TalentDetector

TalentDetector2026_Summer
INTERNATIONAL STUDENTS SCIENTIFIC CONFERENCE

Scientific editor:
Mirosław Bonek

Department of Engineering Materials and Biomaterials,
Faculty of Mechanical Engineering,
Silesian University of Technology
07-09 June 2026
Gliwice, Poland

Katedra Materiałów
Inżynierskich i Biomedycznych

Opiniodawcy
Prof. Eva Tillova – University of Zilina, Slovakia
Prof. Martin Kusy – Slovak University of Technology in Bratislava, Slovakia

Kolegium redakcyjne
REDAKTOR NACZELNY – dr hab. inż. Małgorzata KRÓL, prof. PŚ
REDAKTOR DZIAŁU – dr h.c., dr hab. inż. Mirosław BONEK, prof. PŚ
SEKRETARZ REDAKCJI – mgr Monika MOSZCZYŃSKA-GŁOWACKA

Wydano za zgodą
Rektora Politechniki Śląskiej

Redakcja techniczna i skład komputerowy
dr h.c. dr hab. inż. Mirosław Bonek, prof. PŚ

Materiały są opublikowane na podstawie oryginałów dostarczonych przez autorów, zaopiniowanych przez zespół recenzentów.

Wszystkie opublikowane materiały stanowią utwór, podlegający ochronie na mocy prawa autorskiego. Utwór ten ani w całości, ani we fragmentach nie może być powielany oraz rozpowszechniany za pomocą urządzeń elektronicznych, mechanicznych, kopiujących, nagrywających i innych. Ponadto utwór ten nie może być umieszczany i rozpowszechniany w postaci cyfrowej zarówno w Internecie, jak i w lokalnych sieciach, bez pisemnej zgody właściciela praw autorskich.

Seria wydawnicza
Prace Katedry Materiałów Inżynierskich i Biomedycznych
Wydział Mechaniczny Technologiczny
Politechnika Śląska

ISBN 978-83-68390-68-1

© Copyright by
Wydawnictwo Politechniki Śląskiej
Gliwice 2026

INTERNATIONAL STUDENTS SCIENTIFIC CONFERENCE

TALENTDETECTOR2026_SUMMER

SILESIAN UNIVERSITY OF TECHNOLOGY, GLIWICE, POLAND

07-09 June 2026

The International Student Scientific Conference TalentDetector2026_Summer aims to integrate the student and scientific community dealing with topics related to material technologies. It is a place that gives the opportunity to exchange experiences, knowledge, skills and present current scientific achievements, developing and expanding students' interests in the field of materials engineering, surface engineering, biomaterials and biomedical engineering, nanotechnology, pro-ecological technologies and computer materials science. The conference allows for the presentation of projects conducted with the industry as part of the activities of Student Scientific Circles, doctorates, projects implemented in the form of PBL - Project Based Learning as part of the Excellence Initiative - Research University at the Silesian University of Technology, projects in the framework of EURECA PRO/European University in Responsible Consumption and Production and international bilateral cooperation between Universities.

CONFERENCE ORGANIZER

Materials Science Circle of the Association of Alumni of the Silesian University of Technology, Gliwice, Poland

CONFERENCE CO-ORGANIZER

Department of Engineering Materials and Biomaterials, Faculty of Mechanical Engineering, Silesian University of Technology, Gliwice, Poland

INTERNATIONAL SCIENTIFIC COMMETTEE

prof. Mirosław Bonek dr h.c., Silesian University of Technology, Gliwice, Poland - *President of the International Scientific Commette*

prof. Marcin Adamiak, Silesian University of Technology, Gliwice, Poland
prof. Sedat Alkoy, Gebze Technical University, Gebze, Turkey
prof. Arsen Babajanyan, Yerevan State University, Yerevan, Armenia
prof. Rafał Babilas, Silesian University of Technology, Gliwice, Poland
dr. Dimitrios Diamantis, City University Qatar, Doha, Qatar
dr. Stela Dinescu, University of Petroșani, Petroșani, Romania
prof. Ahmet Durgutlu, Gazi University, Ankara, Turkey
prof. Boris Gitolendia, Georgian Technical University, Tbilisi, Georgia
prof. Afrim Gjelaj, University of Pristina, Pristina, Kosovo
prof. Adam Grajcar, Silesian University of Technology, Gliwice, Poland
prof. Alexander Horn, Laserinstitut Hochschule Mittweida, Mittweida, Germany
prof. Volkan Kılıçlı, Gazi University, Ankara, Turkey
doc. Lenka Kuchariková, University of Zilina, Zilina, Slovakia
prof. Martin Kusy, Slovak Technical University in Bratislava, Trnava, Slovakia
prof. Grzegorz Matula, Silesian University of Technology, Gliwice, Poland
prof. Serhii Matiukh, Khmelnitskyi National University, Khmelnitskyi, Ukraine
prof. Cemal Meran, Pamukkale University, Denizli, Turkey
dr Melody Neaves, Stellenbosch University, Stellenbosch, South Africa
prof. Oleh Polishchuk, Khmelnitskyi National University, Khmelnitskyi, Ukraine
prof. Mykola Skyba, Khmelnitskyi National University, Khmelnitskyi, Ukraine
prof. Tomasz Tański, Silesian University of Technology, Gliwice, Poland
doc. Miroslava Tavodova, Technical University in Zvolen, Zvolen, Slovakia
prof. Eva Tillova, University of Zilina, Zilina, Slovakia
prof. Zheng Zhanguo, SCISE Yanshan University, Qinhuangdao, China
prof. Yao Jing, Yanshan University, Qinhuangdao, China

ORGANIZING COMMETTEE

Chairman
prof. Mirosław Bonek dr h.c.

prof. Rafał Babilas
prof. Klaudiusz Gołombek
prof. Mariusz Krupiński
prof. Sabina Lesz
prof. Małgorzata Musztyfaga-Staszuk
prof. Daniel Pakuła
prof. Marek Sroka
prof. Marcin Staszuk
prof. Agata Śliwa
dr. Katarzyna Cesarz-Andraczke
dr. Aleksandra Drygała
dr. Ewa Jonda
dr. Aneta Kania
dr Monika Kciuk
dr. Anna Kloc-Ptaszna
dr. Marek Kremzer
dr. Mariusz Król
dr. Beata Krupińska
dr. Agnieszka J. Nowak
dr. Magdalena Polok-Rubiniec
dr. Magdalena Szindler
dr. Marek Szindler
dr. Anna Włodarczyk-Fligier
dr. Anna Woźniak

TalentDetector HISTORY

The International Student Scientific Conferences TalentDetector since 2018 have been a place for the exchange of experience, knowledge, skills and presentation of students' current scientific achievements in the field of materials engineering, surface engineering, biomaterials and biomedical engineering. As part of the conference, two international scientific monographs, TalentDetector_Summer and TalentDetector_Winter, are published annually, which already contain over 900 scientific articles resulting from the implementation of PBL, EURECA PRO, Students Scientific Cyrcles projects and projects with secondary school students with international authors. Participation in the form of presentations and posters in TalentDetector International Student Scientific Conferences allows members of the project teams to integrate the student and scientific community of the Silesian University of Technology as well as young staff from foreign research centres in Armenia, Austria, Brazil, China, Czech Republic, Ethiopia, Ghana, Georgia, Iran, Qatar, Romania, Slovakia, South Africa, Ukraine and Turkey, dealing with topics related to materials technologies.
Scientific monographs are prepared based on articles, mostly with international authors, reviewed by an international scientific committee.
The initiative of the cyclical organization of the International Student Scientific Conference TalentDetector significantly expands activities in the field of student education, organizational and popularization activities for the scientific community related to materials engineering at the national and international level.
Thanks to extensive international cooperation, over 310 articles were published free of charge.

Number of cooperating universities: 17

City University Qatar, Doha, Qatar
Federal University of Rio Grande do Sul, Porto Alegre, Brazil
Gazi University, Ankara, Turkey
Gebze Technical University, Gebze, Turkey
Georgian Technical University, Tbilisi, Georgia
Khmelnitskyi National University, Khmelnitskyi, Ukraine
Laserinstitut Hochschule Mittweida, Mittweida, Germany
Pamukkale University, Denizli, Turkey
Silesian University of Technology, Gliwice, Poland
Slovak Technical University in Bratislava, Trnava, Slovakia
Stellenbosch University, Stellenbosch, South Africa
Technical University in Zvolen, Zvolen, Slovakia
University of Petroșani, Petroșani, Romania
University of Pristina, Pristina, Kosovo
University of Zilina, Zilina, Slovakia
Yanshan University, Qinhuangdao, China
Yerevan State University, Yerevan, Armenia

The history of TalentDetector in numbers:

2018
TalentDetector 2018 (Gliwice), 18.11.2018
Number of articles: 59
Number of authors: 206
Number of countries: 1

2021
TalentDetector2021_Winter (Gliwice), 29.01.2021
Number of articles: 37
Number of authors: 134
Number of countries: 2

TalentDetector2021_Summer (Zawiercie), 25.06.2021
Number of articles: 57
Number of authors: 173
Number of countries: 3

2022
TalentDetector2022_Winter (Gliwice), 28.01.2022
Number of articles: 79
Number of authors: 179
Number of countries: 4

TalentDetector2022_Summer (Wisła), 13.06.2022
Number of articles: 79
Number of authors: 176
Number of countries: 4

2023
TalentDetector2023_Winter (Gliwice), 27.01.2023
Number of articles: 73
Number of authors: 143
Number of countries: 6

TalentDetector2023_Summer (Brenna), 26.06.2023
Number of articles: 105
Number of authors: 173
Number of countries: 9

2024
TalentDetector2024_Winter (Gliwice), 29.01.2024
Number of articles: 82
Number of authors: 135
Number of countries: 7

TalentDetector2024_Summer (Gliwice-Zilina), 17.06.2024
Number of articles: 84
Number of authors: 147
Number of countries: 8

2025
TalentDetector2025_Winter (Gliwice), 31.01.2025
Number of articles: 95
Number of authors: 173
Number of countries: 9

TalentDetector2025_Summer (Brenna), 23.06.2025
Number of articles: 87
Number of authors: 143
Number of countries: 10

TalentDetector2025_Yanshan (Gliwice), 26.09.2025
Number of articles: 12
Number of authors: 29
Number of countries: 2

TalentDetector2025_Prom (Gliwice), 20.11.2025
Number of authors: 15
Number of countries: 6

2026
TalentDetector2026_Winter (Gliwice), 09.01.2026
Number of articles: 87
Number of authors: 182
Number of countries: 8

TalentDetector2026_Yanshan (Gliwice), 13.02.2026
Number of authors: 21
Number of countries: 2

TalentDetector2026_Summer (Brenna), 07.06.2026
Number of articles: 102
Number of authors: 137
Number of countries: 10

Contents

The impact of carbon fiber on the reinforcement of motorcycle helmets: differences in fiber arrangement, impact on resistance and abrasion
Mikołaj Adamczyk, Konrad Skorupka, Radosław Byczek, Krzysztof Bizoń 1

Advanced materials and modern steels in the automotive industry – synergy of lightweight design, safety and sustainability
Krystian Adamiec, Filip Derbin, Barbara Grzegorczyk 5

A proprietary expert system supporting the selection of steel grade for bridge elements
Dankhara Akshay, Mohammad Meran Vasseem, Rafał Honysz 12

Production of Biopolymer Blended Sustainable Cable Compounds
Alara Aytekin, Pakize Pinar Erbeyin, Mert Cavus, Cemal Meran, Omer Eren 18

Structure and properties of the TiAlN coating deposited onto a hot-work steel substrate
Piotr Bailner, Kacper Owczarek, Sebastian Zimoląg, Matěj Macák, Filip Škoda, Michal Lattner, Antonin Kříž, Jakub Polis, Marcin Staszuk, Daniel Pakuła 24

Comparative analysis of the microstructure of butt-welded joint variants of S304H steel manufactured from materials before and after service exposure
Wiktoria Borowiec, Zuzanna Zielińska, Marek Sroka 34

Spersonalizowana hybrydowa osłona balistyczna oparta na kompozytach polimerowo-ceramicznych
Szymon Branc, Jakub Niziołek, Paweł Wilk, Edita Illichmanová, Melisa Šnircová, Lenka Kuchariková, Grzegorz Chladek, Klaudiusz Gołombek 40

Simulation of the automation of a selected dye-sensitized solar cell manufacturing process
Jakub Budzynowski, Judyta Drygała, Aleksandra Drygała 46

Analysis of the stress distribution in the rear upper hitch pin of the Ursus C-330 tractor
Jakub Budzynowski, Justyna Janoszka, Agata Śliwa 54

Design And Manufacturing of An Adjustable Air Wipe Nozzle
Emrullah Cangi, Kutay Ates, Huseyin Ali Gok, Cemal Meran, Koksal Ilhan..... 60

Structure and properties of a silicon-based coating deposited onto a hot-work steel substrate
Martyna Ciaś, Alexandra Kuś, Matěj Macák, Filip Škoda, Michal Lattner,
Antonin Kříž, Jakub Polis, Marcin Staszuk, Daniel Pakuła..... 67

Jakościowa identyfikacja mikrowłókien polimerowych uwalnianych podczas modelowego prania odzieży syntetycznej i mieszanej
Marta Cygrimus, Mateusz Szymański, Maksymilian Męcik, Katarzyna Dąbrowska,
Piotr Sakiewicz, Klaudiusz Gołombek 76

Konštrukčný návrh zdvíhacieho mechanizmu do 3,5t pre parkovanie pod zemou
Sebastián Dlugosch, Matúš Vereš, Milan Uhríčik, Mirosław Bonek 88

Comparison of different types of fiducial markers
Maciej Dymkowski, Michał Zientek, Tomasz Kukuczka, Tomasz Moroń..... 96

Condition Monitoring and Fault Diagnosis of Electric Motors in Cable Extrusion Lines
Elber Erkul, Ali Sevgili, Mustafa Arslan Karakaya, Cemal Meran, Fatih Oztekin 104

Development of Antibacterial Hybrid Coatings on Titanium Implants Using Plasma Electrolytic Oxidation: A Conference Review
Sichale W. Fita, Mirosław Bonek , Sebastian Sławski, Anna Woźniak 111

Analysis of the Protective Properties of Wax and Ceramic Coatings Applied to Automotive Paints – Stage II: Testing Under Real Operating Conditions
Marta Fizia, Max Ignacy, Daniel Bujara, Maciej Nogieć, Mateusz Sadowski,
Marek Kremzer, Rafał Duda 119

Structural aspects of laser surface remelting of modern steels using material databases
Marek Flak, Mirosław Bonek 127

Structural aspect of laser surface remelting of modern steels using microprocessor systems and microcontroller programming
Marek Flak, Mirosław Bonek 133

Biomaterials for implantology applications
Martyna Gawlas, Marcin Majnusz, Aneta Kania..... 138

Historia szelaku w przemyśle fonograficznym
Wiktoria Groelich, Jan Grzybicki, Bogusław Ziębowicz, Anna Ziębowicz 143

Visualizing the Invisible: Real-Time Instruction Tracing for Computer Architecture Education
Mateusz Grzanka, Maciej Guja, Jan Jezierski, Bartosz Malich, Patrycja Nessing, Adam Wolany, Aleksander Żak, Jarosław Paduch 150

Application of 3D scanner as an engineering tool during the design and construction of a C-class yacht
Karol Hachuła, Jakub Ciupka, Habiba Abdelhakiem, Beniamin Kurcoń, Jakub Nabiałek, Eryk Olszówka, Jakub Michalak, Antonio J. Paleo, Mariem Messaada, Zakia Aribou, Najoia Aribou, Marcin Bilewicz 157

Electrochemical Methods for Hydrogen Detection in Steels: Comparison of the Barnacle Cell and the Devanathan–Stachurski Permeation Cell
Branislav Hajas, Denisa Straková, František Nový, Mirosław Bonek 163

Simulation studies of the diffusion bonding process of dissimilar materials using the Gleeble 3800 simulator
Dawid Hoim, Kamil Czajkowski, Filip Szyguła, Stanisław Mendrek, Wiktor Wnuk, Wojciech Borek, Saad Ebied 171

Numerical analysis of plate implants for spinal fusion using different types of materials
Monika Honisz, Agata Śliwa 176

Analýza štrukturálnych zmien v austenitických oceliach vplyvom únavového poškodenia
Edita Illichmanová, Milan Uhríčik, Melisa Šnircová, Peter Palček, Klaudiusz Gołombek 186

Corrosion Phenomena in Structural Steels: Mechanisms, Influencing Factors and Anticorrosion Protection Methods
Alicja Jankiewicz, Emilia Komendarczyk, Kamila Krus, Mirosław Bonek 194

The review of regulatory changes regarding the introduction of construction products to the European Union market – the perspective of producers and work on new products
Ewelina Kaputa-Kuc, Elżbieta Nawrot- Sadłoń, Ewa Jonda 202

Mechanical properties and corrosion resistance of Ti6Al4V alloy
Norbert Klęk, Marek Opiela, Monika Kciuk 209

Sinterhardening of PM Cr-Mo prealloyed steels with hybrid alloying powders
Dmitriy Koblik, Miroslava Ťavodová, Richard Hnilica 217

The effect of heat treatment on the structure and corrosion resistance of X2CrNiMoN22-5-3 steel
Bartosz Kowalski, Monika Kciuk 228

Laser Surface Textured Mg and Ti Alloys for Enhanced Performance
Milan Kozik , Mikołaj Grabowski, Monika Kraszewska, Hanna Kostyrko, Gabriela Suchańska, William Vincent Appiah, Edwinner Ohema Animuonyam Ayitey, Magdalena Wyszyńska, David Sasu Konadu, Benjamin Agyei-Tuffour, Guadelupe Carrillo, Monika Nitsze-Wierzba, Grzegorz Chladek, Augustine Appiah, Marcin Adamiak..... 232

Implementation of a Smart Aquarium Using IoT Technology
Magdalena Koźlik, Kamil Kołodziej, Kacper Strukowski, Marcin Jaroszek , Karol Tlałka, Maurycy Frydecki, Mariusz Król..... 238

Mechanical Properties of LPBF Tool Steels after Heat Treatment
Mariusz Król, Juraj Beniak..... 246

Properties and structure of Cu-Cr alloys used in electrical engineering
Beata Krupińska, Maciej Marcinkowski..... 252

Struktura, skład fazowy oraz właściwości mechaniczne i tribologiczne jedno- i dwuwarstwowych powłok na bazie węglika wolframu natryskiwanych płomieniowo
Waldemar Kwaśny, Wojciech Kała, Bartłomiej Kazek, Szymon Wyrwa, Amelia Siemińska, Rafał Łosoń, Grzegorz Sikorski, Oliwier Koprowski, Magdalena Mazur, Patryk Stelmach..... 259

Geochemical differentiation of pyrite from Spanish and Romanian deposits
Kinga Kwiecień, Katarzyna Bloch, Jacek Nowak..... 269

Sustainable fabrication of porous ceramics from glass cullet, slag and fly ash
Lew Lewandowski, Mikołaj Łysień, Emilia Jackow, Jakub Niziołek, Paweł Wilk, Marek Kremzer, Błażej Tomiczek..... 277

Microstructural and chemical study of the antibacterial TiAgN coating
Paulina Lukaszkowicz, Tiara Ogórek, Ewa Adamek, Wojciech Baran, Jozef Sondor, Krzysztof Lukaszkowicz, Klaudiusz Gołombek, Krzysztof Matus, Paweł Nuckowski..... 285

Modeling the level of happiness in the world using machine learning methods and multidimensional data analysis
Aleksandra Mikuła, Mirosław Bonek..... 289

Analysis of dimensional accuracy and surface roughness in additive manufacturing processes
Besart Misini, Afrim Gjelaj, Tomasz Tanski, Brytan Zbigniew, Besart Berisha, Kaltrinë Jakupi, Mehmet Zeqiraj..... 297

Infiltration Processing of Ceramic Fiber-Reinforced AlSi12 Matrix Composites
Jakub Niziołek, Paweł Wilk, Emilia Jackow, Lew Lewandowski,
Mikołaj Łysień, Anna Tomiczek, Klaudiusz Gołombek 304

Powłoki konwersyjne chromianowe
Nadia Nocoń, Wiktoria Ledwig, Jakub Nowak, Tobiasz Wypchol, Bartosz Gonciarz,
Amelia Krupińska, Agnieszka Zaleska, Mariusz Krupiński 312

Powłoki konwersyjne chromianowe stosowane na elementach ze stopów aluminium
Nadia Nocoń, Jakub Nowak, Tobiasz Wypchol, Wiktoria Ledwig, Bartosz Gonciarz,
Amelia, Krupińska, Agnieszka Zaleska, Marcin Staszuk, Mariusz Krupiński 317

Modernization of the sheet metal cutting process
Piotr Nogły, Aneta Kania, Magdalena Polok-Rubiniec, Anna Włodarczyk-Fligier 324

Topological optimization of a structural component with consideration of structural analysis
Karolina Nowak, Julia Wawrzynek, Agata Śliwa 329

Microstructural and chemical characterisation of biochar derived from plant-based waste materials
Tiara Ogórek, Paulina Lukaszkowicz, Ewa Adamek, Wojciech Baran,
Krzysztof Lukaszkowicz, Klaudiusz Gołombek 337

Modeling and optimization of geometric parameters of a chopping knife for wood chopping
Daniel Pella, Filip Bejm, Milen Pawlas, Joanna Tokarz, Adam Zygłowicz, Jakub Polis,
Agata Śliwa, Marek Sroka, Jan Komendák, Samuel Zachar, Miroslava Tavodova 342

Design of the electrode positioning system and selection of the power supply for a laboratory arc furnace
Łukasz Piecha, Maurycy Frydecki, Mateusz Konsek, Patryk Sobota, Mateusz Liszka,
Mariusz Król, Vojtěch Macejko, Řezníček Daniel 353

Printed auxetic materials
Jakub Pluskota, Anna Kloc-Ptaszna 358

Occupational health and safety at a laboratory workstation for electrochemical coating deposition
Michał Podgórski, Monika Spilka 365

Engineering solutions for the filament cooling system during its production on an extrusion machine
Andrii Polishchuk, Mirosław Bonek, Oleh Polishchuk, Serhii Matiukh,
Svitlana Lisevich, Serhii Bobuch 371

Filllers in polymers composites
Magdalena Polok-Rubiniec 377

High-energy cutting methods in modern manufacturing technologies
Katarzyna Ptasznik, Jan Wypiór, Piotr Herian, Natalia Rupala, Bartosz Dziki, Mirosław Bonek, Oleh Polishchuk 383

A Miniaturized Telemetry and Avionics System for Model Rockets
Igor Puchała, Wiktor Bujak, Maja Rudnicka, Kamil Moszumański, Michał Lasak 389

The influence of varying illumination conditions on the performance of solar cells
Stanisław Rasiński, Marcin Mrugała, Oskar Stelmach, Michał Szczęsny, Marcin Szumski, Yurii Humeniuk, Oleksandr Maliarchuk, Judyta Drygała, Janusz Wyrwał, Oleh Polishchuk, Andrii Polishchuk, Sabina Lesz, Aleksandra Drygała 396

Thin films of zinc oxide doped with aluminum produced by the sol-gel method
Jakub Rusinek, Martyna Pasieka, Karolina Kornecka, Michalina Ziółkowska, Magdalena Szindler, Marek Szindler, Grzegorz J. Nowak 404

Defining a Suitable Wind Tunnel Design
Jovani Samir Sabri, Givi Sanadze 411

Assessment of the Degradation Process of a ZnMg1.2 wt% Alloy with a ZnO Coating for Biomedical Applications
Mateusz Słonka, Igor Szymiczek, Zofia Wolska, Aleksandra Wierzbicka, Martyna Rzepiela, Jakub Wierciński, Magdalena Skonieczna, Katarzyna Cesarz-Andraczke, Mateusz Smolarz, Marcin Staszuk 418

Structural characterization of Zn–Mg alloys and development of a decision support tool for material selection
Mateusz Słonka, Igor Szymiczek, Zofia Wolska, Aleksandra Wierzbicka, Martyna Rzepiela, Gabriel Sroka, Jakub Wierciński, Magdalena Skonieczna, Katarzyna Cesarz-Andraczke, Mateusz Smolarz, Marcin Staszuk 425

Geopolymer construction mortars prepared from waste materials. Laboratory tests
Barbara Słomka-Słupik, Tomasz Jaśniok, Hanna Kaźmierczak, Krystyna Skulimowska, Kuba Szlachta 432

Sequestration capacity of RCP: powder fraction of recycled concrete, in relation to CO_2. Calcium looping method
Słomka-Słupik Barbara, Małgorzata Labus, Jakub Piasecki, Nicole Kocierz, Anna Słupik, Kacper Popielarczyk, Paulina Wiśniewska, Kuba Szlachta 438

Properties of building mortars with recycled concrete as a partial replacement for natural sand
Słomka-Słupik Barbara, Dalibor Matýsek, Sylwia Antończyk, Maja Maciaszek, Kuba Szlachta, Kacper Popielarczyk 445

Possibilities for improving the application of magnesium alloys in biomedical engineering through the formation of surface treatments
Melisa Šnircová, Peter Palček, Katarína Marušincová, Martin Slezák, Edita Illichmanová 452

Impact of External Factors on the Durability of Screen-Printed Metallic Interconnections
Jacek Sopala, Jakub Janus, Julian Marszałek, Martyna Pasieka, Karolina Kornecka, Magdalena Szindler, Marek Szindler, Wojciech Sitek, Marko Kršulja, Lovro Liverić 461

Understanding Primary and Secondary Aluminium Alloys: Production, Microstructure, and Properties
Zuzana Straková, Eva Tillová, Lenka Kuchariková, Milan Uhríčik, Mária Chalupová 468

Surface modification of materials manufactured by SLM for implantology
Kamil Szewczulak, Marek Machura, Wojciech Hytry, Zofia Kozak, Magdalena Szindler, Mariusz Król, Marek Szindler, Wojciech Sitek, Lovro Liverić, Marko Kršulja 476

An Example of Applying a Genetic Algorithm for the Identification of Steel Chemical Composition with Required Phase Transformation Temperatures
Jacek Trzaska, Sabina Lesz, Dominika Gajczowska 482

Optymalizacja procesów recyklingu odpadów poprodukcyjnych technologii druku 3D na przykładzie materiału PLA
Klaudia Twardzik, Dominika Zajdel, Natalia Nowrot, Mirosław Bonek 490

Aplikácia multiaxiálnych únavových kritérií pri hodnotení nízkocyklovej a vysokocyklovej únavy konštrukčných materiálov
Milan Uhríčik, Veronika Chvalníková, Edita Illichmanová, Melisa Šnircová, Zuzana Straková, Martin Slezák, Mirosław Bonek 495

Structural aspect of laser surface remelting
Martyna Urbańska, Kinga Stępska, Marek Flak, Felicjan Glenc, Piotr Konieczny, Mirosław Bonek, Eva Tillová 504

Design and Development of an Experimental Setup for Leak Tightness Testing of FDM Prints
Julia Wawrzynek, Wojciech Tokarz, Łukasz Połap, Mikołaj Jędrzejek, Mikołaj Figołuszka, Marek Kremzer, Błażej Tomiczek 511

Leak Tightness Optimization of PETG and TPU 3D Prints Through Printing Parameter Selection
Julia Wawrzynek, Wojciech Tokarz, Łukasz Połap, Mikołaj Jędrzejek, Mikołaj Figołuszka, Marek Kremzer, Błażej Tomiczek 519

Polymer composites with natural fillers as an alternative to traditional materials
Anna Włodarczyk-Fligier 528

Design of the Main Structure for a Self-Lifting Crane in Wind Power Operation and Maintenance
Shengkai Yang, Jing Wang, BoRui Zhang 533

Principles for placing pressure equipment on the market in accordance with Pressure Equipment Directive 2014/68/EU, with particular emphasis on welding processes and the role of the Notified Body
Leszek Zadroga, Tomasz Pfeifer, Artur Czupryński 541

Probabilistic Modeling and Monte Carlo Simulation of Defect Formation in Laser Powder Bed Fusion
Zeshi Zou 548

The design of a complex manipulator manufactured using 3D printing technology
Karol Żyrek, Maja Rudnicka, Kamil Moszumański, Michał Lasak 555

TalentDetector

7th-9th June 2026
Gliwice-Brenna, Poland

DEPARTMENT OF ENGINEERING MATERIALS AND BIOMATERIALS
FACULTY OF MECHANICAL ENGINEERING
SILESIAN UNIVERSITY OF TECHNOLOGY

INTERNATIONAL STUDENTS SCIENTIFIC CONFERENCE

The impact of carbon fiber on the reinforcement of motorcycle helmets: differences in fiber arrangement, impact on resistance and abrasion

Mikołaj Adamczyk, Konrad Skorupka, Radosław Byczek, Krzysztof Bizoń,

a Silesian University of Technology, Faculty of Mechanical Engineering, Department of Engineering Materials and Biomaterials
email: ks322976@student.polsl.pl

Abstract: The aim of this article is to analyze how the arrangement of carbon fibers in a composite affects the durability of motorcycle helmets. In particular, how different layer configurations affect impact and abrasion resistance, as these are key aspects related to user safety.
In this article, we will focus primarily on the helmet's outer shell, the part directly responsible for load transfer and head protection.

Keywords: motorcycle helmets, carbon fiber, composites, anisotropy, safety

1. INTRODUCTION

Carbon fiber motorcycle helmets are highly regarded in the world of motorsports due to their excellent strength-to-weight ratio. However, it's important to remember that the material itself is only one element determining the final product quality. Carbon fiber-reinforced polymer composites
are characterized by strong anisotropy, meaning their physical and mechanical properties are closely dependent on the direction of forces. Therefore, a key engineering aspect in the production of a safe helmet is the proper, directional arrangement of the fiber layers during shell formation.

1.1. Main Material

Carbon Fiber is a lightweight, extremely strong material made of very thin strands of carbon atoms bonded together in a crystalline structure.
It is known for its high strength-to-weight ratio, meaning it is much stronger and stiffer than many metals, but much lighter. It also has excellent resistance to corrosion, fatigue, and high temperatures.

1.2 Carbon fiber itself is made mostly of thin strands of carbon atoms, but in most carbon fiber composites these fibers are embedded in a special resin matrix. The resin plays a very important role because it binds the fibers together, protects them from damage, and transfers loads between the fibers. The matrix serves three critical functions: it binds the individual fabric layers, protects the fibers from external environmental factors, and, most importantly, facilitates stress transfer between broken or loaded fibers.

2. STRUCTURE AND PROPERTIES OF CARBON COMPOSITES

Carbon fiber has exceptional tensile strength along its axis, but can be much more susceptible to damage under shear or transverse loads.

2.1. Fiber Orientation in Space:

To compensate for susceptibility to forces acting from different directions (typical of motorcycle accidents), helmet manufacturers never use a single, unidirectional layer of material. Instead, advanced techniques are employed, arranging successive sheets of fabric at various angles (e.g., 0°, 90°, 45°, -45°). This technique creates a quasi-isotropic structure that effectively resists impacts from any direction, creating armor.

3. INFLUENCE OF FIBER LAYOUT ON ENERGY ABSORPTION

The main function of the helmet's outer shell is to disperse the force of an impact over the largest possible surface area before the destructive energy reaches the inner absorbing layer of EPS (expanded polystyrene).

3.1. Composite Destruction Mechanisms

Upon a severe impact, a carbon fiber helmet does not undergo plastic deformation in the same way as its cheaper polycarbonate counterparts. Energy absorption occurs through controlled structural damage:

• delamination of individual material layers arranged at different angles.
• fracture of the binder (resin matrix) in which the fibers are embedded.
• tear of the carbon fibers themselves.

By crossing and modifying the weaves (e.g., the twill weave popular in helmets), any cracks that develop are effectively suppressed and retained in subsequent, differently oriented layers. This prevents the entire shell from brittle cracking and drastically reduces the risk of it puncturing completely.

3.2. The influence of fiber arrangement on the absorption of impact force

The orientation of carbon fibers has a major influence on how a composite material absorbs energy during an impact. Carbon fiber composites are anisotropic materials, which means their mechanical properties depend on the direction of the fibers. When the fibers are aligned in one direction, the material becomes very strong and stiff along that axis, but it may be less resistant to impacts coming from other directions. In this case, the impact energy is transferred mainly along the fibers, which can lead to cracking or delamination if the load exceeds the material’s

limits. This type of layup allows the material to dissipate energy more effectively during a collision. The resin matrix also contributes to impact behavior. During impact, the resin can crack or deform, while the fibers may break or separate between layers. These damage mechanisms consume energy and help reduce the force transmitted through the structure.

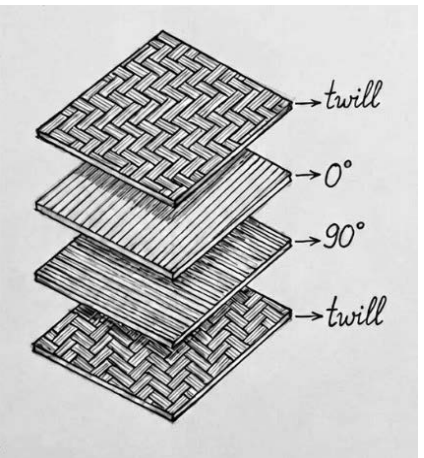

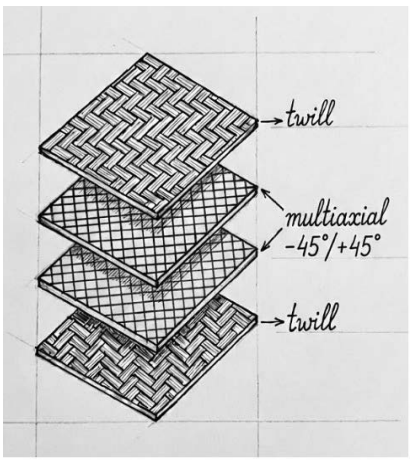

4. SAFETY AND CERTIFICATION

Helmets must meet strict certification standards:

- ECE 22.06 (Europe)
- DOT FMVSS 218 (USA)

Motorcycle-related accidents remain a significant cause of injury and mortality worldwide. According to the World Health Organization (WHO, 2023), wearing a helmet can reduce the risk of death by up to 42% and head injury by 69%. As a result, continuous improvements in helmet technology are critical.

5. WEIGHT REDUCTION

One of the most important benefits is low weight. Carbon helmets can be up to 20–30% lighter than thermoplastic alternatives.
Impact on riders:

- reduced neck strain
- improved comfort during long rides
- better control at high speeds

6. UV DEGRADATION AND STRUCTURAL PROTECTION METHODS

Despite their legendary strength, carbon composites have an "Achilles' heel" in their sensitivity to ultraviolet (UV) radiation. Prolonged exposure to sunlight initiates photo-oxidation within the polymer matrix, leading to the breaking of chemical bonds in the resin. This results not only in aesthetic loss (yellowing, dulling) but, more importantly, in increased shell brittleness. A

degraded matrix ceases to act as a resilient connector; during an impact, this can lead to catastrophic cracking instead of safe energy dissipation.

To mitigate this risk, premium helmet engineering employs multi-level protection:

- Chemical stabilizers: UV absorbers and HALS (Hindered Amine Light Stabilizers) are added to the epoxy resin during production to neutralize free radicals caused by solar energy.
- UV-Filtering Coatings**:** The most effective barrier is an external clear coat enriched with UV-blocking particles. This is crucial for "clear carbon" helmets where the weave is visible.
- User Maintenance**:** From a safety perspective, storing the helmet in a shaded area (bag or locker) when not in use is essential. Due to the irreversible aging of polymers, experts and safety standards (such as ECE 22.06) suggest replacing a carbon helmet every 5–7 years, even without visible damage, to ensure the matrix maintains its critical load-transfer capabilities.

SUMMARY

The exceptional properties of carbon helmets stem not only from the use of a prestigious base material, but primarily from the precise engineering of its formation. The specific arrangement and orientation of the carbon fibers determines how effectively the shell absorbs and dissipates energy in a crash. The correct composite layout guarantees maximum head protection while simultaneously reducing the helmet's weight, which translates into reduced stress on the rider's cervical spine.

BIBLIOGRAPHY

1. https://exatec.pl/myslisz-ze-kazda-plyta-z-wlokna-weglowego-jest-taka-sama-sprawdz-dlaczego-uklad-wlokien-ma-znaczenie/?srsltid=AfmBOooBHhaNmNFGOtEuFi12YQHlvlbgiNE7LSqBPY9yXtmnnht9SihR
2. „Materiały inżynierskie z podstawami technologii procesów materiałowych” Leszek A. Dobrzański
3. „Carbon Fibers: Formation, Structure, and Properties” – Leighton H. Peebles
4. „Kompozyty i techniki ich wytwarzania” – Anna Boczkowska, Grzegorz Krzesiński
5. World Health Organization. (2023). Global status report on road safety .
6. What is Carbon Fiber? Key Properties and Applications Explained
7. https://www.sciencedirect.com/science/article/abs/pii/S1359835X2500034X

TalentDetector

7th-9th June 2026
Gliwice-Brenna, Poland

DEPARTMENT OF ENGINEERING MATERIALS AND BIOMATERIALS
FACULTY OF MECHANICAL ENGINEERING
SILESIAN UNIVERSITY OF TECHNOLOGY

INTERNATIONAL STUDENTS SCIENTIFIC CONFERENCE

Advanced materials and modern steels in the automotive industry – synergy of lightweight design, safety and sustainability

Krystian Adamiec[a], Filip Derbin[a], Barbara Grzegorczyk[b]

[a] Student of the Mechanical and Automotive School Complex in Zabrze
[b] Silesian University of Technology, Faculty of Mechanical Engineering, Department of Engineering Materials and Biomaterials, email: barbara.grzegorczyk@polsl.pl

Abstract: The modern automotive industry faces numerous challenges related to the selection of materials that must be characterized by strength, lightness, affordability and environmental friendliness at the same time. Among the various materials used in car production, steel plays a particularly important role, which still dominates as a raw material used in the construction of car bodies, chassis and many other vehicle components. Increasingly high demands on fuel economy, safety and environmental protection mean that steel must meet increasingly stringent standards and specifications. This article presents the basic characteristics of selected steels used for car body construction elements.

Keywords: materials, steels, automotive industry, AHSS (Advanced High-Strength Steel), UHSS (Ultra High Strength Steel)

1. INTRODUCTION

The automotive industry is currently undergoing a profound transformation driven by global challenges related to environmental protection, energy efficiency, and passenger safety. Increasingly stringent regulations concerning carbon dioxide emissions, combined with the rapid development of electric and autonomous vehicles, are forcing manufacturers to rethink traditional design approaches. In this context, the selection and engineering of materials play a critical role in determining the performance, durability, and sustainability of modern vehicles. One of the key objectives in automotive design is weight reduction, commonly referred to as lightweighting. Lower vehicle mass directly translates into reduced fuel consumption in conventional vehicles and extended driving range in electric vehicles. However, this must be achieved without compromising crashworthiness or structural integrity. Historically, steel has been the primary material used in automotive construction due to its excellent balance of strength, formability, availability, and cost-effectiveness. Over time, advancements in metallurgy have led to the development of advanced high-strength steels (AHSS), enabling thinner and stronger structures. At the same time, alternative materials such as aluminum, magnesium, and titanium alloys are increasingly used. This has led to the concept of multi-material design, where different materials are combined to optimize performance. The concept

of multi-material design and the synergy between lightweight structures, safety, and sustainability is schematically illustrated in Fig. 1 [1–4].

Figure 1. Application of advanced materials in modern automotive structures illustrating the synergy between lightweight design, safety, and sustainability

2. MATERIALS USED IN THE AUTOMOTIVE INDUSTRY

2.1 Steel and its evolution

Steel remains the most important structural material in the automotive industry due to its versatility and continuous development. Initially, automotive bodies were made from low-carbon steels characterized by good formability but relatively low strength. These materials were sufficient for early vehicles but became inadequate as safety requirements increased. The development of High-Strength Steels (HSS) marked the first major step forward. These steels offered improved strength through alloying and controlled rolling processes. However, the real breakthrough came with the introduction of Advanced High-Strength Steels (AHSS), which utilize complex multiphase microstructures. AHSS steels include Dual Phase (DP), Transformation-Induced Plasticity (TRIP), Complex Phase (CP), and martensitic steels. These materials combine high strength with good ductility due to the presence of soft and hard phases within the microstructure. For example, DP steels consist of a ferritic matrix with martensitic islands, providing a favorable balance between strength and formability. Third-generation AHSS steels, such as medium-manganese steels and Q&P (Quenching and Partitioning) steels, represent the latest advancement. These steels aim to bridge the gap between first- and second-generation AHSS by combining high strength, ductility, and reduced alloying costs. Medium-Mn steels, typically containing 3–12% Mn, stabilize retained austenite and exhibit excellent mechanical properties due to the TRIP effect. Microstructure plays a key role in determining

steel properties. Ferrite provides ductility, martensite contributes to strength, bainite offers a compromise between strength and toughness, and retained austenite enhances ductility through phase transformation during deformation. Controlling these phases allows engineers to tailor steel properties for specific applications. In modern vehicles, AHSS and UHSS steels are used in critical components such as A- and B-pillars, crash boxes, and reinforcement beams. Their ability to absorb energy during impact significantly improves passenger safety. Modern cars are constructed from various types of steel appropriately selected for the individual construction elements of the car (Fig. 2) [5–7]

Figure 2. The use of steel in the body construction

2.2 Aluminum alloys

Aluminum alloys are widely used in automotive applications due to their low density and good corrosion resistance. Compared to steel, aluminum is approximately three times lighter, making it an ideal material for reducing vehicle weight. Aluminum alloys used in automotive applications are typically divided into several groups based on their chemical composition. Al–Mg alloys offer excellent corrosion resistance, while Al–Mg–Si alloys provide a good combination of strength and formability. High-strength Al–Zn–Mg alloys can achieve mechanical properties comparable to steel. The use of aluminum significantly contributes to fuel efficiency and emission reduction. For example, replacing steel body panels with aluminum can reduce vehicle weight by several hundred kilograms. This is particularly important for electric vehicles, where weight directly affects battery range. Aluminum is commonly used in body panels, engine components, and structural elements. Modern vehicles such as the Audi A8 and Ford F-150 extensively utilize aluminum in their construction. Despite its advantages, aluminum has limitations, including lower modulus of elasticity and higher cost compared to steel. Additionally, joining aluminum components requires specialized techniques such as adhesive bonding or riveting [8,9].

2.3 Titanium alloys

Titanium alloys offer an exceptional combination of high strength, low density, and corrosion resistance. Their strength-to-weight ratio is among the highest of all structural materials. In automotive applications, titanium alloys are primarily used in high-performance and specialized components. Titanium components can significantly reduce weight while

maintaining excellent mechanical performance. One of the main advantages of titanium alloys is their ability to operate at high temperatures without losing strength. This makes them particularly suitable for exhaust systems and engine components. However, the widespread use of titanium in the automotive industry is limited by its high cost and difficult processing. As a result, titanium is mainly used in luxury and sports cars rather than mass-produced vehicles - Figure 3 [10,11].

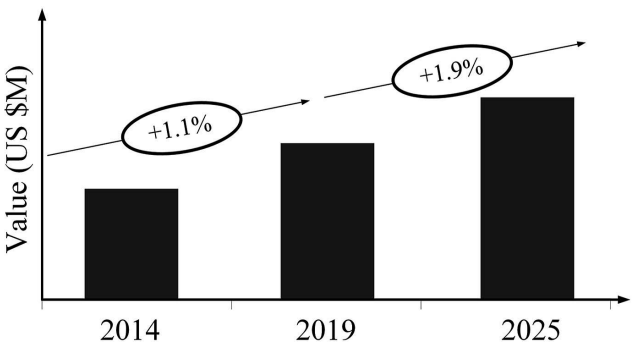

Figure 3. Representation of growth of Ti value in the global automotive market [11].

2.4 Magnesium alloys

Magnesium alloys are the lightest structural metals used in engineering applications. Their density is approximately 75% lower than that of steel, making them highly attractive for lightweight design. Magnesium alloys are commonly used in components such as gearbox housings, steering wheels, and seat frames. Their high strength-to-weight ratio allows for significant mass reduction. However, magnesium alloys present several challenges. Their hexagonal crystal structure limits formability at room temperature, requiring elevated temperatures for forming processes. Additionally, issues such as corrosion resistance and flammability must be carefully addressed. Ongoing research focuses on improving the properties of magnesium alloys and developing new processing techniques to expand their applications in the automotive industry - Figure 4. [12,13].

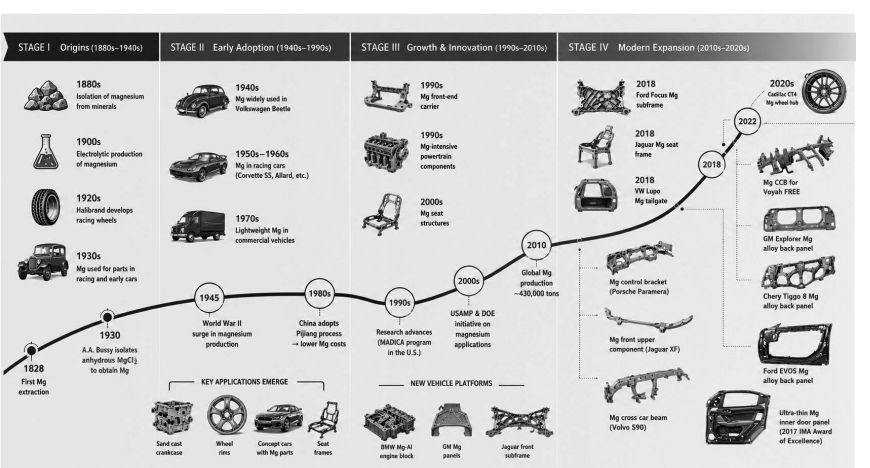

Figure 4. Progression of Magnesium Alloy Technologies for Lightweight Vehicle Design [13]

3. MULTI-MATERIAL DESIGN AND MANUFACTURING TECHNOLOGIES

Modern automotive engineering increasingly relies on multi-material design strategies. Instead of using a single material, engineers combine different materials to optimize the performance of each component. For example, high-strength steels are used in safety-critical areas, while aluminum and magnesium alloys are applied in components where weight reduction is crucial. This approach allows for significant improvements in overall vehicle performance. Advanced manufacturing technologies (Figure 5.) play a key role in enabling multi-material structures. Hot stamping allows for the production of ultra-high-strength steel components with complex geometries. Additive manufacturing enables the creation of lightweight and customized parts. Joining techniques are also evolving to accommodate different materials. Methods such as laser welding, friction stir welding, and adhesive bonding are used to join dissimilar materials [14,15,16].

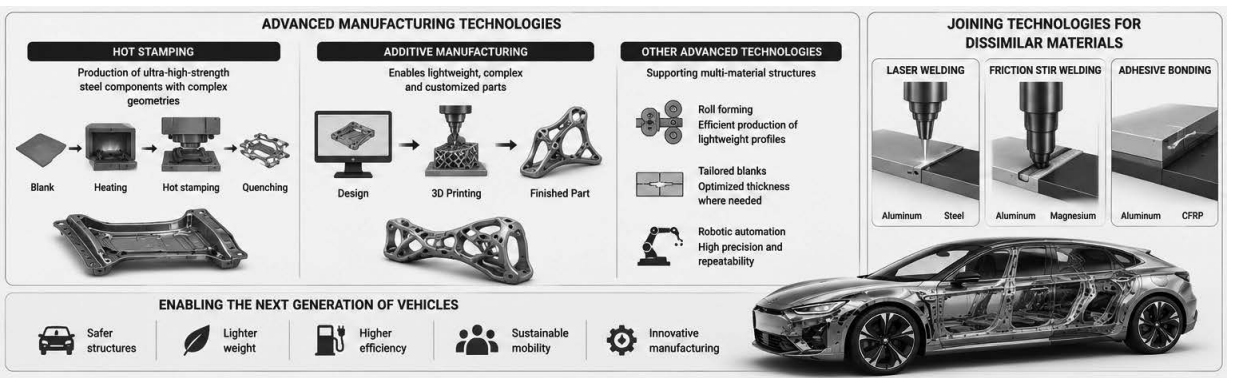

Figure 5. Concept of multi-material vehicle design and advanced manufacturing technologies used in modern automotive engineering

4. CHALLENGES AND FUTURE DIRECTIONS

The automotive industry faces numerous challenges related to materials engineering. These include reducing emissions, improving energy efficiency, and meeting increasing safety requirements. The transition to electric vehicles introduces new challenges, such as the need for lightweight battery enclosures and improved thermal management systems. Materials must also be compatible with advanced electronic systems and sensors. Future developments in materials science will focus on creating materials with improved performance and sustainability. This includes the development of smart materials, advanced composites, and recyclable materials. Steel will continue to play a dominant role due to its cost-effectiveness and recyclability. However, its properties will be further enhanced through advanced processing techniques and alloy design. Another important challenge is the reduction of the environmental impact associated with material production and vehicle manufacturing processes. Automotive companies are increasingly investing in circular economy strategies, including material recycling, remanufacturing, and the reuse of production waste. In the future, artificial intelligence and digital engineering tools will support the optimization of material selection, component design, and manufacturing efficiency. Furthermore, the integration of lightweight multi-material structures will become essential for achieving higher vehicle performance, lower

energy consumption, and improved sustainability in next-generation transportation systems. Figure 6. [16,17].

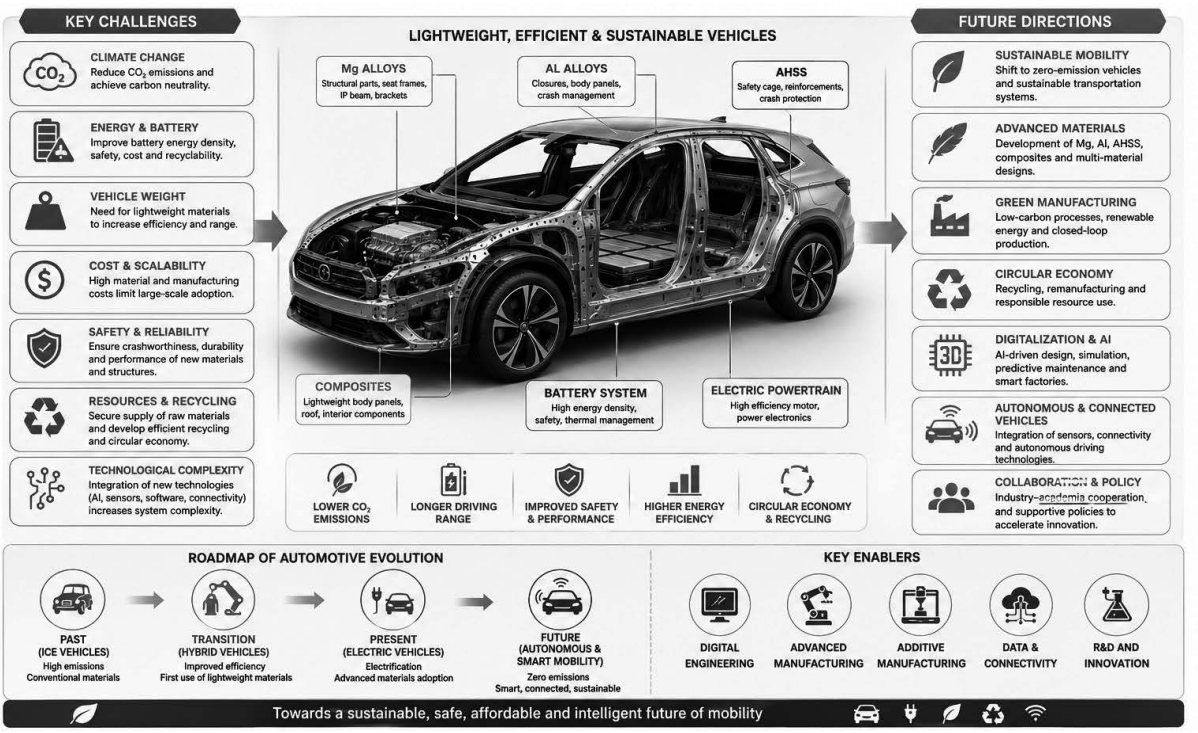

Figure 6. Future challenges and development trends in sustainable automotive engineering.

5. SUMARRY

The automotive industry is undergoing rapid transformation driven by technological advancements and environmental requirements. Material selection plays a critical role in achieving lightweight, safe, and sustainable vehicle designs.

Steel, particularly in the form of AHSS, remains the backbone of automotive construction. At the same time, lightweight materials such as aluminum, magnesium, and titanium alloys are becoming increasingly important.

The future of automotive materials lies in the integration of multiple materials and advanced manufacturing technologies, enabling the development of next-generation vehicles.

BIBLIOGRAPHY

1. A. Candela, G. Sandrini, M. Gadola, D. Chindamo, P. Magri, Lightweighting in the automotive industry as a measure for energy efficiency: Review of the main materials and methods, Heliyon 10 (2024) e29728. doi:10.1016/j.heliyon.2024.e29728.
2. S. Yao, H. Zhu, S. Zhang, H. Chang, H. Wang, Green steel: The future path towards sustainable automotive manufacturing, Resources, Conservation and Recycling 200 (2024) 107319. doi:10.1016/j.resconrec.2023.107319.

3. L. Yan, H. Xu, Lightweight composite materials in automotive engineering: State-of-the-art and future trends, Alexandria Engineering Journal 118 (2025) 1–10. doi:10.1016/j.aej.2024.12.002.
4. A.M. Sherman, A. Krause, P. Friedman, D.Q. Huston, Automotive body materials, in: Encyclopedia of Materials: Science and Technology, Elsevier, (2001) 415–421.
5. A. Grajcar, R. Kuziak, W. Zalecki, Third generation of AHSS with increased fraction of retained austenite for the automotive industry, Archives of Civil and Mechanical Engineering 12 (2012) 334–341. doi:10.1016/j.acme.2012.06.011.
6. K. Notomi, T. Shioura, New stainless steel for cutlery applications, Metal Powder Report 53 (1998) 34. doi:10.1016/S0026-0657(98)80326-3.
7. O. Grässel, L. Krüger, G. Frommeyer, L.W. Meyer, High strength Fe–Mn–(Al, Si) TRIP/TWIP steels development — properties — application, International Journal of Plasticity 16 (2000) 1391–1409. doi:10.1016/S0749-6419(00)00015-2.
8. Innovative Lightweight and High-Strength Alloys, Elsevier, 2024.
9. J. Hirsch, T. Al-Samman, Superior light metals by texture engineering: Optimized aluminum and magnesium alloys for automotive applications, Acta Materialia 61 (2013) 818–843. doi:10.1016/j.actamat.2012.10.044.
10. P. Nyamekye, S. Rahimpour Golroudbary, H. Piili, P. Luukka, A. Kraslawski, Impact of additive manufacturing on titanium supply chain: Case of titanium alloys in automotive and aerospace industries, Advances in Industrial and Manufacturing Engineering 6 (2023) 100112. doi:10.1016/j.aime.2023.100112.
11. Lucintel, Titanium in the Global Automotive Market Report: Trends, Forecast and Competitive Analysis, 2020.
12. V. Balaji, V.K. Bupesh Raja, K. Palanikumar, Ponshanmugakumar, N. Aditya, V. Rohit, Effect of heat treatment on magnesium alloys used in automotive industry: A review, Materials Today: Proceedings 46 (2021) 3769–3771. doi:10.1016/j.matpr.2021.02.017.
13. B. Liu, J. Yang, X. Zhang, Q. Yang, J. Zhang, X. Li, Development and application of magnesium alloy parts for automotive OEMs: A review, Journal of Magnesium and Alloys 11 (2023) 15–47. doi:10.1016/j.jma.2022.12.015.
14. F. Khan, N. Hossain, J.J. Mim, S.M. Rahman, Md.J. Iqbal, M. Billah, M.A. Chowdhury, Advances of composite materials in automobile applications – A review, Journal of Engineering Research 13 (2025) 1001–1023. doi:10.1016/j.jer.2024.02.017.
15. H. Mi, L. Li, F. Liu, Z. Liu, N. Li, C. Zhang, J. Ma, C. Wang, B. Klein, A.J. Gunson, A systematic review on life cycle assessment for sustainable mineral industry: Methodologies, applications, challenges, and future directions, Minerals Engineering 240 (2026) 110131. doi:10.1016/j.mineng.2026.110131.
16. E. Kubińska-Jabcoń, M. Niekurzak, The use of modern materials in the automotive industry to improve the quality and safety of mechanical vehicles, Vehicles 10–11 (2019) 47–52.

ACKNOWLEDGMENTS

The work was created as a result of a project carried out with secondary school pupils as a part of the Excellence Initiative - Research University program (7th competition), Silesian University of Technology. Title: Car body design using modern high-strength steels – lighter, safer, more ecological.

TalentDetector

7th-9th June 2026
Gliwice-Brenna, Poland

DEPARTMENT OF ENGINEERING MATERIALS AND BIOMATERIALS
FACULTY OF MECHANICAL ENGINEERING
SILESIAN UNIVERSITY OF TECHNOLOGY

INTERNATIONAL STUDENTS SCIENTIFIC CONFERENCE

A proprietary expert system supporting the selection of steel grade for bridge elements

Dankhara Akshay, Mohammad Meran Vasseem, Rafał Honysz[a]

[a] Silesian University of Technology, Faculty of Mechanical Engineering, Department of Engineering Materials and Biomaterials
email: rafal.honysz@polsl.pl

Abstract: This article presents a proprietary program developed using the CLIPS expert system, which facilitates the selection of steel grades for structural components of steel bridges based on construction and operating conditions.

Keywords: artificial intelligence, expert system, material selection, bridge elements.

1. INTRODUCTION

A bridge is a structure designed to carry a road, pedestrian walkway, vehicular traffic, railway, wildlife migration route, or other forms of transportation over a water body or terrain obstacle, such as a river or ravine. Bridges connect communities more efficiently than would be possible without them. Like the bridges shown above, they help people cross water and can also span valleys, railways, and roads. Bridges facilitate the faster transportation of goods from one location to another. They are constructed to support the weight or load of anything passing over them and to withstand various weather conditions, including inclement weather. The four most common types of bridges are beam bridges, arch bridges, suspension bridges, and truss bridges [1-7].

Beam bridges are the oldest type of bridge and are also the simplest and most cost-effective to construct. Essentially, a beam bridge consists of a horizontal beam supported by piers at both ends. Longer beam bridges, however, rest on multiple piers, with the weight of the beam pressing directly down on them. Short beam bridges can be made from wood; for example, a wooden beam bridge over a small stream in backyard. Longer beam bridges are typically constructed from prestressed concrete. Under heavy loads, the deck of this type of bridge may begin to sag due to its own weight.

Arch bridges are among the oldest types of bridges. Many of the earliest arch bridges were made of stone or concrete, and those constructed from these materials were relatively low in height. Modern arch bridges are built using steel and concrete. The arch is supported at both ends by structures called abutments, which help distribute the weight evenly throughout the arch. Arch bridges are among the strongest types of bridges, but they generally take longer to construct than other types.

Suspension bridges are structures in which the deck, or decks, are suspended by cables. The main cables are anchored to towers at both ends. These cables are spaced widely apart to evenly distribute the weight of the deck and its load. Suspension bridges can span greater distances than other types of bridges and are often constructed over waterways, allowing tall ships to pass underneath. Many people find suspension bridges visually appealing. However, they have certain drawbacks: cables can break under excessive loads, and strong winds can cause damage to the structure.

Truss bridges are among the strongest types of bridges. A truss is a structure composed of members connected to each other, forming triangular units. Straight steel rods are commonly used to construct truss bridges.

2. STEEL SELECTION FOR STRUCTURAL COMPONENTS OF BRIDGES

Selecting the appropriate steel for a bridge structure is a critical process that requires balancing strength, safety, and operating costs, including maintenance. In modern bridge construction, the goal is not simply to find the "strongest" steel but rather the one that best withstands dynamic loads and resists corrosion. The steel selection process for bridge structures is multi-staged, integrating mechanical requirements, structural physics, and economic considerations. Within the European Union, steel selection must strictly comply with Eurocode 3 (EN 1993-1-10), which provides tables for selecting steel grades based among others on interfacial ductility and the risk of laminar cracking. The following is the detailed procedure that designers follow [8–10]:

1. Determining the operating parameters (loads). The first step is to identify the forces the steel structure must withstand. These include:
   - Static loads: self-weight of the structure, pavement, and equipment.
   - Variable loads: vehicular, pedestrian, or rail traffic (as specified by Eurocode).
   - Exceptional loads: vehicle impacts, ice pressure on piers, and earthquakes.
2. Selecting the strength (Yield Strength) Based on static and strength calculations, the appropriate steel grade is selected. A higher grade permits the design of thinner cross-sections, thereby reducing the overall mass of the bridge.
3. Selecting the quality grade for brittle fracture is the most important step in ensuring fire and winter safety. Steel becomes brittle at low temperatures. The designer must determine the T_{Ed} parameter (lowest design temperature) and select the appropriate impact strength grade accordingly. This procedure is based on EN 1993-1-10, which considers the thickness of the element - the thicker the sheet, the greater the risk of brittle fracture and the higher the impact strength requirements.
4. Verification of resistance to lamellar cracking. In thick sheets (over 15–20 mm) welded with T-shaped or corner welds, there is a risk of steel delamination caused by welding stresses in the thickness direction. The designer calculates the Z_{Ed} parameter and selects the appropriate steel quality class.
5. Selection of the corrosion protection method. This decision determines whether we use ordinary steel for painting or opt for special steel. Some steel grades require sandblasting followed by the application of multi-layer coatings, such as epoxies and polyurethanes. Steels with enhanced resistance to atmospheric corrosion are chosen to avoid costly future painting. This type of steel develops a dense oxide layer (patina) that protects it. Hot-dip galvanizing (also known as electroplating) is one of the most effective corrosion protection methods for steel in bridge construction, especially for

medium-sized structures, pedestrian bridges, and components such as railings, balustrades, and expansion joints. Unlike paint coatings, which provide only barrier protection by blocking oxygen, galvanizing offers electrochemical (cathodic) protection.

3. CLIPS EXPERT SYSTEM

CLIPS (short for C Language Integrated Production System) is a prominent and distinguished programming language designed for creating expert systems. It was developed in 1985 by NASA because commercial tools at the time were prohibitively expensive and difficult to integrate with other software. The following is a detailed description of what makes CLIPS unique. Unlike typical imperative languages such as C or Python, CLIPS is a powerful multi-paradigm tool that supports [11,12]:

- Rule-based programming: Its most important feature is the utilization of heuristic systems.
- Object-oriented programming (COOL): The CLIPS Object-Oriented Language supports classes, inheritance, and polymorphism.
- Procedural programming: It enables the definition of functions and the manipulation of variables in a traditional manner.

At the core of CLIPS is the Inference Engine, which is based on the RETE algorithm. It operates using a forward-chaining model. Its components include:

- Facts: The system stores a knowledge base containing facts about the world.
- Rules: The programmer defines IF... THEN... rules.
- Matches: The mechanism continuously checks which rules are satisfied by the current facts.
- Actions: When a rule is activated, it performs a specific action (e.g., adding a new fact), which can trigger subsequent rules.

The CLIPS syntax is inspired by Lisp [13], which results in the use of many parentheses. However, it remains logical and readable for those working in artificial intelligence. Despite its age, CLIPS continues to be a standard tool in the study of expert systems for several reasons. Written in C, it can be easily compiled on almost any system and integrated with applications written in C++, Java, or Python. The Rete inference algorithm is extremely fast at pattern matching, even with thousands of rules. CLIPS offers an interactive environment (shell) where users can add facts "live" and observe how the system makes decisions. As public domain software, it is available free of charge. CLIPS is used in domains where knowledge is difficult to encode in traditional programming languages and is based on expert experience, such as medical and technical diagnostics, planning systems (e.g., NASA missions), configuration management of complex products, and financial fraud detection etc. [11–15].

4. STEEL SELECTION FOR STRUCTURAL COMPONENTS OF BRIDGES

An proprietary expert system was developed to select the appropriate steel grade for a bridge element. The CLIPS expert system, version 6.24, was used to develop the program. It consists of several components: templates, a steel grade database, a data entry interface, inference rules, and a section displaying the inference results. Figure 1 presents a database of the steel grades most commonly used in bridge construction. Figure 2 shows several selected inference rules for choosing the appropriate steel grade. To do this, the user must answer several questions about the bridge type, its intended use, operating conditions, and other relevant factors. All input parameters and their correct values are listed in Table 1.

```
;;; --- 2. MATERIAL DATABASE (16 GRADES) ---

(deffacts steel-database-full
   ;; --- STANDARD STRUCTURAL STEELS ---
   (steel (grade S235JR)  (yield-strength 235) (impact-temp 20)  (fatigue-resistance standard)
          (corrosion-resistance low)    (weldability-CEV 0.35) (zinc-suitability yes) (relative-cost 1))
   (steel (grade S235J2)  (yield-strength 235) (impact-temp -20) (fatigue-resistance standard)
          (corrosion-resistance low)    (weldability-CEV 0.35) (zinc-suitability yes) (relative-cost 1))
   (steel (grade S275JR)  (yield-strength 275) (impact-temp 20)  (fatigue-resistance standard)
          (corrosion-resistance low)    (weldability-CEV 0.40) (zinc-suitability yes) (relative-cost 2))
   (steel (grade S275J2)  (yield-strength 275) (impact-temp -20) (fatigue-resistance standard)
          (corrosion-resistance low)    (weldability-CEV 0.40) (zinc-suitability yes) (relative-cost 2))
   (steel (grade S355JR)  (yield-strength 355) (impact-temp 20)  (fatigue-resistance high)
          (corrosion-resistance low)    (weldability-CEV 0.45) (zinc-suitability yes) (relative-cost 3))
   (steel (grade S355J0)  (yield-strength 355) (impact-temp 0)   (fatigue-resistance high)
          (corrosion-resistance low)    (weldability-CEV 0.45) (zinc-suitability yes) (relative-cost 3))
   (steel (grade S355J2)  (yield-strength 355) (impact-temp -20) (fatigue-resistance high)
          (corrosion-resistance medium) (weldability-CEV 0.45) (zinc-suitability yes) (relative-cost 3))
   (steel (grade S355K2)  (yield-strength 355) (impact-temp -20) (fatigue-resistance high)
          (corrosion-resistance medium) (weldability-CEV 0.45) (zinc-suitability yes) (relative-cost 3))

   ;; --- WEATHERING STEELS ---
   (steel (grade S355J0WP) (yield-strength 355) (impact-temp 0)   (fatigue-resistance high)
          (corrosion-resistance high)   (weldability-CEV 0.52) (zinc-suitability no)  (relative-cost 4))
   (steel (grade S355J2W)  (yield-strength 355) (impact-temp -20) (fatigue-resistance high)
          (corrosion-resistance high)   (weldability-CEV 0.52) (zinc-suitability no)  (relative-cost 4))
   (steel (grade S355K2W)  (yield-strength 355) (impact-temp -20) (fatigue-resistance high)
          (corrosion-resistance high)   (weldability-CEV 0.52) (zinc-suitability no)  (relative-cost 4))

   ;; --- THERMOMECHANICAL FINE-GRAIN ---
   (steel (grade S420ML)   (yield-strength 420) (impact-temp -50) (fatigue-resistance high)
          (corrosion-resistance medium) (weldability-CEV 0.42) (zinc-suitability yes) (relative-cost 5))
   (steel (grade S460ML)   (yield-strength 460) (impact-temp -50) (fatigue-resistance high)
          (corrosion-resistance medium) (weldability-CEV 0.42) (zinc-suitability yes) (relative-cost 5))

   ;; --- HIGH STRENGTH STEELS ---
   (steel (grade S500QL)   (yield-strength 500) (impact-temp -40) (fatigue-resistance high)
          (corrosion-resistance medium) (weldability-CEV 0.60) (zinc-suitability no)  (relative-cost 6))
   (steel (grade S690QL)   (yield-strength 690) (impact-temp -40) (fatigue-resistance high)
          (corrosion-resistance medium) (weldability-CEV 0.65) (zinc-suitability no)  (relative-cost 7))
   (steel (grade S890QL1)  (yield-strength 890) (impact-temp -60) (fatigue-resistance high)
          (corrosion-resistance medium) (weldability-CEV 0.72) (zinc-suitability no)  (relative-cost 8))
   (steel (grade S960QL)   (yield-strength 960) (impact-temp -40) (fatigue-resistance standard)
          (corrosion-resistance medium) (weldability-CEV 0.75) (zinc-suitability no)  (relative-cost 9)))
```

Figure 1. A database definition (in the form of facts) containing information on the mechanical properties of sixteen steel grades most commonly used in the manufacture of bridge elements.

```
;;; --- 4. LOGIC RULES ---

(defrule filter-strength
   (bridge-project (max-stress ?req) (element-thickness ?t))
   ?s <- (steel (yield-strength ?fy))
   =>
   (bind ?reduction (if (> ?t 40) then 30 else 0))
   (if (< (- ?fy ?reduction) ?req) then (retract ?s)))

(defrule filter-railway-fatigue
   (bridge-project (traffic-type railway))
   ?s <- (steel (fatigue-resistance standard))
   =>
   (retract ?s))

(defrule filter-temp
   (bridge-project (min-service-temp ?t-min))
   ?s <- (steel (impact-temp ?t-i))
   (test (> ?t-i ?t-min))
   =>
   (retract ?s))

(defrule filter-galvanizing
   (bridge-project (galvanizing-required yes))
   ?s <- (steel (zinc-suitability no))
   =>
   (retract ?s))
```

Figure 2. Selected inference rules responsible for the selection of steels most commonly used in the manufacture of bridge elements.

Table 1. Program input parameters and value ranges

Parameter	Values	
	minimum	maximum
Traffic type:	road / pedestrian / railway	
Maximum design stress [MPa]	100	1000
Minimum service temp [ºC]	-60	20
Plate thickness [mm]	5	200
Welding required?	yes / no	
Galvanizing required?	yes / no	
Environment:	rural / urban / industrial / marine	

The program is very simple to use. After loading it into the CLIPS system with the (load) command, reset the system to its initial state using the (reset) command, then run the program using the (run) command. Once launched, the user will be prompted to answer a series of questions. The system uses a text-based interface, so appropriate values must be entered via the keyboard. After all responses are provided, the system displays all steel grades that meet the specified requirements. If multiple grades are available, the cheapest grade is selected as the most advantageous. If no grades meet the specified criteria, an error message is displayed. After reviewing the results, the system can be reset to its initial state to repeat the inference process. An example of the system's operation is shown in Figure 3.

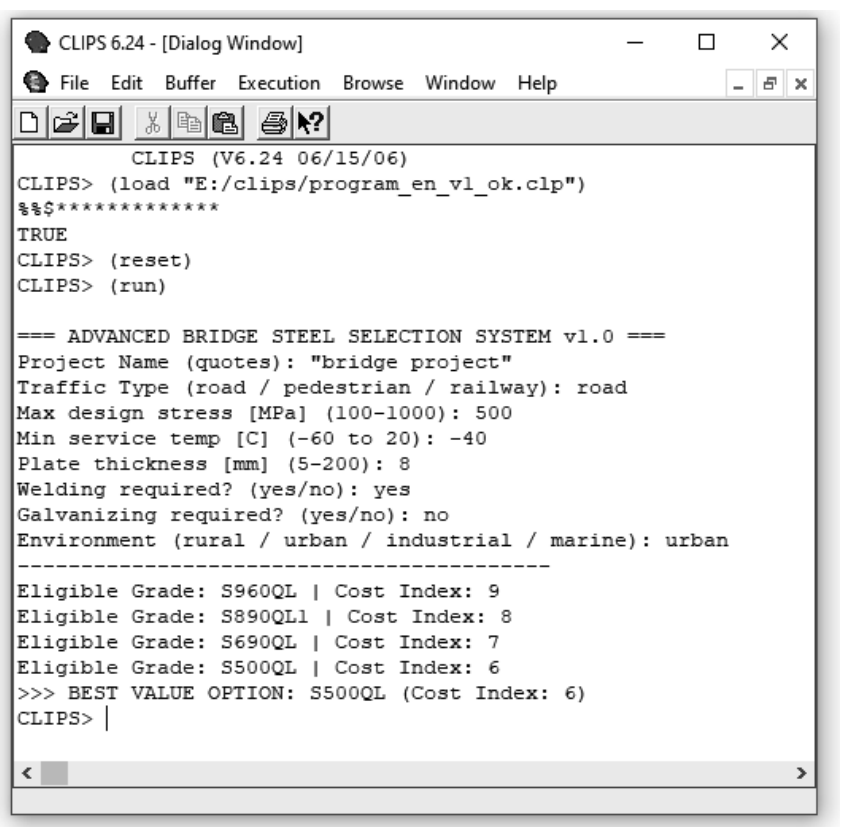

Figure 3. The CLIPS system dialog box after launching the program.

CONCLUSION

The program is easy to use, even for individuals unfamiliar with this type of system. In most cases, it successfully identified steel that met the user's requirements. Issues occurred when the data entered into the system was too inconsistent, incorrect, or outside the acceptable range. This program will serve as the foundation for future expansion, including the addition of new steel grades, more input parameters, and procedures to prevent the entry of invalid values.

BIBLIOGRAPHY

1. W. Radomski, H. Czudek: Podstawy mostownictwa. Warszawa: Państwowe Wydawnictwo Naukowe, 1983 (in polish)
2. B. David, The Creation of Bridges: From Vision to Reality - the Ultimate Challenge of Architecture, Design and Distance. Aurum Press, 2002.
3. J. Biliszczuk, J. Bień, W. Barcik, P. Hawryszków, M. Hildebrand, Bridge Engineering in Poland. In Chen, Wai-Fah; Duan, Lian (eds.). Handbook of International Bridge Engineering. Taylor & Francis, 2014
4. J. A. Sobrino, J. Jordan, D. Topuzi, Bridges Built with Advanced Materials, 9th International Conference on Short and Medium Span Bridges, Calgary, Alberta, Canada, July 15-18, 2014
5. https://scienceandsteamteam.com/seven-different-types-of-bridges-and-why-we-build-them/ (access: 01.05.2026)
6. https://www.harfordcountymd.gov/654/Bridge-Construction-Materials (access: 01.05.2026)
7. https://www.engineeringcivil.com/materials-used-in-bridge-construction.html (access: 01.05.2026)
8. EN 1993-1-10 (2005) (English): Eurocode 3: Design of steel structures - Part 1-10: Material toughness and through-thickness properties [Authority: The European Union Per Regulation 305/2011, Directive 98/34/EC, Directive 2004/18/EC]
9. Yer Kutz (Ed.), Handbook of Materials Selection, John Wiley & Sons, Inc. 2002.
10. P.C. Angelo, B. Ravisankar, Introduction to Steels Processing, Properties, and Applications, CRC Press, 2020.
11. https://www.clipsrules.net/ (access: 01.05.2026)
12. http://siliconvalleyone.com/founder/clips/ (access: 01.05.2026)
13. http://jmc.stanford.edu.articles/lisp/lisp.pdf (access: 01.05.2026)
14. Joseph C. Giarratano, Gary D. Riley, Expert Systems: Principles and Programming. Boston: Thomson, 2005.
15. https://portal.cs.umbc.edu/clips/usersguide/clipsusr.html (access: 01.05.2026)
16. R. Honysz, L. A. Dobrzeński, Materials science virtual laboratory as an example of the computer aid in materials engineering, Journal of Achievements in Materials and Manufacturing Engineering, 2007, Vol. 24/2, p. 219-222

TalentDetector

7th-9th June 2026
Gliwice-Brenna, Poland

DEPARTMENT OF ENGINEERING MATERIALS AND BIOMATERIALS
FACULTY OF MECHANICAL ENGINEERING
SILESIAN UNIVERSITY OF TECHNOLOGY

INTERNATIONAL STUDENTS SCIENTIFIC CONFERENCE

Production of Biopolymer Blended Sustainable Cable Compounds

Alara Aytekin[a], Pakize Pinar Erbeyin[a], Mert Cavus[a], Cemal Meran[a], Omer Eren[b]

[a] Pamukkale University, Faculty of Engineering, Department of Mechanical Engineering, Denizli-Turkiye, email: cmeran@pau.edu.tr
[b] Nexans Turkey Industry, R&D Center, Denizli,Turkiye, omer.eren@nexans.com

Abstract: This article investigates the development and performance of sustainable cable insulation materials produced by blending a conventional halogen-free flame retardant (HFFR) matrix with a bio-friendly polylactic acid (PLA) via single-screw strip extrusion. The research focuses on evaluating the physical, mechanical, and combustion properties of the novel biocomposites formulated under varying PLA mass ratios (0%, 2%, 5%, and 10%). Density measurement, limiting oxygen index testing, and tensile-rupture analysis were conducted to assess the structural integrity and flame retardancy of the blends. Additionally, the environmental stability and joint quality of the composites were validated through thermal and water aging conditions.

Keywords: biopolymer, polylactic acid (PLA), HFFR, cable insulation, flame retardant.

1. INTRODUCTION

Polymer-based materials are widely utilized in the cable industry due to their lightweight nature, high flexibility, excellent dielectric properties, and low production costs. However, traditional cable insulation and sheathing materials, such as polyvinyl chloride (PVC) and hydrocarbon-based polymers, exhibit high flammability. During a fire, these materials pose severe human health and environmental risks by releasing dense smoke and toxic, corrosive gases, such as hydrochloric acid (HCl). To mitigate these safety hazards and comply with international fire safety standards, the integration of HFFR compounds has become mandatory in modern cable manufacturing, particularly for enclosed space applications. HFFR materials retard flame propagation while ensuring low smoke density and the absence of toxic or corrosive emissions.

While conventional HFFR materials provide crucial fire safety, growing environmental awareness and sustainability necessitate a shift from petrochemical-derived materials to renewable, bio-based alternatives. As an example, PLA, synthesized from renewable biological resources such as corn starch and sugarcane, has emerged as a highly promising eco-friendly engineering biopolymer. PLA offers a lower carbon footprint, biocompatibility, and complete biodegradability. However, integrating PLA into highly flexible HFFR matrices presents structural challenges. The rigid structure and moisture-sensitive nature of the PLA phase require

a careful evaluation of its compatibility and long-term stability within the composite. This study aims to provide a comprehensive analysis of the physical, mechanical, and combustion performances of new-generation biopolymer-blended cable insulation composites. As shown in Table 1, the samples were prepared in 200-gram batches with different mass ratios.

Table 1. Mass ratios of samples.

	Sample 1	**Sample 2**	**Sample 3**	**Sample 4**
HFFR %	100	98	95	90
PLA %	0	2	5	10

2. MATERIAL AND METHOD

As detailed in Table 2, the experimental phase utilized an HFFR compound, HS 2400T, as the base matrix, and as given in Table 3, a PLA resin, Luminy® LX175, as the biopolymer additive. Since PLA is highly susceptible to hydrolytic degradation during melt processing, the residual moisture content of the raw polymer granules was controlled and measured prior to the extrusion process.

Table 2. Properties of HS 2400T

Property	**Unit**	**Guaranteed Value**	**Typical Value**	**Test Method**
Hardness	Shore D	-	-	ISO 868
Tensile Strength	MPa	≥ 9	9,5	IEC 60811-501
Elongation at Break	%	≥125	400	IEC 60811-501
High-Temperature Pressure Test (90°C / 4 h)	%	<50	<15	EC 60811-508
Limiting Oxygen Index	% O_2	-	33	EN ISO 4589-2

Table 3. Properties of Luminy® LX175

Property	**Value**	**Test Method**	**Property**	**Value**	**Test Method**
Density	1.24 g/cm³	Literature value	**Tensile Modulus**	3500 MPa	ISO 527-1
MFI (210°C/2.16kg)	6 g/10 min	ISO 1133-A	**Tensile Strength**	45 MPa	ISO 527-1
MFI (190°C/2.16kg)	3 g/10 min	ISO 1133-A	**Elongation at Break**	5%	ISO 527-1
Melting Temperature	155 °C	DSC	**Charpy Notched Impact Strength**	5 kJ/m²	ISO 179-1eA
Residual Monomer	%0.3	TE Corbion Method	**HDT, Amorphous**	60 °C	ISO 75-1

Following weighing and mechanical blending, the polymer mixtures were processed using a laboratory-scale single-screw extruder. The composites were manufactured via the strip extrusion method to form flat, continuous bands. This extrusion process enhanced the surface quality and ensured a stable distribution of the PLA within the HFFR matrix, producing standardized specimens for the subsequent tests.

The physical integrity and composition of the produced bio composites were evaluated through density measurements in accordance with the ISO 1183-1 standard (Method A-

Immersion Method). An OHAUS Voyager Pro VP64C analytical scale with a metrological readability of 0.1 mg was used in test. To prevent the low-density polymer samples from floating and to eliminate the adherence of air bubbles, an ethyl alcohol-water mixture with reduced surface tension was used as the immersion liquid instead of pure water.

The flammability and flame-retardant performance of the specimens were assessed using the Limiting Oxygen Index (LOI) test, conducted according to ISO 4589-2 and ASTM D2863 standards. Test specimens with dimensions of 6.5 ± 0.5 mm in width, 3 ± 0.25 mm in thickness, and 70-150 mm in length were prepared. As shown in Figure 1, each specimen was marked to establish a 50 mm clear combustion observation zone. The samples were ignited under a controlled upward laminar gas flow of 40 mm/s (comprising 93 ± 23 L/s O_2 and 225 ± 55 L/s N_2). The minimum oxygen concentration required to sustain combustion for 3 minutes and to exceed the 50 mm gauge mark was recorded.

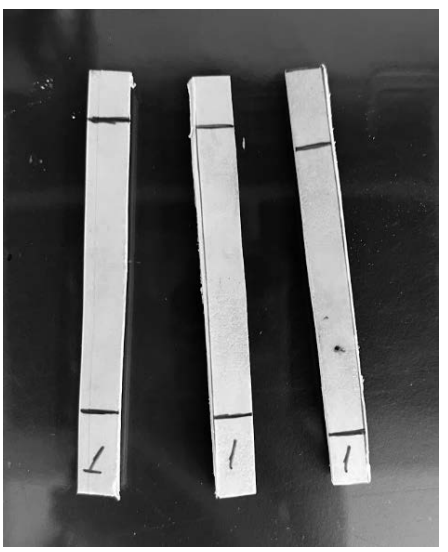

Figure 1. Marked observation zones of samples.

To evaluate the mechanical behavior and environmental stability of the cable insulation materials under external forces, tensile-rupture testing was performed based on the IEC 60811-501 standard. Type 1A dumbbell-shaped samples, with a thickness of 4.0 ± 0.2 mm, were prepared for the evaluations. The standard dimensions and geometrical properties of the tensile test specimens are detailed in Figure 2 [3].

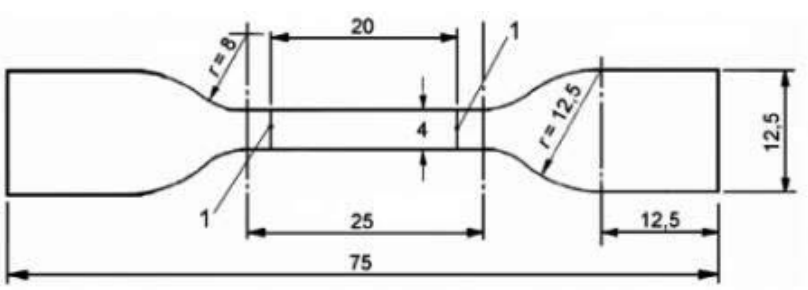

Figure 2: The standard dimensions and geometrical properties of the tensile test specimens

The tests were conducted using a Zwick Roell Z010 universal testing machine equipped with a 10 kN load cell, operating at a constant crosshead speed of 50 mm/min. In order to simulate stressors, the test specimens were divided into three specific conditioning groups: unaged (tested under standard ambient conditions of 23 ± 2 °C and 50 ± 5% relative humidity), thermally aged in an oven at 100 °C for 7 days and water-aged at 70 °C for 7 days.

3. RESULTS AND DISCUSSION

The physical characterization of the biocomposites revealed that the addition of PLA influences the moisture absorption and density of the HFFR matrix, as presented in Table 4. The moisture content increased linearly with the PLA mass fraction, rising from 0.08% in the pure HFFR sample to 0.21% in the 10% PLA composite. This ascending trend is attributed to the hydrophilic nature of the PLA's chemical structure. Conversely, the density profile remained relatively stable at lower PLA ratios but decreased slightly to 1.37 g/cm³ at the 10% PLA fraction. This reduction is explained by the lower theoretical density of the LX175 polymer (1.24 g/cm³), which becomes dominant at higher concentrations.

The flame retardancy of the experimental biocomposites was evaluated using the LOI test, and the results are detailed in Table 4. The pure HFFR matrix exhibited an experimental limiting oxygen index of 34.5% (notably higher than the supplier's typical value of 33% reported in Table 2). A cooperative effect was observed with low PLA additions, where the LOI value reached a maximum of 36% at a 5% PLA fraction. However, increasing the PLA content to 10% led to a reduction in the LOI value to 34%. This decline occurs because the flammable, hydrocarbon-based characteristics of the PLA phase suppress the barrier effect of the inorganic flame retardants at a higher concentration.

Table 4. The moisture, density and LOI test results.

PLA Content (%)	**0**	**2**	**5**	**10**
Moisture Content (%)	0,08	0,11	0,15	0,21
Density (g/cm³)	1,38	1,39	1,38	1,37
Limiting Oxygen Index (%)	34,5	35,9	36	34

The tensile strength and elongation values under unaged, thermally aged, and water-aged conditions are summarized in Table 5. In the unaged state, the pure HFFR matrix demonstrated high flexibility with an elongation of 465% and a tensile strength of 11.34 MPa. The incorporation of PLA compromised the elastic nature of the material, transforming it into a more brittle structure. Due to the high tensile modulus (3500 MPa) and low elongation capacity (≤5%) of the pure PLA, the elongation at break plummeted to 37% for the 10% PLA composite. At the same time, its tensile strength increased to 12 MPa as the highly rigid PLA phase assumed the load-bearing capacity.

The thermal and hydrolytic aging processes exposed the incompatibilities between the polymer chains. Following thermal aging at 100 °C for 7 days, the rigidity of the composites further increased. The 10% PLA sample exhibited a tensile strength of 13.46 MPa, while its elongation plummeted to 21%, indicating a complete loss of elasticity and heightened embrittlement.

Table 5. Tensile and Elongation Test Results

	Unaged State		Thermally Aged State		Water-Aged State		
PLA Fraction (%)	**Tensile Strength (MPa)**	**Elongation at Break (%)**	**Tensile Strength (MPa)**	**Elongation at Break (%)**	**Surface Condition**	**Tensile Strength (MPa)**	**Elongation at Break (%)**
0	11,34	465	9,96	403	-	9,87	404
2	8,32	429	9,16	114	Blistering	8,39	418
5	10,04	57	10,59	41	Blistering	6,65	349
10	12	37	13,46	21	Separation	5,16	250

Water aging at 70 °C for 7 days revealed two critical vulnerabilities of the composites: hydrolytic degradation and poor interfacial adhesion. While pure HFFR maintained its structural integrity, the 2% and 5% PLA composites exhibited surface blistering. Notably, the 10% PLA composite experienced macroscopic phase separation, as shown in Figure 3. Due to this hydrolytic breakdown, the tensile strength of the 10% PLA composite dropped sharply from 12 MPa to 5.16 MPa. Conversely, the elongation values appeared to increase for the 5% and 10% PLA-blended samples after water aging; this does not represent a recovery of true elasticity, but is rather the result of water molecules permeating the polymer matrix and acting as a plasticizer, thereby artificially increasing chain mobility.

Figure 3. The phase seperation of Sample 4.

The observed hydrolytic sensitivity and phase separation are directly correlated with the manufacturing process. Both components being in granule form before extrusion, combined with the absence of a compatibilizer, prevented adequate homogenization between the melt phases. Furthermore, if the residual moisture of PLA granules is not reduced below 250 ppm prior to extrusion, hydrolytic degradation can be triggered, severely weakening the final structural integrity of the cable sheath.

4. CONCLUSIONS

Based on the experimental investigation of the physical, mechanical, and combustion properties of PLA-blended HFFR cable insulation materials, the following conclusions were

drawn:

The integration of PLA into the HFFR matrix increases the moisture absorption of the composite, which is directly attributed to the hydrophilic nature of the PLA. The addition of PLA at low concentrations enhances the flame-retardant properties, elevating the limiting oxygen index. However, excessive PLA content negatively impacts the fire-resistant performance. While the incorporation of PLA improves the tensile strength to a certain extent, it causes a reduction in the elongation at break value, transforming the flexible matrix into a brittle and more rigid structure. Thermal aging exacerbates this embrittlement. As the PLA fraction increases, the material's resistance to long-term thermal degradation decreases, leading to a drop in elongation capacity. Higher PLA contents lead to phase separations and surface blistering, and lowering hydrothermal endurance. Following water-aging, a reduction in tensile strength was observed alongside an increase in elongation. This is not a recovery of true elasticity, but rather the result of water molecules acting as a plasticizer within the polymer matrix, which artificially increases chain mobility. In the next stage of our research, to overcome these limitations and further optimize sustainable cable production, several advanced processing strategies must be implemented. Instead of traditional granule compounds, the utilization of powder-based materials should be investigated to achieve higher performance. Furthermore, pre-drying the granules with industrial dehumidifiers prior to extrusion is recommended to prevent hydrolytic degradation. The application of compatibilizers will also be essential to reduce interfacial tension between the polymer phases and ensure homogeneity. Finally, to broaden the scope of eco-friendly manufacturing, future studies should explore the integration of alternative bio-based polymers, such as Bio-PE and Bio-EVA, into cable insulation and sheathing formulations.

BIBLIOGRAPHY

1. Das, A., Ringu, T., Ghosh, S., & Pramanik, N. (2022). A comprehensive review on recent advances in preparation, physicochemical characterization, and bioengineering applications of biopolymers. *Polymer Bulletin (Berlin, Germany)*, *80*(7), 7247. https://doi.org/10.1007/S00289-022-04443-4
2. Li, Y., Qi, L., Liu, Y., Qiao, J., Wang, M., Liu, X., & Li, S. (2022). Recent Advances in Halogen-Free Flame Retardants for Polyolefin Cable Sheath Materials. *Polymers 2022, Vol. 14, Page 2876*, *14*(14), 2876. https://doi.org/10.3390/POLYM14142876
3. *Tensile Testing Procedure of Nonmetalic Materials of Electric and optical Fibre Cables as per IEC 60811-501 - AHP PLASTIK MAKINA*. (t.y.). Geliş tarihi 25 Mayıs 2026, gönderen https://ahp-makina.com/tensile-testing-procedure-of-nonmetalic-materials-of-electric-and-optical-fibre-cables-as-per-iec-60811-501/

TalentDetector

7th-9th June 2026
Gliwice-Brenna, Poland

DEPARTMENT OF ENGINEERING MATERIALS AND BIOMATERIALS
FACULTY OF MECHANICAL ENGINEERING
SILESIAN UNIVERSITY OF TECHNOLOGY

INTERNATIONAL STUDENTS SCIENTIFIC CONFERENCE

Structure and properties of the TiAlN coating deposited onto a hot-work steel substrate

Piotr Bailner[a], Kacper Owczarek[a], Sebastian Zimoląg[a], Matěj Macák[b], Filip Škoda[b], Michal Lattner[c], Antonin Kříž[c], Jakub Polis[d], Marcin Staszuk[d], Daniel Pakuła[d]

[a] Student of Faculty of Mechanical Engineering, Silesian University of Technology, Poland
[b] Student of Faculty of Mechanical Engineering, Jan Evangelista Purkyně University in Ústí nad Labem, Czech Republic
[c] Faculty of Mechanical Engineering, Jan Evangelista Purkyně University in Ústí nad Labem, Czech Republic
[d] Department of Engineering Materials and Biomaterials, Faculty of Mechanical Engineering Silesian University of Technology, Poland
email: daniel.pakula@polsl.pl

Abstract: This work was carried out as part of the 14th edition of the PBL (Project-Based Learning) project at the Faculty of Mechanical Engineering at the Silesian University of Technology in Gliwice (Poland) and at the Faculty of Mechanical Engineering, Jan Evangelista Purkyně University, Ústí nad Labem, (Czech Republic). The aim of the research project was to investigate the structure and properties of a TiAlN coating deposited on an X40CrMoV5-1 hot-work tool steel substrate. The wear resistance and adhesion of the coating were also investigated. The article presents the results of tribological and structural studies, surface topography, FEM analysis, and chemical composition analysis of the investigated coating.

Keywords: tribological tests, TiAlN coating, PVD method, hot-work tool steel

1. INTRODUCTION

Hot-work steels are widely and extensively used in industry due to their properties, including their ability to maintain their performance characteristics when operating at very high temperatures [1]. One common engineering practice is to apply thin ceramic coatings (approx. 1–3 μm thick) to this type of steel. The main characteristic of these coatings is a significantly higher melting point than that of metals [2]. For example, the melting point of aluminum is approx. 660°C, while that of aluminum oxide is approx. 2020°C. The use of ceramic coatings increases resistance to wear and abrasion and provides a protective barrier against moisture and corrosion [3].

One such coating is the investigated TiAlN coating, which is characterized by high hardness and oxidation resistance. In this coating, titanium is responsible for providing hardness and resistance to mechanical wear. Aluminum increases the chemical stability of the coating,

whereas nitrogen reduces its abrasive wear. TiAlN increases the durability and service life of materials operating under harsh conditions. This coating is deposited by physical vapor deposition (PVD), where the deposition process takes place in a vacuum. The evaporated material deposits onto an appropriate substrate, forming a thin and durable layer [4-6]. The TiAlN coatings find applications, among others, in machining and hot-work tools.

The aim of this study is to investigate the structure and properties of a TiAlN coating deposited on a hot-work steel substrate.

2. MATERIALS AND METHODOLOGY

An alloy tool steel sample of X40CrMoV5-1 was used for the tests, which is characterized by high hardenability, resistance to thermal cracking, high strength, and hardness at elevated temperatures. This steel requires precise heat treatment, preferably in vacuum furnaces, to minimize surface decarburization. After preparation, the material was coated with a TiAlN layer using the physical vapor deposition (PVD) method.

Surface topography was examined using an atomic force microscope (AFM). An area measuring 20 µm × 20 µm was imaged.

Tribological tests were performed using the “ball-on-plate” method on a CSM Instruments device [7-8], under the parameters presented in Table 1. The tests were performed at a temperature of 20°C and a humidity of 50%, using a spherical counter-sample made of zirconium oxide (ZrO_2) with a diameter of 6 mm.

The fretting test was performed using the “ball-on-flat” method on an Anton Paar Revetest RST device [9], with a zirconium ball, for the parameters listed in Table 2.

Table 1. Parameters for tribological tests performed by the "ball-on-plate" method

Sample No.	Substrate	Coating	Parameters				
			Number of cycles	Normal load [N]	Distance [mm]	Acquisition rate [Hz]	Linear speed [cm/s]
1	X40CrMo V5-1	-	5000	5	5	10	5.53
2	X40CrMo V5-1	TiAlN					

Table 2. Parameters for the fretting test performed by the "ball-on-flat" method

Sample No.	Substrate	Coating	Parameters			
			Number of cycles	Normal load [N]	Distance [mm]	Acquisition rate [Hz]
1	X40CrMo V5-1	-	5000	5	13	2
2	X40CrMo V5-1	TiAlN				

The abrasion marks were examined using a ZEISS SEM SUPRA 35 scanning electron microscope at an EHT acceleration voltage of 20 kV, with the use of secondary electrons (SE). Additionally, chemical composition analysis was conducted on the same device using energy-dispersive X-ray spectroscopy (EDS).

A TESCAN VEGA 3 scanning electron microscope (SEM) was also used to conduct a detailed analysis of the chemical homogeneity of the deposited layer. Observations were conducted on prepared metallographic cross-sections. As part of the experiment, elemental mapping was performed to determine the distribution of key elements in the transition zone. The concentrations of elements contained in the coating—titanium (Ti), aluminum (Al), nitrogen (N)—and the alloying elements of the tool steel, particularly iron (Fe), chromium (Cr), vanadium (V), and molybdenum (Mo), were monitored.

Simulations were performed to verify the stresses and strains in the coating. The studies consisted of a numerical analysis of cylindrical samples with a diameter of 20 mm made of X40CrMoV5-1 steel, onto which a protective TiAlN coating with a thickness of 3.5 µm was applied. Modeling was carried out in ANSYS (Static Structural module), assuming perfect adhesion between the coating and the substrate. Thanks to the use of a densified finite element mesh near the surface, it was possible to accurately map the stress distribution in the thin layer deposited by the PVD method. A normal force of 60 N was applied to the model. This force level allowed for obtaining pressures corresponding to the actual operation of hot-work tools, while simultaneously enabling the investigation of the stress distribution prior to permanent damage to the substrate.

3. RESULTS

The TiAlN coating formed a columnar grain structure on the surface of the X40CrMoV5-1 steel, resulting from the method of its application (Fig. 1). Its structure can be classified as Zone II according to the Thornton model, characterized by the presence of columnar grains and surface irregularities. The grains are fine and densely arranged. The coating was uniformly deposited and reached a thickness of 3.5 µm across the entire surface. The coating exhibits high adhesion to the substrate.

a) b)

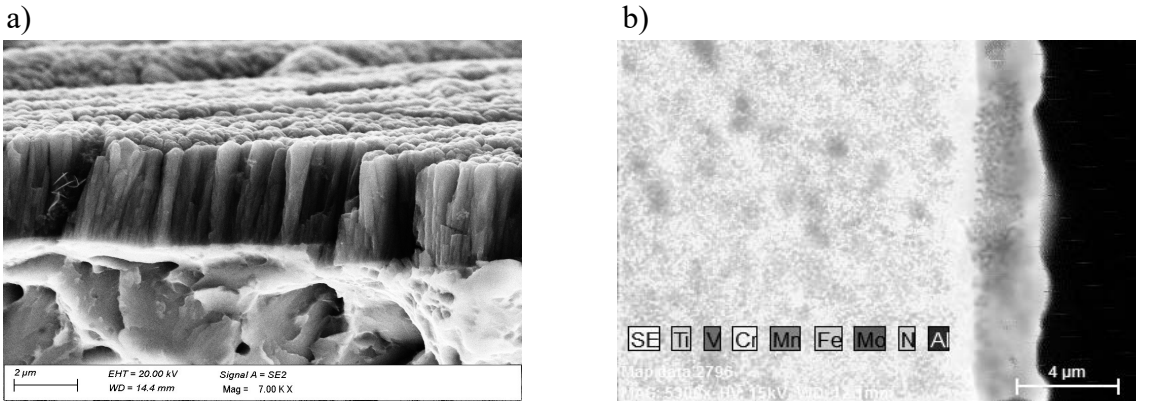

Figure 1. Coating fracture: a) SEM image showing the coating on the substrate, b) distribution of elements in the coating and substrate

a) b)

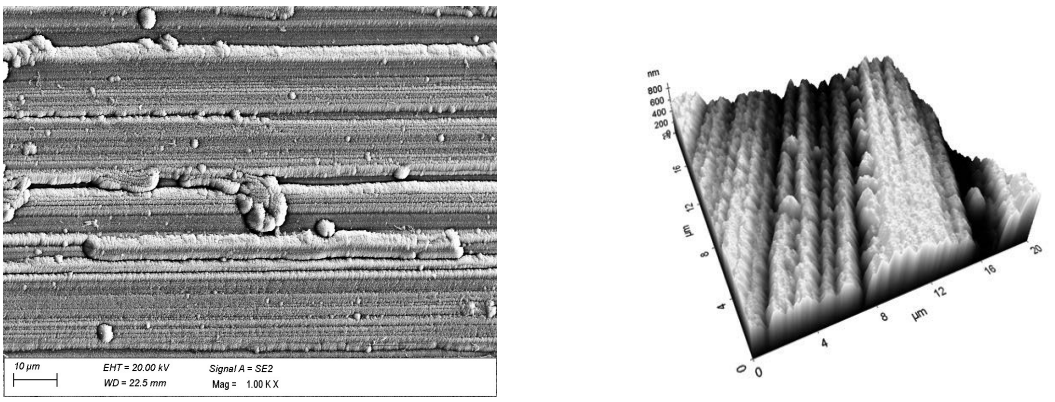

Figure 2. Surface topography of the coating: a) SEM image showing the directional texture, b) 3D visualization of the coating structure via AFM

The surface of the coating exhibits a distinct directional texture resulting from abrasive processing. A dense network of machining marks (so-called grinding marks) oriented parallel to the grinding direction was observed. This does not constitute a coating defect but rather a reflection of the substrate topography. Numerous defects formed during the manufacturing process are also visible on the coating surface. Visible circular macroparticles are characteristic of the cathodic arc evaporation process (Fig. 2).

Based on the analysis of the wear tracks, it was determined that the primary damage mechanism of the investigated material was surface abrasive wear. The average width of the abrasion track is approximately 333.65 µm. In the case of the investigated coating, an irregular wear behavior was observed—the depth and degree of wear vary, and the worn surface is non-homogeneous (Fig. 3). Additionally, the chemical composition analysis revealed oxidation of the substrate.

Iron, most likely originating from the sample substrate, was found in the composition of the investigated coating. EDS analysis also revealed complete abrasion of the coating in some areas. Nevertheless, the presence of the expected elements, i.e., titanium, aluminum, and nitrogen, was confirmed.

A zirconium ball was used as a counter-sample for the tests. Morphological analysis showed uniform abrasive wear of the ball (Fig. 4). Additionally, coating and substrate material were detected on its surface.

The TiAlN-coated steel tested using the “ball-on-plate” method exhibits relatively high friction, with the coefficient of friction stabilizing in the range of 0.6–0.8. The coefficient of friction increases gradually up to approximately 500 cycles. Then, during the next 500 cycles, a rapid increase in the coefficient of friction occurs. This effect could have been triggered by the removal of the outer oxide layer and a change in surface roughness. The fluctuations in the coefficient of friction shown in Fig. 5 are likely due to the test procedure and the grooved surface structure (Fig. 2). Rotation of the sample during the test altered the angle between the direction of the counter-sample’s motion and the directional surface structure, causing variations in the coefficient of friction.

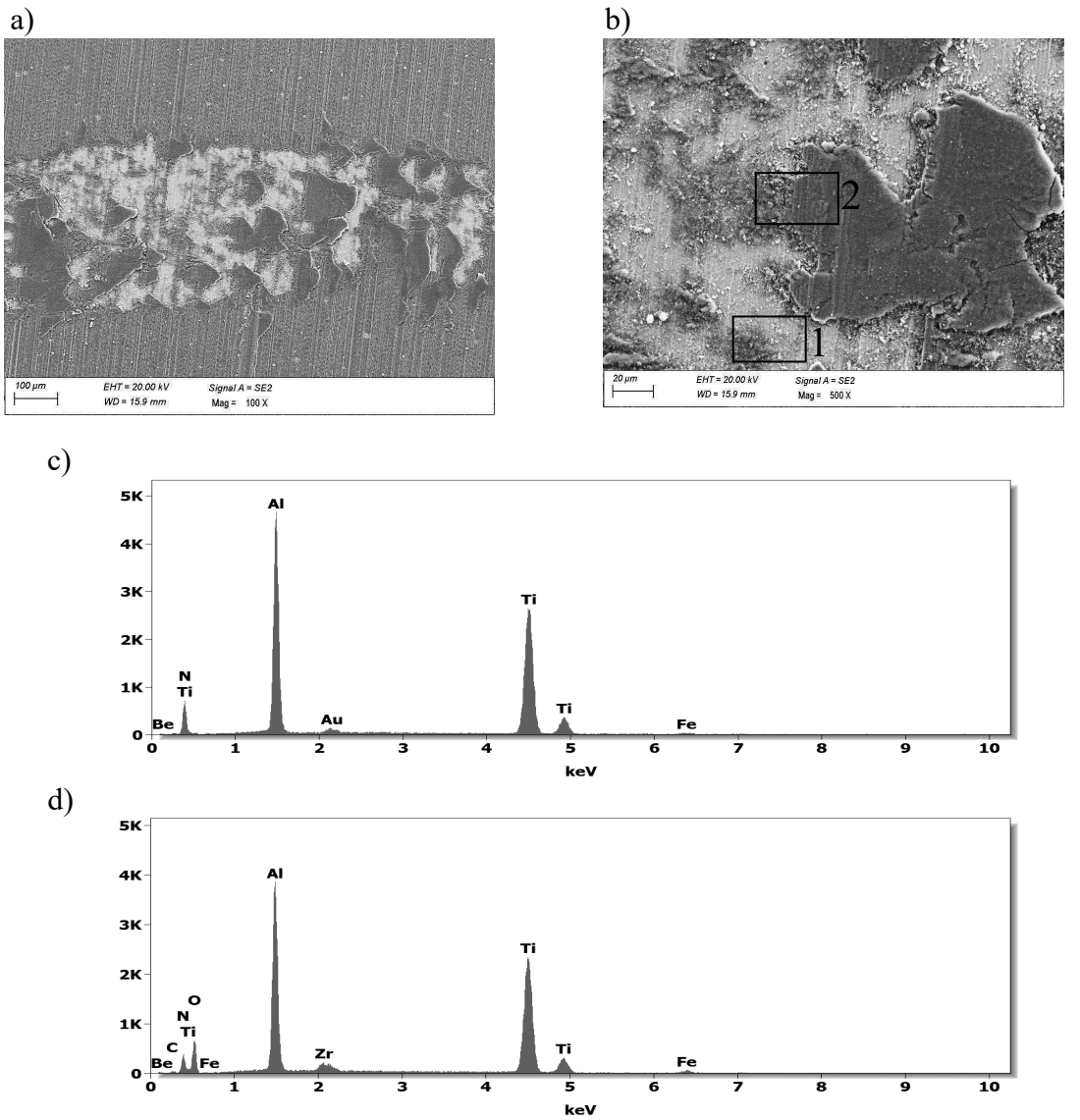

Figure 3. a) Wear track of the investigated coating, b) Magnification of the wear track, c) Chemical composition analysis of area 1, d) Chemical composition analysis of area 2

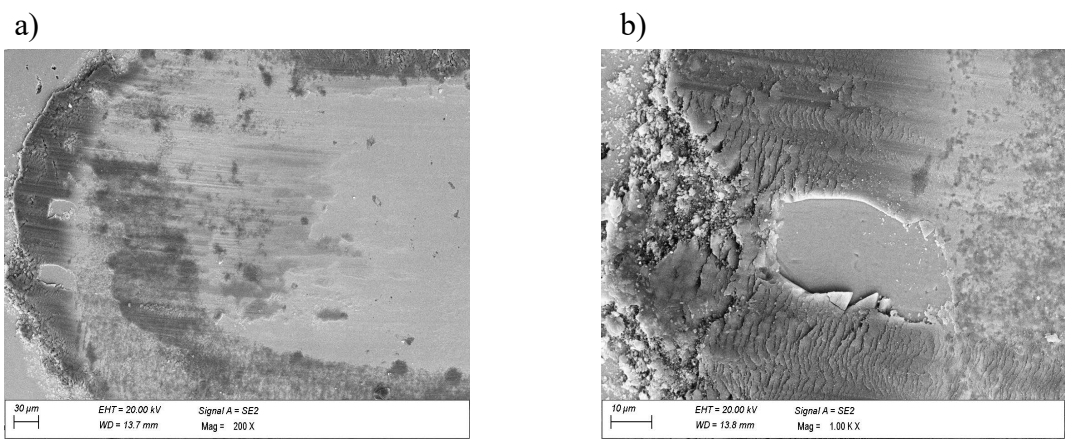

Figure 4. a) Abrasion mark left by the abrasive ball, b) Close-up of the abrasion track

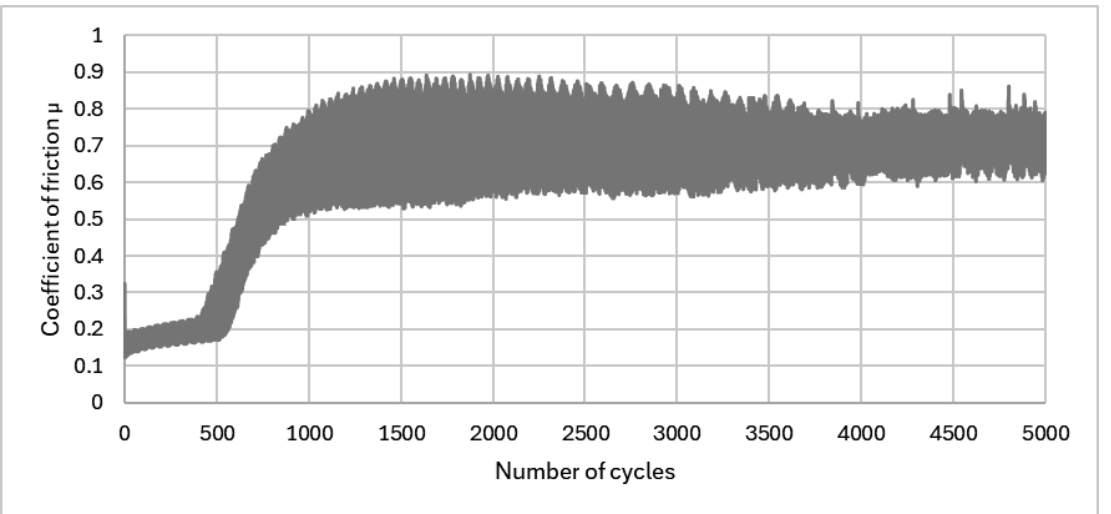

Figure 5. Friction coefficient as a function of the number of cycles for the TiAlN coating ("ball-on-plate" method)

For the test conducted using the "ball-on-flat" method, the coefficient of friction values are presented in Fig. 6. The TiAlN coating exhibits a relatively stable coefficient of friction curve throughout the loading period. A sharp increase in the coefficient of friction values was observed halfway through the test, which may result from increased wear of the counter-sample and the accumulation of zirconium particles in the wear track formed under load.

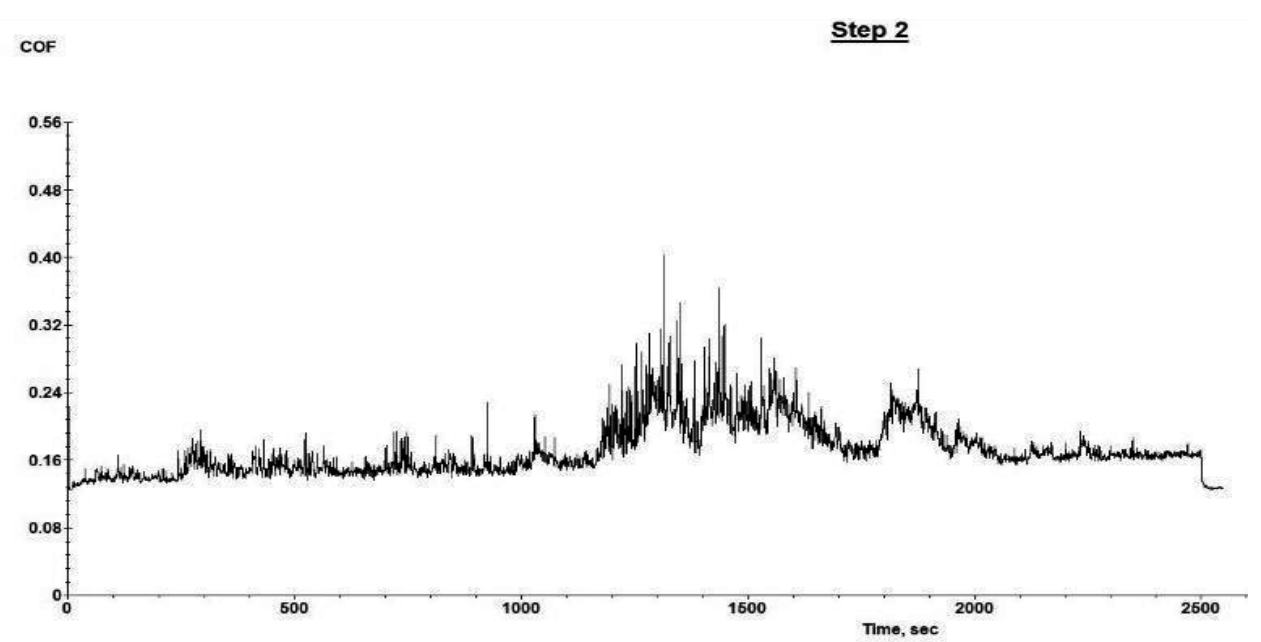

Figure 6. Friction coefficient after using the "ball-on-flat" method

A linear analysis of the traces was performed to assess the condition of the coating after loading during the abrasion test. The results of the linear analysis of the coating are shown in Fig. 7, where no significant coating defects were observed in the indentation area.

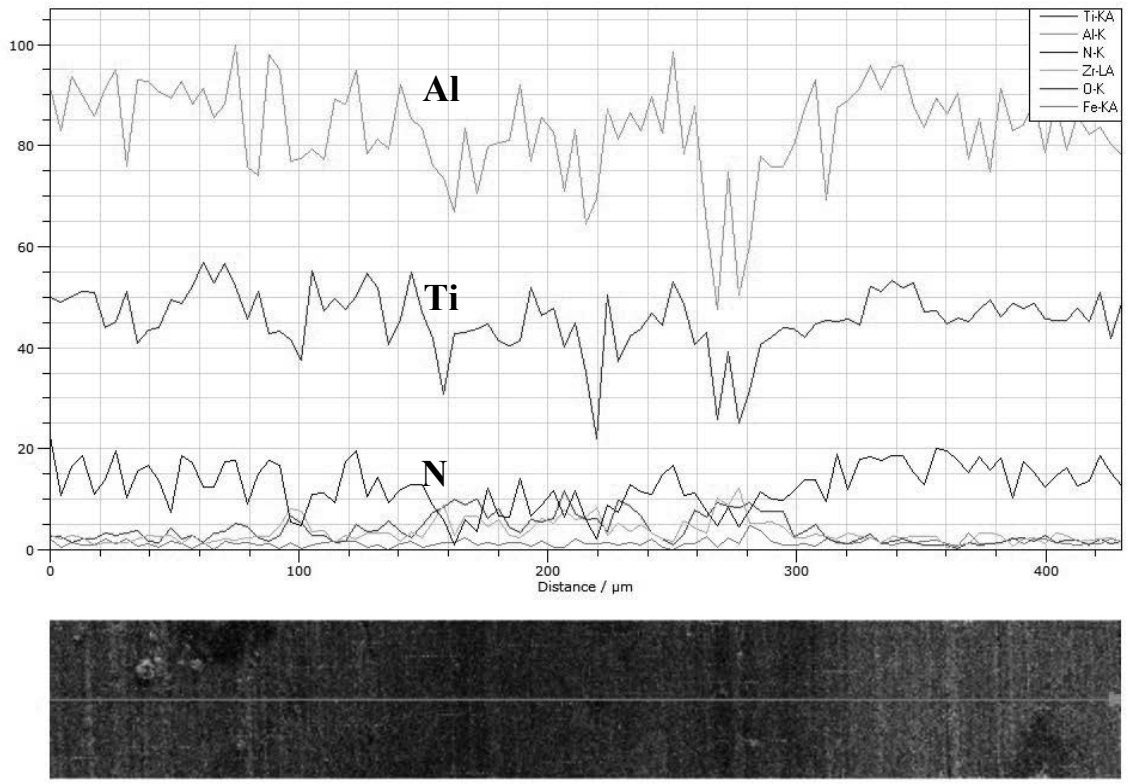

Figure 7. Surface topography after abrasive wear testing with chemical composition analysis

The performed FEM simulations showed that the presence of the protective layer on X40CrMoV5-1 steel improves the mechanical properties of the material, limiting deformations and providing a more favorable stress distribution, as shown in Figs. 8 and 9. For the uncoated X40CrMoV5-1 steel, the largest displacements (8.0 x 10^{-3} µm) and strains (0.663 µm/m) were recorded. The application of the TiAlN coating reduced displacements by approximately 50% (Table 3). This is due to the fact that the hard ceramic has a higher Young's modulus than steel, thereby bearing most of the load and protecting the deeper layers of the material. In the case of TiAlN, solid solution strengthening is critical—the presence of aluminum in the titanium nitride lattice induces stresses that block plastic deformations. The simulation confirmed that the coating effectively protects the steel from degradation, which in practical applications translates into greater wear resistance and an extended service life for tools operating under harsh thermomechanical conditions.

Table 3. Summary of overall results from computer simulations

Material used	**Maximum stress value [kPa]**	**Maximum displacement value [µm]**	**Maximum strain value [µm/m]**
X40CrMoV5-1 steel	95.897	$8.0 \cdot 10^{-3}$	0.663
X40CrMoV5-1 steel coated with TiAlN-based coating	93.371	$4.0 \cdot 10^{-3}$	0.445

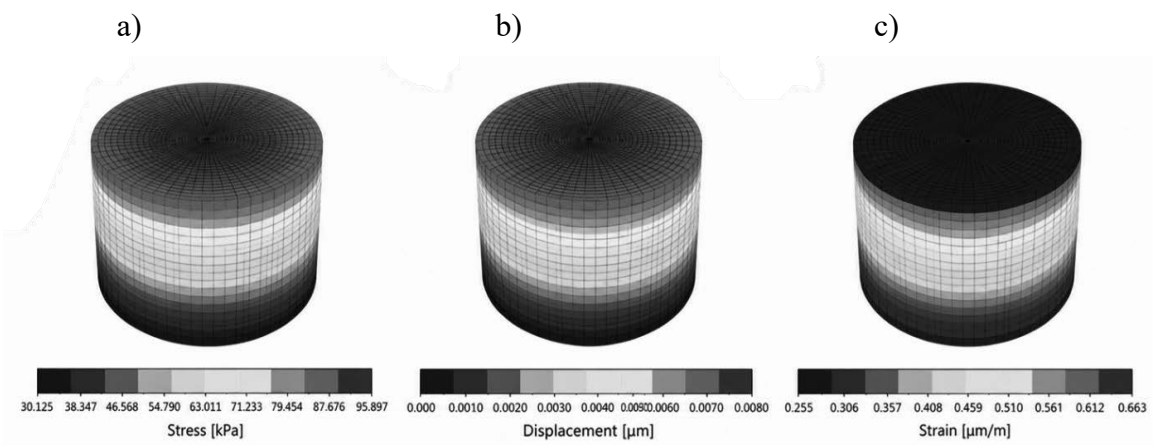

Figure 8. Results of FEM numerical simulations for uncoated X40CrMoV5-1 tool steel: a) stress distribution, b) total displacement, c) strain

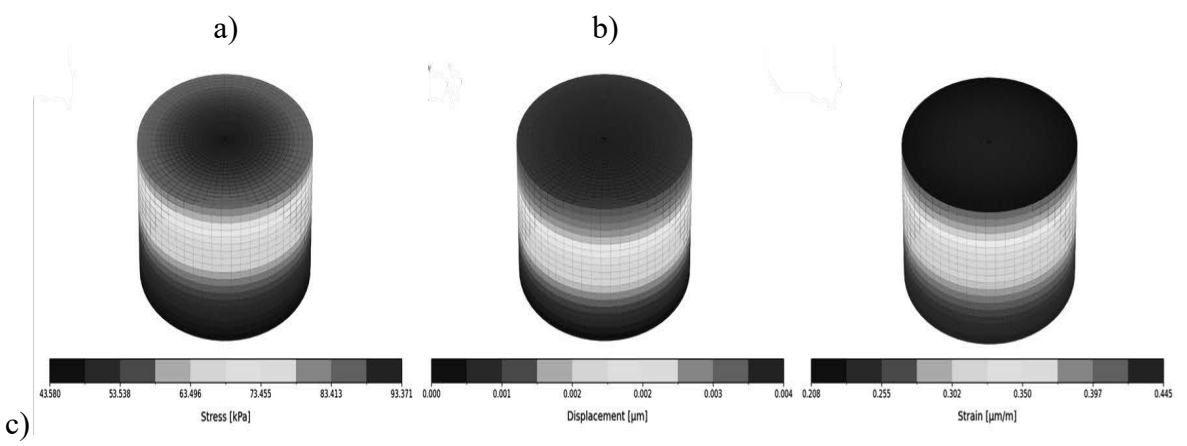

Figure 9. Results of FEM numerical simulations for X40CrMoV5-1 steel with a TiAlN-based protective coating: a) stress distribution, b) total displacement, c) strain

4. CONCLUSIONS

The conducted investigations confirmed that the TiAlN coating effectively improves the abrasive wear resistance of X40CrMoV5-1 steel and enhances its mechanical properties. FEM simulations demonstrated a more favorable stress distribution and a reduction in material displacements by approximately 50% compared to uncoated steel, indicating effective substrate protection provided by the ceramic layer.

Microstructural analysis revealed that the TiAlN coating possesses a dense columnar grain structure characteristic of Zone II in the Thornton model. A directional surface texture and grinding marks reflecting the substrate topography were observed, along with the presence of macroparticles typical of the cathodic arc evaporation PVD process.

The dominant degradation mechanism of the investigated coating was surface abrasive wear. EDS analysis confirmed local complete removal of the coating as well as the presence of iron originating from the substrate and zirconium transferred from the counter-sample, indicating intensive tribological interaction between the cooperating surfaces.

Tribological investigations showed that the coefficient of friction of the TiAlN coating remained at a relatively high level (0.6–0.8) and exhibited local fluctuations during the test. The increase in the coefficient of friction after approximately 500 cycles was associated with progressive wear of the surface layer, changes in surface roughness, and accumulation of wear debris within the wear track.

ACKNOWLEDGMENTS

This work was created as part of a project carried out within the framework of Project-Based Learning (PBL) in the 14th Excellence Initiative Competition—the Scientific Research Program of the Silesian University of Technology.

BIBLIOGRAPHY

1. J. Mikuła, D. Pakuła, L. Żukowska, K. Gołombek, A. Kříž, Wear resistance of (Ti,Al)N Metallic Coatings for Extremal Working Conditions, Coatings 2021, 11(2), 157.
2. M. Staszuk, D. Pakuła, M. Olszowska, A. Kloc-Ptaszna, M. Szindler, A. N. Wieczorek, R. Honysz, E. Jonda, M. Basiaga, Structure and Tribological Properties of TiN/DLC, CrN/DLC, TiAlCN/DLC, AlTiCN/DLC and AlCrTiN/DLC Hybrid Coatings on Tool Steel, Materials 2025, 18(17), 4188.
3. M. Staszuk, D. Pakuła, Ł. Reimann, A. Woźniak, A. Kloc-Ptaszna, J. Kolasa, P. Nuckowski, Investigations of CrN/TiO2 Coatings Obtained in the Hybrid PVD/ALD Process on 316L Steel Substrates, Materials 2026, 19(10), 1921.
4. G.G. Fuentes, M.J. D´ıaz de Cerio, R. Rodriguez, J.C. Avelar-Batista, E. Spain, J. Housden, Y. Qin, Investigation on the sliding of aluminium thin foils against PVD-coated carbide forming-tools during micro-forming, Journal of Materials Processing Technology vol. 177, (2006), 644-648.
5. R. Ferreiraa, Ó. Carvalhoa, L. Sobralb, S. Carvalhoc, F. Silvaa, Influence of morphology and microstructure on the tribological behavior of arc deposited CrN coatings for the automotive industry, Surface & Coatings Technology vol. 397, (2020), 126-127.

6. I. Czaja, M. Staszuk, Struktura i własności powłoki Ti(B,N) uzyskanej na ceramice sialonowej, Prace studenckich kół naukowych, vol. 29, Gliwice 2009, 23-36.
7. M. Basiaga, R. Jendruś, W. Walke, Z. Paszenda, M. Kaczmarek, M. Popczyk, Influence of surface modification on properties of stainless steel used for implants, Arch. Met. Mater., 2016, vol. 6, 2965–2969.
8. C.X. Shan, X. Hou, K.L. Choy, P. Choquet, Improvement in corrosion resistance of CrN coated stainless steel by conformal TiO2 deposition, Surface & Coatings Technology vol. 202, (2008), 2147–2151.
9. S. M. Aktarer, Y. Sert, T. Küçükomeroğlu, Investigation of structural, hardness, adhesion, and tribological properties of CrN and AlCrN coatings deposited on cylinder liner, Surface & Coatings Technology vol. 253, (2025), 1–17.

TalentDetector

7th-9th June 2026
Gliwice-Brenna, Poland

DEPARTMENT OF ENGINEERING MATERIALS AND BIOMATERIALS
FACULTY OF MECHANICAL ENGINEERING
SILESIAN UNIVERSITY OF TECHNOLOGY

INTERNATIONAL STUDENTS SCIENTIFIC CONFERENCE

Comparative analysis of the microstructure of butt-welded joint variants of S304H steel manufactured from materials before and after service exposure

Wiktoria Borowiec[a], Zuzanna Zielińska[a], Marek Sroka[b]

[a] Silesian University of Technology, Faculty of Material Engineering and Digitalisation of Industry, email: wiktbor155@student.polsl.pl, zz304779@student.polsl.pl
[b] Silesian University of Technology, Faculty of Mechanical Engineering, Department of Engineering Materials and Biomaterials, email: marek.sroka@polsl.pl

Abstract: This study investigates the microstructural evolution of Super 304H austenitic steel butt-welded joints fabricated via TIG (GTAW) welding. Joints were produced in three configurations combining as-received (AR) and post-service (EX) materials: AR/AR, AR/EX, and EX/EX. Microstructural characterization was performed using light microscopy under brightfield, darkfield (DF), and differential interference contrast (DIC) modes.The base metals retained an austenitic matrix with annealing twins, while the weld metal exhibited a dendritic structure. The heat-affected zones (HAZs) on both sides displayed local grain growth. Under DF imaging, the HAZ adjacent to the post-service (EX) material exhibited a significantly more advanced precipitation state compared to the as-received (AR) side, where precipitates were solely formed by the weld thermal cycle. This discrepancy stems from the welding heat overlapping with prior service-induced degradation; the EX material already contained operationally induced precipitates, and the subsequent thermal cycle further intensified the precipitation process and caused particle coarsening (coagulation) along boundaries and within grains. Consequently, the EX-side HAZ develops the most heavily evolved precipitation structure, serving as the critical site for future structural failure.

Keywords: S304H, microstructure, welded joints, heat-affected zone, degradation

1. INTRODUCTION

Modern utility-scale power engineering is currently undergoing a gradual transformation, driven by the necessity to ensure energy security, mitigate pollutant emissions, and enhance power generation efficiency. Under domestic conditions, hard coal and lignite-fired power units have long played a critical role, serving as the backbone of the national power system's baseload capacity. Despite the growing share of renewable energy sources (RES), coal remains a vital component of electricity generation in Poland. According to data from *Forum Energii*, in 2024, coal accounted for 56.2% of the gross electricity generation, while RES generation reached 29.4% [1]. The trajectory of changes in the energy sector has also been outlined in the

strategic document "Energy Policy of Poland until 2040" (PEP2040), approved by the Council of Ministers on February 2, 2021. This framework identifies the transition toward a low-emission economy as one of the primary pillars for the development of the energy sector [2].

One of the primary approaches to reducing fuel consumption in conventional power units has been elevating the steam operating parameters and implementing supercritical (SC) and ultra-supercritical (USC) boilers. Operating at higher temperatures and pressures of the working fluid enables an increase in thermal cycle efficiency. This directly translates into lower specific fuel consumption and reduced pollutant emissions per unit of generated electricity [3]. However, the implementation of such solutions imposes stringent requirements on the boiler pressure parts, including steam superheaters, headers, and piping operating under high-temperature, high-pressure conditions and long-term stress exposure. Consequently, the selection of structural materials for supercritical units is directly correlated with their operating parameters. These materials must exhibit high resistance to creep, high-temperature oxidation, and microstructural degradation occurring during decades of commercial operation. For this reason, modern power plants utilize new-generation creep-resistant and heat-resistant steels, including austenitic steels designated for components subjected to the highest thermal loads within the boiler assembly [4].

The group of materials utilized under such conditions includes the X10CrNiCuNb18-9-3 austenitic steel, also designated as Super 304H (S304H). This steel was engineered specifically for service in power boiler components operating at elevated temperatures and under stringent creep resistance requirements. Its in-service performance characteristics stem from a precisely balanced chemical composition and microstructural strengthening mechanisms, driven primarily by the presence of Cu-rich precipitates, MX/NbX-type particles, and $M_{23}C_6$ carbides [5,6].

In the context of boiler components, welded joints also play a critical role. The welding process induces zones with distinct thermal histories, encompassing the base metal (BM), the heat-affected zone (HAZ), and the weld metal (WM). These regions can exhibit variations in grain size, precipitate distribution, grain boundary states, and susceptibility to degradation during subsequent service life. Consequently, microstructural analysis of welded joints fabricated from S304H steel is an essential element in evaluating the structural integrity and lifetime of materials deployed in supercritical power boilers [5,6].

2. RESEARCH OBJECTIVE

In this context, it is highly justified to compare different configurations of butt-welded joints fabricated from materials in pre-service and post-service conditions. Investigating joints formed by combining materials in the as-received state and after long-term service – designated as AR/AR, AR/EX, and EX/EX respectively – enables an assessment of how the initial state of the base metals affects the microstructural evolution within the base metal, the heat-affected zone (HAZ), and the weld metal. This approach allows for determining whether prior service degradation of the material influences the nature of microstructural transformations occurring post-welding.

3. RESEARCH MATERIAL

The research material comprised a section of a pipe made of S304H creep-resistant austenitic steel in both the as-received and post-service conditions. Utilizing the material in these two variants enabled a comparison of the impact of operational service on the microstructure of the welded joints, as well as an assessment of the structural differences within the joint zones between the unexploited material and the material subjected to long-term operation at elevated temperatures.

4. EXPERIMENTAL METHODOLOGY

Using the prepared materials, butt-welded joints were fabricated according to the schematic presented in Figure 1, utilizing a filler metal and welding process parameters suitable for the 141 method (TIG/GTAW).

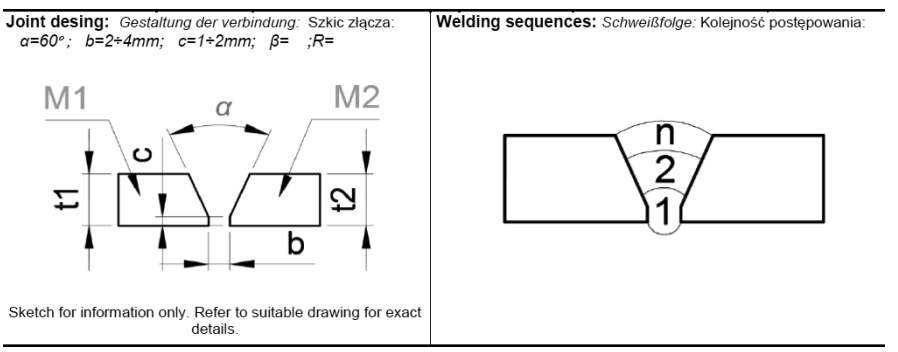

Fig. 1. Schematic diagram of the butt-welded joint configuration.

Within the scope of this study, welded joints were fabricated in three configurations: AR/AR, AR/EX, and EX/EX, where AR designates the material in the as-received state, and EX denotes the post-service material. This matrix enables a comparative evaluation of the base metal – heat-affected zone – weld metal – heat-affected zone – base metal (BM–HAZ–WM–HAZ–BM) assembly as a function of the material condition on both sides of the joint.

a)

b)

c)

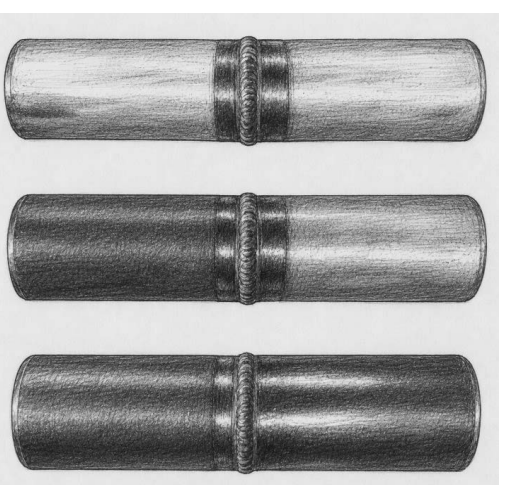

Fig. 2. Schematic view of the post-weld samples for individual butt-joint configurations: a) AR/AR; b) AR/EX and c) EX/EX.

The specimens for microstructural characterization were prepared as transverse cross-sections extracted from the investigated Super 304H steel welded joint. The material was sectioned in a manner that ensured the observation surface encompassed the entire cross-section of the joint, namely the base metal, the heat-affected zone, and the weld metal (Figure 3).

Following the sectioning process, the specimens underwent standard metallographic preparation, which involved grinding with abrasive papers of gradually decreasing grit size, followed by polishing to achieve a mirror-like surface finish. Upon completion of the polishing stage, the metallographic sections were cleaned, degreased, and subjected to electrolytic etching to reveal the joint's microstructure.

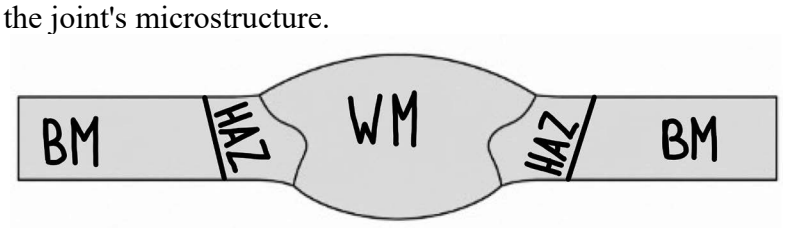

Fig. 3. Representative macrograph showing the cross-sectional view of the welded joint specimen.

5. LIGHT MICROSCOPE OBSERVATION RESULTS

Microstructural observations were performed via light microscopy (LM) on transverse cross-sections after electrolytic etching. Brightfield imaging, darkfield imaging, and differential interference contrast (DIC) were employed to visualize the structure and differentiate microstructural features. The DIC technique provides enhanced contrast for grain boundaries and local surface topography variations on the metallographic section.

Representative areas, in the middle of the thickness, of the base metal, heat-affected zone, and weld metal were selected for microstructural analysis. Initially, the microstructures of the base metal in both the as-received and post-service conditions were documented, serving as a baseline reference for subsequent comparisons of the welded joints (Figure 4).

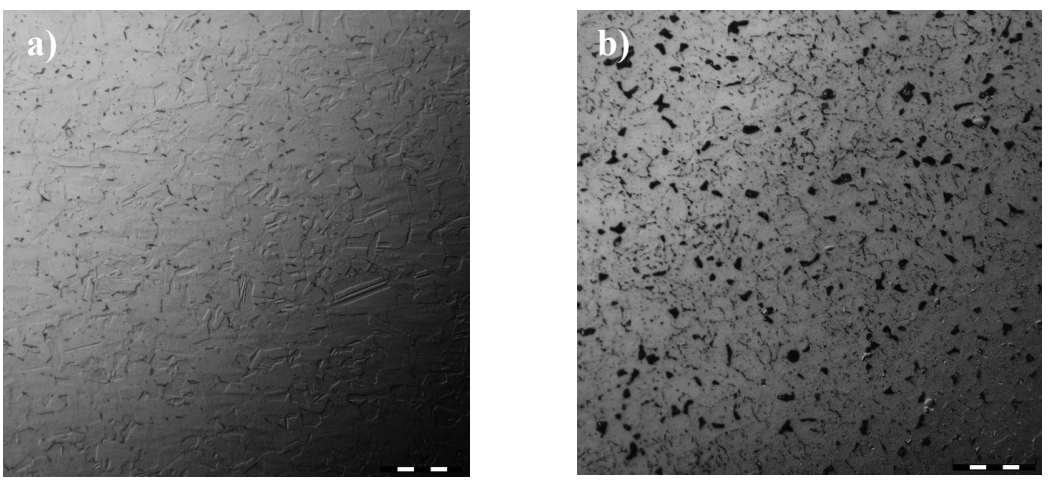

Fig. 4. Light microscopy (LM) microstructure of Super 304H steel utilizing differential interference contrast (DIC): a) as-received (AR), and b) post-service material

Subsequently, the microstructure of the HAZ was presented, where the region adjacent to the as-received material was considered representative of the AR/AR and AR/EX joints, whereas the region adjacent to the post-service material was treated as representative of the EX/EX and EX/AR joints.

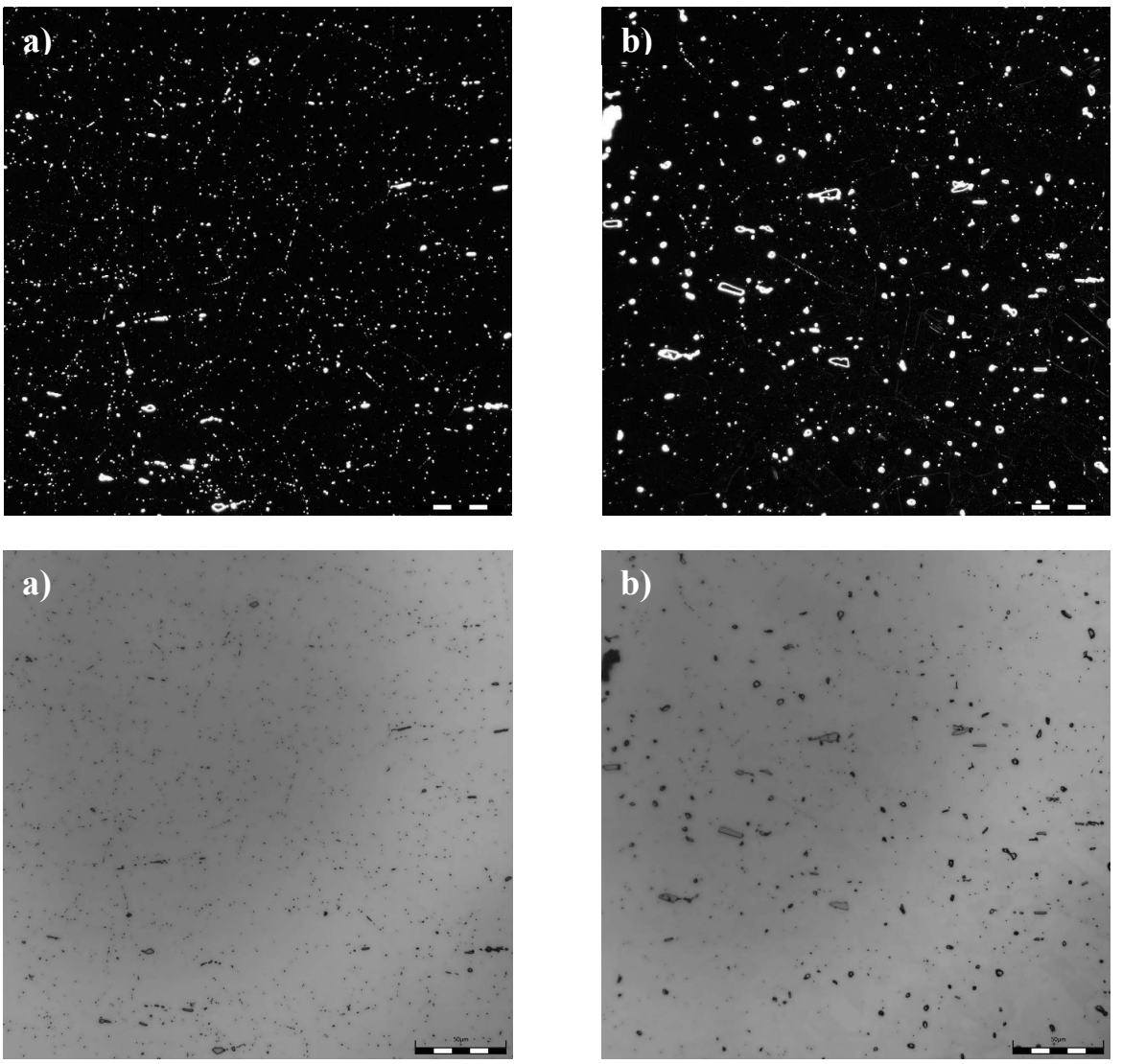

Fig. 5. Comparison of the HAZ microstructure adjacent to the a) AR and b) EX materials within the AR/EX welded joint.

To complete the experimental matrix, the microstructures of the welds fabricated using the filler metal in the individual joint configurations were documented.

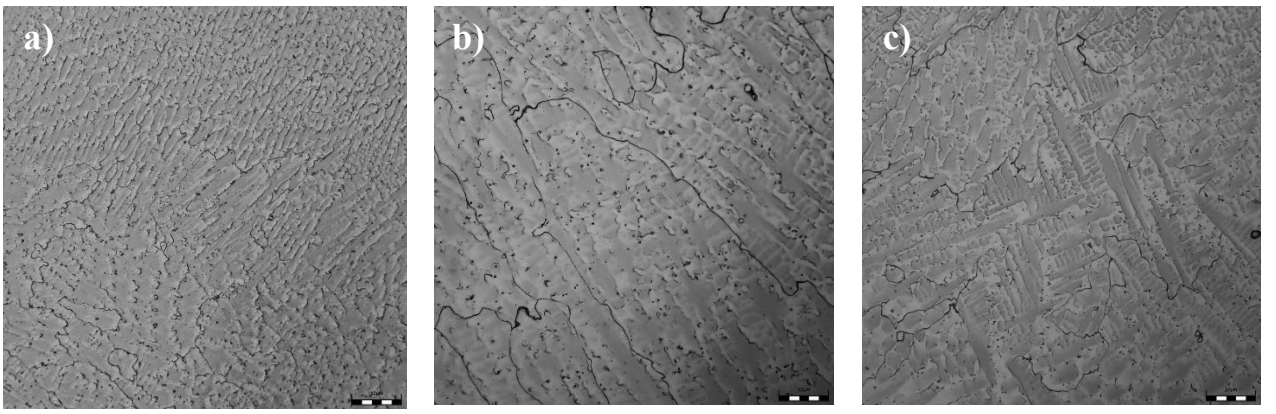

Fig. 6. Microstructure of the newly formed columnar grains; brightfield (BF) light microscopy imaging of the joints: a) AR/EX, b) AR/AR, and c) EX/EX.

5. RESEARCH RESULTS

Light microscopy (LM) observations confirmed a fully austenitic microstructure with prominent annealing twins within the base metal (BM) under both as-received (AR) and post-service (EX) conditions. In contrast, the weld zone exhibited a relatively homogeneous dendritic microstructure typical of the fusion zone (FZ), resulting from rapid weld metal cooling rate. The distinct thermal history of the joined materials led to significant microstructural discrepancies within the heat-affected zones (HAZs) on both sides of the AR/EX joint.

Both HAZ regions exhibited an austenitic matrix with numerous bright precipitates under darkfield (DF) imaging, alongside a local grain growth morphology typical of zones subjected to the weld thermal cycle without melting. The high thermal input accelerated precipitation kinetics and triggered thermally activated phenomena, such as precipitate coarsening (coagulation) both within grain interiors and along boundaries. Consequently, the HAZ possesses the most heavily developed precipitation structure within the entire welded joint, which may ultimately degrade mechanical properties, reduce corrosion resistance, and act as a critical site for future damage initiation or structural failure.

BIBLIOGRAPHY

1. Forum Energii, Rocznik – dane o energetyce, Forum Energii, dane z raportu Transformacja energetyczna w Polsce. Edycja 2025.
2. Ministerstwo Klimatu i Środowiska, Polityka energetyczna Polski do 2040 r.
3. J. Badur, M. Bryk, Krajowe nadkrytyczne bloki węglowe: praca podstawowa czy elastyczna?, „Nowa Energia” 2018, nr 2(62), s. 38–40, https://bibliotekanauki.pl/articles/89591
4. A. Hernas, J. Dobrzański, J. Pasternak, S. Fudali, Charakterystyki nowej generacji materiałów dla energetyki, Wydawnictwo Politechniki Śląskiej, Gliwice 2015.
5. Zieliński, A., Trwałość eksploatacyjna żarowytrzymałych stali o osnowie austenitycznej. Gliwice: Łukasiewicz – Instytut Metalurgii Żelaza, 2021.
6. You Li, Xue Wang, Effect of aging temperatures on the microstructural stability and mechanical properties of Super304H steel, Journal of Materials Research and Technology, Volume 34, 2025, Pages 2651-2661, ISSN 2238-7854, https://doi.org/10.1016/j.jmrt.2024.12.262.

TalentDetector
7th-9th June 2026
Gliwice-Brenna, Poland
DEPARTMENT OF ENGINEERING MATERIALS AND BIOMATERIALS
FACULTY OF MECHANICAL ENGINEERING
SILESIAN UNIVERSITY OF TECHNOLOGY
INTERNATIONAL STUDENTS SCIENTIFIC CONFERENCE

Spersonalizowana hybrydowa osłona balistyczna oparta na kompozytach polimerowo-ceramicznych

Szymon Branc[a], Jakub Niziołek[a], Paweł Wilk[a], Edita Illichmanová [b], Melisa Šnircová [b], Lenka Kuchariková [b], Grzegorz Chladek[c], Klaudiusz Gołombek[c]

[a] student Politechniki Śląskiej, Wydział Mechaniczny Technologiczny, ul. Konarskiego 18A, 44-100 Gliwice
[b] University of Zilina, Faculty of Mechanical Engineering, Department of Materials Engineering, Slovak Republic
[c] Politechnika Śląska, Wydział Mechaniczny Technologiczny, Laboratorium Badania Materiałów, email: klaudiusz.golombek@polsl.pl

Streszczenie: W ramach prac badawczych wytworzono i zbadano hybrydowe kompozyty warstwowe o przeznaczeniu balistycznym składające się z włókien aramidowych oraz stali, spajanych na bazie żywicy epoksydowej.
Abstract: The aim of the study was to manufacture and investigate hybrid layered ballistic composites consisting of aramid fibers and steel, bonded with an epoxy resin matrix.

Słowa kluczowe: kompozyty warstwowe, materiały balistyczne, włókna aramidowe, żywica epoksydowa

1. WSTĘP

Materiały kompozytowe stanowią dynamicznie rozwijającą się grupę materiałów inżynierskich, znajdujących szerokie zastosowanie w obszarach wymagających wysokiej wytrzymałości oraz zdolności do absorpcji energii. Szczególnym obszarem ich wykorzystania jest przemysł obronny oraz systemy bezpieczeństwa, gdzie kluczową rolę odgrywają nowoczesne osłony balistyczne. Tradycyjne, jednorodne materiały konstrukcyjne, takie jak stale pancerne, choć charakteryzują się wysoką odpornością na penetrację, generują znaczny ciężar, co ogranicza mobilność i ergonomię ich użytkowania. Z tego względu współczesne trendy naukowe i technologiczne koncentrują się na projektowaniu lekkich, wielowarstwowych struktur hybrydowych.
Kompozyty hybrydowe łączą w sobie materiały o zróżnicowanych właściwościach mechanicznych i fizycznych, pozwalając na uzyskanie efektu synergii. W materiałach o przeznaczeniu balistycznym powszechnie wykorzystuje się połączenie wysokowytrzymałych włókien polimerowych (np. włókien aramidowych) oraz warstw metalicznych bądź ceramicznych. Włókna aramidowe, charakteryzujące się wybitną wytrzymałością na rozciąganie oraz zdolnością do rozpraszania energii fali uderzeniowej, w połączeniu z

plastyczną lub twardą warstwą zewnętrzną (np. odpowiednio dobraną stalą), tworzą barierę skutecznie zatrzymującą pociski i odłamki. Integralność strukturalną oraz efektywny transfer naprężeń między poszczególnymi warstwami zapewnia osnowa polimerowa, najczęściej w postaci żywicy epoksydowej, cechująca się doskonałą adhezją i stabilnością wymiarową. Ważnym aspektem współczesnego projektowania osłon balistycznych jest ich personalizacja. Dopasowanie geometrii oraz struktury kompozytu do konkretnych wymagań ergonomicznych i operacyjnych pozwala na optymalizację masy pancerza przy jednoczesnym zachowaniu najwyższych parametrów ochronnych.

2. MATERIAŁ I METODYKA BADAŃ

Materiał do badań

Do wytworzenia hybrydowych osłon balistycznych wykorzystano materiały wsadowe pochodzące z odpadów: popioły lotne ze spalania biomasy, a także maty, takie jak kevlar, cordura oraz stal niestopową, a jako osnowę – żywica epoksydowa. Materiały do badań przedstawiono na rysunku 1.

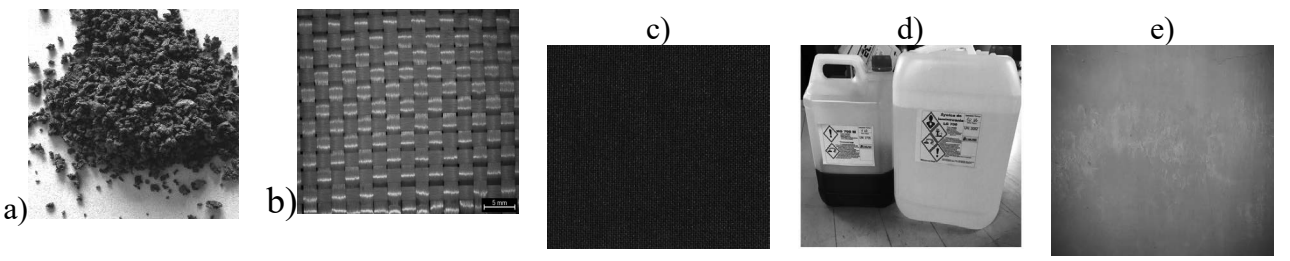

Rys. 1. Materiały: a) popiół lotny; b) kevlar; c) cordura; d) żywica epoksydowa; e) blacha stalowa
Figure 1. Materials: a) fly ash; b) Kevlar; c) Cordura; d) epoxy resin; e) steel sheet

W pierwszym etapie prac przygotowano popiół lotny otrzymany ze spalania biomasy o frakcji <45μm oraz mieszankę żywicy epoksydowej wraz z utwardzaczem w proporcjach 100:30. Następnie pocięto arkusze kevlaru i cordury oraz blachy na odpowiednie wymiary, dostosowane do kieszeni kamizelek kuloodpornych. Osłonę balistyczną złożono z kilku stref: warstw kevlaru, blachy stalowej o grubości 1mm oklejonej cordurą w celu lepszej przyczepności oraz osnowy w postaci żywicy epoksydowej zmieszanej z dodatkiem 5% masowo popiołu lotnego ze spalania biomasy.

Metodyka badań

Na podstawie badań dobrano optymalną ilość warstw kevlaru w celu uzyskania odpowiedniej grubości, dobrano odpowiedni nacisk prasy w procesie łączenia warstw. Obserwację struktury próbek wykonano wykorzystując cyfrowy mikroskop stereoskopowy Leica DVM6 Digital oraz wysokorozdzielczy skaningowy mikroskop elektronowy ZEISS SUPRA 35 wyposażony w detektor składu chemicznego EDS. W celu oceny właściwości

użytkowych wykonano badania odporności na udarowe przebicie tj. testy balistyczne na strzelnicy sportowej z wykorzystaniem amunicji strzeleckiej do broni o kalibrze 9 mm.

3. WYTWORZENIE OSŁON

Proces wytwarzania osłon składał się z kilku etapów: wycięcia arkuszy materiału; przygotowania mieszanki żywicy z popiołem; nasączania warstw kevlaru i ich łączenie; wałkowania w celu równomiernego rozejścia się żywicy; przyklejenia oraz dociążenia blachy w celu uzyskania równego docisku na całej powierzchni styku. Wytworzono kompozyty o następującym układzie warstw:
Kompozyt nr 1 - kordura-blacha-cordura-16 warstw kevlaru-cordura,
Kompozyt nr 2 - 18 warstw naprzemiennych cordura-kevlar.

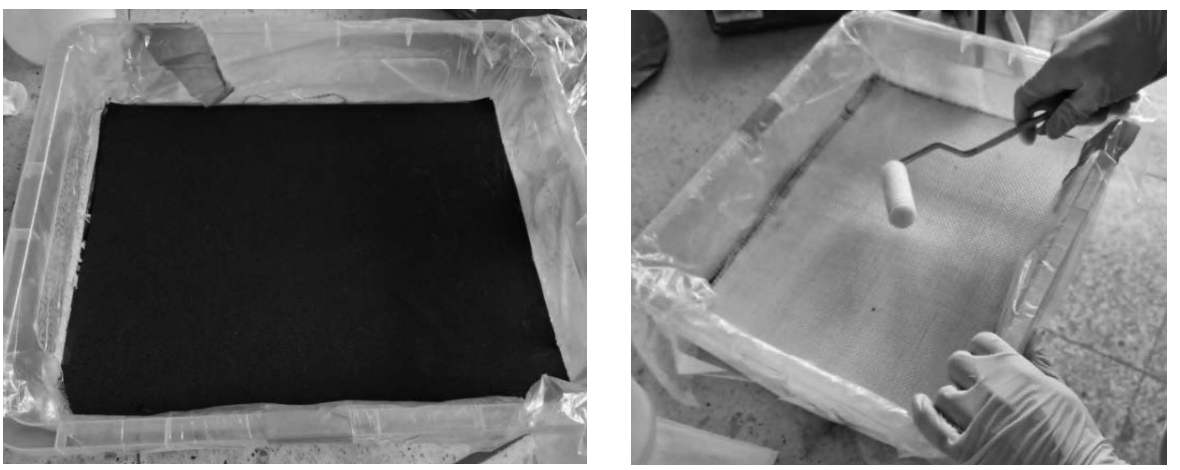

Rys. 2. Proces wytwarzania próbek
Figure 2. Sample production process

3. WYNIKI BADAŃ

Badania powierzchni i mikrostruktury osłon wytworzonych z kompozytów nr 1 i nr 2 wykonano na mikroskopie świetlnym stereoskopowym oraz w wysokorozdzielczym skaningowym mikroskopie elektronowym. Mikrostruktury badanych kompozytów przedstawiono na rysunku 3, a analizy składu chemicznego EDS na rys. 4. Na podstawie badań stwierdzono, że wytworzone osłony charakteryzują się dobrą przyczepnością poszczególnych warstw do siebie oraz do powierzchni stali (dla kompozytu nr 2). Nie zaobserwowano porów i nieciągłości w osnowie z żywicy epoksydowej.

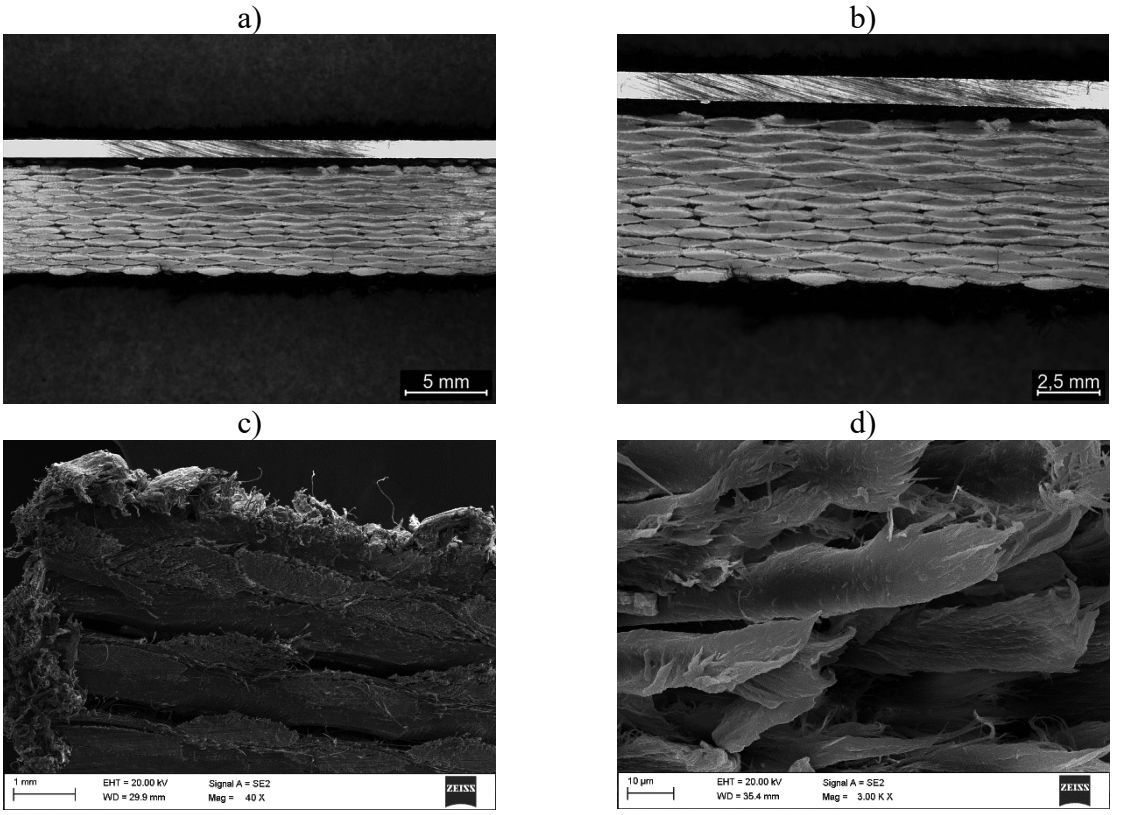

Rys. 3. Struktura badanych próbek: a-b) kompozyt nr.1; c-d) kompozyt nr.2
Figure 3. Structure of tested specimens: a-b) composite no.1; c-*d) composite no.2*

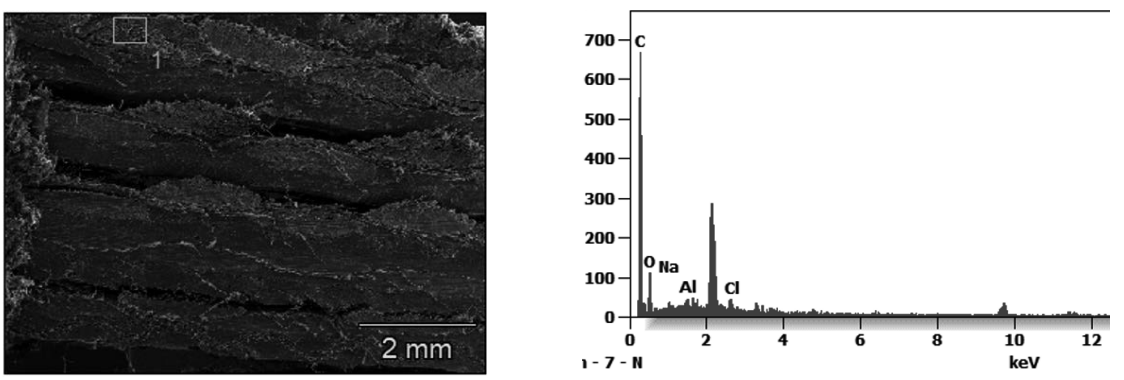

Weight %

	C	*O*	*Na*	*Al*	*Cl*
Area 1	66.9	27.2	1.9	0.7	3.3

Atom %

	C	*O*	*Na*	*Al*	*Cl*
Area 1	74.5	22.8	1.1	0.4	1.2

Rys. 4. Wyniki analizy EDS z zaznaczonego obszaru próbki nr.2
Figure 4. Results of the EDS analysis from the marked area of specimen no. 2

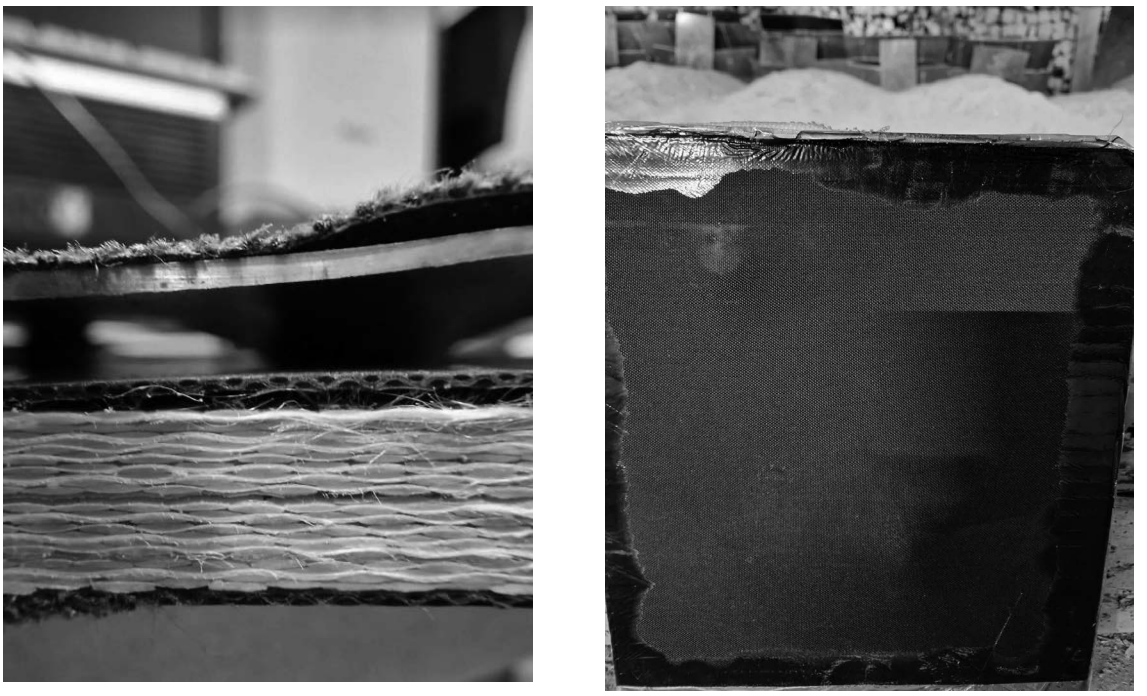

Rys. 5. Widoczne wybrzuszenie w próbce po strzale amunicją 9mm w próbkę nr. 1
Figure 5. Visible bulge in the specimen after firing 9mm ammunition at specimen no. 1

4. WNIOSKI

W ramach badań wytworzono dwie hybrydowe osłony balistyczne o zoptymalizowanym układzie poszczególnych warstw i charakteryzujących się różnymi właściwościami. Głównym materiałem obydwu osłon był kevlar. W jednej z próbek (kompozyt nr 1) zastosowano dodatkowy wkład z płyty wykonanej ze stalowi niestopowej o grubości 1 mm, w celu wzmocnienia konstrukcji, a przede wszystkim rozproszenia energii w trakcie uderzenia pocisku.
Zarówno kompozyt nr 1, jak i kompozyt nr 2 charakteryzują się odpowiednimi właściwościami użytkowymi, przeznaczonych do różnych potencjalnych zastosowań. Podczas testów balistycznych osłona z kompozytu nr 1 skutecznie zatrzymała pocisk kalibru 9 mm wystrzelony z odległości 10 m. Osłona z kompozytu nr 2 wykazuje również dopuszczalne odkształcenie na poziomie poniżej 40 mm, co potwierdza jego zgodność z polską normą PN-V-87000:2011.
Z kolei próbka z kompozytu nr 2 charakteryzuje się innymi zaletami, m.in. znacznie mniejszą masą, lepszą elastycznością oraz łatwością produkcji i obróbki materiału. Niestety osłona wykonana z kompozytu nr 2 w trakcie testów balistycznych nie zatrzymała pocisku 9 mm. Osłona z kompozytu nr 2 ze względu na swoje właściwości, mogłaby z powodzeniem znaleźć zastosowanie jako lekka osłona chroniąca przed bronią białą.

LITERATURA

1. M. Grujicic, B. Pandurangan, B. d'Entremont, The role of adhesive in the ballistic/structural performance of ceramic/polymer-matrix composite hybrid armor, Materials & Design, vol. 41, (2012) 380–393.

2. M. Cegła, W. Habaj, W. Stępniak, P. Podgórzak, Hybrid Ceramic-Textile Composite Armour Structures for a Strengthened Bullet-Proof Vest, Fibres & Textiles in Eastern Europe, vol. 23 1(109), (2015) 82–87.
3. V. Sivakumar, R.S. Pandiyan, R. Sowmiya, Numerical Study on Ballistic Impact Performance of Hybrid Thermoset Composites Subject to Multi-Bullet Hits, Journal of Failure Analysis and Prevention, vol. 23 (1), (2023) 191–205.
4. P. Si, Y. Liu, J. Yan, F. Bai, F. Huang, Ballistic Performance of Polyurea-Reinforced Ceramic/Metal Armor Subjected to Projectile Impact, Materials, vol. 15 (11), (2022) 3918
5. A.K. Bandaru, D.K. Kothandan, H. Chouhan, H. Ma, R.M. O'Higgins, Ballistic impact performance of Kevlar/UHMWPE hybrid composite panels with a liquid thermoplastic resin, Elium, Materials & Design, vol. 252, (2025) 113706.
6. M. Fejdyś, K. Kośla, A. Kucharska-Jastrząbek, M. Łandwijt, Hybride Composite Armour Systems with Advanced Ceramics and Ultra-High Molecular Weight Polyethylene (UHMWPE) Fibres, Fibres & Textiles in Eastern Europe, vol. 24 3(117), (2016) 79–89.
7. M. Grujicic, S. Ramaswami, J. Snipes, Nacre-like ceramic/polymer laminated composite for use in body-armor applications, AIMS Materials Science, vol. 3 (1), (2016) 83–113.
8. A.A. Ramadhan, A.R. Abu Talib, A.S. Mohd Rafie, R. Zahari, High velocity impact response of Kevlar-29/epoxy and 6061-T6 aluminum laminated panels, Materials & Design, vol. 43, (2013) 307–321.
9. M.M. Shokrieh, G.H. Javadpour, Penetration analysis of a projectile in ceramic composite armor, Composite Structures, vol. 82 (2), (2008) 269–276.
10. A. Tasdemirci, G. Tunusoglu, M. Güden, The effect of the interlayer on the ballistic performance of ceramic/composite armors: Experimental and numerical study, International Journal of Impact Engineering, vol. 44, (2012) 1–9.
11. M. Karahan, A. Kus, R. Eren, An investigation into ballistic performance and energy absorption capabilities of woven aramid fabrics, International Journal of Impact Engineering, vol. 35 (6), (2008) 499–510.

PODZIĘKOWANIA

Badania wykonano w ramach XIII edycji projektów badawczych zorientowanych projektowo PBL (Project Base Learning) realizowanych na Politechnice Śląskiej w programie Inicjatywa Doskonałości – Uczelnia Badawcza we współpracy z uczelnią zagraniczną – Uniwersytetem w Żylinie, Słowacja. Szczególne podziękowania Panu Pawłowi Paździorowi (firma *Paweł Paździor Work Project*) za wsparcie techniczne oraz dostarczenie niezbędnych materiałów i specjalistycznych narzędzi.

TalentDetector

7th-9th June 2026
Gliwice-Brenna, Poland

DEPARTMENT OF ENGINEERING MATERIALS AND BIOMATERIALS
FACULTY OF MECHANICAL ENGINEERING
SILESIAN UNIVERSITY OF TECHNOLOGY

INTERNATIONAL STUDENTS SCIENTIFIC CONFERENCE

Simulation of the automation of a selected dye-sensitized solar cell manufacturing process

Jakub Budzynowski[a], Judyta Drygała[b], Aleksandra Drygała[c]

[a] Student, Silesian University of Technology, Faculty of Mechanical Engineering, Konarskiego 18a, 44-100 Gliwice, Poland
[b] Student, Silesian University of Technology, Faculty of Architecture, Akademicka 7, 44-100 Gliwice, Poland
[c] Silesian University of Technology, Faculty of Mechanical Engineering, Department of Engineering Materials and Biomaterials, Konarskiego 18a, 44-100 Gliwice, Poland
email: aleksandra.drygala@polsl.pl

Abstract: Automation of manufacturing processes in photovoltaics plays a crucial role in increasing production efficiency, improving quality, and reducing the manufacturing costs of solar cells. Modern production lines employ advanced control systems, industrial robots, and process monitoring technologies that enable precise execution of individual stages of photovoltaic device fabrication. In this study, a control application for an industrial robot dedicated to substrate handling during the laboratory-scale fabrication of DSSC photoanodes was developed and implemented. The functionality and operational correctness of the proposed system were verified within the FANUC ROBOGUIDE simulation environment.

Keywords: simulation, automation, FANUC ROBOGUIDE, photovoltaics, dye-sensitized solar cells

1. INTRODUCTION

The increasing global demand for electrical energy and the growing environmental degradation issues have led to the intensive development of technologies enabling sustainable and low-emission energy generation. Renewable energy sources are currently gaining particular importance as an alternative to conventional fossil fuel-based energy systems. Among the available renewable energy technologies, photovoltaics represents one of the most rapidly developing fields, utilizing the conversion of solar radiation into electrical energy [1].

The solar effect, consisting in the generation of electromotive force under the influence of Sun radiation, was first observed at the end of the nineteenth century. The intensive advancement of solar energy conversion technologies in subsequent decades led to the classification of photovoltaic devices into four generations, differing in terms of structure, applied materials, and operational parameters (Figure 1) [2].

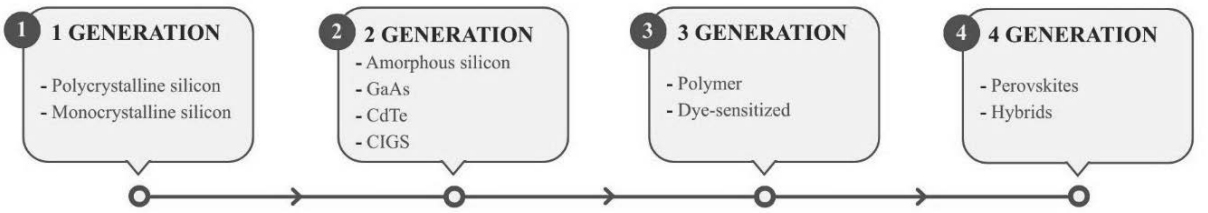

Figure 1. Generations of solar cells [7]

Dye-sensitized solar cells (DSSCs) belong to the third generation of photovoltaic devices. Also referred to as photoelectrochemical cells, they were first developed by Brian O'Regan and Michael Grätzel in 1991 [3]. A characteristic feature of this type of device is the possibility of employing transparent or semi-transparent electrodes, which enables incident radiation to reach the active layer from both sides of the structure, thereby extending the potential application range of the cells [2,4].

The key component responsible for light absorption in DSSCs is the dye layer adsorbed onto the surface of the semiconductor forming the photoanode. Metal oxides, particularly TiO_2, ZnO, and Nb_2O_5, are most commonly used as semiconductor materials due to their favourable electron transport properties and highly developed specific surface area. Transition metal complexes, porphyrin derivatives, phthalocyanines, and organic dyes with high visible-light absorption coefficients are commonly applied as sensitizers. The maximum power conversion efficiency achieved by DSSCs is approximately 15.2% [5,6].

The counter electrode in DSSCs consists of a catalytic layer deposited on a glass substrate coated with a transparent conductive oxide (TCO). Platinum (Pt) is conventionally used as the catalytic material due to its high electrochemical activity in the reduction of the redox couple present in the electrolyte. However, the high cost and limited availability of platinum constitute significant barriers to the large-scale implementation of DSSC technology. Therefore, extensive research has been focused on alternative cathode materials exhibiting comparable catalytic properties. Carbon-based materials, such as graphene, expanded graphite, and carbon nanotubes, are considered particularly promising due to their favourable electrical conductivity and electrochemical performance combined with substantially lower fabrication costs compared to platinum [7,8].

The space between the photoanode and the counter electrode is filled with an electrolyte, typically based on an anhydrous solvent containing a redox system and additives enhancing ionic conductivity and charge carrier mobility. The electrolyte plays a crucial role in dye regeneration and charge transport between the electrodes. In DSSCs, the iodide/triiodide redox couple (I^-/I_3^-) is the most widely used redox system [4]. A schematic representation of the structure of a dye-sensitized solar cell is presented in Figure 2.

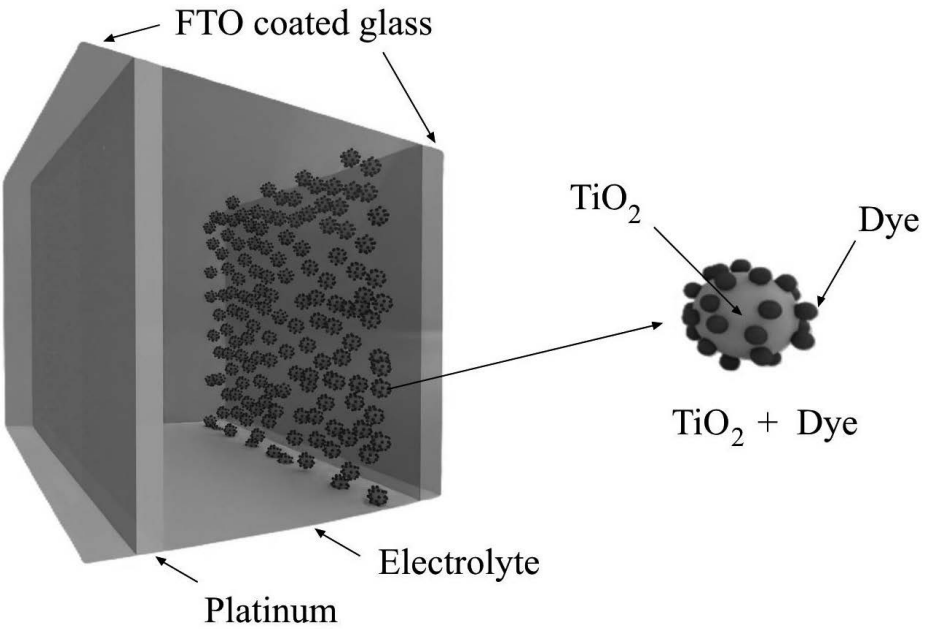

Figure 2. Schematic structure of a dye-sensitized solar cell [4]

Industrial manipulators can be classified according to a variety of structural and operational criteria, with one of the primary classification parameters being the kinematic structure of the system and the associated number of degrees of freedom (DoF). This parameter defines the number of independent motions performed by the manipulator, thereby determining its mobility, positioning capabilities, and ability to execute complex working trajectories. Typical industrial robots are generally equipped with four to six degrees of freedom, enabling simultaneous control of the position and orientation of the end effector in three-dimensional space [9]. The number of degrees of freedom directly results from the configuration of the kinematic chain, consisting of rotational and translational joints that influence both the geometry of the workspace and the dynamic properties of the manipulator, such as stiffness, motion speed, and positioning accuracy [10].

Offline Programming (OLP) constitutes one of the fundamental tools employed in modern industrial robotics systems, enabling the development, analysis, and optimization of robot control programs without interrupting the production process. This approach is based on the use of a virtual workstation model reproducing the geometry of the robot, grippers, peripheral devices, and other components of the technological system within a 3D environment. The digital model enables the design of manipulator motion trajectories, definition of technological operation sequences, and analysis of collisions and workspace accessibility, significantly reducing implementation time and minimizing the risk of integration errors. The application of highly accurate kinematic and dynamic models ensures high consistency between simulated trajectories and the actual motion of the manipulator, allowing optimized control programs to be prepared prior to the physical implementation of the robot in the production environment [11,12].

2. SIMULATION OF THE AUTOMATION OF SUBSTRATE HANDLING FOR DSSC PHOTOANODE FABRICATION

In this study, a simulation of the automation process for substrate handling used in the laboratory-scale fabrication of dye-sensitized solar cell (DSSC) photoanodes was carried out using an industrial robot within the ROBOGUIDE environment. A control program was developed, the operational correctness of the application was verified, and the technological process was visualized in a three-dimensional environment. Due to the required working range and payload capacity, the FANUC M-710iC/45M industrial manipulator was selected, characterized by a working radius of 2606 mm and a payload capacity of 45 kg.

The geometric models of the screen-printing machine (https://grabcad.com/library/silk-screen-printing-machine-1) and the chamber furnace (https://grabcad.com/library/electric-furnace-2) were obtained from the GrabCAD platform and subsequently processed in the Autodesk Inventor CAD environment. As part of the model preparation for simulation purposes, geometry simplification was performed by removing components irrelevant to the technological process analysis, thereby reducing computational complexity and improving the performance of the simulation environment. After the optimization process, the models were exported in the *.stl* format and imported into the ROBOGUIDE environment as components of the robotic workstation infrastructure. The remaining elements of the robotic cell were imported from the internal component library of the FANUC ROBOGUIDE software. The arrangement of the workstation components is presented in Figure 3.

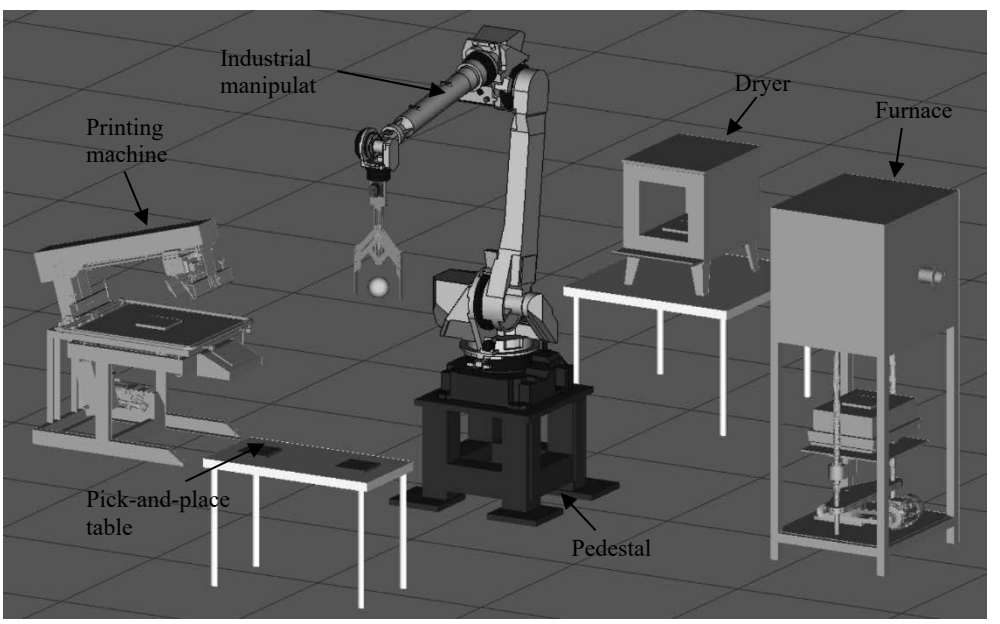

Figure 3. ROBOGUIDE workspace presenting the robotic cell

A 36005f-200 gripper (Figure 4), available in the FANUC ROBOGUIDE component library, was mounted to the mechanical interface of the industrial manipulator. In order to ensure geometric compatibility with the remaining elements of the robotic workstation, the model was scaled along the X, Y, and Z axes by factors of 0.5, 0.7, and 0.2, respectively.

This procedure enabled proper adjustment of the gripper dimensions to the robotic cell configuration and the requirements of the implemented substrate handling process.

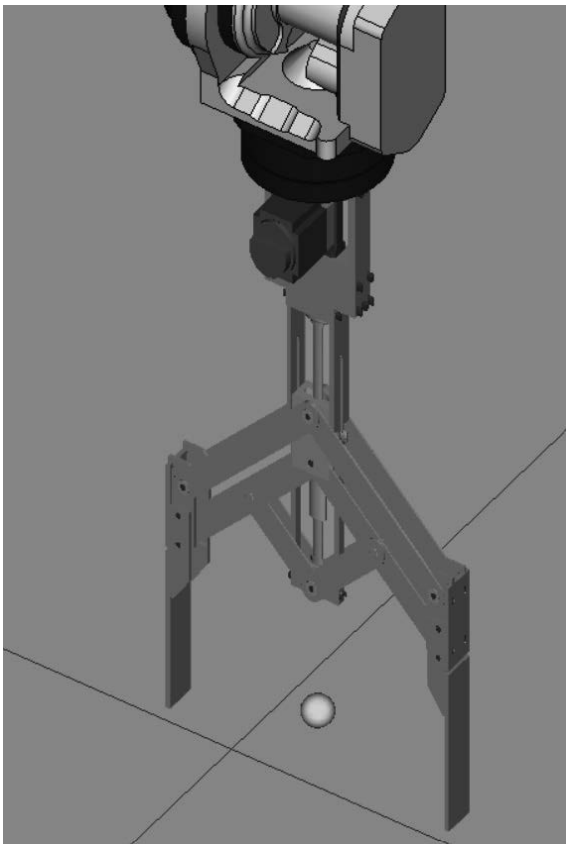

Figure 4. ROBOGUIDE workspace presenting the 36005f-200 gripper

The design of the holder intended for substrate transportation between successive technological workstations was developed in the Autodesk Inventor CAD environment. The designed transport-positioning module (Figure 5) enables simultaneous placement and manipulation of 16 glass substrates, thereby improving the stability of the transport process and the precision of layer deposition within the robotic cell. The implemented solution also contributes to increased process efficiency by reducing the duration of a single technological cycle.

The software architecture of the developed robotic workstation was based on the master program "MAIN", responsible for managing the transport process sequence and calling subroutines dedicated to individual motion operations of the industrial manipulator. The application of a modular program structure enables rapid system reconfiguration through modification of individual subroutines without interfering with the entire control code, thereby significantly simplifying the integration and optimization process of the application.

The adopted control architecture also enables straightforward adaptation of the program to real industrial conditions by replacing temporary *Wait* instructions, used for simulation purposes, with signals generated by automation devices such as sensors or PLC controllers. Each

subroutine contains a complete set of trajectory points associated with a given technological operation, which improves code readability and facilitates subsequent modification of manipulator motion parameters. In the main program, *LBL* labels were implemented before the execution of individual procedures, enabling rapid access to selected sections of the program and supporting diagnostics of the control process.

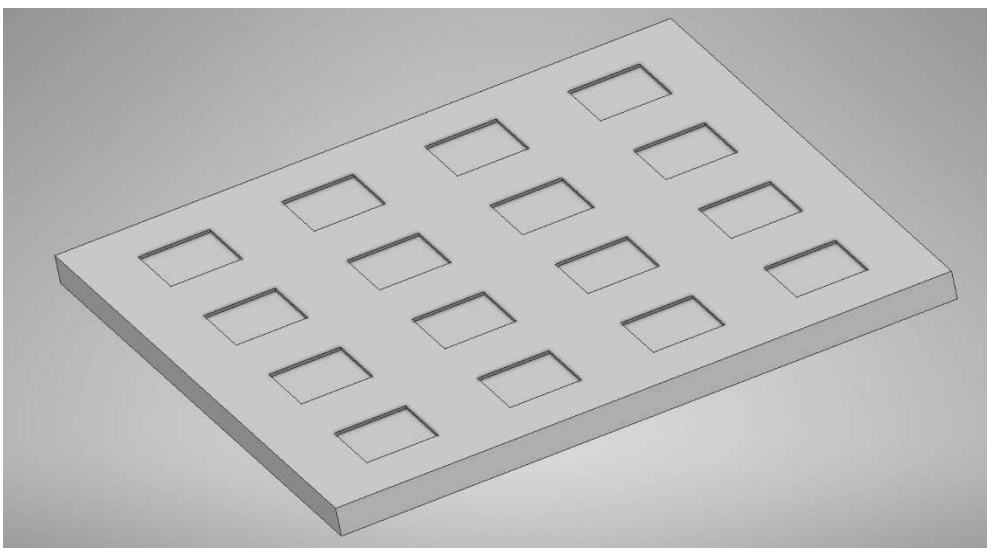

Figure 5. Autodesk Inventor workspace presenting the designed holder intended for substrate transport

The workstation operating cycle is initiated by executing the "HOME" subroutine, responsible for positioning the manipulator in the reference position located above the pick-and-place table. Subsequently, the "pobranie_stol" subroutine is executed, during which the robot picks up the holder containing the substrates. In the next stage, the "zaladunek_druk" procedure is activated, responsible for transporting the substrates to the screen-printing workstation and retracting the manipulator from the machine workspace after completion of the positioning operation. The *Wait* 5s instruction simulates the duration of the TiO_2 layer deposition process, thereby improving the clarity of the process visualization in the virtual environment.

After completion of the printing process, the "rozladunek_druk" procedure is executed, involving retrieval of the holder from the screen-printing machine. Subsequent subroutines, namely "zaladunek_suszarka", "rozladunek_suszarka", "zaladunek_piec", and "rozladunek_piec", are responsible for substrate transport between subsequent technological devices while incorporating time delays corresponding to the actual duration of technological operations. After completion of the heat-treatment process, the "odlozenie_stol" subroutine is executed to place the holder onto the pick-and-place table. The entire cycle concludes with re-execution of the "HOME" procedure, restoring the manipulator to the reference position and preparing the system for the next operating cycle. Figure 6 presents the manipulator motion trajectory in the designed robotic cell, indicated by the light-blue curve.

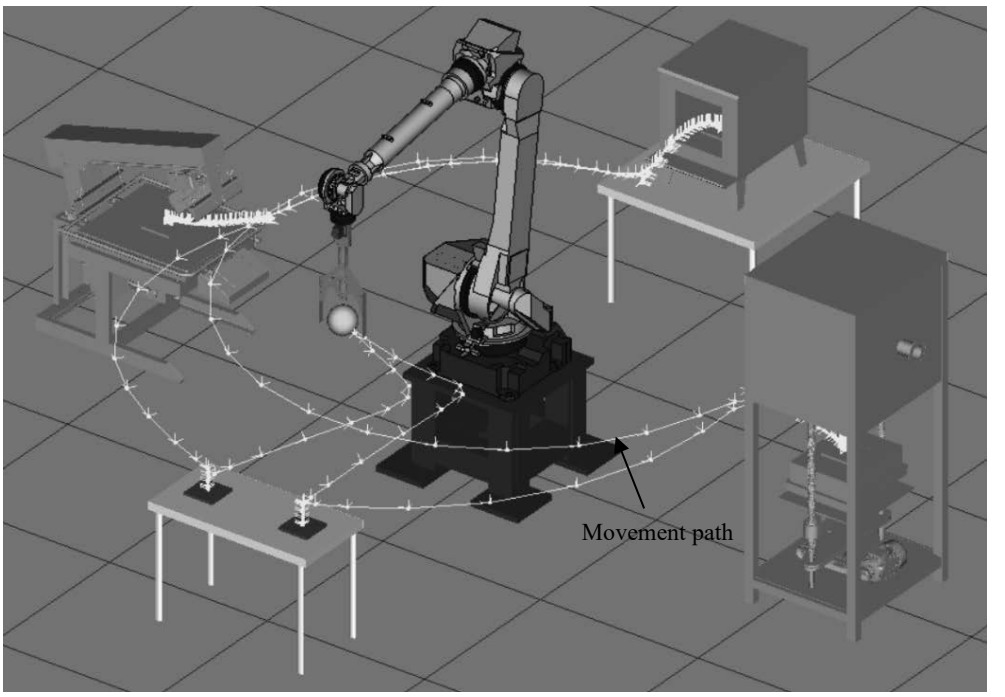

Figure 6. ROBOGUIDE workspace with the industrial manipulator motion trajectory highlighted

3. CONCLUSIONS

The application of the FANUC ROBOGUIDE simulation environment enables the development, implementation, and verification of a control program for an industrial robot dedicated to substrate handling during the laboratory-scale fabrication of DSSCs photoanodes. The developed transport cycle includes the transfer of samples between the pick-and-place table, screen-printing machine, dryer, and chamber furnace according to the predefined technological process sequence. The use of the FANUC M-710iC/45M industrial manipulator ensures high positioning accuracy and repeatability of the end effector, which is crucial for the precise execution of technological operations related to the deposition and processing of photoanode layers.

The virtual simulation environment enables comprehensive analysis of the manipulator motion trajectory prior to the physical implementation of the workstation, allowing optimization of the robot path and elimination of potential collisions with other elements of the technological infrastructure. The application of offline programming makes it possible to develop and test new operating sequences without interrupting the actual production process, while potential logical and collision-related errors can be identified and eliminated at the computer simulation stage.

BIBLIOGRAPHY

1. „Zapotrzebowanie na energię elektryczną”, GLOBALENERGIA, https://globenergia.pl/zapotrzebowanie-na-energie-elektryczna-bedzie-wieksze-niz-kiedykolwiek/, 2026

2. K. Dyndał, G. Lewińska, K. Marszałek, Fotowoltaika. Akademia Górniczo-Hutnicza im. St. Staszica w Krakowie, 2021.
3. B. O'Regan, M. Grätzel, „A low-cost, high-efficiency solar cell based on dye-sensitized colloidal TiO2 films", Nature, t. 353, nr 6346, s. 737–740, 1991.
4. K. Barczak et al., „Wpływ grubości warstwy półprzewodnikowej na własności optoelektryczne barwnikowych ogniw fotowoltaicznych", TalentDetector2023_Summer: International Students Scientific Conference, Brenna, Poland, 26th June 2023, s. 41–49, 2023.
5. M. A. Green et al., „Solar Cell Efficiency Tables (Version 66)", Progress in Photovoltaics, t. 33, nr 7, s. 795–810, 2025.
6. Y. Ren et al., „Hydroxamic acid pre-adsorption raises the efficiency of cosensitized solar cells", Nature, t. 613, nr 7942, s. 60–65, 2023.
7. J. Budzynowski et al., „Co-sensitization of titanium dioxide layers for photovoltaic applications with dyes", TalentDetector2024_Winter : International Students Scientific Conference, Gliwice, Poland, 26th January 2024, s. 55–61, 2024.
8. J. Budzynowski et al., „Application of carbon materials in the production of dye-sensitized solar cells", TalentDetector2025_Winter : International Students Scientific Conference, Gliwice, Poland, 31th January 2025, s. 62–69, 2025.
9. B. Siciliano, Springer Handbook of Robotics, 2nd ed. w Springer Handbooks Ser. Cham: Springer International Publishing AG, 2016.
10. J. J. Craig, Introduction to robotics: mechanics and control, 3. ed., International ed. w Pearson education international. Upper Saddle River, Pearson, Prentice Hall, 2005.
11. S. Mitsi, K.-D. Bouzakis, G. Mansour, D. Sagris, G. Maliaris, „Off-line programming of an industrial robot for manufacturing", Int J Adv Manuf Technol, t. 26, nr 3, s. 262–267, 2005.
12. Z. Pan, J. Polden, N. Larkin, S. Van Duin, J. Norrish, „Recent progress on programming methods for industrial robots", Robotics and Computer-Integrated Manufacturing, t. 28, nr 2, s. 87–94, 2012.

7th-9th June 2026
Gliwice-Brenna, Poland
DEPARTMENT OF ENGINEERING MATERIALS AND BIOMATERIALS
FACULTY OF MECHANICAL ENGINEERING
SILESIAN UNIVERSITY OF TECHNOLOGY
INTERNATIONAL STUDENTS SCIENTIFIC CONFERENCE

Analysis of the stress distribution in the rear upper hitch pin of the Ursus C-330 tractor

Jakub Budzynowski[a], Justyna Janoszka[a], Agata Śliwa[b]

[a] Silesian University of Technology, Faculty of Mechanical Engineering, Student of Engineering and Materials Technologies
email: jb307010@student.polsl.pl; jj307256@student.polsl.pl
[b] Silesian University of Technology, Faculty of Mechanical Engineering, Professor, Department of Engineering Materials and Biomaterials,
email: agata.sliwa@polsl.pl

Abstract: The study presents the results of a numerical simulation of the stress, displacement, and strain distributions occurring in the rear upper hitch pin of the Ursus C-330 tractor, carried out using ANSYS Workbench. The hitch pin was made of C45 steel in a non-heat-treated condition. The component was subjected to loads corresponding to the operating conditions associated with the motion of a medium-sized agricultural trailer.

Keywords: Finite Element Method (FEM), pin, stress distribution, shear

1. INTRODUCTION

Pinned joints are among the most commonly used structural connections in machine design. They constitute a critical component of mechanical systems, as their load-carrying capacity and durability directly affect the reliability, stability, service life, and operational safety of the entire device. In assemblies of working machinery, particularly heavy-duty equipment (including agricultural tractors), articulated joints realized by means of large-size solid pins are widely employed. These components typically operate under highly demanding service conditions, primarily due to the presence of high contact pressures, limited lubrication effectiveness, exposure to corrosive environments, and the necessity of incorporating significant assembly clearances. These factors promote the development of deformations as well as fatigue-related damage [1].

The strength parameters of pinned joints often determine the proper functioning of the entire mechanical system. Overloading or failure of such connections may lead to loss of functional capability, operational downtime, and potential safety hazards for operators. A characteristic feature of pinned joints, classified as detachable connections, is the possibility of repeated assembly and disassembly while maintaining their ability to transmit operational loads [2]. An exemplary pin analysed using the Finite Element Method is presented in Fig. 1.

Fig. 1. Photograph of an exemplary upper hitch pin of the Ursus C-330 tractor [3]

In order to analyse the stress, displacement, and strain fields occurring in the pin under service loading conditions, the Finite Element Method (FEM) was employed. This method constitutes one of the fundamental numerical tools widely used in contemporary engineering calculations and scientific research analyses [4].

The essence of FEM lies in the discretization of a continuous domain by subdividing the geometric model into a finite number of interconnected elements. Subsequently, the governing equations describing the behaviour of the system are solved at characteristic points of the computational mesh, referred to as nodes. Based on the obtained results, the distributions of displacements, strains, and stresses throughout the analysed component are determined [5].

2. MATERIALS AND METHODS

For the preparation of the 3D model, Autodesk Inventor was utilized. The geometric model of the pin was developed based on the manufacturer's design documentation, incorporating a deliberate geometric idealization. During the modelling process, auxiliary components and details not significantly affecting the numerical analysis—such as the cotter pin, chain, and upper handle—were omitted.

Additionally, appropriate surfaces were defined to enable the application of loads and the implementation of boundary conditions. The geometry and dimensions of these surfaces were selected in accordance with ISO 730 and DIN 11026, corresponding to the upper hitch and the trailer drawbar, respectively. The technical drawing of the finalized component is presented in Fig. 2.

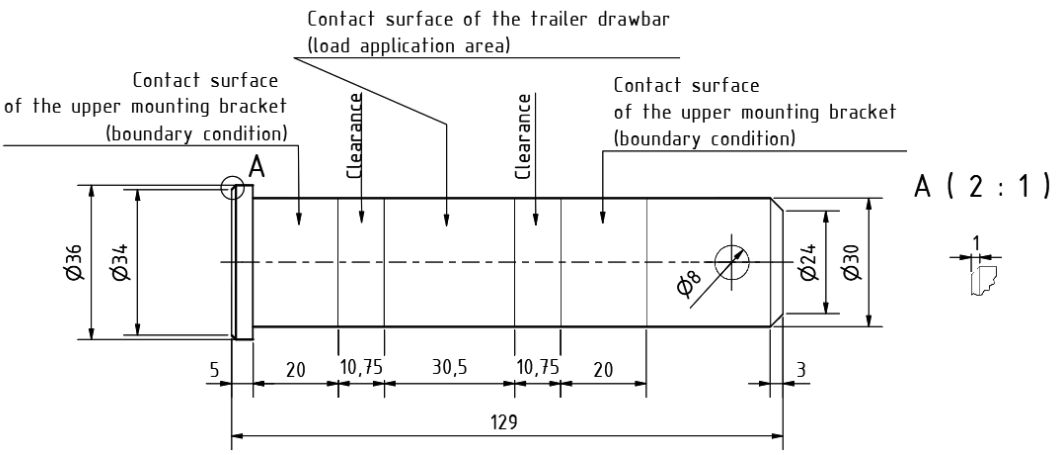

Fig. 2. Technical drawing of the modelled upper hitch pin of the Ursus C-330 tractor

In the next step, the CAD model was imported into the ANSYS Workbench environment. Due to its favourable mechanical properties, high wear resistance, and good machinability, non-heat-treated C45 steel was adopted in the analysis, with the following material parameters: Young's modulus – 210 GPa; Poisson's ratio – 0.3; density – 7800 kg/m³. Considering the type and nature of the applied loading, a "Remote Displacement" boundary condition (Fig. 3) was implemented. In this constraint, translational degrees of freedom were fully restricted in all directions, while rotational freedom was permitted only about the axis coinciding with the longitudinal axis of the pin. Subsequently, a load of 15,000 N was applied, corresponding to the load exerted by a small single-axle agricultural trailer without brakes. The direction of the force and the surface over which it acts are illustrated in Fig. 4. In the numerical meshing process, tetrahedral finite elements were employed, with the element order selected automatically by the software algorithm. A global element size of 2 mm was prescribed. The resulting model discretization is illustrated in Fig. 5.

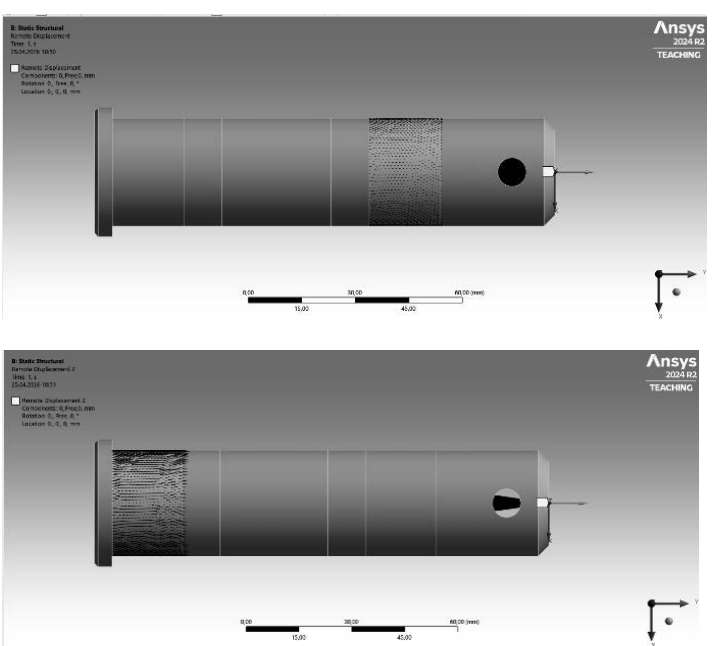

Fig. 3. "Remote Displacement" boundary condition

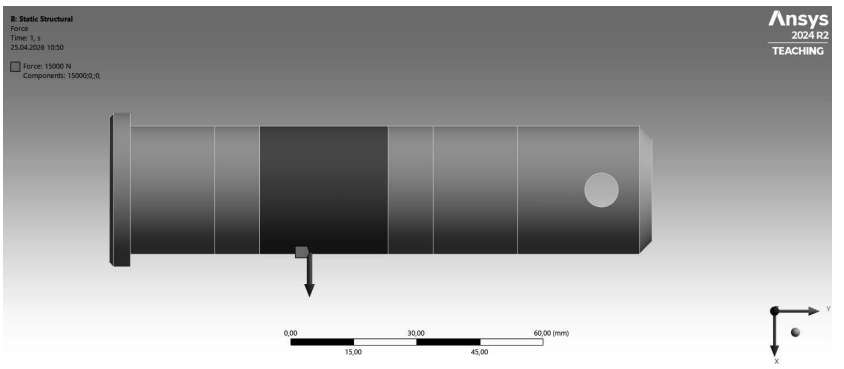

Fig. 4 Applied load

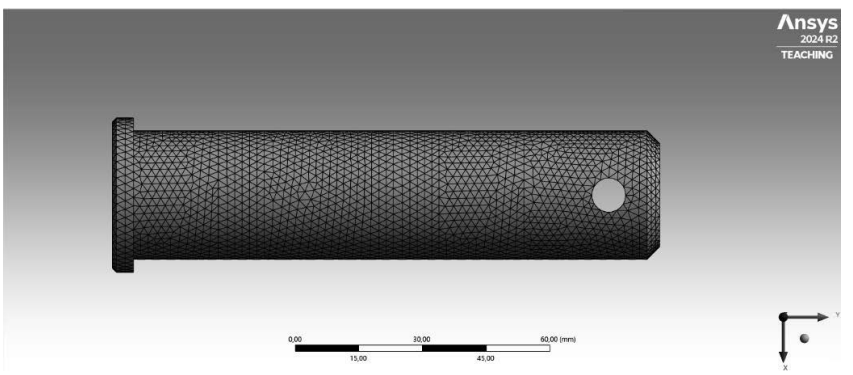

Fig. 5 Model discretization

3. RESULTS

The generated mesh consists of 48,138 elements and 72,948 nodes, and is free of undesirable artifacts. The finite element size was selected appropriately (with a minimum of two elements across the thickness).

Figures 6 and 7 present the distribution of averaged and unaveraged equivalent von Mises stresses. In both cases, the stress distribution is symmetrical, with concentrations at the interface between the upper grip surface and the clearance. A significant discrepancy is observed between the averaged (80.39 MPa) and unaveraged (134.85 MPa) stress values.

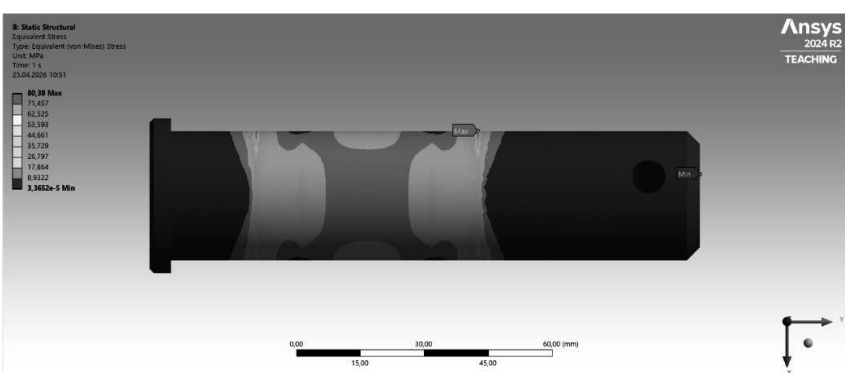

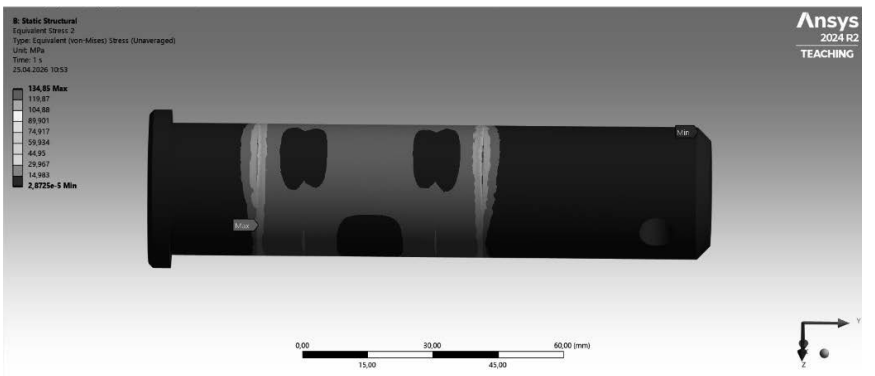

Fig. 7 Unaveraged equivalent von Mises stress

Fig. 8 presents the shear stress distribution on the model surface. According to the legend, the maximum stress value is 38.696 MPa, while the minimum is –42.84 MPa. The highest absolute values (indicated by red and blue colours) are localized in the contact region between the upper mounting bracket surface and the clearance, indicating stress concentrations resulting from load transmission. A more regular stress distribution (green-yellow range) is observed in the central part of the pin.

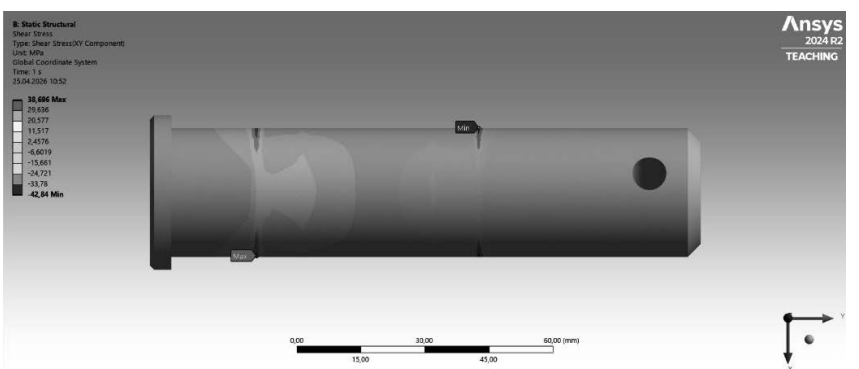

Fig. 8 Shear stress distribution on the model surface

Fig. 9 illustrates the shear stress distribution along the geometric axis of the pin. In this instance, the maximum and minimum values are 12.404 MPa and -12.443 MPa, respectively. The distribution exhibits a more uniform and linear character along the length of the component, which is characteristic of internal cross-sections distant from contact surfaces. Stress extrema occur in the initial and central sections of the pin, coinciding with the peak surface shear stresses. Subsequently, the stress values stabilize near zero (indicated in green), signifying a gradual attenuation of stress concentration effects.

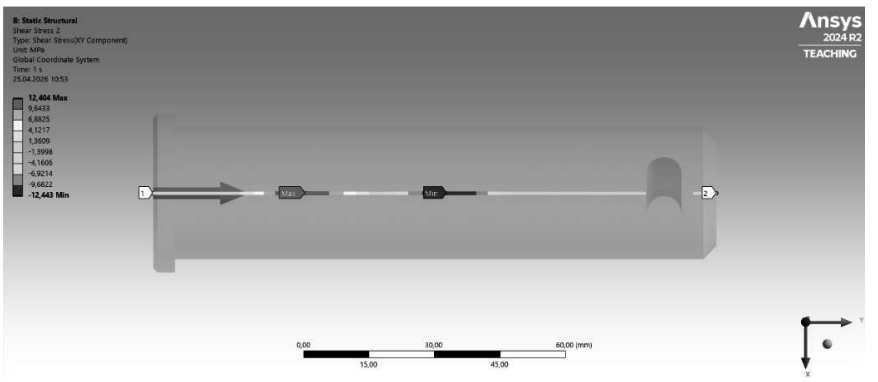

Fig. 9 Shear stress distribution along the geometric axis of the pin

4. CONCLUSIONS

Based on the results of the numerical analysis, it was concluded that the stress distribution induced by the applied load exhibits symmetry relative to the centre of the trailer drawbar contact surface. Simultaneously, significant discrepancies in the equivalent stress values were observed, amounting to 80.39 MPa for averaged results and 134.85 MPa for unaveraged results, respectively. This indicates the necessity for local mesh optimalization in stress concentration areas to achieve a reliable and convergent assessment of these values.

The analysis of the shear stress distribution revealed that the concentration areas coincide with the locations of equivalent stress extrema, both on the model surface and along the geometric axis of the pin. The maximum shear stress value of 42.84 MPa remains below the allowable limits specified in the PN-74/H-84019 standard regarding the mechanical properties of low-alloy steels, which confirms that the strength criteria for the analysed component have been satisfied.

BIBLIOGRAPHY

1. K. Tubilewicz, K. Turczyński, Nowe rozwiązania połączeń przegubowych stosowane w urządzeniach, Technologia i Automatyzacja montażu, Volume 1, 2009.
2. H. Josephs, R. L. Huston, Blake's Design of Mechanical Joints, Boca Raton, 2018.
3. Sworzeń zaczepu górnego C-330, https://www.sklepmaniek.pl/sworzen-zaczepu-gornego-c-330-oryginal-ursus-p-7970.html, dostęp 16.04.2026.
4. A. Fórmaniak, Profesor Olgierd Cecil Zienkiewicz – sylwetka wybitnego inżyniera, Zeszyty naukowe PUNO, Polski Uniwersytet na Obczyźnie w Londynie, 215-223, 2019.
5. A.Z. Fortuna, B. Macukow, J. Wąsowski, Metody numeryczne, WNT, Warszawa, 1993.

TalentDetector

7th-9th June 2026
Gliwice-Brenna, Poland

DEPARTMENT OF ENGINEERING MATERIALS AND BIOMATERIALS
FACULTY OF MECHANICAL ENGINEERING
SILESIAN UNIVERSITY OF TECHNOLOGY

INTERNATIONAL STUDENTS SCIENTIFIC CONFERENCE

Design And Manufacturing of An Adjustable Air Wipe Nozzle

Emrullah Cangi[a], Kutay Ates[a], Huseyin Ali Gok[a], Cemal Meran[a], Koksal Ilhan[b],

[a] Pamukkale University, Faculty of Engineering, Department of Mechanical Engineering, Denizli-Turkiye, email: cmeran@pau.edu.tr
[b] Nexans Turkey Industry, R&D Center, Denizli,Turkiye, koksal.ilhan@nexans.com

Abstract: This study presents the design, aerodynamic analysis, and manufacturing of a novel, adjustable iris-mechanism air knife system for high-speed cable extrusion lines. In continuous manufacturing, residual water on cooled cables causes quality control failures, such as degraded inkjet markings and false spark-test alarms. Conventional air knives use fixed geometries that require costly production shutdowns during cable diameter changes. To solve this, a 4-pin rotary cam iris mechanism was modeled and developed, enabling instantaneous, self-centering adjustments for cable diameters from 30 mm to 100 mm via a single manual control. Operating at an inlet regulator pressure of 1,375 bar (2,38 bar absolute), the system achieves aerodynamic choked flow, accelerating the air curtain to a sonic velocity of 350 m/s to effectively shear off the water film. To avoid the high costs of CNC machining, the entire manifold and link array were produced via Fused Deposition Modeling (FDM) using 4,3 kg of PETG. Experimental validation demonstrates that additive manufacturing can successfully produce high-pressure, hermetically sealed, and functional end-use components for the cable sector.

Keywords: air knife, additive manufacturing, cable drying, fluid mechanics, iris mechanism

1. INTRODUCTION

In modern wire and cable manufacturing plants, such as high-velocity industrial extrusion facilities operating under strict continuous production paradigms, maximizing overall equipment effectiveness (OEE) while maintaining uncompromising surface quality remains a major engineering challenge. During the typical extrusion process, hot polymer insulation jackets or outer sheaths are applied over conductive cores and immediately routed through consecutive water cooling troughs to induce controlled solidification and prevent thermal deformation [6, 8]. While this liquid-immersion cooling phase is indispensable for stabilizing the polymer geometry, the high surface tension of water combined with the high line speed results in a persistent residual moisture film and discrete water macro-droplets adhering to the moving cable jacket. Traditional manufacturing lines require complete surface dryness prior to downstream manufacturing stations. If this liquid layer is not systematically eradicated, it triggers critical defects: the industrial inkjet printers fail to adhere to the wet polymer surface leading to unreadable marking, the continuous high-voltage spark testers generate false ground-fault alarms due to liquid

conductivity, and trapped moisture within tightly wound cable reels initiates rapid micro-structural and microbial degradation. Therefore, non-contact high-velocity air knife systems placed immediately after the cooling bath constitute the most critical pneumatic component of the entire extrusion line topology.

Standard pneumatic drying components deployed across contemporary manufacturing plants predominantly rely on rigid, metallic structures featuring static circular or rectangular discharge orifices [4]. While these traditional configurations perform adequately under unvarying production scenarios, they fail to provide the operational flexibility required by modern agile manufacturing strategies. In industrial environments like Nexans Cable facilities, production schedules frequently dictate rapid transitions between highly diverse product categories, shifting cable outer diameters across a wide spectrum from 30 mm up to 100 mm. Under fixed-diameter air knife regimes, each diameter changeover necessitates an absolute halt of the continuous extrusion line to allow maintenance technicians to mechanically dismantle the existing drying head and replace it with a separate unit matched to the new product geometry. Cooling pool and cable drying line in cable extrusion line was given in Figure 1.

Figure 1. Cooling pool and cable drying line in cable extrusion line

To overcome these structural and economic bottlenecks, this research introduces an interdisciplinary engineering solution that fuses advanced kinematic mechanisms with functional polymer additive manufacturing. The core architecture of the developed system replaces the static orifice with an adjustable rotary cam iris mechanism inspired by high-precision optical camera apertures. By utilizing a coordinated 4-pin arrangement mounted on precision linear guides [2], the mechanism permits real-time, concentric expansion and contraction of the active drying boundary, enveloping any cable diameter between 30 mm and 100 mm in seconds without interrupting the core line feed.

In parallel, rather than using traditional subtractive machining on aluminum or stainless steel blocks, the entire dynamic system—including the complex internal air distribution plenums and nozzle geometries—was manufactured as a functional, end-use product utilizing Fused Deposition Modeling (FDM) 3D printing, with a total material consumption of 4,3 kg of Polyethylene Terephthalate Glycol (PETG). This study explicitly documents the fluid dynamics, kinematic linkages, and material performance criteria under an optimized operational pressure of 1,375 bar, proving that additive manufacturing can successfully transition from rapid visual prototyping into the realm of high-pressure applications

2. ENGINEERING CALCULATIONS AND DESIGN PARAMETERS

The system features four integrated nozzles with an aerodynamic windjet profile and an iris-type central cam mechanism. The thermodynamic, aerodynamic, and static calculations of the system are based on the following operational criteria:

- Operating Diameter Range (D): 30 mm – 100 mm.
- Operating Pressure (P_{op}): 1,375 bar (Gauge) / 2,388 bar (Absolute) at the nozzle entry zone.
- Raw Material: PETG (Polyethylene Terephthalate Glycol — 4.3 kg total structural mass).
- Nozzle Geometry: 4 windjet nozzles with a 1,25 mm fixed throat width, integrated via FDM 3D printing.
- Line Speed (V_L): 200 m/min at minimum cable diameter configuration; 50 m/min at maximum cable diameter configuration.

The 2,388 bar absolute inlet pressure (P_0) utilized in the system exceeds the critical pressure ratio relative to atmospheric pressure (P_{atm} = 1.013 bar). Since the pressure ratio (P_0/P_{atm} = 2.36 > 1.89) is above the critical threshold for air, choked flow conditions occur at the nozzle throat, accelerating the fluid to sonic velocity(Mach 1). The exit velocity (Ve) is determined via the local speed of sound formulation and verified by computational data: $V_e = \sqrt{(\gamma \cdot R \cdot T_t)}$

Based on the system acoustics and stagnation properties, the resulting exit velocity at the throat stabilizes at V_e= 350 m/s.

Using the governing formulations for optimal air jet development, the ideal working distances and corresponding fluid stripping efficiencies were evaluated across various impingement angles. The quantitative assessments are outlined in Table 1.

Table 1: Nozzle Angle and Stripping Efficency Comparison

Nozzle Angle(°)	Optimal Distance(mm)	Water Stripping Efficiency(%)
25	150,2	90,6
30	121,2	86,6
35	100,0	81,9
45	70,0	70,7

Consequent to these evaluations, balances between spatial constraints, aerodynamic performance, and material costs dictated that a 30° angle is ideal for the operational sustainability of the system.

Rapid isentropic expansion and the Joule-Thomson effect cause a drastic temperature drop to -28,8 ℃ the nozzle throat. This sub-zero air stream provides a beneficial secondary cooling (quenching) mechanism for the hot polymer jacket of the extruded cable. Additionally, manufacturing the structure entirely from high-grade PETG ensures the material operates safely above its low-temperature embrittlement threshold, completely mitigating the risk of thermal stress cracking.

Manufacturing the system from PETG via FDM (3D Printing) instead of CNC-machined aluminum increases the internal surface roughness (ε). The resulting localized pressure drop (ΔP) inside the manifold plenum is governed by the Darcy-Weisbach equation: $\Delta P = f \cdot (L/D) \cdot (\rho \cdot V^2/2)$

The high relative roughness (ε/D) stemming from the characteristic 3D-printed layer tracks increases the friction factor (f). To thoroughly compensate for this friction penalty, the design maximizes the volume of the pressure chamber (plenum). The wide internal diameters across the 4,3 kg structural mass effectively reduce the localized flow velocity (V), thereby damping friction losses down to negligible, tolerable levels.

The axial air blast velocity is established at V_e= 350 m/s. When combined counter-currently with the linear line speed (V_L) of the cable, the net relative velocity (V_r) acting on the fluid boundary layer is determined as follows:

- At 30 mm Cable Diameter (200 m/min ≈ 3,33 m/s): V_r = 350 + 3,33 = 353,33 m/s
- At 100 mm Cable Diameter (50 m/min ≈ 0,83 m/s) : V_r = 350 + 0,83 = 350,83 m/s

To mathematically validate the fluid stripping efficiency, the aerodynamic drag force (Fd) acting on a standard spherical water droplet with an average diameter of d_d = 2 mm (drag coefficient C_d = 0,44) adhering to the cable surface was calculated. Referencing the peak relative velocity at the 15 mm cable setup:

$$F_d = 0{,}5 \cdot C_d \cdot \rho \cdot V_r^2 \cdot A_d \;\Rightarrow F_d = 0{,}5 \cdot 0{,}44 \cdot 1{,}225 \cdot 353{,}33^2 \;\cdot (\pi \cdot 0{,}001^2) \approx 0{,}105N$$

Given that the nominal weight of an identical water droplet is roughly 0.00004 N, the 0.105 N aerodynamic drag force exerted by the air knife strips and expels the droplet with an acceleration approximately 2625 times greater than gravity.

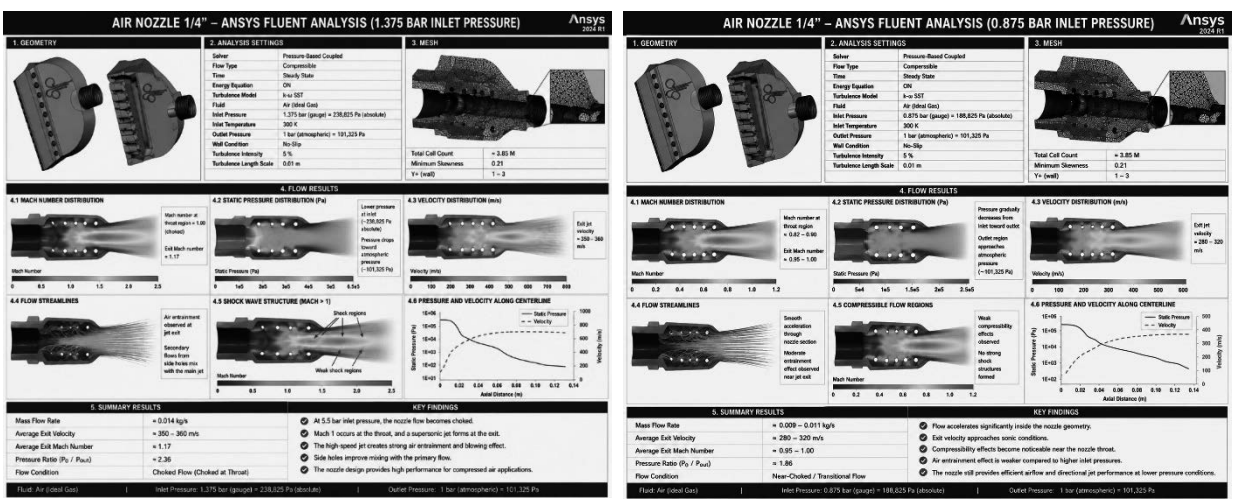

Figure 2. ANSYS CFD Analysis of the Air Knife

Table 2: Fluid dynamics and aerodynamic flow parameters of the system at 0,875 bar and 1,375 bar.

Parameter	**0,875 bar**	**1,375 bar**
Absolute Inlet Pressure	188,825 Pa	238,825 Pa
Exit Velocity	~280–320 m/s	~350–360 m/s
Exit Mach Number	~0,95–1,00	~1,17
Entrainment (Ambient Air Intake)	Moderate level	Strong
Mass Flow Rate	~0,009–0,011 kg/s	~0,014 kg/s
Flow Regime	Near-Choked	Choked Flow

The data presented in the Figures 2 were obtained from the analyses conducted via ANSYS. These data were utilized as a baseline for all other subsequent calculations.

Fluid dynamics and aerodynamic flow parameters of the system at 0,875 bar and 1,375 bar was given in Table 2. Based on the ANSYS CFD analyses, it was observed that the designed air knife successfully meets the theoretical relative velocity calculations down to a minimum operating pressure of 0,875 bar. Since pressure is an intensive thermodynamic property, it is uniform across the internal manifold. Therefore, while the required system pressure remains 0,875 bar, the total minimum mass flow rate ($\dot{m}_{total}$) required from the compressor for the simultaneous operation of the four air knives is calculated as the sum of individual nozzle flows:

$$\dot{m}_{total} = 4 \,.\, 0.11 = 0.044\ kg/s$$

Based on the simulation results, optimizing the drying line's required supply pressure down to the 0.875 - 1.375 bar range decreases the compressor's specific power consumption, resulting in a significant overall energy saving in the operation.

The coordinated radial translation (Δr) of the 4 independent nozzle blocks is precisely adjusted via the manual rotation of the central cam disk by an operator angle (θ):

$$\Delta r = f(\theta)$$

Although the optimal operational pressure is 1,375 bar, the mechanical linkages were designed to safely withstand a maximum factory compressor surge pressure of 5,5 bar (0,55 MPa). This maximum internal gauge pressure exerts a continuous outward pneumatic force trying to push each sliding nozzle block out of its tracks.Assuming a standard nozzle rear projected area(A_{proj}), the individual static pneumatic thrust force (F_p) is formulated as:

$$F_p = P_{surge} \cdot A_{\text{proj}}$$

To keep all 4 nozzles securely centered at the desired setpoint, the manual actuation torque (T_{act}) that the operator must exert to adjust the disk depends on the friction coefficient of the PETG layers (μ) and the meanpitch radius of the cam disk (R_{avg}):

$$T_{act} = 4 \cdot F_p \cdot \mu \cdot R_{avg}$$

This high outward pneumatic force highlights a critical safety requirement: the mechanical actuation lever must incorporate a positive self-locking design to completely prevent the iris mechanism from opening unintentionally under active operational pressures.

3. RESULTS AND DISCUSSION

Experimental evaluations confirmed that the rotary cam iris mechanism smoothly adapts to cable outer diameters ranging from 30 mm to 100 mm. Its inherent self-centering geometry perfectly aligns the aerodynamic focal point with the cable axis at all times, guaranteeing uniform circumferential drying and eliminating the need for production line stoppages. Under an operational regulator setup, the converging nozzles accelerated the compressed air to local sonic velocities (Mach 1), successfully establishing a choked flow regime [3, 5]. Directed at a 30-degree impingement angle, this high-velocity air curtain generated substantial aerodynamic drag to effectively shear the moisture film off the cable surface [1], while the isentropic expansion of the exiting air provided a secondary quenching effect on the hot polymer jacket [7].

Structurally, the integrated pneumatic manifold, printed using 4.3 kg of PETG, successfully withstood continuous internal hoop stresses without any deformation or inter-layer delamination. The optimized printing strategy ensured complete pneumatic hermeticity. Moreover, the rigid

mass of the monolithic unit effectively dampened operational vibrations generated by the high-speed airflow and cable movement, ensuring stable and reliable factory-floor operation.

4. CONCLUSION

The additively manufactured iris-mechanism air knife efficiently resolves chronic downtime issues in high-speed cable extrusion lines. By replacing static metallic nozzles with a dynamic, 3D-printed PETG assembly, production stoppages during 30 mm to 100 mm diameter transitions are completely eliminated. Operating under choked conditions, the system achieves Mach 1 velocities (350 m/s) for superior aerodynamic drying. Producing this complex, 4.3 kg functional unit demonstrates that Fused Deposition Modeling (FDM) is a robust and viable alternative to expensive CNC machining for industrial high-pressure pneumatic equipment. After all design steps, the manufactured of adjustable air wipe nozzle is given in Figure 3.

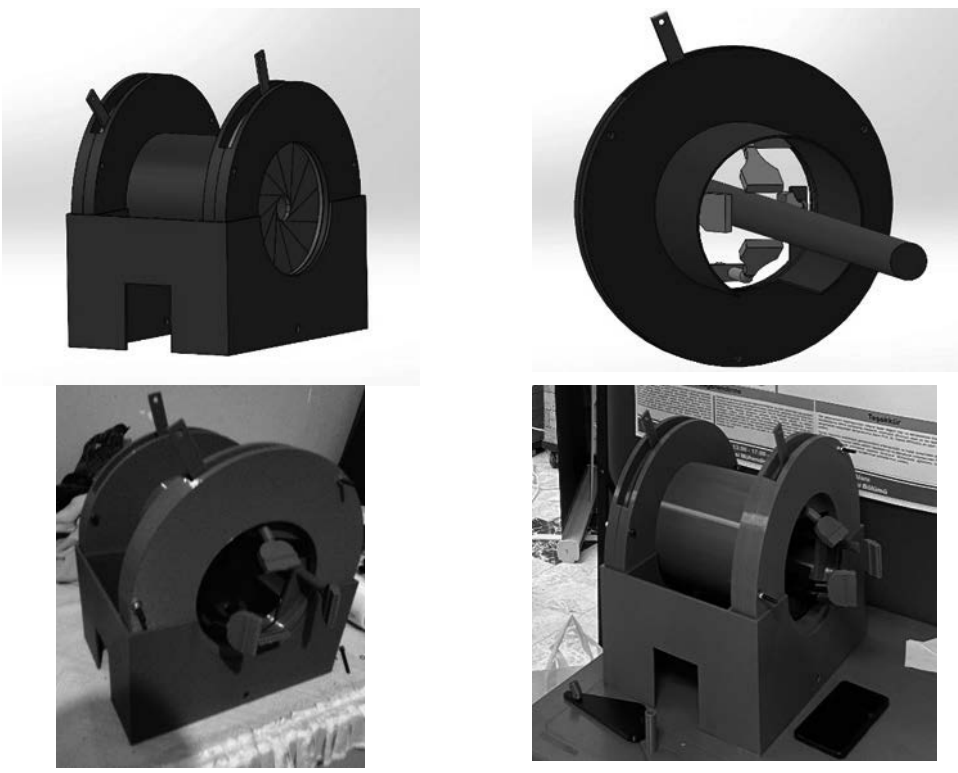

Figure 3. The manufactured of adjustable air wipe nozzle

BIBLIOGRAPHY

[1] Beltaos, S. (1976). Oblique impingement of circular turbulent jets. *Journal of Hydraulic Research, 14*(1), 17-36. https://doi.org/10.1080/00221687609499671
[2] Budynas, R. G., & Nisbett, J. K. (2014). *Shigley's mechanical engineering design* (10th ed.). McGraw-Hill Education.
[3] Çengel, Y. A., & Cimbala, J. M. (2014). *Akışkanlar mekaniği: Temelleri ve uygulamaları* (T. Engin, Çev.; 3. baskı). Güven Bilimsel.

[4] Doe, J. (1995). *Adjustable air wipe apparatus for elongated materials* (U.S. Patent No. 5,432,109). U.S. Patent and Trademark Office. https://patents.google.com/patent/US5432109A/en
[5] Munson, B. R., Okiishi, T. H., Huebsch, W. W., & Rothmayer, A. P. (2013). *Fluid mechanics* (7th ed.). John Wiley & Sons.
[6] Vaynman, H. A., & Fine, M. E. (2001). Continuous extrusion processes in wire and cable manufacturing. *Journal of Materials Engineering and Performance, 10*(2), 154-159. https://doi.org/10.1361/105994901770345150
[7] Viskanta, R. (1993). Heat transfer by single and multiple arrays of impinging two-dimensional jets. *Experimental Thermal and Fluid Science, 6*(2), 111-134. https://doi.org/10.1016/0894-1777(93)90022-B
[8] Wright, R. N. (2011). *Wire technology: Process engineering and metallurgy*. Butterworth-Heinemann. https://doi.org/10.1016/C2009-0-61845-8

TalentDetector

7th-9th June 2026
Gliwice-Brenna, Poland

DEPARTMENT OF ENGINEERING MATERIALS AND BIOMATERIALS
FACULTY OF MECHANICAL ENGINEERING
SILESIAN UNIVERSITY OF TECHNOLOGY

INTERNATIONAL STUDENTS SCIENTIFIC CONFERENCE

Structure and properties of a silicon-based coating deposited onto a hot-work steel substrate

Martyna Ciaś[a], Alexandra Kuś[a], Matěj Macák[b], Filip Škoda[b], Michal Lattner[c], Antonin Kříž[c], Jakub Polis[d], Marcin Staszuk[d], Daniel Pakuła[d]

[a] Student of Faculty of Mechanical Engineering, Silesian University of Technology, Poland
[b] Student of Faculty of Mechanical Engineering, Jan Evangelista Purkyně University in Ústí nad Labem, Czech Republic
[c] Faculty of Mechanical Engineering, Jan Evangelista Purkyně University in Ústí nad Labem, Czech Republic
[d] Department of Engineering Materials and Biomaterials, Faculty of Mechanical Engineering Silesian University of Technology, Poland
email: daniel.pakula@polsl.pl

Abstract: This work was carried out as part of the 14th edition of the PBL (Project-Based Learning) project at the Faculty of Mechanical Engineering at the Silesian University of Technology in Gliwice (Poland) and and at the Faculty of Mechanical Engineering, Jan Evangelista Purkyně University, Ústí nad Labem, (Czech Republic). The paper presents the results of research on the structure and functional properties of a silicon-based nanocomposite protective coating deposited on an X40CrMoV5-1 hot-work tool steel substrate. The study numerically analysed the deformation distribution (FEA), as well as examined the structure, topography of the surface, layer thickness and tribological properties of the coating.

Keywords: X40CrMoV5-1 steel, silicon coating, functional properties, tribology, FEM, SEM

1. INTRODUCTION

The X40CrMoV5-1 hot work tool steel has good tempering resistance, high hardenability and high ductility. Thanks to maintaining high strength parameters, it is widely used in industry, e.g. in the production of forging dies, pressure die-casting molds and extrusion tools. However, in order to protect the surface of the material from extreme thermomechanical loads and intensive tribological wear, it is necessary to use protective coatings deposited with PVD techniques [1, 6].

These coatings play a key role in increasing the durability and resistance of surfaces to wear and contact pressures, which has also been proven for other engineering materials operating under load [2, 3, 4]. Of particular importance in this context are silicon-based hard nanocomposite coatings, which are increasingly being used thanks to their unique functional properties. The introduction of silicon into the coating structure allows for the formation of an

amorphous phase (e.g. Si_3N_4) at the nanocrystalline grain boundaries. This phase effectively blocks the dislocation movement and promotes grain fragmentation (according to the Hall-Petch effect), which leads to a drastic increase in the hardness and resistance of the coating to plastic flow [5].

As shown by previous FEM numerical analyses for top layers, properly designed PVD coatings act as a act as a rigid supporting barrier that effectively reduces the penetration of stresses and deformations into the softer substrate [7]. The use of such layers in industrial applications significantly reduces material consumption and lowers the coefficient of friction, which in turn contributes to a multiple extension of tool life.

The aim of this study is to present and evaluate the functional properties of a silicon coating deposited on a substrate of X40CrMoV5-1 steel, under mechanical and tribological loads.

2. MATERIALS AND METHODOLOGY

The study used samples of X40CrMoV5-1 tool steel in an uncoated state and with a silicon coating applied.

The structure, topography of the surface and traces of tribological damage were analysed using a scanning electron microscope (SEM) at an accelerating voltage (EHT) of 20.00 kV, using the detection of secondary electrons (SE2). In addition, for spatial assessment of morphology, area scans of the surface (e.g. 10x10 µm) were performed using profilometry/AFM. A TESCAN VEGA 3 scanning electron microscope (SEM) was also used to conduct a detailed analysis of the chemical homogeneity of the deposited layer. Observations were conducted on prepared metallographic cross-sections.

Numerical analysis (MES) of the behavior of the coatings under load was performed in the ANSYS (Static Structural) environment. A perpendicular concentrated force of 60 N was simulated on a cylindrical sample with a diameter of 20 mm, analyzing the redistribution of stresses and displacements.

Both coated and uncoated samples were subjected to ball-on-disc tribological studies using a device from CSM Instruments. The counter-sample was a zirconium oxide (ZrO_2) ball with a diameter of 6.00 mm. The tests were carried out over a distance of 5000 cycles, with a linear speed of 5.53 cm/s, under a constant normal load of 5 N, at a temperature of 20°C and a humidity of approx. 50%. The fretting test was performed using the “ball-on-flat” method on an Anton Paar Revetest RST device, with a zirconium ball (Number of cycles 5000; Normal load [N] 5; Distance [mm] 13; Acquisition rate [Hz] 2).

3. RESULTS

Cross-sectional analysis revealed that the resulting coating has a dense, continuous structure with no visible pores and excellent adhesion to X40CrMoV5-1 steel. Point measurements showed an average thickness of approx. 4 µm. In order to verify the material structure, a microanalysis of the chemical composition was performed on the cross-section of the layer. The obtained spectrum unambiguously confirms the dominant share of silicon (Si) as the main building block of the studied coating, which is in line with the technological assumptions of the coatings. The surface of the studied coating shows a spherical morphology, characteristic of columnar growth in gas phase deposition processes (Fig. 1).

a) b)

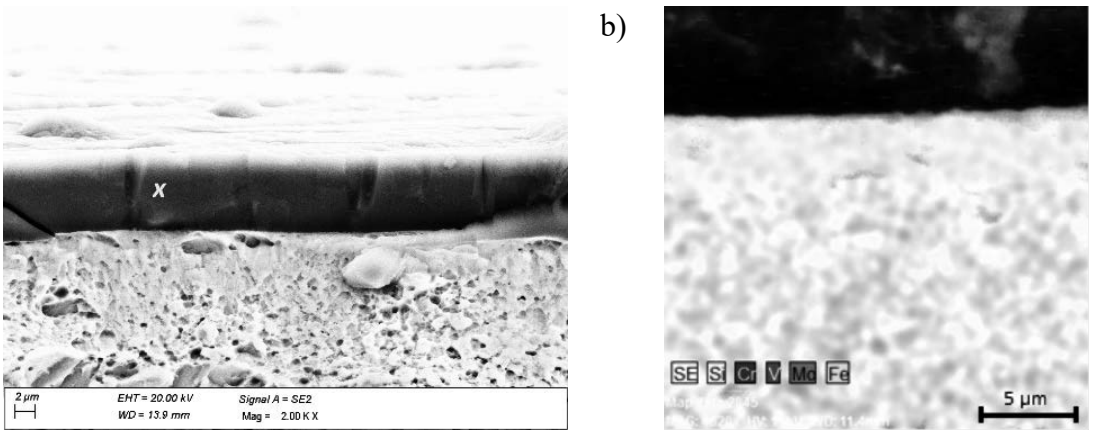

Figure 1. Characteristics of the silicon-based coating on a cross-section: a) Microscopic analysis (SEM), b) Elemental mapping

Microscopic images reveal a uniform structure with visible, isolated microparticles (so-called droplets) that naturally condense on the surface during the application process (Fig. 2a). Apart from these micro-defects, the coating is consistent and free of a network of cracks. A 3D area scan (Fig. 2b) confirms the uniform distribution of spherical elevations, which is crucial for the stabilization of sliding conditions and pressure distribution during tribological interaction.

a) b)

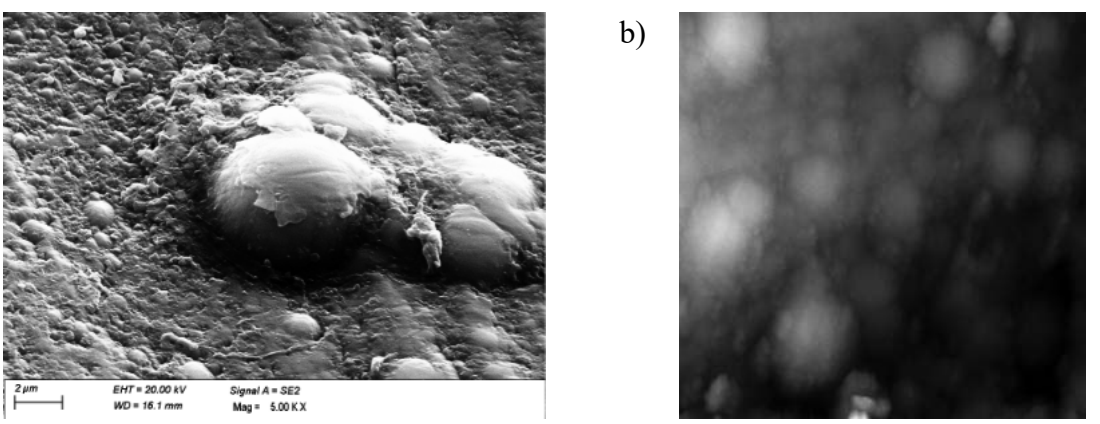

Figure 2. Topography of the silicon coating surface: a) SEM image showing granular morphology with microparticles, b) 3D area scan (10x10 µm)

The uncoated X40CrMoV5-1 tool steel has been subjected to intense wear due to cyclic contact with hard ceramics (ZrO_2). In the SEM image (Fig. 3a), the intensive mechanisms of abrasive and adhesive wear are clearly visible. The hard ball plowed deep grooves in the soft steel substrate, leading to seizure, tearing out fragments of the material and its strong plastic flow in the contact zone.

The application of the coating completely changed the characteristics of the contact area, structure seen in the countersample interaction path corresponds to the original spherical morphology of the silicon coating. The mechanical resistance of the tested layer is so high that the hard ceramic countersample was not able to cause any macroscopic damage, microcracks or delamination on it.

In order to unequivocally prove the lack of penetration into the steel substrate, a chemical composition microanalysis (EDS) was performed (Fig. 3c). The complete absence of a strong iron (Fe) signal from the base material within the contact track is indisputable evidence that the the coating did not wear through, retaining maintained structural continuity and providing an effective barrier to the hard counter sample.

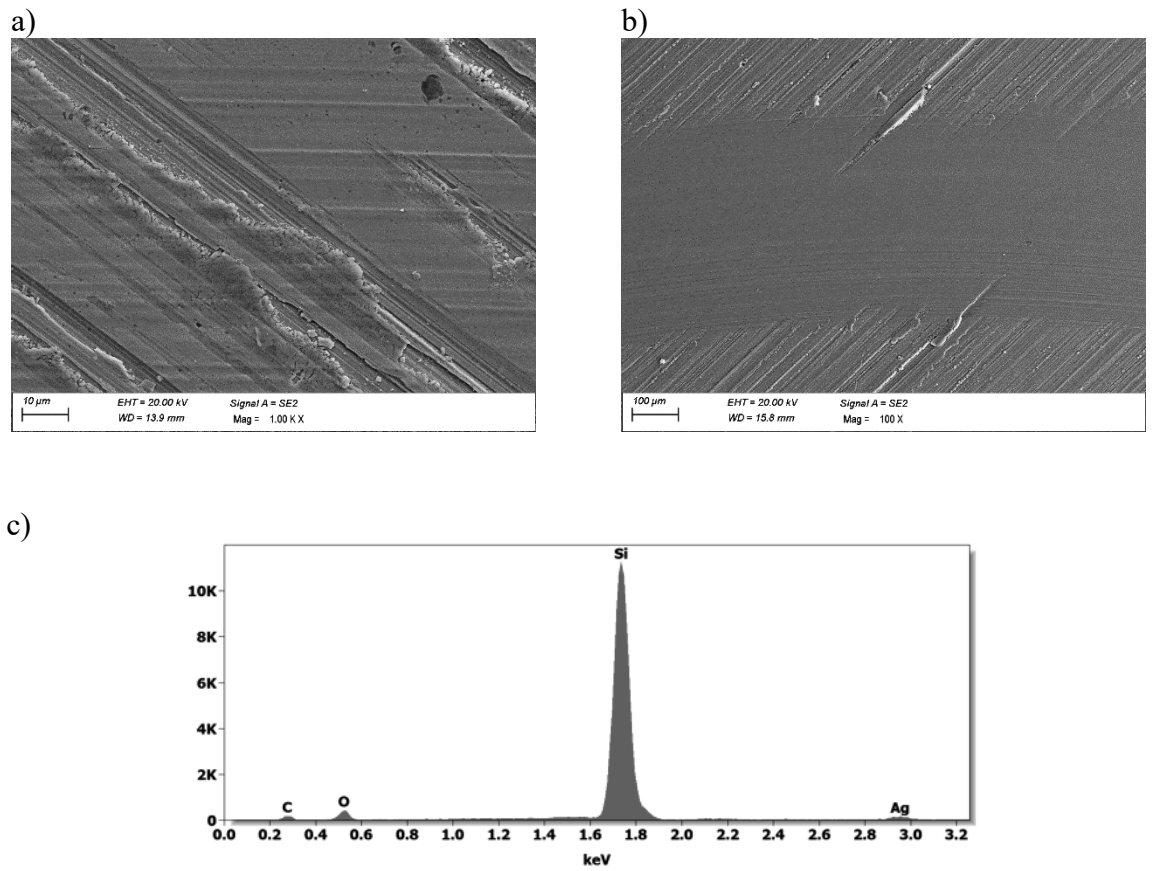

Figure 3. Analysis of the contact zone after the tribological test: a) SEM image of the wear trace on an uncoated X40CrMoV5-1 steel specimen b) SEM image of the wear trace for the silicon coating sample, c) EDS spectrum from inside the friction path for the silicon coated sample.

The SEM image of the countersample after the test (Fig. 4) confirms the benign nature of the system's tribological interaction. Only subtle scratches in the contact zone and signs of material transfer (formation of protective tribofilm) were recorded.

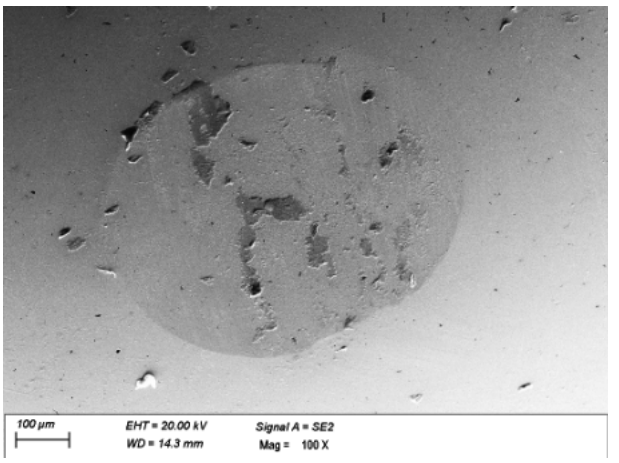

Figure 4. Morphology of the contact zone on zirconium oxide (ZrO_2) counter sample after the test

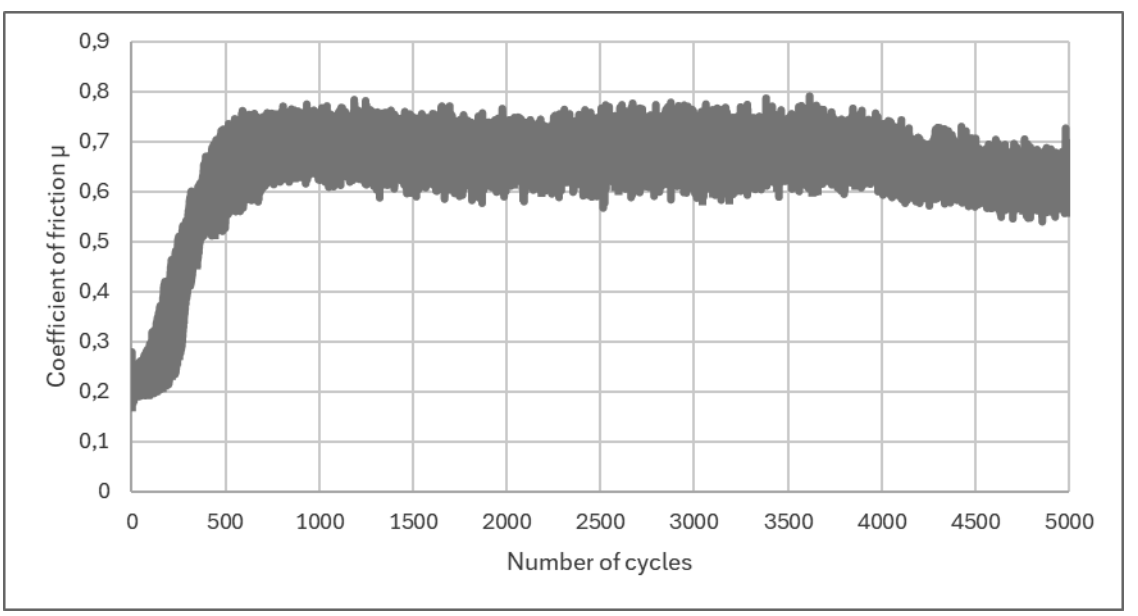

Figure 5. Coefficient of friction (µ) waveform as a function of number of cycles: silicon-based coating

In a coated system, the friction quickly stabilizes at a level of approx. 0.65–0.75, typical for direct contact between two hard materials. The even and stable curve for a full 5000 cycles is direct evidence that the coating has maintained full structural continuity and effectively protected the steel from abrasion (Fig. 5).

The recorded coefficient of friction (COF) waveforms as a function of time (Fig. 6), obtained using a fretting test, show a repeatable, three-step interaction character for both cases. In the initial running-in phase (up to approximately 500–600 s), the movement resistance remains low, at about 0.16–0.20. This is followed by a stage of dynamic friction increase, during which temporary instabilities (visible as fluctuations in the second waveform) may

occur due to the presence of fine wear debris within the contact zone. After approximately 1000 seconds, the process becomes fully stabilized, and the coefficient of friction reaches a steady level of about 0.75–0.80, which is maintained until the end of the test. This behavior confirms that stable conditions of abrasive interaction of the tested coating were achieved under fretting conditions.

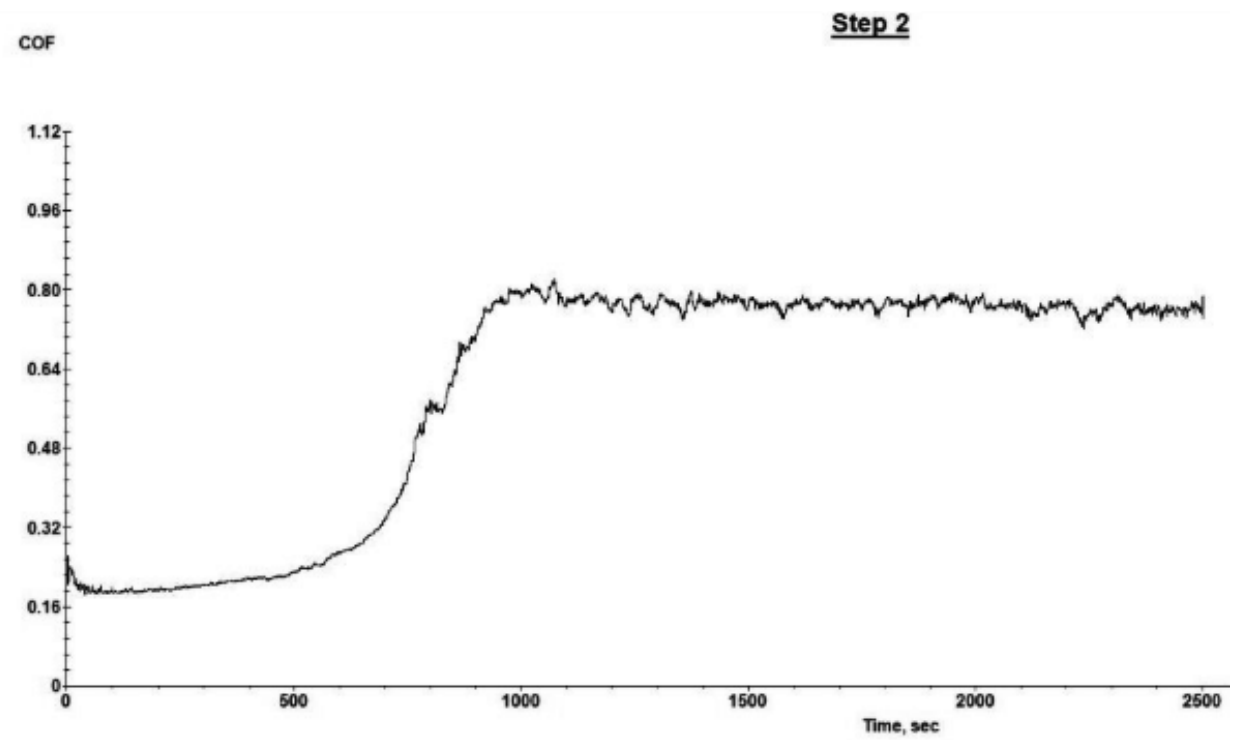

Figure 6. Friction coefficient after using the "ball-on-flat" method

Linear EDS analysis of the chemical composition along the friction path after the fretting test (Fig. 7) enabled a detailed verification of the wear mechanism. Outside the contact zone, a predominant proportion of silicon (Si) was recorded, confirming the presence of a protective coating. However, within the trace of interaction, a drastic decrease in the signal from silicon was observed, with a simultaneous sharp increase in the intensity of the iron (Fe) signal. This indicates that under the accepted conditions of tribological loading, the coating was locally abrased and the countersample exposed the steel substrate (X40CrMoV5-1). This phenomenon suggests that the critical load-bearing capacity of the system is exceeded, resulting in a transition from mild coating wear to intensive abrasion of the base material.

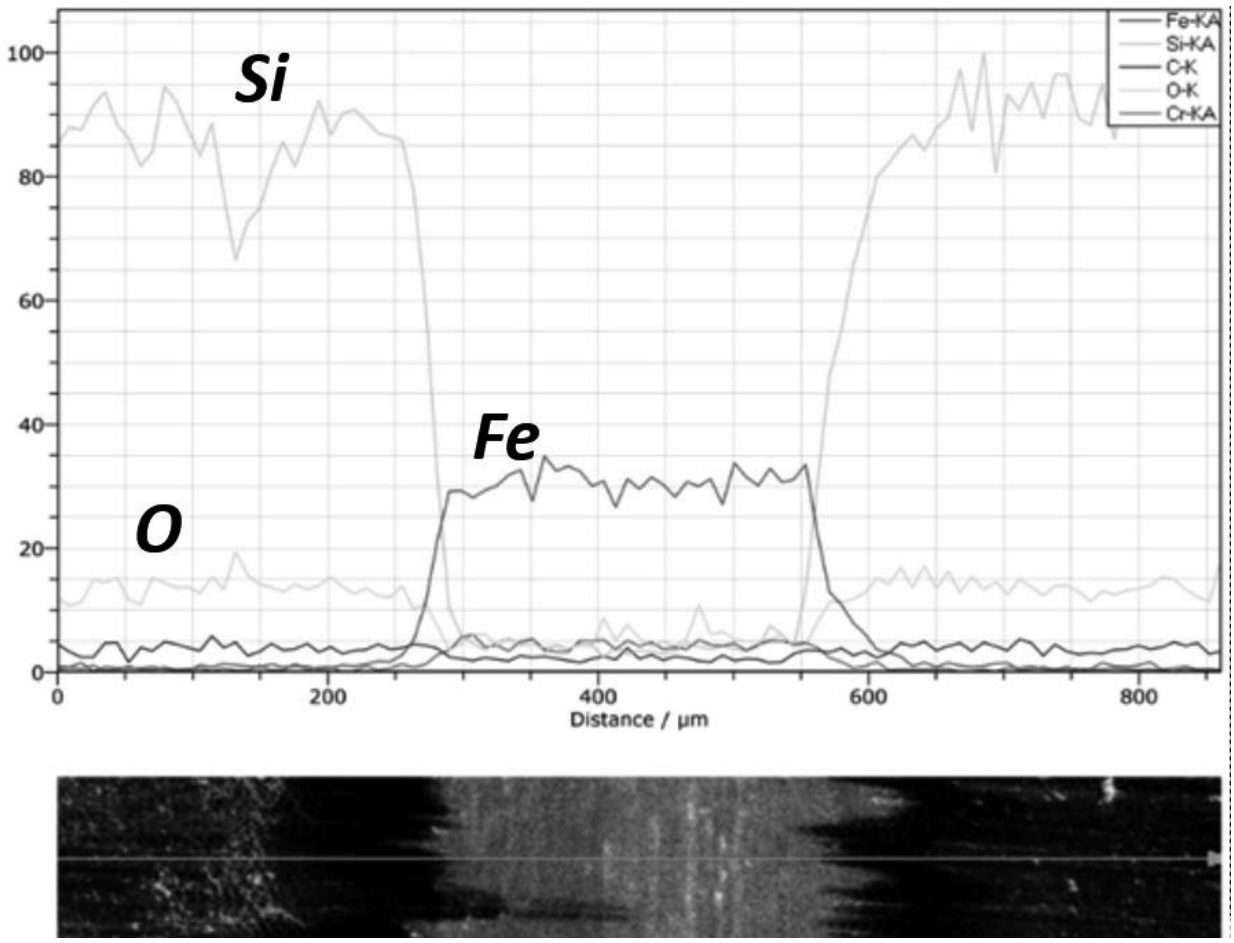

Figure 7. Surface topography after abrasive wear testing with chemical composition analysis

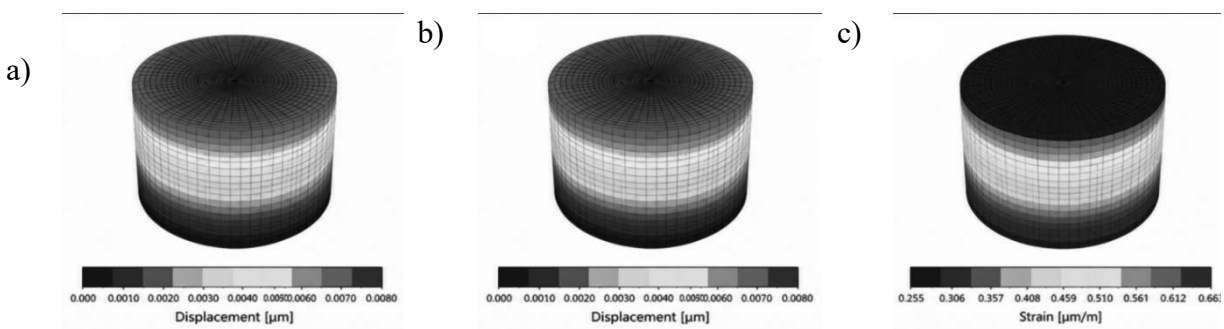

Figure. 8. Results of FEM numerical simulations for X40CrMoV5-1 uncoated tool steel: a) stress distribution, b) total displacement, c) strain.

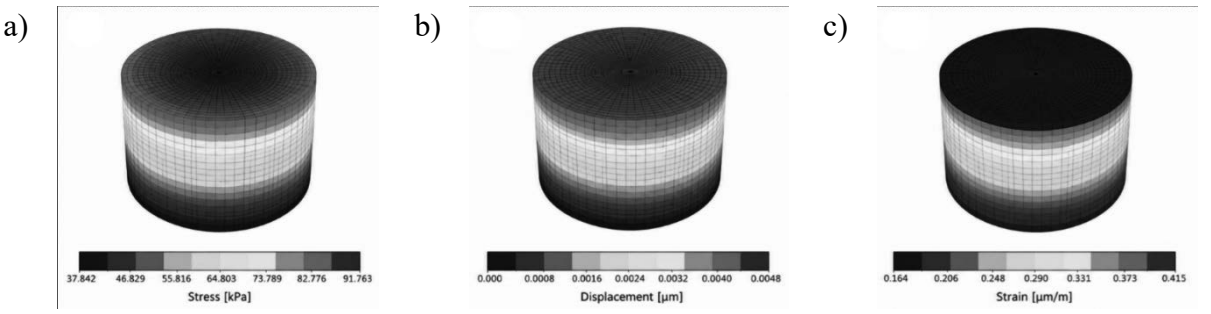

Figure 9. Results of FEM numerical simulations for a system with a protective silicon coating: a) stress distribution, b) total displacement, c) strain.

Numerical analysis of FEM showed that for uncoated steel X40CrMoV5-1, the maximum displacement was 8.0×10^{-3} μm (Fig. 8b), with a deformation equal to 0.663 μm/m (Fig. 8c). The introduction of a 2 μm thickness coating into the model resulted in a displacement reduction of approximately 40% (to 4.8×10^{-3} μm) (Fig. 9b) and a reduction in deformation to 0.415 μm/m (Fig. 9c). These results confirm the beneficial effect of the coating on stress redistribution and increased rigidity of the coating-substrate system. The FEM analysis was simplified and based on the assumption of linearly elastic material properties and an ideal bond between the coating and the substrate. The model did not take into account nonlinear phenomena such as friction, wear or damage initiation, so the results obtained should be considered as a qualitative assessment of the effect of the coating on the mechanical response of the system.

4. CONCLUSIONS

On the basis of simulation and experimental research, the following conclusions were formulated:

- The coating is characterized by dense columnar structure, excellent adhesion and spherical surface topography; Its average thickness is approx. 4 μm.
- The use of a silicon-modified coating significantly stabilizes the system mechanically – in FEM simulations, a reduction in displacement by nearly 40% was observed compared to X40CrMoV5-1 steel.
- Unlike the uncoated X40CrMoV5-1 steel, which underwent intense abrasive and adhesive wear, the silicon coating eliminated catastrophic wear.
- EDS microanalysis confirmed that the original silicon layer (no traces of iron from the substrate) was preserved in the tribological contact area, which confirms its integrity and highest effectiveness in protecting industrial tools.

ACKNOWLEDGMENTS

This work was created as part of a project carried out within the framework of Project-Based

Learning (PBL) in the 14th Excellence Initiative Competition—the Scientific Research Program of the Silesian University of Technology.

BIBLIOGRAPHY

1. D. Pakuła, M. Staszuk, L.A. Dobrzański, Investigations of the structure and properties of PVD coatings deposited onto sintered tool materials, Archives of Materials Science and Engineering 58/2 (2012) 219-226.
2. K. Holmberg, A. Matthews, Coatings Tribology: Properties, Mechanisms, Techniques and Applications in Surface Engineering, Elsevier, (2009).
3. M. Staszuk, L. Reimann, A. Kříž, D. Pakuła, Application of PVD and ALD Methods for Surface Treatment of Al-Si-Cu Alloys, Solid State Phenomena 293 (2019) 97-109.
4. J. Janoszka, N. Puchała, P. Jánský, A. Smetanova, M. Lattner, A. Kříž, M. Staszuk, D. Pakuła, Functional properties of CrN coating obtained by PVD on aluminum alloy surface AlSi9Cu3, Talent Detector Summer, (2025).
5. S. Veprek, The search for novel, superhard materials, Journal of Vacuum Science & Technology A 17 (1999) 2401-2420.
6. D. Pakuła, L.A. Dobrzański, Structure and properties of abrasion-resistant coatings obtained in PVD and CVD processes, Inżynieria Materials XXIV (2003) 463-466.
7. D. Pakuła, L.A. Dobrzański, Computer simulation of stresses in the Ti-B-C-N coatings, Archives of Materials Science and Engineering 34/2 (2008) 99-106.

TalentDetector

7th-9th June 2026
Gliwice-Brenna, Poland

DEPARTMENT OF ENGINEERING MATERIALS AND BIOMATERIALS
FACULTY OF MECHANICAL ENGINEERING
SILESIAN UNIVERSITY OF TECHNOLOGY

INTERNATIONAL STUDENTS SCIENTIFIC CONFERENCE

Jakościowa identyfikacja mikrowłókien polimerowych uwalnianych podczas modelowego prania odzieży syntetycznej i mieszanej

Marta Cygrimus, Mateusz Szymański, Maksymilian Męcik [a], Katarzyna Dąbrowska [b], Piotr Sakiewicz [c], Klaudiusz Gołombek [d]

[a, b] III Liceum Ogólnokształcące im. Wincentego Styczyńskiego w Gliwicach
[c] Politechnika Śląska, Wydział Mechaniczny Technologiczny, Katedra Materiałów Inżynierskich i Biomedycznych
[d] Politechnika Śląska, Wydział Mechaniczny Technologiczny, Laboratorium Badania Materiałów, email: klaudiusz.golombek@polsl.pl, piotr.sakiewicz@polsl.pl

Streszczenie: Artykuł przedstawia projekt badawczy zrealizowany metodą PBL (Project-Based Learning) przez uczniów III Liceum Ogólnokształcącego im. W. Styczyńskiego w Gliwicach we współpracy z Politechniką Śląską. Celem pracy była jakościowa identyfikacja mikrowłókien polimerowych uwalnianych podczas modelowego prania odzieży wykonanej z tkanin syntetycznych i mieszanych. Badania przeprowadzono w warunkach laboratoryjnych z wykorzystaniem pralki turystycznej Botti Aquarina XPB30. Do analizy użyto trzech rodzajów tkanin: koszulki (100% poliester), rajstop (98% poliamid, 2% elastan) oraz bluzy (52% bawełna, 48% poliester). Pranie wykonano w wodzie wodociągowej z Gliwic (pH 7,4; twardość ogólna 325 mg CaCO3/L) bez dodatku detergentu. Rezygnacja z detergentu była świadomym ograniczeniem liczby zmiennych eksperymentalnych. Mikroplastiki i inne cząstki stałe obecne w wodzie popralnej oddzielono przez filtrację z użyciem gazy medycznej jako filtra. Morfologię cząstek oceniono w cyfrowym mikroskopie stereoskopowym Leica DVM6 oraz w wysokorozdzielczym skaningowym mikroskopie elektronowym ZEISS SUPRA 35. Analiza EDS została wykorzystana do oceny składu pierwiastkowego próbek i obecności zanieczyszczeń mineralnych, natomiast identyfikację rodzaju polimeru przeprowadzono metodą spektroskopii FTIR. We wszystkich trzech próbkach stwierdzono obecność mikrowłókien polimerowych o zróżnicowanej morfologii; ich skład był zgodny z charakterem analizowanych materiałów tekstylnych. Realizacja projektu umożliwiła uczniom udział w pełnym toku pracy eksperymentalnej: od przygotowania próbek i filtracji wody poprocesowej po obserwacje mikroskopowe oraz interpretację wyników z użyciem zaawansowanych metod analitycznych.

Abstract: This article reports a Project-Based Learning (PBL) research project conducted by students of III Liceum Ogólnokształcące im. W. Styczyńskiego in Gliwice in collaboration with the Silesian University of Technology. The aim was to qualitatively identify polymer microfibres released during model washing of synthetic and mixed-fabric garments. The research was conducted in a laboratory using a Botti Aquarina XPB30 portable washing machine. Three types of textiles were used: a T-shirt (100% polyester), tights (98% polyamide,

2% elastane), and a sweatshirt (52% cotton, 48% polyester). Washing was carried out in tap water from Gliwice (pH 7.4; total hardness 325 mg CaCO3/L) without detergent. The absence of detergent was adopted to reduce the number of experimental variables. Microplastics and other solid particles retained from the wash water were separated by filtration through gauze/a filter. Particle morphology was assessed using a Leica DVM6 digital stereoscopic microscope and a ZEISS SUPRA 35 high-resolution SEM. EDS analysis was used to assess the elemental composition of the samples and possible mineral contamination, whereas polymer identification was performed by FTIR spectroscopy. Polymer microfibres with varied morphology were observed in all three samples, and their composition was consistent with the analysed textile materials. The project enabled students to develop practical skills in materials science laboratory work and to participate in successive stages of experimental research, including sample preparation, filtration, microscopic observation and interpretation of analytical results.

Słowa kluczowe: mikroplastiki, polimerowe, mikrowłókna syntetyczne, pranie odzieży, SEM/EDS, PBL, edukacja

1. WSTĘP

Masowa produkcja odzieży z włókien syntetycznych, nasilona przez zjawisko szybkiej mody (fast fashion), sprzyja coraz szerszemu wykorzystaniu poliestru, poliamidu i elastanu w przemyśle tekstylnym. Jedną z istotnych, choć często niedostrzeganych konsekwencji eksploatacji i prania takiej odzieży jest uwalnianie mikrowłókien polimerowych, które mogą trafiać do ścieków, a następnie do środowiska wodnego i lądowego. Obecnie nie istnieje jedna, powszechnie przyjęta definicja mikroplastiku. Europejski Urząd ds. Bezpieczeństwa Żywności (EFSA) określa go jako heterogeniczną mieszaninę fragmentów, włókien, elipsoid, granulek i płatków o rozmiarach od 0,1 µm do 5 mm, natomiast cząstki mniejsze niż 0,1 µm klasyfikuje jako nanoplastik [1]. Z kolei Program Środowiskowy ONZ (UNEP) definiuje mikroplastik jako syntetyczny polimer o średnicy poniżej 5 mm, występujący w środowisku wodnym, glebie i powietrzu [2]. Mikroplastiki wykryto dotychczas w wodzie pitnej, soli kuchennej, rybach, produktach rolnych i powietrzu; ich obecność stwierdzono również w ludzkim kale oraz próbkach krwi, co rodzi pytania o możliwe skutki długotrwałej ekspozycji człowieka na te cząstki [3,4]. W literaturze i raportach popularnonaukowych przywoływano szacunek wskazujący, że człowiek może spożywać do około 5 g mikroplastiku tygodniowo, jednak wartość ta powinna być traktowana ostrożnie ze względu na ograniczenia metodyczne takich oszacowań [5,6].

Pod względem pochodzenia wyróżnia się mikroplastiki pierwotne, produkowane od początku w mikroskopijnych rozmiarach i stosowane m.in. w kosmetykach, detergentach i ścierniwach przemysłowych, oraz mikroplastiki wtórne, powstające w wyniku fragmentacji większych odpadów plastikowych pod wpływem procesów mechanicznych i fotochemicznych [7]. Włókna tekstylne uwalniane podczas użytkowania i prania odzieży zalicza się zwykle do mikroplastików wtórnych, jeżeli pochodzą z materiałów syntetycznych. Sektor tekstylny jest wskazywany jako jedno z istotnych źródeł mikrowłókien syntetycznych przedostających się do środowiska wodnego, a w Europie duży udział odzieży zawierającej włókna syntetyczne dodatkowo zwiększa znaczenie tego problemu [8,9,15].

De Falco i współpracownicy wykazali, że w warunkach domowych z jednego kilograma tkaniny może uwolnić się od 124 do 308 mg włókien, co odpowiada nawet 1,5 mln pojedynczych cząstek [10]. Wielkość emisji zależy od rodzaju materiału, temperatury prania, rodzaju detergentu, konstrukcji tkaniny i typu pralki [10,11,18]. Opracowania Europejskiej Agencji Środowiska wskazują, że emisja mikrowłókien z tekstyliów jest istotnym elementem środowiskowego oddziaływania sektora odzieżowego w Europie [9,12]. Dane te pokazują skalę problemu, ale nie mogą być bezpośrednio porównywane z wynikami niniejszego projektu, ponieważ w pracy wykonano eksperyment modelowy o charakterze jakościowym.
Pomimo rosnącej liczby badań, nadal istotne pozostaje rozwijanie prostych i możliwych do odtworzenia procedur identyfikacji mikrowłókien uwalnianych podczas prania, zwłaszcza w warunkach dydaktyczno-laboratoryjnych. Dotyczy to zarówno oceny morfologii uwalnianych mikrowłókien, takiej jak kształt, średnica, długość i stan powierzchni, jak również ich składu chemicznego oraz możliwości zastosowania rozwiązań ograniczających emisję, takich jak filtry pralkowe, woreczki Guppyfriend czy systemy filtracji ścieków [10,11,13,18]. W tym kontekście projekt PBL stanowił próbę połączenia rzeczywistego problemu środowiskowego z praktycznym wykorzystaniem metod analizy materiałowej: mikroskopii optycznej, SEM/EDS.

2. MATERIAŁ I METODYKA BADAŃ

Celem badań była jakościowa identyfikacja i charakterystyka mikrowłókien polimerowych uwalnianych podczas modelowego prania odzieży wykonanej z tkanin syntetycznych i mieszanych. Zastosowano sekwencję metod analitycznych obejmującą: mikroskopię świetlną i stereoskopową, wykorzystaną do wstępnej oceny morfologii cząstek, wysokorozdzielczą skaningową mikroskopię elektronową HRSEM z analizą EDS, zastosowaną do oceny morfologii powierzchni i składu pierwiastkowego, oraz spektroskopię FTIR, wykorzystaną do identyfikacji rodzaju polimeru.
Projekt zrealizowano w formule PBL (Project-Based Learning). Uczniowie uczestniczyli w przygotowaniu próbek, przeprowadzeniu procesu prania, filtracji wody popralnej, obserwacjach mikroskopowych oraz interpretacji wyników uzyskanych z wykorzystaniem aparatury laboratoryjnej Politechniki Śląskiej. Prace z użyciem zaawansowanych technik analitycznych, takich jak HRSEM/EDS i FTIR, prowadzono pod nadzorem opiekunów naukowych. W projekcie zastosowano podejście PBL, w którym uczniowie uczestniczyli w kolejnych etapach pracy badawczej: od przygotowania próbek i przeprowadzenia modelowego prania, przez filtrację wody popralnej, po obserwacje mikroskopowe i interpretację wyników
Do badań wybrano trzy rodzaje odzieży o różnym składzie włókien:

- A - koszulkę wykonaną w 100% z poliestru,
- B - bluzę o składzie 52% bawełny i 48% poliestru,
- C - rajstopy wykonane w 98% poliamidu i 2% elastanu.

Dobór próbek umożliwił porównanie materiału całkowicie syntetycznego, materiału syntetycznego z dodatkiem elastanu oraz tkaniny mieszanej zawierającej zarówno włókna naturalne, jak i syntetyczne. Próbki odzieży wykorzystane w badaniach przedstawiono na rys. 1.
Eksperyment przeprowadzono w pralce turystycznej Botti Aquarina XPB30 o pojemności bębna ok. 15 litrów. Cykl prania obejmował 25 minut aktywnego prania, następnie 15 minut przerwy w celu uniknięcia przegrzania urządzenia, po czym proces kontynuowano przez kolejne 25 minut. Łączny czas aktywnego prania wynosił 50 minut. Łączna objętość wody

użytej podczas prania wynosiła 15 litrów. Pranie przeprowadzono bez dodatku detergentów, w wodzie wodociągowej o temperaturze 30 °C. Rezygnacja z detergentu była świadomym ograniczeniem liczby zmiennych eksperymentalnych i pozwalała ocenić wpływ samego oddziaływania mechanicznego oraz kontaktu materiału z wodą. Skład chemiczny wody odpowiadał normom jakości obowiązującym w sieci wodociągowej dzielnicy Kopernik w Gliwicach [17]. Woda charakteryzowała się następującymi parametrami: pH 7,4; twardość ogólna 325 mg CaCO3/L; chlorki 25,3 mg/L; siarczany 62 mg/L.

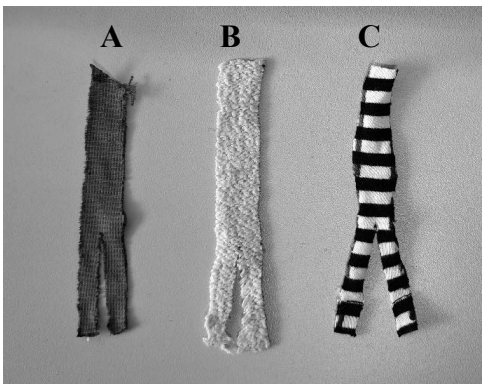

Rys. 1. Próbki odzieży wykorzystane w badaniach
Figure 1. Clothing samples used in the study

Po zakończeniu prania wodę popralną przelano do czystego naczynia i przesączono przez sterylną gazę lub filtr, która zatrzymała cząstki stałe, w tym włókna tekstylne i fragmenty materiału. Ze względu na obecność bluzy zawierającej 52% bawełny, materiał zatrzymany na filtrze mógł obejmować zarówno mikrowłókna syntetyczne, jak i włókna naturalne. Z tego powodu określenie „mikroplastiki" stosowano wyłącznie do cząstek, których syntetyczny charakter potwierdzono na podstawie analizy FTIR. Zebrany materiał pozostawiono do całkowitego wyschnięcia. Analizie poddano zarówno osad zebrany na gazie, jak i próbki włókien wyciętych bezpośrednio z tkanin przed praniem, które stanowiły materiał referencyjny do porównania morfologii i składu chemicznego.

Próbki umieszczono na szklanej płytce i unieruchomiono taśmą węglową. Obserwacje przeprowadzono w cyfrowym mikroskopie optycznym Leica DVM6 przy powiększeniach od 40× do 400×. Metoda umożliwiła wizualną ocenę kształtu cząstek, ich barwy oraz ogólnej morfologii, w tym obecności włókien i fragmentów o nieregularnych formach. Mikroskopia świetlna miała charakter wstępny i nie była traktowana jako metoda jednoznacznej identyfikacji polimeru. Pozwalała natomiast wytypować cząstki do dalszej analizy metodami HRSEM/EDS i FTIR.

Przed obserwacją w SEM próbki napylono cienką warstwą złota w celu zwiększenia przewodnictwa elektrycznego. Obserwacje strukturalne wykonano w mikroskopie HRSEM ZEISS SUPRA 35 przy powiększeniach od 50× do 5000×. Analiza obejmowała szczegółową ocenę morfologii cząstek, obserwację cech powierzchniowych, takich jak pęknięcia, ślady uszkodzeń mechanicznych i struktura włókien, oraz pomiary wymiarów wybranych cząstek.

Skład pierwiastkowy próbek oznaczono z wykorzystaniem detektora EDS firmy Thermo Fisher Scientific z oprogramowaniem Pathfinder. Analizę EDS potraktowano jako metodę wspomagającą, pozwalającą określić obecność pierwiastków charakterystycznych dla analizowanych materiałów i zanieczyszczeń mineralnych.

Metoda EDS nie pozwala jednak jednoznacznie identyfikować rodzaju polimeru, dlatego analizę materiałów polimerowych oparto na wynikach FTiR.
Do identyfikacji rodzaju polimeru zastosowano spektroskopię w podczerwieni z transformatą Fouriera (FTiR). Widma próbek porównano z widmami wzorcowymi z biblioteki referencyjnej, co umożliwiło identyfikację rodzaju polimeru. W przypadku próbek pochodzących z materiałów mieszanych interpretację prowadzono ostrożnie, ponieważ osad po filtracji mógł zawierać zarówno włókna syntetyczne, jak i włókna naturalne pochodzące z bawełny. Ze względu na brak oznaczenia masy lub liczby cząstek uwolnionych podczas prania oraz brak powtórzeń pomiarowych, badanie miało charakter jakościowy. Uzyskane wyniki pozwalają potwierdzić obecność i rodzaj wybranych mikrowłókien polimerowych, ale nie pozwalają na ilościowe porównanie emisji między analizowanymi materiałami.

3. WYNIKI BADAŃ

W obrazach uzyskanych metodą mikroskopii świetlnej stereoskopowej stwierdzono obecność włókien oraz cząstek stałych o zróżnicowanej morfologii i barwie we wszystkich trzech analizowanych próbkach (rys. 2). Dominującą formą były cienkie mikrowłókna, które mogły oddzielać się od powierzchni przędzy pod wpływem ruchu wody oraz oddziaływań mechanicznych występujących podczas prania. Oprócz pojedynczych włókien zaobserwowano również fragmenty materiału o nieregularnym kształcie. W przypadku próbki zawierającej bawełnę należy zaznaczyć, że część obserwowanych włókien mogła mieć charakter naturalny, dlatego ich zaklasyfikowanie jako mikroplastików wymagało potwierdzenia metodą FTIR.
Uwalnianie włókien można wiązać z mechanicznym oddziaływaniem na strukturę tkaniny. Podczas prania włókna ulegają zginaniu, tarciu i naprężaniu, co może prowadzić do ich stopniowej degradacji oraz oddzielania fragmentów od powierzchni przędzy. Na podstawie samych obserwacji mikroskopowych nie można jednak jednoznacznie określić składu chemicznego cząstek, dlatego mikroskopia świetlna została potraktowana jako etap wstępnej selekcji materiału do dalszych analiz.

A) B) C)

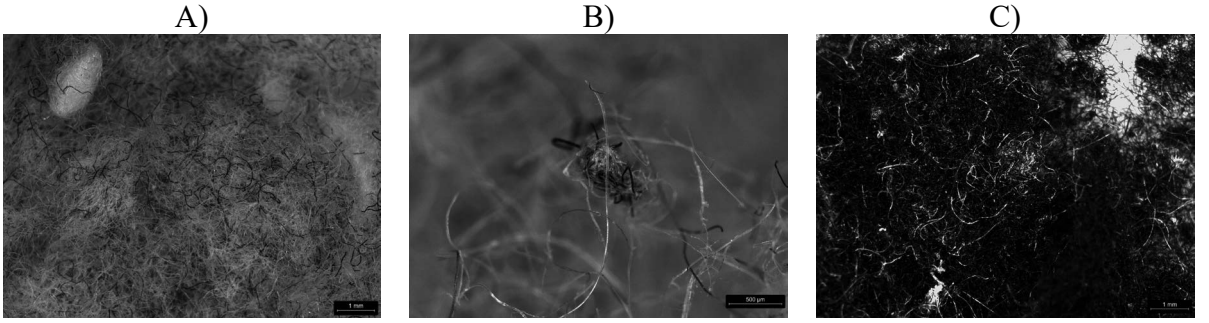

Rys. 2. Mikrostruktura badanych próbek: a-c); mikroskop stereoskopowy
Figure 2. Microstructure of tested specimens: a-c); stereoscopic microscope

Zastosowanie wysokorozdzielczej skaningowej mikroskopii elektronowej (HRSEM) umożliwiło uzyskanie szczegółowych obrazów badanych cząstek oraz ocenę cech powierzchniowych wybranych włókien (rys. 3). Obrazy HRSEM pozwoliły zaobserwować lokalne uszkodzenia powierzchni, nierówności, zakończenia włókien oraz ślady mechanicznego oddziaływania na materiał. Dla części włókien wykonano również pomiary

geometryczne, jednak pełna interpretacja ilościowa wymaga uzupełnienia liczby pomiarów oraz zakresu średnic dla poszczególnych próbek.

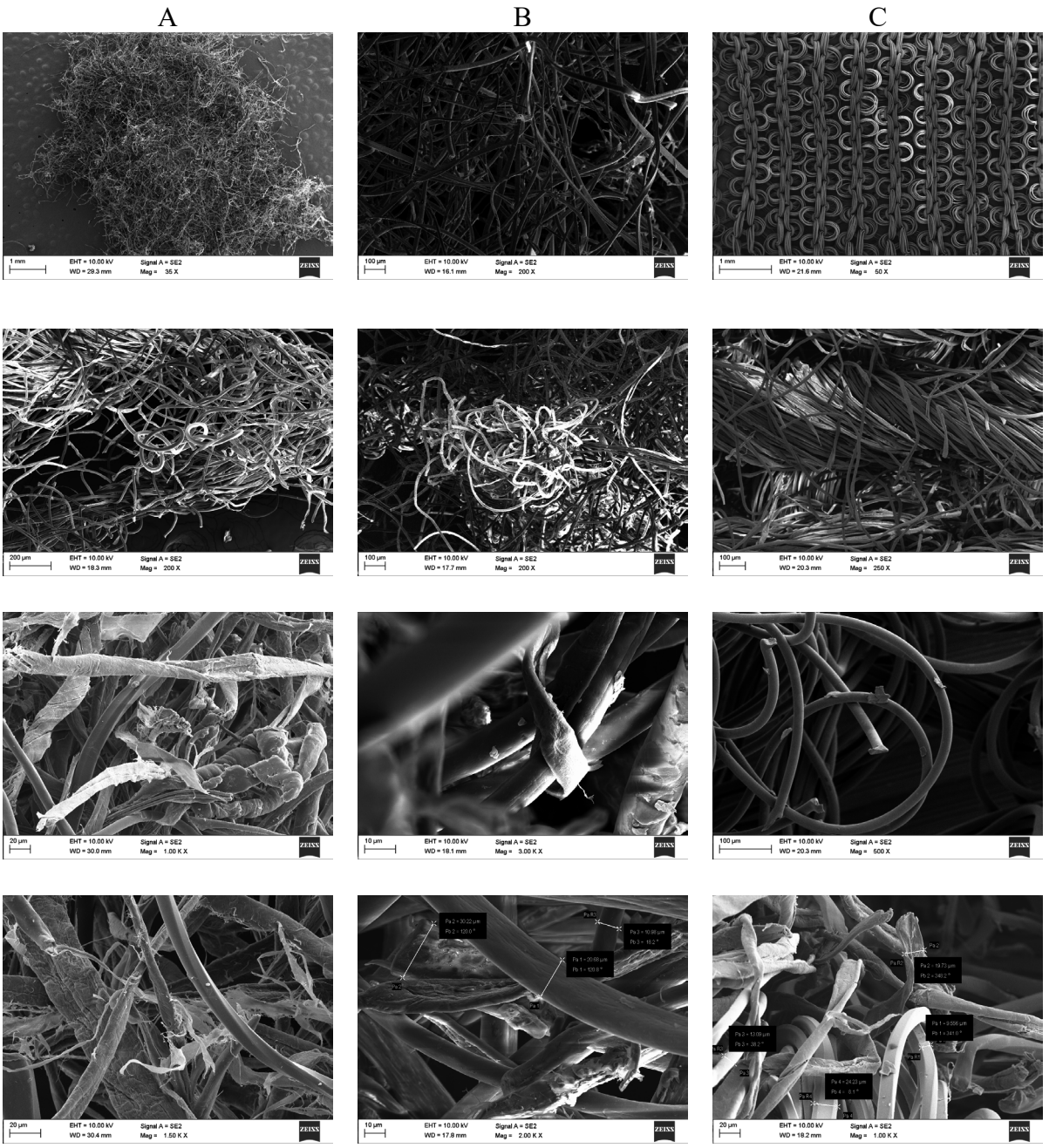

Rys. 3. Mikrostruktura badanych próbek, HRSEM
Figure 3. Microstructure of tested specimens, HRSEM

Analiza EDS umożliwiła określenie składu pierwiastkowego wybranych obszarów próbek (rys. 4-7). W widmach stwierdzono obecność pierwiastków typowych dla analizowanych materiałów organicznych i polimerowych, przede wszystkim węgla (C), tlenu (O) oraz, w przypadku materiałów zawierających poliamid, azotu (N). Zarejestrowano również pierwiastki

śladowe, takie jak siarka (S), magnez (Mg), krzem (Si), glin (Al) i wapń (Ca). Ich obecność może wynikać z zanieczyszczeń mineralnych, składu wody wodociągowej, pozostałości po użytkowaniu tkanin lub osadów zatrzymanych na filtrze. Interpretacja tych pierwiastków powinna być ostrożna, ponieważ badanie nie obejmowało pełnej kontroli źródeł zanieczyszczeń tła.

Analiza EDS nie została potraktowana jako metoda identyfikacji rodzaju polimeru. Jej wyniki wykorzystano jako informację pomocniczą o składzie pierwiastkowym i obecności zanieczyszczeń. Identyfikację polimerów przeprowadzono na podstawie analizy FTiR.

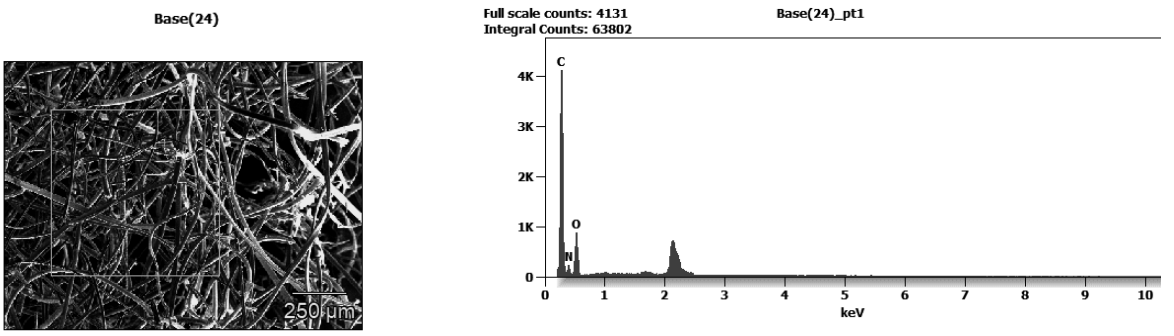

Weight %

	C	N	O
Base(24)_pt1	38.7	21.4	40.0

Atom %

	C	N	O
Base(24)_pt1	44.5	21.1	34.5

Rys. 4. Wyniki analizy EDS z zaznaczonego obszaru dla próbki A
Figure 4. Results of the EDS analysis from the marked area of specimen A

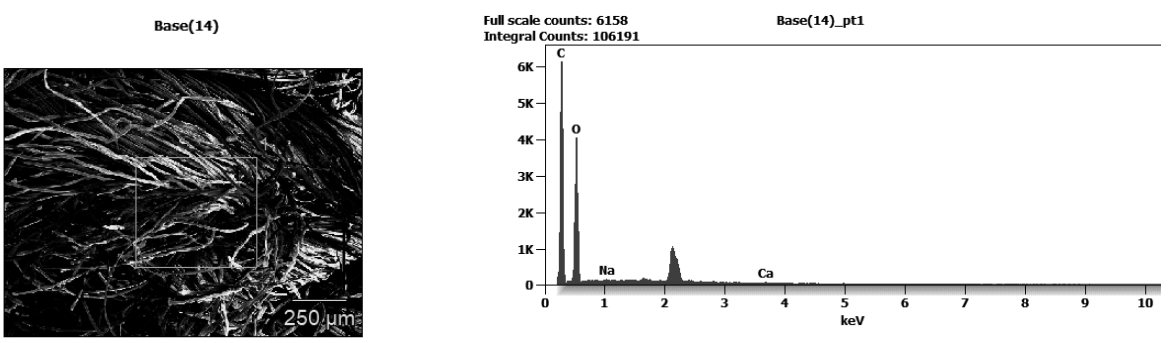

Weight %

	C	O	Na	Ca
Base(14)_pt1	35.7	63.2	0.3	0.9

Atom %

	C	O	Na	Ca
Base(14)_pt1	42.7	56.8	0.2	0.3

Rys. 5. Wyniki analizy EDS z zaznaczonego obszaru dla próbki B
Figure 5. Results of the EDS analysis from the marked area of specimen B

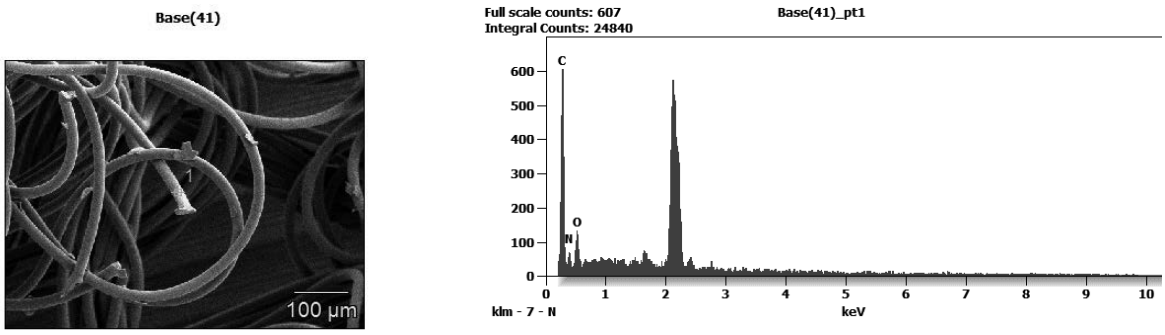

Weight %

	C	*N*	*O*
Base(41)_pt1	38.6	27.3	34.0

Atom %

	C	*N*	*O*
Base(41)_pt1	44.1	26.7	29.2

Rys. 6. Wyniki analizy EDS z zaznaczonego obszaru dla próbki C
Figure 6. Results of the EDS analysis from the marked area of specimen C

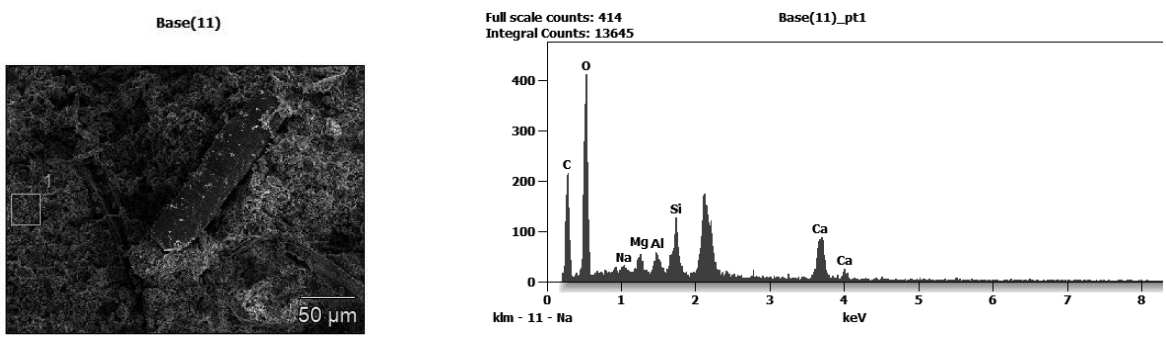

Weight %

	C	*O*	*Na*	*Mg*	*Al*	*Si*	*Ca*
Base(11)_pt1	12.0	44.0	0.6	2.7	3.3	10.2	27.3

Atom %

	C	*O*	*Na*	*Mg*	*Al*	*Si*	*Ca*
Base(11)_pt1	19.8	54.4	0.5	2.2	2.4	7.2	13.5

Rys. 7. Wyniki analizy EDS z zaznaczonego obszaru dla próbki C
Figure 7. Results of the EDS analysis from the marked area of specimen C

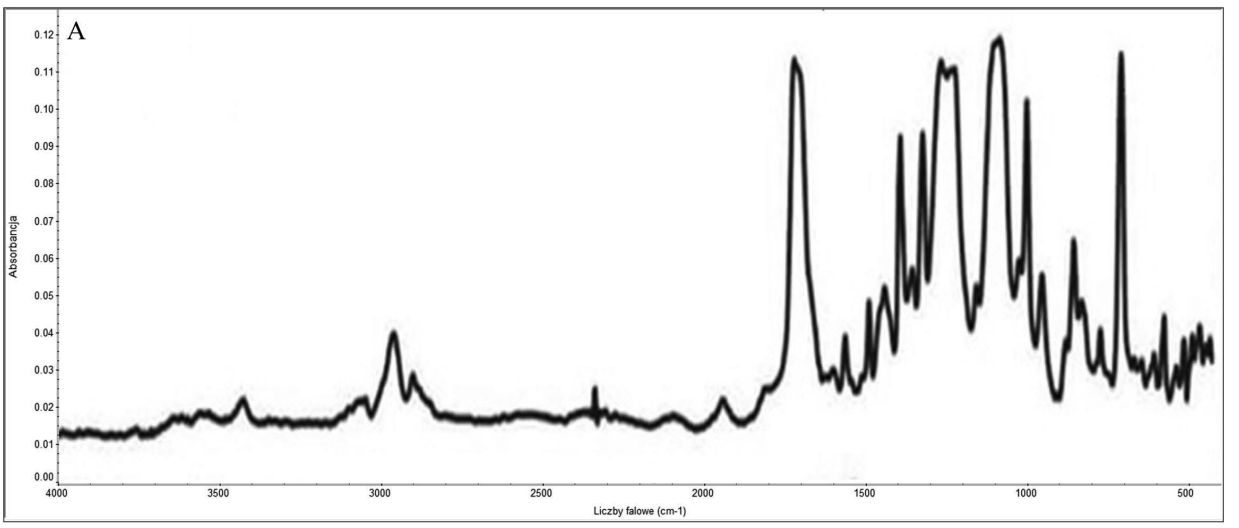

Rys. 8. Wyniki analizy FTiR dla próbki A
Figure 8. Results of the FTiR analysis of specimen A

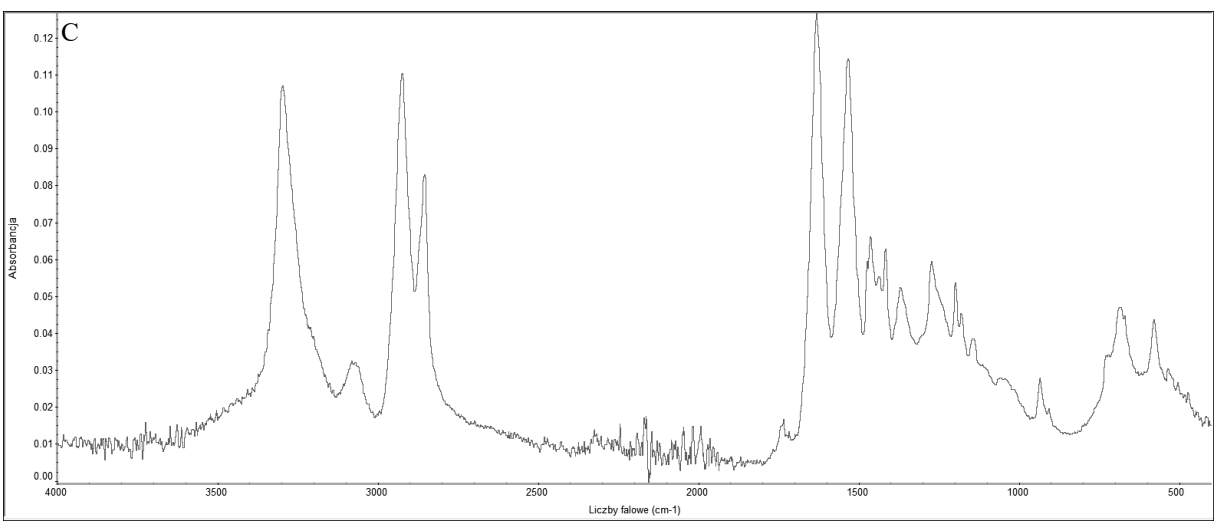

Rys. 9. Wyniki analizy FTiR dla próbki C
Figure 9. Results of the FTiR analysis of specimen C

Spektroskopia FTiR (rys. 8-9) umożliwiła identyfikację rodzaju polimeru w analizowanych próbkach. Uzyskane widma wykazywały obecność pasm odpowiadających charakterystycznym grupom funkcyjnym występującym w badanych materiałach tekstylnych. Na podstawie porównania z widmami referencyjnymi stwierdzono, że próbki pochodzące z koszulki oraz bluzy zawierały sygnały charakterystyczne dla poliestru (rys. 8), natomiast próbki pochodzące z rajstop wykazywały pasma odpowiadające poliamidowi (rys. 9).
W przypadku bluzy, której skład deklarowany obejmował 52% bawełny i 48% poliestru, wynik FTiR należy interpretować ostrożnie. Obecność pasm charakterystycznych dla poliestru potwierdza udział włókien syntetycznych w analizowanym materiale, ale nie wyklucza

obecności włókien celulozowych pochodzących z bawełny. Dlatego próbkę tę należy opisywać jako materiał mieszany, a nie jako próbkę wyłącznie poliestrową.
Na podstawie zestawienia wyników mikroskopii optycznej, HRSEM/EDS oraz FTiR potwierdzono, że w wodzie popralnej po modelowym cyklu prania obecne były mikrowłókna, w tym mikrowłókna polimerowe zgodne ze składem badanych materiałów tekstylnych. Ze względu na brak oznaczenia liczby cząstek, masy osadu oraz powtórzeń pomiarowych wyniki mają charakter jakościowy i nie pozwalają na ilościowe porównanie emisji między poszczególnymi tkaninami.
Wyniki niniejszej pracy są zgodne z ogólnym kierunkiem obserwacji literaturowych, według których proces prania może prowadzić do uwalniania mikrowłókien z materiałów tekstylnych [10,11,14,18]. Vassilenko et al. [18] wykazali, że wielkość emisji zależy od rodzaju włókna, konstrukcji i wykończenia tkaniny, a zastosowanie filtrów pralkowych może istotnie ograniczyć ilość mikrowłókien przedostających się do ścieków. Wartości literaturowe nie są jednak bezpośrednio porównywalne z wynikami niniejszego eksperymentu, ponieważ w pracy wykonano analizę jakościową bez oznaczenia masy lub liczby cząstek.

4. PODSUMOWANIE I WNIOSKI

Przeprowadzone badania wykazały obecność mikrowłókien oraz cząstek stałych we wszystkich trzech badanych próbkach po jednorazowym cyklu prania w kontrolowanych warunkach laboratoryjnych. Na podstawie analizy FTIR potwierdzono obecność mikrowłókien polimerowych zgodnych ze składem analizowanych materiałów tekstylnych: poliestru w próbkach A i C oraz poliamidu w próbce B. Obserwacje HRSEM ujawniły zróżnicowanie morfologiczne włókien oraz ślady uszkodzeń mechanicznych na ich powierzchniach. W przypadku próbki C, wykonanej z mieszanki bawełny i poliestru, należy uwzględnić możliwość współwystępowania włókien celulozowych i syntetycznych; nie każde włókno zatrzymane po filtracji musi więc być mikroplastikiem.
Uzyskane wyniki potwierdzają, że w zastosowanych warunkach modelowego prania dochodziło do uwalniania mikrowłókien z badanych materiałów tekstylnych. Nie stanowią one jednak podstawy do ilościowego porównania emisji między poszczególnymi tkaninami, ponieważ w pracy nie oznaczono masy uwolnionych cząstek, ich liczby ani liczby cząstek odniesionej do masy pranej tkaniny.
Wyniki są spójne z kierunkiem obserwacji opisywanych w literaturze, zgodnie z którym pranie odzieży syntetycznej i mieszanej może prowadzić do uwalniania mikrowłókien [10,11,14,16,18]. Według Vassilenko et al. [18] wielkość emisji zależy od rodzaju włókna, konstrukcji i wykończenia tkaniny, a zastosowanie filtrów pralkowych może istotnie ograniczyć ilość mikrowłókien przedostających się do ścieków. W tej pracy literaturowej wskazano również, że dobór materiału tekstylnego i stosowanie rozwiązań filtracyjnych mogą znacząco zmniejszać emisję mikrowłókien, jednak podawane tam wartości liczbowe dotyczą odmiennych warunków eksperymentalnych. Wartości te należy traktować wyłącznie jako kontekst literaturowy. Nie są one wynikiem niniejszego eksperymentu i nie powinny być używane do bezpośredniego porównania z badanymi próbkami.
Ze względu na jakościowy charakter eksperymentu oraz ograniczenia metodyczne, takie jak brak oznaczenia masy lub liczby cząstek, pojedynczy cykl prania dla analizowanych materiałów, brak powtórzeń pomiarowych, brak próby kontrolnej oraz nieokreślony rozmiar oczek filtra, porównanie emisji między badanymi tkaninami nie jest możliwe na podstawie

zebranych danych. Wyniki należy interpretować jako jakościowe potwierdzenie obecności mikrowłókien polimerowych w materiale zatrzymanym po filtracji wody popralnej, a nie jako pełną ocenę ilościową emisji mikroplastików.
Realizacja projektu metodą PBL pozwoliła uczniom uczestniczyć w kolejnych etapach pracy badawczej, obejmujących przygotowanie próbek, przeprowadzenie modelowego prania, filtrację wody popralnej, obserwacje mikroskopowe oraz interpretację wyników uzyskanych z użyciem metod HRSEM/EDS i FTIR. Prace wymagające obsługi zaawansowanej aparatury laboratoryjnej prowadzono pod nadzorem opiekunów naukowych. Głównym efektem dydaktycznym projektu było powiązanie rzeczywistego problemu środowiskowego z praktycznym wykorzystaniem metod inżynierii materiałowej oraz rozwijanie umiejętności analizy, dokumentowania i krytycznej interpretacji wyników eksperymentalnych.
Dalsze prace powinny obejmować ilościowe oznaczenie masy lub liczby cząstek uwalnianych na kilogram tkaniny, wykonanie powtórzeń pomiarowych, wprowadzenie próby kontrolnej z samą wodą i filtrem, uwzględnienie detergentu jako zmiennej eksperymentalnej, analizę wpływu temperatury prania oraz ocenę skuteczności filtrów pralkowych w zatrzymywaniu włókien o wymiarach odpowiadających zidentyfikowanym w niniejszym badaniu.

LITERATURA

1. European Food Safety Authority. Briefing notes on micro- and nanoplastics in food, EFSA, (2021), https://www.efsa.europa.eu/sites/default/files/2021-05/briefing-notes.pdf
2. United Nations Environment Programme. From Pollution to Solution: A global assessment of marine litter and plastic pollution, UNEP, (2021), https://www.unep.org/resources/pollution-solution-global-assessment-marine-litter-and-plastic-pollution
3. H. A. Leslie, M. J. M. van Velzen, S. H. Brandsma, A. D. Vethaak, J. J. Garcia-Vallejo, M. H. Lamoree, Discovery and quantification of plastic particle pollution in human blood, Environment International, 163, (2022), 107199, https://doi.org/10.1016/j.envint.2022.107199
4. P. Schwabl, S. Köppel, P. Königshofer, T. Bucsics, M. Trauner, T. Reiberger, B. Liebmann, Detection of various microplastics in human stool: A prospective case series, Annals of Internal Medicine, 171(7), (2019), 453-457, https://doi.org/10.7326/M19-0618
5. World Wide Fund for Nature. No Plastic in Nature: Assessing plastic ingestion from nature to people, WWF, (2019), https://www.wwf.org.au/ArticleDocuments/353/pub-no-plastic-in-nature-2019.pdf
6. M. W. Pletz, Ingested microplastics: Do humans eat one credit card per week? Journal of Hazardous Materials Letters, 3, (2022), 100071, https://doi.org/10.1016/j.hazl.2022.100071
7. A. L. Andrady, Microplastics in the marine environment, Marine Pollution Bulletin, 62(8), (2011), 1596-1605, https://doi.org/10.1016/j.marpolbul.2011.05.030
8. M. A. Browne, P. Crump, S. J. Niven, E. L. Teuten, A. Tonkin, T. S. Galloway, R. C. Thompson, (Accumulation of microplastic on shorelines worldwide: Sources and sinks, Environmental Science & Technology, 45(21), 2011), 9175-9179, https://doi.org/10.1021/es201811s
9. European Environment Agency. Microplastics from textiles: Towards a circular economy for textiles in Europe, EEA, (2022), https://www.eea.europa.eu/en/analysis/publications/microplastics-from-textiles-towards-a-circular-economy-for-textiles-in-europe

10. F. De Falco, E. Di Pace, M. Cocca, M. Avella, The contribution of washing processes of synthetic clothes to microplastic pollution, Scientific Reports, 9, (2019), 6633, https://doi.org/10.1038/s41598-019-43023-x
11. U. Pirc, M. Vidmar, A. Mozer, A. Kržan, Emissions of microplastic fibers from microfiber fleece during domestic washing, Environmental Science and Pollution Research, 23, (2016), 22206-22211, https://doi.org/10.1007/s11356-016-7703-0
12. European Environment Agency. Circularity of the EU textiles value chain in numbers, (2025), EEA, https://www.eea.europa.eu/en/analysis/publications/circularity-of-the-eu-textiles-value-chain-in-numbers
13. H. K. McIlwraith, J. Lin, L. M. Erdle, N. Mallos, M. L. Diamond, C. M. Rochman, (Capturing microfibers - marketed technologies reduce microfiber emissions from washing machines, Marine Pollution Bulletin, 139, (2019), 40-45, https://doi.org/10.1016/j.marpolbul.2018.12.012
14. F. De Falco, M. Cocca, M. Avella, R. C. Thompson, Microfiber release to water, via laundering, and to air, via everyday use: A comparison between polyester clothing with differing textile parameters, Environmental Science & Technology, 54(6), (2020), 3288–3296, https://doi.org/10.1021/acs.est.9b06892
15. F. Galgani, G. Hanke, S. Werner, L. De Vrees, Marine litter within the European Marine Strategy Framework Directive, ICES Journal of Marine Science, 70(6), (2013), 1055-1064, https://doi.org/10.1093/icesjms/fst122
16. F. M. Windsor, I. Durance, A. A. Horton, R. C. Thompson, C. R. Tyler, S. J. Ormerod, A catchment-scale perspective of plastic pollution, Global Change Biology, 25(4), (2019), 1207-1221, https://doi.org/10.1111/gcb.14572
17. Przedsiębiorstwo Wodociągów i Kanalizacji Sp. z o.o. w Gliwicach. Tabela parametrów wody, (maj 2025), https://pwik.gliwice.pl/parametry-wody/
18. E. I. Vassilenko, M. Watkins, S. Chastain, J. Mertens, A. M. Posacka, S. Patankar, P. S. Ross, Domestic laundry and microfiber pollution: Exploring fiber shedding from consumer apparel textiles, PLOS ONE, 16(7), (2021), e0250346, https://doi.org/10.1371/journal.pone.0250346

7th-9th June 2026
Gliwice-Brenna, Poland
DEPARTMENT OF ENGINEERING MATERIALS AND BIOMATERIALS
FACULTY OF MECHANICAL ENGINEERING
SILESIAN UNIVERSITY OF TECHNOLOGY
INTERNATIONAL STUDENTS SCIENTIFIC CONFERENCE

Konštrukčný návrh zdvíhacieho mechanizmu do 3,5t pre parkovanie pod zemou

Sebastián Dlugosch[a], Matúš Vereš[b], Milan Uhríčik[a], Mirosław Bonek[c]

[a] Žilinská Univerzita v Žiline, Strojnícka Fakulta, Katedra materiálového inžinierstva, Univerzitná 8215/1, 010 26 Žilina, Slovak Republic
[b] Žilinská Univerzita v Žiline, Strojnícka Fakulta, Katedra konštruovania a častí strojov, Univerzitná 8215/1, 010 26 Žilina, Slovak Republic
[c] Silesian University of Technology, Faculty of Mechanical Engineering, Department of Engineering Materials and Biomaterials, ul. Konarskiego 18A, 44-100 Gliwice, Poland
email: dlugosch@stud.uniza.sk matus.veres@fstroj.uniza.sk milan.uhricik@fstroj.uniza.sk miroslaw.bonek@polsl.pl

Abstract: Cieľom príspevku je popísať konštrukčný návrh zdvíhacieho zariadenia do 3,5t pre parkovanie pod zemou. Práca popisuje vlastný konštrukčný návrh, výpočet návrhu motora, výkresovú dokumentáciu a technickú správu. Pri návrhu zdvíhacieho zariadenia boli zohľadnené dôležité aspekty ako jednoduchosť, efektivita a bezpečnosť.

Keywords: zdvíhacie zariadenie, parkovanie pod zemou, zdvihák, nosnosť 3,5t

1. ÚVOD

K dispozícii boli nasledovné variantné riešenia:

1. Dvojstĺpový zdvihák s hydraulickým zdvihom
2. Dvojstĺpový zdvihák s pneumatickým zdvihom
3. Štvorstĺpový zdvihák s hydraulickým zdvihom
4. Štvorstĺpový zdvihák s pneumatickým zdvihom
5. Štvorstĺpový zdvihák s reťazovým zdvihom
6. Štvorstĺpový zdvihák s lanovým zdvihom
7. Dvojstĺpový zdvihák s hrebeňovým zdvihom
8. Štvorstĺpový zdvihák s hrebeňovým zdvihom
9. **Nožnicový zdvihák so skrutkovicou**
10. Dvojstĺpový zdvihák so skrutkovicou
11. Štvorstĺpový zdvihák so skrutkovicou

11 jednoduchých konštrukčných variantov bolo vzájomne posudzovaných pomocou tzv. dvojbodovej metódy a na základe nižšie uvedených kritérií bol vybraný ako optimálny variant návrh č. 9, t. j. nožnicový zdvihák so skrutkovicou, s technickou hodnotou 0,8654 (tab. 1).

Posudzované kritériá:

- *Nosnosť konštrukcie*: schopnosť konštrukcie odolať maximálnemu možnému zaťaženiu
- *Potreba mazania*: nutnosť častého premazávania komponentov
- *Stabilita konštrukcie*: schopnosť konštrukcie nekonať nežiadúci pohyb pri zaťažení
- *Častá údržba*: Nutnosť častej kontroly a kalibrácie komponentov
- *Rýchlosť zdvihu*: schopnosť konštrukcie konať vertikálny pohyb čo najrýchlejšie bez nutnosti zvýšenia prínosu energie
- *Ekonomická náročnosť*: všetky náklady na materiál, údržbu a prevádzky.

Tab. 1 Výsledky bodového hodnotenia variantov
Table 1 Variant scoring results

Variant konštrukcie	1.	2.	3.	4.	5.	6.	7.	8.	9.	10.	11.	Ideálne riešenie
Technická hodnota	0.830	0.810	0.830	0.826	0.817	0.666	0.801	0.814	0.865	0.814	0.823	1

2. NÁVRH KONŠTRUKCIE S VYUŽITÍM CAD - 3D MODELOV

Konštrukčný návrh bol vytvorený v programe PTC Creo Parametric 9. Pre pohyb zdviháku bolo zvolené riešenie so skrutkovicou. Skrutkovica bude pripojená cez kardanový hriadeľ až k motoru. Vstupné údaje ako napr. výška zdvihu reprezentuje celkovú výšku, o ktorú sa posunie auto na zdviháku a čas zdvihu, ktorý reprezentuje za ako dlho sa automobil znesie alebo vynesie medzi podlažiami.

Pre dostatočne rýchly a efektívny pohyb bol pomocou výpočtov navrhnutý aj motor. Výkon motora musí byť pri výške zdvihu 1,95 m a rýchlosti zdvihu 120 s minimálne 2 kW. Pomocou výpočtov sa dospelo k záveru, že najvhodnejší motor pre nožnicový zdvihák je trojfázový 6-pólový elektromotor s minimálnym výkonom 2 kW spolu s planétovou prevodovkou s prevodom 12:1.

Podstava (obr. 1) by mala byť vyrobená zo železo-betónového podkladu, aby sa dobre upevnil podklad v zemi a zároveň, aby sa zabránilo poškodeniu podstavy, keby sme uvažovali nad oceľovými profilmi ako náhradu za železo-betónový podklad. Podklad má rozmery 4 000 x 7 000 x 200 mm. V podklade sú zároveň umiestnené 2 podpery pre pevnú, nepohyblivú časť nožnicového zdviháku.

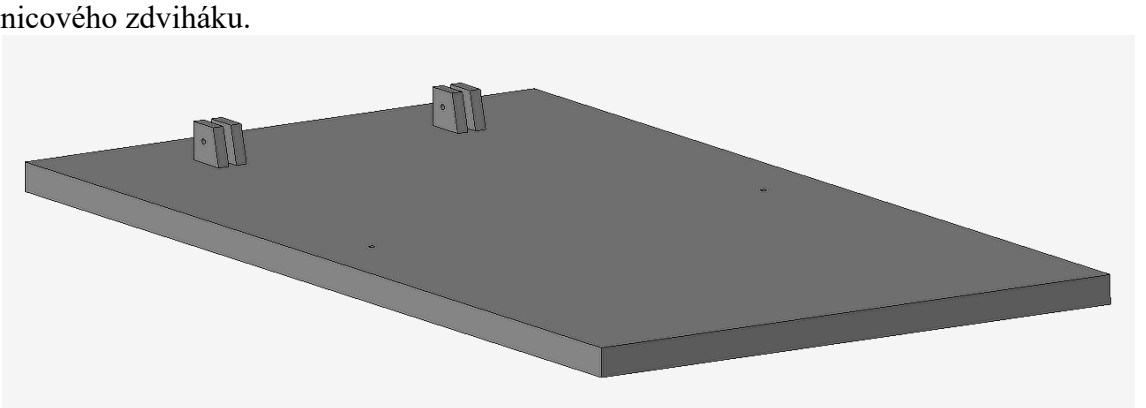

Obr. 1 Podstava
Figure 1. The base

Spodné koľajnice sú rozdelené na ľavé a pravé. Každá je vyrobená z tyče prierezu U z ocele triedy 11 valcovanej za tepla. Ocele triedy 11 sú kvalitnejšie ako ocele triedy 10, spracovávajú sa obdobne. Pre konštrukčné ocele triedy 11 sa zaručuje maximálny obsah uhlíka. Najčastejšie sa tieto ocele používajú na zvárané konštrukcie a na výrobu tyčí, plechov a rúr. Valcovanie za tepla zlepšuje ich trvanlivosť, odstráni vnútorné defekty a má nižšie náklady na spracovanie. Pre konkrétny typ zdviháku bola použitá tyč U280/B STN EN 10279 - S235. Koľajnice sú po bokoch ukotvené pomocou platní.

Pre pohyb nožníc v koľajniciach boli zvolené polyuretánové kolesá (a) TR-ROLL (obr. 2) s tvrdosťou 75 Shore A, ktoré charakterizuje výborná valivosť a pružnosť, dobrá oteruvzdornosť a dobrá odolnosť proti pretrhnutiu. Nosnosť jedného kolesa je 700kg. Maximálne možné zaťaženie, ktoré pôsobí na nožnice je 58 860 N. Váha na jedno koleso je 375kg. Vo vnútri sa nachádzajú dve guličkové ložiská (b) STN 02 4630 s rozmermi 50 x 58 x 25 mm. Kolesá sú uložené na dvoch hriadeľoch (e), kde sú upevnené pomocou podložiek MB4 ISO 2982-2 (d) a maticami KM20 ISO 2982-2 (c).

Obe kolesá sú uložené na platni (f), ktorá bude pripojená na bok nožníc (obr. 3).

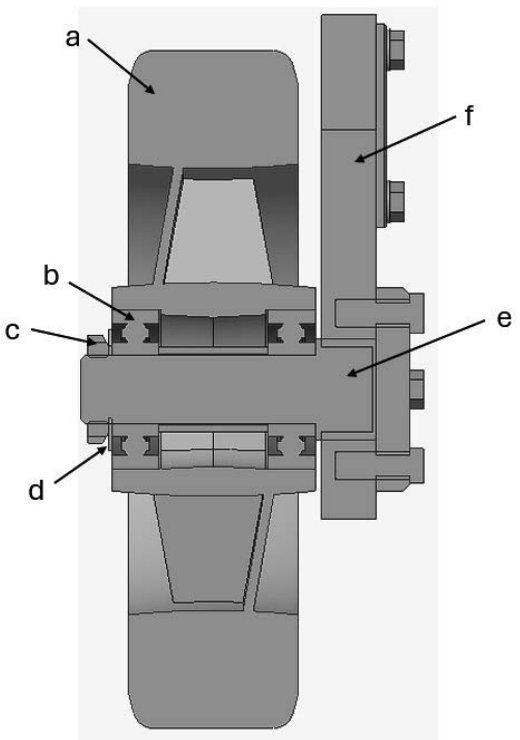

Obr. 2 Rez uloženia kolesa
Figure 2. Wheel bearing section

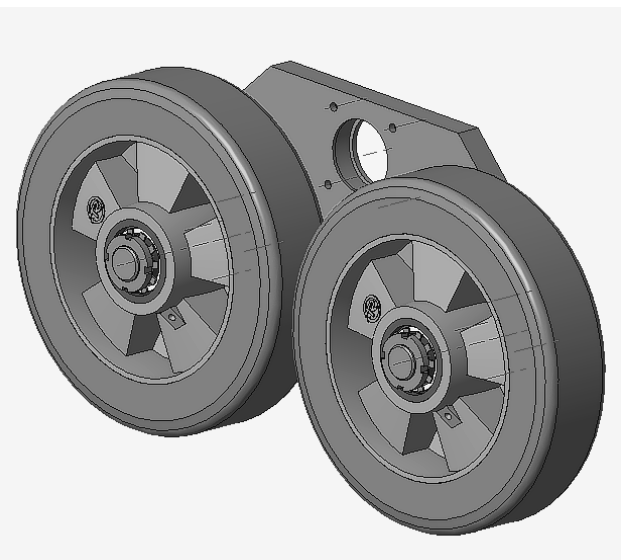

Obr. 3 Uloženie kolies na platni
Figure 3. Storing wheels on a plate

Keďže nožnice sú najviac namáhanou časťou vo zdviháku, boli navrhnuté z tyče prierezu I z ocele triedy 11 valcovanej za tepla, konkrétne tyč s označením I 120/B STN EN 10279 - S355. V prednej časti sa prizváral hriadeľ (a), ktorý je vystužený rúrkou (b) a na ktorom sa uchytili platne s kolesami po oboch stranách. Platne sú uchytené k hriadeli pomocou valivého ložiska NU 204 STN 02 4608 (c), ktoré stabilizujú kolesá proti vykĺznutiu a zaručujú ich plynulý pohyb po koľajniciach (obr. 4 a obr. 5).

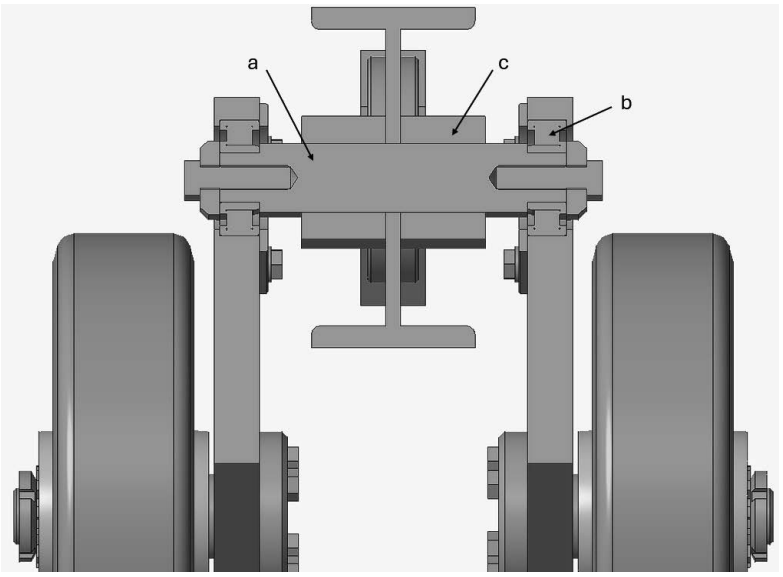

Obr. 4 Rez uloženia plôch s kolesami
Figure 4. Section of the bearing surfaces with wheels

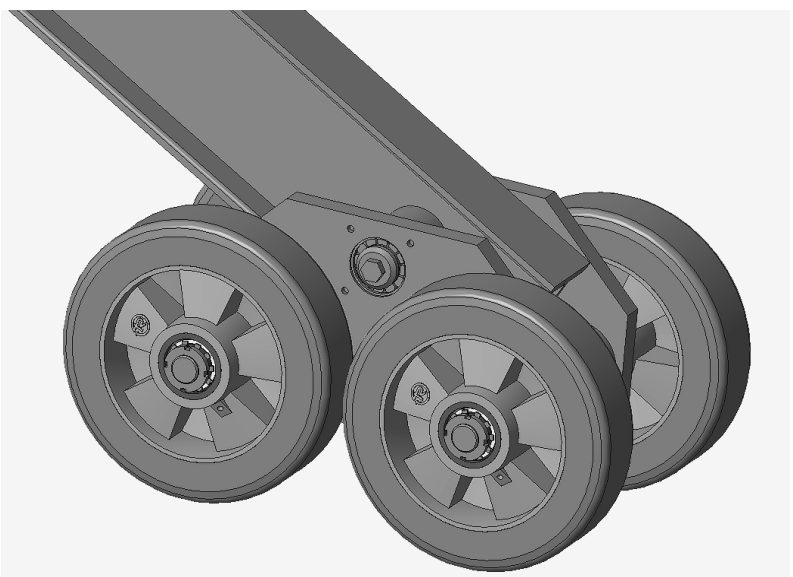

Obr. 5 Uloženie kolies na nožniciach
Figure 5. Wheel storage on scissor stands

Zadný koniec I profilu nožníc je kinematicky fixovaný a umožňuje výhradne rotačný pohyb na rozdiel od prednej časti vybavenej kolieskami (obr. 6). Uloženie je pomocou priváraného hriadeľa (a) k pevnej podstave, na ktorom je uložené valivé ložisko (b) s označením NU 208 STN 02 4608. Ložisko je pevne pripevnené k I profilu nožníc pomocou prírub (c) a skrutiek (d) M10 x 32 ISO 4014 a matice M10 ISO 4032 s podložkou M10 ISO 7069. Na hriadeli je ložisko upevnené pomocou prírub (e). Hriadeľ je upevnený pomocou skrutiek (d) M10 x 32 ISO 4014 a prírub (f).

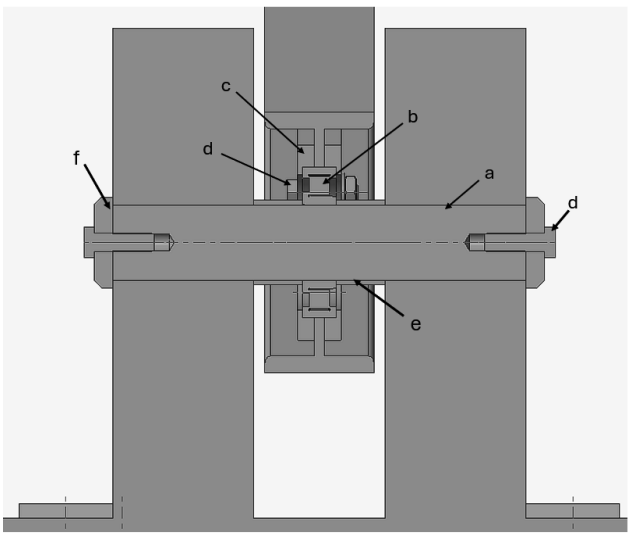

Obr. 6 Rez zadného uloženia nožníc
Figure 6. Section of the rear scissor mount

Horná platňa (obr. 7) je nosná, pretože musí odolať plnej váhe automobilu bez toho aby sa nejakým spôsobom zdeformovala. Preto bola navrhnutá výstuž z nosných tyčí I profilu (a) s označením I100/B STN EN 10279 - S235, ktoré sú umiestnené v strede nosnej plochy. Po obvode sú umiestnené tyče s profilom U (b) otočené o 90° s označením U100/B STN EN 10279 - S235. Všetky tieto nosné tyče sú navzájom pozvárané, aby sa zväčšila tuhosť konštrukcie a zároveň aby sa predišlo ich vzájomnému posunutiu pri zaťažení.

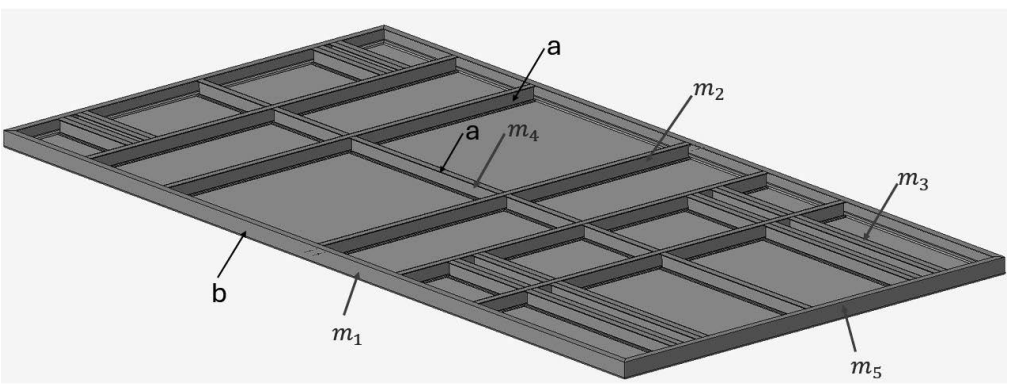

Obr. 7 Profily hornej nosnej platne
Figure 7. Upper support plate profiles

Na hornej strane je prizváraný slzičkový plech (c) s rozmermi 1 500 x 3 000 x 10 mm STN EN 10029. Slzičkový plech je protišmykový a patrí medzi špeciálny druh štruktúrovaných plechov. Je valcovaný za tepla, akosti S235.

Väčšina zdvíhacích zariadení má na okrajoch uhlové skosenie, aby sa automobilom lepšie vchádzalo na plošinu. Avšak len v prípadoch, kedy zdvíhacie zariadenia nemajú platňu v rovine s plochou nájazdu alebo výjazdu automobilu. Keďže zdvihák bol navrhnutý tak, aby nosná platňa bola v rovine s nájazdovou a výjazdovou plochou, bolo rozhodnuté, tieto uhlové skosenia vynechať.

Pre horné koľajnice (obr. 8) boli navrhnuté tyče profilu U s označením U240/B STN EN 10279 - S235. Koľajnice sú uložené pod uhlom 90°, privarené k hornej nosnej platni a k predpripraveným I profilom s označením I100/B STN EN 10279 - S235.

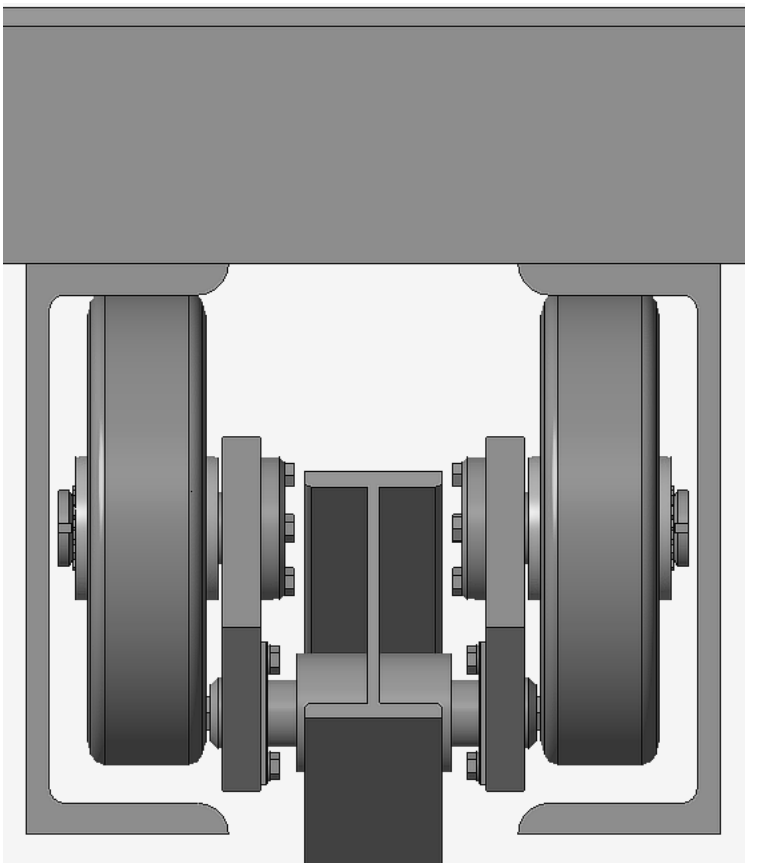

Obr. 8 Uloženie nožnice v hornej koľajnici
Figure 8. Storing the scissors in the upper rail

Skrutkovica bola zvolená o priemere Ø56 mm, aby sa zvýšila jej životnosť a znížil počet kontrol bezpečnosti, čo sa môže neskôr prejaviť hlavne šetrením finančných prostriedkov, ktoré by boli potrebné na opravu, alebo jej výmenu. Uloženie skrutkovice dokumentuje obr. 9.

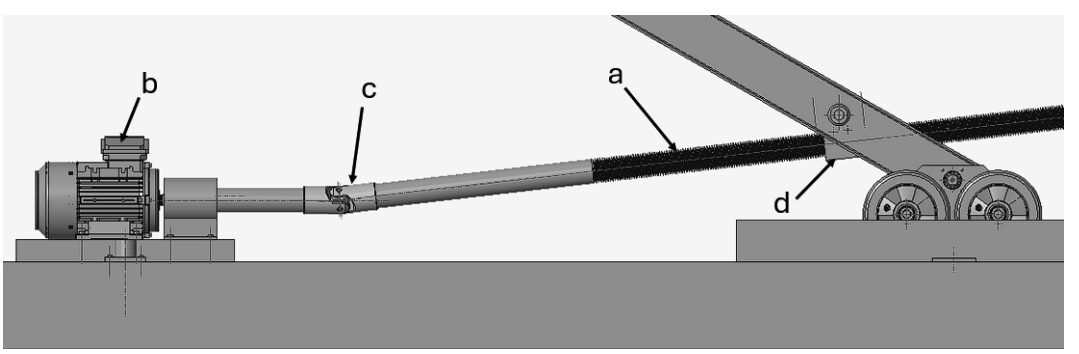

Obr. 9 Uloženie skrutkovice
Figure 9. Screw storage

Skrutkovica (a) je pripojená k trojfázovému 6-pólovému elektromotoru s planétovou prevodovkou (b) s prevodom 12:1 pomocou kardanového hriadeľa (c) s priemerom Ø63 mm (obr. 9). Kardanový hriadeľ zaručuje prenos rotačného pohybu a krútiaceho momentu medzi dvoma nesúosovými hriadeľmi.

Pomocou závitu je skrutkovica pripojená k matici (d), ktorá sa nachádza v strede priečneho hriadeľa medzi nožnicami (obr. 10). Táto matica je pripevnená k hriadeľu pomocou dvoch kĺznych kuželíkových ložísk (e) STN ISO 32 s rozmermi $d_1 = 40\ mm, D = 62\ mm$. Ložiská sú v matici pripevnené pomocou prírub (f) so skrutkami M8x22 ISO 4014 a k hriadeľu pomocou rúrky s kolíkom 10 x 8 ISO 2338 (obr. 11).

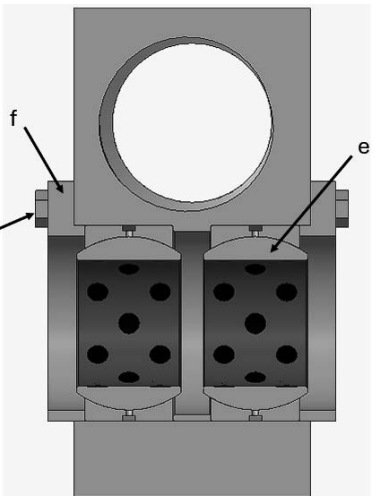

Obr. 10 Rez spodnej matice
Figure 10. Bottom nut cut

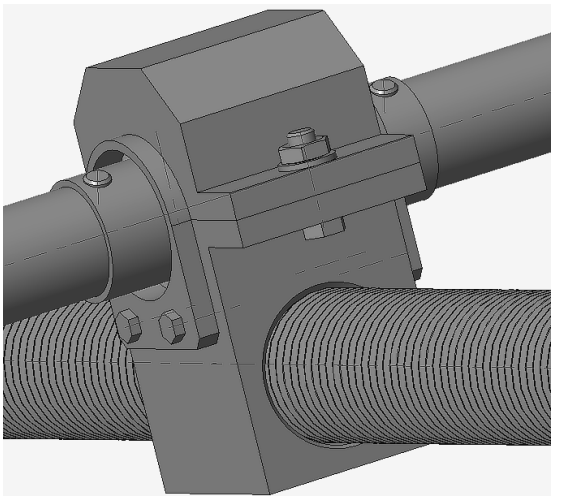

Obr. 11 Uloženie skrutkovice v matici
Figure 11. Storing the screw in the nut

Výsledná zostava bola následne vystužená tyčami Ø40, ktoré sú uložené medzi nožnicami tak, aby zabraňovali pohybu zdviháku do strán. K tomu bola navrhnutá aj vodiaca tyč Ø40, ktorá bola pripevnená k zostave lineárnym ložiskom (a) KBA-20S-UU ISO Standards G20 (obr. 12).

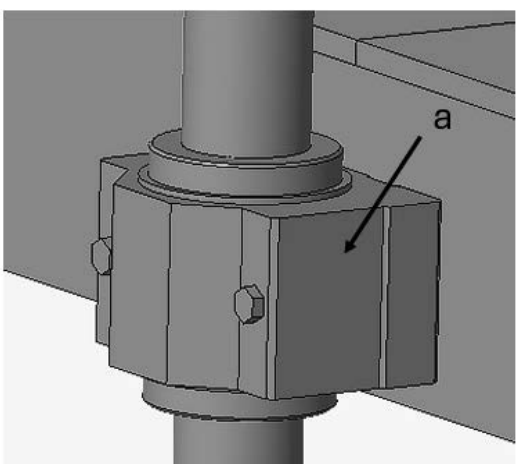

Obr. 12 Detail uloženia lineárneho ložiska
Figure 12. Detail of linear bearing mounting

Na vrchnej časti vodiacej tyče sa nachádza príruba, ktorá bola uchytená k vodiacej tyči a zároveň aj k stene vedľa zdviháku, aby sa zabránilo jeho posúvaniu do strán. Spodné časti ako sú koľajnice a pevné časti boli vystužené platničkami s dierami na kotvu (obr. 13).

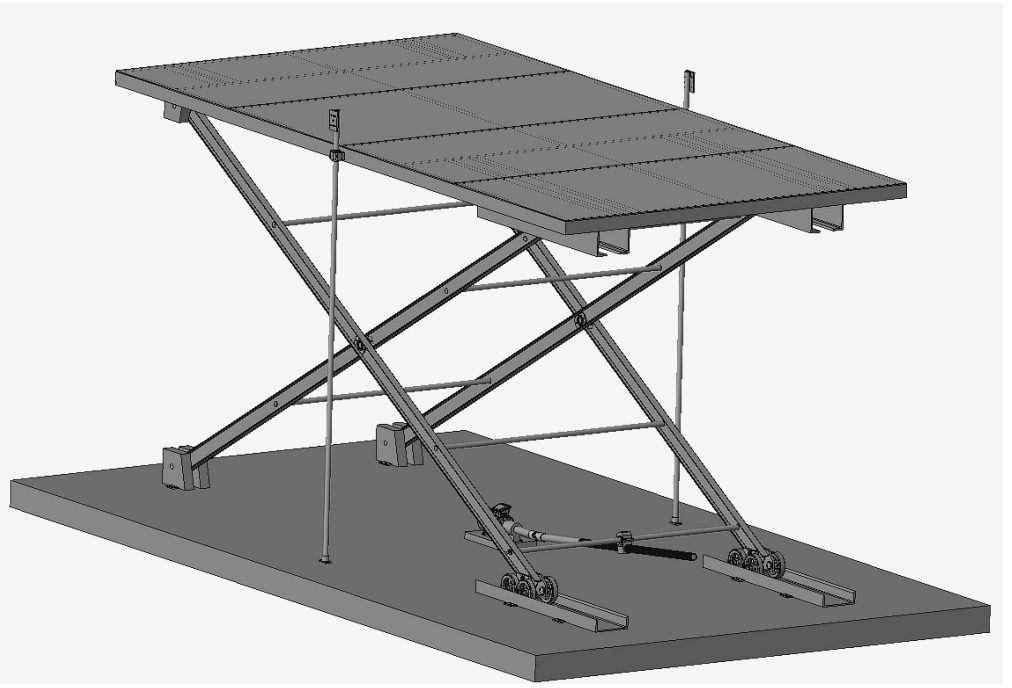

Obr. 13 Výsledný konštrukčný návrh zdviháka
Figure 13. The resulting structural design of the lift

3. ZÁVER

Výsledkom práce je jednoduchý konštrukčný návrh zdvíhacieho mechanizmu do 3,5t pre parkovanie pod zemou vytvorený v programe PTC Creo Parametric 9D vrátane technickej dokumentácie vybraných komponentov podľa platných noriem.

POĎAKOVANIE

Príspevok vznikol v rámci riešenia spoločného slovensko-poľského projektu Project Based Learning ako výsledok spolupráce medzi Politechnikou Slaskou, Gliwice a Žilinskou univerzitou v Žiline a projektov KEGA č. 033ŽU-4/2026 a KEGA č. 039ŽU-4/2026.

LITERATÚRA

1. Bc. Sebastián Dlugosch, Konštrukčný návrh zdvíhacieho mechanizmu do 3,5t pre parkovanie pod zemou, Bakalárska práca, EDIS Žilina, 2024

TalentDetector

7th-9th June 2026
Gliwice-Brenna, Poland

DEPARTMENT OF ENGINEERING MATERIALS AND BIOMATERIALS
FACULTY OF MECHANICAL ENGINEERING
SILESIAN UNIVERSITY OF TECHNOLOGY

INTERNATIONAL STUDENTS SCIENTIFIC CONFERENCE

Comparison of different types of fiducial markers

Maciej Dymkowski[a], Michał Zientek[b], Tomasz Kukuczka[c], Tomasz Moroń[d]

a, b: Silesian University of Technology, Faculty of Automatic Control, Electronics and Computer Science, Informatyka
c: Silesian University of Technology, Faculty of Automatic Control, Electronics and Computer Science, Doctoral School
d: Silesian University of Technology, Faculty of Automatic Control, Electronics and Computer Science, Department of Cybernetics, Nanotechnology and Data Processing
email:[a] md314909@student.polsl.pl

Abstract: This paper presents the initial stage of a mobile robot swarm project developed within a student research group at the Silesian University of Technology. The long-term goal of the project is to develop a cooperative robotic system capable of moving collectively from point A to point B, sharing information about the surrounding environment, and performing mutual localization. The study focuses on the vision-based perception subsystem, specifically on evaluating the detection performance of fiducial markers placed on **JetRacer** Professional Version ROS AI Kit B mobile platforms. A dataset of images containing markers captured at different distances, orientations, and positions within the camera frame was prepared for experimental evaluation. The detection performance of **AprilTag** markers was then compared with **ArUco**. The analysis made it possible to identify how selected factors influence marker detectability and to determine which solution is more suitable for mutual robot localization tasks. The obtained results provide a foundation for future work on relative position estimation between robots and the development of a shared environmental map.

Keywords: fiducial markers, computer vision, object recognition

1. INTRODUCTION

Vision systems are used, among others, in robotics, autonomous driving, localization systems, and navigation. One popular solution for object recognition and determining object position is the use of artificial reference markers[1]. These markers are specially designed with graphical patterns that enable automatic detection and identification in a digital image. Examples of such markers include ArUco markers and AprilTags[3].

ArUco markers and AprilTags belong to the group of two-dimensional graphical patterns, examples of which are shown in Figure 1. They take the form of square binary codes which, after being detected by an image-processing algorithm, make it possible to determine not only their identifier but also their orientation and position relative to the camera. However, estimating the

position and orientation of a marker relative to the camera requires knowledge of the marker's physical size and the camera's calibration parameters. As a result, they can be used, among other applications, for the localization and identification of a robot in a swarm, as well as reference points in space supporting autonomous navigation. The advantages of this approach include relatively simple implementation, low hardware requirements, and, most importantly, in the case of autonomous vehicles, real-time operation.

In practical applications, one of the key factors affecting detection effectiveness is the distance between the marker and the camera. As the distance increases, the marker occupies a smaller part of the image, which may cause difficulties in its correct recognition and identification.

When developing an autonomous driving system, such as one that can be created using the JetRacer platform, correct marker identification within the required operating distance range is essential. The aim of the research described in this article was to compare the most popular types of AprilTags and ArUco markers. The comparison was conducted directly on vehicles that are ultimately intended to move autonomously and included an assessment of detection accuracy, as well as determining which markers are best suited for the development of autonomous mobile platforms[4].

The goal of this study is to evaluate the reliability and detection of the fiducial markers. They are high-contrast patterns that a program can easily detect, identify, and calculate their relative position. These markers are used in augmented reality (AR) applications such as robotic swarms[2], warehouse automation, and product manufacturing.

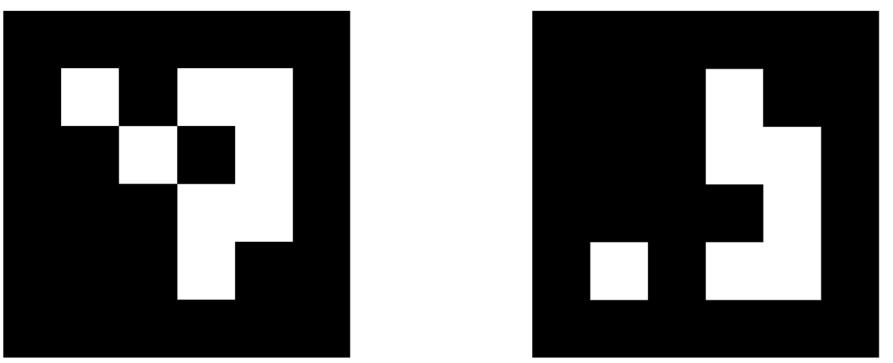

Figure 1. Left tag is an example of ArUco 4x4 marker and the right one is an example of AprilTag tag16h5

2. CHARACTERISTICS OF THE APPLIED FIDUCIAL MARKERS

ArUco markers and AprilTags are square fiducial markers composed of black and white fields that form a unique binary pattern[5]. Their structure is based on a clear contrast between white and black areas, which facilitates their detection in a digital image. The outer border of the marker makes it possible to distinguish it from the background and determine its approximate position during scene analysis. The inner part of the marker contains an encoded pattern that allows a specific identifier to be assigned to it.

2.1. ArUco Markers

Each ArUco marker consists of an outer black border and an inner binary pattern. The border facilitates marker detection in the image and allows the algorithm to determine its boundaries

and corners. The inner part of the marker contains an arrangement of black and white fields that encodes its identifier. As a result, the system can distinguish multiple markers located in the same environment.

ArUco markers are organized into so-called dictionaries. A dictionary defines a set of possible markers, their structure, and the number of available identifiers. For example, the designation 4×4 indicates that the inner binary pattern of the marker consists of a grid of 4 by 4 fields. It does not refer to the physical size of the marker, but to the number of encoding fields.

In robotic applications, ArUco markers can serve as reference points placed within the robot's operating environment. A camera mounted on a vehicle can detect the markers, read their identifiers, and use information about their position to support localization and navigation. For this reason, analyzing the detection effectiveness of different types of ArUco markers depending on the distance from the camera is important when designing autonomous motion systems.

2.2. AprilTag Markers

The basic operating principle of AprilTags is similar to that of ArUco markers. The detection algorithm searches the image for quadrilateral-shaped regions, determines the corners of a potential marker, and then analyzes the binary pattern located inside it. Based on this process, the marker identifier is read. With known camera calibration parameters and the actual physical size of the marker, it is also possible to determine its position and orientation relative to the camera in three-dimensional space.

In the names of AprilTag families, the first number indicates the number of encoding bits inside the marker, while the letter h followed by another number refers to the minimum Hamming distance. For example, the tag36h11 family contains markers whose code consists of 36 bits, and the minimum Hamming distance between codes is 11. This means that individual markers in this family are clearly distinguishable from one another, which increases resistance to incorrect identification.

3. ROBOT PLATFORM

In the experiment we used the WaveShare JetRacer ROS AI Kit platform, shown in Figure 2. It is a mobile robotic platform designed for experiments in vision systems, artificial systems and autonomous driving[6,7]. The use of this platform allowed us to possible conduct tests in approximated conditions similar to the potential target application. This made process of fiducial marker detection more effective.

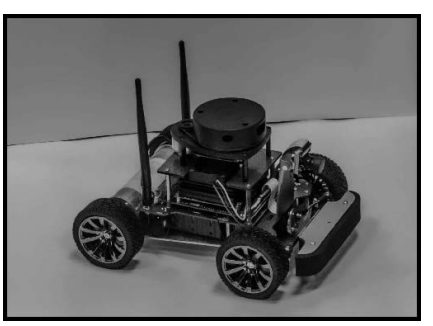

Figure 2. Assembled JetRacer ROS AI Kit platform used as the mobile robotic system in the experiment.

We used Jetson Nano to handle system booting and run detection algorithms[8]. Since it is less powerful than standard desktop computer, it enabled us to assess how the detection performs on the actual small autonomous platform intended for future use[9].

For image acquisition, we utilized 8-megapixel camera equipped with a Sony IMX219 sensor in Figure 3. The camera communicates with the platform via the MIPI CSI-2 interface. Compared to USB cameras, this solution can reduce CPU usage and, in certain cases, minimize data transmission latency. This is critical for real-time systems, where the frame processing time directly impacts the ability to use detection results for tasks such as vehicle control.

Figure 3. 8 MP Sony IMX219 camera used for image acquisition during the marker detection experiments.

The software used in the experiment was developed in Python 3.8, utilizing the OpenCV 4.13.0 library for computer vision tasks. Specifically, the cv2.aruco module was employed for marker detection. The entire image processing pipeline was executed locally on the previously described testing platform. This architecture allowed us to verify whether theses marker types could be effectively detected within the existing hardware constraints.

During the studies, images were processed at a resolution of 1280 × 720 pixels. This resolution was selected due to hardware constraints, representing a compromise between image detail and frames per second (FPS). Such limitations may pose a challenge for the further development of autonomous driving platform.

4. DESCRIPTION OF THE EXPERIMENT

The aim of the experiment was to compare the detection effectiveness of selected ArUco and AprilTag markers depending on the distance between the marker and the camera. The experiment included ArUco markers from the DICT_4X4_250, DICT_5X5_250, DICT_6X6_250, and DICT_7X7_250 dictionaries. In the case of AprilTags, the tag36h11 and tag25h9 families were used[3,10].

Detection was performed on images with a resolution of 1280 × 720 pixels. This resolution was selected due to the hardware limitations of the Jetson Nano platform. Images with higher resolution increased memory usage and the processing time of a single frame, which made real-time detection impossible.

The experiment consisted of recording images of a marker placed at different distances from the camera. Measurements were carried out at distances of 50, 100, 150, 200, and 250 cm. All tested markers had the same physical size of 9 × 9 cm, which made it possible to compare the results under equal conditions[11]. For each combination of marker type and distance, 500 image frames were recorded (example frames shown in Figure 4). The experiment was conducted

under constant artificial lighting to limit the influence of changing lighting conditions on detection effectiveness.

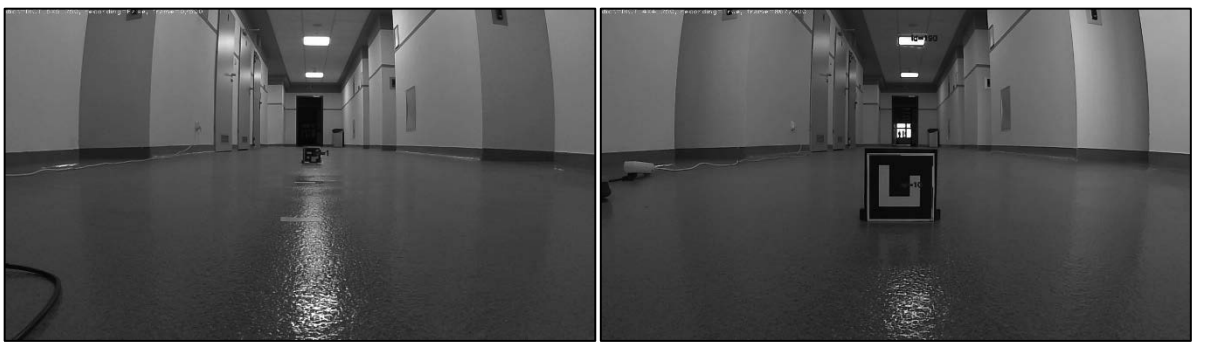

Firugre 4. Example frames from the conducted experiment. The right image shows a case in which the marker detection was classified as correct. The left image shows a frame in which image noise was detected as an additional marker and was therefore classified as a false detection.

For each recorded frame, it was checked whether the marker was detected by the detection algorithm. Next, it was evaluated whether the detected marker was correctly identified; that is, whether the returned identifier corresponded to the actual marker present in the camera field of view. Additionally, the occurrence of false detections was analyzed, including cases in which the algorithm detected a marker that was not present in the analyzed scene, detected an additional non-existent marker, or assigned an incorrect identifier to the detected object.

Based on the collected data, it was possible to determine the detection effectiveness of individual marker types as a function of distance. This made it possible to compare which ArUco dictionaries and AprilTag families maintained the highest effectiveness as the distance between the marker and the camera increased, as well as which of them were most susceptible to incorrect identification or loss of detection.

The software used in the experiment was implemented in Python 3.8 using the OpenCV 4.13.0 library[12]. Marker detection was performed on a Jetson Nano platform running the Linux 5.8 operating system. This setup made it possible to evaluate detection effectiveness under conditions of the target system, in which image processing is carried out directly on board the mobile platform.

5. RESULTS

The experimental results were presented as the detection effectiveness of individual marker types depending on the distance from the camera. Detection effectiveness was determined as the ratio of the number of frames in which the marker was correctly detected and identified to the total number of analysed frames for a given measurement configuration. For each combination of marker type and distance, 500 image frames were analysed. Detection effectiveness was calculated according to the following formula:

$$D_e = \frac{N_c}{N_t} \cdot 100\%$$

where D_e denotes the detection effectiveness, N_c is the number of frames in which the marker was correctly detected and identified, and N_t is the total number of analyzed frames for a given measurement configuration.

Table 1. Comparison of detection effectiveness for selected ArUco dictionaries and AprilTag families at different marker-to-camera distances.

Distance 0.5 m				
Tag Family	True detections	False detections	Non-detections	D_e[%]
ArUco 4x4_250	498	2	0	99.6
ArUco 5x5_250	500	0	0	100
ArUco 6x6_250	500	0	0	100
ArUco 7x7_250	499	0	1	99.8
AprilTag tag25h9	451	0	49	90.2
AprilTag tag36h11	500	0	0	100
Distance 1 m				
ArUco 4x4_250	500	0	0	100
ArUco 5x5_250	500	0	0	100
ArUco 6x6_250	500	0	0	100
ArUco 7x7_250	500	0	0	100
AprilTag tag25h9	178	0	322	35.6
AprilTag tag36h11	137	0	363	27.4
Distance 1.5 m				
ArUco 4x4_250	500	0	0	100
ArUco 5x5_250	483	0	17	96.6
ArUco 6x6_250	275	0	225	55.0
ArUco 7x7_250	350	0	150	70.0
AprilTag tag25h9	43	0	457	8.6
AprilTag tag36h11	43	0	457	8.6
Distance 2 m				
ArUco 4x4_250	500	0	0	100
ArUco 5x5_250	319	0	181	63.8
ArUco 6x6_250	474	0	26	94.8
ArUco 7x7_250	12	0	488	2.4
AprilTag tag25h9	0	0	500	0
AprilTag tag36h11	0	0	500	0
Distance 2.5 m				
ArUco 4x4_250	496	1	3	99.2
ArUco 5x5_250	19	0	481	3.8
ArUco 6x6_250	492	0	8	98.4
ArUco 7x7_250	55	0	455	11.0
AprilTag tag25h9	0	0	500	0
AprilTag tag36h11	85	0	415	17.0

Based on the results presented in Table 1, significant differences in detection effectiveness were observed between the tested marker types. At a distance of 0.5 m, most markers achieved very high detection effectiveness, ranging from 99.6% to 100% for ArUco markers and reaching 100% for AprilTag tag36h11. The exception was AprilTag tag25h9, for which the detection effectiveness was 90.2%.

As the distance increased, a decrease in detection effectiveness was observed for some of the tested markers. The highest stability over the entire measurement range was achieved by ArUco 4x4_250, whose effectiveness remained no lower than 99.2%. ArUco 6x6_250 also achieved high effectiveness; however, in this case, an unusual decrease in effectiveness was observed at a distance of 1.5 m, which may indicate the influence of additional factors, such as a temporary deterioration of image sharpness.

ArUco 5x5_250 and 7x7_250 showed a clear decrease in effectiveness at greater distances. This was particularly visible for ArUco 7x7_250, whose effectiveness at a distance of 2 m was only 2.4%. This may result from the larger number of encoding fields, which, with a fixed physical marker size, occupy fewer pixels in the image, making correct reading of the binary pattern more difficult.

For the tested AprilTag families, a rapid decrease in detection effectiveness was observed already at a distance of 1 m. For tag25h9, the effectiveness was 35.6%, while for tag36h11 it was 27.4%. At subsequent distances, the number of correct detections remained low or zero, indicating that, in the adopted experimental configuration, AprilTags were less resistant to increasing camera-to-marker distance than ArUco markers[11].

The number of false detections was negligible. They occurred only for ArUco 4x4_250, which suggests that the main limitation of the system was not incorrect marker identification, but the lack of marker detection in the image. The obtained results indicate that, for the applied image resolution, physical marker size, and hardware configuration, the highest detection effectiveness was achieved by ArUco 4x4_250.

6. CONCLUSION

The aim of this study was to evaluate the detection effectiveness of selected ArUco dictionaries and AprilTag families at different marker-to-camera distances using a JetRacer-based mobile platform. The experiment was carried out under controlled lighting conditions, with all markers having the same physical size and the image processed at a resolution of 1280 × 720 pixels.

The obtained results confirmed that marker detection effectiveness depends on the marker structure, image resolution, and distance from the camera. In the adopted experimental configuration, ArUco markers generally provided more stable detection results than the tested AprilTag families. Among the analyzed variants, the ArUco 4x4_250 marker showed the highest suitability for the considered application, maintaining reliable detection across the tested distance range.

The low number of false detections indicates that the main limitation of the system was not incorrect marker classification, but rather the loss of detection when the marker became too small or insufficiently clear in the image. This observation is important for autonomous mobile platforms, where reliable marker detection is required for localization, navigation, or object identification.

BIBLIOGRAPHY

1. Wieczorek, Bartosz, et al. "The effects of ArUco marker velocity and size on motion capture detection and accuracy in the context of human body kinematics analysis." *Technical Transactions* 117.1 (2020).
2. Sani, Mohammad Fattahi, and Ghader Karimian. "Automatic navigation and landing of an indoor AR. drone quadrotor using ArUco marker and inertial sensors." *2017 international conference on computer and drone applications (IConDA)*. IEEE, 2017.
3. Patru, George-Cristian, et al. "Fiducial marker systems overview and empirical analysis of ArUco, AprilTag and CCTag." *UPB Sci. Bull., Series C* 85.2 (2023): 49-62.
4. Bacik, Jan, et al. "Autonomous flying with quadrocopter using fuzzy control and ArUco markers." *Intelligent Service Robotics* 10.3 (2017): 185-194.
5. Jurado-Rodriguez, David, et al. "Planar fiducial markers: a comparative study." *Virtual Reality* 27.3 (2023): 1733-1749.
6. Cuervo-Méndez, Saúl J., et al. "Autonomous Navigation Rescue Vehicles: Measuring and Analyzing Trajectories with an Experimental Robot." *2025 IEEE Mexican Humanitarian Technology Conference (MHTC)*. IEEE, 2025.
7. Eswarawaka, Rajesh, et al. "Design and development of autonomous driving car using nvidia jetson nano developer kit." *International Conference on Innovations in Computational Intelligence and Computer Vision*. Singapore: Springer Nature Singapore, 2024.
8. Akdeniz, Fulya, et al. "A review of a research in autonomous vehicles with embedded systems." *The Proceedings of the International Conference on Smart City Applications*. Cham: Springer Nature Switzerland, 2023.
9. Mora-Salinas, Roberto J., and David Antonio-Torres. "Development of engineering skills through low-cost miniature autonomous guided vehicles." *International Conference on Interactive Collaborative Learning*. Cham: Springer International Publishing, 2022.
10. Wang, John, and Edwin Olson. "AprilTag 2: Efficient and robust fiducial detection." *2016 IEEE/RSJ international conference on intelligent robots and systems (IROS)*. IEEE, 2016.
11. Cho, Suyeon, and Euiho Kim. "Analysis in long-range apriltag pose estimation and error modeling." *Proceedings of the 35th International Technical Meeting of the Satellite Division of The Institute of Navigation (ION GNSS+ 2022)*. 2022.
12. Bradski, Gary, and Adrian Kaehler. "OpenCV." *Dr. Dobb's journal of software tools* 3.2 (2000): 1-81.

TalentDetector

7th-9th June 2026
Gliwice-Brenna, Poland

DEPARTMENT OF ENGINEERING MATERIALS AND BIOMATERIALS
FACULTY OF MECHANICAL ENGINEERING
SILESIAN UNIVERSITY OF TECHNOLOGY

INTERNATIONAL STUDENTS SCIENTIFIC CONFERENCE

Condition Monitoring and Fault Diagnosis of Electric Motors in Cable Extrusion Lines

Elber Erkul[a], Ali Sevgili[a], Mustafa Arslan Karakaya[a], Cemal Meran[a], Fatih Oztekin[b]

[a] Pamukkale University, Faculty of Engineering, Department of Mechanical Engineering, Denizli-Turkiye, email: cmeran@pau.edu.tr
[b]Nexans Turkey Industry, R&D Center, Denizli,Turkiye, fatih.oztekin@nexans.com

Abstract: In this study, the feasibility and effectiveness of predictive maintenance strategies were investigated on the cable extrusion line at the Nexans Turkey Denizli Factory. By integrating vibration, current, and temperature analyses rather than relying on traditional reactive or periodic maintenance methods, the actual health condition of the system components was continuously monitored without interrupting production. During the field studies, operational data collected from critical units between 2025 and 2026 were examined utilizing frequency spectrum (FFT) and trend analyses. Based on the findings, hazardous radial vibrations exceeding the upper alarm limits (16,27 mm/s horizontally and 16,12 mm/s vertically) were detected at the 24,17 Hz (1x) running frequency of the Pay-off 1 unit, leading to the diagnosis of a coupling misalignment issue. In the caterpillar unit, advanced rotor unbalance was identified, characterized by a dominant 1x peak reaching an RMS level of 9,202 mm/s. In the filler extruder, early-stage gear fatigue and oil starvation were detected; although these issues were not reflected in standard speed data, they exhibited sudden spikes of up to 270 % in the acceleration spectrum. Furthermore, it was electrically verified that these mechanical faults caused an increase of over 25% in motor current consumption, resulting in facility-wide energy waste. Consequently, critical faults were successfully identified through rigorous predictive maintenance ((PdM) data analysis.

Keywords: Cable extrusion line, predictive maintenance, vibration analysis, motor current analysis

1. INTRODUCTION

In modern industrial production facilities, particularly in cable extrusion lines where continuous production is critical, the operational reliability of rotating equipment—such as electric motors, gearboxes, and caterpillar units—directly influences overall production efficiency. Traditional reactive (breakdown-based) or periodic (time-based) maintenance strategies often lead to high operational costs due to unexpected downtimes, production losses, or the premature replacement of machine components that have not yet reached the end of their useful service life. To overcome these bottlenecks, Predictive Maintenance (PdM) approaches,

which monitor machine health via dynamic parameters, have become a necessity in modern production lines. Vibration analysis, as the cornerstone of predictive maintenance, serves as the most analytical diagnostic method for detecting mechanical anomalies in rotating machinery at an early stage and on a component-specific basis.

When examining the principles of machine dynamics and international standards (e.g., ISO 10816), it is evident that fault characteristics in rotating systems differentiate according to frequency bands. Macroscopic kinematic faults such as rotor unbalance, coupling misalignment, and structural looseness are characterized by vibration velocity (mm/s) parameters in the low-frequency band. In contrast, microscopic tribological defects—such as micro-cracks in bearing raceways, rolling element fatigue, and gear surface wear—generate high-frequency acceleration shock waves (vibration acceleration, mm/s^2) long before they manifest as macroscopic structural vibrations. Therefore, a condition-monitoring strategy based solely on vibration velocity carries the risk of overlooking early-stage fatigue symptoms. Furthermore, mechanical stresses and increased surface friction in rotating equipment directly convert into thermodynamic losses (higher surface temperatures) and electrical resistance (and increased mechanical torque demand). The cross-validation of vibration data with surface temperature measurements and motor current (Amperage) variations provides a holistic approach to machine health. Accordingly, the primary objective of this study is to investigate the dynamic behaviors of rotating equipment on a cable extrusion line by establishing a multi-dimensional condition-monitoring methodology based on vibration velocity, acceleration, temperature, and current data, thereby diagnosing potential faults before they escalate into catastrophic failures.

2. MATERIAL AND METHOD

For calculations and spectrum analyses, it is assumed that all rotating equipment on the extrusion line operated in a steady-state condition and at a constant line speed throughout the measurement periods, that there was a continuous thermal distribution on the electric motor and gearbox housings, and that the mounting bases exhibited perfectly rigid behavior. Within the scope of this study, the Filling, Sheathing, and Color extruders, as well as the Caterpillar, Pay-off 1, and Capstan units located on the cable production line, were evaluated as interactive yet dynamically independent systems. Separate condition assessments were conducted for each machine group using measurement data covering the years 2025 and 2026. The analysis database consists of low-frequency vibration velocity (mm/s), high-frequency vibration acceleration (G), machine surface temperature (°C), and the electrical current (Amperage) drawn by the motors from the grid. Vibration data were systematically collected in three axes [Horizontal (H), Vertical (V), and Axial (A)] from the bearing housings on the input and output shafts of the motor (M) and gearbox (G) groups, in accordance with the kinematic structure. To enhance the accuracy of calculations and diagnoses, ISO 10816 vibration standards were adopted as the academic and industrial reference baseline for evaluating macroscopic structural faults such as unbalance, misalignment, and looseness. Furthermore, Fast Fourier Transform (FFT)-based envelope spectrum methodologies were utilized to detect early-stage bearing fatigue and Gear Mesh Frequency (GMF) wear, and fault characteristics were modeled based on these parameters.

Figure 1. Data acquisition application using an accelerometer

Figure 1 illustrates the data acquisition process performed by a technician using an accelerometer, which is a transducer that converts mechanical vibrations into electrical signals. This sensor plays a critical role in capturing high-frequency data from bearing housings for structural health monitoring. By analyzing these real-time signals, potential faults—such as bearing wear or axial misalignment—can be detected through frequency spectrum analysis before leading to equipment downtime.

2.1 Reel Pay-off 1 Vibration Analysis

Table 1. Pay-off 1 Vibration Data Table

Machine ID	Machine Name	Point ID	Day / Date	Analysis Parameters	Trend Value	%Change Compared to Previous
İK 32	Pay-Off 1	M1H	6.05.2026	General Value	16,267 mm/s	Not Available
İK 32	Pay-Off 1	M1P	6.05.2026	General Value	0,056 mm/s²	Not Available
İK 32	Pay-Off 1	M1V	6.05.2026	General Value	16,125 mm/s	Not Available
İK 32	Pay-Off 1	M2H	6.05.2026	General Value	5,836 mm/s	Not Available
İK 32	Pay-Off 1	M2P	6.05.2026	General Value	0,111 mm/s²	Not Available
İK 32	Pay-Off 1	M2V	6.05.2026	General Value	3,563 mm/s	Not Available
İK 32	Pay Off 1	M2A	6.05.2026	General Value	11,159 mm/s	Not Available
İK 32	Pay-Off 1	G1H	6.05.2026	General Value	1,902 mm/s	Not Available
İK 32	Pay-Off 1	G1P	6.05.2026	General Value	0,113 mm/s²	Not Available
İK 32	Pay-Off 1	G1V	6.05.2026	General Value	1,305 mm/s	Not Available
İK 32	Pay-Off 1	G1A	6.05.2026	General Value	3.764 mm/s	Not Available
İK 32	Pay-Off 1	G3H	6.05.2026	General Value	0,645 mm/s	Not Available
İK 32	Pay-Off 1	G3P	6.05.2026	General Value	0,058 mm/s²	Not Available

As shown in Table 1, high radial vibration amplitudes reaching 16 mm/s were recorded in the horizontal and vertical directions of the Pay-off 1 motor. While the vertical measurements indicate potential weaknesses regarding the unit's frame connections or structural rigidity, the axial data collected from the motor-gearbox interface, when correlated with spectrum analysis, confirm that the primary root cause is Coupling Misalignment.

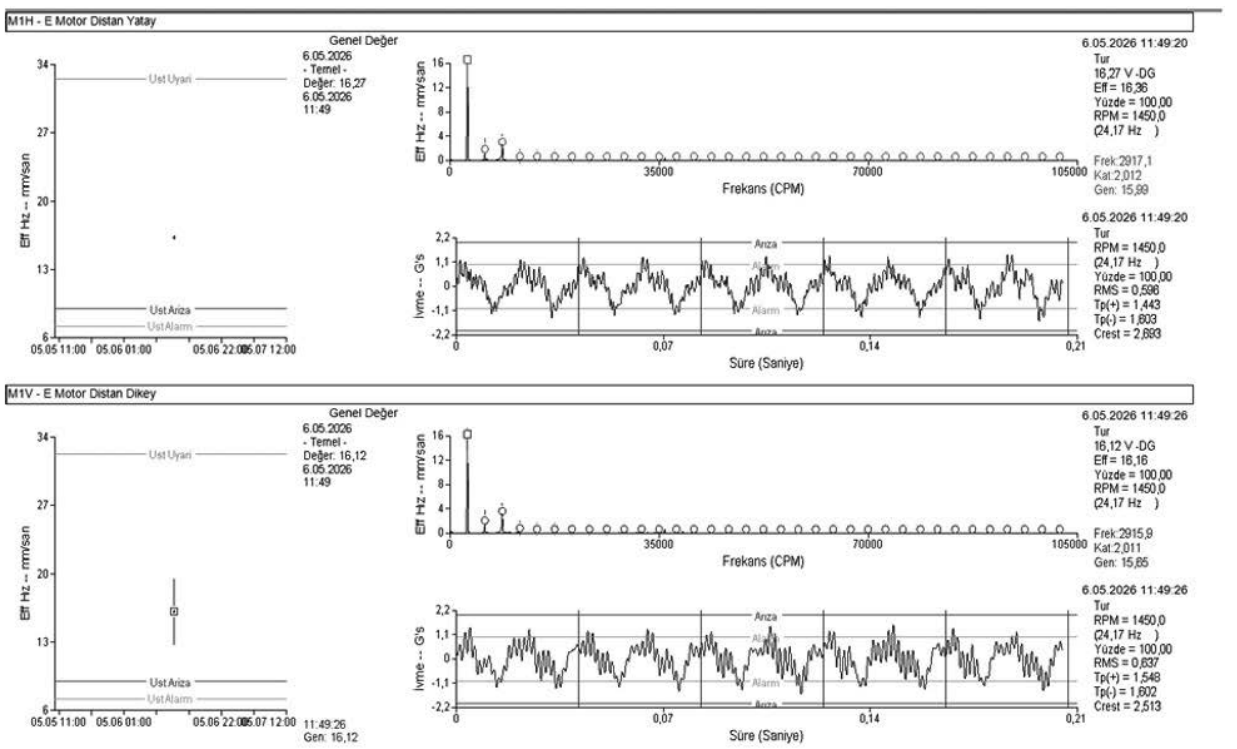

Figure 2. Vibration analysis results for the Pay-off 1 unit motor in horizontal (M1H) and vertical (M1V) directions

Figure 2 presents the horizontal (M1H) and vertical (M1V) vibration spectrum graphs of the motor belonging to the IK-32 line Pay-off 1 unit. The most significant finding in the graph is the high-amplitude vibration peak occurring at the motor's rotational frequency of 1X RPM (1450 RPM / 24,17 Hz). As stated in the predictive maintenance report, this condition elevates the equipment to Category 3 (critical) risk level. This dominant peak at the 1X RPM frequency, accompanied by bearing signals, indicates a mechanical problem (such as misalignment or looseness) in the frame, intermediate connections, or rotating components that requires immediate intervention.

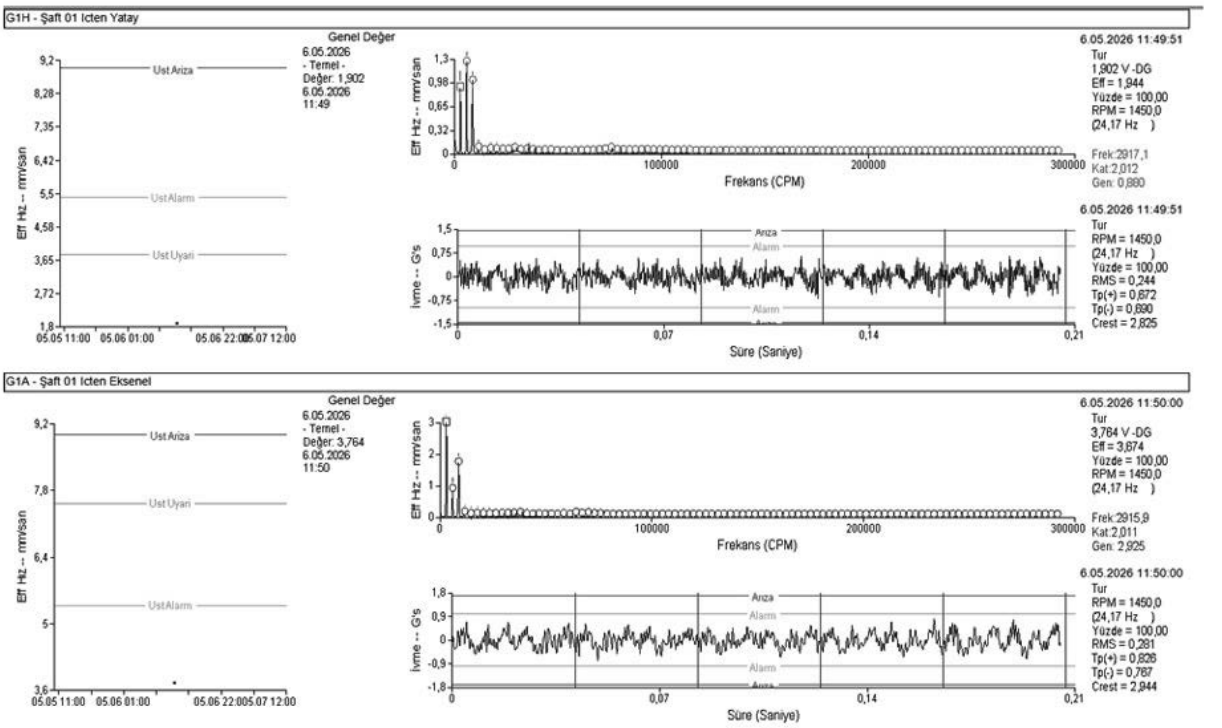

Figure 3. Vibration analysis results for the Pay-off 1 unit gearbox input shaft in horizontal (G1H) and axial (G1A) directions

Figure 3 shows the horizontal (G1H) and axial (G1A) vibration spectrum graphs for the gearbox input shaft of the IK-32 Pay-off 1 unit. Upon examining the graphs, it is observed that the radial (horizontal) vibration level is relatively low at 1,902 mm/s compared to the motor side. This indicates that the root cause of the fault does not originate directly from the internal gearbox components. However, in the axial direction (G1A), a prominent peak is observed at the rotational frequency (1X RPM – 24,17 Hz), and the overall vibration value is measured at 3,764 mm/s. The fact that the axial vibration exceeds the radial vibration and the presence of this dominant amplitude at the 1X frequency conclusively proves the existence of a clear coupling misalignment problem between the motor and the gearbox in the system.

2.2 Temperature Analysis

As shown in Table 2, the operating temperatures of the equipment (24°C–49°C) are well below the damage threshold of 70°C and remain within safe limits. However, thermal data are closely correlated with vibration faults. Despite sudden acceleration (G) spikes of 270% in the acceleration spectrum, the Filler Extruder exhibits a reasonable outlet temperature of 42,7°C, indicating a metal-to-metal friction condition that is still in its early stages. Notably, the Caterpillar unit reached the highest temperature value at 49,0°C; this is thermal evidence of the mechanical power losses caused by the high unbalance fault of 9,2 mm/s detected in the unit. The stable temperature trend in the other units confirms ideal lubrication conditions and healthy vibration profiles.

Table 2. Temperature Measurement Data For The IK-32 Line

Equipment Name	Measurement Point 1 (Inlet)	Measurement Point 2 (Outlet)
IK_32 Filling Extruder	37,9 °C	42,7 °C
IK_32 Sheathing Extruder	31,7 °C	36,7 °C
IK_32 Color Extruder	23,9 °C	36,9 °C
IK_32 Caterpillar	49,0 °C	42,0 °C
IK_32 Pay-Off 1	33,5 °C	37,7 °C
IK_32 Pay-Off 2	23,2 °C	31,1 °C
IK_32 Capstan	28,0 °C	38,0 °C

2.3 Motor Current Signature Analysis (MCSA)

Figure 4. Electrical Control Panel Of The IK 32-Line

Monitoring the electrical current drawn by electric motors from the grid is a critical predictive maintenance method for observing the electrical reflections of mechanical faults. The analyses indicate that mechanical stresses, such as mass unbalance or coupling misalignment, increase internal system friction, which directly reflects on motor current consumption. As can be observed on the panel screen in Figure 4, the 25,5% increase in current observed in the Caterpillar unit compared to the previous year's (2025) data parallels the increase in vibration data (9,2 mm/s) and confirms the electrical load imposed on the motor by the mechanical fault. Current analysis serves as a vital parameter for the cross-validation of fault diagnosis, particularly in situations where vibration data acquisition is limited or structural noise is high, thereby significantly enhancing operational reliability.

3. CONCLUSIONS

This study demonstrates the necessity of a "Multi-Dimensional Condition Monitoring" approach in which vibration, temperature, and current analyses are integrated for cable extrusion lines. As a result of the analysis of operational data from 2025–2026, advanced mass unbalance (9.2 mm/s) in the Caterpillar unit and severe coupling misalignment in the Pay-off 1 unit were identified. It was determined that these mechanical defects cause excessive friction in the system, localized temperature increases reaching 49°C, and excessive current consumption exceeding 25%. To maintain equipment integrity and prevent facility-wide energy waste, it has been decided to urgently perform dynamic balancing on the Caterpillar unit, conduct laser-assisted coupling alignment on the Pay-off 1 unit, and incorporate all critical bearings into routine periodic monitoring schedules.

BIBLIOGRAPHY

1. S. Nandi, H. A. Toliyat, and X. Li, "Condition Monitoring and Fault Diagnosis of Electrical Motors—A Review," IEEE Trans. Energy Convers., vol. 20, no. 4, pp. 719-729, Dec. 2005.
2. M. E. H. Benbouzid, "A Review of Induction Motors Signature Analysis as a Medium for Faults Detection," IEEE Trans. Ind. Electron., vol. 47, no. 5, pp. 984-993, Oct. 2000.
3. A. K. S. Jardine, D. Lin, and D. Banjevic, "A review on machinery diagnostics and prognostics implementing condition-based maintenance," Mech. Syst. Signal Process., vol. 20, no. 7, pp. 1483-1510, Oct. 2006.
4. O. Öztanır, "Predictive Maintenance Using Machine Learning," M.S. thesis, Graduate School of Natural and Applied Sciences, Hacettepe Univ., Ankara, 2018.
5. S. Saraç, "Predictive Maintenance and Early Fault Diagnosis in Electrical Motors via Vibration Analysis," M.S. thesis, Dept. Elect. Eng., Istanbul Technical Univ., Istanbul, 1999.
6. M. Yurtsever, "Vibration Analysis-Based Fault Diagnosis and Predictive Maintenance System Design Using Machine Learning and Deep Learning Methods," Ph.D. dissertation, Dept. Business Administration, Ege Univ., Izmir, 2020.
7. G. Aydın and C. Meran, "Fault Diagnosis and Prevention with Predictive Maintenance in the Cement Industry," Mühendis ve Makina, vol. 59, no. 692, pp. 48-67, 2018.
8. S. S. Erol and C. Meran, "Tribological approach on vibration and electrical current response of experimental misalignment and unbalance failure modes," J. Balkan Tribolog. Assoc., vol. 21, no. 1, pp. 164-177, 2015.
9. S. S. Erol and C. Meran, "A tribological study in the perspective of vibro-electric analysis," Arch. Mater. Sci. Eng., vol. 77, no. 2, pp. 53-61, 2016.
10. M. F. Orha, D. Yavaş, and A. Kabukçu, "Predictive Maintenance in Wire Drawing Machines," Bachelor's thesis, Dept. Mech. Eng., Pamukkale Univ., Denizli, 2025.
11. B. Çeker, S. Kunan, M. Mat, K. İlhan, and C. Meran, "Predictive Maintenance on Medium Voltage Cable Production Extrusion Machine," in Proc. TalentDetector2025 Winter Int. Student Sci. Conf., 2025.

TalentDetector

7th-9th June 2026
Gliwice-Brenna, Poland

DEPARTMENT OF ENGINEERING MATERIALS AND BIOMATERIALS
FACULTY OF MECHANICAL ENGINEERING
SILESIAN UNIVERSITY OF TECHNOLOGY

INTERNATIONAL STUDENTS SCIENTIFIC CONFERENCE

Development of Antibacterial Hybrid Coatings on Titanium Implants Using Plasma Electrolytic Oxidation: A Conference Review

Sichale W Fita [a], Mirosław Bonek [b], Sebastian Sławski [c], Anna Woźniak [d]

[a] Silesian University of Technology, Faculty of Mechanical Engineering, Department of Engineering Materials and Biomaterials, email: sichale.fita@gmail.com
[b] Silesian University of Technology, Faculty of Mechanical Engineering, Department of Engineering Materials and Biomaterials, email: miroslaw.bonek@polsl.pl
c Silesian University of Technology, Faculty of Mechanical Engineering, Department of Theoretical and Applied Mechanics, email: sebastian.slawski@polsl.pl
[d] Silesian University of Technology, Faculty of Mechanical Engineering, Department of Materials Research Laboratory, email: awozniak@polsl.pl

Abstract: Implant-related infection remains a major challenge in orthopaedic and dental applications. Plasma electrolytic oxidation (PEO) is a promising surface modification technique for titanium implants because it produces porous, strongly bonded oxide layers that can be biofunctionalized with antibacterial agents. This paper reviews recent advances in antibacterial hybrid PEO coatings, including metal-based, polymer-assisted, and antibiotic-loaded systems. Key antibacterial mechanisms, biological performance, and major limitations related to release control, cytotoxicity, and clinical translation are discussed. Overall, hybrid PEO coatings offer a flexible platform for balancing antibacterial efficacy with biocompatibility and osseointegration.

Keywords: Plasma electrolytic oxidation, Titanium implants, Antibacterial coatings, Hybrid surface modification, Controlled drug release, Biocompatibility

1. INTRODUCTION

Titanium (Ti) and its alloys are widely recognized as some of the most extensively employed metallic biomaterials in orthopaedic and dental implant applications owing to their excellent mechanical properties, superior corrosion resistance, high fatigue strength, and favorable manufacturability, in addition to their generally satisfactory biocompatibility. Despite these advantageous characteristics, titanium is intrinsically bioinert and therefore exhibits limited ability to form direct biological bonds with surrounding bone tissue during the early post-implantation period. This inherent lack of bioactivity may hinder optimal osseointegration and long-term functional performance unless appropriate surface modification strategies are implemented[1].

Implant infection is a major problem with metallic implants. It begins when bacteria attach to the surface and form a biofilm, making them harder to remove with antibiotics or the immune system[2]. This can cause long-term infection, implant failure, and poor healing. Because antibiotic resistance is increasing, researchers are now focusing on implant surfaces that can better prevent bacterial growth[3]. PEO is a promising way to improve titanium implant surfaces[1], [4]. It creates strong, porous coating that can enhance corrosion resistance, surface properties, and bone bonding. It also allows antibacterial or healing agents to be added, making it a simple and effective method for producing better implant surfaces.

PEO-treated titanium surfaces have been improved in different ways to fight bacteria. One common approach is adding antibacterial metals like silver, copper, and zinc to the porous coating. These metals can help reduce bacterial growth, especially when used together. However, the antibacterial effect also depends on the coating's surface features, such as its porosity, shape, chemical composition, and wettability[1], [2], [3], [4], [5].A second major strategy involves the development of hybrid PEO coatings, in which the oxide layer is combined with polymers, bioactive glasses, or drug-delivery phases to achieve multifunctionality. For example, Kazek-Kęsik et al.[6] reported a hybrid coating on Ti–15Mo alloy in which a PEO-derived oxide layer was combined with a PLGA polymer phase containing doxycycline, resulting in antibacterial performance against Staphylococcus aureus and Staphylococcus epidermidis while preserving cytocompatibility with osteoblast-like cells. In a related but non-PEO titanium surface design, Soylu et al.[7] demonstrated that dopamine-functionalized Ti6Al4V coated with agarose-based hydrogels could provide controlled release of gentamicin and effective inhibition of S. aureus, highlighting the broader relevance of polymer-assisted local drug delivery on titanium surfaces. These studies collectively show that porous titanium-based surface systems can be transformed from passive barriers into active antibacterial reservoirs.

A third and clinically important direction is the use of antibiotic-functionalized oxidized titanium surfaces for local infection prophylaxis. Diefenbeck et al.[8] showed in a rat model that gentamicin-coated plasma chemical oxidized titanium alloy markedly reduced implant contamination and prevented implant-related osteomyelitis, thereby demonstrating that oxidized titanium surfaces can support both osseointegration and local antibacterial delivery in vivo. Likewise, Kranz et al.[1] compared gentamicin-containing, silver nanoparticle-functionalized, and ionic zinc-functionalized TiOB surfaces and showed that all of them exhibited bactericidal activity while retaining cytocompatibility, with zinc displaying antibacterial performance comparable to the gentamicin-containing control and silver showing particularly favourable cell compatibility. Together, these findings support the idea that oxidized titanium surfaces can be tailored using multiple antimicrobial chemistries depending on the intended biological and antibacterial balance.

Despite recent progress, developing antibacterial coatings for implants still requires a careful balance between strong antibacterial action, controlled release, biocompatibility, and long-term integration with surrounding tissue. Recent studies highlight the importance of multifunctional coatings that not only prevent or reduce bacterial growth but also remain safe for host cells, support osseointegration, and reduce possible toxic or environmental concerns linked to some antibacterial agents. In this respect, plasma electrolytic oxidation (PEO) is especially promising because it provides a versatile surface modification platform that can be adjusted through electrolyte composition, processing conditions, and post-treatment methods to achieve both effective infection control and improved tissue response. Therefore, this conference paper focuses on the development of antibacterial hybrid coatings on titanium implants using PEO,

with particular emphasis on how different material combinations, such as metal ions, nanoparticles, polymers, and antibiotics, influence antibacterial activity and biological performance. The paper also outlines the basic principles of PEO, reviews the main hybrid antibacterial strategies, explains their antibacterial mechanisms, and discusses their potential relevance for future orthopaedic and dental implant applications.

2. FUNDAMENTALS OF PLASMA ELECTROLYTIC OXIDATION

Plasma electrolytic oxidation (PEO) is a high-voltage electrochemical surface treatment that generates plasma discharges at the metal-electrolyte interface, producing a thick, porous oxide coating (Fig.1). On titanium, this coating typically contains anatase, rutile, and amorphous TiO_2, together with electrolyte-derived elements such as Ca, P, Si, Ag, Cu, or Zn. The coating structure depends on processing parameters such as voltage, current density, treatment time, and electrolyte composition. For biomedical applications, the tunable porosity, roughness, phase composition, and ion incorporation of PEO coatings are important because they influence corrosion resistance, biological response, and antibacterial performance. In addition, the porous outer layer can act as a reservoir for nanoparticles, polymers, or drugs, while the inner oxide remains strongly bonded to the titanium substrate, making PEO a useful platform for multifunctional implant surfaces.

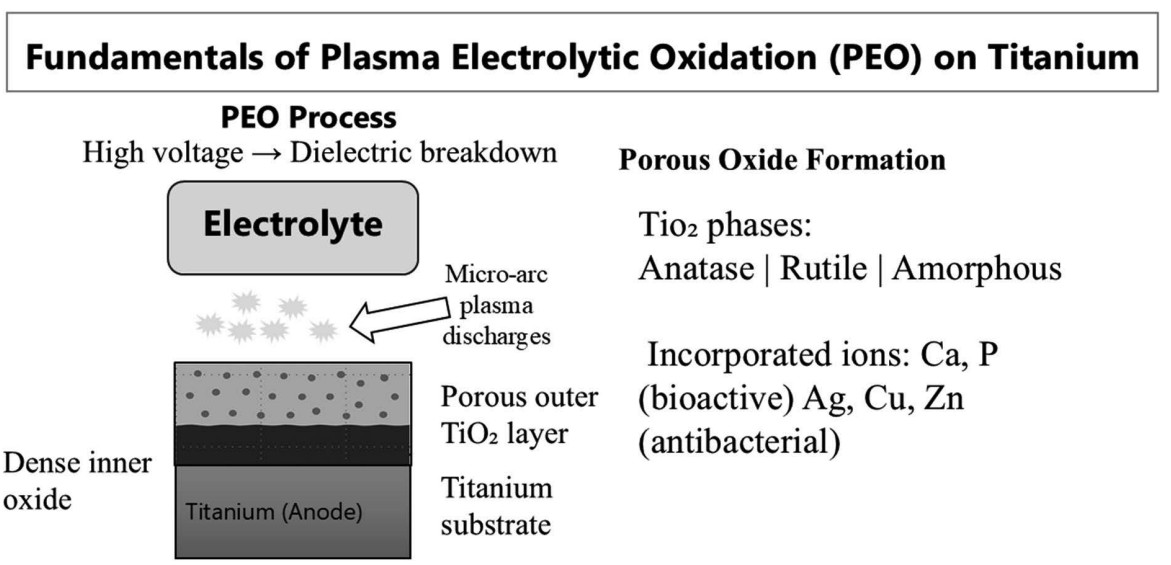

Fig.1 Schematic of plasma electrolytic oxidation (PEO) on titanium showing the process, porous oxide formation, and coating composition.

Diefenbeck et al. [8]showed that plasma chemical oxidation can create a bioactive macroporous titanium-oxide surface suitable for antibacterial functionalization while supporting implant fixation. Kranz et al. [1] similarly reported that plasma chemical oxidized titanium can serve as a bioactive implant surface for antimicrobial functionalization. Van Hengel et al.[9] emphasized that the microporous morphology produced by PEO supports biological interaction and incorporation of antibacterial species, while Rizwan et al.[10] highlighted that PEO forms porous oxide layers on valve metals and can also improve corrosion and wear resistance.

Kazek-Kęsik et al. [6] demonstrated that PEO is an effective first-step treatment for Ti–Mo alloys, producing a porous oxide layer suitable for subsequent polymer and drug incorporation. Van Hengel et al.[9], Pesode and Barve[11] , and Molaei et al.[12] also described PEO as a versatile biomedical surface modification technique capable of producing porous, adherent, and strongly bonded oxide layers that can serve as reservoirs for functional agents.
Soylu et al.[7] showed that titanium alloy surfaces can be modified into local drug-delivery systems using a dopamine-functionalized intermediate layer and an antibiotic-loaded hydrogel coating. Diefenbeck et al.[8] and Kranz et al. [1] further support the concept that oxidized titanium surfaces can serve as multifunctional interfaces combining osseointegration with antibacterial performance. Kazek-Kęsik et al.[6] also highlighted the scaffold-like role of the porous PEO layer in hosting a biodegradable polymer phase, while Pesode and Barve[11] emphasized that the ceramic-like oxide coatings formed by PEO differ from conventional anodized layers and have enhanced biomedical relevance.

3. HYBRID ANTIBACTERIAL STRATEGIES IN PEO COATINGS

Hybrid antibacterial strategies in PEO coatings have emerged as an important approach for improving the infection resistance of titanium implants. By combining the porous oxide layer produced by PEO with antibacterial agents such as metal ions, nanoparticles, polymers, or drugs, these coatings can provide multifunctional surface properties, including antibacterial activity, improved biocompatibility, and favourable biological interactions. Therefore, PEO-based hybrid coatings are increasingly considered promising surface modification strategies for advanced orthopaedic and dental implant applications (Table 1).
Pesode and Barve[11] suggested that the porosity of PEO coatings allows them to act as versatile platforms for biofunctionalization through the incorporation of biologically active species. They also noted that careful control of PEO processing parameters and electrolyte chemistry is essential for tailoring coating composition and achieving favourable biological outcomes. Diefenbeck et al.[8] demonstrated that adding gentamicin to a plasma-oxidized titanium surface can transform a bioactive implant coating into a locally antibacterial system, while Van Hengel et al.[9] reported that PEO-based titanium implants are commonly biofunctionalized with silver, zinc, or copper to enhance antimicrobial performance. These studies show that both antibiotic-based and metal-based functionalization strategies are effective routes for hybrid antibacterial surface design.
Rizwan et al.[10] emphasized that antibacterial PEO coatings are commonly produced by incorporating antibacterial agents into the porous oxide layer, highlighting the adaptability of PEO as a host matrix for multifunctional implant surfaces. Similarly, Kranz et al.[1] showed that plasma-oxidized titanium can be functionalized with gentamicin, silver nanoparticles, or ionic zinc, allowing direct comparison between antibiotic-based and metal-based antibacterial strategies. Molaei et al. [12] further noted that the porous architecture of PEO coatings makes them attractive for localized antibiotic incorporation without significantly altering the underlying implant material.
Kazek-Kęsik et al. [6] demonstrated that combining a PEO-derived oxide layer with a PLGA-based polymer loaded with doxycycline is an effective route for fabricating hybrid antibacterial coatings on titanium alloys. Likewise, Soylu et al. [7] showed that gentamicin-loaded agarose hydrogels can provide controlled antibiotic release from titanium surfaces. Together, these

studies indicate that hybrid PEO coatings can be designed using metal ions, antibiotics, polymers, or hydrogels to balance antibacterial activity with biocompatibility.

Table 1Representative antibacterial hybrid coating strategies and materials used in PEO-based titanium implant systems.

Study	Strategy	Functional agent(s)	Main relevance
van Hengel et al. (2021)	PEO biofunctionalization	Ag, Zn, Cu	Antibacterial metal incorporation on porous titanium oxide
Diefenbeck et al. (2016)	Oxidized Ti + antibiotic	Gentamicin	Local infection prophylaxis and reduced osteomyelitis in vivo
Kranz et al. (2019)	Oxidized Ti + alternative antimicrobials	Gentamicin, Ag nanoparticles, ionic Zn	Comparison of antibiotic-based and metal-based strategies
Kazek-Kesik et al. (2020)	PEO + polymer hybrid	PLGA + doxycycline	Drug-loaded oxide-polymer coating with cytocompatibility
Soylu et al. (2021)	Titanium + hydrogel coating	Gentamicin agarose hydrogel	Controlled antibiotic release from titanium surface

4. MECHANISMS OF ANTIBACTERIAL ACTION

Hybrid PEO coatings inhibit bacterial growth through multiple interacting mechanisms rather than a single antibacterial pathway. One key mechanism is ion-mediated toxicity, where released ions such as Ag^{+}, Cu^{2+}, and Zn^{2+} disrupt bacterial membranes, interfere with essential enzymes, and damage genetic material, with their effectiveness depending on ion distribution, release behaviour, and exposure to body fluids. In addition, direct contact between bacteria and rough, porous surfaces enriched with antibacterial species can lead to contact-based killing at the coating interface. Oxidative stress also plays an important role, as coatings containing copper, zinc oxide, or modified titanium oxides can promote the formation of reactive oxygen species, further enhancing antibacterial activity, especially under external stimuli such as light irradiation. Beyond these direct effects, surface properties such as wettability, charge, composition, and micro- to nanoscale roughness influence early bacterial adhesion and biofilm formation. Importantly, these same features also affect host cell behaviour, highlighting the need to balance antibacterial effectiveness with cytocompatibility and osseointegration. This balance is a major advantage of hybrid coatings, where different components can be designed to provide antibacterial action while simultaneously supporting bone integration and biological safety.

The antibacterial behaviour of Ag-, Zn-, and Cu-functionalized PEO coatings was attributed primarily to metal ion release from the porous oxide layer, which disrupts bacterial metabolism and cell membrane integrity. Van Hengel et al.[9] noted that surface-mediated contact killing and sustained ion release are the dominant antibacterial mechanisms in PEO-treated titanium

implants. Rizwan et al.[10] indicated that the antibacterial functionality of PEO coatings is generally introduced through incorporated antibacterial species within the porous oxide layer, highlighting the importance of coating composition in determining antimicrobial performance. Additionally, Pesode and Barve[11] report that surface characteristics such as roughness, chemical composition, and porosity of PEO coatings play a decisive role in regulating interactions between the implant surface and surrounding biological environments. The review clarifies that while PEO coatings themselves are primarily bioinert, their capability to host functional additives enables indirect antibacterial and bio interactive behaviour. Also, Molaei et al.[12] report that the antibacterial efficacy of antibiotic-loaded PEO coatings is primarily governed by controlled drug release from the porous oxide layer rather than direct contact killing. The review explains that sustained and localized antibiotic release from PEO coatings can effectively inhibit bacterial adhesion and biofilm formation on implant surfaces.

On the other hand, Kranz et al.[1] reported that all tested functionalized TiOB surfaces exhibited bactericidal activity against Staphylococcus aureus, expressed as extended bacterial lag phases, indicating that antimicrobial surface chemistry can effectively delay or suppress early bacterial proliferation. Their results further suggest that the antibacterial response is formulation-dependent, since ionic zinc maintained prolonged bactericidal activity comparable to the gentamicin-containing control, whereas the silver-functionalized surface showed a shorter effective duration. While the antibacterial behaviour described by Kazek-Kęsik et al.[6] is consistent with a release-mediated mechanism, in which doxycycline incorporated within the PLGA layer is gradually made available while the polymer undergoes hydrolytic degradation over time. Their findings suggest that antibacterial performance depends not only on the presence of doxycycline, but also on the microstructure of the hybrid oxide–polymer system, which influences drug distribution, degradation behaviour, and bacteria-surface interaction.

The antibacterial effect reported by Soylu et al.[7] is consistent with a controlled release mechanism, in which gentamicin diffuses gradually from the hydrogel coating into the surrounding medium to suppress bacterial growth. Their findings suggest that prolonging the release profile through hydrogel crosslinking is important for improving medium- and longer-term antibacterial performance beyond the short-term action of conventional coatings. While, according to Diefenbeck et al.[8] the antibacterial performance of gentamicin-functionalized oxidized titanium is governed by a release-based mechanism, whereby gentamicin released from the coated surface effectively suppresses early bacterial colonization and reduces the onset of implant-related infection. Their in vivo results further demonstrate that localized antibiotic delivery from the implant surface can disrupt bacterial establishment at the implantation site, thereby preventing progression toward mature osteomyelitis.

5. BIOLOGICAL AND FUNCTIONAL PERFORMANCE

Most studies on antibacterial PEO coatings focus on pathogens such as Staphylococcus aureus and Escherichia coli, while dental applications often consider anaerobic or multispecies biofilms relevant to peri-implantitis. Overall, PEO coatings containing silver, copper, zinc, or their combinations generally reduce bacterial adhesion and viability compared with untreated titanium or unloaded PEO surfaces. These coatings can also improve corrosion resistance, wear behaviour, and bone-related responses through calcium- and phosphorus-containing oxide layers, while moderate zinc or copper incorporation may additionally support osteogenic activity. However, excessive discharge intensity or antibacterial loading may damage coating

integrity or cause undesirable ion release, indicating that biological performance depends on controlled incorporation within a stable oxide architecture.

Rizwan et al.[10] emphasized that antibacterial PEO coatings should provide more than microbial suppression alone, highlighting bioactive glass-containing coatings for their potential to combine antibacterial behaviour with bioactivity, biocompatibility, and improved osseointegration. Van Hengel et al.[9] similarly reported that zinc- and copper-doped PEO coatings may promote osteogenic responses in addition to antibacterial activity, and that many Ag-, Zn-, and Cu-containing PEO coatings achieve effective antibacterial performance while maintaining acceptable cytocompatibility with osteoblast-like cells. In antibiotic-based systems, Molaei et al.[12] further noted that controlled antibiotic delivery via PEO coatings may prevent early-stage infection without compromising cell adhesion or osteogenic response when drug loading and release are properly optimized.

Consistent with these findings, PEO-treated titanium alloys generally exhibit good biocompatibility, supporting cell attachment, proliferation, and osteogenic activity when appropriately designed. Pesode and Barve[11] emphasized that PEO coatings can enhance bone–implant integration by promoting favourable surface–cell interactions. Soylu et al.[7] showed that gentamicin-releasing agarose-coated titanium surfaces inhibited Staphylococcus aureus while maintaining acceptable cytocompatibility with human cells. Similarly, Kazek-Kęsik et al.[6] reported that doxycycline-loaded hybrid oxide–polymer coatings inhibited Staphylococcus aureus and Staphylococcus epidermidis while remaining cytocompatibility with MG-63 osteoblast-like cells. Together, these findings show that antibacterial efficacy and cytocompatibility can be achieved simultaneously in PEO-based hybrid coatings through careful material and dose selection.

In vivo evidence further supports the clinical relevance of these approaches. Diefenbeck et al. [8] showed in a rat osteomyelitis model that gentamicin-coated plasma-oxidized titanium implants reduced implant contamination and lowered histological and radiographic signs of osteomyelitis. In addition, Kranz et al.[1] reported that MC3T3-E1 cells remained viable on all investigated TiOB surfaces, confirming that antimicrobial functionalization did not compromise biological compatibility. These findings highlight the importance of balancing antibacterial performance with host-cell compatibility in implant design.

6. CONCLUSIONS

Plasma electrolytic oxidation provides a versatile and robust platform for developing antibacterial and bifunctional titanium implant surfaces. By enabling the incorporation of metal ions, polymers, and antibiotics into a porous oxide layer, hybrid PEO coatings can effectively reduce bacterial adhesion while supporting corrosion resistance, cytocompatibility, and bone-related responses. However, optimal performance depends strongly on careful control of coating composition, antibacterial loading, and release behaviour, as excessive ion or drug release may compromise biological safety. Although promising in vitro and in vivo results have been reported, further progress toward clinical translation will require standardized testing protocols, improved control of long-term antibacterial function, and validation under clinically relevant conditions. With continued optimization, hybrid PEO coatings have strong potential for future orthopaedic and dental implant applications.

REFERENCES

[1]S. Kranz *et al.*, "Bactericidal and biocompatible properties of plasma chemical oxidized titanium (TiOB®) with antimicrobial surface functionalization," *Materials*, vol. 12, no. 6, p. 866, 2019.

[2]F. Nowruzi, R. Imani, and S. Faghihi, "Effect of electrochemical oxidation and drug loading on the antibacterial properties and cell biocompatibility of titanium substrates," *Sci Rep*, vol. 12, p. 8595, May 2022, doi: 10.1038/s41598-022-12332-z.

[3]P. Hartjen *et al.*, "Plasma Electrolytic Oxidation of Titanium Implant Surfaces: Microgroove-Structures Improve Cellular Adhesion and Viability," *In Vivo*, vol. 32, no. 2, p. 241, Mar. 2018, doi: 10.21873/invivo.11230.

[4]"Use of Organic Acids as Additives for Plasma Electrolytic Oxidation (PEO) of Titanium." Accessed: May 05, 2026. [Online]. Available: https://www.mdpi.com/2079-6412/14/6/703

[5]M. Magić, B. Čolović, S. Vasilijić, N. Tadić, S. Stojadinović, and V. Jokanović, "Nanodesigned coatings obtained by plasma electrolytic oxidation of titanium implant and their cytotoxicity," *Journal of Applied Biomaterials & Functional Materials*, vol. 19, p. 2280800018822252, Jan. 2021, doi: 10.1177/2280800018822252.

[6]A. Kazek-Kęsik *et al.*, "Physico-chemical and biological evaluation of doxycycline loaded into hybrid oxide-polymer layer on Ti–Mo alloy," *Bioactive materials*, vol. 5, no. 3, pp. 553–563, 2020.

[7]H. M. Soylu *et al.*, "A novel strategy to coat dopamine-functionalized titanium surfaces with agarose-based hydrogels for the controlled release of gentamicin," *Frontiers in cellular and infection microbiology*, vol. 11, p. 678081, 2021.

[8]M. Diefenbeck *et al.*, "Gentamicin coating of plasma chemical oxidized titanium alloy prevents implant-related osteomyelitis in rats," *Biomaterials*, vol. 101, pp. 156–164, 2016.

[9]I. A. J. van Hengel, M. W. A. M. Tierolf, L. E. Fratila-Apachitei, I. Apachitei, and A. A. Zadpoor, "Antibacterial Titanium Implants Biofunctionalized by Plasma Electrolytic Oxidation with Silver, Zinc, and Copper: A Systematic Review," *International Journal of Molecular Sciences*, vol. 22, no. 7, p. 3800, Jan. 2021, doi: 10.3390/ijms22073800.

[10] M. Rizwan, R. Alias, U. Z. Zaidi, R. Mahmoodian, and M. Hamdi, "Surface modification of valve metals using plasma electrolytic oxidation for antibacterial applications: A review," *Journal of Biomedical Materials Research Part A*, vol. 106, no. 2, pp. 590–605, 2018, doi: 10.1002/jbm.a.36259.

[11] P. Pesode and S. Barve, "Biocompatibility of Plasma Electrolytic Oxidation Coated Titanium Alloy for Biomedical Applications," *BioNanoSci.*, vol. 15, no. 2, p. 232, Feb. 2025, doi: 10.1007/s12668-025-01848-z.

[12] M. Molaei, M. Atapour, and E. Mohammadi Zahrani, "Plasma Electrolytic Oxidation (PEO) Coatings for Biomedical Implants: A Review on Enhancing Antibacterial Efficacy Through Controlled Antibiotic Release," *Coatings*, vol. 15, no. 8, p. 925, Aug. 2025, doi: 10.3390/coatings15080925.

7th-9th June 2026
Gliwice-Brenna, Poland
DEPARTMENT OF ENGINEERING MATERIALS AND BIOMATERIALS
FACULTY OF MECHANICAL ENGINEERING
SILESIAN UNIVERSITY OF TECHNOLOGY
INTERNATIONAL STUDENTS SCIENTIFIC CONFERENCE

Analysis of the Protective Properties of Wax and Ceramic Coatings Applied to Automotive Paints – Stage II: Testing Under Real Operating Conditions

Marta Fizia [b], Max Ignacy [b], Daniel Bujara [b], Maciej Nogieć [b], Mateusz Sadowski [b], Marek Kremzer [a], Rafał Duda [c]

a Silesian University of Technology, Faculty of Mechanical Engineering, Scientific and Didactic Laboratory of Nanotechnology and Materials Technology email: marek.kremzer@polsl.pl
b Silesian University of Technology, Faculty of Mechanical Engineering email: mf309372@student.polsl.pl, mi309400@student.polsl.pl, db303946@student.polsl.pl, mn303954@student.polsl.pl, ms303956@student.polsl.pl
c Detailing Studio Mr Cleaner Katowice, email: marketing@mrcleaner.pl

Abstract: This work compares the protective effectiveness of waxes and ceramic coatings applied to automotive paint systems. The mechanisms of their action, the process of applying coatings to automotive paintwork, and their practical limitations are discussed. A separate setup was also prepared to investigate the effect of UV radiation on the samples. In addition, four different tire dressings were applied to the tires of two different vehicles in order to compare their performance under two distinct environmental conditions. All operational tests aimed at evaluating the protective effectiveness of the applied coatings were conducted under natural environmental conditions.

Keywords: waxes, testing under natural environmental condition, automotive paint protection, ceramic coatings, hydrophobicity, wear, coating durability

1. INTRODUCTION

Nowadays, environmental protection is a priority in all manufacturing processes, and human activities should limit the negative impact on the ecosystem as much as possible. This trend in the automotive industry was shown by the introduction of Directive No. 2004/42/EC of the European Parliament, which forced manufacturers to radically change how they produce protective products for paint coatings [1]. As a result, traditional solvent-based paints are increasingly being replaced by water-based systems, which are much safer for both the environment and factory workers.

Despite their clear ecological benefits, modern paint systems used in the automotive industry bring significant challenges during long-term use. Scientific literature shows that using water-based paints requires much stricter quality control, and any application mistakes can lead to an

uneven coating and negatively affect its look [2]. The situation is made worse by the fact that to reduce costs and vehicle weight, modern car manufacturers apply thinner layers of factory paint. All these factors, the lower durability of water-based paints and their reduced thickness, clearly show that vehicle owners need to use additional protective coatings to maintain the paintwork in good shape.

The most traditional method of protecting the surface is applying waxes. In practice, both natural components and synthetic polymer-based systems are used. Waxes create a physical barrier layer that fills microscopic imperfections in the surface, which improves its appearance, increases shine, and provides hydrophobic properties, shown by a high contact angle. However, this layer is not durable because it does not form strong chemical bonds with the surface, it also has limited heat resistance and is easily removed by aggressive detergents [4].

It is this insufficient level of protection and low durability of traditional waxes that forced the automotive industry to introduce advanced ceramic technologies. The effectiveness of these systems, based on a mix of resins and solvents, is mainly determined by the presence of silicon dioxide (SiO_2), which provides much better protection against external factors and UV degradation [4]. Over time, the evolution of these solutions led to the development of hybrid graphene-ceramic coatings, which represent the latest generation of protection today. Compared to classic ceramics, versions with added graphene show a higher contact angle and better flexibility, which prevents the layer from cracking and reduces localized heat buildup [5]. As studies from 2025 prove, the key to optimizing the performance parameters of such protection is precisely determining the graphene content [6].

Although the market currently offers a rich portfolio of such advanced protective products, and their creators claim revolutionary performance in marketing materials, there is still a lack of objective, independent studies to verify these claims. To fill this gap, this project attempts to evaluate the protective and visual parameters of six selected coatings.

1.1. Research methodology

1.1.1 Procedure for Protecting the Automotive Paint Surface

The procedure for protecting the automotive paint surface was carried out in cooperation with the detailing studio Mr Cleaner Katowice. The first stage involved thoroughly washing the entire vehicle twice using a specialist cleaning agent. In addition, the washing process included a pre-wash using Alkaline TFR by Cleantle and washing with Daily Shampoo, a neutral shampoo by Cleantle. Subsequently, tar deposits were removed using Mac Serien Prickbort MAC 124, followed by the removal of metallic contaminants from the paintwork using IronX by CarPro. In addition, the wheels were cleaned using the wheel-cleaning product AUTO GRAPH Detailing Rim Cleaner. The vehicle was then carefully dried with microfiber towels. For the purpose of the study, the vehicle hood and the driver-side door were selected. The selected body panels had to be prepared before the application of the protective coatings. The paintwork was polished using a 15 mm dual action polishing machine equipped with Honey Combination polishing pads and a professional polishing compound — 3D 510 Premium Rubbing Compound. After the polishing stage, the paintwork was degreased using CARPRO Eraser in order to remove polishing compound fillers and to allow for a proper inspection of the corrected surface. The prepared surface was divided into sections, which allowed easy

identification of the individual coatings. The division is presented in Figure 1 and Figure 2. The coatings used are listed in *Table 1 Description and Indication of Used Protection Coatings*. Due to weather conditions, the vehicle remained at the Mr Cleaner Katowice facility for 24 hours, after which it was collected and put into regular use.

Table 1 Description and indication of used protection coatings [7]

Indication	Product	Description
Waxes		
1	Dark Angel	A wax intended for dark and black paintwork, providing protection for up to 6 months. It contains a blend of natural oils and waxes that enhances colour depth, masks minor scratches, and leaves a durable, glossy protective layer with pronounced hydrophobic behaviour.
2	Soft 99 Fusso	A hard protective wax based on fluoropolymers, valued for strong hydrophobic properties. Depending on operating conditions and maintenance, the protective layer can last up to approximately one year.
Coatings		
3	Ultracoat Skyline	A ceramic–graphene coating for paint protection that provides long-term durability and enhances colour depth. According to the manufacturer, it can last up to 3 years and is formulated with SiO_2 and SiC compounds as well as graphene flakes.
4	Ultracoat Aurora	A universal ceramic–graphene spray coating protecting paintwork for up to 9 months, intended for various exterior surfaces such as paint, wheels, and plastics. Owing to its high SiO_2 content and graphene additives, it can be used as a stand-alone product or as a maintenance product for previously applied coatings.
5	Carpro D-quartz	A "nano-diamond" ceramic coating designed to increase the mechanical resistance of the surface. The manufacturer emphasises its focus on reducing micro-scratches and improving resistance to damage.
Top-up products		
6	Ultracoat – Ceramic Qdetailer	A quick detailer with a high SiO_2 content for rapid maintenance of paintwork and other exterior components. It can serve as short-term protection or as a product for regular refreshing and boosting the properties of ceramic coatings, including gloss, slickness, and hydrophobicity.

Figure 1 Division of the car hood surface

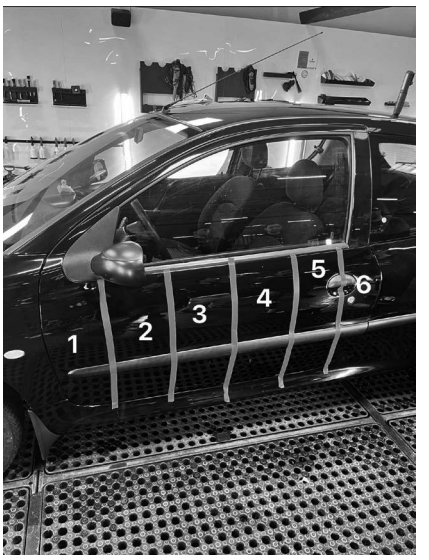

Figure 2 Division of the driver's door surface

1.1.2 UV test setup

A sample stand was constructed using 20 × 20 mm aluminum profiles with lengths ranging from 40 cm to 60 cm. Connectors for joining the profiles were designed in the Autodesk Inventor environment and then 3D-printed using a Bambu Lab P1S printer with PET-G filament [3]. The stand was subsequently assembled, and 14 samples coated with the coatings listed in Table 1 were attached to it (two samples were left uncoated). The stand was placed in a sun-exposed location; seven samples were oriented eastward, while the remaining seven were oriented westward [4].

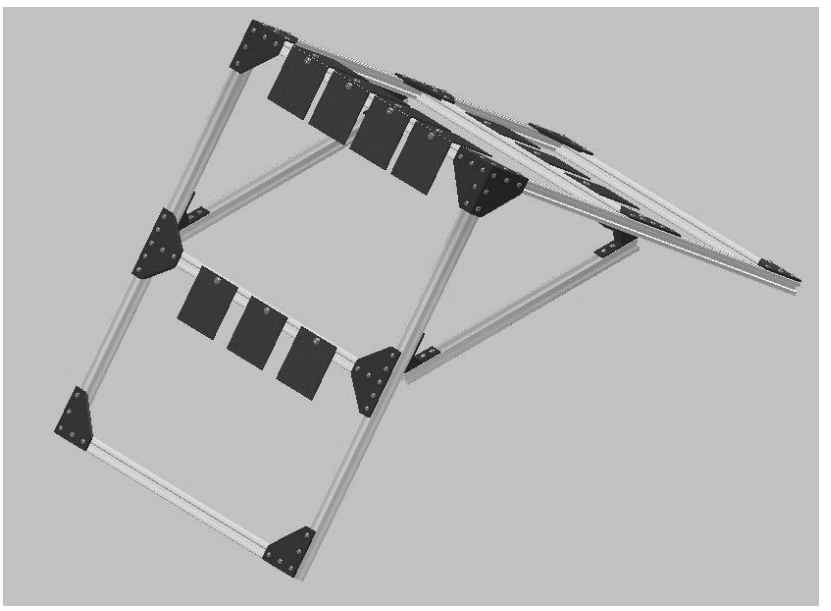

Figure 3 Assembly of the stand in Autodesk Inventor

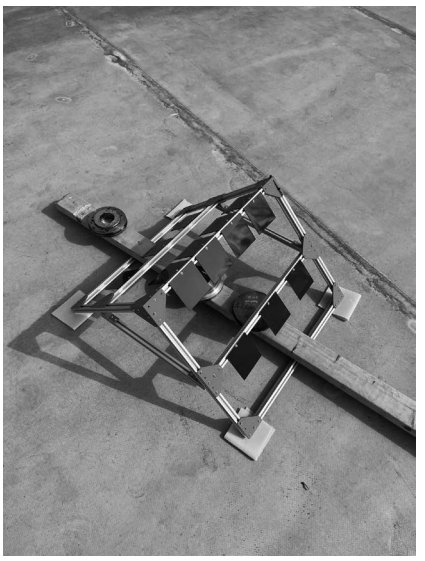

Figure 4 Stand placed in a sunlit location

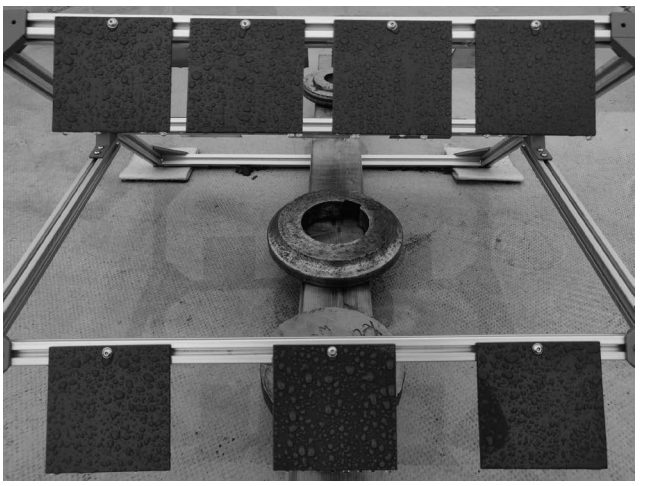

Figure 5 Samples after one and a half months of exposure

1.1.3 Procedure for applying tire dressings to car tires

Tire dressings were applied to two vehicles. The vehicles are used in different ways and operate on different types of roads, as well as cover different distances on a daily basis. Vehicle No. 1 travels approximately 500 km per week, while Vehicle No. 2 covers about 150 km per week.

The application procedure began with thoroughly washing the tires multiple times using a tire-cleaning product — KiurLab Tire-X. The tires were then dried using a car dryer. The cleaned tires were divided into four equal sections (to enable the evaluation of individual products), as shown in Figures 6 and 7. The final stage involved applying the tire dressings according to the numbering presented in *Table 2 Description and Indication of Used Dressings*.

Figure 6 Division of the tire of vehicle No. 1

Figure 7 Division of the tire of vehicle No. 2

Table 2 Description and Indication of Used Dressings.

Indication	Product	Description
1	Ultracoat – Quartz Tire Dressing	Quartz Tire Dressing is a product designed for protecting tires and rubber components. Enriched with silica, it provides a high level of hydrophobicity that lasts for several weeks. It is very easy to apply using a spray applicator. Depending on the application method, it allows either a satin or glossy finish. The product also features a pleasant berry fragrance.
2	FXPROTECT – Graphene Tire Gel	Contains graphene and silicon nanocompounds that provide antistatic, hydrophobic, and dirt-repellent properties. It offers long-lasting protection, UV resistance, and helps prevent fading, cracking, and aging. The gel formula ensures easy application and allows either a satin or glossy finish. It protects rubber from wear and is environmentally safe.
3	Cleantle – Tire Dressing	A modern product designed for the effective care and protection of rubber components such as tires and seals. It also works well on exterior plastic parts. It protects tires against fading and forms a hydrophobic layer that slows down dirt accumulation. The coating helps extend tire lifespan and makes them easier and faster to clean.
4	ONYX – Tire Dressing	Protects tires and gives them a deep black, satin finish. Thanks to a SiO_2-based formula, it provides long-lasting durability, water and dirt repellency, and protection against environmental factors. It also helps maintain rubber flexibility and prevents premature aging. The product is easy to use—simply apply it to an applicator or microfiber cloth and spread evenly over the tire surface.

CONCLUSIONS

Operational testing is still ongoing; however, some changes can already be observed on the tested surfaces, including automotive paint, samples, and tires. Since the application of the coatings, the vehicle has covered approximately 600 km and has been washed once at a public touchless car wash (without the use of brushes).

Due to the ongoing aerobiological season, vehicle soiling is clearly visible. A distinct difference can be observed on the hood, where the highest level of contamination is associated with the Ultracoat Ceramic Soft 99 Fusso coating. On the doors, the level of contamination is similar across all tested areas.

Differences in hydrophobic performance are also noticeable. On the hood, the largest water droplets are retained on the Soft99 Fusso and CarPro D-quartz coatings. In contrast, on the

doors, the best performance is observed for the Ultracoat Aurora coating, as rainwater drains almost immediately from its surface.
Figure 5 shows samples exposed to weather conditions for a period of approximately one and a half months. The prevailing weather conditions made it possible to assess hydrophobicity. The samples coated with Ultracoat Aurora and Ultracoat Ceramic Q-Detailer exhibited the highest hydrophobicity. The reference sample (the sample not coated with any protective layer) retained the most water on its surface.
Clear differences were also observed in the performance of the tire dressings applied to vehicle No. 1. The vehicle covered 500 km and was washed with a neutral shampoo before being dried. After this cycle, the best-performing products were Ultracoat – Quartz Tire Dressing and Cleantle – Tire Dressing. The cycle was then repeated, but no further significant changes were observed.
For vehicle No. 2, the condition of the coatings was evaluated after 100 km of driving, with no significant deterioration observed.
In both vehicles, it can be concluded that all coatings applied to the left tires showed higher levels of wear compared to those applied to the right tires.

ACKNOWLEDGEMENTS

This work was carried out in cooperation with the detailing studio Mr Cleaner Katowice.
This work was created as a result of the project entitled *"Analysis of the Protective Properties of Wax and Ceramic Coatings Applied to Automotive Paints – Stage II: Testing Under Real Operating Conditions"*, carried out within the framework of Project-Based Learning (PBL) in the 13th competition of the *Excellence Initiative – Research University* Program at the Faculty of Mechanical Engineering, Silesian University of Technology.

BIBLIOGRAPHY

[1] Parlament Europejski i Rada Unii Europejskiej, Dyrektywa 2004/42/WE w sprawie ograniczeń emisji lotnych związków organicznych w wyniku stosowania rozpuszczalników organicznych w niektórych farbach i lakierach oraz produktach do odnawiania pojazdów. Dziennik Urzędowy Unii Europejskiej L 143, 2004.
[2] Akafuah, N.K.; Poozesh, S.; Salaimeh, A.; Patrick, G.; Lawler, K.; Saito, K. Evolution of the Automotive Body Coating Process—A Review. Coatings 2016, 6, 24. https://doi.org/10.3390/coatings6020024
[3] Streitberger H.-J., Dössel K.-F., Automotive Paints and Coatings, Weinheim, Wiley-VCH Verlag GmbH & Co. KGaA, 2008.
[4] Nirmal U, Musa MA, Yuhazri MY, Ahmad MMHM. Development of Car Coating Materials over the Past Decade for Paint Protection Applications—An Overview on the Different Types of Paint Protections. Polymers. 2025; 17(23):3114. https://doi.org/10.3390/polym17233114
[5] Priyadharshini R, Xavier JR. Recent Advances in Graphene-Based Nanocomposite Coatings for Corrosion Resistance in the Automotive Industry and Their Smart Functional Applications. Journal of Bio- and Tribo-Corrosion. 2025; 11:113.

[6] BUI, Huyen TT; HOANG, Anh Nguyet; LE, Cuong Manh. Study on the Effect of Graphene on Characteristics of Inorganic Polymer Paint. ACS omega, 2025, 10.6: 5503-5516.
[7] Magdalena Markiewicz, Bartłomiej Wątroba, Julia Wawrzynek, Maciej Nogieć, Mateusz Sadowski, Wojciech Tokarz, Daniel Bujara, Marta Fizia, Marek Kremzer Protective Efficiency of Wax and Ceramic Coatings on Automotive Paints: A Comparative Study, Talent Detector 2026 Winter

TalentDetector

7th-9th June 2026
Gliwice-Brenna, Poland

DEPARTMENT OF ENGINEERING MATERIALS AND BIOMATERIALS
FACULTY OF MECHANICAL ENGINEERING
SILESIAN UNIVERSITY OF TECHNOLOGY

INTERNATIONAL STUDENTS SCIENTIFIC CONFERENCE

Structural aspects of laser surface remelting of modern steels using material databases

Marek Flak[a], Mirosław Bonek[b]

[a] Student of Mechatronics, e-mail: mf310852@student.polsl.pl
[b] Silesian University of Technology, Faculty of Mechanical Engineering, Department of Engineering Materials and Biomaterials, email: miroslaw.bonek@polsl.pl

Abstract: The article presents the impact of laser surface remelting on the microstructure and properties of modern steels used in industry. Structural changes occurring during the process and the importance of technological parameters affecting the quality of the recast layer were discussed. Particular attention was paid to the use of databases and IT systems to collect, analyze and optimize material data and laser processing processes.

Keywords: laser melting, microstructure, data optimization

1. INTRODUCTION

The contemporary development of the materials industry is closely related to the search for methods to increase the durability and operational resistance of structural elements. Technologies for modifying the surface layer of steel are of particular importance, because it is the surface of the material that is most exposed to wear, corrosion and the effects of high temperatures. One of the most effective methods of improving the properties of the surface layer is laser surface melting.

This process involves local melting of a thin layer of material using a concentrated laser beam and then cooling it very quickly. Such a high rate of heating and solidification leads to intensive microstructural changes that directly affect the mechanical and operational properties of steel. Depending on the process parameters, it is possible to obtain a fine-grained martensitic structure, improve abrasion resistance, increase hardness and reduce structural inhomogeneities.

However, the development of laser technologies has led to the creation of a huge amount of data related to processing parameters and material testing results. Each process generates information regarding laser power, beam travel speed, linear energy, process temperature, cooling time and type of shielding gas. Additionally, microstructural tests, hardness measurements, chemical composition analyzes and microscopic observations are performed. In industrial and laboratory practice, it has become necessary to use systems that enable the organization and analysis of this data.

Modern database systems currently play an important role in materials engineering. They allow you to store information about materials, processing parameters and test results in an orderly manner, and enable you to quickly search for relationships between the structure of the material and the parameters of the technological process. As a result, it is possible to more effectively design laser processing processes and predict the properties of the obtained layers.

2. CHARACTERISTICS OF THE LASER MELTING PROCESS

Laser surface melting belongs to a group of technologies enabling controlled modification of the surface layer of metallic materials. In the case of modern steels, this process is particularly important due to the need to improve the operational resistance of elements operating in conditions of intense mechanical wear, high temperatures and variable dynamic loads. Laser technologies are used, among others, in the aviation, energy, automotive and tool industries [1].
The basis of the process is the interaction of a concentrated laser beam with the material surface. The energy supplied by the beam causes the local melting of a thin layer of steel and the creation of a molten metal pool. After passing the laser, the material cools very quickly, the speed of which can reach up to 10^6 K/s [2]. Such intense cooling leads to the formation of non-equilibrium structures and significant fragmentation of the microstructure.
In modern tool and high-alloy steels, a clear influence of process parameters on the nature of the obtained structure is observed. Changing the laser power, scanning speed or spot diameter leads to changes in the melting depth, dendrite morphology and the share of metastable phases [3]. In practice, this means the need to constantly monitor process parameters and archive technological data.
For this purpose, modern industrial systems use relational databases that enable the collection and analysis of information regarding the processing process. Each laser process generates a large amount of technological data, including laser operating parameters, process temperature, cooling time and material test results. This data is then used to analyze the impact of technological parameters on the final properties of the material.

Table 1. Example parameters of the laser surface remelting process used for modern steels

Process parameters	Range of values	Impact on structure
Laser power	500-3000W	Depth of remelting
Scanning speed	0,1-2,0 m/min	Microstructure fragmentation
Spot diameter	0,5-3 mm	Width of the remelting zone
Energy density	20-120 J/mm^2	Process stability
Shielding gas	Ar, N_2, He	Oxidation limitation

One of the most important effects of surface laser melting is the formation of a fine-grained martensitic structure. In H13 and H11 steels, rapid cooling leads to the formation of lath martensite and reduced chemical segregation [4]. This structure is characterized by high hardness and increased abrasion resistance. As a result of the process, three basic areas of the material can be distinguished:

- Zone of complete melting,
- Heat affected zone,
- Native material.

The greatest microstructural changes occur in the melting zone. Dendrites with very small interarm distances and the presence of retained austenite are observed there. In the heat affected zone, transformations occur related to the heating of the material without melting it. However, the native material retains its original structure.

The analysis of such changes requires the use of advanced research methods. The most commonly used:

- Light microscopy,
- Scanning electron microscopy,Analizę EDS,
- X-ray diffraction,
- Microhardness measurements.

Each of these methods generates a large amount of measurement data. In modern laboratories, test results are automatically saved in database systems. This allows you to quickly search for relationships between processing parameters and material properties [5].

3. ANALYSIS OF MICROSTRUCTURE AND STRUCTURAL CHANGES

In practice, it is particularly important to link microstructural data with specific process parameters. For example, an increase in laser power increases the depth of remelting, but at the same time it may lead to an increase in residual stress and the formation of microcracks [6]. Such data is archived in databases, which enables the creation of predictive models used to optimize the process.

Table 2. The influence of selected technological parameters on the properties of the recast layer

Parametr	Changing a parameter	Impact on structure
Increase in laser power	More energy	Depth of remelting
Deceleration	Longer heating time	Increase in the heat affected zone
Faster cooling	Faster crystallization	Grinding of grains
High linear energy	Intense melting	Possibility of microcracks

4. THE USE OF DATABASES IN THE ANALYSIS OF MATERIAL PROCESSES

The importance of databases in material processes increases with the development of the Industry 4.0 concept. In modern production systems, process parameters are monitored in real time and automatically transferred to central IT systems. This makes it possible not only to archive the results, but also to perform statistical analysis and predict the quality of the obtained layer.

Relational databases enable the creation of tables linked by logical relationships. In the case of laser technologies, the following can be distinguished:

- Material table,
- Table of machining parameters,
- Table of test results,
- Table of microstructure images,
- Table of mechanical properties.

This solution allows you to quickly compare results obtained for different materials and process parameters. In engineering practice, this significantly reduces the time needed to design new technologies and reduces the number of costly experimental tests [7].
Non-relational NoSQL databases are also becoming increasingly important, as they enable the storage of unstructured data, such as microscopic images or numerical simulation results. These solutions are particularly useful when analyzing large data sets generated by technological process monitoring systems.

5. INFORMATION SYSTEMS AND ARTIFICIAL INTELLIGENCE IN MATERIALS ENGINEERING

Modern analysis of material data increasingly uses artificial intelligence algorithms. Neural networks are used, among others, to automatically classify microstructures and predict the mechanical properties of materials after laser processing. Learning algorithms analyze data stored in databases and search for relationships between technological parameters and the structure of the material [8].
An example is the automatic analysis of microscopic images, during which the computer system recognizes the grain size, the presence of dendrites and microcracks. The obtained results are then compared with previous data collected in the database. This allows you to predict the properties of the material before performing a full set of laboratory tests.
In the case of modern bainitic and powder steels, it is particularly important to control the cooling rate and the linear energy of the process. These parameters directly affect the dissolution of carbides and the stability of metastable phases [9]. Thanks to the analysis of data collected in database systems, it is possible to more precisely determine the optimal process conditions.

Table 3. Examples of steel properties after surface laser remelting

Type of steel	Dominant structure	Technological effect
H13	Lath martensite	Increase in hardness
H11	Dendritic structure	Improved heat resistance
Bainitic steel	Bainite and martensite	Increased abrasion resistance
Powder steel	Homogeneous structure	Reducing segregation

6. INDUSTRIAL APPLICATION OF LASER TECHNOLOGIES

The integration of laser technologies with databases is currently the basis for the development of intelligent production systems. Process data, microstructural test results and operational information are collected in one IT environment, which enables the creation of digital material models. Such solutions are increasingly used in the modern aviation and automotive industries [10].
Further development of automatic material data analysis systems is expected in the future. Systems using artificial intelligence and machine learning to independently optimize laser process parameters will become increasingly important. The combination of materials engineering with information technologies is becoming one of the key directions in the development of modern industry.

7. SUMMARY

Surface laser remelting of modern steels allows for significant improvement of the properties of the surface layer by changing the microstructure of the material. Rapid crystallization leads to a refinement of the structure, an increase in hardness and improved wear resistance. At the same time, the development of modern research methods results in the creation of huge amounts of technological and material data.
The use of database systems enables effective storage, analysis and interpretation of research results related to laser processing processes. The integration of material technologies with computer science allows the creation of intelligent systems supporting the design of technological processes and predicting material properties.
In the future, we can expect further development of artificial intelligence-based systems that will automatically analyze the microstructure of materials and optimize laser processing parameters. The combination of materials engineering and database technology will play an increasingly important role in the development of modern industry.

ACKNOWLEDGEMENTS

The work was created as part of project based learning - PBL, in the 14th competition under the Initiative of Excellence - Research University, Silesian University of Technology, Gliwice, Poland and as part of project of Students Scientific Circle of Laser Surface Treatment under the Initiative of Excellence - Research University, Silesian University of Technology, Gliwice, Poland.

BIBLIOGRAPHY

1. Colaço R., Vilar R., „Physical metallurgy of laser surface melted plastic mould steels: a case study”, Revista de Metalurgia, 1998.T. Suntola, J. Anlson, U.S. Patent 4,058.430, 1977.

2. Erdoğan A., „Laser Remelting Power Effect on Microstructure, Hardness and Wear Behavior of AISI 1020", Proceedings of the Institution of Mechanical Engineers, Part J: Journal of Engineering Tribology, 2022.
3. Yu Y., Zhang M., Guan Y. i in., „The Effects of Laser Remelting on the Microstructure and Performance of Bainitic Steel", Metals, 2019.
4. Preussner J., Oeser S., Pfeiffer W. i in., „Microstructure and residual stresses of laser remelted surfaces of a hot work tool steel", International Journal of Materials Research, 2014.
5. Jurci P., Cejp J., Brajer J., „Metallurgical Aspects of Laser Surface Processing of PM Cr-V Ledeburitic Steel", Advances in Materials Science and Engineering, 2011.
6. Burakowski T., Wierzchoń T., „Inżynieria powierzchni metali", Wydawnictwo Naukowe PWN, Warszawa, 1999.
7. Dobrzański L.A., „Podstawy nauki o materiałach i metaloznawstwo", Wydawnictwo Naukowo-Techniczne, Warszawa, 2002.
8. Date C.J., „Wprowadzenie do systemów baz danych", Wydawnictwo WNT, Warszawa, 2000.
9. Elmasri R., Navathe S., „Fundamentals of Database Systems", Pearson Education, 2017.
10. Garcia-Molina H., Ullman J.D., Widom J., „Database Systems: The Complete Book", Pearson, 2009.
11. Karkadakattil A., „Laser surface modification of additively manufactured metals: mechanisms, thermal–microstructural evolution, and property enhancement", Journal of Engineering and Applied Science, 2026.
12. Iwaszko J., „Laser surface remelting of powder metallurgy high-speed steel", Bulletin of the Polish Academy of Sciences Technical Sciences, 2020.

TalentDetector

7th-9th June 2026
Gliwice-Brenna, Poland

DEPARTMENT OF ENGINEERING MATERIALS AND BIOMATERIALS
FACULTY OF MECHANICAL ENGINEERING
SILESIAN UNIVERSITY OF TECHNOLOGY

INTERNATIONAL STUDENTS SCIENTIFIC CONFERENCE

Structural aspect of laser surface remelting of modern steels using microprocessor systems and microcontroller programming

Marek Flak[a], Mirosław Bonek[b]

[a] Student of Mechatronics, e-mail: mf310852@student.polsl.pl
[b] Silesian University of Technology, Faculty of Mechanical Engineering, Department of Engineering Materials and Biomaterials, email: miroslaw.bonek@polsl.pl

Abstract: Laser surface remelting of modern steel is one of the most advanced methods of modifying the surface layer of construction materials. The development of microprocessor systems and programmable microcontrollers enables precise control of process parameters, monitoring temperature changes and analysis of technological data in real time. The article presents the influence of microprocessor systems on the control of the laser remelting process and the relationship between control parameters and microstructural changes occurring in modern steels.

Keywords: laser melting, technological data, control parameters

1. INTRODUCTION

The modern materials industry requires the use of technologies that increase the durability and operational resistance of structural elements. The processes of modifying the surface layer are of particular importance, because it is the surface of the material that is most exposed to abrasion, corrosion and thermal loads. One of the most effective methods of improving the functional properties of steel is surface laser melting, which allows to obtain a fine-grained structure and increase the hardness of the surface layer [1].

The development of laser technologies has led to a significant increase in the requirements for the accuracy of process control. Modern technological stations use advanced microprocessor systems responsible for controlling laser power, head travel speed, process temperature and synchronization of measurement sensors. Thanks to the use of microcontrollers, it is possible to monitor machining parameters in real time and quickly respond to changes occurring during the process [2].

In modern industrial systems, microcontrollers cooperate with temperature sensors, thermal cameras and CNC control systems. Appropriately programmed systems enable automatic maintenance of set technological parameters, which directly affects the stability of the process and the quality of the obtained recast layer.

2. CHARACTERISTICS OF THE LASER MELTING PROCESS

Surface laser melting involves the local melting of a thin layer of material using a concentrated laser beam. After passing the energy source, the material cools very quickly, the rate of which can reach values of 10^4–10^6 K/s [3]. Such intense cooling leads to the formation of non-equilibrium structures and significant fragmentation of the microstructure.
The process requires very accurate control of technological parameters. Even small changes in laser power or travel speed can cause significant differences in the depth of melting and the nature of the obtained structure. For this reason, modern stations use microprocessor control systems that analyze data from sensors and dynamically adjust process parameters.

Table 1. Example parameters of the laser surface remelting process used for modern steels

Process parameters	Range of values	Impact on structure
Laser power	500-3000W	Depth of remelting
Scanning speed	0,1-2,0 m/min	Microstructure fragmentation
Spot diameter	0,5-3 mm	Width of the remelting zone
Energy density	20-120 J/mm^2	Process stability
Shielding gas	Ar, N_2, He	Oxidation limitation

Controlling such a dynamic process requires the use of fast microprocessor systems. In practice, STM32, AVR microcontrollers and ARM Cortex systems are used, which are responsible for processing data from temperature sensors and controlling executive systems [4].

3. MICROSTRUCTURE OF MODERN STEELS AFTER PROCESSING

Modern tool and high-alloy steels are characterized by a high content of alloy additives, such as chromium, molybdenum, vanadium and nickel. These elements influence the course of phase transformations that occur during rapid heating and cooling of the material [5].
As a result of surface laser remelting, the following are most often observed in the recast layer:

- Fine needle martensite,
- dendritic structure,
- retained austenite,
- Partial dissolution of carbides,
- Reducing chemical segregation.

The cooling rate and process stability have a direct impact on the nature of the obtained microstructure. For this reason, microcontrollers used in control systems analyze the process temperature in real time and regulate the laser operating parameters. The control system can automatically reduce beam power if the temperature increases excessively or increase the head travel speed to reduce thermal stress.

Table 2. The influence of selected technological parameters on the properties of the recast layer

Parametr	Changing a parameter	Impact on structure
Increase in laser power	More energy	Depth of remelting
Deceleration	Longer heating time	Increase in the heat affected zone
Faster cooling	Faster crystallization	Grinding of grains
High linear energy	Intense melting	Possibility of microcracks

In H13 steels, rapid cooling leads to the formation of lath martensite with very high hardness [6]. At the same time, too high process energy may cause the occurrence of micro-cracks and residual stresses. The use of microprocessor systems makes it possible to reduce these phenomena through continuous control of technological parameters.

4. MICROPROCESSOR SYSTEMS IN CONTROL SYSTEMS

Modern laser processing systems are largely automated. The basic control element are microcontrollers responsible for communication between sensors, actuators and the master system.
The microcontroller performs, among others:

- Reading data from temperature sensors,
- Laser power control,
- Adjustment of travel speed,
- Analysis of measurement data,
- Communication with the control computer,
- Archiving process parameters.

In industrial practice, programming in C and C++ is very often used because they enable quick operations and direct access to the microcontroller's hardware registers [7]. Real-time RTOS systems, on the other hand, allow for simultaneous performance of many tasks, such as sensor operation, communication and drive control.
An important element of the process is also the analysis of signals from temperature sensors and thermal imaging cameras. This data is processed by microprocessor systems and used to dynamically adjust machining parameters. This makes it possible to maintain stable process conditions even with variable material properties.

5. MICROCONTROLLER PROGRAMMING IN MONITORING

Microcontroller programming plays a key role in modern laser processing systems. Properly written algorithms allow you to analyze process data in real time and make decisions regarding process control.

Industrial systems use, among others:

- PID algorithms,
- Adaptive control systems,
- ADC signal analysis,
- UART, SPI and CAN communication,
- Alarm and diagnostic systems.

Microprocessor systems cooperate with temperature sensors, encoders and measurement modules. The data is processed by a microcontroller which adjusts the laser operating parameters based on previously programmed algorithms.

Table 3. Examples of applications of microcontrollers in the laser processing proces

Microcontroller function	Application
Sensor reading	Temperature control
PWM control	Laser power adjustment
CAN communication	Data exchange with the CNC system
ADC support	Analysis of measurement signals
Interrupt system	Response to process changes

6. INDUSTRIAL USE AND DEVELOPMENT

Laser surface melting is used in many industries. In the automotive industry, this technology is used to increase the wear resistance of engine and transmission components. In the aviation industry, it is used for the regeneration of turbine blades and components operating at high temperatures [9].
The development of microprocessor systems enabled the creation of intelligent technological stations capable of independent analysis of process parameters. Modern Industry 4.0 systems use network communication and real-time data processing, which allows for increased accuracy and repeatability of the process.
Embedded systems cooperating with image analysis and thermal cameras are also becoming more and more important. This makes it possible to automatically detect structural defects and monitor the quality of the recast layer without having to stop the production process.

7. SUMMARY

Surface laser remelting of modern steels is an advanced method of modifying the surface layer, which allows obtaining beneficial microstructural changes and improving the operational properties of materials. However, the stability of the process depends on very accurate control

of technological parameters, which requires the use of modern microprocessor systems and appropriately programmed microcontrollers.
The development of control systems enables real-time process monitoring, analysis of measurement data and automatic adjustment of laser operating parameters. The integration of material technologies with microprocessors and embedded systems is currently one of the most important directions in the development of modern industry.

ACKNOWLEDGEMENTS

The work was created as part of project based learning - PBL, in the 14th competition under the Initiative of Excellence - Research University, Silesian University of Technology, Gliwice, Poland and as part of project of Students Scientific Circle of Laser Surface Treatment under the Initiative of Excellence - Research University, Silesian University of Technology, Gliwice, Poland.

BIBLIOGRAPHY

1. Burakowski T., Wierzchoń T., „Inżynieria powierzchni metali", PWN, Warszawa, 1999.
2. Dobrzański L.A., „Podstawy nauki o materiałach i metaloznawstwo", WNT, Warszawa, 2002.
3. Erdoğan A., „Laser Remelting Power Effect on Microstructure, Hardness and Wear Behavior of AISI 1020", Journal of Engineering Tribology, 2022.
4. Mazidi M.A., „AVR Microcontroller and Embedded Systems", Pearson, 2014.
5. Yu Y., Zhang M., Guan Y. i in., „The Effects of Laser Remelting on the Microstructure and Performance of Bainitic Steel", Metals, 2019.
6. Preussner J., Oeser S., Pfeiffer W. i in., „Microstructure and residual stresses of laser remelted surfaces of a hot work tool steel", International Journal of Materials Research, 2014.
7. Yiu J., „The Definitive Guide to ARM Cortex-M3 and Cortex-M4 Processors", Newnes, 2015.
8. Wilmshurst T., „Designing Embedded Systems with PIC Microcontrollers", Elsevier, 2010.
9. Jurci P., Cejp J., Brajer J., „Metallurgical Aspects of Laser Surface Processing of PM Cr-V Ledeburitic Steel", Advances in Materials Science and Engineering, 2011.
10. Karkadakattil A., „Laser surface modification of additively manufactured metals: mechanisms, thermal–microstructural evolution, and property enhancement", Journal of Engineering and Applied Science, 2026.

TalentDetector

7th-9th June 2026
Gliwice-Brenna, Poland

DEPARTMENT OF ENGINEERING MATERIALS AND BIOMATERIALS
FACULTY OF MECHANICAL ENGINEERING
SILESIAN UNIVERSITY OF TECHNOLOGY

INTERNATIONAL STUDENTS SCIENTIFIC CONFERENCE

Biomaterials for implantology applications

Martyna Gawlas[a], Marcin Majnusz[a], Aneta Kania[b]

[a] Silesian University of Technology, Faculty of Mechanical Engineering, Department of Engineering Materials and Biomaterials
email: mg303333@student.polsl.pl
[b] Silesian University of Technology, Faculty of Mechanical Engineering, Department of Engineering Materials and Biomaterials
email: aneta.kania@polsl.pl

Abstract: The article presents a characterization of biomaterials used in contemporary medical engineering. It discusses key requirements for implants, such as biocompatibility and biofunctionality, and presents their classification. Furthermore, the most significant trends in this field were presented, with particular attention given to additive technologies (3D and 4D printing), smart materials, and the increasing role of ecological solutions based on renewable raw materials.

Keywords: biomaterials, biocompatibility, classification of biomaterials, implants

1. INTRODUCTION

Biomaterials are an advanced group of engineering materials designed to interact directly with biological systems to replace, support, or regenerate damaged tissues and organs. A necessary condition for their clinical use is to meet strict criteria of biocompatibility, biofunctionality, and mechanical and corrosion stability in the aggressive environment of body fluids. Current trends in biomedical engineering are moving away from traditional, bioneutral material solutions toward bioactive structures capable of stimulating regenerative processes and controlled osseointegration. In this context, surface layer engineering remains a key area of optimization, determining phenomena at the implant-tissue interface and directly determining the long-term therapeutic effectiveness of implants.

2. CHARACTERIZATION OF BIOMATERIALS

A biomaterial is a material designed to interact with living tissues to support, replace, or regenerate their biological and mechanical functions. Unlike conventional technical materials, biomaterials must meet specific requirements related to safety and biocompatibility. This

means they must not cause toxic, allergic, or immunological reactions, and their presence in the body should be neutral or beneficial to biological processes [1].

Functionality and biocompatibility

Functionality, defined as the ability to perform specific tasks in a biological environment, plays a key role in the design of modern biomaterials. This includes tissue replacement, mechanical load transfer, stimulation of regenerative processes, resistance to infection, controlled drug release, and diagnostic applications [1,2]. Thanks to advanced manufacturing technologies such as 3D printing, functional properties can be precisely shaped by modifying the material's structure and porosity [3].

Biocompatibility is an essential criterion for clinical efficacy. Williams defines it as [4]: 'the ability of a material to elicit the desired body response in a given application without generating cytotoxicity, allergic reactions, or chronic inflammation, while simultaneously supporting tissue integration'.

Traditionally, biomaterials have been classified according to their chemical composition into four main groups: metallic, ceramic, polymer, and composite (Fig. 1). Metals (e.g., titanium and cobalt-chromium alloys) are primarily used in orthopedic and dental implants due to their high strength. Ceramics (e.g., hydroxyapatite, bioglass) are valued for their hardness and bioneutrality, making them ideal for coatings and prosthetics. Polymers (e.g., polyethylene, polytetrafluoroethylene (PTFE), hydrogels) are most commonly used in medicine due to their flexibility and biodegradability. Composites combine the advantages of various materials to achieve properties similar to those of natural tissues [3].

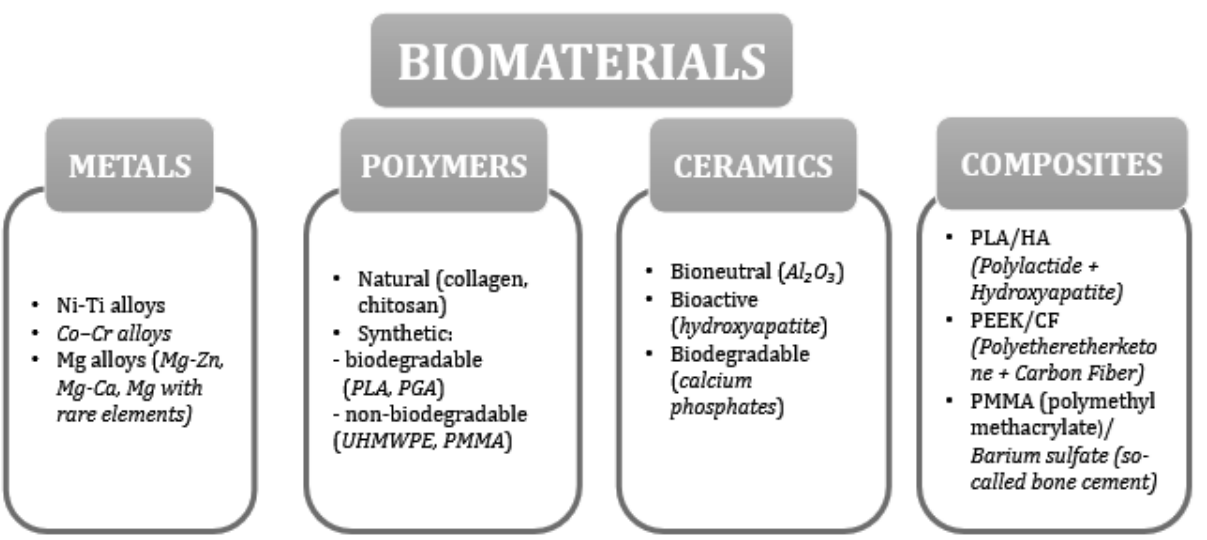

Figure 1. Division of biomaterials according to the type of material

2.1. Metal materials

Metal biomaterials play a key role in implantology and medical engineering, especially where mechanical properties and durability are required, such as in orthopedics (screws, plates, joint implants), dentistry (implants), and cardiology (stents, device components). The most commonly used alloys include titanium and its alloys, cobalt-chromium alloys, and stainless steel. Additionally, shape-memory alloys (NiTi – nickel and titanium alloys) are also used for

special applications. Metal biomaterials are typically non-biodegradable and intended to remain in the body for long periods, so they must consider both mechanical properties and long-term biocompatibility [3].

Cobalt and chromium alloys (Co-Cr)

Cobalt-chromium alloys are characterized by good mechanical properties, corrosion resistance, and good biocompatibility. These materials are used where implants must transfer high mechanical loads and operate stably for many years in the human body. Their applications include orthopedic prostheses (hip and knee joints) and dental components (crowns, bridges, partial dentures). Co-Cr alloys are generally tolerated by human tissues and do not cause severe immunological reactions under normal conditions. However, the presence of metal ions in the biological environment may cause local inflammatory reactions, lead to osteolysis and hypersensitivity reactions in some patients [5].

Polymer materials

Polymer materials constitute one of the most important groups of biomaterials used in contemporary medicine and biomedical engineering. Their popularity is due to the wide range of possibilities for modifying their chemical composition, structure, and physicochemical properties, which allows for precise adaptation of the material to a specific clinical application. Polymers can be both durable and biodegradable, making them suitable for long-term implants, temporary tissue support systems, and drug carriers.

Compared to metallic and ceramic biomaterials, polymers are characterized by low density, good flexibility, and the ability to achieve mechanical properties similar to those of the body's soft and hard tissues. Another significant advantage of polymer materials is their relatively easy processing, which includes methods such as injection molding, extrusion, and 3D printing, enabling the production of implants with complex geometries and controlled porosity. Polymers can be classified according to various criteria, depending on their origin, chemical structure, mechanical properties, and behavior in the environment.

Biodegradable polymers

The most commonly used biodegradable synthetic polymers include polylactide (PLA), polyglycolide (PGA), polylactic acid-glycolic acid copolymer (PLGA), and polycaprolactone (PCL). These materials degrade primarily through hydrolysis of ester bonds, and their degradation products (e.g., lactic acid and glycolic acid) are metabolized in the Krebs cycle or eliminated from the body [6].

Non-biodegradable polymers

In applications where long-term stability is essential, non-biodegradable polymers are employed, such as ultra-high molecular weight polyethylene (UHMWPE), polymethyl methacrylate (PMMA), poly(etheretherketone) (PEEK), and polytetrafluoroethylene (PTFE) [7].

2.2. Ceramic materials

Biomedical ceramics are characterized by high hardness, abrasion resistance, chemical stability, and excellent biocompatibility, making them suitable for long-term implants. Compared to metals and polymers, they exhibit significantly greater resistance to corrosion and

tribological wear, but their significant limitations remain brittleness and relatively low fracture toughness [8].

Bioneutral ceramics

Bioneutral ceramics are a group of ceramic biomaterials that, after implantation, do not cause a significant biological reaction and do not chemically interact with surrounding tissues. Their main characteristics are high chemical stability and resistance to degradation in the physiological environment. This property enables the materials to retain their mechanical properties over an extended period. Integration with the body occurs primarily through mechanical anchoring of the implant, rather than through direct chemical bonds with bone tissue. One of the most important examples of bioneutral ceramics is aluminum oxide (Al_2O_3, alumina), which is characterized by very high hardness, abrasion resistance, and excellent chemical stability [9].

Bioactive ceramics

Bioactive ceramics are a group of biomaterials capable of chemically bonding with bone tissue, promoting osseointegration and bone regeneration. Unlike bioneutral ceramics, these materials are not only tolerated by the body but also actively stimulate a biological response, leading to the formation of a durable implant-bone connection. One of the most important bioactive materials is hydroxyapatite (HA, $Ca_{10}(PO_4)_6(OH)_2$), whose chemical composition is similar to the mineral phase of natural human bone. It demonstrates excellent biocompatibility, osteoconductivity, and the ability to support osteoblast adhesion and proliferation [10].

Biodegradable ceramics

Biodegradable ceramics, also known as resorbable ceramics, are materials that gradually degrade in the physiological environment, and their degradation products are metabolized or eliminated from the body. Their key advantage is the ability to temporarily support the structure of regenerating tissue, after which the material is replaced by natural bone. The most important group of biodegradable ceramics are calcium phosphates, including tricalcium phosphate (TCP) and biphasic calcium phosphates (BCP). The rate of degradation of these materials can be regulated by changing their chemical composition and structural porosity, allowing their properties to be tailored to the rate of bone tissue regeneration [8].

3. DIRECTIONS OF BIOMATERIALS DEVELOPMENT

The development of modern biomaterials resigns from the creation of passive structures in favor of next-generation materials that actively interact with the body and stimulate its regeneration. A major trend is the design of smart biomaterials, capable of adapting to the biological environment and dynamically changing their properties (e.g., releasing drugs) under the influence of external stimuli such as temperature or pH changes. At the same time, advanced additive technologies (3D and 4D printing) are gaining in importance. They enable the development of personalized medicine by producing implants and tissue scaffolds perfectly tailored to the patient's anatomy, which, in the case of 4D printing, can also evolve over time [11].

Surface engineering aims to develop multifunctional and hybrid systems that integrate mechanical, biological, and therapeutic properties. One example of this integration is the

simultaneous provision of bone-forming and antibacterial properties [11]. The ecological aspect is also increasingly emphasized. The role of so-called green biomaterials, i.e., biodegradable solutions based on renewable plant raw materials, is growing. This approach is consistent with the principles of sustainable development [12].

4. CONCLUSIONS

The effectiveness and safety of biomaterials depend primarily on their appropriate interaction with the body's living tissues. Currently, there is a clear shift away from the use of purely passive structures toward modern bioactive materials that can actively stimulate healing processes. The future of regenerative medicine depends on the precise personalization of implants and the integration of advanced surface engineering techniques. These elements, when combined, will facilitate the development of implants that are more durable, safer, and perfectly tailored to the patient's needs.

BIBLIOGRAPHY

1. C. Scheau, A.C. Didilescu, C. Caruntu, Functional Biomaterials: Scaffolds for Innovative Treatments, Journal of Functional Biomaterials 16/5 (2025) 154.
2. G. Lutzweiler, A. Ndreu Halili, N. Engin Vrana, The overview of porous, bioactive scaffolds as instructive biomaterials for tissue regeneration and their clinical translation, Pharmaceutics 12/7 (2020) 602.
3. A. Arjunan, A. Baroutaji, A.S. Praveen, J. Robinson, C. Wang, Classification of biomaterial functionality, Encyclopedia of Smart Materials 1 (2020) 86-102.
4. D.F. Williams, The Williams dictionary of biomaterials. Liverpool University Press, Liverpool, 1999.
5. B. Lohberger, N. Stuendl, D. Glaenzer, B. Rinner, N. Donohue, H.C. Lichtenegger, L. Ploszczanski, A. Leithner, CoCrMo surface modifications affect biocompatibility, adhesion, and inflammation in human osteoblasts, Scientific Reports 10/1 (2020) 1682.
6. J.C. Middleton, A.J. Tipton, Synthetic biodegradable polymers as orthopedic devices, Biomaterials 21/23 (2000) 2335-2346.
7. S.M. Kurtz, J.N. Devine, PEEK biomaterials in trauma, orthopedic, and spinal implants, Biomaterials 28/32 (2007) 4845-4869.
8. S. Punj, J. Singh, K. Singh, Ceramic biomaterials: Properties, state of the art and future prospectives, Ceramics International 47/20 (2021) 28059-28074.
9. J. Chevalier, L. Gremillard, Ceramics for medical applications: A picture for the next 20 years, Journal of the European Ceramic Society 29/7 (2009) 1245-1255.
10. F. Boschetto, A. Rondinella, E. Marin, Biological Activity of Silicon Nitride Ceramics: A Critical Review, Materials 17/22 (2024) 5548.
11. K. Rezwan, Q.Z. Chen, J.J. Blaker, A.R. Boccaccini, Biodegradable and bioactive porous polymer/inorganic composite scaffolds for bone tissue engineering, Biomaterials 27/18 (2006) 3413-3431.
12. Z.U. Arif, M.Y. Khalid, A. Zolfagharian, M. Bodaghi, 4D bioprinting of smart polymers for biomedical applications: recent progress, challenges, and future perspectives, Reactive and Functional Polymers 179 (2022) 105374.

TalentDetector
7th-9th June 2026
Gliwice-Brenna, Poland
DEPARTMENT OF ENGINEERING MATERIALS AND BIOMATERIALS
FACULTY OF MECHANICAL ENGINEERING
SILESIAN UNIVERSITY OF TECHNOLOGY
INTERNATIONAL STUDENTS SCIENTIFIC CONFERENCE

Historia szelaku w przemyśle fonograficznym

Wiktoria Groelich[a], Jan Grzybicki[b], Bogusław Ziębowicz[c], Anna Ziębowicz[d]

[a] Faculty of Biomedical Engineering, Department of Biomaterials and Medical Device Engineering, Silesian University of Technology, Roosevelta 40, 41-800 Zabrze, Poland;
email: wg301436@student.polsl.pl, Science and Culture Student Research Club
[b] Cafted System, ul. Centralna 299, 43-187, Orzesze, j.grzybicki@gmail.com
[c] Faculty of Mechanical Engineering, Department of Engineering Materials and Biomaterials, Silesian University of Technology, Konarskiego 18A , 44-100 Gliwice, Poland;
email: boguslaw.ziebowicz@polsl.pl
[d] Faculty of Biomedical Engineering, Department of Biomaterials and Medical Device Engineering, Silesian University of Technology, Roosevelta 40, 41-800 Zabrze, Poland;
email: anna.ziebowicz@polsl.pl

Streszczenie: Płyta szelakowa była podstawowym nośnikiem dźwięku od końca XIX wieku aż do połowy XX wieku. Zanim rozpowszechniły się płyty winylowe, to właśnie krążki szelakowe umożliwiły masową dystrybucję muzyki rozrywkowej, klasycznej, nagrań operowych, przemówień oraz audycji rozrywkowych. Ich rozwój był ściśle związany z wynalezieniem gramofonu oraz postępem technologii zapisu i reprodukcji dźwięku.

Słowa kluczowe: płyta gramofonowa, szelak, zapis dźwięku, historia, materiał

1. WSTĘP

Płyta szelakowa stanowiła najważniejszy nośnik zapisu dźwięku od schyłku XIX wieku do połowy XX stulecia. Jeszcze przed popularyzacją płyt winylowych krążki wykonywane z szelaku umożliwiały szerokie rozpowszechnianie muzyki, wystąpień publicznych znanych osób oraz programów rozrywkowych. Ich upowszechnienie odegrało istotną rolę w rozwoju przemysłu fonograficznego i przyczyniło się do zmiany sposobu odbioru kultury muzycznej oraz przekazu słownego. Powstanie i rozwój płyt szelakowych były bezpośrednio związane z wynalezieniem gramofonu oraz udoskonalaniem metod rejestracji i odtwarzania dźwięku. Dzięki nowym rozwiązaniom technologicznym możliwe stało się wielokrotne odtwarzanie nagrań, co znacząco wpłynęło na rozwój rynku muzycznego oraz popularyzację fonografii wśród społeczeństwa. Nośnik ten przez wiele dekad pozostawał dominującą formą zapisu audio, mimo ograniczeń wynikających z jego kruchości i niewielkiej pojemności nagraniowej. [1, 2]

Celem niniejszej pracy jest przedstawienie historii szelaku jako materiału stosowanego w fonografii przed erą polichlorku winylu oraz analiza obrazów mikroskopowych płyty szelakowej sprzed stu lat wykonanych przy użyciu mikroskopu skaningowego elektronowego.

2. POCZĄTKI REJESTACJI DŹWIĘKU

Za początek historii fonografii uznaje się rok 1877, kiedy Thomas Edison skonstruował fonograf zapisujący dźwięk na cylindrach pokrytych cynową folią. Urządzenie umożliwiało zarówno nagrywanie, jak i odtwarzanie głosu. Był to pierwszy w historii aparat zdolny do mechanicznej reprodukcji dźwięku (Rys. 1). Przełom nastąpił jednak dzięki pracom Emilea Berlinera, który w 1887 roku opatentował gramofon wykorzystujący płaski dysk zamiast cylindra. Rozwiązanie to okazało się znacznie praktyczniejsze w produkcji seryjnej, ponieważ matryce do produkcji płyt umożliwiały łatwe tłoczenie wielu identycznych egzemplarzy nagrania. Konstrukcja Berlinera stała się podstawą nowoczesnych płyt gramofonowych, w tym szelakowych (Rys. 1). [3, 4]

a) b)

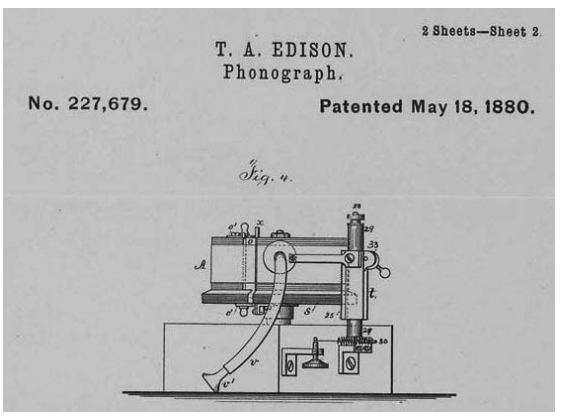

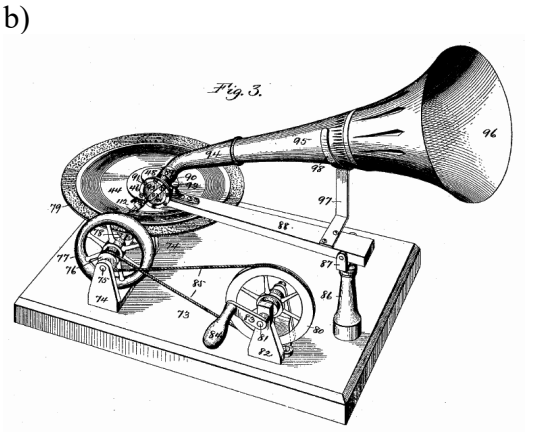

c) d)

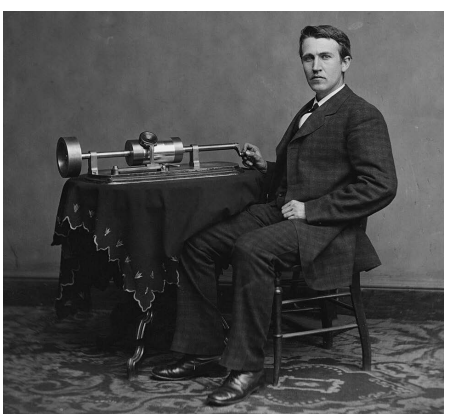

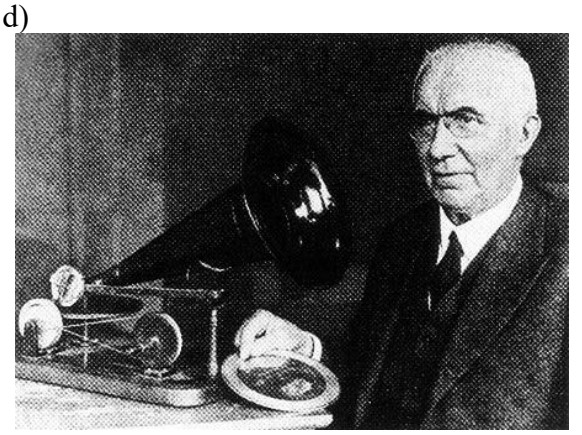

Rysunek 1. Rysunek z patentu: a) Thomasa Edisona – fonograf [5], b) Emila Berlinera – gramofon [6] a) Thomasa Edisona – fonograf. Zdjęcie Thomasa Edisona i jego wynalazku: c). [https://pl.wikipedia.org] Zdjęcie Emila Berlinera i jego wynalazku: d). [https://pl.wikipedia.org]

3. NARODZINY PŁYTY SZELAKOWEJ

Pierwsze płyty gramofonowe wykonywano z różnych mieszanek materiałów, lecz na początku XX wieku standardem stała się masa szelakowa. Szelak jest naturalną żywicą produkowaną przez owady Kerria lacca (Rys. 2). Jest to gatunek czerwca (owada z nadrodziny Coccoidea) należący do rodziny Kerriidae. Jest on jednym z najważniejszych gospodarczo gatunków owadów lakowych, ponieważ stanowi główne źródło naturalnej żywicy zwanej lakiem. Po oczyszczeniu i rafinacji żywica ta wykorzystywana jest do produkcji szelaku oraz innych produktów stosowanych m.in. w przemyśle drzewnym, spożywczym i farmaceutycznym. Gatunek ten występuje naturalnie w Azji południowej i południowo-wschodniej, zwłaszcza na obszarze Indii i Tajlandii. [7]

a) b)

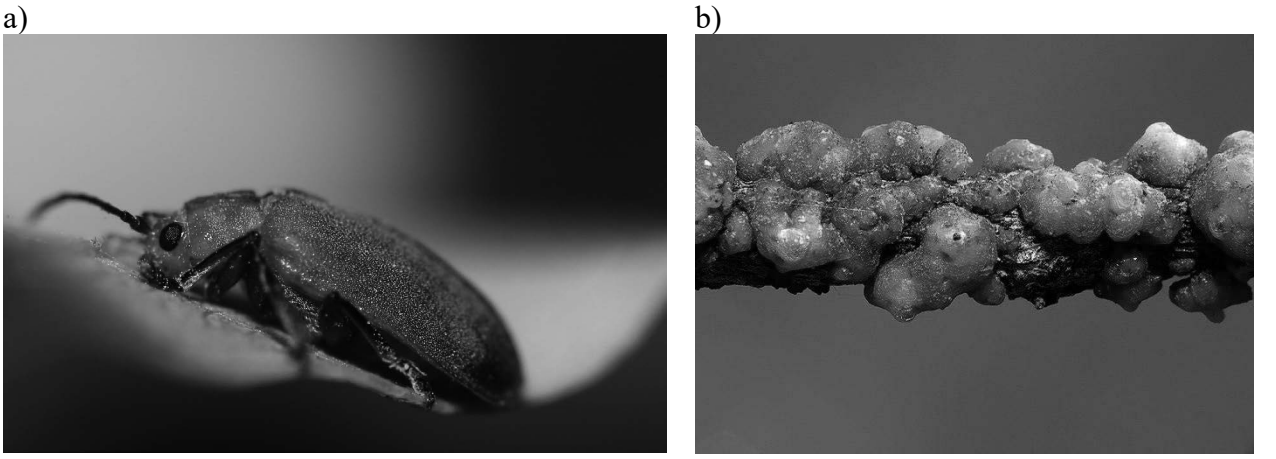

Rysunek 2. a) widok ogólny owada Kerria lacca, b) widok charakterystycznych skupisk owadów i ich żywicznej wydzieliny (laki) pokrywającej gałązki drzew. [https://pl.wikipedia.org]

Płyty szelakowe były ciężkie, kruche i podatne na pękanie, jednak miały dużą odporność na ścieranie. Standardowo obracały się z prędkością 78 obrotów na minutę (78 rpm), dlatego często określa się je mianem „siedemdziesiątek ósemek”. Około 1915 roku format 78 rpm stał się międzynarodowym standardem. Typowa płyta 10-calowa mogła pomieścić około 3–4 minut nagrania na stronę.

4. ROZWÓJ PRZEMYSŁU FONOGRAFICZNEGO

Na początku XX wieku przemysł płytowy rozwijał się niezwykle dynamicznie. Powstały wielkie wytwórnie, takie jak Columbia Records, Victor Talking Machine Company czy Deutsche Grammophon. Gramofon i płyta szelakowa stały się pierwszym masowym medium muzycznym w historii. W latach 1910–1920 sprzedaż gramofonów gwałtownie wzrosła. Muzyka przestała być dostępna wyłącznie podczas koncertów — można jej było słuchać w domu. Rozwój rynku płyt zbiegł się z popularyzacją muzyki rozrywkowej, między innymi ragtime’u, bluesa i jazzu. W latach 20. XX wieku nastąpiło przejście z nagrań akustycznych na elektryczne. Zastosowanie mikrofonów i wzmacniaczy znacząco poprawiło jakość rejestrowanego dźwięku. Od tego momentu płyty szelakowe mogły wierniej oddawać brzmienie orkiestr i głosu ludzkiego. [1-4]

5. TECHNOLOGIA PRODUKCJI

Charakterystyczną cechą płyt szelakowych były szerokie rowki, znacznie większe niż w późniejszych płytach winylowych typu LP. Szerokość rowka w płytach szelakowych wynosiła zazwyczaj około 100–150 µm, dlatego określa się je mianem nagrań standard groove lub 78 rpm groove (Rys. 3). Wymagały one stosowania grubych stalowych igieł o większej średnicy, najczęściej około 65–100 µm oraz specjalnych gramofonów mechanicznych, od końca lat 20. XX wieku zasilanych silnikiem elektrycznym. W porównaniu z późniejszymi płytami winylowymi jakość dźwięku była ograniczona, a poziom szumów stosunkowo wysoki.

Proces produkcji płyt szelakowych należał do najbardziej zaawansowanych technologicznie przedsięwzięć przemysłu fonograficznego pierwszej połowy XX wieku. Wytwarzanie jednej płyty wymagało połączenia technologii mechanicznej, chemicznej i elektrochemicznej.

Pierwszym etapem produkcji było wykonanie nagrania wzorcowego – dysk woskowy. W epoce nagrań akustycznych muzycy grali przed dużą tubą akustyczną połączoną z membraną i rylcem. Drgania dźwięku były mechanicznie przenoszone na obracający się dysk woskowy, w którym ryto spiralny rowek odpowiadający zapisowi dźwięku. Po połowie lat 20. XX wieku zaczęto stosować mikrofony i wzmacniacze elektryczne, co pozwoliło uzyskać znacznie dokładniejszy zapis. Nagrany dysk woskowy był bardzo delikatny, dlatego nie nadawał się bezpośrednio do tłoczenia. Pokrywano go cienką warstwą grafitu lub srebra, a następnie poddawano procesowi galwanizacji. W kąpieli elektrochemicznej osadzała się warstwa metalu — zwykle niklu lub miedzi — tworząc negatyw nagrania zwany „ojcem" (father). Z niego wykonywano kolejne kopie robocze: „matkę" (mother) i stemple tłoczące. Taki system umożliwiał seryjną produkcję tysięcy egzemplarzy bez niszczenia oryginalnego nagrania. Płyty nie były wykonywane z czystego szelaku. Masa produkcyjna zawierała: szelak naturalny, pył łupkowy lub wapienny, sadzę, włókna bawełniane, dodatki utwardzające. Takie połączenie materiałów zwiększało twardość i odporność na ścieranie płyt, choć jednocześnie powodowało ich dużą kruchość. Typowa płyta szelakowa mogła łatwo pęknąć po upuszczeniu. Materiał był jednak stosunkowo odporny na wysoką temperaturę i intensywne użytkowanie. Masa szelakowa była podgrzewana do postaci plastycznej, a następnie umieszczana pomiędzy dwiema metalowymi matrycami w prasie hydraulicznej. Pod wysokim ciśnieniem tłoczono rowki wraz z papierowymi etykietami znajdującymi się po obu stronach płyty. Cały proces trwał zwykle mniej niż minutę. Po wyjęciu z prasy nadmiar materiału przycinano mechanicznie. Gotowa płyta przechodziła kontrolę jakości, po czym trafiała do papierowych kopert i do dystrybucji. W dużych fabrykach produkowano tysiące egzemplarzy dziennie. Technologia płyt szelakowych miała kilka istotnych ograniczeń: szerokie rowki ograniczały długość nagrania, wysoki poziom szumów własnych utrudniał wierne odtwarzanie cichych dźwięków, płyty szybko zużywały się przy użyciu stalowych igieł, kruchość materiału powodowała częste uszkodzenia podczas transportu. Mimo tych wad technologia dominowała na rynku przez ponad 50 lat i stworzyła fundament współczesnego przemysłu muzycznego. [1, 4, 8]

Na rysunku 3 przedstawiono obrazy mikroskopowe płyty szelakowej wyprodukowanej w wytwórni Columbia Records w połowie lat 20. XX wieku wykonane za pomocą skaningowego mikroskopu elektronowego firmy ZEISS Supra 25 w powiększeniach 100x, 250x oraz 1000x. Na podstawie badań mikroskopowych stwierdzono, że średnia szerokość rowka płyty gramofonowej wynosi 162,32 µm. Przełom płyty po pęknięciu jest przełomem typowo kruchym. Na widoku z góry oraz z boku widać wyraźne pasma zużycia oraz zanieczyszczenia powierzchniowe w postaci drobin kurzu.

6. SCHYŁEK ERY SZELAKU

Po II wojnie światowej rozpoczęła się rewolucja technologiczna w fonografii. W 1948 roku Columbia Records zaprezentowała płytę długogrającą LP (long play) wykonaną z polichlorku winylu i odtwarzaną z prędkością 33⅓ rpm. Wkrótce firma RCA Corporation wprowadziła format 45 rpm SP (single play). Polichlorek winylu okazał się materiałem zdecydowanie lepszym od szelaku. Był lżejszy, bardziej elastyczny i mniej kruchy oraz umożliwiał zapis znacznie dłuższych nagrań (około 25 minut na jednej stronie płyty) przy zdecydowanie lepszej jakości dźwięku wynikającej między innymi z mniejszej ziarnistości materiału. [1-4]

Produkcja płyt szelakowych zaczęła szybko zanikać w latach 50. XX wieku, choć w niektórych krajach utrzymywała się jeszcze w latach 60. Wraz z popularyzacją płyt winylowych „78-ki" stały się formatem historycznym i kolekcjonerskim.

a)

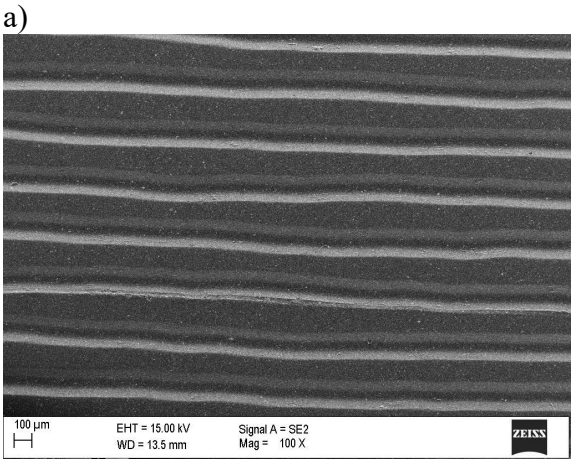

b)

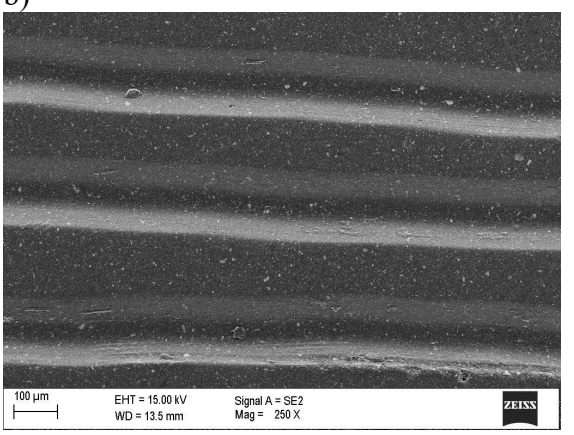

c)

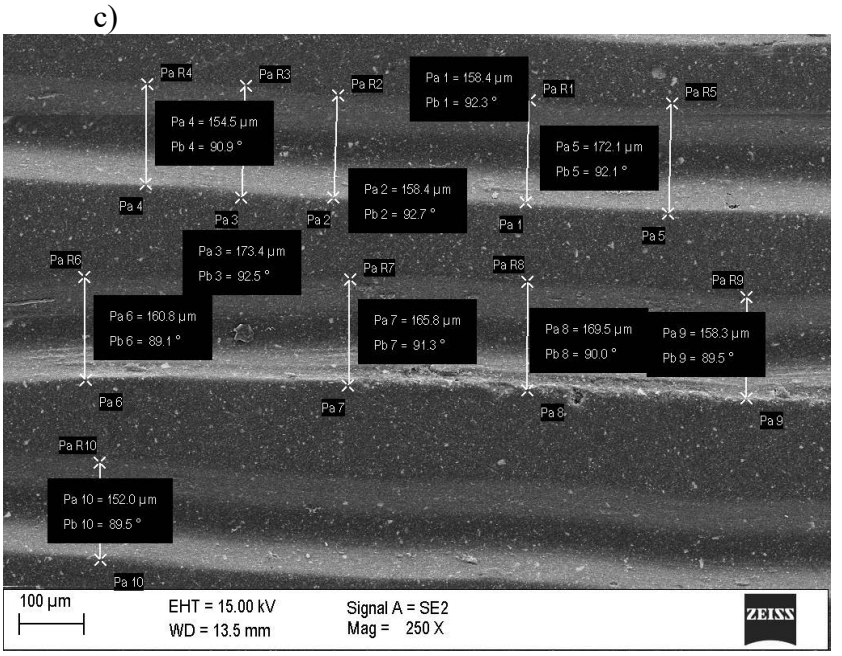

d)

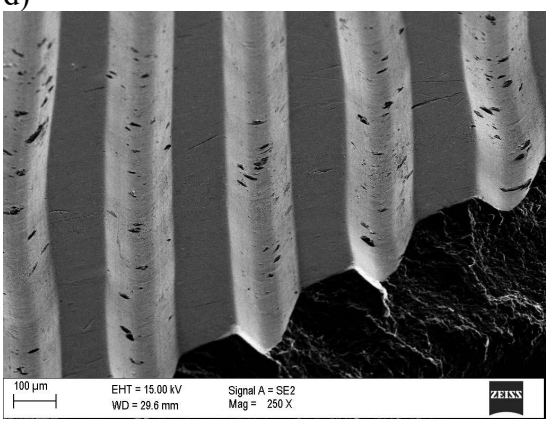

e)

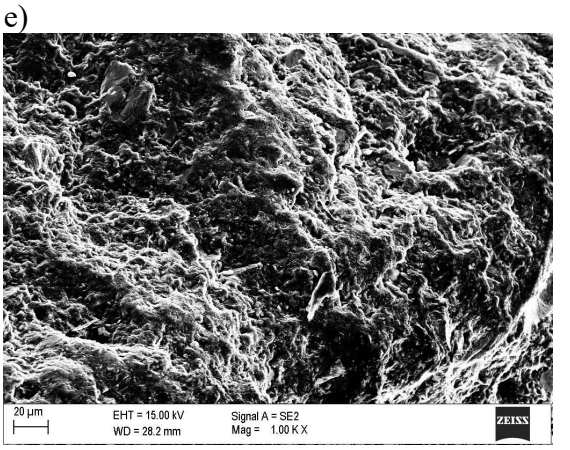

Rysunek 3. Płyta szelakowa: a) widok ogólny z góry, powiększenie 100x, b) widok ogólny z góry, powiększenie 250x, c) wynik analizy szerokości rowka, powiększenie 260x, d) widok z boku z widocznym przełomem po pęknięciu płyty, powiększenie 250x, e) widok przełomu (rodzaj przełomu – kruchy), powiększenie 1000x.

Na rysunku 4 przedstawiono album płyt szelakowych zawierających V Symfonię c-moll op. 67 Ludwiga van Beethovena wytworzonych w latach 20. XX wieku przez wytwórnie Columbia Records. Symfonia zawiera się na czterech krążkach. Aby odtworzyć całą symfonię słuchacz musiał osiem razy zmieniać stronę płyty. Było to bardzo kłopotliwe i wymagało poszukiwań nowych rozwiązań technicznych.

a)

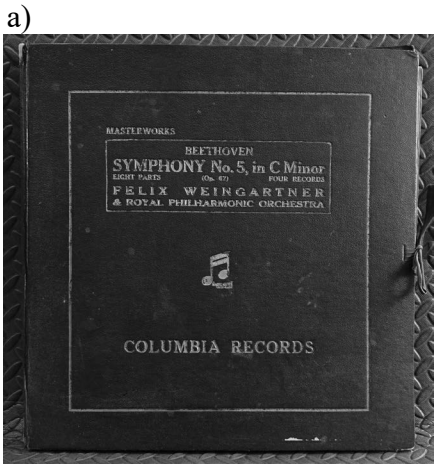

b)

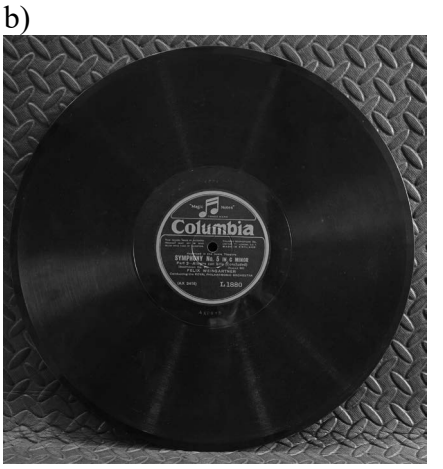

Rysunek 4.Widok albumu płyt szelakowych zawierających V Symfonię c-moll op. 67 Ludwiga van Beethovena wytworzonych w latach 20. XX wieku przez wytwórnie Columbia Records: a) okładka, b) płyta szelakowa z labelem (etykietą).

7. ZNACZENIE KULTUROWE

Płyta szelakowa odegrała fundamentalną rolę w rozwoju kultury masowej. Umożliwiła narodziny przemysłu muzycznego, popularyzację gwiazd estrady oraz globalną dystrybucję muzyki. Dzięki niej po raz pierwszy możliwe było wielokrotne odtwarzanie tego samego wykonania w dowolnym miejscu i czasie. Dla współczesnych kolekcjonerów płyty szelakowe stanowią cenne źródło dokumentacji historycznej. Zachowały się na nich nagrania artystów z

początku XX wieku, w tym wczesne wykonania muzyki, m.in. klasycznej, jazzu, bluesa oraz ragtime'u.

BIBLIOGRAFIA

1. Gavin Williams, Format Friction: Perspectives on the Shellac Disc, University of Chicago Press, 2024.
2. Elodie A. Roy, Shellac in Visual and Sonic Culture: Unsettled Matter, Amsterdam University Press, 2023.
3. Andre Millard, America on Record: A History of Recorded Sound, Cambridge University Press, 2005.
4. Oliver Read, Walter L. Welch, From Tin Foil to Stereo: Evolution of the Phonograph, Howard W. Sams & Co., 1976.
5. U.S. National Archives. (1880). Drawing for a Phonograph (Patent No. 227,679)
6. Berliner, E. (1887). Gramophone: specification forming part of Letters Patent No. 372,786, dated November 8, 1887. United States Patent Office.
7. https://www.britannica.com/topic/shellac
8. David L. Morton, Sound Recording: The Life Story of a Technology, Baltimore: Johns Hopkins University Press, 2006

TalentDetector

7th-9th June 2026
Gliwice-Brenna, Poland

DEPARTMENT OF ENGINEERING MATERIALS AND BIOMATERIALS
FACULTY OF MECHANICAL ENGINEERING
SILESIAN UNIVERSITY OF TECHNOLOGY

INTERNATIONAL STUDENTS SCIENTIFIC CONFERENCE

Visualizing the Invisible: Real-Time Instruction Tracing for Computer Architecture Education

[a]Mateusz Grzanka, [a]Maciej Guja, [a]Jan Jezierski, [a]Bartosz Malich, [a]Patrycja Nessing, [a]Adam Wolany, [a]Aleksander Żak, [b]Jarosław Paduch

[a] Students of Silesian University of Technology, Faculty of Automatic Control, Electronics and Computer Science,
email: mg311306@student.polsl.pl
[b] Silesian University of Technology, Faculty of Automatic Control, Electronics and Computer Science, Department of Graphics, Computer Vision and Digital Systems
email: jaroslaw.paduch@polsl.pl

Abstract: This paper presents the design and implementation of an innovative educational platform aimed at addressing the existing pedagogical gap in computer architecture instruction for engineering students. In contrast to traditional microcontroller programming methodologies, where the processor is often treated as a 'black box', the proposed solution enables direct observation of the Z80 processor's signal layer. Through the integration of a dedicated assembler, a simulator, and a physical hardware platform coupled with a visualisation layer, students can trace the execution of individual instructions decomposed into micro-steps (T-states), thereby facilitating a rigorous comparison between theoretical models and real-time signals on the address and data buses.

Keywords: Z80 processor, computer architecture, educational platform, assembler, embedded systems, laboratory teaching

1. INTRODUCTION

Contemporary computer architecture education frequently relies upon software simulators or off-the-shelf development kits. Whilst these tools are undoubtedly useful, they possess a significant pedagogical drawback: the microcontroller is treated as a 'black box'. Although the programmer provides the code and the integrated circuit executes the task, the underlying processes, specifically how an instruction triggers signals on the buses and how physical circuits respond to control pulses, remain entirely obscured. As a result, concepts such as bus cycles, memory operations, and timing relationships remain abstract and difficult to relate to the physical behaviour of hardware systems [5].

The objective of this paper is to present an integrated educational platform that eliminates this barrier. Rather than focusing solely on running software on a legacy processor, the system emphasises visualising Z80 instruction execution, decomposed into T-states. This approach

enables the transformation of abstract theoretical concepts into observable hardware phenomena.

The Z80 processor was selected for its transparent architecture, comprehensive technical documentation, and the distinct decomposition of instruction execution into machine cycles and T-states [1,2]. These characteristics enable a deterministic analysis of the execution flow, making it an exceptionally powerful educational tool.

2. EXISTING SOLUTIONS AND THEIR LIMITATIONS

Teaching computer architecture typically relies upon three primary categories of educational tools: microcontroller platforms, software simulators, and FPGA-based systems.

Microcontroller development kits, such as Arduino, STM32 Nucleo, and PIC-based platforms, are widely utilised in engineering education due to their low barrier to entry. While they facilitate rapid embedded application development, the underlying mechanisms of instruction execution, bus activity, and signal synchronisation remain entirely obscured from the user.

Software simulators allow the observation of register and memory contents and the analysis of program flow [6]. However, because they operate on abstract behavioural models, they fail to replicate actual bus timing or hardware signal synchronisation. Consequently, students interact with a logical model of the processor rather than the physical signals generated during real-time execution.

FPGA-based platforms provide deep insight into digital systems and allow for the implementation of custom architectures. Nevertheless, they necessitate proficiency in Hardware Description Languages (HDLs), which poses a significant pedagogical barrier for students new to computer architecture. Furthermore, many educational FPGA implementations utilise simplified soft-core processors that lack the comprehensive timing documentation required for granular analysis.

While certain Z80-based projects, such as the Z80 MBC [3] and RC2014 [4], demonstrate the enduring relevance of classic architectures, their primary objective is full-system operation rather than instruction-level analysis. These platforms do not provide synchronised observation of bus activity at the granularity of individual T-states.

The platform presented in this paper addresses these limitations by bridging the gap between physical execution and real-time visualisation. By combining a physical Z80 processor with a system-clock-synchronised bus monitor, the proposed solution enables a direct correlation between assembly instructions and observable hardware behaviour at the level of individual T-states.

3. CONCEPT OF THE PROPOSED PLATFORM

The proposed environment is designed around a single overarching educational objective: making visible the internal micro-operations that typically remain hidden during standard computer execution. Every design decision, across both the hardware and software layers, is subordinated to this goal of transparency.

The pedagogical foundation of the platform lies in the granular analysis of machine cycles. As each instruction is executed as a sequence of T-states corresponding to individual system clock periods [1,2], specific signals emerge on the processor buses, including memory addresses, data transfers, and control signals. The core concept of this platform is to capture these transient hardware events and present them as a continuous, synchronised visual representation. This allows students to perform a step-by-step decomposition of an instruction into its constituent micro-operations.

To realise this concept, the system integrates three functional layers: a hardware execution layer, a software development layer, and a monitoring/visualisation layer (Figure 1). The hardware layer provides the physical execution environment; the software layer handles the translation of low-level code into machine instructions; and the monitoring layer serves as the bridge, capturing real-time signal transitions and decomposing them into a human-readable format.

A key advantage of this approach is the seamless continuity of the educational workflow. By allowing students to first analyse a program in a simulator and then execute it on physical hardware, the platform enables a direct empirical comparison between theoretical predictions and actual hardware behaviour. This process transforms abstract architectural concepts into verifiable, laboratory-based observations.

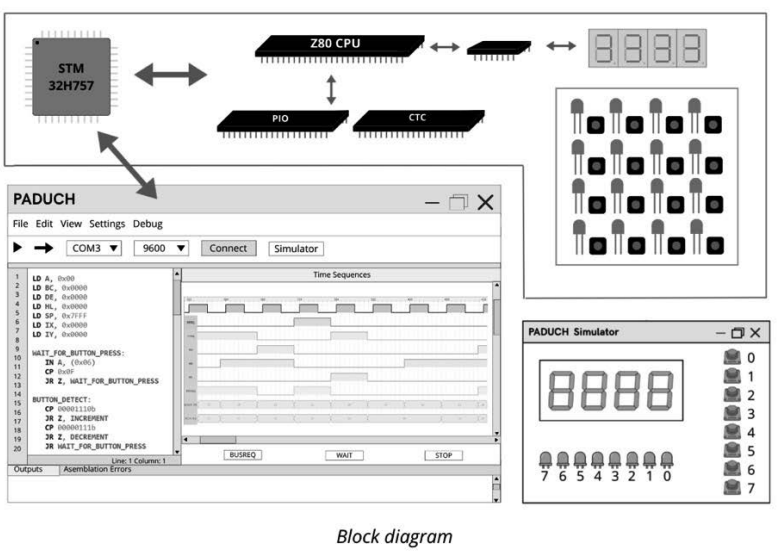

Figure 1. Block diagram of the proposed platform

4. SYSTEM IMPLEMENTATION

The implementation of the proposed platform is realised through an integrated architecture consisting of three interconnected layers: the hardware execution layer, the software development environment, and the signal monitoring/visualisation system. The architecture is designed to create a closed-loop feedback mechanism in which code is developed, transferred to the physical processor, and its internal micro-operations are captured in real time. The following sections describe the technical specifications and the functional role of each component within this ecosystem.

4.1. Hardware Execution Layer (Z80 Platform)

The core of the platform is built around the Z80 microprocessor, chosen specifically for its transparent machine-cycle architecture and the availability of comprehensive technical documentation [1,2]. The fundamental educational value of this processor lies in its deterministic execution: each instruction is decomposed into a strictly defined sequence of T-states [1]. This allows students to perform predictive analysis of bus activity, specifically address and data bus transitions, and subsequently validate these theoretical models through real-time observation of the physical hardware signals.

To provide a complete experimental environment, the processor is integrated into a custom-designed Printed Circuit Board (PCB) that hosts several essential peripheral components.
The hardware layout was implemented on a 4-layer PCB to ensure signal integrity for the high-frequency clock and bus transitions. The system architecture includes:

- Memory Subsystem: A 64kB SRAM module provides the workspace required for program execution and data manipulation.
- Peripheral Controllers: Dedicated Z80-compatible controllers, including a Programmable Interface Device (PIO) for general-purpose I/O and a Counter/Timer Circuit (CTC), are integrated to allow students to interact with hardware-level timing and logic.
- User Interface & I/O Peripherals: To support human-machine interaction, the board features a 4x4 matrix keyboard for inputting low-level commands and a 4x4 LED matrix for visual output. These components are mapped directly to the processor's I/O ports, allowing students to observe the immediate effect of software instructions on the physical hardware state.

4.2. Signal Acquisition and Visualisation Layer (STM32 & Interface)

A key component linking the physical hardware platform to the desktop application is a dual-core STM32 microcontroller, which serves as a high-speed communication bridge and system controller. The microcontroller operates at a clock frequency significantly higher than that of the Z80 processor, providing sufficient computational headroom to perform multiple concurrent tasks:

- Clock Generation: Generating a stable CLK signal with a frequency defined by the user within the desktop application.
- Firmware Deployment: Transferring the assembled machine code from the PC to the platform's SRAM.
- Bus Monitoring: Passive monitoring of the address and data buses, and essential control lines (e.g., \RD, \WR)
- Hardware Control: Actively managing the processor state by generating \WAIT and \BUSRQ signals to enable controlled execution steps.

The signal acquisition process is strictly synchronised with the generated CLK signal. This synchronisation ensures that each sampled state of the monitored lines is precisely mapped to a specific T-state of the executed instruction, preventing data misalignment during high-speed transitions.

Three groups of Z80 processor lines are monitored: the 16-bit address bus (A0–A15), the 8-bit data bus (D0–D7), and the control signals \MREQ, \IORQ, \RD, \WR, and \M1. All 29 lines are sampled synchronously with the generated CLK signal. By operating at a clock frequency significantly higher than the Z80's, the STM32 minimises the risk of capturing transient states and ensures that each sample is precisely assigned to its corresponding T-state.

The acquired data are encapsulated into frames representing consecutive T-states and transmitted via the USB interface to the desktop application. There, they are mapped to machine cycles in accordance with the Z80 architecture documentation [1]. The visualisation layer renders these frames as timing waveforms, enabling a direct comparison between observed bus activity and the theoretical execution model.

To ensure real-time visualisation without latency bottlenecks, the acquired bus states are buffered within the STM32 and transferred to the desktop application via a high-speed USB interface (USB CDC/HID). The desktop application then processes this stream, reconstructing the execution trace into timing waveforms. This allows the student to observe the logical state of each monitored line across consecutive clock cycles, effectively visualising the processor's internal micro-operations.

4.3. Software Development and Assembly Layer

The software ecosystem comprises three interconnected components, the assembler, the simulator, and the visualisation layer, designed to guide the student through a continuous learning workflow from code authoring to physical hardware verification.

The assembler supports the full Z80 instruction set, along with specific directives for memory management, data definition, and conditional execution. Developed from scratch, based on an analysis of existing educational tools, it is optimised for pedagogical use. The source code undergoes a multi-stage process that includes removing comments, expanding macros, tokenising, and validating. Particular attention was devoted to error reporting; each detected issue is described unambiguously, providing both the line number and the nature of the error. This precise feedback is crucial in an educational context, as it forces students to reflect on the underlying cause of the problem rather than merely identifying its location.

The simulator provides a virtual execution environment in which assembled machine code can be analysed before deployment to hardware. It offers full control over the execution flow, allowing the simulation to be paused at any time to observe processor registers, memory contents, and predicted bus activity for each T-state. This stage allows students to build a mental model of the expected processor behaviour.

The visualisation layer (Figure 2) serves as the final stage of the workflow, aggregating data from either the simulator or directly from the physical hardware platform. Presenting both virtual and real-time waveforms in a unified interface enables direct comparison. This capability allows students to verify that the waveforms observed on the actual hardware match the theoretical model, using any discrepancies as a starting point for deeper analysis of hardware-level phenomena [7].

Figure 2. Visualisation of time sequences in a desktop application.

In conclusion, the simulator and the physical hardware platform fulfil complementary educational roles, creating a complete learning cycle. While program execution within the simulator is highly accessible, requiring only the desktop application, it operates in an idealised environment.

The simulator offers superior debugging capabilities and predictable input behaviour, making it an ideal tool for building an initial mental model of instruction execution.

In contrast, the physical hardware platform introduces the essential layer of real-world complexity. Operating on the actual PCB allows students to observe phenomena that a simulator cannot replicate, such as the behaviour of multiplexed displays and the physical interaction with push buttons. While the simulator provides a controlled environment for error-free testing, the physical platform offers unparalleled realism and flexibility by integrating software logic with tangible electronic systems. Together, these two environments ensure that students can progress from theoretical understanding to practical mastery of hardware.

5. EDUCATIONAL APPLICATION

A typical laboratory exercise using the proposed system is conducted in three distinct stages. The process begins with writing a program in Z80 assembly language; even a minimal instruction sequence demands a rigorous understanding of memory organisation and register operations. Crucially, the assembler provides precise error messages that direct the student's attention to the underlying cause of the issue, rather than merely identifying its location, thereby fostering deeper analytical reflection.

In the second stage, the program is executed within the simulator, which presents a predicted execution flow decomposed into individual T-states. This includes the sequence of signals on the address and data buses, the duration of each machine-cycle phase, and the transitions in processor register states [7]. This stage allows students to construct a robust mental model of the expected hardware behaviour.

The final and most critical step involves running the same program on the physical Z80-based hardware. Here, the captured bus signals, synchronised with the system clock, are directly compared with the simulation results. Consistency between these two environments verifies the accuracy of the theoretical model, while any discrepancies serve as a powerful teaching tool, highlighting real-world hardware phenomena that the simulator does not capture, such as signal propagation delays or subtle memory access timings.

6. CONCLUSIONS AND FUTURE WORK

The presented system addresses a critical gap in computer architecture education by enabling direct observation of Z80 processor bus activity, decomposed into individual T-states and synchronised with the system clock. By integrating a dedicated hardware platform, assembler, simulator, and visualisation layer into a single coherent environment, this work provides a unique pedagogical tool that bridges the gap between theoretical instruction and the behaviour of physical hardware.

While the hardware platform has undergone preliminary validation, the assembler and simulator are fully functional and ready for integration into laboratory curricula. The deployment of this system will transform previously purely theoretical exercises into hands-on, practical learning experiences.

Furthermore, the modular hardware design and open-source software foundation provide a scalable framework adaptable to various processor architectures. Future work will focus on collecting empirical data after a full teaching cycle to quantitatively assess the system's educational effectiveness and its impact on student learning outcomes.

BIBLIOGRAPHY

1. Zilog, *Z80 CPU User Manual*. Available: https://www.zilog.com/docs/z80/um0080.pdf
2. J. Karczmarczuk, *Mikroprocesor Z80*. Silesian University of Technology. Available: https://delibra.bg.polsl.pl/Content/1265/Mikroprocesor_Z80.pdf
3. “Z80 MBC - A 4 ICs Z80 Homemade Computer on Breadboard”. Available: https://hackaday.io/project/19000-a-4-4ics-z80-homemade-computer-on-breadboard
4. S. Owen, *RC2014 Homebrew Z80 Computer*. Available: https://rc2014.co.uk/
5. I. McLoughlin, “A Perspective on the Experiential Learning of Computer Architecture,” in *Proceedings of the 2010 IEEE International Conference on Microelectronic Systems Education*, 2010. Available: https://ieeexplore.ieee.org/document/5724933
6. B. Nikolic, “A Survey and Evaluation of Simulators Suitable for Teaching Courses in Computer Architecture and Organisation,” in *2010 33rd International Convention MIPRO*, 2010. Available: https://ieeexplore.ieee.org/document/5490468
7. T. Sondag, “Frances: A Tool for Understanding Computer Architecture and Assembly Language,” in *Proceedings of the 43rd ACM Technical Symposium on Computer Science Education (SIGCSE ’12)*, 2012. Available: https://dl.acm.org/doi/10.1145/2157136.2157225

TalentDetector
7th-9th June 2026
Gliwice-Brenna, Poland
DEPARTMENT OF ENGINEERING MATERIALS AND BIOMATERIALS
FACULTY OF MECHANICAL ENGINEERING
SILESIAN UNIVERSITY OF TECHNOLOGY
INTERNATIONAL STUDENTS SCIENTIFIC CONFERENCE

Zastosowanie skanera 3D jako narzędzia inżynierskiego podczas konstruowania i budowy jachtu klasy C

Karol Hachuła[1], Jakub Ciupka[1], Habiba Abdelhakiem[1], Beniamin Kurcoń[1], Jakub Nabiałek[1], Eryk Olszówka[1], Jakub Michalak[1], Antonio J. Paleo[2], Mariem Messaada[2], Zakia Aribou[2], Mateusz Bilewicz[3], Eryk Kuczera[3], Aleksander Macurek[3], Olaf Sas[3], Maciej Tański[4], Marcin Bilewicz[1*]

[1]Politechnika Śląska, Wydział Mechaniczny Technologiczny, Katedra Materiałów Inżynierskich i Biomedycznych, Gliwice
[2]University of Minho, Guimarães, Portugal
[3]Zespół Szkół Leśnych i Ekologicznych w Brynku
[4]Technikum nr2, Górnośląskie Centrum Edukacyjne
*email: marcin.bilewicz@polsl.pl

Streszczenie: W artykule przedstawiono prace z wykorzystaniem współczesnych, nadal rozwijanych, narzędzi inżynierskich w postaci skanera 3D, wykorzystującego światło strukturalne. Celem jest wykorzystanie możliwości skanera w odniesieniu do skanowanych gabarytów oraz rodzajów obiektów możliwych do skanowania. Przewodnim tematem jest skan jachtu we współpracy z przemysłem, umożliwiający zeskanowanie poszczególnych elementów jachtu. Praca przy budowie jachtu wymaga zaplanowania, konstruowania i ewentualnego modyfikowania wstępnych założeń. Praca ze skanerem 3D jest przedsięwzięciem umożliwiającym w przyszłości wykorzystanie współczesnych technik inżynierskich do szybkiego i sprawnego monitorowania prac przy budowie jachtu.

Abstract: This article presents work using modern, still-developed engineering tools, such as a 3D scanner using structured light. The goal is to leverage the scanner's capabilities in terms of scanned dimensions and the types of objects that can be scanned. The main topic is yacht scanning in collaboration with industry, enabling the scanning of individual yacht components. Working on a yacht requires planning, designing, and potentially modifying initial assumptions. Working with a 3D scanner is intended to enable the future use of modern engineering techniques for the rapid and efficient monitoring of yacht construction.

Słowa kluczowe: skaner 3D, skaner światła strukturalnego, jacht klasy C

1. WPROWADZENIE

Współczesny przemysł coraz częściej wykorzystuje technologie cyfrowe wspomagające projektowanie, kontrolę jakości oraz monitorowanie procesów produkcyjnych [1]. Jedną z

dynamicznie rozwijających się w ostatnich latach technologii cyfrowych są skanery 3D [2]. Umożliwiają one szybkie pozyskanie dokładnych modeli geometrycznych rzeczywistych obiektów. Technologia ta znajduje zastosowanie w wielu dziedzinach, a w szczególności w inżynierii odwrotnej, metrologii, projektowaniu CAD oraz prototypowaniu [3].
Skanowanie 3D pozwala na tworzenie cyfrowych modeli obiektów o złożonej geometrii. W zależności od rodzaju skanera możliwe jest skanowanie zarówno niewielkich komponentów mechanicznych, jak i dużych konstrukcji przemysłowych [4]. Szczególnie problematyczne podczas digitalizacji są duże obiekty o gładkich i błyszczących powierzchniach, takie jak kadłuby jachtów, gdzie konieczne jest odpowiednie przygotowanie powierzchni skanowanej oraz zastosowanie dużej liczby markerów referencyjnych [5].
Budowa jachtu jest procesem niewątpliwie wieloetapowym, obejmującym projektowanie cyfrowe CAD, wykonanie form, laminowanie, montaż oraz końcowe wykończenie konstrukcji. Skanowanie 3D pozwala na kontrolę geometrii jachtu na wielu etapach produkcji poprzez porównanie rzeczywistej geometrii z modelem CAD [6]. Zastosowanie technologii skanowania 3D może znacząco usprawnić proces projektowo-produkcyjny oraz ograniczyć ryzyko występowania błędów konstrukcyjnych, w szczególności podczas prac nad prototypami nowych jednostek.
Celem pracy jest przedstawienie możliwości wykorzystania skanera 3D wykorzystującego światło strukturalne podczas budowy jachtu klasy C. W pracy skupiono się na analizie możliwości skanowania dużych obiektów, jakości uzyskiwanej chmury punktów oraz problemach pojawiających się podczas digitalizacji elementów jachtu. Badania wykonano we współpracy z Silesian Yachts, gdzie przeprowadzono skanowanie wybranych elementów konstrukcji jachtu.

2. BADANIA

Na wielu etapach budowania jachtu istnieje możliwość wspomagania procesu inżynierią odwrotną poprzez skanowanie 3D. Etapy budowania jachtu to m.in.:
- Cyfrowy projekt
- Tworzenie konstrukcji formy
- Ręczne wyprowadzanie powierzchni
- Wypełnianie formy, w tym żelkot, przekładki z mat szklanych
- Laminowanie
- Łączenie połówek kadłuba
- Wykończenia pokładowe i wnętrze (rys. 1).

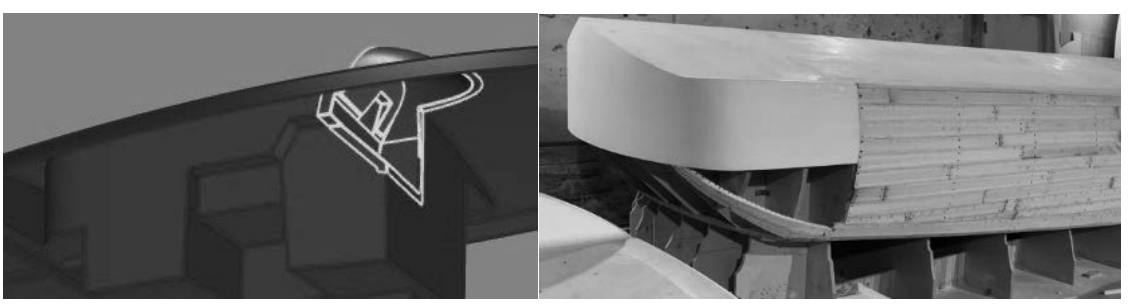

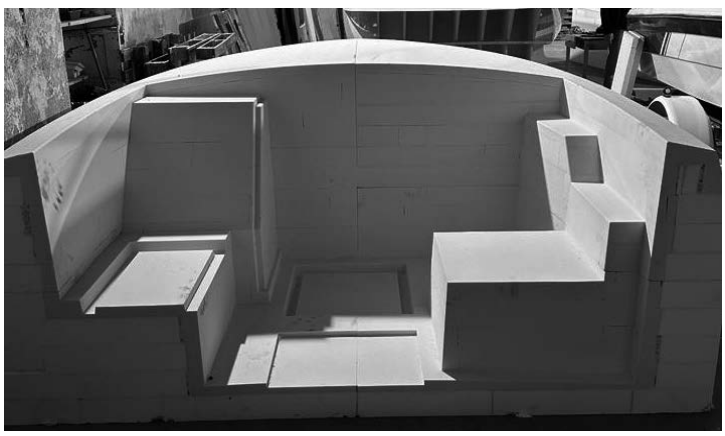

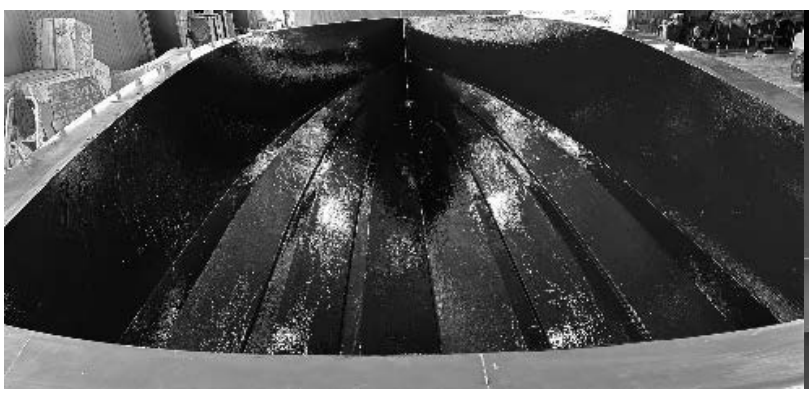

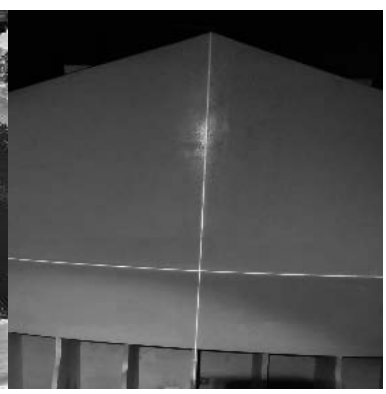

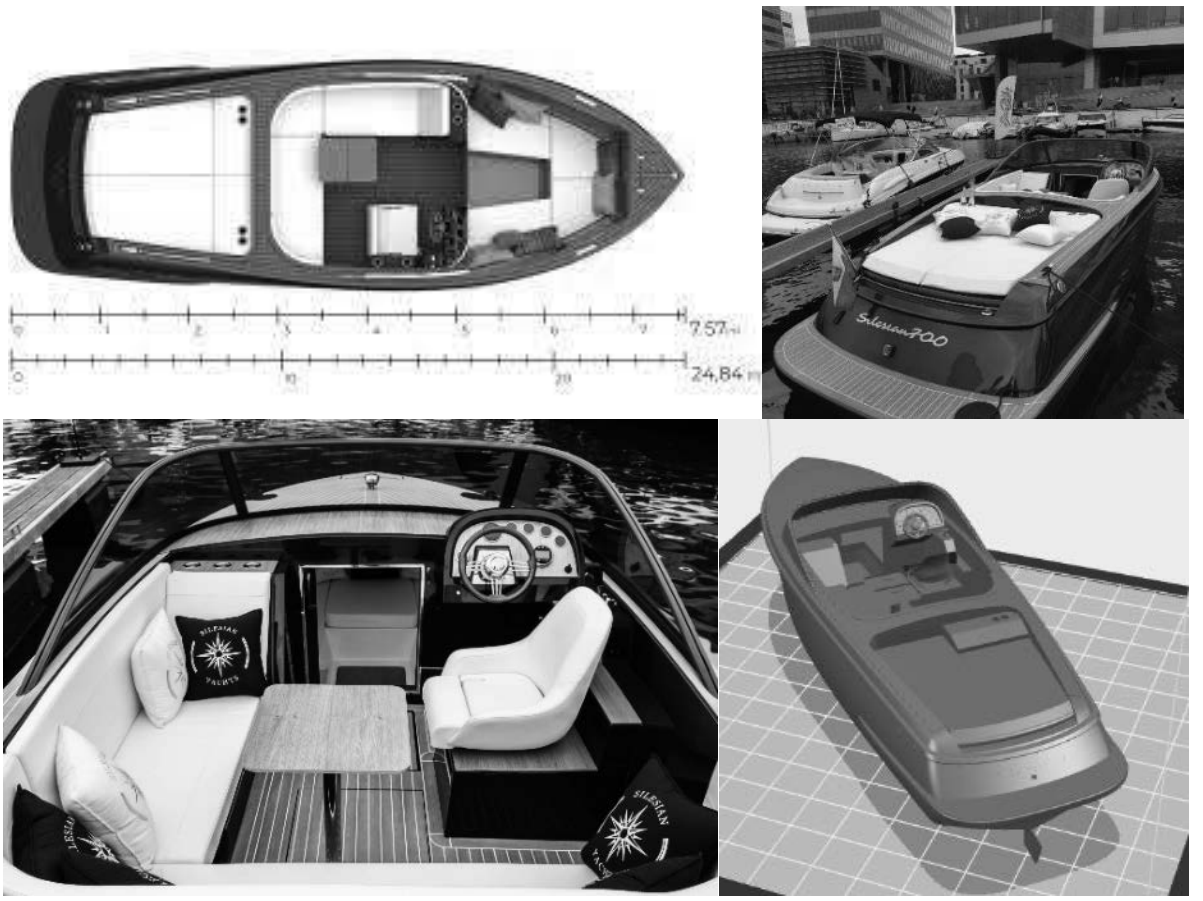

Rysunek 1. Przedstawienie poszczególnych etapów procesu tworzenia jachtu na przykładzie Silesian 700 firmy Silesian Yachts; *model jachtu widoczny w programie typu sllicer gotowy do drukowania (u dołu)*
Figure 1. Presentation of the individual stages of the yacht creation process using the Silesian 700 by Silesian Yachts as an example; yacht model visible in a slicer program, ready for printing (bottom)

Skanowanie jachtu przeprowadzono w hali dzięki współpracy z firmą Silesian Yachts. Do digitalizacji elementów jachtu wykorzystano skaner 3D (rys. 2). Każdy zeskanowany element generował plik o dużym rozmiarze (nawet do 10 GB), co wiązało się z czasochłonnym przetwarzaniem i tworzeniem chmury punktów liczącej około 1,5 miliona punktów.

Rysunek 2. Zastosowanie skanera 3D do stworzenia modelu przestrzennego jachtu; skan kadłuba (u góry); zastosowanie markerów w celu rozpoznania przez skaner gładkich powierzchni (u dołu).
Figure 2. Application of a 3D scanner to create a spatial model of a yacht; scanning the hull (top); using markers to help the scanner recognize smooth surfaces (bottom).

Skanowanie poszczególnych elementów jachtu przedstawiono na zdjęciach poniżej (rys. 3).

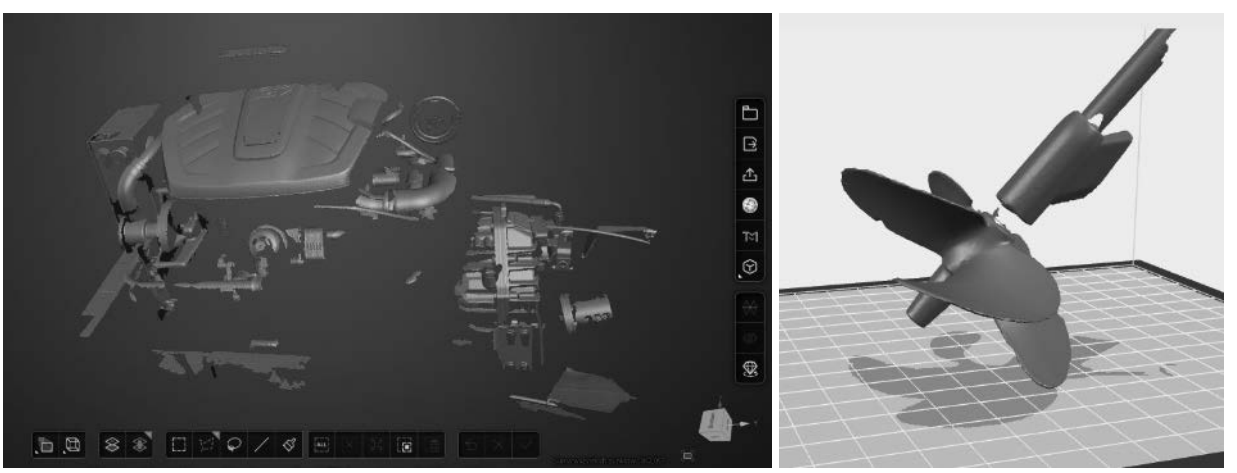

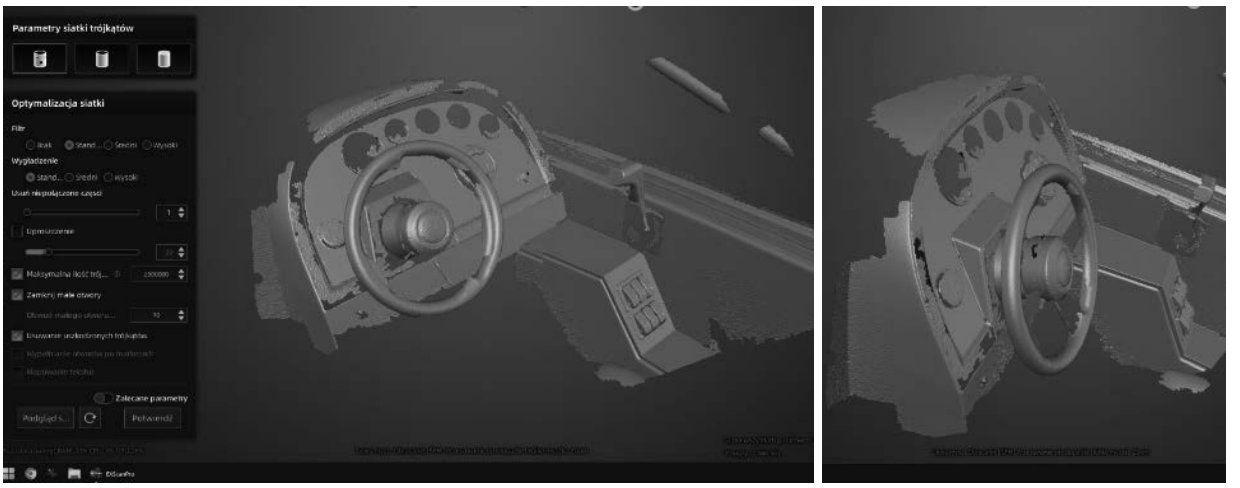

Rysunek 3. Interfejs programu z możliwymi parametrami optymalizacji siatki punktów wygładzania/domykania powierzchni; Widok zeskanowanych elementów silnika oraz śruby napędowej (u góry); widok kokpitu na pokładzie głównym (u dołu).
Figure 3. Program interface with possible parameters for optimizing the mesh of smoothing/closing surface points; View of the scanned engine and propeller components (top); view of the cockpit on the main board (bottom).

3. WNIOSKI

Podczas skanowania dużego obiektu typu jacht, sformułowano następujące wnioski:

- Skanowanie możliwe jest w dość krótkim czasie nie przekraczającym 5 minut,
- Podczas przetwarzania punktów w chmurze, których liczba może wynosić ok 1,5 miliona, potrzebna jest dobra moc obliczeniowa komputera i może to zająć ok 10 minut,
- Skaner wykorzystujący światło strukturalne ma ograniczony dostęp do trudno dostępnych miejsc,
- Podczas skanowania wystąpiły problemy z odbiciem światła od powierzchni gładkich oraz o ciemnych kolorach,
- Przy dużych i gładkich powierzchniach wymagane jest użycie markerów.

4. BIBLIOGRAFIA

1. Groover M.P., *Automation, Production Systems, and Computer-Integrated Manufacturing*, Pearson, 2020.
2. Bernadini F., Rushmeier H., *The 3D Model Acquisition Pipeline*, Computer Graphics Forum, 2002.
3. Varady T., Martin R., Cox J., *Reverse Engineering of Geometric Models*, Computer-Aided Design, 1997.
4. Geng J., *Structured-light 3D Surface Imaging: A Tutorial*, Advances in Optics and Photonics, 2011.
5. Sansoni G., Trebeschi M., Docchio F., *State-of-The-Art and Applications of 3D Imaging Sensors in Industry*, Sensors, 2009.
6. Tang Y. et al., *3D Scanning in Shipbuilding and Marine Engineering Applications*, Journal of Marine Science and Engineering, 2021.

TalentDetector

7th-9th June 2026
Gliwice-Brenna, Poland

DEPARTMENT OF ENGINEERING MATERIALS AND BIOMATERIALS
FACULTY OF MECHANICAL ENGINEERING
SILESIAN UNIVERSITY OF TECHNOLOGY

INTERNATIONAL STUDENTS SCIENTIFIC CONFERENCE

Electrochemical Methods for Hydrogen Detection in Steels: Comparison of the Barnacle Cell and the Devanathan–Stachurski Permeation Cell

Branislav Hajas[a], Denisa Straková[a], František Nový[a], Mirosław Bonek[b]

[a] Žilinská univerzita v Žiline, Strojnícka fakulta, Katedra materiálového inžinierstva, Univerzitná 8215/1, 010 26 Žilina, Slovak Republic
[b] Silesian University of Technology, Faculty of Mechanical Engineering, Department of Engineering Materials and Biomaterials, ul. Konarskiego 18A, 44-100 Gliwice, Poland
email: hajas@stud.uniza.sk

Abstract: This paper presents a comparative study of two electrochemical methods used for the detection and evaluation of hydrogen in steels: the Devanathan-Stachurski permeation cell and the Barnacle cell. Hydrogen embrittlement (HE) is a critical degradation mechanism where hydrogen diffusion and accumulation lead to a significant deterioration of mechanical properties in high-strength materials. The study analyses the measurement principles, experimental arrangements, and limitations of both techniques. The Devanathan-Stachurski cell is identified as a reference laboratory method for monitoring hydrogen permeation through a membrane to determine diffusion coefficients and trapping effects. In contrast, the Barnacle cell is evaluated as a practical, non-destructive tool for in-service surface measurements on real components without the need for specimen extraction. The comparison concludes that the choice of method depends on the objective: the permeation cell is superior for detailed scientific analysis of transport mechanisms, while the Barnacle cell offers significant advantages for rapid diagnostic applications in the field.

Keywords: hydrogen, steels, hydrogen embrittlement (HE), electrochemical methods, Devanathan-Stachurski permeation cell, Barnacle cell, hydrogen diffusion.

1. INTRODUCTION

Hydrogen embrittlement is a serious problem in modern materials engineering, particularly in high-strength steels, where even a small amount of hydrogen can lead to a significant deterioration of mechanical properties. Since hydrogen transport and accumulation in metals are closely related to failure mechanisms, reliable methods for its detection and evaluation are of considerable importance.

Among the methods used for studying hydrogen in metallic materials, electrochemical techniques play a particularly important role. They make it possible to analyse hydrogen transport, estimate diffusion-related parameters, and evaluate the interaction of hydrogen with the microstructure.

The aim of this paper is to compare two electrochemical approaches used for hydrogen investigation in steels, namely the Devanathan–Stachurski permeation cell and the Barnacle cell. The comparison is focused on their measurement principle, experimental arrangement, practical applicability, and main limitations.

2. HYDROGEN DIFFUSION IN METALS

Hydrogen diffusion in metals occurs through the movement of atomic hydrogen between interstitial sites of the crystal lattice. Hydrogen usually enters the material after the dissociation of molecular hydrogen at the metal surface. The diffusion process is driven by a concentration gradient and is commonly described by Fick's laws [1,2].

In real metallic materials, hydrogen transport is strongly influenced by the microstructure. Structural defects such as dislocations, grain boundaries, precipitates, and inclusions may act as hydrogen traps. Depending on their nature, these traps can bind hydrogen either reversibly or irreversibly. As a result, they reduce the effective diffusion rate and cause a non-uniform distribution of hydrogen within the material [1,2].

The interaction of hydrogen with these microstructural features may lead to local hydrogen accumulation. This can increase internal stresses, promote crack initiation and propagation, and cause deterioration of the mechanical properties of the metal. Therefore, hydrogen diffusion is closely related to the problem of hydrogen embrittlement (Fig. 1) [1,2].

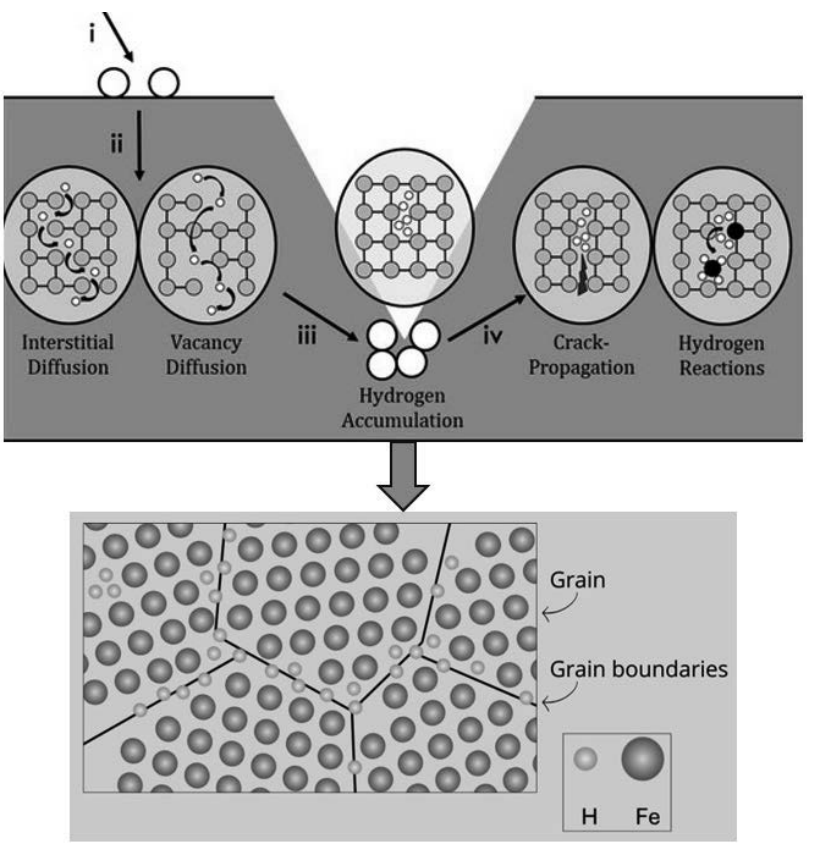

Fig. 1 Schematic representation of hydrogen transport in metals, including interstitial diffusion, vacancy-assisted diffusion, hydrogen accumulation, and its role in crack initiation and propagation [3,4].

Since hydrogen is present in metals mainly in atomic form and in very low concentrations, its direct detection is difficult. For this reason, indirect experimental methods are commonly used. These methods usually focus either on hydrogen diffusion through the material or on its electrochemical behaviour at the surface. Electrochemical techniques are among the most widely used methods for studying hydrogen behaviour in metals. Their importance lies in the possibility of monitoring hydrogen transport indirectly through an electrical response. Among these methods, the Devanathan–Stachurski permeation cell and the Barnacle cell represent two approaches with different objectives: the first is primarily intended for laboratory investigation of hydrogen transport through a specimen, whereas the second is designed for direct surface measurement on real components.

3. ELECTROCHEMICAL METHODS FOR HYDROGEN DETERMINATION

3.1 DEVANATHAN–STACHURSKI PERMEATION CELL

The Devanathan–Stachurski permeation cell is one of the most important electrochemical methods used for studying hydrogen diffusion in metallic materials. It is a classical laboratory technique that enables monitoring of hydrogen permeation through a Metal Membrane (Specimen) and subsequent determination of parameters such as the diffusion coefficient, permeability, and the effect of hydrogen traps within the microstructure of the material. The method is still regarded as a reference experimental approach in research on hydrogen embrittlement and hydrogen–metal interactions [5].

Principle and Experimental Arrangement

The method is based on dividing the system into two electrochemical compartments separated by the Metal Membrane (Specimen) representing the investigated material. One side of the membrane forms the Hydrogen Entry Cell, while the opposite side forms the Hydrogen Exit Cell (Fig. 2). On the entry side, atomic hydrogen is generated by cathodic polarization through the reduction of hydrogen ions. A portion of the generated hydrogen is absorbed into the metal and subsequently diffuses through the bulk of the material toward the opposite side of the membrane [5].

Each compartment contains an Electrolyte, a Reference Electrode, and a Counter Electrode. The membrane is fixed between both compartments using Seals, which ensure leak-tight operation and define the active measurement area [5].

On the Hydrogen Exit Cell side, an anodic potential is maintained, under which hydrogen emerging from the metal is oxidized. This oxidation produces an electric current whose magnitude is directly proportional to the hydrogen flux through the membrane. This current represents the main measured signal of the entire method [5].

The cell is typically constructed from chemically resistant materials such as acrylic polymers or glass. Leak-tight sealing is ensured by O-rings, which also define the active measurement area. Each compartment contains an Electrolyte, a Reference Electrode (e.g., Ag/AgCl or mercury/mercurous sulphate electrode, Hg/Hg_2SO_4), and a Counter Electrode, most made of platinum. The potentials on both sides of the Metal Membrane (Specimen) are controlled by a bipotentiostat, allowing independent adjustment of conditions in the Hydrogen Entry Cell and Hydrogen Exit Cell [7].

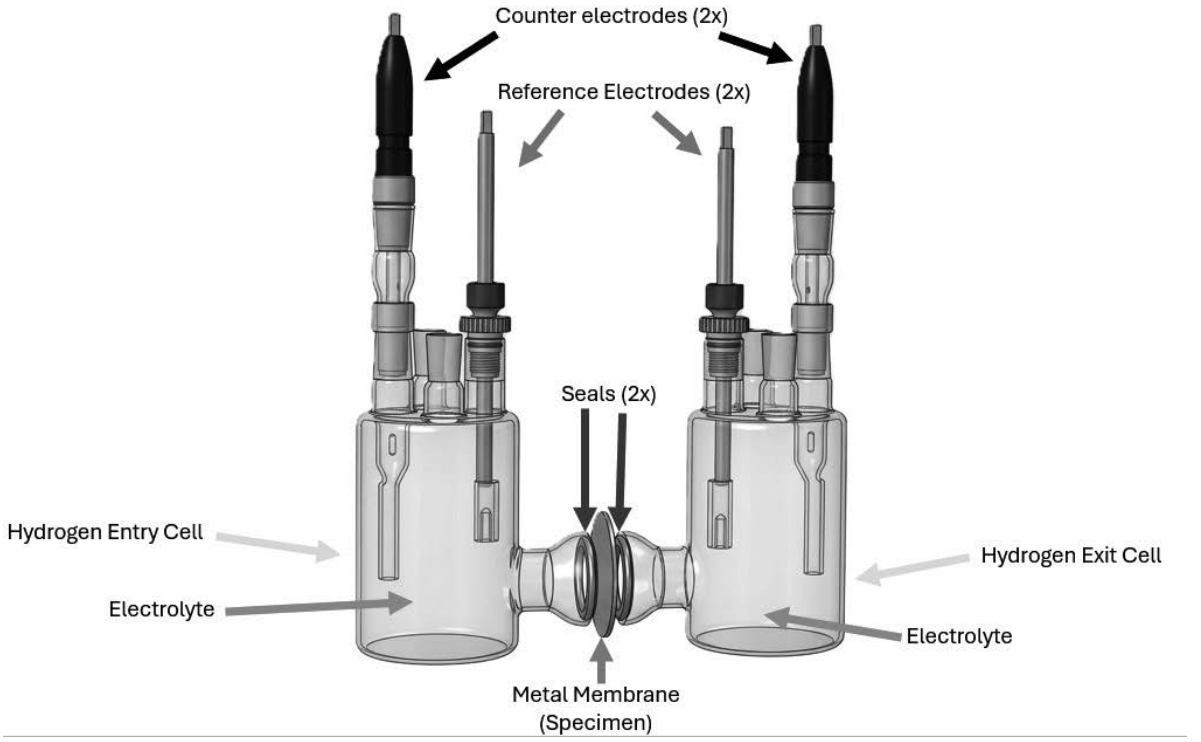

Fig. 2 Scheme of Devanathan–Stachurski permeation cell [6]

3.2 BARNACLE CELL

The Barnacle Cell represents a modification of the classical electrochemical permeation method developed to enable determination of hydrogen concentration directly on the surface of steel components without the need for sample extraction or preparation of a thin membrane. The device was designed for practical use in the evaluation of hydrogen in aerospace, marine, and other structural components exposed to the risk of hydrogen embrittlement. The name "barnacle" originates from the magnetic attachment of the device to the steel surface, where the cell adheres in a manner like a marine organism attached to a solid substrate [8].

The method is based on the same electrochemical principle as the Devanathan–Stachurski permeation cell, but it utilizes only the detection part of the process. Hydrogen already present in the material diffuses toward the surface of the Hydrogen-Charged Specimen, where it is electrochemically oxidized. The resulting current serves as a measure of hydrogen concentration near the surface. This eliminates the need for a conventional two-compartment laboratory arrangement and creates a system suitable for in-service field measurements [8].

Construction of the Device and Field Application

The Barnacle Cell consists of a compact Cell Body made of chemically resistant Kel-F polymer, which is embedded in a cylindrical Magnet Holder manufactured from Alnico 5. The magnetic attachment enables rapid and stable fixation of the device to the ferromagnetic surface of the investigated Hydrogen-Charged Specimen.

The internal cavity of the cell contains an Electrolyte, a Counter Electrode of Ni/NiO type, and a Reference Electrode of Ni/Nb type. Electrical contact with the investigated material is

ensured by spring-loaded nickel Conductors (2x). The system also includes a Vent for gas release and pressure equalization, as well as a silicone Seal, which defines the active measurement area and prevents electrolyte leakage (Fig. 3) [8].

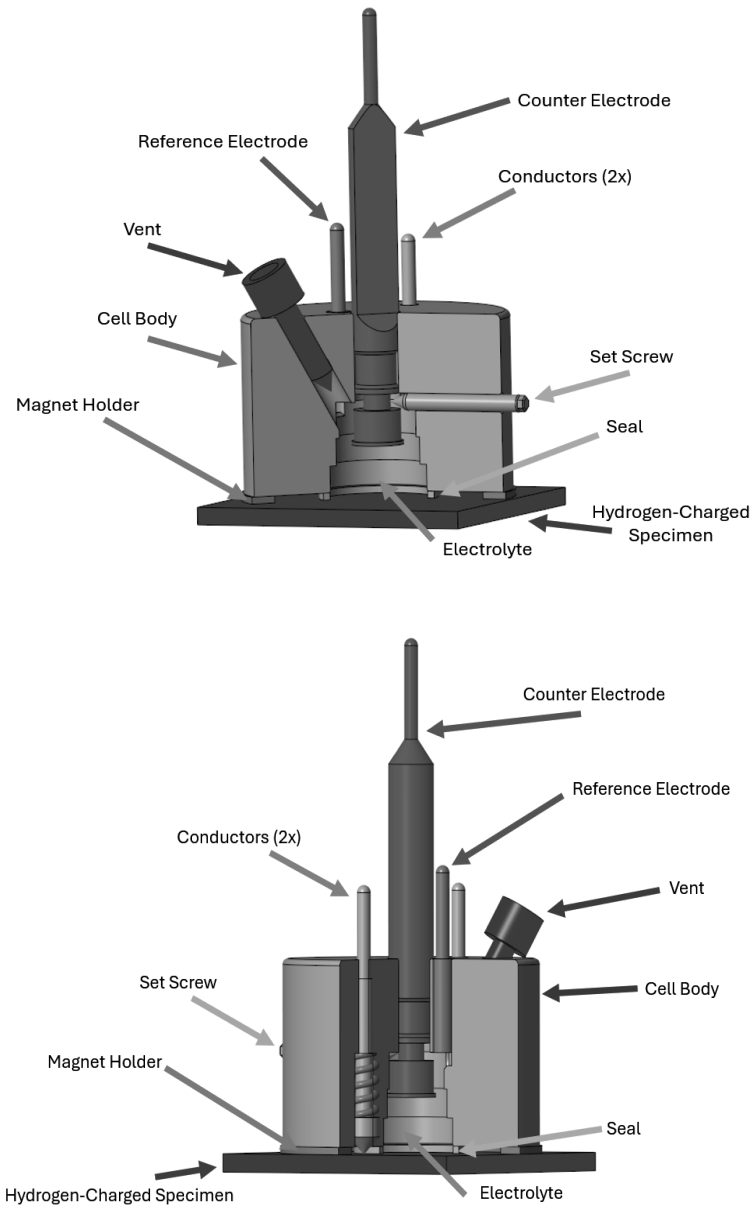

Fig. 3 Barnacle cell schematic showing the main structural components [8].

During measurement, the cell is attached to a cleaned material surface and filled with Electrolyte. After stabilization of the system, the time dependence of the oxidation current generated by oxidation of hydrogen diffusing from the metal is recorded. A major advantage of this approach is the possibility of performing measurements directly on real components without the need for their disassembly [8].

Limitations Compared with the Permeation Cell

Compared with the Devanathan–Stachurski permeation cell, the Barnacle cell provides more limited information. Its response reflects hydrogen emerging near the surface rather than hydrogen transport through the full thickness of the material. Therefore, it does not directly provide diffusion coefficients or a detailed description of bulk permeation kinetics [8].

Its results are also more sensitive to surface-related factors, including oxide films, surface roughness, sealing quality, and the quality of contact between the device and the specimen. In addition, the method is less suitable for components with complex geometry. Although these limitations reduce its analytical precision, the Barnacle cell remains valuable as a practical diagnostic tool for in-service measurements [8].

4. DISCUSSION

The comparison (tab.1) of the two methods shows that they serve different, although related, purposes in hydrogen research. The Devanathan–Stachurski permeation cell is primarily a laboratory technique suitable for detailed investigation of hydrogen transport through a specimen. Its main strength lies in the possibility of obtaining quantitative information on diffusion behaviour and trapping effects. In contrast, the Barnacle cell is intended mainly for practical surface measurements on real components. Its greatest advantage is the possibility of performing non-destructive measurements directly under service conditions, without the need for specimen extraction or preparation of a thin membrane.

However, this practical convenience is achieved at the expense of lower analytical detail. From this perspective, the two techniques should not be seen as competing methods, but rather as complementary tools. The permeation cell is more appropriate when the aim is to understand transport mechanisms in detail, whereas the Barnacle cell is more suitable when rapid and localized hydrogen assessment is required in practice.

Table1 Comparison of the Devanathan–Stachurski permeation cell and the Barnacle cell

Parameter	Devanathan–Stachurski permeation cell	Barnacle cell
Type of measurement	hydrogen permeation through membrane	hydrogen detection near surface
Main use	laboratory research	field/service diagnostics
Output	diffusion-related parameters	indicative surface hydrogen response
Sample requirement	thin membrane specimen	real component surface
Main advantage	analytical detail	practical applicability
Main limitation	demanding specimen preparation	limited quantitative detail

5. CONCLUSION

This paper compared two electrochemical approaches used for hydrogen investigation in metallic materials: the Devanathan–Stachurski permeation cell and the Barnacle cell. Although both methods are based on electrochemical detection of hydrogen, they differ substantially in their purpose, arrangement, and application.

The Devanathan–Stachurski permeation cell is more suitable for laboratory investigation of hydrogen transport through the bulk of a material and for obtaining diffusion-related parameters. The Barnacle cell, on the other hand, is better suited for practical surface measurements on real components under service conditions.

Their comparison shows that the choice of method depends mainly on the purpose of the investigation. For detailed scientific analysis, the permeation cell is more appropriate, whereas for rapid practical diagnostics, the Barnacle cell offers important advantages.

ACKNOWLEDGEMENT

The work was created as part of project based learning - PBL, in the 14th competition under the Initiative of Excellence - Research University, Silesian University of Technology, Gliwice, Poland and as part of project of Students Scientific Circle of Laser Surface Treatment under the Initiative of Excellence - Research University, Silesian University of Technology, Gliwice, Poland as a result of collaboration between the Silesian University of Technology (Poland) and the University of Žilina (Slovakia).

The research was supported by the Ministry of Education, Research, Development and Youth of the Slovak Republic by following grants: project VEGA 1/0831/25 and projects KEGA č. 033ŽU-4/2026 and KEGA č. 039ŽU-4/2026.

REFERENCES

1. MOHTADI-BONAB, M.A. – MASOUMI, M. 2023. Different aspects of hydrogen diffusion behaviour in pipeline steel. In: Journal of Materials Research and Technology [online]. 2023, vol. 24, s. 4762-4783. [accessed.10.4.2026]. ISSN 2238-7854. Available on: https://doi.org/10.1016/j.jmrt.2023.04.026
2. LI, H et al. 2024. Hydrogen diffusion and hydrogen embrittlement of a 1500 MPa hot-stamped steel 22MnB5 in different austenitizing conditions. In: Materials Science and Engineering: A [online]. 2024, vol. 897. [accessed.10.4.2026]. ISSN 9215093. Available on: https://doi.org/10.1016/j.msea.2024.146349
3. ILYUSHECHKIN, A et al. 2023. Material Challenges and Hydrogen Embrittlement Assessment for Hydrogen Utilisation in Industrial Scale. In: Hydrogen [online]. 2023, vol. 2. [accessed.10.4.2026]. ISSN 2673-4141. Available on: https://doi.org/10.3390/hydrogen4030039
4. TUROLA, Jéssica. Understanding hydrogen embrittlement [online image]. LinkedIn. 20 March 2026 [accessed. 20 April 2026].
5. Available on: https://www.linkedin.com/posts/jturola_engineering-materialsscience-hydrogen-activity-7433556602672005121-obUm/#

6. VECCHI, L. et al. 2019. Numerical interpretation to differentiate hydrogen trapping effects in iron alloys in the Devanathan-Stachurski permeation cell. In: Corrosion Science [online]. 2019, vol. 154, s. 231-238. [accessed.10.4.2026]. ISSN 0010938X. Available on: https://doi.org/10.1016/j.corsci.2019.04.008
7. PINE RESEARCH. Devanathan-Stachurski Hydrogen Permeation Cell Kit [online]. [accessed. 20.04.2026]. Available on: https://pineresearch.com/products/devanathan-stachurski-hydrogen-permeation-cell-kit/
8. FUSHIMI, K. et al. 2016. Hydrogen Permeation into a Carbon Steel Sheet Observed by a
9. Micro-capillary Combined with a Devanathan-Stachurski Cell. In: ISIJ International [online]. 2016, vol. 56, p. 431-435. [accessed.10.4.2026]. ISSN 9151559. Available on: https://doi.org/10.2355/isijinternational.ISIJINT-2015-191
10. MANSFELD, F. 1979. BARNACLE ELECTRODE MEASUREMENT SYSTEM FOR HYDROGEN IN AIRCRAFT STEEL [online]. 1979 [accessed.3.4.2026]. Available on https://apps.dtic.mil/sti/citations/ADA065945

TalentDetector

7th-9th June 2026
Gliwice-Brenna, Poland

DEPARTMENT OF ENGINEERING MATERIALS AND BIOMATERIALS
FACULTY OF MECHANICAL ENGINEERING
SILESIAN UNIVERSITY OF TECHNOLOGY

INTERNATIONAL STUDENTS SCIENTIFIC CONFERENCE

Simulation studies of the diffusion bonding process of dissimilar materials using the Gleeble 3800 simulator

Dawid Hoim [a], Kamil Czajkowski [a], Filip Szyguła [a], Stanisław Mendrek [a], Wiktor Wnuk [b], Wojciech Borek [c,*], Saad Ebied [d]

[a] Student of Silesian University of Technology, Faculty of Mechanical Engineering, Konarskiego 18A, 44-100 Gliwice, Poland
[b] Student of Silesian University of Technology, Institute of Physics – Centre for Science and Education, Konarskiego 22B, 44-100 Gliwice, Poland
[c] Silesian University of Technology, Faculty of Mechanical Engineering, Department of Engineering Materials and Biomaterials
[d] Department of Production Engineering and Mechanical Design, Faculty of Engineering, Tanta University, Tanta, 31527, Egypt, * email: wojciech.borek@polsl.pl

Abstract: The study investigates the effect of heating rate on temperature overshoot and interlayer behavior during diffusion bonding of 304L/316L stainless steels using a Gleeble 3800 simulator. A copper interlayer (99.9% Cu) was applied. The results show that increasing the heating rate from 10°C/s to 500°C/s leads to a significant temperature overshoot (up to 1140°C), exceeding the melting point of copper (1084°C). This results in partial melting and expulsion of the interlayer from the bonding interface. The findings highlight the critical importance of heating rate control in diffusion bonding processes involving low-melting interlayers.

Keywords: diffusion bonding, Gleeble 3800, heating rate, dissimilar materials, stainless steel, copper interlayer

1. INTRODUCTION

Contemporary realities necessitate the pursuit of innovative technologies. In industrial sectors such as aerospace, automotive, and energy, new methods are being sought for joining materials with vastly different physicomechanical properties. The durable and reliable bonding of dissimilar materials constitutes one of the greatest challenges in materials engineering. Despite extensive research on diffusion bonding, the effect of rapid heating rates on interlayer behavior-especially in systems using copper interlayers-remains insufficiently understood. It requires precise control of the processes occurring at the interface between the materials [1-5].

The aim of this paper is to present the activities undertaken during the implementation of a PBL (Project-Based Learning) student project. The study focuses on improving the method

of diffusion bonding of dissimilar materials using the Gleeble 3800 thermomechanical simulator [1-5].

2. RESEARCH OBJECTIVE AND METHODOLOGY

The main objective of this study is to investigate the effect of heating rate on the thermal response and interlayer behavior during diffusion bonding of dissimilar stainless steels. Particular emphasis is placed on the joining of dissimilar materials exhibiting significantly different physical and mechanical properties. To achieve this, the Gleeble 3800 thermomechanical simulator is employed to accurately reproduce process conditions. The Gleeble 3800 system is equipped with a direct resistance heating system. This solution enables achieving a highly uniform temperature distribution within the sample volume, while the maximum heating rate can reach up to 10,000°C/s. The heating and cooling rates of the samples depend primarily on the applied specimen dimensions and geometry, the grips used, and the material under investigation. The direct resistance heating system allows for maintaining a constant temperature with an accuracy of up to 1°C. Nevertheless, high heating rates may sometimes lead to overheating of the specimen at the moment the target temperature is reached. Therefore, the initial stage of this project focused on investigating the effect of the heating rate on the actual temperature value.

Based on literature data as well as preliminary experiments, two stainless steels, 304L and 316L, were selected for the study. These steels belong to the group of austenitic grades and are widely used in industry due to their good corrosion resistance and favorable mechanical properties. However, they differ in chemical composition, which affects their corrosion resistance, range of applications, and high-temperature performance. Figure 1 presents the technical drawing of the specimen as well as the actual view of the samples used for diffusion bonding experiments performed using the Gleeble simulator.

a) b)

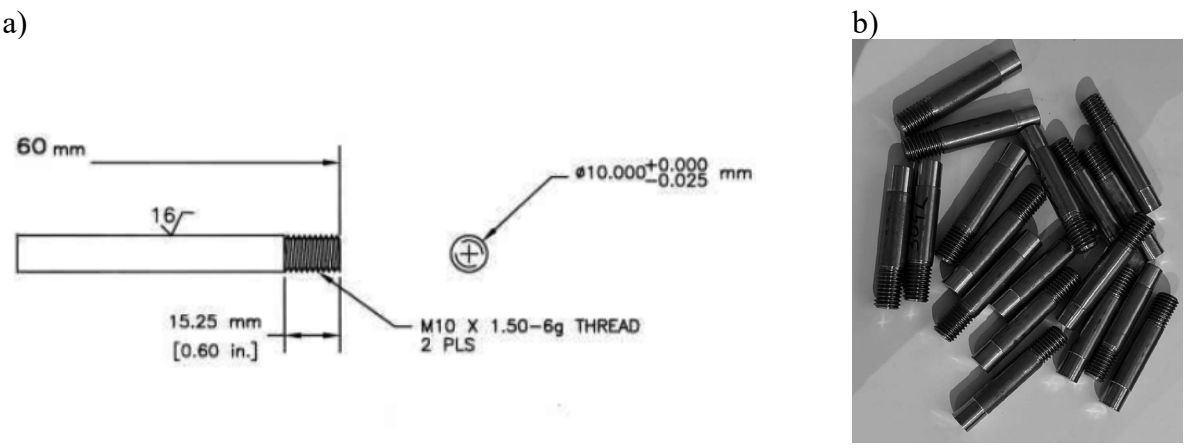

Figure 1. Technical drawing of the specimen (a) as well as the actual view of the samples (b) used for diffusion bonding experiments performed using the Gleeble simulator

A copper interlayer (99.9% Cu) with a thickness of 0.3 mm and dimensions of 10 × 10 mm was placed between the joined stainless steel specimens. Prior to the bonding process, all prepared samples were cleaned with isopropyl alcohol to remove surface contaminants and to ensure the highest possible surface quality. The prepared specimens were then positioned in specially designed grips, ensuring proper alignment and adequate contact pressure between the

components (Figure 2). The entire assembly was mounted in the Gleeble 3800 thermomechanical simulator. Additionally, K-type thermocouples were welded to the surface of the 304L steel specimen, enabling precise measurement and control of temperature throughout the entire bonding process.

The bonding experiments were carried out in a protective argon atmosphere under the following technological parameters:

- Diffusion bonding temperature: 1000°C,
- Heating rate: 10°C/s, 50°C/s, 100°C/s, 200°C/s, and 500°C/s,
- Isothermal holding time at temperature 1000°C: 2s.

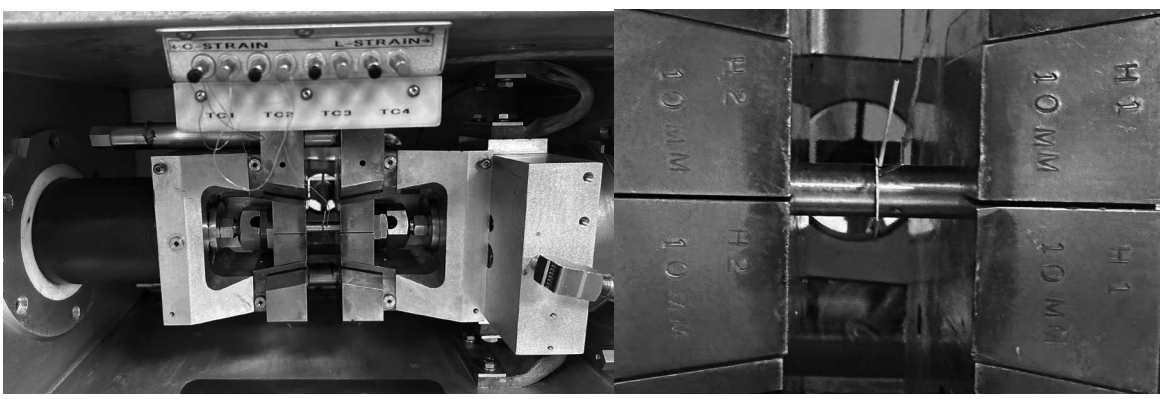

Figure 2. Actual view of the specimen installed in the Gleeble 3800 simulator prior to the resistance bonding test with copper interlayer placed between the joined stainless steel specimens

3. RESULTS

Figure 3 presents captured images from the heating process of the specimens to the target temperature 1000°C. Figure 4 shows images of the actual specimens after the heating process to the target temperature: (a) heating rate of 10°C/s, (b) heating rate of 500°C/s. Based on the conducted tests, it was found that specimens heated at low rates exhibited stable thermal behavior, while the copper interlayer placed between the steel samples did not exhibit significant deformation. However, increasing the heating rate to 500°C/s resulted in uncontrolled overheating of the entire system, leading to partial melting of the copper interlayer, as presented in Figure 4b in the form of metal droplets.

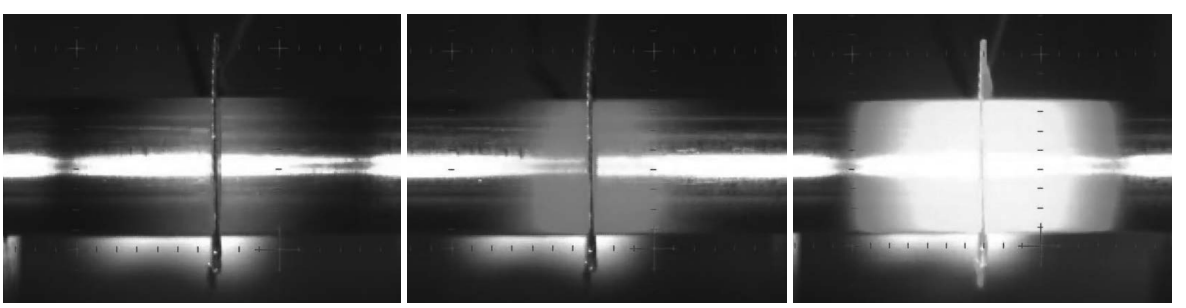

Figure 3. Captured state of the specimen during heating to the target temperature in the Gleeble 3800 simulator

a)

b)

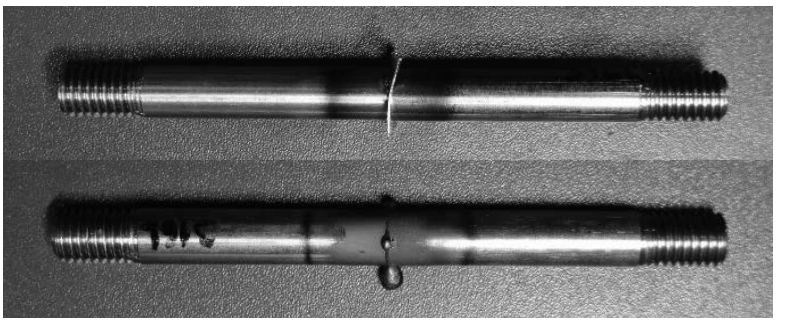

Figure 4. Selected images of the specimens after the heating process to the target temperature: (a) heating rate of 10°C/s, (b) heating rate of 500°C/s

Based on the data recorded by the Gleeble 3800 thermomechanical simulator, a temperature–time plot was prepared (Figure 5), enabling the determination of the actual temperature reached at the moment when the target temperature (1000°C) was assumed to be achieved. The obtained results allow for an assessment of whether the designed technological process is suitable in the case of using copper interlayers. The results are summarized in Table 1 for easier data analysis. An overshoot of approximately 140°C was observed at a heating rate of 500°C/s.

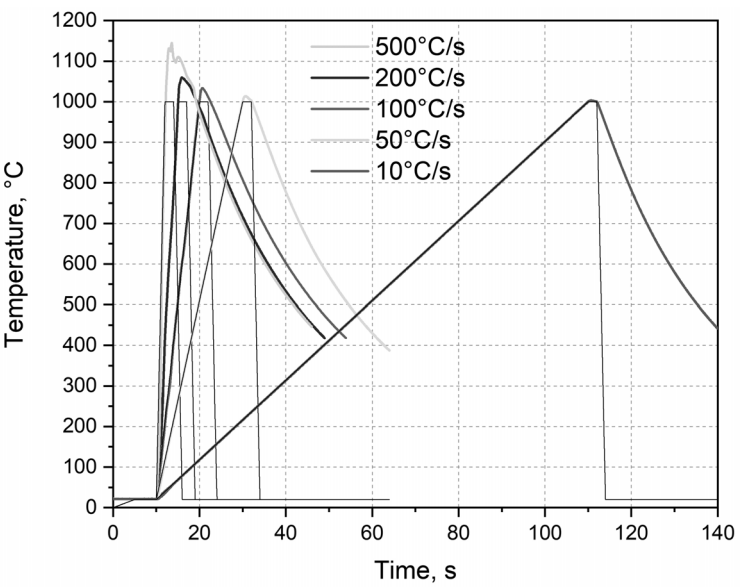

Figure 5. Temperature versus time graph of resistance welded samples using the Gleeble 3800 simulator

Table 1. Temperature values recorded by the Gleeble 3800 metallurgical simulator with assumed heating to 1000°C

Heating rate	Recorded temperature value
500°C/s	1140°C
200°C/s	1060°C
100°C/s	1030°C
50°C/s	1013°C
10°C/s	1003°C

Based on the conducted studies, it can be concluded that excessively high heating rates may lead to uncontrolled overheating of the bonded joint. In the case of using an interlayer material such as copper (99.9% Cu), with a melting temperature of 1084°C, this may result in the transition of the material into the liquid state and its subsequent expulsion from the contact zone. When selecting the bonding process parameters, it is therefore essential to consider a temperature range, and consequently a heating rate, that prevents melting of the interlayer material. Despite the use of an interlayer, in the specimen bonded at a heating rate of 500°C/s, the joint remained intact; however, the majority of the interlayer material was expelled from the joint region.

5. CONCLUSIONS

The following conclusions can be drawn:

- High heating rates (>200°C/s) lead to significant temperature overshoot.
- Overheating results in partial melting of the copper interlayer.
- Excessive melting causes expulsion of the interlayer from the bonding interface.
- Optimal heating conditions must balance thermal efficiency and interlayer stability.
- Temperature overshoot increases nonlinearly with heating rate.

Future work will focus on microstructural analysis and optimization of bonding parameters.

BIBLIOGRAPHY

1. A. AlHazaa, N. Haneklaus, Diffusion Bonding and Transient Liquid Phase (TLP) Bonding of Type 304 and 316 Austenitic Stainless Steel - A Review of Similar and Dissimilar Material Joints, Metals 10 (2020) 613.
2. A.A.A. Akbar, S.A.A. Ajeel, and S.M. Hassoni, “Optimization of Diffusion Bonding of Pure Copper (OFHC) with Stainless Steel 304L: Al-Khwarizmi Engineering Journal 14/2 (2019) 30-39
3. S. Sebastian, V.A. Suyamburajan, K. Ramar, P. Rajagopal, Effect of Surface Roughness on Diffusion Bonding of Copper with Stainless Steel, NanoWorld Journal 9/S3 (2023) S486-S489.
4. T. Baross, H.B.Z. Rachid, P. Bereczki, M. Palánkai, K. Balázsi, C. Balázsi, G. Veres, Diffusion Bonding of Al_2O_3 Dispersion-Strengthened 316L Composite by Gleeble 3800, Materials 17 (2024) 2300.
5. X. Yuan, K. Tang, Y. Deng, J. Luo, G. Sheng, Impulse pressuring diffusion bonding of a copper alloy to a stainless steel with/without a pure nickel interlayer, Materials & Design 52 (2013) 359-366.

TalentDetector

7th-9th June 2026
Gliwice-Brenna, Poland

DEPARTMENT OF ENGINEERING MATERIALS AND BIOMATERIALS
FACULTY OF MECHANICAL ENGINEERING
SILESIAN UNIVERSITY OF TECHNOLOGY

INTERNATIONAL STUDENTS SCIENTIFIC CONFERENCE

Numerical analysis of plate implants for spinal fusion using different types of materials

Monika Honisz[1], Agata Śliwa[2]

[1] Student of the Medical University of Silesian, Faculty of Medical Sciences in Zabrze
email: honiszmonika@gmail.com
[2] Silesian University of Technology, Faculty of Mechanical Engineering, Department of Engineering Materials and Biomaterials, email: agata.sliwa@polsl.pl

Abstract: The work includes the comparative strength analysis of platelet implant for stabilizing the spine made of three different types of materials: Ti, Ti-6Al-4V and X3CrNiMo13-4. Model and FEM calculations were made with the aid of SolidWorks.

Keywords: plate implant for spine stabilization, FEM analysis, Von Mises stresses, displacements

1. INTRODUCTION

The spine is a fundamental pillar of the human skeletal system. It is one of the most important and complex bone structures, and its components are susceptible to damage. Advances in technology have significantly reduced the need for humans to perform tasks that are particularly dangerous and require significant physical exertion. However, the convenience of everyday life, often sedentary work, and inactivity contribute to numerous disorders and dysfunctions of the musculoskeletal system, including the spine. On the other hand, excessive strain on bone structures also leads to pathological changes and dysfunctions of joint systems. Spinal disorders can be treated using two methods: invasive and non-invasive. Non-invasive treatment encompasses a wide range of procedures that can significantly improve spinal health. These methods include massage, hydrotherapy, balneotherapy, cryotherapy, ultrasound, electrotherapy, laser therapy, kinesiotherapy, and pharmacological treatment. The vast majority of back pain cases are treated conservatively. Despite non-invasive treatment, there are also situations in which the degeneration of the spine progresses or, as a result of an accident, the doctor is forced to decide on a surgical procedure (Fig.1) [4].

The basic tasks that should be performed during surgical treatment of spinal injuries include[4]:

1) decompression of the nervous system structures;
2) restoration of the spinal axis (correction – reduction of kyphosis);
3) restoration of the integrity (support) of the anterior column;
4) restoration of stiffness and stability of the spine as a result of the procedure;

5) ensuring conditions for natural spinal fusion in the future (ensuring the stability of the achieved correction);

6) enabling the fastest and most complete mobilization of the patient.

Both implants and implants used in surgical treatment are assigned certain basic tasks, from a mechanical perspective: [4]:

• maintaining deformation continuity;

• maintaining appropriate stiffness of the stabilized system (as close to the stiffness of the healthy spine as possible).

The basic tasks assigned to the clinic are [4]:

• eliminating pain;

• restoring selected spinal functions;

• decompression of the spinal cord from compression.

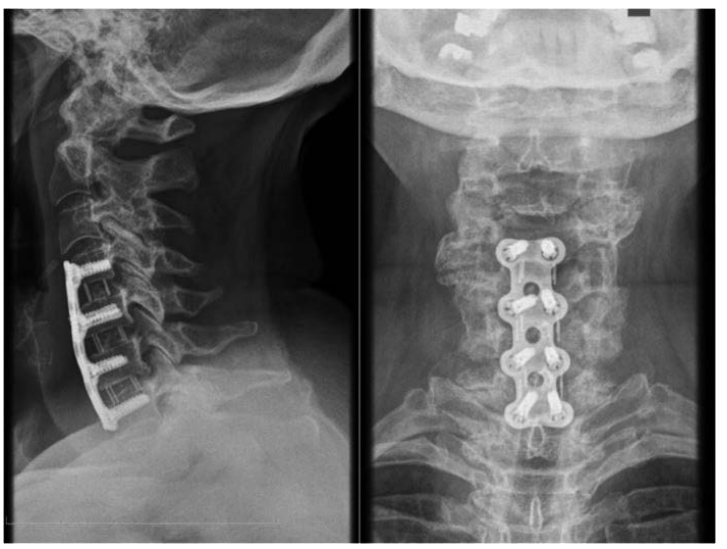

Figure 1. X-ray of the spine after invasive surgery - implantation of a platelet implant [1]

Stabilizers

In the surgical treatment of spinal instability, technical measures are typically used, such as various types of stabilizers. The primary therapeutic purpose of spinal stabilizers is to preserve or restore the structure of the spinal mobility segment and to fuse the damaged vertebra with the healthy adjacent vertebrae [2]. Stabilizers with screws and plates or rods are characterized by a simple design and a limited number of components. The entire system consists of plates, rods, screws, pins, and the necessary instrumentation for assembly. These stabilizers are manufactured by foreign companies such as ABC Aesculap, Globus Medical, and Synthes. They are also supplied by Polish implant companies, including LfC and ChM. Plate implants are flat plates, generally rectangular in shape. However, depending on the manufacturer, the plates come in various shapes [2], (Fig. 2-4):

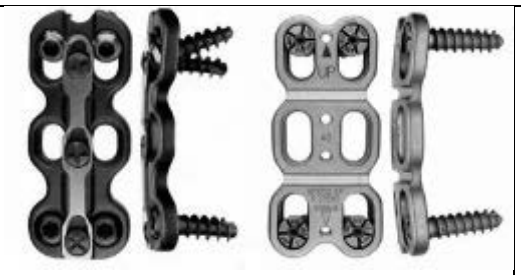		
Figure 2. Platelet stabilizer of the lumbar spine ABC Aesculap [2	*Figure 3. Plate stabilizer from Globus Medical [2]*	*Figure 4. Synthes plate stabilizer [2]*

Please note that the presented types and types of plate implants are made of titanium and its alloys in accordance with the ISO 5832-3 and ISO 5832-11 standards. The high-quality workmanship of these implants is guaranteed by Quality Management Systems, ISO 9001, EN ISO 13485, and compliance with the requirements of Directive 93/42/EEC [2].

2. SELECTED MATERIALS

Titanium (Ti) is a chemical element from the transition metal group in the periodic table with atomic number 22. It is a light metal with a grayish color. It has high mechanical strength and is resistant to corrosion (including seawater and chlorine). Titanium is added as an alloying element to iron, aluminum, vanadium, molybdenum, and others. It occurs in the Earth's crust in quantities of around 0.61%, in the form of the minerals ilmenite, rutile, and titanite, which are widely distributed throughout the Earth. Titanium metal is obtained by processing ores using the Kroll process. Its most common compound, titanium dioxide, is used in the production of white pigments. Titanium and its alloys are currently most popular in biomedicine. They are characterized primarily by corrosion resistance and low density. It is mainly used for joint endoprostheses, bone fracture fixation components, dental prosthetics, cardiac surgery, and interventional cardiology [3, 8].

Cold working of titanium causes it to harden very quickly: the Rm of cold-pressed rods is 420 MPa, while after 85% work hardening, the value reaches 860 MPa. The effects of work hardening are removed by recrystallization annealing at temperatures between 600 and 700°C. Hot working at temperatures between 750 and 1000°C. Titanium and its alloys exhibit resistance to pitting, intergranular, and stress corrosion [7].

Among the broad spectrum of metallic biomaterials, titanium and its alloys are excellent materials used for various types of implants. They exhibit good mechanical properties, excellent corrosion resistance, and are biocompatible. Titanium also has the lowest specific gravity and Young's modulus, making it a candidate for the best metal in bioengineering, surpassing even materials such as austenitic steels and cobalt alloys. The excellent biotolerance of this element allows for the occurrence of osseointegration in the living organism, a process involving the fusion of bone tissue with the titanium implant surface. This metal's high affinity for oxygen causes the formation of a passive TiO2 layer on its surface, which protects the material against corrosion. The high cost of titanium implants is related to the complex manufacturing processes. Titanium and its alloys can be used to produce joint and knee endoprostheses; intramedullary nails, plates, and bone screws; as well as various prosthetic

devices such as bridges – these materials also find applications in cardiac surgery and interventional cardiology [5].

There are five types of titanium alloys [7]:
• Single-phase α alloys;
• Two-phase α + β alloys;
• Single-phase β alloys;
• In bone surgery, mainly Ti - 6Al - 4V with a two-phase structure (Protasul 64WF);
• New alloys: Ti - 6Al - 7Nb (Protasul R100), Ti - 6Al - (3-6)Nb - (1-6)Ta,
Ti - 5Al - 2.5Fe (two-phase).

Heat treatment of two-phase alloys [7]:
• Solution annealing, aging;
• Solution annealing: heating to the α+β or β phase region;
• Homogenization, rapid cooling; single-phase or two-phase structure;
• Instability of the β phase causes it to age after each heating;
• Rapid cooling of the β phase of Ti-V-Nb-Ta alloys can cause a transition to the α ̅ phase, which is soft and ductile – the transformation occurs diffusionlessly, similarly to the martensitic transformation;
• High concentrations of alloying elements can prevent the material from undergoing a diffusionless transformation – the concentration should lower the onset temperature of the martensitic transformation below room temperature.

Two-phase titanium alloys are subjected to heat treatment consisting of solution annealing and aging (Tab.1).

Table 1. Chemical composition of the Ti6Al4V titanium alloy according to ISO 5832/3 [6]

Stężenie pierwiastków % masowy							
O	V	Al	Fe	H	C	N	Ti
<0,20	3,5	5,5	<0,30	<0,0015	<0,08	<0,05	reszta

The negative impact of the element vanadium, which, when released, disrupts the proper functioning of the body, contributed to the creation and development of subsequent titanium alloys, so-called vanadium-free alloys. In these alloys, the β-phase of titanium is stabilized by elements that are tolerated by the body in even larger quantities, such as niobium, tantalum, and iron. These new titanium alloys are more resistant to corrosion and exhibit better biotolerance compared to the Ti6Al4V alloy. They are also characterized by a lower Young's modulus and excellent mechanical properties, primarily fatigue strength and hardness (Tab.2) [5].

Table 2. Mechanical properties of titanium alloys used for implants [6]

Stop	Moduł sprężystości E [GPa]	Wytrzymałość na rozciąganie R_m [MPa]	Granica plastyczności $R_{p0,2}$ [MPa]	Wytrzymałość zmęczeniowa R_z [MPa] dla 107 cykli
Ti	105	785	692	430
Ti-6Al-4V	110÷114	960÷970	850÷900	620÷725
Ti-6Al-4V ELI	101÷110	860÷965	795÷875	598÷816
Ti-6Al-7Nb	105	1024	921	500÷600
Ti-5Al-2,5Fe	110	1033	914	580
Ti-13Nb-13Zr	79	1030	900	500

3. CAD GEOMETRIC MODEL

The spinal stabilization implant (Fig. 5) was analyzed based on examples from the ChM catalog. The plate height was 39 mm and width 19 mm. The plate thickness was 2 mm. The distance between the hole centers was 10 mm. The inner diameter of the holes was 2.25 mm, and the outer diameter was 4.5 mm. Figure 6 shows the technical documentation with the dimensioned spinal stabilization plate.

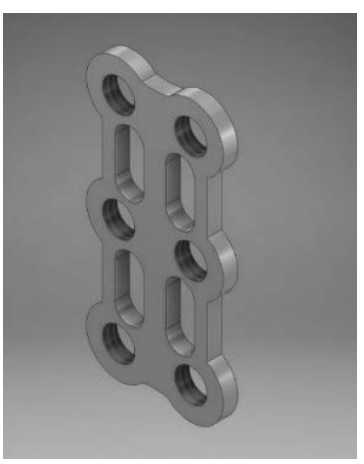

Figure 5. Implant for stabilization of the spine made in Inventor

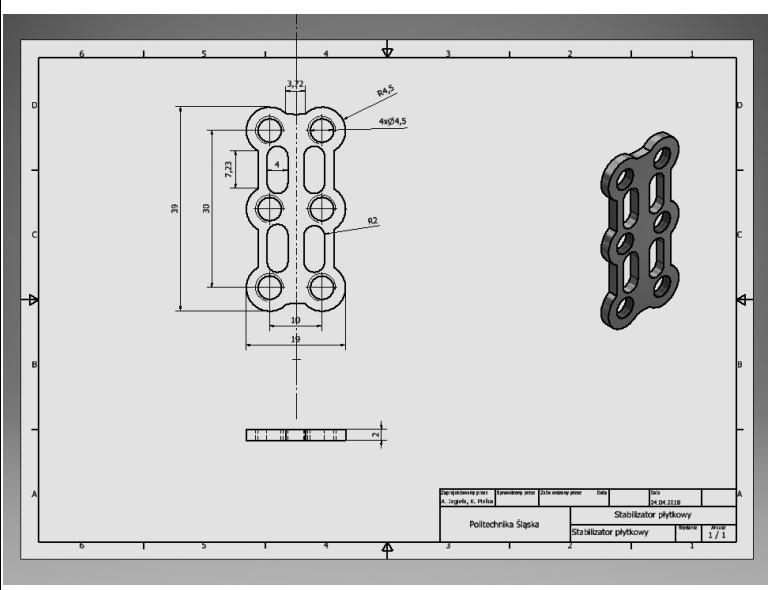

Figure 6. Technical documentation of the implant for stabilizing the spine

Boundary conditions

Computer simulations were conducted in SolidWorks software using static displacement and stress analysis. The plate was fixed on the shorter sidewall, as indicated by green arrows in Figure 7. Forces of 20 N, 60 N, and 100 N were applied to the implant's top surface in subsequent simulations. In Figure 7, the forces are indicated by purple arrows. The plate was meshed with a standard SolidWorks mesh (Fig. 8) with a total of 15,219 nodes and 8,534 elements. To obtain varied results, material variations were applied for each of the applied forces. The materials used in the analysis were Ti, Ti-6Al-4V, and X3CrNiMo13-4.

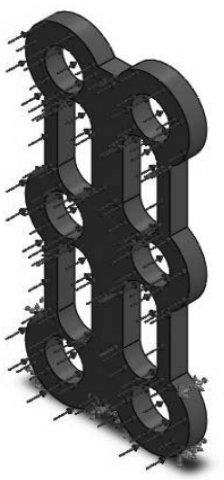

Figure 7. Boundary conditions of the plate to stabilize the spine

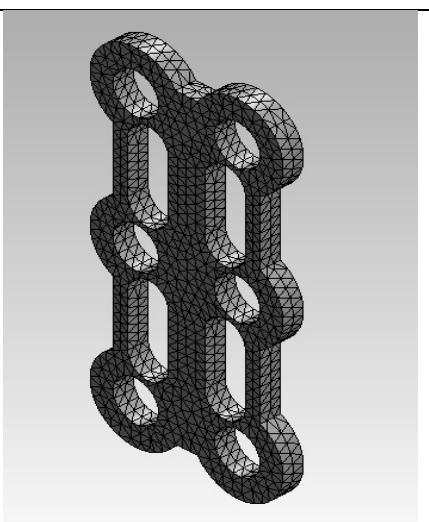

Figure 8. Solid mesh applied to the implant

4. NUMERICAL ANALYSIS RESULTS

Bending Stress Analysis Results

Implant analysis was performed for all selected materials and presented using Huber-Mises stresses. Figures 9-17 graph the resulting maximum stresses in MPa for the selected materials.

Based on the simulation results, it was determined that the highest stresses occurred for Ti-6Al-4V at a load of 100 N, reaching 684.6 MPa. These stresses occurred above the lower holes, on the outer side. For the titanium plate and the X3CrNiMo13-4 alloy, the stresses were 683.3 MPa and 681.2 MPa, respectively. The plate was additionally analyzed with an applied force of 20 N and 60 N. For the same loads, the resulting maximum stresses were very similar.

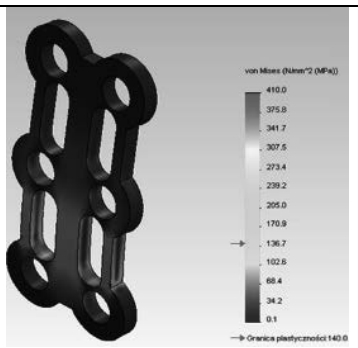

Figure 9. Stress value, force 20N, material Ti

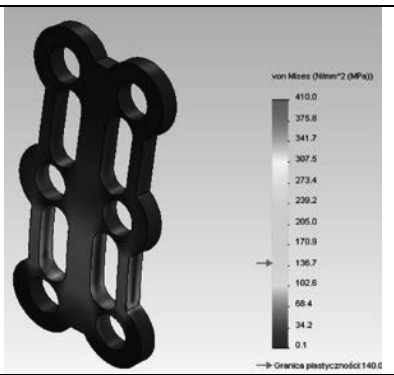

Figure 10. Stress value, force 60N, material Ti

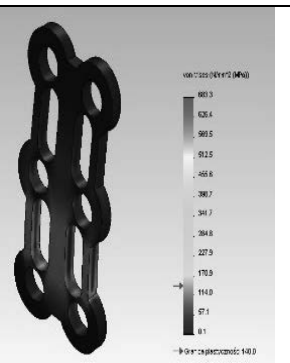

Figure 11. Stress value, force 100N, material Ti

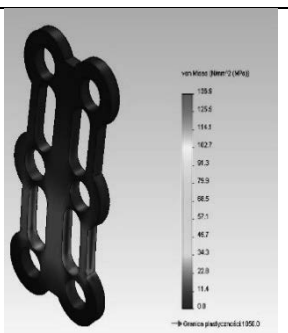

Figure 12. Stress value, force 20N, material Ti-6Al-4V

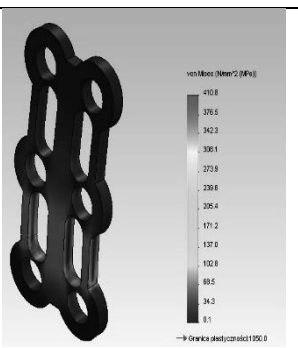

Figure 13. Stress value, force 60N, material Ti-6Al-4V

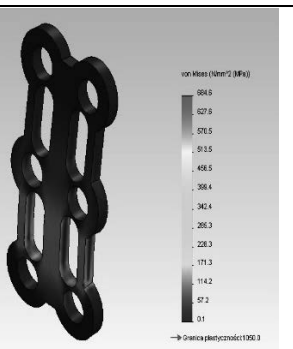

Figure 14. Stress value, force 100N, material Ti-6Al-4V

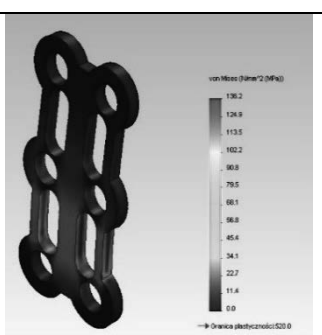

Figure 15. Stress value, force 20N, material X3CrNiMo13-4

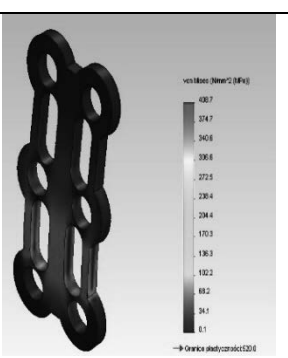

Figure 16. Stress value, force 60N, material X3CrNiMo13-4

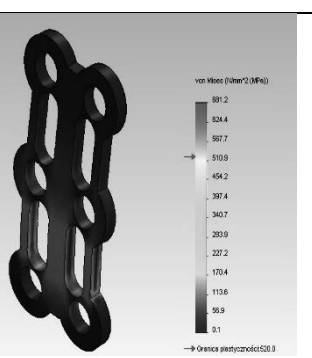

Figure 17. Stress value, force 100N, material X3CrNiMo13-4

Bending displacement analysis results

The next part of the study involved simulating displacements. Figures 18-26 present the results of displacement analysis for all three selected materials under various forces of 20 N, 60 N, and 100 N. For all materials, displacement values increased with increasing force.

For titanium, during the simulation with a force of 20 N, the displacement was approximately 0.143 mm (Fig. 18). During the test with a force of 60 N, the displacement was 0.429 mm (Fig. 19), and the test with a force of 100 N yielded a value of 0.716 mm (Fig. 20). Comparing the obtained

results with the other two selected materials, it is easy to see that the obtained values are intermediate between the values obtained for the two selected alloys.

The titanium alloy Ti-6Al-4V is the material for which the highest displacement values were obtained in each simulation. In the first test with a force of 20 N, the resulting displacement was 0.15 mm (Fig. 21); in the test with a force of 60 N, the displacement was 0.451 mm (Fig. 22); in the last test, the displacement reached 0.751 mm (Fig. 23). The obtained displacement values are larger but comparable to the results obtained for pure titanium – the difference in displacements between both materials at each applied force is approximately 5%. Of the selected materials, the X3CrNiMo13-4 material showed the smallest displacement. At an applied force of 20 N, the displacement was 0.0828 mm (Fig. 24), for a force of 60 N, the value was 0.248 mm (Fig. 25), and for the highest force of 100 N, the result was 0.4141 mm (Fig. 26). In each simulation, the displacement value for this material was approximately 55% of the value obtained for the titanium alloy.

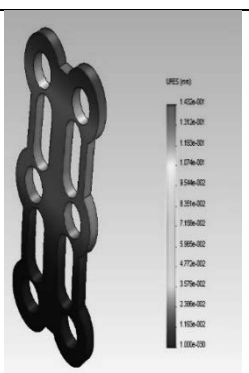	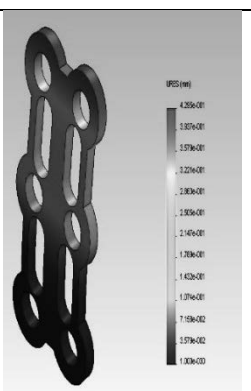	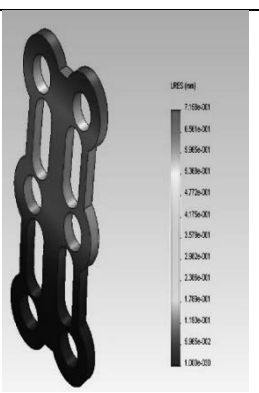
Figure 18. Value of displacement analysis, 20N force, Ti material	*Figure 19. Value of displacement analysis, 60N force, Ti material*	*Figure 20. Value of displacement analysis, 100N force, Ti material*
		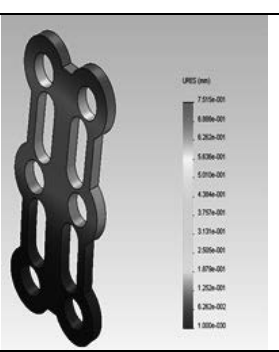
Figure 21. Value of displacement analysis, 20N force, Ti-6Al-4V material	*Figure 22. Value of displacement analysis, 60N force, Ti-6Al-4V material*	*Figure 23. Value of displacement analysis, 100N force, Ti-6Al-4V material*

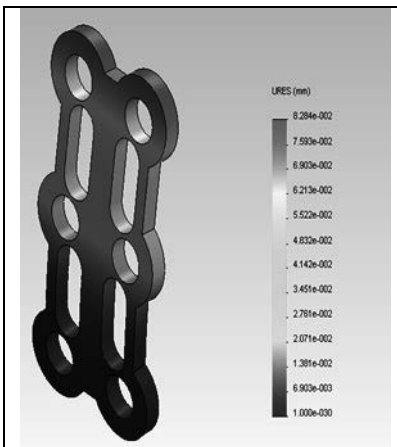

Figure 24. Value of displacement analysis, 20N force, X3CrNiMo13-4 material

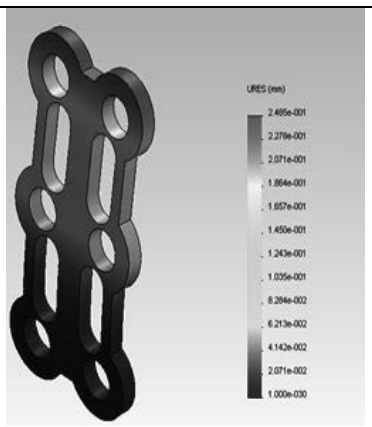

Figure 25. Value of displacement analysis, 60N force, X3CrNiMo13-4 material

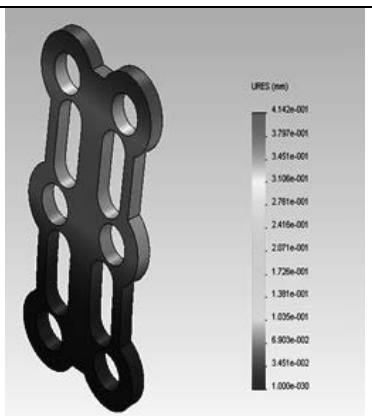

Figure 26. Value of displacement analysis, 100N force, X3CrNiMo13-4 material

SUMMARY OF RESULTS

The obtained results of all simulations are summarized in Table 3 (stress results) and Table 4 (displacement results).

Table 3. Results of stress analysis for individual materials and forces

Strength \ Material	Ti	Ti-6Al-4V	X3CrNiMo13-4
20 N	Max: 136.668 MPa	Max: 136.923 MPa	Max: 136.236 MPa
60 N	Max: 410.005 MPa	Max: 410.77 MPa	Max: 408.708 MPa
100 N	Max: 683.342 MPa	Max: 684.617 MPa	Max: 681.179 MPa

Table 4. Results of displacement analysis for individual materials and forces

Strength \ Material	Ti	Ti-6Al-4V	X3CrNiMo13-4
20 N	Max: 0.143157 mm	Max: 0.150292 mm	Max: 0.082836 mm
60 N	Max: 0.42947 mm	Max: 0.450876 mm	Max: 0.248508 mm
100 N	Max: 0.715783 mm	Max: 0.75146 mm	Max: 0.41418 mm

The best results in the simulations were achieved by the X3CrNiMo13-4 material. While the stress analysis values were very similar to those for the other two materials, a significant difference was noticeable in the displacement analysis – in this case, the material showed the lowest displacement value in each of the three simulations, with the results being approximately 55% of the value obtained for the titanium alloy. Based on the simulation results, it could be assumed that the worst-performing material is the Ti-6Al-4V titanium alloy. In the stress analysis, it does not differ significantly from the other materials, but the displacement analysis showed that this material

achieved the highest displacement value in each case – almost twice as high as the results obtained for the X3CrNiMo13-4 alloy. However, the initial dimensions of the tested plate should not be forgotten. In the third test, using 100N, the displacement value obtained was 0.715783mm – the largest displacement observed in this study – which still represents only 1.8% of the plate length.
The results obtained during the titanium analysis are very similar to those obtained for the Ti-6Al-4V titanium alloy. In the stress analysis, titanium behaves almost identically to the alloy, but in the displacement analysis, the values differ by approximately 5%.

5. SUMMARY

This article presents the results of computer simulations of stresses and displacements for various force values and materials used to manufacture a plate implant for spinal stabilization.

The materials selected for this study were titanium, a Ti-6Al-4V titanium alloy, and an X3CrNiMo13-4 alloy. All three materials are biocompatible and suitable for use in this type of prosthesis.

The simulations were conducted to examine the behavior of a plate made of these materials—the internal stresses and maximum displacements of the element—for three different loading forces: in the first simulation, the force was 20 N, then 60 N, and then 100 N.

All the selected materials exhibited very similar values during the tests; only the displacement analysis results for the X3CrNiMo13-4 alloy were very low compared to the other two materials. For this reason, this material appears to be the best option for manufacturing this type of component.

BIBLIOGRAPHY

[1]https://www.fizjologika.pl/10-pytan-po-operacji-szyi/ [dostęp: 20.11.2019];
[2]Prof. dr hab. inż. Konstanty SKALSKI, dr inż. Józef SKOWORODKO, Prof. dr hab. Inż. Monika GIERZYŃSKA - DOLNA „Stabilizatory oraz implanty krążka międzykręgowego kręgosłupa – przegląd konstrukcji”
[3] J. Adamus „Tytan i jego stopy jako materiał stosowany na elementy tłoczone”;
[4] R. Będziński, C. Pezowicz, „Mechaniczne aspekty stabilizacji kręgosłupa szyjnego”;
[5]iim.p.lodz.pl/media/materialy/mat-kier-MiBM-AiR-PiP-Trans/Cwiczenie%2013.pdf
[dostęp: 20.11.2019];
[6] Norma ISO 5832/3;
[7] mech.pg.edu.pl/documents/174709/23717562/STOPY%20Ti%205.2014.pdf
[8] B. Jedynak, E. Mierzwińska – Nastalska, „Tytan – właściwości I zastosowanie w protetyce stomatologicznej”

7th-9th June 2026
Gliwice-Brenna, Poland
DEPARTMENT OF ENGINEERING MATERIALS AND BIOMATERIALS
FACULTY OF MECHANICAL ENGINEERING
SILESIAN UNIVERSITY OF TECHNOLOGY
INTERNATIONAL STUDENTS SCIENTIFIC CONFERENCE

Analýza štrukturálnych zmien v austenitických oceliach vplyvom únavového poškodenia

Edita Illichmanová[a*], Milan Uhríčik[a], Melisa Šnircová[a] , Peter Palček[a], Klaudiusz Gołombek[b]

[a] Žilinská univerzita v Žiline, Strojnícka fakulta, Katedra materiálového inžinierstva, Univerzitná 8215/1, 010 26 Žilina, Slovak Republic
*email: edit.illichmanova@fstroj.uniza.sk
[b] Politechnika Śląska, Laboratorium Badania Materiałów, Wydział Mechaniczny Technologiczny ul. Konarskiego 18a, PL - 44-100 Gliwice, Poland

Abstract: Únavové poškodenie predstavuje jeden z najvýznamnejších degradačných mechanizmov kovových materiálov, ktorý vedie k ich postupnému zlyhaniu v dôsledku pôsobenia cyklického zaťaženia. Tento proces je charakterizovaný akumuláciou plastickej deformácie na mikroštruktúrnej úrovni, pričom jeho priebeh je výrazne ovplyvnený štruktúrou materiálu a podmienkami zaťaženia. V prípade austenitických ocelí dochádza počas únavového procesu k významným štrukturálnym zmenám, ktoré zahŕňajú zmenu dislokačných štruktúr, vznik perzistentných sklzových pásov, iniciáciu a šírenie trhlín, ako aj deformačne indukovanú martenzitickú transformáciu. Cieľom príspevku je analyzovať uvedené mechanizmy a ich vzájomné interakcie s dôrazom na mikroštruktúrne aspekty únavového poškodenia.

Kľúčové slová: austenitické ocele, únava materiálu, plastická deformácia, magnetizmus

1. INTRODUCTION

Únavové poškodenie kovových materiálov predstavuje komplexný fyzikálny proces, ktorý vzniká v dôsledku dlhodobého pôsobenia cyklického mechanického zaťaženia. Na rozdiel od statického porušenia je charakteristické tým, že k zlyhaniu materiálu dochádza postupne, pričom jednotlivé štádiá degradácie prebiehajú na mikroštruktúrnej úrovni a často nie sú makroskopicky pozorovateľné až do konečného štádia lomu. Tento fakt robí únavové poškodenie mimoriadne nebezpečným z hľadiska prevádzky technických zariadení, keďže môže viesť k náhlym a neočakávaným poruchám konštrukčných prvkov aj pri napätiach výrazne nižších ako je medza klzu materiálu [1].

Z mikroštruktúrneho hľadiska je únavový proces úzko spätý s pohybom a interakciou dislokácií, ktoré predstavujú základné nositele plastickej deformácie v kryštalických materiáloch. Pri opakovanom zaťažení dochádza k ich postupnej reorganizácii, k tvorbe dislokačných buniek a vzniku lokalizovaných oblastí plastickej deformácie, ktoré sú známe ako perzistentné sklzové pásy. Tieto oblasti predstavujú kritické miesta, kde dochádza k koncentrácii napätia a následnej iniciácii únavových trhlín [2].

Austenitické ocele sú z hľadiska únavového správania špecifické vďaka svojej kryštalickej štruktúre (mriežka K12), ktorá umožňuje aktiváciu viacerých sklzových systémov a tým aj vysokú schopnosť plastickej deformácie. Táto vlastnosť síce zvyšuje húževnatosť materiálu, ale súčasne vedie k intenzívnej dislokačnej aktivite počas cyklického zaťaženia, čo môže urýchliť vznik mikroštruktúrnych poškodení [3].

Významným faktorom ovplyvňujúcim správanie austenitických ocelí je aj ich schopnosť podliehať deformačne indukovanej martenzitickej transformácii. Tento proces predstavuje bezdifúznu zmenu kryštalickej štruktúry, ktorá je iniciovaná mechanickým napätím a vedie k vzniku martenzitu v oblastiach s vysokou hustotou dislokácií. Transformácia má zásadný vplyv na mechanické vlastnosti materiálu, keďže spôsobuje jeho lokálne spevnenie, ale zároveň môže znižovať húževnatosť a podporovať iniciáciu trhlín [4].

Z uvedeného vyplýva, že analýza únavového poškodenia austenitických ocelí si vyžaduje komplexný prístup, ktorý zohľadňuje interakciu medzi mikroštruktúrou, mechanickým zaťažením a fázovými transformáciami. Pochopenie týchto mechanizmov je kľúčové pre návrh materiálov s vyššou odolnosťou voči únave a pre optimalizáciu ich použitia v technickej praxi [5].

2. AUSTENITICKÉ OCELE

Austenitické nehrdzavejúce ocele patria medzi najvýznamnejšie konštrukčné materiály používané v technickej praxi, najmä v prostrediach so zvýšenými nárokmi na koróznu odolnosť, tvárniteľnosť a húževnatosť. Ich vlastnosti sú determinované predovšetkým stabilnou austenitickou štruktúrou, ktorá je výsledkom vhodného chemického zloženia a technologického spracovania. Vďaka špecifickej kryštalickej mriežke a interakciám legujúcich prvkov vykazujú tieto ocele odlišné mechanické a fyzikálne správanie v porovnaní s feritickými alebo martenzitickými ocelami, čo sa výrazne prejavuje aj pri ich namáhaní a porušovaní [3,4].

2.1 Charakteristika a štruktúra austenitických ocelí

Austenitické nehrdzavejúce ocele predstavujú skupinu vysoko legovaných ocelí, ktorých základnou charakteristikou je austenitická štruktúra stabilná pri izbovej teplote. Táto štruktúra je tvorená tuhým roztokom uhlíka v železe γ s kubickou plošne centrovanou (FCC) kryštalickou mriežkou, ktorá umožňuje rozpúšťanie väčšieho množstva intersticiálnych prvkov, najmä uhlíka a dusíka. V porovnaní s feritickou (BCC) štruktúrou poskytuje austenitická mriežka väčší intersticiálny priestor, čo má zásadný vplyv na mechanické a fyzikálne vlastnosti materiálu [3].

Stabilita austenitu pri nižších teplotách je dosahovaná legovaním prvkami, ako sú nikel, mangán alebo dusík, ktoré znižujú teplotu premeny $\gamma \rightarrow \alpha$. Tieto prvky zároveň ovplyvňujú mechanizmy plastickej deformácie a energetické pomery v kryštalickej mriežke. Významnú úlohu zohráva aj energia vrstevných chýb, ktorá rozhoduje o tom, či bude deformácia prebiehať sklzom, dvojčatením alebo martenzitickou transformáciou [4].

Austenitické ocele sa vyznačujú vysokou plasticitou a húževnatosťou, čo súvisí s ich kryštalickou štruktúrou. Táto štruktúra umožňuje aktiváciu veľkého počtu sklzových systémov, čím sa zvyšuje schopnosť materiálu plasticky deformovať bez porušenia. V dôsledku toho vykazujú tieto ocele dobrú tvárniteľnosť a odolnosť voči lomovým mechanizmom aj pri nízkych teplotách [4].

2.2 Tepelné spracovanie a stabilita austenitických ocelí

Z hľadiska technologického spracovania je pre austenitické nehrdzavejúce ocele typické rozpúšťacie žíhanie, ktoré sa vykonáva pri teplotách približne 950 až 1050°C, po ktorom nasleduje rýchle ochladenie. Tento proces zabezpečuje rozpustenie karbidov a zabraňuje ich opätovnému vylučovaniu, čím sa zachováva homogénna austenitická štruktúra a vysoká korózna odolnosť materiálu [6,7].

Pri nedostatočne rýchlom ochladzovaní alebo nevhodne zvolených teplotách môže dochádzať k precipitácii karbidov na hraniciach zŕn, čo vedie k zhoršeniu koróznej odolnosti. Z tohto dôvodu je potrebné dodržiavať minimálnu rýchlosť ochladzovania a vyhýbať sa príliš vysokým žíhacím teplotám, pri ktorých sa môže v štruktúre tvoriť δ-ferit [6].

V prípade stabilizovaných austenitických ocelí legovaných prvkami ako titán alebo niób sa po rozpúšťacom žíhaní môže aplikovať aj stabilizačné žíhanie pri teplotách 850 až 950°C. Tento proces podporuje viazanie uhlíka a dusíka do stabilných karbidov a nitridov, čím sa znižuje riziko medzikryštalickej korózie a zvyšuje dlhodobá stabilita štruktúry pri zvýšených teplotách [7].

Okrem klasických postupov tepelného spracovania sa v špecifických prípadoch využívajú aj ďalšie nízkoteplotné režimy, ktoré umožňujú optimalizovať kombináciu mechanických vlastností a koróznej odolnosti. Tieto postupy sú navrhované tak, aby nedošlo k narušeniu stability austenitickej štruktúry, pričom sa zachovajú požadované pevnostné charakteristiky materiálu [6].

3. MECHANIZMY ÚNAVOVÉHO POŠKODENIA

Únavový proces možno charakterizovať ako sekvenciu na seba nadväzujúcich mechanizmov, ktoré zahŕňajú cyklickú plastickú deformáciu, vznik lokalizovaných deformačných štruktúr, iniciáciu mikrotrhlín a ich následné šírenie až po konečné porušenie materiálu. Každá z týchto fáz je sprevádzaná špecifickými mikroštruktúrnymi zmenami, ktoré ovplyvňujú celkové únavové správanie materiálu [1].

3.1 Cyklická deformácia a vývoj dislokačných štruktúr

V počiatočných štádiách únavového zaťažovania dochádza k intenzívnemu pohybu dislokácií, ktoré sa aktivujú v sklzových rovinách v dôsledku pôsobenia striedavého napätia. Tento pohyb nie je náhodný, ale vedie k postupnej reorganizácii dislokácií do stabilnejších konfigurácií, ako sú dislokačné bunky alebo steny. Vznik týchto štruktúr predstavuje energeticky výhodný stav, ktorý umožňuje materiálu efektívnejšie reagovať na opakované zaťaženie [1,8].

S pokračujúcim cyklickým zaťažovaním dochádza k zvyšovaniu hustoty dislokácií a k ich vzájomnej interakcii, čo vedie k zmene mechanických vlastností materiálu. Tento jav sa prejavuje ako cyklické spevňovanie alebo zmäkčovanie (obrázok 1), pričom konkrétny priebeh závisí od počiatočného stavu materiálu a jeho mikroštruktúry. V prípade austenitických ocelí je často pozorované cyklické spevňovanie, ktoré je spojené s akumuláciou dislokácií a vznikom prekážok ich pohybu [9].

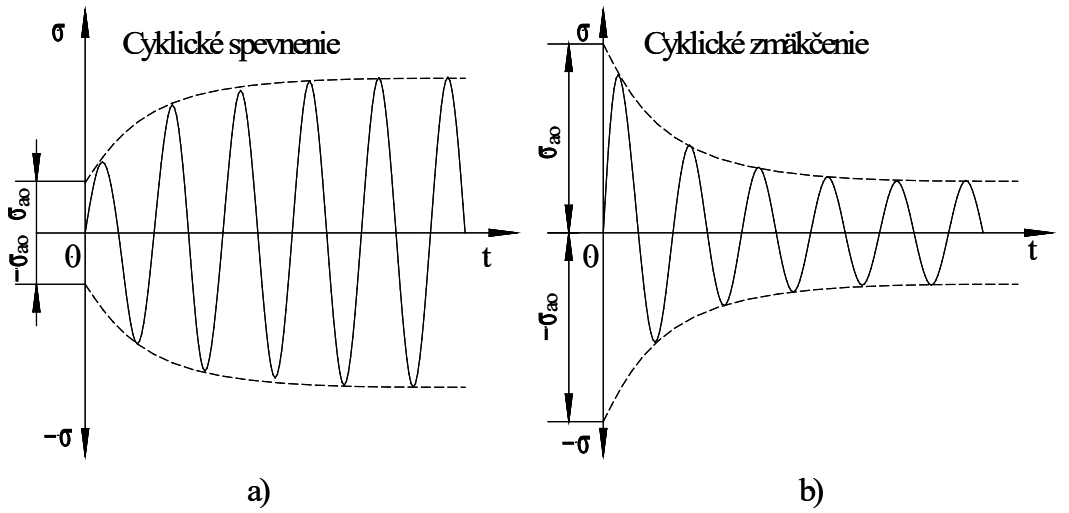

Obr. 1 Priebehy cyklického spevnenia a zmäkčenia [9]
Figure 1. Cyclic hardening and softening processes [9]

3.2 Nukleácia únavových trhlín

Jedným z najvýznamnejších prejavov cyklickej deformácie je vznik perzistentných sklzových pásov, ktoré predstavujú úzke oblasti intenzívnej plastickej deformácie orientované v smere sklzových rovín. Tieto pásy vznikajú v dôsledku opakovaného pohybu dislokácií po rovnakých sklzových rovinách, čo vedie k ich postupnému zosilňovaniu a stabilizácii [2].

Perzistentné sklzové pásy (obrázok 2) majú zásadný význam pre iniciáciu únavových trhlín, keďže sú miestami zvýšenej koncentrácie napätia. Na povrchu materiálu sa prejavujú ako E – extrúzie (materiál vyčnieva z povrchu) a I – intrúzie (materiál je vtlačený do povrchu), ktoré vznikajú v dôsledku nerovnomerného plastického toku materiálu. Intruzie predstavujú kritické miesta, kde dochádza k vzniku mikrotrhlín, ktoré sa následne šíria do objemu základného materiálu (M)[1,8].

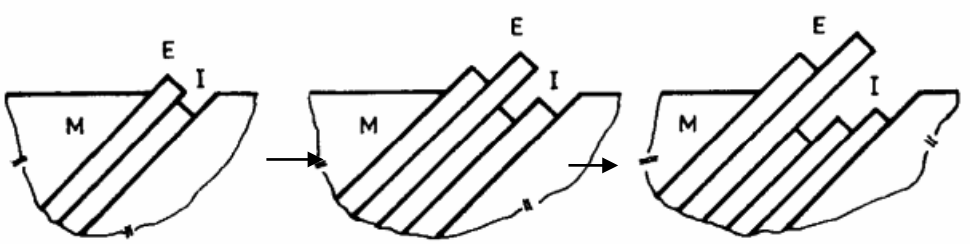

Obr. 2 Schéma vzniku a rozvoja únavových sklzových pásov [8]
Figure 2. Scheme of the formation and development of fatigue slip bands [8]

3.3 Iniciácia únavových trhlín

Proces iniciácie trhlín je ovplyvnený kombináciou mikroštruktúrnych faktorov a podmienok zaťaženia. V austenitických oceliach dochádza k iniciácii trhlín najčastejšie na povrchu materiálu, kde sú najvyššie koncentrácie napätia a kde sa nachádzajú perzistentné sklzové pásy.

Okrem toho môžu trhliny iniciovať aj na vnútorných defektoch, ako sú inklúzie, póry alebo hranice zŕn [5].

Iniciácia trhlín je postupný proces, ktorý zahŕňa nukleáciu mikrotrhlín, ich rast a spájanie do väčších trhlín. Tento proces je ovplyvnený veľkosťou zŕn, distribúciou fáz a prítomnosťou nehomogenít v materiáli [2].

3.4 Šírenie únavových trhlín

Po iniciácii trhlín nasleduje ich šírenie, ktoré prebieha v niekoľkých štádiách (obrázok 3). Krátke trhliny sú silne ovplyvnené mikroštruktúrou materiálu, pričom ich rast môže byť nepravidelný a závislý od lokálnych vlastností. S rastúcim počtom cyklov dochádza k ich koalescencii a rastu, pričom väčšina sa stabilizuje na dĺžkach do desiatok μm. U časti trhlín pokračujúcich v raste dochádza k zmene mechanizmu šírenia z kryštalografického (po sklzových rovinách) na nekryštalografický, orientovaný kolmo na hlavné napätie. Tento prechod predstavuje ukončenie štádia krátkej trhliny; následne sa zvyčajne vyvíja jedna dominantná (magistrálna) trhlina s dĺžkou do niekoľkých desatín mm. Väčšina únavovej životnosti materiálu sa spotrebuje v štádiu pomalého šírenia trhlín, ktoré prebieha transkryštalicky. Dlhé trhliny sú definované ako trhliny presahujúce približne desaťnásobok veľkosti štruktúrnych prvkov. Únavové poškodenie je sústredené v plastickej zóne na čele trhliny a je charakterizované únavovým žliabkovaním (striáciami), ktorých rozstup približne zodpovedá prírastku trhliny za cyklus. Jeho vznik súvisí s opakovaným otupovaním a zaostrovaním špičky trhliny [1,8].

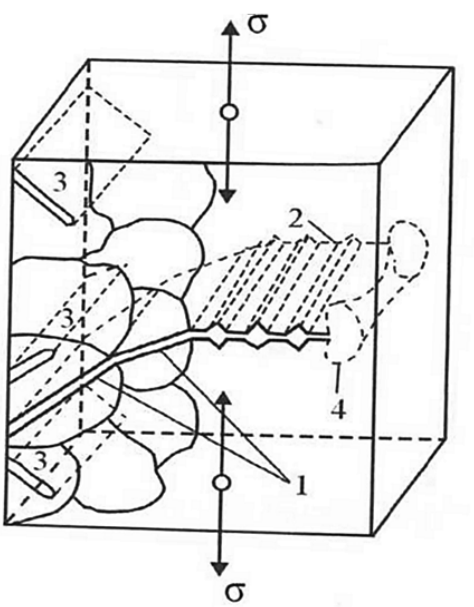

Obr. 3 Etapy šírenia únavovej trhliny: 1 - transkryštalické šírenie trhliny (1. etapa), 2 - nekryštalografické šírenie trhliny (2. etapa), 3 - neefektívne trhliny, 4 - plastická zóna na čele trhliny [8]

Figure 3. Stages of fatigue crack propagation: 1 - transcrystalline crack propagation (stage 1), 2 - non-crystallographic crack propagation (stage 2), 3 - ineffective cracks, 4 - plastic zone at the crack tip [8]

Parisov zákon predstavuje základný nástroj pre opis rýchlosti rastu trhlín v závislosti od rozsahu súčiniteľa intenzity napätia. Tento vzťah umožňuje predikciu životnosti materiálu a je široko využívaný v inžinierskej praxi [1].

3.5 Únavový lom

Typickým znakom únavových lomov je, že k nim dochádza náhle, bez predošlej makrodeformácie materiálu, aj v prípade húževnatých materiálov, ktoré sa pri statickej skúške porušia až po výraznej plastickej deformácii. Výsledkom šírenia únavovej trhliny je zoslabenie nosného prierezu súčiastky. Ak dosiahne trhlina kritickú veľkosť, dôjde k náhlemu lomu zvyšného prierezu (obrázok 4). Preto má každý únavový lom dve rozlíšiteľné oblasti: oblasť únavového poškodenia a zvyškový lom (oblasť dolomenia). Oblasť únavového poškodenia, v ktorej prebieha pozvoľný nárast trhliny, má vzhľad jemného lomu, ktorý je spôsobený opakovaným otváraním a zatváraním trhliny. Na lomovej ploche v tejto oblasti je viditeľné východisko lomu (ohnisko) a tzv. rastové čiary. Zvyškový lom vzniká dolomením zvyšnej časti nosného prierezu [5].

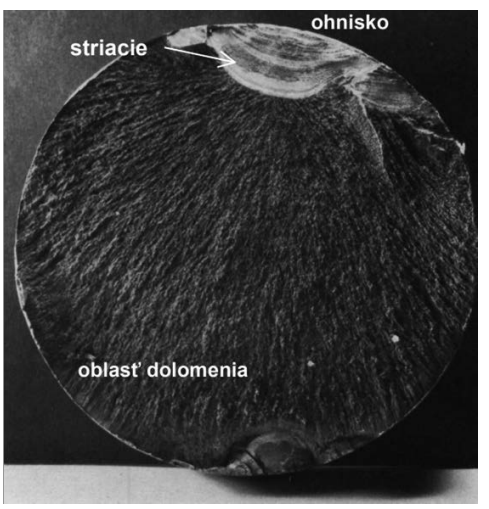

Obr. 4 Charakter únavového lomu piestu
Figure 4. Character of piston fatigue fracture

3. MARTENZITICKÁ TRANSFORMÁCIA A MIKROŠTRUKTÚRNY VÝVOJ

V nadväznosti na mikroštruktúrnu stabilitu austenitu a jeho schopnosť plastickej deformácie predstavuje martenzitická transformácia jeden z kľúčových mechanizmov ovplyvňujúcich správanie austenitických ocelí pri mechanickom zaťažení. Ide o bezdifúzny proces, pri ktorom dochádza k náhlej zmene kryštalickej štruktúry z kubickej plošne centrovanej (FCC) na martenzitickú fázu. Transformácia prebieha šmykovým mechanizmom a je sprevádzaná charakteristickou ihlicovou alebo doskovitou morfológiou novovzniknutej fázy. V metastabilných austenitických oceliach sa počas deformácie najčastejšie vytvára deformačne indukovaný α′-martenzit, pričom v niektorých prípadoch môže byť jeho vzniku predchádzané prechodnou ε-fázou [1,5].

Mechanické napätie a plastická deformácia zohrávajú rozhodujúcu úlohu pri iniciácii tejto transformácie. V dôsledku lokálneho nahromadenia plastickej deformácie dochádza k vzniku martenzitu predovšetkým v oblastiach s vysokou hustotou dislokácií, ako sú perzistentné sklzové pásy, hranice zŕn alebo oblasti v blízkosti koncentrátorov napätia, napríklad hrotov trhlín. Tento proces úzko súvisí s mechanizmami popísanými pri plastickej deformácii austenitu, pričom transformácia predstavuje ďalší spôsob adaptácie deformácie. Vznik martenzitu vedie k výraznej zmene lokálnych mechanických vlastností, keďže táto fáza je tvrdšia a pevnejšia ako pôvodný austenit [3,5].

Počas cyklického zaťaženia sa martenzitická transformácia uplatňuje ako súčasť deformačných mechanizmov a prispieva k postupnému spevňovaniu materiálu. Lokálne spevnenie spôsobené prítomnosťou martenzitu môže viesť k redistribúcii napätí v mikroštruktúre a spomaleniu šírenia existujúcich trhlín. Súčasne však vznik fázových rozhraní medzi austenitom a martenzitom predstavuje potenciálne miesta iniciácie nových mikrotrhlín v dôsledku nekompatibility deformácie jednotlivých fáz. Vplyv martenzitickej transformácie na únavové správanie je preto komplexný a závisí od miery jej rozvoja a od charakteru zaťaženia. Pri dlhodobom cyklickom namáhaní dochádza k postupnej akumulácii martenzitu, čo vedie k vývoju mikroštruktúry a zmene mechanických vlastností materiálu. Tento proces je sprevádzaný objemovými zmenami, ktoré generujú vnútorné napätia a podporujú vznik ďalších mikroštruktúrnych defektov. Interakcia medzi dislokáciami, sklzovými pásmi a novovzniknutými martenzitickými oblasťami vedie k výraznej heterogenite mikroštruktúry, ktorá následne ovplyvňuje iniciáciu a šírenie únavového poškodenia. Výsledné správanie materiálu je tak výsledkom kombinácie plastickej deformácie a transformačných mechanizmov prebiehajúcich na mikroskopickej úrovni [1,5].

4. ZÁVER

Únavové poškodenie austenitických ocelí predstavuje komplexný proces, ktorý je výsledkom interakcie medzi mikroštruktúrnymi zmenami a mechanickým zaťažením. Kľúčovými mechanizmami sú cyklická deformácia, vznik perzistentných sklzových pásov, iniciácia a šírenie trhlín a martenzitická transformácia. Pochopenie týchto procesov umožňuje efektívnejší návrh materiálov a konštrukcií s vyššou odolnosťou voči únave, čo je nevyhnutné pre bezpečnú a spoľahlivú prevádzku technických zariadení.

POĎAKOVANIE

Tento príspevok vznikol v rámci spoločného slovensko-poľského projektu ako výsledok spolupráce medzi Politechnikou Slaskou (Poľsko) a Žilinskou univerzitou v Žiline (Slovensko) a bol podporený projektami KEGA č. 033ŽU-4/2026, KEGA č. 039ŽU-4/2026 a VEGA č. 1/0729/26.

BIBLIOGRAPHY

1. KLESNIL, M. Cyklická deformácia a únava kovov. Bratislava: VEDA. ISBN 71-018- 87, 1987.

2. VĚCHET, S., a kol. Únavové vlastnosti tvárné litiny. Žilina: EDIS - vydavateľstvo Žilinská univerzita. ISBN 80-7100-910-5, 2001.
3. PTÁČEK, L., a kol. Nauka o materiálu II. Brno: Akademické nakladatelství CERM, s.r.o.. ISBN 80-7204-130-4, 1999.
4. OLSON, G.B., OWEN, W.S. Martensite. A tribute to Morris Cohen. Ohio: ASM International. ISBN: 0-87170-434-X, 1992.
5. SKOČOVSKÝ, a kol. Náuka o materiáli. Žilina: EDIS - vydavateľstvo Žilinská univerzita. ISBN 978-80-554-0871-2, 2014.
6. FREMUNT, P., PODRÁBSKÝ, T. Konstrukční oceli. Brno: Akademické nakladatelství CERM. ISBN 80-85867-95- 8, 1996.
7. ČÍHAL, V. Korozivzdorné oceli a slitiny. Praha: Academia, nakladatelství AVČR. ISBN 80-2000-671-0, 1999.
8. PLUHAŘ, J., a kol. Fyzikální metalurgie a medzní stavy materiálu. Praha: SNTL – Nakladatelství technické literatury a Bratislava: Alfa, vydavateľstvo technickej a ekonomickej literatúry, 1987.
9. VELES, P. Mechanické vlastnosti a skúšanie kovov. Bratislava: Alfa. ISBN 063-552- 89, 1985.

TalentDetector

7th-9th June 2026
Gliwice-Brenna, Poland

DEPARTMENT OF ENGINEERING MATERIALS AND BIOMATERIALS
FACULTY OF MECHANICAL ENGINEERING
SILESIAN UNIVERSITY OF TECHNOLOGY

INTERNATIONAL STUDENTS SCIENTIFIC CONFERENCE

Corrosion Phenomena in Structural Steels: Mechanisms, Influencing Factors and Anticorrosion Protection Methods.

Alicja Jankiewicz[a], Emilia Komendarczyk[b], Kamila Krus[c], Mirosław Bonek

[a] Silesian University of Technology, Faculty of Mechanical Engineering, Department of Engineering Materials and Biomaterials
email: aj319519@student.polsl.pl
[b] Silesian University of Technology, Faculty of Mechanical Engineering, Department of Engineering Materials and Biomaterials
email: ek322978@student.polsl.pl
[c] Silesian University of Technology, Faculty of Mechanical Engineering, Department of Engineering Materials and Biomaterials
email: kk317217@student.polsl.pl

Abstract: The article concerns the phenomenon of corrosion in metals, including an analysis of the influence of alloying elements and heat treatment in structural steels. It also discusses the corrosion process, the use of structural steels and corrosion prevention methods.

Keywords: corrosion, structural steels, anti-corrosion protection

1. INTRODUCTION

Corrosion is one of the most critical issues encountered in the operation of metallic materials. Although it develops slowly and is often hard to see, its impact on the durability and safety of structures is a serious problem.

1.1. Hazards Associated with Corrosion

Corrosion reduces the cross-sectional area and mechanical strength of elements, which can lead to serious structural damage or collapse. It also causes crack growth in the material, further reducing its mechanical properties. Additionally, corrosion increases operating costs because of the need for regular inspections, maintenance, and replacing damaged parts. As a result, it is a technical, economic, and safety hazard for both human life and the environment.

1.2. Corrosion in Structural Steels

Corrosion can be divided into chemical (direct reaction with gases or at high temperatures) and electrochemical (happening in the presence of an electrolyte due to potential differences on the surface). In structural steels, electrochemical corrosion is much more common and includes:

- Pitting corrosion – Localized damage that forms deep holes (pits) due to corrosion cells. The bottom of the pit is the anode (where metal dissolves) and the area around it is the cathode (where reduction happens, e.g., of oxygen).

- Crevice corrosion – Localized electrochemical corrosion in narrow, hard-to-reach places like bolted or riveted joints.

- Intergranular corrosion – Destruction that goes along grain boundaries, weakening the material structure.

- Uniform corrosion – Even destruction of the material over its entire surface.

- Stress corrosion cracking – Cracks caused by the simultaneous action of a corrosive environment and mechanical tensile stresses, which can cause sudden failure of an element.

1.3. Classification of Structural Steels

Structural steels are widely used because they have good mechanical properties and are relatively cheap. They are divided into non-alloy and alloy steels:

Non-alloy steels (e.g., S235, S355) – Mainly used in construction up to around 300°C and in low-corrosion environments. They are easy to machine, weld, or bolt. Their properties depend on chemical composition, and the most important parameter is yield strength. They rust easily under atmospheric conditions, so they need protective coatings.

Alloy steels – Used for more demanding applications with high static and dynamic loads. Thanks to alloying elements, they have higher strength and better corrosion resistance, but they can still corrode in tough conditions.

1.4. Properties of Structural Steels

Structural steel usually contains from 0.15% to 0.30% carbon, which changes its strength and hardness. Its main mechanical properties are strength (especially tensile strength), hardness, impact toughness, ductility, and elasticity.

The long-term effect of atmospheric corrosion on structural steel is presented in **Fig. 1.1**. The graph compares thickness loss over four years between standard carbon steel and weathering steel. While carbon steel degrades rapidly, weathering steel shows much higher resistance thanks to specific alloying elements that form a stable protective layer on its surface.

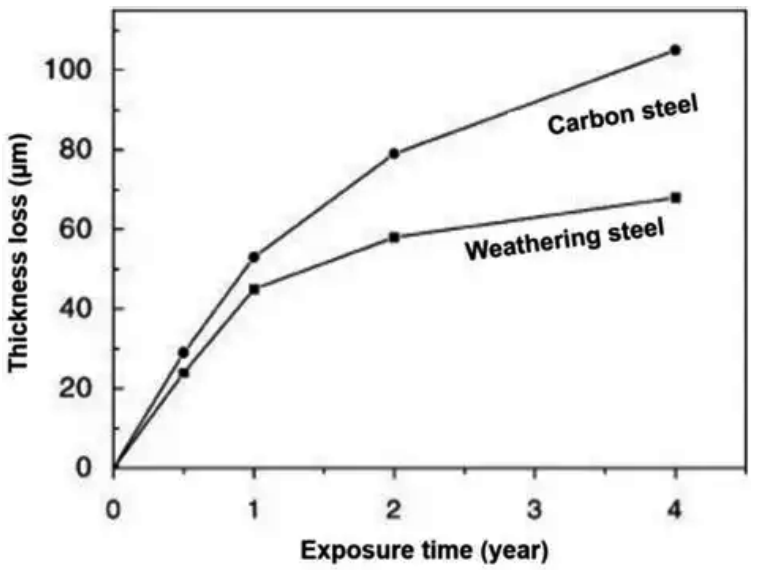

Fig. 1.1. Comparison of corrosion-induced thickness loss over exposure time between standard carbon steel and weathering steel.

2. THE INFLUENCE OF CHEMICAL COMPOSITION AND HEAT TREATMENT

One of the criteria for material selection by a designer is corrosion resistance, At the design stage of a given component, it is necessary to anticipate the environmental conditions to which it will be exposed.

2.1. The influence of Alloying Elements

The properties of structural steel depend on the alloying elements used. The addition of alloying elements allows the properties of steel to be better tailored to specific service conditions.

Corrosion-resistant structural steels are low-alloy steels containing up to 0.16% of carbon and alloying elements such as chromium (0.3-1.25%), copper (0.25-0.55%) and others. A protective passive layer forms on their Surface, composed mainly of chromium or copper oxides, as well as copper sulfates and carbonates, which limits the corrosion process. Elements such as Cr, Ni, and Mo are mainly used to improve hardenability.

Corrosion-resistant steels exhibit higher corrosion resistance than carbon steels. In humid or marine environments, additional protection of surface, such as paint coating, may be needed. Resistance to atmospheric corrosion and seawater is provided by the alloying addition of copper.

One of the primary alloying elements used in corrosion-resistant steels is chromium, which significantly improves corrosion resistance. If chromium concentration is over 13% in the ferrous alloy, an increased tendency for the formation of passive layers may be observed. The durability of those layers is greater than those forming on pure iron. A layer like this protects the steel against further oxidation. Stainless steel contains at least 10.5% of chromium.

High-chromium steels with ferritic, ferritic-martensitic and martensitic structure are specifically resistant to chemical corrosion. They are resistant to oxidation in air, natural water

and water vapor environment, as well as to the action of cold alkaline solution, diluted acids and salts (excluding chlorides and iodides) and to contact with crude oil.

Resistance to electrochemical corrosion is exhibited by chromium-nickel and chromium-nickel-manganese steels with austenitic structure. Particularly in environments such as acids, nitrogen compounds, salt solutions and food products.

Austenitic steels exhibit high corrosion resistance and a lower tendency to grain growth than ferritic steels.

Prevention of intergranular corrosion is based on not letting the chromium carbides to discharge. It can be done by repeated solution heat treatment of steel or reducing the carbon content below 0.03%.

The addition of 1-3% Mo leads to an increase in the corrosion resistance of Cr-Ni steels (with an austenitic structure) in sulfuric and acetic acid environments. These steels are also resistant to pitting and crevice corrosion in the presence of chloride ions. As an alloying element, molybdenum enables the use of steels under high-temperature conditions.

The risk of stress corrosion cracking in Cr-Ni steels can be minimalized by the addition of approximately 3% Cu.

Steels characterized by very high corrosion resistance are fully austenitic steels containing the highest possible concentrations of Cr, Ni and Mo.

2.2. The influence of heat treatment

The corrosion resistance of steel also depends on the applied heat treatment. Annealing is used to reduce internal stresses and homogenize the microstructure. This process has a positive effect on the corrosion resistance of steel by eliminating dislocations that could act as the cause of corrosion. Annealing ensures a more uniform distribution of alloying elements, which is a significant advantage in aggressive environments.

Normalizing, by prompting the dissolution of phases, improves the microstructure and makes it even more homogeneous. This results in increased resistance to intergranular corrosion.

Hardening may reduce corrosion resistance due to rapid structural changes that can generate internal stresses and microcracks. This process is often combined with tempering (to reduce internal stresses) or passivation.

2.3. Examples of structural steels

- Stainless steel A2 (AISI 304) – 18-20% Cr; 8-10,5% Ni. Widely used in general structural applications where the corrosion environment is not extreme. It is applied in typical atmospheric conditions.
- Stainless steel A4 (AISI 316) – 16-18% Cr; 10-14% Ni; 2-3% Mo. Due its molybdenum content, it exhibits higher corrosion resistance, particularly in chloride-containing environments such as seawater. It is used in marine and chemical industries. Owing to its more complex chemical composition and higher corrosion resistance, it is more expensive.
- Stainless steel AISI 410 – 12-14% Cr; 0.08-0.15% C. It is characterized by good corrosion resistance in moderately aggressive environments. It is used where both corrosion resistance and mechanical strength are required, e.g. turbine components.
- Steel 18CrMo4 – 0,16-0,23% C; 0,9-1,2% Cr; 0,9-1,2% Mn; 0,2-0,3% Mo. It is used in components subjected to high stress and variable loads, such as gears, shafts and bushings.

Fig. 2. Progressive corrosion of a structural element.

3. APPLICATIONS OF STRUCTURAL STEELS IN THE AUTOMOTIVE INDUSTRY

Nowadays, the automotive industry faces one of the greatest engineering challenges: the need to simultaneously increase passenger safety and reduce vehicle weight. In a time of strict emission standards and the rapid growth of electric vehicles, the weight of the chassis directly affects the driving range and energy efficiency of the vehicle. Although lightweight aluminum alloys and carbon composites are becoming more popular, structural steel remains a key engineering material due to its versatility and relatively low production costs.

3.1. Structural Steel Elements in Passenger Cars

- **Subframe and Load-Bearing Components (The Structural Foundation)**
  - **Front subframe:** Isolates the unibody (monocoque) body from engine vibrations and front suspension forces.
  - **Rear subframe:** Holds the suspension components, differential, and exhaust system; it increases stiffness and dampens vibrations.
  - **Chassis frame rails (longitudinal members):** Long steel or aluminum beams running along the vehicle. They form the main skeleton of the car, defining its geometry, bending stiffness, and crash energy absorption.

- **Wheel Guiding Elements (Suspension System)**
  - **Control arms / Wishbones (lower/upper):** Connect the steering knuckle to the vehicle body or subframe. They allow the wheel to move only vertically (up and down).
  - **Torsion beam (twist-beam axle):** A simple rear axle used in compact cars. It consists of two trailing arms connected by a crossbeam that twists to provide stability.
  - **Steering knuckles / Spindles:** Keep the wheel in the position required by the suspension geometry and steering system.

- **Elastic and Stabilizing Elements**

- **Stabilizer links (sway bar links):** Connect the anti-roll bar (stabilizer bar) to the control arm or MacPherson strut. They reduce body roll in corners.
- **Torsion bars:** Springs in the form of a solid bar or tube (used instead of coil or leaf springs) that use the metal's resistance to twisting.

- **Steering System Components**
  - **Tie rods and tie rod ends:** Transmit movement from the steering gear to the steering knuckle, allowing the car to turn. Ball joints allow them to work at the same time as the suspension moves vertically.
  - **Steering gear housing:** Protects internal gear mechanisms from dirt and mechanical damage.

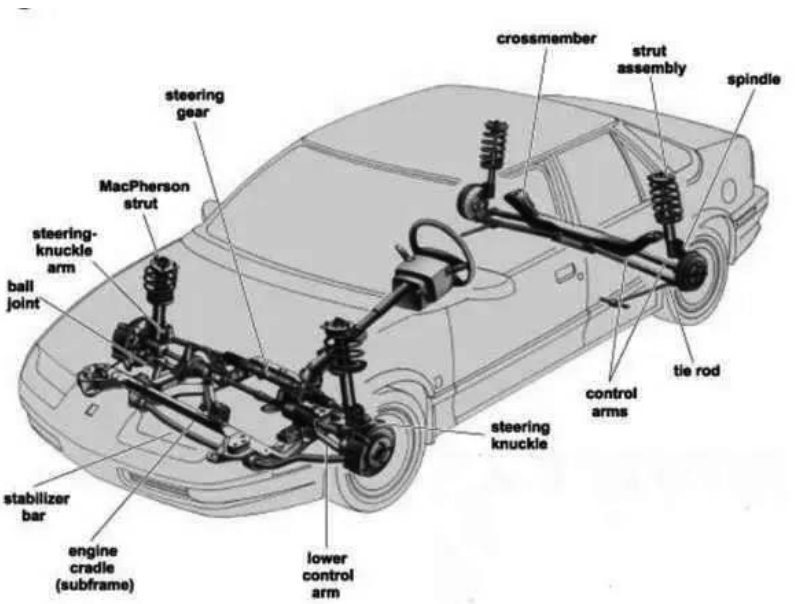

Fig. 3. The Parts of a Car Suspension System

3.2 Analysis of Operating Conditions of Structural Steel in Chassis Elements

<u>Mechanical Loading and Material Fatigue</u>

- **Operating Characteristics:** Chassis components (control arms, subframes) work in the high-cycle fatigue regime (10^4 cycles and above) and under elastic deformation.
- **Hazards:** Fatigue strength decreases as stress amplitudes increase; fully reversed stress cycles are the most dangerous.
- **Failure Mechanism:** Microcrack initiation →macrocrack propagation →sudden brittle fracture. Internal defects (e.g., in welds) eliminate the initiation stage – the destruction starts directly with crack propagation.
- **Geometric Effects (Notches):** Mounting holes, changes in cross-section, and welded joints act as notches that concentrate stresses. The smaller the transition radius from the weld into the base metal, the lower the fatigue life of the element.

Corrosive Environment

- **Corrosion Fatigue:** Pitting corrosion creates micro-notches, which drastically reduces the fatigue strength of steel compared to working in clean air.
- **Critical Areas:** Joints and welds. Weld defects (pores, inclusions) collect moisture and road salt, which starts dangerous crevice corrosion.

Impact Loading and Erosion

- **Mechanical Degradation:** Impacts from stones, gravel, and ice act as abrasive blasting on the underbody, stripping away factory protective coatings.
- **Chemical Consequences:** Unprotected steel exposed to water, mud, and de-icing salts undergoes rapid electrochemical corrosion (pitting and rust propagation), which degrades the load-bearing integrity.

Thermal Extremes

- **Elevated Temperatures:** Cause thermal expansion in steel (introducing risks of chassis geometry distortion) and increase its ductility, rendering it more susceptible to permanent plastic deformation.
- **Low Temperatures (Sub-Zero Conditions):** Induce material contraction (generating residual stresses in rigidly constrained structures) and reduce toughness. The steel exhibits a ductile-to-brittle transition; combined with impact loads, this dramatically escalates the risk of sudden structural brittle fracture.

4. CONCLUSION

Corrosion is one of the biggest threats to the durability and safety of steel structures, especially in automotive operating conditions. Correctly selected alloying elements and proper heat treatment improve steel properties and extend the life of structures. Choosing the right structural steel grade and effective anti-corrosion protection methods is key to ensuring a long service life for vehicle chassis elements. Modern alloy steels and processing technologies make it possible to design lighter, high-strength structures that resist aggressive environments.

BIBLIOGRAPHY

1. Rowiński S., Wprowadzenie do problematyki wytrzymałości zmęczeniowej konstrukcji stalowych, Politechnika Gdańska.
2. Kułakowski M., Rokosz K., Zastosowanie stali stopowych w środkach transportu, „Autobusy: technika, eksploatacja, systemy transportowe”, R. 19, nr 6, s. 536–539, 2018.
3. Kolenda J., Porównawcze miary odporności materiałów na udarowe wgniecenia, nakłucia i nacięcia, „Zeszyty Naukowe Akademii Marynarki Wojennej”, R. 49, nr 2 (173), s. 19–24, 2008.
4. L. Dobrzański, Materiały inżynierskie i projektowanie materiałowe. Podstawy nauki o materiałach i metaloznawstwo, 2006, Wydawnictwo Naukowo-Techniczne, Gliwice-Warszawa
5. Korozja – Wikipedia, wolna encyklopedia
6. https://pl.wikipedia.org/wiki/Dodatek_stopowy

7. https://pl.wikipedia.org/wiki/Stal_konstrukcyjna_niskostopowa
8. https://motofocus.pl/
9. https://www.autocentrum.pl/motoslownik/zwrotnica-kola/
10. https://motostacja.com/blog/porady/drazki-stabilizatora-jak-dzialaja-i-dlaczego-sa-wazne.html
    https://sprez-mot.pl/p/7/sprezyny-srubowewalcowenaciskowe
11. https://www.autocentrum.pl/motoslownik/drazek-skretny/
12. https://www.oponeo.pl/artykul/drazek-kierowniczy
13. https://autokult.pl/przekladnia-zebatkowa-uklad-kierowniczy,6808013724072065a
14. https://www.rustcheckcorolon.pl/blog/189-dlaczego-podwozie-jest-najbardziej-narazone-na-korozje
15. https://wyrobyzestali.pl/pl/blog/wplyw-wysokich-i-niskich-temperatur-na-wlasciwosci-stali-w-gotowych-konstrukcjach-1720415797.html
16. Korozja konstrukcji stalowych: przyczyny, skutki i sposoby zapobiegania | Metikam
17. Kompleksowy przewodnik po właściwościach stali konstrukcyjnej | Artizono
18. Korozja Stali - Rodzaje, przyczyny, mechanizmy | Świat Korozji
19. Stal konstrukcyjna – właściwości, rodzaje i zastosowania | moris.eu
20. Jakie_sa_rodzaje_korozji.pdf
21. Skutki korozji – co powoduje i jak wpływa na bezpieczeństwo, koszty i trwałość konstrukcji? | HMS
22. https://wyrobyzestali.pl/pl/blog/jaki-jest-wplyw-pierwiastkow-stopowych-na-wlasciwosci-stali-1737012016.html
23. https://kalla.pl/blog/dlaczego-sklad-chemiczny-materialu-ma-kluczowe-znaczenie-dla-odpornosci-na-korozje/
24. https://wagnertrade.pl/stal-czym-jest-jakie-ma-skladniki-stopowe-i-ich-wplyw-na-wlasciwosci/?srsltid=AfmBOortasoxBRfmc62LHXg4XDxR6f4Gxkb3LBvE4aClVv--F6sUrqoX
25. https://karbaz.com.ua/pl/blog-pl/wplyw-obrobki-cieplnej-na-odpornosc-metali-na-korozje/
26. https://marcopol.pl/glowne-roznice-miedzy-stalami-nierdzewnymi-a2-aisi-304-i-a4-aisi-316/
27. https://www.kronosedm.pl/stal-18hgm-1-7262/

Figures:
Figure 1: https://www.researchgate.net/figure/Thickness-loss-of-weathering-steel-and-carbon-steel-x-exposure-time-10_fig1_373013577
Figure 2: https://wyrobyzestali.pl/pl/blog/jak-stal-zachowuje-sie-pod-woda-wlasciwosci-ktore-warto-znac-1736941713.html
Figure 3: https://www.gswautoparts.com/what-are-all-the-parts-of-a-car-suspension/

TalentDetector

7th-9th June 2026
Gliwice-Brenna, Poland

DEPARTMENT OF ENGINEERING MATERIALS AND BIOMATERIALS
FACULTY OF MECHANICAL ENGINEERING
SILESIAN UNIVERSITY OF TECHNOLOGY

INTERNATIONAL STUDENTS SCIENTIFIC CONFERENCE

Regulatory changes regarding the introduction of construction products to the European Union market – the perspective of manufacturers and work on new products

Ewelina Kaputa - Kuc[a], Elżbieta Nawrot - Sadłoń[a], Ewa Jonda[b,*]

[a] Łukasiewicz Research Network - Warsaw Institute of Technology, Building Materials Laboratory "IZOLACJA" in Katowice, 193A Al. W. Korfantego St., 40157 Katowice, Poland.
[b] Department of Engineering Materials and Biomaterials, Faculty of Mechanical Engineering, Silesian University of Technology, 18a Konarskiego St., 44100 Gliwice, Poland.
*email: ewa.jonda@polsl.pl

Abstract: The paper presents an overview of the key regulatory changes introduced by Regulation (EU) 2024/3110 (Regulation (EU) 2024/3110 of the European Parliament and of the Council of 27 November 2024 on laying down harmonised rules for the marketing of construction products and repealing Regulation (EU) No 305/2011) concerning construction products. The analysis focuses on the impact of the new regulations on the development and market launch of innovative construction products in the European Union from the perspective of manufacturers and product development. Particular attention is paid to the importance of integrating regulatory, environmental and information requirements at early stages of research and development, as well as to the opportunities and challenges arising from the new regulatory framework.

Keywords: construction products, CPR 2024/3110, manufacturers, innovations, EU market, regulations

1. INTRODUCTION

For decades, the construction sector in the European Union has operated under a harmonized legal framework aimed at ensuring the free movement of construction products within the internal market while guaranteeing their safety and quality. This framework was established by Regulation (EU) No 305/2011 (Regulation (EU) No 305/2011 of the European Parliament and of the Council of 9 March 2011 laying down harmonised conditions for the marketing of construction products and repealing Council Directive 89/106/EEC) of the European Parliament and of the Council of 9 March 2011, commonly known as the Construction Products Regulation (CPR). This document, repealing the previous Council Directive 89/106/EEC, established harmonized conditions for the marketing of construction products and introduced mandatory CE marking as proof of product conformity with declared performance [2].

After more than twelve years of implementing the CPR, it has become clear that introducing new construction products to the European Union market is an increasingly complex process, combining technical, research, and regulatory issues. In recent years, new civilizational challenges, such as ecological transformation, digitalization, and the circular economy, have required a thorough update of the regulations [3,4].
The result of many years of legislative work and extensive consultations is the current Regulation (EU) 2024/3110 of the European Parliament and of the Council of 27 November 2024 on laying down harmonised rules for the marketing of construction products and repealing Regulation (EU) No 305/2011, commonly referred to as the new CPR or CPR2 [1,2].

This publication discusses the most significant changes introduced by the new regulation from the perspective of manufacturers of construction products and from the point of view of the scientific and research community involved in the development of new materials and products.

2. SCOPE AND PURPOSE OF THE REGULATION

Regulation (EU) 2024/3110 of the European Parliament and of the Council defines the rules for placing and making available on the European Union market construction products intended for permanent incorporation into construction works or parts thereof. It covers products whose properties affect the fulfillment of basic requirements for the safety, functionality, and durability of construction works [1,7]. Compared to Regulation No. 305/2011, the scope of the new regulations has been expanded to include innovative products manufactured using new technologies, and in certain cases, also used products. This means that the regulations cover an increasingly broader range of solutions developed through research and development [1,2].

The new CPR is also significantly more extensive than the previous legislation, encompassing 96 articles and 11 annexes, reflecting the greater level of detail in the regulations and the expansion of manufacturers' obligations [1,6,7].

The primary goal of the regulation is to harmonize the rules for assessing and declaring the performance of construction products to ensure the smooth functioning of the internal market while maintaining a high level of security and transparency of information.

Another important element of the new regulations is the stronger link between technical requirements and environmental objectives and the gradual implementation of digital tools, including the digital product passport, which influences the design and documentation of new construction products [1].

Visual examples related to the CPR and the principles of the circular economy in construction are presented in Figure 1.

Figure 1. Visual examples related to CPR and the principles of the circular economy in construction: 1) modular building element, 2) building material recycling symbol, 3) digital product passport concept, 4) neutral building materials ready for assembly or recycling. [Source: Generated using artificial intelligence]

2.1. Key changes from CPR6 305/2011

The new CPR 2024/3110 regulation introduces a number of changes that directly impact the way construction products are designed, tested, and marketed in the European Union. Of particular importance are those changes that impact the research and development phase.

One of the most important changes is the strengthening of the harmonized principles for assessing product performance. The new CPR aims to achieve greater consistency and transparency in the description of performance characteristics, which is intended to facilitate product comparison and their free circulation on the EU market. This requires a clearer link between design solutions and regulatory requirements [8].

Another significant change is the increased emphasis on environmental aspects. The new regulations strongly emphasize the need to limit the negative impact of construction products on the environment, which translates into the need to consider issues such as raw material selection, product durability, and reusability. The new regulation allows the use of the requirements of the EN ISO 14024 ecolabel standard to confirm compliance with minimum environmental sustainability requirements. At the same time, the scope of assessment has been expanded to include new essential environmental characteristics, not included in the previous regulation.

The essential environmental characteristics that will ultimately need to be declared include:

1. Impacts of climate change (global warming):
   - Global warming potential (GWP) over the entire life cycle;
   - Emissions related to fossil fuel use;
   - Emissions related to biogenic carbon;
   - Effects of land use change (including impacts).

2. Other environmental impacts:
   - Ozone depletion potential;
   - Soil and water acidification;
   - Water eutrophication in freshwater and marine waters;
   - Ground-level ozone formation;

- Abiotic resource depletion: minerals and metals;
- Water resource depletion rate.

3. Other characteristics:
   - Particulate matter: Dust emission;
   - Ionizing radiation: Effects on human health;
   - Ecotoxicity: Effects on freshwater;
   - Toxic effects on the human body (carcinogenic): Health effects;
   - Toxic effects on the human body (other than carcinogenic): Health effects.

For manufacturers and researchers, this means considering life cycle analysis (LCA) at the product design stage, not just during commercialization. From the academic perspective, this opens up a vast research field: LCA methods, eco-design, and carbon footprint assessment of building materials are becoming not only a fashionable topic but a direct regulatory requirement [7,8,14]. Figure 2 shows the life cycle of building materials.

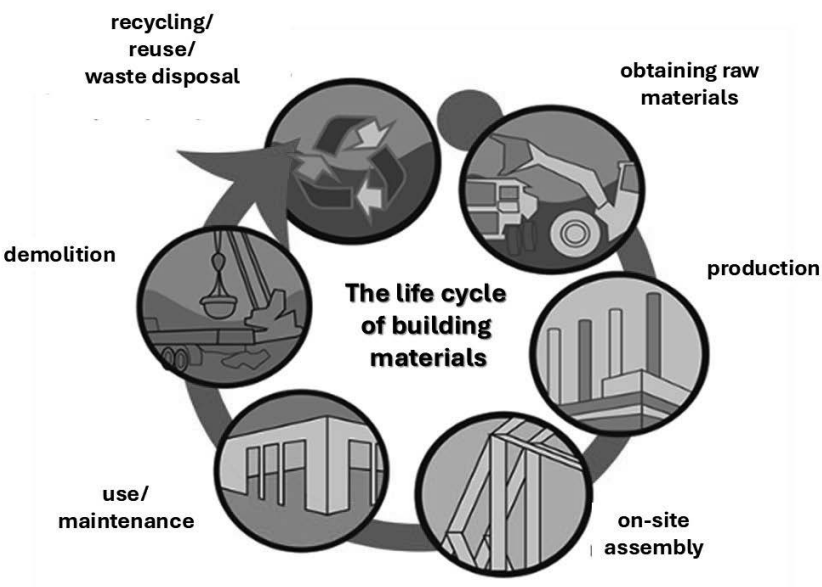

Figure 2. Life cycle of building materials [18].

One of the most innovative changes to the new CPR is the Digital Product Passport (DPP). Its introduction is intended to enable better access to technical, environmental, and operational information about construction products. The DPP is intended to be a key tool supporting the circular economy in construction, facilitating the recycling and reuse of building materials. In practice, the DPP is a digital "passport" for a product, accompanying it from production throughout its entire life cycle, to dismantling and recycling. It collects data on material composition, performance properties, assembly and dismantling instructions, maintenance requirements, and environmental impact [1,12,13,15].

A significant procedural change is the introduction of a new system for assessment and verification of performance – the 3+ system. Under this system, the manufacturer prepares an EPD (Environmental Product Declaration) according to the PN-EN 15804+A2:2020-03 standard [14], which is verified by a notified body. In the 3+ system, external verification

applies only to environmental data, not the product itself. Its essence is an approach based on modeling and input data, not solely on direct laboratory test results. For innovative products whose environmental properties are difficult to measure using traditional methods, the 3+ system opens up new assessment path possibilities [14,7].

System 3+ will be assigned to products by harmonized standards, specifically their Annexes ZA. The European Commission expects the 3+ system to become the standard system for products whose key performance characteristic to be declared is carbon footprint (GWP) or, more broadly, LCA data. In practice, this applies to, among others [7,8,14]:

- concrete and aggregate products,
- insulation materials (mineral wool, polystyrene, foams),
- wood and wood-based products,
- steel and aluminum products,
- many other categories where LCA/GWP becomes a key parameter.

Additionally, the changes involve revising the definitions. The definition of "construction product" has been expanded to include 3D-printed products. The concept of "construction work" has also been revised to include above-ground, underground, and water structures, including roads, bridges, and tunnels [1,16]. New definitions have been introduced: "repair," "maintenance," and "reclaimed product." The regulation's target groups have also been expanded. In addition to the traditional categories—manufacturers, importers, distributors, and authorized representatives—the new regulations explicitly introduce the category of order fulfillment service providers. This expansion stems from the increasing complexity of supply chains and the dynamic growth of e-commerce in the construction materials trade.

In summary, the key changes introduced by the new CPR make the process of introducing construction products to the EU market more complex. Manufacturers must consider technical, environmental, and information requirements early in the development of a new product, which influences research planning and product development strategies.

3. PERSPECTIVE OF RESEARCH AND WORK ON NEW PRODUCTS

For the scientific community involved in materials engineering and construction, the new CPR is a document of direct practical importance. It defines the requirements that a newly developed product must meet before it can be introduced to the European market.

3.1. Environmental aspect

Life-cycle assessment (LCA), carbon footprint, recycled content, disassembly and reusability – all these parameters, previously considered voluntary additions to documentation, are gaining regulatory importance. Scientists developing new building materials will need to conduct these analyses in parallel with characterizing mechanical, thermal, and fire properties [7,8,14,5,15].

3.2. Digital Product Passport

The digital product passport (Fig. 3) creates a new area of information requirements.

Already at the research stage, it is worth designing the product data structure so that it is ready to feed into the DPP system. Integration with BIM (Building Information Modeling - a digital building model) means that laboratory data must increasingly be made available in interoperable formats that enable automatic reading by computer systems [12,15].

Figure 3. Symbolic illustration of a digital product passport.[Source: Generated using artificial intelligence]

3.3. 3D printed products

Including 3D-printed products in the definition of a construction product sends a clear regulatory signal to the growing field of 3D printing in construction. Although detailed standards for this product category are still being developed, the mere fact that they are included in the scope of the CPR opens a formal path to certification and market access [1,16].

3.4. Recycled and remanufactured products

New definitions and the possibility of marketing used products after dismantling provide a framework for research into the reuse of building materials. This is an area of growing interest from both industry and EU policy, and is particularly important for academic centers conducting research on the recycling of concrete, steel, building ceramics, and thermal insulation materials [5,15].

4. IMPLEMENTATION SCHEDULE

The implementation schedule for the new CPR is crucial for the construction products market. The regulation entered into force on 7 January 2025, and full application of most provisions began on 8 January 2026, replacing CPR 305/2011, some of whose articles remain in a transitional period until 2040. Phased implementation allows for the development of new harmonized standards, adaptation of documentation and assessment processes by manufacturers, and preparation of notified bodies for verification. Application of the new CPR requirements depends on the availability of standards for specific product groups; until then, the provisions of the existing CPR apply, which could take up to 15 years, although most new standards will appear within 3-5 years [2].

SUMMARY

Regulation (EU) 2024/3110 introduces significant changes to the way construction products are introduced to the European Union market, directly impacting the process of their design, testing, and preparation for sale. The new CPR emphasizes the need to consider regulatory, environmental, and information requirements from an early stage of product development.

The growing importance of research, data analysis, and an interdisciplinary approach to the design of construction products fosters collaboration between the scientific community and industry. The new CPR identifies areas where academic knowledge can be directly applied in practice.

BIBLIOGRAPHY

[1] Regulation (EU) 2024/3110 of the European Parliament and of the Council of 27 November 2024 laying down harmonised rules for the marketing of construction products and repealing Regulation (UE) nr 305/2011, Dz.U. UE L 2024/3110.
[2] Regulation (EU) No 305/2011 of the European Parliament and of the Council of 9 March 2011 laying down harmonised conditions for the marketing of construction products.
[3] European Commission, Evaluation of the Construction Products Regulation (CPR), 2019.
[4] Ministry of Development and Technology, Placing construction products on the market – revision of regulations, 2024.
[5] PARP – Centrum Rozwoju MŚP, analiza CPR 2024/3110.
[6] Website: www.nowycpr.pl
[7] Polish Standard PN-EN ISO 14040:2009/A1:2021-03 "Environmental management - Life cycle assessment - Principles and structure".
[8] Polish Standard PN-EN ISO 14044:2009/A1:2018-05 "Environmental management -- Life cycle assessment -- Requirements and guidelines".
[9] European Commission, Digital Product Passport – Ecodesign for Sustainable Products Regulation (ESPR), 2022–2024.
[10] European Commission, Circular Economy Action Plan, 2020.
[11] Polish Standard PN-EN 15804+A2:2020-03 "Sustainability of construction works - Environmental product declarations - Basic principles for the categorization of construction products".
[12] Pomponi F., Moncaster A., Circular economy for the built environment, Journal of Cleaner Production, 2017.
[13] Website: http://mieszkajenergooszczednie.pl

TalentDetector

7th-9th June 2026
Gliwice-Brenna, Poland

DEPARTMENT OF ENGINEERING MATERIALS AND BIOMATERIALS
FACULTY OF MECHANICAL ENGINEERING
SILESIAN UNIVERSITY OF TECHNOLOGY

INTERNATIONAL STUDENTS SCIENTIFIC CONFERENCE

Mechanical properties and corrosion resistance of Ti6Al4V alloy

Norbert Klęk, Marek Opiela[a], Monika Kciuk[a]

[a] Silesian University of Technology, Faculty of Mechanical Engineering, Department of Engineering Materials and Biomaterials
email: marek.opiela@polsl.pl

Abstract: This article presents the results of research into the mechanical properties and corrosion resistance of the Ti6Al4V alloy in a high-salinity environment. Corrosion tests were conducted using gravimetric and potentiodynamic methods. To determine mass loss, some of the prepared samples were placed in a 35% NaCl solution. Other samples were exposed to a 5% salt spray in a salt spray chamber. The mechanical properties of the tested alloy were evaluated using a universal testing machine. The conducted research showed that the Ti6Al4V alloy possesses high mechanical properties and very good corrosion resistance in an atmosphere of concentrated NaCl solutions.

Keywords: mechanical properties, corrosion resistance, Ti6Al4V alloy

1. INTRODUCTION

The corrosion resistance of metals is a critical factor affecting the performance and lifetime of manufactured products, particularly those exposed to aggressive environments. Corrosion resistance should be taken into account during the design phase, e.g., in electronic circuits, where corrosion of the track can cause a circuit break, or in structures operating under load, where corrosion leading to a reduction in the effective cross-sectional area of their components can result in unexpected failures. Titanium alloys constitute a structural material with very good mechanical properties (at both low and high temperatures) characterized by a favorable strength-to-density ratio, very good corrosion resistance, and good biocompatibility. These alloys are used in industries such as the military, aviation, nuclear, chemical, medical, marine, and aerospace sectors. The primary raw material for the production of titanium alloys is titanium sponge, obtained mainly in the Kroll process, which is based on the reduction of titanium tetrachloride (TiCl4) with liquid magnesium [1, 2]. Titanium alloys are most commonly classified based on their structure, which depends significantly on the amount of additives introduced. Titanium alloys can be classified into those with α, α + β, and β structures. The α phase, with a hexagonal close-packed structure, transforms at 882°C into the β phase, characterized by a body-centered cubic structure. The Ti6Al4V alloy, which have an α + β structure, account for approximately 60% of global titanium alloy production [3, 4]. Despite many desirable properties, this alloy exhibits high reactivity with oxygen, hydrogen, and nitrogen at increased temperatures, leading

to the formation of compounds that cause its fragility. Chemical affinity for these gases is also problematic during heat treatment or plastic deformation, which requires these operations to be performed in a protective gas atmosphere. Despite its good biocompatibility, which makes it a common choice for implants, the Ti6Al4V alloy contains vanadium. When released, this element migrates into human tissues, causing cytotoxic effects and potentially leading to inflammation, and in the long term, lymphadenopathy. For this reason, research has begun on replacing harmful vanadium with other elements such as niobium, tantalum, zirconium, or chromium. The Ti6Al4V alloy exhibits excellent passivation properties, creating a passive layer on the material's surface consisting of titanium dioxide up to 10 nm thick, which protects the material from reacting in aggressive environments [4, 5]. If the protective layer is damaged, Ti ions react spontaneously with the oxygen present almost immediately, and the coating is rebuilt, reforming a tight barrier [6]. The effect of tribocorrosion is also particularly significant for loaded titanium alloy components; this involves the synergistic wear of the material through both electrochemical and mechanical processes, leading to accelerated material degradation. It occurs, for example, in joint implants during their use. This results in accelerated destruction of the passive layer through abrasion and the release of fine oxide particles, which have adverse consequences for human tissues. This effect can also be observed in pipe components, heat exchangers, and connecting elements operating in a marine environment, where water with increased salinity, combined with mechanical vibrations at the contact point between two components, destroys the passive layer formed on the Ti6Al4V alloy. Faster material wear in this case is also due to pitting corrosion caused by the action of chloride ions. The nature of the damage resulting from tribocorrosion is strongly dependent on the magnitude of the load. At low loads, mechanical damage is minor, and destruction through the abrasion of the passive layer becomes dominant. In contrast, under high loads, mechanical wear begins to dominate, leaving no time for pitting corrosion to develop [5, 7].

Nowadays, there has been a significant increase in the production of Ti6Al4V alloy components manufactured using selective laser melting (SLM). This technology allows for the production of components with complex geometries while using significantly less raw material, which has greatly expanded the possibilities for implant manufacturing. However, these components require heat treatment, as the material immediately after fabrication consists mainly of the needle-like martensitic α' phase, which is very hard but brittle at the same time. Therefore, stress-relief annealing and aging are applied to reduce residual stresses and improve mechanical properties. The Young's modulus of a Ti6Al4V alloy print is approximately 110 – 130 GPa. Compared to the Young's modulus of human bone, which ranges of 10 – 30 GPa, this is a significantly different value, which can lead to weakening of the bone tissue. The consequence of this effect is loosening of the implant, which ultimately makes it necessary to perform additional surgeries. To ensure that human joints respond properly to the implant, the porosity and microstructure of the implant are strictly modified [8].

The aim of this study is to evaluate the mechanical properties and corrosion resistance of the Ti6Al4V alloy in a high-salinity environment (35% NaCl solution and 5% salt spray).

2. MATERIALS AND METHODS

The research material consisted of a Ti6Al4V alloy containing 0.012% C, 0.118% Fe, 6.39% Al, and 4.12% V (with the remainder being Ti), supplied in the form of a 10-mm-diameter rod [9]. A static tensile test was performed on a Zwick Z100 universal testing machine using samples with a diameter of 6 mm and a measured length of 30 mm [10]. The strain rate was 0.008 s^{-1}. The neck diameter of the scrap at the fracture point and the measured length after the test were measured with a caliper to determine narrowing and elongation.

To conduct corrosion resistance tests, 12 samples with a length of 5 mm were prepared. Sample preparation included grinding and polishing the surfaces. The samples were then placed under a light microscope to take photographs of the surface before the corrosion tests and immediately after their completion. The photographs were taken at magnifications ranging from 25x to 100x.

The samples were degreased with acetone and then dried. The mass of the prepared samples was measured on an analytical balance with an accuracy of 0.0001 g. Three samples were placed in a laboratory vessel in a 35% NaCl solution at a constant temperature of 20°C. After 336 hours (14 days), the samples were removed, rinsed with water, and weighed again to determine the loss in mass.

The next three samples were prepared for accelerated corrosion testing in a salt spray chamber. The test was conducted using an ASCOT CC450iP instrument in accordance with EN ISO 9227:2012 [11]. The samples were subjected to continuous spraying with a 5% NaCl solution for 1,008 hours (42 days) at a constant temperature of 35°C and 100% humidity. After the test was completed, the samples were rinsed with water, dried, and weighed again. The speed of corrosion in both cases was evaluated based on the calculation of mass loss (Vc) using the following equation [12-14]:

$$V_c = \Delta m/(S \cdot t) \tag{1}$$

where: Δm – the difference in sample mass before and after corrosion test, S – sample surface area, m^2, t – time of corrosion test, day.

Next, the average of cross-sectional loss rate (V_p) was calculated, which represents a 1 mm of reduction in cross-sectional dimension of the sample over one year. The average corrosion rate was determined using following equation:

$$V_p = (V_c \cdot 365)/(1000 \cdot \rho) \tag{2}$$

where: ρ – density.

The potentiodynamic tests were performed using an ATLAS 0531 potentiostat-galvanostat. Before the tests began, the surface of the samples, with an average area of 78.5 mm^2, was cleaned with ethyl alcohol and then mounted in the device. The working electrode (WE) was the sample of the analysed alloy, and the reference electrode (RE), immersed in the conductive solution, was an Ag/AgCl electrode. The corrosive environment was a 35% NaCl solution with a volume of 160 ml.

After the gravimetric test, the samples were again placed under a ZEISS AXIO OBSERVER Z1M light microscope to observe changes in the alloy's surface structure. This made it possible to determine the characteristics of the corrosion damage resulting from prolonged contact with the aggressive medium.

3. RESULTS

The tensile stress-strain curves are presented in fig.1, while the detailed results of the mechanical property tests for the Ti6Al4V alloy are presented in table 1. The tensile test was performed to determine the key mechanical and plastic properties of the Ti6Al4V alloy. Due to the inability to determine a noticeable yield point, a conventional yield point ($R_{p0.2}$) was determined. The average value of the conventional yield point ($R_{p0.2}$) – obtained from three tests – was 686 MPa. Meanwhile, the average tensile strength (R_m) for the tested alloy was 1031 MPa. After exceeding the tensile strength, a decrease in stress values was observed. This effect was associated with the formation of a neck, where the samples finally broke. The elongation of the tested alloy reached an average value of 15.36%, and the average reduction in area reached a value of 48.72%.

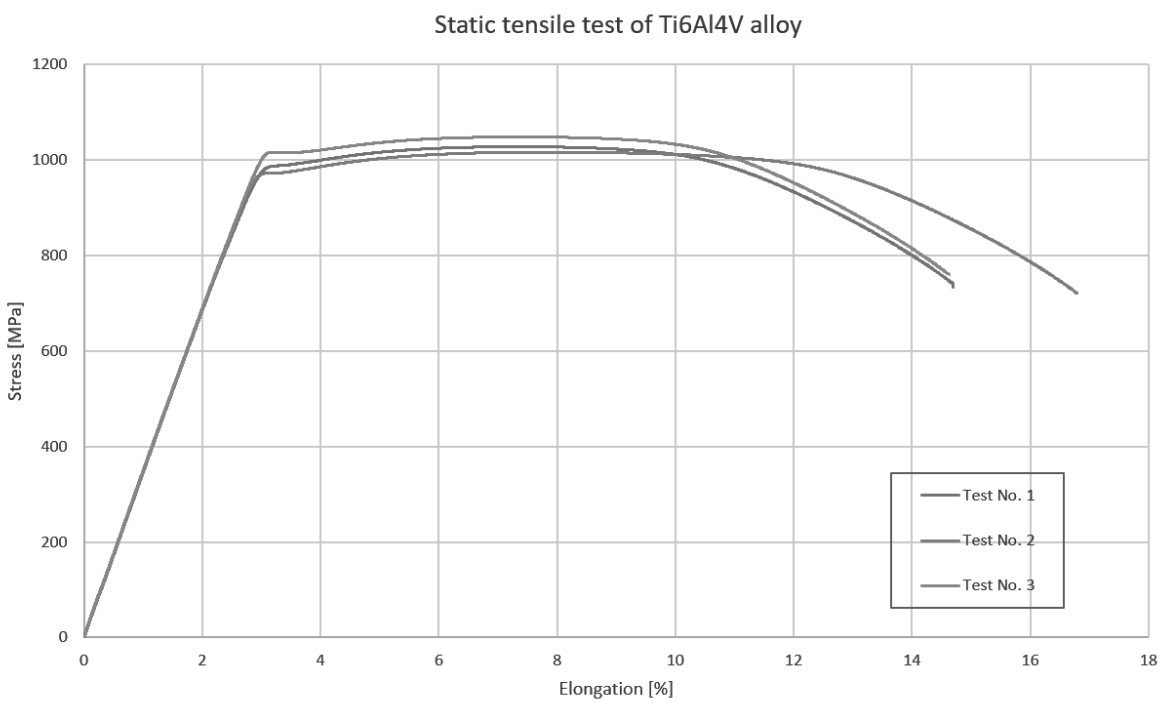

Fig 1. Tensile test curves for Ti6Al4V alloy samples

Table 1. Mechanical properties of the Ti6Al4V alloy

No.	$R_{p0.2}$, MPa	R_m, MPa	$R_{p0.2}/R_m$	A, %	Z, %
1	685	1028	0.67	14.67	45.12
2	685	1016	0.67	16.79	54.21
3	688	1048	0.66	14.62	46.83
Σ	**686**	**1031**	**0.67**	**15.36**	**48.72**

The results of the gravimetric test, expressed as the corrosion velocity i.e., the decrease in the effective cross-sectional area of the sample in mm/year for samples exposed for 14 days to a 35% NaCl solution, are summarized in Table 2.

Table 2. Results of gravimetric analysis.

Sample number	Difference in mass before and after immersion in the 35% solution of NaCl, g	V_c, $g/m^2 \cdot day$	V_p, mm/year
1	0.0001	0.022736	0.001873
2	0.0001	0.022736	0.001873
3	0.0001	0.022736	0.001873

The research showed a mass loss of 0.0001 g for each of the three samples. After filling in the required data for equations 1 and 2, an average corrosion rate of 0.001873 mm/year was obtained. The result was then compared with the data in Table 3, which contains a corrosion resistance scale.

Table 3. Corrosion resistance scale for metal and their alloy [15]

Corrosion resistance group		**Corrostion resistance degree**	**Corrostion rate, V_p, mm/year**	**Corrosion durability, Tr, mm/ year**
definition	**class**			
completely resistant	I	1	> 0.001	not specified
highly resistant	II	2	0.001 ÷ 0.005	not specified
		3	0.005 ÷ 0.01	
resistant	III	4	0.01 ÷ 0.05	10 ÷ 100
		5	0.05 ÷ 0.1	
less resistant	IV	6	0.1 ÷ 0.5	1 ÷ 10
		7	0.5 ÷ 1.0	
low resistant	V	8	1.0 ÷ 5.0	0.1 ÷ 1.0
		9	5.0 ÷ 10.0	
non-resistant	VI	10	< 10.0	> 0.1

The tested material ranks in corrosion resistance group 2, which makes it highly resistant to corrosion caused by environments with increased salinity.

After completing the salt spray test and cleaning the samples, the surface condition was analyzed using a light microscope (Fig. 2).

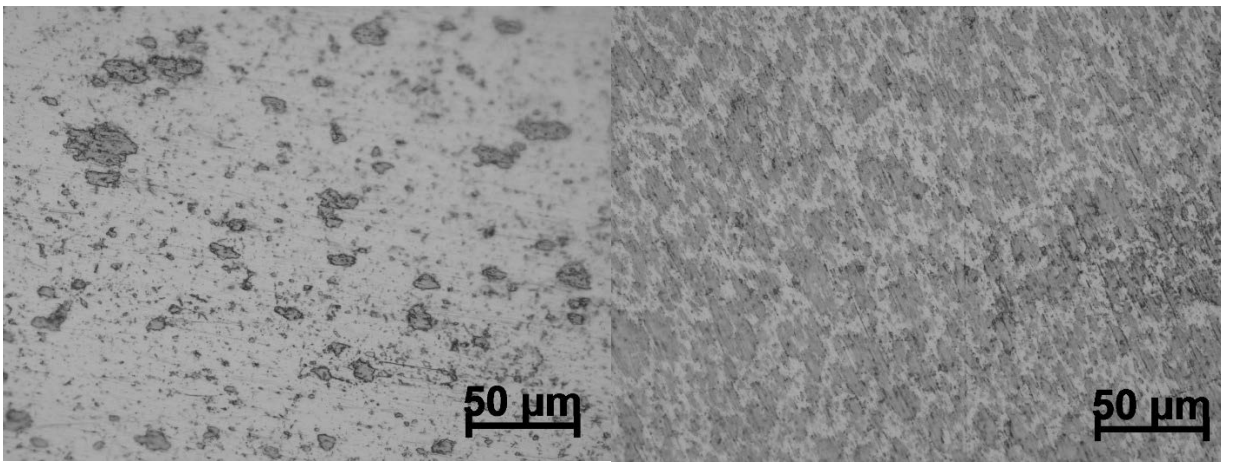

Fig 2. Surface structure of Ti6Al4V alloy after a 1008 hour test in salt spray chamber

No visible corrosion products were observed on the surface of the samples, which signifies very good corrosion resistance. After testing, the samples were weighed, and the data were then substituted into equations 1 and 2. The results of the calculations are presented in table 4.

Table 4. Results of the salt chamber test

Sample number	Difference in mass before and after immersion in the salt spray chamber, g	V_c, $g/m^2 \cdot day$	V_p, mm/year
5	0.0001	0.007579	0.000624
6	0.0001	0.007579	0.000624
7	0.0001	0.007579	0.000624

A comparison of the results obtained (table 4) with the data in Table 3 indicates that the Ti6Al4V alloy is completely resistant to corrosion.

The potentiodynamic test made it possible to determine the important parameters of the tested material's corrosion resistance presented in table 5.

Table 5. Results of the potentiodynamic test

Sample number	E_{kor}, V	I_{kor}, A/cm^2	R_p, Ω	V_p, mm/year
8	-0.278	$9.011 \cdot 10^{-10}$	$9.925 \cdot 10^{8}$	$7.678 \cdot 10^{-6}$
10	-0.244	$6.708 \cdot 10^{-9}$	$1.107 \cdot 10^{8}$	$5.716 \cdot 10^{-5}$
Average	-0.261	$3.8045 \cdot 10^{-9}$	$5.516 \cdot 10^{8}$	$3.2419 \cdot 10^{-5}$

Parameters such as E_{kor} – corrosion potential, I_{kor} – current density, and R_p – corrosion resistance determine the dynamics of the processes occurring on the material's surface. The average corrosion potential value was -0.261 V, which with a current density of $3.8045 \cdot 10^{-9}$ A/cm^2 and a resistance of $5.516 \cdot 10^{8}$, indicates the material's high electrochemical stability. The determined average corrosion rate of $3.2419 \cdot 10^{-5}$ mm/year allows the Ti6Al4V alloy to be classified as completely resistant to chloride ions under the tested conditions. The results of the potentiodynamic test also include graphs of the potential as a function of time (Fig.3a) and the current density as a function of potential (Fig.3b).

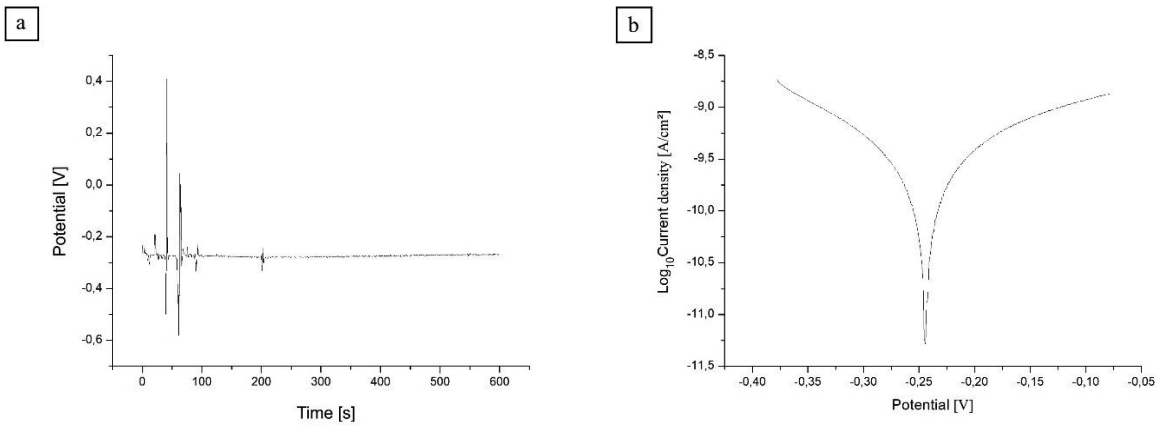

Fig 3. Graph of correlation between: a) potential and time, b) current density and potential

Figure 3a. shows significant fluctuations of the potential in the early seconds of the test, suggesting alternating changes in the corrosion rate and the growth of the passive layer until a state of equilibrium was reached, in which the oxidation and passivation reactions balanced each other out. Figure 3b. shows a graph of current density versus potential. This allows, among other things, the corrosion potential to be determined from the point of lowest current density, or the corrosion current density to be calculated using the Taffel extrapolation method. There is a clear coincidence between the results in table 5 and the graphs shown in fig. 3.

4. CONCLUSIONS

The static tensile test showed that the Ti6Al4V alloy retains a very smooth transition from the linear-elastic to the plastic range, which is a characteristic feature of titanium alloys with an α+β structure and leads to the determination of a conventional yield strength. This also means that the material's hardening is minimal. The strength parameters obtained for the Ti6Al4V alloy (a conventional yield strength of 686 MPa and a tensile strength of 1031 MPa) are similar to the strength properties of 42CrMo4 steel, but with a density that is nearly half as low (4.42 g/cm^3). This makes the Ti6Al4V alloy a very attractive structural material where the weight of the structure is a critical factor.

Tests involving continuous exposure to an atmosphere with increased salinity have demonstrated that the Ti6Al4V alloy is highly corrosion-resistant. This is evidenced by corrosion results obtained using gravimetric and potentiodynamic methods, as well as the results of accelerated chamber tests. This is confirmed by the absence of noticeable corrosion products (fig. 2). The correlations shown in fig. 3 indicate that the Ti6Al4V alloy is a material with very good passivation ability, forming a thin, tight film on the surface that protects the material from corrosion. The corrosion potential of the Ti6Al4V alloy, which is -0.261 V, is also an indicator of good corrosion resistance, and the low corrosion current density of $3.8045 \cdot 10^{-9}$ indicates a low intensity of corrosion processes occurring on the alloy's surface.

BIBLIOGRAPHY

1. N. Senthilkumar, G. Perumal, S. Sivaguru, S. Anandhakumar, Optimization of duplex heat treatment settings with the MOORA-PCA technique to customize the mechanical and wear response of Ti6Al4V alloy, Tribology International 192 (2024) 109232
2. Li Kaihua, Sheng Zhuo, Zhu Fuxing, Li Jun, Ma Zhanshan,Li Zhanjun, Yang Xin, Liu Ying, Identification of source and control of oxygen and nitrogen impurities in Kroll process for preparation of Ultra-soft titanium sponge, Journal of Materials Research and Technology 36 (2025) 3104–3111
3. Seyed Alireza Etesami, Behzad Fotovvati, Ebrahim Asadi, Heat treatment of Ti-6Al-4V alloy manufactured by laser-based powder-bed fusion: Process, microstructures, and mechanical properties correlations, Journal of Alloys and Compounds 895 (2022) 162618
4. Michał Tarnowski, Wpływ parametrów technologicznych procesu azotowania jarzeniowego na strukturę i właściwości warstw otrzymanych na stopie tytanu Ti6Al4V, praca dyplomowa, Politechnika Warszawska, Wydział Inżynierii Materiałowej Warszawa, lipiec 2010
5. Saman Nikpour, Ren´e Daniel Pütz, Ayush Khurana, Sina Matin, Anna Neus Igual Muno, Stefano Mischler, Yolanda S. Hedberg, Tribocorrosion of additively manufactured and wrought Ti6Al4V in a saline environment, Wear 586 (2026) 206440
6. Ladislav Vrsalović, Senka Gudić, Antonia Talijančić, Jelena Jakić, Jure Krolo, Iman Danaee, Corrosion Behavior of Ti and Ti6Al4V Alloy in Brackish Water, Seawater, and Seawater Bittern, Corros. Mater. Degrad. 2024, 5, 641–656.
7. Qi Feng, Pengwei Ren, Hao Liu, Jianzhang Wang, Quande Li, Yanhua Shi, Effect of load on the fretting tribocorrosion behavior of Ti6Al4V in seawater, Journal of Materials Research and Technology 36 (2025) 8576–8590
8. Anh Tai Le, Van Huan Dau, Tien Dat Hoang, H. Nguyen-Xuan, Heat treatment of Ti6Al4V alloy fabricated by selective laser melting (SLM) for medical implant: A comprehensive review, Journal of Materials Research and Technology 36 (2025) 7643–7665
9. ASTM B265-13 Standard Specification for Titanium and Titanium Alloy Bars, and Brillets.
10. PN-EN 10002-1:2004 Metale – próba rozciagania – Część 1:Metoda badania w temperaturze otoczenia.
11. EN ISO 9227:2012 Badania korozyjne w sztucznych atmosferach – Badania w rozpylonej solance.
12. Glinicka. A, Imiełowski. S, Ajdukiewicz. C, Influence of uniformly distributed corrosion on the compressive capacity of selected thin – walled metal columns, Procedia Engineering 2015, t. 111, 262–268.
13. Paik J. K, Lee J. M. Park J. H, Hwang J.S, Kim C.W, Time – variant ultimate longitudinal strength of corroded bulk carriers. Marine Structures 2003, t. 16, 567–600.
14. Fakuda M, Fujii K, Nakayama T, Matsui S, An evaluation method for the remaining strength of plate girder with local corrosion under sleepers, Procedia Engineering 2011, t. 14, 2285–2293.
15. PN-H-04608: 1978. Metal corrosion – the scale of resistance of metals to corrosion (in Polish)

TalentDetector

7th-9th June 2026
Gliwice-Brenna, Poland

DEPARTMENT OF ENGINEERING MATERIALS AND BIOMATERIALS
FACULTY OF MECHANICAL ENGINEERING
SILESIAN UNIVERSITY OF TECHNOLOGY

INTERNATIONAL STUDENTS SCIENTIFIC CONFERENCE

Sinterhardening of PM Cr-Mo prealloyed steels with hybrid alloying powders

Dmitriy Koblik, Miroslava Ťavodová, Richard Hnilica

Technical University in Zvolen, Faculty of Technology, Department of Manufacturing Technologies and Quality Management
email: xkoblik@is.tuzvo.sk, tavodova@tuzvo.sk

Abstract: In powder metallurgy (PM), there are several methods of introducing alloying elements into PM ma-terials in order to adjust the alloying element content. Each alloying method has its advantages and disadvantages. Master alloys (MA), powders with a high content of typically a few alloying elements, can be added in small amounts to the base powder, especially to introduce oxygen-sensitive elements such as Cr, Mn and Si. In addition, MA can be designed to form a liquid phase during the sintering process to improve the distribution of alloying elements in the material and accelerate homogeniza-tion. In this study, such MA were combined with pre-alloyed base powders to form hybrid alloy mix-tures with the aim of improving the hardenability of the material during sinterhardening. The hybrid alloys were compared with mixtures of MA and pure iron as a reference material. The hardenability during sinterhardening of all materials was determined by generating CCT diagrams recorded at dif-ferent cooling rates. The results were verified by HV30 and HV0.1 hardness measurements.

Keywords: sinterhardening, prealloyed material, master alloy (MA), macrohardness, microhardness, CCT diagram

1. INTRODUCTION

Industrial trends have significantly increased the demands on mass production of parts over the past decade. Cost reduction, high quality standards for millions of manufactured parts, such as high precision, mechanical properties, environmental requirements have contributed to the accelerated development of powder metallur-gy. For the further expansion of PM into new industrial areas and applications, materials with improved properties are needed. One such method is the sinterhardening process. The sinterhardening process signifi-cantly simplifies the production of parts, as sintering and hardening are integrated into one cycle. This solu-tion achieves the controlled formation of a martensitic structure that occurs during cooling after sintering. As a result, hardness and mechanical properties are improved. The process uses special sintering furnaces in which a well-designed controlled cooling zone is applied. Thanks to this, it is no longer necessary to perform a separate thermomechanical hardening procedure, which eliminates the need to design additional operations and thus minimizes costs and production time [1]. Another major advantage is the achievement of high di-mensional

accuracy of components. Since the entire thermal transformation occurs within a single operation, the risk of thermal deformation and subsequent distortion of the part is significantly reduced. This accuracy is particularly valued in areas where tolerances are crucial – for example, in the automotive, aerospace or military industries. In addition, automated process integration ensures consistency of the resulting properties of the parts, which is important in terms of the quality and reliability of the final products [1,2].

The energy efficiency of sinterhardening is another significant benefit. Compared to traditional methods, where it is necessary to perform separate heat treatments (for example, heating, rapid cooling in oil, washing and subsequent tempering). Sinterhardening can reduce energy consumption by up to 60%. Manipulating the temperature profile directly during sintering reduces not only energy consumption, but also the need for addi-tional processing of parts, which also reduces operating costs. This environmentally friendly approach is also beneficial for manufacturers who are striving for more sustainable production [3].

Sinterhardening allows for improved mechanical properties of parts. The resulting martensitic structure provides a combination of high hardness and wear resistance, which is especially important for components exposed to high mechanical stress. From a safety point of view, this approach is particularly advantageous in applications where components are exposed to impacts or dynamic stress. Thanks to the optimized process, minimal variability in properties between individual products is also ensured, which significantly contributes to the overall reliability and performance of the products [1,3,4].

The main limitation is the low cooling rate achieved during sinterhardening. In current industrial furnaces, cooling rates of 2-5°C.sec^{-1} can be achieved. In addition, as shown by Bocchini [4], the surface to volume ratio also plays an important role, since the factor determining the cooling rate is the heat transfer between the part and the atmosphere. The thermal conductivity in the part itself is usually fast enough to ensure relatively uni-form cooling (and therefore transformation) in the part; this is an advantage since most PM parts have com-plex shapes and therefore high surface to volume ratios and usually thin walls [5].

To compensate for the slow cooling compared to oil quenching, the alloying system has to be adjusted accordingly, requiring a higher content of alloying elements. Special grades of PM steel have been developed for sintering, for example based on pre-alloyed Fe-Mo powder with diffusion-bonded Cu or Cu + Ni [2,6]. These alloying elements are often used in PM due to their low affinity for oxygen. Therefore, any oxides in “green parts” can be easily reduced during sintering and the risk of oxygen capture from the sintering atmos-phere is also minimal. However, these elements are expensive and Ni is classified as carcinogenic, as result elements such as Cr are increasingly considered advantageous, and pre-alloyed Cr and Cr-Mo powders are now commercially available at a reasonable price [2,7]. These powders have more precise requirements regard-ing the chemical composition and the quality of the sintering atmosphere, but this is now feasible and this class of materials has also been shown to be suitable for sintering [8], at least if a martensitic structure is the desired result. Carbon control is also essential for sintered steels and is more difficult than for metallic steels, especially for sintered steels alloyed with elements with high oxygen affinity such as Cr, Mn and Si, which makes carbon loss during sintering a key issue. This is also true for high-temperature sintering, where deoxi-dation is greater but at the cost of higher carbon loss [9].

Unlike metal parts, in PM, not only the choice of alloying elements but also the alloying method is a pa-rameter that affects the properties of the final material. One way to add several alloying elements is to admix master alloys (MA). MA is a powder with a high alloying element content, which usually contains several ele-ments combined in one powder. It is a good

way to supplement oxygen-sensitive elements such as Cr, Mn and Si. In addition, MA can be designed to form a liquid phase during the sintering process to improve the distribution of alloying elements in the material and to accelerate homogenization. Master alloyed powders show a homogeneous distribution of alloying elements, but due to solution hardening, the powders are hard-er and therefore less compactable than pure elemental powders of each element [9,10]. It has been shown that it is difficult to sinterharden steels from most pre-alloyed powders under standard conditions without the admixture of additional alloying elements, except for powders with relatively high alloying element content, which multiplies the cost and the problem of compaction [11]. By implementing new automation techniques, such as high-pressure water atomization of the powder, it is now possible to produce MA powders containing Fe, Si, C, Cr and Mn with low oxygen content [12]. These MAs have been further modified to improve liquid phase formation, infiltration properties and alloying element content compared to previous studies [13].

2. MATERIALS AND METHODS

The article presents the results of sinterhardening of materials ASC100.29, Astaloy85Mo, AstaloyCrA, AstaloyCrM and Astaloy CrS with MA addition. The composition of the materials used is given in Table 1[15,16], the composition of the powder mixes is given in Table 2 [15,16]. The alloying elements were meas-ured using laser ablation mass spectrometry and inductively coupled plasma and the carbon content was de-termined by C-LECO measurements. The standard used for this measurement was the standard for steel pins 501-679 with a content of 0.799±0.011 wt. % carbon. The powders were mixed in a Turbula mixer for 10 minutes according to the standard industrial procedure. Rectangular pieces (10 x 7 x 4 mm) were cut from impact strength samples according to ISO 5754 [14], which were pressed at a pressure of 600 MPa and using Multical calibration oil. The pressings were isothermally sintered at 1 300°C for 1 hour under defined condi-tions in an electrically heated furnace with a gas-tight tubular retort under a high-purity argon atmosphere and cooled to room temperature in the exit zone of the furnace with water cooling at rates of 1.5 and 3.0 °C.sec^{-1}.

Table 1 Composition of basic materials [15,16]

Basic material	Composition wt. [%]					
	Fe	Si	Mn	Cr	Mo	C
ASC100.29	99.81	0.00	0.13	0.05	0.01	0.00
Astaloy85Mo	98.93	0.00	0.17	0.05	0.85	0.00
AstaloyCrA	98.01	0.03	0.13	1.80	0.03	0.00
AstaloyCrM	96.32	0.03	0.15	3.00	0.50	0.00
AstaloyCrS	98.82	0.03	0.15	0.85	0.15	0.00
H45	56.00	8.00	0.00	32.00	0.00	4.00
H46	48.00	6.00	42.00	0.00	0.00	4.00
H47	35.30	6.00	28.00	27.00	0.00	3.70
H166	56.10	7.50	33.00	0.00	0.00	3.4
H200	49.50	9.00	40.00	0.00	0.00	1.5

Table 2 Composition of powder mixes [15,16]

Powder mix	Composition wt. [%]					
	Fe	Si	Mn	Cr	Mo	C
ASC + 4%H45	97.89	0.39	0.13	1.09	0.01	0.49
ASC + 4%H46	97.83	0.21	1.46	0.05	0.01	0.44
ASC + 4%H47	97.49	0.32	0.88	0.82	0.01	0.48
Ast85Mo + 4%H45	96.89	0.38	0.17	1.24	0.83	0.49
Ast85Mo + 4%H46	97.23	0.24	1.23	0.05	0.81	0.44
Ast85Mo + 4%H47	96.50	0.34	0.94	0.91	0.82	0.49
AstCrA + 4%H45	96.31	0.47	0.13	2.60	0.03	0.46
AstCrA + 4%H46	96.15	0.31	1.44	1.65	0.03	0.42
AstCrA + 4%H47	95.45	0.44	1.03	2.58	0.03	0.47
AstCrM + 4%H45	95.01	0.44	0.15	3.49	0.47	0.44
AstCrM + 4%H46	94.91	0.28	1.07	2.87	0.48	0.39
AstCrM + 4%H47	94.26	0.45	0.91	3.48	0.46	0.44
Ast85Mo + 4%H166	96.39	0.32	1.44	0.03	0.84	0.69
Ast85Mo + 4%H200	96.34	0.35	1.72	0.02	0.86	0.71
AstCrS + 4%H166	96.53	0.31	1.45	0.84	0.13	0.74
AstCrS + 4%H200	96.20	0.36	1.73	0.85	0.13	0.73

3. RESULTS

The results of this study are presented in comparisons of Masters alloys (MA) combined with pre-alloyed base powders to form hybrid alloy mixtures and to improve the hardenability of the material during sinter-hardening. The hybrid alloys were compared with mixtures of MA and pure iron as a reference material. The hardenability during sinterhardening of all materials was determined by creating CCT diagrams recorded at different cooling rates. The results were verified by hardness measurements of HV30 and HV0.1.

3.1. Hardness

For the determination of hardness for materials with MA H45, H46 and H47, the HV30 and HV0.1 values were recorded to obtain both the hardness of the metal matrix and the “integral” or apparent hardness; the latter includes the effect of porosity. For materials with MA H166 and H200, only the HV30 hardness was evaluated.

For materials with MA H45, H45 and H46 additions, the results are shown in Fig. 1 and 2 [15]. For mate-rials with MA H166 and H200 additions, the results are shown in Table 3 [16]. For the microhardness meas-urements, 14 indentations per sample were evaluated. The shapes of the indentations were visually inspected to verify whether the pores influenced the indentation. If this was the case, a new measurement was per-formed at a different location.

For the inhomogeneous microstructure, 7 indentations were made in each of the different microstructural components. The microhardness values shown in the bar graphs in Fig. 2 are the average values of all indentations to give an idea of the inhomogeneity of the hardness using the standard deviation bar. As expected, the results are also confirmed by the CCT diagrams, the hybrid alloying technique leads to significantly better hardness values. At a cooling rate of 3 °C.sec^{-1}, H47 in combination with ASC100.29 iron powder forms a hard microstructure that can compete with samples prepared from pre-alloyed powder, although it showed a heterogeneous microstructure.

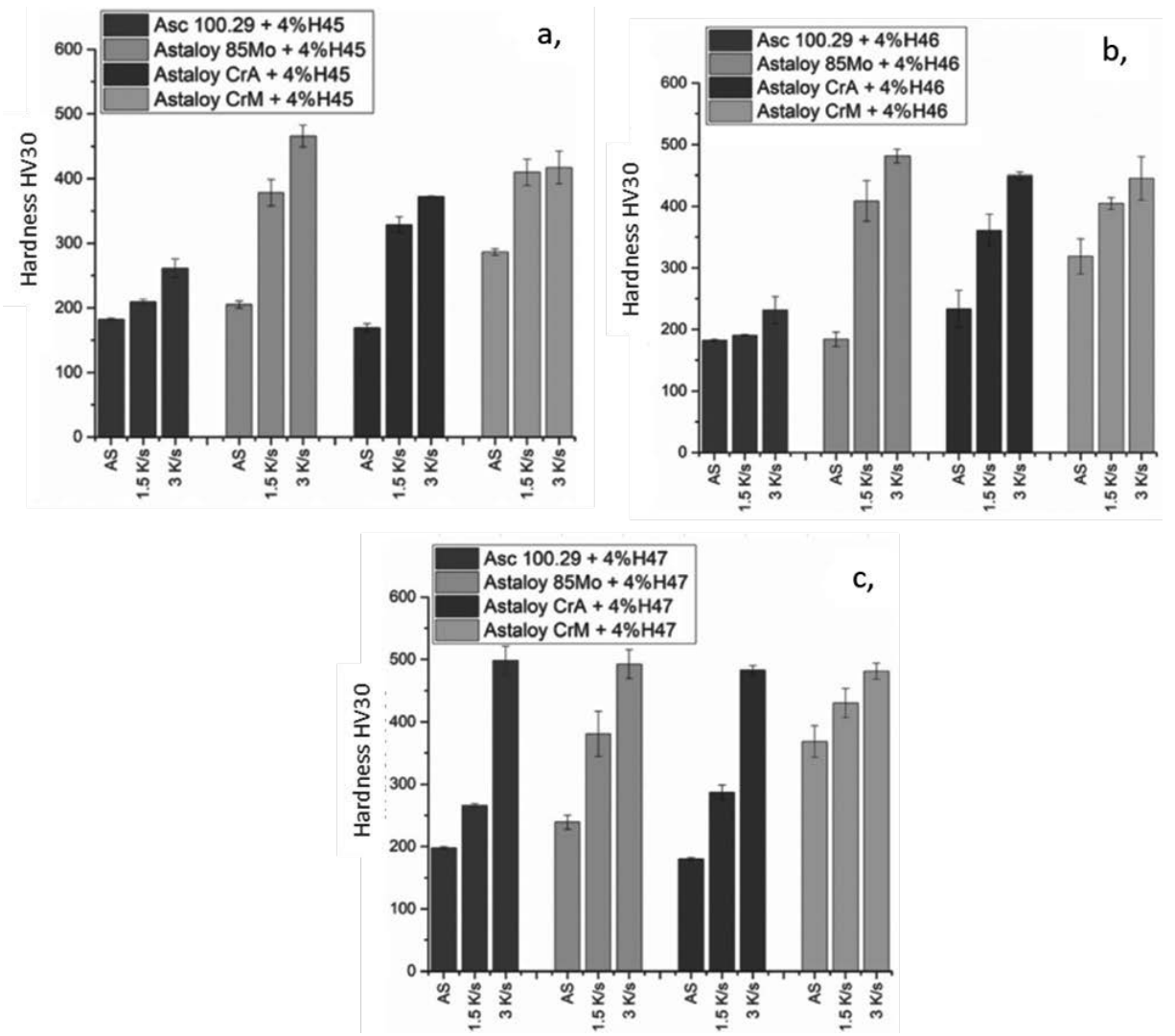

Figure 1. Macrohardness HV30 [15]

Surprisingly, the combination of MA + Astaloy85Mo achieved even higher hardness levels than MA + AstaloyCrM or AstaloyCrA. A possible explanation is that the heat treatment profile used for the samples, especially the authentication conditions, could be closer to the optimum for MA + Astaloy85Mo. This means that MA was originally designed for the combination with iron powder and the heat treatment conditions used were designed for the combination of MA + ASC100.29. The authentication temperature strongly de-pends on the

alloying elements [17] leading to the assumption that the pre-alloyed powders of AstaloyCrA and CrM containing Cr require a higher authentication temperature, while the base powder pre-alloyed only with Mo can be hardened well at lower temperatures.
AstaloyCrS and especially Astaloy85Mo show relatively high hardness already after sintering with a relative-ly slow cooling rate of approximately 25°C.min^{-1} (linearized). This suggests that the combination of Cr and Mo from the base powder with MA Mn and Si leads to better sintering.

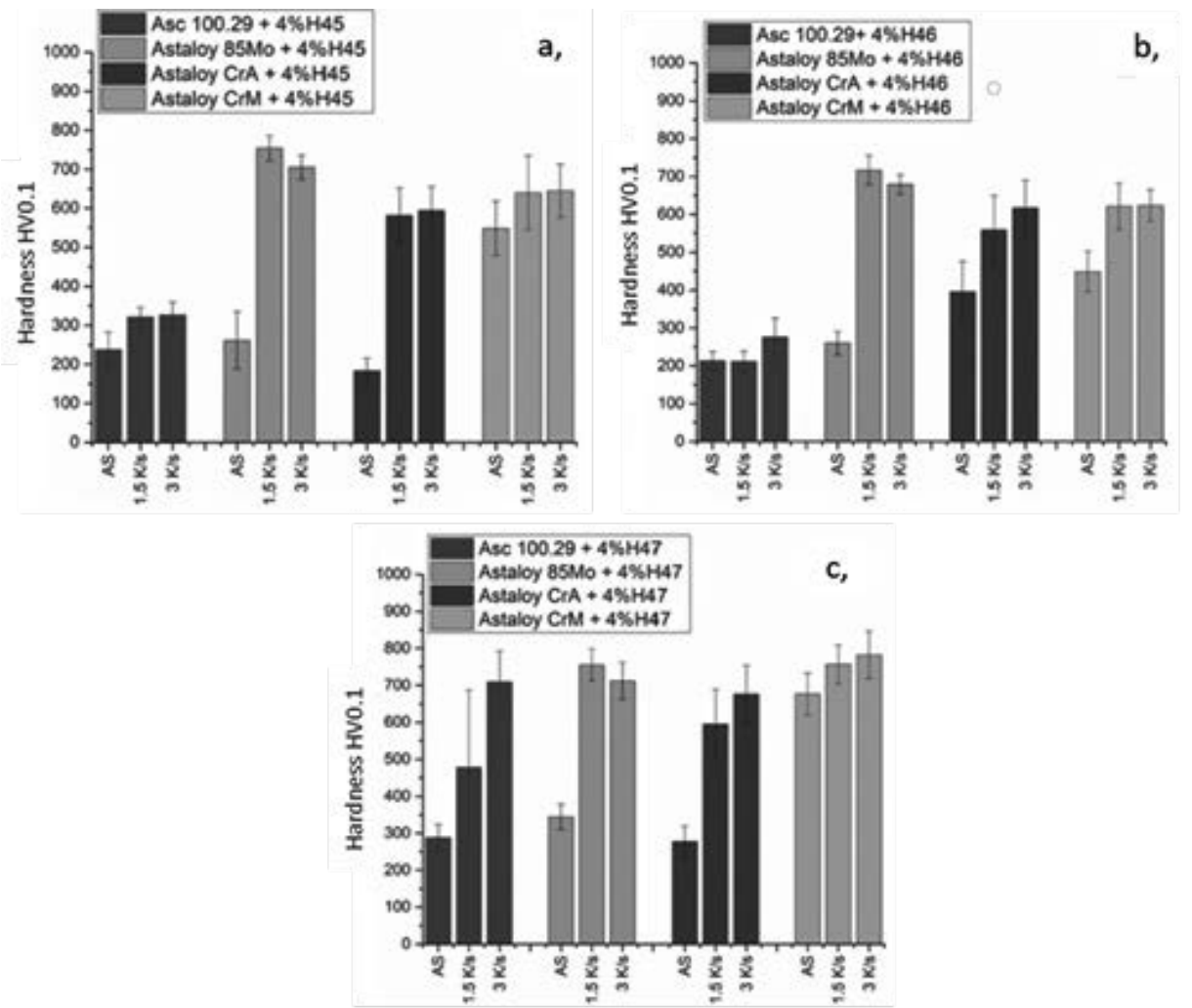

Figure 2. Macrohardness HV0,1 [15]

To verify the effect of actual sinter-ing, test bars austenitized for 30 minutes at 1100°C in N_2 atmosphere and gas quenched in a rapid cooling unit of the furnace were evaluated. The hardness values obtained confirm that the addition of MA significant-ly improves the sintering ability. The addition of MA leads to a significant increase in hardness even in the quenched state compared to the sintered state, from 290 – 340 to 500 – 540 HV30. Here too, Astaloy85Mo is slightly better, indicating that the combination of pre-alloyed Mo with MA (Mn + Si) is more synergistic than Cr. In addition, the lower dissolution of MA in the AstaloyCrS matrix may also contribute to these results.

Table 3 Hardness HV30 of materials with MA H166 and H200 [16]

Material	Hardness HV30	
	Sintering	Sinterhardening (3°C. sec^{-1})
Ast85Mo + 4%H166 + 0.7%C	319	528
Ast85Mo + 4%H200 + 0.7%C	340	492
AstCrS + 4%H166 + 0.75%C	288	494
AstCrS + 4%H200 + 0.75%C	336	472

3.2 CCT Diagrams

It is evident that the iron powder steels ASC100.29 and lower alloyed pre-alloyed powders, such as Astaloy85Mo and AstaloyCrA, cannot be hardened by sinterhardening at industrially achievable cooling rates, at least at this carbon content. AstaloyCrM can form a martensitic microstructure without any additional alloy-ing elements, as previously reported by G. Kalss [18]. For all other steels it is evident that if martensitic hard-ening is desired at conventional sinterhardening cooling rates, additional alloying elements need to be added to the material.

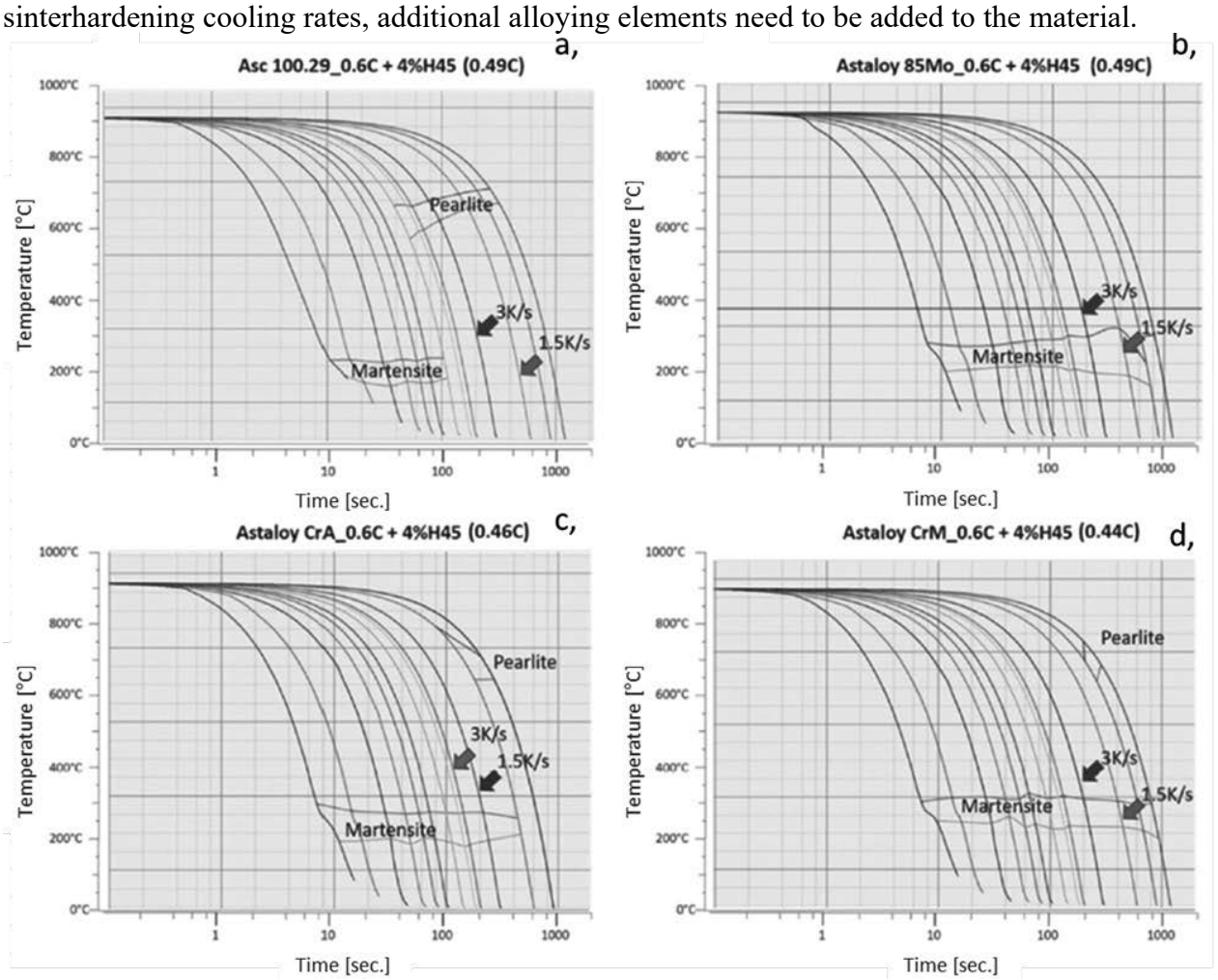

Figure 3. CCT diagrams of powders admixed with 4%H45 [15]

Figure 3 shows the CCT diagrams of various base powders + 4% H45 (MA Cr-Si) [15]. These CCT diagrams are shown here as examples. Similar CCT diagrams have been produced with other base powder + MA combinations. Sintered steels made from Asc100.29 (Fig. 3a,) iron

powder, at least with the carbon content chosen here, cannot be hardened under standard sintering conditions, not even in combina-tion with MA, with the exception of H47 (MA Mn-Cr-Si). In contrast, hybrid alloy powder mixtures can be hardened by sinterhardening at a cooling rate of 1.5°C.sec^{-1}, sometimes even lower. This means that at the carbon content considered in this study, pre-alloyed powders should be combined with MA powder (hybrid alloying) if a martensitic microstructure is desired. Although it is possible to achieve a martensitic microstruc-ture with AstaloyCrM (Fig. 3c,) without MA, the combination with MA leads to even higher macro- and mi-crohardness. Fig. 3d, shows the CCT diagram of the hybrid powder mixture AstaloyCrM + 4% H45. It can be observed that at cooling rates of 1 °C.sec^{-1} and 0.75 °C.sec^{-1} pearlite formation occurs in the hybrid alloy material. The reason for this finding is that the heat treatment at the investigated temperatures and times may not be sufficient to completely dissolve the carbides in the material, and therefore less dissolved carbon is available in the austenitic matrix than should be nominally [19].

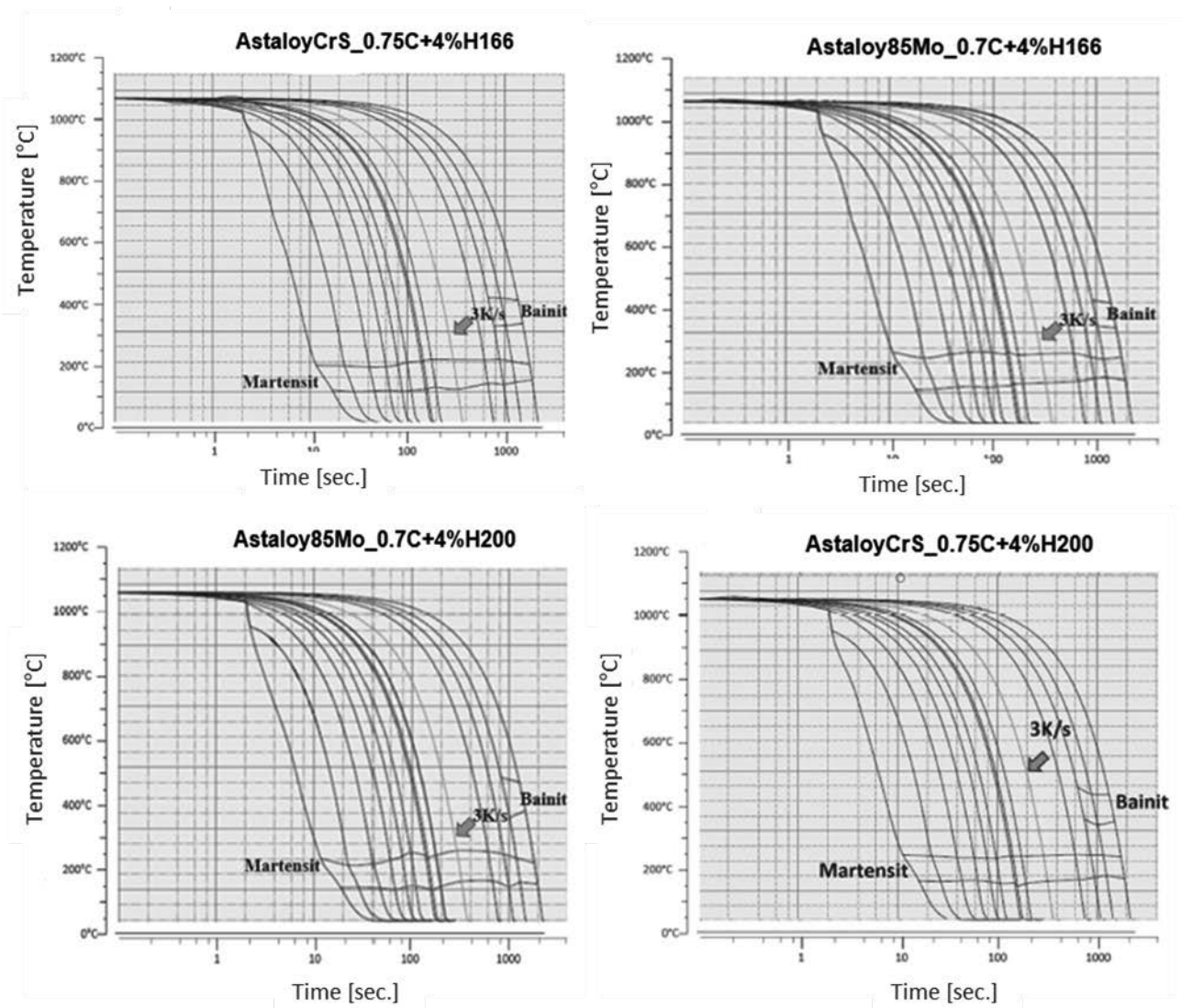

Figure 4. CCT diagrams of powders admixed with 4%H166 and 4%H200 [16]

Regarding the combination of MA with Astaloy85Mo and AstaloyCrS, to characterize the sinterhardening and in particular to reliably estimate the effective cooling rates leading to martensitic microstructures, CCT dia-grams were evaluated in a quenching dilatometer. These are shown in Fig.4 [16], the transformations were identified from the cooling graphs. These diagrams clearly confirm that the pre-alloyed materials do not sinter and do not harden even at higher carbon levels; quenching would require cooling rates that are significantly higher than those possible in industrial furnaces. The addition of pre-alloyed MA drastically increases the hardenability: even at cooling rates as low as 1 °C.sec^{-1}, no bainite or pearlite transformation is visible.

This is in agreement with the relatively high hardness levels after sintering and the partial martensitic mi-crostructures after sintering. However, it should be considered that, as reported for example by Geroldinger et al. [15], small areas of bainitic or pearlitic transformation are not shown in the CCT diagram. Although the diagram predicts a fully martensitic microstructure, metallography may reveal some pearlite or bainite, especial-ly in the cores of the largest particles of the former base powder [20]. In practice, the system tolerance is rele-vant in terms of cooling rate. For Astaloy85Mo-MA-C, the CCT diagram indicates bainite at cooling rates <1°C.sec^{-1}. In this material, the cores of the larger particles were also sufficiently alloyed, leading to a full mar-tensitic transformation at 3°C.sec^{-1}.

As shown in the article, the admixture of master alloys has a high impact on the hardenability of the material, and, therefore, the mechanical and fatigue properties. This type of alloying is very promising for improving the properties of low-alloy steels (such as AstaloyCrS and AstaloyCrA) while maintaining a competitive price.

Based on the results of this article, it is possible to further improve the properties of the material by selecting the base powder, the type of master alloy and optimizing the carbon content.

4. CONCLUSION

Based on the above facts, we can conclude the following:

- the hybrid alloying technique, which means the combination of pre-alloyed powder and MA powder, significantly improves hardenability compared to steels made from pure iron powder;
- CCT diagrams of PM-steel were created and hardness measured;
- martenitic hardening of pure iron powder could be achieved at a rate of 3°C.sec^{-1} and MA of the Fe-Mn-Cr-Si-C type;
- the use of a base powder pre-alloyed with 0.85% Mo in combination with MA leads to hybrid alloy mix-tures with high hardness and good hardenability;
- fully martensitic homogeneous microstructures can be achieved with all hybrid alloy materials using AstaloyCrM as the base powder;
- materials based on AstaloyCrM show the smallest differences in hardness at cooling rates of 3 and 1.5°C.sec^{-1}, these steels are the best in sinterhardening;
- for microhardness and macrohardness, the type of base powder is more important than the choice of MA, at least for the MA types investigated here.

ACKNOWLEDGEMENT

This work was supported by Scientific Grant Agency of the Ministry of Education, science, research and sport of the Slovak Republic and the Slovak Academy of Sciences under the grant number VEGA 1/0073/24 „Experimental analysis of shapes and materials of working tools of additional equipment of forestry mechanization technology “.

BIBLIOGRAPHY

[1] KALSS, G., et al. (2020). Sinter Hardening of Cr-Mo Pre-Alloyed Steels as a Function of the Carbon Con tent. In: Powder Metallurgy Progress. Vol. 20, No. 2, Slovak Academy of Sciences, 2020, pp. 81- 93. https://doi.org/10.2478/pmp-2020-0008

[2] ENGSTRÖM, U., MC. LELLAND, J., MAROLI, B. (2002). Effect of sinter hardening on the properties of high temperature sintered PM steels. In. Adv. Powder Metall. & Partic. Mater. MPIF, Princeton NJ, Part 13, 2002, p. 1.

[3] KOBLIK, D., ŤAVODOVÁ, M., VARGOVÁ, M. (2025). Evaluation of selected mechanical properties of Astaloy CrS material produced by sinterhardening process. In: TalentDetector2025_Summer: international students scientific conference. 2025. s. 211–216. ISBN 978-83-65138-44-6. Dostupné z: https://pimib.polsl.pl/pdf/Talent-Detector-Summer-2025.pdf.

[4] BOCCHINI, GF., et al. (2002). Influence of density and surface/volume ratio on the cooling speed of sinter-hardening materials, Part two: Microstructure and microhardness distribution inside parallelepi-peds. In: Adv. Powder Metall. & Patric. Mater., MPIF, Princeton NJ, Part13, 2002, p.60.

[5] GÁBRIŠOVÁ, Z., BRUSILOVÁ, A., ŠVEC, P. (2019). Study of Sintering Parameters and Sintering Addi-tives Effect on selected properties of Silicon Nitride. In: Manufacturing Technology. Vol. 19, No. 2, pp. 222-227. doi: 10.21062/ujep/273.2019/a/1213-2489/MT/19/2/222.

[6] KARAMCHEDU, S., HATAMI, S., NYBORG, L., ANDERSSON, M. (2014). Sinter-hardening re-sponse of sintered steel based on astaloy mo and its diffusion bonded derivatives In: Powder Metall. Progress, vol.14, no.2, 2014, p.93.

[7] BERG, S., MAROLI, B. (2002). Properties obtained by chromium-containing material. In: Adv. Powder Metall.&Patric. Mater. MPIF, Princeton NJ, Part 8, 2002, p.1.

[8] NOVÁK, P., NOVÁ, K., VANKA, T., PRŮŠA, F. (2018). High-temperature Behaviour of New Fe-Al-Si Alloy Produced by Powder Metallurgy. In: Manufacturing Technology. Vol. 18, No. 2, pp. 299-302. doi: 10.21062/ujep/95.2018/a/1213-2489/MT/18/2/299.

[9] DANNINGER, H., GIERT, C. (2001). Processes in PM steel compacts during the initial stages of sinter ing, Mater. In: Chem. Physics. 67 1, pp. 49-55, DOI:0.1016/S0254-0584(00)00419-3.

[10] MARDAN, M., BLAIS, C. (2016). Development of Novel of Pre-alloyed PM Steels for Optimization of Machinability and Fatigue Resistance of PM Components. In: Journal of Materials Engineering and Per for-mance. pp. 764-773, DOI:10.1007/s11665-016-1900-3.

[11] HOGANAS (2017). Iron and steel powders of sintered components. Hoganas, Sweden, 2017. ISBN: 978-91- 983614-0-7.

[12] DE ORO CALDERON, R.; DUNKLEY, J.; GIERL, C.; DANNINGER, H. (2019). New opportunities for master alloys: Ultra-high pressure water atomized powders. In: Powder Metall. Review 8 1, pp. 55-66.
[13] GEROLDINGER, S. (2019). Optimization of iron-based Master Alloys for liquid phase sintering of PM steels. Mas-ter Thesis, TU Wien, 2019.
[14] ISO 5754 (2023). Sintered metal materials, excluding hardmetals - Unnotched impact test piece.
[15] GEROLDINGER, S., DE ORO CALDERON, R., GIERTL-MAYER, C., DANNINGER, H. (2021). Sinter hardening PM steels prepared through hybrid alloying, In: J. Heat. Treatm. Mat. 76, 2; pp. 105-119, DOI:10.1515/htm-2020-0007.
[16] GEROLDINGER, S., HOJATI, M., DE ORO CALDERON, R, GIERTL-MAYER, C., DANNINGER, H., HELLEIN, R. (2024). Hybrid alloyed sinter hardening steels based on different pre-alloyed powders. In: J. Heat. Treatm. Mat. 79, 3; pp. 147-158.
[17] KRAUSS, G. (2015). Steels: processing, structure and performance. In: ASM International, Ohio, 2015, p.705. ISBN: 978-0871708175.
[18] KALSS, G. (2007). Sinterhärten von Cr-Mo-legierten PM-Stählen fur hochbelastbare Präzisionsteile, Dissertation, TU Wien, 2007, p.321.
[19] KOZOVÝ, P., ŠAJGALÍK, M., DRBÚL, M., HOLUBJÁK, J., MARKOVIČ, J., JOCH, R., BALŠIANKA, R. (2023). Identification of Residual Stresses after Machining a Gearwheel Made by Sintering Metal Powder. In: Manufacturing Technology. 23(4):468-474. doi: 10.21062/mft.2023.054.
[20] KNAISLOVÁ, A., ŠIMŮNKOVÁ, V., NOVÁK, P., PRŮŠA, F., CYGAN, S., JAWORSKA, L. (2017). The Optimization of Sintering Conditions for the Preparation of Ti-Al-Si Alloys. In: Manufacturing Technolo-gy. 2017;17(4):483-488. doi: 10.21062/ujep/x.2017/a/1213-2489/MT/17/4/483.

TalentDetector

7th-9th June 2026
Gliwice-Brenna, Poland

DEPARTMENT OF ENGINEERING MATERIALS AND BIOMATERIALS
FACULTY OF MECHANICAL ENGINEERING
SILESIAN UNIVERSITY OF TECHNOLOGY

INTERNATIONAL STUDENTS SCIENTIFIC CONFERENCE

The effect of heat treatment on the structure and corrosion resistance of X2CrNiMoN22-5-3 steel

Bartosz Kowalski[a], Monika Kciuk[b]

[a] Silesian University of Technology, Faculty of Mechanical Engineering
[b] Silesian University of Technology, Faculty of Mechanical Engineering, Department of Engineering Materials and Biomaterials
email: monika.kciuk@polsl.pl

Abstract: The paper presents the influence of heat treatment on the structure and corrosion resistance of X2CrNiMoN22-5-3 steel. To determine the material's structure after heat treatment the method of light microscopy microanalysis was used.The corrosion resistance experiments were performed using a salt spray chamber.

Keywords: materials, corrosion resistance, gravimetric method.

1. INTRODUCTION

Duplex steels are a modern group of stainless steels that combine the properties of ferritic and austenitic steels. Thanks to their two-phase structure, they are characterized by very high corrosion resistance and high mechanical strength. They perform particularly well in chloride-exposed environments where traditional stainless steels may suffer from pitting or crevice corrosion [1-4].

Duplex stainless steels are widely used in the chemical, petrochemical, energy, and marine industries, where high durability and structural reliability are essential. They are commonly applied in the production of storage tanks, chemical vessels, pressure equipment, process installations, and load-bearing structures operating under demanding service conditions [5,6].

These materials are also utilized in desalination systems, peroxide reactors, fermentation chambers, expansion tanks, pipelines, and flexible industrial hoses. In addition, duplex steels are frequently used in heating devices and hot water storage systems. Owing to their excellent resistance to aggressive environments, including seawater, hydrogen sulfide, and carbon dioxide, they are well suited for heat exchangers, dryers, and dynamically loaded structures exposed to severe operating conditions [7].

Compared to traditional stainless steels, duplex steels offer improved resistance to stress corrosion cracking and a more favorable strength-to-weight ratio. This allows for the design of lighter, yet more durable components for installations and equipment. An additional advantage is their good weldability and ability to operate in demanding environmental conditions.

The growing popularity of duplex steels is also due to their cost-effectiveness. The material's higher durability translates into lower operating and maintenance costs, making them an increasingly popular choice for modern industrial projects [8].

2. MATERIALS AND METHODS

The investigations were carried out on commercially available X2CrNiMoN22-5-3 steel. The chemical composition of analyzed steel is presented in Table 1.

Table 1. Chemical composition of the investigated steel

Chemical element	C	Si	Mn	P	S	Cr	Ni	Mo	N
wt [%]	0,03	1	2	0,03	0,02	23	6,5	3,5	0,2

The heat treatment was carried out in electric resistance furnace Nabertherm HTCT 03/16. Heat treatment was carried out on the tested samples at a temperature of 1100°C and cooling of the samples after heat treatment was performed in water.

Metallographic preparation was performed using conventional procedures for specimens in the initial stae and after heat treatment. The samples were mounted in Duracryl resin, mechanically ground using SiC abrasive papers of progressively finer grit sizes, and subsequently polished with an Al_2O_3 aqueous suspension. Final etching was carried out using aqua regia. Microstructural observations were conducted with a Carl Zeiss AG Zeiss Axio Observer Z1m optical microscope at a magnification of 200 and 500×.

Corrosion resistance tests were conducted in accordance with the requirements of the PN-EN ISO 9227 standard using a CC450iP salt spray chamber manufactured by Ascott Analytical Equipment. The specimens were exposed to a 5 wt.% NaCl aqueous solution in the form of a neutral salt spray at a temperature of 35°C and relative humidity of 100%. The total exposure time was 96 h.

The corrosion resistance of the tested material in its initial state and after heat treatment was determined using a gravimetric method. For this purpose, mass loss V_c (1) and linear corrosion rate V_p (2, 3) were calculated.

$$V_c = \frac{\Delta m}{A \cdot t} \tag{1}$$

where:
Δg - mass loss [g],
A - total surface area of the sample [m^2],
t – time of corrosion [days].

$$V_p = V_c \cdot \alpha \tag{2}$$

$$\alpha = \frac{365}{1000 \cdot d} \tag{3}$$

where:
α - conversion factor
d – density of the material [g/cm^3]

3. EXPERIMENT RESULTS

Microscopic metallographic studies allowed to determine the effect of heat treatment on the structure of X2CrNiMoN22-5-3 steel. The initial microstructure was characteristic of duplex stainless steel, consisting of a dual-phase ferritic–austenitic matrix. (Fig. 1). The structure is also characterized by banding characteristic of rolled products.

As a result of solution heat treatment of the samples at temperatures 1100°C, a significant increase in grain size, particularly of austenite, is observed. Grain globulization is also noticeable in the sample solution heat treated at 1100°C.

a)

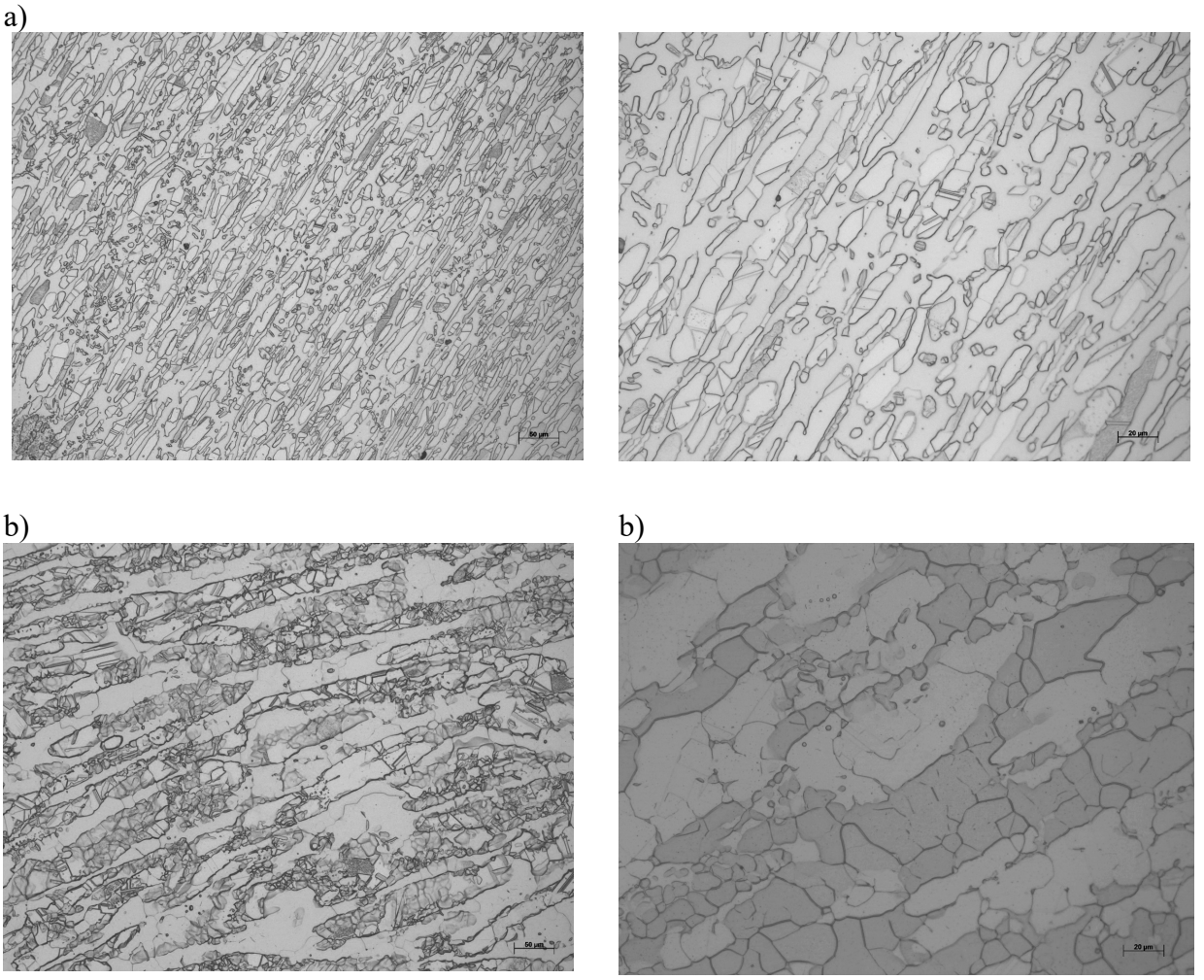

Figure 1. Structure od the X2CrNiMoN22-5-3 steel in initial stateure (a) 200x and 500x, after heat treatment (b) 200x and 500x

The main aim of the work was to determine the corrosion resistance of the tested material in its initial state and after heat treatment. The characterization of the specimens after the corrosion test are presented in Table 2. It was found that the values of corrosion rate determined for samples in the initial state exposed to 5% sodium chloride showed worse corrosion properties compared to samples subjected to solution heat treatment at a temperature of 1100°C.

Presence of Cl ions in an environment will cause the native oxide layer to be thinner. This however is not a result of a smaller defect density but a negative effect of chloride on film thickness. Chloride ions are small in size and exhibit high diffusivity, and they are responsible for developing punctual defects in passive films, leading to punctate corrosion.

Table 2. Result of corrosion tests

Material condition	Mass loss V_c [g/ m^2*day]	Linear corrosion rate V_p [mm/year]
Initial state	0,152	0,007
Supersaturation 1100 °C	0,065	0,003

4. CONCLUSIONS

The obtained experimental results have enabled the formulation of the following conclusions:

1. The initial microstructure was characteristic of duplex stainless steel, consisting of a dual-phase ferritic–austenitic matrix.
2. Following heat treatment at 1100°C, a significant increase in grain size was observed, with the most pronounced growth occurring in the austenitic phase.
3. The heat treatment performed improves the corrosion resistance of the tested material.
4. Aggressive Cl^- ions penetrate the passive film due to their small diameter, locally destroy the passive layer and cause pit nucleation.

BIBLIOGRAPHY

1. A. I. Zhiteneva, A. S. Fedorova, P. V. Kovaleva, D. A. Strekalovskaya, A. A. Al'khimenko, Cast Structure and Properties of Duplex Stainless Steels, Steel in Translation, Vol. 52, No. 5 (2022) 479–486.
2. P. Quadros 1, J. Ribeiro, B. Kurelo, , O. Calabokis, A. Turin, P. Borges, Influence of Heat Treatment Temperature on Microstructure, Hardness and Sensitization of UNS S32205 Duplex Stainless Steel, Materials,17 (2024) 4715 1-22.
3. Z. Ren, L. Fang, H. Wang, P. Ding, X. Zeng, Seawater Corrosion Resistance of Duplex Stainless Steel and the Axial Compressive Stiffness of Its Reinforced Concrete Columns, Materials,16 (2023)7249, 3-20.
4. J. Zdunek, P. Maj, M. Kulczyk, J. Mizera: Texture, residual stresses and mechanical properties analysis in the commercial 1.4462 duplex stainless steel subjected to hydrostatic extrusion, Archives of civil and mechanical engineering 19 (2019) 525-534.
5. L. A. Dobrzański, M. Osojca: Struktura i własności stali duplex typu X2CrNiMoN22-5-3, Proceedings of AMME'2003, vol. 12, 263-266
6. L. Duprez, B. De Cooman, N. Akdut: Microstructure evolution during isothermal annealing of astandard duplex stainless steel type 1.4462, Steel Research 71 (2000) 417-422
7. Y. Han, R. Chi, Q. Chen, B. Wang, W. Liu, Y. He, Microstructural evolution and coarsening behavior of the precipitates in 2205 duplex stainless steel aged at 850°C, Journal of Materials Research and Technology Volume 26 (2023), 2560-2574.
8. G. Chail, P. Kangas: Super and hyper duplex stainless steels: structures, properties and applications, Procedia Structural Integrity 2 (2016) 1755–1762.

TalentDetector

7th-9th June 2026
Gliwice-Brenna, Poland

DEPARTMENT OF ENGINEERING MATERIALS AND BIOMATERIALS
FACULTY OF MECHANICAL ENGINEERING
SILESIAN UNIVERSITY OF TECHNOLOGY

INTERNATIONAL STUDENTS SCIENTIFIC CONFERENCE

Laser Surface Textured Mg and Ti Alloys for Enhanced Performance

Milan Kozik, Mikołaj Grabowski, Monika Kraszewska, Hanna Kostyrko, Gabriela Suchańska, William V. Appiah, Edwinner O.A Ayitey, Magdalena Wyszyńska, María Guadalupe Carrillo, David Sasu Konadu, Benjamin Agyei-Tuffour, Monika Nitsze-Wierzba, Grzegorz Chladek, Augustine Appiah, Marcin Adamiak

Silesian University of Technology, Gliwice, Poland
Medical University of Silesia in Katowice, Katowice, Poland
University of Ghana, Legon, Ghana
Kwame Nkrumah University of Science and Technology, Kumasi, Ghana
Grupo SG, Salvador, El Salvador

Abstract: This study investigates the effects of Laser Surface Texturing (LST) on the topographical and mechanical properties of Ti-6Al-4V and Mg RZ5 alloys for biomedical applications. LST successfully generated controlled topographies: a square grid on Ti-6Al-4V and a honeycomb pattern on Mg RZ5, achieving a penetration depth of ~30 μm. Mg RZ5 exhibited a rougher surface profile (Pt = 14.4 μm) and a narrower heat-affected zone (26 μm) compared to Ti-6Al-4V (Pt = 8.16 μm; HAZ = 61 μm). Additionally, LST induced localized hardening, increasing the Vickers microhardness of Mg RZ5 (65 to 74 HV) and Ti-6Al-4V (340 to 354 HV). These surface modifications demonstrate strong potential for improving osseointegration and wear resistance in implants.

Keywords: Laser Surface Texturing, Ti-6Al-4V, Mg RZ5, Surface Roughness, Microhardness, Biomedical Implants

1. INTRODUCTION

Titanium and magnesium alloys represent two of the most critical classes of metallic biomaterials in modern orthopedic and dental applications [1]. Titanium alloys, particularly Ti-6Al-4V, are the established standard for permanent load-bearing implants due to their exceptional mechanical strength, corrosion resistance, and biocompatibility [2]. Conversely, magnesium alloys such as Mg RZ5 are increasingly investigated as revolutionary biodegradable materials for temporary fixation devices, designed to safely dissolve in vivo and eliminate the need for secondary removal surgeries [3], [4].

Despite their respective advantages, optimizing the tissue-implant interface remains essential for long-term clinical success [5]. Both permanent and temporary implants require specific surface properties to promote rapid osseointegration, ensure mechanical stability, and mitigate wear or particulate generation. Laser Surface Texturing (LST) has emerged as a highly precise,

non-contact technique to engineer surface topography and tailor these critical interface properties without compromising the bulk material. By creating controlled micro-architectures, LST can significantly increase functional surface area and induce localized mechanical improvements through rapid thermal cycling [6].

This study aims to evaluate the efficacy of LST in modifying the surface characteristics of Mg RZ5 and Ti-6Al-4V alloys. By applying distinct micro-patterns, specifically honeycomb and square grids, this research investigates the resulting microstructural evolution, topographical changes, and microhardness enhancements, ultimately assessing how these targeted surface modifications can be leveraged for advanced biomedical performance.

2. METHODOLOGY

Commercial Mg RZ5 and Ti-6Al-4V alloys were sectioned, ground with silicon carbide (SiC) abrasive papers, polished with 0.04 μm colloidal silica and cleaned in ethanol, to establish a uniform baseline. Surface modification was performed using a pulsed laser system optimized to achieve a consistent ablation depth of approximately 30 μm. A single-pass honeycomb pattern was applied to the Mg RZ5 alloy, while a square grid pattern was generated on the Ti-6Al-4V alloy.

The morphological and topographical effects of the LST process were evaluated using digital microscopy and scanning electron microscopy (SEM). SEM, including cross-sectional imaging, was used to characterize the laser tracks, verify penetration depth, and examine the heat-affected zones (HAZ) and microstructural changes. Energy-dispersive X-ray spectroscopy (EDS) point analysis and elemental mapping were conducted to assess chemical stability and elemental distribution across the textured regions. Additionally, surface profilometry quantified the topographical impact, extracting linear roughness profiles to determine peak-to-valley (Pt) heights over designated measurement lengths (4000 μm for Mg RZ5 and 2791 μm for Ti-6Al-4V).

To evaluate localized mechanical alterations induced by the LST thermal cycling, Vickers microhardness testing was performed. Multiple indentations were recorded and averaged on both the untextured baseline surfaces and the processed zones of the Mg RZ5 and Ti-6Al-4V specimens to accurately quantify the degree of surface hardening achieved through the laser treatment.

3. RESULTS AND DISCUSSION

3.1. Microstructure

Figure 1 illustrates the microstructural evolution of the Mg RZ5 alloy following LST. The digital and scanning electron microscopy (SEM) micrographs reveal the successful formation of a distinct honeycomb pattern on the surface. The localized thermal input resulted in a heat-affected zone (HAZ) measuring approximately 26 μm in width, accompanied by the formation of distinct precipitates along the pattern edges. EDS analysis confirmed the primary composition within the textured region as 97.58 wt% magnesium, with minor constituents including 0.63 wt% zinc and 0.29 wt% silicon. Subsequent EDS mapping demonstrated the distribution of oxygen and carbon within the newly formed precipitates, highlighting the oxidative nature of the alloy in response to thermal interactions.

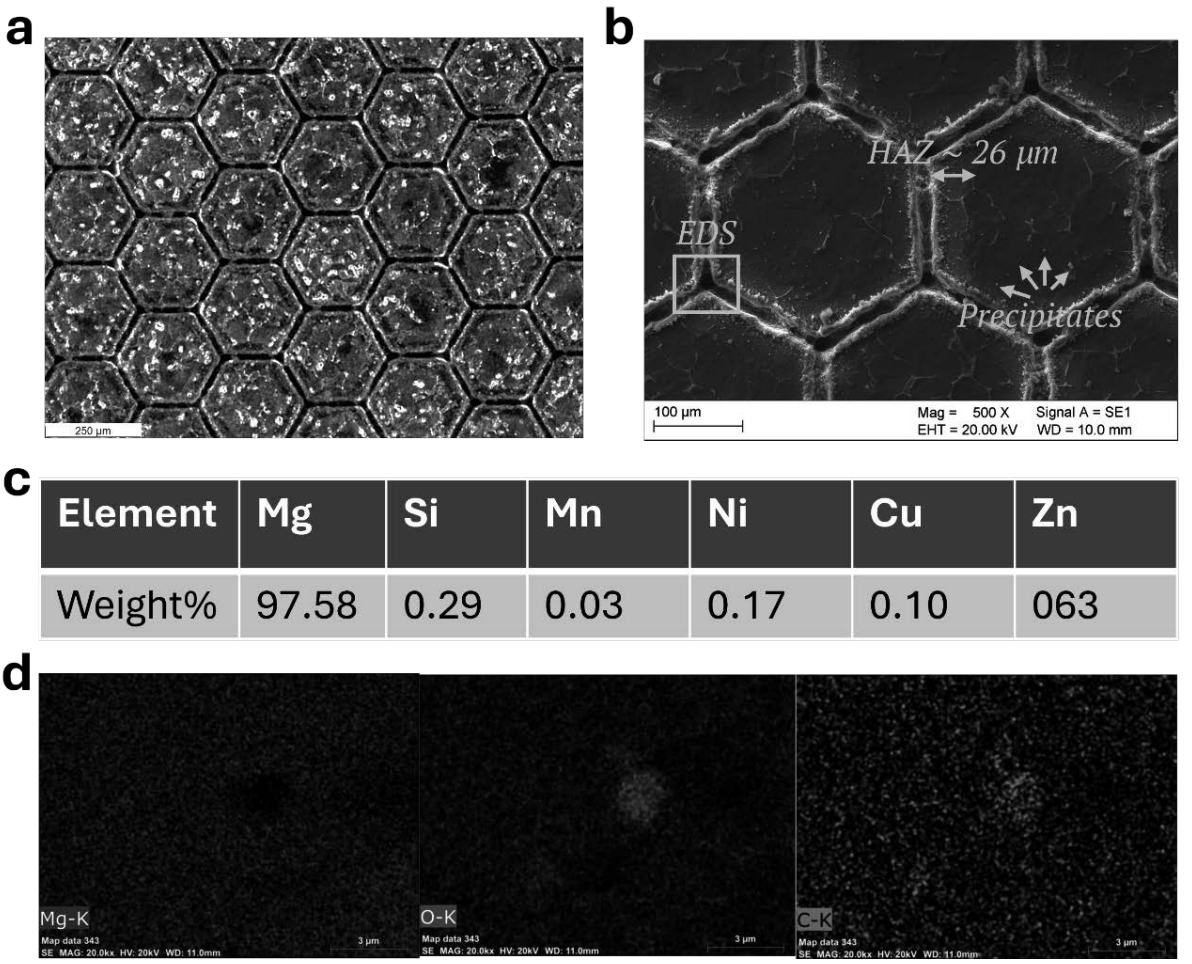

Element	Mg	Si	Mn	Ni	Cu	Zn
Weight%	97.58	0.29	0.03	0.17	0.10	063

Figure 1. a. Digital micrograph of the surface of Mg RZ5 after LST processing, b. SEM image of the honeycomb LST patterns showing the heat-affected zone (HAZ) and precipitates, c. EDS chemical composition analysis obtained across the LST pattern indicated in b, and d. EDS chemical composition mapping of the precipitates indicated in b.

Figure 2 details the microstructural characteristics of the LST-processed Ti-6Al-4V alloy. In contrast to the magnesium substrate, the laser processing generated a well-defined square pattern grid on the titanium alloy. SEM imaging shows a comparatively wider heat-affected zone of approximately 61 µm adjacent to the laser tracks, reflecting the differing thermal properties and beam interaction with the material. Quantitative EDS analysis verified the expected elemental makeup within the textured region, indicating 90.3 wt% titanium, 6.4 wt% aluminum, and 3.3 wt% vanadium. The corresponding elemental mapping further confirmed the distribution of these primary alloying elements across the processed surface area, with Al exhibiting preferential segregation a the node of the surface texture.

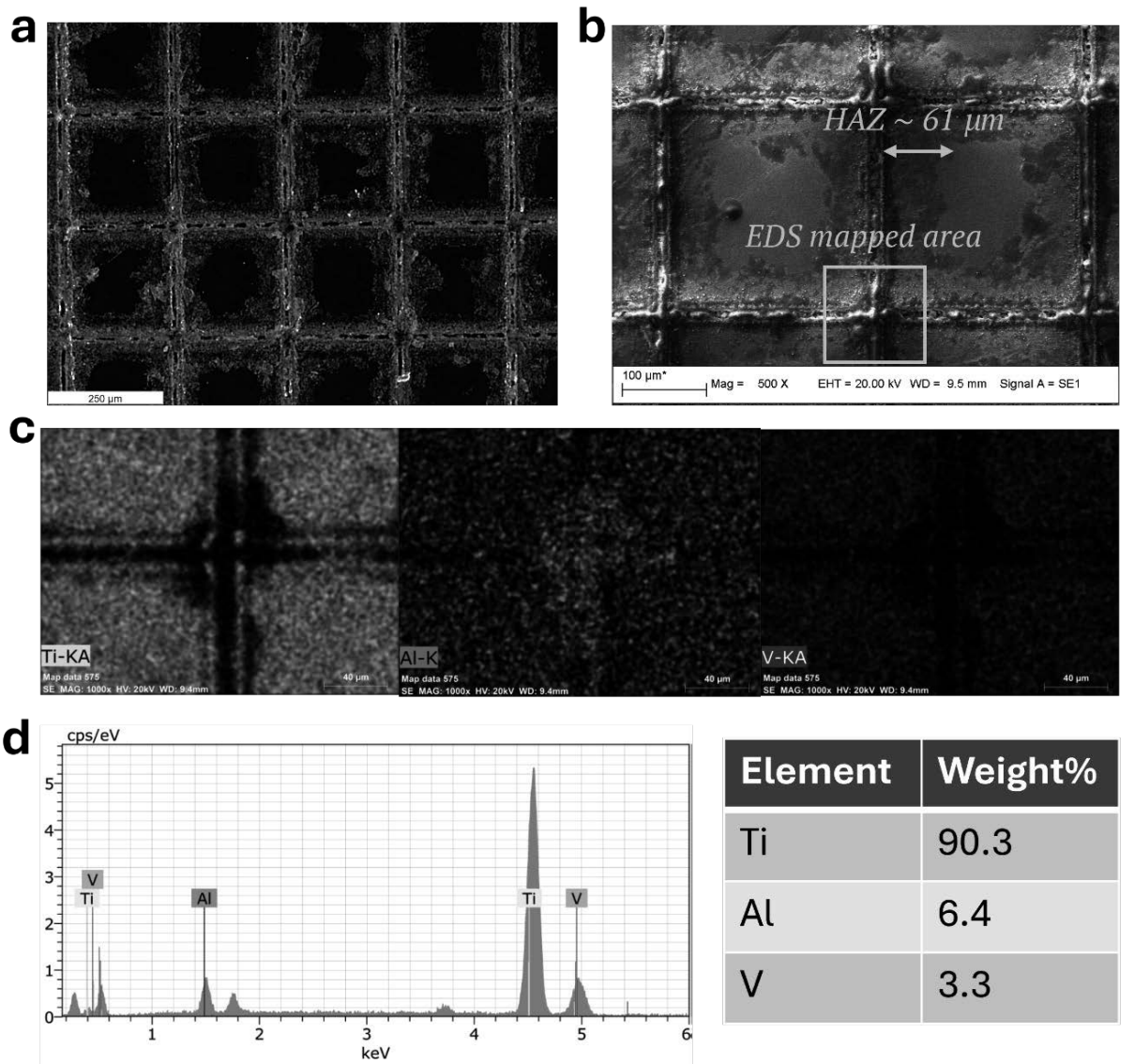

Element	Weight%
Ti	90.3
Al	6.4
V	3.3

Figure 2. a. Digital micrograph of the surface of Ti-6Al-4V after LST processing, b. SEM image of the square LST patterns showing the heat-affected zone (HAZ) c. EDS chemical composition mapping obtained across the LST pattern indicated in b, and d. Corresponding quantitative EDS chemical composition analysis in c.

3.2. Surface Roughness

Figure 3 provides a topographical (Figure 3a) and cross-sectional (Figure 3b) analysis of the textured surfaces, detailing the physical impact of the laser ablation. Cross-sectional SEM imaging reveals that the laser tracks achieved a consistent penetration depth of approximately 30 µm into both substrates. However, surface roughness profiles highlight distinct variations in the resulting topography. The linear profiles capture a peak-to-valley (Pt) value of 14.4 µm over a 4000 µm measurement length for the Mg RZ5 alloy, indicating a more pronounced structural variation. Conversely, the Ti-6Al-4V alloy exhibited a comparatively smoother profile with a Pt of 8.16 µm measured over a 2791 µm length.

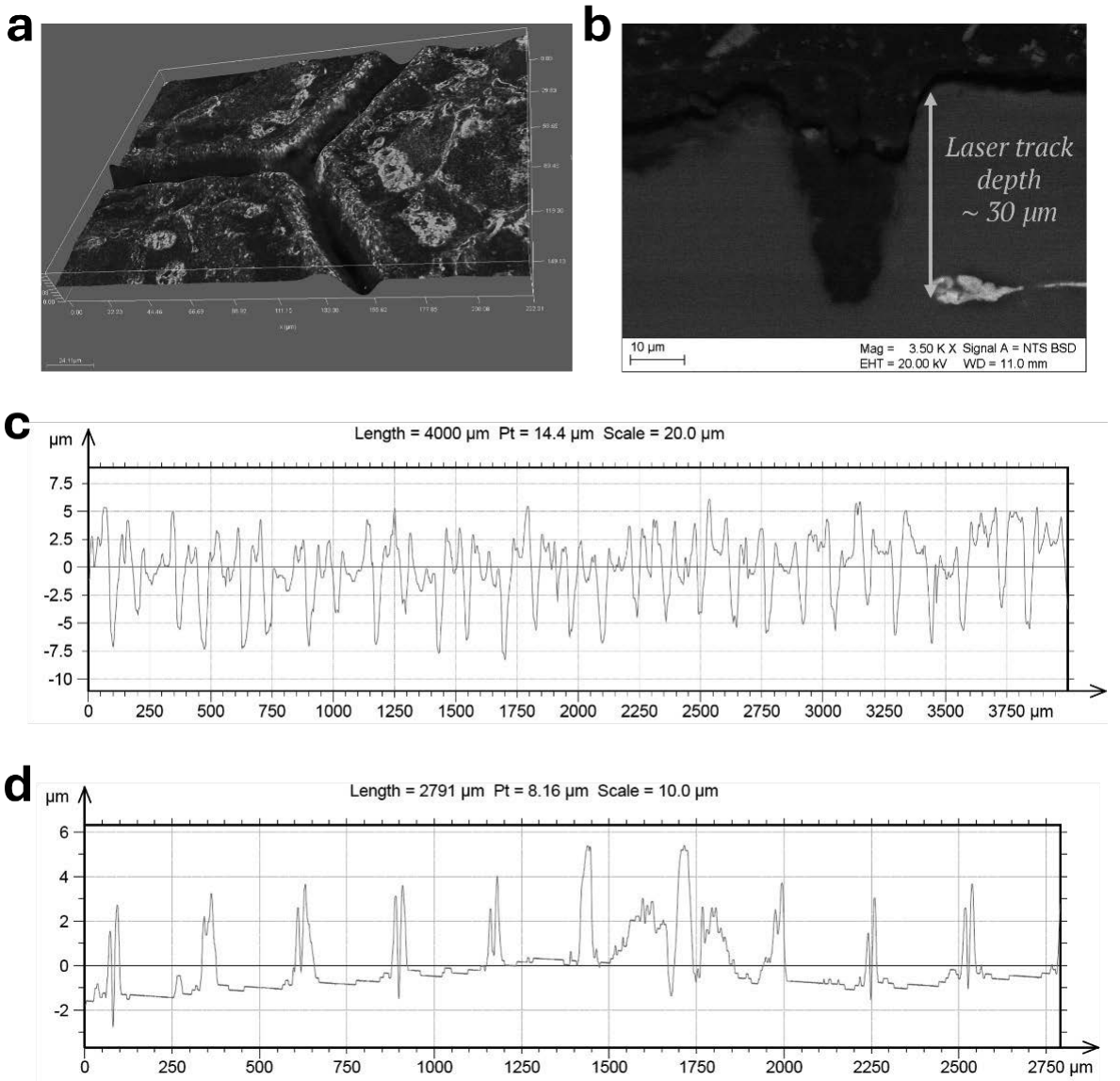

Figure 3. a. 3D digital visualization of the honeycomb LST pattern, b. SEM image of the cross-section of the laser track detailing the depth of penetration of the track from the surface of the Mg RZ5 alloy, c and d. Surface rough profiles of the laser surface textured Mg RZ5 and Ti-6Al-4V alloys, respectively.

3.3. Mechanical Properties

Figure 4 presents a comparative Vickers microhardness evaluation, demonstrating the mechanical impact of the LST process on the surfaces of both alloys. The rapid thermal cycling and microstructural refinement associated with the texturing procedure successfully induced a measurable hardening effect. For the Mg RZ5 alloy, the microhardness increased from a pre-treatment baseline of 65 $\pm$ 7 HV to 74 $\pm$ 7 HV following LST. Similarly, the Ti-6Al-4V alloy exhibited a notable enhancement in surface hardness, rising from 340 $\pm$ 10 HV before texturing to 354 HV $\pm$ 11 after the laser processing.

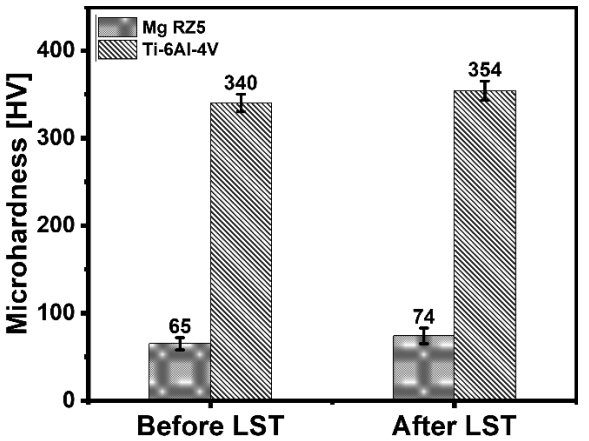

Figure 4. Vickers microhardness analysis of the surface of the samples before and after LST processing.

3.4. Relevance in Biomedical Applications

The morphological and mechanical modifications induced by LST hold significant promise for the deployment of these alloys in biomedical applications. Titanium alloys like Ti-6Al-4V are widely utilized for permanent orthopedic and dental implants, while magnesium alloys are increasingly investigated for temporary, biodegradable fixation devices. The controlled topographical patterns, such as the honeycomb and square grids, substantially increase the functional surface area, which is highly advantageous for promoting cellular adhesion, proliferation, and ultimately, enhanced osseointegration at the implant-bone interface. Furthermore, the localized increase in surface microhardness observed in both materials can contribute to improved wear resistance, reducing the risk of particulate debris generation and supporting the biomechanical stability of the implants under physiological loading conditions.

BIBLIOGRAPHY

[1] Y. Liu *et al.*, "Biomaterials for endometriosis treatment: Design, advances, and prospects," *Acta Biomater.*, vol. 216, pp. 1–21, Jun. 2026, doi: 10.1016/j.actbio.2026.03.034.

[2] S. Vazirian and A. Farzadi, "Dissimilar transient liquid phase bonding of Ti–6Al–4V and Co–Cr–Mo biomaterials using a Cu interlayer: Microstructure and mechanical properties," *J. Alloys Compd.*, vol. 829, p. 154510, Jul. 2020, doi: 10.1016/j.jallcom.2020.154510.

[3] S. Riyaz *et al.*, "Inflammatory response toward a Mg-based metallic biomaterial implanted in a rat femur fracture model," *Acta Biomater.*, vol. 185, pp. 41–54, Sep. 2024, doi: 10.1016/j.actbio.2024.06.040.

[4] J. E. Ampah-Essel *et al.*, "Enhancing wettability, wear, and corrosion resistance of magnesium RZ5 biomaterial via pulsed laser surface texturing (LST)," *Tribol. Int.*, vol. 211, p. 110835, Nov. 2025, doi: 10.1016/j.triboint.2025.110835.

[5] R. Feiner and T. Dvir, "Tissue–electronics interfaces: from implantable devices to engineered tissues," *Nat. Rev. Mater.*, vol. 3, no. 1, p. 17076, 2017.

[6] L. Ge *et al.*, "Synergistic enhancement of mechanical interlocking and chemical bonding in Al alloy/CFRTP joints prepared by friction stir lap welding: Effect of laser surface texturing," *J. Mater. Process. Technol.*, vol. 353, p. 119365, Jul. 2026, doi: 10.1016/j.jmatprotec.2026.119365.

TalentDetector
7th-9th June 2026
Gliwice-Brenna, Poland
DEPARTMENT OF ENGINEERING MATERIALS AND BIOMATERIALS
FACULTY OF MECHANICAL ENGINEERING
SILESIAN UNIVERSITY OF TECHNOLOGY
INTERNATIONAL STUDENTS SCIENTIFIC CONFERENCE

Implementation of a Smart Aquarium Using IoT Technology

Magdalena Koźlik[a], Kamil Kołodziej[a], Kacper Strukowski[a], Marcin Jaroszek[a] , Karol Tlałka[b], Maurycy Frydecki[b], Mariusz Król[c]

[a] Silesian University of Technology, Faculty of Mechanical Engineering, Automation and Industrial Robotics,
[b] Silesian University of Technology, Faculty of Mechanical Engineering, Industrial Mechatronics,
[c] Silesian University of Technology, Faculty of Mechanical Engineering, Department of Engineering Materials and Biomaterials, e-mail: mariusz.krol@polsl.pl

Abstract: This article presents the design and implementation of a smart aquarium that utilizes Internet of Things (IoT) technology. The developed system is based on an Arduino Uno board with integrated temperature, pH, and turbidity sensors. The system enables real-time monitoring of aquatic environment parameters, displays data on an LCD screen, and archives it as CSV files. Additionally, the data is transmitted to a mobile app developed using MIT App Inventor. Tests confirmed that the system operates correctly and demonstrated the potential of IoT technology for monitoring aquatic environments.
Keywords: smart aquarium, mobile app, IoT, Arduino Uno, water parameter monitoring, mobile app, MIT App Inventor, measurement system

1. INTRODUCTION

The rapid development of Internet of Things (IoT) technology means that it is increasingly being used in systems related to aquatic environment monitoring. Smart measurement systems enable automatic monitoring of water parameters and a rapid response to any abnormalities that arise. Solutions of this type are used not only in industry but also in home aquariums [1,2].
The purpose of this article is to present the design and implementation of a smart aquarium based on the Arduino Uno. The developed system enables the monitoring of basic water parameters, such as temperature, pH, and turbidity. The measurement data is displayed on an LCD screen, saved to a file, and transmitted to a mobile app. The system allows for real-time monitoring of conditions in the aquarium and reduces the need for constant user intervention.

2. LAYOUT STRUCTURE

The smart aquarium system was built around an Arduino Uno microcontroller working in conjunction with a set of sensors responsible for measuring aquatic environment parameters

(Fig. 1). The microcontroller's main task is to periodically collect measurement data, process it, and display the results to the user [3, 4].

The project utilizes a DS18B20 temperature sensor, a pH sensor, and an analog turbidity sensor. Additionally, the system is equipped with an LCD display that allows for local monitoring of the aquarium's current operating parameters. The data is also transmitted to a mobile app and saved as a CSV file, enabling subsequent analysis of the measurements and notifying the user of any deviations from normal values.

The entire system was designed as a compact unit that enables continuous monitoring of the aquatic environment with minimal user intervention [1, 2]. Additionally, a dedicated enclosure was designed for the electrical components to protect them from water exposure (Fig. 2).

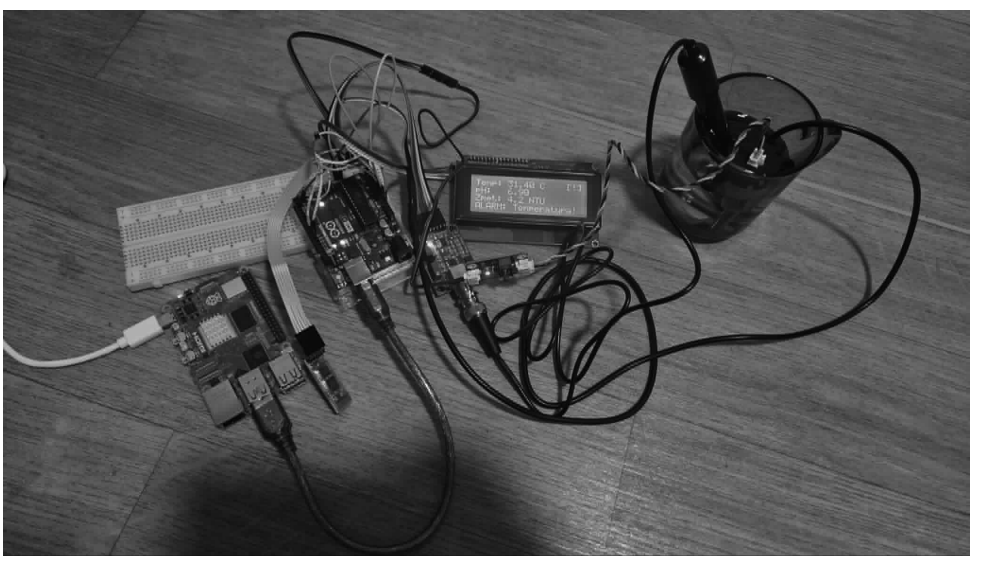

Figure 1 Measurement setup

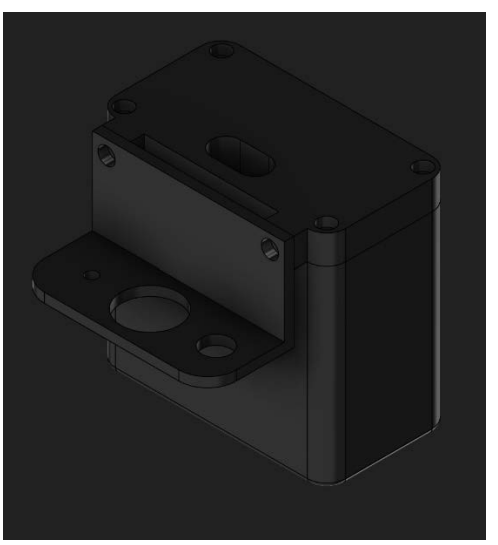

Figure 2 Equipment enclosure

3. HARDWARE LAYER

The central component of the system is the Arduino Uno microcontroller, which is responsible for controlling the operation of the entire system. This module was chosen due to its simplicity of implementation, the large number of available libraries, and its easy integration with sensors[5].

The Arduino Uno reads measurement data, analyzes water parameters by comparing current measurement values with predefined thresholds set in the control program, controls the LCD display, and communicates with a mobile device. Thanks to the built-in Bluetooth module, data can be transmitted wirelessly to the user's application. A diagram illustrating the interaction between the microcontroller, sensors, and output components is shown in Fig. 3.
Descriptions of tables justified: in Polish (simple text) and in English (italics), as shown in the example below. Board border ½ point, width 16 cm.

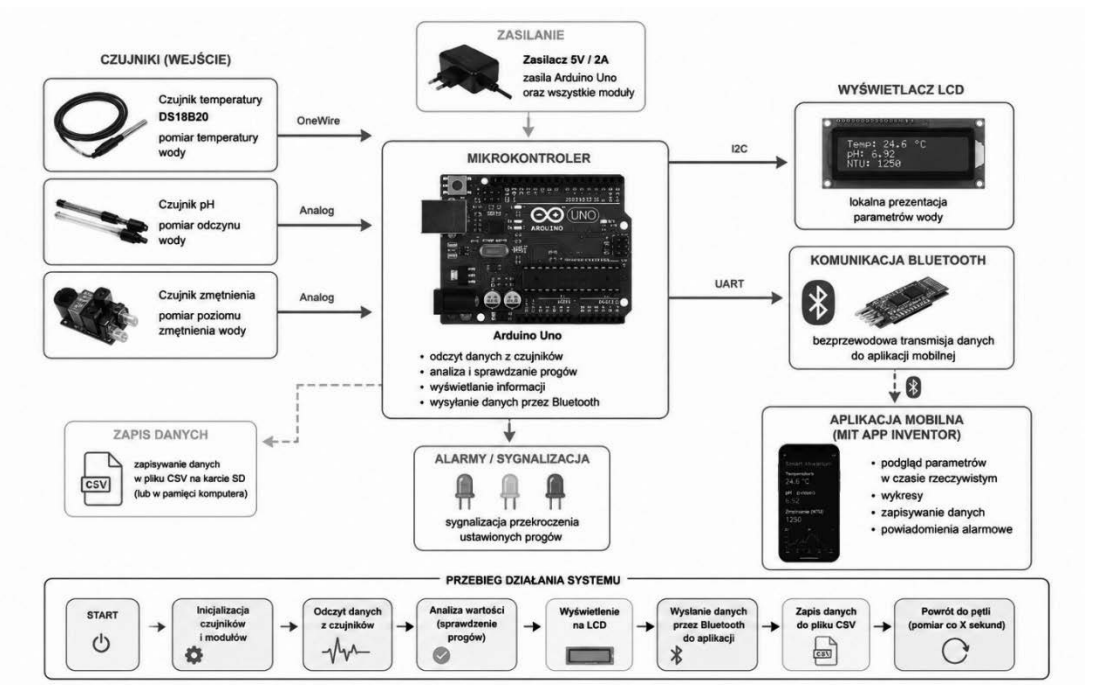

Figure 3. System operation diagram and sequence of operations

Three basic measurement sensors were used to monitor environmental conditions. Water temperature was measured using a waterproof DS18B20 digital sensor, which features simple communication and high measurement accuracy. It operates based on the 1-wire communication method [6,7].

An analog pH sensor was used to measure water pH, enabling continuous monitoring of changes in chemical parameters in the aquarium [7]. Additionally, a turbidity sensor was used to determine the degree of water contamination by analyzing light transmittance.

All sensors were connected directly to the Arduino Uno microcontroller and operated continuously, enabling regular measurements.
The system is equipped with an LCD display that allows for the local display of the aquarium's current operating parameters. The screen displays information on water temperature, pH, and turbidity levels.

The use of a local display allows the user to quickly check the system's status without having to use a mobile app. This solution enhances user convenience and improves the readability of the displayed data [1].

Additionally, the system incorporates a set of LED lights as a warning mechanism for deviations from the set parameters; depending on the color, these lights will indicate the current condition of the water.

4. SOFTWARE IMPLEMENTATION

The system software was developed using the Arduino IDE. The program runs in a loop and is based on regularly taking measurements of water parameters.

Upon startup, the system initializes all sensors and the LCD display. Then, the main program loop begins, which is responsible for collecting measurement data, analyzing it, and presenting the results to the user.

The obtained data is displayed on the LCD screen, transmitted to a mobile app, and saved to a file. If abnormal values are detected, the system can generate a warning informing the user of the need to take appropriate action.

The following standards (Table 1) have been adopted for the parameters read from the sensors; if these standards are exceeded, an alert will be signaled both via LED lighting and a message on the display.

Table 1.
Standards Adopted for the Measured Parameters [1]

PARAMETER	SCOPE APPROVED	NOTICE WHEN THE LIMIT IS EXCEEDED
Water pH	6.8 - 7.5	„Temperature too low/too high"
Water temperature	24- 28 °C	„Water pH too low/too high"
Water Turbidity	0 – 5 NTU	„Excessive water turbidity"

The system regularly reads the aquarium's environmental parameters. Temperature is measured by a DS18B20 sensor, while pH and turbidity values are read from analog sensors connected to the microcontroller's inputs.

The measurement results are converted to actual values and presented to the user in an easy-to-read format on the LCD display or in the mobile app. Data was logged every 1 second.

An important feature of the system is the ability to archive measurement data. All recorded parameters are saved in a CSV file containing the date, time, and values of individual measurements. The code that implements the method of saving data in CSV format is shown in Fig. 4. Analysis of the saved data allows for monitoring the stability of environmental parameters and detecting temporary measurement deviations. Data archiving also enables the assessment of the impact of environmental changes on conditions within the aquarium.

```
========================================
   SYSTEM SMART AKWARIUM - START
========================================
TEMP: 24.56 *C | pH: 13.09 | ZMETNIENIE: 1871.48 NTU (3.57 V)
TEMP: 24.56 *C | pH: 13.00 | ZMETNIENIE: 1860.44 NTU (3.57 V)
TEMP: 24.56 *C | pH: 13.02 | ZMETNIENIE: 1893.39 NTU (3.56 V)
TEMP: 24.56 *C | pH: 13.02 | ZMETNIENIE: 1882.46 NTU (3.56 V)
TEMP: 24.56 *C | pH: 13.05 | ZMETNIENIE: 1904.27 NTU (3.55 V)
TEMP: 24.56 *C | pH: 13.00 | ZMETNIENIE: 1904.27 NTU (3.55 V)
TEMP: 24.56 *C | pH: 12.98 | ZMETNIENIE: 1882.46 NTU (3.56 V)
TEMP: 24.56 *C | pH: 12.97 | ZMETNIENIE: 1849.35 N
```

☑ Autoscroll ☐ Show timestamp

File Edit Search View Document Help

```
Data i Godzina,Temperatura (C),pH,Zmetnienie (NTU)
2026-05-13 12:49:49,23.87,12.95,2657.90
2026-05-13 12:49:49,23.87,13.00,2675.92
2026-05-13 12:49:50,23.87,12.95,2669.96
2026-05-13 12:49:54,23.87,12.92,2675.92
2026-05-13 12:49:56,23.87,12.86,2669.96
2026-05-13 12:49:58,23.87,12.90,2675.92
2026-05-13 12:50:00,23.87,12.92,2687.66
2026-05-13 12:50:02,23.87,12.85,2669.96
2026-05-13 12:50:04,23.87,12.98,2699.19
2026-05-13 12:50:06,23.87,13.02,2710.50
2026-05-13 12:50:08,23.87,12.98,2914.77
2026-05-13 12:50:10,23.87,13.00,2908.48
2026-05-13 12:50:12,23.87,12.92,2935.07
2026-05-13 12:50:14,23.87,12.88,2914.77
2026-05-13 12:50:16,23.87,12.90,2929.54
2026-05-13 12:50:18,23.87,12.88,2942.97
2026-05-13 12:50:20,23.87,12.83,2905.26
2026-05-13 12:50:22,23.87,12.85,2895.27
2026-05-13 12:50:24,23.87,12.71,2858.50
2026-05-13 12:50:26,23.87,12.81,2870.10
2026-05-13 12:50:28,23.87,12.85,2881.21
2026-05-13 12:50:30,23.87,12.78,2873.85
2026-05-13 12:50:32,23.87,12.86,2891.84
2026-05-13 12:50:34,23.87,12.74,2877.56
```

Figure. 3 Example of a generated CSV file and a preview from the Arduino monitor

```python
import serial
import csv
import time
import re
import os

# Konfiguracja sciezek
desktop_path = os.path.join(os.path.expanduser("~"), "Desktop")
folder_path = os.path.join(desktop_path, "dane")
filename = os.path.join(folder_path, "dane_akwarium.csv")

if not os.path.exists(folder_path):
    os.makedirs(folder_path)

serial_port = '/dev/ttyACM0'
baud_rate = 9600

print("Uruchomiono skrypt Smart Akwarium...")

while True:
    try:
        # Proba nawiazania polaczenia
        with serial.Serial(serial_port, baud_rate, timeout=1) as ser:
            print(f"Polaczono z {serial_port}")
            time.sleep(2)

            with open(filename, mode='a', newline='') as file:
                writer = csv.writer(file)
                if os.path.getsize(filename) == 0:
                    writer.writerow(["Data i Godzina", "Temperatura (C)", "pH", "Zmetnienie (NTU)"])

                while True:
                    if ser.in_waiting > 0:
                        line = ser.readline().decode('utf-8', errors='ignore').strip()
                        numbers = re.findall(r"[-+]?\d*\.\d+|\d+", line)

                        if len(numbers) >= 3:
                            timestamp = time.strftime('%Y-%m-%d %H:%M:%S')
                            writer.writerow([timestamp, numbers[0], numbers[1], numbers[2]])
                            file.flush()
                            print(f"Zapis: {timestamp} | T:{numbers[0]} pH:{numbers[1]} NTU:{numbers[2]}")

    except (serial.SerialException, FileNotFoundError):
        print("Blad: Nie znaleziono Arduino. Proba ponownego polaczenia za 5 sekund...")
        time.sleep(5)
    except Exception as e:
        print(f"Nieoczekiwany blad: {e}")
        time.sleep(5)
```

Figure 4. Program that writes data to a CSV file

Communication between the smart aquarium system and the user is facilitated by Bluetooth technology. Data is transmitted wirelessly to a mobile app, where the user can monitor the aquarium's current status.

This solution provides quick access to the system's most important parameters without the need to connect the device directly to a computer. Additionally, the user can receive notifications when specific threshold values are exceeded.

5. MOBILE APP

The mobile app serves as a key tool for interacting with the user. It allows users to monitor the condition of the aquarium in real time, analyze water parameters, and quickly respond to any abnormalities. The app's interface was developed using MIT App Inventor [8] and presents real-time data in a clear and easy-to-understand way, allowing the user to quickly assess the situation in the aquarium.

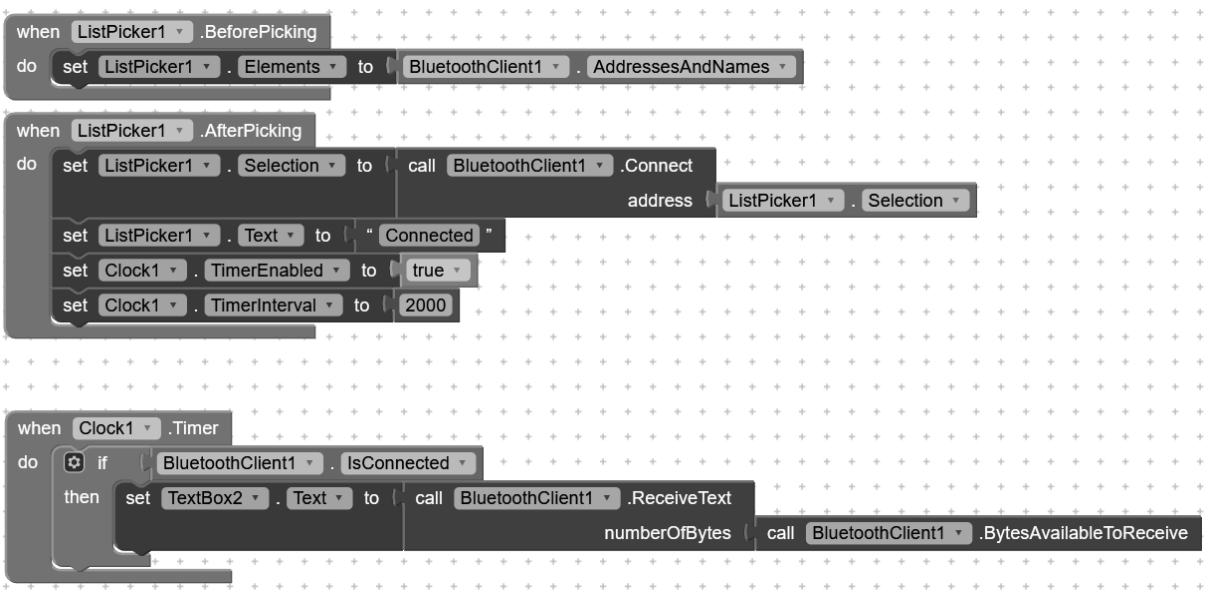

Figure 5. A program that reads the value of one of the variables from an Arduino Uno, written using Mit App Inventor

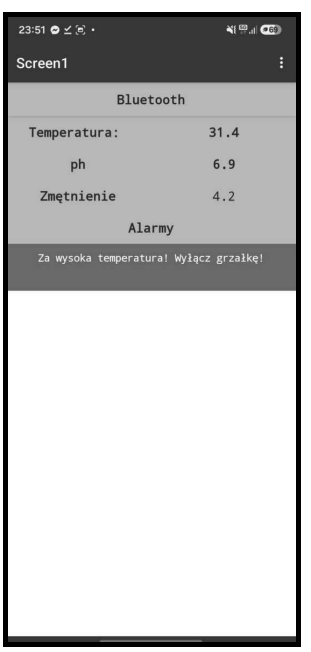

Figure 6. Mobile app for monitoring aquarium water parameters

Upon detecting any anomalies, the system automatically alerts the user by sending a notification that immediately appears on the mobile device's screen. Additionally, the app provides detailed information about the detected issues. Users can check which parameter is out of range, when the anomaly occurred, and the recommended actions to restore optimal conditions in the aquarium. This is a significant help for people who do not have in-depth knowledge of aquarium care.

The entire design is focused on simplicity and ease of use. The app does not overwhelm the user with excessive information [1], but instead focuses on clearly presenting the necessary data.

6. SYSTEM PERFORMANCE ANALYSIS

During the system performance tests, it was observed that the DS18B20 temperature sensor exhibited the greatest measurement stability. The measured values varied only slightly, which is due to the sensor's digital communication method and its resistance to electromagnetic interference. The temperature readings were stable and did not require additional data filtering.

Significantly greater fluctuations were observed in the case of the analog pH sensor and the liquid turbidity sensor. This is primarily due to the characteristics of analog measurement signals and the system's susceptibility to electrical interference and changes in supply voltage. In particular, the turbidity sensor exhibited momentary spikes in readings during liquid movement and changes in the sensor's position relative to the light source.

It was also observed that the measurement frequency has a direct impact on the system's operational stability and the amount of data generated. A reading interval that was too short led to a large number of entries in the CSV file and an increased number of temporary measurement deviations. To improve system stability, periodic readings taken every few seconds were implemented.

Bluetooth communication between the Arduino Uno and the mobile app also proved to be an important aspect. During testing, no issues were observed with data transmission over short distances; however, connection stability decreased as the distance between the devices increased. Nevertheless, the use of Bluetooth communication significantly simplified the integration of the system with the mobile app created in the MIT App Inventor environment.

7. CONCLUSION

This article presents the design and implementation of a smart aquarium based on the ESP32 microcontroller. The developed system enables automatic monitoring of basic aquatic environment parameters, such as temperature, pH, and water turbidity.

The use of measurement sensors, an LCD display, and wireless communication made it possible to create a functional system that assists in monitoring aquarium conditions. An additional advantage of this solution is the ability to archive data and analyze it later.

The results confirm the potential for using IoT technology in simple aquatic environment monitoring systems. In the future, the system can be expanded to include additional features, such as automatic lighting control, automatic feeding, or integration with cloud-based data storage.

BIBLIOGRAPHY

1. M. Frydecki, K. Tkałka, M. Koźlik, K. Strukowski, K. Kołodziej, M. Jaroszek, M. Król, M. Bilewicz, V. Macejko, E. Posmyková *Smart aquarium as an example of modern methods of water environment control,* TalentDetector2026_Winter INTERNATIONAL STUDENTS SCIENTIFIC CONFERENCE, Gliwice 2026, str. 113- 119, ISBN 978-83-68390-55-1,
2. M.Sahaya Sheela, S.RaviChand, S. Gopalakrishnan, Shruti Bhargava choubey, M Gopianand, J.Jasmine Hephzipah *Empowering Aquarists a Comprehensive Study On IOT-Enabled Smart Aquarium Systems For Remote Monitoring And Control,* Babylonian Journal of Internet of ThingsVol.2024, pp. 33–43 https://doi.org/10.58496/BJIoT/2024/005
3. T. A. Taher, *Development of IoT based fish monitoring system for aquaculture,* in Intelligent Automation and Soft Computing, vol. 32, no. 1, pp. 55-71, 2022
4. Balasubramani S., Aakash Ram S., Akshay Bharadwaj S., Bennet Niffin N. *Smart Aquarium Management System,* 2020, doi:10.3233/APC200196
5. *A Balanced Aquarium – Testing and Analysis*, https://en.zolux.com/tips-from-the-pros/balanced-aquarium [dostęp 16.12.2025].
6. Shamshulbahrin, A. S., & Ahmad, I. *Aquarium Monitoring System via IOT*. Journal of Engineering Technology, 10(1), 13-16, 2022
7. A.T. Tamim , H. Begum , S. A. Shachcho , M. M. Khan, B. Yeboah-Akowuah , M. Masud J. F. Al-Amri *Development of IoT Based Fish Monitoring System for Aquaculture,* Intell, Autom. Soft COmput.. 2022, 32, 0215, DOI:10.32604/iasc.2022.021559
8. https://appinventor.mit.edu/

TalentDetector

7th-9th June 2026
Gliwice-Brenna, Poland

DEPARTMENT OF ENGINEERING MATERIALS AND BIOMATERIALS
FACULTY OF MECHANICAL ENGINEERING
SILESIAN UNIVERSITY OF TECHNOLOGY

INTERNATIONAL STUDENTS SCIENTIFIC CONFERENCE

Mechanical Properties of LPBF Tool Steels after Heat Treatment

Mariusz Król[a], Juraj Beniak[b],

[a] Silesian University of Technology, Faculty of Mechanical Engineering, Department of Engineering Materials and Biomaterials, e-mail: mariusz.krol@polsl.pl
[b] Slovak University of Technology in Bratislava, Faculty of Mechanical Engineering, Bratislava e-mail: mariusz.krol@polsl.pl

Abstract: This study investigates the influence of heat-treatment parameters on the mechanical properties of W722 and M789 tool steels fabricated using the Laser Powder Bed Fusion (LPBF) process. Hardness, tensile strength, and impact toughness were evaluated for samples subjected to various heat-treatment conditions. The results demonstrated that W722 steel exhibited considerably superior mechanical performance compared with M789 steel. The highest hardness and tensile strength values for W722 steel, reaching 57.2 HRC and 2164 MPa respectively, were obtained after combined solution heat treatment and aging. In addition, solution heat treatment alone provided high impact toughness (53.2 J), indicating a broad potential for tailoring the material properties through controlled thermal processing.

Keywords: LPBF, Heat Treatment, Mechanical Properties, Tool Steels.

1. INTRODUCTION

Laser Powder Bed Fusion (LPBF) has significantly expanded the manufacturing possibilities for the tool industry by enabling the production of complex geometries and conformal cooling channels unattainable with conventional methods. However, the rapid solidification and cyclic thermal loading characteristic of LPBF strongly affect the microstructure and mechanical behavior of tool steels, making post-process heat treatment essential for achieving optimal properties (Fig. 1).

Among LPBF tool steels, W722 and M789 represent two advanced materials with distinct strengthening mechanisms and application potential. W722 maraging steel is characterized by very high strength and toughness, while M789 combines maraging hardening with improved corrosion resistance due to chromium addition. Their final mechanical performance strongly depends on heat-treatment parameters, particularly solution annealing and aging conditions.

This study investigates the influence of aging and heat-treatment parameters on the microstructure and mechanical properties of LPBF-produced W722 and M789 steels. The analysis focuses on hardness, yield strength, tensile strength, and impact toughness, aiming to identify heat-treatment conditions that provide the best balance between high strength and sufficient ductility for industrial tooling applications [1-10].

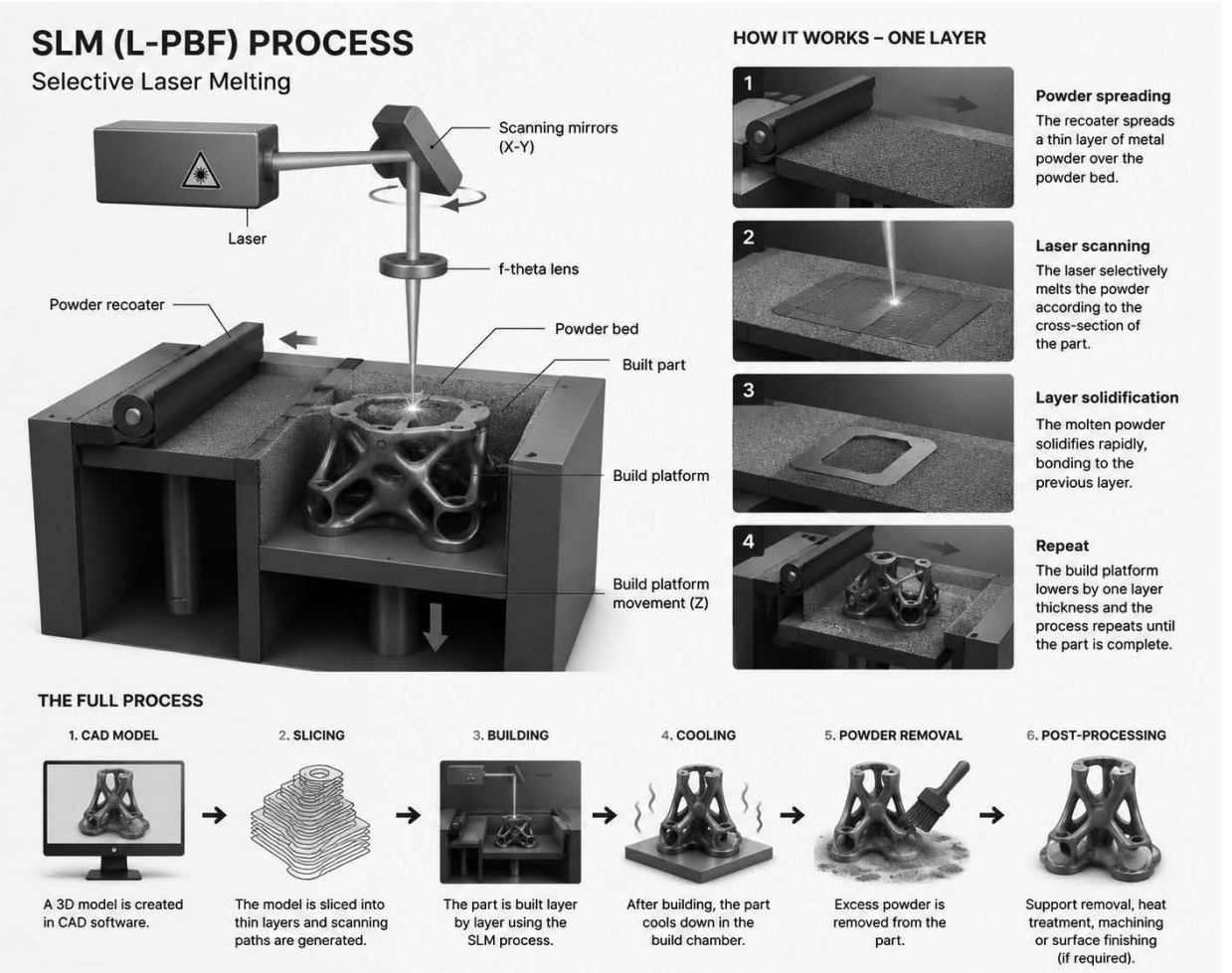

Fig. 1. Schematic illustration of the Laser Powder Bed Fusion (LPBF) process.

2. MATERIALS AND EXPERIMENT

The study was carried out on W722 and M789 tool steels manufactured by the laser powder bed fusion (LPBF) process using powders supplied by Voestalpine BÖHLER Edelstahl GmbH & Co KG. The chemical compositions of the investigated powders (Table 1) were characterized by low carbon content and alloying additions such as nickel, chromium, molybdenum, aluminum, and titanium. Both materials were produced by gas atomization and consisted of spherical particles with sizes ranging from 15 to 45 µm.

To evaluate the suitability of the powders for the LPBF process, detailed powder characterization was performed. Particle morphology was analyzed using scanning electron microscopy (SEM, Zeiss Supra 35), while particle size distribution was determined by laser diffraction (Fraunhofer model) in wet dispersion using an Analysette 22 MicroTec analyzer.

Table 1. Chemical composition of the W722 and M789 tool steels powder, wt%

	C	Cr	Ni	Mo	Al	Ti	Mn	C
W722	<0.03	-	18.00	4,90	0.60	1.10	<0.15	9.30
M789	<0.02	12.2	10.00	1.00	0.60	1.00		-

Specimens for hardness, Charpy impact, and tensile testing were manufactured in a horizontal orientation relative to the build direction. Separate sample sets were prepared for each testing method and heat-treatment condition, enabling the evaluation of four material states: as-built, solution annealed, aged, and solution annealed + aged.

The heat treatment of W722 steel consisted of solution annealing at 820°C for 1 h followed by air cooling, and subsequent aging at 490°C for 6 h in an argon atmosphere with furnace cooling. For M789 steel, solution annealing was performed at 1000°C for 1 h with air cooling, followed by aging at 510°C for 3 h in argon and furnace cooling. The applied parameters were selected based on literature data and manufacturer recommendations.

Mechanical properties were determined by tensile testing using a Zwick Z100 machine in accordance with PN-EN ISO 6892-1. Dogbone specimens were prepared according to ISO 2740. Charpy impact tests were conducted on V-notched specimens following PN-EN ISO 148-2, while hardness measurements were performed using a Zwick ZHR 4150TK hardness tester.

3 RESULTS AND DISCUSSION

Laser diffraction analysis confirmed the high dimensional homogeneity of both powders, as evidenced by the narrow and symmetrical particle size distribution curves (Fig. 2). The average particle size (D50) was approximately 40 µm for W722 and 29.0 µm for M789, while the D10–D90 ranges were 23.9–63.7 µm and 15.7–48.3 µm, respectively. SEM observations (Fig. 3) revealed that both powders were predominantly spherical in shape; however, individual particles with irregular geometry and visible satellite formations were also identified.

The W722 steel exhibited superior strength and significantly higher impact toughness compared with M789 steel.

For W722 steel, the lowest hardness (34.6 HRC) and tensile strength (1079 MPa) were recorded after solution heat treatment alone. Aging, particularly when combined with solution treatment, substantially improved these properties, leading to maximum values of 57.2 HRC and 2164 MPa. At the same time, solution heat treatment provided the highest impact toughness of 53.2 J, whereas aging reduced impact toughness to approximately 15–17 J due to increased material hardening.

A similar trend was observed for M789 steel, where the lowest hardness and tensile strength values (32.1 HRC and 886 MPa) occurred after solution heat treatment, while aging resulted in peak values of 53.1 HRC and 1639 MPa. However, the tensile strength of M789 remained noticeably lower than that of W722 under comparable conditions. Moreover, M789 steel exhibited consistently low impact toughness, ranging from 5.8 to 14.3 J, with the poorest performance observed after combined solution treatment and aging.

In summary, the application of W722 steel powder appears to be a more amenable material to heat treatment in terms of combining high strength with good impact toughness, while M789 achieves lower strength parameters and is characterized by greater brittleness.

a) b)

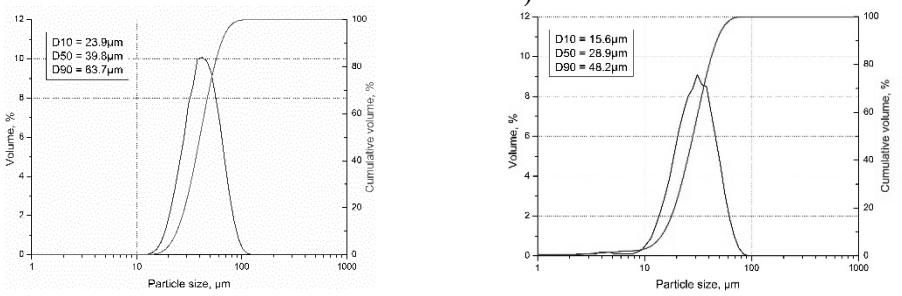

Fig. 2. Graph depicting the particle size distributions of the: a) W722 and b) M789 powder.

a) b)

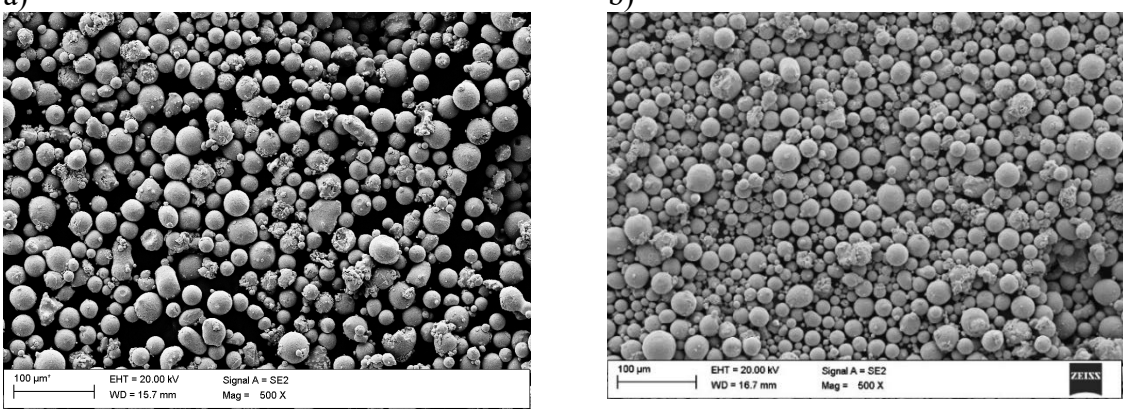

Fig. 3. Morphology of steel powders (SEM, 500×): (a) grade W722, (b) grade M789.

The observed differences between W722 and M789 steels are primarily related to their chemical composition and precipitation-hardening mechanisms. W722 steel, enriched with nickel, cobalt, and molybdenum, enables the formation of a high density of fine intermetallic precipitates during aging, resulting in very high tensile strength exceeding 2000 MPa. In contrast, M789 steel contains chromium to improve corrosion resistance, which is accompanied by lower strength parameters compared with cobalt-containing maraging steels.

The aging process promotes the precipitation of strengthening phases that hinder dislocation movement and significantly increase hardness. This effect was particularly pronounced for W722 steel, where hardness increased from approximately 37 to 57 HRC after aging. For M789 steel, however, the combined solution treatment and aging cycle produced lower hardness than aging alone, suggesting that high-temperature solution annealing may have induced unfavorable grain growth or phase separation, reducing the effectiveness of precipitation hardening.

Heat treatment also affected the impact toughness of both steels in different ways. In W722 steel, aging caused a substantial reduction in toughness due to intensive precipitation strengthening, which increased hardness at the expense of ductility. In M789 steel, solution treatment significantly decreased impact toughness, while subsequent aging partially restored ductility. This behavior may be associated with the formation of reverted austenite during aging.

Austenite reversion is known to improve toughness in maraging steels when present in limited amounts. In W722 steel, the precipitation of a small fraction of reverted austenite after the full heat-treatment cycle likely contributed to maintaining relatively favorable impact toughness. In contrast, M789 steel retained a more brittle microstructure, or the reverted austenite formed in a less beneficial morphology, resulting in inferior fracture resistance.

4. CONCLUSIONS

Based on the obtained mechanical properties of LPBF-manufactured W722 and M789 steels, it can be concluded that W722 steel demonstrated significantly superior performance, achieving over 30% higher tensile strength (Rm > 2100 MPa) and greater hardness than M789 steel due to effective precipitation strengthening associated with Ni, Co, and Mo alloying additions. Furthermore, the applied heat-treatment procedures enabled effective tailoring of W722 properties, ranging from high ductility after solution treatment, reflected by an impact toughness of 53.2 J, to very high hardness and strength after the combined solution treatment and aging cycle. In contrast, M789 steel exhibited a pronounced reduction in impact toughness after solution treatment, which may indicate the occurrence of unfavorable microstructural changes such as grain coarsening or carbide precipitation.

ACKNOWLEDGEMENT

The scholar would like to acknowledge the International Visegrad Fund for the financial support during the realization of the research project. The most thanks are directed to prof. MSc. Juraj Beniak, PhD. from the Institute of Production Engineering and Quality, Faculty of Mechanical Engineering, Slovak University of Technology in Bratislava for friendship and invaluable help while doing the research.

Visegrad Fund

BIBLIOGRAPHY

[1] Behl, B., Dong, Y., Pramanik, A., Bandyopadhyay, T.K.: Evolution of Microstructures and Mechanical Properties of Laser-Welded Maraging Steel for Aerospace Applications: The Past, Present, and Future Prospect, Journal of Manufacturing and Materials Processing 9(9), 394 (2025)

[2] Brytan, Z., Król, M., Benedyk, M., Pakieła, W., Tanski, T., Dagnaw, MJ., Snopiński P., Pagác, M., Czech, A.: Microstructural and mechanical properties of novel co-free maraging steel manufactured by laser powder bed fusion, Materials 15(6) 2089 (2022)

[3] Ni, C., Zhu, J., Zhang, B., An, K., Wang, Y., Liu, D., Liu, C.: Recent advance in laser powder bed fusion of Ti–6Al–4V alloys: microstructure, mechanical properties and machinability. Virtual and Physical Prototyping, 20(1), (2025)

[4] Bheemavarapu, S.R., Thella, B.R., Mondi R.K.: Effect of Direct Aging Heat Treatment on Microstructure and Mechanical Properties of Laser Powder Bed Fused Maraging Steel 300-Grade Alloy. Journal of Tribology 146(11), 111701 (2024)

[5] Böhler Edelstahl GmbH, BÖHLER M789 AMPO – Additive Manufacturing Powder, Technical Datasheet, 2024

[6] Böhler Edelstahl GmbH, BÖHLER W722 AMPO – Hot Work Tool Steel for Additive Manufacturing, Technical Datasheet, 2024

[7] Palad, R., Tian, Y., Chadha, K., Rodrigues, S., Aranas, C.: Microstructural features of novel corrosion-resistant maraging steel manufactured by laser powder bed fusion, Materials Letters. 275, 128026, (2020)
[8] Kučerová, L., Burdová, K., Jeníček, Š., Volkmannová, J.: Microstructure and mechanical properties of 3D printed tool steel after various precipitation hardening treatments. Manufacturing Technology 22(2), 215-223 (2022)
[9] Pustički, D., Alar Ž., Bandov, Zvonimir, Aditively manufactured maraging steel: Influence of heat treatment on mechanical properties and microstructure. Materials 18(9), 1999 (2025)
[10] Li, Y., Yu, J., Li, S., Wang, S., Ren, Y., Yang, K., Wang, YD.: The influence of post-aging treatment on the microstructure and micromechanical behaviors of additively manufactured maraging steel investigated by in situ high-energy X-ray diffraction. Journal of Materials Science & Technology 200, 1-12 (2024)

TalentDetector

7th-9th June 2026
Gliwice-Brenna, Poland

DEPARTMENT OF ENGINEERING MATERIALS AND BIOMATERIALS
FACULTY OF MECHANICAL ENGINEERING
SILESIAN UNIVERSITY OF TECHNOLOGY

INTERNATIONAL STUDENTS SCIENTIFIC CONFERENCE

Properties and structure of Cu-Cr alloys used in electrical engineering
Własności i struktura stopów Cu-Cr stosowanych w elektrotechnice

Beata Krupińska[a], Maciej Marcinkowski[b]

[a] Silesian University of Technology, Faculty of Mechanical Engineering, Department of Engineering Materials and Biomaterials
email: beata.krupinska@polsl.pl
[b] Student of Materials Engineering 2022, Silesian University of Technology, Faculty of Mechanical Engineering,

Streszczenie: Celem pracy było określenie wpływu odkształcenia plastycznego oraz obróbki cieplnej na wybrane własności mechaniczne i mikrostrukturę stopu miedzi CuCrZr. Materiał poddano analizie termiczno-derywacyjnej w celu ustalenia temperatury obróbki cieplnej a następnie wykonano obróbkę cieplno-plastyczną przy ustalonych parametrach. Wykonano badania mikrostruktury, twardości oraz konduktywności w celu porównania własności stopów.
Abstract: The aim of this study was to determine the effect of plastic deformation and heat treatment on selected mechanical properties and microstructure of a CuCrZr copper alloy. The material was subjected to thermal derivation analysis to determine the heat treatment temperature, followed by thermoplastic treatment at established parameters. Microstructure, hardness, and conductivity tests were performed to compare the alloy properties.
Keywords: Cu-Cr, thermal-derivative analysis, microstructure, microhardness, conductivity.

1. WSTĘP

Stopy Cu-Cr zawierają od ok. 0,6 do 1,2% chromu. Charakteryzuje je wysoka wytrzymałość, odporność korozyjna oraz przewodność elektryczna. W porównaniu do czystej miedzi, odporność korozyjna jest znacznie wyższa ze względu na własności czystego chromu. Są one doskonałymi materiałami na elektrody do zgrzewania oporowego, rozdzielnice, złącza kablowe, części wyłączników, formy oraz końcówki do zgrzewania punktowego. Również świetnie nadają się na różnego rodzaju przewodniki elektryczne oraz termiczne od których wymagana jest duża wytrzymałość. Stopy te można poddać starzeniu. Podczas starzenia chrom jest wytrącany z roztworu stałego powodując tym samym zmianę własności stopu. Po starzeniu wytrzymałość tego stopu charakteryzuje prawie dwukrotnie większa wytrzymałość niż w przypadku czystej miedzi. Operacja starzenia w dalszym ciągu utrzymuje przewodnictwo na wysokim poziome, którego wartość wynosi 85% czystej miedzi. Wytrzymałość tych stopów jest wysoka nawet w podwyższonych temperaturach [1-6].

Materiały z miedzi chromowej (Cu-Cr) przeważnie stosuje się w przemyśle elektrotechnicznym. Jest to związane z korzystnymi własnościami mechanicznymi i jednocześnie bardzo wysoką przewodnością elektryczną oraz cieplną. Wysoka wytrzymałość uzyskiwana jest w wyniku utwardzania wydzieleniowego. W stopach miedzi chromowej o dużej zawartości chromu, chrom jest uważany za drugą fazę. Już bardzo małe ilości chromu (0,7% wag.) rozpuszczają się w osnowie miedzi. Skutkuje to tworzeniem się roztworu stałego w temperaturze eutektycznej. Jednakże trzeba pamiętać, iż większość chromu jest nierozpuszczona, więc efekt wzmocnienia drugiej fazy jest częściowo ograniczony. Powodem takiego ograniczenia są zbyt duże rozmiary cząstek jak również stosunkowo niewystarczająca wytrzymałość fazy wzmacniającej. Z tych powodów w stopach nie jest możliwe skuteczne zahamowanie ruchu dyslokacji. Opierając się na przykładach dla stopów Cu-Cr, gdzie zawartość chromu jest mniejsza niż 1% wag. i jest wykonany proces starzenia, wytrzymałość na rozciąganie sięga wartości ok. od 450 do 500 MPa. Natomiast w stopach zawierających aż 15% wag. chromu, zauważono stosunkowo niewielki wzrost wartości wytrzymałości, gdyż jest to wartość tylko o 100–150 MPa większa. Powoduje to, że przyrost wytrzymałości tych stopów jest uważany za za niewystarczający [1-6].

2. BADANY MATERIAŁ ORAZ METODOLOGIA

Badanym materiałem był stop CuCrZr o składzie chemicznym przedstawionym w tabeli 1. Stop poddano analizie termiczno-derywacyjnej w celu ustalenia parametrów obróbki cieplnej (przesycania i starzenia) a następnie dla różnych parametrów obróbki cieplnej wykonano pomiary twardości i konduktywności w celu zbadania wpływu obróbki cieplnej na uzyskane wyniki.

Table 1. Chemical composition of analysed copper alloys
Tablica 1. Skład chemiczny badanych stopów miedzi

	Stężenie masowe pierwiastków, %		
	Cr	Zr	Cu
CuCrZr	0.85	0.15	reszta
CuCrZr (przesycany, odkształcany plastycznie, starzony	0.85	0.15	reszta

W celu określenia wpływu odkształcenia plastycznego oraz obróbki cieplnej na wybrane własności mechaniczne i mikrostrukturę stopu miedzi CuCrZr:

Analizę termiczno-derywacyjną wykonano z wykorzystaniem urządzenia UMSA wyposażonego w sterowany komputerowo układ chłodzenia, który pozwala na elastyczne ustawienie szybkości chłodzenia stopów CuCrZr. Przygotowano próbki do analizy termiczno-derywacyjnej o średnicy Ø12 mm i wysokości 12 mm. Wykonano również otwory na termopary, w których występuje węzeł cieplny dla tego typu i układu geometrii próbki.

Temperatura przesycenia wyznaczona w wyniku analizy termiczno-derywacyjnej) CuCrZr wynosiła 950°C, czas nagrzewania 1 godzinę w atmosferze argonu ochronnego, następnie odkształcenie plastyczne 50%, a następnie wykonano starzenia w temperaturze 450°C, czas grzania 1 godzinę w atmosferze argonu ochronnego.

Badania mikrostruktury i składu chemicznego wykonano z wykorzystaniem mikroanalizy EDS na skaningowym mikroskopie elektronowym Zeiss Supra 25 oraz mikroskopie optycznym

MEF4A dostarczonym przez firmę Leica wraz z oprogramowaniem do analizy obrazu, a także skaningowym mikroskopie elektronowym z wykorzystaniem urządzenia Zeiss Supra 25 w trybie wysokiej rozdzielczości.

Pomiar przewodności elektrycznej wykonano za pomocą urządzania Sigmascope SMP350 z sondą FS40.

Mikrotwardość zmierzono przy użyciu twardościomierza Vickers Future-Tech (FM-ARS 9000) z obciążeniem 1000 gf przez 10 s.

3. WYNIKI

Analiza Termiczno-Derywacyjna wykonana z wykorzystaniem UMSA MT5 (Universal Metallurgical Symulator and Analyzer) pozwoliła określić temperatury T_L i T_{sol} (Rys.1, tab. 2).

Analiza termiczno-derywacyjna jest kluczowym badaniem w celu określenia kinetyki krystalizacji stopu. Dzięki uzyskanym krzywym na wykresie można określić w jakiej temperaturze przebiega proces przesycania. Na podstawie uzyskanych wykresów można wyznaczyć temperaturę początku krystalizacji (T_L) oraz temperaturę końca krystalizacji (T_{SOL}). Proces przesycania według literatury powinno przeprowadzać się w temperaturze poniżej temperatury T_{SOL} stopu [7,8].

Próbki zostały podgrzane do temperatury 1120°C i utrzymywane w niej przez 300 sekund. Po wytrzymaniu próbek w temperaturze 1120°C rozpoczęło się swobodne chłodzenie. Badanie te wykonano w atmosferze gazu ochronnego - argonu. Na podstawie otrzymanych wykresów wyznaczono temperaturę przesycania wynosi 950°C.

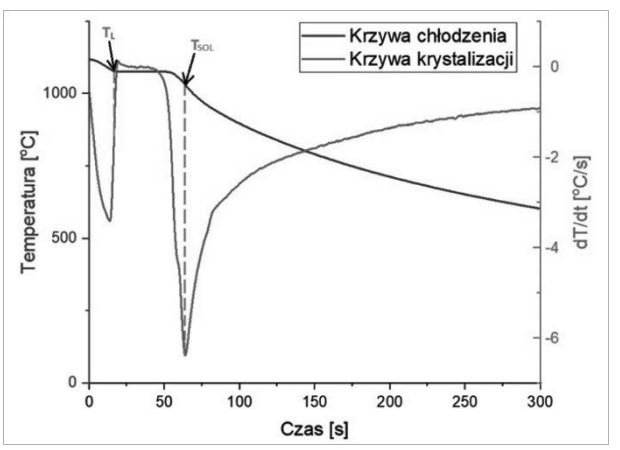

Figure 1. ATD analysis graph during cooling of CuCrZr alloy.
Rysunek 1. Wykres analizy ATD podczas chłodzenia stopu CuCrZr.

Table 2. Determined temperatures at points T_L and T_{SOL}.
Tablica 2. Wyznaczone temperatury w punktach T_L oraz T_{SOL}.

	T_L [°C]	T_{SOL} [°C]
CuCrZr	1077	1033

Na rys. 2, który przedstawia morfologie stopu CuCrZr w stanie wyjściowym można zauważyć strukturę dendrytyczną. Na granicach ziaren widoczne są wydzielenia chromu, które zostały przedstawione na rysunku 3. Mikrostruktury po procesie przesycania widzimy na rysunku 4. Z kolei na rysunku 5 można zauważyć, że w stopie CuCrZr po przesycaniu oraz starzeniu

wydzielenia chromu są dużo większe i gromadzą się w dużym stopniu na granicach ziaren, lecz pojawiły się również drobne wydzielenia w osnowie. Cząstki chromu mają zdolność do tworzenia się podczas krzepnięcia. Na podstawie uzyskanych wyników można zauważyć, że chrom jest wypierany przez miedź ze względu na zbyt duże rozmiary cząstek chromu.

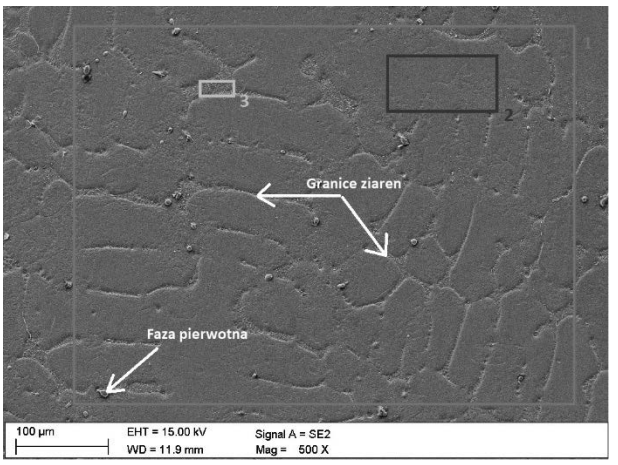

Figure 2. Microstructure of the CuCrZr alloy (initial state).
Rysunek 2. Mikrostruktura stopu CuCrZr (stan wyjściowy).

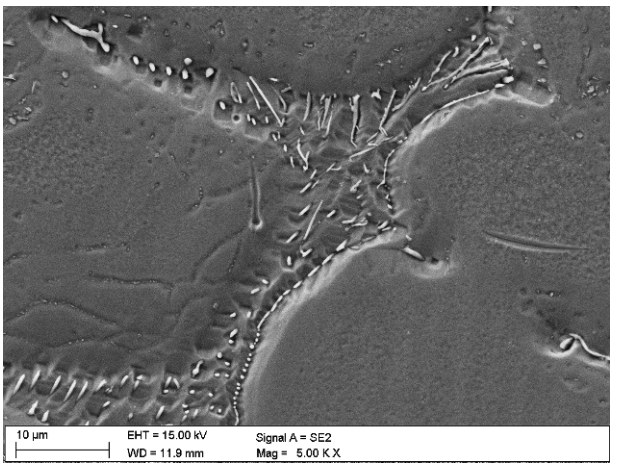

Figure 3. Chromium precipitation and morphology of the CuCrZr alloy in the initial state (magnification 5000x).
Rysunek 3. Wydzielenia chromu oraz morfologia stopu CuCrZr w stanie wyjściowym (powiększenie 5000x).

Table 3. EDS analysis results in areas 1-3 in Fig. 2.
Tablica 3. Wyniki analizy EDS w obszarach 1-3 na rys. 2.

	Cr	***Cu***
Obszar 1	1.4	98.6
Obszar 2		100.0
Obszar 3	4.9	95.1

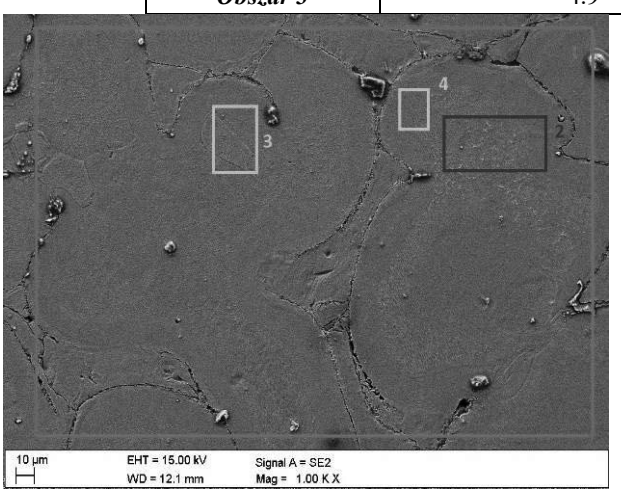

Figure 4. Microstructure of the CuCrZr alloy (state after solution annealing).
Rysunek 4. Mikrostruktura stopu CuCrZr (stan po przesycaniu).

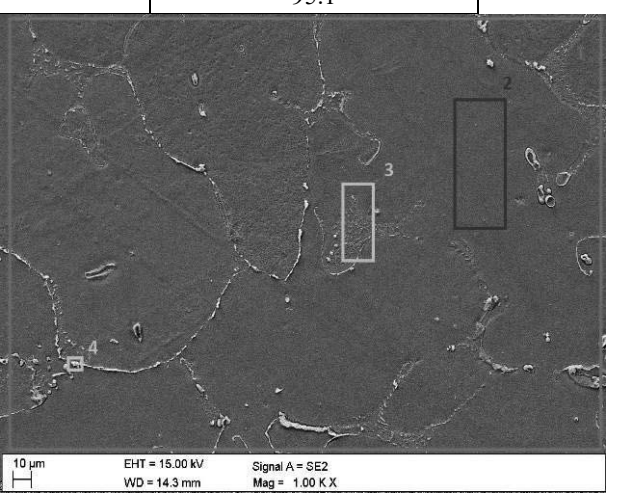

Figure 5. Microstructure of the CuCrZr alloy (state after solution heat treatment and aging).
Rysunek 5. Mikrostruktura stopu CuCrZr (stan po przesycaniu i starzeniu).

Table 4. EDS analysis results in areas 1-4 in Fig. 4.
Tablica 4. Wyniki analizy EDS w obszarach 1-4 na rys. 4.

	P	***Cr***	***Cu***
Obszar 1	1.5	0.9	97.6
Obszar 2	1.9	0.4	97.7
Obszar 3			100.0
Obszar 4		1.0	99.0

Table 5. EDS analysis results in areas 1-4 in Fig. 5
Tablica 5. Wyniki analizy EDS w obszarach 1-4 na rys. 5.

	O	***Cr***	***Cu***	***Zr***
Obszar 1		1.6	98.4	
Obszar 2			100.0	
Obszar 3	2.7	5.8	91.5	
Obszar 4	9.4	26.8	53.2	10.5

Mikrostruktury stopu CuCrZr przedstawiono na rysunkach 6-8. Na rysunku 6 widzimy stan wyjściowy – struktura dendrytyczna. Po przesycaniu stopu CuCrZr wydzielenia chromu dyfundują do fazy α (rys. 7). Chrom podczas przesycania częściowo rozpuszcza się w miedzi. W wyniku starzenia stopu CuCrZr pojawiły się pojedyncze wydzielenia chromu, które mają na celu blokować ruch dyslokacji (rys. 8). W próbkach, które poddano starzeniu wydzielenia chromu występują na granicy ziaren.

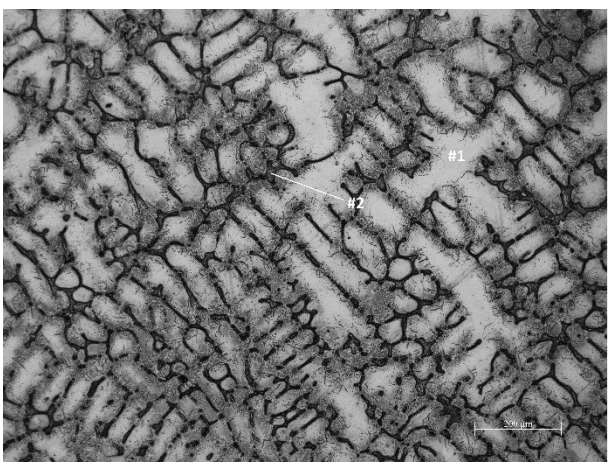

Figure 6. Structure of the CuCrZr alloy in its initial state (100x magnification). #1 - α, #2 – β
Rysunek 6. Struktura stopu CuCrZr w stanie wyjściowym (powiększenie 100x). #1 - α, #2 – β

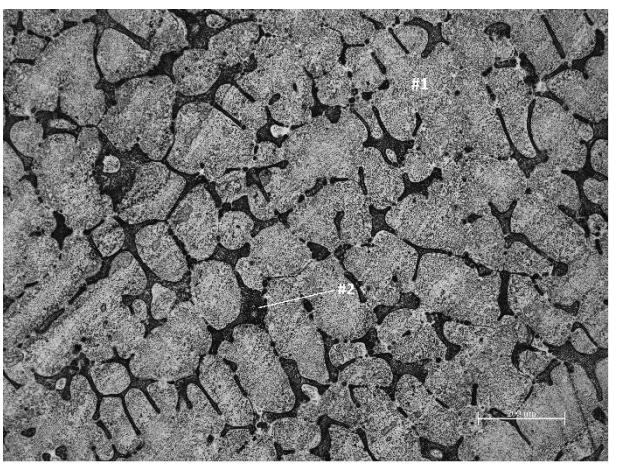

Figure 7. Structure of the CuCrZr alloy supersaturation treated at 950°C (100x magnification). #1 – CuCr, #2 – β
Rysunek 7. Struktura stopu CuCrZr przesycanego w temperaturze 950°C (powiększenie 100x). #1 – CuCr, #2 - β

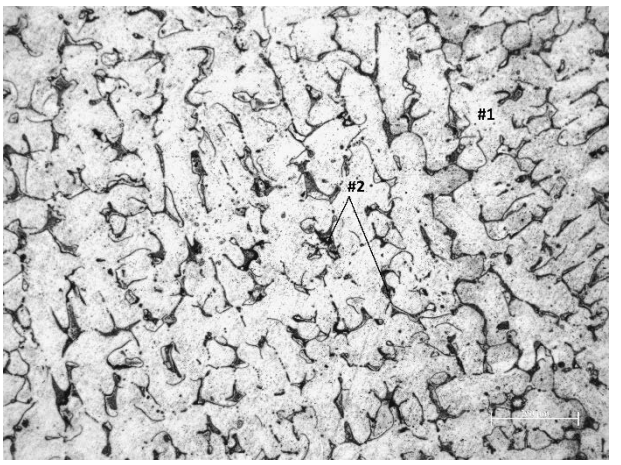

Figure 8. Structure of the CuCrZr alloy solution annealed at 950°C and aged at 450°C (100x magnification). #1 – α, #2 - β
Rysunek 8. Struktura stopu CuCrZr przesycanego w temperaturze 950°C i starzonego w temperaturze 450°C (powiększenie 100x). #1 – α, #2 - β

Wyniki pomiarów twardości i konduktywności przedstawiono w tablicy 6.

Table 6. Results of hardness and conductivity measurements for the CuCrZr alloy in its initial state and after thermoplastic treatment
Tablica 6. Wyniki pomiarów twardości i konduktywności dla stopu CuCrZr w stanie wyjściowym i po obróbce cieplno-plastycznej

	Konduktywność [Ms/m]	Twardość [HV]
CuCrZr	19	93
CuCrZr (przesycany, odkształcany plastycznie, starzony	30	126

WNIOSKI

Na podstawie przeprowadzonych badań sformułowano następujące wnioski:
W stanie wyjściowym w stopie CuCrZr wydzielenia chromu wystąpiły na granicach ziaren. W wyniku przesycania stopów CuCrZr w temperaturze 950°C chrom częściowo rozpuszcza się w osnowie miedzi. Natomiast efektem starzenia jest powstanie pojedynczych wydzieleń.
Porównując wartość twardości badanych stopów po przeprowadzonej obróbce cieplno-plastycznej z stanem wyjściowym zaobserwowano znaczny wzrost rzędu ok. 30%.
Wartość konduktywności stopu CuCrZr w stanie wyjściowym wynosiła 19Ms/m natomiast po obróbce cieplno-plastycznej 30 Ms/m co oznacza wzrost ponad 50%

LITERATURA

1. Z. Rdzawski monografia “Miedź stopowa” Wydawnictwo Politechniki Śląskiej Gliwice 2009.

2. B. Krupińska, W. Borek, M. Krupiński, T. Karkoszka, The Influence of Ag on the Microstructure and Properties of Cu-Ni-Si, Materials 13 (2020) 3416.
3. Deutsches Kupferinstitut Berufsverband "Low-Alloyed Copper Alloys".
4. M. Krancy, Rozprawa doktorska "Uszlachetnianie miedzi oraz stopów Cu-Cr preparatami utleniająco - modyfikującymi w aspekcie poprawy przewodności elektrycznej" AGH 2019.
5. H. Jiang, L. Peng, X. Mi, H. Guo, H. Xie, D. Liu, F. Liu, Z. Yang "Simultaneously enhancing the strength and electrical conductivity of Cu-Ni-Sn alloy through plastic deformation of an intermetallic compound" Materials & Design Volume 235 (2023) 112445.
6. S. Fassbinder, Miedź w elektrotechnice - Praktyczne zastosowania materiałów przewodzących, Niemiecki Instytut Miedzi (2010).
7. http://www.tungsten-copper.com/Polish/chromium-copper-alloy.html
8. Liyuan Shan, Xueliang Wang, Yanli Chang, Yaping Wang, „Improving the mechanical performance of CuCr alloy by dissolving Cu in the Cr second phase", Materials Characterization, Volume 176, 2021

TalentDetector
31th January 2025
Gliwice, Poland
DEPARTMENT OF ENGINEERING MATERIALS AND BIOMATERIALS
FACULTY OF MECHANICAL ENGINEERING
SILESIAN UNIVERSITY OF TECHNOLOGY
INTERNATIONAL STUDENTS SCIENTIFIC CONFERENCE

Struktura, skład fazowy oraz właściwości mechaniczne i tribologiczne jedno- i dwuwarstwowych powłok na bazie węglika wolframu natryskiwanych płomieniowo

Waldemar Kwaśny [a], Wojciech Kała [b], Bartłomiej Kazek [b], Szymon Wyrwa [c], Amelia Siemińska [d], Rafał Łosoń[b], Grzegorz Sikorski[b], Oliwier Koprowski[b], Magdalena Mazur[e], Patryk Stelmach[e]

[a] Politechnika Śląska Wydział Mechaniczny Technologiczny, Katedra Spawalnictwa, ul. Konarskiego 18A, 44-100 Gliwice, email: waldemar.kwasny@polsl.pl
[b] Student: Wydział Mechaniczny Technologiczny, kierunek Mechanika i Budowa Maszyn
[c] Student: Wydział Mechaniczny Technologiczny (studia międzywydziałowe), kierunek Inżynieria Lotnicza i Kosmiczna
[d] Student: Wydział Mechaniczny Technologiczny, kierunek Inżynieria Ogólna
[e] Student: Wydział Mechaniczny Technologiczny, kierunek Automatyka i Robotyka Przemysłowa

Abstract: The aim of this study was to determine the effect of thermal spraying conditions on the structure and properties of coatings obtained using NiTec 10224 and PE 8215 powders. The study included penetration tests, metallographic observations, and measurements of mechanical properties. The phase composition of the coatings, including the residual stress state, was determined using X-ray diffraction (XRD). Furthermore, abrasion resistance tests were performed on the analyzed layers. Single-layer coatings produced from PE 8215 powder were compared with two-layer coatings containing an intermediate layer made of NiTec 10224 powder. The tests showed that the coating sprayed based on PE 8215 powder with an intermediate layer made of NiTec 10224 powder was characterized by higher hardness, greater abrasion resistance, and higher compressive stress values compared to the single-layer coating.
Streszczenie: Celem pracy było określenie wpływu warunków procesu natryskiwania cieplnego na strukturę oraz właściwości powłok otrzymanych z wykorzystaniem proszków NiTec 10224 oraz PE 8215. W ramach badań przeprowadzono próby penetracyjne, obserwacje metalograficzne oraz pomiary właściwości mechanicznych. Skład fazowy powłok, w tym stan naprężeń własnych, określono z zastosowaniem metody dyfrakcji rentgenowskiej (XRD). Ponadto wykonano testy odporności na zużycie ścierne analizowanych warstw. Porównano powłoki jednowarstwowe wytworzone z proszku PE 8215 z powłokami dwuwarstwowymi, zawierającymi dodatkowo warstwę pośrednią wykonaną z proszku NiTec 10224. Przeprowadzone badania wykazały, że powłoka natryskiwana na bazie proszku PE 8215 z międzywarstwą wykonaną z proszku NiTec 10224 charakteryzuje się wyższą twardością, większą odpornością na ścieranie oraz wyższymi wartościami naprężeń ściskających w porównaniu z powłoką jednowarstwową.

Keywords: thermal spraying, XRD analysis, abrasion resistance, hardness
Słowa kluczowe: natryskiwanie cieplne, analiza XRD, odporność na ścieranie, twardość

1. WSTĘP

Współczesne wymagania eksploatacyjne stawiane elementom maszyn i urządzeń, związane ze wzrostem obciążeń, prędkości pracy oraz oddziaływaniem agresywnych środowisk, prowadzą do intensyfikacji procesów zużycia powierzchni roboczych [1,2]. W odpowiedzi na te problemy rozwijają się technologie inżynierii powierzchni, wśród których szczególne znaczenie mają procesy natryskiwania cieplnego, umożliwiające kształtowanie właściwości warstw wierzchnich bez ingerencji w strukturę materiału podłoża.

Natryskiwanie cieplne polega na nanoszeniu stopionego lub uplastycznionego materiału powłokowego na odpowiednio przygotowaną powierzchnię, bez jej przetopienia, co skutkuje powstaniem połączenia o charakterze mechanicznym i adhezyjnym [2,4]. Powłoki te charakteryzują się specyficzną strukturą lamelarną, wynikającą z osadzania się spłaszczonych cząstek materiału, a także obecnością porowatości i tlenków, co w istotny sposób wpływa na ich właściwości eksploatacyjne [2].

Jedną z najczęściej stosowanych metod jest natryskiwanie płomieniowe (gazowe), w którym źródłem ciepła jest płomień gazowy, najczęściej acetylenowo-tlenowy. Technologia ta wyróżnia się stosunkowo prostą aparaturą, niskimi kosztami oraz dużą uniwersalnością zastosowań, szczególnie w procesach regeneracyjnych części maszyn [5]. Umożliwia ona nanoszenie powłok metalicznych, ceramicznych oraz kompozytowych o grubości rzędu od dziesiątek do setek mikrometrów, przy zachowaniu dobrych właściwości tribologicznych i odporności na zużycie [6-9].

2. CEL ORAZ ZAKRES BADAŃ

Celem badań było określenie wpływu zastosowania międzywarstwy wykonanej z proszku NiTec 10224 na strukturę oraz właściwości powłok wytwarzanych z proszku SF PE 8215, nanoszonych na podłoże ze stali konstrukcyjnej S235JR. Do otrzymania warstw wykorzystano proces natryskiwania płomieniowego. W ramach badań przeprowadzono analizę porównawczą próbek bez międzywarstwy oraz z jej zastosowaniem. Zakres przeprowadzonych badań obejmował:

- obserwację zgładów metalograficznych w skali mikro oraz makroskopowej,
- jakościową analizę składu fazowego uzyskanych powłok ,
- analizę mikrostruktury przy wykorzystaniu skaningowej mikroskopii elektronowej (SEM), wraz z zastosowaniem analizy składu chemicznego EDS,
- badania penetracyjne,
- pomiary twardości,
- pomiar naprężeń własnych uzyskanych powłok,
- ocenę odporności na zużycie tribologiczne.

3. MATERIAŁY WYKORZYSTANE DO BADAŃ

Materiałem podłoża wykorzystanym podczas natryskiwania płomieniowego z wykorzystaniem proszków NiTec 10224 oraz SF PE 8215 była niskowęglowa stal konstrukcyjna S235JR.

Proszek Eutalloy 10224 (NiTec) został wykorzystany jako materiał na warstwę pośrednią. Jest to proszek należący do grupy stopów Ni-B-Si, przeznaczonych do stosowania zarówno na nowych, jak i zużytych elementach, w szczególności wykonanych z żeliwa.

Na warstwę zewnętrzną wykorzystano proszek Eutalloy SF PE 8215. Jest to proszek stopowy na bazie niklu typu Ni-Cr-B-Si z dodatkiem żelaza oraz węglików wolframu (ok. 60% WC), przeznaczonym do wytwarzania powłok o wysokiej odporności na zużycie ścierne.

4. PRZEBIEG PROCESU NAKŁADANIA POWŁOK

Proces natryskiwania cieplnego przeprowadzono z wykorzystaniem palnika SuperJet-S-Eutalloy, co umożliwiło uzyskanie dyfuzyjnego połączenia materiałów dodatkowych z materiałem podłoża. Gazy techniczne wykorzystane podczas procesu natryskiwania podawane były z następującym ciśnieniem roboczym: acetylen - 0,5 bara, tlen - 2,0 bara.

Istotnym etapem poprzedzającym właściwe nanoszenie powłok było wstępne podgrzanie materiału podłoża do temperatury w zakresie 100 - 200°C. Zabieg ten miał na celu ograniczenie dostępu tlenu do powierzchni podłoża oraz wytworzenie warstwy buforowej.

5. OBSERWACJE METALOGRAFICZE

Proces przygotowania zgładów metalograficznych obejmował: cięcie próbek, inkludowanie w żywicy, szlifowanie, polerowanie oraz trawienie w odpowiednim odczynniku chemicznym.

Analizę metalograficzną powłok natryskiwanych płomieniowo oraz materiału podłoża przeprowadzono z wykorzystaniem dwóch technik obserwacyjnych. Do oceny i obserwacji makrostruktury zastosowano mikroskop stereoskopowy Olympus SZX9. Natomiast szczegółową analizę mikrostruktury wykonano przy użyciu mikroskopu Nikon Eclipse MA100, który umożliwił również sporządzenie odpowiedniej dokumentacji obrazowej.

Zdjęcia mikrostruktury natryskiwanej powłoki dwuwarstwowej oraz materiału rodzimego przedstawiono na rysunku 1. Na podstawie obserwacji metalograficznych, zidentyfikowano w strukturze warstw natryskiwanych płomieniowo z wykorzystaniem proszku PE 8215 węgliki chromu i wolframu, co potwierdzono badaniami XRD i przedstawiono w dalszej części pracy.

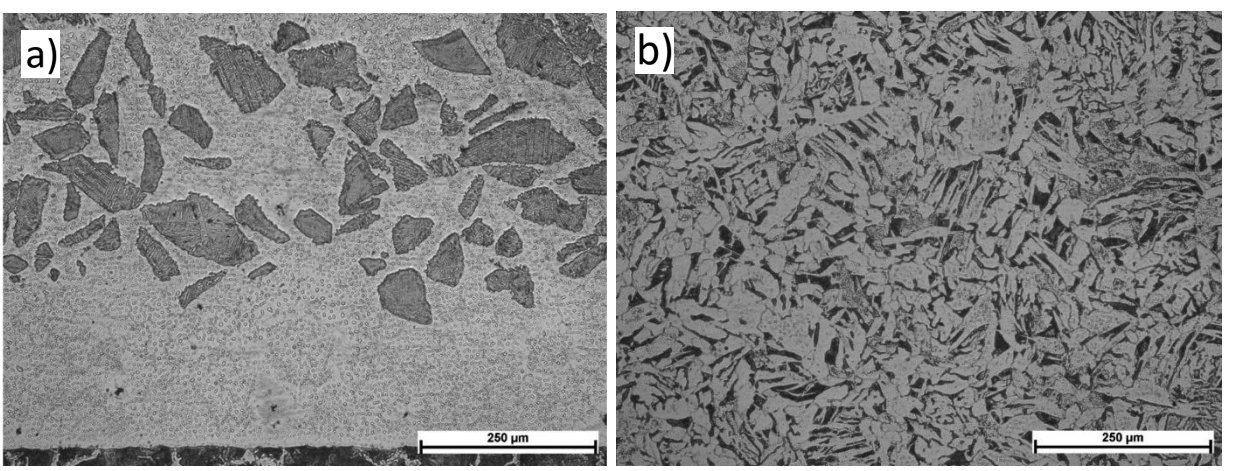

Rysunek 1.a) Zdjęcie mikroskopowe przedstawiające linię wtopienia oraz warstwę natryskiwaną proszkiem Eutalloy SF PE 8215 z międzywarstwą NiTec 10224 b) Zdjęcie mikroskopowe przedstawiające strukturę materiału podłoża

6. BADANIA SEM WRAZ Z ANALIZĄ SKŁADU CHEMICZNEGO

W ramach badań struktury powłok natryskiwanych płomieniowo zastosowano skaningowy mikroskop elektronowy SUPRA 25 firmy ZEISS. Urządzenie to umożliwia prowadzenie obserwacji w wysokiej rozdzielczości, co pozwala na szczegółową ocenę struktury wytworzonych warstw oraz obszaru przejściowego pomiędzy powłoką a materiałem podłoża.

Mikroskop wyposażono w zestaw detektorów, obejmujący detektor elektronów wtórnych (SE), detektor wewnątrz soczewkowy (In-Lens) oraz detektor elektronów wstecznie rozproszonych (BSE). Dzięki temu możliwe było uzyskanie obrazów o zróżnicowanym kontraście, co ułatwiło analizę jednorodności struktury oraz identyfikację poszczególnych składników materiału.

Dodatkowo przeprowadzono lokalną analizę składu chemicznego z wykorzystaniem zintegrowanego systemu EDS, co umożliwiło identyfikację pierwiastków oraz ocenę ich rozmieszczenia. Na rysunku 2 przedstawiono strukturę powłoki dwuwarstwowej (SF PE 8215 + NiTec 10224) oraz wyniki analizy składu chemicznego (EDS) dla wskazanych punktów.

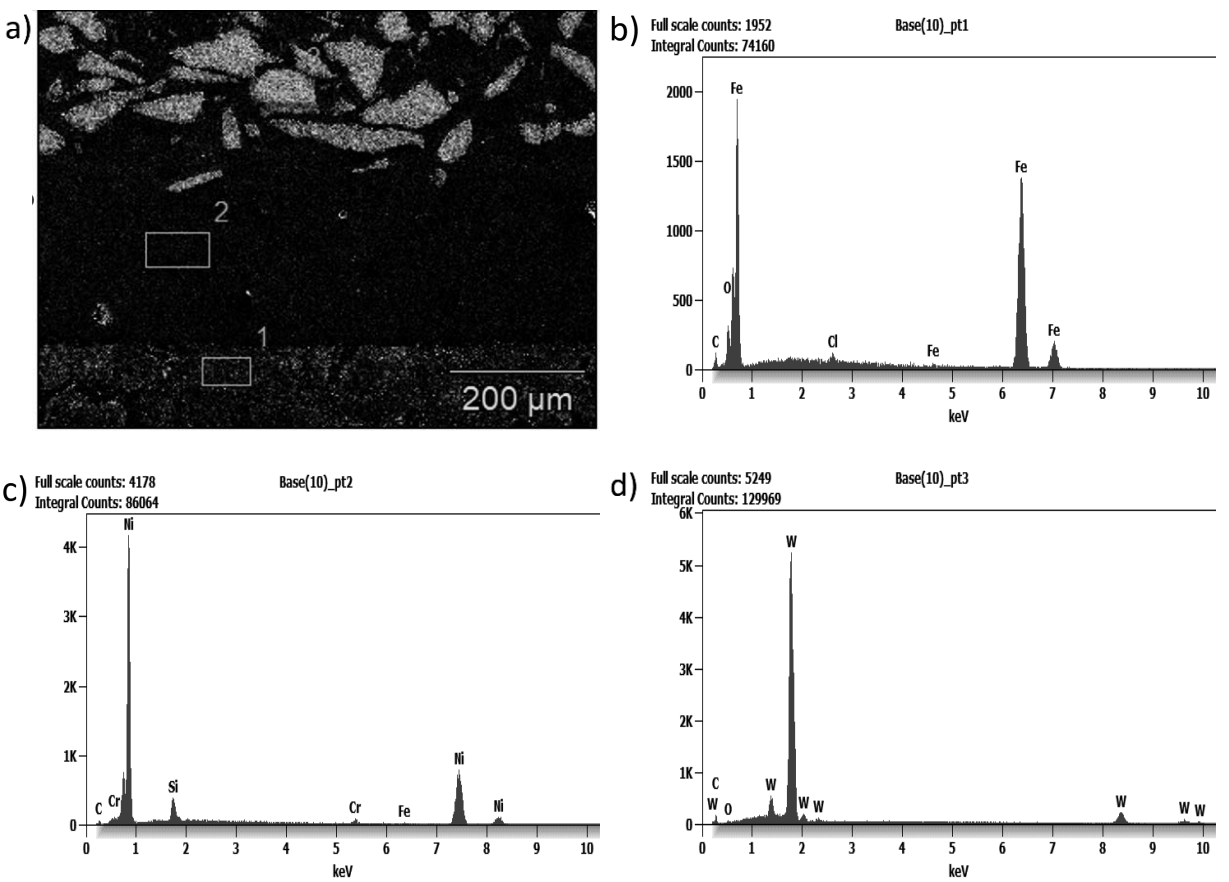

Rysunek 2. a) Obraz struktury (SEM) przedstawiający powłokę dwuwarstwową oraz materiał podłoża b) Analiza składu chemicznego (wykres rozproszonego promieniowania rentgenowskiego) z obszaru oznaczonego 1 (materiał rodzimy) c) z obszaru oznaczonego 2 – warstwa pośrednia d) z obszaru oznaczonego 3 – wydzielenie WC

7. BADANIA PENETRACYJNE

Na podstawie przeprowadzonych badań penetracyjnych w oparciu o normę PN-EN ISO 3452 uzyskanych próbek stwierdzono brak nieciągłości spawalniczych w postaci pęknięć. Jednocześnie w materiale stwierdzono wysoki poziom porowatości.

8. POMIARY TWARDOŚCI

Pomiary twardości wykonano w trzech charakterystycznych strefach próbek: w osnowie powłoki, w strefie pośredniej oraz w materiale podłoża. Badania przeprowadzono z wykorzystaniem mikrotwardościomierza FM-810, stosując metodę Vickersa.

W celu wyznaczenia twardości osnowy wykonano po 5 odcisków dla każdej próbki, natomiast w strefie pośredniej oraz w materiale rodzimym przeprowadzono po 6 pomiarów. Odciski rozmieszczono równomiernie, zachowując jednakowe odstępy pomiędzy punktami pomiarowymi. Wszystkie pomiary realizowano przy obciążeniu 0,5 kg oraz czasie działania wgłębnika wynoszącym 12 s.

Zestawienie uzyskanych wyników pomiaru twardości przedstawiono na rysunku 3. Analiza danych wykazała, że wyższą twardością charakteryzuje się powłoka wykonana z proszku Eutalloy SF PE 8215 z międzywarstwą z proszku NiTec 10224. Dla próbki bez międzywarstwy wartość twardości wyniosła 525,26HV.

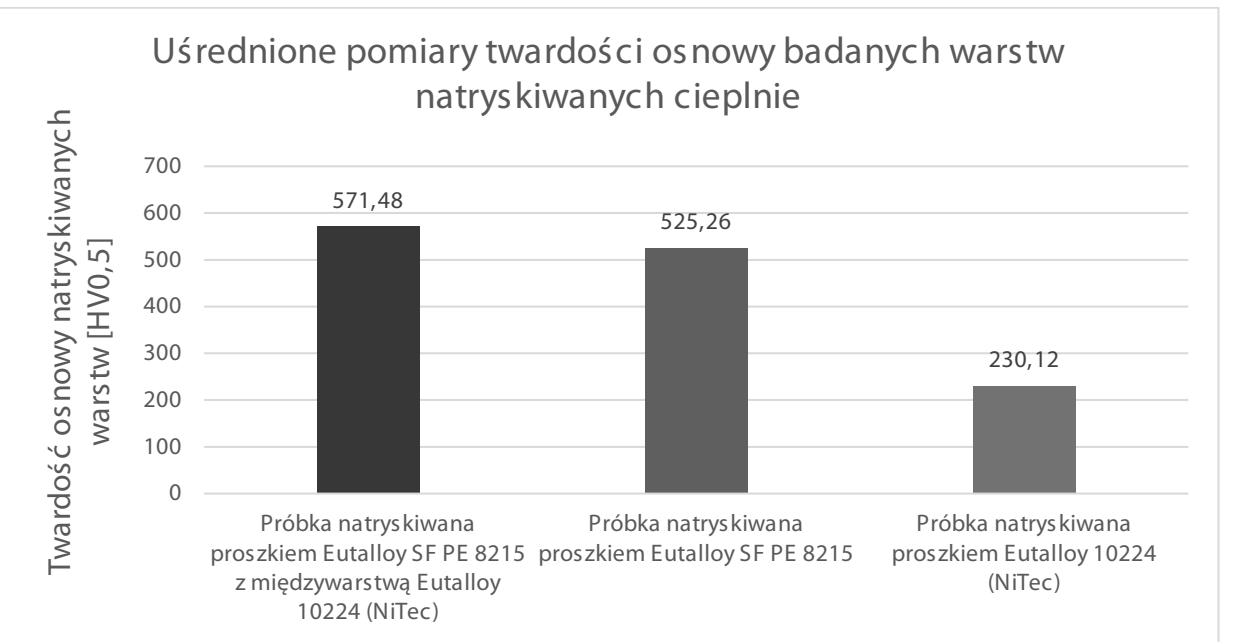

Rysunek 3. Wykres uśrednionych pomiarów twardości badanych próbek

Tabela 1. Pomiary twardości warstwy, SWC oraz materiału rodzimego badanych próbek

Seria	Numer pomiaru	Eutalloy SF PE 8215 + NiTec 10224	Eutalloy SF PE 8215	Eutalloy 10224 (NiTec)
I	1	556,7	384,9	323,9
	2	730,3	512,3	271,9
	3	519,6	491,8	231,1
	4	528,4	604,6	168,9
	5	522,4	632,7	154,8
	Średnia	**571,48**	**525,26**	**230,12**
II	6	170,9	323,1	150,8
	7	141,5	252,1	142,3
	8	136,9	180,8	123,2
	9	149,9	161,7	130,3
	10	146,9	156,6	132,6
	11	148,5	155,9	144,6
	Średnia	**149,1**	**205,03**	**137,3**

9. BADANIE SKŁADU FAZOWEGO I POMIAR NAPRĘŻEŃ METODAMI RTG

Badania składu fazowego przeprowadzono z wykorzystaniem dyfraktometru rentgenowskiego PANalytical X'PERT PRO pracującego w geometrii Bragga–Brentano. Do identyfikacji jakościowej faz występujących w powłokach natryskiwanych cieplnie zastosowano promieniowanie lampy o anodzie kobaltowej i długości fali λCo = 1,78897 Å, przy parametrach pracy: napięcie anody 40 kV oraz natężenie prądu 30 mA. Rejestrację dyfraktogramów prowadzono w zakresie kąta dyfrakcji 2Θ od 30° do 120°.

Analizę naprężeń własnych wykonano metodą $\sin^2\psi$, przy czym pomiary realizowano w kierunku równoległym do kierunku natryskiwania cieplnego próbek.

Wyznaczanie wartości naprężeń własnych oparto na analizie refleksu dyfrakcyjnego odpowiadającego płaszczyźnie krystalograficznej niklu (311). Obliczenia przeprowadzono z wykorzystaniem oprogramowania X'Pert Stress (XSTRESS Plus), zawierającego bazę danych materiałowych niezbędnych do realizacji analizy naprężeń w badanych próbkach.

Dla obu analizowanych powłok (SF PE 8215 oraz SF PE 8215 + NiTec10224) stwierdzono obecność tych samych refleksów w warstwie zewnętrznej. Refleksom tym odpowiadają fazom niklu, węglika chromu oraz węglika wolframu (WC), dotyczy to zarówno powłoki wytworzonej z proszku Eutalloy SF PE 8215, jak i próbki z warstwą wykonaną z proszku Eutalloy SF PE 8215 z zastosowaną międzywarstwą Eutalloy NiTec 10224 (rys. 4). Natomiast dla powłoki wykonanej wyłącznie z proszku Eutalloy NiTec 10224 zidentyfikowano głównie obecność niklu oraz węglika chromu (rys. 5). Uzyskane przykładowe wyniki dotyczące naprężeń w warstwach natryskiwanych zostały szczegółowo zaprezentowane na rysunku 6 i 7 oraz zestawione w tablicy 2.

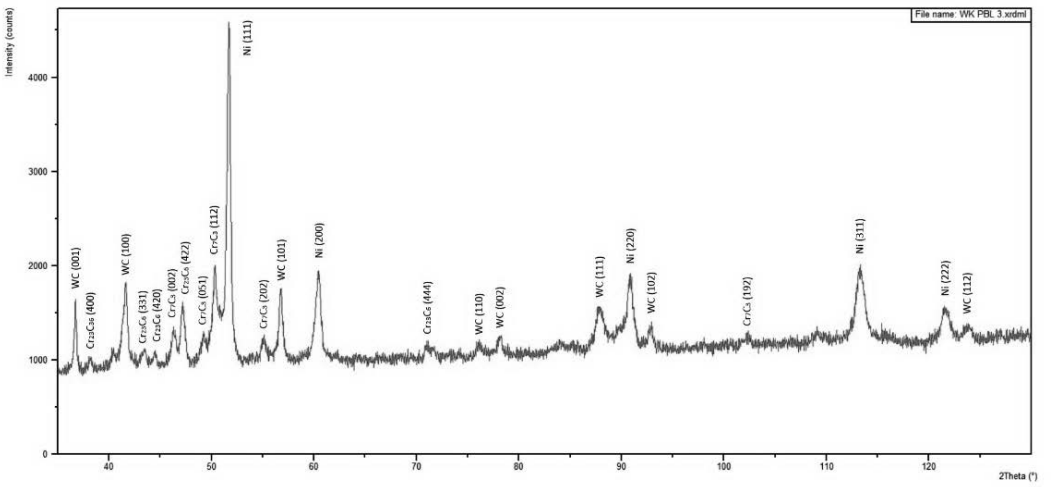

Rysunek 4. Dyfraktogram rentgenowski powłoki dwuwarstwowej

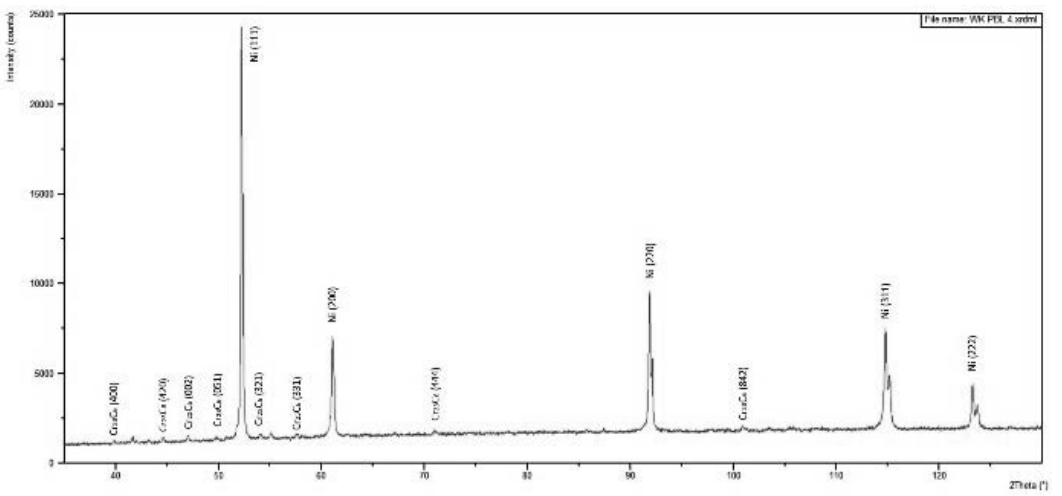

Rysunek 5. Dyfraktogram rentgenowski warstwy wykonanej z proszku Eutalloy 10224(NiTec)

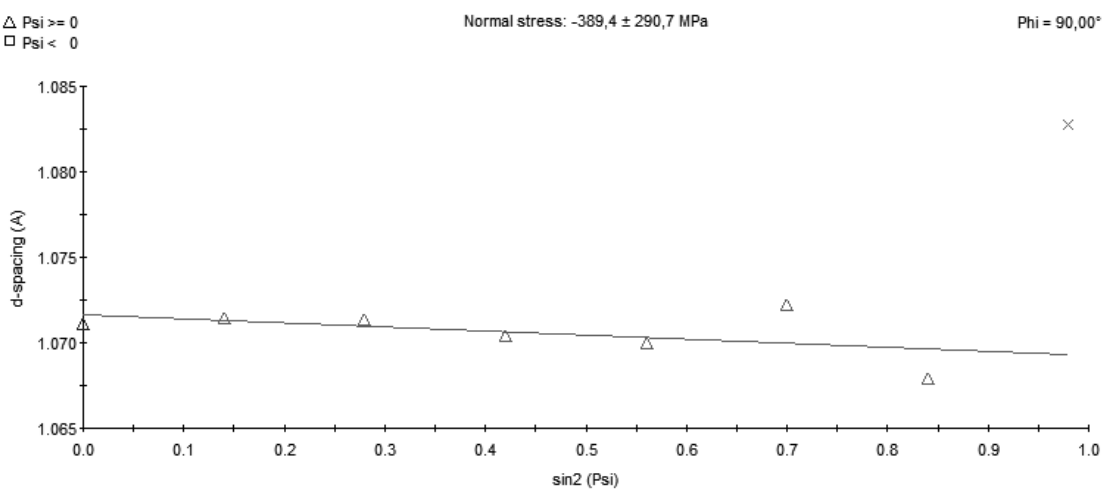

Rysunek 6. Wykres zmian odległości międzypłaszczyznowej d refleksu Ni(311) powłoki dwuwarstwowej w funkcji $\sin^2\psi$

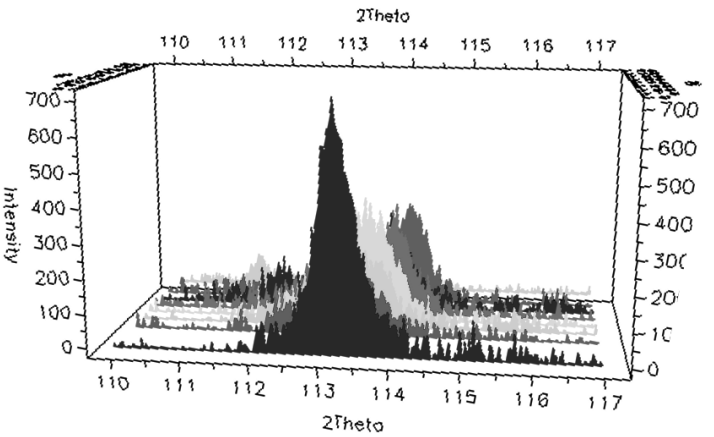

Rysunek 7. Wykres zmian położenia refleksu Ni (311) w funkcji $\sin^2\psi$

Tabela 2. Zestawienie uzyskanych wyników pomiaru naprężeń analizowanych powłok

Wariant próbki	**Wartość naprężeń, równolegle do kierunku natryskiwania [MPa]**
Próbka natryskiwana Eutalloy SF PE 8215	- 175,9 ± 27,5
Próbka natryskiwana Eutalloy NiTec 10224+Eutalloy SF PE 8215	- 389,4 ± 290,7
Próbka natryskiwana Eutalloy 10224 NiTec	- 42,4 ± 61,0
Stal S235JR	108,3 ± 21,1

10. BADANIE ODPORNOŚĆI NA ZUŻYCIE CIERNE

Badania odporności na zużycie ścierne powłok wytworzonych metodą natryskiwania cieplnego przeprowadzono z wykorzystaniem stanowiska badawczego spełniającego wymagania normy ASTM G65-00 (procedura A). Próbki zostały zamocowane w dedykowanym uchwycie w taki sposób, aby powierzchnia z naniesioną warstwą pozostawała w bezpośrednim kontakcie z kołem ciernym urządzenia.

Proces ścierania realizowano przez około 1500 obrotów koła, pracującego z prędkością 200 obr./min. Siła docisku koła do powierzchni próbki wynosiła 15 N. Jako ścierniwo wykorzystano piasek A.F.S. Testing Sand 50 - 70 o wilgotności poniżej 0,5%, dozowany ze stałym natężeniem przepływu równym 335 g/min. Zastosowane ścierniwo charakteryzowało się uziarnieniem w zakresie 0,1 - 0,4 mm. W celu porównania wyników jako materiał odniesienia zastosowano stal typu HARDOX, znaną z wysokiej odporności na ścieranie. Wyniki pomiarów masy próbek przed i po przeprowadzonym teście, wraz z obliczonym procentowym ubytkiem masy, zestawiono w tablicy 3. Dodatkowo, na rysunku 7 przedstawiono graficzną interpretację uzyskanych wyników. Analiza uzyskanych danych wykazała, że próbka natryskiwana proszkiem PE 8215 z zastosowaniem międzywarstwy na bazie proszku NiTec 10224 cechowała się około znacznie niższym ubytkiem masy w porównaniu do próbki wykonanej wyłącznie z użyciem

proszku PE 8215. Wynik ten jednoznacznie wskazuje na istotne zwiększenie odporności na zużycie ścierne w przypadku zastosowania międzywarstwy.

Tabela 3. Zestawienie wyników po przeprowadzonej próbie ścieralności

Próbka	Masa próbki przed badaniem [g]	Masa próbki po badaniu [g]	Ubytek masy próbki [g]	Procentowy ubytek masy [%]
Próbka natryskiwana proszkiem Eutalloy SF PE 8215	164,176	163,663	0,513	0,312
Próbka natryskiwana proszkiem Eutalloy 10224 (NiTec)	162,279	161,778	0,501	0,309
HARDOX	116,579	116,346	0,233	0,200
Próbka natryskiwana proszkiem Eutalloy SF PE 8215 z międzywarstwą Eutalloy 10224 (NiTec)	163,04	162,745	0,295	0,181

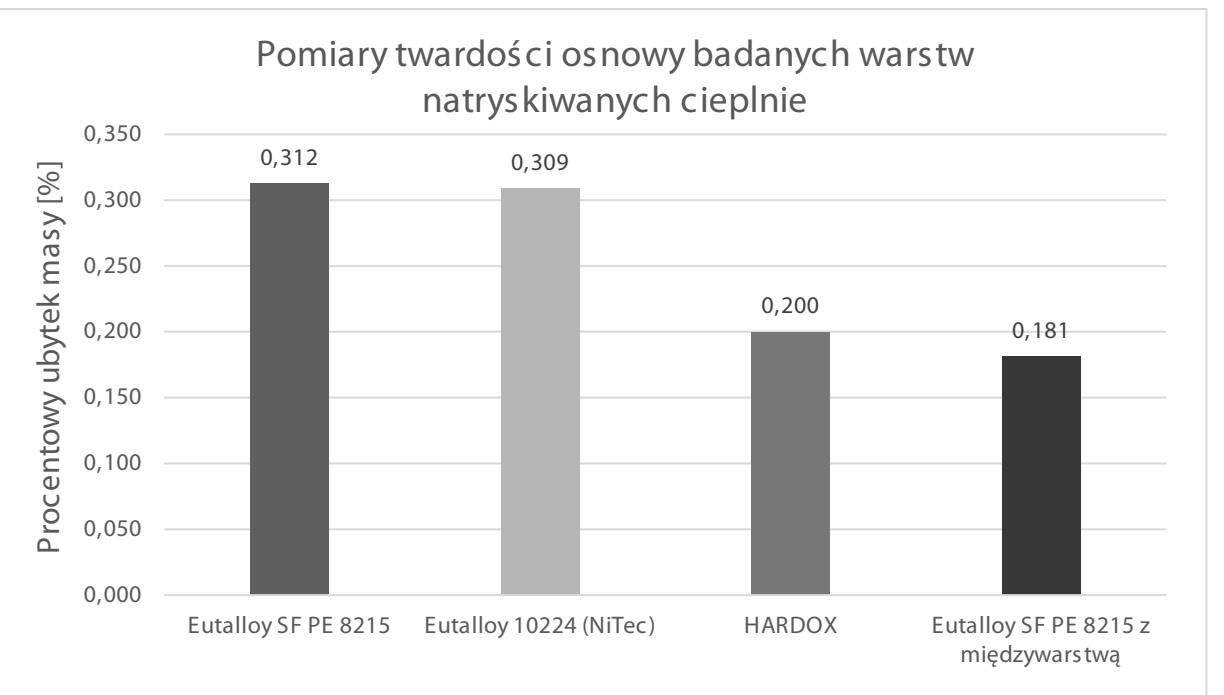

Rysunek 7. Graficzna interpretacja przedstawiająca procentowy ubytek masy próbek po przeprowadzonej próbie ścieralności

11. WNIOSKI

- Przeprowadzone badania penetracyjne wykazały brak nieciągłości w postaci pęknięć w analizowanych powłokach, przy jednoczesnym występowaniu charakterystycznej dla natryskiwania cieplnego podwyższonej porowatości.
- Jakościowa analiza fazowa XRD wykazała obecność tych samych głównych faz (Ni, WC oraz węgliki chromu) w warstwach zewnętrznych zarówno powłok jedno-, jak i dwuwarstwowych, natomiast w warstwie pośredniej na bazie proszku NiTec 10224 dominującą fazą jest nikiel z udziałem węglików chromu.
- Pomiary naprężeń własnych wykazały, że zastosowanie międzywarstwy prowadzi do istotnego wzrostu naprężeń ściskających (z ok. -176 MPa do ok. -389 MPa), co korzystnie wpływa na własności trybologiczne powłok.
- Stwierdzono wyraźną korelację pomiędzy twardością, stanem naprężeń własnych oraz odpornością na zużycie. Powłoki o wyższej twardości i większym udziale naprężeń ściskających wykazują większą odporność na zużycie ścierne.

LITERATURA

1. Adamiec Piotr, Dziubiński Jerzy.: „Regeneracja i wytwarzanie warstw wierzchnich elementów maszyn transportowych”. Wydawnictwo Politechniki Śląskiej, rok wydania: 1999, ISSN 0434-0825,
2. Klimpel Andrzej Adam, Mazur Marceli.: „Podręcznik spawalnictwa”. Wydawnictwo Politechniki Śląskiej, rok wydania: 2004,
3. Klimpel Andrzej, Dziubiński Jerzy.: „Technologia napawania”. Wydawnictwo Politechniki Śląskiej, rok wydania: 1983, ISSN 0434-0825,
4. Pawłowski Lech.: „The Science and Engineering of Thermal Spray Coatings”. Wydawnictwo John Wiley & Sons, rok wydania: 2008, ISBN 978-0-470-49049-4,
5. Tucker Robert C. (red.).: „Thermal Spray Technology Handbook”. Wydawnictwo ASM International, rok wydania: 2013, ISBN 978-1-61503-996-8,
6. Sampath Sanjay, Jiang Xiaoyan.: „Flame spraying and its applications”. Czasopismo: Journal of Thermal Spray Technology, Volume 10, Issue 1, Rok: 2001, ISSN 1059-9630,
7. Matejicek Jiri.: „Thermal spraying of advanced materials”. Czasopismo: Surface and Coatings Technology, Volume 202, Issues 4–7, Rok: 2007, ISSN 0257-8972,
8. Miś Klaudia, Majdecka Patrycja, Czech A., Bonek Mirosław.: „Naddźwiękowe natryskiwanie płomieniowe HVOF”. Wydawnictwo Politechniki Śląskiej. Prace Instytutu Materiałów Inżynierskich i Biomedycznych, Rok: 2019, Zeszyt 1/2019, s. 154–157,
9. Sanhita Pal, Rakesh Bhaskaran Nair, André McDonald.: „Effect of tungsten and vanadium additions on the dry abrasive wear and solid particle erosion of flame-sprayed AlCoCrFeMo high entropy alloy coatings”. Czasopismo: International Journal of Refractory Metals and Hard Materials, Volume 114, Article 106245, Rok: 2023, ISSN 0263-4368,

TalentDetector

7th-9th June 2026
Gliwice-Brenna, Poland

DEPARTMENT OF ENGINEERING MATERIALS AND BIOMATERIALS
FACULTY OF MECHANICAL ENGINEERING
SILESIAN UNIVERSITY OF TECHNOLOGY

INTERNATIONAL STUDENTS SCIENTIFIC CONFERENCE

Geochemical differentiation of pyrite from Spanish and Romanian deposits

Kinga Kwiecień[a], Katarzyna Bloch[a], Jacek Nowak[b]

[a] Silesian University of Technology, Faculty of Energy and Environmental Engineering
email: kk300651@student.polsl.pl
[b] Silesian University of Technology, Faculty of Mining, Safety Engineering and Industrial Automation, Department of Applied Geology

Abstract: This article presents the results of chemical and mineralogical analyses of pyrite samples collected from well-known deposits located in distinct geological environments: Navajún (Spain) and Baia Mare (Romania). The laboratory investigations included X-ray diffraction (XRD), X-ray fluorescence (XRF), and thermogravimetric analysis coupled with evolved gas detection (TGA-FTIR). XRD analysis of the Spanish sample revealed the presence of chloritoid – a silicate mineral occurring as inclusions within the Navajún pyrite – in addition to the primary pyrite phase. These chloritoid inclusions originate from the host rock, consisting of Cretaceous marls. Conversely, thermogravimetric analysis showed more intense oxidation in the pyrite sample from the Romanian deposit, indicating that this sulfide is mineralogically more reactive. This increased reactivity is attributed to the hydrothermal origin of the pyrite in the Baia Mare deposit**.**

Keywords: pyrite, chloritoid, Navajún (Spain), Baia Mare (Romania)

1. INTRODUCTION

The aim of the project was to compare pyrites from two deposits with different geological conditions: Spain (Navajún) and Romania (Baia Mare). Pyrite is one of the most common sulfides, often found in metal deposits. As part of the project, differences in elemental composition and structure were analyzed, which may indicate different origins and mineralization conditions. According to the literature, instrumental studies are usually conducted using techniques such as XRD, XRF, TGA/FTIR, as well as SEM and Mössbauer spectroscopy. Microscopic silicate inclusions, composed primarily of iron-rich chloritoid, can be found in the pyrite matrix. Analysis of these crystals reveals distinct structural and chemical differences, indicating different local physicochemical conditions.

The following stages were carried out as part of the project: 1 - a field trip to Spain, where pyrite samples were collected from Navajun - one of the most famous sulphide deposits in the world, 2 - laboratory analyses, including XRF and XRD methods, 3 - assessment of the influence of geological conditions on the chemical composition of pyrites, 4 - enrichment of the educational minerals collection of Silesian University of Technology.

1.1 Field trip and collection of pyrite samples from the Navajun site (La Rioja province)

In January 2026, a five-person group of representatives from our SILESIAN Student Geology Scientific Association traveled to Spain to search for the world-famous pyrites from Navajún. The pyrite deposit in Navajún is one of the most famous mineralogical sites in the world. The pyrites in this deposit crystallized in Cretaceous marls—a sedimentary limestone-clay rock—under conditions where chemistry, temperature, and pressure favor the growth of exceptionally regular FeS_2 crystals, which today delight collectors and scientists worldwide. This area is normally strictly protected and completely inaccessible to tourists. Thanks to the courtesy of the owners of the Victoria mine, we were able to enter the premises and see firsthand what we usually see in museum display cases—perfect cubes of pyrite embedded in the rock (Fig. 1). We also observed sedimentary structures left by the undulations of the Cretaceous sea—so-called "ripplemarks". Meeting with the quarry manager provided us with a wealth of substantive information. We learned details about the history of mining in the area and the geological processes responsible for such unusual crystal growth.

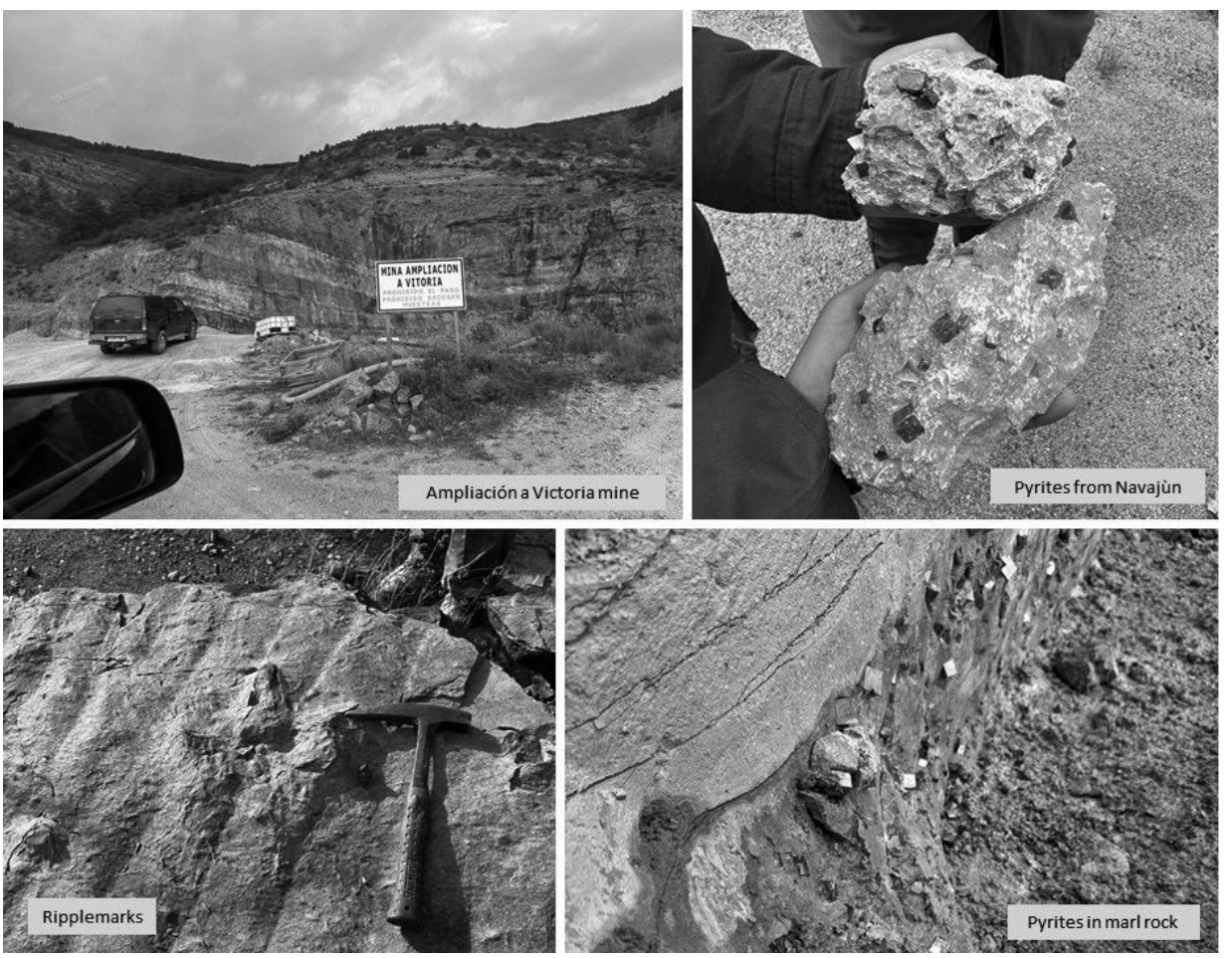

Figure 1. Photoreport from a visit to the Victoria Mine (Navajun)
Rysunek 1. Relacja fotograficzna z wizyty w kopalni Victoria (Navajun)

1.2. Macroscopic description of pyrite specimens

Navajún pyrite forms perfectly formed cubic crystals with even edges and a metallic luster (Fig. 2a). The crystals are embedded in Cretaceous talc marl. Characteristic are the intergrowing cubic crystals of a golden-yellow color, often with variegated coatings. The crystals range in size from a few millimeters to 19 cm (cube edge).

During previous trips by members of our Association, pyrite specimens were collected from the Baia Mare region (Maramureș, Romania) – an area characterized by complex, hydrothermal polymetallic mineralization (Au–Ag–Pb–Zn–Cu and others). Pyrite here is not a typical, isolated collectible crystal – it usually occurs in complex parageneses with other minerals (such as galena, sphalerite, arsenopyrite, etc.) in hydrothermal veins, for example, in the Herja, Săsar, Cavnic mines, etc.

Pyrite from the Baia Mare region can have various crystalline forms, but rarely forms perfectly regular large cubes like those found in Navajún. The photograph below (Fig. 2b) shows intergrown brass-yellow crystals with striations on their walls. The Baia Mare pyrite represents a gold-bearing type, in which gold occurs in dispersed form – as atoms in the crystal lattice or as submicroscopic inclusions, often stabilized by the presence of arsenic.

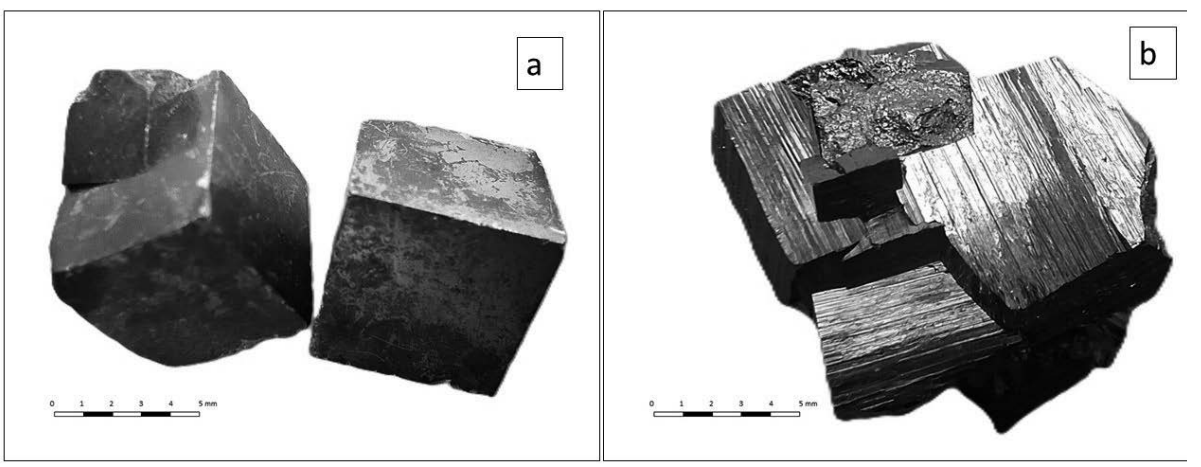

Figure 2. Macro photographs of pyrite crystals: a – from Navajun, b – from Baia Mare
Rysunek 2. Makrofotografie kryształów pirytu: a – z Navajun, b – z Baia Mare

1.3. Instrumental analysis

Instrumental studies (XRD, XRF, TGA/FTIR) were performed on samples of pyrite from Navajun (marked with the symbol H) and pyrite from Baia Mare (marked with the symbol R). Phase and chemical composition analyses were preceded by appropriate preparation: the mineral samples were ground in an agate mortar to form a homogeneous powder.

X-ray Diffraction (XRD) measurements were performed using a D2 PHASER diffractometer (Bruker). The powder was placed in metal measuring holders. The radiation source was a Cu lamp. Measurements were performed at a voltage of 30 kV and a current of 20 mA, in the angular range of 2°–72° 2Theta, with a step size of 0.01° and a counting time of 0.4 s/step. DIFFRAC.EVA v6.1 software, supported by the ICDD PDF-4+ database, was used for data processing and phase identification.

Elemental composition was determined by X-ray fluorescence (XRF) using a Bruker S2 PUMA spectrometer. Measurements were performed in an air atmosphere on powder samples placed in measuring cuvettes. The device enabled qualitative and quantitative analysis of elements ranging from sodium (Na) to americium (Am).

Thermogravimetric analysis (TGA) was performed using a STA F3 analyzer. Approximately 20 mg of each sample was heated to 1000°C at a heating rate of 10°C/min in ceramic crucibles with a perforated lid. Nitrogen was the inert gas used in the experiment. A Bruker "alpha" FTIR spectrometer, directly coupled to the STA analyzer, was used to measure the released volatiles. Spectra were recorded every 16 s in the range from 400 to 4000 cm−1 with a resolution of 4 cm−1. The gas chamber was maintained at a constant temperature of 200°C to prevent condensation of volatile substances. The results were analyzed using dedicated OPUS software (Bruker).

2. RESULTS

2.1. XRD diffraction analysis

X-ray diffraction analysis allowed the identification of the crystalline phases present in the analyzed pyrite samples from Romania and Spain. In both cases, the predominant crystalline phase is pyrite FeS , as confirmed by intense reflections consistent with the structural pattern.

Sample R (Romania): This sample exhibits very high phase purity. The diffraction pattern is characterized by the presence of reflections originating exclusively from pyrite. The absence of additional peaks suggests that the elemental impurities identified in the XRF analysis are dispersed within the pyrite crystal lattice or are present in amounts below the detection limit of the XRD method (Fig. 3.).

Sample H (Spain): In addition to the dominant pyrite phase, the diffraction pattern also revealed distinct reflections of a secondary phase – chloritoid (aluminum and iron silicate). The highest intensity of chloritoid reflections was observed for 2Θ angles around 18.3˚ and 20.1˚ (Fig. 4). The presence of this phase is a distinctive feature of the Spanish sample in relation to the Romanian one.

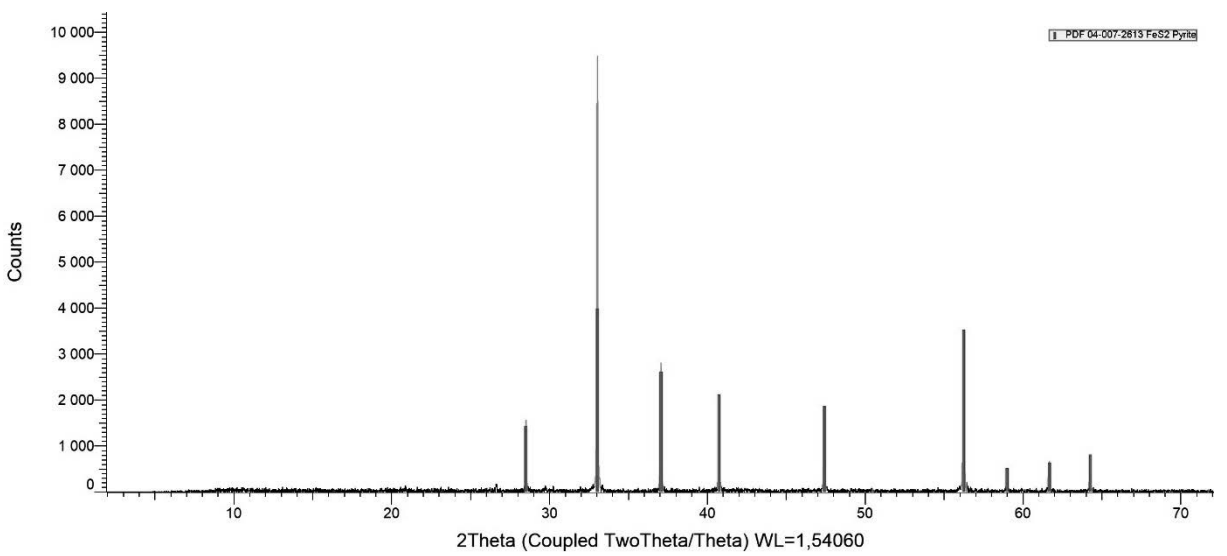

Figure 3. XRD analysis of sample R
Rysunek 3. Analiza XRD próbki R.

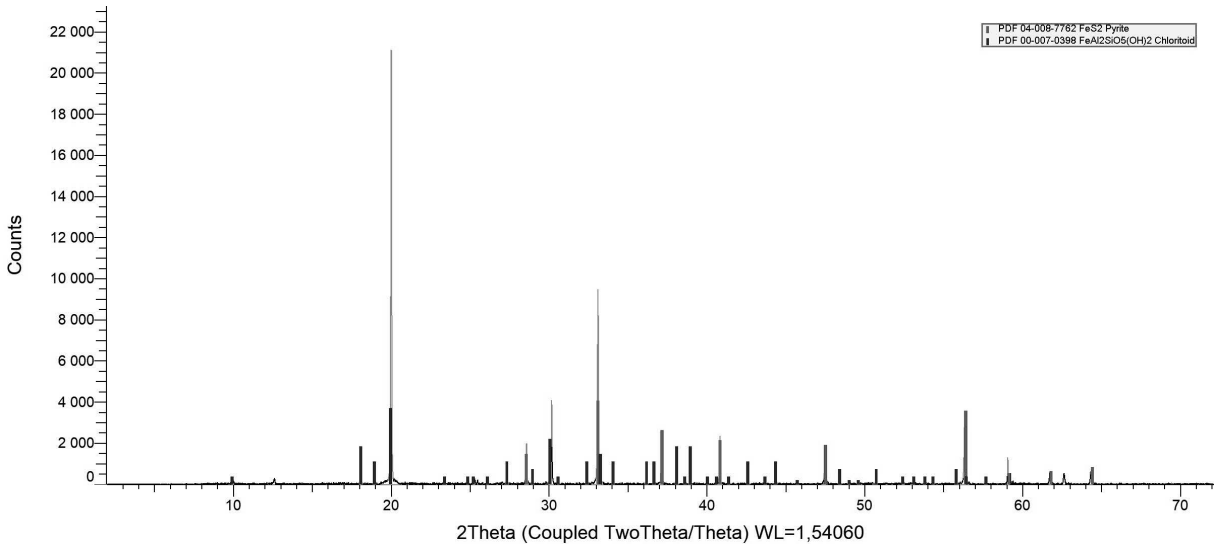

Figure 4. XRD analysis of sample H
Rysunek 4. Analiza XRD próbki H.

The presence of chloritoid in Navajún pyrite crystals has been documented in the literature. Lodders et al. [1] describe microscopic silicate inclusions (chloritoid) in octahedral positions of the crystal structure, which are the result of local oxidation processes. The chloritoid found as inclusions in pyrite is an almost pure, ferrous variety of this mineral, crystallizing exclusively in the triclinic system. It takes the form of needles up to 100 µm long, in which microinclusions of rutile and quartz were identified. Spectroscopic studies cited in the aforementioned publication [1] revealed variable Fe^{3+} ion content – typically around 7%, although in selected samples this value reached as high as 22%. This indicates local oxidation processes, in which Fe^{2+} ions in the octahedral layers of the crystal structure were replaced by Fe^{3+}.

2.2. X-ray fluorescence analysis

The elemental composition results (Table 1) correlate with the XRD data, indicating significant differences in the geochemistry of both samples.

Table 1. Chemical composition [%] of the tested pyrite samples determined by the XRF method
Tabela 1. Skład chemiczny [%] badanych próbek pirytu oznaczony metodą XRF

Element	Sample R	Sample H
S	49.49	47.67
Fe	45.69	46.25
Al	2.57	3.9
Si	1.31	1.36
As	0.65	< 0.01
Ti	< 0.01	0.33
Ca	0.04	0.19
Ni	< 0.01	0.08

Sample H is characterized by a higher aluminum content (3.9%) and the presence of titanium (0.33%). These results confirm the presence of chloritoid, identified in the XRD

analysis. Sample R shows a lower aluminum content (2.57%) and trace titanium content. Furthermore, the pyrite sample from Romania has a high arsenic content (As = 0.65%), while in the sample from Spain this element is present in negligible amounts. Sample R contains trace amounts of heavy metals, such as lead (Pb = 0.05%) and gold (Au = 0.01%). Sample H, on the other hand, contains nickel (Ni = 0.08%) and a slightly elevated calcium content.

2.3. Thermal analysis (TGA/FTIR)

The thermal decomposition process of pyrite, both under oxidizing and neutral conditions, has been the subject of numerous studies (e.g., [2, 3, 4, 5]), which served as the basis for the interpretation presented below.

The thermograms (Figs. 5 and 6) show the TG curves (red), illustrating mass loss with increasing temperature, the DTG curves (dashed green), and the GS curves (blue). The DTG curve is a derivative of the mass loss (TG), allowing for the interpretation of the temperature at which the sample loses its mass most rapidly. The GS curves reflect the total gas emission from the sample during the experiment.

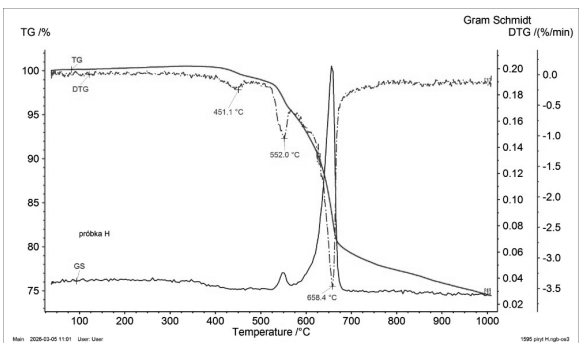

Figure 5. Thermogram of sample H
Rysunek 5. Termogram próbki H

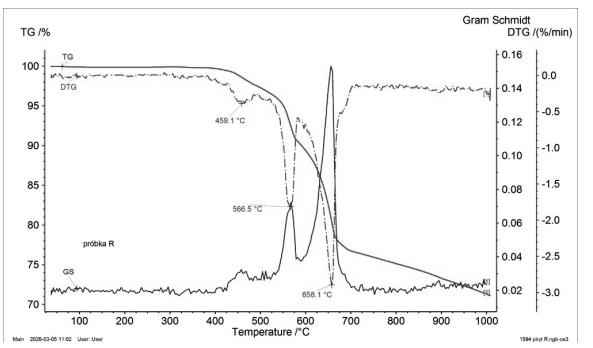

Figure 6. Thermogram of sample R
Rysunek 6. Termogram próbki R

Pyrite decomposition reactions are a combination of oxidation, reduction, and thermal dissociation. These reactions partially or completely overlap [2]. The first mass loss effect occurs at 450-460°C and results from the oxidation reaction. In the case of sample R, this reaction is combined with gas emission, as shown by the GS curve (Fig. 6). This is manifested by the presence of symmetric stretching vibrations S=O (Fig. 8), indicating the release of SO_2 from the sample. The next effect visible in the thermograms (Figs. 5 and 6) occurs at a temperature of approximately 555°C and is associated with another episode of iron and sulfur oxidation. The FTIR spectra (Figs. 7 and 8, red spectrum) show relatively weak vibrations originating from sulfur compounds in the wavelength ranges of 2515, 1420-1300 and 1160-1130 cm^{-1}. In the case of sample R, an additional effect of elemental sulfur emission appears in the band of 834 cm^{-1}, which is typical for pyrites already partially modified under the influence of hydrothermal processes.

The last, strongest effect of gas emission during TGA experiments reaches a maximum at 658°C and is associated with the decomposition of sulfide: FeS2→FeS+S. This is related to SO_2 emission, which is visible in the FTIR spectra (Figs. 7 and 8, pink spectrum) as S=O stretching vibrations.

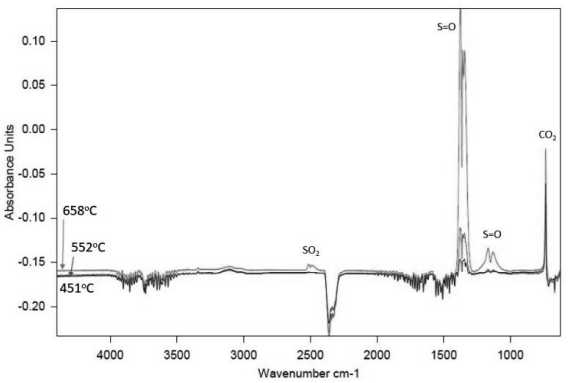

Figure 7. Sample H FTIR spectra in temperatures: 451, 552 and 658°C
Rysunek 7. Widma FTIR próbki H w temperaturach 451, 552 i 658°C

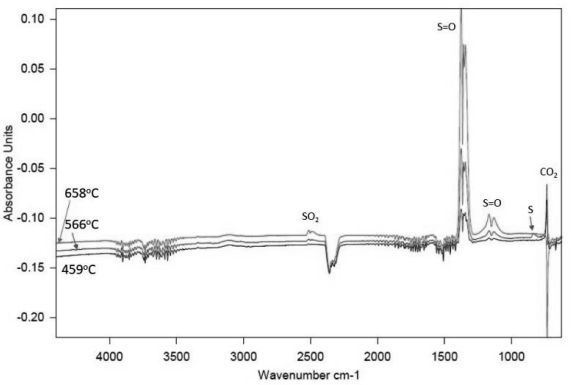

Figure 8. Sample R FTIR spectra in temperatures: 459, 556 and 658°C
Rysunek 8. Widma FTIR próbki R w temperaturach 459, 556 i 658°C

Comparing the thermograms of both pyrite samples tested, stronger oxidation is observed in the initial phase of thermal decomposition in the case of sample R.

The FTIR spectra of sample H do not reveal vibrations associated with the dehydroxylation of chloritoid, which was detected by XRD in this sample. This may be due to the relatively low content of this phase in the sample volume tested or the masking of the signal by intense sulfide oxidation processes occurring in a similar temperature range.

3. SUMMARY AND CONCLUSIONS

Comparative studies of pyrites from the Navajún (Spain) and Baia Mare (Romania) deposits allowed for the characterization of both similarities and differences in their mineral composition, clearly confirming the genetic diversity of both deposits.

X-ray diffraction analysis (XRD) combined with elemental composition studies (XRF) showed that the presence of chloritoid in the Navajún (H) sample results directly from the mineral inclusions originating from the parent rock, i.e., Cretaceous marl. The chloritoid contained is a remnant of the sedimentary growth environment of pyrite and was incorporated into the FeS_2 crystal during its diagenesis in the Cameros Basin, which determines the high thermal stability of this sample and its unique, idiomorphic form.

In turn, pyrite from the Baia Mare (R) deposit represents a different origin, closely related to Neogene hydrothermal activity within the Carpathian Arc, as evidenced by the presence of arsenic admixtures (0.65%). The increased chemical reactivity of sample R, documented by intense oxidation in the temperature range of 450-460°C and elemental sulfur emission, determined by the 834 cm^{-1} FTIR band, indicates the presence of a significant crystal lattice defect, typical of rapid crystallization in vein systems.

The obtained research results demonstrate that radically different geological conditions – from low-energy sedimentary-metasomatic environments to dynamic hydrothermal systems – determine not only the chemical composition of pyrites but also their degree of structural order.

BIBLIOGRAPHY

1. Lodders K., Klingerhöfer G., Kremser D.T., 1998, Chloritoid inclusions in pyrite from Navajún, Spain, The Canadian Mineralogist 36, 137-145.
2. Földvári M., 2011, Handbook of thermogravimetric system of minerals and its use in geological practice, Occasional Papers of the Geological Institute of Hungary, vol. 213.
3. Hu H., Chen Z., Yin P., Zhang P., 2003, Thermal behaviours of mechanically activated pyrites by thermogravimetry, Thermochim. Acta 398, 233-240.
4. Labus M., 2021, Pyrite thermal decomposition in source rocks, Fuel 287
5. Paulik F., Paulik J., Arnold M., 1982, Kinetic and mechanism of the decomposition of pyrite under conventional and quasi-isothermal – quasi-isobaric thermoanalytical conditions, Journal of Thermal Analysis, 25, 313-325.

TalentDetector

7th-9th June 2026
Gliwice-Brenna, Poland

DEPARTMENT OF ENGINEERING MATERIALS AND BIOMATERIALS
FACULTY OF MECHANICAL ENGINEERING
SILESIAN UNIVERSITY OF TECHNOLOGY

INTERNATIONAL STUDENTS SCIENTIFIC CONFERENCE

Sustainable fabrication of porous ceramics from glass cullet, slag and fly ash

Lew Lewandowski[a], Mikołaj Łysień[a], Emilia Jackow[a], Jakub Niziołek[b], Paweł Wilk[b], Marek Kremzer[c], Błażej Tomiczek[c]

[a] Student of Aeronautical and Aerospace Engineering, Silesian University of Technology
email: ej316587@student.polsl.pl, ll316600@student.polsl.pl, ml316562@student.polsl.pl
[b] Student of Industrial Mechatronics, Silesian University of Technology
email: jn316720@student.polsl.pl, pw316704@student.polsl.pl
[c] Silesian University of Technology, Faculty of Mechanical Engineering, Scientific and Didactic Laboratory of Nanotechnology and Materials Technology
email: marek.kremzer@polsl.pl , blazej.tomiczek@polsl.pl

Abstract: Porous ceramics were successfully fabricated using glass cullet as a matrix and waste-derived additives (slag and fly ash), demonstrating their potential for sustainable, resource-efficient ceramic processing within a circular economy. The type of additive strongly influenced the microstructure and properties: slag promoted higher densification and formation of a rough, highly porous coral-like structure, while fly ash enhanced sintering and resulted in a smoother microstructure with preserved microsphere features. Processing parameters such as sintering temperature and compaction pressure significantly affected density, shrinkage, and porosity, enabling controlled tailoring of the material for structural, filtration, and insulation applications.

Keywords: Sustainable production, porous ceramics, glass cullet, slag, fly ash

1. INTRODUCTION

Porous ceramic materials are widely utilised across various industries for their exceptional physical and chemical properties, including low density, high thermal resistance, superior thermal insulation, and chemical stability. These materials play an indispensable role in the aerospace, energy, metallurgical, environmental, and construction sectors, particularly where lightweight structures and resistance to extreme temperatures or corrosive environments are required [1-3]. In recent years, significant research has pivoted toward sustainable ceramic processing, focusing on utilising industrial by-products and waste-derived raw materials to reduce the environmental footprint of this energy-intensive industry [4]. Secondary raw materials such as glass cullet, coal fly ash, and metallurgical slags are considered highly valuable due to their favourable chemical compositions, which are often rich in silica and alumina [5]. Fly ash is a critical precursor for promoting the formation of high-value ceramic phases, such as mullite, through deep-desilication technologies that optimise the alumina-to-silica ratio [6]. Metallurgical slags, often rich in metal oxides, can be used to obtain both dense and highly porous composites (with porosities reaching up to 65%) that exhibit excellent mechanical strength and durability in acidic environments [7].

Furthermore, waste glass (sodalime or borosilicate) serves as a potent fluxing agent, enabling a dramatic reduction in sintering temperatures—successfully lowering them from conventional levels of 1050°C to as low as 650°C—thereby accelerating sintering kinetics and enhancing densification [8]. The integration of these secondary resources aligns with the principles of sustainable development and the circular economy. Life Cycle Assessments (LCA) indicate that energy consumption during the firing process is the dominant contributor to the environmental impact and carbon emissions of ceramic production [9]. By replacing virgin minerals with reprocessed waste, manufacturers can reduce raw material extraction, minimise landfill disposal, and lower greenhouse gas emissions [10]. This transition not only mitigates environmental degradation but also offers substantial economic benefits, as waste-derived materials such as foamed slag glass can be produced at costs 2 to 3 times lower than those of their commercial counterparts [11]. Moreover, recycling industrial waste into functional ceramics directly lowers the energy demand of the production cycle. Additives like glass cullet improve sintering behaviour, allowing lower processing temperatures and shorter firing cycles, which directly translate into reduced consumption of fossil fuels and electricity. As a result, implementing secondary raw materials not only supports global environmental protection strategies but also significantly enhances the economic competitiveness and resource efficiency of modern ceramic manufacturing systems [12]. The aim of this project is to investigate the sustainable production of porous ceramics based on glass cullet, fly ash, and slag. The study evaluates the influence of these waste-derived materials on the microstructure and properties of the ceramics, as well as their benefits and limitations in ceramic technology.

2. MATERIALS

The experimental studies were carried out using waste-derived materials in the form of glass cullet, fly ash, and slag, which were applied as raw materials for the fabrication of porous ceramics. These materials originate from industrial processes and recycling operations and represent a promising source of secondary raw materials for applications in ceramic technology. The glass cullet was obtained from the recycling of waste glass used in the construction industry. This material is characterized by favorable physical properties, particularly an appropriate bulk density and good sintering ability, which make it suitable for ceramic processing. Fly ash and slag, on the other hand, are by-products generated during high-temperature coal combustion processes. Due to their chemical composition rich in silica, alumina, and other oxide compounds, these materials can actively participate in the formation of ceramic phases and influence the final microstructure of the obtained materials. Their incorporation into ceramic systems may also contribute to improved thermal and mechanical performance while reducing the demand for natural mineral resources. The morphology and chemical composition of the applied waste materials were analyzed using scanning electron microscopy (SEM) equipped with an energy-dispersive spectroscopy (EDS) detector. Microscopic investigations enabled detailed observation of the surface morphology, pore distribution, particle geometry, and microstructural characteristics of the processed materials. Furthermore, light microscopy (LM) and scanning electron microscopy (SEM) analyses (Fig. 1) provided valuable insight into the influence of the applied waste-derived additives on the microstructure, homogeneity, and porosity of the produced ceramic materials. The chemical composition of the base powders used in the study is presented in Table 1. The true and apparent densities of the selected powders are presented in Table 2.

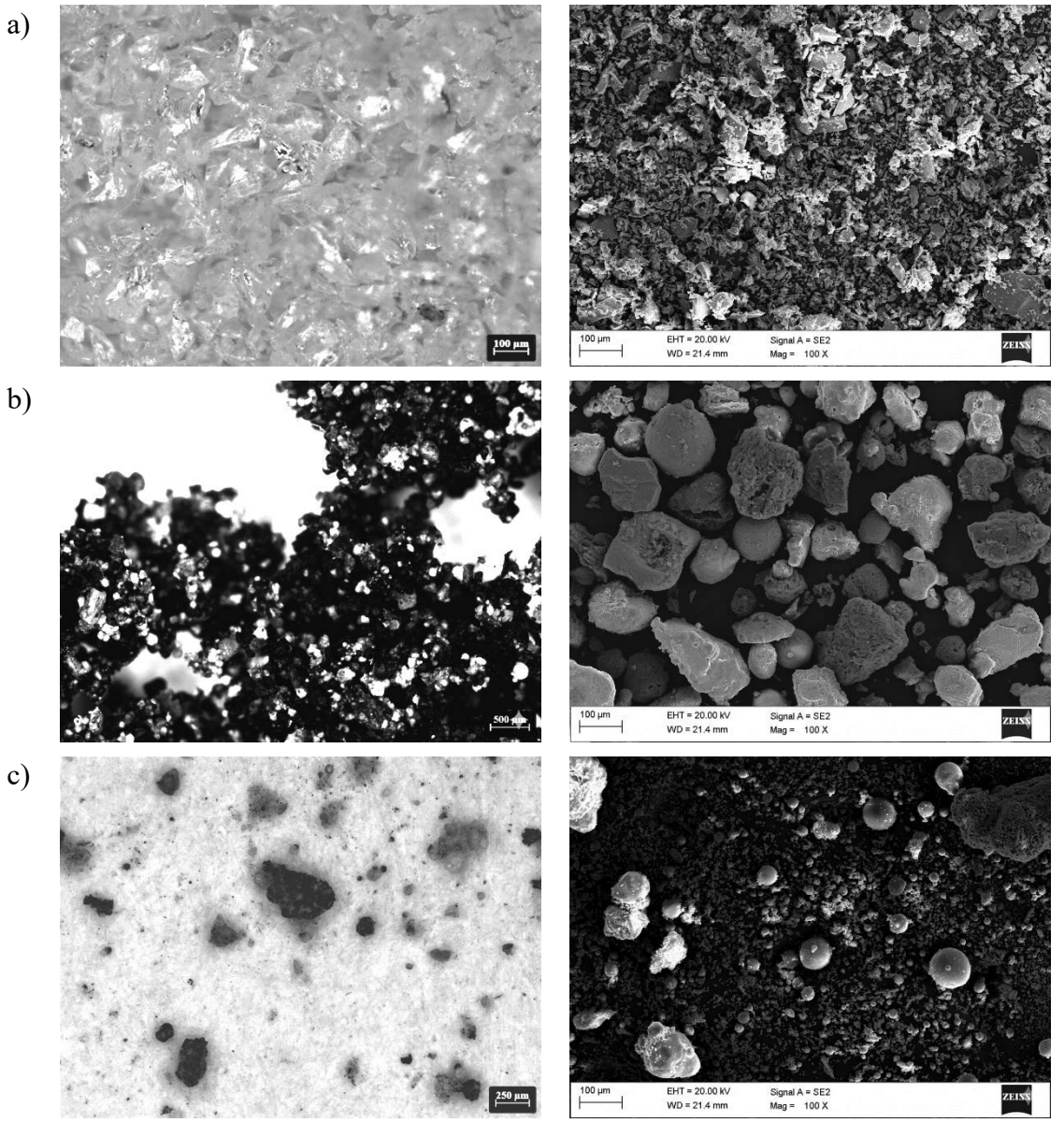

Fig. 1. Morphology of base powders a) glass cullet, b) slag and c) fly ash

Table 1. Chemical composition determined using EDS analysis

	C	O	Na	Mg	Al	Si	K	Ca	Ti	Fe	Mn
Glass cullet											
Weight %	26.1	37.5	0.5	1.5	0.7	3.8	3.4	24.6	0	1.1	0.8
Atom %	39.5	42.6	0.4	1.1	0.5	2.5	1.6	11.1	0	0.4	0.3
Bottom slag											
Weight %	26.0	37.0	0.7	1.9	8.3	13.9	1.7	4.5	0.6	5.4	0
Atom %	38.3	40.9	0.5	1.4	5.5	8.7	0.7	2.0	0.2	1.7	0
Fly ash											
Weight %	29.9	37.6	0.5	0.9	9.6	15.3	1.4	1.6	0.5	2.7	0
Atom %	42.0	39.5	0.4	0.6	6.0	9.2	0.6	0.7	0.2	0.8	0

Table 2. The true and apparent densities of the selected powders.

Powder	Glass cullet	Slag	Fly ash
True density [g/cm^3]	2,50	2,19	2,13
Apparent density [g/cm^3]	1,64	0,59	0,75

The EDS analysis shows clear differences in the chemical composition of the investigated materials. Glass cullet is characterised by a very high calcium content (24.6 wt.%) and a relatively low silicon and aluminium content, whereas slag is distinguished by an elevated silicon content (13.9 wt.%) and iron (5.4 wt.%). Fly ash, in turn, contains a higher amount of carbon (29.9 wt.%) and silicon (15.3 wt.%), with a moderate aluminium content (9.6 wt.%), indicating a more heterogeneous composition. Differences are also observed in density values. The highest true density is found for glass cullet (2.50 g/cm³), followed by slag (2.19 g/cm³), while fly ash exhibits the lowest value (2.13 g/cm³). Apparent density is significantly higher for glass cullet (1.64 g/cm³) and considerably lower for slag (0.59 g/cm³) and fly ash (0.75 g/cm³). Results of particle size analysis of selected powders has been shown on Figure 2. Differences in particle size distribution were determined using the laser particle size analyser Analysette 22 manufactured by Fritsch Company. All three obtained distributions are asymmetric and unimodal. As can be clearly seen in the graphs, the finest powder was fly ash, while bottom slag exhibited the coarsest particle size distribution. The median particle sizes were 15.8 µm for glass cullet, 13.7 µm for fly ash, and 47.3 µm for slag.

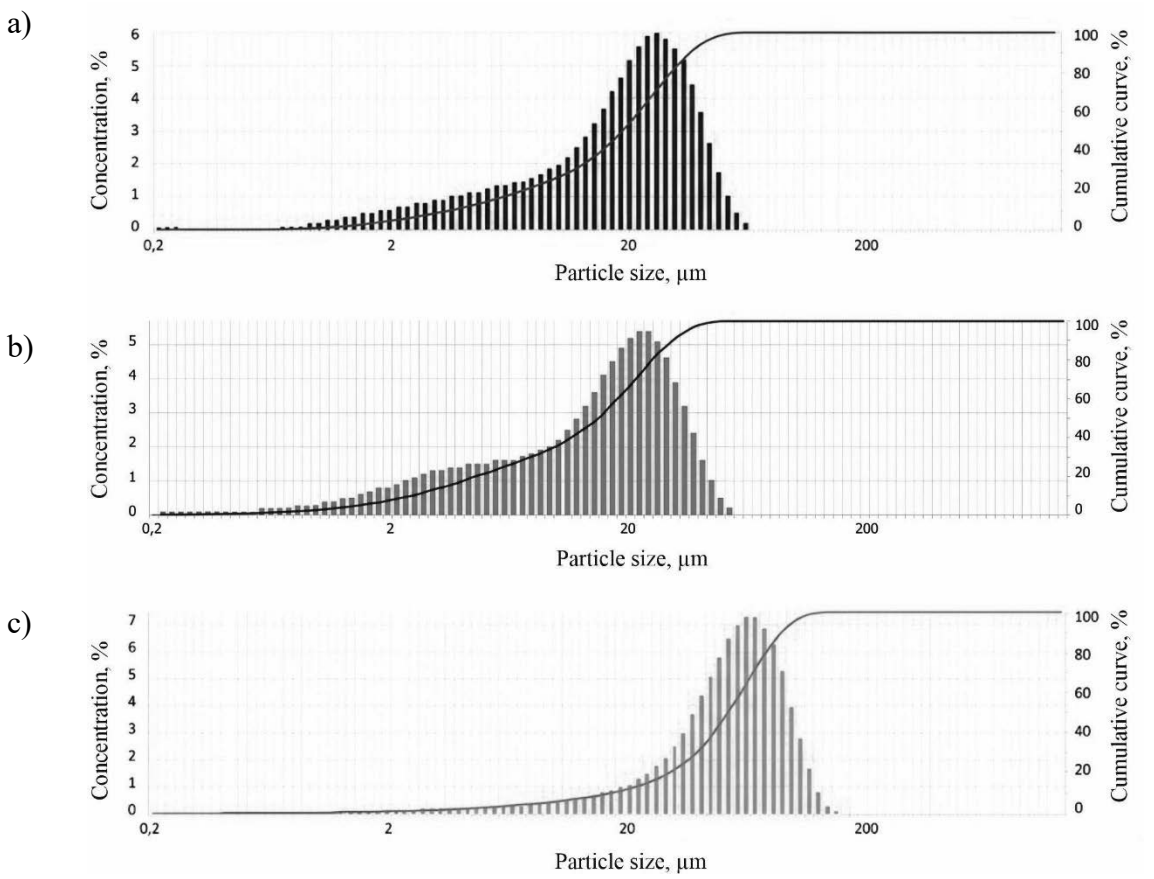

Fig. 2. Particle size distribution of a) glass cullet, b) fly ash and c) bottom slag

3. SAMPLE PREPARATION

To obtain porous ceramics, several series of powder samples were prepared, with glass cullet as the primary matrix component. The entire technological process is illustrated in the diagram presented in Fig. 3.

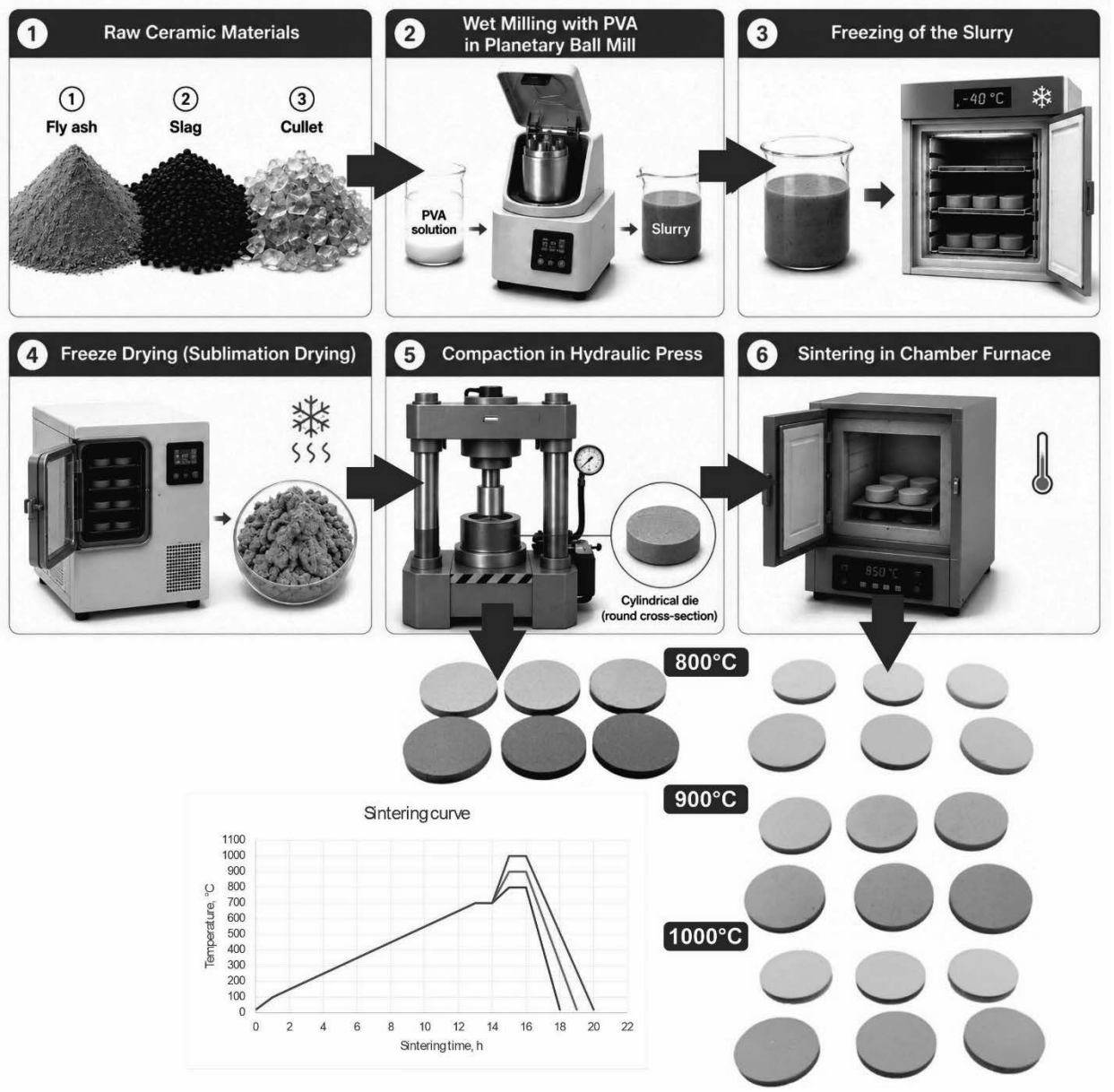

Fig. 3. Process flow diagram of the technological route

The individual samples differed in the type of waste additive used in the mixture—either slag or fly ash. The preparation process for both powders followed the same technological procedure. For the preparation of the first sample, 50 g of glass cullet and 50 g of slag were used. Subsequently, 100 g of deionised water was added to the mixture to reduce impurities that could affect the final composition of the material, along with 1 g of a polyvinyl alcohol (PVA) solution as a binder. All components were placed in a milling vessel made of yttria-stabilised zirconia, to which 20 mm diameter milling balls were added. The mass ratio of powder to grinding media was 1:7. The prepared vessel was placed in a Fritsch Pulverisette 6 planetary mill, where

homogenization was carried out for 10 minutes at 300 rpm. After milling, the resulting suspension was transferred into a laboratory container. Due to the need to completely remove water from the material, the sample was frozen at −20°C and, after full solidification, freeze-dried to remove water without disturbing the material's structure. The dried sample was then sieved, yielding a homogeneous powder intended for pressing. The second mixture was prepared analogously, replacing the slag with fly ash. In the next step, compacts with a diameter of 30 mm were produced from the prepared powder mixtures using uniaxial single-sided pressing in a closed-die hydraulic frame press. Three pressing pressures were applied: 70, 140, and 210 MPa. The pressing time was 10 s. After compaction, the samples were measured and then placed in a high-temperature chamber furnace. Three sintering temperatures were applied: 800, 900, and 1000°C, with a heating rate of 50°C/h.

4. RESULTS AND DISSCUSION

To precisely characterise the ceramic materials obtained, a series of investigations was carried out, the main objective of which was to conduct a detailed analysis of surface morphology and to evaluate shrinkage and porosity in the produced ceramic samples. A key stage of this work was determining how individual waste components, such as slag and fly ash, affected the final structure of the obtained sinter compared with the matrix based on glass cullet. Images of the samples after sintering at different temperatures are presented in Figure 3. The results of the geometric measurements of the obtained samples are summarised in Table 3. The analysis of the results indicates that the apparent density of the samples increases with both rising sintering temperature and pressing pressure, reaching a maximum value of 2.02 g/cm³ for the material containing slag, sintered at 1000°C and compacted under 210 MPa. This trend suggests that higher thermal energy and compaction pressure enhance particle rearrangement and pore elimination, leading to a more densely packed microstructure. The lowest apparent density, equal to 1.59 g/cm³, was observed for samples containing fly ash, pressed at 70 MPa and sintered at 800°C. In this case, the relatively low pressure, combined with an insufficient sintering temperature, likely limited diffusion and particle bonding, resulting in a more porous structure with incomplete densification. Regarding linear shrinkage, higher values are observed for slag-containing samples. The maximum shrinkage reaches 8.11% (1000°C, 70 MPa), indicating intensified densification and significant pore closure during sintering. In contrast, the minimum value across the entire dataset is −3.84% for the fly ash material (800°C, 70 MPa), indicating initial structural expansion. This anomalous behavior may be associated with gas release, thermal decomposition of residual phases, or early-stage pore growth dominating over densification mechanisms at lower processing conditions. Overall, the results clearly demonstrate that the use of slag promotes densification and higher linear shrinkage, consistent with improved sinterability and particle reactivity. Conversely, fly ash leads to more heterogeneous volumetric behaviour of the samples, likely due to its more complex phase composition, lower reactivity, and the presence of unburned residues or stable glassy phases that hinder uniform densification.

An important step in the research process was the detailed microstructural analysis of the produced ceramic materials using scanning electron microscopy (SEM). Since the investigated porous ceramics are electrically insulating and do not conduct electric current, appropriate sample preparation, involving the application of a thin gold coating, was required prior to placing them in the microscope chamber.

Table 3. Dimensional measurements of the obtained ceramic samples

Powder mixture	Sintering temp., °C	Compaction pressure, MPa	Sample					
			diameter	thickness	mass	volume	apparent density	shrinkage
Glass cullet + bottom slag	800	70	30,16	3,82	4,75	2,73	1,74	4,12%
		140	30,25	3,57	4,74	2,57	1,85	2,55%
		210	30,25	3,41	4,75	2,45	1,94	2,71%
	900	70	30,12	3,78	4,75	2,69	1,76	5,37%
		140	30,17	3,58	4,74	2,56	1,85	2,79%
		210	30,19	3,50	4,74	2,51	1,89	0,82%
	1000	70	29,72	3,77	4,74	2,62	1,81	8,11%
		140	29,78	3,50	4,73	2,44	1,94	7,41%
		210	29,81	3,36	4,75	2,35	2,02	6,90%
Glass cullet + fly ash	800	70	30,20	3,92	4,47	2,81	1,59	-3,84%
		140	30,30	3,61	4,46	2,60	1,71	-1,61%
		210	30,19	3,47	4,46	2,48	1,80	0,26%
	900	70	30,15	3,78	4,45	2,70	1,65	0,20%
		140	30,19	3,54	4,45	2,53	1,75	1,08%
		210	30,21	3,47	4,45	2,49	1,79	0,13%
	1000	70	29,99	3,80	4,45	2,68	1,66	0,73%
		140	29,99	3,54	4,45	2,50	1,78	2,38%
		210	30,04	3,33	4,45	2,36	1,89	5,24%

For this purpose, a thin gold layer was applied to the dried and cleaned samples by sputter coating to ensure charge dissipation and optimal imaging conditions, after which SEM analysis was performed to examine microstructure and pore characteristics within the ceramic matrix. As shown in the microstructure (Fig. 4), the produced ceramic exhibits uniformly distributed, homogeneous porosity resulting from the degradation of the binding additive (PVA) and other substances in fly ash or slag, which released gases during heating to the sintering temperature. The microstructural study shows that slag addition to glass cullet increases specific surface area and forms a rough, coral-like structure rich in intergranular pores. In contrast, fly ash promotes more intensive sintering, likely involving a liquid phase, leading to smoother pore walls and preserved microsphere traces.

a) b)

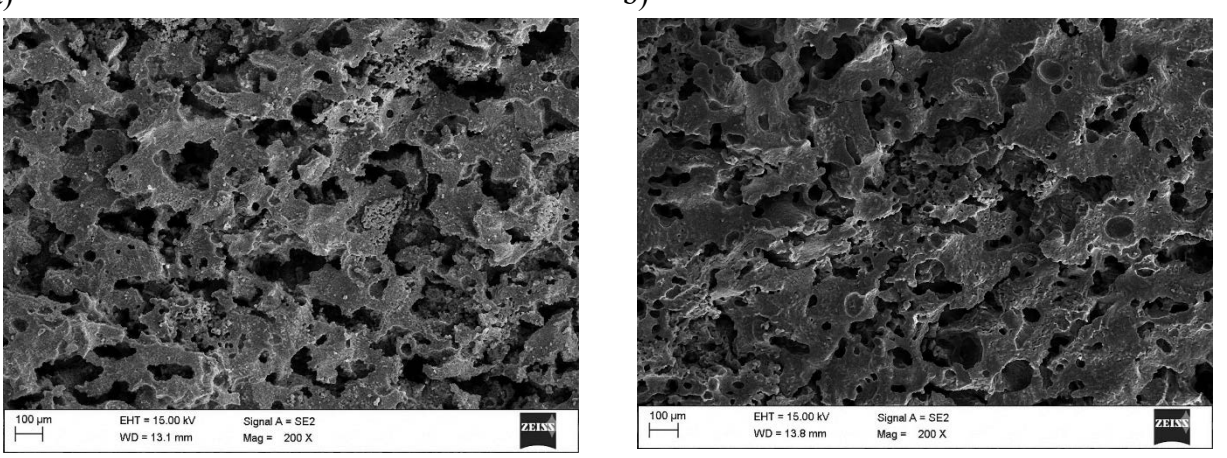

Fig. 4. Microstructure of manufactured ceramics consist on mixture of a) cullet + slag and b) cullet + fly ash, sintered at 900°C, SEM

5. CONCLUSIONS

It has been demonstrated that industrial waste materials (glass cullet, slag, and fly ash) can be effectively used as secondary raw materials for the fabrication of porous ceramics, supporting the principles of the circular economy and reducing the consumption of primary resources. The type of additive significantly influences the microstructure and final properties of the material: slag promotes densification and a rough, highly porous structure, whereas fly ash enhances sintering and yields a smoother microstructure with preserved microsphere features. Technological parameters (sintering temperature and compaction pressure) play a crucial role in determining density, shrinkage, and porosity, enabling controlled tailoring of the ceramic structure for structural, filtration, or insulating applications.

ACKNOWLEDGMENTS

This publication was supported under the „Excellence Initiative – Research University" program at the Silesian University of Technology, within the framework of the 14th Project Based Learning (PBL) funding competition.

BIBLIOGRAPHY

1. A. Kelly, Why engineer porous materials? Philosophical Transactions of the Royal Society A: Mathematical, Physical and Engineering Sciences 364.1838 (2006) 5-14.
2. Y. Chen, N. Wang, O. Ola, Y. Xia, Y. Zhu, Porous ceramics: Light in weight but heavy in energy and environment technologies, Materials Science and Engineering: R 143 (2021) 100589.
3. T. Ohji, M. Fukushima, Macro-porous ceramics: Processing and properties, International Materials Reviews 57/2 (2012) 115-31. https://doi.org/10.1179/1743280411Y.00000000
4. Z. Zhang, H. Ma, C. Wu, Y. Sun, R. Chen, X. Guo, Properties of Glass-Ceramics Prepared from Industrial Multi-Wastes, Separations 10 (2023) 498.
5. S.S. Hossain, P.K. Roy, Sustainable ceramics derived from solid wastes: a review. Journal of Asian Ceramic Societies, 8/4 (2020) 984–1009.
6. X. Chen, Y. Tan, H. Yan, J. Shi, J. Wu, B. Ding, A review of cleaner production of glass-ceramics prepared from MSWI fly ash, Journal of Environmental Management 370 (2024) 122855.
7. Q. Wu, Z. Huang, Preparation and performance of lightweight porous ceramics using metallurgical steel slag, Ceramics International 47/18 (2021) 25169-25176.
8. S. Akhtar, U. M. Zaman, M. S. Islam, F. Nigar, M.K. Hossain, Effect of Different Types of Glasses as Fluxing Agent on the Sintering Temperature of Bricks. Transactions of the Indian Ceramic Society 76/2 (2017) 128–132.
9. H. Monteiro, P.L. Cruz, B. Moura, Integrated environmental and economic life cycle assessment of improvement strategies for a ceramic industry, Journal of Cleaner Production 345 (2022) 13173.
10. A. Waterkemper Vieira, L. Savi Rosso, A. Demarch, D. Pasini, S. Pereira Ruzza, S. Arcaro, M. J. Ribeiro, E. Angioletto, Life cycle assessment in the ceramic tile industry: a review, Journal of Materials Research and Technology 23 (2023) 3904-3915..
11. E. A. Yatsenko, B. M. Goltsman, V. A. Smolii and A. S. Kosarev, "Foamed slag glass - eco-friendly insulating material based on slag waste," 2015 IEEE 15th International Conference on Environment and Electrical Engineering (EEEIC), Rome (2015) 819-823
12. J. Zhang, Y. Fan, X. Zhai, V.V. Kumar, Investigating the effects of sintering additives and heating regimes on the performances of glass–ceramic proppants derived from industrial wastes, Materials & Design 250 (2025) 113634.

TalentDetector

7th-9th June 2026
Gliwice-Brenna, Poland

DEPARTMENT OF ENGINEERING MATERIALS AND BIOMATERIALS
FACULTY OF MECHANICAL ENGINEERING
SILESIAN UNIVERSITY OF TECHNOLOGY

INTERNATIONAL STUDENTS SCIENTIFIC CONFERENCE

Microstructural and chemical study of the antibacterial TiAgN coating

Paulina Lukaszkowicz[a], Tiara Ogórek[a], Ewa Adamek[b], Wojciech Baran[b], Jozef Sondor[c], Krzysztof Lukaszkowicz[d], Klaudiusz Gołombek[e], Krzysztof Matus[e], Paweł Nuckowski[e]

[a] Medical University of Silesian in Katowice, Faculty of Pharmaceutical Sciences in Sosnowiec, Student Scientific Club at the Department of Inorganic Chemistry
email: s86990@365.sum.edu.pl; s87046@365.sum.edu.pl
[b] Medical University of Silesian in Katowice, Faculty of Pharmaceutical Sciences in Sosnowiec, Department of Inorganic Chemistry
email: eadamek@sum.edu.pl; wbaran@sum.edu.pl
[c] LISS, a.s., Dopravni 2603, 756 61 Roznov pod Radhostem, Czech Republic
email:j.sondor@liss.cz
[d] Silesian University of Technology, Faculty of Mechanical Engineering, Department of Engineering Materials and Biomaterials
email: krzysztof.lukaszkowicz@polsl.pl
[e] Silesian University of Technology, Faculty of Mechanical Engineering, Materials Research Laboratory
email: klaudiusz.golombek@polsl.pl; krzysztof.matus@polsl.pl; pawel.nuckowski@polsl.pl

Abstract: The research subject was the microstructural and chemical characterisation of the TiAgN coating deposited by magnetron sputtering. The TiAgN coating was characterised using scanning electron microscopy (SEM), transmission electron microscopy (TEM), energy-dispersive spectroscopy (EDS), and X-ray diffraction (XRD) for structural, chemical composition, and phase analysis, respectively.

Keywords: TiAgN coating, magnetron sputtering, SEM, TEM, EDS, XRD

1. INTRODUCTION

The TiAgN coating combines the protective properties of titanium nitride with the antibacterial properties of silver. The concept of depositing silver within the titanium nitride structure arose from the observation that silver exhibits strong antibacterial properties, yet its direct use as a coating has limitations: silver is soft and not hard enough for practical applications. The antibacterial properties of TiAgN coatings are their main advantage and the motivation for research. TiAgN has been shown to exhibit significant antibacterial activity against a wide range of pathogens, including Streptococcus mutans, Staphylococcus aureus, E. coli, and many others [1-5]. One of the most widely used methods for depositing a TiAgN coating is magnetron sputtering [6].

2. MATERIALS AND METHODS

The tests were performed on samples of X6CrNiMoTi17-12-2 austenitic steel and on polished silicon wafers coated with TiAgN coating. The coating deposition process was carried out by the magnetron sputtering method in an argon-nitrogen atmosphere. During the deposition process, targets containing pure metals (Ti and Ag) were used. The cross-section and chemical composition of the investigated coating were examined using a high-resolution scanning electron microscope, HRSEM SUPRA 35 by Zeiss, equipped with an EDS spectrometer. Chemical composition analyses in micro-areas were performed using the EDS detector with Pathfinder software. Phase analysis of the investigated coating was performed using a PANalytical X'Pert PRO X-ray diffractometer with Co Kα radiation. Analysis was performed using the step registration method over a 2θ angular range of 10–100°. Qualitative X-ray analysis was performed using HighScore Plus 3.0e version software and a dedicated PAN-ICSD phase identification card database. A microstructural study was performed using a transmission electron microscope (TEM) Titan 80-300 equipped with an energy-dispersive X-ray spectrometer (EDS), for chemical composition analysis. The thin cross-section lamellas for TEM observations were prepared by the focused ion beam (FIB) technique using a Quanta 200i instrument with gallium ions. The following TEM techniques (bright-field BF, dark-field DF, and selected area diffraction) were used for imaging.

3. RESULTS AND DISCUSSION

The cross-sectional image of the TiAgN coating is presented in Fig. 1a. The coating exhibits a compact, columnar structure, with no signs of delamination or defects. Based on scanning electron microscope images, the coating thickness was estimated to be approximately 1.3 µm. The chemical composition tests performed using an EDS spectrometer confirmed the presence of individual elements in the analysed TiAgN coating (Fig. 1b).

a) b)

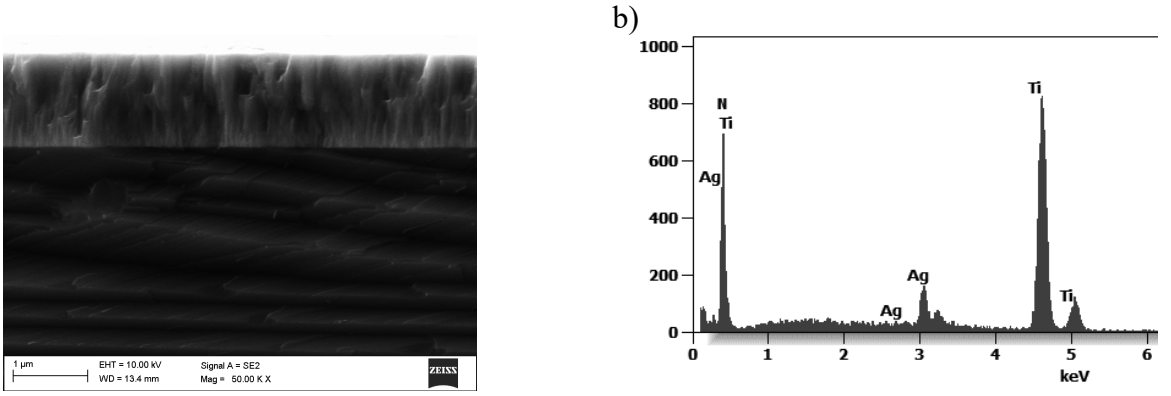

Figure 1. TiAgN coating deposited on the silicon wafer: a) cross-section image (SEM), b) EDS spectrum of the area as in fig. a

Based on the results of the XRD pattern for TiAgN coating (Fig. 2), four reflexes (111), (200), (220), (311) are shown. The reflexes correspond to interplanar spacings of 2.45, 2.12, 1.50 and 1.28 Å, respectively, which are characteristic of the TiN cubic phase. The intensity ratio of the detected reflexes indicates the presence of an fcc-type crystal structure in the TiAgN coating.

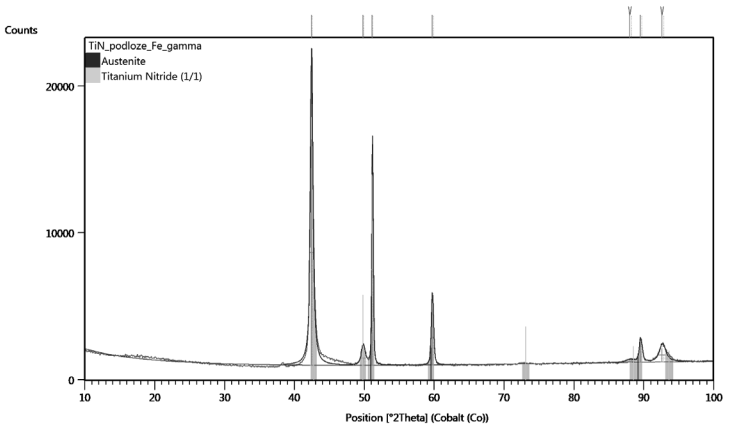

Figure 2. X-ray diffraction pattern of TiAgN coating

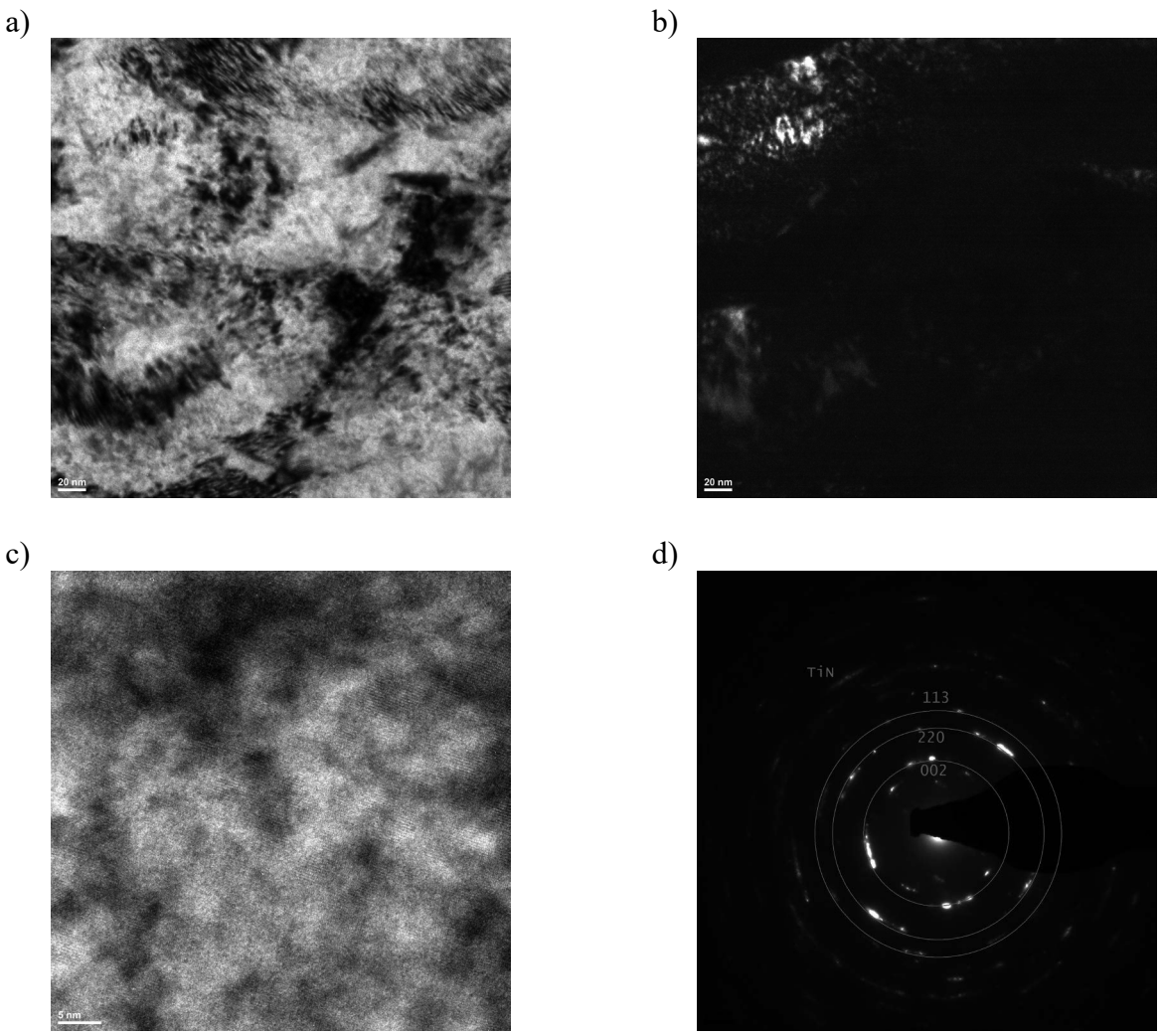

Figure 3. Structure of the TiAgN coating: a) TEM-BF image, b) TEM-DF image, c) HRTEM image, d) SAED obtained from the area as in fig. b

The structure examination performed in a transmission electron microscope (TEM) confirmed the homogeneous polycrystalline character of TiAgN coating (Fig. 3a-c). The coating exhibits a columnar structure with column widths ranging from 60 to 180 nm. Based on SAED (Fig. 3d), the cubic phase of TiN was identified, confirming the above XRD results. The results of EDS chemical composition analysis performed in TEM confirm the high chemical quality of the tested coating. The chemical composition of the investigated coating is presented in Table 1.

Table 1. Chemical composition of TiAgN coating

Element	Weight %	Atomic %
N	24,90	55,53
Ti	62,65	40,86
Ag	12,45	3,61

4. CONCLUSION

Based on SEM observations, the TiAgN coating was found to have a uniform thickness and tight adhesion to the substrate throughout its entire area. The results of X-ray qualitative phase analysis confirm the presence of the TiN phase in the tested coating. Transmission electron microscopy analysis revealed that the deposited coating possesses a crystalline structure composed of columns oriented perpendicular to the substrate surface.

BIBLIOGRAPHY

1. S. Hojda, M. Biegun-Żurowska, A. Skórkowska, K. Klesiewicz, M. Ziąbka, A weapon against implant-associated infections: antibacterial and antibiofilm potential of biomaterials with titanium nitride and titanium nitride-silver nanoparticle electrophoretic deposition coatings, International Journal of Molecular Sciences 26 (2025) 1646.
2. B.-M. Kang, W.-J. Jeong, G.-C. Park, D.- J. Yoon, H.-G. Ahn, Y.- S. Lim, The characteristics of an antibacterial TiAgN thin film coated by physical vapor deposition technique, Journal of Nanoscience and Nanotechnology 15/8 (2015) 6020-6023.
3. C.P. Priyanka, K.K. Krishnan, U. Sudeep, K.K. Ramachandran, Osteogenic and antibacterial properties of TiN-Ag coated Ti-6Al-4V bioimplants with polished and laser textured surface topography, Surface and Coatings Technology 474 (2023) 130058.
4. L. Geyao, D. Yang, C. Wanglin, W. Chengyong, Development and application of physical vapor deposited coatings for medical devices: A review, Procedia CIRP 89 (2020) 250-262.
5. X. Fang, R. Tu, J. Liu, H. Dai, L. Zheng, S. Zhu, S. Zhang, T. Goto, Improvement of antibacterial activity and mechanical properties of titanium alloy by TiAlV/Ag gradient multilayer coating, Journal of Vacuum Science & Technology A 41 (2023) 033107.
6. J.T. Gudmundsson, Physics and technology of magnetron sputtering discharges, Plasma Sources Science and Technology 29 (2020) 113001.

TalentDetector

7th-9th June 2026
Gliwice-Brenna, Poland

DEPARTMENT OF ENGINEERING MATERIALS AND BIOMATERIALS
FACULTY OF MECHANICAL ENGINEERING
SILESIAN UNIVERSITY OF TECHNOLOGY

INTERNATIONAL STUDENTS SCIENTIFIC CONFERENCE

Modeling the level of happiness in the world using machine learning methods and multidimensional data analysis

Aleksandra Mikuła [a], Mirosław Bonek

[a] Silesian University of Technology, Faculty of Organization and Management
email: am320737@student.polsl.pl

Abstract: The aim of the paper is to develop an analytical tool that enables modeling and interpretation of the level of happiness in the world using data analysis and machine learning methods. The analysis used data from the World Happiness Report, and the research process was carried out in the Google Colab environment using the Python language. The developed tool combines statistical analysis, interactive visualization and elements of predictive modeling, constituting an example of the application of data science in the analysis of social phenomena.

Keywords: happiness modeling, machine learning, data science, multivariate data analysis

1. INTRODUCTION

In recent years, the issue of measuring and modelling social well-being has gained significant importance both in scientific research and in public policy practice. Traditional approaches based solely on economic indicators, such as gross domestic product, prove insufficient to fully describe the quality of life of societies. In response to this gap, multidimensional measures of happiness and well-being are being developed, taking into account social, health, institutional and environmental factors. One of the most recognizable sources of this type of data is the *World Happiness Report*, which provides comparable information on the level of happiness in individual countries and its determinants [1-5}.
At the same time, there is a dynamic development of data analysis and machine learning methods that enable the identification of complex dependencies in high-dimensional data. These techniques allow not only for the construction of predictive models, but also for an in-depth interpretation of relationships between variables, which is of particular importance in the analysis of multifactorial social phenomena. The integration of statistical tools, exploratory data analysis methods, and machine learning algorithms creates new research opportunities, enabling more precise modeling and visualization of complex relationships [6-10].
The aim of this paper is to develop an analytical tool that enables modeling and interpretation of the level of happiness in the world using data analysis and machine learning methods. The study used data from the *World Happiness Report*, which includes a set of indicators describing various aspects of social and economic life. The research process was carried out in

the Google Colab environment using the Python language, which allowed for the integration of various analytical libraries and provided high flexibility in data processing and visualization.
The developed tool combines elements of statistical analysis, interactive visualization and predictive modeling. In particular, it enables the exploration of data structure, the identification of key determinants of the level of happiness and the construction of models that allow for forecasting the value of well-being indicators. The use of interactive forms of visualization supports the process of interpreting the results and allows for a better understanding of the relationships between the analyzed variables [11-14].
The work uses the Google Colab environment – a cloud platform enabling data analysis without local configuration. The following libraries are used:

- **pandas** – allows you to work on tabular data (DataFrame), including filtering, aggregation and transformations,
- **numpy** – used for mathematical operations and work on matrices,
- **plotly** – allows you to create interactive data visualizations,
- **scikit-learn** – used to build machine learning models.

The aim of the article is to create a tool that allows you to analyze and model the level of happiness.

2. MATERIALS AND METHODS

2.1 Data

The analysis used data from the World Happiness Report [1], which includes a set of indicators describing the quality of life in different countries of the world. This dataset is one of the most important sources of data in the field of social welfare research and is widely used in scientific analyses and reports of international institutions. The central element of the set is a variable defined as the happiness result, taking values on a scale from 0 to 10 and reflecting the respondents' subjective assessment of life, which allows for a quantitative understanding of the phenomenon of a qualitative nature.
In addition, the collection contains explanatory variables related to the level of economic development, the state of health of the society, social relations or the level of trust in public institutions, which together create a multidimensional picture of factors affecting well-being. Such a wide range of variables allows for the construction of analytical and predictive models, which are part of the so-called computational social science.
It should be emphasized that this data is the basis for further visual and interactive analyses presented in the following parts of the article, where modern data visualization tools will be used to explore relationships in a dynamic way.

2.2 Analytical process

The analytical process is designed as a multi-stage data processing pipeline. In the first step, the data was imported using the pd.read_csv function, which allowed it to be further processed in the DataFrame structure typical of the pandas library. Next, a data quality analysis was performed, which consisted in identifying the missing values using the df.isnull().sum() method. The results of this analysis indicated that there were no data gaps, which made it possible to move on to the next stages without the need for imputation.

The next stage was to clean the data by using the dropna method, which ensures the consistency of the set in further calculations. In order to increase the readability of the data, the names of the columns were also translated into Polish, which facilitates the interpretation of the results and adapts the analysis to the recipient.
An important element of the process was the engineering of features, which consisted in the creation of a new variable describing the level of wealth of countries. For this purpose, the average value of GDP was calculated and on its basis countries were divided into two groups: countries with a level of wealth above the average and countries below this value. This allowed for additional comparative analysis and identification of differences between groups.
The final stage was to conduct a correlation analysis and prepare interactive visualizations, which are a key part of the developed tool.

3. MATHEMATICAL MODEL

The paper uses a linear regression model describing the relationship between the level of happiness and selected socio-economic factors. The model presents the happiness score as a linear combination of variables such as GDP, social support, health, freedom of decision, and the level of corruption. The model coefficients reflect the strength of the influence of individual variables, while the random component takes into account factors not directly included in the model.
This approach allows not only to describe the relationships occurring in the data, but also provides the basis for building predictive models that can predict the level of happiness based on the observed indicators.

4. RESULTS AND VISUALS

4.1 Heatmap

The heatmap was generated using the px.imshow function and shows a correlation matrix between the variables being analyzed. The use of the text_auto=".2f" parameter allows for the automatic display of numerical values in matrix cells with an accuracy of two decimal places, which significantly increases the precision of interpretation. The RdBu_r color scale used allows you to quickly distinguish the direction and strength of the relationship, where shades of red indicate strong positive correlations, and shades of blue indicate negative relationships.
The interactivity of the chart is also an important element (Fig. 1). By using the hovertemplate parameter, the user can get detailed information about the analyzed pair of variables and the exact value of the correlation coefficient after hovering. This solution transforms the graph into an exploratory tool, allowing you to analyze relationships in a dynamic and detailed way.

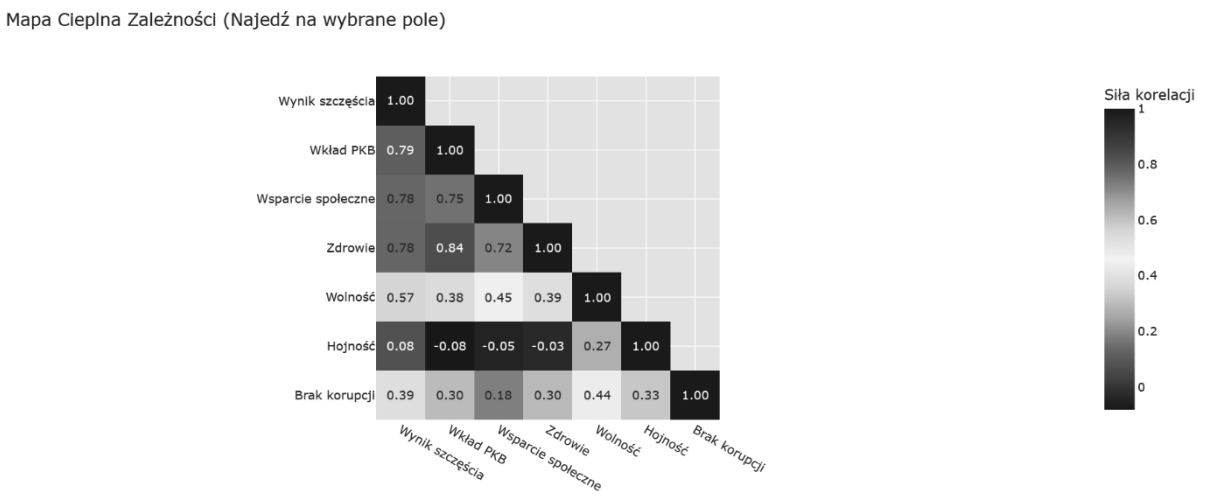

Fig.1 Interactive chart overview

After hovering over the selected field, we get (Fig. 2):

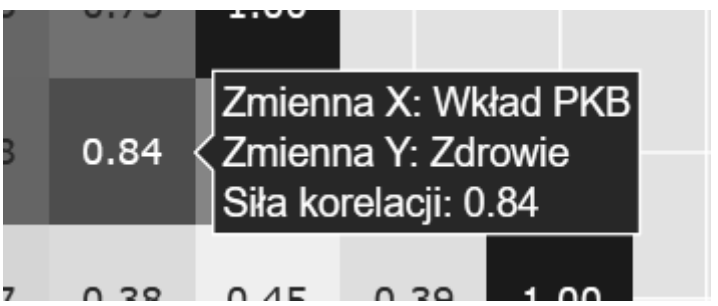

Fig.2. Interactive chart functionality

4.2 Regression Chart (Scatter + OLS)

The scatter chart was created using the px.scatter function and shows the relationship between GDP contribution and happiness levels (Fig. 3). The color parameter assigns a color to points based on the value of the dependent variable, allowing you to analyze an additional dimension of the data at the same time. The viridis color scale has been selected due to its high legibility and smooth transitions between values.

Using the trendline="ols" parameter allows for automatic least squares regression line adjustment, allowing for a visual assessment of the direction and strength of the relationship. The interactivity of the chart, implemented among others by the hover_name parameter, allows for the identification of individual countries and the analysis of their position in relation to the global trend. This allows the user not only to observe general dependencies, but also to study individual cases.

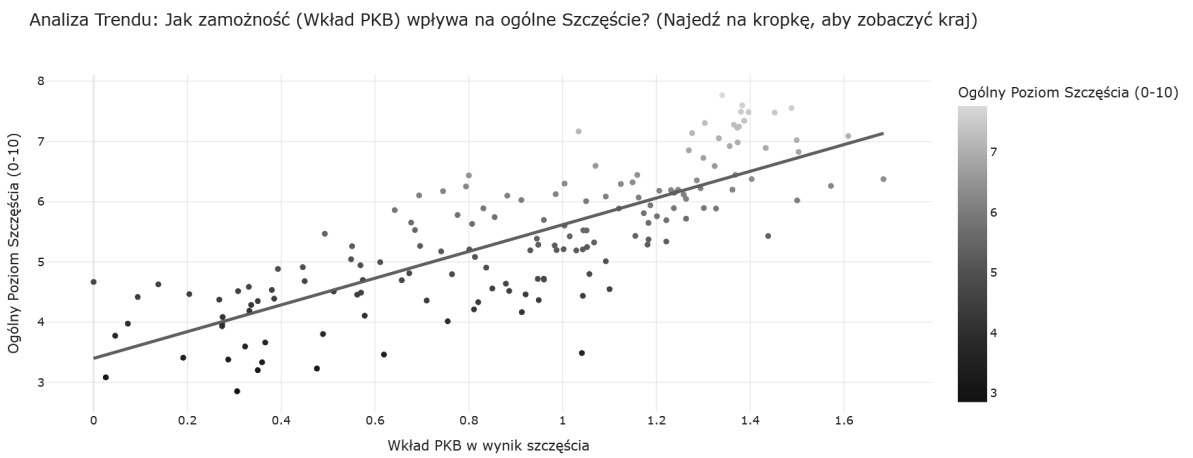

Fig. 3. Trend analysis: how wealth contributes to GDP and overall happiness

After hovering over the selected field, we get (Fig. 4):

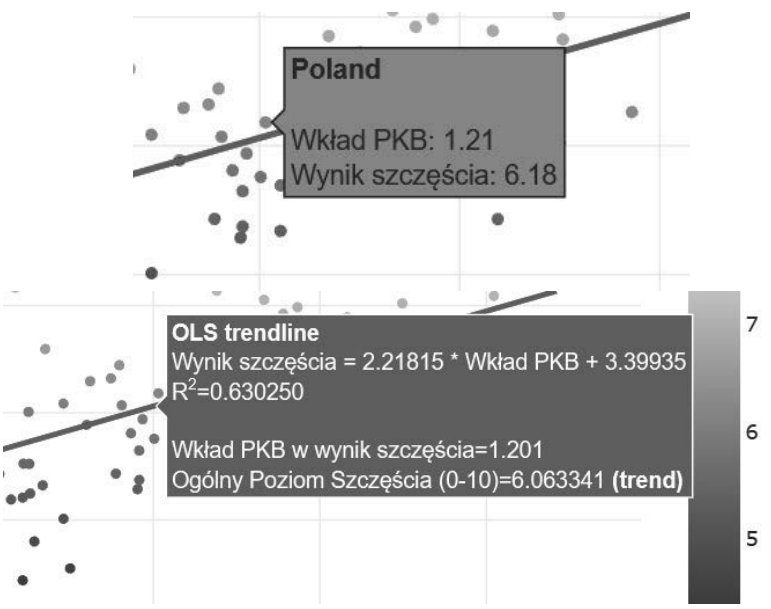

Fig. 4. Interactive chart functionality

4.3 Boxplot

The box chart was used to analyze the distribution of happiness levels in groups of countries with different levels of wealth (Fig. 5). The points="all" parameter allows you to display all observations, which significantly increases the amount of information available and allows you to analyze typical values and potential outliers at the same time.
The additional use of interactivity allows each point to be identified, which means that the user can check the exact values for a specific country. As a result, the graph has not only a presentational function, but also an analytical function, allowing for in-depth data mining.

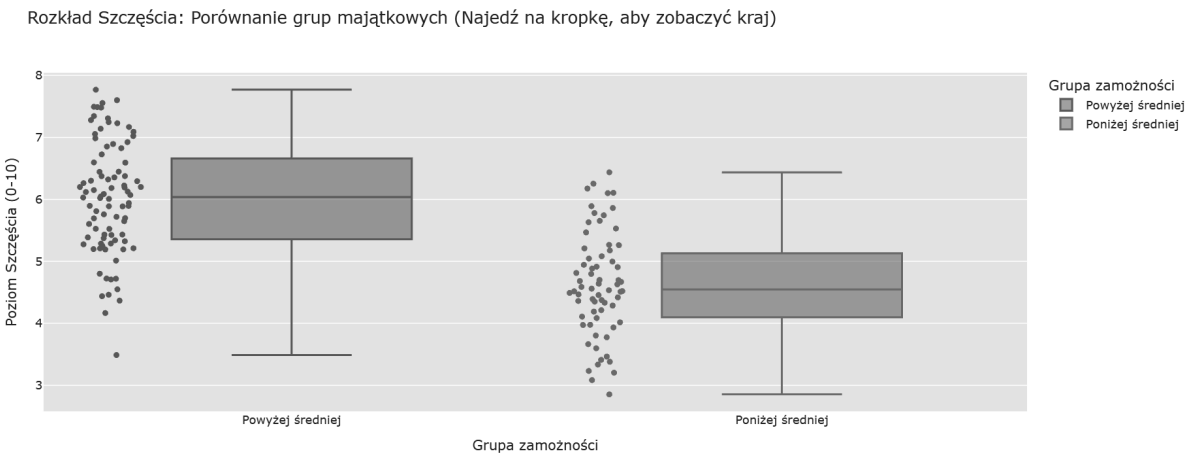

Fig. 5. Distribution of happiness: comparison of wealth groups

After hovering over the selected field, we get (Fig. 6):

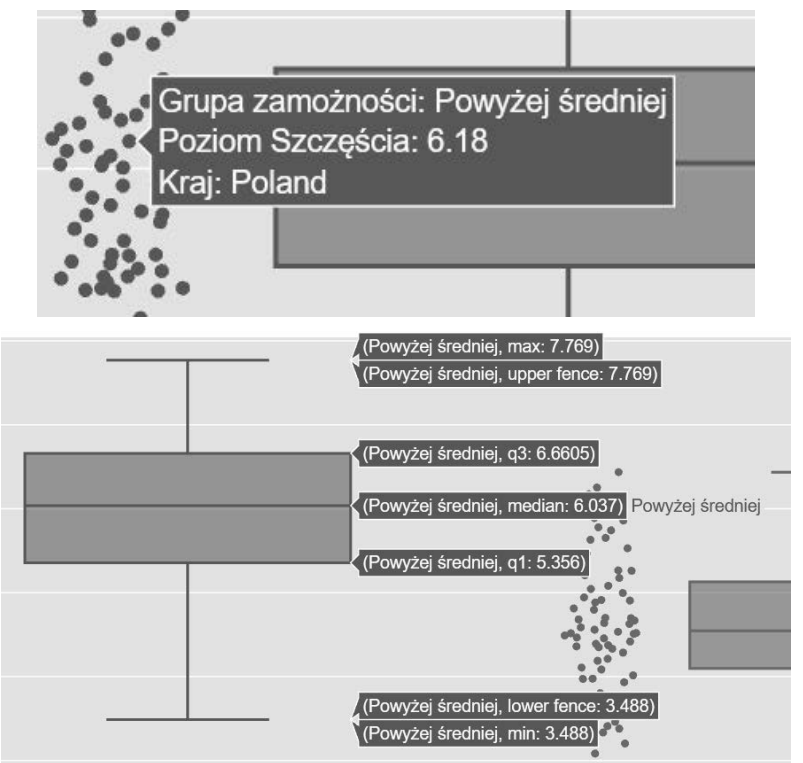

Fig. 6. Interactive chart functionality

4.4. The importance of interactive visualizations

Interactive visualizations are a key element of the developed tool, as they allow the user to actively explore the data instead of passively receiving the results. Thanks to the ability to hover the cursor over the elements of the chart, zoom in on the view or analyze individual observations in detail, the user gains much more control over the process of data interpretation.

Such an approach is in line with modern standards of data analysis, in which visualization no longer performs only an illustrative function, but becomes an integral part of the research process. As a result, the developed solution can be treated as an interactive analytical tool.

4.5. Implementation of the tool

The developed solution is a modular analytical system, in which the subsequent stages of data processing are logically ordered and interconnected. The first element is the data layer, which includes the input set and its preparation. The data is then processed using libraries such as pandas and numpy, which are responsible for transformation operations and preparing the data for analysis.
The next layer is modeling, which uses statistical methods and approaches characteristic of machine learning. At this stage, it is possible to both explain the observed relationships and build predictive models. The results are then presented using interactive visualizations based on the Plotly library, allowing them to be analyzed in real time.
The last element of the system is the user, who, by interacting with the visualizations, can analyze the data and formulate conclusions. Such a tool can be developed into a web application in the future, for example by using frameworks such as Dash, which further increases its application potential.

8. CONCLUSION

The results obtained indicate a strong link between the level of economic development and the level of happiness. At the same time, it is noticeable that social factors, such as social support or a sense of security, are equally important. This means that the well-being of societies is a multidimensional phenomenon and cannot be analysed solely in an economic context.

The analysis confirms that it is possible to model the level of happiness using data analysis methods. The results obtained indicate the key role of economic and social factors, and the use of interactive visualizations significantly increases the interpretative possibilities of the tool. The approach developed can provide a basis for further research and development of decision support systems.

BIBLIOGRAPHY

1. Helliwell, J. F., Layard, R., & Sachs, J. (2019). *World Happiness Report 2019*. New York: Sustainable Development Solutions Network
2. OECD (2013). *OECD Guidelines on Measuring Subjective Well-being*. Paris: OECD Publishing
3. OECD (2025). *OECD Guidelines on Measuring Subjective Well-being (2025 Update)*. Paris: OECD Publishing
4. Durand, M. (2015). The OECD Better Life Initiative: How's Life? and the measurement of well-being. *Review of Income and Wealth*, 61(1), 4–17
5. Decancq, K., & Schokkaert, E. (2016). Beyond GDP: Using equivalent incomes to measure well-being in Europe. *Social Indicators Research*, 126(1), 21–55

7. Hair, J. F., Black, W. C., Babin, B. J., & Anderson, R. E. (2010). *Multivariate Data Analysis* (7th ed.). Upper Saddle River, NJ: Pearson
8. VanderPlas, J. (2016). *Python Data Science Handbook*. O'Reilly Media
9. McKinney, W. (2018). *Python for Data Analysis*. O'Reilly Media
10. Raschka, S., & Mirjalili, V. (2019). *Python Machine Learning*. Packt Publishing.
11. Yang, B., & Xie, X. (2025). Analyzing and predicting global happiness index via integrated multilayer clustering and machine learning models. *PLOS ONE*, 20(4)
12. Naveen, & Bhatia, A. (2025). Unveiling the landscape of happiness prediction with machine learning: A systematic review
13. Machine learning in the prediction of human wellbeing. *Nature Scientific Reports*
14. Happiness prediction with domain knowledge integration and explanation. *IEEE Xplore*

TalentDetector

7th-9th June 2026
Gliwice-Brenna, Poland

DEPARTMENT OF ENGINEERING MATERIALS AND BIOMATERIALS
FACULTY OF MECHANICAL ENGINEERING
SILESIAN UNIVERSITY OF TECHNOLOGY

INTERNATIONAL STUDENTS SCIENTIFIC CONFERENCE

Analysis of dimensional accuracy and surface roughness in additive manufacturing processes

Besart Misini[a], Afrim Gjelaj[a*], Tomasz Tanski[b], Brytan Zbigniew[b], Besart Berisha[a], Kaltrinë Jakupi[a], Mehmet Zeqiraj[a]

[a] University of Prishtina, Faculty of Mechanical Engineering, Department of Manufacturing and Industrial Engineering
email: besart.misini@student.uni-pr.edu, afrim.gjelaj@uni-pr.edu, besart.berisha@uni-pr.edu, kaltrinë.jakupi@uni-pr.edu, mehmet.zeqiraj@uni-pr.edu
[b] Silesian University of Technology, Faculty of Mechanical Engineering, Department of Engineering Materials and Biomaterials
email: tomasz.tanski@polsl.pl, zbigniew.brytan@polsl.pl
Correspondent author: afrim.gjelaj@uni-pr.edu

Abstract: Describe briefly what the article is about and what has been done.
For example: The article describes the idea of the atomic layer deposition method and its possible applications. Also presented are the exemplary test results of Al2O3 thin layers deposited by the ALD method on the Picosun R-200 system.
Technology day by day creates and develops production processes to facilitate work processes, improve quality, automate functions, eliminate mass labor, reduce financial costs, and especially shorten time. We have witnessed a rapid development of technology in recent years, which has actually pushed the increase in the variety of shapes and constructions of different products that constitute important parts for the realization of functions and the performance of work. Such technology undoubtedly increases the range of materials. This is a very modern process in terms of the paths a product takes to be produced and the materials that are made available for working.
Previously, production relied on processes that removed material in different forms, which from experience we have known as conventional and non-conventional processes, and now the process that we will elaborate on creates similar products but with a completely opposite process by not removing but adding material layer by layer.
The 3D printing process uses a wide range of materials, but polymer materials and their combinations stand out. Then, we will analyze the dimensional accuracy and surface roughness measurement of a flange, which we will elaborate on.

Keywords: PLA materials, 3D printing, dimensional acuracy and surface roughness

1. INTRODUCTION

Additive manufacturing is the technique of parts, workpieces and products through providing the necessary material. Additive manufacturing is now commonly known as 3D Printing. 3D printing has revolutionized manufacturing of parts and goods and it has gotten more complex and cost effective [1-4]. Two of the major influences on the look of printed parts and their usefulness in diverse sectors such as mechanical engineering, medical and industrial design are the surface roughness and accuracy dimensional. Surface roughness of appearance is a term that refers to the structure, the physical finish of the printed thing. In 3D printing the surface is made up of the structures of the material deposited, and this has nothing to do with a particular model [5-9].

The quality of surface roughness is defined by various major elements such as thickness of the layer, printing temperature - speed and infill parameter. Therefore, further finishing steps such as mechanical polishing, chemicals and application of protective coatings are often carried out as post-processing on these alterations.

Dimensional accuracy is the ability of the 3D printer to produce the design with the same dimensions as the original design (CAD model). This is critical for the workpieces that need to be as accurate as other components or have rigorous functioning requirements. Dimensional deviations may arise from shrinkage of materials, printer calibration and model design and orientation.

For practical applications, such as mechanical components, dimensional precision is crucial, as any variation can spell the end of the part or system. The search for an ideal finish with high dimensional precision is applied in the development of functional prototypes, custom parts and esthetical models. It covers the optimization of printing parameters and in certain cases post processing procedures.

3D printing has a huge challenge that is the balance between the roughness of the same and the dimensional precision. For example, increasing the resolution to increase the features often increases the printing time and consumes more resources. However, an exclusive concentration on the dimensional accuracy can neglect the aesthetic appeal of the part. In this review, we discuss the analysis of the effect of several printing settings, such as infill pattern, nozzle temperature and feed rate on the analysis of research and dimensional accuracy of products printed with PL A.

The research of this feature aims at obtaining the ideal arrangements, which are outstanding in all respects. If you want to get sharpness, clarity and dimensional precision with a 3D printer utilizing PLA filament, you will want to be careful.

1.1. Flange manufacturing using 3D printing

Product manufacturing, related to all production processes, typically commences with design, specifically utilizing CAD design software. We have selected Autodesk Inventor program for design purposes. The component to be manufactured is a mechanical flange, a shape frequently encountered in practice. Flanges are utilized to join pipes to one another, to valves, and to other specialized equipment.

The flange will be produced using the Ender 3 Pro, a Fused Deposition Modeling (FDM) 3D printer manufactured by Creality. The dimensions and form into 2D and 3D view of the flanges are showed in figure 1.

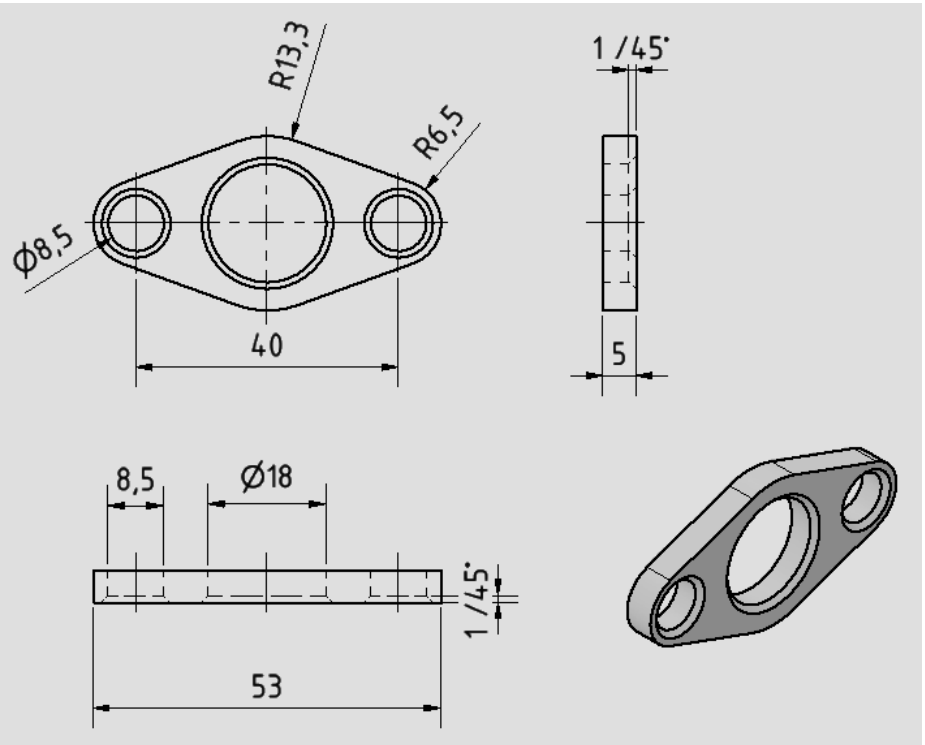

Figure 1. 2D and 3D view of flange

The primary parameters considered during the 3D printing process are the filament temperature and the print bed temperature. The filament temperature was maintained at a constant 210 °C across all 9 experimental situations, while the bed temperature was consistently set at 55 °C. These parameters were selected to guarantee stability and uniform quality throughout the printing process.

Other parameters are changed like: printing speed, printing quality, and printing density (infill density). The printer software autonomously computes supplementary parameters for each parameter combination, including sample weight, filament length utilized, and predicted print duration.

Upon completion of the process, the actual print duration is juxtaposed with the duration forecasted by the program to evaluate the precision and efficacy of the printing procedure. The experimental investigation utilized three distinct levels of print speed, three levels of print quality, and three levels of print density as a foundation. The amalgamation of these criteria yielded a total of 9 distinct experimental combinations, resulting in the production of 9 samples for testing and analysis.

Table 1. Printing parameter

Printing speed [mm/s]	45	50	55
Layer height [mm]	0.12	0.16	0.20
Infill density [%]	30	50	70
Filament temperature [°C]	210 °C		
Bed temperature [°C]	55 ° C		

The combined values of the main printing parameters, i.e. printing speed [mm/s], layer height [mm] and infill ensdity [%] are presented in the table 2. These parameters are the main factors

which directly affect the printing quality, the time of production, the material consumption and the mechanical properties of the printed samples. These parameters were combined at different levels, creating a total of 9 experimental combinations. Test samples were created and the impact of each parameter on the 3D printing process was analyzed.

Table 2. Combination of parameters

No. of experiments	Printing speed [mm/s]	Quality layer high [mm]	Infill density [%]	Length of filament [mm]	Predicted time from Software [min]	Real time printing [min]
1	45	0.12	30	970	46	51
2	45	0.16	50	1080	34	34
3	45	0.20	70	1100	36	37
4	50	0.12	50	1060	50	50
5	50	0.16	70	1160	35	35
6	50	0.20	30	880	26	27
7	55	0.12	70	1150	54	54
8	55	0.16	30	1010	28	27
9	55	0.20	50	980	30	30

In accordance with these parameters, as illustrated in table 2, a total of nine printing samples were created for testing and experimental analysis as in figure 3.

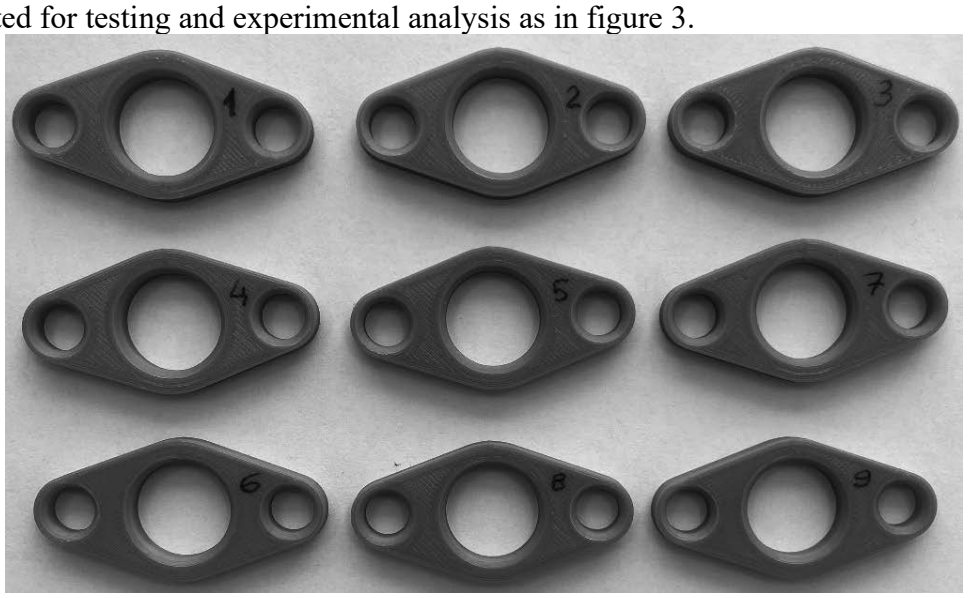

Figure 2. 3D printing flange of the nine specimens depend of the parameters

2. DIMENSIONAL ACCURACY AND SURFACE ROUGHNESS STUDY

Surface roughness is one of the most important characteristics of the surface finish of manufactured components because it directly affects the functional performance of the part as well as the contact with the external environment or with other parts. It is a measurement of the

extent of unevenness or microscopic variations in the surface profile and is measured by various parameters, such as Ra (arithmetic mean roughness), Rq (root mean square roughness), Rz (maximum profile height), etc.

These parameters are required to judge the quality of the processing and the effect of the processes such as mechanical processing, 3D printing or surface treatment [14, 15, 16]. The choice of proper process parameters has a great influence on the obtained roughness values. For example, in 3D printing, the print speed, layer thickness and infill density, among others, can greatly alter the quality of the final surface. A lower roughness is generally required for parts that require smooth contact or limited wear. In structural or non - functional parts, a higher roughness might be acceptable. Thus, the control and optimization of surface roughness are important for the performance and durability of manufactured products.

Dimensional accuracy was achieved at approximately 99%, considering the PLA material, the printing temperature and then the cooling, where the printer was open. For example, the hole in the middle with the dimension according to the drawing was D = 18 mm, after printing the measurement came out to be 17.85 mm. Similarly for the other dimensions. Where the measurements were made with a vernier.

After measuring the surface roughness, the results for all 9 cases are described as in table 3, for the parameter Rz.

Table 3. Combination of parameters

Nr.	Printing speed [mm/s]	Quality layer high [mm]	Infill density [%]	Rq [μm]
1	45	0.12	30	7.85
2	45	0.16	50	14.29
3	45	0.20	70	12.28
4	50	0.12	50	11.46
5	50	0.16	70	17.28
6	50	0.20	30	10.42
7	55	0.12	70	9.49
8	55	0.16	30	10.78
9	55	0.20	50	7.03

The roughness measurement findings for the printed samples were analyzed using Minitab software.

In the 3D view, the plot is presented as a function of print quality, print density and surface roughness parameter Rq as in Figure 3. This 3D surface plot shows the relationship between layer quality (Quality, mm), fill density (Infill, %) and root-mean-square roughness (Rq, μm).

Through this representation, the influence of printing parameters on the change in the Rq value is visualized simultaneously. From the corrugated surface, it is observed that Rq is affected non-linearly by both parameters. There are pronounced areas where Rq increases significantly with increasing infill, especially when the layer quality is thinner (around 0.12 mm). On the other hand, for larger layer thicknesses (0.20 mm), Rq appears more stable, despite changes in density.

This suggests that increasing the layer thickness may have a stabilizing effect on the surface profile, while high density may contribute to irregularities. Such graphs are useful for finding the optimal combinations of parameters that minimize roughness.

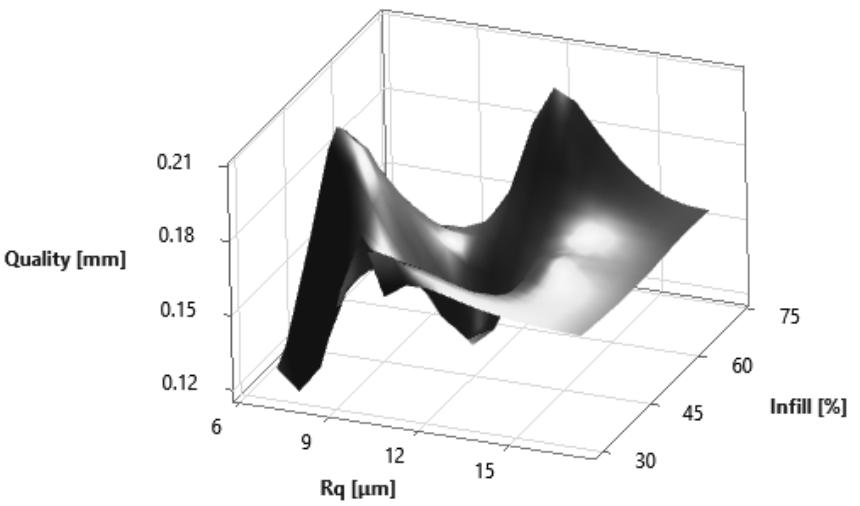

Figure 3. 3D view of the roughness diagram Rq, as a function of print quality and infill density.

CONCLUSION

This study has addressed the impact of key 3D printing parameters — such as printing speed, layer thickness (quality), and infill density — on the final surface quality of the manufactured parts, assessed through the roughness parameter Rq. From the analysis of the results, it was observed that layer thickness has the most significant impact on surface roughness values. In general, thinner layers (higher quality) contribute to a smoother surface, reducing Rq values.

It was also observed that a higher infill density is often associated with increased roughness, which can be related to excessive material accumulation and the creation of surface irregularities. Printing speed did not have a direct linear impact in all cases, but it was found that for some combinations it contributes to improving or worsening the surface. This suggests that the effects of the parameters should not be analyzed separately, but in interaction with each other to find the optimal configurations.

Sample 9 showed the lowest Rq (7.03 µm). This confirms that the combinations of parameters have a clear impact on the entire spectrum of roughness measurements. Finally, it can be said that the optimization of the layer thickness and the management of the infill density are key to improving the surface finish in the 3D printing process. It is recommended that for parts requiring a smooth surface, higher layer thickness (0.2 mm), medium density and maximum infill should be avoided.

This study provides a valid basis for adjusting parameters in order to achieve a balance between quality and efficiency in production. Based on the dimensional accuracy after measurement with Vernier, we obtained measurement values of approximately 99%, in terms of dimensional accuracy of 3D printing. In conclusion, the results show that optimizing 3D printing parameters is essential to guarantee the surface quality of products.

BIBLIOGRAPHY

1. Relatori: prof. Carrera Erasmo, prof. Montemurro Marco dott. Pagani Alfonso, dott.ssa Catapano Anita dott. Zappino Enrico, dott. Panettieri Enrico, Candidato: Micali Lorenzo - Characterization of mechanical properties of 3D printed continuous carbon fiber reinforced composites - POLITECNICO DI TORINO - Facolt`a di Ingegneria Meccanica e Aerospaziale - Corso di Laurea in Aerospace Engineering. 2018
2. Otfinofski, Steven - 3D Printing, Science, Technology, Engineering - 2017
3. Ciara O'Driscoll, Olamide Owodunni, Umar Asghar - Optimization of 3D printer settings for recycled PET filament using analysis of variance (ANOVA). Volume 10, Issue 5. 2024
4. Ian Gibson & David Rosen & Brent Stucker - Aditive Manufacturing Technologies
   Chee Kai Chua, Kah Fai Leong - 3D Printing and Additive Manufacturing: Principles and Applications, 2010.
5. Nor Aiman Sukindar, Ahmad Shah Hizam Md Yasir, Muhammad Danial Azhar, Muhammad Afif Md Azhar, Nor Farah Huda Abd Halim, Mohd Hafis Sulaiman, Ahmad Syamaizar Haji Ahmad Sabli, Mohd Khairol Anuar Mohd Ariffin, Evaluation of the surface roughness and dimensional accuracy of low-cost 3D-printed parts made of PLA–aluminum, Heliyon, Volume 10, Issue 4, 2024,
6. Gjelaj, A., Berisha, B., Sitek, W. (2022). An Experimental Based Approach Using Artificial Intelligence Algorithm for Determining the Surface Roughness by Milling Process. International Transaction Journal of Engineering, Management, & Applied Sciences & Technologies, 13(5), 13A5B, 1-11. 2022
7. Jin Young Choi, Modelling of 3D Printed Fiber-Reinforced Plastic Composites by Classical Laminate Theory, Master of Applied Science, 2019.
8. Redyarsa Dharma Bintara et al. The effect of layer height on the surface roughness in 3D Printed Polylactic Acid (PLA) using FDM 3D printing, 2021_IOP Conference Series: MaterialsScience and Engineering.
9. Besart Berisha, Zoran Pandilov, Gligorche Vrtanoski, Application of additive manufacturing technologies for medical purposes. ACTA TECHNICA CORVINIENSIS – Bulletin of Engineering. 2025.

TalentDetector

7th-9th June 2026
Gliwice-Brenna, Poland

DEPARTMENT OF ENGINEERING MATERIALS AND BIOMATERIALS
FACULTY OF MECHANICAL ENGINEERING
SILESIAN UNIVERSITY OF TECHNOLOGY

INTERNATIONAL STUDENTS SCIENTIFIC CONFERENCE

Infiltration Processing of Ceramic Fiber-Reinforced AlSi12 Matrix Composites

Jakub Niziołek[a], Paweł Wilk[a], Emilia Jackow[b], Lew Lewandowski[b], Mikołaj Łysień[b], Anna Tomiczek[c], Klaudiusz Gołombek[d]

[a] Student of Industrial Mechatronics, Silesian University of Technology
email: jn316720@student.polsl.pl, pw316704@student.polsl.pl
[b] Student of Aeronautical and Aerospace Engineering, Silesian University of Technology
email: ej316587@student.polsl.pl, ll316600@student.polsl.pl, ml316562@student.polsl.pl
[c] Silesian University of Technology, Faculty of Mechanical Engineering, Scientific and Didactic Laboratory of Nanotechnology and Materials Technology
email: anna.tomiczek@polsl.pl
[d] Silesian University of Technology, Faculty of Mechanical Engineering, Materials Research Laboratory, email: klaudiusz.golombek@polsl.pl

Abstract: This study investigated the fabrication of aluminium matrix composites reinforced with ceramic fibres and foamed glass using gas-pressure infiltration. Morphological and chemical analyses of the porous reinforcements were performed using SEM and EDS, revealing highly heterogeneous, porous structures. Initial pressureless infiltration attempts were unsuccessful due to insufficient penetration of the molten aluminium alloy into the porous preforms and degradation of the foamed glass structure. Significantly improved results were obtained with a gas pressure of 3 MPa, enabling effective infiltration of the ceramic fibre preform with the AlSi12 alloy. The produced composites exhibited good structural integrity, uniform reinforcement distribution, and strong bonding between the ceramic and metallic phases, confirming the effectiveness of pressure-assisted infiltration for the manufacture of lightweight metal-matrix composites.

Keywords: aluminium matrix composites, pressure infiltration, ceramic fibres

1. INTRODUCTION

Composite materials constitute a widely used group of advanced engineering materials, finding broad applications in the aerospace, automotive, safety, and ballistic industries, among others. By combining different phases, such as a matrix responsible for protection and stress transfer together with reinforcing fibres or particles, entirely new and exceptional properties can be achieved that are not exhibited by the individual components alone [1]. A particularly important group of structural materials is Fibre Metal Laminates (FMLs), such as GLARE and CARALL, composed of alternating layers of metals, including titanium or aluminium, and polymer

composites reinforced, for example, with glass fibres [2,3]. These materials are characterised by an excellent strength-to-weight ratio, very good interfacial adhesion between layers, and outstanding fatigue resistance, including an effective crack-bridging and crack-arrest mechanism [4,5]. However, the design of FML structures requires careful analysis of thermal stresses in adhesive joints arising from differences in the coefficients of thermal expansion of the constituent materials [6]. An equally important functional group is represented by aluminium matrix composites (AMCs) reinforced with various particulate reinforcements [7]. Compared to conventional aluminium alloys, these materials exhibit a superior strength-to-weight ratio, higher hardness, yield strength, and improved wear and corrosion resistance [8]. In turn, layered polymer-matrix composites combined with advanced technical fibers, such as aramid or polyethene fibres, and hard ceramic materials have become indispensable in the design of modern hybrid protective structures and armour systems [9], used, among others, for protecting patrol vehicles against improvised explosive devices (IEDs) and fragment impacts [10,11]. The high-performance requirements imposed on composite structures necessitate the use of dedicated manufacturing technologies. In the case of FML laminates, autoclave processing, often combined with precise preforming operations, ensures high repeatability and excellent dimensional tolerances, while significantly reducing the risk of structural defects such as delamination or gas porosity [12]. Metal matrix composites, on the other hand, are frequently manufactured using diffusion bonding with hot pressing or advanced casting techniques [13]. An important aspect of the manufacturing of many modern composite systems, such as AMCs and resin-based composites, is the implementation of sustainable development principles by using recycled materials [14]. The incorporation of low-cost waste fly ash as reinforcement in aluminium matrices, or the use of recycled polyurethane foam, reduces production costs, supports environmental protection, and simultaneously optimises the coefficient of thermal expansion and improves the hardness of the resulting material [15].

Generally, among these trends, improvements in plastic forming methods, casting techniques, powder metallurgy, and pressure infiltration of porous ceramic skeletons can be distinguished. The latter is a hybrid technology that combines powder metallurgy for forming a porous skeleton with pressure casting to fill it with a liquid metal alloy. The use of the infiltration process as a highly cost-effective technology forms the basis for obtaining a wide variety of composite materials and enables the realisation of several technological advantages [16-18]:

- the possibility of obtaining near-net-shape composite products with high surface quality,
- adaptation of the process for mass production,
- the possibility of using various reinforcing phases and matrix materials,
- high process efficiency at relatively low production costs,
- the possibility of local reinforcement of cast components.

Depending on the agent responsible for infiltration, the process can be divided into the following modifications [19-21]:

- vacuum infiltration, during which the ceramic skeleton is subjected to reduced pressure relative to atmospheric pressure, while gas pressure acts as the driving force for liquid metal infiltration,
- low-pressure infiltration, which involves applying a pressure of about several tens of pascals (but less than one hundred pascals) on the gas above the liquid metal surface; this variant may also include pressureless infiltration when penetration of the skeleton is driven by hydrostatic pressure,

- pressure (squeeze) infiltration, in which metal under a pressure of several tens to several hundreds of MPa enters and solidifies within the pores of the skeleton. The pressure may be generated by gas above the melt surface, a punch in a die press or centrifugal forces.

2. MATERIALS AND METHOD

Within the scope of this study, an attempt was made to fabricate metal matrix composite materials reinforced with ceramic fibres (Fig. 1a) and foamed glass (Fig. 1b). A refractory ceramic paper supplied by VITCAS, made from a mixture of aluminosilicate fibres, was used as the source of ceramic fibres. The foamed glass was provided by FOAMGLASS.

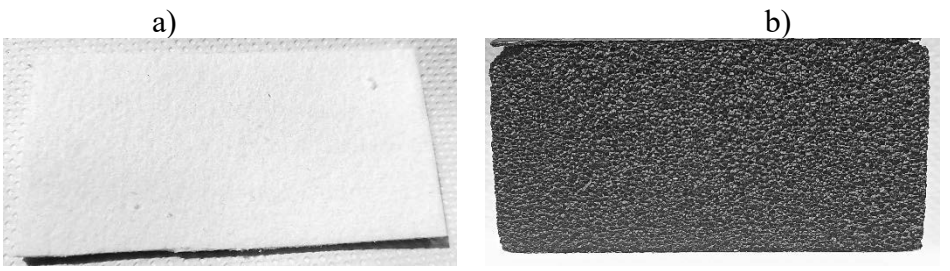

Fig. 1. View of as-received: (a) refractory ceramic paper and (b) foam glass.

The results of the morphological analysis of the ceramic fibres (SEM) and the chemical composition analysis obtained by EDS are presented in the Figure 2. The fracture surface morphology of the refractory mat composed of aluminosilicate ceramic fibres is characterised by a highly heterogeneous, fibrous structure, with elongated, randomly oriented fibres forming a porous network. The fibres exhibit smooth to slightly rough surfaces and variable diameters, typical of materials produced via melt-blowing or fiberising from the molten state. In addition to the fibrous phase, larger droplet-like particles are observed, most likely originating from incompletely fiberised melt or re-solidified amorphous droplets. The results of the morphology tests of the foamed glass (SEM) and the results of the chemical composition tests using the EDS method are presented in the Figure 3. The fracture surface morphology of the foamed glass is characterised by a highly developed, irregular, and porous structure, resulting from numerous closed pores and, less frequently, partially open pores (Fig. 3a). Gas cells of various sizes and shapes can be observed on the fracture surface, separated by thin glassy walls. Small closed pores are also visible within the thicker cell walls (Fig. 3b). The material exhibits brittle fracture, as confirmed by sharp-edged fracture surfaces and the absence of plastic deformation features. In many regions, local interconnections between pores, microcracks, and structural heterogeneities resulting from the foaming process can also be observed. The chemical composition (Fig. 3c), rich in silicon, oxygen, sodium, and calcium, is typical of glass cullet, which is most commonly used as a raw material for the production of this type of glass foam.

As a first step of the experimental procedure, 10 mm thick slices were prepared from both materials, wrapped in nickel mesh, and secured with Kanthal wire. A special apparatus for gas-pressure infiltration of porous preforms with light alloys was designed and manufactured by the Czylok Company (Fig. 4). The porous preforms were attached to a movable plunger located in the upper part of the infiltration device (PTA-8/PrGC2P, Czylok). The AlSi12 alloy was placed in a silicon carbide crucible positioned in the lower section of the infiltration chamber. After placing both the preform and the aluminium alloy inside the chamber, the device was sealed, the

air was displaced with nitrogen gas, and the chamber was evacuated. The crucible was then heated to 800°C and held at this temperature for 1h to ensure complete melting and homogenization of the aluminium alloy. Subsequently, the plunger carrying the porous preform was immersed in the molten alloy, and the gas pressure was gradually increased up to 3 MPa.

a)

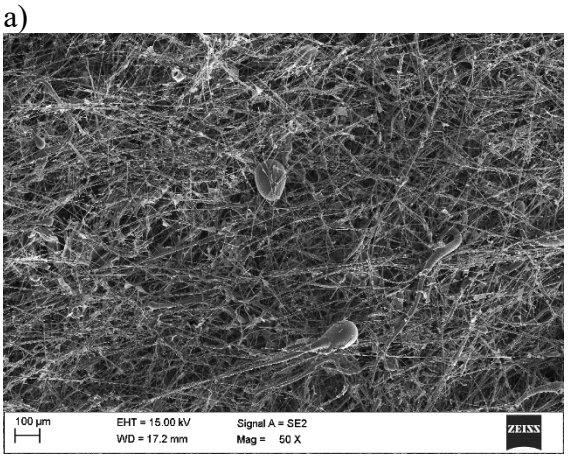

b)

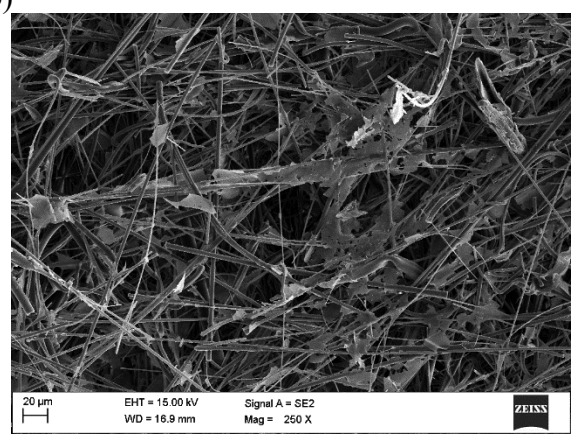

c)

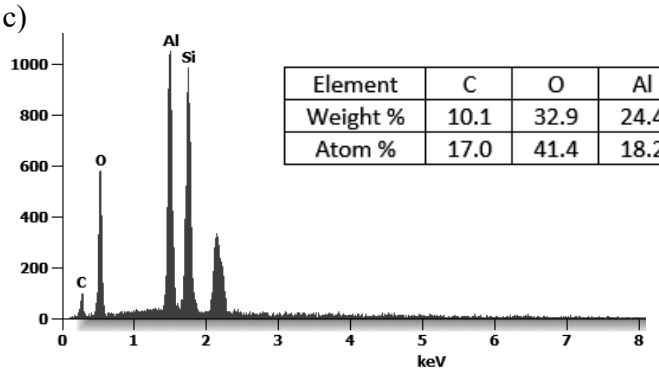

Element	C	O	Al	Si
Weight %	10.1	32.9	24.4	32.6
Atom %	17.0	41.4	18.2	23.4

Fig. 2. SEM micrograph showing: (a) (b) the morphology of ceramic fibers and (c) EDS chemical composition.

a)

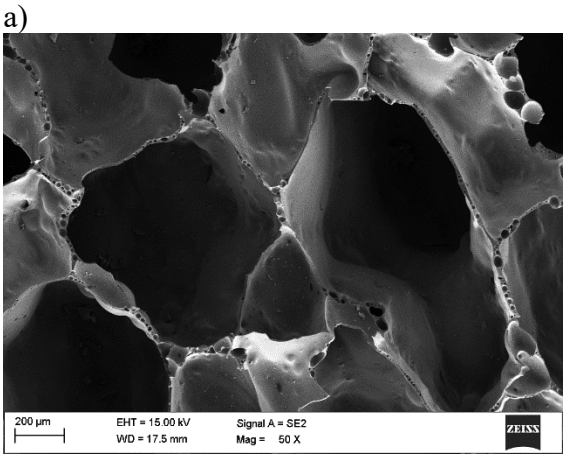

b)

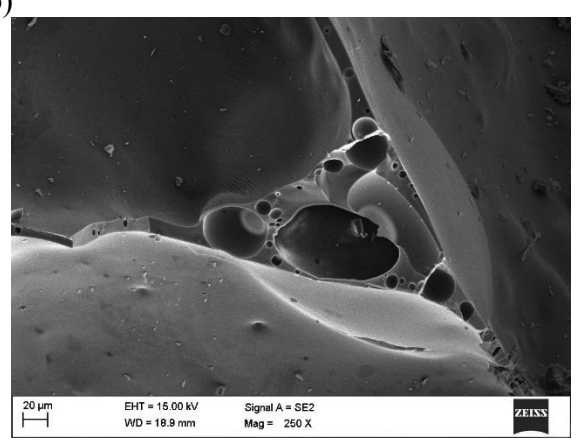

c)

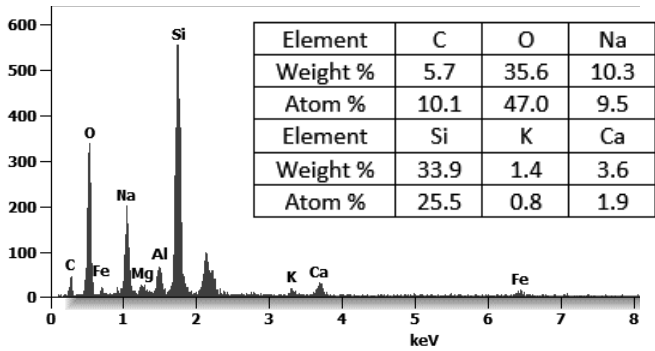

Element	C	O	Na	Mg	Al
Weight %	5.7	35.6	10.3	1.1	2.8
Atom %	10.1	47.0	9.5	0.9	2.2
Element	Si	K	Ca	Fe	-
Weight %	33.9	1.4	3.6	5.6	-
Atom %	25.5	0.8	1.9	2.1	-

Fig. 3. SEM micrograph showing: (a) (b) the morphology of foam glass and (c) EDS chemical composition.

This pressure forced the molten metal into the ceramic preform's pores. After 5 minutes, the plunger with the fabricated composite sample was lifted, and the gas was released from the chamber. The prepared composite samples were removed and cooled using a stream of compressed air. Finally, the samples were polished for microstructural observations and examined using light microscopy. The structure of the samples was observed using a Leica DVM6 Digital stereoscopic microscope and a ZEISS SUPRA 35 high-resolution scanning electron microscope equipped with an EDS chemical composition detector.

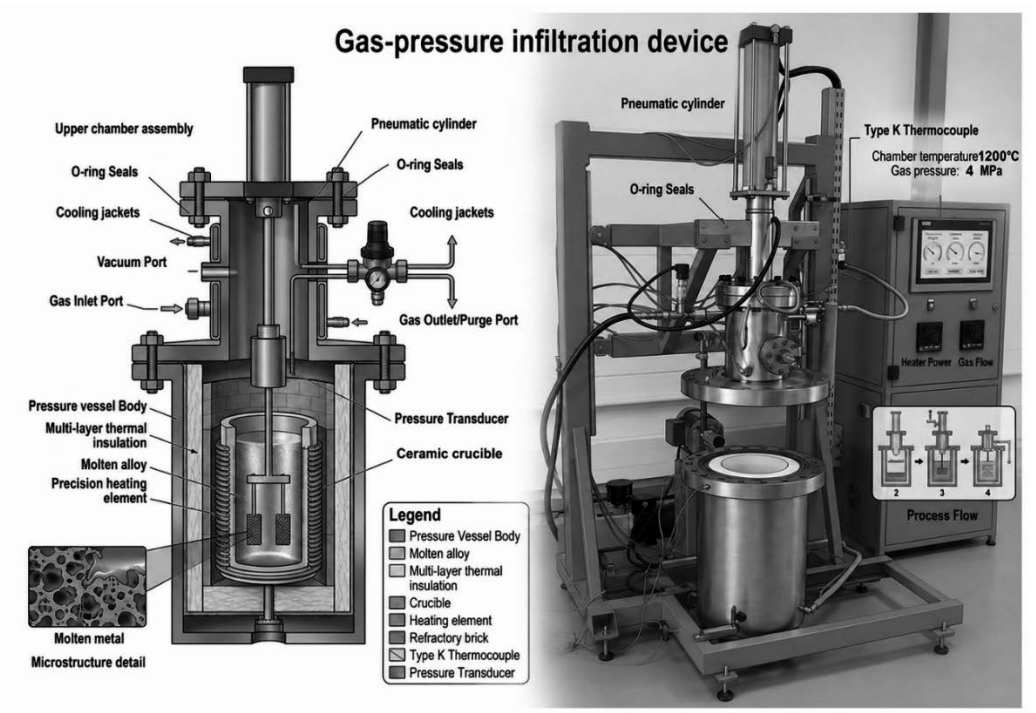

Fig. 4. Diagram of a device designed for the gas-pressure infiltration of a porous ceramics.

3. RESULTS AND DISCUSSION

The first attempt at pressureless (spontaneous) infiltration was unsuccessful. The pressure difference was insufficient to enable spontaneous filling of the pores between the ceramic fibers

(Fig. 5a). In the case of the glass foam, this process led unfortunately to its degradation and loss of structural integrity (Fig. 5b).

a) b)

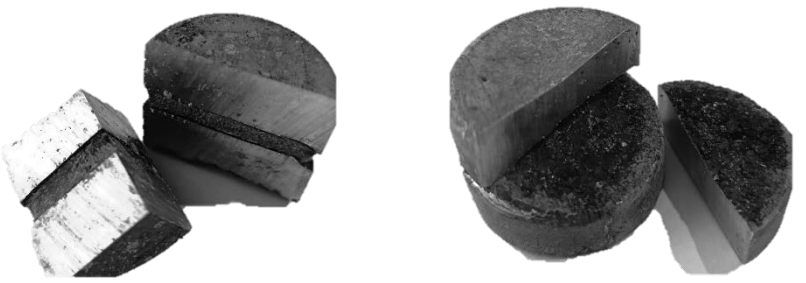

Fig. 5. Samples subjected to pressureless infiltration: (a) ceramic fibers, (b) glass foam.

Significantly better results were obtained after applying a pressure of 3 MPa, which enabled effective infiltration of the ceramic mat with liquid AlSi12. Light microscopy imaging characterisation showed that the obtained composites had no detectable porosity and demonstrated good filling of the ceramic preform with the aluminium alloy (Fig. 6). A more detailed analysis revealed microfiltration within the ceramic matrix, which ensures a strong connection between the ceramic and metallic phases and provides good mechanical properties. The examinations confirmed the uniform distribution of sintered ceramic fibres, the percolative nature of the microstructure, and the absence of unfilled pores and reinforcement agglomeration. The ceramic grains retained their shape, which indicates a proper infiltration pressure. The grains were also closely connected to the metallic matrix, which contributed to achieving appropriate mechanical properties and indicated a sufficient temperature during the infiltration process.

a) b)

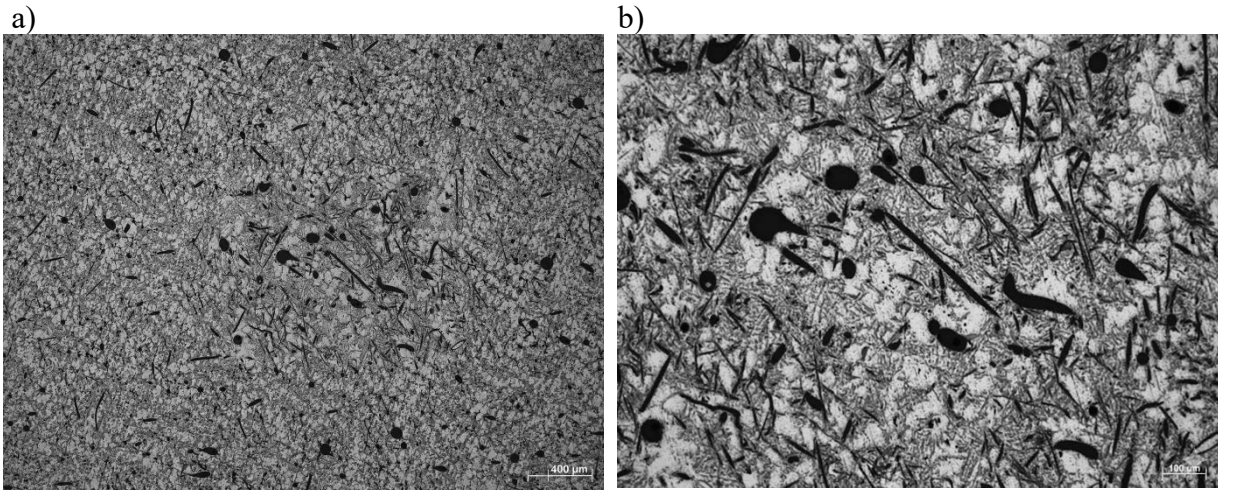

Fig. 6. Microstructure of infiltrated AlSi12 aluminium alloy matrix composites reinforced with ceramic fibres.

4. CONCLUSIONS

The conducted study confirmed that gas-pressure infiltration is an effective method for manufacturing aluminium matrix composites reinforced with porous ceramic preforms. The results demonstrated that pressureless infiltration was insufficient to achieve effective

penetration of molten aluminium into the porous structures and, in the case of foamed glass, resulted in material degradation and loss of structural integrity. The application of a gas pressure of 3 MPa enabled the successful infiltration of the ceramic fibre preform with the AlSi12 alloy, resulting in composites characterised by good filling of the porous structure and the absence of significant porosity. Microstructural observations confirmed the formation of a well-connected metallic–ceramic interface and a uniform distribution of reinforcing phases within the matrix. The SEM and EDS analyses showed that both ceramic fibres and foamed glass exhibited highly porous, heterogeneous morphologies, which strongly influenced infiltration behaviour and the final microstructure of the composites. The ceramic fibre preform demonstrated significantly greater structural stability during infiltration than foamed glass. The results indicate that the selection of reinforcement type, pore morphology, and infiltration parameters is crucial for determining the quality and structural integrity of the produced metal matrix composites. The study also confirmed the potential of pressure-assisted infiltration techniques for the fabrication of lightweight composite materials intended for advanced engineering applications.

ACKNOWLEDGMENTS

This publication was supported under the „Excellence Initiative – Research University" program at the Silesian University of Technology, within the framework of the 14th Project Based Learning (PBL) funding competition, entitled: „Layered aluminium alloy composites reinforced with waste mineral materials".

BIBLIOGRAPHY

1. P.D. Srivyas, M.S. Charoo, Aluminum metal matrix composites a review of reinforcement; mechanical and tribological behavior, International Journal of Engineering & Technology, vol. 7 (2.4), (2018) 117–122.
2. M. Balkundhi, S.S. Baloor, G. Bolar, Effect of temperature and stacking sequence on the impact behavior of CARALL fiber metal laminates, Materials Research Express, vol. 12 (10), (2025).
3. M. Ostapiuk, B. Surowska, Charakterystyka mikrostrukturalna wybranych laminatów metalowo-włóknistych, Przetwórstwo Tworzyw, vol. 18 (3), (2012) 262–265. (in polish)
4. J. Bieniaś, P. Jakubczak, B. Surowska, Odporność laminatów aluminium/kompozyt epoksydowo-szklany na uderzenia o małej prędkości, Composites Theory and Practice, nr (6), t. 33, (2012) 651-654 (in Polish).
5. B. Dahshan, A.M. El-Habbak, M. Adly, M. Shazly, Experimental and numerical study on the tensile, three-point-bending, and interlaminar fracture toughness of GLARE, Journal of Mechanical Science and Technology, vol. 34 (8), (2020) 3273–3282.
6. W. He, L. Wang, H. Liu, C. Wang, L. Yao, Q. Li, G. Sun, On impact behavior of fiber metal laminate (FML) structures: A state-of-the-art review, Thin-Walled Structures 167 (2021) 108026.
7. S.S. Nordin, E.E. Mhd Noor, P. Chockalingam, Chemical and Thermal Analysis of Fly Ash-Reinforced Aluminum Matrix Composites (AMCs), Journal of Composites Science, vol. 8 (5), (2024) 170.

8. M.Y. Jiang, X.Y. Meng, J. Zhou, Z.Y. Wei, H.F. Zhang, P. Shen, Design and manufacture of near-net-shape metal-ceramic composites with gradient-layered structure and optimized damage tolerance, Additive Manufacturing 84 (2024) 104112.
9. M. Fejdyś, M. Landwijt, M. Struszczyk, Hybride Composite Armour Systems with Advanced Ceramics and Ultra-High Molecular Weight Polyethylene Fibres, Fibres & Textiles in Eastern Europe, vol. 24, nr 3 (117), (2016) 79–85.
10. M. Szudrowicz, Layered composite increasing the resistance of patrol and intervention vehicles to the impact of improvised explosive devices (IED) from below, Eksploatacja i Niezawodność – Maintenance and Reliability, 20/1 (2018) 9-15.
11. R. Studziński, W. Sumelka, M. Malendowski, T. Gajewski, H. Al-Rifaie, P. Sielicki, Sandwich panel subjected to blast wave impact and accelerated fragments, Eksploatacja i Niezawodność – Maintenance and Reliability, 26/2 (2024) 183698.
12. H. He, J. Xu, B. Su, X. Wang, Y. Su, X. Zheng, Y. Li, Z. Li, Improved mechanical performance of fiber metal laminates: Effects of interlaminar reinforcement process and lay-up structure optimization, Thin-Walled Structures 226 (2026) 114906.
13. B. Yang, W. Zhao, X. Guo, Y. Lu, H. Xiao, J. Du, Microstructure evolution, elemental diffusion behavior, and bonding strength of TA1/AZ31B laminated composite fabricated by hot pressing, Journal of Materials Research and Technology 33 (2024) 6045-6057.
14. E. Liu, H. Li, Z. Li, J. Li, H. Hao, M. Su, Mechanical properties of Al based-aluminum foam/resin interpenetrating porous composites with different interface types, Composite Structures 380 (2026) 120030.
15. A. Jain, Utilisation of fly ash as a potential reinforcement material for better mechanical properties of Aluminum, International Journal of Advanced Production and Industrial Engineering 5 (3), (2020) 23–27.
16. L.A. Dobrzański, M. Kremzer, A.J. Nowak, A. Nagel, Composite materials based on porous ceramic preform infiltrated by aluminium alloy, Journal of Achievements in Materials and Manufacturing Engineering 20/1-2 (2007) 95-98.
17. B. Tomiczek, M. Kujawa, G. Matula, M. Kremzer, T. Tanski, L. A. Dobrzański, Aluminium AlSi12 alloy matrix composites reinforced by mullite porous preforms, Materialwissenschaft und Werkstofftechnik 46 (2015) 4–5.
18. K. Matus, G. Matula, M. Pawlyta, J. Krzysteczko-Witek, B. Tomiczek, TEM Study of the Microstructure of an Alumina/Al Composite Prepared by Gas-Pressure Infiltration, Materials 15 (2022) 6112.
19. Y. Ma, J. Wang, Y. Zhao, X. Wei, L. Ju, Y. Chen, A New Vacuum Pressure Infiltration CFRP Method and Preparation Experimental Study of Composite, Polymers 12 (2020) 419.
20. Y. Jiang, P. Xu, C. Zhang, F. Jin, Y. Li, X. Cao, L. Yu, Simulation and Experimental of Infiltration and Solidification Process for $Al_2O_{3(3D)}$/5083Al Interpenetrating Phase Composite for High Speed Train Prepared by Low-Pressure Infiltration, Materials 16 (2023) 6634.
21. N. Kota, M.S. Charan, T. Laha, S. Roy, Review on development of metal/ceramic interpenetrating phase composites and critical analysis of their properties. Ceramics. International 48 (2022) 1451–1483.
22. R. Etemadi, B. Wang, K.M. Pillai, B. Niroumand, E. Omrani, P. Rohatgi, Pressure infiltration processes to synthesize metal matrix composites—A review of metal matrix composites, the technology and process simulation. Materials and Manufacturing Processing 33 (2018) 1261–1290.

TalentDetector
7th-9th June 2026
Gliwice-Brenna, Poland
DEPARTMENT OF ENGINEERING MATERIALS AND BIOMATERIALS
FACULTY OF MECHANICAL ENGINEERING
SILESIAN UNIVERSITY OF TECHNOLOGY
INTERNATIONAL STUDENTS SCIENTIFIC CONFERENCE

Powłoki konwersyjne chromianowe

Nadia Nocoń[a], Wiktoria Ledwig[a], Jakub Nowak[a], Tobiasz Wypchol[a], Bartosz Gonciarz[b], Amelia Krupińska[c], Agnieszka Zaleska[d] Mariusz Krupiński[e].

[a] Politechnika Śląska wydział Mechaniczny Technologiczny, Mechanika i Budowa Maszyn
[b] Politechnika Śląska, wydział Mechaniczny Technologiczny, Inżynieria Produkcji i Zarządzanie
[c] Zespół Szkół Chemiczno-Medycznych i Ogólnokształcących w Tarnowskich Górach
[d] I Liceum Ogólnokształcące im. Stefanii Sempołowskiej w Tarnowskich Górach
[e] Politechnika Śląska, Wydział Mechaniczny Technologiczny, Katedra Materiałów Inżynierskich i Biomedycznych, 44-100 Gliwice, ul. Konarskiego 18a
email: mariusz.krupinski@polsl.pl

Streszczenie: W artykule przedstawiono charakterystykę powłok konwersyjnych chromianowych stosowanych na elementach wykonanych ze stopów aluminium. Omówiono rodzaje powłok, ze szczególnym uwzględnieniem powłok zawierających chrom sześciowartościowy [Cr(VI)] oraz trójwartościowy [Cr(III)], wskazując na ich właściwości, zalety i ograniczenia. Przedstawiono również metody nakładania powłok, takie jak metody zanurzeniowa i natryskowa, oraz ich wpływ na jakość uzyskiwanej warstwy ochronnej. W pracy opisano także właściwości uzyskanych powłok, w tym ich strukturę, odporność korozyjną oraz zdolność do poprawy przyczepności powłok lakierniczych. Dodatkowo zaprezentowano wybrane metody badawcze i techniki analityczne stosowane do oceny jakości i składu powłok.

Abstract: The article presents the characteristics of chromate conversion coatings applied to aluminium alloy components. Different types of coatings are compare, with particular attention on coatings containing hexavalent chromium [Cr(VI)] and trivalent chromium [Cr(III)], highlighting their properties, advantages, and limitations. Methods of coating application, such as immersion and spraying, are also described, along with their impact on the quality of the resulting protective layer. The article also describes the properties of coatings, including their structure, corrosion resistance, and ability to improve the adhesion of painting coatings. Additionally, selected research methods and analytical techniques used for the evaluation of coating quality and composition are presented.

Słowa kluczowe: Chromianowanie aluminium, ochrona antykorozyjna, przyczepność powłok

1. WPROWADZENIE

Chromianowe powłoki konwersyjne stanowią wysoce skuteczną metodę wstępnej obróbki stopów aluminium przeznaczonych do pracy w środowiskach korozyjnych. Powłoki te łączą doskonałe właściwości jako podłoże pod farby, prostotę aplikacji oraz długotrwałą odporność korozyjną [1].

2. 1. Rodzaje powłok konwersyjnych chromianowych oraz metody ich nakładania

Chromianowanie, jako proces konwersyjny, prowadzi do wytworzenia cienkiej warstwy ochronnej bezpośrednio związanej z podłożem metalicznym. W zależności od zastosowanej technologii oraz składu chemicznego kąpieli możliwe jest uzyskanie powłok o zróżnicowanych właściwościach, spełniających wymagania różnych gałęzi przemysłu. Najbardziej klasycznym i przez wiele lat stosowanym typem są powłoki chromianowe zawierające chrom w stopniu utlenienia sześciowartościowego, określane jako powłoki Cr(VI). Charakteryzują się one bardzo wysoką odpornością na korozję, wynikającą z obecności związków chromu zdolnych do tzw. samoregeneracji. W przypadku uszkodzenia powłoki jony chromianowe mogą migrować i ponownie pasywować odsłoniętą powierzchnię metalu. Ich istotną zaletą jest także dobra przewodność elektryczna oraz bardzo dobra przyczepność dla kolejnych warstw, takich jak farby czy lakiery. Wadą pozostaje jednak wysoka toksyczność chromu(VI) oraz jego właściwości rakotwórcze. W odpowiedzi na wymagania środowiskowe opracowano powłoki chromianowe oparte na chromie trójwartościowym, czyli Cr(III). Stanowią one bardziej przyjazną dla środowiska alternatywę. Ich właściwości ochronne są nieco słabsze niż w przypadku powłok Cr(VI), przede wszystkim ze względu na brak efektu samonaprawy. Ważnym aspektem jest również fakt, iż owe powłoki są znacznie cieńsze niż te wykonane z chromu sześciowartościowego [2, 3].
Metodyka nakładania powłok konwersyjnych chromianowych stanowią istotny element całego procesu technologicznego, ponieważ w dużym stopniu determinuje jednorodność, grubość oraz właściwości ochronne uzyskanej warstwy. Najbardziej rozpowszechnioną metodą jest nakładanie powłok poprzez zanurzenie w kąpieli roztworowej. Proces polega na całkowitym umieszczeniu elementu w roztworze zawierającym odpowiednie związki chromu. W wyniku reakcji chemicznej pomiędzy powierzchnią metalu, a składnikami kąpieli dochodzi do wytworzenia cienkiej warstwy konwersyjnej. Metoda ta zapewnia bardzo dobre pokrycie nawet skomplikowanych geometrycznie detali, w tym powierzchni trudno dostępnych. Alternatywą dla zanurzania jest metoda natryskowa, polegająca na nanoszeniu roztworu chromianowego na powierzchnię elementu w postaci rozpylonej cieczy. Proces ten umożliwia ograniczenie zużycia chemikaliów oraz skrócenie czasu obróbki. Metoda ta jednak stawia większe wymagania kontrolne parametrów, tj. równomierność rozpylania [3].

Proces zachodzi wedle określonych reakcji chemicznych:
Etap 1: Częściowe rozpuszczenie się metalu
$2Al \rightarrow 2Al^{3+} + 6e^{-}$
Uwalnianie elektronów powoduje redukcję jonów chromianowych.
Etap 2: Reakcja redukcji do chromu(III)
$Cr_2O_7^{2-} + 8H^{+} + 6e^{-} \rightarrow 2Cr(OH)_3 + H_2O$
Reakcja tworzy ochronną warstwę Cr_2O_3 lub $Cr(OH)_3$. [2]

Rysunek 1 oraz rysunek 2 przedstawiają budowę warstwy po wykonaniu procesu chromianowania zielonego [Cr(III)] oraz żółtego [Cr(VI)].

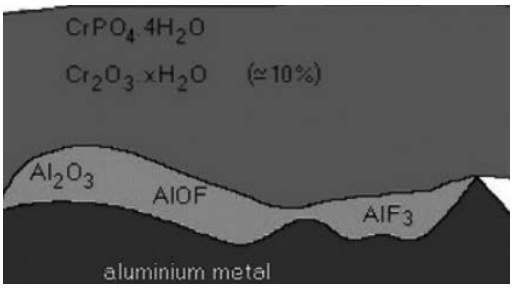

Rysunek 1 – budowa warstwy po wykonaniu procesu chromianowania Cr(III) [7]

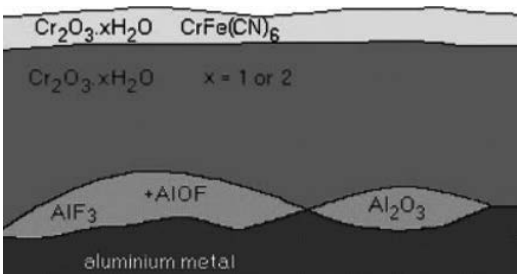

Rysunek 2 – budowa warstwy po wykonaniu procesu chromianowania Cr(VI) [7]

2. 2. Właściwości powłoki konwersyjnej chromianowej.

Kluczowym powodem stosowania chromianowych powłok jest ochrona antykorozyjna. Korozja zachodzi wskutek kontaktu powierzchni metalu z wilgocią, środkami chemicznymi lub innymi czynnikami środowiska zewnętrznego. W przypadku aluminium samoczynnie tworzy się cienka warstwa Al_2O_3 [3]. Podczas chromianowania tworzy się dodatkowa warstwa ochronna, która ma na celu odizolowanie metalu od otaczającego środowiska. Ponadto zmniejsza ona szybkość zachodzących reakcji anodowych i katodowych, a także hamuje rozwój korozji wżerowej. Powłoka chromianowa ma strukturę mikroporowatą i pewnym stopniu nieregularną.
Tworzy zatem trwałą warstwę, do której klej lub powłoka lakiernicza wiąże się skuteczniej. Przede wszystkim oznacza to mniejsze ryzyko odpadania lakieru lub farby, a także odspajania się nałożonego kleju.[2, 3, 5]

2. 3. Metodyka badawcza i techniki analityczne

W celu zbadania mechanizmów formowania się warstw konwersyjnych i określenia roli pierwiastków stopowych, stosuje się zaawansowane techniki inżynierii materiałowej, pozwalające na analizę w skali nanometrycznej:
- Mikroskopia skaningowa (m.in. AFM, SEM). Metoda badawcza umożliwiająca ocenę parametrów materiału. Mikroskopia elektronowa umożliwia np. przeprowadzenie analizy składu chemicznego oraz grubości powłoki. Z użyciem mikroskopu sił atomowych można zbadać w trybie bezkontaktowym topografię powłoki.
- Testy korozyjne w obojętnej mgle solnej. Polegają na ekspozycji elementów w komorach nasyconych rozpylonym chlorkiem sodu. Proces ten symuluje przyspieszoną degradację

materiału w agresywnym środowisku, dostarczając danych o ogólnej skuteczności barierowej powłoki w warunkach zbliżonych do rzeczywistej eksploatacji.
- Techniki spektroskopowe (RBS i XPS). Spektroskopia wstecznego rozpraszania Rutherforda oraz spektroskopia fotoelektronów rentgenowskich są aplikowane do precyzyjnej analizy chemicznej. Pozwalają na wyznaczenie ilościowych stosunków atomowych pomiędzy składnikami powłoki a utlenionymi atomami podłoża oraz ocenę rozkładu poszczególnych domieszek.
- Napylanie magnetronowe i markery nanocząsteczkowe: Próbki syntezuje się w warunkach wysokiej próżni w celu uzyskania metastabilnych roztworów stałych, pozbawionych segregacji faz wtórnych. Dodatkowo w strukturze umieszcza się chemicznie obojętne nanocząstki złota, które pełnią funkcję markerów lokalizacyjnych. Pozwala to na jednoznaczną identyfikację pierwotnej granicy faz metal–powłoka i śledzenie kierunku jej wzrostu [3, 4].

2. 4. Przykłady zastosowania powłok konwersyjnych chromianowych.

Chromianowanie znajduje zastosowanie w wielu gałęziach ówczesnego przemysłu. Niektórymi z nich są:
- Przemysł lotniczy, w którym stosuje się elementy konstrukcji aluminiowych, poszycia, a także przygotowanie części pod powłoki lakiernicze.
- Motoryzacja, gdzie często wykorzystuje się części aluminiowe, śruby lub wsporniki.
- Budownictwo, ze względu na wykorzystanie profili aluminiowych i elementów konstrukcyjnych.
- Wojskowość i przemysł morski: materiały muszą wytrzymać agresywne warunki w środowisku o wysokim zasoleniu oraz narażenie na wilgoć.

Chromianowanie w lotnictwie odgrywa ważną rolę ze względu na fakt, iż samoloty pracują w ciężkich warunkach atmosferycznych. Aluminiowe elementy samolotu są narażone na duże wilgotności, częste zmiany temperatury lub np. mgłę solną, która często pojawia się na lotniskach nadmorskich. Ochrona antykorozyjna jest tu zatem kluczowa. Warto również zauważyć, że chromianowanie poprawia przyczepność powłok lakierniczych [1], które bez wspomnianego przygotowania mogłyby się łuszczyć, co pogarszałoby efektowność wizualną maszyn [2, 3, 5].

3. PODSUMOWANIE

Powłoki konwersyjne chromianowe stanowią efektywną i szeroko stosowaną metodę ochrony stopów aluminium przed korozją, znajdującą zastosowanie w wielu gałęziach przemysłu, takich jak lotnictwo, motoryzacja czy budownictwo. Ich skuteczność wynika z tworzenia cienkiej, dobrze przylegającej warstwy ochronnej, która ogranicza dostęp czynników korozyjnych do powierzchni metalu oraz poprawia przyczepność różnych powłok. W pracy wskazano, że zarówno rodzaj zastosowanej powłoki [Cr(VI) lub Cr(III)], jak i metoda jej nanoszenia mają istotny wpływ na właściwości końcowe systemu ochronnego. Zarówno rodzaj zastosowanego procesu technologicznego oraz analiza wyników zastosowanych metod badawczych potwierdza, że kluczowe znaczenie dla jakości powłoki ma odpowiednie przygotowanie powierzchni oraz ścisła kontrola parametrów procesu.

PODZIĘKOWANIA
Praca powstała w wyniku realizacji projektu „Powłoki konwersyjne chromianowe stosowane na elementach ze stopów aluminium" w ramach kształcenia zorientowanego projektowo – PBL, w XIII konkursie Programu Inicjatywa Doskonałości – Uczelnia Badawcza, Wydział Mechaniczny Technologiczny, Politechnika Śląska.

BIBLIOGRAFIA

1. Joseph H Osborne, "Observations on chromate conversion coatings from a sol–gel perspective", Progress in Organic Coatings, 2001
2. J. Zhao, L. Xia, A. Sehgal, D. Lu, R. L. McCreery, and G. S. Frankel, "Effects of chromate and chromate conversion coatings on corrosion of aluminum alloy 2024-T3". Surface and Coatings Technology, 2001
3. E. Gralak, „Technologie chromianowania trójwartościowego stopów odlewniczych aluminium z zastosowaniem związków fluorokompleksowych metali grup przejściowych", Politechnika Wrocławska, Wrocław 2024.
4. Y. Liu,P. Skeldon,G.E. Thompson,H. Habazaki,K. Shimizu, „Chromate conversion coatings on aluminium: influences of alloying", Corrosion Science, 2004
5. Shixiinproto, „Powłoka konwersyjna chromianowa": https://shixinproto.com/pl/chromate-conversion/
6. Chemly, Alufinish partner, „Konwersja chromianowa": https://chemly.pl/konwersja-chromianowa/
7. Lakiernictwo.net, "Trwałe i odporne powłoki": https://www.lakiernictwo.net/dzial/143-artykuly-branzowe/artykuly/trwale-i-odporne-powloki,813/2

TalentDetector
7th-9th June 2026
Gliwice-Brenna, Poland
DEPARTMENT OF ENGINEERING MATERIALS AND BIOMATERIALS
FACULTY OF MECHANICAL ENGINEERING
SILESIAN UNIVERSITY OF TECHNOLOGY
INTERNATIONAL STUDENTS SCIENTIFIC CONFERENCE

Powłoki konwersyjne chromianowe stosowane na elementach ze stopów aluminium

Nadia Nocoń[a], Jakub Nowak[a], Tobiasz Wypchol[a], Wiktoria Ledwig[a], Bartosz Gonciarz[b], Amelia, Krupińska[c], Agnieszka Zaleska[d], Marcin Staszuk[e], Mariusz Krupiński[e]

[a]Politechnika Śląska, Wydział Mechaniczny Technologiczny, Mechanika i Budowa Maszyn
[b] Politechnika Śląska, Wydział Mechaniczny Technologiczny, Inżynieria Produkcji i Zarządzanie
[c]Zespół Szkół Chemiczno-Medycznych i Ogólnokształcących w Tarnowskich Górach
[d]I Liceum Ogólnokształcące im. Stefanii Sempołowskiej w Tarnowskich Górach
[e]Politechnika Śląska, Wydział Mechaniczny Technologiczny, Katedra Materiałów Inżynierskich i Biomedycznych, 44-100 Gliwice, ul. Konarskiego 18A
email: mariusz.krupinski@polsl.pl

Streszczenie: Celem pracy było zbadanie struktury i własności powłok konwersyjnych chromianowych na elementach ze stopów aluminium. Na elementy ze stopu AlSi6Cu4 w stanie odlanym oraz przesyconym, nałożono powłokę chromianową trójwartościową. Twardość próbek zmierzono metodą Vickersa korzystając z twardościomierza FUTURE-TECH FM-ARS 9000. Korzystając z trybometru firmy CSM Instruments metodą Pin-On-Disk zmierzono odporność na ścieranie powłok. Zmierzono z użyciem mikroskopu SEM grubość powłok, skład chemiczny w mikroobszarach wykonano metodą EDS. Wykonane badania wskazują, że na własności powłok konwersyjnych na stopach aluminium, mają wpływ zarówno przygotowanie powierzchni jak i stan obróbki stopu (stan odlany, obrobiony cieplnie).

Abstract: The aim of this study was to investigate the structure and properties of chromate conversion coatings on aluminum alloy components. For the tests, a trivalent chromate conversion coating, was applied to AlSi6Cu4 alloy samples in both the as-cast and solution-treated conditions. The hardness of the samples was measured using the Vickers method with a FUTURE-TECH FM-ARS 9000 hardness tester. The wear resistance of the coatings was evaluated using the Pin-on-Disk method with a tribometer manufactured by CSM Instruments. The coating thickness was measured using a SEM microscope. The chemical composition of the coating was determined by the EDS method. The tests performed indicate that the properties of conversion coatings on aluminum alloys are influenced by both the surface preparation and the alloy processing condition (as cast, heat-treated).

Słowa kluczowe: stopy aluminium, konwersyjne powłoki chromianowe, struktura i własności

1. WPROWADZENIE

Aluminium jest termodynamicznie aktywnym metalem nieszlachetnym, który wykazuje dużą odporność na korozję przy niskim potencjale normalnym wynoszącym 1,67 V wzgl. nasyconej elektrody wodorowej. W środowisku zawierającym tlen zawarty w powietrzu lub rozpuszczony w wodzie na powierzchni metalicznego aluminium tworzy się jednak warstwa tlenków i metal ten przechodzi w stan pasywny. Warstwa pasywna wytworzonego tlenku jest odporna na korozję atmosferyczną (w normalnych warunkach lądowych i przy umiarkowanym zanieczyszczeniu siarką). W przypadku stosowania aluminium w warunkach sprzyjających korozji konieczne jest jednak jego zabezpieczenie. Jednym z sposobów jego zabezpieczania jest chromianowanie. Chromianowanie aluminium jest procesem polegającym na nałożeniu powłoki chromianowej na aluminium lub jego stop. Powłoka ta jest zazwyczaj stosowana jako podkład pod powłoki lakiernicze, gdyż poza zapewnieniem odporności korozyjnej zwiększa ona także adhezyjność tych powłok. Powłoka ta pozwala również na zachowanie przewodności elektrycznej, co jest kluczowe dla niektórych zastosowań. Chromianowanie jest procesem powszechnie stosowanym w przemyśle motoryzacyjnym, lotniczym oraz kosmonautyce. Aktualnie najczęściej do tego procesu wykorzystuje się chromianowanie chromem trójwartościowym. Zastąpił on chromianowanie chromem sześciowartościowym, posiadającym wyższą odporność korozyjną oraz zdolność do samo regeneracji kosztem wysokiej toksyczności w trakcie wytwarzania [1,2,3].

2. MATERIAŁ I METODYKA BADAŃ

Powłoka konwersyjna chromianowa została naniesiona na stopie aluminium AlSi6Cu4 w stanie odlanym i obrobionym cieplnie. Proces chromianowania realizowany był na linii galwanicznej składającej się z kolejnych etapów:
Przygotowanie powierzchni (odtłuszczanie). Etap polegający na eliminacji zanieczyszczeń powierzchniowych. Ewentualne depozyty mogą powodować nierównomierne tworzenie powłoki oraz gorszą jej przyczepność.
Płukanie pierwsze. Dwukrotne płukanie w wodzie demineralizowanej wykonywane w celu usunięcia chemicznych składników używanych w pierwszym etapie.
Trawienie. Proces służący do oczyszczenia warstwy wierzchniej m. in. z tlenków a także pozostałych zanieczyszczeń. Wykonywany w mieszaninie kwasów: kwas fluorowodorowy 1,5% oraz kwas siarkowy 1,5%.
Płukanie drugie. Ponowne dwukrotne płukanie w wodzie demineralizowanej.
Pasywacja (kąpiel chromianowa). Elementy zanurza się w roztworze zawierającym jony Cr(III). W trakcie procesu cienka warstwa aluminium częściowo się rozpuszcza, a w jej miejsce powstaje powłoka konwersyjna. Generowanie powłoki wiąże się ze stałą degradacją materiału bazowego i wymaga ścisłego monitorowania parametrów m.in. tj. temperatura, czas.
Płukanie w wodzie demineralizowanej. Wykonywane w celu zatrzymania procesów chemicznych poprzez usunięcie nadmiaru odczynników, co zapewnia wykształcenie powłoki o równomiernej grubości i adekwatnej optyce.
Suszenie w 60°C. Operacja realizowana w wymuszonym obiegu ciepłego powietrza, powodująca zamknięcie mikro porów i utrwalenie powłoki.
Skaningowa mikroskopia elektronowa została zastosowana do pomiaru grubości powłoki oraz analizy jej składu chemicznego. Do obserwacji wykorzystano technikę elektronów wtórnych

(SE) oraz spektroskopię rentgenowską z dyspersją energii (EDS). Grubość powłoki została zmierzona bezpośrednio w jej przełomie. Badania wykonano na wysokorozdzielczym skaningowym mikroskopie elektronowym SUPRA 35 firmy ZEISS z przystawką do analizy EDS. Badanie za pomocą mikroskopu AFM zostało wykonane w trybie bezkontaktowym (NC-AFM). Skan wykonano na powierzchni kwadratu o boku 20 mikrometrów. Do badań zastosowano mikroskop sond skanujących: XE-100 firmy Park Systems.
Do zbadania twardości powłoki na stopie AlSi6Cu4 został zastosowany twardościomierz Vickersa FUTURE-TECH FM-ARS 9000. Badanie wykonano pod małym obciążeniem 300 gf, co jest porównywalne do ok. 2,94 N, w czasie 10 sekund. Badania tribologiczne wykonano metodą Pin-On-Disk trybometrem firmy CSM Instruments wyposażony w profilometr Tylor-Hubson Sutronic 25. Wyznaczono z pomiarów wartość średnią oraz odchylenia standardowe. Wykonano kilka pomiarów oraz obliczono wartość średnią i odchylenie standardowe.

3. WYNIKI BADAŃ WŁASNYCH

3.1. Badanie za pomocą mikroskopu SEM

W ramach wykonanych badań została określona grubość powłoki konwersyjnej chromianowej na podłożu ze stopu AlSi6Cu4 (rys. 1). Pomiary wykonane na przełomie próbki wykazały, że powłoka ma grubość ok. 980 nanometrów. Tak mała grubość powłoki (poniżej 1 mikrometra) powoduje, że wiązka elektronów w badaniu składu chemicznego metodą EDS przenika przez powłokę, w związku z czym wykrywane są pierwiastki z podłoża.
Obecność dodatków stopowych istotnie wpływa na grubość powłoki ochronnej. W miejscach, gdzie występują przy powierzchni fazy międzymetaliczne (np. β i Al_2Cu), warstwa chromianowa charakteryzuje się mniejszą grubością w porównaniu do obszaru osnowy aluminiowej.

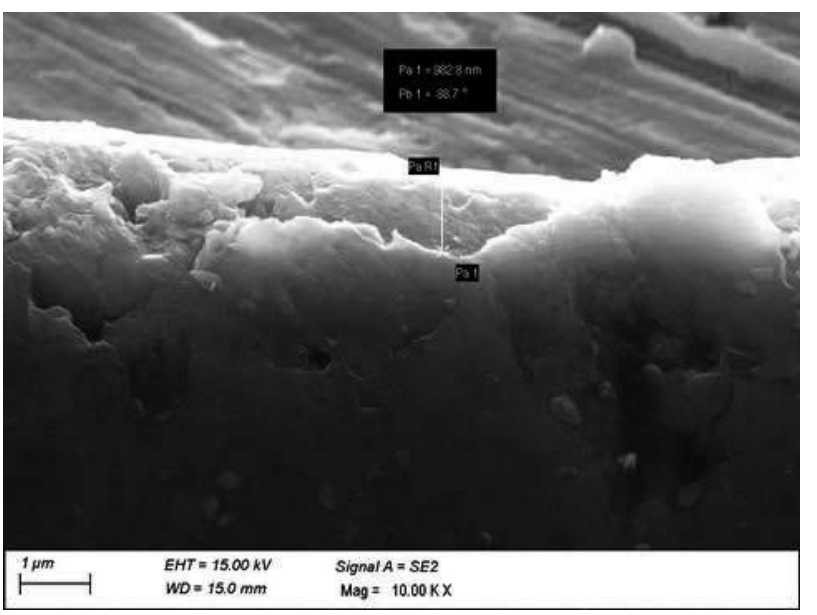

Rysunek 1 - Wynik pomiaru grubości konwersyjnej powłoki chromianowej na stopie AlSi6Cu4

Wyniki pomiaru składu chemicznego powłoki konwersyjnej (rys. 2), uzyskane metodą spektroskopii rentgenowskiej z dyspersją energii (EDS), pozwalają na identyfikację pierwiastków tworzących powłokę ochronną oraz będących w składzie stopu aluminium. W tabeli 1. zestawiono punkty pomiaru EDS oraz stężenie masowe pierwiastków.

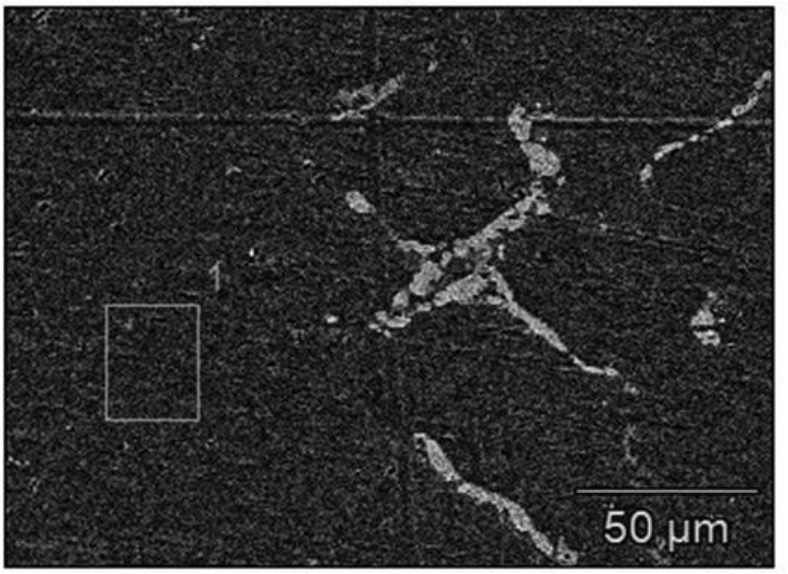

Rysunek 2 – Zaznaczone miejsca wykonania pomiaru EDS dla stopu AlSi6Cu4

Tabela 1. Miejsce analizy pomiaru EDS dla stopu AlSi6Cu4 oraz stężenie masowe pierwiastków.
Table 1. EDS analysis locations for the AlSi6Cu4 alloy and the weight concentrations of elements.

Miejsce analizy na rys. 2	Stężenie masowe pierwiastków, %					
	Al	Si	C	Cu	Cr	O
#1	74.28	20.82	2.59	2.14	0.17	-
#2	61.88	33.35	1.97	1.77	-	1.03

3.2. Badanie za pomocą mikroskopu AFM

Mikroskopia sił atomowych pozwoliła na trójwymiarowe zobrazowanie topografii powierzchni powłoki w skali nanometrycznej na podłożu ze stopu AlSi6Cu4 (rys. 3). Zarejestrowany zakres wysokości nierówności na badanej powierzchni znajduje się między 0 do około 700 nanometrów. Na wykonanym obrazie topograficznym powierzchni widoczne są podłużne pasma o preferowanym kierunku. Specyficzna struktura powierzchni jest wynikiem wpływu podłoża - cienka powłoka chromianowa nie posiada zdolności wyrównywania materiału. Oznacza to, że powłoka konwersyjna odwzorowuje nierówności podłoża powstałe przed procesem chromianowania. Histogram rozkładu wysokości potwierdza zróżnicowanie topografii powierzchni powłoki (rys. 3).

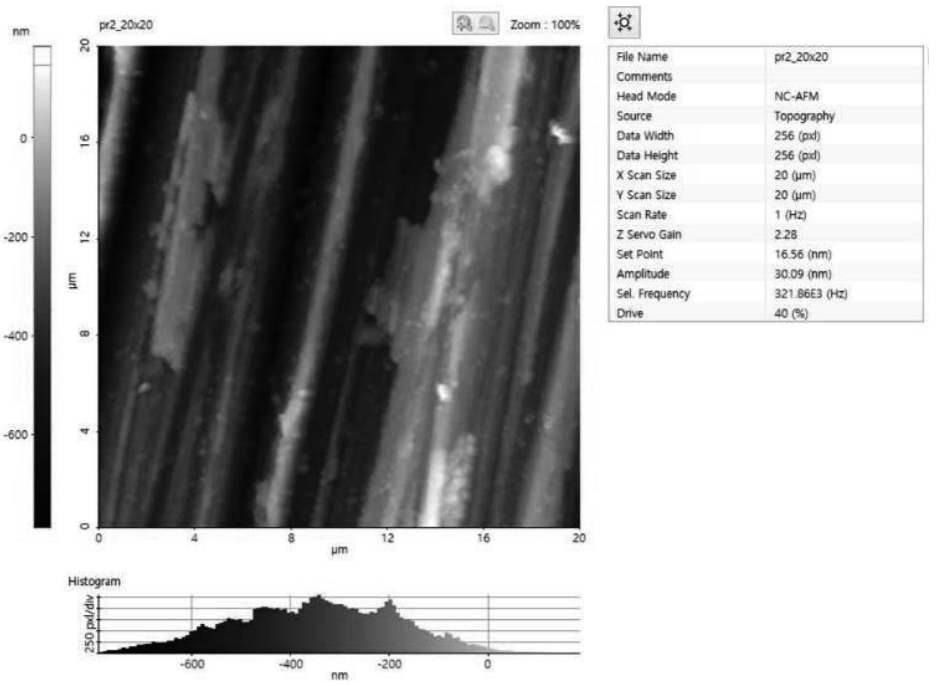

Rysunek 3 - Analiza topografii powłoki dla stopu AlSi6Cu4

3.3. Badanie twardości przy małej sile obciążenia

Wyniki pomiarów spowodowane są głównie twardością samego podłoża, gdyż nałożona powłoka nie jest wystarczająco gruba by mieć znaczący wpływ na wynik pomiaru. Wykonane badania twardości przy małym obciążeniu pokazano w tabeli 2. Przykładowy odcisk po badaniu pokazano na rysunku 4.

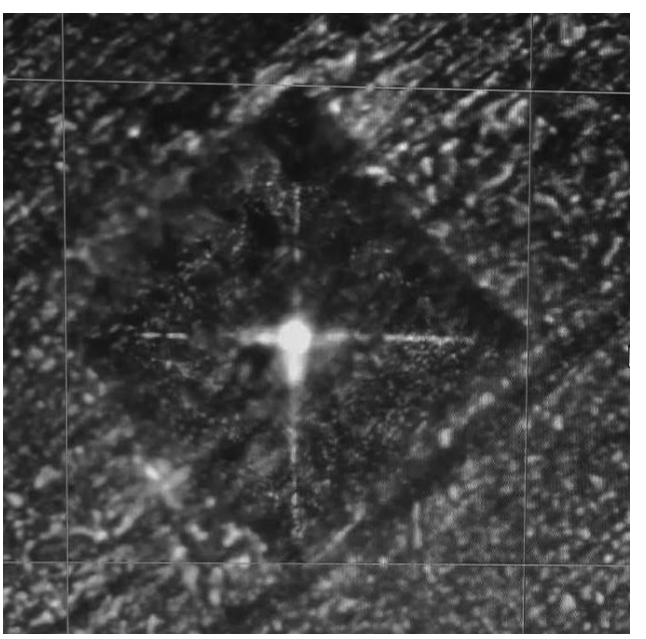

Rys.4. Przykładowy odcisk pomiaru twardości metodą Vickersa stopu aluminium w stanie przesyconym

Tabela 2. Wartość średnia oraz odchylenie standardowe pomiaru twardości AlSi6Cu4 (stan odlany i obrobiony cieplnie)
Table 2. Mean value and standard deviation of the hardness measurement of AlSi6Cu4 (as-cast and heat-treated).

	Wartość średnia pomiarów, $HV_{0,3}$	Odchylenie standardowe, $HV_{0,3}$
AlSi6Cu4 stan odlany	84,07	4,60
AlSi6Cu4 stan obrobiony cieplnie	122,43	10,18

Wyniki pomiarów twardości przy małej sile obciążenia wskazują, że stop który został przesycony w temperaturze 480°C wykazuje wzrost twardości w wyniku samorzutnego starzenia.

3.4. Badanie odporności na ścieranie powłok

Jednym z najważniejszych właściwości mechanicznych powłok jest ich odporność na ścieranie. Średnie wyniki pól przekroju śladów zużycia oraz odchylenie standardowe przedstawiono w tabeli 3. Przykładowy przekrój pomiaru pokazano na rysunku 5.

Tabela 3. Wartość średnia oraz odchylenie standardowe pomiarów pól przekrojów śladów zużycia stopu AlSi6Cu4 (stan odlany i obrobiony cieplnie) wykonanych z użyciem metody Pin-On-Disk.
Table 3. Mean value and standard deviation of the cross-sectional area measurements of wear tracks in the AlSi6Cu4 alloy (as-cast and heat-treated) obtained using the Pin-on-Disk method.

	Wartość średnia pól przekroju śladów zużycia, μm^2	Odchylenie standardowe, μm^2
AlSi6Cu4 stan odlany	50697,5	2144,13
AlSi6Cu4 stan obrobiony cieplnie	79595,2	4707,78

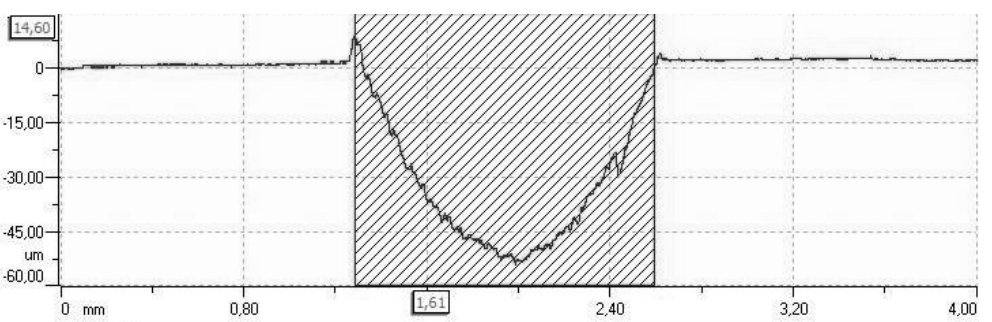

Rys.5 Przykładowe pole przekroju śladu zużycia wykonane metodą Pin-On-Disc dla stopu AlSi6Cu4 (stan odlany)

4. PODSUMOWANIE

W wyniku badań została określona struktura badanego materiału oraz jego własności. Badania strukturalne pozwoliły określić grubość powłoki oraz jej topografię, a także pozwoliły na analizę składu chemicznego podłoża. Analiza wyników skaningowej mikroskopii elektronowej

wykazała, że grubość powłoki konwersyjnej chromianowej wynosi ok. 980 nanometrów. Badania za pomocą mikroskopu sił atomowych pozwoliły na zobrazowanie topografii powierzchni powłoki, która okazała się odwzorowywać nierówności podłoża powstałe przed nałożeniem powłoki. Podłużne pasma o preferowanym kierunku są charakterystyczne dla mechanicznego przygotowania powierzchni. W związku z bardzo cienką warstwą powłoki chromianowej, zostały wykryte pierwiastki podłoża. Warstwa chromianowa jest cieńsza w miejscach występowania faz międzymetalicznych. Przesycanie powoduje zmianę morfologii faz międzymetalicznych bądź ich rozpuszczenie w roztworze, co może mieć wpływ na jakość uzyskanej powłoki.

PODZIĘKOWANIA

Praca powstała w wyniku realizacji projektu „Powłoki konwersyjne chromianowe stosowane na elementach ze stopów aluminium" w ramach kształcenia zorientowanego projektowo –PBL, w XIII konkursie Programu Inicjatywa Doskonałości – Uczelnia Badawcza, Wydział Mechaniczny Technologiczny, Politechnika Śląska.
Podziękowania dla Elektrocarbon-Galwan Spółka z o.o. w Tarnowskich Górach za pomoc w realizacji projektu badawczego.

BIBLIOGRAFIA

1. E. Gralak, Technologie chromianowania trójwartościowego stopów odlewniczych aluminium z zastosowaniem związków fluorokompleksowych metali grup przejściowych, Rozprawa doktorska, 2024.
2. https://metale.pl/wiedza/aluminium/korozja
3. Y. Liu, P. Skeldon, G.E. Thompson, H. Habazaki, K. Shimizu, „Chromate conversion coatings on aluminium: influences of alloying" Corrosion Science 46/2 (2004), pp. 297-312.

TalentDetector

7th-9th June 2026
Gliwice-Brenna, Poland

DEPARTMENT OF ENGINEERING MATERIALS AND BIOMATERIALS
FACULTY OF MECHANICAL ENGINEERING
SILESIAN UNIVERSITY OF TECHNOLOGY

INTERNATIONAL STUDENTS SCIENTIFIC CONFERENCE

Modernization of the sheet metal cutting process

Piotr Nogły [a], Aneta Kania[b], Magdalena Polok-Rubiniec[b], Anna Włodarczyk-Fligier[b]

[a] Silesian University of Technology, Faculty of Mechanical Engineering, Department of Engineering Materials and Biomaterials
email: pn308680@student.polsl.pl
[b] Silesian University of Technology, Faculty of Mechanical Engineering, Department of Engineering Materials and Biomaterials
email: aneta.kania@polsl.pl

Abstract: The article presents an analysis of the effectiveness of modernizing the sheet metal laser cutting process at a company producing heating boilers. The modernization involved replacing the CO_2 laser with a modern fiber optic laser. Actual production data including the technological process, operation times, edge quality, and workflow organization was analyzed.

Keywords: sheet metal cutting proces, laser cutting, fiber laser, process optimization.

1. INTRODUCTION

Modern manufacturing companies operate in a dynamic market environment, with growing competition and increasing quality and cost requirements. In such a climate, the efficiency of manufacturing processes is crucial, determining a company's competitiveness.

In the heating boiler industry, one of the fundamental technological stages is the cutting of steel sheets. The quality and accuracy of the resulting components directly influence subsequent technological operations, such as bending, welding, and assembly of structural components. Simultaneously, the efficiency of the cutting process determines the pace of order fulfillment and the company's production capacity.

The development of laser technology has led to significant advances in the efficiency and energy efficiency of cutting processes. Older technological solutions, such as CO_2 lasers, despite their reliability, are characterized by high energy consumption and limited performance compared to modern fiber lasers. Therefore, many companies are choosing to modernize their machinery by implementing fiber laser technology.

2. LASER CUTTING TECHNOLOGY IN PRODUCTION PROCESSES

Laser cutting represents a contemporary method of material separation that has gained significant importance in the metalworking industry. The process involves the impact

of a concentrated, high-energy laser beam on the material's surface, causing it to melt or vaporize. The removal of molten material from the cutting kerf is facilitated by the application of an assisting gas [1-4].

The most important advantages of laser cutting technology include [1,5]:
- high dimensional accuracy,
- narrow cutting kerf,
- small heat-affected zone,
- high process repeatability,
- possibility of automation and integration with CNC systems.

This technology is particularly useful in the production of components with complex geometry and in short-run and serial production.

3. COMPARISON OF CO_2 AND FIBER LASER TECHNOLOGIES

Two types of laser sources are most commonly used in the sheet metal processing industry: CO_2 lasers and fiber lasers. CO_2 lasers generate radiation with a wavelength of approximately 10.6 μm. The beam is guided by a system of mirrors, which increases the complexity of the optical system. The main advantages of these lasers include [1,2,6]:
- good beam quality,
- ability to cut thick materials.

Disadvantages include:
- low energy efficiency,
- high operating costs,
- complicated maintenance,
- high energy and process gas consumption.

Fiber lasers use a semiconductor radiation source, and the beam is transmitted via optical fiber. The wavelength (~1.06 μm) facilitates efficient energy absorption by steel. Advantages of fiber lasers are [3]:
- high energy efficiency,
- high cutting speeds,
- process stability,
- low operating costs,
- simplified design.

This technology is currently the dominant solution in modern manufacturing enterprises.

4. CHARACTERISTICS OF THE ANALYZED PROCESS

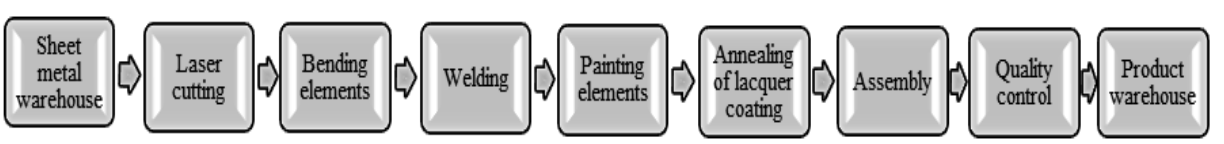

Figure 1. Diagram of the boiler production process

The research was conducted at a company specializing in the production of heating boilers. The production process uses 5-6 mm thick P265GH boiler sheets, which require high-quality edges due to subsequent welding operations (Fig. 1).

Before the modernization, the process was performed using a Mazak Super Turbo X510 MK II CO_2 laser (Fig. 2). In 2019, a Han's Laser G3015-F fiber laser was implemented (Fig. 3).

Figure 2. Mazak Super Turbo X510 MK II laser

Figure 3. Han's Laser G3015-F

Process limitations before modernization

Process analysis revealed significant technological and organizational limitations. The most important included:

- low cutting speed,
- long material penetration time,
- high proportion of interruption time,
- frequent operator intervention,
- deteriorated edge quality requiring rework,
- high energy and gas consumption,
- risk of production bottlenecks.

The cutting process could have limited the efficiency of the entire production system.

4.1. Effects of process modernization

The implementation of the fiber laser has yielded significant technological and organizational benefits. A comparison of cutting times showed an average reduction of approximately 70% in operation time (Tab. 1). The greatest differences were observed for components with complex geometries and a large number of punctures. The increased efficiency results from:

- higher cutting speed,
- shorter puncture time,
- higher energy efficiency,
- greater head movement dynamics.

It was observed that the use of a fiber laser resulted in:

- reduced burr,

– reduced surface roughness (Fig. 4),
– greater repeatability,
– elimination of finishing operations.

Table 1. Comparison of detail cutting times

Detail	Mazak Super Turbo X510 MK II laser, s	Han's Laser G3015-F, s	**Time reduction**
Logo	270	85	**68.5%**
Ash pan frame	60	15	**75%**
Cover	140	40	**71%**
Flue	180	55	**69%**

a) **b)**

Figure 4. Comparison of the cut surface quality of steel elements: a) edge after CO_2 laser cutting – visible scale and larger heat-affected zone, b) edge after fiber laser cutting – smooth surface, high perpendicularity, and minimal slag

The improvement in the quality of the components contributed to a significant improvement in the welding process.

In addition, after implementing the modernization, the following improvements were observed:
– shorter workstation preparation time,
– reduced operator intervention,
– greater process stability (Tab. 2),
– increased machine operating time utilization,
– improved production flow,
– the laser was no longer a bottleneck in the process.

The modernization also reduced operating costs by:
– reducing electricity consumption,
– reducing the consumption of process gases,
– simplifying maintenance,
– increasing operational reliability.

5. THE IMPORTANCE OF MODERNIZATION IN THE CONTEXT OF INDUSTRY 4.0

Process modernization aligns with the principles of Industry 4.0, which assumes increasing the efficiency of production processes through automation, digitization, and the implementation of modern technologies. The use of modern CNC systems, integration with CAD/CAM software, and high process stability enable increased production flexibility and better adaptation to changing market needs.

Table 2. Quality non-conformities in elements after laser cutting

Type of non-conformity	Mazak Super Turbo X510 MK II laser, %	Han's Laser G3015-F, %	**Reduction**
Burr requiring removal	18	3	↓ 83%
Miscut edges	5	1	↓ 80%
Melting zones and roughness	7	2	↓ 71%
Details requiring manual machining	22	4	↓ 82%
Rejected parts	2	<1	↓ ~75%

6. CONLUSIONS

Modernizing the sheet metal cutting process by implementing a fiber laser significantly increased the efficiency of the production process. The most important effects of the modernization include:

- reducing operation time by approximately 70%,
- improving edge quality and eliminating finishing,
- increasing process stability,
- improving production flow,
- reducing operating costs,
- eliminating production bottlenecks.

The obtained results confirm the validity of investing in modern laser technologies and point to directions for further optimization of manufacturing processes.

BIBLIOGRAPHY

1. W.M. Steen, J. Mazumder, Laser Material Processing, Springer, London, 2010.
2. J.C. Ion, Laser Processing of Engineering Materials: Principles, Procedure and Industrial Application, Elsevier Butterworth-Heinemann, Oxford, 2005.
3. A.K. Dubey, V. Yadava, Laser beam machining – A review, International Journal of Machine Tools and Manufacture 48 (2008) 609-628.
4. J. Dutta Majumdar, I. Manna, Laser processing of materials, Sadhana – Academy Proceedings in Engineering Sciences 28 (2003) 495-562.
5. J.F. Ready, Industrial Applications of Lasers, Academic Press, 1997.
6. J. Powell, CO_2 Laser Cutting, Springer-Verlag, London 1993.

TalentDetector

7th-9th June 2026
Gliwice-Brenna, Poland

DEPARTMENT OF ENGINEERING MATERIALS AND BIOMATERIALS
FACULTY OF MECHANICAL ENGINEERING
SILESIAN UNIVERSITY OF TECHNOLOGY

INTERNATIONAL STUDENTS SCIENTIFIC CONFERENCE

Topological optimization of a structural component with consideration of structural analysis

Karolina Nowak[a], Julia Wawrzynek[a], Agata Śliwa[b]

[a] Student of Silesian University of Technology, Faculty of Material Engineering
email: kn308350@student.polsl.pl, jw305636@student.polsl.pl
[b] Silesian University of Technology, Faculty of Mechanical Engineering, Department of Engineering Materials and Biomaterials
email: agata.sliwa@polsl.pl

Abstract: This article presents a comparative analysis of the shape optimization of a connector manufactured using 3D printing technology from PETG material. The aim of the study was to evaluate the capabilities and effectiveness of the Autodesk Inventor and ANSYS environments in the optimization of structural component surfaces. For the adopted geometric model, boundary conditions and loads were defined, followed by an optimization process aimed at reducing mass while maintaining the required strength. The obtained geometric variants were then subjected to finite element method (FEM) analysis to determine the distributions of stresses and displacements.

Keywords: shape optimization, 3D printing, PETG, finite element method (FEM), strength analysis, Autodesk Inventor, ANSYS, topology optimization.

1. INTRODUCTION

Modern engineering design aims to achieve structures characterized by high strength while simultaneously minimizing mass and material consumption. One of the most important tools enabling the realization of these objectives is shape and topology optimization, which involves distributing material within a given design space in such a way as to satisfy specific strength and functional criteria [1–2]. This process is widely applied in the design of mechanical components, particularly in the context of additive manufacturing technologies, which enable the production of complex geometries unattainable by conventional manufacturing methods.

Shape (surface) optimization involves modifying the geometry of a component in order to reduce stress concentrations, improve stiffness, and increase material utilization efficiency. In engineering practice, the finite element method (FEM) is frequently used for this purpose, as it enables the analysis of stress, strain, and displacement distributions within a structure and forms the basis of optimization algorithms [1,3]. Owing to the iterative approach, it is possible to gradually eliminate excess material from regions subjected to low loads, leading to structures with optimized mechanical properties. Optimization is of particular importance in 3D printing

technology, where the absence of technological limitations associated with subtractive machining allows the realization of structures with complex, often organic shapes. However, materials used in additive manufacturing exhibit specific mechanical properties, including anisotropy resulting from the layer-by-layer manufacturing process, which must be considered during design and analysis [3–4].

One of the popular software environments used in this field is Autodesk Inventor, which combines parametric modeling functions with strength analysis modules. The software enables static analyses and the use of optimization tools such as the Shape Generator, based on iterative algorithms employing FEM. This tool allows for the automatic identification of regions containing excess material and the generation of geometry proposals that satisfy predefined design criteria, such as mass minimization or stiffness maximization. A significant advantage of this environment is its intuitiveness and the integration of all design stages within a single system, making it particularly useful for engineering applications of moderate complexity [5].

Advanced capabilities in the field of numerical analysis and optimization are offered by ANSYS, one of the most widely used CAE-class systems. The software enables detailed strength, nonlinear, and multiphysics analyses, as well as advanced topology optimization. The application of different computational environments in the optimization process may lead to different results due to variations in the implementation of numerical methods, finite element mesh generation techniques, and optimization algorithms. Therefore, it is important to conduct a comparative analysis in order to evaluate their suitability for designing components intended for manufacturing using 3D printing technology.

2. MATERIALS AND METHODOLOGY

In this study, PETG (polyethylene terephthalate glycol-modified), a material commonly used in FDM 3D printing technology, was analyzed. This material is characterized by good mechanical properties and resistance to damage, which makes it widely used in the production of structural components. In the calculations, a linear elastic material model was adopted, and isotropic behavior was assumed, which constitutes a simplification compared to the actual behavior of materials manufactured using a layer-by-layer process.

Table 1 Material Properties of PETG

Parameter	Symbol	Value	Unit
Young's Modulus	E	2590	MPa
Poisson's Ratio	ν	0,4	–
Yield Strength	Rp 0,2	47,3	MPa
Density	ρ	1,3	g/cm³

Numerical analyses were carried out using the finite element method (FEM), which enables the determination of stress, displacement, and strain distributions in the analyzed component. To ensure the comparability of results, consistent assumptions regarding boundary conditions and loading were adopted in both computational environments. The numerical analysis was performed using two software packages: Autodesk Inventor and ANSYS. In both cases, strength analysis and shape optimization of the investigated component were conducted. In the Autodesk Inventor environment, the Shape Generator tool was applied, enabling geometry optimization through the iterative removal of material from regions subjected to low stress

levels. This process allows for the development of structures with reduced mass while maintaining the required mechanical properties.

In the ANSYS environment, topology optimization was carried out, involving the determination of the optimal material distribution within a specified design space. This method enables the automatic generation of geometry that satisfies the adopted design criteria while taking into account loading and boundary conditions. The applied methodology enables a direct comparison of the results obtained in both computational environments. The analysis includes the evaluation of stress and displacement distributions, as well as the effectiveness of material reduction, allowing for the identification of differences in optimization approaches and the assessment of the suitability of individual tools for the design of components intended for 3D printing.

3. CAD GEOMETRIC MODEL

The analyzed structural component is a connector designed in the Autodesk Inventor environment. The geometry of the model was developed considering its function and the anticipated operating conditions. The dimensions and views of the connector are presented in Figures 1a and 1b. The component includes a distinguished load application surface and a mounting surface. Additionally, due to structural requirements, two M6 threaded holes were incorporated into the connector to enable its fastening.

a) b)

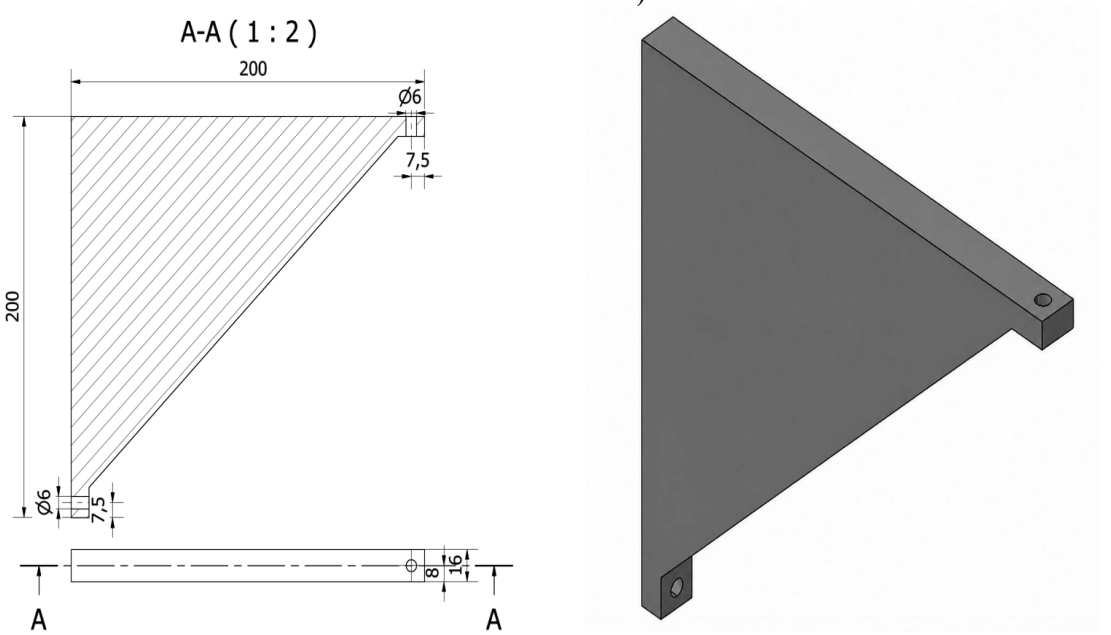

Figure 1 Geometric model of the connector: a) technical drawing with dimensions, b) spatial view of the 3D model.

4. BOUNDARY CONDITIONS

To ensure the comparability of the analysis results obtained in the Autodesk Inventor and ANSYS environments, identical boundary conditions and material properties were adopted for the model:

1. In both cases, the same material model corresponding to the properties of PETG was applied, enabling direct comparison of the obtained results.
2. An external load was applied to the upper surface of the component in the form of a force of 2500 N, acting in a direction corresponding to the actual operating conditions of the connector.
3. Boundary conditions were defined by completely constraining selected surfaces of the model. The following constraints were applied:

- fixed support on the mounting surface,
- fixed support in the region of the mounting holes.

4. In the optimization process, a mass reduction criterion of 60% relative to the initial model was adopted while maintaining the required mechanical properties.

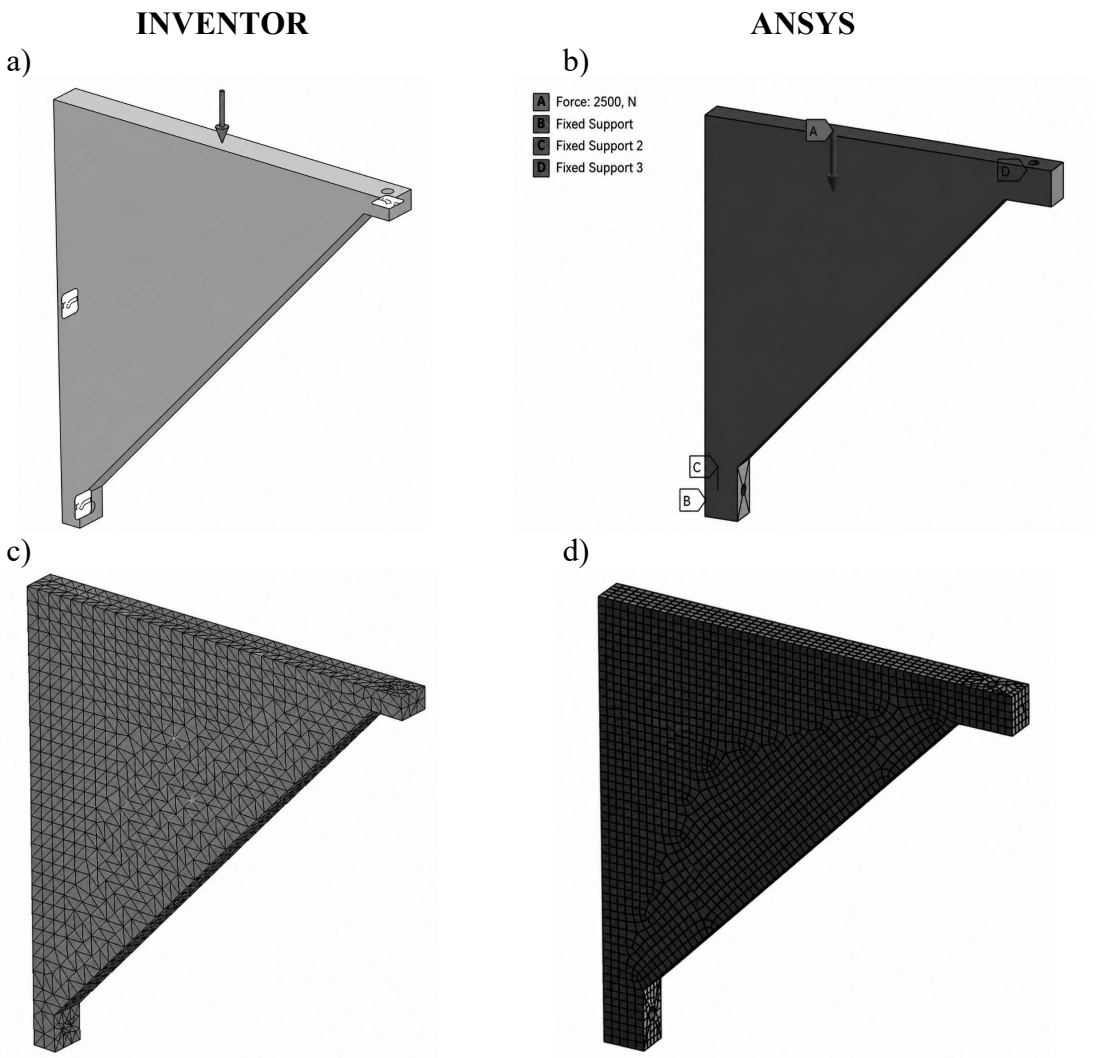

Figure 2 Definition of boundary conditions and model discretization: a) boundary conditions in Autodesk Inventor, b) boundary conditions in ANSYS, c) FEM mesh in Autodesk Inventor, d) FEM mesh in ANSYS.

5. TOPOLOGY OPTIMIZATION

The methods used to perform topology optimization differ depending on the applied software. Despite the similar approach to defining boundary conditions and material properties, differences occur primarily in the available functionalities and the optimization workflow. The main difference concerns the method of defining regions that should remain unchanged during the optimization process.

In the Autodesk Inventor environment, this is achieved by manually indicating the preserved regions of the structure (Fig. 3a). The user specifies the areas that are excluded from modification, which allows key geometric features to be maintained. In the case of ANSYS, the approach is different. Preserved regions are determined automatically based on numerical calculations using topology optimization tools (e.g., the ETOPO function). This process enables a more automated determination of material distribution within the design space (Fig. 3b).

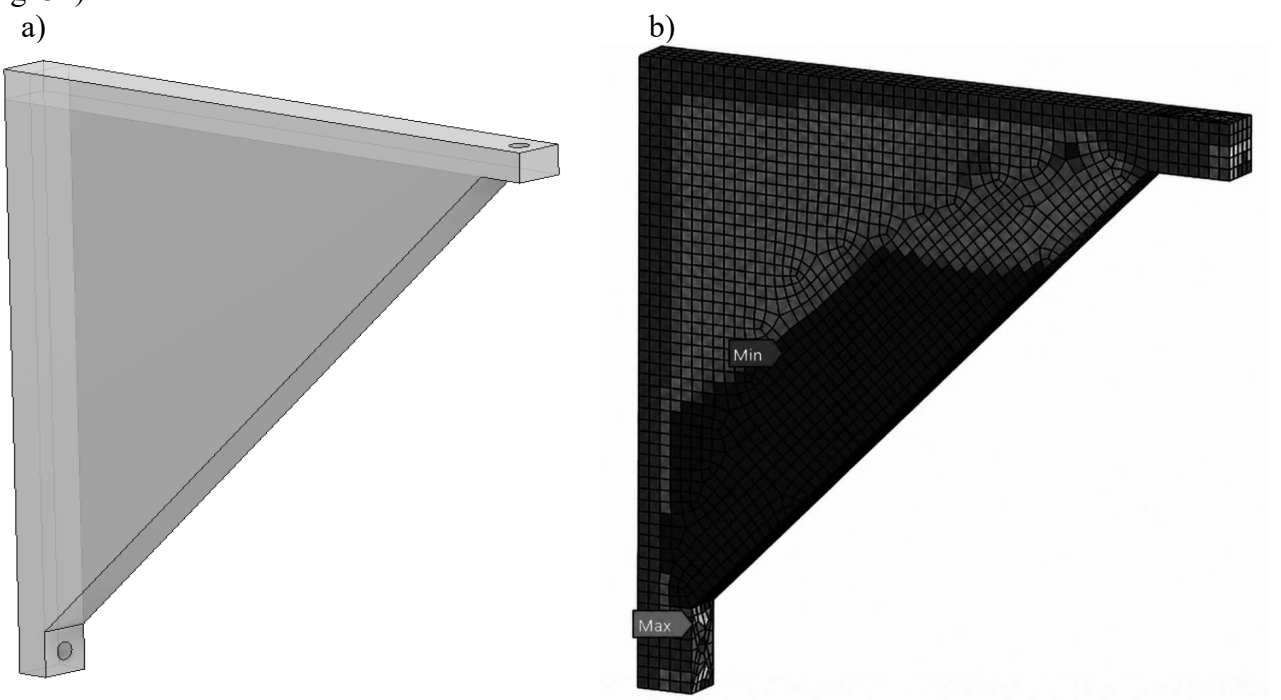

Figure 3 Comparison of the topology optimization process: a) manual definition of preserved regions in Autodesk Inventor, b) automatic determination of regions in ANSYS.

After the topology optimization process, the obtained geometry requires appropriate preparation for manufacturing. In the ANSYS environment, it is possible to take technological limitations into account already at the optimization stage by applying the Manufacturing Constraints and Design Constraints functions. As a result, the generated geometry is directly adapted to the manufacturing process without requiring additional user intervention (Fig. 4d). In the case of Autodesk Inventor, the optimized structure is obtained in the form of a mesh, which requires further processing (Fig. 4a). In order to simplify and smooth the geometry, manual remodeling is necessary, involving the reconstruction of the shape based on the optimization result (Fig. 4c). This process is more time-consuming and depends on the user's experience, which may affect the accuracy of reproducing the optimized structure. Differences

in the approach to the final model preparation have a significant impact on the efficiency of the design process and the level of sophistication of the applied software.

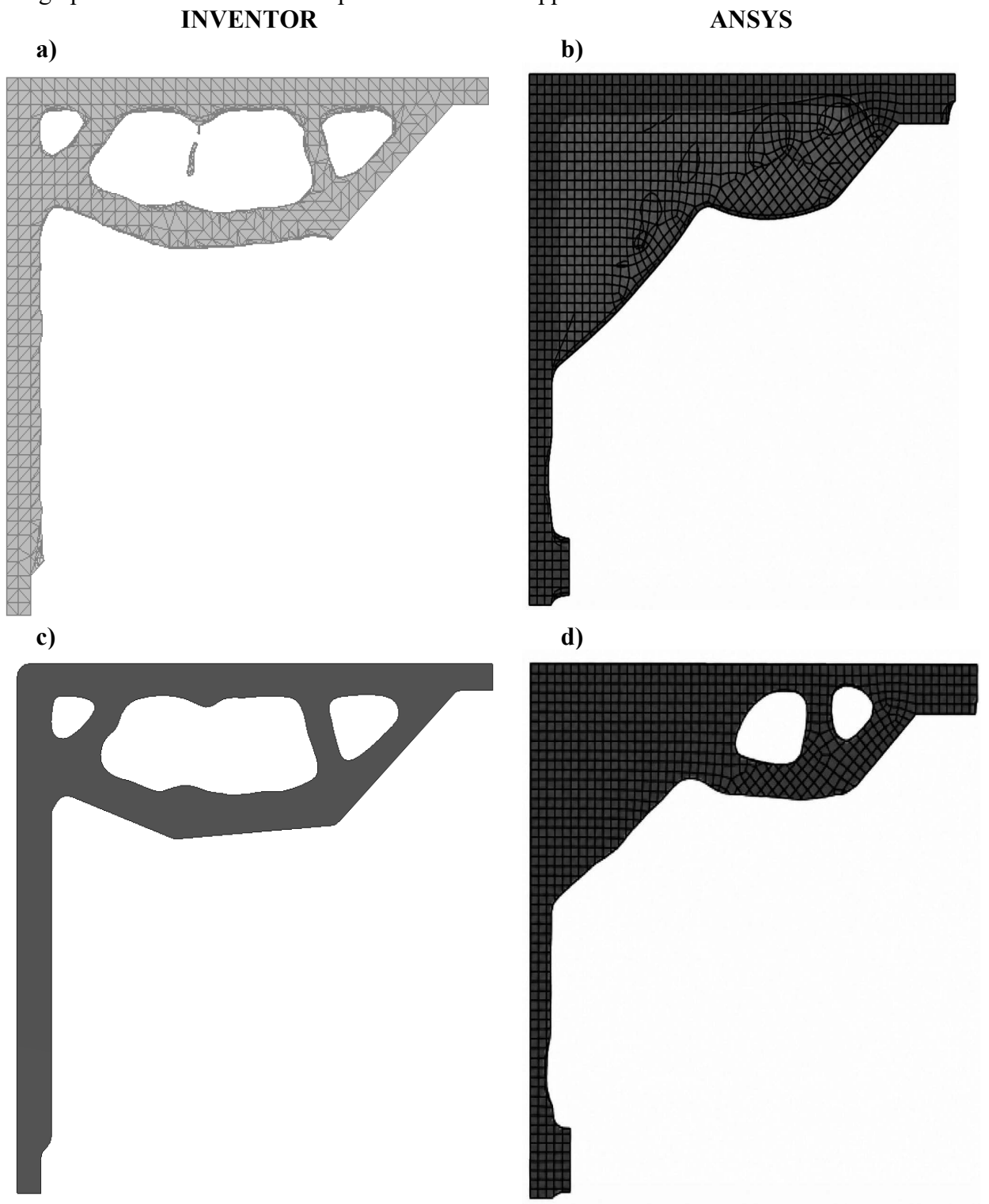

Figure 4. Stages of geometry preparation after topology optimization: a) mesh generated in Autodesk Inventor, b) mesh generated in ANSYS, c) model after manual post-processing in Autodesk Inventor, d) geometry obtained in ANSYS with manufacturing constraints considered.

6. ANALYSIS OF RESULTS

6.1 Numerical stress analysis results

The numerical stress analysis was performed based on the Huber von Mises hypothesis. As a result of the applied load, distributions of equivalent stresses were obtained, with values expressed in MPa. Figure 5 presents a comparison of the stress distributions for the optimized geometries.

a) b)

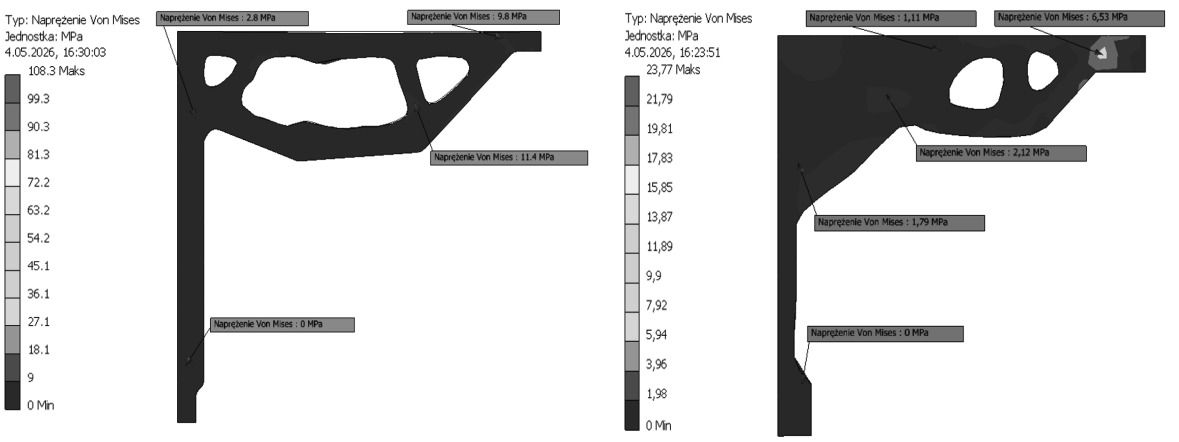

Figure 5 Huber von Mises stress analysis for the topologies obtained in: a) Autodesk Inventor, b) ANSYS

6.2 Numerical displacements analysis results

Within the numerical analysis, the displacements caused by the applied force were determined, and their distribution throughout the structure was calculated. The results are shown in Figure 6. The applied load causes the model to deform, resulting in a change in its geometry.

a) b)

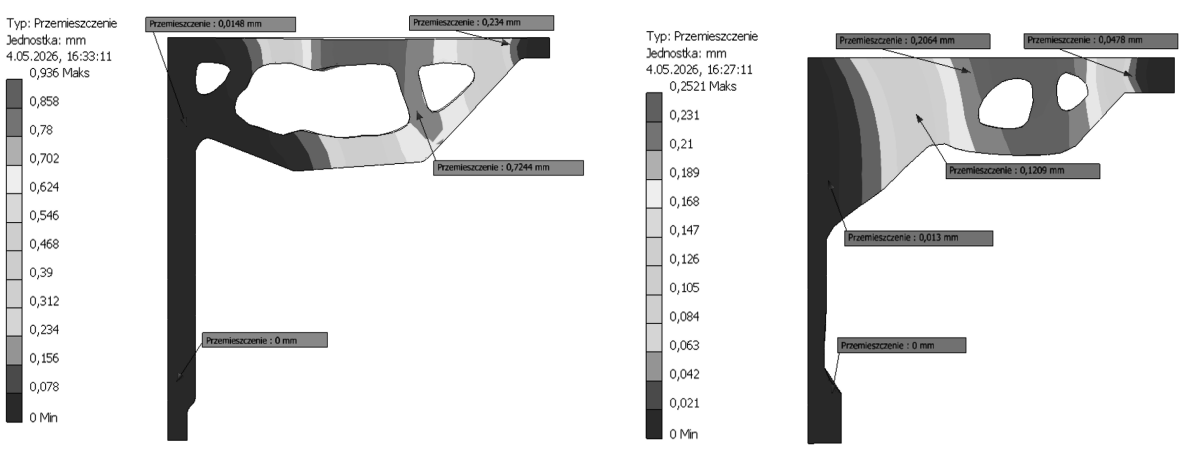

Figure 6 Displacement analysis for topologies generated in: a) Autodesk Inventor, b) Ansys

7. CONCLUSIONS

An important aspect of the conducted analyses is the noticeable difference in stress and displacement values obtained in the Autodesk Inventor and ANSYS environments, despite the application of identical boundary conditions and loads. In the case of Autodesk Inventor, the maximum displacements reached approximately 0.9 mm, whereas in ANSYS they were about 0.25 mm. A similar discrepancy was observed for stresses in the main part of the structure, the average stresses in Inventor were approximately 9 MPa, while in ANSYS they were about 2.5 MPa.

The observed differences result primarily from the different levels of advancement of the two computational environments. ANSYS, as an advanced CAE-class tool, enables more precise control over the model discretization process, including the quality and density of the finite element mesh, as well as a more accurate representation of boundary conditions. The applied topology optimization algorithms also allow for a more efficient material distribution, leading to reduced stress concentrations and smaller displacements. In contrast, Autodesk Inventor employs a more simplified approach to numerical analysis, which may result in higher stress and displacement values. Limited control over FEM mesh parameters and the solution process may lead to local stress concentrations and overestimation of deformations.

The obtained results indicate that ANSYS provides more reliable and accurate results of strength analysis, particularly in the case of complex topology optimization problems. At the same time, the noticeable differences suggest the need for further model verification, including the unification of analysis parameters, mesh refinement, and consideration of the influence of the adopted material simplifications.

BIBLIOGRAPHY:

1. J. Alexandersen, O. Sigmund, A detailed introduction to density-based topology optimization, Structural and Multidisciplinary Optimization, 2023, odnośnik do strony internetowej: https://portal.findresearcher.sdu.dk/files/226815117/s00158_022_03420_9.pdf (data dostępu: 01.05.2026).
2. M. Nowak, Topology optimization without volume constraint, Bulletin of the Polish Academy of Sciences, 2021, odnośnik do strony internetowej: https://journals.pan.pl/Content/119995/PDF/20_02338_Bpast.No.69%284%29_27.08.21_druk.pdf (data dostępu: 01.05.2026).
3. G. Misiun, E. van de Ven, M. Langelaar, Topology Optimization for additive manufacturing with process simulation, 2021, odnośnik do strony internetowej: https://ris.utwente.nl/ws/files/265091435/1_s2.0_S0045782521004266_main.pdf (data dostępu: 01.05.2026).
4. C. Hagnell, Topology Optimization, praca naukowa, 2021, odnośnik do strony internetowej: https://www.diva-portal.org/smash/get/diva2%3A1575804/FULLTEXT01.pdf (data dostępu: 01.05.2026).
5. Autodesk Inc., Autodesk Inventor – Shape Generator and Simulation Documentation, odnośnik do strony internetowej: https://help.autodesk.com/view/INVNTOR/ (data dostępu: 01.05.2026).
6. ANSYS Inc., Topology Optimization in ANSYS – Application Overview, odnośnik do strony internetowej: https://www.ansys.com/products/structures/ansys-mechanical (data dostępu: 01.05.2026).

TalentDetector
7th-9th June 2026
Gliwice-Brenna, Poland
DEPARTMENT OF ENGINEERING MATERIALS AND BIOMATERIALS
FACULTY OF MECHANICAL ENGINEERING
SILESIAN UNIVERSITY OF TECHNOLOGY
INTERNATIONAL STUDENTS SCIENTIFIC CONFERENCE

Microstructural and chemical characterisation of biochar derived from plant-based waste materials

Tiara Ogórek[a], Paulina Lukaszkowicz[a], Ewa Adamek[b], Wojciech Baran[b], Krzysztof Lukaszkowicz[c], Klaudiusz Gołombek[d]

[a]Medical University of Silesian in Katowice, Faculty of Pharmaceutical Sciences in Sosnowiec, Student Scientific Club at the Department of Inorganic Chemistry
email: s87046@365.sum.edu.pl; s86990@365.sum.edu.pl
[b]Medical University of Silesian in Katowice, Faculty of Pharmaceutical Sciences in Sosnowiec, Department of Inorganic Chemistry, email: eadamek@sum.edu.pl; wbaran@sum.edu.pl
[c]Silesian University of Technology, Faculty of Mechanical Engineering, Department of Engineering Materials and Biomaterials, email: krzysztof.lukaszkowicz@polsl.pl
[d]Silesian University of Technology, Faculty of Mechanical Engineering, Materials Research Laboratory, email: klaudiusz.golombek@polsl.pl

Abstract: The aim of the study was to evaluate the microstructure and chemical composition of biochars produced from various waste materials of natural origin. Scanning electron microscopy (SEM) and energy-dispersive X-ray spectroscopy (EDS) were used for the analysis, which made it possible to determine the morphological characteristics and identify the elements present in the materials. It was observed that the properties of the obtained biochars depend on the type of biomass used, which is reflected in the varied surface structure. All samples showed a high content of elemental carbon as well as the presence of inorganic components, which may be associated with the occurrence of metal oxides on the material surface.

Keywords: biochar, waste biomass, SEM, EDS, chemical analysis

1. INTRODUCTION

The intensive production of waste has led to the search for inexpensive methods for its management and reuse. One way to utilize animal and plant waste (biomass) with a high carbon content is to convert it into a carbonaceous material known as biochar.

Biochar is a high-carbon product of biomass pyrolysis, produced under conditions of limited oxygen access at temperatures above 500°C. It is manufactured from a variety of natural organic materials, namely plant-derived feedstocks (e.g., corn cobs, sunflower stalks, straw, pits, husks, shells, empty fruit bunches, or wood chips) or animal-derived materials (manure) [1]. Its composition consists primarily of elemental carbon (approximately 90%). The remaining fraction is made up of inorganic compounds containing mainly oxygen (O),

hydrogen (H), nitrogen (N), calcium (Ca), potassium (K), and silicon (Si), as well as smaller amounts of magnesium (Mg), aluminium (Al), sulphur (S), iron (Fe), phosphorus (P), chlorine (Cl), and sodium (Na). Variations in the percentage content of these elements in biochar are the result of the type and origin of the biomass. Due to its high degree of graphitization (structures rich in π-bond systems), the presence of lattice defects and oxygen-containing functional groups, as well as small amounts of heteroatoms (mainly O, N, and S), unmodified biochar also exhibits catalytic activity. This activity can be enhanced, for example, by modifying surface functional groups through heteroatom doping (P, B) or modification with transition metals (Fe, Cu, Ag) [2,3].

The most important characteristics of biochars include porosity and specific surface area, as well as the associated adsorption capacity. These properties depend on the type of feedstock used, the process parameters, and the possible activation method. For example, the use of woody biomass with a high lignin content can yield biochars with a high degree of graphitization and a highly developed specific surface area. Biochar is used in industry and energy production (as a renewable fuel and additive to materials such as concrete), in agriculture and horticulture (as a fertilizers carrier and an additive to compost), and in environmental protection (for carbon sequestration, bioremediation, or as an adsorbent) [4].

The aim of this study was to investigate the microscopic properties of biochars obtained from various waste feedstocks of natural origin (non-woody biomass) and to determine their elemental composition.

2. MATERIALS AND METHODS

A powdered biochar was used in the study. The unmodified biochar was obtained by carbonizing of natural waste materials at temperatures ranging from 400 to 1100°C for 4–10 h. The feedstocks used for biochar synthesis differed in their chemical composition:

- material A: cellulose <65%, hemicellulose <20%, lignin <20%;
- material B: cellulose <85%, hemicellulose <15%, lignin <2%;
- material C: cellulose <95%.

The carbonization procedure was developed by staff of the Department of General and Inorganic Chemistry, Faculty of Pharmaceutical Sciences. The morphology and chemical composition of the biochars were analyzed using a SUPRA 35 high-resolution scanning electron microscope (HRSEM) manufactured by ZEISS and equipped with an EDS detector. The investigations were carried out at an accelerating voltage in the range of 10–20 kV using both secondary electron detector (SE) and backscattered electron detector (BSE). Chemical composition analysis in micro-areas was performed using the EDS system and Pathfinder software.

3. RESULTS AND DISCUSSION

The study revealed differences in the morphology of biochars depending on the origin of the feedstock. The biochar samples retained their original macrocellular morphology, probably due to only partial degradation of the raw materials. The fiber size was on the order of several micrometers. Differences were observed between individual grains and within single particles (inclusions, bright deposits, heterogeneities). The presence of elemental carbon (>80%) and

other typical elements characteristic of biochars was confirmed. Numerous bright structures were observed on the surface of the products, most likely corresponding to metal oxides such as CaO, SiO_2, and Al_2O_3.

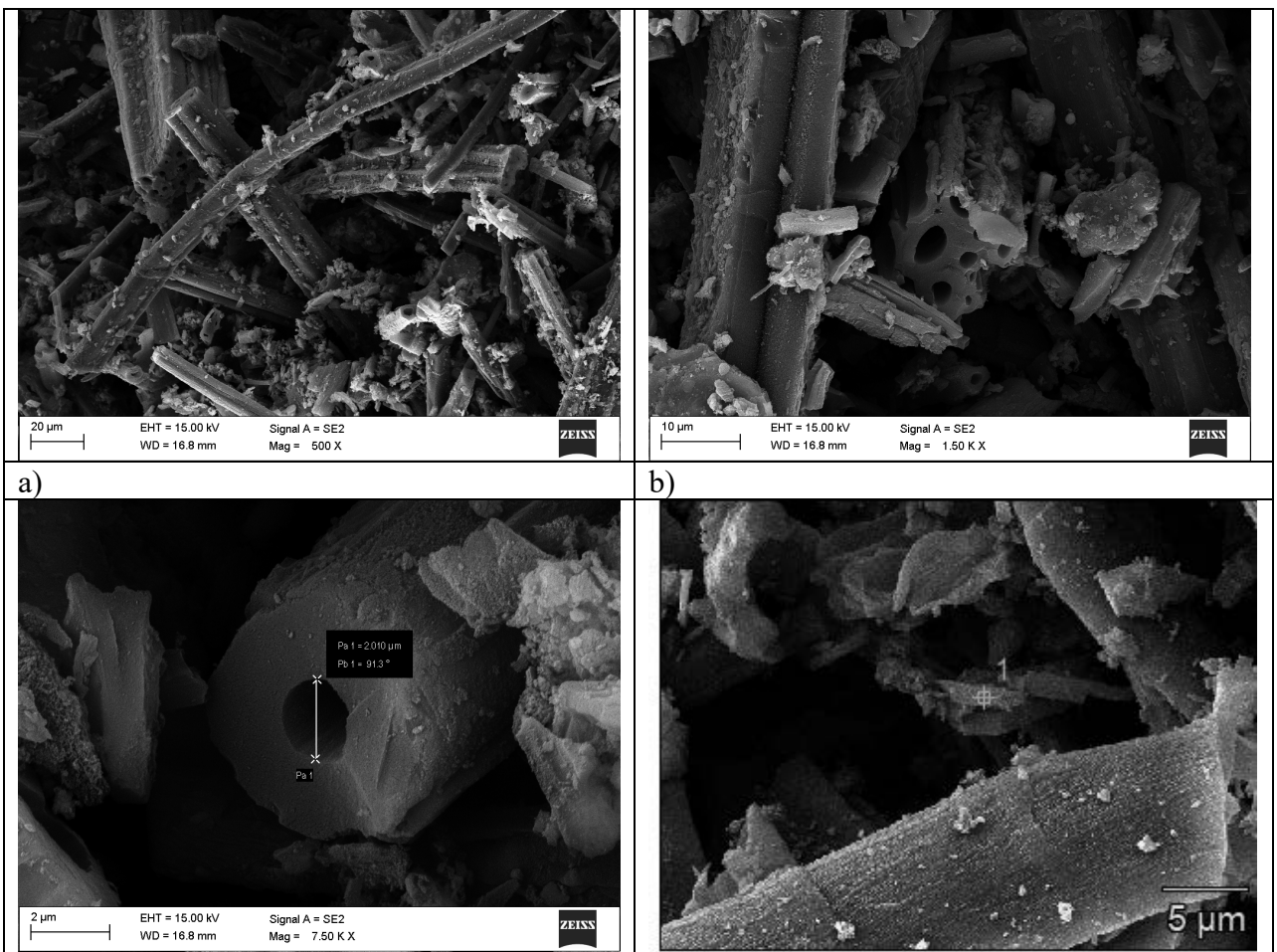

	C	*O*	*Ca*
Base(10)_pt1	85.08	13.10	1.82

Figure 1. Longitudinal (a, b, c) and cross-sectional (d) views of a single fiber of material A together with elemental composition analysis

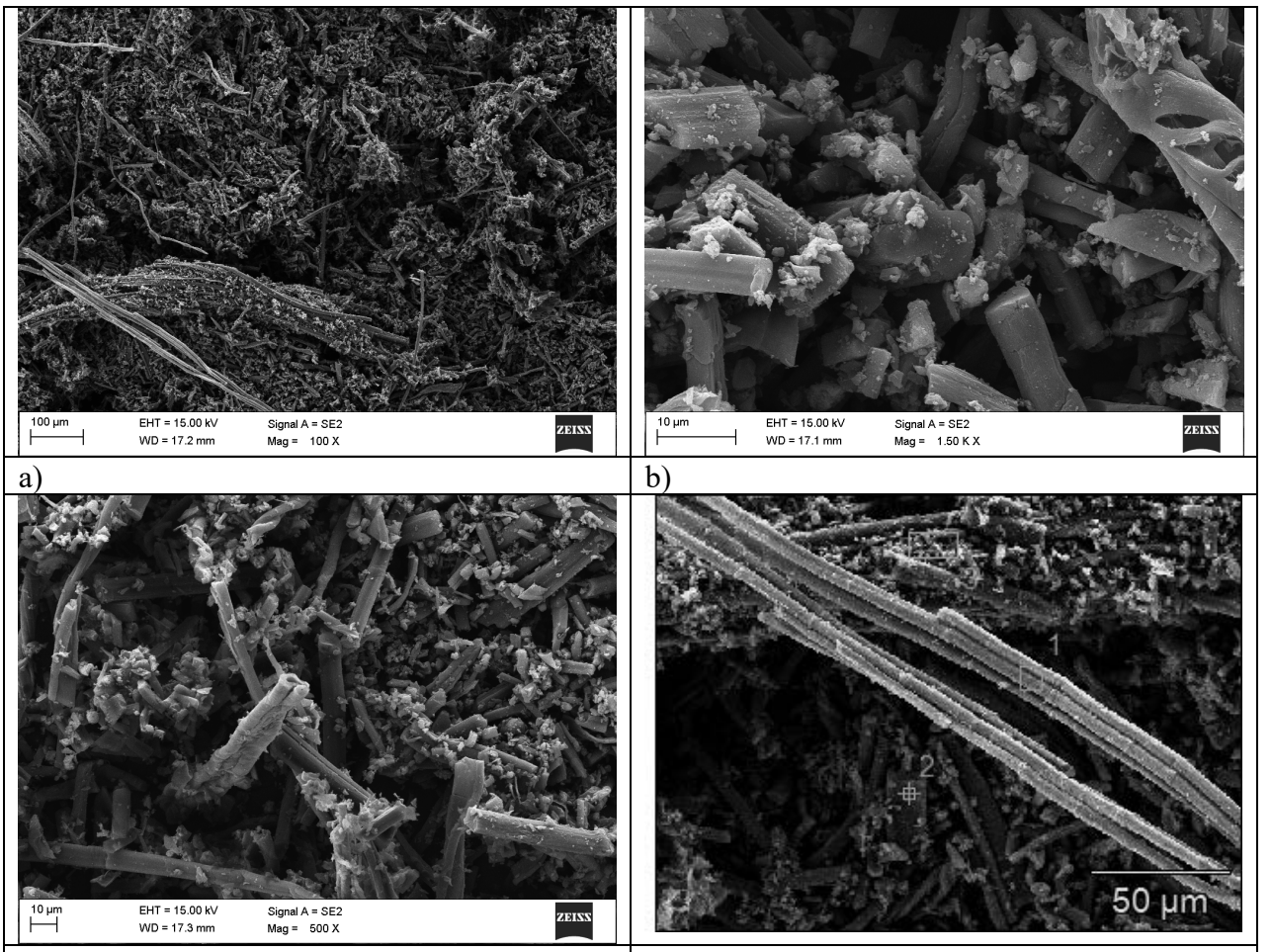

	C	O	Al	Si	Cl	K	Ca
Base(12)_pt1	83.39	15.02				0.66	0.92
Base(12)_pt2	91.59	8.41					
Base(12)_pt3	74.32	10.30	1.19	4.77	1.06	1.58	6.79

Figure 2. Longitudinal view of single fibers of material B and elemental composition analysis

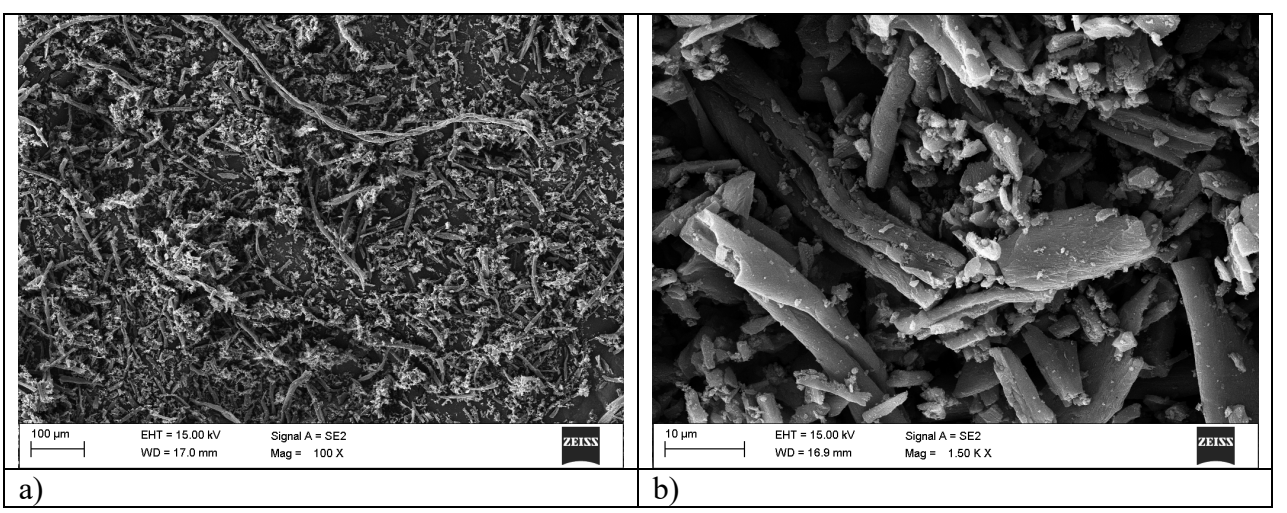

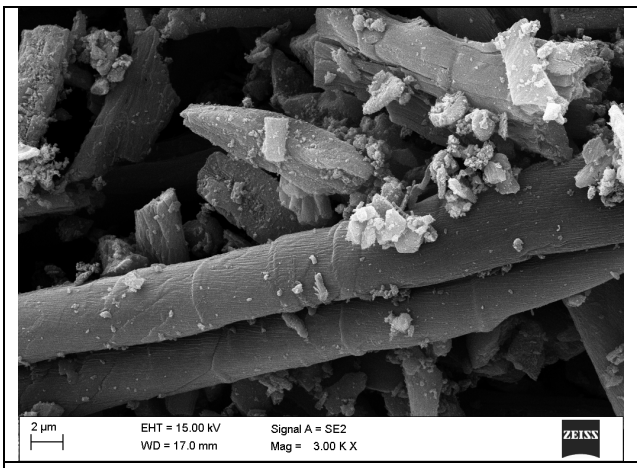

c)

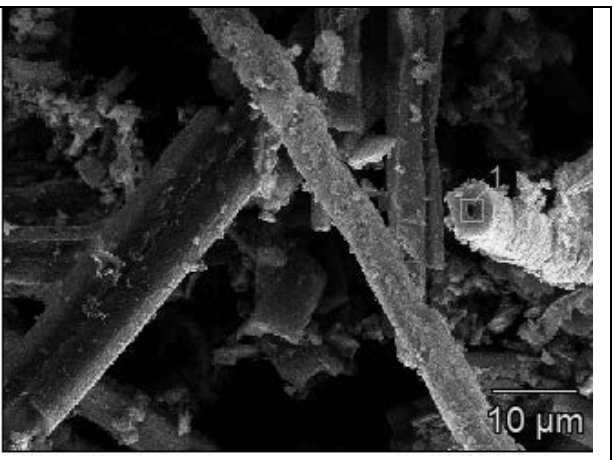

d)

	C	*O*	*Ca*
Base(5)_pt1	89.20	10.17	0.64

Figure 3. Longitudinal view of single fibers of material C and elemental composition analysis

4. CONCLUSION

The properties of the biochars strongly depended on the type of biomass used. The obtained materials were characterized by a developed and heterogeneous structure as well as a high content of elemental carbon, confirming the effectiveness of the carbonization process. The presence of inorganic phases on the sample surfaces suggests that the biochars may exhibit additional adsorption and catalytic properties.

BIBLIOGRAPHY

1. F. Tian, Y. Wang, Y. Zhao, R. Sun, M. Qi, S. Wu, L. Wang, A Review of Biochar-Industrial Waste Composites for Sustainable Soil Amendment: Mechanisms and Perspectives, Water 17(15), 2025.
2. K. Jatuwong, W. Aiduang, T. Kiatsiriroat, W. Kamopas, S. Lumyong, A Review of Biochar from Biomass and Its Interaction with Microbes: Enhancing Soil Quality and Crop Yield in Brassica Cultivation, Life 15(2), 2025.
3. P. Li, K. Wan, H. Chen, F. Zheng, Z. Zhang, B. Niu, Y. Zhang, D. Long, Value-Added Products from Catalytic Pyrolysis of Lignocellulosic Biomass and Waste Plastics over Biochar-Based Catalyst: A State-of-the-Art Review, Catalysts 12, 1067, 2022.
4. P. Li, K. Wan, H. Chen, F. Zheng, Z. Zhang, B. Niu, Y. Zhang, D. Long, Recent advancements and challenges in emerging applications of biochar-based catalysts, Biotechnology Advances 67, 108181, 2023.

TalentDetector

7th-9th June 2026
Gliwice-Brenna, Poland

DEPARTMENT OF ENGINEERING MATERIALS AND BIOMATERIALS
FACULTY OF MECHANICAL ENGINEERING
SILESIAN UNIVERSITY OF TECHNOLOGY

INTERNATIONAL STUDENTS SCIENTIFIC CONFERENCE

Modeling and optimization of geometric parameters of a chopping knife for wood chopping

Daniel Pella[a], Filip Bejm[a], Milen Pawlas[b], Joanna Tokarz[b], Adam Zygłowicz[b], Jakub Polis[a], Agata Śliwa[a], Marek Sroka[a], Jan Komendák[c], Samuel Zachar[c], Miroslava Tavodova[c]

[a] Silesian University of Technology, Faculty of Mechanical Engineering, Department of Engineering Materials and Biomaterials
email: dp316755@student.polsl.pl, fb316756@student.polsl.pl, jakub.polis@polsl.pl, agata.sliwa@polsl.pl, marek.sroka@polsl.pl
[b] Silesian University of Technology, Institute of Physics
email: mp317594@student.polsl.pl, jt317600@student.polsl.pl, az317598@student.polsl.pl
[c] Technical University in Zvolen, Faculty of Technology, Department of Manufacturing Technology and Quality Management
email: xkomendakj@is.tuzvo.sk, xzachars@is.tuzvo.sk, tavodova@tuzvo.sk

Abstract: Chipping machines, including woodchippers and specialized processing equipment, are essential for the valorization of woody biomass and logging residues. These machines produce wood chips utilized extensively across the energy, pulp and paper, chemical, and furniture industries, with particle dimensions tailored to specific industrial requirements. To withstand the rigorous conditions of the wood-processing environment, chopping knives are fabricated from high-alloy tool steels engineered for superior hardness, toughness, and wear resistance. The efficiency of the chipping process is governed by complex wood-metal interactions, where the optimization of cutting forces and blade geometry is critical for enhancing component longevity. Given that cyclic and random operational loads frequently lead to structural failure, fatigue performance remains a primary concern in blade design. This study presents a fatigue analysis of a chopping knife design conducted using SOLIDWORKS simulation software. This study presents a fatigue analysis of a shredding blade design performed using SOLIDWORKS simulation software. The study evaluates the structural integrity of the component to predict fatigue damage and mitigate the risk of component failure.

Keywords: Wood chippers, chopping knives, tool steel, wood-metal interaction, fatigue analysis, S-N method, SOLIDWORKS.

1. CHIPPING MACHINES

The use of wood waste for both energy and industrial purposes is linked to the development of technologies for its processing. Various mechanical pre-treatment methods (chipping,

shredding, grinding, etc.) can effectively reduce the particle size of wood waste. One of the most important pieces of equipment in wood processing is the wood chipper. It is a device for chip-free wood splitting, achieved by the cutting action of the chopping blades across the grain and, at the same time, by splitting the wood to the desired thickness along the grain due to the blade's wedge shape. A wood chipper is therefore a machine that uses the mechanical action of chopping blades to remove small fragments—wood chips—from the wood [1, 2].

A wood chipper is a machine that processes wood waste (twigs, branches, small-diameter wood, etc.) to facilitate its transport and further use. The cutting mechanism acts on the wood material being processed, mechanically cutting and chipping it into particles ranging from 3 to 50 mm in length. This product is called wood chips (figure 1). Chippers cut through the wood fibers with the cutting edge of their blades (unlike shredders, which break down, tear, or crush the wood material using pressure or the impact of hammer heads) [1, 2].

Figure 1. Wood chips [2]

1.2 Disc chippers

The working component of a disc chipper (figure 2) is the disc, which has cutting blades arranged radially on its front surface. The disc rotates in a vertical position. It is mounted on a horizontal shaft, which is supported by bearings within the machine frame. The wood being processed is fed to the disc through a feed chute (trough) inclined at an angle. The disc is equipped with ejection blades that ensure the chips are discharged through the exhaust chute. Additionally, there are openings beneath the blades to allow the chips to pass through the disc. The length of the chips is adjusted by the overhang of the blades. The disc is characterized by the mounted blades, their number and arrangement, as well as the number of revolutions, i.e., the cutting speed. The disc must be sufficiently strong to withstand the impacts generated during chipping.A counter-blade is mounted at the bottom of the feed chute. The size of the inlet opening depends on the radius of the cutting disc [3].

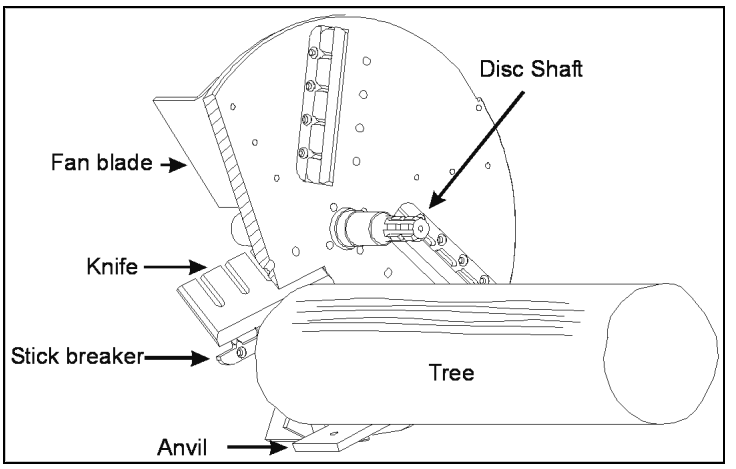

Figure 2. Schematic representation of disc chipper [4]

Advantages of a disc wood chipper [5,6]:

- Mobile disc chippers are characterized by high quality chips.
- They allow chopping wood of large diameters up to 500 mm with acceptable weight and strength dimensions.
- The large moment of inertia allows installing a combustion engine of lower power, with the chipping being done by interrupting the feed until the engine power is sufficient for chopping with respect to the thickness of the wood.
- Disc chippers do not require a special fan, since the chipping disc itself, equipped with blades, has a large throwing and ventilation effect, which ensures the transport of chips into cars or parked containers.

Disadvantages of a disc wood chipper [5,6]:

- The size of the inlet hole is limited by the radius of the cutting disc.
- Unsuitability for use in cutting chaotic material due to the limited size of the inlet hole.

Figure 3 shows an example of such a machine.

Figure 3. Disc wood chipper [7]

2. CUTTING BLADES IN WOOD CHIPPERS

Cutting blades (figure 4) are among the key functional components of wood chippers and significantly influence chipping efficiency, operational reliability, and the quality of the produced wood chips. Parameters such as cutting edge sharpness, wear resistance, and material quality directly affect machine performance, energy consumption, and the uniformity of the final product. Within wood chipping systems, the blades serve as the primary working element responsible for the mechanical processing of wood biomass. The process involves the treatment of various materials, including coniferous and deciduous wood, small diameter logs, branches, stumps, bamboo, veneer waste, and post-harvest residues. In addition to woody biomass, selected agricultural residues, such as cotton stalks and similar plant materials, may also be processed. The resulting wood chips are widely utilized as a renewable energy source in heating and power generation systems, while also serving as a valuable secondary raw material in agricultural and industrial applications [8-10].

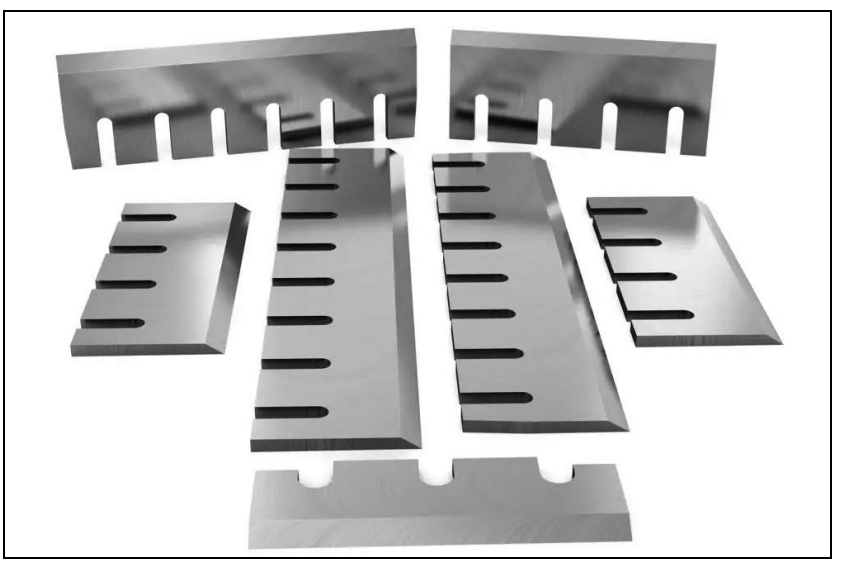

Figure 4. Chipper knives (blades) [11]

2.1 Chipping knives construction and chipping process

Despite significant differences among wood chippers in terms of design, dimensions, and performance parameters, the cutting tools used in these machines exhibit a high degree of structural similarity. The blades are predominantly rectangular in shape, with widths typically ranging from 50.8 to 101.6 mm and lengths from 101.6 to 304.8 mm. Their thickness ranges from approximately 38.1 to 50.8 mm. The height of the blade is determined by the machine design and must correspond to the spacing between individual cutting elements. In addition to geometry, cutting parameters must also be considered, as they significantly influence the wood chipping process. Figure 5 illustrates the distribution of cutting forces and the orientation of the cutting edge during the chipping process. The cutting knives serve as the primary cutting element, ensuring material separation and the formation of wood chips. Technical literature also points to several design solutions for blade mounting and holder systems. Among more modern approaches is an optimized blade holder design that eliminates the need for a separate counter blade and conventional holder. In this configuration, the cutting tool is mounted

directly onto the disc using a screw connection. The design also includes an adjacent surface inclined at 120° relative to the plane of the disc, which simplifies installation and operation of the equipment. The main technical limitations of the chipping process include, above all, an inappropriate selection of the cutting tool (blade type) and an inefficient material feeding method during operation. In the past, there was limited pressure to improve equipment addressing these shortcomings, primarily due to the low economic value of processed wood waste. Although existing chipping and reprocessing technologies have served the forestry and wood processing industries for several decades, current technological developments highlight the need to optimize the dynamic performance of these systems. The aim of such improvements is to increase efficiency and adapt the equipment to the requirements of end users in both primary and secondary utilization of wood biomass [12].

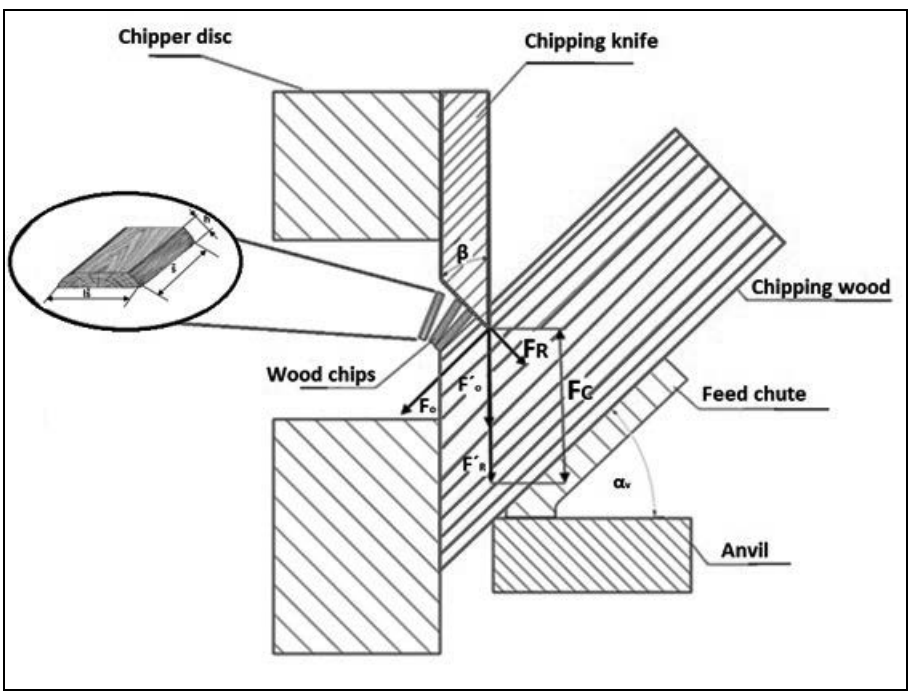

Figure 5. Wood splitting scheme and force analysis of the splitting process [13]

2.2 materials and properties of wood chipper knives

The selection of an appropriate material is a key factor in the design and performance of high quality chipper knives. Cutting tools used in wood chipping processes are typically manufactured from tool steels or alloy steels with modified mechanical properties, although in demanding applications manufacturers may also employ hardened tool steels or carbide materials. Most chipper knives are therefore produced from high-alloy steels, which are characterized by exceptional strength, durability, and resistance to wear, enabling them to withstand the harsh conditions associated with processing dense wood and abrasive particles. The choice of a specific material is primarily determined by the properties of the processed wood and the operating conditions of the equipment. A fundamental functional requirement is the long-term retention of cutting edge sharpness and geometric stability, which directly influences the uniformity and efficiency of wood chip production. From a material science perspective, cutting blades are evaluated based on a combination of physical, mechanical, and

chemical properties, including wear resistance, hardness, strength, resistance to abrasive loading, and corrosion resistance [14].
Different material groups exhibit distinct operational behaviour; consequently, their application is defined by the specific requirements of the technological process and the characteristics of the processed material. Carbon steels offer favourable machinability and low production costs; however, their service life is limited, particularly under conditions involving hard or highly abrasive materials. Alloy steels with improved corrosion resistance are suitable for operation in environments with increased humidity, but generally exhibit lower hardness, which leads to accelerated wear of the cutting edge. The highest performance level is achieved by tools produced using powder metallurgy techniques, which combine high hardness, extended service life, and excellent cutting performance. These properties make them particularly suitable for the most demanding operational conditions in wood chipping applications [15].

3. MATERIALS AND METHODOLOGY

The examined element is a wood chopping knife made of X48CrMoV8-1-1 tool steel, whose chemical composition and material properties are presented below in Table 1 and Table 2.
Table 1. Chemical composition of X48CrMoV8-1-1 steel [16].

Element	Min [%]	Max [%]
C	0.45	0.50
Cr	7.3	7.8
Mo	1.3	1.5
V	1.3	1.5
Si	0.7	0.9
Mn	0.35	0.45
P	-	0.02
S	-	0.005

Table 2. Mechanical and physical properties of X48CrMoV8-1-1 steel [17].

Property	Value
Young's modulus [GPa]	207
Poisson's ratio	0.28
Shear modulus [GPa]	79
Density [kg/m^3]	7750
Tensile strength [MPa]	1135
Yield strength [MPa]	935
Coefficient of thermal expansion [K^{-1}]	$11*10^{-6}$
Thermal conductivity [W/(m*K)]	14
Specific heat [J/(kg*K)]	440

4. CAD GEOMETRIC MODEL

A digital model of wood chopping knife was prepared in SOLIDWORKS to carry out strength check using a computer-based simulation. The crafted knife model is shown in Figure 6a. The aim of this analysis is to assess how a standard load of 4143 N on the surface of the chopping knife affects it during use (i.e., +30% from the initial value). This elevated load condition represents a critical operational scenario designed to evaluate the structural integrity and safety margins of the blade under increased mechanical stress.

5. BOUNDARY CONDITIONS

In the computer simulation, the following setup conditions were applied:

- A finite element mesh was laid over the knife model (Figure 6b),
- The model was then subjected to forces of 4683 N, each directed onto the cutting edge of the blade at an angle of 36°,
- The location where the force is applied, along with the way the knife was immobilized is illustrated in Figure 6c.

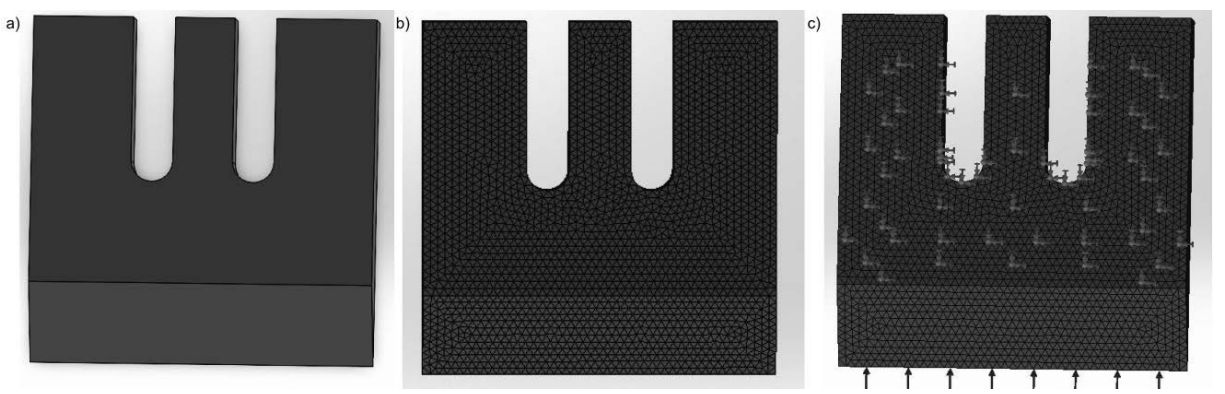

Figure 6. CAD model of wood chopping knife (a); with laid over finite element mesh (b); with laid over finite element mesh, visible direction of forces and immobilized knife geometry (c)

Next, a high-cycle fatigue analysis was performed using the previously determined Von Mises stress distributions as input data. The simulation was programmed to achieve a fatigued life of one million operating cycles. This stage of the analysis is scientifically justified and serves to evaluate the structural durability and strength limit of the blade under repeated loading conditions.

6. ANALYSIS RESULTS

Numerical stress assessment was conducted according to the Huber-Mises hypothesis. Upon loading the component, stress distribution maps were generated with magnitudes expressed in MPa. Figure 7 illustrates the stress distribution under the applied loads, showing a maximum Von Mises stress of 395,611 MPa. This peak value occurs at the neck region, indicated in red.

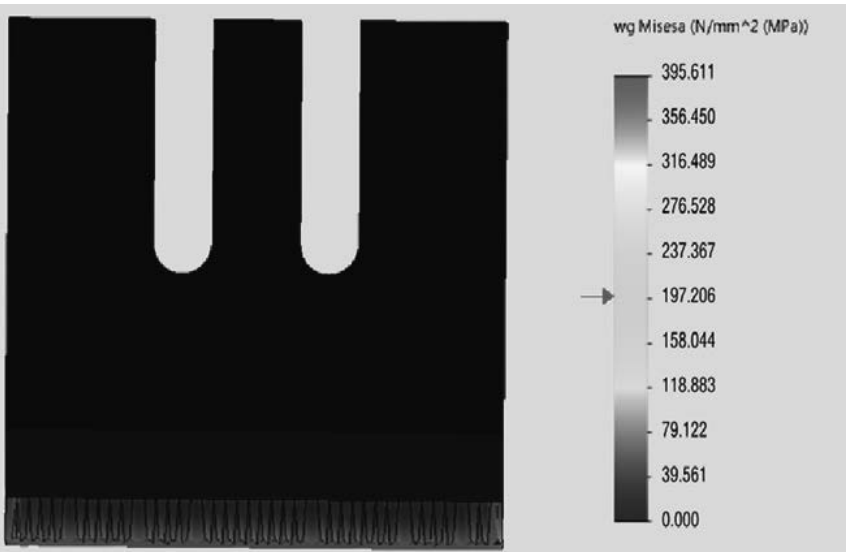

Figure 7. Huber-Mises stress reduction distribution of wood chipping knife

Building upon the obtained stress distribution results, a fatigue analysis was subsequently carried out to assess the component's durability under cyclic loading, assuming a target service life of one million cycles. The results of this analysis, presented in Figure 8, indicate that the predicted fatigue life is 69,158 cycles. This value fails to satisfy the specified design requirement of 10^6 cycles. The critical zone, representing the highest risk of fatigue failure, is located at the fillet (neck) region, indicated in red on the fatigue map, which correlates directly with the areas of maximum stress concentration identified in the static analysis.

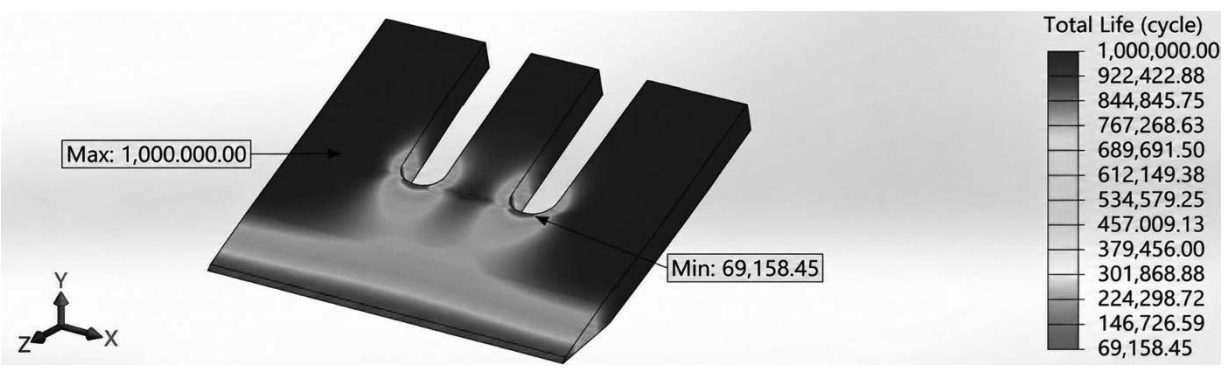

Figure 8. Plot of total life of component and failure affected area

Figure 9 shows the distribution of percentage damage within the component, highlighting critical stress concentrations at the base of the grooves. A maximum damage value of 144.60% was observed, which allows these areas to be identified as high-risk zones for potential structural failure.

Figure 9. Plot of total life of component and failure affected area

7. CONCLUSION

This study performed a comprehensive numerical evaluation of the structural durability and fatigue behavior of an chopping knife fabricated from X48CrMoV8-1-1 chromium-molybdenum-vanadium alloy steel. Utilizing the Finite Element Method (FEM), the blade was subjected to a functional load of 4683 N applied at a 36° angle to the cutting edge to simulate operational conditions. The resulting Von Mises stress distribution reached peak values of approximately 395.6 MPa, primarily localized along the cutting edge and within the geometric notches.

Subsequent high-cycle fatigue analysis, targeting a design life of 10^6 operating cycles, identified critical failure points due to geometric stress concentrations. While the bulk of the component maintains structural integrity through the target life, the notch bases exhibit significant fatigue accumulation. The analysis revealed a minimum service life of 69,158 cycles in these localized zones, corresponding to a maximum damage percentage of 144.60%. These results indicate that despite the high toughness and fatigue resistance of the X48CrMoV8-1-1 steel, the current notch geometry acts as a primary limiting factor for the blade's operational longevity.

Consequently, future research and design iterations must prioritize the optimization of the slot base geometry, specifically by increasing the fillet radii to mitigate stress concentration factors. Furthermore, implementing advanced surface treatment techniques or localized heat treatment adjustments for this specific alloy should be investigated to enhance the fatigue threshold in these high-risk zones, ensuring the blade achieves the required operational durability across its entire structure.

ACKNOWLEDGMENTS

The authors are grateful for the financial support of the Slovak Research and Development Agency under the Contract no. APVV-21-0180 Innovative approaches to increase the lifetime and reduce the energy consumption of cutting tools in wood processing in forestry.
This study was conducted as part of the project-oriented education - PBL, in the XIV competition within the Excellence Initiative - Research University program.

BIBLIOGRAPHY

1. ČABALOVÁ, Iveta, Tatiana BUBENÍKOVÁ, Viera KUČEROVÁ, Jozef KRILEK, Michal JABLONSKÝ a Vladimír HÖNIG. *Technológie a technika spracovania drevnej a rastlinnej biomasy: vysokoškolská učebnica*. Zvolen: Technická univerzita vo Zvolene, 2021. ISBN 978-80-228-3278-6.
2. Pine wood chips – 10 Cubic Meters. Online. 10.05.2026. Available at: https://www.pavementmaterials.co.za/products/pine-wood-chips-supplier-cape-town-johannesburg-pretoria-durban-south-africa?srsltid=AfmBOooLBPKGfu4FzA6nK3DIXxE1AMsvBhtZSj1d3wx82LswedBY2Tlv
3. KOVÁČ, Ján, Jozef KRILEK, Ján JOBBÁGY a Jiří DVOŘÁK. *Technika a mechanizácia v lesníctve: vysokoškolská učebnica*. Zvolen: Technická univerzita vo Zvolene, 2017. ISBN 978-80-228-3021-8.
4. Wood Harvesting Equipment. Online. 10.05.2026. Available at: http://www.woodenergy.ie/woodharvestingequipment/
5. MIKLEŠ, Milan. *Lesnícke stroje a zariadenia* [online]. Zvolen: Technická univerzita vo Zvolene, 2011 [cit. 2026-5-10]. ISBN 978-80-228-2302-9.
6. SVOREŇ, Ján. *Drevárske stroje* [online]. Zvolen: Technická univerzita vo Zvolene, 2009, Časť III. ISBN 978-80-228-2036-3.
7. Carlton 1712 (12” Disk Chipper). Online. 10.05.2026. Available at: https://radiusindustrial.ca/products/carlton-1712-series-12-disk-chipper?srsltid=AfmBOorOdrJDROdEhVkyu3XUiUxjW0lR4MHRykQA9gSPp76wGG1TGQ4l
8. RDM PARTS, 2026. Wood chipper blades. Online 10.5.2026. Available at: https://www.rdmparts.com/en/c-627-houtversnipperaar-beitels?srsltid=AfmBOop-a9qxDWYFZplNQm-MdXTSkwS5VPh2PKXoZWAGyTCRkJf9iqBM
9. TROKNIVES, 2026. Chipper knives (wood chip production). Online 10.5.2026. Available at: https://www.troknives.com/Products/Knives-for-recycling/chipper-knives-wood-chip-production
10. PILANA®, 2026. Bruks chipper knives (blades). Online 10.5.2026. Available at: https://www.pilanagroup.com/en/wood-industry/wood-chipping/bruks/bruks-chipper-knives.html
11. BELLO, R., S., ONILUDE, A., M., 2011. Force Relations and Dynamics of Cutting Knife in a Vertical Disc Mobile Wood Chipper. Leonardo Electronic Journal of Practices and Technologies Issue 18, p. 17-34, ISSN 1583-1078.

12. KRILEK, J., TICHÝ, B., KOVÁČ, J., MELICHERČÍK, J., AND KUVIK, T., 2021. Design of a stationary disc chipper project for dendromass chipping with stress analysis FEM methods. BioResources 16(4), 8205-8218.
13. *CEISUPPLY, 2026.* Online 10.5.2026. Available at: https://www.ceisupply.com/blog-the-science-behind-chipper-knife-design-what-makes-a-great-blade
14. BRENNDÖRFER, M., DREINER, K., KALTSCHMITT, M. and SAUER, N. 1994. Energtische Nutzung von Biomasse, Kuratorium für Technik und Bauwesen in der Landwirtschaft (KTBL), Darmstadt, 149 p.
15. https://virgamet.pl/oferta/1-2360-x48crmov811-stal-narzedziowa - access date 10.05.2026
16. Solidworks material base.

TalentDetector

7th-9th June 2026
Gliwice-Brenna, Poland

DEPARTMENT OF ENGINEERING MATERIALS AND BIOMATERIALS
FACULTY OF MECHANICAL ENGINEERING
SILESIAN UNIVERSITY OF TECHNOLOGY

INTERNATIONAL STUDENTS SCIENTIFIC CONFERENCE

Design of the electrode positioning system and selection of the power supply for a laboratory arc furnace

Łukasz Piecha [a], Maurycy Frydecki [b], Mateusz Konsek [b], Patryk Sobota [c], Mateusz Liszka [d], Mariusz Król [e], Vojtěch Macejko [f], Řezníček Daniel [f]

[a] Silesian University of Technology, Faculty of Automatic Control, Electronics and Computer Science, Automatic Control and Robotics, Gliwice, Poland
[b] Silesian University of Technology, Faculty of Mechanical Engineering, Industrial Mechatronics, Gliwice, Poland
[c] Silesian University of Technology, Faculty of Electrical Engineering, Computer Science in Electronic Systems and Circuits, Gliwice, Poland
[d] Silesian University of Technology, Faculty of Mechanical Engineering, Mechanical Engineering - Dual Studies, Gliwice, Poland
[e] Silesian University of Technology, Faculty of Mechanical Engineering, Department of Engineering Materials and Biomaterials, Gliwice, Poland
[f] The Department of Machining, Assembly and Engineering Metrology Faculty of Mechanical Engineering, VSB - Technical University of Ostrava, Ostrava, Czech Republic
e-mail: mariusz.krol@polsl.pl

Abstract: The article presents an interdisciplinary design process of a laboratory arc furnace. The main goal of the work was to develop a concept for a mechatronic manipulation system for precise electrode positioning and to select an optimal high-power supply source. As part of the work, a 3D CAD model was created, and the system's kinematic and thermal assumptions were analysed. An analytical and experimental verification of the adaptation of a toroidal transformer into a current source was also carried out. Physical tests revealed critical geometric limitations of the core window and mechanical issues with the wires, leading to the rejection of this concept in favour of adopting an industrial welding transformer.

Keywords: laboratory arc furnace, mechatronic system, kinematics, high-current transformer, CAD prototyping, power supply.

1. INTRODUCTION

Electrometallurgical processes carried out in arc furnaces require precise control of many physical parameters. The stability of the ignition and maintenance of the electric arc depends mainly on two factors: a reliable power source with appropriate characteristics and a precise electrode positioning system relative to the charge. Errors in mechanical control or power supply

instability can cause arc breakage, short circuits, or an uneven temperature distribution in the crucible.

The purpose of this article is to present the interdisciplinary design process of a laboratory arc furnace. The study includes the concept of a mechatronic manipulation system and the analytical-experimental verification of the selection of a high-power supply source. The article presents the design path from preliminary assumptions and modelling in the CAD environment, through verification tests of the construction limitations of toroidal transformers, to the selection of the optimal power supply solution [1-8].

2. CONCEPT AND DESIGN OF THE MECHATRONIC POSITIONING SYSTEM

The designed mechatronic station features a modular structure based on a supporting frame made of V-slot aluminium profiles and welded steel profiles, ensuring adequate system rigidity. The workspace was defined around the crucible casing, made of fireclay brick to ensure optimal thermal insulation, which is illustrated in Figure 1.

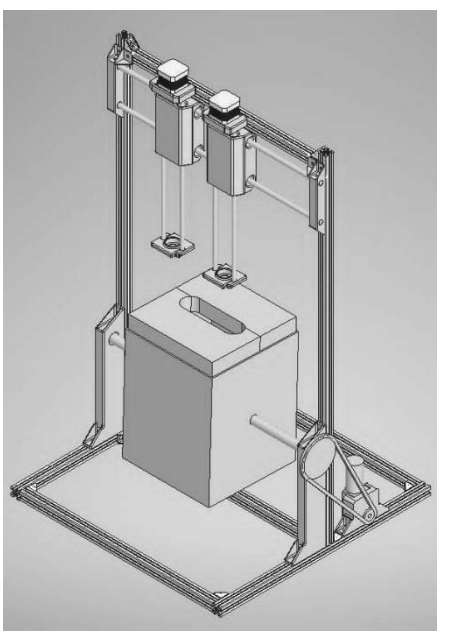

Figure. 1. 3D CAD spatial model of the laboratory station's supporting structure and crucible casing.

2.1. Kinematics and drive system

The electrode positioning and charge manipulation system is based on the coordinated action of five independent drive axes. Movement in the vertical axis (Z) is carried out independently for each electrode using NEMA 17 stepper motors integrated with trapezoidal screws. The stability of this mechanism, with an assumed maximum electrode stroke of 330 mm, is ensured by four linear ball bearings moving along two guide shafts for each side. To regulate the horizontal spacing of the electrodes, a rack-and-pinion mechanism driven by a Waveshare 22414 servomotor with a high torque of 40 kg·cm was used, which guarantees their symmetrical movement away from the central axis of the crucible to a distance of at least 130 mm. The tilt

angle of the electrodes in the theoretical range of 0 to 45 degrees is regulated by two independent PowerHD HD-1501MG servomotors with a torque of 17 kg·cm, which allows for optimal arc focusing relative to the charge level. The final axis is the crucible rotation mechanism driven by a 12 V DC motor with a worm gear and an additional chain transmission with a ratio of approximately 3:1. To eliminate undesirable bending moments, the drive shaft of this system was welded exactly in the geometric center of the crucible base. The applied gearmotor has a nominal torque of 25 kg·cm at 15 rpm and a holding torque with a locked rotor of 75 kg·cm. The motion system are presented in the kinematic diagram in Figure 2.

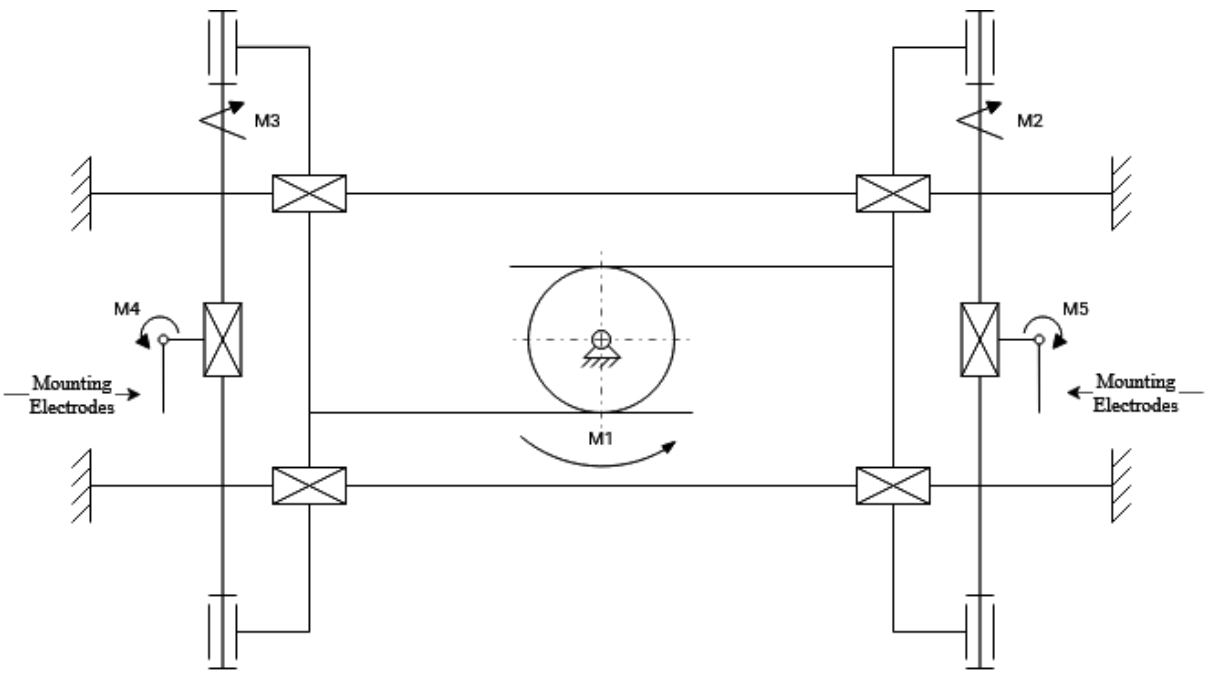

Figure. 2. Kinematic diagram of the mechatronic mechanism for electrode positioning.

2.2. Material selection and thermal aspects

Due to the specific operation of the arc furnace, a key design aspect was selecting appropriate materials resistant to temperature gradients. Structural and connecting elements exposed to lower temperatures were designed to be manufactured using FDM additive technology from ASA polymer, characterised by high resistance to UV radiation and environmental conditions. In zones with increased thermal risk near the crucible, a print made from an advanced PA6-CF composite (polyamide doped with carbon fibre) was used, providing dimensional stability and a thermal barrier for mechanical components. The flow of working current to the electrodes was realised using industrial universal terminals 35-240 mm², adapted for voltages up to 1000 V and continuous currents up to 425 A.

3. DESIGN AND ANALYSIS OF THE HIGH-POWER SUPPLY SYSTEM

The power supply system is a critical component of the arc furnace, ensuring stable ignition and the maintenance of the electric arc. In the design process, several concepts for the current

source were analysed, with each evaluated for feasibility, electrical parameters, and ease of implementation.

3.1. Analytical and experimental verification of toroid design limitations

In the initial phase of the project, the adaptation of an off-the-shelf toroidal transformer with external dimensions of 170 mm, a height of 110 mm, and an internal window diameter of 70 mm was assumed. It was assumed to make 16 turns using a bundle consisting of 16 parallel DN2E type wires with a diameter of d = 2.12 mm.

To verify the technological assumptions, an attempt was made to wind a test bundle, reduced to 14 wires. Empirical tests revealed significant discrepancies between the theoretical copper cross-section and the actual dimensions of the bundle. Physical measurements showed that the formed bundle reached an outer diameter of 12-13 mm. This is due to wire crossovers, the thickness of the enamel insulation, and natural empty air spaces.

Verification of the internal circumference of the transformer window, approximately 220 mm, revealed a critical geometric collision. An attempt to lay 16 turns would require a space of over 200 mm, which constitutes more than 90% of the available internal circumference on the core itself, making it physically impossible to execute the winding. Additionally, the technological test showed significant mechanical problems. The bundle was extremely stiff, which prevented it from adhering closely to the core, leading to an undesirable increase in leakage inductance. These results forced a change in the power supply concept.

3.2. Analysis of alternative solutions and selection of the target power source

In response to the identified geometric and mechanical limitations of the original project, two alternative approaches to the construction of the power source were analyzed. The first concept assumed changing the core to a larger one and using copper flat bars instead of round wire bundles. This solution maximizes the copper fill factor in the transformer window and eliminates empty spaces, which positively affects the stiffness of the source's characteristics. Nevertheless, machining a thick flat bar in workshop conditions is technologically demanding, and the risk of edge deformation and insulation damage would pose a serious threat.

The second option was the adaptation of an industrial welding transformer, for example, the Bester 1500 type. Such an approach, based on the reuse of existing equipment, directly implements the principles of eco-friendly design and sustainable development. Welding transformers have windings factory-adapted to high current densities, and their key advantage is a built-in current regulation mechanism using a magnetic shunt, facilitating arc stabilization. The only disadvantage of this solution is the larger dimensions and total mass of the system compared to toroidal transformers.

Based on the multi-criteria analysis conducted, it was decided to implement the concept based on the welding transformer. This solution completely eliminates the risk of error when manually executing high-current windings and drastically simplifies the implementation of the power supply, allowing the main design work to focus on the development of proprietary control electronics and the integration of the machine's complex kinematics.

4. CONCLUSIONS

Designing a laboratory arc furnace required the strict integration of issues across mechanics, electronics, and materials engineering. The developed mechatronic drive system and the conscious selection of the heat-resistant PA6-CF composite ensure precision in shaping the electric arc geometry and the stability of the entire structure. Experimental tests conducted on the toroidal core showed that pure theoretical calculations are insufficient when designing high-current circuits, because the physical stiffness of thick wires and the spatial limitations of the internal window constitute a critical technological barrier. Therefore, the adaptation of an industrial welding transformer was considered the optimal solution, as it guarantees operational safety and significantly simplifies the control of the furnace's current parameters.

ACKNOWLEDGEMENTS

This work was carried out as part of a PBL project under the XIV competition of the Initiative of Excellence – Research University program at the Faculty of Mechanical Engineering, Silesian University of Technology.

BIBLIOGRAPHY

[1] Hering M., Podstawy elektrotermii, Wydawnictwa Naukowo-Techniczne (WNT), Warszawa, 1998.
[2] Jezierski E., Transformatory: budowa i projektowanie, Wydawnictwa Naukowo-Techniczne (WNT), Warszawa, 1983.
[3] Olszewski M. (red.), Podstawy mechatroniki, Wydawnictwa Naukowo-Techniczne (WNT), Warszawa, 2006.
[4] Schmid S.R., Kalpakjian S., Manufacturing Engineering and Technology, Pearson, 2013.
[5] Kurbiel A., Urządzenia i instalacje elektrotermiczne, Wydawnictwo AGH, Kraków, 2011.
[6] HD-1501MG Servo Specifications, https://servodatabase.com/servo/power-hd/hd-1501mg, 2026.
[7] Waveshare 22414, https://www.waveshare.com/st3215-servo.htm, 2026.
[8] JK42HS40-0504, https://datasheet4u.com/datasheets/ETC/JK42HS/1380131, 2026.

TalentDetector

7th-9th June 2026
Gliwice-Brenna, Poland

DEPARTMENT OF ENGINEERING MATERIALS AND BIOMATERIALS
FACULTY OF MECHANICAL ENGINEERING
SILESIAN UNIVERSITY OF TECHNOLOGY

INTERNATIONAL STUDENTS SCIENTIFIC CONFERENCE

Printed auxetic materials

Jakub Pluskota[a], Anna Kloc-Ptaszna[b]

[a] Student of Silesian University of Technology, Faculty of Mechanical Engineering, Konarskiego 18A, 44-100 Gliwice, Poland
email: jp307654@student.polsl.pl
[b] Silesian University of Technology, Faculty of Mechanical Engineering, Department of Engineering Materials and Biomaterials, Konarskiego 18A, 44-100 Gliwice, Poland
email: anna.kloc@polsl.pl

Abstract: This article, based on an engineering thesis, investigates and compares the structures of auxetic materials to determine their influence on the mechanical properties of 3D-printed specimens. The scope of work included the design and modelling of auxetic and standardized specimens, their additive manufacturing, static tensile testing to evaluate mechanical properties, and structural examination using light microscopy.

Keywords: auxetic materials, re-entrant, honeycomb, 3D-printing, FDM method, mechanical properties, structure

1. INTRODUCTION

Auxetic materials belong to a group of mechanical metamaterials with unique properties that distinguish them from conventional industrial materials. A key characteristic of these materials is their negative Poisson ratio (NPR), which results in expansion (rather than contraction) in the transverse direction when stretched. First described by Lakes [1], auxetic structures have undergone continuous development. Figure 1 illustrates the difference between materials with positive and negative Poisson ratios during tensile loading [1–5].

Over the years, various auxetic geometries have been proposed and tested for mechanical performance, such as load-bearing capacity and energy absorption. Common types include re-entrant (RE), chiral, and anti-chiral structures, as well as rotating polygons. These can be implemented in two- and three-dimensional configurations [2,3,6-9].

Auxetic structures are primarily fabricated from polymers and metals. Frequently used thermoplastics include ABS, ASA, PLA, and PETG [2,10–15]. Additive manufacturing (AM) is the preferred production method due to its precision in reproducing complex geometries. Fused Deposition Modelling (FDM), which involves extruding layer by layer melted plastic filament, is widely utilized [2,10,16]. Applications span several sectors, including the automotive, aerospace, and biomedical industries [2,10].

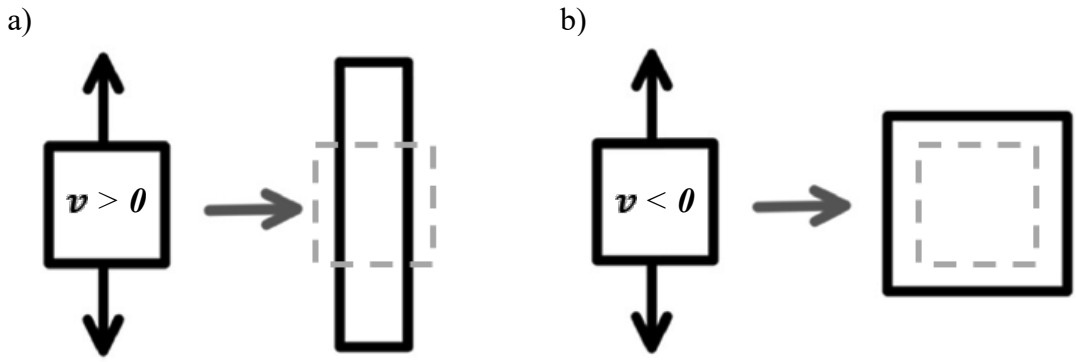

Figure 1. Uniaxial tensile testing of a material a) with a positive Poisson's ratio, b) with a negative Poisson's ratio [2,5].

2. MATERIALS AND METHODOLOGY

The investigation focused on auxetic and standardised specimens produced via 3D printing using an original Prusa i3 printer. ABS+ polymer filament (ROSA3D filaments) was used, with the following parameters: 1.75mm diameter, extrusion multiplier of 1, and a density of 1.08 g/cm³.

A static uniaxial tensile test on standardised and auxetic specimens, aimed at determining their mechanical properties, was carried out on a Zwick Roell Z020 testing machine. The initial test force was 5 N. The test speed was 5 mm/min for most specimens. The force cut-off threshold was 80% of the maximum force F_{max}, and the force threshold for fracture detection was 0.1% of the nominal force F_{nom}. The dimensions of the reference sample are shown in Figure 2. Three auxetic geometries (Figure 3) were designed based on Tang et al. [17] with custom modifications:

1. RAH: Re-entrant Auxetic Honeycomb (base geometry);
2. ARH: Arc-shaped Re-entrant Honeycomb;
3. ERH: Elliptic-profile Re-entrant Honeycomb.

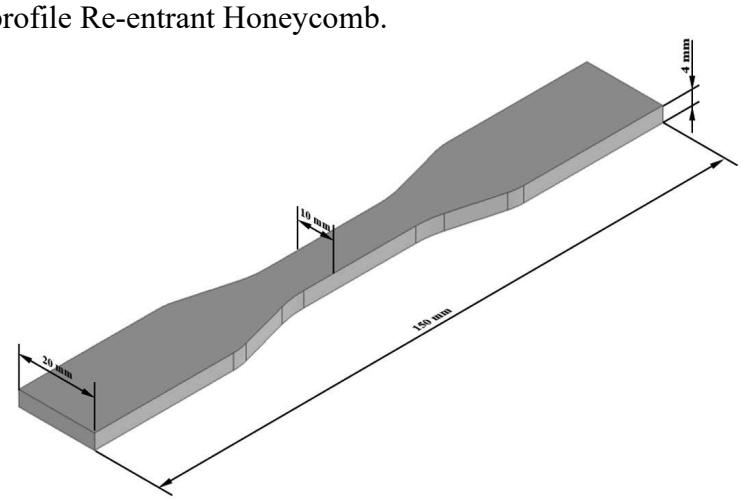

Figure 2. The dimensions of the reference sample [2].

Models were created using Autodesk Inventor Professional 2025. Due to the limitations of the construction plate, the specimens were scaled by a factor of 0.39. A layer height of 0.2 mm was maintained for all prints. Standardised samples were modelled as Type 1B moldings according to ISO 527-2:2025 [18]. Table 1 present the cell geometries and dimensions.

Table 1. Dimensions of the designed auxetic cells [mm].

Cell geometry	H	H_0	H_1	W		T	L_1	L_2	l_1	l_2
RAH	300	40	380	149.5		10	29.9	20	18.5	18
ARH										
ERH										
Cell geometry	g_1	g_2	d	φ [°]	r_1	r_2	r_3	r	a	b
RAH	1	1.5	5.7	75	0.2	2	2	-	-	-
ARH				-		-	1	15.7	-	-
ERH				-		-	1	-	15.7	19.885

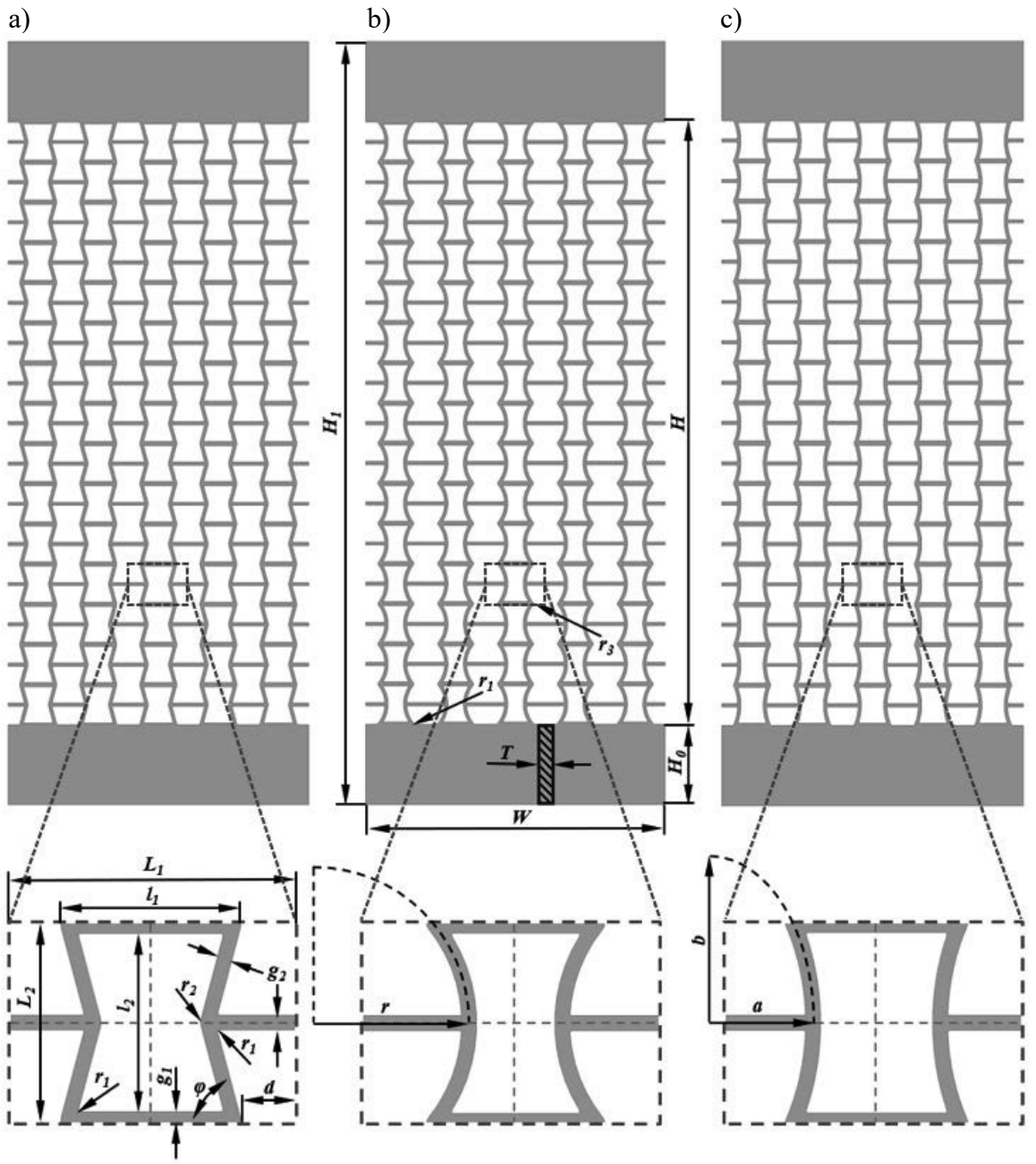

Figure 3. Designed auxetic samples: a) RAH, b) ARH, c) ERH [2].

3. RESULTS AND DISCUSSION

3.1. Base Material Properties

The mechanical properties of the bulk ABS+ material were first established. As shown in Table 2 and Figure 4, the material exhibited a tensile strength (R_m) of 30.86 MPa, a maximum force (F_m) of 1.23 kN and a strain at break (ε) of 14.57%.

Table 2. Average mechanical properties of ABS+ bulk material.

Material	Tensile strength R_m [MPa]	Strain ε [%]	Maximum force F_m [kN]
ABS+	30.86	14.57	1.23

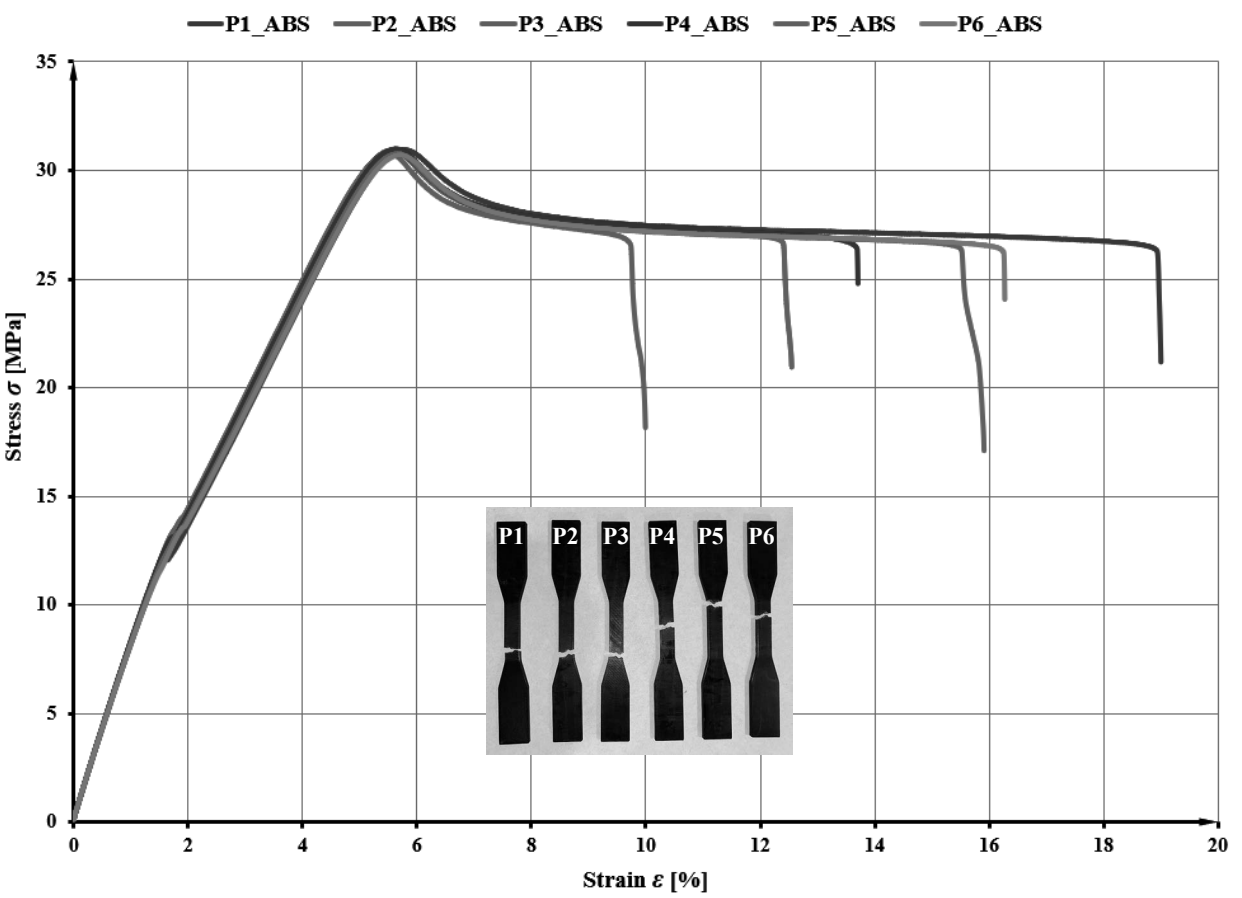

Figure 4. Stress-strain curve for samples made of ABS+ [2].

3.2. Auxetic Specimen Performance

The mechanical performance of the auxetic specimens is summarised in Table 3 and Figure 5. The results indicate that cell geometry significantly influences the mechanical response.

The ERH geometry achieved the highest maximum force (F_m = 0.34 kN), representing a significant improvement over the base RAH geometry (F_m = 0.24 kN). The ARH configuration showed intermediate performance (F_m = 0.28 kN). In particular, ERH samples showed the lowest strain (ε = 2.23%), while ARH specimens showed the highest ductility (ε = 2.78%).

Visual analysis during testing confirmed the auxetic effect; The samples underwent transverse expansion under tension, validating the negative Poisson ratio.

Table 3. Average mechanical properties of auxetic specimens.

Cell geometry	Material	Strain ε [%]	Maximum force F_m [kN]
RAH	ABS+	2.28	0.24
ARH		2.78	0.28
ERH		2.23	0.34

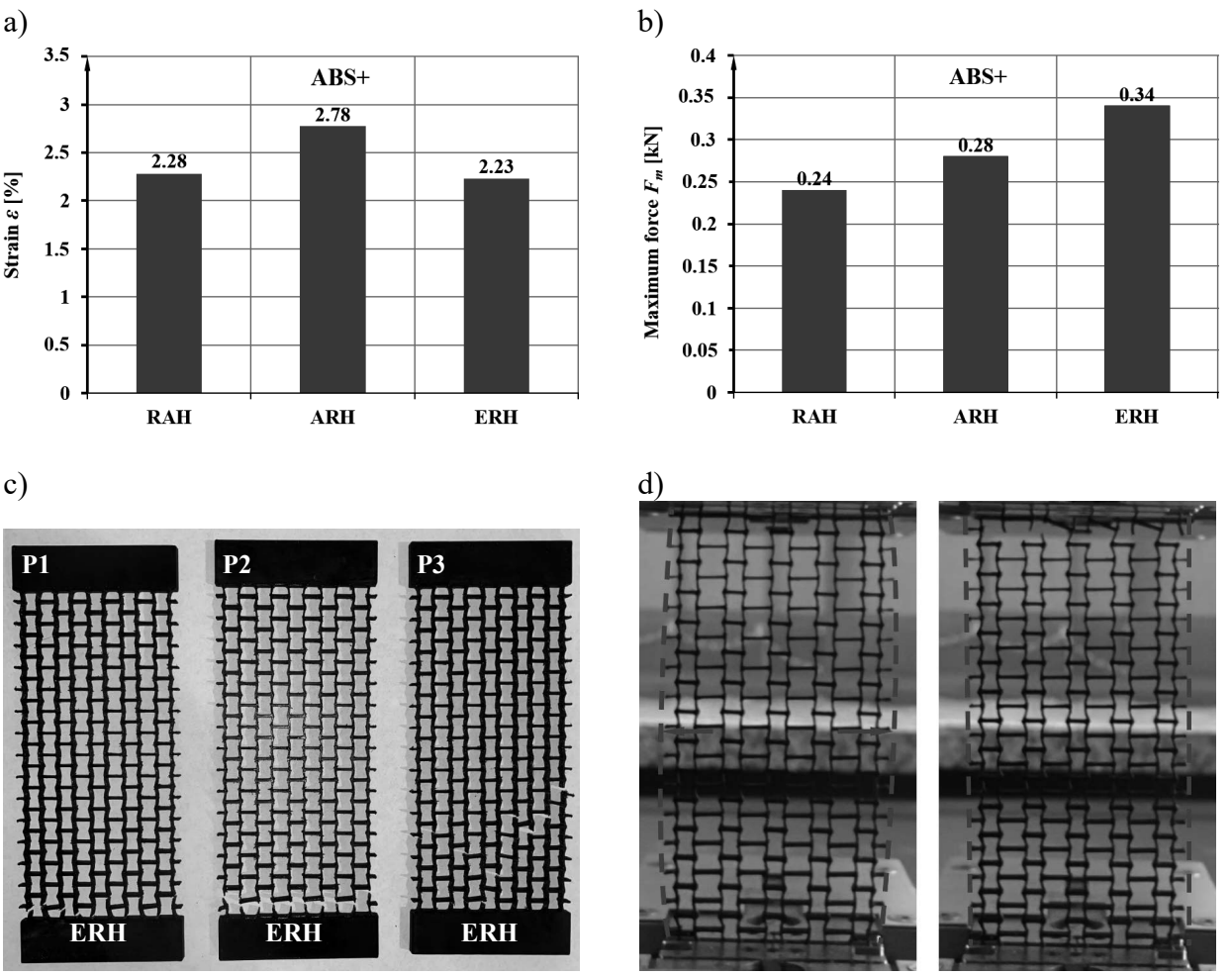

Figure 5. Bar chart showing the average values for auxetic specimens: a) strain ε, b) maximum force Fm, c) ERH geometry specimen after tensile testing, d) ARH auxetic specimen just before and after failure [2].

3.3. Microstructural Analysis

Light microscopy (Figure 6) allowed the verification of geometric accuracy and failure modes. Specimens after testing showed evidence of brittle ductile fracture, tearing, and localized bending of the cell struts.

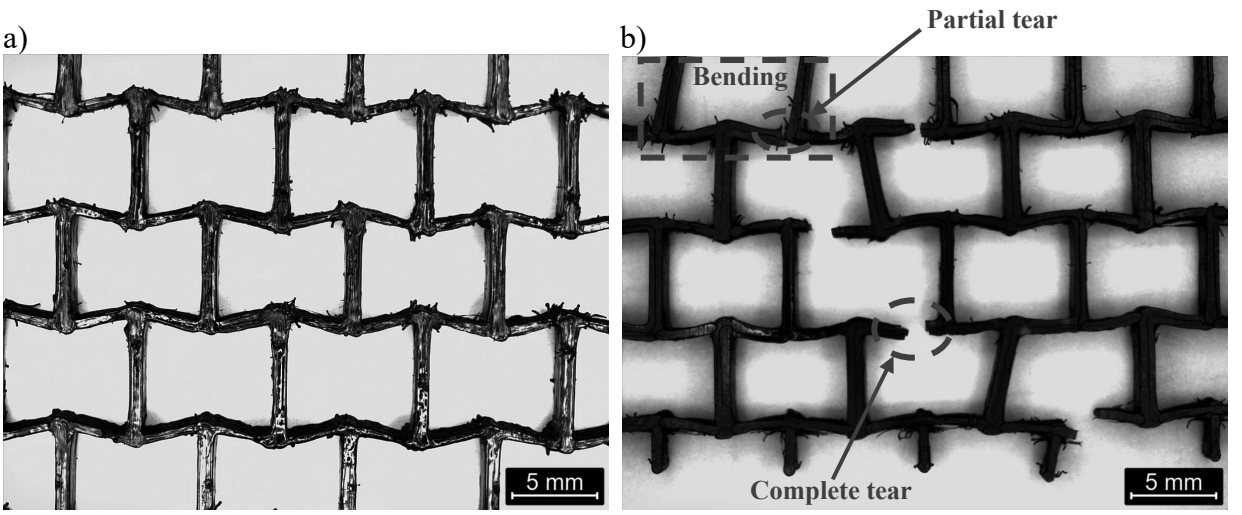

Figure 6. Sample, magnification ×10: a) RAH before stretching, b) ERH after stretching [2].

4. CONCLUSIONS

Static tensile testing confirmed that the geometry dictates the mechanical properties of the auxetic metamaterials. The ERH geometry provided the highest load-bearing capacity (F_m = 0.34 kN).

Modifying the traditional RAH geometry by introducing elliptical (ERH) or circular (ARH) profiles reduces stress concentrations at the re-entrant corners. This stress redistribution improves the overall strength of the structure, consistent with findings in the literature [17,19].

All tested geometries exhibited a clear auxetic effect (transverse expansion), confirming their functionality as negative Poisson ratio materials.

Microscopic analysis revealed failure mechanisms such as strut rupture and bending, which are critical to understanding the limits of 3D printed auxetic components.

BIBLIOGRAPHY

1. R. S. Lakes, Deformation mechanisms in negative Poisson's ratio materials: structural aspects, Journal of Materials Science, 26 (1991) 2287–2292.
2. J. Pluskota, Porównanie struktury i własności mechanicznych drukowanych materiałów auksetycznych, Praca inżynierska, Wydział Mechaniczny Technologiczny, Politechnika Śląska, Gliwice, 2026.
3. R. Hasanzadeh, S. Jolaiy, M. Mojaver, T. Azdast, C. B. Park, Auxetic 3D printed metastructure stents for enhanced mechanical and structural performance and biocompatibility in coronary artery treatments, Acta Biomaterialia 202 (2025) 641–659.

4. P. Roberjot, J. L. Herder, A unified design method for 2D auxetic metamaterials based on a minimalauxetic structure, International Journal of Solids and Structures 295 (2024) 112777.
5. T. Marotta , M. Vlasea , S. McLachlin, Applications of auxetic structures in orthopaedics: A scoping review, Bioprinting 44 (2024) e00375.
6. M. Lorenzo, Auxetic structures: towards bending-active architectural applications, Politecnico di Milano, 2015, Mediolan.
7. W. Beluch, M. Hatłas, J. Ptaszny, A. Kloc-Ptaszna, Computational Homogenisation and Identification of Auxetic Structures with Interval Parameters, Materials, 2025, 18(19), 4554.
8. C. Lu, M. Hsieh, Z. Huang, C. Zhang, Y. Lin, Q. Shen, F. Chen, L. Zhang, Architectural Design and Additive Manufacturing of Mechanical Metamaterials: A Review, Engineering 2022, 17, 44–63.
9. W. T. Nugroho, Y. Dong, A. Pramanik, M. C. P. Selvan, Z. Zhang, S. Ramakrishna, Additive manufacturing of re-entrant structures: Well-tailored structures, unique properties, modelling approaches and real applications, Additive Manufacturing, 2023, 78, 103829.
10. M. Periyasamy, N. Srinivasan, A review on auxetic structures: Applications, properties, classifications, finite element analysis, manufacturing methods, and selective laser melting process parameters, Results in Engineering 28 (2025) 107660.
11. M. Sadeghzade, A. Dadashi, H. Gharehbaghi, Mechanical behavior, process innovations, and future directions of 3d-printed continuous fiber-reinforced polymeric lattice structures: A comprehensive review, Materials & Design 260 (2025) 114970.
12. R. A. Gomes, L. A. de Oliveira, M. B. Francisco, G. F. Gomes, Tubular auxetic structures: A review, Thin-Walled Structures 188 (2023) 110850.
13. Z. Chen, Z. Li, J. Li, C. Liu, C. Lao, Y. Fu, C. Liu, Y. Li, P. Wang, Y. He, 3D printing of ceramics: A review, Journal of the European Ceramic Society 39 (2019) 661-687.
14. J. S. Hu, B. L. Wang, J. E. Li, K. F. Wang, Thermal shock resistance behavior of auxetic ceramic honeycombs with a central crack or an edge crack, Ceramics International 46 (2020) 11835-11845.
15. D. Jiang, H. Thissen, T. C. Hughes, K. Yang, R. Wilson, A. B. Murphy, V. Nguyen, Advances in additive manufacturing of auxetic structures for biomedical applications, Materials Today Communications 40 (2024) 110045.
16. W. T. Nugroho, Y. Dong, A. Pramanik, M. C. P. Selvan, Z. Zhang, S. Ramakrishna, Additive manufacturing of re-entrant structures: Well-tailored structures, unique properties, modelling approaches and real applications, Additive Manufacturing, 2023, 78, 103829.
17. T. Yuxin, P. L. Hien, Z. Yifeng, L. Rong, Enhanced tensile performance and energy absorption in elliptic-profile re-entrant honeycombs, International Journal of Mechanical Sciences 304 (2025) 110708.
18. ISO 527-2:2025, Plastics — Determination of tensile properties, Part 2: Test conditions for moulding and extrusion plastics, International Organization of Standardization, Geneva, Switzerland, 2025.
19. Y. Schneider, V. Guski, S. Schmauder, J. Kadkhodapour, J. Hufert, A. Grebhardt, C. Bonten, Deformation Behavior Investigation of Auxetic Structure Made of Poly(butylene adipate-co-terephthalate) Biopolymers Using Finite Element Method, Polymers 2023, 15, 1792.

TalentDetector
7th-9th June 2026
Gliwice-Brenna, Poland
DEPARTMENT OF ENGINEERING MATERIALS AND BIOMATERIALS
FACULTY OF MECHANICAL ENGINEERING
SILESIAN UNIVERSITY OF TECHNOLOGY
INTERNATIONAL STUDENTS SCIENTIFIC CONFERENCE

Occupational health and safety at a laboratory workstation for electrochemical coating deposition

Michał Podgórski[a], Monika Spilka[b]

[a] Student, Silesian University of Technology, Faculty of Mechanical Engineering, Department of Engineering Materials and Biomaterials
[b] Silesian University of Technology, Faculty of Mechanical Engineering, Department of Engineering Materials and Biomaterials
email: monika.spilka@polsl.pl

Abstract: This article concerns the provision of occupational health and safety at a laboratory workstation for electrochemical coating deposition. Hazards were identified and an occupational risk assessment was carried out using the JSA method.

Keywords: occupational health and safety, laboratory workstation, electrochemical coating deposition, occupational risk assessment

1. INTRODUCTION

Ensuring occupational health and safety (OHS) is one of the key elements influencing the organization of work in modern enterprises. Its primary goal is to protect the life and health of employees, as well as to reduce and eliminate occupational risks that may occur in the work environment [1].

Occupational health and safety is a system of technical, organizational and social solutions regulated by law, the aim of which is to protect employees from hazards occurring in the work environment. According to the definition of the Central Institute for Labor Protection - National Research Institute (CIOP-PIB), occupational health and safety covers all conditions that should be met in an enterprise so that employees can perform their duties safely, without negative impact on health. [2].

In Poland, ensuring occupational health and safety is regulated by a legal system comprising constitutional and statutory provisions and implementing acts. The right to safe and hygienic working conditions is guaranteed to every employee by Article 66, paragraph 1 of the Constitution of the Republic of Poland [3]. Detailed obligations of the employer in the field of occupational health and safety are specified in Section X of the Labour Code, according to which the employer is obliged, among others, to ensure safe and hygienic working conditions, conduct occupational risk assessment and organize occupational health and safety training for employees [4].

An important element of the occupational health and safety system is occupational risk assessment, which involves the systematic identification of hazards occurring in the workplace, the analysis of the possible consequences of their impact, and the determination of the probability of their occurrence. The purpose of occupational risk assessment is to undertake preventive and protective measures aimed at eliminating hazards or reducing them to an acceptable level [5].

2. CHARACTERISTICS OF THE ELECTROCHEMICAL COATING DEPOSITION WORKSTATION INCLUDING HAZARDS IDENTIFICATION

The electrochemical metal coating deposition workstation, used for research and educational purposes, was analyzed. The coating deposition process includes surface preparation operations involving grinding, degreasing and etching. Then, the actual electrochemical treatment is carried out, during which the element is immersed in a properly prepared electrolyte, enabling the controlled deposition of the metallic coating. Between each operation, rinsing is carried out to remove residual chemicals and ensure the cleanliness of the workpiece surface. The workstation is equipped with, among other things, galvanic baths, heating plates, local exhaust hoods, devices for measuring current parameters, a precision scale, and the necessary laboratory glassware.

A person working at the analyzed workstation is exposed to many hazards related to the electrochemical coating deposition process, as presented in Table 1.

Table 1. Hazards at the electrochemical coating deposition workstation

Hazards category	Type of hazard	Location of the hazard (source of the hazard)	Possible consequences of the hazard
Dangerous	Wet and slippery floor	Laboratory room, open laboratory beakers	Injury, absence from work, first aid treatment
	Electric current	Laboratory room, electrical equipment	Death, body burns, absence from work, first aid treatment
	Hot surfaces	Laboratory room, heating plates	Injury, absence from work, first aid treatment
	Flammable solvents	Laboratory room	Death, body burns, absence from work, first aid treatment
	Explosion hazard	Laboratory room	Death, body burns, absence from work, first aid treatment
	Cuts, lacerations	Laboratory room	Injury, first aid treatment
Harmful	Noise	Laboratory room, local exhaust ventilation	Absence from work, headaches, fatigue, hearing disorders, first aid treatment
	Corrosive and toxic substances (sulfuric acid, hydrochloric acid, chromium(VI) compounds, nitric acid, sodium cyanide, potassium cyanide, ammonia)	Laboratory room	Skin and eye burns, allergies, carcinogenic and mutagenic effects, absence from work, first aid treatment

	Electrolytic mist vapors (sulfuric acid, hydrochloric acid, nickel, cadmium, chromium)	Laboratory room, electroplating baths	Irritation of the mucous membranes, upper respiratory tract diseases, headaches, carcinogenic effects, allergic reactions, nausea, absence from work, first aid treatment
	Contact with solvents (methanol, ethanol)	Laboratory room	Skin irritation, nausea, vomiting, headaches, absence from work, first aid treatment
	Heavy metal salts (nickel, copper, chromium(VI), cadmium)	Laboratory room	Allergic reactions, poisoning, carcinogenic effects, nausea, vomiting, headaches, absence from work, death, first aid treatment
	Metal dusts	Laboratory room, samples preparation	Respiratory irritation, allergic reactions, absence from work, first aid treatment
Burdensome	Standing work position	Laboratory room	Absence from work, musculoskeletal disorders, first aid treatment
	The need to bend down	Laboratory room	Absence from work, back pain, overload of the back and neck muscles, development of posture defects, first aid treatment
	Stress	Laboratory room	Decreased concentration, sleep disturbances, irritability, burnout, absence from work
	The need to remain highly concentration	Laboratory room	Mental fatigue, risk of mistakes, absence from work
	Monotony	Laboratory room	Decreased attention, risk of mistakes, absence from work
	Time pressure	Laboratory room	Errors, risk of accidents, absence from work
	The need to use personal protective equipment	Laboratory room	Mental fatigue, discomfort
	Unpleasant smell	Laboratory room	Mental fatigue, discomfort

3. OCCUPATIONAL RISK ASSESSMENT USING THE JOB SAFETY ANALYSIS METHOD

The occupational risk assessment at the analyzed workstation was carried out using the Job Safety Analysis (JSA) method, in accordance with the developed methodology [6], which defines the risk of an incident based on three parameters: the frequency of hazard occurrence (F), the ability to avoid or limit damage (A) and the probability of event occurrence (O). The parameters take values from 1 to 5, and their sum determines the probability of the consequence of the event (P). Another value taken into account in risk estimation using this method is the consequence of the event (C) defined in four classes. Risk valuation is performed after parameter estimation and is read from the risk matrix presented in Table 2.

Table 2. Risk matrix in the JSA method [6]

The JSA method – risk valuation					
Consequence class – C	Probability of the consequences – P				
	3-4	5-7	8-10	11-13	14-15
C1	1	2	3	4	5
C2	2	3	4	5	6
C3	3	4	5	6	7
C4	4	5	6	7	8

Three risk levels are defined: 1-2 – negligible risk; 3-5 – acceptable risk; 6-8 –unacceptable risk.

For each identified hazard, values were assigned to the parameters of the frequency of hazard occurrence, probability of event and possibility of avoiding or limiting damage. Then, the probability of consequences was calculated and a consequence class was assigned, which is presented for selected hazards in Table 3.

Table 3. Occupational risk assessment using the JSA method at the electrochemical coating deposition workstation

Hazard	Frequency of hazard occurrence (F)	Probability of event occurrence (O)	Ability to avoid or limit damage (A)	Probability of event consequence (P)	Consequence class (C)
Wet and slippery floor	4 (once a week)	3 (imaginable)	2 (likely)	9 (acceptable risk)	C3 (prolonged inability to work)
Electric current	2 (once a year)	2 (unlikely)	2 (likely)	6 (acceptable risk)	C4 (death)
Hot surfaces	5 (daily)	4 (likely)	3 (possible)	12 (acceptable risk)	C2 (short inability to work)
Flammable solvents	3 (once a month)	2 (unlikely)	2 (likely)	7 (acceptable risk)	C3 (prolonged inability to work)
Explosion hazard	3 (once a month)	2 (unlikely)	2 (likely)	7 (acceptable risk)	C4 (death)
Cuts, lacerations	4 (once a week)	4 (likely)	3 (possible)	11 (acceptable risk)	C1 (not causing incapacity for work)
Noise	5 (daily)	5 (usually)	4 (unlikely)	14 (acceptable risk)	C1 (not causing incapacity for work)
Corrosive and toxic substances	5 (daily)	4 (likely)	2 (likely)	11 (unacceptable risk)	C3 (prolonged inability to work)

Electrolytic mist vapors	4 (once a week)	3 (imaginable)	2 (likely)	9 (acceptable risk)	C2 (short inability to work)
Contact with solvents	5 (daily)	4 (likely)	2 (likely)	11 (acceptable risk)	C2 (short inability to work)
Heavy metal salts	4 (once a week)	3 (imaginable)	2 (likely)	9 (acceptable risk)	C3 (prolonged inability to work)
Metal dusts	3 (once a month)	2 (unlikely)	2 (likely)	7 (acceptable risk)	C2 (short inability to work)
Standing work position	5 (daily)	5 (usually)	4 (unlikely)	14 (unacceptable risk)	C2 (short inability to work)
The need to bend down	5 (daily)	5 (usually)	3 (possible)	13 (acceptable risk)	C2 (short inability to work)
Stress	4 (once a week)	3 (imaginable)	2 (likely)	9 (acceptable risk)	C1 (not causing incapacity for work)
The need to remain highly concentration	4 (once a week)	3 (imaginable)	2 (likely)	9 (acceptable risk)	C1 (not causing incapacity for work)
Monotony	5 (daily)	3 (imaginable)	3 (possible)	11 (acceptable risk)	C1 (not causing incapacity for work)
Time pressure	4 (once a week)	4 (likely)	3 (possible)	11 (acceptable risk)	C1 (not causing incapacity for work)
The need to use personal protective equipment	5 (daily)	5 (usually)	4 (unlikely)	14 (acceptable risk)	C1 (not causing incapacity for work)
Unpleasant smell	4 (once a week)	4 (likely)	3 (possible)	11 (acceptable risk)	C1 (not causing incapacity for work)

Based on the risk matrix, the risk was determined and evaluated at three levels, as shown in Table 4.

Table 4. Risk level for hazards according to the analysis using the JSA method

Hazards	Risk level
no hazards identified	Negligible risk
wet and slippery floor; electric current; hot surfaces; flammable solvents; explosion hazard; cuts, lacerations; noise; electrolytic mist vapors; contact with solvents; heavy metal salts; metal dusts; the need to bend down; stress; the need to remain highly concentration; monotony; time pressure; the need to use personal protective equipment; unpleasant smell	Acceptable risk
corrosive and toxic substances; standing work position	Unacceptable risk

As a result of the assessment conducted using the JSA method, no hazards with a negligible level of risk were identified. The majority of workplace hazards are within the acceptable risk level group. Two hazards were classified as presenting an unacceptable level of risk, namely corrosive substances and a standing work position.

4. SUMMARY

At the analyzed laboratory workstation for deposition metallic coatings using the electrochemical method, the greatest risk is posed by contact with chemical substances and the dominant standing work position. For this reason, when developing the concept of a safe and ergonomic coating deposition workstation, attention should be focused on isolating the laboratory worker from hazardous factors and ensuring a more ergonomic body position during work. This would be possible through the use of automated robot arms, which allow for the safe and convenient control and execution of the process from behind a protective shield. Automating the process would make it possible to change the predominant standing position to a sitting position, which would reduce the strain on the musculoskeletal and circulatory systems that occurs during long-term work in a standing position.

BIBLIOGRAPHY

1. R. Dębkowski, Podstawy BHP, Wydawnictwo Politechniki Łódzkiej, Łódź, 2022.
2. D. Koradecka, Bezpieczeństwo i higiena pracy, Wydawnictwo Centralnego Instytutu Ochrony Pracy, Warszawa, 2008.
3. Konstytucja Rzeczypospolitej Polskiej z dnia 2 kwietnia 1997 r. (Dz.U. 1997 nr 78 poz. 483 z późn. zm.).
4. Ustawa z dnia 26 czerwca 1974 r. Kodeks pracy (Dz.U. 2023, poz. 1465 z późn. zm.).
5. I. Romanowska-Słomka, A. Słomka, Ocena ryzyka zawodowego, Wydawnictwo Tarbonus, Kraków, 2025.
6. https://www.bhpex.pl/bhp/ocena-ryzyka-zawodowego/metoda-jsa/

TalentDetector

23th-25th June 2025
Gliwice-Brenna, Poland

DEPARTMENT OF ENGINEERING MATERIALS AND BIOMATERIALS
FACULTY OF MECHANICAL ENGINEERING
SILESIAN UNIVERSITY OF TECHNOLOGY

INTERNATIONAL STUDENTS SCIENTIFIC CONFERENCE

Engineering solutions for the filament cooling system during its production on an extrusion machine

Andrii Polishchuk [a], Mirosław Bonek [b], Oleh Polishchuk [c], Serhii Matiukh [d], Svitlana Lisevich [e], Serhii Bobuch [f]

[a] Khmelnytskyi National University, Faculty of Mechanical Engineering, Transport and Architecture, Khmelnytskyi, Ukraine, email: andrepol215@gmail.com.
[b] Silesian University of Technology, Faculty of Mechanical Engineering, Department of Engineering Materials and Biomaterials, Gliwice, Poland , email: miroslaw.bonek@polsl.pl.
[c] Khmelnytskyi National University, Faculty of Mechanical Engineering, Transport and Architecture, Khmelnytskyi, Ukraine, email: opolishchuk7l@gmail.com.
[d] Khmelnytskyi National University, Faculty of International Relations and Law, Khmelnytskyi, Ukraine, email: matuh@khmnu.edu.ua.
[e] Khmelnytskyi National University, Faculty of Mechanical Engineering, Transport and Architecture, Khmelnytskyi, Ukraine, email: lisevichsv@gmail.com.
[f] Khmelnytskyi National University, Faculty of Engineering Mechanics, Khmelnytskyi, Ukraine email: bobukhs@gmail.com.

Abstract: This paper examines engineering solutions for the cooling system used during filament production on an extrusion machine. The study compares water-bath, air, and combined cooling concepts and justifies the choice of a compact forced-air system with four fans for stabilizing the filament after it exits the extrusion head. The proposed solution provides non-contact cooling, preserves filament geometry, and is well suited for compact extrusion equipment. The results show that controlled air cooling offers a practical balance between cooling efficiency, structural simplicity, and ease of maintenance.

Keywords: filament production; extrusion machine; cooling system; forced-air cooling; polymer extrusion; dimensional stability; heat transfer; extrusion head.

1. INTRODUCTION

Filament production for material-extrusion applications is a technologically complex process that combines polymer melting, pressure-driven flow through an extrusion head, strand formation, controlled cooling, dimensional stabilization, and winding. Each of these stages affects the final quality of the product, but the cooling stage is especially important because the filament leaves the die in a highly heated and mechanically unstable state, and therefore requires carefully controlled heat removal to preserve its geometry.

In modern extrusion practice, the quality requirements for filament are quite strict, because the product must have stable diameter, sufficient roundness, smooth surface, and predictable mechanical behavior during its subsequent use. Open-access studies on thermoplastic filament manufacturing show that deviations in cooling conditions may lead to ovality, dimensional instability, surface defects, or changes in material properties, all of which reduce the technological suitability of the filament [1].

The thermal state of the filament immediately after exiting the die determines how quickly the polymer solidifies and how uniformly internal temperature gradients are formed across its cross-section. If cooling is too slow, the strand may deform under its own weight, deviate from the desired path, or undergo unstable diameter variation. If cooling is too intensive, the outer layer may solidify much faster than the core, which can contribute to residual stresses and non-uniform shrinkage [2].

For this reason, the design of a filament cooling system is not only a question of heat transfer efficiency, but also a broader engineering task involving product stability, machine layout, and process controllability. The cooling zone must be coordinated with extrusion productivity, die geometry, take-up speed, and the overall dimensions of the machine. In compact extrusion systems, this requirement becomes even more significant because the designer must achieve sufficient cooling performance within a limited installation space.

Open-access engineering literature describes several cooling strategies used in polymer extrusion. The most common approaches include water-bath cooling, natural or forced air cooling, and combined systems in which different stages of heat removal are distributed along the extrudate path. The selection of a specific method depends on the material, the cross-sectional dimensions of the product, the required line speed, and the acceptable compromise between cooling intensity, simplicity of operation, and dimensional stability.

In the context of filament production on an extrusion machine, the search for a rational cooling solution is especially relevant for laboratory, educational, and compact manufacturing equipment. Such systems must remain structurally simple, easy to maintain, and reliable in operation, while still providing the thermal conditions necessary for stable production of filament with acceptable geometric accuracy. Therefore, the development and justification of engineering solutions for cooling the filament after extrusion is an important practical problem in the design of extrusion machines.

2. FORMULATION OF THE PROBLEM

The engineering problem is to choose a rational cooling system for a filament formed on an extrusion machine, ensuring stable heat removal after the die and preserving the required product shape. This issue is especially relevant for compact extrusion systems, where the cooling section must be integrated into a limited machine space.

The design objective is to justify an effective cooling solution for filament production on an extrusion machine, taking into account process compactness, cooling uniformity, ease of maintenance, and the need to avoid mechanical interaction with the still-soft polymer strand. Open-access studies confirm that the way heat is removed from the extrudate directly affects further process stability and product quality [3].

3. RESULTS AND DISCUSSION

Different engineering solutions can be used to remove heat from a filament immediately after it exits the die, and each of them offers a different balance between cooling intensity, machine complexity, and process controllability. In extrusion practice, the most widely known solutions are water-bath cooling, air cooling, and combined cooling systems. Their applicability depends on the material being processed, the required productivity, the dimensions of the product, and the structural limitations of the extrusion machine.

A water-bath cooling system is one of the most intensive methods of heat removal because water has significantly higher heat capacity and thermal conductivity than air. Studies on filament production indicate that water-bath temperature, the distance from the die to the cooling bath, and the cooling length can substantially affect filament roundness and other quality indicators. This means that water cooling can be highly effective, but only if the thermal regime and geometric configuration of the cooling section are selected properly [4].

At the same time, water-based systems have several practical disadvantages for compact extrusion equipment. They require additional structural elements, including a bath, guides, liquid containment, and often temperature control or circulation components. The presence of liquid in the production zone may also complicate maintenance and increase the number of operating factors that must be monitored during continuous filament production. In small machines, such systems may occupy too much space or make the layout more difficult.

Air cooling is another common engineering approach. In this case, heat is removed from the filament by convection between the polymer surface and the surrounding air, and the rate of heat transfer can be increased by forced airflow generated by fans. Compared with water cooling, air cooling is usually less intensive, but it is structurally much simpler, cleaner in operation, and easier to integrate into compact machines. For systems intended for educational laboratories, pilot lines, or small-scale manufacturing, this simplicity becomes a significant advantage [5].

The thermal efficiency of air cooling depends on several parameters, including air velocity, exposure length, orientation of the airflow relative to the filament, ambient temperature, and the temperature of the extrudate at the die exit. From an engineering standpoint, the main task is to provide sufficiently uniform convective cooling along the filament path so that the strand gradually loses heat without abrupt thermal gradients that could distort its shape. This is why multi-point airflow systems are often more rational than a single local air jet.

A combined cooling concept may also be considered. In such systems, one stage of cooling prepares the strand for subsequent stabilization, while another stage intensifies heat removal further downstream. For example, a filament may first pass through an air-cooling zone to avoid sudden deformation near the die and then enter a more intensive cooling medium. Research on polymer cooling shows that non-uniform thermal history leads to residual stresses, differential shrinkage, and shape instability, so the combined method can be useful when one cooling mechanism alone does not provide the required balance between stability and productivity.

For the extrusion machine considered in this work, the first element of interest is the extrusion head, through which the polymer melt leaves the machine and begins to form the filament. The geometry of this zone is important because it defines the initial cross-section of the strand and the starting thermal conditions for the cooling process. Immediately after leaving the die, the material is highly sensitive to external thermal influences and must be cooled in a controlled manner to preserve the required filament shape and direction of movement.

Fig. 1. Extrusion head.

After analyzing the possible variants, the most rational solution for the considered machine is a forced-air cooling system. This solution is shown in Fig. 2. The selected cooling unit consists of four fans arranged vertically along the path of the formed filament. These fans generate directed airflow that blows over the filament surface and removes heat by convection as the strand moves upward toward the take-up section. Such a design makes it possible to distribute the cooling effect over a certain distance rather than concentrate it in a single point.

Fig. 2. Cooling system of composite thread.

The choice of four fans is justified by several engineering considerations. First, multiple fans allow the cooling intensity to be distributed along the trajectory of the filament, which supports gradual solidification of the strand and reduces the risk of local overheating or sudden temperature drops. Second, a multi-fan system provides more flexibility in adjusting the thermal regime, since the designer may change fan performance, spacing, and orientation depending on

the extrusion conditions and polymer type. Third, the use of forced air avoids direct contact between the cooling medium and the polymer, which simplifies maintenance and preserves a dry operating environment.

An additional advantage of the selected solution is its compatibility with compact machine architecture. Unlike a water bath, the fan-based system can be mounted directly on the machine frame and does not require separate tanks or liquid handling units. This reduces the overall size of the installation and simplifies the integration of the cooling section into the full extrusion line. From the standpoint of machine design, such compactness is valuable because it makes the unit easier to manufacture, operate, and service.

The proposed cooling system also improves control over the filament formation process. Since the polymer strand cools progressively while moving through the airflow zone, the designer can achieve a more stable transition from melt to solid state. This gradual stabilization is important for controlling the final diameter and reducing the tendency of the filament to bend, oscillate, or deviate from the required path. Literature on polymer extrusion and cooling confirms that the thermal regime in the post-die zone plays a critical role in determining final product geometry and residual stress distribution.

Thus, in comparison with water-based and combined cooling concepts, the selected air-cooling system offers the most balanced solution for the considered extrusion machine. It is less complicated structurally, suitable for compact installation, easy to maintain, and capable of providing sufficient cooling performance for filament production when properly configured. For a machine of this type, where simplicity and operational convenience are important design criteria, the four-fan air system can be regarded as a rational and technically justified engineering solution.

As a summary of the adopted design solution, Fig. 3 shows the complete extrusion machine. The machine includes the housing with a heating system, the loading block, the filament cooling system, and the spool with filament. This overall arrangement demonstrates that the cooling system is not an isolated element, but an integrated part of the entire extrusion unit, ensuring the transition from melt extrusion to stable filament winding within one compact design scheme.

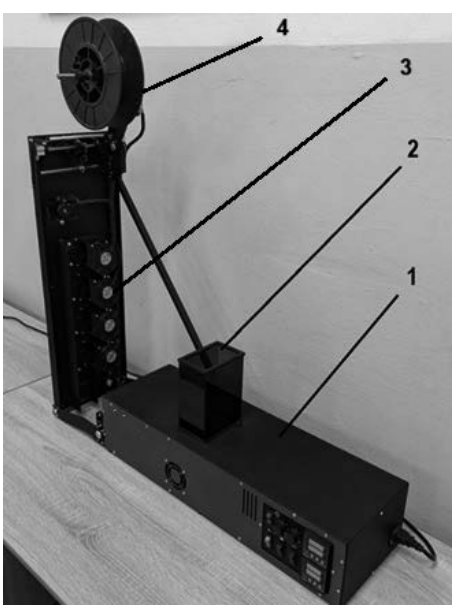

Fig. 3. Extrusion machine: 1 - housing with a heating system; 2 - loading block; 3 - filament cooling system; 4 - spool with filament

4. CONCLUSIONS

For the considered extrusion machine, the most rational solution is a forced-air cooling system with fans installed after the extrusion head. This system ensures effective non-contact cooling of the filament, is easy to integrate into a compact machine layout, and provides a practical engineering solution for stable filament production.

GRATITUDE

The publication is the result of cooperation within the Visegrad Scholarship Program 2025/2026.

Visegrad Fund

BIBLIOGRAPHY

1. Hardy, Patrick; Angermayer, Cole; Lokey, Rhett; Book, Rebeca; and Norton, Jeanne H., "Extrusion Production of 3D Printer Filament for Additive Manufacturing" (2019). Posters. 24. https://digitalcommons.pittstate.edu/posters_2019/24
2. Michelle M. A. Spanjaards, Martien A. Hulsen, Patrick D. Anderson. Numerical Study of Residual Stresses Due to External Cooling in Extruded Polymer Profiles. Macro-Molecular Theory and Simulations. 30 December 2021. https://doi.org/10.1002/mats.202100074Digital Object Identifier (DOI)
3. Farh M.M., Gribniak V. Thermo-Mechanical Approach to Material Extrusion Process During Fused Filament Fabrication of Polymeric Samples. Materials. 2025, 18, 4537.
4. High-Quality PLA Filament Production: Extrusion and Auxilliary Equipment Setup. [Electronic resource]. - Access mode: https://dgchemtech.com/pla-filament-production-line-setup.html
5. Strand Cooling Belt PFS [Electronic resource]. - Access mode: https://www.azurr-tech.cz/file/40f9522aa38cf668a457ff4f3ca73247/13649/strand_cooling_EN.pdf

TalentDetector
7th-9th June 2026
Gliwice-Brenna, Poland
DEPARTMENT OF ENGINEERING MATERIALS AND BIOMATERIALS
FACULTY OF MECHANICAL ENGINEERING
SILESIAN UNIVERSITY OF TECHNOLOGY
INTERNATIONAL STUDENTS SCIENTIFIC CONFERENCE

Fillers in polymers composites

Magdalena Polok-Rubiniec[a]

[a] Silesian University of Technology, Faculty of Mechanical Engineering, Department of Engineering Materials and Biomaterials
email: magdalena.polok-rubiniec@polsl.pl

Abstract: The paper presents the polymer composites with carbon fillers characterization. These materials are more and more often used as construction materials, because of their interesting properties, they can competitive, in some cases even with carbon steels. Their influence on the properties of various polymer matrices, depends on the filler content and application possibilities of the obtained composites were presented.

Keywords: polymer composites, carbon fillers, properties, application

1. INTRODUCTION

The continuous development of industry and the growing interest in polymer materials for new applications necessitates research into improving the properties of materials through their modification. Active fillers play a crucial role in the modification of polymer materials, improving mechanical, tribological, rheological, thermal, dielectric, chemical, and processing properties [1-5]. Fillers also reduce polymer shrinkage and viscosity, limit jet expansion, and improve heat dissipation during cooling. Composites based on polymer materials with the addition of fillers in the form of powders, fibers, and nanoadditives are becoming increasingly important among construction materials. A filler can be defined as solid particles whose share in the polymer matrix exceeds 10% by weight. In the case of plastics processed by injection molding or extrusion, the filler content can reach up to 60%, and in the case of resins, even 90%. It has been found that at this degree of filler filling, the macromolecular material acts as a binder for the filler. The most commonly used powdered fillers include: powdered mica, quartz sand, chalk, quartz flour, kaolin, graphite, dolomite flour, and mica. Commonly used nanoadditives in polymer composites include silver nanoparticles and carbon black nanoparticles, as well as allotropic forms of carbon – carbon nanotubes and graphene. The most commonly used fibers include carbon, glass, and ceramic fibers. In recent years, carbon fillers, including various forms of carbon black and graphite, as well as hard coal, shungite, and anthracite, have also been successfully used as an alternative to expensive carbon nanotube fillers [1-8].

The use of fillers does not guarantee the improvement of all properties; there is no such thing as a universal filler; actual improvement of some properties results in deterioration of

others. A filler that is designed to fulfill specific functions should demonstrate: low absorption and water content, low specific gravity, chemical inertness towards the polymer and hardener, good wettability, and thermal resistance. A pleasant color and lack of odor are also important. The most common undesirable side effects of filler use include: sedimentation (which can cause material inhomogeneity), agglomeration (which reduces mechanical properties), deterioration of processing properties, increased density, and increased moisture absorption, which affects dielectric properties. The effects of filler interactions with the polymer matrix should be determined individually for each composite type and tested experimentally. Powder fillers also influence the type and size of the formed crystallites; they can act as artificial crystallization nuclei at low filler volume fractions. A large filler content reduces the maximum degree of polymer crystallization. The use of powder fillers allows for shaping material properties according to application needs and reducing material costs. The characteristics of carbon fillers themselves depend significantly on their production conditions, dimensions, shapes, and specific surface area [8-15].

1.1. Carbon fillers used in polymer composites

Carbon fillers in powder form are an important component of polymer composites used in the automotive, mining, and chemical industries. Carbon fillers increase the heat resistance of polymers, as well as environmental factors and UV radiation. Depending on the type of carbon filler, the desired volume and surface resistivity, as well as magnetorestrictive properties, can be achieved, primarily in composites with a polypropylene matrix. Such materials can be used as shields against the effects of electric and magnetic fields, sensors for measuring various physical quantities, thermistors, protective coatings against the accumulation of electrostatic charges, and infrared heating elements. In addition to improving electrical properties, carbon fillers are expected to improve mechanical properties, particularly abrasive wear resistance and hardness. Besides surface phenomena, the interaction of polymers with fillers also influences the density of matrix particles within the filler particles. The filler volume plays an important role; too high a filler content does not always improve abrasive wear resistance. When we want to modify dielectric properties, graphite is used, which increases electrical conductivity [8-10]. In recent years, fossil coal has been successfully used as a filler in polymeric materials. Coal is primarily known as an energy resource and is a natural rock of organic origin with a complex chemical structure. Fossil coal consists of organic compounds, mineral inorganic components, and water. It contains carbon, oxygen, hydrogen, nitrogen, sulfur, arsenic, and uranium. The primary component is maceral, the type of which significantly influences the coal's properties. An advantage of coal is its thermal resistance; the degree of carbon metamorphism (the percentage of C) influences the decomposition temperature of the organic substance.

The most commonly used carbon fillers in polymer composites are in the form of: carbon fibers, graphite, carbon nanotubes, carbon black (amorphous carbon), powdered fossil coal (pure hard coal, shungite, anthracite) [8-16].

1.2. Carbon fibers in polymer matrices

The large-scale production of carbon and graphite fibers, as well as nanotubes, has led to increased interest in these materials as fillers in polymer composites. Carbon fibers (containing 80-98% C) have been used for a long time, including in the production of electric lamps. Graphite fibers (containing approximately 99% C) emerged as an interesting engineering material in the 1950s. Compared to graphite fibers, carbon fibers are characterized by a less

ordered structure and poorer mechanical properties, but are significantly cheaper. Carbon fibers (CF) are obtained by pyrolysis of polyacrylonitrile (PAN), accounting for approximately 90% of global production. The properties of the fibers are primarily influenced by their production parameters. They can also be produced from other raw materials: cellulose, asphalt, mesophase pitches (residues from the distillation of coal tars), and phenolic resins. Graphite fibers have a tensile strength of 2500 MPa, while carbon fibers have a tensile strength of 900 MPa. In terms of strength, graphite fibers can even compete with steel, with a Young's modulus of up to 420 GPa, while carbon fibers have a tensile strength of 90 GPa. Carbon fibers are characterized by thermal and chemical resistance, and their properties remain unchanged in non-oxidizing atmospheres up to 2000°C. Advantages of carbon fibers used in polymer matrices include low density, good thermal and electrical conductivity, low coefficient of friction, vibration damping, and low X-ray absorption, high fatigue strength and creep resistance, high dimensional stability, and resistance to sudden temperature changes. The undoubted disadvantages of carbon fibers include their brittleness and high price, which prevents their reuse. Carbon fibers in a polymer matrix can also be present as a nanofiller in the form of carbon nanotubes (CNTs), composed of graphene layers. Their addition to polymer composites has been found to produce nanocomposites that are electrically conductive and eliminate the accumulation of electrostatic charges. Nanotubes have been added to polymer matrices made of polyester, polycarbonate, and polyamide. The advantage of nanocomposites is that the introduction of 1-5% of nanoadditives into the composite is sufficient to achieve high properties of the nanocomposites compared to traditional polymer composites, where the same properties are achieved only with a 15-30% filler content [8, 17-19].

Both thermoplastic polymers and thermosets are used to create nanocomposites filled with carbon nanotubes. In thermosets, nanotubes are typically incorporated directly into a low-viscosity resin (with the addition of a solvent), then mechanically mixed, and the resin is cured. In thermoplastics, CNTs are incorporated into the matrix by introducing molten nanotubes and mechanically mixing. An in-situ method is also used, where CNTs are incorporated into the polymer during its synthesis. This seems to be a good way to achieve the desired filler distribution throughout the volume of the synthesized polymer matrix.

Due to their properties, carbon fiber-reinforced polymers are used in the production of yacht and boat masts, bicycle frames, in the production of heat-resistant, flame-retardant, and electrically heated fabrics, and in the production of skis, golf clubs, tennis rackets, and protective helmets. They are also used in construction, in aircraft and space structures, in the production of Formula 1 racing car bodies, and in ablative coatings made of carbon fiber-reinforced epoxy resins in spacecraft cabins [8, 17-20, 21-22].

1.3. Polymer composites with carbon black filler

Carbon black is formed as a result of the incomplete combustion (pyrolysis) of fuels and other materials containing significant amounts of the element carbon. Its main component is amorphous carbon, making carbon black the cheapest source of amorphous carbon. Carbon black typically contains fine graphite-like structures, small amounts of fullerenes and fullerene-like structures, and residues of burned organic substances, such as fats and ash [8-10].

Carbon black, as a nanofiller in polymer composites, increases the hardness, abrasion resistance, and resistance to permanent deformation of elastomers. It is used in the production of car tires and lubricants. It is also used as a pigment in paint production, for coloring and photostabilizing plastics, and for printing inks. Carbon black is most often used as a filler in rubber mixtures, increasing their mechanical strength and reducing abrasion. It also increases

the resistance to natural aging of rubber products as a result of UV absorption. The use of carbon black evenly distributed in the polypropylene matrix significantly increases the modulus of longitudinal elasticity and causes a slight increase in the mechanical strength of the material [8-10, 23-26].

An increasingly important application of carbon black is to fill a polymer matrix to increase electrical conductivity. The use of carbon blacks with different structures will have different effects on the conductivity in a polymer composite. A polymer filled with a "high" structure of carbon black (composed of many carbon black particles fused together in a clustered structure) will have lower electrical resistivity compared to the same polymer filled with a "low" structure of carbon black (composed of a small number of carbon black particles fused together in an aggregate) at the same carbon black concentration. The method of dispersing the carbon black in the polymer matrix is important; small changes during processing (e.g., mixing time, speed) can drastically affect the resistivity of the composite [25-26].

Electrically conductive polymer composites are characterized by low specific gravity, deformability, and ease of processing. These advantages have led to their widespread use: as a shielding layer in cables and devices sensitive to electromagnetic fields, in hoses and pipes conveying media susceptible to explosions due to electrostatic charge accumulation, in medicine, electronics, and the automotive industry. They are also used as materials with potential sensory properties (sensors, "electronic noses") [26-28].

1.4. Polymer composites with powdered hard coal

An interesting carbon filler is shungite, a fossil raw material containing approximately 30% carbon and 70% silicate compounds. It is an intermediate form of carbon between anthracite and graphite. It is a product of the metamorphism of petroleum derivatives, which most often occur as deep-sea veins among highly metamorphosed Proterozoic rocks. It also contains carbon nanotubes and fullerenes. Shungite is primarily used as a rubber filler, replacing carbon black as a component of paints and varnishes with increased electrical conductivity, and as a shield for plastics against electromagnetic radiation. As a polypropylene filler, it exhibits good adhesion to macromolecules and increases its electrical conductivity. The addition of approximately 4% shungite by weight improves tensile strength and stress at break. Strength decreases with increasing filler content (for 5% shungite by weight, the composite strength is 25% lower than for pure PP). Shungite has a positive effect on increasing the modulus of elasticity and stiffness of the material, reducing impact strength and elongation at maximum stress and stress at break, lowering the melt flow index, and increasing the crystallization and melting temperature. The addition of approximately 20% by weight of shungite improves the thermal stability of the composite, and increasing the shungite content reduces mass loss at 700°C. A significant decrease in volume and surface resistivity was observed, which worsens the electrical insulating properties of the composites. However, a significant improvement in antistatic properties was also observed – reduced surface resistivity facilitates the discharge of electrical charges on the composite's surface layer. Composites containing shungite are hydrophobic [17-19, 26, 29-30].

Studies were also conducted on pure hard coal with varying degrees of carbonization; the addition of this filler to polyamide increased viscosity. Polyethylene with carbon filler did not exhibit significant changes in tensile strength, but reduced deformability and impact strength, increased hardness, and reduced the electrical resistance of the composites. Furthermore, the introduction of approximately 7% by weight of carbon filler into thermoplastics inhibited jet

expansion. An increase in abrasion resistance was also observed for cast gradient polymer composites based on epoxy resin with the addition of powdered orthocoke and anthracite dust. At contents below 26% by weight, samples with orthocoke exhibited improved abrasion resistance, while at higher filler values above 26% by weight, composites with anthracite exhibited improved abrasion resistance, and an increase in composite hardness was also observed. The addition of anthracite to the epoxy-carbon composite improved its thermomechanical properties. Carbon powder added to thermosets improves their heat resistance (brown coal powder filler) [31-33].

BIBLIOGRAPHY

1. T. Klepka, Collective work edited by Klepka T., Modern polymer materials and their processing, part 1, Lublin University of Technology, Lublin (2014) 26-28, in polish
2. M. Olejnik, Polymer nanocomposites with montmorillonite - preparation, evaluation methods, properties and applications, Technical Textile Products, Łódź (2008) 67-74, in polish.
3. J. Janik, Properties and structure of polypropylene/layered silicate composites, Kompozyty (Composite) 4/10 (2004) 2005-2011, in polish.
4. G. Sionkowski, H. Kaczmarek, Polymers with silver nanoparticles - selected systems - preparation, properties, applications, Polymers 55 7-8 (2010) 545-551, in polish.
5. A. Boczkowska, G. Grzesiński, Composites and their production techniques, OWPW, Warsaw (2016) 50-56, in polish.
6. J. Stabik, M. Rojek, Ł. Suchoń, M. Chomiak, Research on the rheological properties of polyamide filled with hard coal, Przetwórstwo Tworzyw 6 (2011) 521-524, in polish
7. D. Żuchowska, Structural polymers, WNT, Warsaw (2000), in polish.
8. J. Stabik, M. Chomiak, Ł. Suchoń, A. Dybowska, K. Mrowiec, Chosen manufactured methods of polymeric graded materials with electrical and magnetic properties gradation, Archives of Materials Science and Engineering 54/2 (2012) 218-226.
9. M. Żenkiewicz et. al, Selected properties of polypropylene-shungite composites, Polymers 55/2 (2010) 119-126, in polish.
10. M. Chomiak, J. Stabik, The influence of hard coal particles on the hardness and abrasion of polymer gradient materials, Przetwórstwo Tworzyw 6 (2013) 582-591, in polish.
11. Z. Majchrzak, J. Lipczyński, Preparation and characterization of polypropylene composites, Polymers 52/3 (2007) 190-194, in polish.
12. A. Gnatowski, The influence of the type of filler on the properties of selected polymer mixtures, Composites 2 (2005) 63-67, in polish.
13. *J.* Stabik, Selected issues in the rheology of plasticized filled polymers, Wydawnictwo Politechniki Śląskiej, Gliwice, 2004, in polish.
14. K. J. Kurzydłowski, A. Boczkowska, J. Schmidt, at. al., Monitorowanie uszkodzeń w kompozytach metodami nieniszczącymi, Polymers 50/4 (2005) 255-261, in polish.
15. Yui H., Wu G., Sano H., i inni, Morphology and electrical conductivity of injceton-molded polypropylene/carbon black composites with addition of high-density polyethylene, Polymer 47 3599-3608.
16. D. W. Van Krevelen, *Coal-topology, physics, chemistry constitution,* 3rd ed., Elsevier, Amsterdam, London, NY, Tokyo, 1993.

17. P. Mayer, J. W. Kaczmar, Properties and applications of carbon and glass fibers, Tworzywa sztuczne i Chemia 6 (2008) 52-56, in polish.
18. M. Fejdyś, M. Łandwijt, Włókna techniczne wzmacniające materiały kompozytowe, Techniczne Wyroby Włókiennicze (2010) 12-22, in polish.
19. J. Barton et.al, Polymer composites, biocomposites, and nanocomposites. Preparation, composition, properties, and application directions, Chemik 68/4 (2014) 280-287, in polish.
20. M. Kwiatkowska et.al, Preparation and characterization of PBT/carbon nanotube polymer nanocomposites, Kompozyty (Composite) 5/2 (2005) 99-104, in polish.
21. W. Królikowski, Z. Rosłaniec, Polymer nanocomposites, Kompozyty (Composites), 4/9 (2004) 3-16, in polish.
22. L. Zapór, Nanomaterial Hazards in the Plastics Industry: Recommendations for Assessing and Reducing Occupational Risks, CIOPPIB, Warsaw, 201, in polish.
23. P-Ch. Ma, et.al, Enhanced electrical conductivity of nanocomposites containing hybrid fillers of carbon nanotubes and carbon black, Applied Materials and Interfaces 1/5 (2009) 1090-1096.
24. W. Zhang, A.A. Dehghani-Sanij, R.S. Blackburn, Carbon based conductive polymer composites, Journal of Materials Science 42 (2007) 3408-3418.
25. P. J. Mather, K. M. Thomas, Carbon black/high density polyethylene conducting composite materials, Part II, Journal of Materials Science 32 (1997) 1711-1715.
26. P. M. Ajayan, L. S. Schradler, P. V. Braun, Nanocomposites science and technology, Wiley-VCH, Verlag, Weinheim, 2003.
27. S. Frąckowiak, M. Kozłowski, Electrically conductive polymer composites as a material with sensory potential, Polymers 55/5 (2010) 390-398, in polish.
28. P. J. Mather, K.M. Thomas, Carbon black/high density polyethylene conducting composite materials, Part I, Journal of Materials Science 32 (1997) 401-407, in polish.
29. Bieliński D. M., Dobrowolski O. Ślusarski L., *Dyspersja napełniacza matrycy w kauczuku. Cz. II. Metody ocena stopnia dyspersji,* Polimery, 2007, 52,9, 640-647
30. R. Steller, J. Iwko, Modeling the plasticization process of polymer materials during injection molding. Part I. Model establishment and solid fuel transport, Polymers, 53/11-12 (2008), 834-840, in polish
31. L. Kurzeja, K. Hennek, M. Rojek, J. Stabik, Heat resistance testing of epoxy-carbon compositions, NT Conference Materials, Polymers and structural composites, Kozubnik (1995) 213-217, in polish
32. B. Kumanek, Polymer composites with anthracite fillers with different degrees of structural order, Abstract of doctoral dissertation, Centrum Materiałów Polimerowych i Węglowych PAN.
33. Z. Wei, et. al, Comprehensive technical support for high-quality anthracite production: A case study in the Xinqiao Coal Mine, Yongxia Mining Area, China, Minerals 5/4 (2015) 919-935.

TalentDetector

7th-9th June 2026
Gliwice-Brenna, Poland

DEPARTMENT OF ENGINEERING MATERIALS AND BIOMATERIALS
FACULTY OF MECHANICAL ENGINEERING
SILESIAN UNIVERSITY OF TECHNOLOGY

INTERNATIONAL STUDENTS SCIENTIFIC CONFERENCE

High-energy cutting methods in modern manufacturing technologies

Katarzyna Ptasznik[a], Jan Wypiór[b], Piotr Herian[c], Natalia Rupala[d], Bartosz Dziki[e], Mirosław Bonek[f], Oleh Polishchuk[g]

[a] Silesian University of Technology, Faculty of Mechanical Engineering,
Student of Production and Management Engineering, email: kp309682@student.polsl.pl
[b] Silesian University of Technology, Faculty of Mechanical Engineering,
Student of Production and Management Engineering, email: jw309692@student.polsl.pl
[c] Silesian University of Technology, Student of Electrical Engineering,
email: ph305443@student.polsl.pl
[d] Silesian University of Technology, Faculty of Automatic Control, Electronics and Computer Science, Student of Teleinformatics, email: nr310520@student.polsl.pl
[e] Silesian University of Technology, Faculty of Electrical Engineering, Student of Mechatronics, email: bd310822@student.polsl.pl
[f] Silesian University of Technology, Faculty of Mechanical Engineering
[g] Khmelnytskyi National University, Faculty of Mechanical Engineering, Transport and Architecture, Khmelnytskyi, Ukraine

Abstract: The article describes the historical evolution and technical characteristics of modern material cutting technologies, tracing the transition from traditional mechanical tools to high-energy systems. Also presented is a detailed comparative analysis of laser, plasma, and waterjet cutting methods, highlighting their operational principles, industrial applications, and inherent advantages or limitations. Furthermore, the paper examines the role of CNC-aided nesting software in optimizing sheet layouts to minimize production waste and improve manufacturing cost-effectiveness.

Keywords: Material cutting, Laser cutting, Plasma cutting, Waterjet cutting (WJ/AWJ), CNC nesting optimization, Waste reduction, Heat-Affected Zone (HAZ).

1. INTRODUCTION

The rapid development of modern industry has created a growing demand for cutting technologies that are not only fast and precise, but also efficient and environmentally conscious. Traditional mechanical methods are increasingly being replaced by advanced high-energy cutting technologies such as laser, plasma, and waterjet cutting. These methods have revolutionized manufacturing by enabling the processing of complex shapes with exceptional accuracy while minimizing material waste and production time.

Today, high-energy cutting systems play a key role in industries ranging from automotive and aerospace engineering to electronics and heavy manufacturing. Their integration with CNC-controlled systems and modern nesting software has further increased production efficiency and reduced costs. This article presents the evolution of cutting technologies, explains the operating principles of the most widely used methods, and compares their advantages and limitations. Understanding these technologies is essential for appreciating the direction in which modern manufacturing continues to develop.

2. HISTORY OF MATERIAL CUTTING

The process of material cutting developed together with technological progress and the growing industrial demand for more accurate and faster machining. Initially, mainly mechanical methods were used, such as hand saws, chisels, and shears. In the 19th century, thermal techniques began to be used, including gas cutting using an oxy-acetylene flame [1].

In the 20th century, high-energy technologies developed rapidly. Modern methods appeared that used concentrated energy sources, such as plasma, laser, or a high-pressure water jet. These technologies made it possible to achieve greater cutting accuracy, reduce the amount of waste, and automate production processes [1][2].

Nowadays, cutting technologies are constantly being improved in terms of energy efficiency, edge quality, and minimization of material losses. CNC numerically controlled systems are of particular importance, as they allow elements to be arranged very precisely on sheets of material and reduce the amount of production waste [2].

3. CUTTING METHODS

Due to constantly growing customer demands, the market is constantly evolving and striving to advance cutting techniques and technologies. [4] Cutting machines can be categorized according to the type of working medium used into:

- laser cutting machines
- waterjet cutting machines
- Plasma cutting machines

Several other cutting methods could also be mentioned, but the ones listed above are the most common and widely used. The most important variables in the process are cost and the quality of the manufactured product. These factors determine subsequent sales costs, which directly impact the company's revenue [5].

3.1 Laser cutting

Laser cutting involves the direct application of laser beam energy to the cutting zone. Cutting is performed in three ways: burning, melting, or sublimation. The laser cutting process involves directing a high-energy laser beam at the material, causing it to heat up, melt, and in some cases also vaporize or burn. During this process, a supply of gas is directed into the cutting zone. A separate gas stream removes the molten material and its vapors. When cutting metals, primarily steel, oxygen is used, which increases the heat and ensures higher-quality cut edges. Lasers are used to cut various metallic materials up to a thickness of approximately 32

mm. Cutting materials up to 40 mm thick is possible but requires specialized lasers and adjustment of the process time [6]. The process is also regulated by global standards, such as ISO 9013:2017.

Among the many advantages of laser cutting, the most important are:

- ease of process automation
- the ability to arrange components very closely together on a sheet
- the speed of the cutting process
- a narrow cutting gap
- the non-contact nature of the process
- Minimal deviations, allowing for the cutting of complex patterns

Unfortunately, there are also several disadvantages:

- The power of the laser itself directly affects the cutting thickness
- Laser cutting is nearly twice as expensive as plasma cutting [4]
- Equipment is required to filter harmful gases
- Material quality on the underside (burrs, with thicker sheets or improperly selected speed)
- Materials with a high reflectivity coefficient (copper, brass) cut very poorly [4]

3.2 Plasma Cutting

Plasma cutting is one of the modern methods of thermal processing of electrically conductive materials. The process involves the use of a highly concentrated plasma arc with a very high temperature, which can exceed 20,000°C [1][3].

Plasma is formed as a result of the ionization of a working gas, such as compressed air, nitrogen, or argon. The electric arc generated between the electrode and the material being processed causes the gas to transform into plasma. The plasma stream blows the molten material out of the cutting gap, creating a narrow line separating the material [3].

This method is mainly used for cutting:

- structural steel,
- stainless steel,
- aluminum,
- copper and other conductive metals [3].

The most important advantages of plasma cutting include:

- high cutting speed,
- the ability to cut thick materials,
- relatively low operating cost,
- good edge quality,
- the possibility of automating the process,
- reduction of material losses [3].

Plasma cutting plays an important role in modern waste-free technologies. Thanks to its high accuracy and the possibility of working with CNC systems, it is possible to optimally arrange elements on a sheet of material. This allows the amount of post-production waste to be reduced and production costs to be lowered [2].

3.3 Waterjet Cutting

Operating Principle and Applications

Modern cutting machines use intensifier pumps that compress water to extreme pressures of 400–600 MPa (4,000–6,000 bar) [10]. The water is forced through a tiny sapphire or diamond nozzle, reaching supersonic speeds. Depending on the hardness of the workpiece, this method is divided into:

- **WJ (Pure Waterjet)**: Used for soft materials like rubber, paper, foam, and extensively in the food industry.
- **AWJ (Abrasive Waterjet):** A fine abrasive (e.g., garnet) is added to the water stream in a mixing chamber. This allows for the cutting of the hardest metal alloys, structural steels, armored steels, non-ferrous metals, glass, and composites [11][12].

Advantages of Waterjet Cutting

The key advantages of this method include:

- **No Heat-Affected Zone (HAZ):** As it is a cold cutting process, the material does not melt, thermally deform, harden, or change its metallurgical or chemical structure [9].
- High edge quality, often requiring no further finishing (no burrs).
- Extreme versatility – a single machine can cut almost any material.
- Environmental safety (no harmful fumes, smoke, or dust released into the air) [10].
- Narrow kerf width, facilitating high nesting density on the sheet and minimizing waste.

Disadvantages of Waterjet Cutting

Despite its many benefits, the method has certain limitations:

- Lower cutting speed for thin sheets compared to laser or plasma cutting [10].
- High operating and maintenance costs (consumption of abrasive, nozzles, and high-pressure pump components).
- The need for sludge disposal (a mixture of used abrasive, water, and material particles).
- High noise levels generated during the process [11].

4. SHEET LAYOUT OPTIMIZATION

This method stands out from others due to its excellent material usage. In practice, the goal is to minimize production waste, which helps reduce manufacturing costs. The process uses “nesting,” or computer-aided optimization of part placement on the sheet of material. CAM software arranges the parts in such a way that they take up as little space as possible. At the same time, it maintains the previously specified required technological clearances. This reduces material loss and increases the cost-effectiveness of the process.

However, achieving zero waste is difficult. Sheet margins, technological bridges, and beam penetration points must always be taken into account.

Cutting designs should be prepared at a 1:1 scale [7]. It is possible to import files from popular CAD programs such as SolidWorks or AutoCAD (DWG, DXF formats). The design should clearly show the contours; no additional dimensions should be included – only the information necessary for the laser. Layers or colors may indicate different processing operations. The laser cutting path is shown in red.

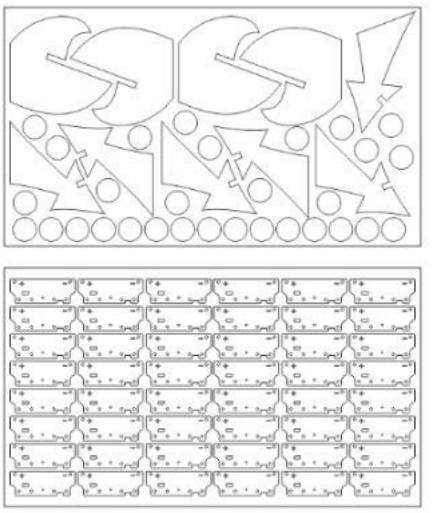

Figure 1. An example of nesting, the layout of sheet metal [8]

5. CONCLUSION

Modern industrial manufacturing is defined by a diverse range of cutting technologies, each offering specific trade-offs cost, speed, and edge quality. While laser and plasma methods dominate the thermal cutting sector due to their speed and automation potential, waterjet technology remains indispensable for cold processing and material versatility.

The integration of CNC systems and advanced CAM nesting software represents the most significant contemporary advancement in the field. By optimizing the arrangement of parts on a sheet, companies can drastically reduce material loss. Ultimately, the choice of cutting method is determined by the specific material properties and economic requirements of the project, with a clear industry-wide trend toward maximizing energy efficiency and achieving zero-wast production.

ACKNOWLEDGEMENTS

The work was created as part of project based learning - PBL, in the 14th competition under the Initiative of Excellence - Research University, Silesian University of Technology, Gliwice, Poland and as part of project of Students Scientific Circle of Laser Surface Treatment under the Initiative of Excellence - Research University, Silesian University of Technology, Gliwice, Poland.

BIBLIOGRAPHY

[1] A. Klimpel, *Welding, Resistance Welding and Metal Cutting*, Scientific and Technical Publishers, Warsaw, 1999.
[2] A. Klimpel, *Welding Handbook. Welding and Cutting Technologies*, Silesian University of Technology Publishing House, Gliwice, 2013.

[3] A. Klimpel, *Technology of Welding and Metal Cutting*, Silesian University of Technology Publishing House, Gliwice.
[4] TECHNIKI WYSOKOENERGETYCZNE CIĘCIA – STAN OBECNY I KIERUNKI ROZWOJU, Marek KOWALIK1, Tomasz TRZEPIECIŃSKI
[5] Cięcie laserowe K. Musiała , K. Studnika , M. Bonek, Gliwice 2014
[6]https://www.researchgate.net/publication/323326207_Podstawy_teoretyczne_ciecia_laserowego_metali (dostęp: 15.05.2026)
[7] https://darko-steel.pl/blog/najpopularniejsze-sposoby-ciecia-stali (dostęp: 15.05.2026)
[8] https://laserem.pl/ciecie-laserem/przygotowanie/ (dostęp: 15.05.2026)
[9] Borkowski J., Fundamentals of Abrasive Waterjet Machining, Scientific and Technical Publishers (WNT), Warsaw 2001.
[10] Klimpel A., Laser and Plasma Technologies and Waterjet Cutting, Silesian University of Technology Publishing House, Gliwice 2011.
[11] Cichosz P., Machining, Scientific and Technical Publishers (WNT), Warsaw 2006.
[12] Hashish M., The Waterjet Machine Tool, Springer-Verlag, New York 2010.

TalentDetector

7th-9th June 2026
Gliwice-Brenna, Poland

DEPARTMENT OF ENGINEERING MATERIALS AND BIOMATERIALS
FACULTY OF MECHANICAL ENGINEERING
SILESIAN UNIVERSITY OF TECHNOLOGY

INTERNATIONAL STUDENTS SCIENTIFIC CONFERENCE

A Miniaturized Telemetry and Avionics System for Model Rockets

Igor Puchała[a], Wiktor Bujak[a], Maja Rudnicka[a], Kamil Moszumański[a], Michał Lasak[a]

[a] Silesian University of Technology, Faculty of Automatic Control, Electronics and Computer Science, SKN SpaceCoffee, email: igor.puchala@gmail.com, wb322602@student.polsl.pl, mr322241@student.polsl.pl, km322442@student.polsl.pl, Michal.Lasak@student.polsl.pl

Abstract: This paper presents the design and implementation of a miniaturized telemetry and avionics system intended for use in amateur rockets. The task of the system is to rapidly acquire and process data from an onboard accelerometer, gyroscope, and barometer. The onboard software processes sensor readings to calculate current altitude, velocity, and spatial orientation, allowing autonomous software-based detection of individual flight phases. The system is designed to support electronic parachute deployment systems as well as two-stage rockets. The complete flight telemetry is recorded on an SD card. The data collected was used for post-flight analysis.

Keywords: telemetry system, avionics, rocket modeling, data analysis, aerodynamics

1. INTRODUCTION

Model rockets are an engineering topic of high interest in the context of continuous development of autonomous navigation strategies, as well as the potential these types of models have for experimental purposes. The design of such inexpensive small-scale constructions also offers a versatile educational experience for students in fields such as aerospace engineering, electronics or engineering design [1].

The project discussed in this paper is a comprehensive implementation of an experimental rocket designed for educational and research purposes. The core assumptions were the development of a modular avionics system, as well as an efficient custom telemetry system [2]. These software structures are responsible for the basic flight control logic and for ensuring the completion of the rocket's mission objectives and successful recovery.

An additional objective for improving the practical aspects of the project was providing the support of an electronic parachute deployment system and automatic ignition of the second stage in two-stage rockets.

2. SYSTEM ARCHITECTURE AND HARDWARE INTEGRATION

2.1. Telemetry system

The implementation of the system follows the principles of Integrated Modular Avionics (IMA), which centralizes multiple flight functions onto a single computing platform to optimize weight and power efficiency [3]. The architecture is built around the Raspberry Pi Pico microcontroller, which acts as the primary On-Board Computer (OBC). Unlike industrial aerospace solutions, this project prioritizes the use of commercial off-the-shelf (COTS) components to demonstrate that high-fidelity activities can be developed at a low cost [3, 4]. To maintain a small form factor suitable for restricted airframe volumes, all electronic components are integrated into a miniature soldered prototyping board [2]. While this prototype lacks the aesthetic finish of a professional PCB, it serves as an essential functional validation stage before transitioning to a refined PCB design.

Fig. 1. Render of the rocket model developed and manufactured for testing purposes

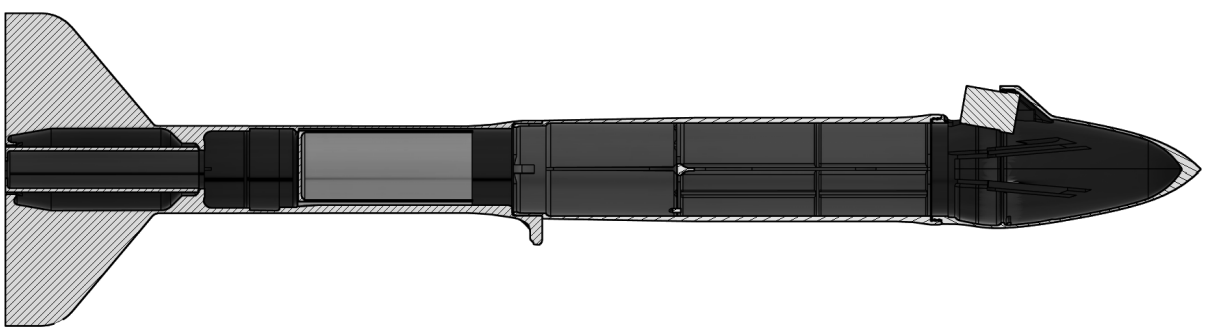

Fig. 2. Render of the rocket model, cross-section

2.2. Avionics system integration

The sensory segment of the avionics suite comprises a digital inertial sensor with a 16-bit-per-axis analog-to-digital converter that communicates via an interface for 6-axis motion tracking. Also employed is a high-linearity absolute pressure sensor for precision measurements of atmospheric pressure and temperature. Data persistence is managed via a microSD module, functioning as a "black box" to store raw telemetry for post-flight assessment, such as drag

coefficient calculations [5]. Visual documentation is provided by an integrated HD camera, while a high-decibel buzzer acts as a recovery aid to facilitate vehicle retrieval post-landing. The entire system is powered by a small LiPo cell, which provides the high energy density required to sustain the camera and microcontroller while keeping the total mass fraction within the stability requirements of a mid-power model rocket.

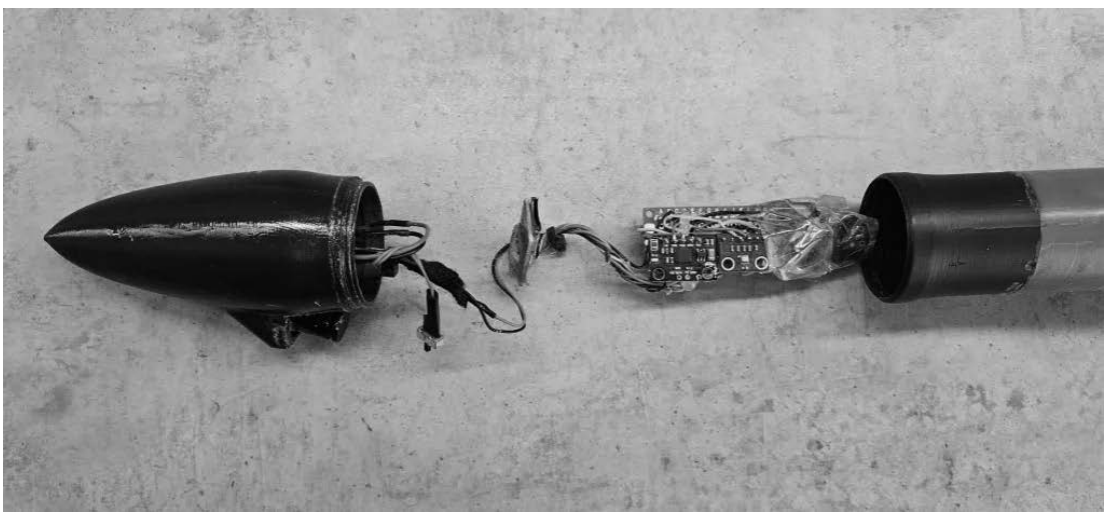

Fig. 3. Prototype electrical assembly used on Flights 3 and 4

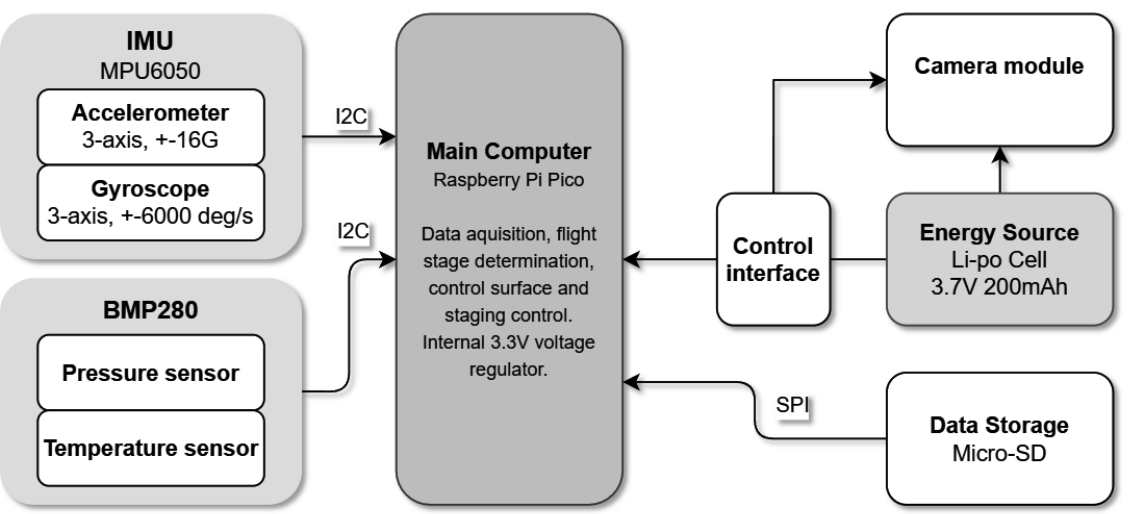

Fig. 4. Block diagram of the system

Fig. 5. Frame of onboard video from Flight 4, near the apogee at 280 meters.

3. SOFTWARE LOGIC AND FLIGHT PHASE DETECTION

The flight management software is designed as a time-driven finite-state machine (FSM). This centralized data management approach processes real-time sensor readings through a sequence of logical states including Ground/Idle, Powered Flight, Coasting, Apogee, and Recovery. To ensure reliability, moving average filters are applied to the barometric and inertial data to reduce measurement noise and prevent premature parachute deployment, which is a common failure mode in experimental rocketry. The software utilizes the dual-core processing capability of the Raspberry Pi Pico to poll sensors and log data to the SD card simultaneously, making high-frequency sampling without interrupting critical flight control tasks possible [6].

4. EXPERIMENTAL RESULTS AND ANALYSIS

All experimental flight data presented in this article originates from two specific launches, designated as Flight 3 and Flight 4. To facilitate a clear comparative analysis, the time axis in all presented graphs has been normalized to a relative flight time, where T=0 s corresponds to the exact moment of engine ignition.

As presented in the net longitudinal acceleration data [Fig. 6], the motor ignition resulted in a rapid spike, reaching a peak acceleration of 121 m/s². The thrust phase was followed by a coasting phase until the highest point of the trajectory was reached. The avionics successfully detected the apogee at approximately T+9.2 s for the analyzed flight profile.

A comparative analysis of the altitude reference data [Fig. 6] reveals the dynamic differences between the two launches. Flight 3 peaked at 195 meters, while Flight 4 reached a higher altitude of nearly 283 meters. Flight 4 used the same Klima9D rocket motor, but the airframe had numerous upgrades to reduce its mass and aerodynamic drag.

Flight 3 was a fully successful launch with nominal operation of all subsystems and exceptional roll stability due to perfectly aligned tail fins which were printed as a single part along with the aft end of the airframe. Flight 4 experienced a parachute deployment failure, but was recovered

intact due to its low terminal velocity. Flight 4 reached a peak velocity of nearly 540 km/h. The differences in flight characteristics of both models can be seen in Fig. 6-8.
These different descent profiles are clearly reflected in the sensor data. For Flight 3, sharp fluctuations visible on the acceleration graphs during the descent phase correlate perfectly with the parachute ejection and the subsequent stabilization of the rocket. The accurate logging of such inertial data is crucial for evaluating vehicle dynamics and post-flight performance, as emphasized in studies of larger launch vehicle tracking systems [7]. Despite the hard landing during Flight 4, the miniaturized avionics system demonstrated exceptional reliability. The hardware survived the impact, and the software successfully tracked and logged all flight phases in both the nominal and the failure scenarios.

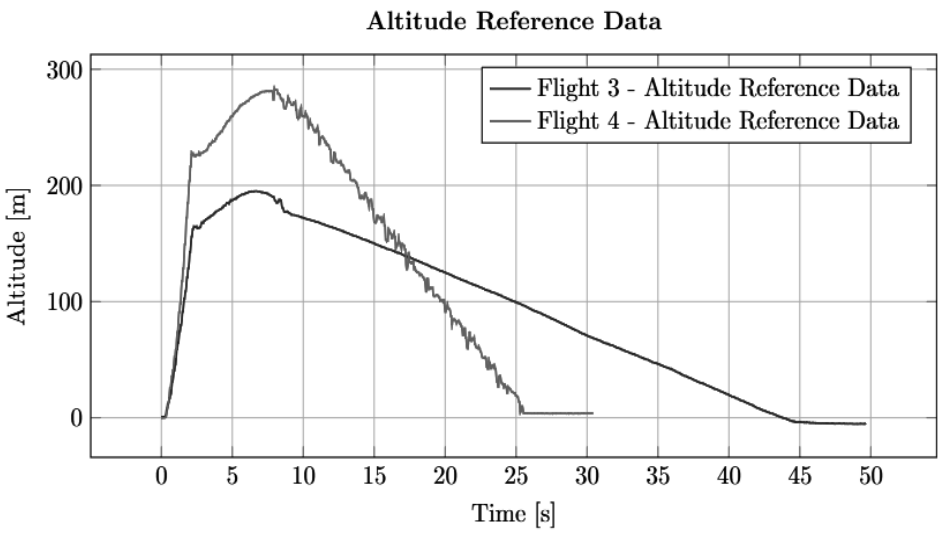

Fig. 6: Plot of Barometric Altitude vs. Time

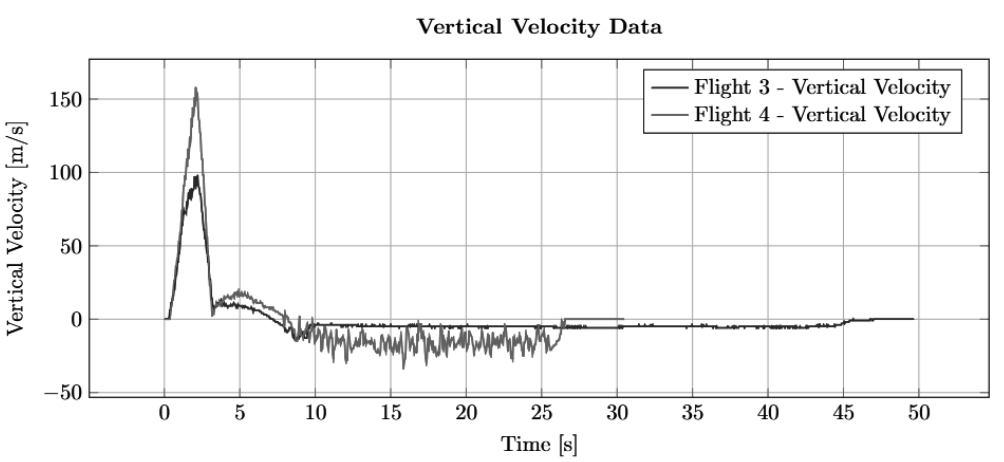

Fig. 7: Plot of Barometric Vertical Velocity vs. Time

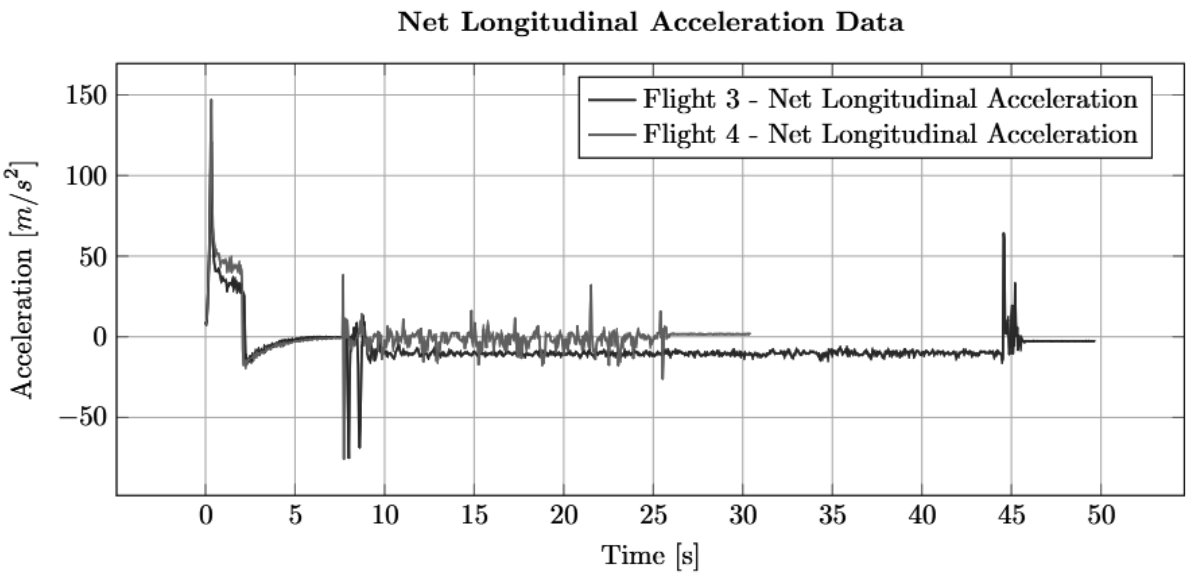

Fig. 8: Plot of Barometric Longitudinal Acceleration vs. Time

5. FUTURE DEVELOPMENTS

Future developments of this model rocket will focus on upgrading its avionics, telemetry, and overall accessibility. Key technical improvements include refining the sensor acquisition and Kalman fusion algorithms for more accurate flight data processing and orientation estimation [8]. To enhance tracking and recovery—especially during high-altitude flights—the system will integrate an ATGM336H module for GNSS capability alongside an nRF24 radio module. This telemetry upgrade will enable a live connection to a ground station, providing real-time flight milestone callouts and precise landing coordinates. Furthermore, the hardware architecture will be consolidated into a custom, all-in-one PCB equipped with an intuitive end-user interface for seamless customization. Ultimately, these advancements aim to make the platform widely available as a reliable, low-cost solution for amateur rocket hobbyists and student-led aerospace teams. The upcoming upgrades will be tested to support active control loops for roll stabilization and automatic ignition sequences for two-stage motor configurations [9].

6. CONCLUSIONS

The deployment of this miniaturized telemetry system provided highly reliable data acquisition for post-flight analysis. Utilizing dual-core processing and filtered sensor inputs, the system continuously logged high-resolution inertial and barometric data without dropping frames or interrupting flight control logic—even surviving a high-impact crash landing. During flight testing, the avionics successfully captured critical vehicle dynamics, recording a peak thrust acceleration of 147 m/s², maximum velocities approaching 540 km/h, and precise apogee detection at 283 m. This reliable data collection enabled a direct comparative analysis between two different airframe configurations and accurately mapped the descent profiles and

stabilization events. Ultimately, the acquired telemetry was used to empirically reconstruct the rocket motor's thrust curve and determine the vehicle's aerodynamic drag coefficients [10].

BIBLIOGRAPHY

1. Rojas, J., Prats, X., Montlaur, A. & Garcia-Berro, E. (2008). Model Rocket Workshop: A Project-Based Learning Experience for Engineering Students. International Journal of Emerging Technologies in Learning (iJET), 3(4), 70-77. Kassel, Germany: International Journal of Emerging Technology in Learning.
2. de Almeida Souza, Gabriel & Barbosa, Larissa & Ramalho, Glênio & Guarato, Alexandre. (2019). LOW COST REAL TIME ROCKET TELEMETRY SYSTEM DESIGN. 10.26678/ABCM.COBEM2019.COB2019-1585.
3. A. Y. Botero, J. S. Rodríguez, J. G. Serna, A. Gómez and M. J. García, "Design, construction and testing of a data transmission system for a mid-power rocket model," 2017 IEEE Aerospace Conference, Big Sky, MT, USA, 2017, pp. 1-14, doi: 10.1109/AERO.2017.7943739.
4. A. Williams, J. Puig-Suari and M. Villa, "Low-cost, low mass avionics system for a dedicated Nano-Satellite launch vehicle," 2015 IEEE Aerospace Conference, Big Sky, MT, USA, 2015, pp. 1-8, doi: 10.1109/AERO.2015.7119081.
5. A. D. Adamos, "Design, development, and flight testing of a modular avionics and vehicle monitoring system," M.S. thesis, Dept. Aerosp. Eng., Naval Postgraduate School, Monterey, CA, USA, 2021.
6. M. Klugherz, "Lightweight embedded thrust vector control on the RP2040," Cornell University, Ithaca, NY, USA, 2024.
7. Braun, Benjamin & Markgraf, Markus & Montenbruck, Oliver. (2016). Performance analysis of IMU-augmented GNSS tracking systems for space launch vehicles. CEAS Space Journal. 8. 10.1007/s12567-016-0113-9.
8. D. Vallverdú, C. Pou, M. Badenas, and E. Diez, "Application of a hybrid navigation system for an autonomous space air-launched vehicle," in *Proc. 9th European Congress on Embedded Real Time Systems and Services (ERTS 2018)*, Toulouse, France, 2018.
9. Posta, A., Monk, A., Durollet, A., Martin, O., & Bruton, S. (2024). Improved Attitude Stabilisation System Augmented Sounding Rocket Design, Integration, Verification & Launch. IFAC-PapersOnLine, 58(30).
10. A. M. Rauf, B. G. Kilberg, C. B. Schindler, S. A. Park and K. S. J. Pister, "Towards Aerodynamic Control of Miniature Rockets with MEMS Control Surfaces," 2020 IEEE 33rd International Conference on Micro Electro Mechanical Systems (MEMS), Vancouver, BC, Canada, 2020, pp. 523-526, doi: 10.1109/MEMS46641.2020.9056431.

7th-9th June 2026
Gliwice-Brenna, Poland
DEPARTMENT OF ENGINEERING MATERIALS AND BIOMATERIALS
FACULTY OF MECHANICAL ENGINEERING
SILESIAN UNIVERSITY OF TECHNOLOGY
INTERNATIONAL STUDENTS SCIENTIFIC CONFERENCE

The influence of varying illumination conditions on the performance of solar cells

Stanisław Rasiński[a], Marcin Mrugała[a], Oskar Stelmach[a], Michał Szczęsny[a], Marcin Szumski[b], Yurii Humeniuk[c], Oleksandr Maliarchuk[c], Judyta Drygała[d], Janusz Wyrwał[e], Oleh Polishchuk[f], Andrii Polishchuk[f], Sabina Lesz[g], Aleksandra Drygała[g]

[a] Student, Silesian University of Technology, Faculty of Mechanical Engineering, Konarskiego 18a Str., 44-100 Gliwice, Poland
[b] Student, Silesian University of Technology, Faculty of Mining, Safety Engineering and Industrial Automation, Akademicka 2 Str., 44-100 Gliwice, Poland
[c] Student, Faculty of Engineering, Transport and Architecture, Khmelnytskyi National University, Instytuts'ka 11 Str., 29016 Khmelnytskyi, Ukraine
[d] Student, Silesian University of Technology, Faculty of Architecture, Akademicka 7 Str., 44-100 Gliwice, Poland
[e] Silesian University of Technology, Faculty of Automatic Control, Electronics and Computer Science, Department of Measurements and Control Systems, Akademicka 16 Str., 44-100 Gliwice, Poland
[f] Faculty of Engineering, Transport and Architecture, Department of Machines and Apparatus, Electromechanical Energy Systems, Khmelnytskyi National University, Instytuts'ka 11 Str., 29016 Khmelnytskyi, Ukraine
[g] Silesian University of Technology, Faculty of Mechanical Engineering, Department of Engineering Materials and Biomaterials, Konarskiego 18a Str., 44-100 Gliwice, Poland
email: aleksandra.drygala@polsl.pl

Abstract: In this work, the influence of varying illumination conditions on the electrical properties of silicon solar cells were investigated. These are devices that enable the generation of free electrical energy from the Sun in an environmentally friendly way. They are characterized by a compact design, quiet operation, and zero air pollution emissions. In the face of growing energy demand, they constitute an ecological, economical, and technologically advanced solution. Scientists around the world are striving to improve the efficiency of solar cells. Although they can operate even on cloudy days, their performance is strongly dependent on the intensity of solar radiation. Any deviations from optimal sunlight conditions result in reduced energy efficiency and, in extreme cases, may lead to damage to the photovoltaic system components.

Keywords: photovoltaics, silicon solar cells, illumination, electrical properties, cells shading

1. INTRODUCTION

1.1. General characteristics of silicon solar cells

Silicon solar cells dominate modern photovoltaics due to their favorable combination of high efficiency, durability, and well-developed manufacturing technology. A silicon solar cell consists of two layers of semiconductor material: p-type silicon and n-type silicon, which together form a p–n junction. Electrical contacts are located on the front and rear surfaces of the solar cell to enable the collection of generated charge carriers, while an antireflection coating is applied to reduce light reflection. The operating principle of solar cells is based on the photovoltaic effect, which involves the generation of charge carriers through the excitation of electrons into the semiconductor conduction band under the influence of solar radiation. Photons with energy greater than the semiconductor band-gap energy generate electron–hole pairs. Within the p–n junction region, charge carriers are separated: electrons move toward the n-type region, whereas holes migrate toward the p-type region, resulting in the creation of a potential difference [1, 2].

Silicon solar cells are characterized by relatively high efficiency and long operational lifetimes, often exceeding 25 years. Three main types of silicon cells can be distinguished: monocrystalline, polycrystalline, and amorphous. Monocrystalline cells achieve the highest efficiency; however, their manufacturing process is more expensive. Polycrystalline cells are less costly to produce but exhibit slightly lower performance. In contrast, amorphous silicon cells are lightweight and flexible, although they provide the lowest efficiency among silicon-based photovoltaic technologies. Owing to their advantageous properties, silicon solar cells are widely applied in both small-scale residential systems and large photovoltaic power plants [3, 4].

1.2. Environmental factors affecting the performance of solar cells

Solar cells used in photovoltaic modules and panels are exposed to numerous external factors, often related to weather conditions as well as other environmental phenomena. These factors may significantly affect the operation and performance of solar cells [5].

The primary factor determining the efficiency of solar cells is the intensity of solar irradiance. The greater the amount of solar energy reaching the surface of the cell, the higher the electrical energy production. Consequently, the performance of photovoltaic devices depends on the time of day, season, geographical latitude, atmospheric clarity, fog, rainfall, snowfall, and cloud cover. Clouds, fog, and precipitation reduce the amount of solar radiation reaching the solar cells, thereby limiting electricity generation. Heavy wet snowfall may cause temporary snow accumulation on photovoltaic modules. Due to its high albedo coefficient, or ability to reflect solar radiation, even a several-centimeter layer of snow may reduce the power output of solar cells almost to zero. The efficiency of solar cells is also influenced by the angle of incidence of solar radiation. The highest energy yield is achieved when solar rays strike the surface of the photovoltaic cell or module perpendicularly. Therefore, the proper orientation of photovoltaic installations relative to the Sun, as well as an appropriate tilt angle, are of considerable importance [5, 6].

Ambient temperature and the temperature of the photovoltaic device itself also have a significant impact on solar cell performance. As temperature increases, the current intensity rises slightly, whereas the voltage decreases noticeably, leading to a reduction in both efficiency and output power. For most silicon solar cells, an increase in temperature of 1 °C above standard test conditions results in an efficiency decrease of approximately 0.4–0.5% [5, 6].

The efficiency of solar cells is further affected by various environmental contaminants, such as dust, dirt, and soot originating from road traffic, industrial activity, or coal combustion, as well as leaves, plant pollen, bird droppings, and snow accumulating on the surface of photovoltaic installations. These contaminants reduce the current generated by the device and consequently limit its performance [7]. Another important operational issue is the partial shading of photovoltaic modules. Even slight shading of a small fragment of a solar cell may result in a significant decrease in the efficiency of the entire photovoltaic module, particularly in series-connected systems. Under such conditions, the shaded solar cell may operate in reverse bias mode and act as an energy receiver, leading to local temperature increases known as the "hot-spot" effect. Long-term occurrence of this phenomenon may result in degradation of the semiconductor material, damage to protective layers, and, in extreme cases, permanent failure of the photovoltaic module. To minimize the adverse effects of shading, bypass diodes, maximum power point tracking (MPPT) systems, and appropriate photovoltaic module configuration and arrangement are employed [8].

All the aforementioned environmental factors influence the amount of energy produced by a photovoltaic installation. Therefore, the design and operation of photovoltaic systems must take local climatic and environmental conditions into account [5]. Within the scope of this study, the influence of shading on the electrical properties of silicon solar cells was investigated.

2. MATERIALS AND METHODOLOGY

For the purposes of this study, a monocrystalline silicon solar cell of unknown origin, with dimensions of 50 × 50 mm, was used in the investigation (Fig. 1).

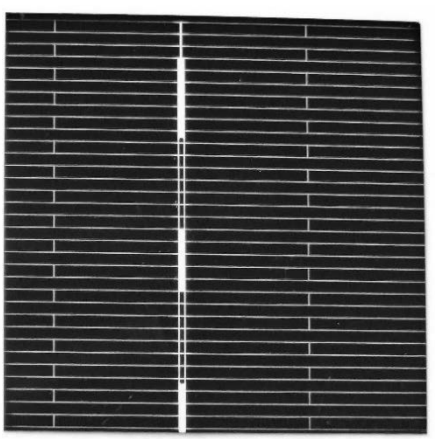

Figure 1. Monocrystalline silicon solar cell

To partially shade the surface of the solar cell, five masking materials with different levels of transparency were used:

- PVC film A with a thickness of 150 μm (Fig. 2a),
- film C– film A coated with a layer of carbon dust originating from coke combustion in a heating furnace (Fig. 2b),
- film B – film A covered with a layer of transparent 3M™ ElectroCut™ Series 1170C plotter film of 76.2 μm thickness, commonly used for road-sign applications (Fig. 2c),

- toploader of 1 mm thickness , typically used for the protection of collectible cards (Fig. 2d),
- carbon paper with a thickness of 20 μm, used for automatic duplication of written documents (Fig. 2e).

The masking materials (with the exception of the carbon paper) were cleaned using 99.9% isopropyl alcohol (Sigma Aldrich).

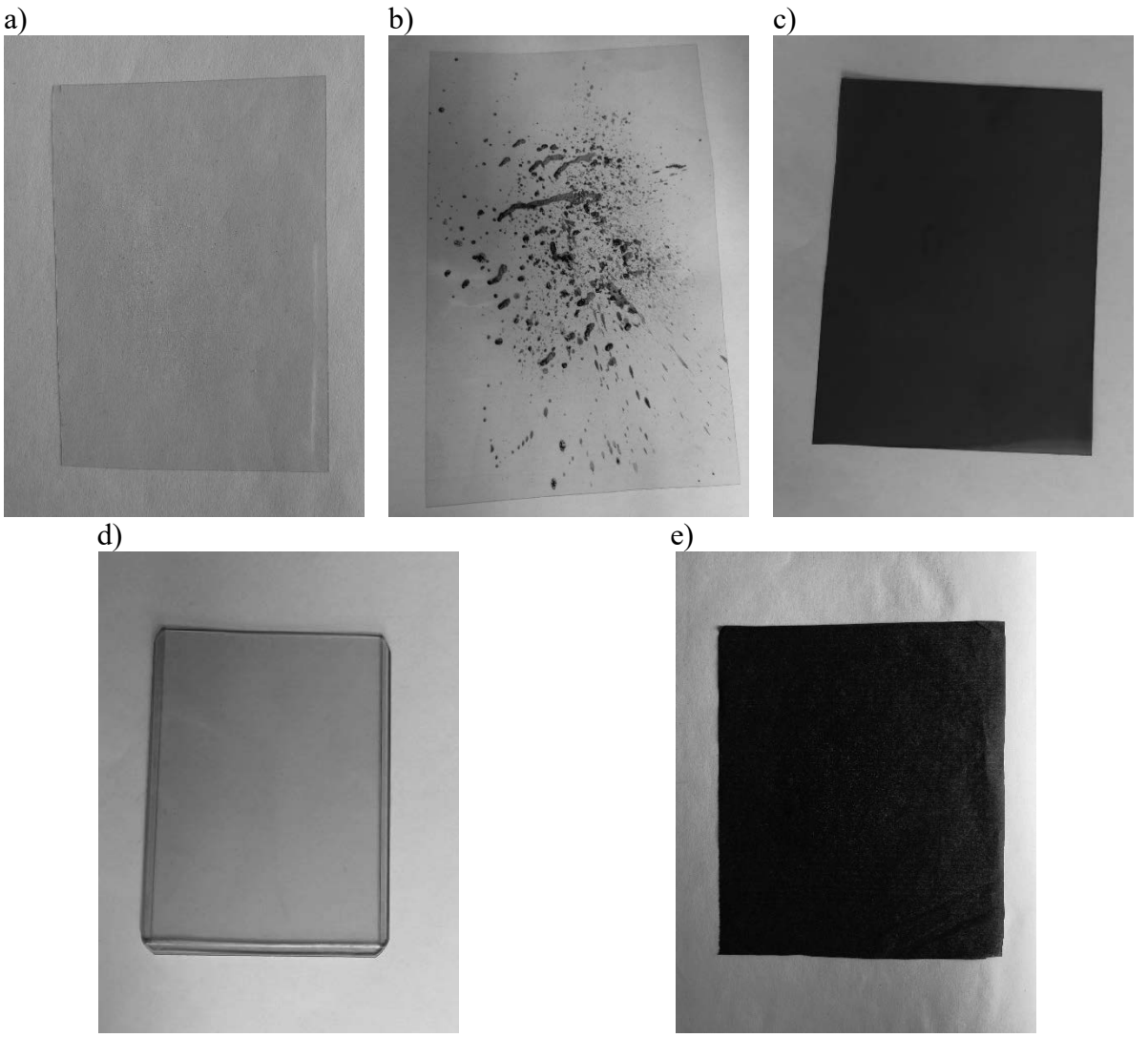

Figure 2. Applied masking materials: a) film A, b) film C, c) film B, d) toploader, e) carbon paper

The electrical properties of the monocrystalline silicon solar cell with partially shaded surfaces were determined on the basis of the measured current–voltage (I–V) characteristics using the SS IV CT 02 system manufactured by PV Test Solutions Tadeusz Żdanowicz, equipped with a PhotoEmission Tech SS150AAA Solar Simulator (Fig. 3).

Prior to the measurements, the system was calibrated against a reference solar cell in order to ensure the highest possible accuracy and reliable reproduction of the obtained measurement results. The measurements were carried out under solar irradiance of 1000 W/m², AM 1.5 spectral distribution, and a solar cell temperature of 25 °C. The masking materials were positioned at a distance of 70 mm from the measurement stage.

The transmittance of the applied masking materials was determined using a Thermo Scientific Evolution 220 UV-Vis Spectrophotometer (Fig. 4) within the wavelength range of 190–1100 nm.

Figure 3. SS IV CT 02 system for measuring the current-voltage characteristics of solar cells

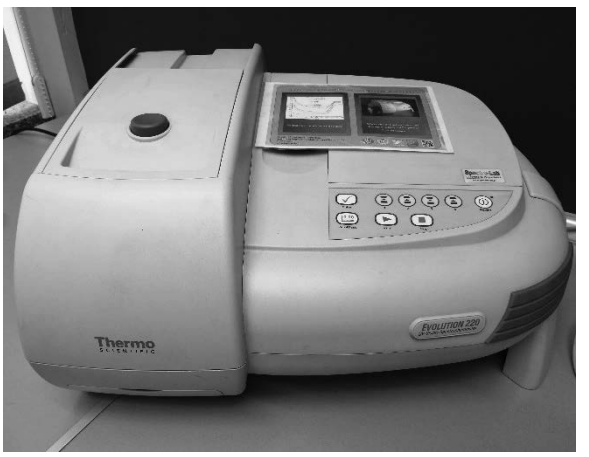

Figure 4. Evolution 220 UV-Vis spectrophotometer

3. RESULTS

Figure 5 presents the relationship between transmittance and wavelength for the masking materials used to shade the front surface of the monocrystalline silicon solar cell. It was found that film A transmitted more than 90% of light for wavelengths above 350 nm. For film C, the shape of the transmittance curve was comparable; however, its transparency above 290 nm was lower. At a wavelength of 500 nm, the transmittance was approximately 16% lower than that of film A. The application of the road-sign film onto film A (masking material designated as film B) significantly altered the shape of the transmittance curve. Two main peaks were observed: a narrow peak at approximately 460 nm and a broad peak centered around 980 nm. Film B exhibited limited transmission of orange and red light and was opaque to ultraviolet radiation.

For the toploader material, the following characteristics were obtained:

- an increase in transmittance above 280 nm,
- transparency exceeding:
  - 80% within the wavelength range of 412–523 nm,
  - 85% for wavelengths greater than 672 nm.

The lowest transmittance within the visible and infrared regions was observed for carbon paper. However, it should be emphasized that carbon paper was the only investigated material exhibiting partial transmission of ultraviolet radiation below 280 nm.

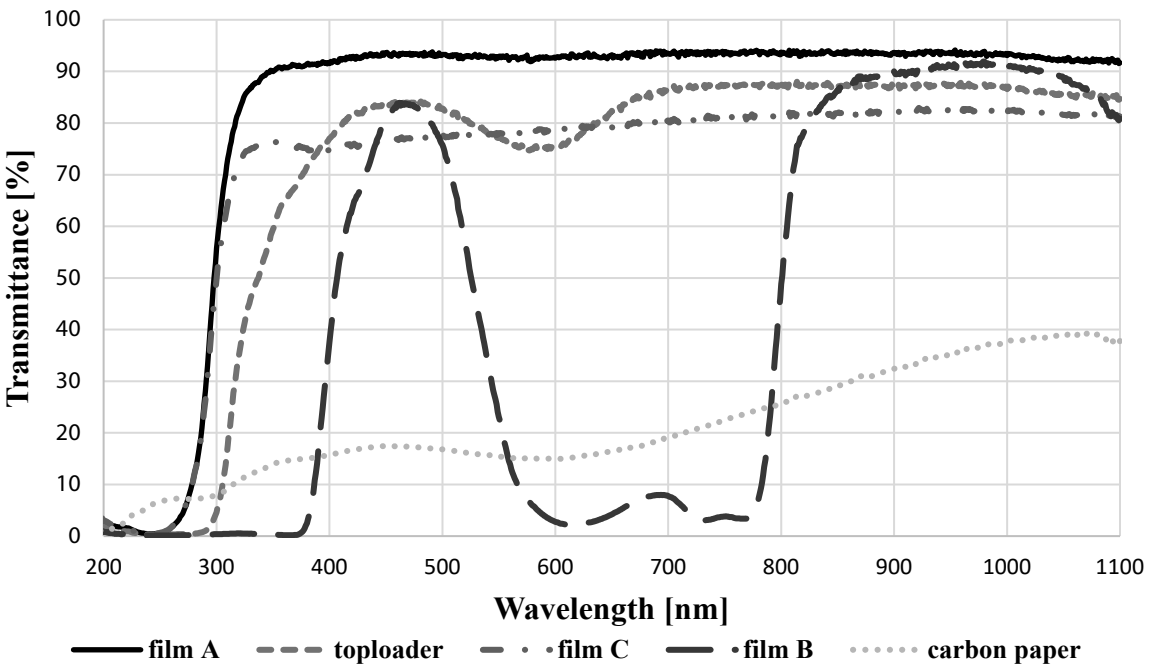

Figure 5. Dependence of the transmittance on the light wavelength of the masking materials

Figure 6 presents the current–voltage (I–V) characteristics of the monocrystalline solar cell shaded with masking materials of different transparency levels. Table 1 summarizes the electrical properties, including the short-circuit current (I_{sc}), open-circuit voltage (V_{oc}), current (I_m) and voltage (V_m) at the maximum power point, maximum power (P_m), fill factor (FF), and solar cell efficiency (E_{ff}). It was found that the application of the masking materials significantly affected the electrical properties of the monocrystalline silicon solar cell. Compared with the device operating without any filter, the efficiency of the solar cell decreased by 2.06%, 3.99%, 5.50%, 13.85%, and 18.33% for film A, toploader, film C, film B, and carbon paper, respectively.

The highest open-circuit voltage, equal to 0.634 V, was obtained for the solar cell without surface shading. The application of film A, the toploader, and film C resulted in only a slight reduction in Voc, whereas the use of film B and carbon paper caused a decrease of 0.03 V and 0.061 V, respectively. It was also observed that shading significantly affected the value of the short-circuit current, which is consistent with literature reports [6, 8]. Compared with the unshaded cell, the short-circuit current of the monocrystalline silicon solar cell decreased by 0.12 A, 0.22 A, 0.30 A, 0.72 A, and 0.96 A for film A, toploader, film C, film B, and carbon paper, respectively. The application of the masking materials did not significantly influence the fill factor, apart from low-transparency material, namely carbon paper, for which the FF value decreased by 0.02.

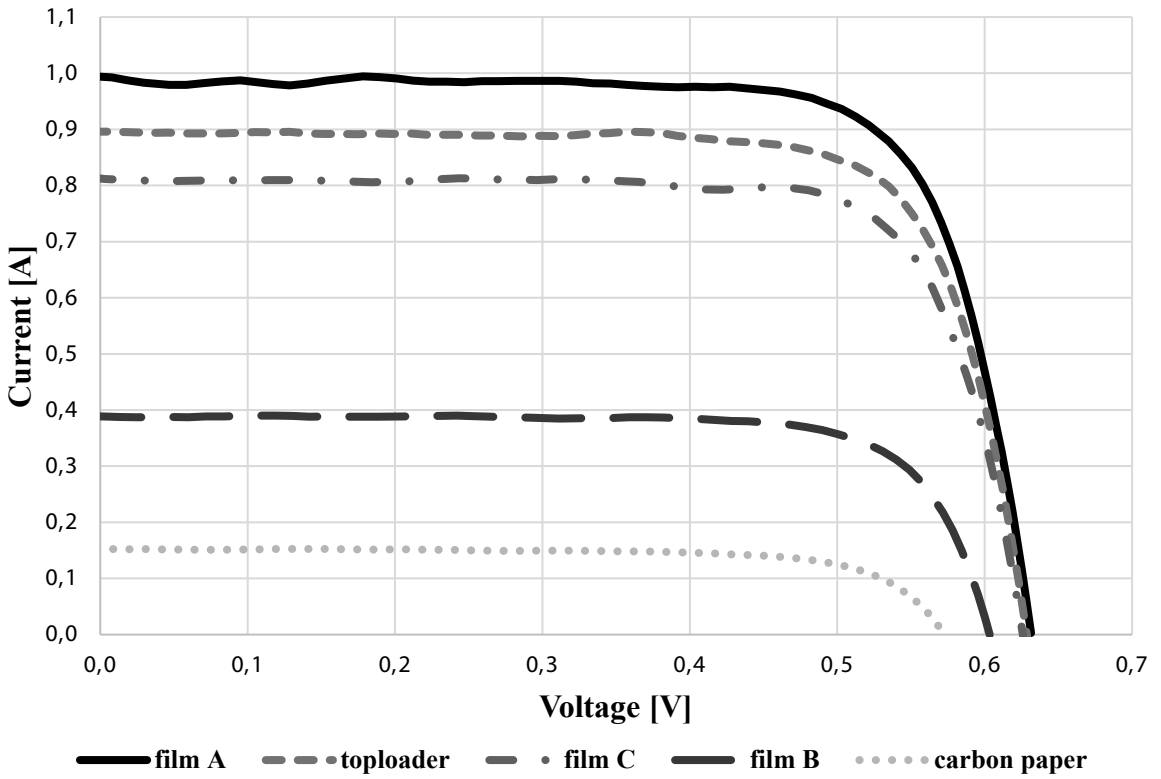

Figure 6. The current-voltage characteristics of monocrystalline silicone solar cell with shaded front surface

Table 1. Electrical properties of monocrystalline cells with shaded front surface

Type of masking materials	Electrical properties of solar cell						
	I_{sc} [A]	V_{oc} [V]	I_m [A]	V_m [V]	P_m [W]	FF	E_{ff} [%]
without masking	1.11	0.634	1.03	0.516	0.53	0.76	20.92
film A	0.99	0.632	0.92	0.515	0.47	0.76	18.86
toploader	0.89	0.628	0.83	0.514	0.43	0.76	16.93
film C	0.81	0.626	0.76	0.512	0.39	0.76	15.42
film B	0.39	0.604	0.36	0.499	0.18	0.76	7.07
carbon paper	0.15	0.573	0.14	0.470	0.06	0.74	2.59

4. CONCLUSION

Researchers worldwide continuously strive to improve the efficiency and reliability of solar cells, as photovoltaic energy plays an increasingly important role in the global energy system. Solar cells are capable of operating under cloudy conditions; however, their performance strongly depends on the intensity of solar radiation reaching the surface of the device.

Based on the investigations carried out in the present study, it was found that the highest light transmittance (exceeding 90% for wavelengths above 350 nm) was identified for film A, whereas the lowest transmittance was observed for carbon paper (below 40% across the entire investigated spectral range). However, it is worth noting that compared to the other investigated materials, carbon paper was the only one exhibiting the highest ultraviolet transmittance in the 210–280 nm wavelength range. The results demonstrated that the application of masking materials significantly affected the electrical properties of the monocrystalline silicon solar cell. The highest efficiency was recorded for the device operating without any masking material (20.92%), while the lowest efficiency was obtained for carbon paper (2.59%), which correlates well with the measured transmittance characteristics of the investigated materials. It was also found that shading of the solar cell significantly influenced the short-circuit current. This is due to the fact that the short-circuit current is directly proportional to the solar radiation incident on the cell surface. Under conditions of partial or complete shading, the number of generated charge carriers decreases, leading to a reduction in photocurrent and, consequently, a decrease in the output power of the system.

ACKNOWLEDGMENTS

The work was created as a result of the project PBL (Project Based Learning) - 14th edition – of the Excellence Initiative - Research University, Silesian University of Technology.

BIBLIOGRAPHY

1. M. Bošnjaković, Advance of Sustainable Energy Materials: Technology Trends for Silicon-Based Photovoltaic Cells. Sustainability 16 (2024) 7 962
2. M. Wacławek, T. Rodziewicz, Ogniwa słoneczne, Wydawnictwo Naukowo-Techniczne WNT, Warszawa 2011
3. Z. U. Khan, A. D. Khan, K. Khan, S. A. K. Al Khatib, S. Khan, M. Q. Khan, and A. Ullah, A Review of Degradation and Reliability Analysis of a Solar PV Module, IEEE Access 12, (2024) 185036–185056
4. M.A. Green, Solar Cells: Operating Principles, Technology and System Applications, Prentice-Hall, Englewood Cliffs NJ, 1982
5. O. Bamisile, C. Acen, D. Cai, Q. Huang, I. Staffell, The environmental factors affecting solar photovoltaic output, Renewable and Sustainable Energy Reviews 208 (2025) 115073
6. E. F. A. Al-Showany. The Impact of the Environmental Condition on the Performance of the Photovoltaic Cell. American Journal of Energy Engineering. 4/1 (2016) 1-7
7. M. T. Chaichan, B. A. Mohammed, H. A. Kazem, Effect of pollution and cleaning on photovoltaic performance based on experimental study, International Journal of Scientific & Engineering Research 6/4 (2015) 594-601
8. G. Álvarez-Tey, J.A.Clavijo-Blanco, Á. Gil-García, R. Jiménez-Castañeda, C. García-López, Electrical and Thermal Behaviour of Crystalline Photovoltaic Solar Modules in Shading Conditions. Applied Science 9/15 (2019) 3038

TalentDetector

7th-9th June 2026
Gliwice-Brenna, Poland

DEPARTMENT OF ENGINEERING MATERIALS AND BIOMATERIALS
FACULTY OF MECHANICAL ENGINEERING
SILESIAN UNIVERSITY OF TECHNOLOGY

INTERNATIONAL STUDENTS SCIENTIFIC CONFERENCE

Thin films of zinc oxide doped with aluminum produced by the sol-gel method

Jakub Rusinek[a], Martyna Pasieka[a], Karolina Kornecka[a], Michalina Ziółkowska[b], Magdalena Szindler[c], Marek Szindler [d], Grzegorz J. Nowak[ef]

[a] Students of the Silesian University of Technology, Faculty of Mechanical Engineering
[b] Students of the Silesian University of Technology, Faculty of Applied Mathematics
[c] Silesian University of Technology, Faculty of Mechanical Engineering, Department of Engineering Materials and Biomaterials
[d] Silesian University of Technology, Faculty of Mechanical Engineering, Didactic Laboratory of Nanotechnology and Material Technologies, Gliwice, Poland
[e]Lukasiewicz Research Network – Krakow Institute of Technology, Zakopianska Str. 73, 30-418 Krakow, Poland,
[f]Department of Biomaterials and Medical Devices Engineering, Faculty of Biomedical Engineering, Silesian University of Technology
email: marek.szindler@polsl.pl

Abstract: Aluminum-doped zinc oxide (AZO) thin films were fabricated on glass substrates using the sol–gel spin-coating method at a rotation speed of 2000 rpm with six deposited layers. The microstructure, surface morphology, and optical properties of the coatings were investigated using SEM, AFM, and UV–Vis spectroscopy. SEM and AFM analyses revealed a compact, homogeneous, and continuous surface morphology with favorable roughness parameters. Tauc plot analysis showed a direct optical band gap of approximately 3.71 eV, confirming the good optoelectronic properties of the obtained AZO thin films for transparent conductive applications.

Keywords: Aluminum-doped zinc oxide (AZO), Sol–gel spin coating, Thin films

1. INTRODUCTION

All Thin films based on metal oxides constitute an important group of modern engineering materials widely used in electronics, optoelectronics, energy conversion systems, and surface engineering. Their significance results from the possibility of tailoring functional properties through the control of chemical composition, microstructure, deposition conditions, and post-treatment processes. Thin films are generally defined as surface layers with thicknesses ranging from several nanometers to a few micrometers, where surface and interface phenomena strongly influence the overall behavior of the material. Depending on the selected oxide system and preparation method, thin films may exhibit optical transparency, electrical conductivity,

photocatalytic activity, corrosion resistance, antibacterial properties, or enhanced mechanical durability. Owing to this combination of properties, metal oxide coatings are extensively applied as protective layers, transparent electrodes, antireflective coatings, sensing materials, and functional interfaces in semiconductor devices. The functional behavior of metal oxide thin films is closely related to their structural organization. Parameters such as crystallographic orientation, grain size, porosity, surface roughness, and defect concentration determine optical, electrical, and mechanical performance. Thin films may possess amorphous, polycrystalline, or nanocrystalline structures depending on the deposition technique and thermal treatment. In nanocrystalline oxide films, the large fraction of grain boundaries significantly modifies charge transport, light interaction, and surface reactivity compared with bulk materials. Consequently, nanostructured oxide coatings are particularly attractive for transparent electronics, photovoltaic systems, gas sensing devices, and photocatalytic applications [1-4].

Various techniques are used for the fabrication of metal oxide thin films and can generally be divided into physical and chemical deposition methods. Physical approaches include thermal evaporation, electron beam evaporation, pulsed laser deposition, sputtering, and arc deposition, whereas chemical methods involve chemical vapor deposition (CVD), atomic layer deposition (ALD), spray pyrolysis, and solution-based techniques such as sol–gel processing. Among these methods, sol–gel technology has attracted considerable attention because of its relatively low processing cost, compositional flexibility, simplicity of equipment, and ability to produce homogeneous coatings on large-area substrates. In addition, the method enables easy incorporation of dopants directly into the precursor solution, which is particularly important for transparent conductive oxide systems [4-6].

Zinc oxide (ZnO) is one of the most extensively investigated metal oxides in thin-film technology. ZnO is a II–VI semiconductor crystallizing predominantly in the hexagonal wurtzite structure with lattice parameters of approximately a = 0.325 nm and c = 0.521 nm. Thin ZnO films commonly exhibit preferential orientation along the (002) plane, corresponding to the alignment of the c-axis perpendicular to the substrate surface. ZnO possesses a direct wide band gap of approximately 3.3–3.4 eV and a high exciton binding energy of about 60 meV, which enables efficient ultraviolet absorption and emission at room temperature. At the same time, ZnO films maintain high transparency in the visible spectral range, making them attractive for optoelectronic applications. An important advantage of ZnO is the possibility of modifying its electrical and optical properties through controlled doping. Among numerous dopants, aluminum is one of the most commonly used because of its small ionic radius, low cost, and high effectiveness as a donor impurity. Aluminum-doped zinc oxide (AZO) is formed when Al^{3+} ions substitute Zn^{2+} ions within the ZnO crystal lattice. This substitution introduces additional free electrons into the conduction band, increasing carrier concentration and reducing electrical resistivity. As a result, AZO behaves as a highly doped n-type semiconductor with properties suitable for transparent conductive oxide (TCO) applications [6-10].

The incorporation of aluminum influences not only the electrical conductivity but also the microstructure and optical response of ZnO thin films. Moderate Al doping generally improves conductivity while preserving high optical transparency. Increasing carrier concentration causes a shift of the Fermi level toward the conduction band, leading to the Burstein–Moss effect and an apparent widening of the optical band gap. Simultaneously, excessive doping may introduce structural disorder, lattice strain, and defect-related scattering centers, which can deteriorate crystallinity and charge carrier mobility. Therefore, the optimization of aluminum concentration and deposition parameters is essential for obtaining AZO films with balanced

optoelectronic properties. AZO thin films can be fabricated using numerous techniques, including sputtering, ALD, CVD, and sol–gel processing. Among them, the sol–gel spin coating method offers several technological advantages. In this process, metal precursors are dissolved in a suitable solvent to form a stable sol, which is deposited onto the substrate by spin coating. During spinning, centrifugal forces distribute the solution uniformly across the substrate surface, producing a thin liquid layer that subsequently transforms into a gel during drying. Final thermal annealing removes residual organic compounds and promotes crystallization of the oxide structure. The properties of the resulting AZO films strongly depend on precursor concentration, aluminum content, spin speed, number of coating cycles, drying conditions, and annealing temperature. AZO thin films are widely investigated as low-cost alternatives to indium tin oxide (ITO), particularly because zinc and aluminum are abundant, inexpensive, and less environmentally critical than indium. Their combination of high transparency and low resistivity makes them suitable for photovoltaic cells, flat-panel displays, touch screens, transparent heaters, UV photodetectors, gas sensors, and flexible electronic systems. In photovoltaic devices, AZO serves as a transparent conductive electrode and may additionally contribute to light trapping through surface texturing. In sensing applications, electrical conductivity changes in response to gas adsorption processes occurring at the film surface. Due to these versatile functional properties and the scalability of solution-based fabrication methods, AZO thin films remain an important subject of research in advanced materials engineering and modern optoelectronic technologies [10-15].

2. MATERIALS AND METHODOLOGY

Aluminum-doped zinc oxide (AZO) thin films were fabricated using the sol–gel spin-coating technique. Zinc acetate dihydrate was applied as the zinc source, while aluminum nitrate served as the dopant precursor. Ethanol was used as the solvent and acetic acid acted as a stabilizing agent during solution preparation. All chemicals were of analytical purity and were used as received. Glass substrates with dimensions of 2 × 2 cm were selected as deposition supports. Prior to coating, the substrates were cleaned sequentially in detergent solution, acetone, and ethanol using an ultrasonic cleaner, and then dried under ambient laboratory conditions. The precursor solution was prepared by dissolving zinc acetate in ethanol with continuous magnetic stirring at elevated temperature until a homogeneous and transparent solution was obtained. Subsequently, the aluminum precursor dissolved in a small amount of deionized water was slowly introduced into the zinc-containing solution. After additional stirring, the prepared sol was left for aging to improve its stability and ensure uniform precursor distribution.

AZO coatings were deposited by spin coating using a constant rotation speed of 2000 rpm. Each deposition cycle lasted 30 s, and a total of six successive layers were applied to obtain multilayer thin films. After each coating step, the samples were pre-heated at 200 °C for several minutes in order to evaporate residual solvents and partially densify the deposited layer. Following the deposition of all six layers, the coatings were subjected to final thermal annealing to promote crystallization of the oxide structure and removal of remaining organic compounds. The aluminum concentration in the deposited films was controlled through the precursor ratio in the sol and corresponded to approximately 2–3 at.% Al relative to zinc content. The applied deposition parameters were selected to achieve homogeneous coatings with good surface coverage and controlled thickness. The resulting six-layer films exhibited

increased thickness compared with single-layer coatings due to the cumulative deposition effect associated with repeated spin-coating cycles.
Surface morphology and microstructural features of the obtained AZO thin films were investigated using scanning electron microscopy (SEM, ZEISS SUPRA 35). Surface topography and roughness measurements were carried out using atomic force microscopy (AFM, Park Systems XE-100) operating in non-contact mode with a scanning area of 5 × 5 μm^2. Optical properties were analyzed by UV–Vis spectrophotometry in the wavelength range of 250–950 nm. The combination of SEM, AFM, and optical measurements enabled evaluation of the relationship between deposition conditions and the structural as well as optoelectronic properties of the AZO coatings.

3. RESULTS AND DISCUSSION

The morphology of the ZnO:Al 2000 (6×) thin film was analyzed using scanning electron microscopy (SEM). The SEM image presented in Figure 1a reveals a compact and homogeneous surface morphology composed of densely packed fine crystallites forming a continuous network across the entire observed area. No major cracks, discontinuities, or large agglomerates were detected, indicating good surface coverage and high structural integrity of the multilayer coating. Such morphology suggests that successive deposition cycles promoted gradual filling of surface irregularities and enhanced continuity of the coating. The EDS spectrum shown in Figure 1b confirms the presence of Zn, O, and Al elements in the deposited layer, verifying the successful incorporation of aluminum into the ZnO structure.

Surface topography and roughness were further investigated using atomic force microscopy. The AFM 2D and 3D images presented in Figure 2a–b demonstrate that the film surface remains continuous and free from dominant high-profile defects. Although local height variations are visible, the overall structure is relatively uniform and compact. The multilayer sample exhibits a more developed local topography compared to the single-layer coatings, which may result from the accumulation and partial interpenetration of successive deposited layers during the spin-coating process. Nevertheless, the measured roughness parameters indicate favorable surface quality. The maximum surface height reached only 13.536 nm, which was the lowest value among all investigated samples. Additionally, the root mean square roughness (Rq) and average roughness (Ra) were equal to 4.136 nm and 3.148 nm, respectively. These results confirm that the multilayer ZnO:Al coating maintained good surface continuity despite the increased thickness of the film.

The optical properties of the ZnO:Al 2000 (6×) coating were evaluated using UV–Vis spectroscopy and Tauc plot analysis. The corresponding Tauc plot is shown in Figure 3. The absorption edge exhibits the characteristic behavior of a wide-band-gap semiconductor with a direct optical transition. In comparison with the single-layer samples, the absorption edge of the multilayer film is slightly less steep, which may be associated with increased thickness and a higher density of structural defects or localized states within the band structure. Based on the extrapolation of the linear region of the Tauc plot, the optical band gap energy (Eg) of the ZnO:Al 2000 (6×) thin film was determined to be approximately 3.71 eV. The slightly lower band-gap value compared to the other investigated samples may facilitate carrier excitation and improve electrical conductivity. Despite this reduction, the film preserved high optical transparency and retained the characteristic optoelectronic properties of aluminum-doped zinc oxide thin films.

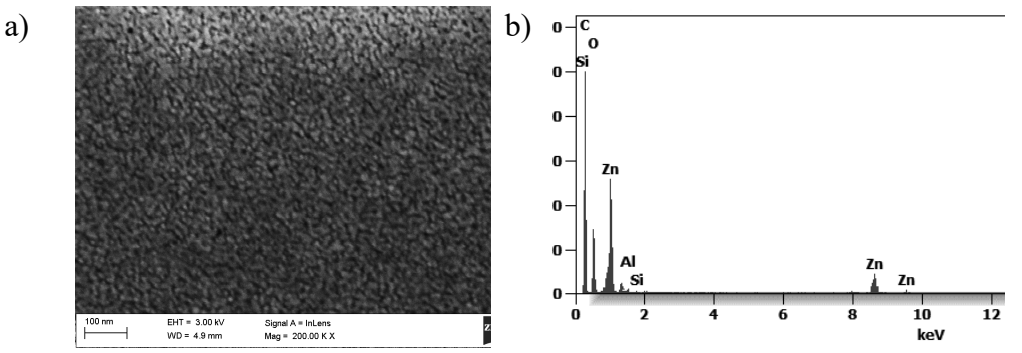

Figure 1. SEM micrograph (a) and Energy-dispersive X-ray spectroscopy (EDS) spectrum (b) of ZnO:Al (2 at.%) thin film produced by the sol–gel spin coating method

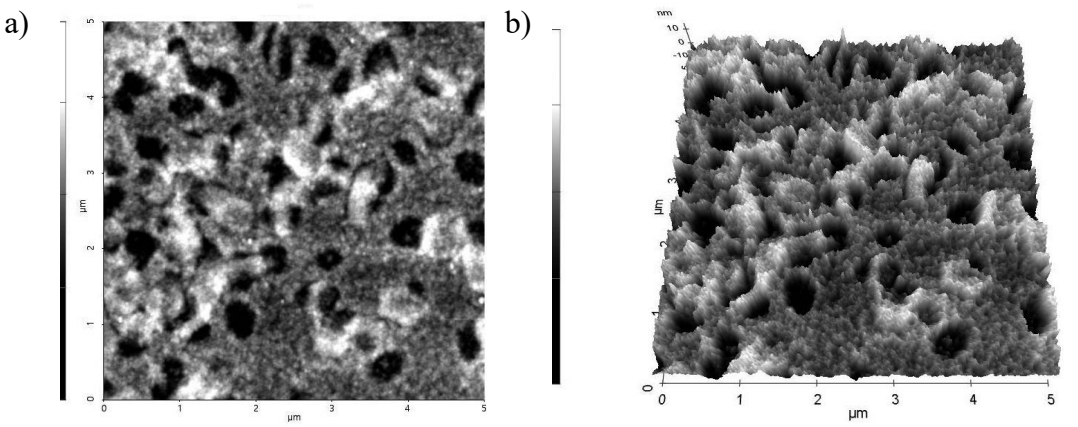

Figure 2. AFM 2D (a) 3D (b) images of ZnO:Al (2 at.%) thin film produced by the sol–gel spin coating method

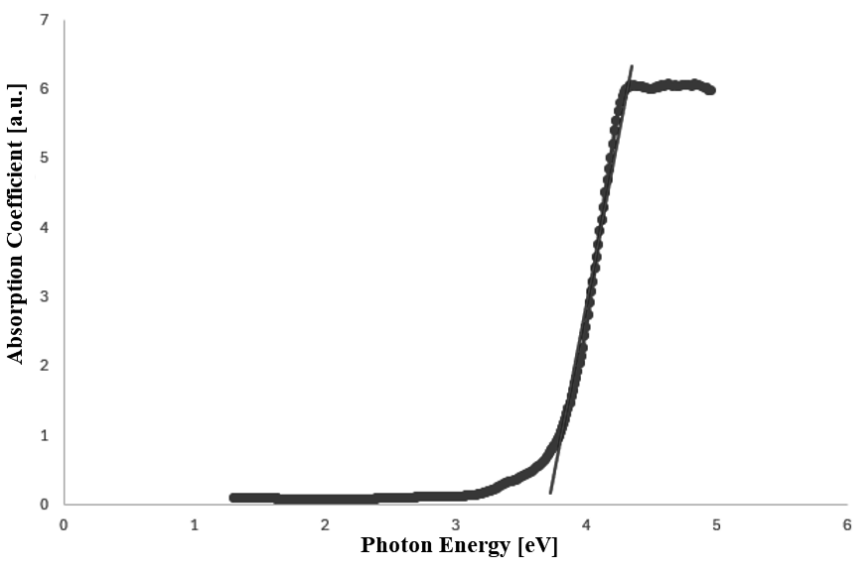

Figure 2. Tauc diagrams for ZnO:Al layers based on UV/VIS measurements

4. SUMMARY AND CONCLUSIONS

In this study, aluminum-doped zinc oxide (AZO) thin films were successfully fabricated on glass substrates using the sol–gel spin-coating technique with a constant rotation speed of 2000 rpm and six successive deposition cycles. The applied technological parameters enabled the formation of homogeneous multilayer coatings with good surface coverage and favorable structural as well as optical properties. SEM observations demonstrated that the ZnO:Al 2000 (6×) coating possessed a compact and continuous microstructure composed of densely packed fine crystallites. No significant cracks, discontinuities, or large agglomerates were observed, indicating good adhesion and high integrity of the deposited film. EDS analysis confirmed the presence of zinc, oxygen, and aluminum, verifying successful incorporation of the Al dopant into the ZnO structure. AFM investigations revealed that the multilayer coating exhibited a relatively uniform and continuous surface morphology despite local height variations associated with the multilayer architecture. The obtained roughness parameters confirmed favorable surface quality, with the maximum height parameter equal to 13.536 nm, while the average roughness (Ra) and root mean square roughness (Rq) reached 3.148 nm and 4.136 nm, respectively. The results indicate that repeated deposition cycles improved coating continuity and densification without generating dominant surface defects. Optical investigations performed using UV–Vis spectroscopy showed that the AZO thin film retained the characteristic transparency and wide-band-gap behavior typical for ZnO-based semiconductor coatings. Analysis of the Tauc plot confirmed the direct optical transition and allowed determination of the optical band-gap energy at approximately 3.71 eV. The slightly reduced band-gap value compared with thinner coatings may be associated with increased film thickness and structural effects related to multilayer deposition, which can contribute to improved charge carrier excitation. The obtained results demonstrate that the sol–gel spin-coating method is an effective and low-cost approach for the fabrication of AZO thin films with controlled microstructure and favorable optoelectronic properties. The investigated ZnO:Al 2000 (6×) multilayer coating exhibited good structural uniformity, compact morphology, and suitable optical characteristics, making this type of material promising for potential applications in transparent electronics, optoelectronic devices, photovoltaic systems, and transparent conductive coatings.

BIBLIOGRAPHY

1. T. Hryniewicz, *Technologia powierzchni i powłok*, Politechnika Koszalińska, 1999.
2. T. Nimalan, M. R. Begam, *Physical and Chemical Methods: A Review on the Analysis of Deposition Parameters of Thin Film Preparation Methods*, International Journal of Thin Films Science and Technology, 2024.
3. J. Ziaja, *Cienkowarstwowe struktury metaliczne i tlenkowe. Właściwości, technologia, zastosowanie w elektrotechnice*, Oficyna Wydawnicza Politechniki Wrocławskiej, Wrocław, 2012.
4. Z. Wiliński, L. Lipińska, R. Batjewski, A. Marcjaniuk, *Chemiczne i elektrochemiczne wytwarzanie warstw tlenku cynku*, Instytut Technologii Materiałów Elektronicznych, 2009.
5. S. Vyas, *A Short Review on Properties and Applications of Zinc Oxide Based Thin Films and Devices*, Johnson Matthey, 2020.

6. L. Schmidt-Mende, J. L. MacManus-Driscoll, *ZnO – nanostructures, defects, and devices*, Materials Today, 2007.
7. J. G. Cuadra, *Functional properties of transparent ZnO thin films synthetized by using spray pyrolysis for environmental and biomedical applications*, Ceramics International, 2023.
8. T. J. Coutts, J. D. Perkins, D. S. Ginley, T. O. Mason, *Transparent Conducting Oxides: Status and Opportunities in Basic Research*, NREL, 1999.
9. A. Shabani, M. Khazaei Nezhad, N. Rahmani et al., *Revisiting the Optical Dispersion of Aluminum-Doped Zinc Oxide*, Wiley-VCH GmbH, 2021.
10. S. Khan, E. Stamate, *Comparative Study of Aluminum-Doped Zinc Oxide, Gallium-Doped Zinc Oxide and Indium-Doped Tin Oxide Thin Films Deposited by RF Magnetron Sputtering*, Nanomaterials, 2022.
11. G. M. Wu, Y. F. Chen, H. C. Lu, *Aluminum-Doped Zinc Oxide Thin Films Prepared by Sol-Gel and RF Magnetron Sputtering*, Acta Physica Polonica A, 2011.
12. L. Znaidi, T. Touam, D. Vrel et al., *AZO Thin Films by Sol-Gel Process for Integrated Optics*, Coatings (MDPI), 2013.
13. J. B. Hahn, N. Ehrmann, R. Reineke-Koch et al., *Aluminum-doped zinc oxide sol–gel thin films: Influence of the sol's water content on the resistivity*, Thin Solid Films, 2014.
14. M. H. Nateq, R. Ceccato, *Enhanced Sol–Gel Route to Obtain a Highly Transparent and Conductive Aluminum-Doped Zinc Oxide Thin Film*, Materials (MDPI), 2019.
15. J. Patel, R. K. Sharma, M. A. Quijada et al., *A Review of Transparent Conducting Films (TCFs): Prospective ITO and AZO Deposition Methods and Applications*, Nanomaterials, 2024.

TalentDetector
7th-9th June 2026
Gliwice-Brenna, Poland
DEPARTMENT OF ENGINEERING MATERIALS AND BIOMATERIALS
FACULTY OF MECHANICAL ENGINEERING
SILESIAN UNIVERSITY OF TECHNOLOGY
INTERNATIONAL STUDENTS SCIENTIFIC CONFERENCE

Defining a Suitable Wind Tunnel Design

Jovani Samir Sabri[a], Givi Sanadze[b]

[a] Georgian Technical University, Faculty of Transport Systems and Mechanical Engineering, Department of Mechanical Engineering and Industrial Technology
email: samirsabrinasip.jovani25@gtu.ge
[b] Georgian Technical University, Faculty of Transport Systems and Mechanical Engineering, Department of Mechanical Engineering and Industrial Technology, Professor
email: sanadzegivi05@gtu.ge

Abstract: This article examines the importance of wind tunnel applications for engineering problem solving and training. The article is based on a wind tunnel project at the Georgian Technical University. For this purpose, various design options were studied and evaluated.

SolidWorks was used for the wind tunnel design, simulation, and study. We propose a multifunctional wind tunnel design suitable for confined spaces. We developed this design to maximize the ability to generate multiple types of flows within the tunnel. The design methodology incorporates various flow optimization parameters to ensure homogeneity across tunnel sections using computational fluid dynamics (CFD) simulations. The proposed tunnel's ability to simulate cyclones, downdrafts, and atmospheric boundary flows was also evaluated.

Keywords: Wind Tunnel, Aerodynamics, Design, Computational Fluid Dynamics Simulation (CFD), Turbulence intensity, Test-Section, Velocity, Open circuit wind tunnel, Closed circuit wind tunnel, Mach number, Reynolds number.

1. INTRODUCTION

A wind tunnel is an experimental device used by aerodynamic engineers to study the phenomena and processes that influence proposed aircraft designs. Within the tunnel, engineers can precisely control the flow conditions that affect aircraft performance [4]. The model is placed in a test section of the tunnel and equipped with instruments to study flow in the surface layers of the atmosphere [3]. To obtain meaningful data, engineers must ensure that flow parameters, such as Mach number and Reynolds number, correspond to flight conditions. The model often includes small ports for measuring pressure, or it can be mounted on a scale to directly measure the aircraft's lift or drag [4].

It is essential to understand when using a wind tunnel is appropriate and when better alternatives may exist. The advantages of wind tunnel tests are: This system provides real-world validation of aerodynamic theories. Iterative design optimization is enhanced through experimental feedback. Student engagement in STEM subjects is improved through hands-on

learning. Computational fluid dynamics simulations are complemented by physical verification. But it also has the following disadvantages: High-quality models can be expensive. They require space, power, and regular calibration. Smaller devices may not accurately replicate real-world Reynolds numbers. Not all consumer models publish performance data for verification [5].

2. TYPES OF WIND TUNNELS

There are two main types of wind tunnels and two main types of test section designs. However, the specific characteristics of each tunnel vary considerably. The two main types of test section designs are the open test section design and the closed test section design, although these are now considered opposite ends of the spectrum, as test sections with slotted walls are used in both low-speed wind tunnels and supersonic wind tunnels.

In an open circular wind tunnel, air flows in a nearly straight path from the inlet, through the compressor, to the test section, then to the air distributor, fan section, and vent. Construction costs are typically much lower. If the goal is to film smoke flow on a large scale, cleaning is not a problem, provided the intake and exhaust pipes are open to air. If the tunnel is placed in a room, depending on the size of the tunnel and the room, a large-scale protective layer at the inlet may be required to ensure high-quality airflow. The same applies if the exhaust inlet is open to the air, as both wind and cold can affect performance. For a given size and speed, the tunnel will require more power to operate. This is usually only a significant factor when used in development experiments, where tunnel utilization rates are high. Generally, open-circuit tunnels tend to generate noise. in large tunnels, this noise can cause environmental problems, limit operating hours, or require extensive acoustic treatment of the tunnel and surrounding room.

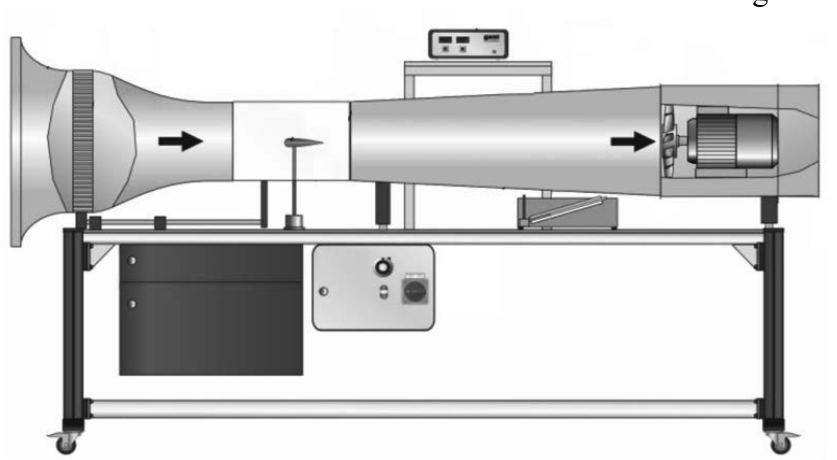

Figure 1. open-circuit(open-jet) wind tunnel

In a closed-circuit (Recirculating) wind tunnel, such as the Prandtl or Göttingen tunnels, the air circulates continuously with little to no exchange with the outside air. The vast majority of closed- loop wind tunnels are based on a single-loop system, although double-loop and annular tunnels also exist. Using angled rotating vanes and screens, flow quality can be precisely controlled, and, importantly, it will be independent of other activities in the building and weather conditions. It requires less energy for a given size and velocity of the test section. This is crucial for tunnels used in high-load development experiments. Ambient noise levels during operation are also reduced. The initial cost is higher due to the presence of return pipes and inclined fins.

If the tunnel is used extensively for smoke flow imaging experiments or for running internal combustion engines, a dedicated cleaning area is required. If the tunnel is used frequently, an air exchanger or another cooling method may be necessary [2].

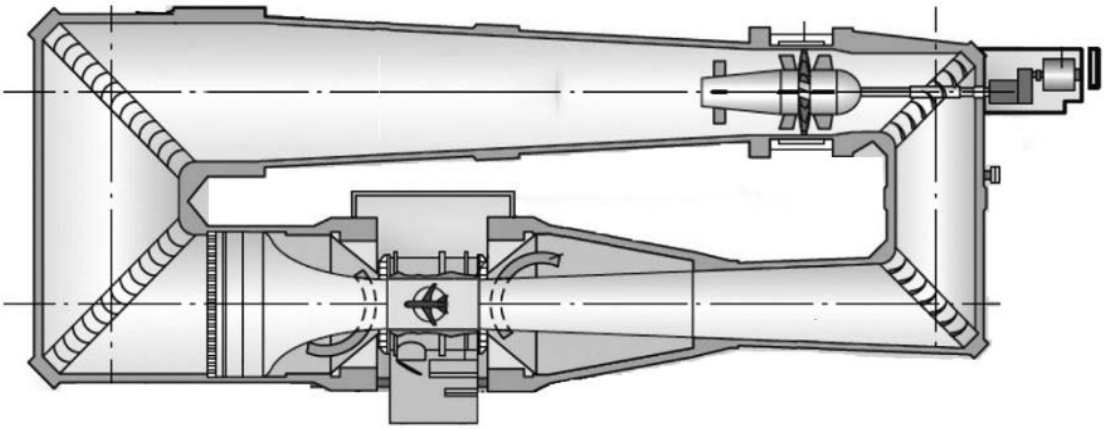

Figure 2. Closed-circuit wind tunnel

3. DESIGN REQUIREMENTS FOR WIND TUNNELS

The fundamental requirement for a wind tunnel is the ability to produce a straight and uniform airflow. Achieving this requirement is extremely difficult. As a preliminary approximation, the straightness and uniformity of the flow are ensured through the engineering of the tunnel walls and internal structural elements [2]. The basic requirements can be summarized as follows:

- Define your use case: Are you teaching basic airflow concepts? Designing drones? Testing structural models? Design the tunnel capabilities to suit your primary purpose.
- Determine the required dimensions for the test section. Measure the largest planned model and add a safety margin (at least 20% on all sides).
- Choose the type based on your accuracy requirements: For qualitative demonstrations, an open-jet configuration may suffice. For quantitative research, choose a closed-loop, low-turbulence system.
- Verify the airflow specifications. Confirm the maximum velocity and flow consistency. Request independent test reports if available.
- Evaluate the measuring devices. Integrated Pitot tubes, load cells, and pressure gauge ports save time and improve consistency.
- Assess the build quality. check the materials, connection integrity, and vibration resistance.
- Review calibration options. Is the system recalibrable? Is NIST certification available?
- Check safety features. Look for emergency stop buttons, safety barriers, and an engine overload protection system.

4. CAD DESIGNS OF WIND TUNNELS

SolidWorks was used for the wind tunnel design, simulation, and study. We propose a multifunctional wind tunnel design suitable for confined spaces. We developed this design to maximize the ability to generate multiple types of flows within the tunnel. The design

methodology incorporates various flow optimization parameters to ensure homogeneity across tunnel sections using computational fluid dynamics (CFD) simulations. The proposed tunnel's ability to simulate cyclones, downdrafts, and atmospheric boundary flows was also evaluated.

Multiple simulations were performed for each of these wind flow models, varying the tunnel parameters that control these phenomena [6]. We made sure that the initial conditions and the dimensional space were at the same stage so that we could make a fair comparison. The dimensions of the entire design were determined between: length=7m, height=3m, width=2m. the flow speed was set to 25 km/h. We present design options and streamlined modeling of closed wind tunnels.

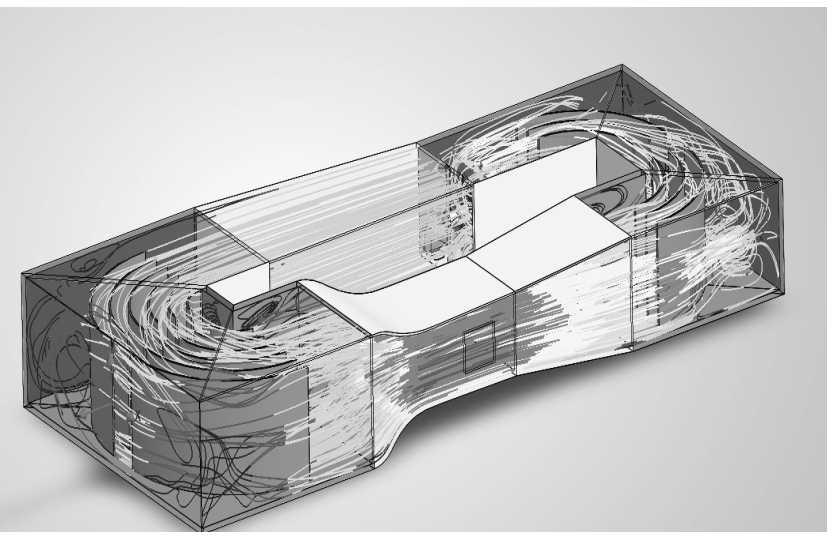

Figure 3. Rounded Horizontal Tunnel

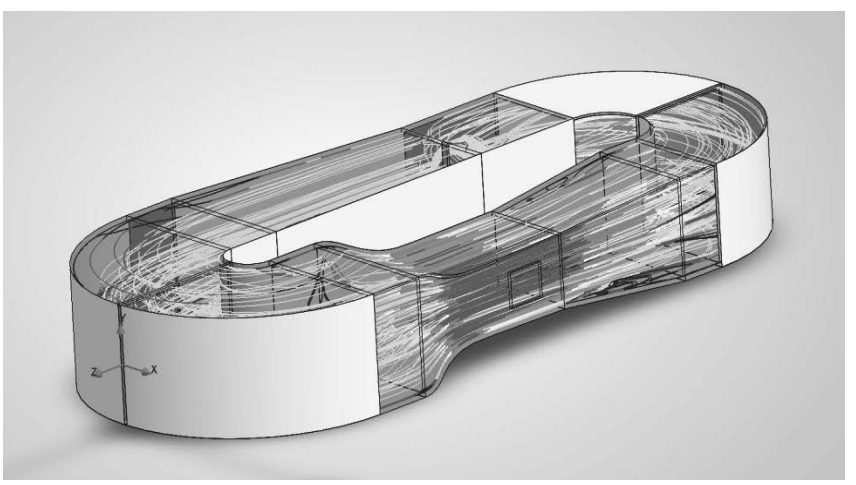

Figure 4. Rounded Horizontal Tunnel with Optimized Outer Surface

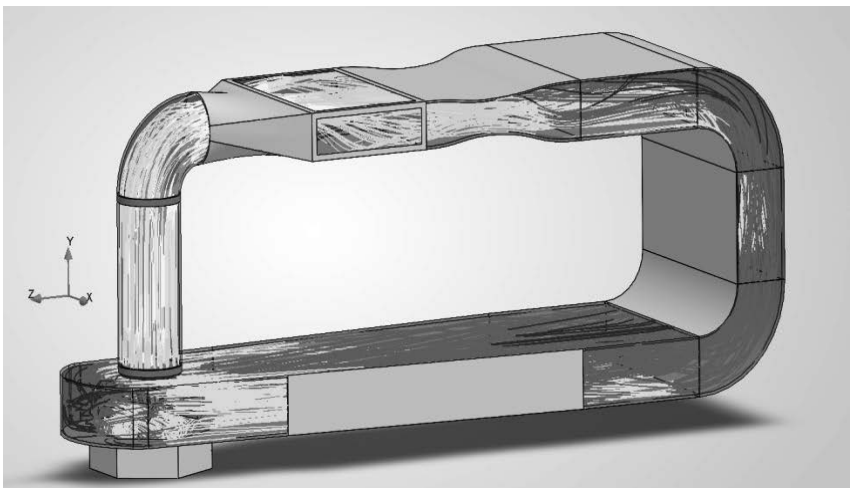

Figure 5. Rounded Vertical Tunnel (Compact Layout)

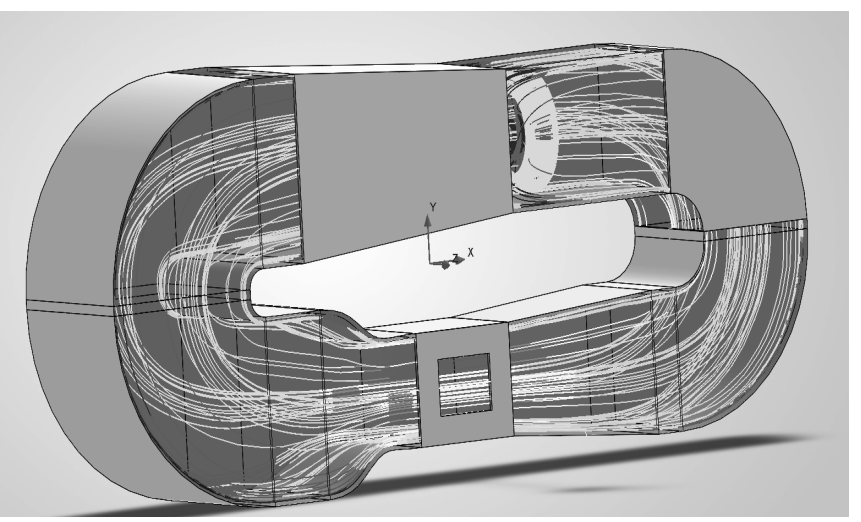

Figure 6. Rounded Vertical Tunnel with lower test-section

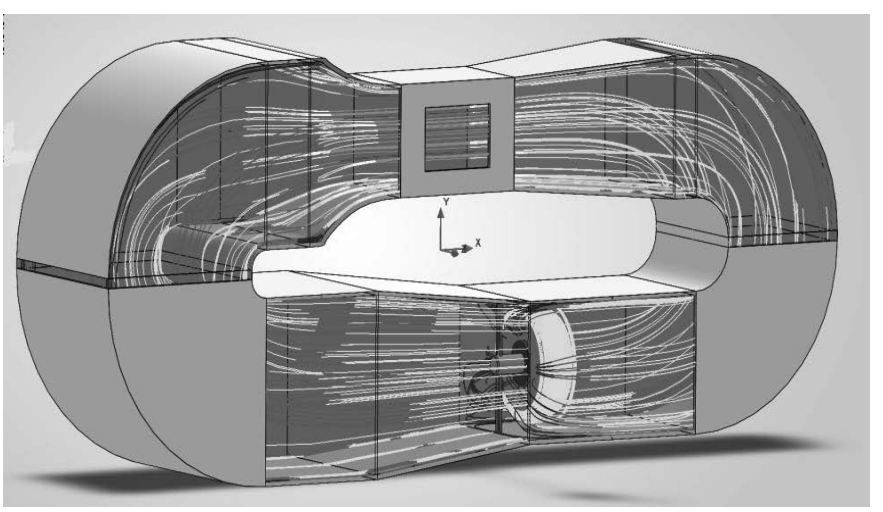

Figure 7. Rounded Vertical Tunnel with upper test-section

Table 1. Simulation setup and goals conditions:

Wind Tunnel	Rounded horizontal tunnel	Rounded horizontal tunnel with optimized outer surface	Rounded vertical tunnel (compact layout)	Rounded vertical tunnel with lower test section	Rounded vertical tunnel with upper test section
Min. pressure [Pa]	101271.70	101320.45	101262.61	101309.96	100309.72
Max. pressure [Pa]	101529.00	147484.86	101436.78	158303.68	183891.01
Velocity [Km/H]	47.261	711.276	35.919	771.087	903.625
Min. density (fluid) [Kg/M^3]	1.18	1.31	1.18	1.40	1.18
Max. density (fluid) [Kg/M^3]	1.18	1.72	1.18	1.84	2.15
Mach number	0.04	0.59	0.03	0.64	0.76
Turbulence intensity [%]	0.91	0.84	0.70	0.94	0.68
Velocity uniformity [%]	151.6	28.3	24.4	33	10.9
Mass flux [Kg/(M^2·S)]	8.0295	-0.9554	0.0107	-0.6155	-1.2222

5. CONCLUSION

Choosing the right wind tunnel requires balancing application needs, specifications, and budget. For educators, a high-quality open-type or smoke-filled wind tunnel may suffice to demonstrate airflow principles. Researchers and engineers, however, should prioritize closed-loop designs with proven low turbulence and digital instruments. Always review detailed specifications, consult customer reviews, and verify supplier reliability before making any decisions. By focusing on key parameters such as pressure ratio, flow uniformity, and test section size, you can select a wind tunnel that delivers meaningful and reproducible results.

BIBLIOGRAPHY

1. S. M. Gorlin and I. I.Slezinger. Wind Tunnels And Their Instrumentation -NASA - IPST - 1966.
2. J.B.Barlow, W.H.Rae, Jr, A. Pope Low Speed Wind Tunnel Testing ,published simultaneously in Canada,1999 by John Wiley.
3. Study of Parameters and Characteristics of Turbulent Flow in the Working Zone of a Wind Tunnel, Received April 7, 2024; Moscow State University of Civil Engineering (MGSU), Research Institute of Mechanics, Moscow State University, revised May 22, 2024; accepted July 4, 2024.

4. Wind Tunnel Aerodynamics-Glenn Research center -by Tom Benson - Engine Systems Technology Branch 21000 Brookpark Road Cleveland, Ohio 44135- https://www.grc.nasa.gov/www/k-12/VirtualAero/BottleRocket/airplane/benson.html.
5. How to Choose the Best Wind Tunnel for Your Needs: Buying Guide 20 December 2025- By Rachel Williams .
6. Designing a multi-purpose wind tunnel suitable for limited spaces-Author links open overlay panel - Mohamed Abdelwahab, Tarek Ghazal, Haitham Aboshosha -Received 28 April 2022, Revised 20 May 2022, Accepted 21 May 2022, Available online 27 May 2022, Version of Record 10 June 2022.

TalentDetector

7th-9th June 2026
Gliwice-Brenna, Poland

DEPARTMENT OF ENGINEERING MATERIALS AND BIOMATERIALS
FACULTY OF MECHANICAL ENGINEERING
SILESIAN UNIVERSITY OF TECHNOLOGY

INTERNATIONAL STUDENTS SCIENTIFIC CONFERENCE

Assessment of the Degradation Process of a ZnMg1.2 wt% Alloy with a ZnO Coating for Biomedical Applications

Mateusz Słonka[a], Igor Szymiczek[b], Zofia Wolska[c], Aleksandra Wierzbicka[d], Martyna Rzepiela[e], Jakub Wierciński[f], Magdalena Skonieczna[g], Katarzyna Cesarz-Andraczke[h], Mateusz Smolarz[i], Marcin Staszuk[j],

[a] Student of Silesian University of Technology, email: ms309483@student.polsl.pl
[b] Student of Silesian University of Technology, email: is309487@student.polsl.pl
[c] Student of Silesian University of Technology, email: zw313185@student.polsl.pl
[d] Student of University School of Physical Education, email: 49098@awfkatowice.edu.pl
[e] Student of Silesian University of Technology, email: mr303355@student.polsl.pl
[f] Student of University School of Physical Education, email: kuba.wiercinski@op.pl
[g] Silesian University of Technology, Institute of Automation, Department of Systems Engineering and Biology, email: magdalena.skonieczna@polsl.pl
[h] Silesian University of Technology, Faculty of Mechanical Engineering, Department of Engineering Materials and Biomaterials email: katarzyna.cesarz-andraczke@polsl.pl
[i] University School of Physical Education, Institute of Physiotherapy and Health Sciences, email:m.smolarz@awf.katowice.pl
[j] Silesian University of Technology, Faculty of Mechanical Engineering, Department of Engineering Materials and Biomaterials email: marcin.staszuk@polsl.pl

Abstract: In this study, structural investigations and degradation tests were carried out on samples of a cast ZnMg1.2 wt% alloy, as well as on the same alloy coated with a ZnO layer using the Atomic Layer Deposition (ALD) method. Due to the potential application of zinc alloys as resorbable materials for medical implants, the effectiveness of the applied coating was evaluated in terms of its ability to homogenize the degradation process of the zinc alloy during the first two weeks of degradation under simulated service conditions. The ZnO protective coating deposition process was selected as a method to enhance corrosion resistance and reduce the degradation rate of the substrate material.

Keywords: biomaterials, degradation, structure, ALD, ZnO

1. INTRODUCTION

The use of resorbable implants in orthopedic surgery can offer a number of benefits. The most significant potential advantage of this approach is the elimination of the need for a second surgical procedure to remove implants whose function is only temporary stabilization of the tissue, enabling its remodeling in a manner as close as possible to physiological structure.

Reducing the number of surgical procedures is associated with shorter patient immobilization time and, consequently, a lower risk of complications from the circulatory, respiratory, and musculoskeletal systems. Immobilization lasting longer than three days after surgery is already associated with more than a twofold increase in the risk of thromboembolic complications (OR = 2.21) [1].

When selecting an appropriate material for biomedical applications, in addition to properties such as mechanical strength, particular attention must be paid to the degradation process of the material and whether the compounds released during implant degradation are non-toxic to the recipient's body. Studies have shown that degradation kinetics are directly related to cell proliferation, tissue synthesis, and regeneration, influencing the composition and structure of the final extracellular matrix and the overall host response [2].

A potential metallic biomaterial that has recently attracted considerable attention from many research groups is zinc-based alloys with the addition of bio-compatible elements. It should be noted that zinc, a trace element present in the human body, is also essential for many biological processes. Corrosion products of zinc after 4.5 and 6 months in vivo are largely compact and consist mainly of zinc oxide with a contribution of zinc carbonate. Data indicate that both Zn- and Mg-based biomaterials support adhesion and proliferation of hMSCs and induce cytoskeletal reorganization and extracellular matrix mineralization in vitro.

The results reported by Tang et al. [3] show that during long-term immersion of zinc in Ringer's solution, the corrosion product layer consists of a relatively compact, banded inner layer of $CaCO_3$ formed at the early stage, and a more porous, mixed outer layer composed of $CaCO_3$ and $Zn_5(CO_3)_2(OH)_6$, formed at a later stage, which provides good protection and stability. However, due to the multiphase nature of zinc alloys, protective coatings are often applied to homogenize this process in order to preserve the mechanical integrity of a future implant.

ALD (Atomic Layer Deposition) is a technique first introduced by Suntola and Antson in 1977 for coating a flat ZnS display. In general, this method involves the deposition of various materials from the gas phase in thin, most often monolayer films on selected surfaces. The ability to precisely control the deposition process and film thickness is the main advantage of ALD compared to other methods such as Chemical Vapour Deposition (CVD). This is possible due to the self-limiting nature of the process, which results in the formation of only a single precursor layer during its interaction with the surface of the coated material. ALD is widely used in many industrial sectors, including microelectronics, the fabrication of transistors and capacitors, energy storage and conversion, as well as desalination and the development of biomimetic membranes [4].

In addition to zinc alloys themselves, zinc oxide (ZnO) has also found wide application in medicine due to its antibacterial, anti-inflammatory, and biocompatible properties. It has been used for many years in dermatology, dentistry, and as a wound dressing that promotes healing. It is considered a safe and biocompatible material, and its activity is associated with the generation of reactive oxygen species and the release of Zn^{2+} ions, which disrupt bacterial cell function. ZnO coatings applied to medical materials have been shown to exhibit strong antibacterial activity against microorganisms such as *Escherichia coli*, *Staphylococcus aureus*, and *Pseudomonas aeruginosa*, which are among the pathogens responsible for hospital-acquired infections and therefore pose a serious threat, particularly to immunocompromised patients [5].

1.1. Materials and methods

The investigated material was a cast ZnMg1.2 wt% alloy. The elements used for alloy preparation were Zn with a purity of 99.95% and Mg with a purity of 99.95%. The initial charge was weighed,

and magnesium was then melted in liquid zinc at approximately 520 °C in a ceramic (Al_2O_3) crucible under an argon protective atmosphere. The ZnO coating on the ZnMg1.2 wt% alloy was deposited using the Atomic Layer Deposition (ALD) technique at 200 °C (1500 cycles). The surface topography and structure of the ZnO coating deposited by ALD on the ZnMg1.2 wt% alloy were examined using Atomic Force Microscopy (AFM). The first step after material preparation was cutting the samples into sections for embedding in resin. The ZnMg1.2 wt% alloy samples were then ground using abrasive papers with grit sizes of 500, 800, and 1200. Polishing was carried out using diamond suspensions with particle sizes of 9, 6, 3, and 1 µm, respectively. The samples were subsequently etched in nital. Structural investigations of the ZnMg1.2 wt% alloy were performed using a Zeiss optical microscope at magnifications of 100× and 200×. Immersion degradation tests of coated and uncoated samples were carried out in Ringer's solution at 37 °C. The chemical composition of the Ringer's solution was as follows: sodium chloride (NaCl): 8.60 g, potassium chloride (KCl): 0.30 g, calcium chloride dihydrate: 0.33 g (or 0.24 g anhydrous), and distilled water up to 1000 ml. Sample immersion lasted 264 hours. After immersion testing, the surface condition of the coated sample was evaluated using Scanning Electron Microscopy (SEM). A preliminary analysis of the chemical composition of degradation products formed on the surface of both coated and uncoated samples was performed using Energy Dispersive X-ray Spectroscopy (EDS). The removal of corrosion products was carried out in the following sequence. Four cleaning attempts were performed using an ultrasonic bath operating at 90% power, and after each attempt the condition of a reference (blank) sample surface was evaluated. The first attempt was conducted in distilled water at 40 °C for 60 seconds. The second attempt was carried out under the same conditions, except that the temperature was increased to 50 °C to evaluate whether this would more effectively remove residual salt deposits from the sample surface. The third attempt was performed identically to the second one without major modifications. The fourth attempt was conducted at 20 °C using acetone due to the lack of effectiveness of the previous procedures. After removal of corrosion products and deposits, the sample surface was observed using a stereomicroscope at magnifications of 50× and 100×.

1.2. Results and discussion

The results of structural investigations of the uncoated ZnMg1.2 wt% alloy are presented in Fig. 1. The microstructure of the alloy shows bright precipitates of the primary zinc phase in the form of dendrites, as well as dark gray regions corresponding to a magnesium-rich phase. Based on the Zn–Mg phase equilibrium diagram, it can be inferred that this is the Mg_2Zn_{11} phase.

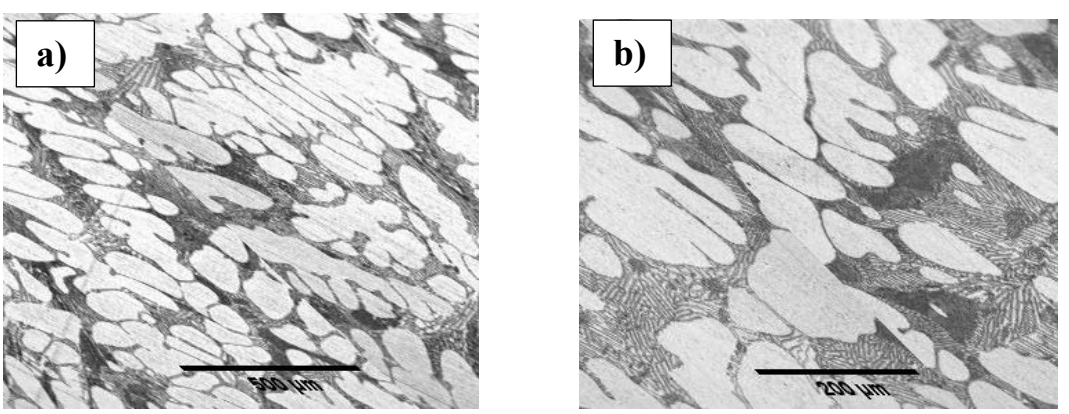

Figure 1. Microstructure of the ZnMg1.2 wt% alloy at magnification 100× (a) and 200× (b)

The surface topography of the ZnO coating deposited on the ZnMg1.2 wt% alloy, examined using Atomic Force Microscopy (AFM), is presented in Fig. 2. The surface topography reveals a granular and polycrystalline character. The AFM images show a uniform distribution of nanocrystalline grains as well as local surface irregularities. Such a morphology is typical for ZnO coatings obtained by thin-film deposition methods and has a beneficial effect on the optical and sensing properties of the material.

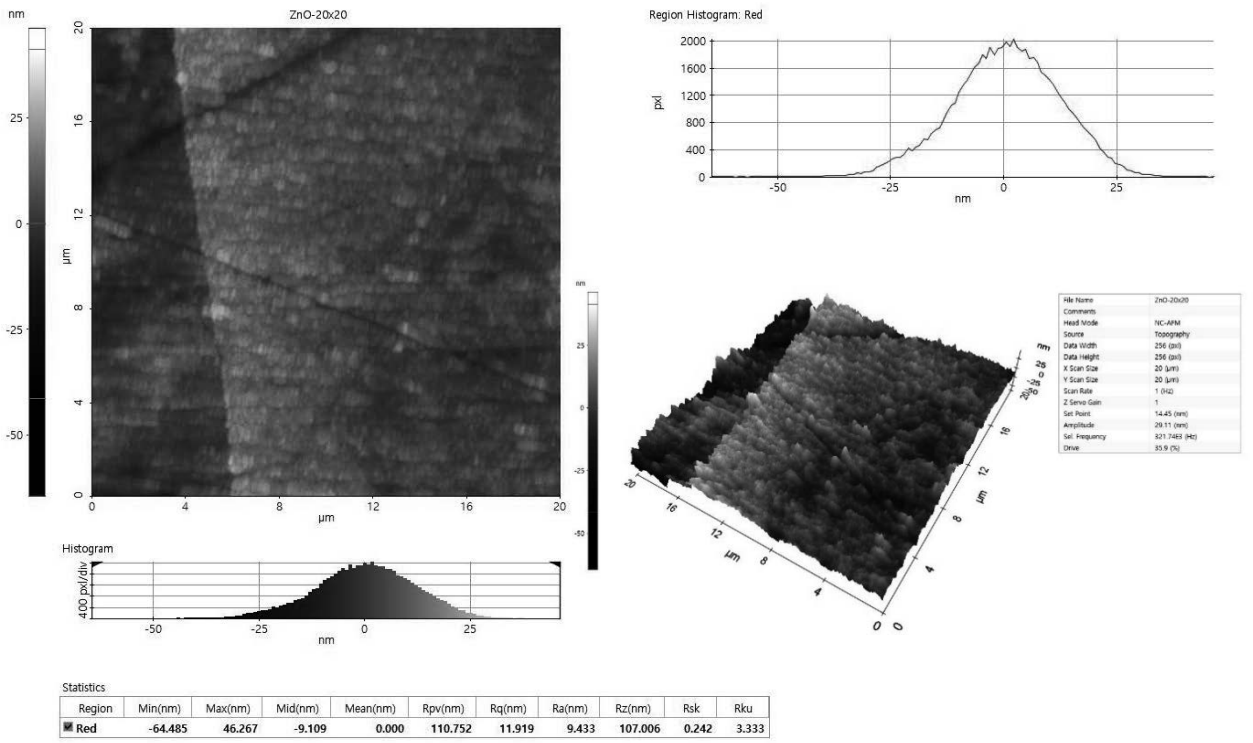

Figure 2. Surface topography of the ZnO coating on the ZnMg1.2 wt% alloy

The results of observations performed using Scanning Electron Microscopy (SEM) showing deposits and degradation products of the ZnMg1.2 wt% alloy with a ZnO coating after 264 h of immersion in Ringer's solution at 37 °C are presented in Fig. 3. The layer of deposits and corrosion products is non-uniform. At least three distinct regions can be identified, as shown in Figs. 3b, 3c, and 3d.

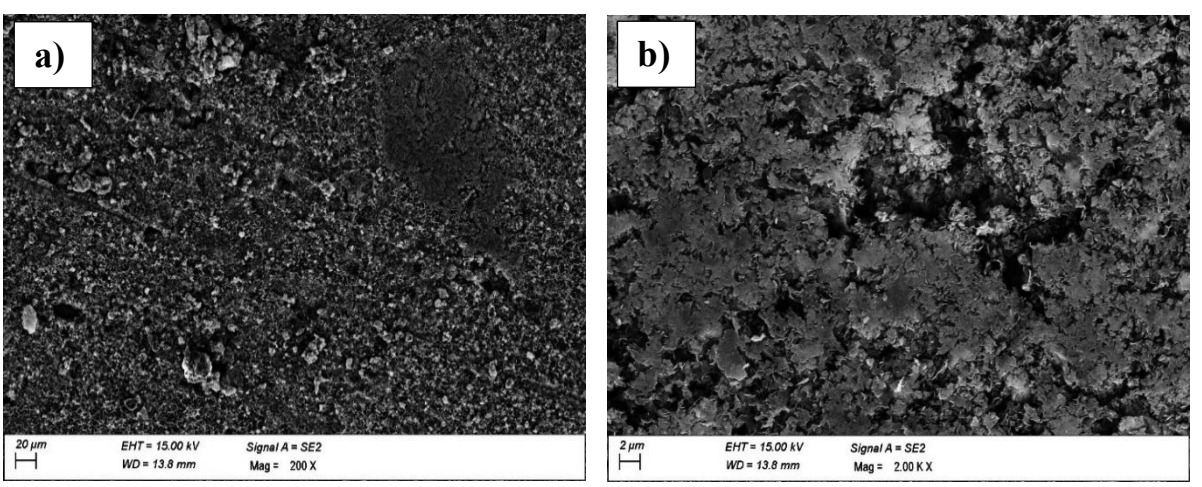

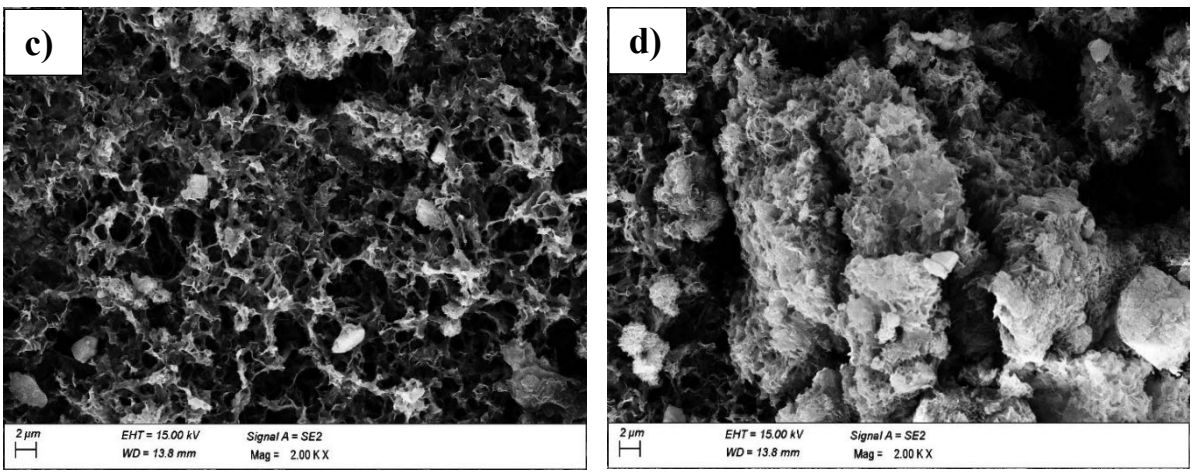

Figure 3 SEM images of the surface of the ZnMg1.2 wt% alloy with a ZnO coating after 264 hours of immersion in Ringer's solution at 37 °C.

The morphology of the region shown in Fig. 3b is the most compact, although it exhibits discontinuities resulting from the free drying of the sample.

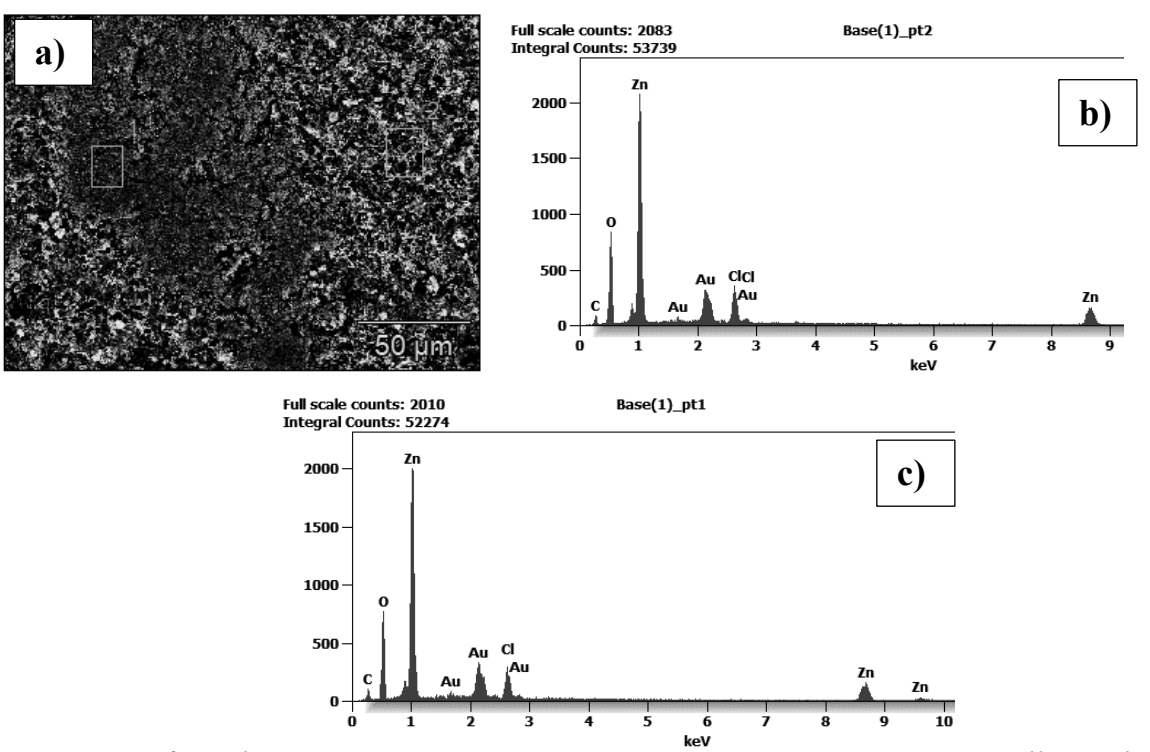

Figure 4 Surface chemical composition analysis (a, b, c) of the ZnMg1.2 wt% alloy with a ZnO coating after 264 hours of immersion in Ringer's solution at 37 °C.

Fig. 3c shows a significantly developed surface of the deposit layer, while Fig. 3d presents one of the salt agglomerates originating from the deposit formed after immersion in Ringer's solution. Energy Dispersive X-ray Spectroscopy (EDS) analysis (Fig. 4) revealed the dominant presence of zinc originating from the substrate, chlorine from the Ringer's solution, and gold, which is

present due to sputter coating of the sample for SEM observations. The qualitative composition of the deposits and corrosion products on the surface of the ZnMg1.2 wt% alloy with a ZnO coating, both in region 1 and region 2, indicates the presence of the same elements.The zinc detected in the analysis most likely originates not only from the alloy substrate but also partially from residual coating material intentionally applied for the study. Due to the complete coverage of the sample surface by salt deposits from the Ringer's solution and corrosion products, it is not possible to assess the progression of degradation or analyze the potential corrosion mechanism. Therefore, corrosion products and deposits were removed using distilled water, acetone, and an ultrasonic cleaner (fig.5).

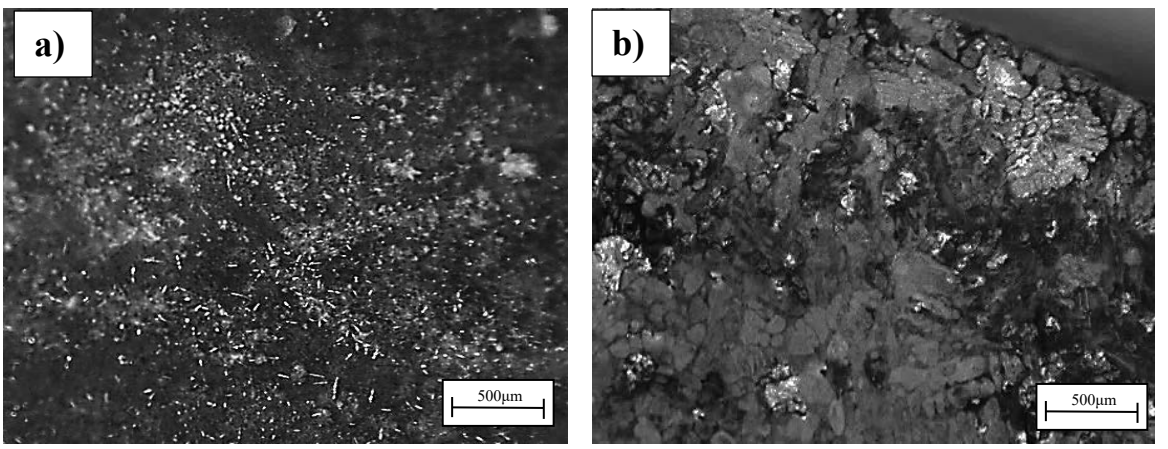

Figure 5 Surface image of the ZnMg1.2 wt% alloy sample with a ZnO coating after 264 hours of immersion in Ringer's solution at 37 °C, before (a) and after (b) removal of deposits and degradation products.

On the surface of the ZnO-coated alloy after removal of the degradation products, shown in Fig. 5b, partial degradation in the form of pits can be observed. The ZnO coating has largely degraded, exposing the substrate surface, which consequently led to further degradation progressing into the bulk of the alloy.

2. CONCLUSIONS

The conducted investigations in this work enabled a critical assessment of the degradation progression of the studied material in a simulated body fluid, which is crucial for evaluating its suitability for biomedical applications. The study presents the results of a developed technology for the fabrication of a ZnO layer on a ZnMg1.2 wt% substrate. Due to the multiphase nature of the ZnMg1.2 wt% alloy, an attempt was made to improve its corrosion resistance by applying a protective ZnO coating using the ALD method. The coating provides partial protection in the initial stage of immersion (up to approximately one week in Ringer's solution); however, it degrades too rapidly and non-uniformly, exposing the substrate surface. As a consequence, pitting corrosion occurs, which could lead to a loss of mechanical integrity of a potential implant made from the investigated alloy. In the next step, the research team plans to increase the thickness of the ZnO layer and to implement multilayer ZnO–TiO_2 coatings in order to achieve a more uniform degradation process and to reduce the degradation rate in simulated body fluids.

ACKNOWLEGMENTS

The work was carried out thanks to the financing of Project Based Education - PBL (Excellence Initiative - Research University program), in accordance with the Regulations No. 54/2020 and 55/2020 of the Rector of the Silesian University of Technology of March 13, 2020

BIBLIOGRAPHY

1. Aydin, S., Kurtulus, B. Silent Threats After Surgery: Incidence and Predictors of Deep Vein Thrombosis and Pulmonary Embolism in Orthopedic Patients. (2025) Diagnostics (Basel, Switzerland), 15(18), 2352. https://doi.org/10.3390/diagnostics15182352
2. Wang L , Wang C , Wu S , Fan Y , Li X . Influence of the mechanical properties of biomaterials on degradability, cell behaviors and signaling pathways: current progress and challenges. Biomater Sci. 2020 May 21;8(10):2714-2733. doi: 10.1039/d0bm00269k. Epub 2020 Apr 20. PMID: 32307482.
3. Shuai TANG, Wentai ZHANG, Junyu QIAN, Peng XIAN, Xiaoshan MO, Nan HUANG, Guojiang WAN. Long-term in Vitro Corrosion Behavior of Zinc in Ringer's Solution[J]. Journal of Inorganic Materials, 2020, 35(4): 461
4. Oviroh, P. O., Akbarzadeh, R., Pan, D., Coetzee, R. A. M., & Jen, T. C. (2019). New development of atomic layer deposition: processes, methods and applications. Science and Technology of Advanced Materials, 20(1), 465–496. https://doi.org/10.1080/14686996.2019.1599694
5. Helena Teterycz, Patrycja Suchorska-Woźniak, Marta Fiedot,, Iwona Karbownik, Deposition of Zinc Oxide on the Materials Used in Medicine. Preliminary Results, Engineering of Biomaterials (2013) 32–35.

TalentDetector

7th-9th June 2026
Gliwice-Brenna, Poland

DEPARTMENT OF ENGINEERING MATERIALS AND BIOMATERIALS
FACULTY OF MECHANICAL ENGINEERING
SILESIAN UNIVERSITY OF TECHNOLOGY

INTERNATIONAL STUDENTS SCIENTIFIC CONFERENCE

Structural characterization of Zn–Mg alloys and development of a decision support tool for material selection

Mateusz Słonka[a], Igor Szymiczek[b], Zofia Wolska[c], Aleksandra Wierzbicka[d], Martyna Rzepiela[e], Gabriel Sroka[f] Jakub Wiercińskі[g], Magdalena Skonieczna[h], Katarzyna CesarzAndraczke[i], Mateusz Smolarz[j], Marcin Staszuk[k],

[a] Student of Silesian University of Technology, email: ms309483@student.polsl.pl
[b] Student of Silesian University of Technology, email: is309487@student.polsl.pl
[c] Student of Silesian University of Technology, email: zw313185@student.polsl.pl
[d] Student of University School of Physical Education, email: 49098@awfkatowice.edu.pl
[e] Student of Silesian University of Technology, email: mr303355@student.polsl.pl
[f] Student of Silesian University of Technology, email: gs321484@student.polsl.pl
[g] Student of University School of Physical Education, email: kuba.wiercinski@op.pl
[h] Silesian University of Technology, Institute of Automation, Department of Systems Engineering and Biology, email: magdalena.skonieczna@polsl.pl
[i] Silesian University of Technology, Faculty of Mechanical Engineering, Department of Engineering Materials and Biomaterials email: katarzyna.cesarz-andraczke@polsl.pl
[j] University School of Physical Education, Institute of Physiotherapy and Health Sciences, email:m.smolarz@awf.katowice.pl
[k] Silesian University of Technology, Faculty of Mechanical Engineering, Department of Engineering Materials and Biomaterials email: marcin.staszuk@polsl.pl

Abstract: Based on the results of structural investigations and microhardness tests of cast ZnMg1.2 wt% and ZnMg3.2 wt% alloys, the influence of magnesium concentration on the structural changes and hardness of zinc alloys considered as potential resorbable biomaterials was determined. A literature review was conducted, on the basis of which a database was created. By applying the principles of engineering materials selection and experimental design depending on the intended application of the investigated potential biomaterial, a software tool was developed to support the decision-making process in selecting materials for experimental studies.

Keywords: resorbable materials, implants, structure, microhardnes, Zn-Mg alloys

1. INTRODUCTION

The development of resorbable biomaterials is currently highly intensified across many international research groups. Titanium and its alloys, which are among the most commonly used materials in surgical implantology, have long been considered biologically inert. However, clinical reports indicate that they may induce allergic reactions as well as peri-implant responses

at the implant–bone interface. For this reason, resorbable implants may represent a beneficial alternative [1,2,3]. Studies show that bioresorbable materials are associated with a statistically lower risk of surgical site infections. Additionally, no significant differences have been found between conventional and resorbable implants with respect to the total number of complications, implant failures, pain symptoms, functional outcomes, or the time required to achieve bone union [4].

Biodegradable, bioresorbable, and bioactive materials are of significant interest in both medicine and implantology due to their ability to gradually degrade within the body, eliminating the need for additional surgical procedures to remove implants. In this context, zinc-based alloys attract particular attention. In contrast to conventional metallic biomaterials used in biomedical applications (e.g., stainless steel and titanium alloys), zinc-based alloys exhibit a moderate degradation rate in the body—more favorable than that of magnesium, which degrades too rapidly, and iron, which degrades too slowly. This makes them promising candidates for biodegradable orthopedic implants such as screws, pins, and scaffolds supporting bone regeneration [5]. Zinc is an element naturally present in the human body, found mainly in bones and muscles. It influences, among other processes, osteoblast activity and bone mineralization. Moreover, it is considered non-toxic and biocompatible [6]. In the study by Patrick K. Bowen, Jaroslaw Drelich, and Jeremy Goldman [7], zinc was investigated for the first time as a bioresorbable material for cardiovascular stents, where preliminary results indicated that it meets the requirements for stent applications. At the same time, it was observed that pure zinc remains largely intact for at least four months in a mouse model, after which the corrosion process accelerates, enabling timely implant degradation.

In orthopedics, the primary function of an implant is to replace damaged or lost bone tissue and to transfer mechanical loads in a manner similar to the natural structures of the musculoskeletal system. The appropriate selection of material mechanical properties is crucial to ensure implant stability, durability, and proper integration with bone.

For orthopedic implants, the most important parameters include compressive, bending, and tensile strength, as well as the elastic modulus, which should be close to that of cortical bone (approximately 10–30 GPa). A large mismatch between the stiffness of the implant and that of bone can lead to the so-called stress shielding effect, i.e., excessive load transfer by the implant. As a consequence, mechanical stimulation of bone tissue is reduced, leading to its gradual resorption and structural weakening in the vicinity of the implant [2].

Therefore, materials intended for orthopedic implants should combine moderate stiffness with adequate resistance to fatigue and fracture. These properties must ensure the transfer of both static loads (e.g., standing) and dynamic loads (e.g., walking or running), while minimizing the risk of permanent deformation and fatigue failure.

In biomaterials research, the process of selecting an appropriate material is complex, as it must simultaneously satisfy multiple criteria such as biocompatibility, mechanical strength, chemical resistance, ability to integrate with tissues, and biodegradability. Computational tools play a key role in supporting decision-making processes related to material selection, particularly in the field of biomaterials. They enable faster analysis of large datasets, prediction of material properties, and reduction of both laboratory testing time and experimental costs. A simple software tool based on a database derived from scientific literature can serve as an effective instrument for supporting the selection of zinc alloys intended for resorbable biomaterials. The scientific literature increasingly emphasizes the growing role of computational tools and materials informatics in decision-support systems for material selection. Systems based on data analysis, artificial intelligence, and multi-criteria decision-making methods enable more efficient

comparison of material properties and prediction of their behavior under specific service conditions [8]. In this study, a software tool was developed which, based on an analysis of the requirements for implants used in different types of bone fractures and predefined input parameters—such as required mechanical strength, implant resorption time, or loading conditions—identifies the most suitable zinc and magnesium alloys and suggests their potential clinical applications. Based on the research direction proposed by the program, two alloys were selected for structural investigations and for evaluation of the influence of composition on alloy microhardness.

1.1. Materials and methods

The investigated materials were cast ZnMg1.2 wt% and ZnMg3.2 wt% alloys. The constituent elements, namely Zn with a purity of 99.95% and Mg with a purity of 99.95%, were weighed and subsequently melted by dissolving magnesium in liquid zinc at approximately 520 °C in a ceramic crucible (Al_2O_3) under an argon protective atmosphere. Structural investigations of the ZnMg1.2 wt% alloy were performed using a Zeiss optical microscope at 500× magnification. Metallographic samples were prepared by grinding (500, 800, and 1200 grit) followed by polishing using diamond suspensions with particle sizes of 9, 6, 3, and 1 µm. The samples were etched with nital. Microhardness measurements were carried out using a Vickers hardness tester under a load of 100 g. The software supporting material selection for the study is based on a self-developed database containing results of investigations on Zn- and Mg-based alloys with biocompatible additions such as Ca, Mg, and Zn, as well as information regarding bone fractures and implant designs. Based on the input data, the program analyzes and dynamically selects suitable alloys that meet the defined requirements. The software was developed using the Python programming language together with the pandas library for data analysis.

1.2. Results and discussion

Based on the developed database, the decision-support program for selecting biomaterials for orthopedic implants interacts with the user by asking a series of questions that progressively narrow the research scope. Finally, based on the selected responses, it provides a range of proposed solutions to the defined engineering problem. Fig. 1 presents the set of questions used to select a specific injury case for analysis.

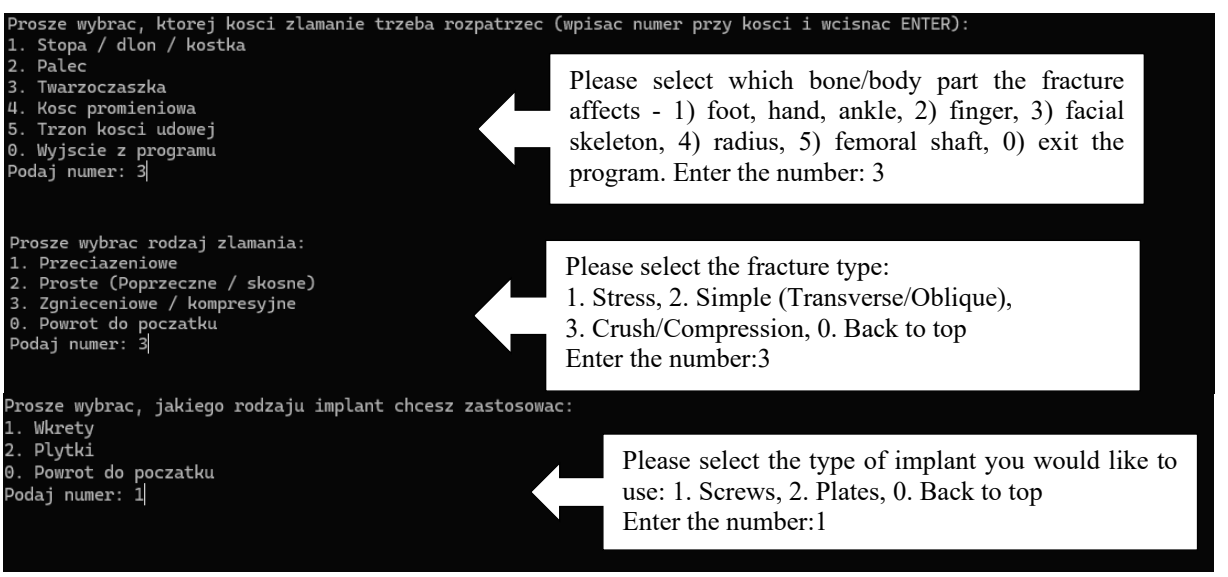

Figure 1 Initial identification of the application area for the proposed material solution.

The next stage involves selecting the material for the target implant, including the type of function it is intended to perform as well as the range of chemical composition (Fig. 2).

```
Prosze wybrac grupe materialowa:
1. Metale
2. Polimery
3. Ceramika
0. Powrot
Podaj numer: 1
```

Please select a material group: 1. Metals, 2. Polymers, 3. Ceramics, 0. Return
Enter the number: 1

```
1. Obojetne
2. Resorbowalne
0. Powrot
```

1. Neutral, 2. Resorbable, 0. Return
Enter the number: 2

```
1. Mg + Zn
2. Mg + Zn + Ca
3. Mg + Ca
0. Powrot
Podaj numer: 2
```

1. Mg + Zn, 2. Mg + Zn + Ca, 3. Mg + Ca
0. Return
Enter the number:2

Figure 2 Characterization of the biomaterial concept and function.

Once all selections are confirmed, the program generates an information sheet that includes the type of bone, type of fracture, and implant specifications calculated based on the previously defined conditions.

```
============== Specyfikacja kosci ==================
Kosc:  Twarzoczaszka
Typ kosci:  krotka
Wytrzymalosc:  40
Wydluzenie:  2.0
***************************
Rodzaj zlamania:  Zgnieceniowe / kompresyjne
***************************

============== Specyfikacja implantu ==================
Konstrukcja:  Wkrety
Material:  Metale
Minimalna wytrzymalosc:  60
Maksymalna wytrzymalosc:  100
Minimalne wydluzenie:  5
Maksymalne wydluzenie:  10

============== Rozwiniecie ==================
      Nazwa stopu    Mg   Zn   Ca  Rm [MPa]  A [%]
25    MgZnCaODL26  95.0  4.0  1.0        60    8.0
86    MgZnCaODL87  98.0  1.0  1.0       125    5.7
90    MgZnCaODL91  97.0  2.0  1.0       143    7.3
105  MgZnCaODL106  93.0  6.0  1.0       145    4.5
```

== Bone Specifications ==
Bone: Craniofacial
Bone Type: Short
Strength: 40
Elongation: 2.0
Fracture Type: Compression/Compression
==Implant Specifications ==
Construction: Screws
Material: Metals
Minimum Strength: 60
Maximum Strength: 100
Minimum Elongation: 5
Maximum Elongation: 10

Alloy Name	Mg	Zn	Ca	Rm [MPa]	A [%]
25 MgZnCaODL26	95.0	4.0	1.0	60	8.0
86 MgZnCaODL87	98.0	1.0	1.0	125	5.7
90 MgZnCaODL91	97.0	2.0	1.0	143	7.3
105 MgZnCaODL106	93.0	6.0	1.0	145	4.5

Figure 3 Results of the database analysis and the proposed range of materials for experimental testing.

Based on the analysis of the developed database, an alloy was selected for basic experimental investigations aimed at determining structural changes and their influence on microhardness in relation to the phase composition of the alloy. Due to biocompatibility criteria and the results of the database analysis, a zinc alloy composition with magnesium additions in the range of 1.2 wt% to 3.2 wt% was selected. In the first step, the microstructure of the investigated alloys was analyzed (Fig. 4). The structure shows bright regions corresponding to the α-Zn matrix, while the dark areas represent the intermetallic Mg_2Zn_{11} phase. Phase identification was performed

based on the Zn–Mg phase equilibrium diagram. It should be noted that an increase in magnesium concentration led to an increased fraction of the Mg_2Zn_{11} phase (Fig. 4b).

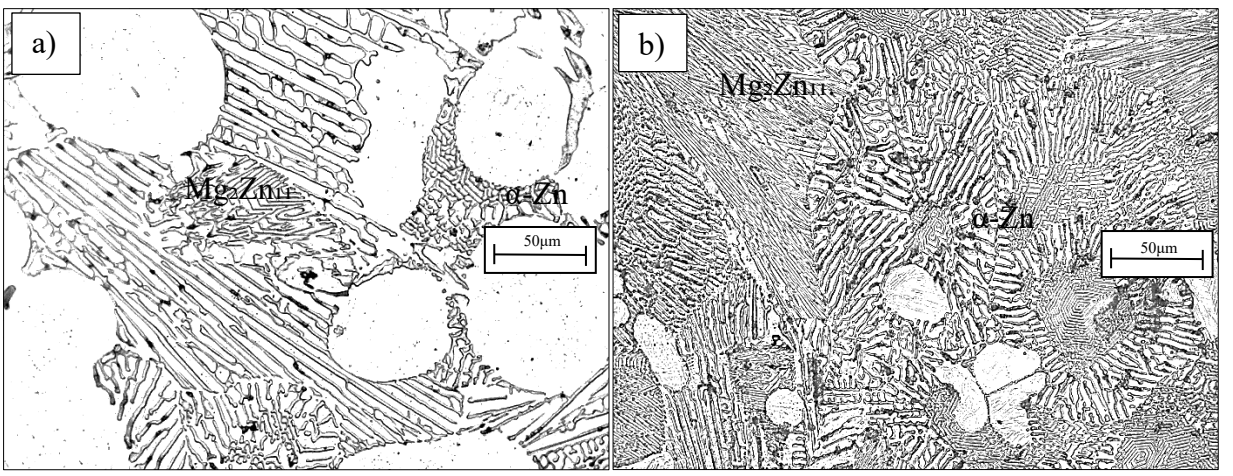

Figure 4. Microstructure of the ZnMg1.2 wt% alloy (a) and ZnMg3.2 wt% alloy (b) at 500× magnification

Next, Vickers microhardness measurements were performed for the investigated alloys. The measurements were carried out in regions corresponding to the occurrence of individual phases. Images of representative indentations are shown in Fig. 5.

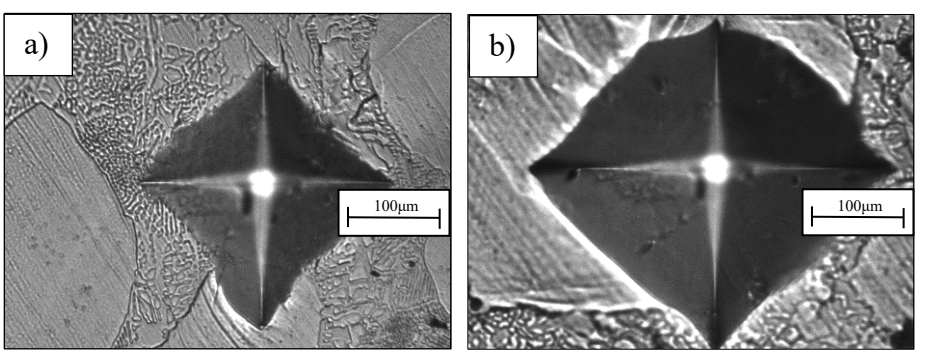

Figure 5. Representative indentation after microhardness measurement for the ZnMg1.2 wt% alloy (a) and the ZnMg3.2 wt% alloy (b) at 200× magnification.

In the ZnMg1.2 wt% alloy, measurements were performed both in the α-Zn matrix regions and in the Mg_2Zn_{11} intermetallic phase regions (Table 1).

Table 1. Microhardness measurements for ZnMg1.2 wt% and ZnMg3.2 wt% alloys with characterization of the measured regions.

Microhardness ZnMg1,2 wt% [HV]	**characterization of the measured region**	**Microhardness ZnMg3,2 wt% [HV]**	**characterization of the measured region**
101	around the Mg_2Zn_{11} phase	186	around the Mg_2Zn_{11} phase
105	around the Mg_2Zn_{11} phase	168	around the Mg_2Zn_{11} phase

86	around the α-Zn phase	170	around the Mg_2Zn_{11} phase
70	around the α-Zn phase	167	around the Mg_2Zn_{11} phase
81	around the α-Zn phase	172	around the Mg_2Zn_{11} phase
84	around the α-Zn phase	192	around the Mg_2Zn_{11} phase
92	around the α-Zn phase	169	around the Mg_2Zn_{11} phase
93	around the α-Zn phase	178	around the Mg_2Zn_{11} phase

The obtained microhardness values for the α-Zn phase were as follows: 92 HV, 93 HV, 86 HV, 70 HV, 81 HV, 84 HV, and 85 HV, resulting in an average value of approximately 84 HV. For the Mg_2Zn_{11} phase, the measured values were 101 HV and 105 HV, with an average of approximately 103 HV. In the case of the ZnMg3.2 wt% alloy, all measurements were performed on the Mg_2Zn_{11} phase. The obtained microhardness values were: 186 HV, 168 HV, 170 HV, 167 HV, 172 HV, 192 HV, 169 HV, and 178 HV. The average microhardness of this phase was approximately 175 HV, which is significantly higher than in the ZnMg1.2 wt% alloy. The substantial increase in the microhardness of the Mg_2Zn_{11} phase in the ZnMg3.2 wt% alloy is associated with the higher magnesium concentration in the alloy and the increased fraction of intermetallic phases in the microstructure. With increasing Mg content, the fraction of the α-Zn + Mg_2Zn_{11} eutectic increases, and the structure becomes refined [9]. This results in stronger dispersion strengthening and greater resistance to dislocation motion, leading to an increase in microhardness. The obtained results are consistent with literature data, according to which intermetallic phases in the Mg–Zn system exhibit significantly higher hardness than the α-Zn zinc matrix [10,11]. An increased fraction of the Mg_2Zn_{11} phase leads to improved hardness of the alloy; however, it may also increase material brittleness. The results confirm that the α-Zn matrix is characterized by lower microhardness due to the high ductility of the zinc-rich phase. At the same time, the presence of the Mg_2Zn_{11} intermetallic phase causes a local increase in material hardness. The Mg_2Zn_{11} phase acts as a hard reinforcing phase that restricts dislocation motion and increases resistance to plastic deformation [9,10]. In the ZnMg1.2 wt% alloy, the dominant constituent of the microstructure is the α-Zn matrix. This phase is characterized by relatively low hardness and high ductility, which results in greater susceptibility of the material to plastic deformation [11]. A small fraction of the α-Zn + Mg_2Zn_{11} eutectic is observed in the microstructure, occurring mainly in the interdendritic regions. The limited amount of intermetallic phases causes the microhardness of the ZnMg1.2 wt% alloy to remain relatively low.

2. CONCLUSIONS

The developed database and the decision-support software, together with the microhardness tests, demonstrated a significant influence of the phase composition of the microstructure on the microhardness of the analyzed Zn–Mg alloys. Hard intermetallic phases distributed within the zinc matrix act as barriers to dislocation motion, leading to an increase in hardness measured by the Vickers method. It can therefore be stated that the α-Zn phase is primarily responsible for the

ductility and reduction of alloy microhardness, whereas the Mg_2Zn_{11} phase plays a strengthening role. With increasing magnesium content, the fraction of the Mg_2Zn_{11} phase increases, resulting in higher microhardness of Zn–Mg alloys. For this reason, the ZnMg3.2 wt% alloy exhibits higher microhardness than the ZnMg1.2 wt% alloy.

ACKNOWLEGMENTS

The work was carried out thanks to the financing of Project Based Education - PBL (Excellence Initiative - Research University program), in accordance with the Regulations No. 54/2020 and 55/2020 of the Rector of the Silesian University of Technology of March 13, 2020

BIBLIOGRAPHY

1. Chou, H., Lin, Y. Y., Huang, Y. C., Yeh, P. C., Chang, S. H. (2026). Allergic Reaction to Titanium Alloy Osteosynthesis Implants: A Case Report of Three Patients. Life (Basel, Switzerland), 16(3), 388. https://doi.org/10.3390/life16030388
2. Ajarrag, S., Torchon, M. C. (2026). Suspected Hypersensitivity Reaction to Titanium Screws Following Kalish Osteotomy for Hallux Valgus. Cureus, 18(3), e104709. https://doi.org/10.7759/cureus.104709
3. Music, A., Thapa, A. A., Shipovskaia, M., Pramchand, A., Moushon, B., Tiesenga, F. (2026). Titanium Allergy: A Case of Foreign Body Reaction Following Laparoscopic Cholecystectomy. Cureus, 18(3), e104781. https://doi.org/10.7759/cureus.104781
4. Blackman, B., Okunbor, S., Sowa, A. M., McDonnell, J. M., Ross, T. D., Rigney, B., Darwish, S., Butler, J. S. (2025). Bioabsorbable implants are a viable alternative to traditional metallic implants in orthopaedic surgery: a systematic review and meta-analysis. Journal of orthopaedics, 65, 257–269
5. P. Pesode, S. Barve, Surface Modification of Biodegradable Zinc Alloy for Biomedical Applications, BioNanoSci. 13 (2023) 1381–1398. https://doi.org/10.1007/s12668-023-01139-5.
6. L. Kong, Z. Heydari, G.H. Lami, A. Saberi, M.S. Baltatu, P. Vizureanu, A Comprehensive Review of the Current Research Status of Biodegradable Zinc Alloys and Composites for Biomedical Applications, Materials 16 (2023) 4797. https://doi.org/10.3390/ma16134797.
7. Bowen PK, Drelich J, Goldman J. Zinc exhibits ideal physiological corrosion behavior for bioabsorbable stents. Adv Mater. 2013 May 14;25(18):2577-82. doi: 10.1002/adma.201300226. Epub 2013 Mar 14. PMID: 23495090.
8. Fatima Z, Kaplarevic M., Grujovic N., Stojanovic B., Ivanovic M., Materials informatics: A review of AI and machine learning tools, platforms, data repositories, and applications to architectured porous materials, Materials Today Communications, Volume 48, 2025, 113525, https://doi.org/10.1016/j.mtcomm.2025.113525.
9. Akdeniz M., Wood J., Microstructures and phase selection in rapidly solidified Zn-Mg alloys, Journal of Materials Science 31 (1996) 545-550.
10. Talita F., Crystopher B., Thiago S., Lima S.,. Spinelli J. E, Cheung N., Garcia A., Near-eutectic Zn-Mg alloys: Interrelations of solidification thermal parameters, microstructure length scale and tensile/corrosion properties, Current Applied Physics, 19(5) (2019) 582-598
11. Zhang Z., Zhang J., Zhao X., Cheng X., Liu X., Zhang Q., Thermodynamic Simulation Calculations of Phase Transformations in Low-Aluminum Zn-Al-Mg Coatings, *Materials 17 (2024)* 2719.

TalentDetector

7th-9th June 2026
Gliwice-Brenna, Poland

DEPARTMENT OF ENGINEERING MATERIALS AND BIOMATERIALS
FACULTY OF MECHANICAL ENGINEERING
SILESIAN UNIVERSITY OF TECHNOLOGY

INTERNATIONAL STUDENTS SCIENTIFIC CONFERENCE

Geopolymer construction mortars prepared from waste materials. Laboratory tests

Słomka-Słupik Barbara[a], Tomasz Jaśniok[a], Hanna Kaźmierczak[a], Krystyna Skulimowska[a], Kuba Szlachta[a]

[a]Silesian University of Technology, Faculty of Civil Engineering, Department of Building Structures, email: barbara.slomka-slupik@polsl.pl

Abstract: This article discusses the use of cementless binders, which include recycled materials, primarily biomass ash from wood combustion and a waste activator: concentrated NaOH. The aim of the study was to compare the strength of mortar beams obtained under different hardening conditions and depending on the type of alkaline activator. It was demonstrated that prolonged curing at elevated temperatures and soaking the mortars in CO_2 gas had a beneficial effect on their strength.

Keywords: geopolymer mortars, alkali activators, compressive strength, CO_2, climatic chamber, biomass wood ash

1. INTRODUCTION

The production of ordinary Portland cement (OPC) significantly contributes to the worldwide carbon dioxide (CO_2) emission, therefore, solutions that are less harmful to the environment are being sought. Alkaline-activated binders, mainly based on aluminosilicates, are being analyzed. Such binders are called geopolymer binders, in which the activator is most often a concentrated solution of NaOH, KOH, or water glass, and the precursor is mainly metakaolin (MK), fly ash (FA), blast furnace slag (BFS), rice husk ash, and many others containing SiO_2 and Al_2O_3 as their main components. A distinction is made between calcium-free and calcium-containing geopolymers, particularly those based on BFS. After hardening, a predominantly amorphous phase is formed: (N/K)-A-S-H or C-(A)-S-H (where N=NaOH, K=KOH, A= Al_2O_3, S=SiO_2, H= H_2O, C=CaO). Therefore, the enormous potential in creating geopolymer binders prompts researchers to continually explore the relationships within them. In particular, they are leaning towards geopolymers with an increasingly smaller carbon footprint, which can be achieved by using waste raw materials such as ash. FA is the most popular, although considerable attention is also paid to residual biomass wood ash (BWA) resulted as a by-product of burning the wood wastes. This is due to the increasingly popular production of energy from biomass in the world [1-9]. Candamano et al. [3] analyzed the possibility of replacing metakaolin with forest biomass ash in geopolymer mortars. The mechanical strength and microstructure of the material were studied. Paper [4] concerns the use

of high-calcium wood ash as a partial replacement for fly ash in geopolymer mortars. The authors demonstrated improved mechanical properties and durability. The effect of granulation and thermal treatment of wood ash (grinding + calcination) on the properties of geopolymer mortars was also studied. The results showed improved porosity and strength after appropriate ash modification [5]. Paper [6] describes the effect of the type of activator, curing conditions, and biomass ash content on the properties of geopolymer mortars. It was noticed that biomass fly ash often contains high levels of unburned carbon and irregular particle morphology, which can influence its suitability for geopolymer applications, so biomass fly ash was modified through flotation method, which reduces unburned carbon content. Additionally, it was shown that the addition of BFA decreases the flowability of geopolymer mortar. Replacing 40% of Coal fly ash (CFA) by BFA achieves highest compressive strength under water curing conditions. An alkali activator with SiO_2/Na_2O ratio of 2.31 exhibits higher compressive strength and lower porosity. In contrast, lower SiO_2/Na_2O ratios negatively affected strength development, possibly due to excessive Na_2O causing overreaction of fly ash, weakening interfacial bonding, increasing porosity, and thus reducing strength. Prochon et al. [7] also compared the effect of alkaline activators on the strength of geopolymer mortars based on biomass and coal ash. This team in turn showed that biomass fly ash due to low alumina and silica content is not adequate for alkali-activation. The main chemical structures related to hydration of active CaO and formation of $CaCO_3$. Strength tests, SEM, FTIR and chemical durability analysis were included in a comprehensive study on geopolymer mortars with the addition of rice husk ash (RHA) and sugarcane bagasse ash (SCBA) [8], in turn.
The aim of this study was to test the strength of six mortars made from biomass ash and various activators. Four different curing conditions were developed. In addition to high temperature, the possibility of curing the beams in CO_2 gas was also investigated to further reduce the product's carbon footprint.

2. EXAMINATION

2.1. Materials and Methods

The mortar mixtures were prepared using biomass ash from a Polish power plant (precursor) called EP-5, alkaline solutions (activators), and dolomite sand with a granulation size of up to 2 mm (filler). The results of the phase composition analysis of the biomass ash showed a 100% crystalline phase (Fig. 1). The main components were quartz, calcite, and microcline, so there was little hope of creating strong mortars. Additionally, SEM-EDS elemental composition studies indicated a relatively high amount of calcium and carbon atomically (Fig. 2). However, SEM-SE microscopic observations revealed significant differences in the granulation of the sand and dust (Fig. 3).
The mortar mixtures were prepared in the proportions given in the table below (Table 1). They shared the same aggregate and precursor, but differed in the activator. The following activators were used: GKA1-cn – supernatant of contaminated concentrated NaOH (slightly less than 6%, approximately 1.5M) as a waste solution from industrial processes; 10M and 12M sodium hydroxide (10M NaOH and 12M NaOH); and the "B5" in the mortar name denotes the addition of 5 mm basalt fibers, 9 grams in mixes 2 and 6. The activator amount was selected so that, according to expert assessment, all mixtures achieved a flow of approximately 13 cm. Flow was tested using a standard flow test table. As can be seen, the addition of fibers increased the need for liquid activator in the mix to be workable. Comparing mortars CPG-20260423NH10M

with CPG-20260423NH10MB5 and CPG-20260423 with CPG-20260423B5, rapid hardening of the mixes with more concentrated NaOH was also observed during mixing. The mixes were placed in standard molds (4×4×16 cm), gently mechanically vibrated, and 1-2 hours after mixing, transferred to a climatic chamber where the conditions were 60°C and relative humidity RH = 20%. Curing, or curing, of the samples was differentiated into four series, as shown in Table 2. The samples stayed in the chamber for the time shown in Table 2, and otherwise matured at room temperature, tightly insulated. Strength testing was performed at the specified times. Samples exposed for 3 days at 60°C and 20% RH were tested on the 4th day, while those exposed for the first 5 days at 60°C and 20% RH were tested on the 24th day, just before CO_2 impregnation began.

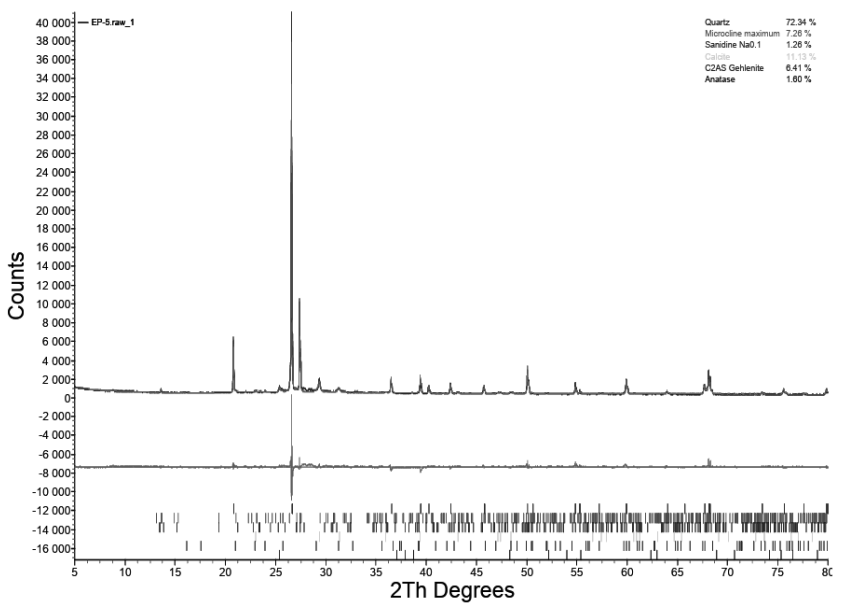

Quartz, SiO - 72,34%

Calcite, $CaCO_3$ - 11,13%

Microcline $KAlSi_3O_8$ - 7,26%

Sanidine Na0.1 $(K;Na)(Al;Si)_4O_8$ - 1,26%

Gehlenite, C_2AS - 6,41%

Anatase TiO_2 - 1,6%

Figure 1. XRD pattern of biomass wood ash

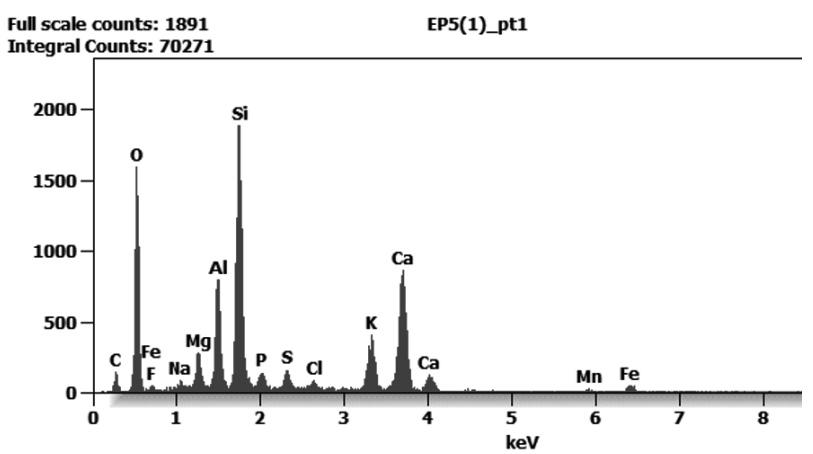

C – 6.97	O – 57.22
Na – 0.4	S – 0.91
Al – 4.75	Mg – 1.86
P – 0.86	Si – 12.47
Cl – 0.40	K – 3.27
Ca – 9.28	Mn – 0.49
Fe – 1.13	

Figure 2. SEM-EDS pattern of biomass wood ash and atom% content

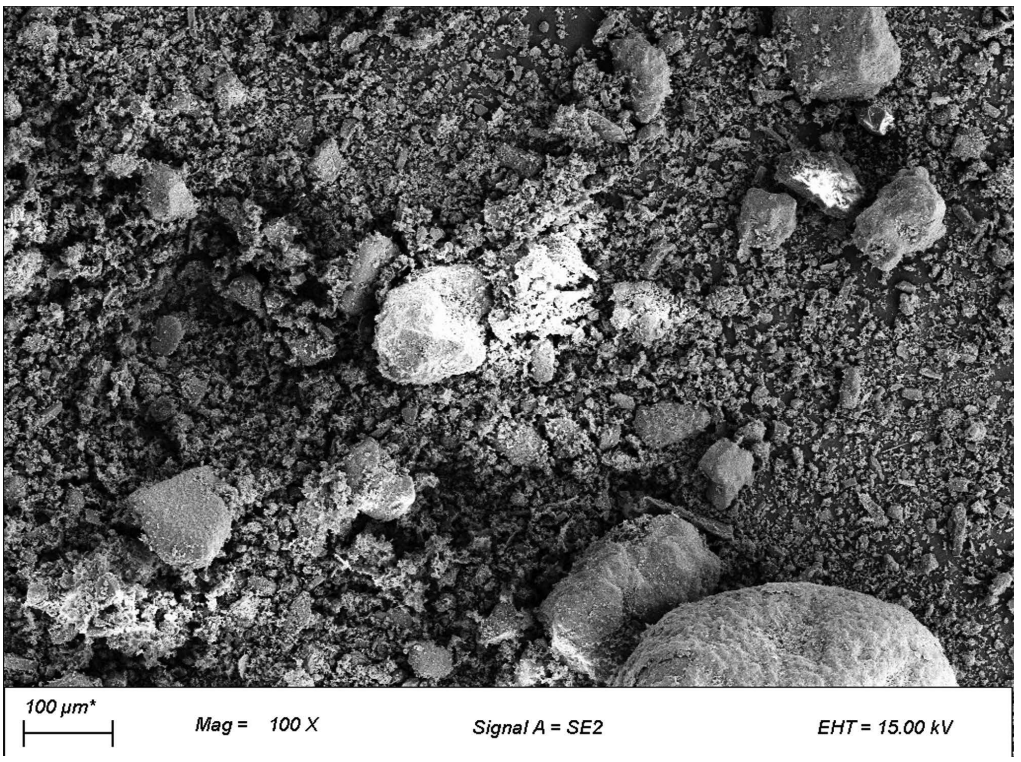

Figure 4. SEM-SE image of biomass wood ash

Table 1. Composition of mortar mixtures with geopolymer binder

Name of the mortar	Ash amount EP-5, g	Sand amount, g	Amount of activator, g	Activator type	Flow, cm
CPG-20260423	450	1400	367,8	GKA1-cn	13
CPG-20260423B5	450	1400	402	GKA1-cn	13,5
CPG-20260423NH10M	450	1400	340	10M NaOH	13
CPG-20260423NH10MB5	450	1400	369,4	10M NaOH	13
CPG-20260423NH12M	450	1400	340	12M NaOH	-
CPG-20260423NH12M+	450	1400	395	12M NaOH	12

Table 2. Types of mortar care before strength testing, in the shown hardening day

Series name	T = 60°C RH = 20%	Strength test	T = 60°C RH = 20% 10% CO_2	Strength test
S.3d	1-3	4	-	-
S.3dCO_2	1-3	-	25 - 29	34
S.5d	1-5	22	-	-
S.5dCO_2	1-5	-	25 - 29	34

2.2. Results and analysis

Compressive strength test results (Fig. 4) clearly show that the longer the curing time at higher temperatures, the stronger the mortars. However, testing of the S.3d series on day 22 would also be required. Testing the beam strength on day 34 also shows that the initial curing time at higher temperatures plays a role in carbonation processes. The strength values of samples with the waste activator, designated GKA1-cn, were similar, but significantly lower without carbonation. In essence, this study shows that the curing time for geopolymers is not as important as the curing conditions, as there is a significant difference in the values between days 22 and 34 of these samples. Clearly, the waste activator (contaminated with NaOH) can provide high strength, but the samples should be additionally carbonated. The effect of basalt fibers was not observed here. However, in the case of samples activated with 10 molar pure NaOH, it can be seen that basalt reduced the strength, although the higher amount of NaOH in CPG-20260423NH10MB5 could also be responsible for this. A higher NaOH concentration in CPG-20260423NH12M samples increased the strength compared to the use of 10M NaOH in CPG-20260423NH10M. However, this sample was unworkable, non-plastic, and non-castable, so a larger amount of 12M NaOH (CPG-20260423NH12M+) was added. This treatment had a worse effect on the strength.

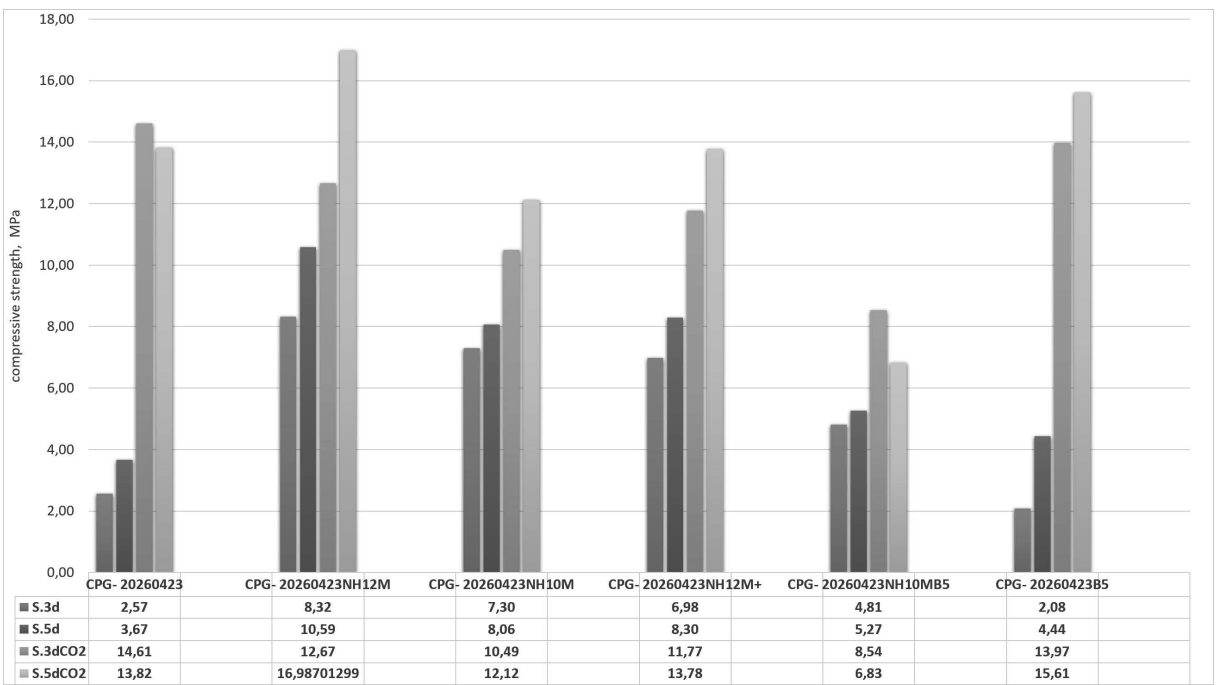

Figure 4. Compressive strength values of carbonated and uncarbonated mortars

3. SUMMARY and CONCLUSIONS

The mixtures used are undoubtedly eco-friendly due to the reduced carbon footprint achieved through the use of biomass ash and waste NaOH activator from post-production processes. Another advantage is the binding of carbon dioxide within the mixture. This process not only reduces the carbon footprint but also increases the strength of the mortars. Unfortunately, the

carbon footprint is increased by using pure hydroxides, but this article demonstrates that quite good results can be achieved with 1.5 molar NaOH, compared to 10M or 12M, which are used with ash from coal combustion, not wood. Since phase studies did not reveal the presence of alkali-reactive phases, it is worth considering the contribution of the aggregate used to the hardening and CO_2 binding reactions. Further work should focus on this issue.
The challenge with these mixtures is achieving the desired workability and flow. Therefore, different preparation technology should be considered, e.g., vibro-pressing for blocks. Basalt fibers were not visible in fractures of hardened mortars. All indications are that they were degraded in the highly alkaline NaOH environment. This phenomenon was also confirmed by other researchers, who noted that it depends on the type and concentration of the activator [9]. The mechanism of alkaline attack on basalt increases at higher temperatures and, in its simplest form, is as follows: $Si{-}O{-}Si + OH^- \rightarrow Si{-}OH + {}^-O{-}Si$.

BIBLIOGRAPHY

1. Yalcinkaya, B.; Spirek, T.; Bousa, M.; Louda, P.; Růžek, V.; Rapiejko, C.; Buczkowska, K.E. Unlocking the Potential of Biomass Fly Ash: Exploring Its Application in Geopolymeric Materials and a Comparative Case Study of BFA-Based Geopolymeric Concrete against Conventional Concrete. Ceramics 2023, 6, 1682-1704. https://doi.org/10.3390/ceramics6030104
2. R. Siddique. Waste Materials and By-Products in Concrete, 1st ed.; Springer-Verlag Berlin Heidelberg: Berlin, Germany, 2008; ISBN 978-3-540-74294-4
3. S. Candamano, P. De Luca, P. Frontera, F. Crea. Production of Geopolymeric Mortars Containing Forest Biomass Ash as Partial Replacement of etakaolin. *Environments* 2017, *4*, 74.
4. A.A. Omar, R. Mahyuddin, J.C. Matthews. Production of geopolymer mortar system containing high calcium biomass wood ash as a partial substitution to fly ash: An early age evaluation, Composites Part B: Engineering, Volume 174, 2019, 106941, ISSN 1359-8368
5. F. Ates, K.T. Park, K.W. Kim, B.-H. Woo, H.G. Kim. Effects of treated biomass wood fly ash as a partial substitute for fly ash in a geopolymer mortar system. Construction and Building Materials, Volume 376, 2023, 131063, ISSN 0950-0618
6. H. Qi, L. Shilun, L. Zihao, T. Koji, P. Kevin, K. Xinyuan, S. Hiroki. Factors influencing the performance of biomass fly ash-based geopolymers, Construction and Building Materials, Volume 489, 2025, 142415, ISSN 0950-0618
7. P. Prochon, Z. Zhao, L. Courard, T. Piotrowski, F. Michel, A. Garbacz. Influence of Activators on Mechanical Properties of Modified Fly Ash Based Geopolymer Mortars. Materials. 2020; 13(5):1033
8. P.J. Ardhira, S.K. Shukla, D. Sathyan, Synthesis of geopolymer mortar from biomass ashes and forecasting its compressive strength behaviour, Case Studies in Construction Materials, Volume 21, 2024, e03581, ISSN 2214-5095
9. A. Mahmood, M. Pechočiaková, B. Tomková, M.T. Noman, M. Gheibi, K. Behzadian, J. Wiener, L. Hes, Machine Learning-Driven Optimization for Evaluating the Durability of Basalt Fibers in Alkaline Environments. *Fibers* 2025, *13*, 137

TalentDetector

7th-9th June 2026
Gliwice-Brenna, Poland

DEPARTMENT OF ENGINEERING MATERIALS AND BIOMATERIALS
FACULTY OF MECHANICAL ENGINEERING
SILESIAN UNIVERSITY OF TECHNOLOGY

INTERNATIONAL STUDENTS SCIENTIFIC CONFERENCE

Sequestration capacity of RCP: powder fraction of recycled concrete, in relation to CO_2. Calcium looping method

Słomka-Słupik Barbara[a], Małgorzata Labus[b], Jakub Piasecki[a], Nicole Kocierz[a], Anna Słupik[c], Kacper Popielarczyk[a], Paulina Wiśniewska[a], Kuba Szlachta[a]

[a] Silesian University of Technology, Faculty of Civil Engineering, Department of Building Structures
email: barbara.slomka-slupik@polsl.pl
[b] Silesian University of Technology, Faculty of Mining, Safety Engineering and Industrial Automation, Department of Applied Geology, email: malgorzata.labus@polsl.pl
[c] Silesian University of Technology, Faculty of Architecture

Abstract: The article shows the possibility of reusing concrete rubble in construction but pays particular attention to the reabsorption of carbon dioxide by the powdered fraction of ground concrete. The calcium looping method was used in this work.

Keywords: recycled concrete, calcium looping, TGA analysis, PBL (project-based learning)

1. INTRODUCTION

Contemporary trends in construction increasingly emphasize the need to implement the principles of a circular economy, in which materials from demolition are treated as valuable secondary raw materials. Of particular importance here are technologies enabling the recovery and reuse of concrete, which is one of the most commonly used construction materials in the world. Progressive urbanization processes and the growing scale of demolition work generate the need to develop solutions that reduce waste and the carbon footprint of building material production. One research direction in support of the "zero waste" policy is the use of ground concrete as a component of new cement, concrete, and mortars composites [1], including both as an aggregate and as an active additive with binding properties. Standardization for this type of aggregate is included in [2], [3], [4].

An additional value is the phenomenon of recarbonation, which involves the secondary binding of CO_2 by a material containing cement hydration products, which opens the way to the creation of more sustainable and low-emission concrete production technologies.

The aim of the work undertaken within PBL XIII (Winter-2025/2026) and described in this paper was to assess the potential for reusing ground concrete crumb from demolition, provided by a recycler, in construction. It was initially assumed that the coarser fractions could be used as aggregate in concrete, while the finest, dusty fractions could be used as a binder component. The aggregate from Dąbrowa Górnicza, from EkoCem, a Heidelberg Group

company, is prepared in a special way; the crumbs are not broken, and as a result, they are close to globular. The aim of the research presented in this article was to determine the sequestration potential of the finest fraction of ground concrete from demolition. Therefore, the dusty fraction, abbreviated as **RCP** (recycled concrete powder), was calcined and recarbonated in a thermogravimeter. This fraction should generally consist primarily of hydrated cement and aggregate residues. Reports suggest that this fraction can be a cement component with CO_2 absorption properties. One ton of uncalcined RCP can absorb up to 150 kg of CO_2 [5]. Therefore, it can be argued that after calcination, this capacity should be greater, and CO_2 binding more durable.

2. MATERIALS AND RESEARCH METHODS

Samples of waste material were obtained from the EkoCem concrete recycling plant in Dąbrowa Górnicza (Fig. 1), owned by the Heidelberg Group. The recycler provided samples with the following granulation sizes: 0-0.125; 0.125-4; 4-8; and 8-16 mm, which were to be used by us as a component of new concrete mixtures. For the purposes of this work, the 0-0.125 mm fraction was analyzed using TGA, XRD, and SEM methods.

Figure 1. The EkoCem concrete recycling plant in Dąbrowa Górnicza (photo: own)
Rysunek 1. Zakład recyklingu betonu EkoCem w Dąbrowie Górniczej (fot. własne)

2.1. Thermal analysis – calcium looping method

Thermal testing (DTG) was performed using a NETZSCH thermal analyzer, model STA 449 F3 Jupiter. Measurements were performed on sample RCP.8.2025, representing aggregate with a fraction of 0-0.125 mm, in two temperature programs, described below.

I. Standard thermogravimetric analysis to determine the composition of tested samples. Measurement parameters: sample weight approximately 20 mg, dynamic gas flow (synthetic air) at 50 ml/min; heating rate 10°C/min in the temperature range 30-1030°C, Al_2O_3 crucibles with lids.

II. Measurement in a so-called calcium looping to determine CO_2 sorption capacity [6]. Measurement parameters: approximately 20 mg of rock sample, dynamic gas flow (CO_2 – working gas, N2 – shielding gas) at a rate of 20 ml/min; heating rate of 20°C/min in a temperature range of 40-900°C, Al_2O_3 crucibles without lids.
The temperature program developed for calcium looping is shown in Fig. 2.

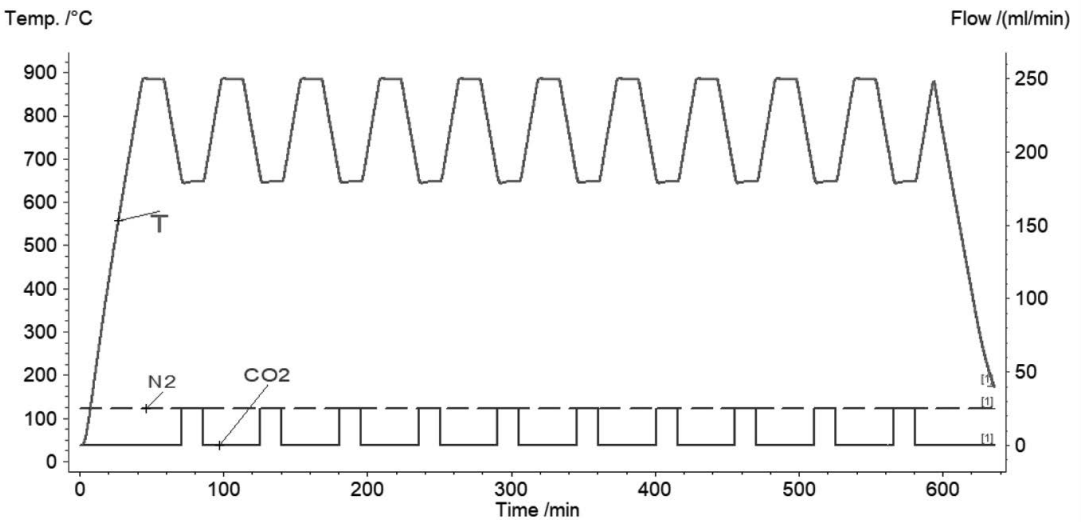

Figure 2. Temperature program of the so-called calcium looping (Program II). T – temperature, N2 – flow of protective gas (nitrogen), CO_2 – flow of working gas (carbon dioxide).
Rysunek 2. Program temperaturowy tzw. pętli wapniowej (Program II). T – temperatura, N_2 – przepływ gazu ochronnego (azotu), CO_2 – przepływ gazu roboczego (dwutlenku węgla).

Temperature changes are shown in the red curve (T). Initially, the sample was heated to 900°C at a rate of 20°/min in an inert atmosphere (N_2). The temperature was maintained at 900°C for 10 minutes, followed by cooling to 650°C. The sample was held at this temperature for 10 minutes, with a simultaneous flow of carbon dioxide (CO_2) as the working gas. The sample was then heated again to 900°C. This calcination and carbonation cycle was repeated 10 times. Sample mass changes were recorded during the experiment.

2.2. Diffraction and microscopic examination of RCP before thermal processes

Phase composition studies of the raw dust fraction from RCP.8.2025 were conducted using X-ray diffraction (XRD). Quantitative analysis was performed using Rietveld computational methods, which indicated 100% crystalline phase content, consisting of the phases shown in Figure 3. In particular, over half of the mass was quartz. Calcite accounted for almost 23%, and albite, ettringite, microcline, and muscovite accounted for over 20% in total. As is known, calcium carbonate begins to decompose from temperatures of 650°C to 900(±50)°C, so this compound, among those detected by XRD, could be the one undergoing recarbonation. Both phase and scanning electron microscope studies confirm a relatively large proportion of ettringite ($Ca_6Al_2(SO_4)_3(OH)_{12}\cdot 26H_2O$), visible as a rod-like phase in the micro-area shown – Fig. 4. Phase composition studies show that it is necessary to test recycled concrete,

as the tested 0-0.125 mm fraction was expected to contain a larger amount of amorphous phase, i.e., the C-S-H phase. This fraction was supposed to contain mainly cement paste. However, it can be concluded that it is paste, but originating from highly carbonated concrete. Therefore, the dusty fractions should be calcined to re-bind CO_2 in the new binder material.

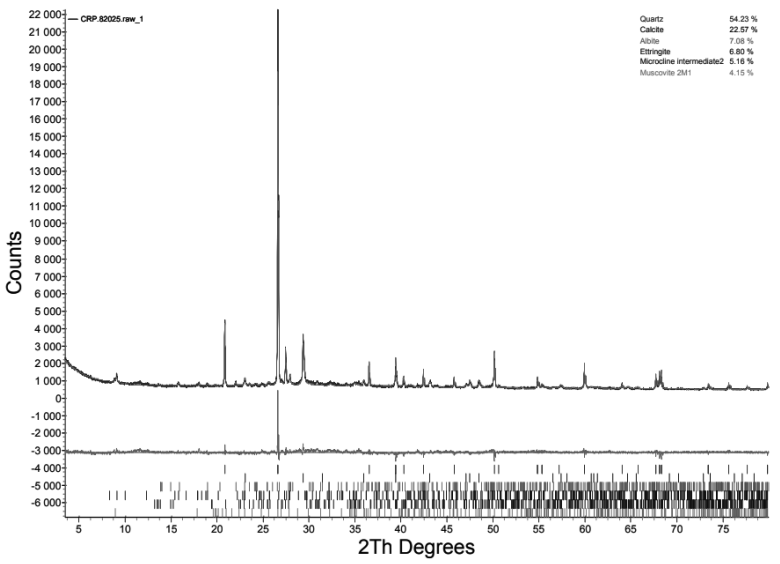

Quantitative Analysis

Quartz: 54.23%
Calcite: 22.57%
Albite: 7.08%
Ettringite: 6.80%
Microcline: 5.16%
Muscovite 2M1: 4.15%

Figure 3. Phase composition of the RCP.8.2025 sample, determined by diffractometric method and results of quantitative analysis.
Rysunek 3. Skład fazowy próbki RCP.8.2025, określony metodą dyfraktometryczną oraz wyniki ilościowej analizy.

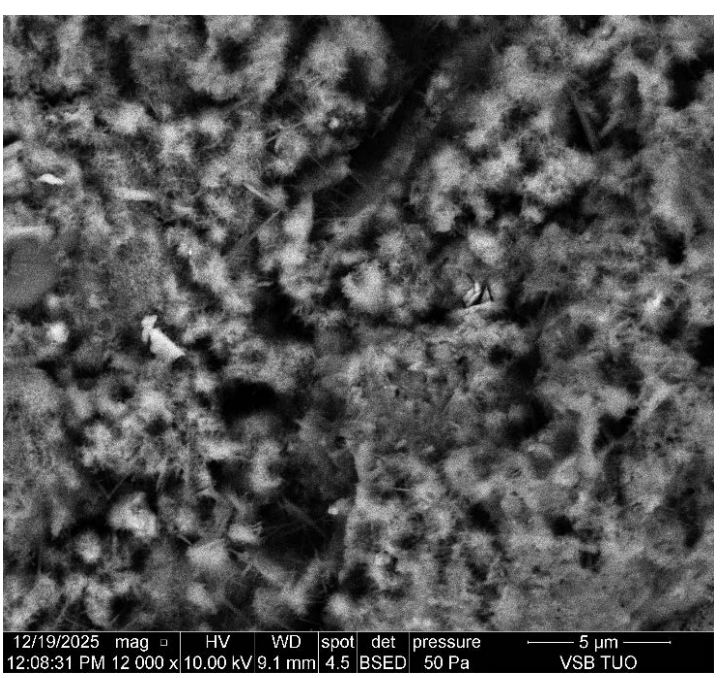

Figure 4. RCP.8.2025 specimen microarea
Rysunek 4. Mikroobszar próbki RCP.8.2025

3. TGA RESULTS OF THE RCP SEQUESTRATION CAPACITY TESTS

As mentioned above, thermogravimetric analysis was performed using two temperature programs. Program I was used to determine the sample's composition in terms of thermoreactive components. Thermal analysis of concrete or cement mortar allows for the determination of the content of bound water in hydration and hydrolysis products, as well as the content of calcium hydroxide and calcium carbonate [7, 8]. The graph (Fig. 5) shows the following thermal effects.

- in the range of 35-225°C - a complex endothermic effect associated with the dehydration of C-S-H silicates, hydrated calcium aluminates and aluminosulfates, and the decomposition of gypsum. The double peak visible on the DSC and DTG curves indicates the decomposition of ettringite – hydrated calcium and aluminum sulfate ($Ca_6Al_2(SO_4)_3(OH)_{12} \cdot 26H_2O$).
- in the range of 225-700°C - an endothermic effect with a maximum at 477°C, attributed to the dehydroxylation of $Ca(OH)_2$,
- at 574°C - an effect that does not cause a mass change, originating from the polymorphic transformation of quartz ($\beta \rightarrow \alpha$),
- in the range of 700-1000°C - an endothermic effect associated with the decomposition of $CaCO_3$.

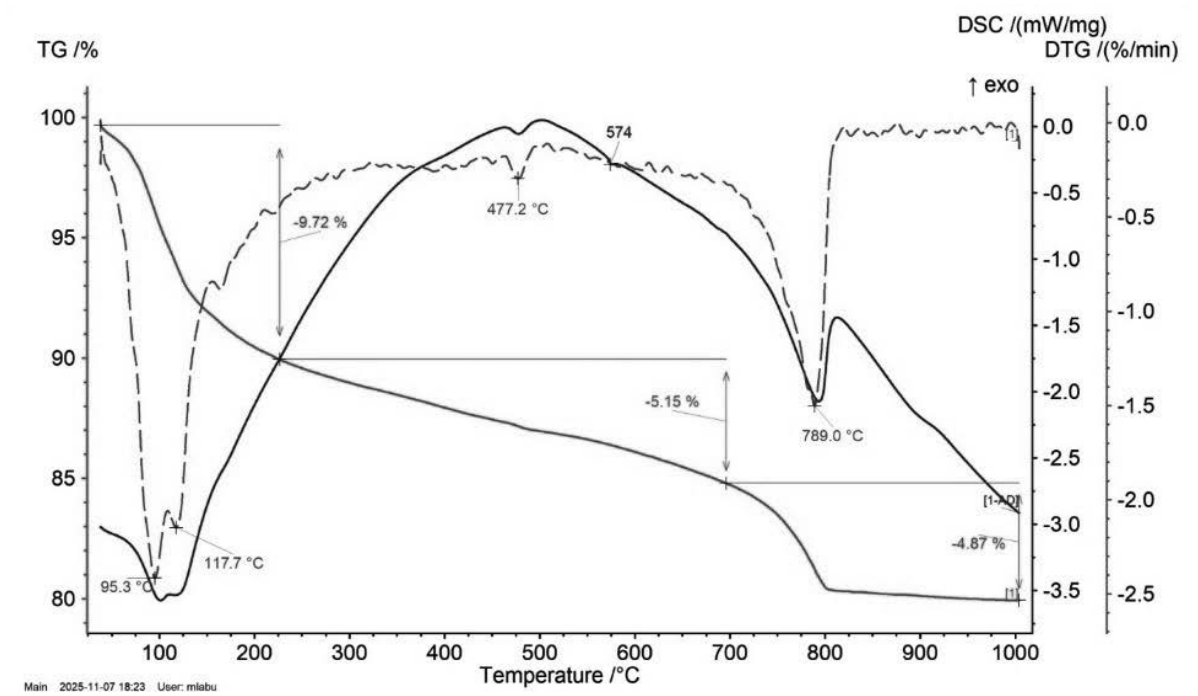

Figure 5. TGA analysis result (temperature program I) for sample RCP.8.2025. Curves: TG – red, DTG – green dashed, DSC – blue

Rysunek 5. Wynik analizy TGA (program temperaturowy I) dla próbki RCP.8.2025. Krzywe: TG – czerwona, DTG – zielona przerywana, DSC - niebieska

Based on the above results, the content of individual thermoreactive components was determined. Determination of bound water content (Hzw) by thermal analysis in cement and cement paste is based on the assumption that all bound water in all hydration

products of cement and cement paste is removed by 580°C. Bound water is first determined as contained in hydration products (hydrated calcium silicates, aluminosulfates, aluminates, and aluminoferrates) in the temperature range up to approximately 300°C and is designated by the symbol HI. Water bound from calcium hydroxide is then added in the temperature range up to approximately 600°C and designated by the symbol HCH. Mass losses associated with thermal effects within the above-mentioned temperature ranges constitute the bound water content in cement and cement paste. For the CRP.8.2025 sample, the bound water content was calculated as the sum of the sample mass losses recorded on the TG curve in the temperature range from 35°C to approximately 700°C, i.e.:

$$H_{zw} = H_I + H_{CH}: 9.72\% + 5.15\% = 14.87\%.$$

In turn, the determination of $Ca(OH)_2$ content by thermal analysis assumes that all $Ca(OH)_2$ in cement and cement paste decomposes according to the reaction:

$$Ca(OH)_2 \rightarrow CaO + H_2O.$$

The mass loss caused by dehydroxylation of $Ca(OH)_2$, when multiplied by the appropriate factor (4.11), will indicate the content of $Ca(OH)_2$ in the tested sample; in this case: 5.15% × 4.11 = 21.17%

The determination of calcium carbonate content assumes that all $CaCO_3$ in cement and cement mortar decomposes in the temperature range from 700 to 1000°C.:

$$CaCO_3 \rightarrow CaO + CO_2.$$

The mass loss caused by the decomposition of calcium carbonate, after multiplying by the appropriate factor (2.27), will indicate the $CaCO_3$ content in the tested sample, i.e.: 4.87% × 2.27 = 11.05%.

In the calcination and carbonation process (program II), mass increases were obtained in the TG curve in subsequent stages, indicating CO_2 sorption (Fig. 6). During the carbonation of the sample, the mass increase in subsequent cycles ranged from 0.93% (in the first cycle) to 0.31% (in the 10th cycle). This indicates a moderate sequestration capacity of the tested sample.

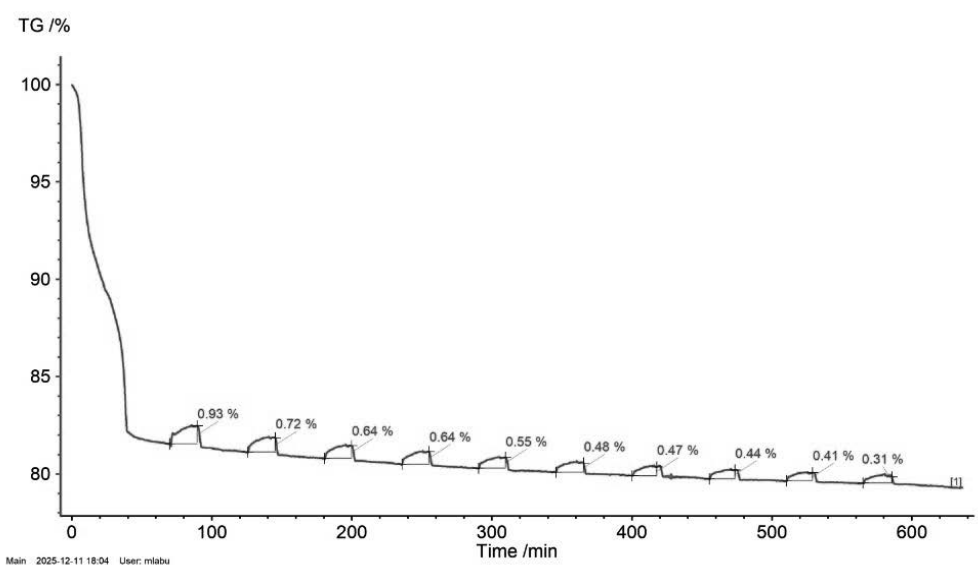

Figure 6. Experimental result (TG curve) in the calcium looping for sample RCP.8.2025
Rysunek 6. Wynik eksperymentu (krzywa TG) w pętli wapniowej dla próbki RCP.8.2025

4. SUMMARY AND CONCLUSIONS

Crushed concrete, recycled concrete, crushed concrete from demolitions, or concrete rubble from demolitions or renovations is undoubtedly ecological and cheaper substituent for natural aggregates. After testing, in appropriate fractions, they can even be used as a concrete component, not just for landscaping, soil stabilization, road bases, or drainage. The powdered fraction, which was the subject of this study, can be a component that reabsorbs CO_2, but as studies have shown, only to a small extent, within 10 hours after subsequent decarbonization (calcination) stages.
It is worthwhile conducting research on the carbonization or recarbonation of recycled aggregates to understand their reactivity as a new concrete component. Moreover, one cannot forget about the prior testing of recycled concrete, because each building structure has its own history.

ACKNOWLEDGEMENT

The article is part of the work entitled: "*CO_2 sequestration in recycled concrete*", carried out within the framework of PBL-IDUB 13th edition.

BIBLIOGRAPHY

1. Paweł Tokarz: „Beton w zgodzie z naturą, czyli „ZERO WASTE (zero marnowania) - kruszywo z recyklingu w połączeniu z cementami niskoemisyjnymi w betonie jako przyszłość budownictwa”, XIII Konferencja Dni Betonu 13-15 X 2025, Wisła; online: https://www.dnibetonu.com/wp-content/uploads/2025/10/Tokarz_bs.pdf
2. PN-EN 12620+A1 Kruszywa do betonu
3. PN-EN 206+A2:2021-08 Beton. Wymagania, właściwości użytkowe produkcja i zgodność
4. PN-B-06265:2022-08 Beton. Wymagania, właściwości użytkowe produkcja i zgodność. Krajowe uzupełnienie PN-EN 206+A2:2021-08
5. Strona internetowa: PropertyNews.pl: „W Dąbrowie Górniczej rusza zakład recyklingu betonu”, online: 18 lip 2024 https://www.propertynews.pl/tereny-inwestycyjne/w-dabrowie-gorniczej-rusza-zaklad-recyklingu-betonu,165130.html?mp=promo \
6. Labus K., 2021, Comparison of the Properties of Natural Sorbents for the Calcium Looping Process, Materials 14, 548
7. Majchrzak A., Nowak W., 2017, Optimization of novel sorbents for CO_2 removal based on FTIR and TG analysis, Mineralogia 48, 47-62
8. Villain G., Thiery M., Platret G., 2007, Measurement methods of carbonation profiles in concrete: Thermogravimetry, chemical analysis and gammadensimetry, Cement & Concrete Research 37, 1182-1192

TalentDetector
7th-9th June 2026
Gliwice-Brenna, Poland
DEPARTMENT OF ENGINEERING MATERIALS AND BIOMATERIALS
FACULTY OF MECHANICAL ENGINEERING
SILESIAN UNIVERSITY OF TECHNOLOGY
INTERNATIONAL STUDENTS SCIENTIFIC CONFERENCE

Properties of building mortars with recycled concrete as a partial replacement for natural sand

Słomka-Słupik Barbara[a], Dalibor Matýsek[b], Sylwia Antończyk[a], Maja Maciaszek[a], Kuba Szlachta[a], Kacper Popielarczyk[a]

[a] Silesian University of Technology, Faculty of Civil Engineering, Department of Building Structures, email: barbara.slomka-slupik@polsl.pl
[b] Technical University of Ostrava, Faculty of Mining and Geology, Department of Geological Engineering

Abstract: The article presents the possibility of reusing concrete in construction. Demolition concrete was ground into fine fractions and reused in mortars. The compressive strength of the mortars was tested at different curing times, divided into wet and dry curing. The degree of replacement of natural sand with recycled concrete sand was 10%, 20%, 30%, 50%, 100% by weight.

Keywords: recycled concrete sand (RCS), mortars, compressive strength

1. INTRODUCTION

Circular Economy, sustainable construction, low-emission construction, and local content are not just slogans, but an entire machine of processes leading to savings in both energy and non-energy raw materials. The construction materials industry, as one of the more energy-intensive sectors, follows designated ecological goals in various ways. One example is the reuse or incorporation of worn-out structural elements into a construction product. In this work, we will focus on demolition concrete, which in fragmented form as crushed concrete, can serve many construction purposes. It is used as base courses under roads and parking lots, reinforces embankments, but can also constitute aggregate in lower-class concrete mixes.
As of January 1, 2025, new regulations regarding construction and demolition waste have been in force. According to Art. 3, point 6a) of the Waste Act [1], this waste must be collected selectively, and concrete is among it. Once crushed, concrete rubble should meet the appropriate standards to be considered an aggregate for concrete or mortars [2, 3]. Large-scale global research shows the possibilities of using crushed concrete in mortars. Neno et al. [4] replaced natural sand with recycled concrete sand, but the grains maintained the same particle size distribution. Mortars were prepared with natural sand replacement levels of 20%, 50%, and 100%. The compressive strength and many other factors were analyzed. The best results were obtained for the replacement ratios of 20% and 100%; consequently, considering other tests, the mortar with a 20% replacement ratio performed better than the reference mortar. On the other hand, Zhao and

his team [5] analyzed the impact of fine recycled concrete aggregates on the properties of fresh and hardened mortars, as well as the interfacial transition zone (ITZ) microstructure. They investigated the effect of the saturation state of the recycled material on the properties of mortars with an identical composition. The results showed that the consistency of mortars containing dried concrete sand is always greater than that of mortars containing water-saturated concrete sand. Furthermore, the compressive strength of mortars containing dried concrete sand was higher in each case compared to mortars made with saturated sand, which is attributed to a thinner interfacial transition zone (ITZ) that improves its mechanical properties. The compressive strength of the mortars decreased almost linearly with the increase in the percentage of recycled sand. Additionally, it was demonstrated that the finest, silty fraction of the recycled sand had a worse effect on the mechanical properties of the mortars.
Braga et al. [6] conducted studies on the properties of masonry mortars with the addition of recycled concrete sand at various natural aggregate replacement proportions. The materials obtained from the recycling plant were sieved through a 4 mm mesh sieve and used directly to prepare the mixes, maintaining their original particle size distribution. CEM-IV/A(V) 32.5 N cement, containing 29% fly ash, was used, and the mortars were prepared with a cement-to-aggregate volume ratio of 1:7. Five mortars with different volumetric replacement levels were tested: 0%, 5%, 10%, 20%, and 40%. The results proved that a replacement ratio of even up to 40% constitutes a viable alternative to produce environmentally friendly masonry mortar.
Meanwhile, three years ago, Bendimerad et al. [7] described alternative methods of recycling concrete sand and their impact on the mechanical and performance properties of mortars. Attention was focused on the cost-effectiveness and valuation of sand and concrete aggregates derived from recycling. An environmentally friendly, alternative recycling process was investigated; mortar mixes based on recycled sand and concrete aggregates with 50% and 100% volumetric substitution of natural sand combined with 20% natural perlite were developed and analyzed; the efficiency of the recycling process to obtain useful mortars based on recycled aggregates was determined; and an improvement in the quality of the composition and main properties of mortars with waste aggregates was noted. On the other hand, more recent articles present a multi-criteria analysis of cement mortars with the addition of recycled sand, covering mechanical properties, durability, and environmental aspects [8], or, for example, investigated the effect of recycled concrete sand on the durability of mortars, particularly resistance to carbonation and chloride penetration when using limestone calcined clay cements (LC^3) [9].

2. EXAMINATIONS

1.1. Materials and Methods

The materials used in the study were:

- CEM II/A-LL 52,5R cement – Portland-limestone cement with very high early and standard strength
- standard sand (fraction < 2 mm)
- recycled concrete sand (fraction < 4 mm)
- distilled water

The recycled concrete sand, obtained from a local concrete recycling plant, was produced in such a way that the construction demolition rubble was subjected to specialized fragmentation – not

crushing, but rather grinding – so that the edges of the aggregates were not sharp but rounded, like in the case of natural river aggregate.
The cement used was a modern, eco-friendly cement, free of ash and slag content in its composition, providing rapid strength development to the mortars.
By replacing the natural sand with recycled concrete sand, it was examined how the mass shares of individual fractions are distributed in a sample with a mass of, for example, 1000 grams. The sieving of the concrete sand was performed on a set of sieves with the mesh sizes specified in Table 1. Table 1 also shows the quantities of individual fractions in 1000 grams of both types of sand. Meanwhile, Figure 1 compares the cumulative quantities of individual fractions of both sands up to 100% of their mass. Comparing both types of sand, it can be noticed that the natural sand contained much more of the 0.125-0.25 mm fraction, as well as the 0.5-1 and 1-2 fractions, but contained no 2-4 fraction at all and only trace amounts of larger grains. When preparing samples with partial substitution, the 2-4 fraction was not removed from the recycled concrete sand, as this could be unjustified on an industrial scale. However, it can be assumed that such differences had an impact on strength.

Table 1. Mass of the fractions of standard sand and recycled concrete sand in 1000 grams

Fraction, mm	Mass fraction of natural sand, g, in 1000 g	Mass fraction of recycled concrete sand, g, in 1000 g
< 0.063	9	28
0.125 – 0.063	54	43
0.25 – 0.125	191	95
0.5 – 0.25	76	171
1 – 0.5	309	160
1 - 2	361	168
2 - 4		285
> 4		51
sum	1000	1000

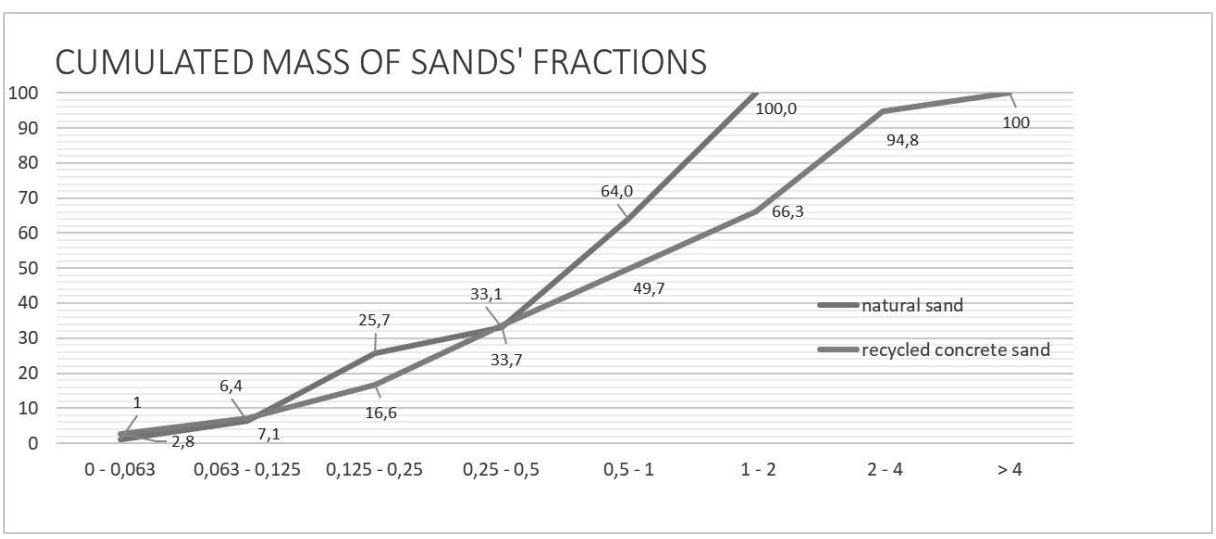

Figure 1. Cumulated mass of natural sand and recycled concrete sand fractions

The Z1 mortar mix was prepared using standard quantities of ingredients, as shown in Table 2, and was subsequently modified by replacing natural sand (P) with recycled concrete sand (RB) in the mass ratios specified in the names of the mixes. They were demoulded after 7 days and further cured either at their own moisture level – in zip lock plastic bags – or immersed in lime water, to check how the curing method affects the strength of the mortars. Therefore, the strength tested on the 7th day of curing could only be reported for the dry sample.

Table 2. Weights of ingredients in individual mortar mixtures, in grams

name of the mixture	cement	water	recycled concrete sand	natural sand
Z1	450	225	-	1350
Z2.P70.RB30	450	225	405	945
Z3.P80.RB20	450	225	270	1080
Z4.P90.RB10	450	225	135	1215
Z5.P50.RB50	450	225	675	675
Z1.R (RB100)	450	225	1350	-
Z2.Rw+ (RB100)	450	264.6	1350	-

1.2. Compressive strength test results

The results of the compressive strength tests of the mortars are shown in the graph in Figure 2. Analyzing the 7-day strength values, it can be seen that they decrease as the amount of recycled sand increases relative to the amount of standard (natural) sand. However, the complete replacement of natural sand with the recycled material (Z1.R and Z2.Rw+) yielded the highest strength, particularly in the case of the mix with a lower water content. The strength values after 28 days were higher than after 7 days, and they were greater in the case of dry curing. In contrast, after six months of hardening, the mixes showed less clear dependencies, but internal curing generally yielded better results than water curing. The highest strength value, nearly 64 MPa, was obtained after 6 months for the Z3.P80RB20.s sample, which is the sample with a 20% replacement of natural sand with concrete sand. The complete replacement of natural sand with recycled concrete (Z1.R and Z2.Rw+) showed very strange mortar strength values after a longer hardening period. This issue undoubtedly needs to be investigated in further studies. It is possible that unfavorable reactions occurred between the components of the cement and the ground demolition concrete. In the Z1.R and Z2.Rw+ mortars, concrete sand was used, but the fractions were prepared in the same way as for the standard sand, meaning they ranged from 0 to 2 mm; hence, Z1.R can be compared to Z1.s. The differences in strength on the 7th day were very minor, but over a longer period, they became highly divergent.

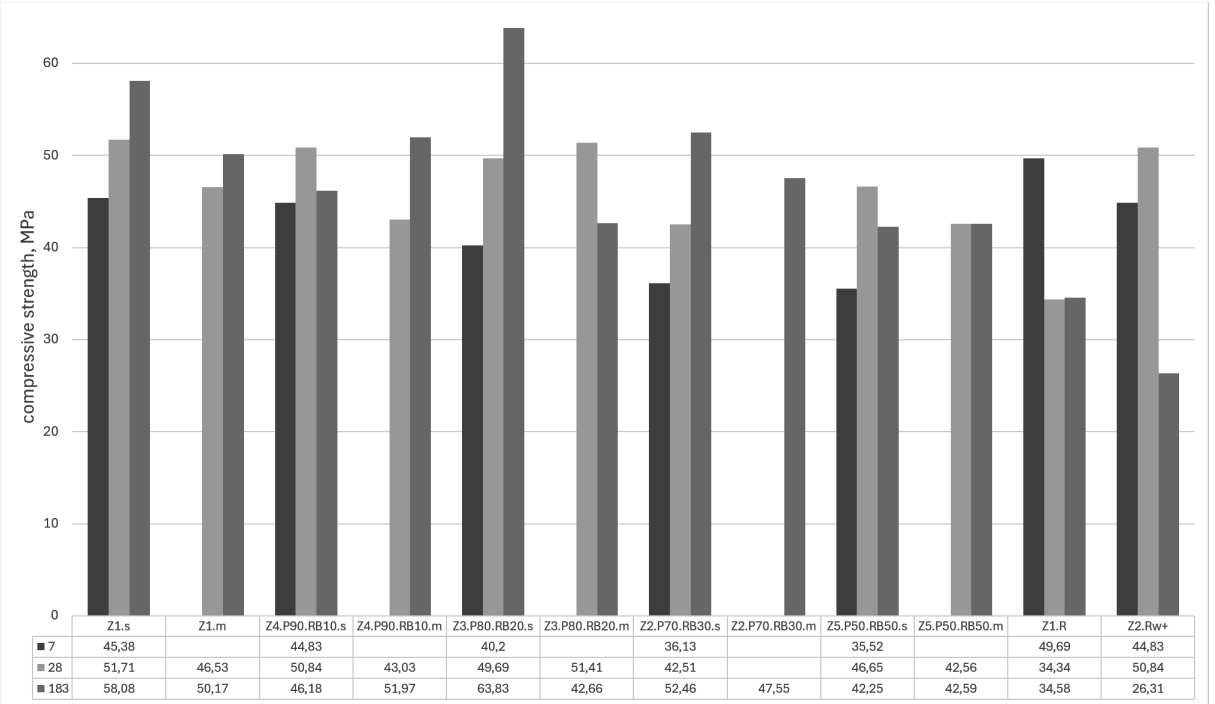

Figure 2. Compressive strength of wet (m) and dry (s) cured samples at different hardening times (7 days, 28 days, 6 months), MPa

2.2. Microscopic test results

Replacing natural sand with recycled concrete sand may also affect the microstructure of the mortars. Therefore, microscopic observations were conducted. Below are compiled images of the microstructure of the Z1 mortar without the addition of the recycled material, cured under dry conditions (Fig. 3a) and in a solution like the pore solution (Fig. 3b). The images suggest that wet curing causes leaching of the binder, which appears less dense in Z1.m. The visible darker, larger grains are natural sand particles. An attempt was also made to compare the Z1.R and Z2.Rw+ mortars (Fig. 4), which contained no natural sand, but only recycled concrete sand. Both cured in bags at their own moisture level. The fresh mix of Z1.R mortar was unworkable due to high water sorption by the porous recycled concrete; therefore, more water than the standard amount was added to it (Table 2), and it was named Z2.Rw+. It appears that the mix with the lower water content has a more cohesive binder matrix, but cracking is also present. On the other hand, the microstructure of the Z2.Rw+ binder has significantly more fine pores. Subsequent images show micro-areas at higher magnifications, and it can be noticed that the limestone cement used contributes to the formation of large amounts of portlandite, visible as plates located in the ITZ or on the surface of an air void (Fig. 5), as well as to the formation of significant amounts of ettringite (Fig. 6). Microscopic observations showed that it is difficult to determine which part in the images constitutes the recycled concrete.

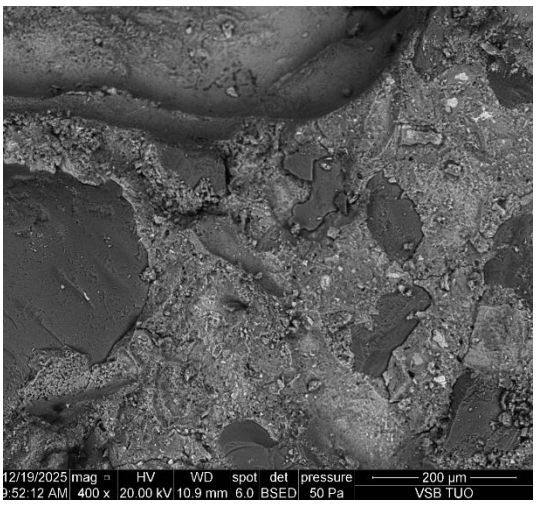

a) Z1.s cured in dry conditions

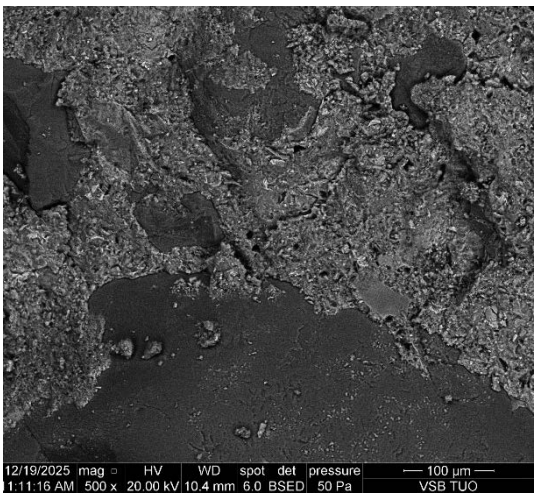

b) Z1.m cured in wet conditions

Figure 3. SEM images of Z1 mortar cured in dry (a) and wet (b) conditions

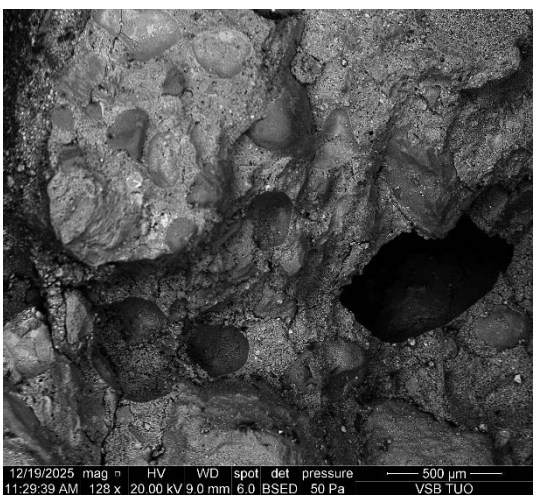

a) Z1.R cured in dry conditions

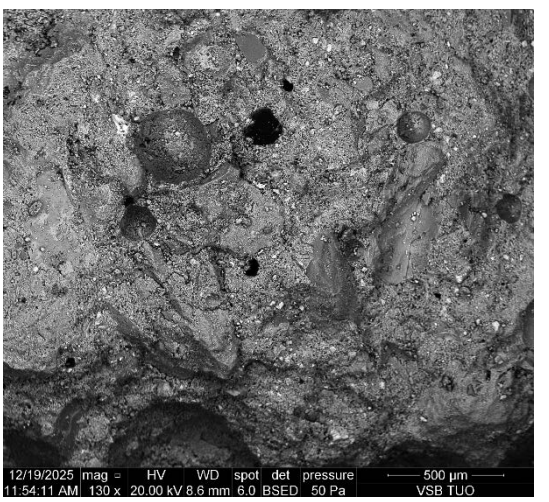

b) Z2.Rw+ cured in dry conditions

Figure 4. SEM images of Z1.R mortar and Z1.Rw+ mortar

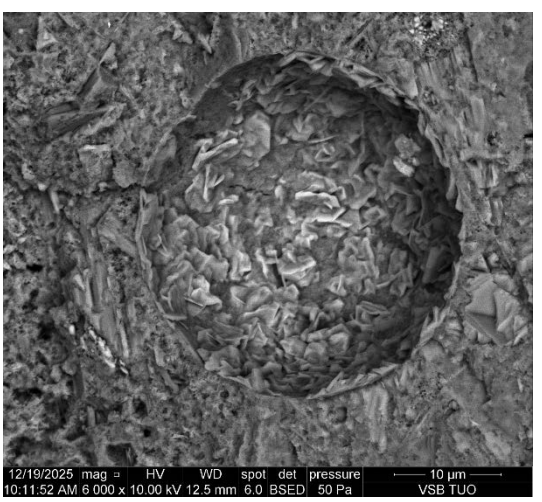

Figure 5. SEM images of Z1.s microarea

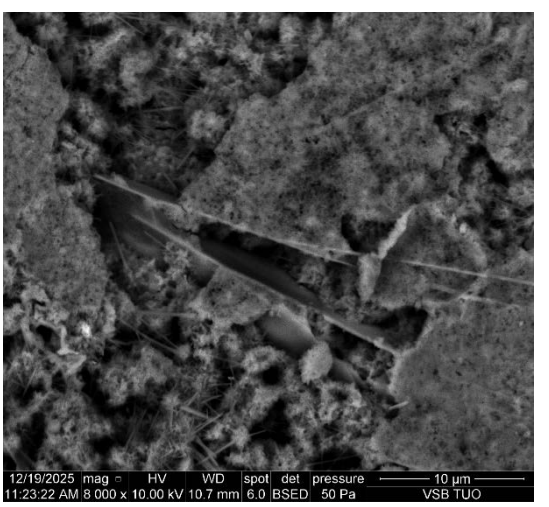

Figure 6. SEM images of Z1.m microarea

3. ANALYSIS AND CONCLUSIONS

This paper presents the study of compressive strength and microscopic observations of mortars in which natural sand was replaced with a locally available, fine-fraction concrete crush (< 4mm), with mass substitutions of 10%, 20%, 30%, 50%, and 100% of recycled sand. The Portland-limestone cement used, CEM II/A-LL 52.5R, characterized by very high early and standard strength, provided the samples with very high strengths ranging from 35 MPa to 45 MPa after just 7 days. It was also noted that in the case of standard sand, the strength steadily increased over time, whereas in the case of the complete replacement of natural sand with the recycled material, the changes in strength over time were highly unstable. This could potentially be caused by impurities within the demolition concrete. Therefore, demolition concrete should be tested for its corrosiveness before being applied as an aggregate in fresh mixes. Microstructural observations, on the other hand, confirmed a greater number of discontinuities in the case of samples cured in water. Meanwhile, the mortar sample without natural sand and with a lower water content exhibited higher strength; however, shrinkage should be investigated in this case, as dried recycled sand can absorb the water required for cement hydration.

Fine recycled concrete aggregates (FRCA) also called recycled sand, having particle sizes smaller than 5 mm, are essentially composed of mortar and hardened cement paste. Therefore, their properties differ from those of natural aggregate, for example they induce a large water demand which can make them hard to recycle into mortar and concrete.

Therefore, research must continue to identify various factors affecting the durability of mortars, particularly those with 100% natural sand replacement. It is also recommended to test the concrete before crushing and using it in a new mix to verify its purity and rule out the occurrence of internal corrosion over time.

BIBLIOGRAPHY

1. Dz.U. 2013 poz. 21. Ustawa z dnia 14 grudnia 2012 r. o odpadach. Tekst ujednolicony.
2. PN-EN 12620:2013 "Kruszywa do betonu".
3. PN-EN 13242:2013 "Kruszywa do niezwiązanych i hydraulicznie związanych materiałów stosowanych w obiektach budowlanych i budownictwie drogowym".
4. Neno C., de Brito J., Veiga R., “Using fine recycled concrete aggregate for mortar production”, *Materials Research*, Vol. 17, No. 1, 2014, s. 168–177..
5. Zhao Z., Remond S., Damidot D., Xu W., “Influence of fine recycled concrete aggregates on the properties of mortars”, *Construction and Building Materials*, Vol. 81, 2015, s. 179–186.
6. Braga M., de Brito J., Veiga R., “Properties of masonry mortars manufactured with fine recycled concrete aggregates”, *Construction and Building Materials*, Vol. 71, 2014, s. 289–298.
7. Elaboration of recycled concrete sand aggregates-based mortars, Bendimerad A. Z. i in., “Elaboration of recycled concrete sand aggregates-based mortars: An alternative recycling process”, *Construction and Building Materials*, Vol. 398, 2023, 132333.
8. Multicriteria Analysis of Cement Mortar with Recycled Sand, Kępniak M., Łukowski P., “Multicriteria Analysis of Cement Mortar with Recycled Sand”, *Sustainability*, Vol. 16, No. 5, 2024, 1773.
9. Chloride ingress and carbonation assessment of mortars prepared with recycled sand and calcined clay-based cement, Jan A., Ferrari L., Mikanovic N. i in., “Chloride ingress and carbonation assessment of mortars prepared with recycled sand and calcined clay-based cement”, *Construction and Building Materials*, Vol. 456, 2024, 139337.

TalentDetector

7th-9th June 2026
Gliwice-Brenna, Poland

DEPARTMENT OF ENGINEERING MATERIALS AND BIOMATERIALS
FACULTY OF MECHANICAL ENGINEERING
SILESIAN UNIVERSITY OF TECHNOLOGY

INTERNATIONAL STUDENTS SCIENTIFIC CONFERENCE

Possibilities for improving the application of magnesium alloys in biomedical engineering through the formation of surface treatments

Melisa Šnircová[a], Peter Palček[a], Katarína Marušincová, Martin Slezák[a], Edita Illichmanová[a]

[a]University of Žilina, Faculty of Mechanical Engineering, Department of Materials Engineering, Univerzitná 8215/1, 010 26 Žilina, Slovakia
email: melisa.snircova@fstroj.uniza.sk

Abstract: This paper focuses on modern surface modification techniques for magnesium alloys intended for biodegradable implant applications. The study summarizes current knowledge regarding combined surface treatment methods based on plasma electrolytic oxidation (PEO) and polymer coatings (PVA), with emphasis on their potential to improve the corrosion resistance and functional properties of magnesium alloys in physiological environments. Attention is devoted to the mechanisms of coating formation, surface characteristics, degradation behaviour, and the influence of surface modifications on biocompatibility and mechanical stability. The paper also discusses the advantages, limitations, and future perspectives of these surface engineering approaches in biomedical applications. The presented overview contributes to a better understanding of the possibilities for extending the applicability of magnesium alloys in biomedical engineering and supports further research in the development of advanced biodegradable implant materials.

Keywords: magnesium alloys, biodegradable implants, corrosion, plasma, electrolytic oxidation, polymer coatings

1. INTRODUCTION

Magnesium alloys have become a key subject of research in the field of materials science, particularly due to their potential use in medical applications. However, their main disadvantage remains the high degradation rate in bodily fluids, which reduces their service life as biodegradable implants. Therefore, one of the main objectives in their development is to reduce the degradation rate through various surface treatments. These modifications improve biocompatibility and protect the implant against corrosion without permanently altering its properties. [1] [2] [3] [4]

Plasma electrolytic oxidation (PEO) is a commonly used technique for the formation of protective surface layers on magnesium and its alloy substrates. PEO is considered a more suitable approach for biomedical applications compared to other traditional surface treatment methods. However, the main limitation of PEO layers in terms of long-term corrosion resistance is their porosity. [5] [6] [7]

In biomedicine, biocompatible polymer coatings are also widely used because they improve surface properties and positively influence the corrosion resistance of magnesium alloys while remaining safe in terms of degradation within the human body. Synthetic polymers, such as polyvinyl alcohol (PVA), provide better control over the degradation process and minimize the risk of undesirable immune responses. [8] [9]

2. BIOCOMPATIBLE SURFACE TREATMENTS OF MAGNESIUM ALLOYS

Among the most critical limitations of using magnesium and its alloys as implant materials are rapid corrosion, the formation of large amounts of hydrogen gas, the accumulation of gas bubbles near the implant, and an increase in the local pH of bodily fluids. For magnesium to be used as a biodegradable implant material, it should meet the following requirements:

- It should maintain sufficient mechanical strength and integrity until the affected part of the body has healed.
- It should exhibit corrosion resistance in bodily fluids during the initial implantation period and subsequently corrode in a controlled and uniform manner.
- Its corrosion products should not exceed the acceptable absorption level for the human body. [10]

The most suitable solution is to reduce the corrosion rate of magnesium, since a low corrosion rate of a magnesium implant leads to a reduction in hydrogen evolution and alkalization, allowing the human body to gradually absorb or consume the corrosion products. To reduce the corrosion rate, surface modification of magnesium alloys is required, which also improves the biocompatibility, bioactivity, and mechanical properties of the implant. [10] [5]

For biodegradable magnesium-based implants, the aim of surface treatments is only to control the degradation rate and improve the surface biocompatibility, rather than permanently altering the surface structure and properties, as this could lead to the non-degradability of implants or toxicity to surrounding tissues. Surface modification can be understood in terms of surface treatment (modification of the surface by changing its composition, microstructure, or both), surface coating (adding a separate material layer onto the original surface), and combined treatment. A coating (a layer with an appropriate thickness) represents a promising solution for minimizing severe localized corrosion of magnesium and its alloys during the initial stage after implantation because it acts as a protective barrier for the substrate. Furthermore, as a temporary surface, a properly designed coating can gradually degrade in vivo without causing harmful effects on surrounding tissues. However, combined treatments exhibit better properties compared to the coating or substrate alone. [4] [11]

Interactions between the biological environment and biomaterials occur at the material surface, while the initial biological response of living tissues to these foreign biomaterials depends on the properties of their surface. The reasons for surface modification of magnesium alloys are as follows:

- The properties of magnesium alloys rarely perfectly satisfy all the requirements of specific applications.
- Appropriate surface treatment techniques make it possible to preserve the excellent bulk properties of the magnesium alloy substrate while improving specific surface properties required for various clinical applications. For example, surface modification can reduce surface energy, neutralize surface potential, and smooth the surface texture. These changes

can directly influence thrombosis and neointimal proliferation, thereby reducing the risk of restenosis.

- Although bulk properties determine the mechanical characteristics of biomaterials, interactions between tissues and biomaterials are surface phenomena governed by surface properties. In various applications, it is necessary to ensure an appropriate lifetime of medical implants; therefore, it is important to find a balance between substrate and surface properties.
- Requirements in modern medicine include not only the need for improved biomedical devices but also greater functionality and bioactivity of medical implants. [11]

The classification of surface treatments in the scientific literature varies slightly, as different authors use different criteria for their categorization. Marulanda et al. roughly classified surface treatment techniques as chemical modifications and physical modifications. Chemical modification can be defined as the use of chemical or electrochemical methods to create a new phase on the metal surface through chemical bonding, which includes fluoride treatment, alkaline treatment, acid etching, or anodizing (anodic oxidation). Physical modification can be defined as the application of physical processing techniques or the deposition of new adhesive phases on a metal surface without chemical bonding between the metallic substrate and the coating. These techniques include laser surface processing, electron beam processing, ion implantation, and metal oxide implantation. Apatite coatings and organic polymer coatings can be prepared using both chemical and physical methods. [12] Mahto et al. classified surface modification techniques into two main categories, namely conversion coatings and non-conversion coatings. The overall classification is shown in Figure 1. [5]

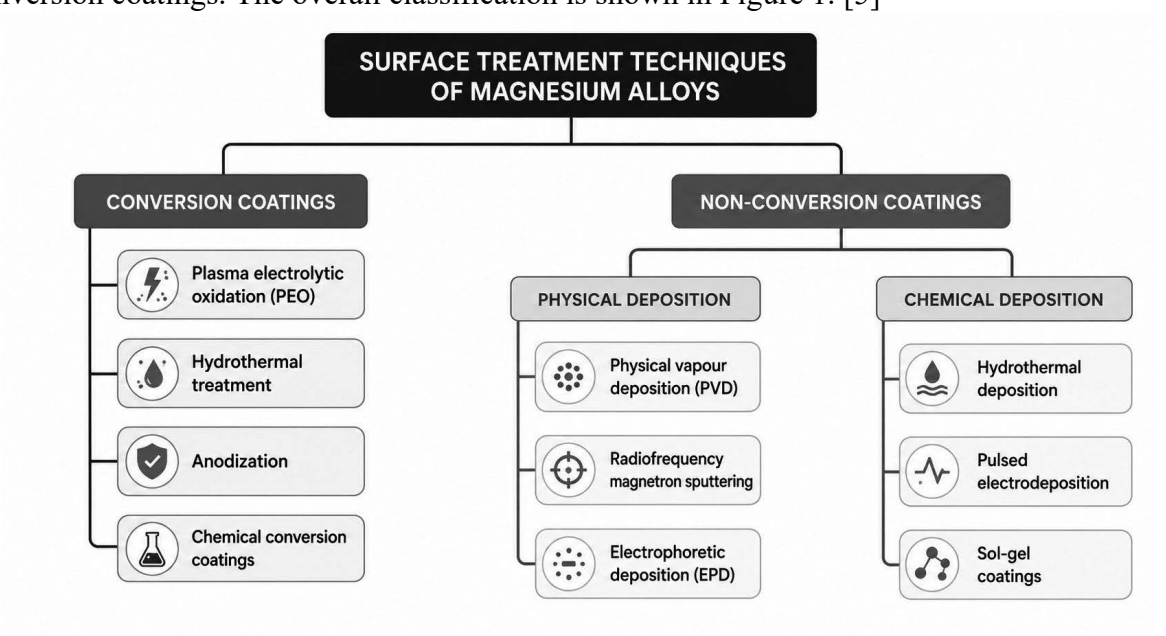

Figure 1. Classification of surface treatment techniques for magnesium alloys (Generated by AI- ChatGPT-version GPT- 5.5.) [5]

2.1. Conversion layers

Conversion layers for magnesium alloys consist of magnesium oxide or hydroxide layers. Oxidation of the substrate surface leads to the formation of oxide or hydroxide layers that act as

corrosion barriers. Techniques falling under conversion coatings include plasma electrolytic oxidation, hydrothermal treatment, or anodizing. Plasma electrolytic oxidation is the simplest, most versatile, and most environmentally friendly coating technique among all conversion processes. [5]

Hydrothermal treatment. The surface treatment of pure magnesium and the magnesium alloy AZ91 using hydrothermal treatment with deionized water or sodium hydroxide (NaOH) has been studied by many researchers. In their study, Sankara Narayanan et al. performed hydrothermal treatment of a magnesium alloy at a temperature of 160 °C using a 5.66 wt.% NaOH solution. Subsequently, a compact, uniform, and adherent magnesium hydroxide $Mg(OH)_2$ layer was formed on the surface of the magnesium alloy after the hydrothermal treatment. The thickness of the $Mg(OH)_2$ layer was strongly dependent on pH and treatment time, meaning that higher pH values and longer treatment times resulted in a greater layer thickness. However, the ability of $Mg(OH)_2$ to provide long-term corrosion protection for magnesium and its alloys in simulated body fluid remains an ongoing subject of research. [10]

Anodizing. Anodizing is a simple surface treatment technique for magnesium alloys that operates at low voltage and is environmentally friendly. It involves electrode reactions combined with the diffusion of metal and oxygen ions driven by an electric field, resulting in the formation of a stable coating layer with a thickness of up to 200 μm. The main advantages of anodizing, from a biomedical perspective, include improved adhesion and the formation of porous surface layers. [5] [11]

Chemical conversion coatings. In this technique, magnesium alloy substrates are immersed in solutions containing calcium phosphates. Calcium phosphates, such as hydroxyapatite (HA) or brushite, are the most formed layers, while $Mg(OH)_2$ is a less significant component. Substrates treated using this method have demonstrated good corrosion resistance, biocompatibility, and enhanced cell growth. [5]

2.2. Non-conversion coatings

In non-conversion coatings, the coating material is not derived from the base metal. The composition and properties of the substrate and the coating material may differ from each other. [6]

Physical coating deposition methods. Various physical deposition methods are used for applying coatings on magnesium alloys. These methods include physical vapor deposition (PVD), radio-frequency magnetron sputtering, and electrophoretic deposition (EPD). [5]

In physical vapor deposition, the material intended to form the coating is first converted into vapor and subsequently deposited onto the magnesium alloy substrate. This method is used for applying thin coatings that tend to seal porous oxide layers and improve the corrosion resistance of the alloy. [5] [13]

Radio-frequency magnetron sputtering is another physical technique for depositing thin surface layers onto a substrate using a magnetic field. It enables faster deposition at lower pressure compared to other coating techniques. [5]

Electrophoretic deposition is a versatile technique in which charged particles dispersed in an electrolyte are deposited onto the surface of a sample under the influence of an applied electric field. Various biomaterials such as hydroxyapatite, polymer materials, carbon nanotubes, and others are used. Morphological studies show that at low surface roughness and high annealing temperature, the resulting coatings are homogeneous and uniform with a minimal number of cracks. [5] [14]

Chemical coating deposition methods. In chemical deposition methods, coatings are formed by exposing the substrate surface to one or more volatile precursors. These precursors react or decompose on the substrate surface, forming the desired coating layer. [5]

Kaabi Falahieh Asl et al. deposited calcium phosphate onto AZ31 alloy using hydrothermal deposition and subsequently investigated the corrosion behaviour and biocompatibility of the alloy with the formed surface layer. Various studies confirmed that the corrosion protection of the coating depends on deposition temperature and time. In simulated body fluid, the weight loss was higher for the uncoated sample, while the coated sample showed a significantly reduced corrosion current density. [5] Pulse electrodeposition is a versatile and cost-effective method used for forming surface layers. Its unique advantage is the control of coating thickness and chemical composition by adjusting the current during deposition. The use of pulsed current instead of conventional direct current expands the possibilities for preparing high-quality coatings. In surface treatment of magnesium and its alloys, hydroxyapatite deposition is particularly important, as it improves corrosion resistance and provides better bioactivity. [10] Sol-gel surface treatment creates a thin gel layer on the magnesium surface through polycondensation after immersion in a colloidal solution. During immersion tests in modified simulated body fluid, the coating significantly reduced magnesium ion release and maintained the pH below 7.6 throughout the test. [14]

3. PLASMA ELECTROLYTIC OXIDATION (PEO)

Plasma electrolytic oxidation (PEO) or micro-arc oxidation (MAO) is the most commonly used surface treatment technique for creating thick and dense ceramic oxide layers on magnesium substrates and their alloys. PEO utilizes environmentally friendly weak alkaline or acidic electrolytes, in which oxide layers are formed by the application of high electrical voltage. During this process, the coating thickness can range from 5 to 200 μm depending on the operating conditions. Many different parameters influence the process, such as the type and geometry of the substrate, electrolyte concentration, voltage, temperature, and process duration. The PEO process has been the subject of extensive research for a long time and is considered a superior approach for biomedical applications compared to other conventional surface treatment methods. [5] [6]

3.1. Principle of the method

In the PEO process, a wide range of voltages is applied together with either direct or alternating current between the anode and cathode. When the electrical circuit is closed, Ohm's and Faraday's laws apply to both the anode and cathode. The metallic substrate (sample) acts as the working electrode (anode), while the counter-electrode (cathode) is usually made of stainless steel. Both electrodes are immersed in a weakly alkaline electrolyte and then connected to an external power source to initiate the formation of a surface layer. During the process, stirring ensures continuous mixing of the electrolyte, which is essential to maintain a uniform composition and to dissipate the generated heat. An external cooling system is used to keep the electrolyte temperature at room level. [6] [15]

The mechanism of oxide layer formation via PEO is the result of plasma-chemical, electrochemical, and thermochemical reactions. The main electrochemical reactions include oxidation of magnesium (at the anode), reduction of oxygen (at the cathode), and evolution of hydrogen gas (at the cathode). At the anode, magnesium is oxidized, producing magnesium

ions, which subsequently react with oxygen and hydroxide ions to form the primary component of the surface layer, magnesium oxide. At the cathode, oxygen reduction and hydrogen gas evolution help maintain charge balance in the system. [16]

For PEO processes, the constant current mode is typically used, while monitoring voltage changes over time helps identify the main stages of the process. The PEO process is based on electrical discharges occurring on the anode surface at higher voltages. When voltage is applied between the electrodes, the process begins. In the first stage, voltage increases linearly with time, and no visible discharges are observed on the substrate surface during the initial seconds; a transparent, thin passive oxide layer is formed. The first inflection point in the voltage curve is associated with the breakdown voltage, which occurs as the oxide layer grows and resists current flow. In the second stage, voltage continues to increase linearly, but with a lower slope. Molten oxide is ejected through discharge channels formed on the oxide layer surface, and upon cooling, a rough and porous coating is formed across the substrate surface. In this stage, small and evenly distributed discharges are visible, changing in colour from white at the beginning to yellow as the process continues. The second inflection point represents the critical voltage. After exceeding this level, surface phenomena change significantly. In the third stage, voltage reaches an approximately constant value, and stable sparking is observed on the metal surface. The discharges appear orange and slowly move across the entire surface, while their density gradually decreases and their size increases. The voltage-time graph for the PEO process on a magnesium alloy substrate is shown in Figure 2. [17] [15] [18]

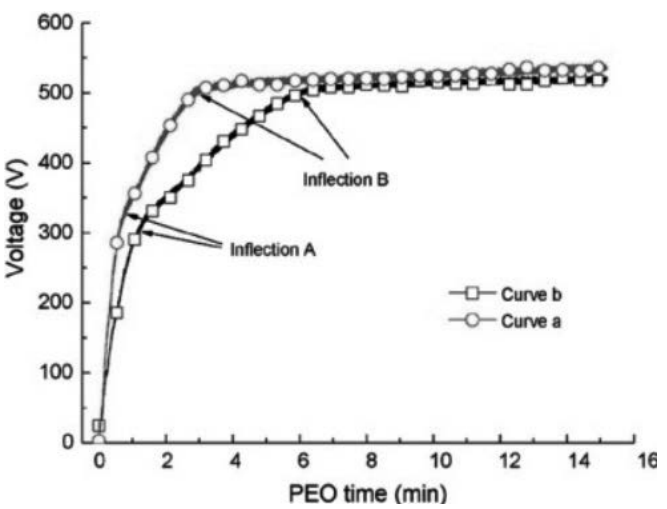

Figure 2. Voltage as a function of time for the PEO process on magnesium alloys: Curve a - current density of 100 mA/cm² and curve, b - current density of 50 mA/cm² over 15 min. [18]

It is assumed that the PEO layer on magnesium substrates consists of a three-layer structure, as shown in Figure 3. This structure comprises a porous outer layer, a compact intermediate layer, and a thin compact inner layer. The compact intermediate layer provides excellent corrosion resistance and is also responsible for good mechanical properties. [18]

The surface of PEO layers usually contains circular structures with a discharge channel located at the centre of each structure. Individual structures are separated by distinct boundaries formed because of the process in which molten material flows through the discharge channels and subsequently cools upon exposure to the cold electrolyte. The pore diameters in magnesium alloys typically range from 0.5 to 50 μm, and their size depends on the density or

magnitude of the discharges and the process duration. During the PEO process, local microcracks also form on the coating surface because of the cooling of molten material upon contact with the cold electrolyte. [17] [18]

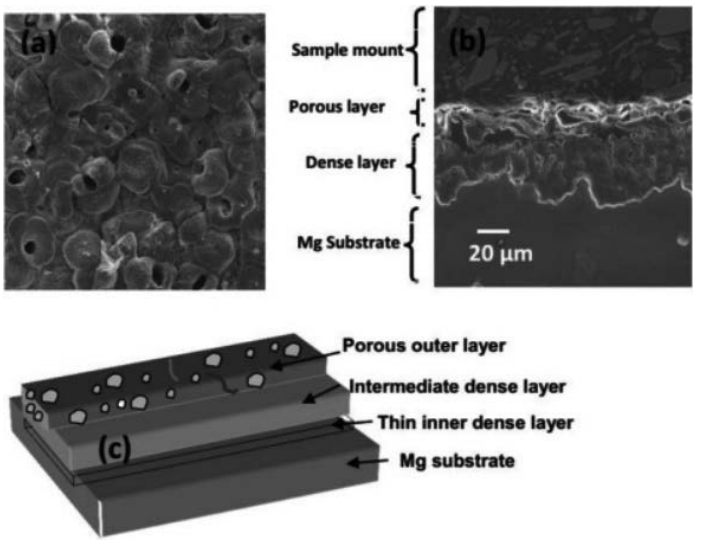

Figure 3. Structure of the PEO layer [18]

3.2. Biocompatibility of PEO layers

The biocompatibility and corrosion resistance of magnesium alloys with a PEO layer depend on many factors. In their study, Esmaeili et al. provided a detailed overview of how the selection of key PEO process parameters influences the corrosion resistance and biocompatibility of magnesium alloys intended for biomedical applications.

It has been demonstrated that current density is a significant factor affecting corrosion resistance; however, it has no substantial influence on the biocompatibility of the surface layer. Another factor is increased surface roughness, which may negatively affect corrosion resistance but positively influence biocompatibility. The hardness of the surface layer also has a direct effect on biocompatibility, while the hardness of PEO layers on magnesium alloys is governed by the crystalline phases present in the layers, which can be influenced by the electrolyte used as well as the chemical composition of the substrate. These findings were also supported by Fattah-alhosseini et al., who stated in their study that PEO layers have great potential as a surface treatment for biodegradable magnesium-based materials because the composition and properties of the layers can be adjusted over a wide range in order to control degradation and ensure biocompatibility. [19] [7]

Ma et al. focused in their article on comparing two magnesium samples: an untreated pure magnesium sample and a pure magnesium sample with a PEO layer. The results of in vitro cytotoxicity tests demonstrated that both samples were safe for use as implants. Furthermore, animal implantation experiments showed that no disorders of the heart, liver, kidneys, or spleen were observed, and no negative effects related to magnesium release were recorded, indicating that both implants exhibited good in vivo biocompatibility. Greater new bone formation was also observed around the sample with the PEO layer because this layer reduced the corrosion rate and magnesium ion concentration, resulting in improved osteoblastic activity and stimulation of new bone tissue growth. [20]

ACKNOWLEDGEMENT

The research was supported by the Ministry of Education, Research, Development and Youth of the Slovak Republic through the projects KEGA č. 033ŽU-4/2026 and KEGA č. 039ŽU-4/2026.

BIBLIOGRAPHY

1. A.R. Khan et al., Recent advances in biodegradable metals for implant applications: Exploring in vivo and in vitro responses, Results in Engineering 2023 https://doi.org/10.1016/j.rineng.2023.101526
2. S. Dobatkin et al., Mechanical Properties, Biodegradation, and Biocompatibility of Ultrafine Grained Magnesium Alloy WE43, Materials, vol.12 (2019)
3. J. Liu et al., Biodegradable magnesium alloy WE43 porous scaffolds fabricated by laser powder bed fusion for orthopedic applications: Process optimization, in vitro and in vivo investigation, Bioactive Materials, vol. 16 (2022) pp. 301-319
4. P. Tian, X. Liu, Surface modification of biodegradable magnesium and its alloys for biomedical applications, Regenerative Biomaterials, vol. 2 (2015) pp. 135-151
5. V.K. Mahto, K.A. Singh, A. Malik, Surface modification techniques of magnesium-based alloys for implant applications, Journal of Coatings Technology and Research, vol. 20 (2023) pp. 163-181
6. S. Sikdar et al., Plasma Electrolytic Oxidation (PEO) Process - Processing, Properties, and Applications, Nanomaterials, vol. 11 (2021
7. A. Fattah-alhosseini et al., A review of effective strides in amelioration of the biocompatibility of PEO coatings on Mg alloys, Journal of Magnesium and Alloys, vol. 11 (2023) pp. 1045-1068
8. L.F. Francis, C.C. Roberts, Chapter 6 - Dispersion and Solution Processes, Material Processing - A Unified Approach to Processing of Metals, Ceramics and Polymers, 2016
9. Y. Zhu, W. Liu, T. Ngai, Polymer coatings on magnesium-based implants for orthopaedic applications, Journal of Polymer Science vol.60 (2022) pp. 1234-1248,
10. T.S.N. Sankara Narayanan, I. Park, M. Lee, Surface modification of magnesium and its alloys for biomedical applications: Opportunities and challenges, Biological Interactions, Mechanical Properties and Testing, 2015
11. J. Yang, F. Cui, I.S. Lee, Surface Modifications of Magnesium Alloys for Biomedical Applications, Annals of Biomedical Engineering vol. 39 (2011) pp. 1857-1871
12. X. He et al., An overview of magnesium-based implants in orthopaedics and a prospect of its application in spine fusion, Bioactive Materials 2024.
13. S. Abela, Protective Coatings for Magnesium Alloys, Magnesium Alloys - Corrosion and Surface Treatments, 2011 https://doi.org/10.5772/14100
14. S.A. Rahim et al., Recent Progress in Surface Modification of Mg Alloys for Biodegradable Orthopedic Applications, Frontiers in Materials vol. 9 (2022)
15. H. Sampatirao et al., Developments in plasma electrolytic oxidation (PEO) coatings for biodegradable magnesium alloys, Materials Today: Proceedings vol. 46 (2021) pp. 5489-5494

16. Y.Q. Almajidi, Unveiling the effect of particle incorporation in PEO coatings on the corrosion and wear performance of magnesium implants, Lubricants, vol. 11 (2023)
17. D. Kajánek, Štúdium mechanizmov korózneho napadnutia povrchovo upravených horčíkových zliatin, Dizertačná práca, Žilinská univerzita v Žiline, SjF, KMI, 2019.
18. G.B. Darband et al., Plasma electrolytic oxidation of magnesium and its alloys: Mechanism, properties and applications, Journal of Magnesium and Alloys vol. 5 (2017) pp. 74-88
19. M. Esmaeili, M. Tadayonsaidi, B. Ghorbanian, The effect of PEO parameters on the properties of biodegradable Mg alloys: a review, Surface Innovations vol.9 (2021) pp. 1-15
20. W.H. Ma et al., Improved biological performance of magnesium by micro-arc oxidation, Brazilian Journal of Medical and Biological Research vol. 48 (2015) pp. 798-806

TalentDetector

7th-9th June 2026
Gliwice-Brenna, Poland

DEPARTMENT OF ENGINEERING MATERIALS AND BIOMATERIALS
FACULTY OF MECHANICAL ENGINEERING
SILESIAN UNIVERSITY OF TECHNOLOGY

INTERNATIONAL STUDENTS SCIENTIFIC CONFERENCE

Impact of External Factors on the Durability of Screen-Printed Metallic Interconnections

Jacek Sopala[a], Jakub Janus[a], Julian Marszałek[a], Martyna Pasieka[a], Karolina Kornecka[a], Magdalena Szindler[b], Marek Szindler [c], Wojciech Sitek[c], Marko Kršulja[d], Lovro Liverić[d]

[a] Student of the Silesian University of Technology
[b] Silesian University of Technology, Faculty of Mechanical Engineering, Department of Engineering Materials and Biomaterials
[c] Silesian University of Technology, Faculty of Mechanical Engineering, Didactic Laboratory of Nanotechnology and Material Technologies, Gliwice, Poland
[d] Faculty of Engineering, Juraj Dobrila University of Pula, Negrijeva 6, 52100 Pula, Croatia
email: marek.szindler@polsl.pl

Abstract: Screen-printed Ag contacts based on nano- and microsized silver particles, glass frit, and barium oxide were fabricated on silicon substrates and thermally fired in a tunnel belt furnace. The microstructure and electrical properties were investigated using SEM, EDS, and ShereScan measurements before and after climatic chamber testing. SEM observations revealed homogeneous and well-adhered metallization layers, while EDS analysis confirmed the presence of Ag and Si within the contact region. The contacts exhibited low sheet resistance and specific resistivity values of 1.279 mΩ/sq and 1.919 μΩ·cm, respectively. After climatic aging, only a moderate increase in resistive parameters was observed, confirming good electrical stability of the developed metallization system for photovoltaic applications.

Keywords: screen printing; silver metallization; photovoltaic contacts

1. INTRODUCTION

Modern manufacturing engineering and energy management systems face a significant challenge related to reducing greenhouse gas emissions and combating climate change [1]. One of the key areas of development is solar energy, particularly photovoltaic technology, which enables the direct conversion of solar radiation into electricity [5, 11]. It should be emphasized, that the overall environmental impact of this technology, assessed on a life-cycle basis, depends primarily on the resource intensity of the manufacturing process and the operational lifespan of the modules [1, 9]. Consequently, the identification and elimination of degradation mechanisms in solar cell components, including electrical connections, is of critical importance from both an economic and environmental perspective. To enable the collection and transport of charge carriers generated within the semiconductor structure, a network of metallic contacts is formed on the surface of the silicon cell [5, 8, 10, 11].

The most commonly used method for their production is screen printing (Figure 1), due to its high efficiency and relatively simple technological implementation [1, 12]. This process involves mechanically forcing conductive paste through a printing screen using a squeegee, with the pattern of conductive paths being reproduced on the screen using a photosensitive emulsion [11, 12].

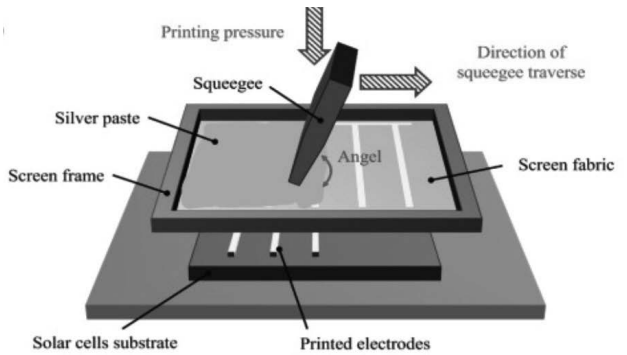

Figure 1. Schematic Representation of the Screen Printing Process

In modern production lines, it is possible to achieve a yield of 1500 cells per hour [8, 11]. The screen, typically made of thin steel wires, is kept at a controlled distance from the surface of the silicon base. During the process, a squeegee made of elastomer moves at a constant speed, causing the screen to contact the substrate and the paste to flow through the open mesh openings. After the squeegee passes, the screen separates from the surface, leaving a precisely reproduced pattern of conductive paths [4, 8, 11]. From a materials engineering perspective, the conductive paste constitutes a complex dispersion system consisting of three basic components: the functional phase (metal powder), the inorganic phase (glass frit), and the organic carrier [2, 6, 8, 11]. Controlling the particle size distribution and the homogeneity of their distribution within the system's volume is of key importance. After the paste is applied, the cells are subjected to a drying process at temperatures within the range of 150–250°C, the purpose of which is to remove the volatile components of the organic carrier and to fix the geometry of the tracks [11, 12]. The next stage is the high-temperature burnout process, performed in multi-zone furnaces. At temperatures ranging from 300–400°C, the organic components decompose and are removed. Subsequently, the maximum process temperature, typically 750–900°C, is reached within a short time. During this stage, the glass frit melts and reacts with the anti-reflective layer (e.g., silicon nitride), enabling electrical contact between the metal particles and the emitter region. During cooling, the structure crystallizes, resulting in a permanent, low-resistance connection between the metallization and the semiconductor [5, 8, 10]. Rapid cooling restricts excessive metal diffusion, which could lead to damage to the p–n junction.

Despite obtaining high-quality junctions under laboratory conditions, during operation the cells are subjected to changing environmental conditions [9, 11]. A significant degradation factor is cyclic temperature changes, leading to the formation of thermomechanical stresses result from differences in the thermal expansion coefficients of the materials [7, 9]. Additionally, the presence of moisture and chemically active agents promotes the initiation of electrochemical corrosion processes, particularly under applied voltage conditions [7, 9, 12]. Therefore, evaluation of the durability of metallic connections requires the use of accelerated environmental tests, such as thermal cycles and tests under increased temperature and humidity conditions. Analysis of degradation mechanisms, performed using microscopic methods and

measurements of electrical properties, forms the foundation for improving photovoltaic cell manufacturing technology [7, 9, 12].

2. MATERIALS AND METHODOLOGY

Metal contacts were deposited by the screen-printing method using a paste composed of nano- and microsized silver particles, glass frit, and barium oxide. The paste was applied using a semi-automatic screen-printing machine S5070. After deposition, the contacts were fired in a tunnel belt furnace PFO-200. The firing process was carried out in three temperature zones: a drying zone at approximately 250–300°C, a burnout zone at 450–550°C for removal of organic binders, and a peak firing zone at 750–820°C to ensure proper sintering of the silver particles and formation of conductive contacts.

The morphology and microstructure of the metallized contacts were investigated using a SEM Supra 35 microscope manufactured by Zeiss. Cross-sectional SEM micrographs were obtained to evaluate the thickness, porosity, and adhesion of the metallization layer. In addition, energy-dispersive X-ray spectroscopy (EDS) analysis and EDS line profile measurements were performed to determine the elemental composition and distribution of the metallic and glass phases across the contact cross-section.

Electrical characterization of the screen-printed contacts was performed before and after climatic chamber testing using the ShereScan measurement system. The resistance of the front metallization should remain as low as possible in order to minimize series resistance losses, while maintaining a limited metallized area to reduce optical shading. The ShereScan system enables characterization of metallic fingers and busbars through local sheet resistance measurements. Since the conductive lines have very small widths, the conventional sheet resistance equation cannot be directly applied. Therefore, the system uses the measured line width, introduced by the operator, to calculate the sheet resistance of the metallic line. When the line thickness is additionally provided, the instrument also calculates the specific resistivity of the metallization according to the relation $\rho = Rs \times t$, where Rs is the sheet resistance and t is the line thickness. To ensure accurate measurements, the four probe tips must be positioned precisely along the centerline of the metallic contact. The ShereScan system automatically performs multiple measurements across the width of the conductive path and identifies the point corresponding to the minimum measured resistance value as the actual centerline position. Climatic reliability tests were carried out using a Weiss WKL 100/40 climatic chamber, which enables investigations under controlled temperature and humidity conditions in the range from −40°C to 180°C. To simulate realistic environmental operating conditions of photovoltaic devices, thermal and humidity cycling tests were performed in the temperature range from −20°C to 85°C with relative humidity varying between 20% and 85%. These conditions were selected to reproduce typical day–night and seasonal environmental fluctuations occurring during long-term outdoor operation. The climatic tests were conducted to evaluate the influence of thermo-mechanical and humidity-related stresses on the structural stability, electrical performance, and degradation behavior of the screen-printed silver contacts.

3. RESULTS AND DISCUSSION

Figure 2a presents the cross-sectional SEM micrograph of the Ag contact metallization deposited by the screen-printing method. A typical morphology of a screen-printed front contact can be observed, consisting of a relatively dense silver layer well adhered to the silicon

substrate. The metallization exhibits a continuous conductive structure with visible sintered Ag particles and limited porosity, indicating proper firing conditions during the thermal treatment process. No significant delamination or large structural defects were observed at the Ag/Si interface, which confirms appropriate interaction between the silver paste and the silicon surface during the firing process. The EDS spectrum shown in Figure 2b confirms the presence of the main constituent elements of the contact structure. The dominant peaks correspond to silver (Ag) and silicon (Si). The Si signal observed at approximately 1.74 keV corresponds to the characteristic Si Kα line, while the Ag peaks appearing near 2.98 keV and 3.15 keV are associated with the characteristic Ag Lα and Ag Lβ transitions, respectively. The relatively high intensity of the Ag peaks confirms the formation of a conductive silver-rich metallization layer, whereas the presence of Si originates from the silicon substrate beneath the contact region. Figure 3a presents a SEM image of the cross-section of the screen-printed Ag contact together with the EDS line profile analysis shown in Figure 3b. The line scan analysis confirms the distribution of the principal elements across the metallization thickness and the Ag/Si interface. A high concentration of silver is observed within the upper contact region, while the silicon concentration increases significantly near the substrate area. The gradual transition between Ag and Si regions indicates good adhesion and proper interfacial contact formation after the firing process. Moreover, the EDS profile suggests limited elemental diffusion and no significant discontinuities within the analyzed cross-section.

a) b)

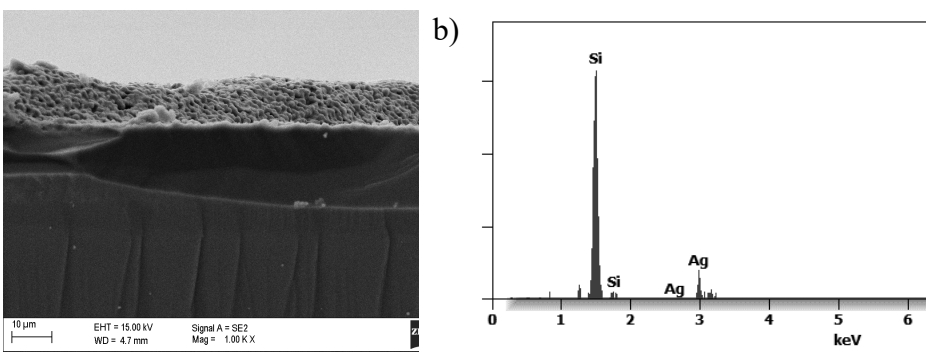

Figure 2. SEM micrograph (a) and energy-dispersive X-ray spectroscopy (EDS) spectrum (b) of the cross-section of an Ag contact metallization deposited by the screen-printing method.

a) b)

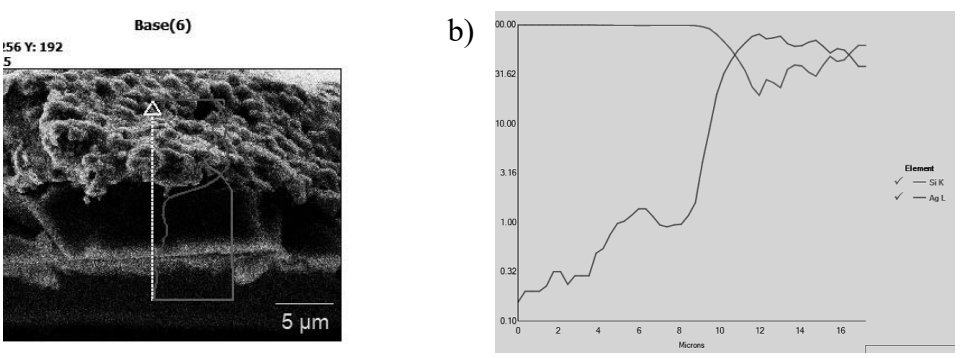

Figure 3. SEM micrograph (a) and line profile of energy-dispersive X-ray spectroscopy (EDS) spectrum (b) of the cross-section of an Ag contact metallization deposited by the screen-printing method.

Electrical characterization of the metallized contacts was performed using the ShereScan system before and after climatic chamber testing. The obtained results are presented in Figure 4. Prior to climatic aging, the sheet resistance of the metal contacts was equal to 1.279 mΩ/sq, while the specific resistivity reached 1.919 μΩ·cm. These values indicate very good electrical conductivity of the screen-printed Ag metallization and are close to the resistivity of bulk silver, confirming efficient sintering and good electrical continuity between Ag particles. After climatic chamber exposure, an increase in both sheet resistance and specific resistivity was observed. The sheet resistance increased to 1.758 mΩ/sq, whereas the specific resistivity reached 2.638 μΩ·cm. The increase in electrical resistance after climatic testing may be associated with thermo-mechanical stresses, microstructural degradation, partial oxidation processes, and the formation of microcracks within the metallic network during cyclic temperature and humidity exposure. Despite the observed degradation, the metallization layer maintained relatively low resistivity values, indicating satisfactory environmental stability of the developed Ag paste composition. The obtained results demonstrate that the applied nano- and microsilver-based paste enables fabrication of conductive and structurally stable contacts using the screen-printing method. Although climatic aging caused a measurable increase in resistive parameters, the electrical properties of the metallization remained within the range acceptable for photovoltaic applications.

a)

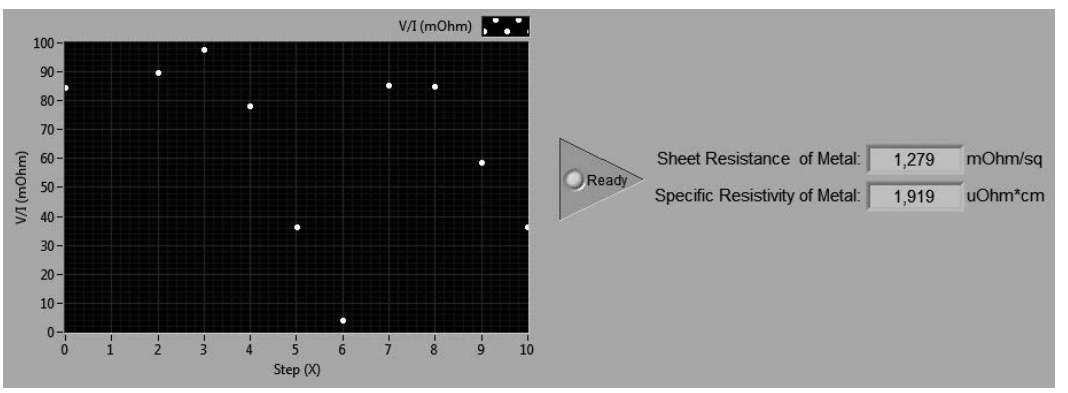

b)

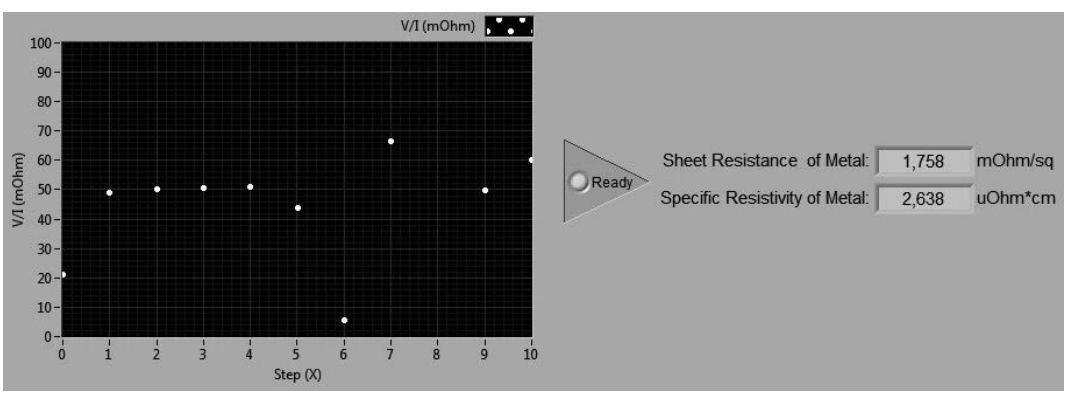

Figure 4. Specific resistivity of the screen-printed Ag metallization measured using the ShereScan system: (a) before climatic chamber testing and (b) after climatic chamber exposure.

4. SUMMARY AND CONCLUSIONS

The conducted investigations confirmed that the developed screen-printable paste based on nano- and microsized silver particles, glass frit, and barium oxide enables the fabrication of conductive and structurally stable metallization contacts for silicon photovoltaic applications. The screen-printing process followed by thermal firing in a tunnel belt furnace resulted in the formation of homogeneous Ag conductive paths with good adhesion to the silicon substrate and a relatively low level of structural defects.

SEM cross-sectional observations demonstrated a typical morphology of properly fired screen-printed contacts, characterized by a continuous metallic structure and good interfacial connection between the Ag layer and the silicon substrate. EDS analysis confirmed the presence and uniform distribution of the principal elements within the metallization region, while the EDS line profile indicated a stable Ag/Si interface without significant discontinuities or excessive elemental diffusion.

Electrical characterization performed using the ShereScan system revealed very low resistive parameters before climatic aging, with a sheet resistance of 1.279 mΩ/sq and a specific resistivity of 1.919 μΩ·cm. These values are close to the resistivity of bulk silver, indicating efficient sintering of the silver particles and high electrical quality of the fabricated contacts.

After climatic chamber exposure under variable temperature and humidity conditions, an increase in both sheet resistance and specific resistivity was observed, reaching 1.758 mΩ/sq and 2.638 μΩ·cm, respectively. The increase in resistance is most likely associated with thermo-mechanical stresses, local microstructural degradation, and partial deterioration of conductive pathways occurring during cyclic environmental loading. Nevertheless, the metallization maintained relatively low resistive values after aging, confirming satisfactory environmental stability and durability of the developed contact system.

The obtained results demonstrate that the proposed Ag paste composition and technological process provide a promising approach for the fabrication of low-resistance screen-printed metallization suitable for silicon solar cell applications operating under realistic environmental conditions.

BIBLIOGRAPHY

1. J. M. Kopania, *Techniczno-organizacyjne aspekty inżynierii produkcji*, Wydział Zarządzania i Inżynierii Produkcji, 2018.
2. M. Ziółko, *Utylizacja i recykling ogniw fotowoltaicznych*, „Inżynieria Środowiska – Młodym Okiem”, t. 17, Politechnika Białostocka, 2015.
3. P. Ostrowski, *Procesy termiczne i chemiczne w recyklingu ogniw i modułów fotowoltaicznych z krystalicznego krzemu*, Rozprawa doktorska, Politechnika Gdańska, Gdańsk, 2010.
4. P. Panek, K. Drabczyk, *Technologie wytwarzania krzemowych ogniw słonecznych*, Wydawnictwo Instytutu Metalurgii i Inżynierii Materiałowej PAN, Kraków, 2014.
5. M. Musztyfaga-Staszuk, *Nowe kompozyty na bazie miedzi w zastosowaniu do wytwarzania krzemowych ogniw fotowoltaicznych*, Wydawnictwo Politechniki Śląskiej, Gliwice, 2019.
6. S. Werle, J. Ferdyn-Grygierek, *Ochrona klimatu i środowiska. Nowoczesna energetyka. Wybrana problematyka*, Wydawnictwo Politechniki Śląskiej, Gliwice, 2024.

7. A. Mroziński, *Recykling ogniw fotowoltaicznych*, Inżynieria i Aparatura Chemiczna, nr 5, 2010.
8. E. Klugmann-Radziemska, P. Ostrowski, A. Cenian, M. Sawczak, *Chemical, Thermal and Laser Processes in Recycling of Photovoltaic Silicon Solar Cells and Modules*, Ecological Chemistry and Engineering S, vol. 17, no. 3, 2010.
9. A. Kuczyńska-Łażewska, E. Klugmann-Radziemska, *Kluczowe zagadnienia procesu recyklingu zużytych modułów fotowoltaicznych I i II generacji*, Zeszyty Naukowe Instytutu Gospodarki Surowcami Mineralnymi PAN, 2018.
10. J. Lach, *Recykling paneli fotowoltaicznych*, Chemia Przemysłowa, nr 1, 2023.
11. M. Niekurzak, A. Brelik, W. Lewicki, *Economic Potential of Recovery and Recycling of Silicone Photovoltaics Cells and Non-Ferrous Metals as Part of the Transition Towards a Circular Economy*, Economics and Environment, vol. 86, no. 3, 2023.
12. H. A. Cheema, S. Ilyas, H. Kang, H. Kim, *Comprehensive Review of the Global Trends and Future Perspectives for Recycling of Decommissioned Photovoltaic Panels*, Waste Management, vol. 174, 2024.

7th-9th June 2026
Gliwice-Brenna, Poland
DEPARTMENT OF ENGINEERING MATERIALS AND BIOMATERIALS
FACULTY OF MECHANICAL ENGINEERING
SILESIAN UNIVERSITY OF TECHNOLOGY
INTERNATIONAL STUDENTS SCIENTIFIC CONFERENCE

Understanding Primary and Secondary Aluminium Alloys: Production, Microstructure, and Properties

Zuzana Straková[a], Eva Tillová, Lenka Kuchariková, Milan Uhríčik, Mária Chalupová

[a] University of Žilina, Faculty of Mechanical Engineering, Department of Materials Engineering
email: zuzana.strakova@fstroj.uniza.sk

Abstract: Aluminium alloys are among the most widely used materials due to their excellent mechanical properties. Increasing global demand for lightweight and sustainable materials has led to continuous development of production technologies for both primary and secondary aluminium alloys. The article provides an overview of the production routes, microstructure, and properties of primary and secondary aluminium production. Primary aluminium alloys are produced from bauxite ore through the Bayer and Hall-Héroult processes, with predictable chemical compositions and therefore predictable and consistent mechanical properties. Secondary aluminium alloys are produced by recycling and remelting aluminium scrap, significantly reducing the energy consumption, but with a less predictable chemical composition. Special attention is given to the challenges associated with secondary aluminium production, including impurity accumulation, porosity and the formation of Fe-rich intermetallic phases. This article also highlights the importance of aluminium recycling and, therefore, supports sustainable manufacturing and the circular economy.

Keywords: aluminium, primary production, secondary production, automotive, recycling

1. INTRODUCTION

Aluminium and its alloys are among the most widely used engineering materials due to their good corrosion resistance, high strength and excellent recyclability. These properties make aluminium alloys highly suitable for applications in the automotive, aerospace, and packaging industries. In these industries, lightweight materials and energy efficiency are becoming increasingly important. Over the recent years and decades, the global demand for aluminium has grown significantly. That led not only to increased primary aluminium production but also to an expansion of secondary aluminium recycling [1,2].

Primary aluminium alloys are produced from bauxite ore through the Bayer and Hall-Héroult processes. These processes require large amounts of energy, but they provide high-purity aluminium, with predictable properties and well-controlled chemical composition. In comparison, secondary aluminium alloys are produced via a process that includes recycling and remelting aluminium scrap. Since aluminium recycling requires only a fraction of the energy

needed for primary production, it makes secondary alloys environmentally and economically attractive. As a result, recycled aluminium is becoming a crucial part of the circular economy and sustainable manufacturing techniques [2,3].

Despite the environmental advantages, the production of secondary aluminium alloys poses several metallurgical difficulties. These issues arise from the mixing of materials sourced from various products like beverage cans, engine blocks, and electrical components, leading to impurity accumulation and reduced quality in the recycled Al. The recycling process often introduces impurities (Fe, Si, Cu and Zn), leading to the formation of intermetallic phases, thus reducing the mechanical properties of the final product. Understanding the relationship between production methods, microstructure, and final properties is essential for producing a higher-quality alloy and, therefore, expanding the use of recycled aluminium in demanding automotive applications [3,4].

The production processes for primary and secondary aluminium alloys are given in this article, along with a discussion of the key differences in their microstructure and characteristics. The difficulties in recycling processes and their effect on secondary aluminium alloys' performance are given special consideration.

2. PRIMARY ALUMINIUM PRODUCTION

Primary aluminium production begins with the extraction of bauxite, the main raw material that is used for aluminium production. Bauxite is primarily extracted using open-pit mining. The majority of bauxite comes from laterite-type deposits located at or near the surface, which are mined with heavy machinery. The principal aluminium hydroxide minerals found in varying proportions within bauxite are gibbsite (trihydrated) and boehmite and diaspore (both monohydrated). The aluminium oxide content is around 30 – 60%. After mining, the ore is crushed, washed and prepared for further processing [4-6].

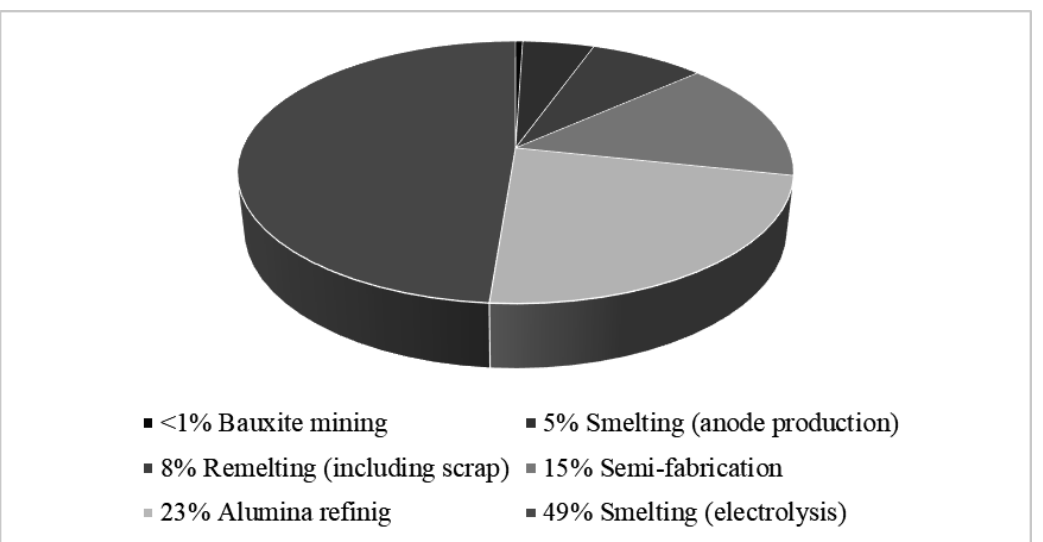

Figure 1. Global aluminium industry energy use required to produce primary aluminium by stage, 2013 [7]

Primary aluminium production involves two independent energy-intensive processes to transform the ore into the metal – the Bayer process and the Hall-Héroult process. In the Bayer

process, bauxite is treated at high temperatures, with sodium hydroxide solution under pressure (dissolving the aluminium-containing compounds and separating them from impurities – Fe oxides, silica). The solution is then cooled off, and aluminium hydroxide precipitates. This is followed by calcination, and finally, the anhydrous alumina (Al_2O_3 free of water) is produced. Aluminia has a very high melting point, above 2050 °C, and is a chemically very stable compound. These are the reasons for the large amount of energy needed to produce aluminium from alumina [5,6].

The alumina is converted to aluminium through the Hall-Héroult process. Alumina is dissolved in molten cryolite and is then subjected to electrolysis in large reduction cells. A strong electric current is passed through the electrolyte, causing aluminium ions to be reduced to molten aluminium at the cathode, while oxygen reacts with carbon anodes to form carbon dioxide. The alumina content in the electrolyte is usually maintained within the limited range of 2 to 3 wt. % Al_2O_3. Higher alumina content may lead to excessive amounts of undissolved alumina sludge collecting underneath the metal pad [8,9].

2.1 Alloy Production

Alloying elements are added to the molten pure aluminium to improve its properties, since it is relatively soft and has limited strength. The most commonly used elements are silicon, copper, magnesium, and zinc. Silicon improves castability, magnesium enhances strength and corrosion resistance, copper increases hardness, and zinc is used for aluminium alloys used in the aerospace industry [10].

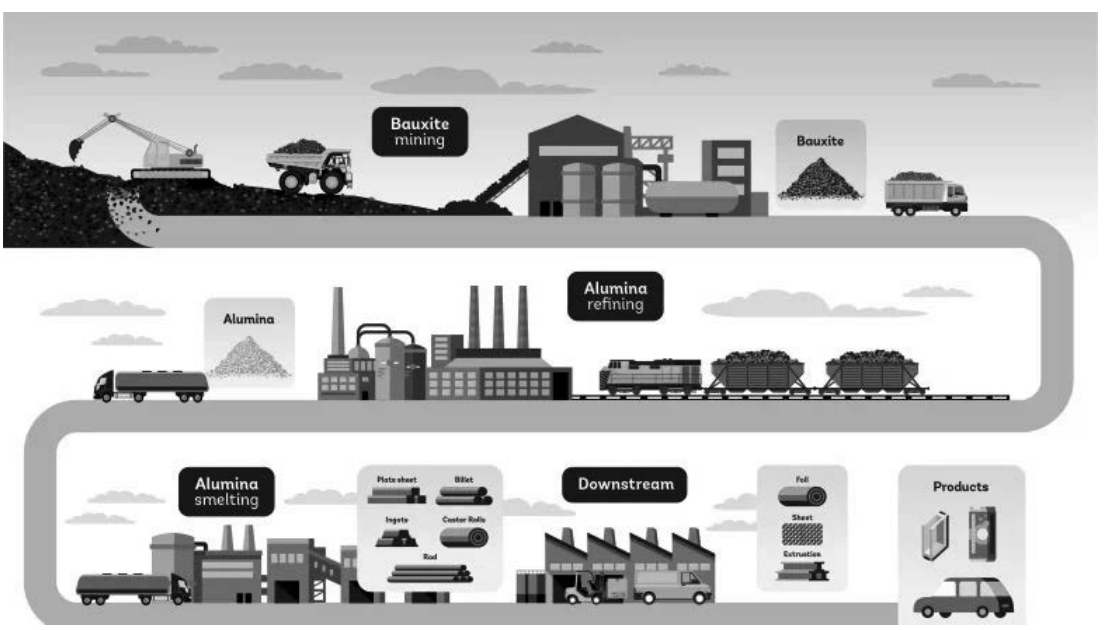

Figure 2. Primary aluminium production process [11]

The molten aluminium is then cast into semi-finished products – ingots, blooms, billets and slabs, using various casting techniques. After that, they are divided into those used for wrought alloys and cast alloys. Wrought alloys are used mostly for shaping processes such as extrusion, forging, and rolling. They are both heat-treatable and non-heat-treatable; they represent about 85% of all aluminium alloys. Cast aluminium alloys are manufactured by pouring molten metal into moulds, filling them, and subsequently solidifying. They can be divided into heat-treatable

and non-heat-treatable cast aluminium alloys; they have a comparatively low tensile strength but help create cost-efficient products [12].

2.2 Advantages and Challenges

Primary aluminium alloys offer several important advantages. Because they are produced from high-purity aluminium under carefully controlled conditions, they have low impurity content and controlled chemical composition. Therefore, the manufacturers can easily predict the microstructure and achieve the desired mechanical properties, which is essential in the automotive and aerospace industries [13].

However, primary aluminium production is associated with several environmental and economic challenges. Primary production is one of the most energy-intensive metallurgical processes due to the large amount of electrical energy required by the Hall-Héroult process. Furthermore, the use of carbon anodes during electrolysis results in significant CO_2 emissions, which adds to the environmental issues associated with greenhouse gas production. In comparison to secondary aluminium obtained through recycling, production costs are higher due to the high energy requirements and intricate processing pathways [9,13].

3. SECONDARY ALUMINIUM PRODUCTION

Secondary aluminium is produced from secondary raw materials, specifically from old and new scrap. Aluminium is considered highly sustainable for recycling because it can be repeatedly recycled without a significant loss of its fundamental properties. This, combined with the growing need to reduce emissions and the costs associated with manufacturing new products, makes aluminium an essential part of the modern metallurgical industry. Compared to primary aluminium production, recycling requires only 5% of the energy required to produce new aluminium, reducing carbon emissions. [6,14].

3.1 Alloy Production

The recycling process begins with the collection and sorting of aluminium scrap. The scrap materials come from waste generated during the production of aluminium products, such as cans, machining chips, used beverage cans, automotive components, construction materials, or end-of-life products. The sorting process is especially important because aluminium scrap often contains impurities that can negatively affect the quality of the recycled alloy. Depending on the type of scrap and the desired product quality, different types of furnaces for melting aluminium scrap are used. Scrap for the production of casting alloys is commonly melted in rotary furnaces under a layer of liquid melting salt. Producers of wrought alloys prefer open-hearth furnaces in varying designs (aluminium alloys) [3,9,14].

Secondary aluminium alloys can be cast into castings or further mechanically processed into wrought products. Thanks to its advantageous combination of low density, acceptable mechanical properties, and reduced environmental impact, recycled aluminium is widely used in the automotive and construction industries [6,15].

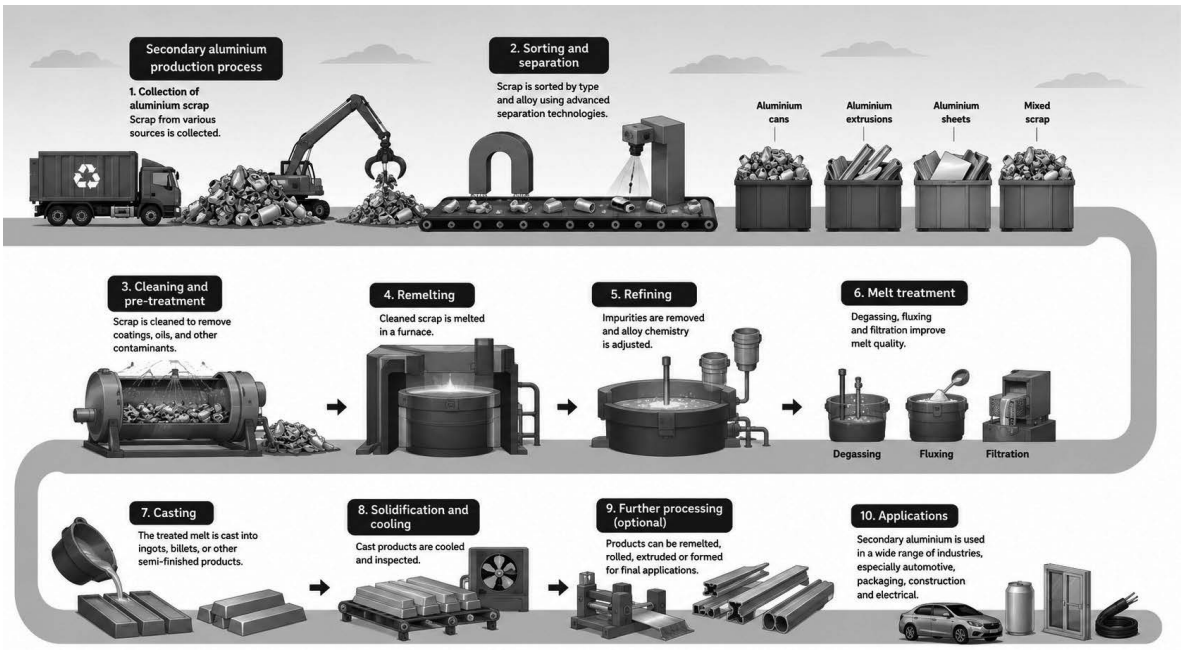

Figure 3 Secondary aluminium production process [16 – OpenAI]

3.2 Advantages and Challenges

Although secondary aluminium alloys offer many benefits, their production also presents many challenges. The most significant of these is iron contamination, which enters the alloys from aluminium scrap or during the casting process. Iron is very difficult to remove during remelting. Excessive iron content promotes the formation of brittle intermetallic phases, which negatively impact ductility, fatigue and corrosion resistance [17].

The presence of oxide inclusions is another significant issue. Aluminium readily interacts with oxygen during handling and remelting, forming oxide films on the melt surface. These oxide layers could become trapped in the molten metal, causing internal flaws (bifilms) in the finished casting. During service, oxide inclusions can lower mechanical strength and start crack formation [17].

The inconsistency of scrap composition further complicates the production of secondary alloys. Recycled scrap often contains mixtures of various aluminium alloys, coatings, lubricants, and impurities, making it difficult to precisely control the composition.

4. MICROSTRUCTURE OF PRIMARY AND SECONDARY ALUMINIUM ALLOYS

Aluminium alloys' microstructure plays a crucial role in determining their mechanical properties. Fatigue and corrosion resistance, strength, ductility and other properties are influenced by grain size, the number and distribution of intermetallic phases and porosity in these alloys. Since primary and secondary aluminium alloys are produced differently, their microstructure differs [15].

4.1 Microstructure of Primary Aluminium Alloys

These alloys are obtained by the Bayer and the Hall-Héroult processes, which means their chemical composition is controlled, and they have lower impurity levels. Therefore, these alloys have a cleaner microstructure, with a lower concentration of impurities such as iron, copper or silicon [3].

Intermetallic phases are generally smaller, better distributed and therefore less detrimental to the mechanical performance. Strengthening precipitates like Mg_2Si or Al_2Cu can be purposefully created through heat treatment to increase hardness and strength, depending on the alloy system. Improved ductility, fatigue resistance, and structural dependability are all facilitated by the relatively low levels of oxide inclusions and porosity [15,18].

4.2 Microstructure of Secondary Aluminium Alloys

Due to the presence of impurities, secondary aluminium alloys exhibit a more heterogeneous microstructure in comparison to the primary alloys. Scrap contamination and variable chemical composition contribute to the formation of intermetallic phases and increased porosity. Iron contamination is difficult to eliminate, and therefore, it leads to the formation of brittle Fe-rich intermetallic phases. These phases include β-Al_5FeSi and α-Al(Fe,Mn)Si. The β-Al_5FeSi phase usually forms platelet-like phases acting as stress-concentrators. In contrast, α-Al(Fe,Mn)Si phases have a more compact ”Chinese script” morphology and are considered less harmful to mechanical properties. This is due to the manganese addition, which is often used to mitigate the negative effects of iron [10].

5. FUTURE PERSPECTIVES

In recent years, sustainability has become one of the most important factors when developing new aluminium products. Due to its high recyclability, aluminium is considered a key material in the transition toward a circular economy. Meaning that the materials can be reused continuously, minimising waste and without losing their fundamental properties, which makes them highly sustainable for long-term use [8].

The aluminium recycling plays a crucial role in reducing the environmental impact of material production. Secondary aluminium production requires only about 5% of the energy needed for primary production, reducing the energy consumption and greenhouse gas emissions. Since these alloys are made from aluminium scrap, the need for bauxite mining is also lower. However, only a limited amount of aluminium scrap is used in the production of secondary aluminium, as waste sorting is not 100% accurate, and significant adjustments to the chemical composition are required [8,19].

At the same time, modern techniques used in sorting, refining and melt treatment methods continue to enhance the quality of recycled aluminium. Advanced sorting technologies, including laser-induced breakdown spectroscopy (LIBS) or X-ray sorting, allow for more precise identification and separation of aluminium scrap. Modern refining methods include advanced filtration systems, improved degassing, and even the optimisation of the fluxing process. This leads to a reduction in the amount of oxide inclusions, porosity and other defects in the final material [19].

The automotive sector is among the fastest-growing areas for the use of secondary aluminium. Manufacturers increasingly incorporate recycled aluminium into engine parts, wheels, and structural components to lower vehicle weight, enhance fuel efficiency, and reduce

environmental impact. As regulations tighten and the demand for sustainable materials rises, secondary aluminium alloys are set to become even more important. Future research in aluminium production is likely to focus on advancing recycling technologies, managing impurity levels, and creating new alloy systems tailored for efficient recycling. These developments will help close the performance gap between primary and secondary aluminium alloys and advance sustainable materials engineering [20].

CONCLUSION

Low density, high corrosion resistance, and favourable mechanical properties make primary and secondary aluminium alloys vital components in contemporary engineering applications. However, due to their production processes and raw materials sources, these two material groups differ significantly from one another. High-purity aluminium obtained by the Bayer and Hall-Héroult processes is used to make primary aluminium alloys, which enable precise control of chemical composition and generate cleaner microstructures and more predictable mechanical properties. Primary alloys are especially well-suited for demanding applications in the automotive and aerospace sectors because of these qualities. On the other hand, because secondary aluminium alloys are manufactured using recycling techniques that utilise significantly less energy than primary production, they provide significant economic and environmental advantages.

Recycling aluminium is essential for lowering greenhouse gas emissions and promoting the shift to a circular economy. However, secondary alloys generally contain more impurities, oxide inclusions, and Fe-rich intermetallic phases, which can detrimentally affect the material's final microstructure and mechanical properties. One of the most crucial elements of aluminium production is the connection between material attributes, microstructure, and processing conditions. The performance and dependability of aluminium alloys are ultimately determined by factors such as impurity levels, melt treatment, and solidification conditions, which significantly impact grain structure, porosity, and intermetallic phase development.

Therefore, it is crucial to understand these interactions to improve the production of both main and secondary alloys. Future advancements in aluminium production need to focus on developing alloy systems that are more suitable for environmentally friendly production, enhanced sorting and refining techniques, and sophisticated recycling technology.

Secondary aluminium alloys are anticipated to acquire greater quality and broader applicability in high-performance engineering industries as recycling methods continue to advance. Therefore, the development of sustainable aluminium production will be essential to the future of ecologically conscious materials engineering.

ACKNOWLEDGEMENT

The Ministry of Education, Research, Development and Youth of the Slovak Republic supported the research by projects VEGA 1/0461/24, VEGA 1/0729/26 and KEGA no. 033ŽU-4/2026 and KEGA no. 039ŽU-4/2026.

BIBLIOGRAPHY

1. Primary and Secondary Aluminum, Clinton Aluminum,https://clintonaluminum.com/ primary -and-secondary-aluminum/, 2021.

2. Primary Aluminium Production, UK Aluminium Industry Fact Sheet 17, https://alfed.org.uk/files/Fact%20sheets/17-aluminium-primary-production.pdf.
3. H.R. Kotadia, N. Bareker, M.H. Khan, J.I. Ahuir-Torres, A. Das, Aluminium recycling: A critical review of iron-bearing intermetallics in aluminium alloys, Materials Today Sustainability 30 (2025) 1-33.
4. H. Kvande, Production of primary aluminium, Fundamentals of Aluminium Metallurgy (2011) 46-69.
5. S. H. Patterson, H. F. Kurtz, J. C. Olson, C. L. Neeley, World Bauxite Resources, United States Government Printing Office, Washington, 1986.
6. H. G. Schwarz, Aluminum Production and Energy, Encyclopedia of Energy, (2004) 81-95.
7. M. Stacey, Aluminium Recyclability and Recycling – Towards Sustainable Cities, Cwningen Press 2015.
8. A. T. Tabereaux, R. D. Peterson, Aluminium Production, Treatise on Process Metallurgy, Vol. 3 (2014) 839-917.
9. Primary Aluminum: Inert Anode and Wettable Cathode Technology in Aluminum Electrolysis, Light Metal Age, https://www.lightmetalage.com/resources/patents/primary-aluminum-inert-anode-and-wettable-cathode-technology-in-aluminum-electrolysis/, (2020).
10. Z. Straková, E. Tillová, L. Kuchariková, M. Mikolajčík, The Study of Porosity in A356 Secondary Aluminium Alloys with Higher Iron Content, System Safety Human - Technical Facility – Environment, 6 (2025) 430-438.
11. Competitiveness of Global Aluminum Supply Chains Under Carbon Pricing Scenarios for Solar PV, World Bank Group, https://www.worldbank.org/en/topic/extractiveindustries/publication/competitiveness-of-global-aluminum-supply-chains-under-carbon-pricing-scenarios-for-solar-pv, (2023).
12. Differences Between Cast and Wrought Aluminum Alloys, Howard, https://www.howardprecision.com/differences-between-cast-and-wrought-aluminum-alloys/, (2020).
13. B. Zeng, Ch. Chen, H. Zhao, C. Zhang, P. Liu, G.Wang, A. He, F. Liu, A systematic review of the production of high-purity aluminum: Applications, preparation, and mechanisms, Journal of Materials Research and Technology 34 (2025) 987-1009.
14. Infinitely Recyclable, The Aluminium Assotiation, https://www.aluminum.org/Recycling, (2025).
15. H. Nunes, O. Emadinia, R. Soares, M. F. Vieira, A. Reis. Adding Value to Secondary Aluminum Casting Alloys: A Review on Trends and Achievements, Materials 16(3) 895 (2023).
16. OpenAI, ChatGPT Image – Secondary Aluminium Production Process, Available at: https://chatgpt.com.
17. X. Cao, J. Campbell, Oxide inclusion defects in Al-Si-Mg cast alloys, Canadian Metallurgical Quarterly 44 (2005) 435-448.
18. M. Baruah, A. Borah, Processing and Precipitation Strengthening of 6xxx Series Aluminium Alloys: A Review, International Journal of Materials Science1 (2020) 40-48.
19. Advanced sorting technologies drive innovation in aluminum recycling, Waste Management World, https://waste-management-world.com/recycling/advanced-sorting-technologies-drive-innovation-in-aluminum-recycling/ (2025).
20. A. Nocivin, C. Tudor, C. Illie, D. Raducanu, L. V. Melnic, Recycled Versus Primary Aluminum in European Automotive Industry: Trends, Challenges, and Opportunities, Recycling 11 (2026).

TalentDetector

7th-9th June 2026
Gliwice-Brenna, Poland

DEPARTMENT OF ENGINEERING MATERIALS AND BIOMATERIALS
FACULTY OF MECHANICAL ENGINEERING
SILESIAN UNIVERSITY OF TECHNOLOGY

INTERNATIONAL STUDENTS SCIENTIFIC CONFERENCE

Surface modification of materials manufactured by SLM for implantology

Kamil Szewczulak[a], Marek Machura[a], Wojciech Hytry[a], Zofia Kozak[a], Magdalena Szindler[b], Mariusz Król[b], Marek Szindler [c], Wojciech Sitek[c], Lovro Liverić[d] Marko Kršulja[d]

[a] Student of the Silesian University of Technology
[b] Silesian University of Technology, Faculty of Mechanical Engineering, Department of Engineering Materials and Biomaterials
[c] Silesian University of Technology, Faculty of Mechanical Engineering, Didactic Laboratory of Nanotechnology and Material Technologies, Gliwice, Poland
[d] Faculty of Engineering, Juraj Dobrila University of Pula, Negrijeva 6, 52100 Pula, Croatia
email: magdalena.szindler@polsl.pl

Abstract: ZnO/TiO_2 oxide coatings were deposited on SLM-manufactured CoCr (Mediloy) alloy using the Atomic Layer Deposition (ALD) technique in order to improve the corrosion resistance of biomaterial surfaces. The surface morphology and chemical composition of the coatings were investigated using stereoscopic microscopy, SEM, and EDS analysis. Microscopic observations revealed a uniform and continuous coating covering the rough surface characteristic of additively manufactured materials, while EDS analysis confirmed the presence of Zn, Ti, and O originating from the deposited oxide layers. Corrosion resistance was evaluated by potentiodynamic polarization tests performed in Ringer's solution at 37 °C. The coated samples exhibited a significant decrease in corrosion current density and an increase in polarization resistance compared with the uncoated alloy, indicating improved electrochemical stability under simulated physiological conditions.

Keywords: Atomic Layer Deposition (ALD); CoCr alloy; corrosion resistance

1. INTRODUCTION

Modern dental implantology focuses on the development of materials with high mechanical durability, full biocompatibility, and safety of use in the patient's body [1]. Among metallic materials, cobalt–chromium alloys are particularly important, as they have been widely used in prosthetics and maxillofacial surgery for many years due to their favorable strength and wear resistance properties [1,2].

The development of modern manufacturing technologies has led to the gradual replacement of conventional casting methods with additive techniques. One of the most advanced methods in this group is selective laser melting (SLM), which enables the production of components by layer-by-layer melting of metal powder using a laser beam [3,4].

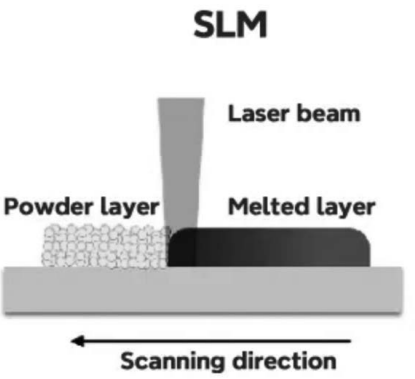

Figure 1. Schematic of the Selective Laser Melting Process

This technology enables the creation of structures with high geometric complexity and individual adaptation to the patient's anatomical conditions. Despite its numerous advantages, the selective laser melting process is associated with specific physical phenomena resulting from local temperature gradients and the material's solidification kinetics. As a result, a characteristic microstructure is formed, along with discontinuities in the form of micropores and increased surface roughness [3,4]. From the point of view of biomedical applications, this is a significant limitation, as the surface properties of the material play a key role in its interaction with the biological environment. The oral cavity environment is characterized by high chemical aggressiveness and variable operating conditions. Implants are exposed to variable environmental conditions, the presence of electrolytes containing chloride ions, as well as cyclic mechanical and thermal loads [2,5]. Under such conditions, the presence of micropores and surface irregularities promotes the initiation of localized corrosion processes [5]. The increased active surface area and structural heterogeneity can lead to intensified electrochemical interactions. The development of corrosion processes on the surface of the implant is undesirable, as it may result in the release of metal ions into the surrounding tissues [6]. This phenomenon is clinically significant because it can lead to inflammatory and allergic reactions, as well as other adverse biological effects. Therefore, limiting these processes remains a significant challenge from both a materials engineering and medical perspective.

One of the effective ways to improve the operational properties of additively manufactured materials is the application of advanced surface engineering techniques. Of particular importance is the atomic layer deposition (ALD) method, which enables the controlled deposition of thin coatings with high uniformity. This process allows for the formation of oxide coatings, such as aluminum oxide, which are characterized by high impermeability and bioinertness [7, 8, 9, 10]. Thanks to the ability to uniformly cover geometrically complex surfaces, it is possible to effectively protect the material from the effects of the biological environment. The resulting coating acts as a protective barrier, limiting corrosion processes and reducing the release of alloy components into the surrounding tissue [6,9].

2. MATERIALS AND METHODOLOGY

SLM-manufactured CoCr (Mediloy) alloy samples were coated using the atomic layer deposition (ALD) technique in an R200 reactor. The coating process consisted of 500 cycles of ZnO deposition followed by 100 cycles of TiO_2 deposition. Diethylzinc (DEZ) was used as the

zinc precursor for ZnO deposition, while titanium tetrachloride ($TiCl_4$) was applied as the titanium precursor for TiO_2 deposition. In both processes, deionized water served as the oxygen-reactive precursor.

The surface morphology and macroscopic quality of the coatings were initially evaluated using a Leica stereoscopic microscope. Detailed microstructural observations were subsequently performed using a Supra 35 scanning electron microscope (SEM, Zeiss) operating in InLens mode. Additionally, elemental composition analysis was carried out using an energy-dispersive X-ray spectroscopy (EDS) detector integrated with the SEM system.

To evaluate the corrosion resistance of SLM-manufactured Mediloy (Co–Cr–Mo alloy) samples, both uncoated and coated with ALD ZnO/TiO_2 layers, electrochemical tests were performed in Ringer's solution (NaCl—8.6 g/L; KCl—0.3 g/L; $CaCl_2 \cdot 6H_2O$—0.48 g/L) at 37 ± 1 °C and pH 7.0 ± 0.2. Measurements were carried out using an Autolab PGSTAT302N potentiostat in a three-electrode system, with the sample as the working electrode, a saturated calomel electrode (SCE) as the reference electrode, and platinum wire as the counter electrode. Prior to polarization measurements, the open-circuit potential (EOCP) was monitored for 3600 s. Potentiodynamic polarization curves were then recorded from −300 mV vs. EOCP to +1000 mV vs. SCE at a scan rate of 1 mV/s. Additional scans within ±250 mV vs. EOCP were used for Tafel analysis. Corrosion potential (Ecorr), corrosion current density (icorr), polarization resistance (Rp), and passive current density (ipass) were determined from the obtained curves.

3. RESULTS AND DISCUSSION

Figure 2 presents stereoscopic microscope images of the CoCr samples fabricated by Selective Laser Melting before and after ALD coating deposition. The uncoated sample (Figure 2a) exhibited a characteristic rough and heterogeneous surface morphology typical of SLM-manufactured materials. Numerous partially melted powder particles and irregular surface features resulting from the layer-by-layer manufacturing process were observed. After deposition of the ZnO/TiO_2 coating (Figure 2b), the surface appeared more homogeneous and uniform. The coating covered the substrate continuously without visible macroscopic defects such as cracks or delamination. Additionally, a slight change in surface coloration was observed, indicating successful deposition of the oxide layers on the CoCr substrate.

SEM micrographs presented in Figure 3 revealed characteristic differences between the uncoated and coated CoCr surfaces. The uncoated sample (Figure 3a) showed an irregular surface morphology with visible surface asperities, unmelted or partially melted particles, and local microstructural heterogeneities associated with the SLM process. In contrast, the ZnO/TiO_2-coated sample (Figure 3b) exhibited a more compact and uniform surface morphology. The ALD coating effectively covered the substrate, reducing the visibility of sharp surface irregularities. Single surface agglomerates or particles were locally observed; however, no significant coating discontinuities or cracks were detected, confirming good coating conformity and surface coverage. The EDS spectrum of the uncoated sample (Figure 3c) confirmed the presence of the main alloying elements characteristic of CoCr alloys, including cobalt (Co), chromium (Cr), molybdenum (Mo), tungsten (W), and silicon (Si). The dominant chromium and cobalt peaks corresponded to the chemical composition of the Mediloy alloy. After deposition of the ZnO/TiO_2 coating (Figure 3d), additional peaks corresponding to zinc (Zn), titanium (Ti), and oxygen (O) were registered, confirming successful formation of the oxide coating on the CoCr substrate. Simultaneously, the intensity

of the substrate-related peaks decreased due to attenuation of the electron signal by the deposited coating layers. The EDS results confirmed the presence and continuity of the ZnO/TiO_2 coating deposited by the ALD process.

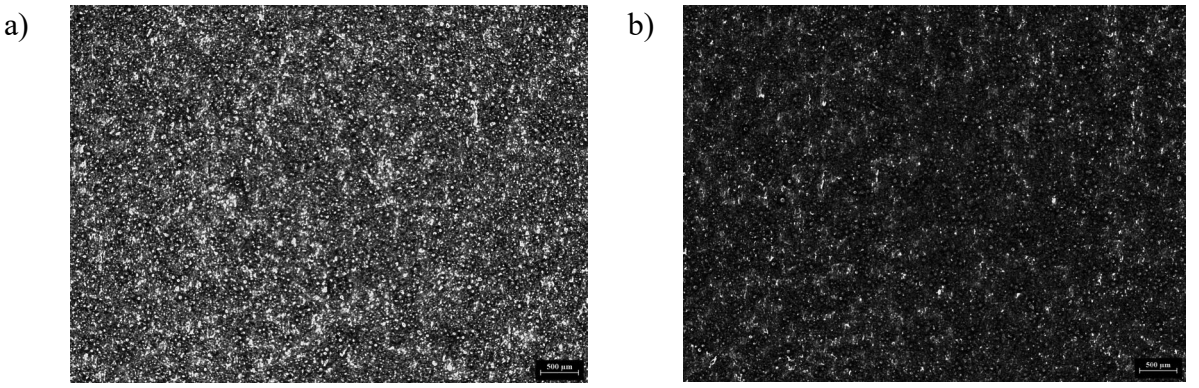

Figure 2. Stereoscopic microscope images of the CoCr sample fabricated by Selective Laser Melting: (a) uncoated surface and (b) surface coated with ZnO/TiO_2 by Atomic Layer Deposition.

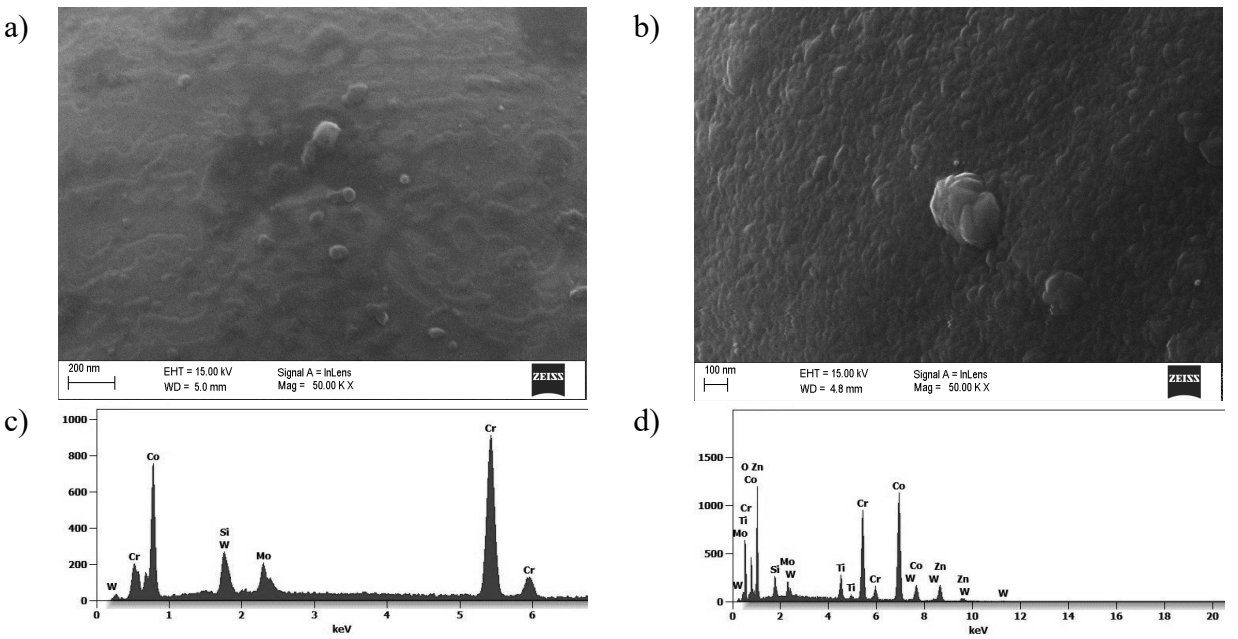

Figure 3. SEM images of the CoCr sample fabricated by Selective Laser Melting: (a) uncoated surface, (b) surface coated with ZnO/TiO_2 by Atomic Layer Deposition, (c) EDS analysis of the uncoated sample, and (d) EDS analysis of the coated sample.

The results of potentiodynamic polarization measurements are summarized in Table 1. The uncoated CoCr SLM sample exhibited the lowest corrosion resistance, characterized by a relatively negative open-circuit potential (−612 mV vs. SCE) and corrosion potential (−548 mV vs. SCE). In addition, the sample showed the highest corrosion current density (8.92 $\mu A/cm^2$) and the lowest polarization resistance (5.8 $k\Omega \cdot cm^2$), indicating intensified electrochemical activity in Ringer's solution. The application of the 500 nm ZnO / 1000 nm TiO_2 coating significantly improved the electrochemical performance of the alloy. A positive shift in both EOCP and Ecorr values was observed, reaching −384 mV and −352 mV vs. SCE,

respectively. Simultaneously, the corrosion current density decreased to 0.58 μA/cm², while the polarization resistance increased to 74.6 kΩ·cm². The obtained results indicate that the ALD ZnO/TiO_2 coating effectively enhanced the corrosion resistance of the SLM CoCr alloy by limiting electrolyte access to the substrate surface and reducing the rate of electrochemical corrosion processes.

Table 1. Results of potentiodynamic polarization measurements conducted in Ringer's solution at 37 °C after 60 min stabilization of the working electrode

Sample	Open-Circuit Potential EOCP [mV vs. SCE]	Corrosion Potential Ecorr [mV vs. SCE]	Ba [mV/dec]	Bc [mV/dec]	Corrosion Current Density icorr [μA/cm²]	Polarization Resistance Rp [kΩ·cm²]
CoCr SLM (uncoated)	−612	−548	126	94	8.92	5.8
CoCr SLM + 500 nm ZnO / 1000 nm TiO_2	−384	−352	168	116	0.58	74.6

4. SUMMARY AND CONCLUSIONS

The conducted study demonstrated that the application of ALD ZnO/TiO_2 coatings significantly improved the surface properties and corrosion resistance of SLM-manufactured CoCr (Mediloy) alloy. Microscopic observations confirmed that the deposited coating uniformly covered the complex and irregular surface morphology characteristic of additively manufactured materials. SEM analysis revealed improved surface homogeneity and good coating continuity, while EDS measurements verified the presence of Zn, Ti, and O, confirming successful formation of the oxide layers on the CoCr substrate. Electrochemical investigations performed in Ringer's solution showed a considerable enhancement of corrosion resistance after coating deposition. The coated samples exhibited a positive shift in open-circuit and corrosion potentials, a substantial decrease in corrosion current density, and a significant increase in polarization resistance compared with the uncoated alloy. These results indicate improved electrochemical stability and effective limitation of electrolyte penetration to the substrate surface. Overall, the obtained findings confirm that the ALD process enables the fabrication of uniform and protective ZnO/TiO_2 coatings on SLM-manufactured CoCr alloys. The applied oxide layers effectively reduced the intensity of electrochemical corrosion processes under simulated physiological conditions, suggesting that ALD coatings may represent a promising strategy for improving the durability and long-term performance of CoCr biomaterials intended for biomedical and dental applications.

BIBLIOGRAPHY

1. Dobrzański, L. A., i in. (2014). Structure and properties of Co-Cr-Mo alloy manufactured by selective laser melting. "Archives of Materials Science and Engineering", vol. 65, nr 2, s. 53-59. Wydawnictwo Politechniki Śląskiej, Gliwice.
2. Walke, W., i in. (2015). Electrochemical corrosion resistance of Co-Cr-Mo alloy. "Journal of Achievements in Materials and Manufacturing Engineering", vol. 73, nr 2, s. 142-149. Wydawnictwo International OCSCO World Press, Gliwice.
3. Arias, S. L., i in. (2016). Corrosion resistance and ion release of ALD-coated CoCrMo alloys in simulated physiological fluids. "Materials Science and Engineering: C", vol. 62, s. 251-260.
4. Dobrzańska-Danikiewicz, A. D., i in. (2015). Atomic layer deposition of thin oxide coatings onto the metallic substrates. "Archives of Materials Science and Engineering", vol. 72, nr 1, s. 28-35. Wydawnictwo Politechniki Śląskiej, Gliwice.
5. George, S. M. (2010). Atomic Layer Deposition: An Overview. "Chemical Reviews", vol. 110, nr 1, s. 111-131.
6. Plocek, J., i in. (2021). Atomic layer deposition of Al2O3 and TiO2 on Co-Cr-Mo alloys for biomedical applications. "Surface and Coatings Technology", vol. 422, art. 127532.
7. Vladescu, A., i in. (2016). Ariel View on ALD Coatings for Biomedical Applications. "Coatings", vol. 6, nr 4, art. 45.
8. Staszuk, M., Pakuła, D., Reimann, Ł., Król, M., Basiaga, M., Mysłek, D., & Kříž, A. (2020). Structure and Properties of ZnO Coatings Obtained by Atomic Layer Deposition (ALD) Method on a Cr-Ni-Mo Steel Substrate Type. *Materials*, vol. 13, nr 19, art. 4223. MDPI.
9. Łosiewicz, B., Osak, P., & Górka-Kulikowska, K. (2023). Electrophoretic Deposition of Multi-Walled Carbon Nanotube Coatings on CoCrMo Alloy for Biomedical Applications. Micromachines, vol. 14, nr 11, art. 2122. MDPI

TalentDetector

7th-9th June 2026
Gliwice-Brenna, Poland

DEPARTMENT OF ENGINEERING MATERIALS AND BIOMATERIALS
FACULTY OF MECHANICAL ENGINEERING
SILESIAN UNIVERSITY OF TECHNOLOGY

INTERNATIONAL STUDENTS SCIENTIFIC CONFERENCE

An Example of Applying a Genetic Algorithm for the Identification of Steel Chemical Composition with Required Phase Transformation Temperatures

JacekTrzaska[a], Sabina Lesz[a], Dominika Gajczowska[b]

[a] Silesian University of Technology, Faculty of Mechanical Engineering, Department of Engineering Materials and Biomaterials
[b] Student of Silesian University of Technology, Faculty of Mechanical Engineering
email: jacek.trzaska@polsl.pl

Abstract: This paper presents an example of implementing a genetic algorithm for the identification of steel chemical composition corresponding to a required martensite start temperature (Ms). The study demonstrates the use of the Python programming language, the PyGAD library, and the Google Colaboratory environment for solving an engineering optimization problem. In the presented example, the chemical composition of steel was treated as a set of optimization variables, while the required Ms temperature was adopted as the optimization criterion. The results confirm the usefulness of Python-based tools for the implementation of evolutionary optimization methods in materials engineering applications.

Keywords: materials engineering, steel chemical composition, genetic algorithm

1. INTRODUCTION

Optimization methods are increasingly used in engineering problems related to materials design, process parameter selection, and numerical modeling. In many practical cases, classical optimization techniques are difficult to apply due to nonlinear relationships between variables, the presence of multiple local optima, or the lack of analytical models. For such problems, evolutionary algorithms, including genetic algorithms (GAs), provide an effective alternative. Genetic algorithms are optimization methods inspired by biological evolution processes such as selection, crossover, and mutation. Their main advantage is the ability to search complex solution spaces without requiring derivatives of the objective function.

One of the important parameters considered in steel heat treatment is the martensite start temperature (Ms), which defines the temperature at which the martensitic transformation begins during cooling from the austenitizing temperature. The value of Ms strongly influences the final microstructure and properties of steel after quenching. Carbon and most alloying elements decrease the Ms temperature, which may increase the risk of cracking and promote retained austenite formation after heat treatment. Consequently, the prediction and control of the Ms temperature are important issues in materials engineering and in the selection of heat treatment conditions.

The rapid development of Python-based computational tools has significantly simplified the implementation of optimization algorithms in engineering applications. Python is widely used in scientific and technical computing due to its readability, extensive ecosystem of libraries, and ease of integration with numerical and data analysis tools. One of the libraries dedicated to evolutionary optimization is PyGAD (Python Genetic Algorithm Development), which enables relatively simple implementation of genetic algorithms for solving optimization problems [1]. The library provides built-in mechanisms for population generation, fitness evaluation, selection, crossover, and mutation operations, allowing users to focus mainly on defining the optimization problem itself. An additional advantage of modern Python tools is the possibility of using cloud-based computational environments such as Google Colaboratory (Google Colab). Google Colab enables execution of Python code directly in a web browser without the need for local software installation or configuration. The platform supports interactive notebooks combining executable code, text descriptions, equations, and graphical outputs in a single environment, making it particularly useful for educational and research purposes.

The aim of this paper is to present an example of implementing a genetic algorithm in the Google Colaboratory environment using the PyGAD library. As an illustrative engineering problem, the identification of steel chemical composition corresponding to a required martensite start temperature was selected. The presented example demonstrates the practical use of Python-based optimization tools in materials engineering applications.

2. GENETIC ALGORITHM

Genetic algorithms belong to a group of optimization methods inspired by processes occurring in nature. Their operation is based on an analogy to biological evolution mechanisms such as natural selection, crossover, and mutation. During successive iterations of the algorithm, new populations of solutions are generated and gradually evolve toward solutions that better satisfy the adopted optimization criteria [2]. As a result, genetic algorithms enable the search for near-optimal solutions even for complex, nonlinear, or difficult optimization problems that are challenging to solve using classical methods.

The basic element of a genetic algorithm is a population, which represents a set of potential solutions analyzed simultaneously. Each solution is represented by an individual corresponding to a single point in the search space. Information describing a solution is stored in the form of a chromosome composed of genes. Individual genes correspond to specific problem parameters, such as numerical values, coefficients, or selected solution variants. Depending on the nature of the problem, a chromosome may be represented as a binary string, a vector of integers, or a vector of real numbers. In practical engineering applications, direct real-valued encoding is often preferred because it simplifies the representation of technological or material parameters.

The operation of the algorithm begins with the generation of an initial population. In most cases, the population is created randomly in order to ensure a high diversity of solutions at the beginning of the optimization process. Next, a fitness function is evaluated for each individual. The fitness function determines the quality of a given solution and serves as the main criterion for assessing its suitability for the considered optimization problem.

The next stage is selection, in which individuals are chosen to participate in the creation of the next generation. The purpose of selection is to increase the proportion of better solutions while maintaining an appropriate level of population diversity. In practice, various selection methods are used, including proportional (roulette wheel) selection and tournament selection. In

roulette wheel selection, the probability of selecting an individual is proportional to its fitness value, meaning that better solutions have a higher chance of passing their features to the next generation. Tournament selection, on the other hand, involves randomly choosing a small group of individuals and selecting the best one among them. This method is simple to implement and widely used in practice due to its stability and efficiency.

After selection, the crossover operation is performed. Its purpose is to create new solutions by combining information from two parent individuals. In the simplest case, crossover consists of exchanging fragments of chromosomes between parents. As a result, offspring may inherit beneficial features from both solutions, increasing the probability of discovering improved parameter combinations.

Another important component of the algorithm is mutation, which introduces random modifications into offspring chromosomes. The main role of mutation is to maintain population diversity and enable exploration of new regions of the search space. Mutation prevents the population from converging too quickly toward a single solution, which could lead to premature convergence to a local optimum. However, the mutation probability must be chosen carefully, since an excessively high mutation rate may turn the optimization process into a largely random search.

After the application of selection, crossover, and mutation operators, a new population is created. The evolutionary process is repeated until a termination condition is satisfied. This condition may correspond to reaching a maximum number of iterations, observing no further improvement in solution quality, or obtaining a fitness value that satisfies user-defined requirements. Many implementations additionally employ elitism, which preserves the best individuals in subsequent generations to prevent the loss of high-quality solutions due to random modifications.

Genetic algorithms possess several advantages that make them widely applicable in optimization problems. They do not require knowledge of derivatives of the objective function and can therefore be applied to nonlinear, discontinuous, and multidimensional problems. They are also effective in problems characterized by numerous local optima. However, their limitations include relatively high computational cost and sensitivity to the proper selection of algorithm parameters such as population size, crossover probability, and mutation probability. Despite these limitations, genetic algorithms remain effective and versatile tools for solving optimization problems in many areas of science and engineering.

2. EXAMPLE OF GENETIC ALGORITHM IMPLEMENTATION

In the presented example, the optimization problem consists in identifying the chemical composition of steel for which the martensite start temperature reaches a required target value. The optimization procedure was implemented in Python using the PyGAD library and executed in the Google Colaboratory environment. In this approach, the concentrations of selected alloying elements were treated as decision variables of the genetic algorithm, while the objective function was formulated on the basis of the difference between the calculated and target Ms temperatures.

The martensite start temperature was calculated using the empirical relationship given by:

$$M_s = 541 - 401 \cdot C - 36 \cdot Mn - 10{,}5 \cdot Si - 14 \cdot Cr - 18 \cdot Ni - 17 \cdot Mo$$

where the alloying element concentrations are expressed in mass percent. The applied equation was adopted from the literature [3, 4]. The relationship may be used within the range of chemical compositions presented in Table 1.

Table 1 Ranges of mass concentrations of elements (wt.%)

	C	Mn	Si	Cr	Ni	Mo
Minimum	0.10	0.28	0.13	0	0	0
Maximum	0.68	1.98	1.90	2.50	3.85	1.05

The optimization task considered in this study does not have a unique solution. Different combinations of alloying element concentrations may lead to the same or very similar Ms temperature values within the assumed range of variables. Consequently, repeated executions of the genetic algorithm may produce different solutions while still satisfying the optimization criterion. Furthermore, modifying the allowable concentration ranges or changing the genetic algorithm parameters may also lead to different optimized chemical compositions. This behavior is characteristic of evolutionary optimization methods applied to multidimensional engineering problems.

```
# PyGAD library installation
!pip install pygad

# Import required libraries
import pygad
import numpy as np
import pandas as pd
import matplotlib.pyplot as plt

# Target martensite start temperature
MS_TARGET = 400

# Chemical elements considered in the optimization process
# A single individual in the population represents the steel chemical composition:
# [C, Mn, Si, Ni, Cr, Mo]
elements = ["C", "Mn", "Si", "Ni", "Cr", "Mo"]

# Search ranges for the mass concentration of individual alloying elements [wt.%]
bounds = {
    "C":  (0.10, 0.68),
    "Mn": (0.28, 1.98),
    "Si": (0.13, 1.90),
    "Ni": (0.00, 3.85),
    "Cr": (0.00, 2.50),
    "Mo": (0.00, 1.05),
}
# Lower and upper bounds of decision variables
lower_bounds = np.array([bounds[e][0] for e in elements])
upper_bounds = np.array([bounds[e][1] for e in elements])

# Function for calculating the martensite start temperature
def calculate_ms(solution):
```

```
    """
    Calculates the martensite start temperature Ms [°C].
    Parameters:
        solution: individual of the genetic algorithm,
                  containing the mass concentrations of elements:
                  [C, Mn, Si, Ni, Cr, Mo]
    Returns:
        Ms temperature in °C
    """
    C, Mn, Si, Ni, Cr, Mo = solution

    Ms = 541 - 401*C - 36*Mn - 10.5*Si - 14*Cr - 18*Ni - 17*Mo
    return Ms
```

Fitness function

```
def fitness_func(ga_instance, solution, solution_idx):
    """
    Evaluates the quality of an individual.
    PyGAD maximizes the fitness function. In this problem, the objective
    is to minimize the absolute difference between the calculated Ms
    temperature and the target value.
    The fitness value is therefore defined as:
        fitness = 1 / (1 + error)
    where:
        error = |Ms - MS_TARGET|
    """
    Ms = calculate_ms(solution)
    error = abs(Ms - MS_TARGET)

    fitness = 1.0 / (1.0 + error)
    return fitness
```

Definition of the gene space.
Each gene corresponds to one alloying element and has its own allowed range.

```
gene_space = [
    {"low": bounds["C"][0],  "high": bounds["C"][1]},
    {"low": bounds["Mn"][0], "high": bounds["Mn"][1]},
    {"low": bounds["Si"][0], "high": bounds["Si"][1]},
    {"low": bounds["Ni"][0], "high": bounds["Ni"][1]},
    {"low": bounds["Cr"][0], "high": bounds["Cr"][1]},
    {"low": bounds["Mo"][0], "high": bounds["Mo"][1]},
]
```

List used to store the best error value in each generation

```
best_history = []
```

Progress monitoring function

```
def on_generation(ga_instance):
    """
    Function called automatically after each generation.
    It stores the current best error value and prints the calculation
    progress every 10 generations.
    """
    solution, solution_fitness, solution_idx = ga_instance.best_solution()
```

```
    Ms = calculate_ms(solution)
    error = abs(Ms - MS_TARGET)
    best_history.append(error)

    if ga_instance.generations_completed % 10 == 0:
        print(
            f"Generation {ga_instance.generations_completed:3d} | "
            f"Ms = {Ms:.4f} °C | "
            f"Error = {error:.6f} °C | "
            f"Fitness = {solution_fitness:.6f}"
        )
```

```
# Genetic algorithm configuration
ga_instance = pygad.GA(
    num_generations=100,    # number of generations
    sol_per_pop=100,        # number of individuals in the population
    num_genes=6,            # number of genes: C, Mn, Si, Ni, Cr, Mo

    gene_space=gene_space,       # constraints for gene values
    fitness_func=fitness_func,   # fitness function
    num_parents_mating=50, # number of parents selected for crossover

    parent_selection_type="tournament",  # tournament selection
    K_tournament=3,                       # tournament size

    crossover_type="single_point",   # single-point crossover
    mutation_type="random",          # random mutation
    mutation_percent_genes=30, #percentage of genes selected for mutation
    on_generation=on_generation # callback after each generation
)

# Run the genetic algorithm
ga_instance.run()

# Read the best solution found by the algorithm
solution, solution_fitness, solution_idx = ga_instance.best_solution()

best_ms = calculate_ms(solution)
best_error = abs(best_ms - MS_TARGET)

# Prepare results in tabular form
result = pd.DataFrame({
    "Element": elements,
    "Concentration [wt.%]": solution
})

# Format the concentration values
result["Concentration [wt.%]"] = result["Concentration [wt.%]"].apply(lambda
x: f"{x:.2f}")

# Display the obtained chemical composition
print("Chemical composition of steel:")
display(result)
print(f"Calculated Ms temperature = {best_ms:.1f} °C")
print(f"Error = {best_error:.1f} °C")
```

```
print(f"Fitness value = {solution_fitness:.2f}")
```

Chemical composition of steel:

	Element	Concentration [wt.%]
0	C	0.12
1	Mn	0.85
2	Si	0.40
3	Ni	1.87
4	Cr	0.91
5	Mo	0.64

Calculated Ms temperature = 400.0 °C
Error = 0.0 °C
Fitness value = 1.00

Figure 1. Example solution obtained by the genetic algorithm

```
# Plot the convergence of the genetic algorithm
plt.figure(figsize=(8, 5))
plt.plot(best_history)
plt.xlabel("Generation", fontsize=12)
plt.ylabel(f"Error |Ms - {MS_TARGET}| [°C]", fontsize=14)
plt.title("Genetic Algorithm Convergence", fontsize=16)
plt.tick_params(axis="both", which="major", labelsize=12)
plt.grid(True)
plt.show()
```

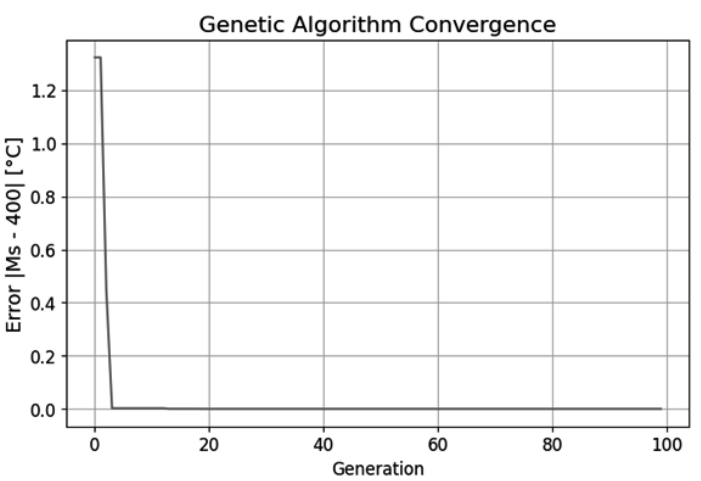

Figure 2. Optimization error as a function of generation number

3. SUMMARY

The presented example demonstrates that genetic algorithms can be effectively implemented using Python-based computational tools for solving engineering optimization problems related to materials science. The combination of the PyGAD library and the Google Colaboratory environment enables relatively simple development and execution of evolutionary optimization

procedures, while the process of code creation and modification can be effectively supported by modern AI-assisted programming tools.

A deliberately simple and basic implementation of the genetic algorithm was presented in order to emphasize the accessibility and educational value of the proposed approach. The developed example may be easily adapted to other optimization tasks by modifying selected elements of the code, such as the objective (fitness) function, the set of decision variables, the allowable ranges of variables, or the genetic algorithm parameters including population size, mutation rate, and selection method.

The performed calculations confirmed that the applied genetic algorithm was capable of identifying steel chemical compositions corresponding to the required martensite start temperature. At the same time, the study showed that the optimization problem may possess multiple acceptable solutions, which is characteristic of multidimensional optimization tasks. Consequently, repeated executions of the algorithm or modifications of optimization constraints may lead to different solutions while still satisfying the assumed optimization criterion. The presented implementation may therefore serve both as an educational example of genetic algorithm programming in Python and as a starting point for developing more advanced optimization procedures in materials engineering and related fields.

BIBLIOGRAPHY

1. A. F. Gad, "PyGAD Documentation," Read the Docs. [Online]. Available: https://pygad.readthedocs.io/en/latest/. [Accessed: May 11, 2026].
2. D. E. Goldberg, Genetic Algorithms in Search, Optimization and Machine Learning, 1st ed. Boston, MA, USA: Addison-Wesley Longman Publishing Co., 1989.
3. J. Trzaska, Prediction Methodology for the Anisothermal Phase Transformation Curves of the Structural and Engineering Steels. Gliwice, Poland: Silesian University of Technology Press, 2017 (in Polish).
4. J. Trzaska, "Empirical formulas for calculating Continuous Cooling Transformation diagrams," Journal of Achievements in Materials and Manufacturing Engineering, vol. 97, no. 1, pp. 21–30, 2019, doi: 10.5604/01.3001.0013.7946.

TalentDetector
7th-9th June 2026
Gliwice-Brenna, Poland
DEPARTMENT OF ENGINEERING MATERIALS AND BIOMATERIALS
FACULTY OF MECHANICAL ENGINEERING
SILESIAN UNIVERSITY OF TECHNOLOGY
INTERNATIONAL STUDENTS SCIENTIFIC CONFERENCE

Optymalizacja procesów recyklingu odpadów poprodukcyjnych technologii druku 3D na przykładzie materiału PLA

Klaudia Twardzik[a], Dominika Zajdel[b], Natalia Nowrot[c]

[abc] Studenci kierunku Innowacyjne Technologie w Przemysle., Wydział Mechaniczny Technologiczny, Politechnika Śląska

Streszczenie: Niniejsza analiza dotyczy procesu recyklingu materiału „polilaktyd" (PLA), jako materiału powszechnie stosowanego w procesach technologii druku 3D.

Słowa kluczowe: polilaktyd, PLA, druk 3D, recykling, polimery, biodegradacja

1. WPROWADZENIE

Procesy wykorzystujące druk 3D pozostawiają znaczną ilość odpadów. Odpady te generowane są głównie w postaci nieudanych wydruków, struktur wsporczych oraz pozostałości po procesach kalibracji. Nie spełniają one żadnych funkcji oraz nie posiadają zastosowań w innych procesach wytwórczych. Jedyną opcją ich ponownego zastosowania w druku 3D jest ich przetopienie i dostosowanie do formatu filamentu.

W niniejszej pracy skupiono się na porównaniu parametrów pierwotnego materiału oraz materiału poddanego procesowi recyklingu, na przykładzie materiału PLA, jako materiału najczęściej stosowanego w druku 3D. Porównano zasadność ponownego przetwórstwa materiału, z możliwością jego naturalnej biodegradacji.

2. CHARAKTERYSTYKA MATERIAŁU

Polilaktyd (PLA) jest tworzywem termoplastycznym i biodegradowalnym. Od wielu lat jest wykorzystywany nie tylko w druku 3D, lecz także jako materiał wytwórczy w wielu dziedzinach przemysłu. Jest on poliestrem alifatycznym o dużej przezroczystości i połysku. Barwa zależy od barwników dodanych w procesach produkcyjnych. Cechuje się łatwością formowania z wykorzystaniem typowych urządzeń przetwórczych stosowanych dla klasycznych tworzyw sztucznych.

Możemy wyróżnić dwie charakterystyczne metody powstawania polilaktydu: polimeryzację kondensacyjną zwaną również polikondensacją oraz polimeryzację w trakcie której następuje otwarcie pierścienia laktydu. Pierwsza z nich jest procesem stopniowym, zachodzi na skutek reakcji grup funkcyjnych które znajdują się w monomerach, ponadto polikondenscaji towarzyszy powstanie małocząsteczkowego produktu ubocznego, którym może być np. woda,

kwas solny czy amoniak. Jednakże efektywniejszą metodą jest druga z podanych, w wyniku której następuje otwarcie pierścienia laktydu. Związek ten jest cyklicznym dimerem kwasu mlekowego, który powstaje w efekcie fermentacji wielu różnorodnych węglowodanów, takich jak skrobia czy celuloza.

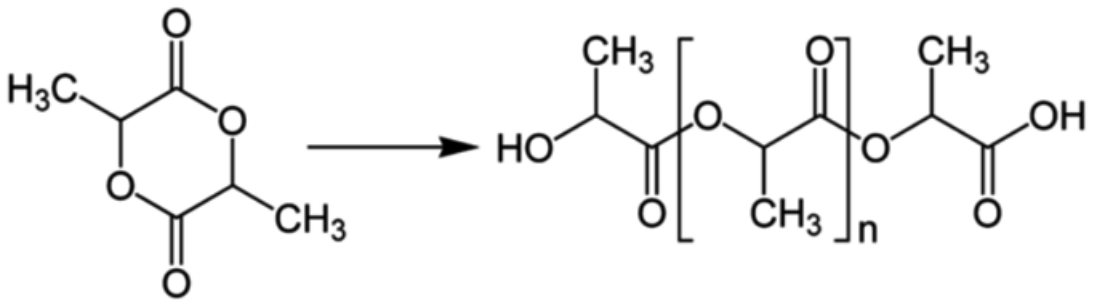

Rysunek 1. Polimeryzacja PLA poprzez otwarcie pierścienia laktydu.

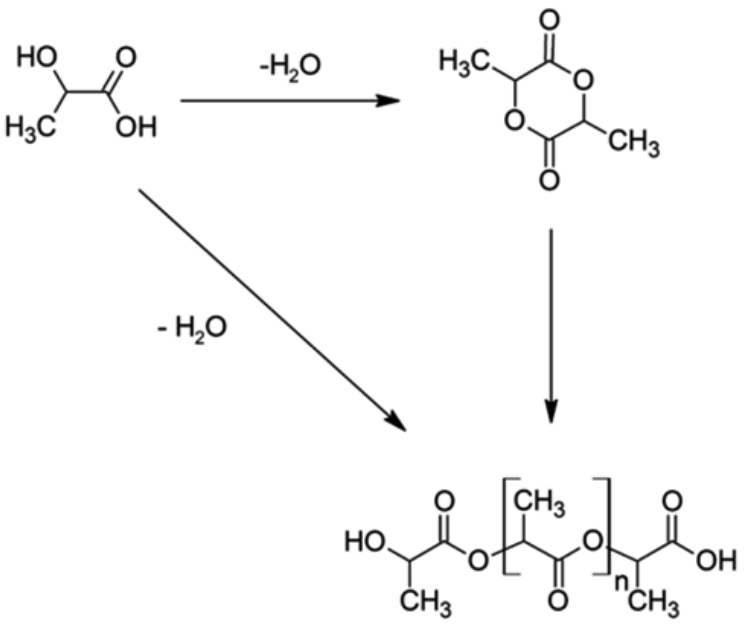

Rysunek 2. Polikondensacja kwasu mlekowego

2.1. Własności materiału PLA

Tabela 1. Specyfikacja polilaktydu

Gęstość	1,0-1,5 g/cm³
Temperatura topnienia	140-210 °C
Moduł Younga	2534±85 MPa
Wytrzymałość na rozciąganie	48±5 Mpa
Wytrzymałość udarowa Izod (X-Y)	22±2 kJ/m²
Wydłużenie przy zerwaniu	8±1%
Moduł zginania	3360±100 MPa

PLA cechuje się dobrą wytrzymałością na rozciąganie, sztywnością oraz niską udarnością i ograniczoną elastycznością, co czyni go mniej wytrzymałym od innych materiałów. Jest on natomiast tworzywem łatwym w obróbce, dzięki stosunkowo niskiej temperaturze topnienia. Dzięki temu jest on dobrze przystosowany do projektów, w których liczy się estetyka lub prędkość produkcji.

2.2. Proces wytwarzania polilaktydu w formie cienkiej żyłki

Proces formowania polilaktydu w postać filamentu (żyłki o precyzyjnie określonej średnicy) opiera się na technologii wytłaczania jednoślimakowego. Proces dzieli się na kilka kluczowych etapów, od których zależą późniejsze właściwości reologiczne materiału:

1. Przygotowanie poprzez suszenie surowca
Ze względu na wysoką higroskopijność PLA, granulat przed przetwórstwem musi zostać poddany osuszaniu. Wilgoć zamknięta w polimerze podczas wytłaczania mogłaby prowadzić do hydrolizy łańcuchów polimerowych oraz powstawania pęcherzyków gazu wewnątrz żyłki, co drastycznie obniża jej jakość.

2. Plastyfikacja w wytłaczarce
Granulat trafia do układu plastyfikującego, gdzie pod wpływem ciepła dostarczanego przez grzałki oraz tarcia generowanego przez obracający się ślimak, przechodzi w stan wysokolepkiej cieczy. Proces zachodzi w temperaturch w przedziale od 180 do 210°C.

3. Formowanie
Stopiony polimer jest przetłaczany przez dyszę formującą o przekroju kołowym. Zaraz po opuszczeniu dyszy, gorąca żyłka trafia do układu chłodzenia kąpielą wodną lub powietrzem.

4. Stabilizacja wymiarów
Żyłka trafia do systemu odciągu, który poprzez regulację prędkości obrotowej pozwala na precyzyjne wyciągnięcie żyłki do pożądanej średnicy, z tolerancją nieprzekraczającą 0,05 mm.

5. Nawijanie
Gotowy produkt jest nawijany na szpule. Na tym etapie można stosować laserowe czujniki średnicy, które w czasie rzeczywistym monitorują jakość produktu.

2.3. Proces biodegradacji

Polilaktyd jest najłatwiej degradowany przez mikroorganizmy produkujące enzymy, a także enzymy innego pochodzenia. Degradacja materiału zachodzi podczas procesu hydrolizy poprzez działanie substancji z grupy hydrolaz serynowych, zawierających aktywne centrum w postaci triady katalitycznej (Ser-His-Asp). PLA degraduje najlepiej w środowisku kompostu, co wynika z obecności większej różnorodności enzymów oraz mikroorganizmów. Obecność wody przyspiesza proces hydrolizy oraz zwiększa przyczepność enzymów i mikroorganizmów do materiału. Temperatura wyższa niż pokojowa sprzyja zmianom w mikrostrukturze polimeru oraz znacznie przyspiesza zachodzenie procesu rozkładu.

3. ANALIZA PROCESU RECYKLIGU

Proces recyklingu rozpoczyna się pozyskaniem odpadów poprodukcyjnych, a następnie ich oczyszczeniem oraz wysuszeniem. Pozbawiony zanieczyszczeń i suchy materiał jest rozdrabniany do formy granulatu. Gotowy regranulat może zostać wykorzystany w procesach produkcyjnych jako samodzielny materiał, a także jako dodatek do granulatu, który nie został jeszcze poddany żadnej obróbce.

4. ANALIZA WŁASNOŚCI PO PROCESIE PRZETWÓRSTWA WTÓRNEGO

Wielokrotne przetwarzanie materiału biodegradowalnego jakim jest polilaktyd skutkuje niewielkim pogorszeniem właściwości wytrzymałościowych, w stosunku do stanu pierwotnego. Największe zmiany zachodzą podczas pierwszego procesu. Następne próby przetwarzania nie skutkują już znacznymi ubytkami we własnościach materiału. Przy wielokrotnym przetwarzaniu polilaktydu znacznemu pogorszeniu ulegają jedynie jego właściwości reologiczne. Nie zachodzą zmiany we właściwościach cieplnych – temperatura zeszklenia i topnienia są wartościami stałymi. Zalecane jest przetwarzanie materiału maksymalnie 3-krotnie, ponieważ taka obróbka nie wpływa w sposób istotny na jego podstawowe właściwości mechaniczne oraz cieplne. Materiał traci wtedy głównie wartości wizualne – staje się coraz ciemniejszy.

4.1. Wykorzystanie i właściwości wyrobów wytworzonych z udziałem recyklatu

Właściwości użytkowe elementów wydrukowanych z materiału pochodzącego z recyklingu są bezpośrednią wypadkową zmian zachodzących w strukturze molekularnej polimeru. Zastosowanie domieszki regranulatu na poziomie do 10-25% pozwala na zachowanie niemal pełnej wytrzymałości pierwotnej materiału. Pomimo niewielkiego spadku właściwości mechanicznych regranulat w pełni nadaje się do produkcji:
1. prototypów i modeli,
2. oprzyrządowania warsztatowego,
3. produktów hobbistycznych niespecjalistycznych.

5. WNIOSKI

Recykling materiałowy może być stosowany w przypadku PLA, gdyż pogorszenie jego właściwości wytrzymałościowych jest nieznaczne i nie wyklucza jego zastosowania w procesach wytwórczych niektórych wyrobów. Trzykrotne przetwarzanie PLA nie wpływa w sposób istotny na jego podstawowe właściwości mechaniczne oraz cieplne, a mieszaniny zawierające do 10% regranulatu wykazują zbliżone właściwości do surowca pierwotnego. Możliwość biodegradacji materiału nie wyklucza zasadności ponownego jego wykorzystania. Oba procesy mogą być wykorzystane w zależności od potrzeb użytkownika. Recykling daje jednak możliwość wykorzystania materiału już wytworzonego, co minimalizuje koszty materiałów potrzebnych do wytworzenia produktu, a także zmniejsza liczbę generowanych odpadów i potrzebę ich utylizacji.

LITERATURA

1. epodreczniki.open.agh.edu.pl, Podstawy chemii polimerów, 2021
2. W. Frącz, Przetwórstwo tworzyw polimerowych, 2016.
3. Z. Florjańczyk, S. Penczak, Chemia polimerów tom I, 2001.
4. G. W. Ehrenstein, Ż. Brocha-Krzemińska, Materiały Polimerowe, 2016
5. A. Żmihorska-Gotfryd, Wybrane zagadnienia biologicznej degradacji polimerów, 2015
6. R. Malinowski, S. Richert, Wpływ trzykrotnego przetwarzania polilaktydu na jego właściwości wytrzymałościowe, reologiczne i cieplne, 2010
7. R. Malinowski, D. Łubkowski, Zmiany wybranych właściwości polilaktydu zachodzące pod wpływem jego trzykrotnego przetwarzania, 2012

7th-9th June 2026
Gliwice-Brenna, Poland
DEPARTMENT OF ENGINEERING MATERIALS AND BIOMATERIALS
FACULTY OF MECHANICAL ENGINEERING
SILESIAN UNIVERSITY OF TECHNOLOGY
INTERNATIONAL STUDENTS SCIENTIFIC CONFERENCE

Aplikácia multiaxiálnych únavových kritérií pri hodnotení nízkocyklovej a vysokocyklovej únavy konštrukčných materiálov

Milan Uhríčik[a], Veronika Chvalníková[a], Edita Illichmanová[a], Melisa Šnircová[a], Zuzana Straková[a], Martin Slezák[a], Mirosław Bonek[b]

[a] University of Žilina, Faculty of Mechanical Engineering, Department of Materials Engineering, Žilina, Slovakia
[b] Silesian University of Technology, Faculty of Mechanical Engineering, Department of Engineering Materials and Biomaterials, Gliwice, Poland
email: milan.uhricik@fstroj.uniza.sk, veronika.chvalnikova@fstroj.uniza.sk, edit.illichmanova@fstroj.uniza.sk, melisa.snircova@fstroj.uniza.sk, zuzana.strakova@fstroj.uniza.sk, martin.slezak@fstroj.uniza.sk, peter.palcek@fstroj.uniza.sk

Abstrakt: Článok sa zaoberá problematikou odhadu únavovej životnosti konštrukčných materiálov pri multiaxiálnom cyklickom zaťažení kombinovaným namáhaním ohyb-krut. Hlavným cieľom bolo analyzovať správanie vybraných multiaxiálnych únavových kritérií v oblasti nízkocyklovej a vysokocyklovej únavy a porovnať ich citlivosť pri predikcii počtu cyklov do porušenia. Experimentálna a numerická analýza bola realizovaná na skúšobnej vzorke zo zliatiny hliníka EN AW 2007.T3 (AlCu4PbMg), ktorá patrí medzi často používané konštrukčné materiály v strojárskej praxi vzhľadom na priaznivý pomer pevnosti a hmotnosti.

Kľúčové slová: multiaxiálna únava, únavové kritériá, MKP, Wöhlerova krivka, hliníková zliatina

1. ÚVOD

Únavové porušovanie patrí medzi najvýznamnejšie mechanizmy degradácie konštrukčných materiálov namáhaných cyklickým zaťažením. V technickej praxi sa veľké množstvo strojových súčiastok a konštrukčných prvkov nachádza v podmienkach opakovane sa meniaceho zaťaženia, ktoré môže viesť k postupnému vzniku a šíreniu únavových trhlín až po konečné porušenie materiálu. Charakteristickým znakom únavového poškodenia je skutočnosť, že k porušeniu môže dôjsť aj pri napätiach výrazne nižších, ako je medza pevnosti alebo medza klzu materiálu [1,2].

Proces únavového poškodenia prebieha spravidla v troch základných etapách. V počiatočnej fáze dochádza k iniciácii mikrotrhlín, ktoré vznikajú najmä v miestach koncentrácie napätia, ako sú povrchové nerovnosti, vruby, inklúzie alebo geometrické diskontinuity. Následne dochádza k stabilnému šíreniu trhlín pôsobením cyklického zaťaženia. Poslednou etapou je

nestabilné porušenie pri prekročení kritickej veľkosti trhliny, ktoré vedie k náhlemu lomu súčiastky [1,2].

Z hľadiska veľkosti plastických deformácií sa únava rozdeľuje na nízkocyklovú a vysokocyklovú únavu. Nízkocyklová únava (LCF – Low Cycle Fatigue) je charakteristická výrazným podielom plastických deformácií a typicky sa prejavuje pri nižších počtoch cyklov do porušenia. Naopak vysokocyklová únava (HCF – High Cycle Fatigue) prebieha prevažne v elastickej oblasti materiálu a je charakteristická vysokým počtom cyklov do lomu pri relatívne nízkych amplitúdach napätia [2,3].

Pri jednoduchom jednoosovom zaťažení možno únavové správanie materiálu pomerne spoľahlivo opísať klasickými Wöhlerovými krivkami, ktoré vyjadrujú závislosť amplitúdy napätia od počtu cyklov do porušenia. Reálne prevádzkové podmienky však vo väčšine prípadov predstavujú kombináciu viacerých druhov namáhania, napríklad ťahu, tlaku, ohybu a krutu. Takéto zaťaženie sa označuje ako multiaxiálne cyklické namáhanie a jeho analýza je výrazne komplikovanejšia vzhľadom na vzájomné pôsobenie normálových a šmykových zložiek napätia a deformácie[4].

Významným aspektom multiaxiálnej únavy je aj charakter vzájomného časového priebehu jednotlivých zložiek zaťaženia. Pri proporcionálnom zaťažení dosahujú všetky zložky maxima súčasne, zatiaľ čo pri neproporcionálnom zaťažení vzniká medzi nimi fázový posun. Práve neproporcionálne zaťaženie môže viesť k dodatočnému cyklickému spevňovaniu materiálu a výraznému zníženiu únavovej životnosti[5].

V súčasnosti zohrávajú významnú úlohu pri analýze multiaxiálnej únavy numerické metódy, predovšetkým metóda konečných prvkov (MKP). Kombinácia numerických simulácií s výpočtovými nástrojmi na odhad únavovej životnosti umožňuje efektívne analyzovať zložité napäťovo-deformačné stavy a predikovať správanie konštrukčných komponentov ešte pred ich reálnym nasadením do prevádzky. Takýto prístup významne znižuje náklady na experimentálne testovanie a zároveň umožňuje optimalizáciu návrhu konštrukcií z hľadiska ich životnosti a bezpečnosti[3-5].

2. ÚNAVOVÉ KRITÉRIÁ

Na opis iniciácie a rastu únavových trhlín pri multiaxiálnom namáhaní bolo vyvinutých viacero únavových kritérií. Tieto kritériá sa snažia transformovať zložitý stav napätosti a deformácie do ekvivalentného parametra, ktorý možno porovnať s materiálovými charakteristikami získanými z experimentov [6].

Multiaxiálne únavové kritériá možno rozdeliť do niekoľkých základných skupín, a to kritériá založené na napätí, kritériá založené na deformácii, energetické kritériá a kritériá založené na kritickej rovine. Kritériá kritickej roviny patria medzi najrozšírenejšie prístupy, pretože umožňujú fyzikálnu interpretáciu procesu iniciácie únavovej trhliny na rovine s maximálnym poškodením [7].

2.1. Brown–Millerovo únavové kritérium

Brown–Millerovo kritérium patrí medzi deformačné kritériá kritickej roviny. Vyvinuli ho M. W. Brown a K. J. Miller s cieľom opísať nízkocyklovú multiaxiálnu únavu materiálov, pri ktorej zohrávajú významnú úlohu plastické deformácie. Kritérium predpokladá, že iniciácia

únavovej trhliny je riadená kombináciou amplitúdy šmykovej deformácie a normálovej deformácie pôsobiacej na kritickej rovine [6].

Brown a Miller vychádzali z pozorovania, že únavové trhliny sa často iniciujú na rovinách maximálnej šmykovej deformácie, pričom normálová deformácia ovplyvňuje otváranie trhliny a urýchľuje poškodenie [6].

Únavové kritérium má nasledovný tvar:

$$\frac{\Delta\gamma_{max}}{2} + S \times \Delta\varepsilon_n = A \times \frac{\sigma_f^{'} - 2\sigma_{n,mean}}{E} \times \left(2 \times N_f\right)^b + B \times \varepsilon_f^{'} \times \left(2 \times N_f\right)^c \tag{1}$$

2.2. Fatemi–Socieho únavové kritérium

Fatemi–Socieho kritérium je modifikáciou Brown–Millerovho prístupu. Kritérium vyvinuli A. Fatemi a D. F. Socie s cieľom zohľadniť vplyv normálového napätia na kritickej rovine. Predpokladá sa, že poškodenie je riadené amplitúdou šmykovej deformácie a maximálnym normálovým napätím. Normálové napätie podporuje otváranie mikrotrhlín a urýchľuje rast poškodenia [7].

Únavové kritérium má nasledovný tvar:

$$\frac{\Delta\gamma}{2} \times \left(1 + k \times \frac{\sigma_{n,max}}{\sigma_y}\right) = \frac{\tau_f^{'}}{G} \times \left(2 \times N_f\right)^{b_\gamma} + \gamma_f^{'} \times \left(2 \times N_f\right)^{c_\gamma} \tag{2}$$

2.3. Smith–Watson–Topperovo kritérium (SWT)

Smith–Watson–Topperovo kritérium patrí medzi deformačno-napäťové kritériá. Bolo vyvinuté na zohľadnenie vplyvu stredného normálového napätia na únavovú životnosť. Kritérium predpokladá, že poškodenie závisí od kombinácie maximálneho normálového napätia a amplitúdy normálovej deformácie [8].

Únavové kritérium má nasledovný tvar:

$$\sigma_{n,max} \times \frac{\Delta\varepsilon_1}{2} = \frac{\sigma_f^{'2}}{E} \times \left(2 \times N_f\right)^{2b} + \sigma_f^{'} \times \varepsilon_f^{'} \times \left(2 \times N_f\right)^{b+c} \tag{3}$$

2.4. Liuovo únavové kritérium

Liuovo kritérium patrí medzi energetické kritériá kritickej roviny. Je založené na predpoklade, že únavové poškodenie je riadené hustotou deformačnej energie na kritickej rovine. Model kombinuje normálovú deformačnú energiu a šmykovú deformačnú energiu.

Únavové kritérium má nasledovný tvar [8]:

$$\Delta W^t = 4 \times \sigma_f^{'} \times \varepsilon_f^{'} \times \left(2 \times N_f\right)^{b+c} + \frac{4 \times \sigma_f^{'2}}{E} \times \left(2 \times N_f\right)^{2b} \tag{4}$$

2.5. Goodmanovo únavové kritérium

Goodmanovo kritérium patrí medzi klasické napäťové kritériá. Používa sa na zohľadnenie vplyvu stredného napätia na únavovú pevnosť. Predpokladá lineárny vzťah medzi amplitúdou napätia a stredným napätím [8].

Únavové kritérium má nasledovný tvar:

$$\frac{K_f \times \sigma_{amp}}{S_e} + \frac{\sigma_{mean}}{S_{ut}} = \frac{1}{f_f} \tag{5}$$

2.6. Findleyho únavové kritérium

Findleyho kritérium je jedno z najznámejších kritérií kritickej roviny založených na napätí. Predpokladá, že únavové poškodenie závisí od amplitúdy šmykového napätia a maximálneho normálového napätia. Findley predpokladal, že normálové napätie podporuje rast trhliny vzniknutej v dôsledku šmykového namáhania [8].

Únavové kritérium má nasledovný tvar:

$$\frac{\Delta\tau}{2} + k \times \sigma_n = \tau_f^{'} \times \left(N_f\right)^b \tag{6}$$

2.7. Sinesovo únavové kritérium

Sinesovo kritérium patrí medzi invariantné napäťové kritériá. Je založené na predpoklade, že únavové poškodenie závisí od amplitúdy deviátorického napätia a hydrostatického napätia. Kritérium využíva invarianty tenzora napätia [8].

Únavové kritérium má nasledovný tvar:

$$\frac{\Delta\tau_{oct}}{2} + \alpha \times (3 \times \sigma_h^{mean}) = \tau_f^{'} \times \left(N_f\right)^b \tag{7}$$

2.8. Kritérium minimálnej opísanej elipsy (MCE)

Kritérium minimálnej opísanej elipsy (Minimum Circumscribed Ellipse – MCE) patrí medzi moderné geometrické prístupy k hodnoteniu multiaxiálnej únavy. Základnou myšlienkou je aproximovať priebeh napäťovej alebo deformačnej trajektórie v priestore pomocou minimálnej opísanej elipsy. Tvar, orientácia a rozmery elipsy charakterizujú proporcionalitu namáhania, neproporcionálnosť cyklu a intenzitu multiaxiálneho poškodenia [8].

Pri proporcionálnom namáhaní degeneruje trajektória na priamku. Pri neproporcionálnom namáhaní vznikajú eliptické alebo kruhové trajektórie, ktoré vedú k dodatočnému cyklickému spevneniu materiálu [8].

Únavové kritérium má nasledovný tvar:

$$\tau_a = \sqrt{R_A^2 + R_B^2} \tag{8}$$

Kde γ_f' je koeficient tvárnej únavy v krute; ε_f' je súčiniteľ únavovej ťažnosti; σ_f' je súčiniteľ únavovej pevnosti; σ_h^{mean} je stredné hydrostatické napätie; σ_n je normálové napätie; $\sigma_{n,max}$ je maximálne napätie; $\sigma_{n,mean}$ je stredná hodnota napätia; σ_y je napätie v smere osi y; τ_a je ekvivalentné šmykové napätie; τ_f' je súčiniteľ únavovej pevnosti v šmyku; Δy_{max} je maximálny rozsah šmykového napätia; $\Delta\varepsilon_1$ je rozsah hlavnej deformácie; $\Delta\varepsilon_n$ je rozsah normálovej deformácie; $\Delta\tau/2$ je striedavé napätie v šmyku; $\Delta\tau_{oct}$ je oktaedrické šmykové napätie; ΔW je virtuálna deformačná energia; N_f je počet cyklov do lomu; S_{ut} je medza pevnosti v ťahu; f_f je faktor bezpečnosti; E je modul pružnosti v ťahu; G je modul pružnosti v krute; R_A je hlavná os elipsy; R_B je maximálna vzdialenosť bodu napätia; b je exponent únavovej pevnosti; b_γ je exponent únavovej pevnosti v šmyku; c je exponent únavovej ťažnosti; c_γ je exponent únavovej ťažnosti v šmyku; A, B, S, k, α sú materiálové parametre.

3. EXPERIMENT

Experimentálna časť bola zameraná na numerické modelovanie multiaxiálneho cyklického namáhania skúšobnej vzorky a následný výpočet únavovej životnosti pomocou vybraných multiaxiálnych kritérií poškodenia. Analýza bola realizovaná na skúšobnej tyči zo zliatiny hliníka EN AW 2007.T3 (AlCu4PbMg). Materiál bol zvolený vzhľadom na jeho časté využitie v technickej praxi pri dynamicky namáhaných súčiastkach.

Skúšobná vzorka mala valcovitý tvar so zúženým prierezom v strednej časti, pričom práve táto geometrická diskontinuita predstavovala potenciálnu oblasť zvýšenej koncentrácie napätia a iniciácie únavového poškodenia. Geometria vzorky bola následne implementovaná do programu ANSYS, v ktorom bol vytvorený trojrozmerný MKP model (Obr.1). Pri definovaní materiálových vlastností boli použité nasledovné parametre: Youngov modul pružnosti $E=0.817\times10^{11}$ Pa, Poissonovo číslo $\mu=0.3$ a medza pevnosti materiálu Rm=491 MPa.

Okrajové podmienky numerického modelu boli definované tak, aby simulovali kombinované zaťaženie ohyb-krut. Jeden koniec skúšobnej tyče bol zaťažený ohybovým momentom a druhý koniec krútiacim momentom. Zaťaženie malo harmonický sínusový priebeh s nulovou strednou hodnotou napätia, pričom fázový posun medzi jednotlivými zložkami zaťaženia bol nastavený na hodnotu $\varphi=0°$. Tento typ zaťaženia predstavuje proporcionálne multiaxiálne namáhanie, pri ktorom maximá jednotlivých napäťových zložiek nastávajú súčasne.

Pomocou statickej numerickej analýzy boli identifikované oblasti s najvyššími hodnotami ekvivalentného napätia a deformácie. Kritická oblasť bola lokalizovaná v krčku skúšobnej vzorky, kde dochádzalo ku koncentrácii napätia v dôsledku geometrického zúženia. Z tejto oblasti boli extrahované hodnoty napäťových a deformačných veličín reprezentujúce rozhodujúci stav materiálu pre ďalšiu únavovú analýzu.

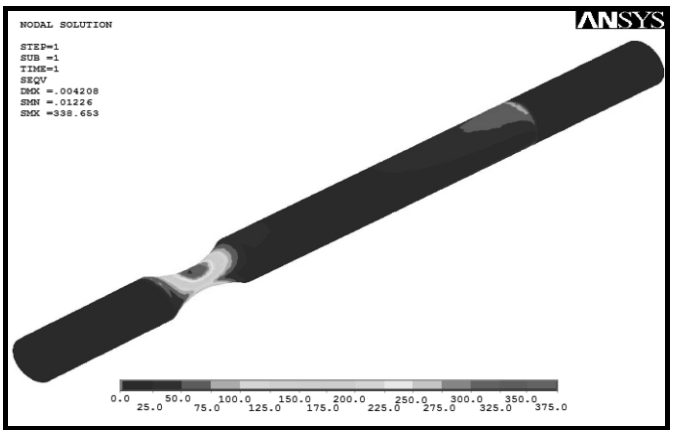

Obrázok 1. Výsledok MKP analýzy

Takto získané výsledky boli následne použité ako vstupné parametre pre výpočtový program Fatigue Calculator, ktorý umožňuje numerické hodnotenie únavovej životnosti na základe rôznych multiaxiálnych kritérií poškodenia. Program poskytol odhady počtu cyklov do porušenia pre jednotlivé únavové modely v oblasti nízkocyklovej aj vysokocyklovej únavy. Pre oblasť nízkocyklovej únavy boli použité únavové kritériá Fatemi–Socie, Smith–Watson–Topper (SWT), Brown–Miller a Liu. V oblasti vysokocyklovej únavy boli analyzované modely Goodman, Findley, Sines a MCE. Na základe vypočítaných hodnôt počtu cyklov do porušenia boli zostavené Wöhlerove krivky (Obr.2 a Obr.3)

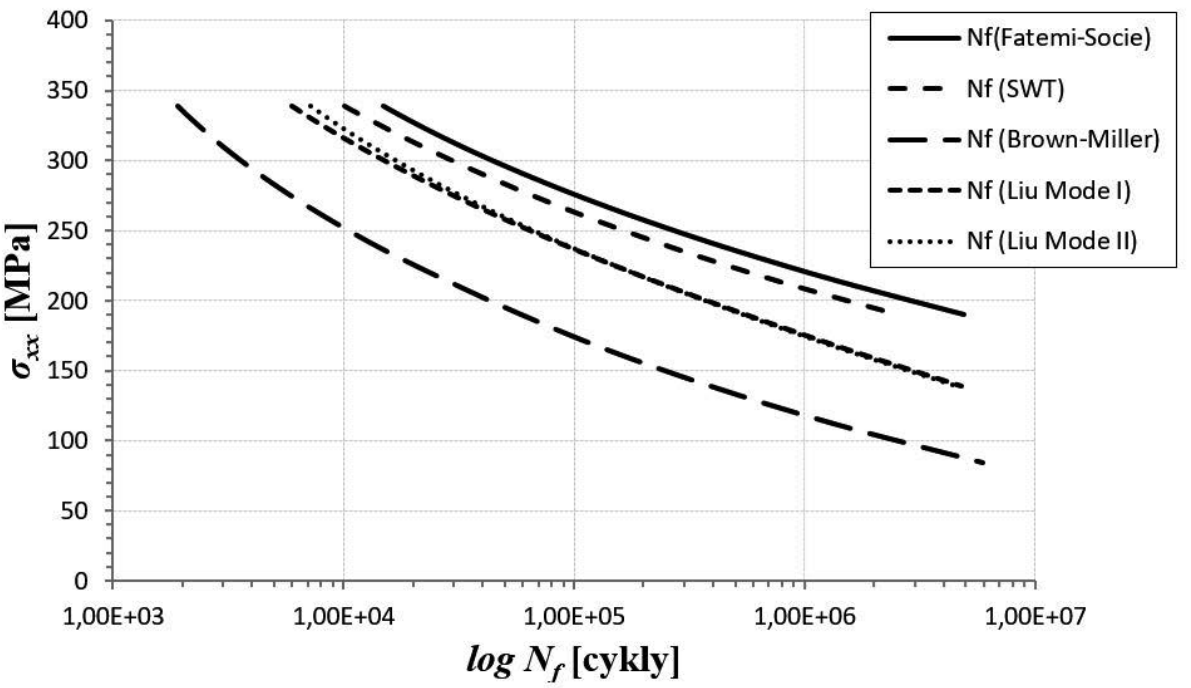

Obrázok 2. Wöhlerove krivky pre multiaxiálnu nízkocyklovú únavu

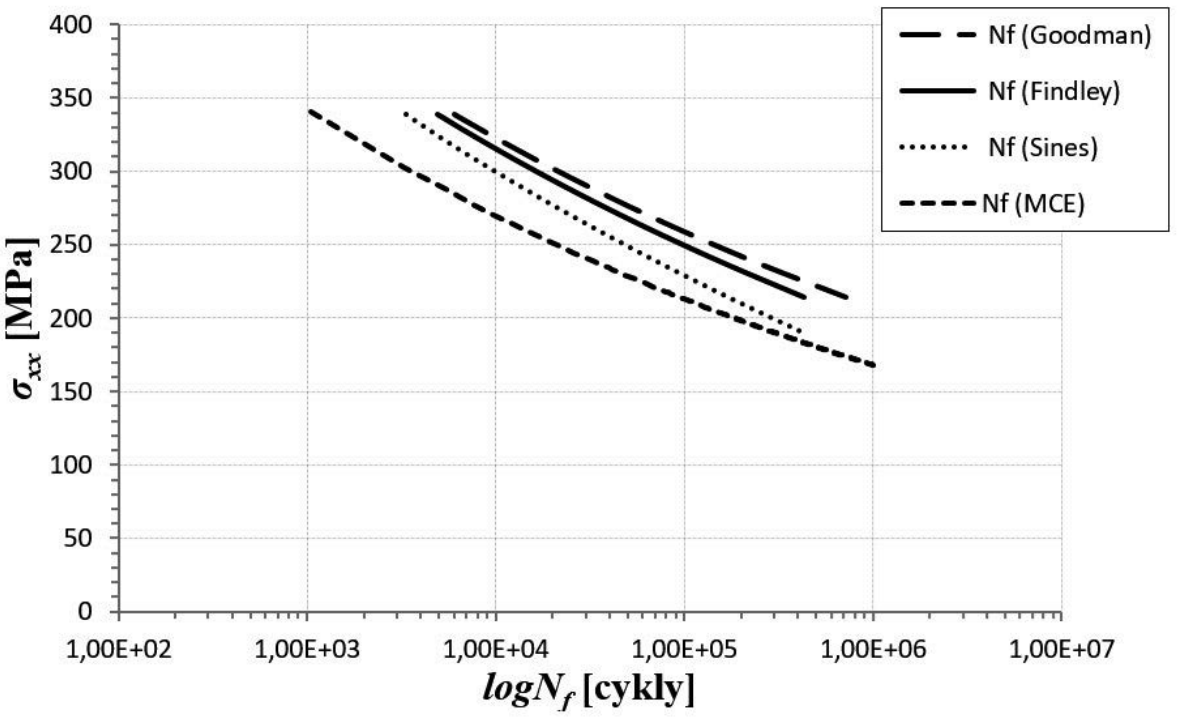

Obrázok 3. Wöhlerove krivky pre multiaxiálnu vysokocyklovú únavu

4. DISKUSIA

Na základe výsledkov získaných vo výpočtovom programe Fatigue Calculator boli zostavené Wöhlerove krivky únavovej životnosti pre jednotlivé multiaxiálne kritériá poškodenia. Výsledné priebehy umožnili vzájomné porovnanie predikcií životnosti v oblasti nízkocyklovej a vysokocyklovej únavy pri kombinovanom namáhaní ohyb-krut.

Výsledky ukázali, že všetky hodnotené modely vykazujú typický klesajúci charakter únavových kriviek, čo znamená, že so zvyšujúcim sa počtom cyklov do porušenia dochádza k poklesu prípustnej amplitúdy napätia. Tento trend je v súlade so základnou teóriou únavového poškodenia materiálov.

V oblasti nízkocyklovej únavy boli analyzované modely Fatemi–Socie, SWT, Brown–Miller a Liu. Z porovnania jednotlivých Wöhlerových kriviek bolo možné pozorovať veľmi dobrú zhodu medzi modelmi Fatemi–Socie, SWT a Liu v celom rozsahu sledovaných cyklov. Tieto modely poskytovali podobné odhady únavovej životnosti a ich priebehy boli charakteristické porovnateľným sklonom aj úrovňou amplitúd napätia. Odlišné správanie však vykazoval Brown–Millerov model, ktorého krivka sa nachádzala výrazne nižšie v porovnaní s ostatnými modelmi. Tento model teda predikoval kratšiu únavovú životnosť pri rovnakých úrovniach zaťaženia. Uvedený jav môže súvisieť so samotnou formuláciou Brown–Millerovho kritéria, ktoré vychádza zo šmykovej deformácie modifikovanej účinkom normálovej deformácie. Zvýšená citlivosť modelu na kombináciu šmykových a normálových zložiek deformácie môže viesť ku konzervatívnejšiemu odhadu životnosti, najmä pri proporcionálnom multiaxiálnom namáhaní.

Pri vysokocyklovej únave boli hodnotené modely Goodman, Findley, Sines a MCE. Výsledné Wöhlerove krivky pre modely Goodman, Findley a Sines vykazovali veľmi podobný

priebeh v celom intervale sledovaného počtu cyklov. Rozdiely medzi nimi boli relatívne malé, čo naznačuje podobnú citlivosť týchto kritérií na pôsobenie kombinovaného zaťaženia ohyb-krut. Najvýraznejšie odlišné výsledky poskytol MCE model, ktorého Wöhlerova krivka bola posunutá do oblasti nižších amplitúd napätia. Tento model teda predikoval výrazne nižšiu odolnosť materiálu voči únavovému poškodeniu. Príčinou môže byť skutočnosť, že MCE kritérium nezohľadňuje niektoré materiálové parametre a mechanizmy poškodenia tak podrobne ako ostatné analyzované modely. V dôsledku toho môže dochádzať ku konzervatívnejšiemu odhadu únavovej životnosti.

Z výsledkov je taktiež zrejmé, že jednotlivé multiaxiálne kritériá reagujú rozdielne na kombináciu normálových a šmykových napätí. Kritériá založené prevažne na šmykovej zložke deformácie vykazovali vyššiu citlivosť na charakter multiaxiálneho namáhania.

5. ZÁVER

Na základe vykonaných numerických analýz a porovnania jednotlivých multiaxiálnych kritérií poškodenia možno formulovať nasledujúce závery:

- všetky analyzované Wöhlerove krivky vykazovali typický klesajúci charakter, pričom s rastúcim počtom cyklov do porušenia dochádzalo k poklesu prípustnej amplitúdy napätia,
- v oblasti nízkocyklovej únavy vykazovali modely Fatemi–Socie, SWT a Liu veľmi podobné priebehy únavových kriviek a porovnateľné odhady životnosti v celom rozsahu sledovaných cyklov,
- Brown–Millerov model poskytoval výrazne nižšie hodnoty únavovej životnosti oproti ostatným kritériám, pričom jeho priebeh bol konzistentne konzervatívny v celom rozsahu analyzovaného zaťaženia,
- v oblasti vysokocyklovej únavy sa modely Goodman, Findley a Sines vyznačovali veľmi dobrou zhodou výsledkov a podobným charakterom priebehov únavových kriviek,
- MCE model predikoval výrazne nižšiu únavovú odolnosť materiálu v porovnaní s ostatnými vysokocyklovými kritériami, čo môže súvisieť s odlišnou formuláciou kritéria a absenciou niektorých materiálových parametrov vo výpočte,
- výsledky potvrdili, že voľba vhodného multiaxiálneho kritéria poškodenia má zásadný význam pri spoľahlivom hodnotení únavovej životnosti konštrukčných komponentov namáhaných kombinovaným cyklickým zaťažením.

POĎAKOVANIE

Tento príspevok vznikol v rámci spoločného slovensko-poľského projektu ako výsledok spolupráce medzi Politechnikou Slaskou (Poľsko) a Žilinskou univerzitou v Žiline (Slovensko) a bol podporený projektami VEGA 1/0729/26, VEGA 1/0461/24, KEGA 033ŽU-4/2026 a KEGA 039ŽU-4/2026.

LITERATÚRA

1. Bathias, C. Fatigue in the very high cycle regime. Vienna, Austria 2001.
2. Bokůvka, O., Nicoletto, G., Kunz, L., Palček, P., Chalupová, M. Low & high frequency fatigue testing. CETRA and Univerzity of Žilina, Žilina 2002.

3. Nový, F., Kopas, P., Bokůvka, O., Chalupová, M. Vplyv zlievarenských chýb na únavovú životnosť perliticko – feritickej LGG. Materiálové inžinierstvo, 3, 10, SK, 2003.
4. Leger, J. Fatigue life testing of crane drive shafts under crane-typical torsional and rotary bending loads. Schenck Hydropuls Mag., Issue 1/89 (1989), pp. 8–11.
5. Gough, H.J., Pollard, H.V. Some experiments of the resistance of metals to fatigue under combined stresses. Min. of Supply, Aero Res. Council, RSM 2522, Part I (1951).
6. Brown, M. W., Miller, K. J. A theory for fatigue under multiaxial stress-strain conditions. In: Proc. Inst. Mech. Engrs, Vol. 187 (1973),745-755.
7. Fatemi, A., Socie, D. F. A critical plane approach to multiaxial fatigue damage including out-of-phase loading. Fatigue Fract. Eng. Mater. Struct. 11 3 (1988),149-166.
8. Yan, X. Multiaxial notch fracture and fatigue. CRC Press, 2025.

TalentDetector

7th-9th June 2026
Gliwice-Brenna, Poland

DEPARTMENT OF ENGINEERING MATERIALS AND BIOMATERIALS
FACULTY OF MECHANICAL ENGINEERING
SILESIAN UNIVERSITY OF TECHNOLOGY

INTERNATIONAL STUDENTS SCIENTIFIC CONFERENCE

Structural aspect of laser surface remelting

Martyna Urbańska[a], Kinga Stępska[b], Marek Flak[c], Felicjan Glenc[d], Piotr Konieczny[e], Mirosław Bonek[f], Eva Tillova[g]

[a] Student of Production and Management Engineering, e-mail: mu309689@student.polsl.pl
[b] Student of Production and Management Engineering, e-mail: ks309686@student.polsl.pl
[c] Student of Mechatronics, e-mail: mf310852@student.polsl.pl
[d] Student of Mechanical Engineering, e-mail: fg316671@student.polsl.pl
[e] Student of Electrical Engineering, e-mail: pk308597@student.polsl.pl
[f] Silesian University of Technology, Faculty of Mechanical Engineering, Department of Engineering Materials and Biomaterials, email: miroslaw.bonek@polsl.pl
[g] University of Žilina, Faculty of Mechanical Engineering, Department of Materials Engineering, Žilina, Slovakia

Abstract: Laser Surface Remelting (LSR) is an advanced surface engineering technique that enables localized modification of the surface layer of metallic materials without significantly affecting the properties of the core material. This paper presents the characteristics of the LSR process, with particular emphasis on phase transformations, microstructural evolution, and the influence of the resulting microstructure on the functional properties of modern structural, tool, and stainless steels. The structure of the remelted layer, including the remelted zone and the heat-affected zone (HAZ), is discussed together with the mechanisms responsible for the formation of martensitic, bainitic, and dendritic structures during extremely rapid heating and cooling cycles. Particular attention is paid to the influence of technological parameters such as laser power, beam scanning speed, and cooling rate, which determine the final microstructure and service properties of the processed material. The study also presents the effect of laser surface remelting on hardness enhancement, wear resistance, tribological performance, and corrosion resistance. Both the advantages of the LSR technology, resulting from its high precision and capability for localized surface strengthening, and its limitations related to residual stresses and the risk of microcrack formation are discussed.

Keywords: Laser Surface Remelting (LSR), microstructure, surface modification, grain refinement, martensitic structure, bainitic structure, surface hardness, wear resistance, corrosion resistance, tribological properties, thermophysical properties, modern steels, laser processing, surface engineering

1. INTRODUCTION

In materials engineering, increasing attention is being focused on the modification of the surface layer of materials, as it is responsible for wear, corrosion, the initiation of fatigue

cracks, and direct contact with aggressive environments. One of the most advanced methods of surface modification is Laser Surface Remelting (LSR), which enables localized surface remelting, microstructural modification, and the improvement of service properties while maintaining the core properties of the material.

This method is particularly applicable to modern engineering steels, including Advanced High-Strength Steels (AHSS), where the strength-to-weight ratio is of primary importance; stainless steels, which require high corrosion resistance; and tool steels, whose durability strongly depends on the hardness of the surface layer.

In AHSS steels, LSR makes it possible to create localized martensitic zones, thereby increasing strength while preserving ductility. In the case of stainless steels, LSR technology is used for the so-called carbide dissolution process. Rapid remelting followed by cooling above the critical cooling rate prevents the precipitation of chromium carbides at grain boundaries, which improves resistance to intergranular corrosion.

For tool steels, LSR enables significant refinement of the surface-layer microstructure, resulting in increased hardness and the elimination of casting defects formed during the solidification proces. [1]

2. LASER SURFACE REMELTING

Laser surface melting is a modern method for modifying the surface layer of metallic materials. The core principle of this process is rapid heating and, consequently, melting of the material, which leads to the formation of a liquid metal pool. This rapid temperature spike occurs only within the micro-area of the laser beam's interaction. Once the beam is removed, the melted layer undergoes rapid cooling and solidification. Such phenomena occurring on the material's surface allow for the creation of a unique microstructure with enhanced physical and mechanical properties, such as improved corrosion resistance, wear resistance, or increased hardness.

A characteristic feature of this process is the material's heating rate which, depending on the laser used, reaches levels of 10^3-10^{10} K/s. When combined with relatively low energy densities (typically 0,1-10 J/cm^2), this allows for temperature changes exclusively within the near-surface zone, preventing the entire component from overheating and minimizing distortion. Another key aspect is the ability to achieve high precision in controlling technological parameters. By adjusting the laser power, melting depth, or the beam scanning speed, it is possible to precisely control the structure and properties of the processed area.

Despite its numerous advantages, the process involves high investment costs, primarily related to expensive equipment and control systems. Another technological challenge is the very high temperature gradient. Such sudden changes lead to the formation of residual stresses and increase the risk of cracks within the melted layer.

Due to the possibilities offered by the aforementioned process, laser surface melting finds applications in many branches of industry. It is utilized in the processing of shafts, gears, and engine components, as well as in the production of implants and surgical instruments and many more. [2,3]

3. CHARACTERISTIC ZONES OF THE LASER-REMELTED LAYER

3.1. Remelted Zone (Melted Zone)

The remelted zone is the area of the material that was completely melted during laser action and then cooled very rapidly. During laser surface remelting, the laser beam delivers a large amount of energy to a very small surface area, causing the temperature to rise rapidly. After the beam passes, the material transfers heat just as quickly to the deeper layers of the steel, which results in rapid solidification of the molten metal. [4]

As a result of this process, a very fine microstructure is formed, which differs from the structure of the material before treatment.

In the remelted zone, martensite is most commonly present, which is responsible for increasing the hardness of the material. A dendritic structure, formed during the solidification of the liquid metal, can also be observed. Due to rapid cooling, the grains are significantly smaller, which usually improves resistance to abrasion and surface wear. In modern high-alloy steels, partial dissolution of carbide precipitates and a more uniform distribution of alloying elements also occur.

The structure of the remelted zone mainly depends on process parameters such as laser power, beam travel speed, and material heating time. Too much energy may lead to the formation of residual stresses and microcracks caused by the very rapid heating and cooling of the material. [5]

Nevertheless, a properly conducted laser remelting process allows significant improvement of the surface layer properties of steel without changing the properties of the entire component.

3.2. HAZ

The heat-affected zone (HAZ) is the area located directly next to the remelted zone. The material in this part does not melt, but it is strongly heated. The high temperature causes changes in the steel microstructure, which affect its mechanical properties. [6]

The extent of these changes mainly depends on the temperature reached by the material and the rate at which it cools after the process.

Various structural transformations may occur in the HAZ, such as grain growth, phase transformations, or partial tempering of previously formed martensite. In areas where the temperature was the highest, austenite grains may grow larger, which after cooling leads to the formation of a harder but more brittle structure. [7]

In other areas, finer grains may form, which positively affect the mechanical properties of the material. [6]

In modern high-strength steels, local softening of the HAZ may become a problem. This happens when high temperature causes partial tempering of martensite or dissolution of precipitates strengthening the steel structure. This may lead to a reduction in strength and fatigue resistance of the material.

One of the most important advantages of laser processing is the very small width of the heat-affected zone. Due to the concentration of energy on a small surface area and short heating times, structural changes affect only a thin layer of the material. This makes it possible to limit thermal distortions and maintain good core properties of the component, which is particularly important in the case of modern steels used in the aerospace, automotive, and tool industries.

4. PHASE TRANSFORMATIONS AND STRUCTURAL EVOLUTION DURING LASER SURFACE REMELTING

The fundamental mechanism of laser processing involves delivering a high-power density beam to the material, resulting in extremely rapid heating followed by rapid cooling due to heat dissipation into the cold core of the material once the interaction ceases. The cooling rate is of particular importance in this process; in thin layers with low heat capacity, it is comparable to, and sometimes even greater than, the heating rate. Controlling this parameter allows for the management of desired phase transformations, such as martensitic quenching, vitrification, or the creation of nanocrystalline structures. [8,9]

The specific nature of the laser thermal cycle, characterized by heating rates in the range of 10^3 - 10^6 K/s, forces significant changes in the kinetics of solid-state transformations. A shift of the critical points Ac_1 and Ac_3 towards higher temperatures is observed; at extreme heating rates, these points may even shift toward the melting temperature. This leads to the overlapping of individual transformations or a change in their sequence. Furthermore, the character of the transformation often changes from diffusional to diffusionless; in hypoeutectoid steels, this can result in the formation of austenite from pearlite without carbon diffusion until the liquidus line is reached. [3]

In the melt zone (MZ), where the temperature exceeds the liquidus line, the final phase composition is determined by the dynamics of the liquid metal pool and the crystallization conditions. Intense liquid circulation induced by thermocapillary convection (the Marangoni effect) promotes high homogenization of the chemical composition. During solidification, which occurs epitaxially on the partially melted grains of the substrate, the ratio of the temperature gradient (G) to the crystallization rate (R) has a crucial influence on morphology. As the G/R value decreases from the bottom of the pool toward the surface, the crystallization front evolves from planar to cellular, and finally to dendritic. Very high speeds of the crystallization front promote the "solute trapping" phenomenon, allowing for the obtainment of solid solutions with element concentrations significantly exceeding the solubility limits derived from equilibrium systems. [3,10]

In the group of high-alloy steels, such as 17-4 PH martensitic steel, laser remelting significantly modifies the balance between phases. This steel solidifies in a ferritic mode; however, due to the high cooling rate, the transformation of ferrite into austenite is partially suppressed. Upon reaching room temperature, residual ferrite with vermicular or lath morphology is retained within the martensitic matrix. [11,12]

Conversely, alloying austenitic steels with Fe-Al type powders leads to the synthesis of intermetallic phases FeAl and Fe_3Al, resulting in a significant increase in layer hardness while maintaining high structural refinement.

- In tool steels (e.g., SWV9) and HSLA micro-alloyed steels, laser remelting achieves hardness levels reaching 600 - 800 HV.
- In SWV9 steel, the process promotes the dissolution of vanadium carbides in the liquid phase and their subsequent crystallization in a highly dispersed form within the martensitic-austenitic matrix.
- In HSLA steels (e.g., 28MnTiNbVB), a fine lath martensite structure is formed, where carbide precipitates are arranged much more densely than in the parent material. [10,13]

It should be noted, however, that the violence of the process promotes gas entrapment, which can lead to the formation of gas pores within the remelted volume.

Light alloys and nanocrystalline claddings constitute a separate group.

- In Al-Mg-Sc-Zr aluminum alloys, laser remelting generates a bimodal structure: primary Al_3(Sc, Zr) phases serve as nucleation sites for fine equiaxed grains at the pool boundaries, while columnar grains dominate in the center.
- In Mg-Al-Zn magnesium alloys, the post-remelting structure consists of α-Mg solution grains and precipitates of the γ-$Mg_{17}Al_{12}$ phase.
- Interesting effects are achieved during the texturing of nanocrystalline claddings, where repeated beam interaction leads to high microstructural heterogeneity and an increase in hardness to approximately 1150 HV0.5 while maintaining structural stability. [14,15]

The final result of these phase transformations is a surface layer with unique functional properties. A significant increase in hardness reaching up to 1400 HV in certain alloying systems like $MoSi_2$ and structural refinement improve resistance to wear and corrosion. However, one must account for the formation of residual stresses, which are a combination of thermal and structural stresses (resulting from changes in the specific volume of phases, e.g., during martensitic transformation); in some materials, this necessitates the use of preheating to avoid cracking. [3,10]

5. INFLUENCE OF MICROSTRUCTURE ON FUNCTIONAL PROPERTIES

The microstructure obtained as a result of Laser Surface Remelting (LSR) significantly determines the service properties of modern steels. This process is characterized by a high energy concentration and extremely high heating and cooling rates, which lead to the formation of non-equilibrium microstructures and significant grain refinement. Compared with conventional heat treatment methods, laser remelting enables the production of a more homogeneous and fine-grained surface layer, which may improve the mechanical and functional properties of the material. [16,17]

One of the most important effects of microstructural modification is the increase in the hardness of the surface layer. A refined microstructure impedes dislocation movement within the crystal lattice, resulting in material strengthening. In the remelted zone, martensitic and bainitic structures are frequently observed, both characterized by high hardness and increased resistance to plastic deformation. The strengthening effect is further enhanced by the rapid solidification of the molten metal and the limited diffusion of alloying elements during cooling. [17,18]

The microstructure of the remelted layer also influences the material's resistance to abrasive and erosive wear. A fine-grained and homogeneous structure promotes a more uniform stress distribution within the material and limits the initiation of microcracks during component operation. Particularly beneficial effects are associated with finely dispersed carbide precipitates, which increase the surface resistance to wear and improve tribological properties. As a result, components subjected to laser remelting may exhibit improved service life under conditions of intensive friction, contact loading, and exposure to abrasive media. [18,19]

Another important aspect is the influence of microstructure on the corrosion resistance of steels. The remelting process leads to chemical homogenization of the surface layer and reduces the segregation of alloying elements. A more homogeneous structure limits the In addition, the reduction of porosity and the elimination of structural discontinuities may improve the integrity of the surface layer and increase resistance to aggressive environments. This effect is particularly significant for steels operating under corrosive conditions. [17,20]

The microstructure obtained after laser remelting also affects the thermophysical properties of the material. Changes in grain size and phase distribution may influence thermal conductivity, thermal expansion, and structural stability during operation at elevated temperatures.[16,21]

6. SUMMARY

Laser Surface Remelting is one of the most advanced methods for modifying the surface layer of metallic materials. Owing to extremely high heating and cooling rates, the process enables the formation of fine-grained, non-equilibrium microstructures that significantly improve the service properties of engineering materials. The process allows localized enhancement of hardness, wear resistance, and corrosion resistance while preserving the mechanical properties of the material core.

The conducted analysis demonstrated that the technological parameters of the process, particularly laser beam power, interaction time, and cooling rate, play a crucial role in determining the final effects of laser remelting. Proper selection of these parameters enables control over phase transformations and microstructural development within both the remelted zone and the heat-affected zone. Particularly beneficial effects are observed in modern high-strength, stainless, and tool steels, where the LSR process promotes the formation of martensitic structures and refinement of carbide precipitates.

Despite its numerous advantages, Laser Surface Remelting also involves certain limitations, including high equipment costs, the formation of residual stresses, and the possibility of microcracks and porosity within the remelted layer. Nevertheless, LSR remains a highly promising surface engineering technology with broad applications in the automotive, aerospace, tooling, and biomedical industries. Further advancements in laser processing technologies and process control methods are expected to expand the industrial applicability of this technique in modern engineering materials.

BIBLIOGRAPHY

1. H.S. Nalwa (ed.), Handbook of thin film materials Vol. 1, Deposition and processing of thin films, Academic Press, San Diego, 2002.
2. Majumdar J., Manna I., Laser processing of materials, Sadhana, Vol. 28, No. 3–4, 2003, s. 495–562
3. Radziejewska J., Laserowa modyfikacja właściwości warstwy wierzchniej wspomagana nagniataniem, Prace IPPT – IFTR Reports, nr 3/2011, Instytut Podstawowych Problemów Techniki PAN, Warszawa 2011.
4. Colaço R., Vilar R., Physical metallurgy of laser surface melted plastic mould steels: a case study, Revista de Metalurgia, 1998.
5. Preussner J. i in., Microstructure and residual stresses of laser remelted surfaces of a hot work tool steel, International Journal of Materials Research, 2014.
6. *Laser surface remelting enhances microstructure uniformity and improves corrosion resistance of low-alloy steel weld metals*, Materials Characterization, 2025.

7. *The effect of laser energy density on the microstructure, residual stress and phase composition of H13 steel treated by laser surface melting, Journal of Alloys and Compounds*, 2021.
8. *Wpływ przetapiania laserowego na strukturę i własności powłok ceramicznych ZrO2 – Y2O3 jako barier cieplnych*, wydawnictwo Politechnika Śląska PODRECZNIK
9. *Technologie laserowe przebiegające z odparowaniem warstwy wierzchniej obrabianego materiału,* Agnieszka Twardowska, Łukasz Łetocha
10. *Przetapianie laserowe* T. Targośa, Ł. Ciszeka , M. Bonek
11. *Effect of laser remelting processing on microstructure and mechanical properties of 17-4 PH stainless steel during laser direct metal deposition*, Zhiyuan Yu, Yi Zheng, Junmei Chen, Chuanfeng Wu, Jijin Xu, Hao Lu, Chun Yu
12. *Skład fazowy i mikrostruktura warstwy wierzchniej na podłożu stali austenitycznej 18-8 po laserowej modyfikacji*
13. *Przetapianie laserowe stali mikrostopowej typu HSLA*, Jacek Górka, Marek Opiela, Sebastian Stano
14. *Struktura i własności stopów Mg-Al-Zn*, L.A. Dobrzański, T. Tański, A.D. Dobrzańska-Danikiewicz, M. Król, S. Malara, J. Domagała-Dubiel
15. *Teksturowanie laserowe nanokrystalicznych napoin wojciech napadłek*, Agnieszka LABER Instytut Pojazdów Mechanicznych i Transportu, Wydział Mechaniczny, Wojskowa Akademia Techniczna
16. A. Twardowska, Ł. Łętocha, *Technologie laserowe w inżynierii powierzchni*, Annales Universitatis Paedagogicae Cracoviensis, Studia Technica IV, 2011.
17. J.-P. Kruth, J. Deckers, E. Yasa, *Experimental Investigation of Laser Surface Remelting for the Improvement of Selective Laser Melting Process*, 2008.
18. L.A. Dobrzański, *Warstwy powierzchniowe kształtowane z wykorzystaniem technologii laserowych*.
19. L.E. dos Santos Paes et al., *Understanding the behavior of laser surface remelting after directed energy deposition additive manufacturing through comparing the use of iron and Inconel powders*, Journal of Manufacturing Processes, 70 (2021), 494–507
20. A. Temmler et al., *Surface Structuring by Laser Remelting of Metals*, 2017
21. P. Radkiewicz, *Symulacja numeryczna procesu kształtowania lokalnych umocnień za pomocą przetapiania laserowego*, rozprawa doktorska, Wrocław, 2024.

TalentDetector

7th-9th June 2026
Gliwice-Brenna, Poland

DEPARTMENT OF ENGINEERING MATERIALS AND BIOMATERIALS
FACULTY OF MECHANICAL ENGINEERING
SILESIAN UNIVERSITY OF TECHNOLOGY

INTERNATIONAL STUDENTS SCIENTIFIC CONFERENCE

Design and development of an experimental setup for leak tightness testing of FDM prints

Julia Wawrzynek[a], Wojciech Tokarz[a], Łukasz Połap[b], Mikołaj Jędrzejek[b], Mikołaj Figołuszka[b], Marek Kremzer[c], Błażej Tomiczek[c]

[a] Student of Materials Engineering and Technologies, Silesian University of Technology
email: jw305636@student.polsl.pl, wt303939@student.polsl.pl
[b] Student of Mechanics and Machine Design, Silesian University of Technology
email: mj309401@student.polsl.pl, lp309478@student.polsl.pl, mf309370@student.polsl.pl
[c] Silesian University of Technology, Faculty of Mechanical Engineering, Scientific and Didactic Laboratory of Nanotechnology and Materials Technology
email: marek.kremzer@polsl.pl, blazej.tomiczek@polsl.pl

Abstract: Pressure-induced material failure is a major operational concern in many engineering and industrial systems, leading to significant construction and maintenance costs. This paper presents the design and analysis of an experimental setup developed to investigate leakage in 3D-printed materials subjected to gas pressure. The proposed system enables testing under controlled laboratory conditions with adjustable process parameters, including pressure profile, duration, and cyclic pressurization. The study primarily focuses on a detailed analysis of the boundary conditions required to ensure reliable and repeatable experimental results. Additionally, aspects related to the integration of control systems for partial automation of the testing procedure are discussed. The developed setup provides stable and repeatable testing conditions, enabling comparative analysis of additive manufacturing parameters, materials, and geometries. The proposed solution can be applied in both scientific research and engineering practice, supporting the development of manufacturing techniques and structures optimized for pressure-resistant applications.

Keywords: Fatigue strength, pressure resistance, experimental setup, process parameter optimization, material failure, tightness-testing, Fussed Deposition Modeling

1. INTRODUCTION

Material degradation caused by gas pressure is an important issue in many engineering and industrial applications [1,4], particularly in systems where components are exposed to internal pressure or cyclic pressurization [2]. Such loading conditions may lead to deformation, leakage, and, in extreme cases, material failure. With the growing use of additive manufacturing technologies, especially FDM, understanding their response to pressure loading conditions has become increasingly important.

The behavior of materials under gas pressure depends on numerous factors, including material properties, geometry, manufacturing parameters, and loading conditions [1,3]. In the case of additively manufactured parts, internal structure, layer adhesion, and porosity can significantly influence deformation and leakage mechanisms. Repeated pressurization may additionally lead to progressive material degradation and changes in structural response over time [5]. Depending on the applied pressure level and loading cycle, the tested samples may exhibit elastic or permanent deformation, while under higher stresses local damage or rupture can occur. However, in many practical applications the main issue is not catastrophic failure, but rather the gradual loss of tightness and dimensional stability. Therefore, reliable experimental methods are required to evaluate the behavior of 2D and 3D printed specimens under controlled gas pressure conditions.

The increasing application of additively manufactured components in functional engineering systems requires reliable methods for evaluating their pressure resistance and leak tightness. Due to the layer-based manufacturing process, printed parts often exhibit anisotropic behavior and internal imperfections that may affect their response under pressure loading. Furthermore, variations in additive manufacturing parameters may result in significant differences in the mechanical and sealing performance of printed structures. Consequently, controlled and repeatable experimental investigations are necessary for proper evaluation and comparative analysis of different materials, geometries, and manufacturing conditions. An additional challenge in the analysis of pressure-loaded printed components is the difficulty in obtaining stable and repeatable testing conditions. Even small variations in pressure level, loading duration, or specimen mounting may significantly affect the obtained results. For this reason, the experimental setup should ensure precise control of operating conditions and reliable measurement capability. Proper sealing of the testing chamber and stable mounting of the specimens are also essential to minimize measurement uncertainty and eliminate uncontrolled leakage outside the tested sample. Moreover, the possibility of performing both static and cyclic pressurization tests enables a broader assessment of material behavior under different operating conditions. This study focuses on the development and analysis of an experimental setup designed for testing additively manufactured samples subjected to static and repeated gas pressurization [4,6]. The proposed system enables controlled laboratory investigations of deformation, leakage, and pressure resistance, providing repeatable conditions for comparative analysis of different materials, geometries, and manufacturing parameters [7]. Particular attention was given to ensuring stable operating conditions and precise control of the testing process.

2. CONCEPT OF THE EXPERIMENTAL SETUP

2.1. Experimental setup requirements and design assumptions

To investigate the gas tightness of printed components under controlled conditions, an experimental setup was designed to enable systematic laboratory testing. The main objective was to develop a system capable of analyzing the influence of key process parameters, such as operating pressure, exposure time, and repeated pressurization, on the leak tightness of the tested components. The developed setup enables the regulation of compressed air pressure inside the system and the stable maintenance of a pressure level of 8 bar for a specified period of time. The interaction of compressed air with the printed specimens may lead to leakage, deformation, or failure of the sample, the nature and intensity of which depend on the selected

operating conditions. The system allows precise control of flow parameters and ensures the repeatability of experiments, which is essential for reliable comparative analysis of materials. During the design process, particular attention was given to defining the boundary conditions that the setup had to fulfill. The system was required to have a compact structure suitable for laboratory applications, use compressed air as the working medium, and ensure adequate sealing together with easy assembly and disassembly.

An important requirement was also the possibility of adjusting process parameters, including operating pressure and the duration of sample exposure to pressure conditions. Additionally, the setup was designed as an open system, enabling controlled pressure reduction inside the chamber. This approach improves operational safety. The construction also includes the use of water inside the chamber in order to minimize the danger caused by possible fragments originating from a damaged or destroyed specimen.

2.2 Structure and Operating Principles of the Experimental Setup

The conceptual design of the experimental setup was developed to meet the previously defined boundary conditions required for reliable operation under controlled laboratory conditions. The primary objective was to create a compact and modular system capable of testing both 2D and 3D printed specimens subjected to gas pressure. The developed setup enables investigations under different pressurization profiles, including static pressurization with gradual pressure increase, dynamic pressurization with rapid pressure application, and cyclic repeated pressurization. The overall structure of the developed setup is presented in Fig. 1. An important design requirement was the ability to adjust key process parameters, including operating pressure, pressurization rate, test duration, and the number of pressure cycles. Particular emphasis was also placed on implementing partial automation of the experimental procedure in order to improve the repeatability and reliability of the obtained results. The modular design facilitates easy assembly, disassembly, and potential modification of individual components. Furthermore, the setup was designed to ensure stable operation during both static and dynamic pressure loading under controlled laboratory conditions.

a) b)

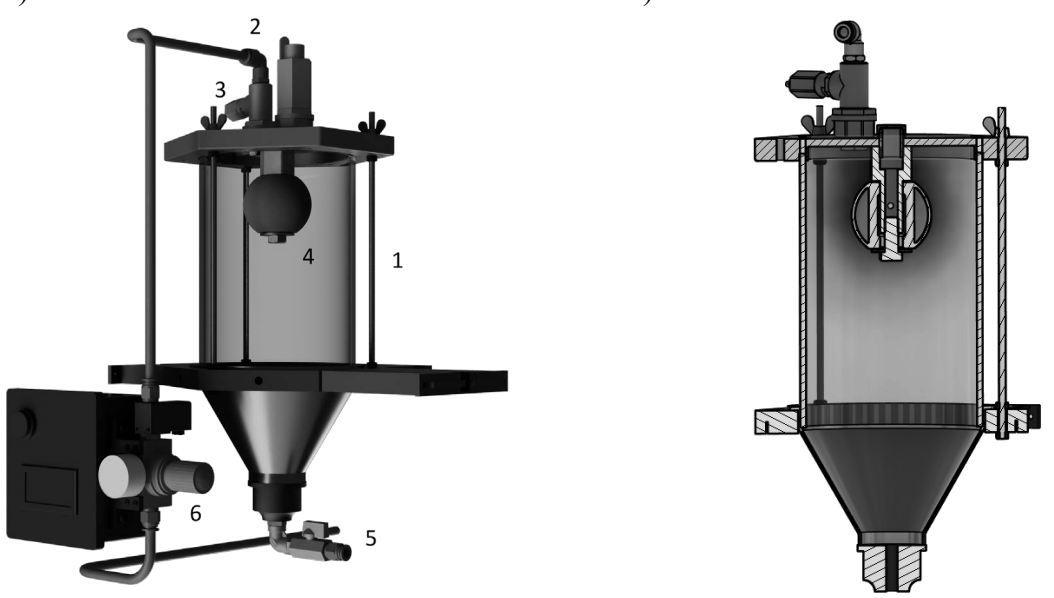

Fig. 1 Designed experimental setup: a) general view, b) cross-sectional view

The proposed concept enables testing of both flat disk-shaped samples and spatial geometries such as spheres and cuboids. Depending on the applied loading conditions, the tested specimens may undergo elastic deformation, permanent deformation, leakage, or, in extreme cases, material rupture. For this reason, the setup was additionally designed to ensure safe operation during rupture tests. The chamber can also be partially filled with water to reduce the risk associated with fragments originating from damaged specimens. The developed system enables controlled and repeatable experiments, providing suitable conditions for comparative analysis of different materials, geometries, and additive manufacturing parameters. The main components of the experimental setup and their corresponding functions are summarized in Table 1.

Table 1. Main components of the experimental setup and their functions

No.	Component	Function
1	Test chamber	Provides a protected testing space filled with water during rupture tests
2	Compressed air inlet module	Supplies and transports the working medium
3	Safety valve	Ensures safety by preventing overpressurisation
4	Sample holder	Allows mounting of different types of samples
5	Water valve	Enables water drainage
6	Pressure regulator with gauge	Controls the pressure and allows easy pressure reading

Safety features

The developed experimental setup incorporates several safety features intended to ensure controlled and reliable operation during pressure testing. Since the system is designed for experiments involving static, dynamic, and cyclic gas pressurization, particular attention was given to protection against overpressurization and safe containment of the tested samples. A safety valve is installed in the gas supply system to limit the maximum pressure delivered to the setup and protect the system components from excessive pressure levels. Additionally, the experimental chamber was designed as a reinforced enclosure equipped with a pressure release valve, enabling rapid depressurization of the system when required. This solution improves operational safety and allows better control of the testing process under varying pressurization conditions. To further improve safety, a water layer is placed at the bottom of the chamber. In the event of specimen rupture, the water helps absorb part of the released energy and reduces the propagation of fragments inside the chamber. This solution increases operator safety and minimizes the risk of damage to surrounding equipment. The system configuration also limits the uncontrolled release of gas, contributing to safer working conditions. Overall, the implemented safety solutions enable controlled, safe, and repeatable operation of the experimental setup under various pressurization conditions.

Specimen holder

An important element of the experimental setup is the specimen holder, whose purpose is to ensure stable mounting of the printed sample and adequate sealing, so that the airflow

passes exclusively through the structure of the tested specimen. The holder design enables easy installation and removal of samples, which improves the efficiency of the testing procedure and increases the repeatability of the obtained results.

The study considered two types of specimens corresponding to different operating conditions: flat and three-dimensional samples. To ensure proper sealing, both holder designs utilize a threaded mechanism that provides uniform and constant compression of rubber seals located on opposite sides between the holder and the specimen. This solution prevents air leakage and specimen displacement caused by pressure forces. More detailed design solutions are presented in Fig. 2.

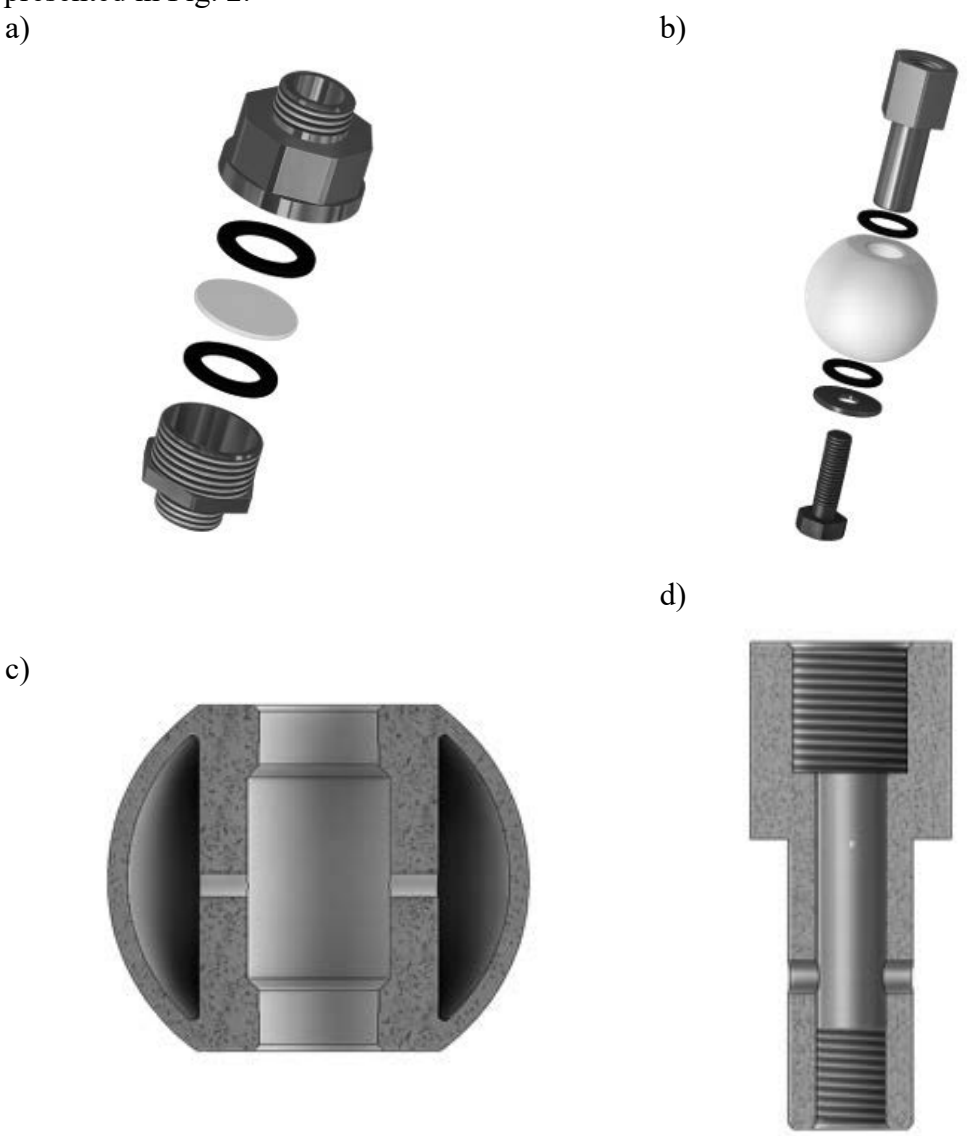

Fig. 2 Handle design: a) holder for flat samples, b) holder for 3D samples, c) cross-section view of 3D sample, d) cross-section view of air injection sleeve

2.3 The Design and Construction Process of the Test Rig

The design process of the experimental setup involved the development of a structural concept and modelling of individual components using Autodesk Inventor software. The application of CAD tools enabled precise representation of component geometries, analysis of their mutual fit, and verification of proper system operation during the design stage. Furthermore, CAD modelling facilitated the early identification of potential assembly issues and supported optimization of the overall structure prior to prototype manufacturing. Examples of the designed structural components are presented in Fig. 3.

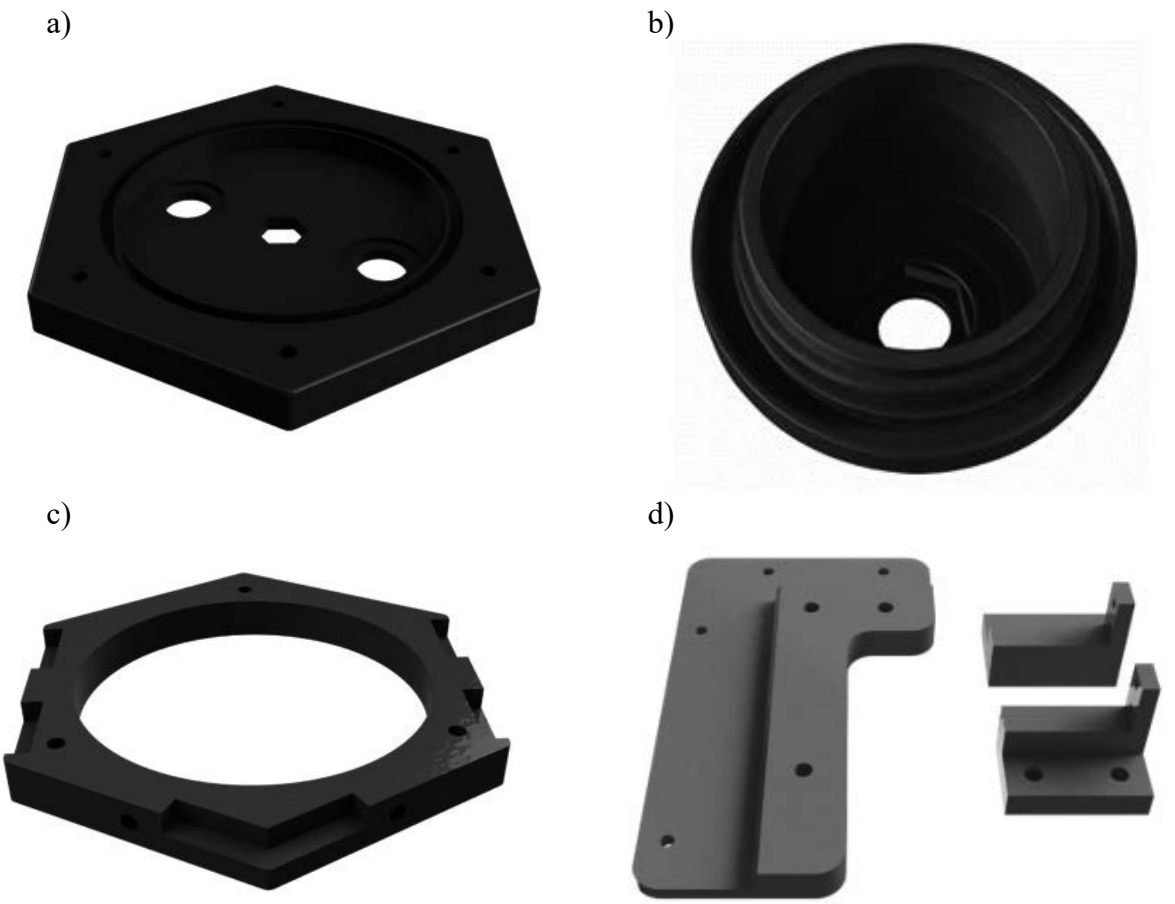

Fig. 3 Selected structural components of the test rig: a) top cover, b) threaded component, c) bottom holder, d) mounting elements

Selected components were subsequently manufactured as prototypes using FDM 3D printing technology. During the manufacturing process, appropriate printing parameters and filament materials were selected with consideration of operational requirements such as mechanical strength, dimensional stability, and leak tightness. The printed components were designed to ensure compatibility with standardized pneumatic fittings, enabling reliable integration within the system. To improve the repeatability of experimental conditions, the setup was partially automated through the implementation of a timer relay controlling the actuator responsible for gas flow regulation. This solution enabled precise control of test duration and cyclic pressurization, thereby increasing the repeatability and reliability of the conducted experiments. The completed experimental setup is presented in Fig. 4.

a) b)

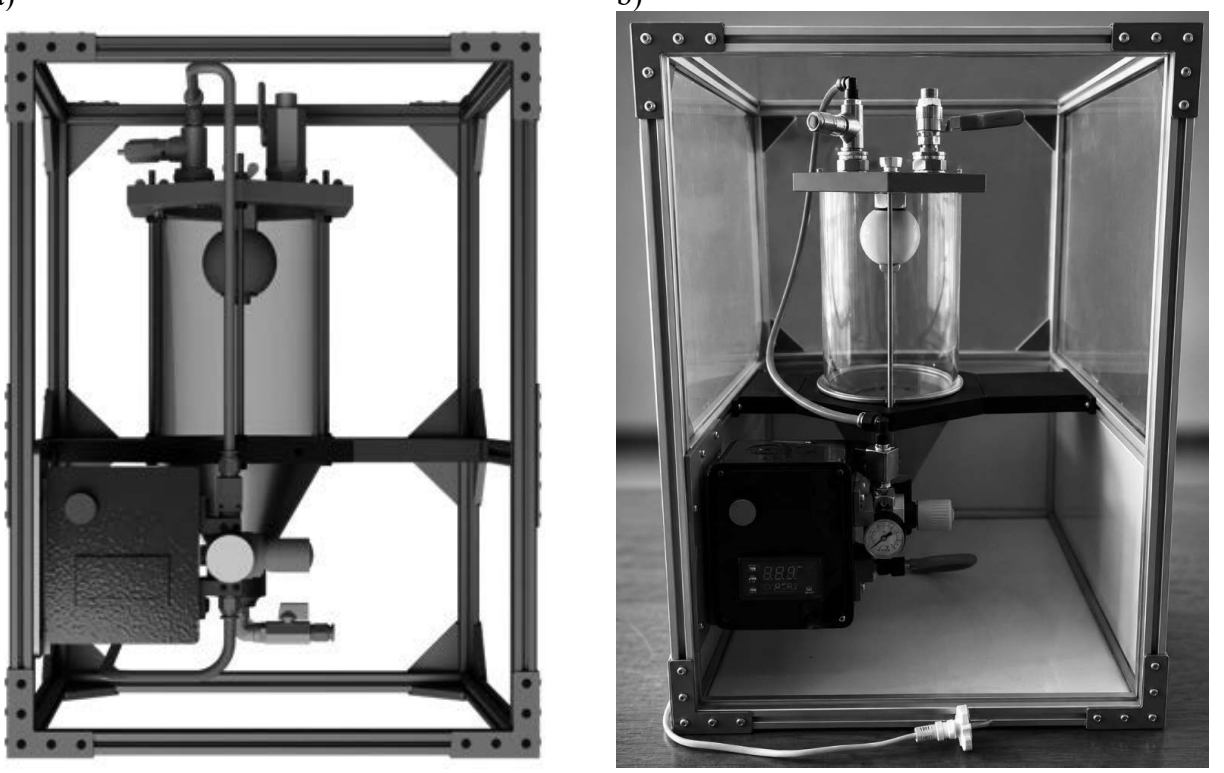

Fig. 4 The developed experimental setup: a) CAD model created in Autodesk Inventor, b) assembled experimental test rig

3. CONCLUSIONS

The conducted work enabled the design and construction of a test rig intended for evaluating the leak tightness of specimens manufactured using FDM technology. The developed setup fulfilled the assumed design requirements, allowing experiments to be carried out under controlled pressure conditions using compressed air with a working pressure of up to 8 bar. The test rig enabled the analysis of the influence of printing parameters, specimen geometry and pressure loading conditions on leak tightness and resistance to leakage. To ensure stable and repeatable measurement conditions, the system was equipped with a pressure regulator enabling precise adjustment of operating parameters, as well as an electronically controlled valve responsible for regulating the flow of the working medium. The implementation of partial process automation improved both the measurement accuracy and the repeatability of the experimental results. The performed tests confirmed the correct operation of the designed test rig and its suitability for investigating the leak tightness of components produced using the additive manufacturing method. During the experiments, the influence of the different parameters alters the occurrence and intensity of leakage observed, which allowed the assessment of specimen quality and the identification of potential leakage locations. The obtained results confirm the possibility of using the developed setup both in laboratory investigations and in the verification of components intended for operation under pressure conditions up to 8 bar. The developed construction may serve as a basis for further research

focused on the influence of water exposure on the leak tightness and functional properties of printed components.

ACKNOWLEDGMENTS

This publication was supported under the "Excellence Initiative – Research University" program at the Silesian University of Technology, within the framework of the 14th Project Based Learning (PBL) funding competition, entitled Design and Construction of an Experimental setup for Assessing the pressure resistance and leakage of materials manufactures using FDM.

LITERATURE

[1] J. Backiel, P. Dzienis, K. Golak, P. Zamojski, M. Rećko, R. Grądzki, J. E. Martínez, R. Valdés, Feasibility study of manufacturing hydraulic fittings using additive manufacturing technologies: Comparative analysis of FDM and SLA methods. Materials 19/4 (2026) 799. https://doi.org/10.3390/ma19040799

[2] Formlabs, How to make watertight 3D printed parts. Website: https://formlabs.com/blog/watertight-3d-printing/ (accessed 18.05.2026).

[3] P. Sapkota, K. S. Al-Rubaie, Effect of process parameters on the leakage resistance of FDM-printed pressure vessels. Journal of Manufacturing and Materials Processing 6/3 (2022) 64

[4] D.R. Baraboi, G. Năstase, M. Pavel, Leakage testing of 3D-printed vacuum enclosures for smart facade applications. Preprints.org (2026). https://www.preprints.org/manuscript/202602.0058, doi: 10.20944/preprints202602.0058.v1

[5] P. Sreejith, K. Kannan, K. R. Rajagopal, A thermodynamic framework for additive manufacturing using amorphous polymers capable of predicting residual stress, warpage and shrinkage. International Journal of Engineering Science 159 (2021) 103412. https://doi.org/10.1016/j.ijengsci.2020.103412

[6] R. Flitney, Seals and Sealing Handbook. 6th ed., Butterworth-Heinemann, Oxford 2014.

[7] M. Chen, Q. Ji, X. Zhang, L. Feng, X. V. Wang, L. Wang, Study on efficient fused deposition modelling of thermoplastic polyurethane inflatable wall features for airtightness. In: Proceedings of the International Conference on Manufacturing Research (ICMR), KTH Royal Institute of Technology, Sweden 2020. https://www.diva-portal.org/smash/get/diva2:1512474/FULLTEXT01.pdf

TalentDetector

7th-9th June 2026
Gliwice-Brenna, Poland

DEPARTMENT OF ENGINEERING MATERIALS AND BIOMATERIALS
FACULTY OF MECHANICAL ENGINEERING
SILESIAN UNIVERSITY OF TECHNOLOGY

INTERNATIONAL STUDENTS SCIENTIFIC CONFERENCE

Leak Tightness Optimization of PETG and TPU 3D Prints Through Printing Parameter Selection

Julia Wawrzynek[a], Wojciech Tokarz[a], Łukasz Połap[b], Mikołaj Jędrzejek[b], Mikołaj Figołuszka[b], Marek Kremzer[c], Błażej Tomiczek[c]

[a] Student of Materials Engineering and Technologies, Silesian University of Technology
email: jw305636@student.polsl.pl, wt303939@student.polsl.pl
[b] Student of Mechanics and Machine Design, Silesian University of Technology
email: mj309401@student.polsl.pl, lp309478@student.polsl.pl, mf309370@student.polsl.pl
[c] Silesian University of Technology, Faculty of Mechanical Engineering, Scientific and Didactic Laboratory of Nanotechnology and Materials Technology
email: marek.kremzer@polsl.pl, blazej.tomiczek@polsl.pl

Abstract: This paper presents an investigation of the influence of FDM 3D printing parameters on the leak tightness and surface quality of PETG and TPU printed parts. The experimental plan was developed using the Taguchi method to identify the most significant process parameters while reducing the number of required experiments. The manufactured samples were evaluated in terms of surface roughness, visual quality, and leak tightness under pressure conditions using a dedicated test setup. Based on the obtained results, the key parameters affecting the sealing performance of the printed components were identified.

Keywords: FDM 3D printing, leak tightness, PETG, TPU, additive manufacturing, surface roughness, pressure testing, print quality

1. INTRODUCTION

Fused Deposition Modelling (FDM) is currently one of the most widely used additive manufacturing technologies due to its low production cost, accessibility, and ability to manufacture geometrically complex components. Initially used mainly for rapid prototyping, FDM technology is increasingly applied in the production of functional engineering parts intended for industrial, medical, and fluid transport applications. In such applications, leak tightness becomes one of the key functional requirements. However, due to the layer-by-layer deposition process, FDM-manufactured parts often contain internal voids, insufficiently fused layers, and microscopic defects that may lead to leakage of gases or liquids [1,2].

The sealing performance of FDM-printed components strongly depends on the selection of printing parameters. Parameters such as nozzle temperature, layer height, printing speed, extrusion flow rate, wall thickness, infill density, and cooling conditions directly influence the quality of interlayer bonding and porosity formation within the printed structure. Higher nozzle temperatures may improve material fusion between adjacent layers, while excessive printing

speed can reduce bonding quality and increase the occurrence of internal defects. Similarly, lower layer heights are often associated with improved surface quality and reduced leakage paths due to better layer adhesion [3,4]. Wall thickness and infill structure also play an important role in determining the tightness of printed parts. Increasing the number of wall perimeters and infill density may significantly reduce internal porosity and improve resistance to fluid leakage. Previous studies demonstrated that insufficient extrusion flow or improperly selected infill parameters may result in the formation of continuous microchannels inside the structure, which negatively affects the sealing performance of FDM components [2,5]. Surface roughness is another important factor associated with print quality and tightness, since irregular surface morphology may indicate unstable material deposition and poor fusion between deposited layers.

Among commercially available FDM materials, Polyethylene Terephthalate Glycol (PETG) and Thermoplastic Polyurethane (TPU) are considered particularly suitable for manufacturing functional and sealing components. PETG is characterised by good mechanical strength, chemical resistance, dimensional stability, and relatively strong interlayer adhesion. Due to these properties, PETG is commonly used for manufacturing technical housings, containers, and fluid-handling components. TPU, in contrast, is a flexible elastomeric material distinguished by high elasticity, impact resistance, and good vibration-damping capabilities. Its flexibility and relatively good layer bonding make TPU suitable for sealing structures and flexible engineering applications [6]. Several methods are currently used to evaluate the leak tightness and structural quality of FDM-manufactured parts. The most common approaches include air pressure tests, hydrostatic pressure tests, vacuum decay methods, and visual inspection of leakage zones. Additionally, surface roughness measurements and microscopic analysis are frequently used to identify defects associated with insufficient fusion between deposited layers. Previous studies demonstrated that reducing porosity and improving interlayer adhesion significantly enhances the sealing performance of FDM-printed components [1,5].

Therefore, this study focuses on the investigation of the influence of selected FDM printing parameters on the leak tightness and surface quality of PETG and TPU printed parts. The selected process variables were analysed experimentally in order to determine their influence on sealing performance and identify parameter configurations leading to improved print quality and reduced leakage. Additionally, surface roughness measurements and visual inspection were performed to evaluate the quality of the manufactured samples. Leak tightness tests under pressure conditions were carried out using a dedicated experimental setup developed for this study.

2. MATERIALS AND METHODOLOGY

Two commercially available thermoplastic materials dedicated to Fused Deposition Modelling (FDM) technology were selected for the experimental investigation: Polyethylene Terephthalate Glycol (PETG) and Thermoplastic Polyurethane (TPU). Both materials were chosen due to their widespread use in functional engineering applications requiring sufficient mechanical properties and leak tightness. PETG is characterised by good dimensional stability, relatively high mechanical strength, low material shrinkage, and strong interlayer adhesion. Due to these properties, PETG is commonly used for manufacturing technical housings, containers, and fluid-handling components. TPU, in contrast, is a flexible elastomeric material

distinguished by high elasticity, impact resistance, and good vibration-damping behaviour, making it suitable for sealing structures and flexible engineering applications.

The experimental investigation was focused on determining the influence of selected FDM process parameters on the leak tightness and surface quality of PETG and TPU printed parts. Based on preliminary analysis and literature review, five process parameters were selected as the most significant variables affecting the quality and sealing performance of the manufactured components:

- nozzle temperature
- extrusion flow rate
- printing direction
- layer height
- printing speed

Each parameter was investigated on three different levels. In the case of printing direction, the samples were manufactured in three different orientations relative to the build plate: horizontal (0°), angled (45°), and vertical (90°), as presented in Figure 1. The experimental plan was developed using the Taguchi L27 orthogonal array, which enabled the reduction of the number of required experiments while maintaining the ability to evaluate the influence of individual process variables [7].

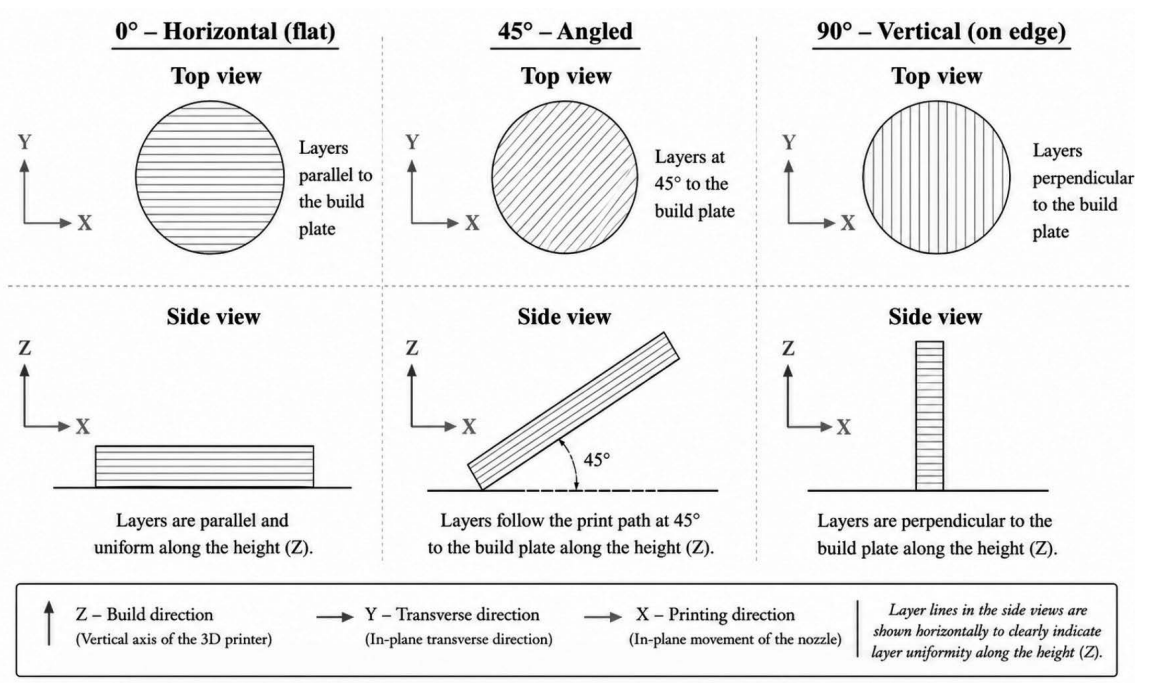

Fig. 1 Specimen printing orientation

The experimental samples were designed as cylindrical specimens with a diameter of 30 mm and specified heights. Identical sample geometry was maintained for all experiments to ensure repeatability and minimise the influence of geometrical variations on the obtained results. A total of 27 experimental samples were manufactured according to the developed experimental matrix. Following the printing process, all specimens were subjected to visual inspection to identify visible surface defects and potential leakage zones. The surface quality of the printed samples was evaluated using profilometer-based surface roughness measurements. Leak tightness tests were carried out using a dedicated experimental pressure test setup developed for this study. During the experiments, the printed samples were exposed to controlled pressure conditions and evaluated for leakage occurrence.

Following the preliminary analysis, the number of investigated process parameters was reduced to three variables showing the greatest influence on the leak tightness and surface quality of the printed samples:

- layer height,
- specimen height,
- extrusion flow rate.

A second experimental stage was subsequently performed using the reduced parameter set. In this phase, 18 PETG samples and 18 TPU samples were manufactured and tested. The repeated experiments enabled a more detailed evaluation of the relationship between the selected process parameters and the sealing performance of the manufactured PETG and TPU components.

Table 1 Printing Parameters for TPU and PET-G Samples Based on the Taguchi L27 Method

TPU				PET-G			
No.	**Layer height [mm]**	**Specimen height [mm]**	**Material flow rate [%]**	**No.**	**Layer height [mm]**	**Specimen height [mm]**	**Material flow rate [%]**
1	0,2	0,8	100	**19**	0,2	0,8	100
2			105	**20**			105
3			110	**21**			110
4	0,1		100	**22**	0,1		100
5			105	**23**			105
6			110	**24**			110
7	0,2	0,6	100	**25**	0,2	0,6	100
8			105	**26**			105
9			110	**27**			110
10	0,1		100	**28**	0,1		100
11			105	**29**			105
12			110	**30**			110
13	0,2	0,4	100	**31**	0,2	0,4	100
14			105	**32**			105
15			110	**33**			110
16	0,1		100	**34**	0,1		100
17			105	**35**			105
18			110	**36**			110

3. RESULTS

3.1. Visual Evaluation of Printed Samples

Some of the preliminary printed samples exhibited relatively poor, non-uniform surface quality, with numerous visible defects that could significantly affect the obtained leak-tightness results (Fig. 2 and 3). Surface irregularities, such as layer discontinuities, uneven extrusion paths, and local material accumulation, were frequently observed, indicating unstable processing conditions during manufacturing. One of the most influential factors affecting the print quality was the printing orientation. Samples manufactured at a printing angle of 45° required the use of support structures, resulting in a higher incidence of surface defects, poor surface finish, and

local discontinuities after support removal. In several cases, the printed specimens were additionally damaged, partially delaminated, or fractured during the manufacturing process, making them unsuitable for reliable leak-tightness evaluation.
Printing speed also significantly influenced the quality of the manufactured samples. Excessively high printing speed caused interruptions in the extrusion path and insufficient bonding between adjacent layers, leading to discontinuities in the outer walls of the printed structure. These defects were considered potential leakage zones during subsequent pressure testing and could substantially reduce the sealing performance of the printed parts. Based on the visual evaluation and preliminary inspection of the manufactured samples, the final experimental stage was conducted using reduced, optimised printing speeds for both PETG and TPU. Additionally, the investigated printing orientations were limited to vertical printing and 45° orientation in order to reduce the occurrence of critical manufacturing defects and improve the repeatability and overall quality of the printed specimens.

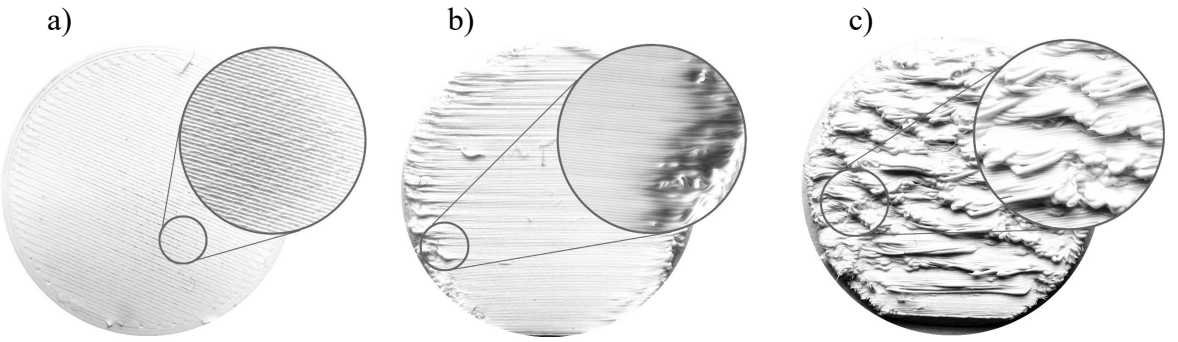

Fig. 2 Samples printed from TPU in orientations: (a) 0°, (b) 45°, and (c) 90°

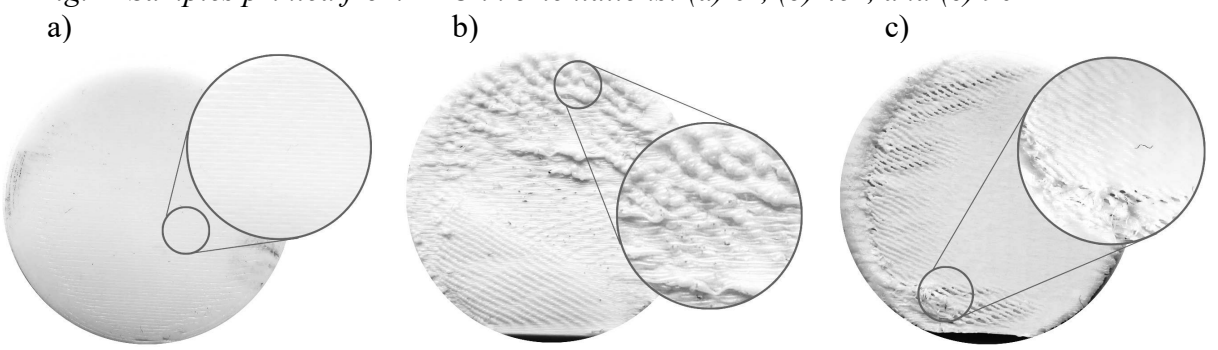

Fig. 3 Samples printed from PETG in orientations: (a) 0°, (b) 45°, and (c) 90°

3.2 Surface Roughness Analysis

The initially manufactured 2 mm-thick samples were subjected to profilometer measurements to evaluate the surface roughness of the printed specimens. In both investigated materials, smooth build plate sheets without visible surface texture were used during printing, which minimised the influence of the build surface on the resulting roughness. It should be noted that, due to the profilometer's limited measurement range, several samples exceeded the device's measurable range. This effect was particularly observed for specimens printed at a 45° orientation, which exhibited the highest surface irregularities and the largest roughness values. Figure 4 presents the average surface roughness values for PETG and TPU samples, respectively. Figure 5 presents a comparative set of representative surface roughness profiles obtained for PETG and TPU samples manufactured at different printing orientations. Based on the results, the highest average surface roughness was observed for samples printed at 45°,

regardless of the investigated material, while the lowest roughness was observed for horizontally printed specimens (0° orientation).

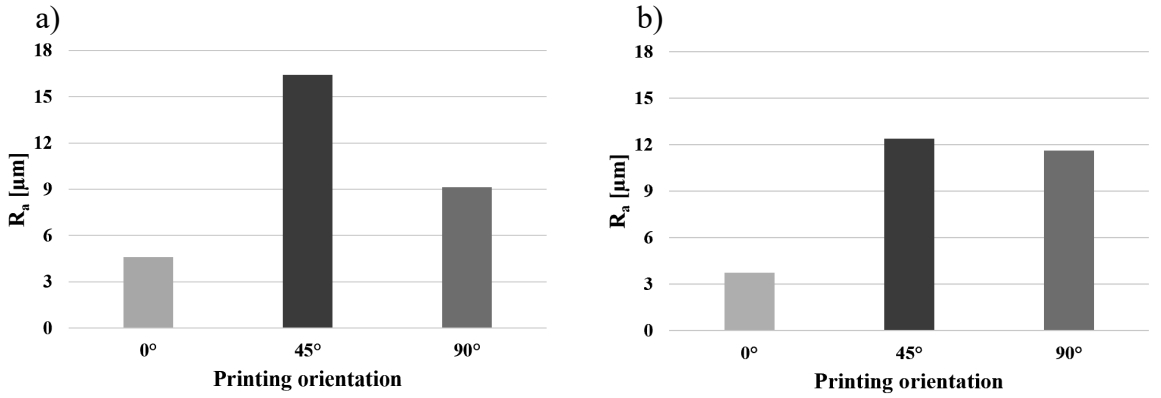

Fig. 4 Influence of printing orientation on average surface roughness: a) PETG, b) TPU.

Printing orientation [°]	PETG
0	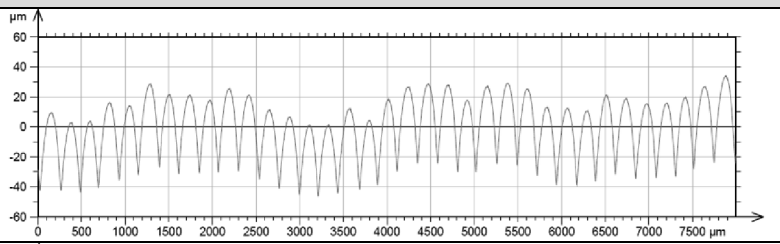
45	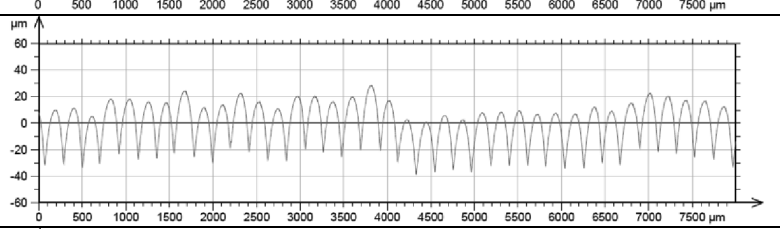
90	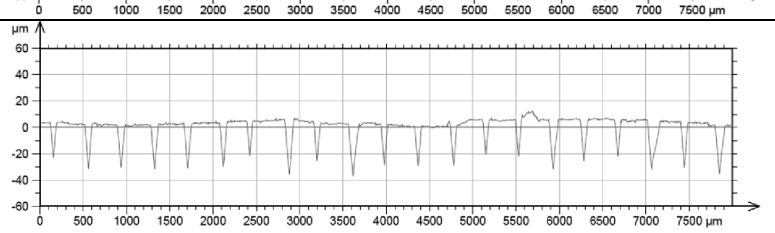
Printing orientation [°]	**TPU**
0	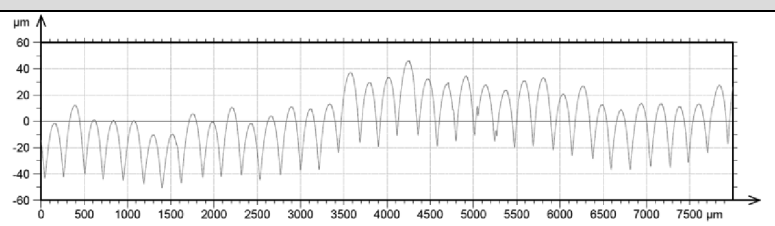
45	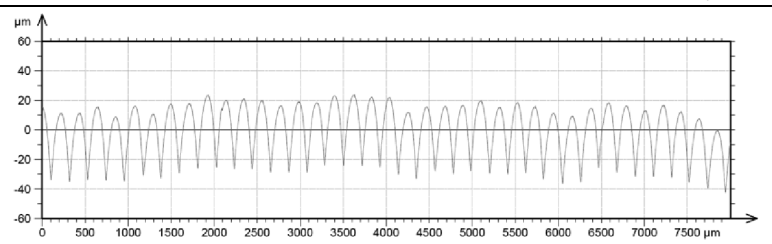

90	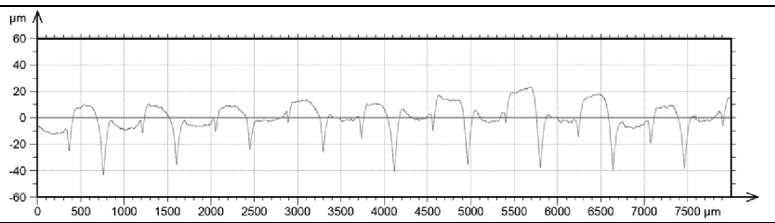

Fig. 3 Representative profilometer surface roughness profiles for PETG and TPU samples printed at different orientations

3.3 Leak Tightness Evaluation

During the preliminary stage of the investigation, all samples were manufactured with a specimen height of 2 mm. Due to the relatively large thickness of the printed walls, all specimens successfully passed the leak tightness tests under the applied pressure conditions. In order to determine the minimum specimen height ensuring sufficient sealing performance, additional experiments were subsequently performed with reduced sample heights. Based on the preliminary analysis, the investigation was focused on specimen heights of 0.4 mm, 0.6 mm, and 0.8 mm. Additionally PETG and TPU samples were then manufactured using the reduced parameter set, including layer height and extrusion flow rate, followed by leak tightness testing using the developed experimental setup. For PETG samples, regardless of specimen thickness, all samples withstood the maximum pressure of 8 bar during all three tests. Figure 6 represents the PETG and TPU samples after the leak tightness testing process. Figure 7 presents the maximum pressure values ensuring leak-tightness for individual TPU samples.

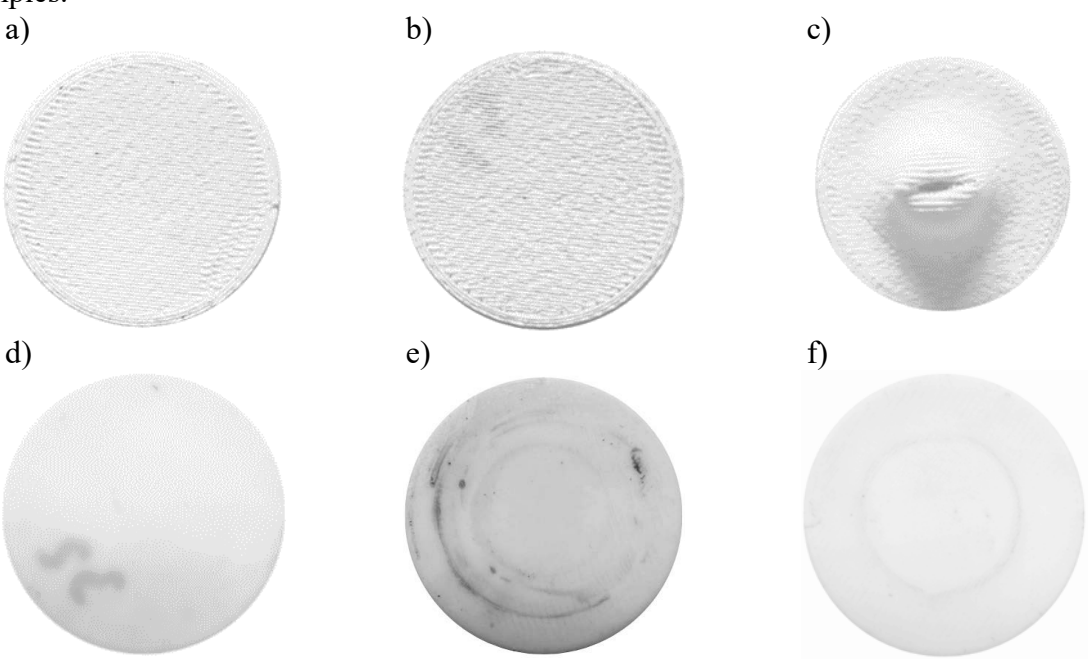

Fig. 6 Representative samples after the leak-tightness test: TPU specimens with heights of (a) 0.8 mm (3), (b) 0.6 mm (13), and (c) 0.4 mm (17); PET-G specimens with heights of (d) 0.8 mm, (e) 0.6 mm, and (f) 0.4 mm.

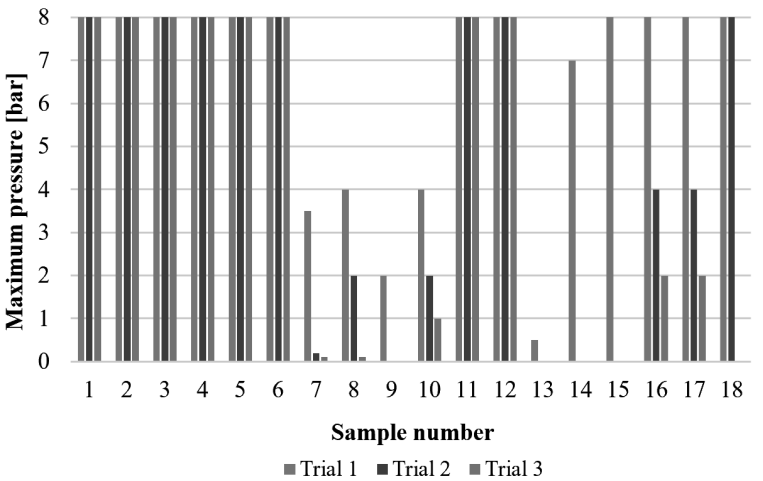

Fig. 7 Maximum pressure values ensuring leak-tightness for individual TPU samples

4 CONCLUSIONS

The conducted investigations confirmed a significant influence of FDM printing parameters on the leak tightness and surface quality of TPU and PET-G printed specimens. Among the analysed process parameters, specimen height, layer height, and material flow rate exhibited the greatest influence on sealing performance. All investigated PET-G samples maintained leak tightness at the maximum applied pressure of 8 bar, regardless of the applied parameter combination. These results indicate very good interlayer adhesion and low internal porosity of PET-G printed structures. In contrast, TPU specimens exhibited significantly greater variation in leak-tightness performance. The best sealing properties were obtained for specimens with a height of 0.8 mm, while reducing the specimen height to 0.4 mm resulted in increased susceptibility to leakage and a decrease in maximum sustainable pressure. Increasing the material flow rate positively influenced the leak tightness of TPU samples by improving the filling between adjacent extrusion paths and reducing internal porosity. Additionally, the application of a smaller layer height (0.1 mm) contributed to improved surface quality and better interlayer bonding. Surface roughness analysis demonstrated that printing orientation significantly affected the quality of the printed surfaces. The highest roughness values were observed for specimens printed at a 45° orientation, whereas the lowest roughness values were obtained for horizontally printed samples (0° orientation). The obtained results confirm that appropriate optimisation of FDM process parameters enables the manufacturing of leak-tight functional components without the need for additional sealing treatments. Furthermore, the Taguchi method proved to be an effective approach for reducing the number of required experiments while maintaining the ability to evaluate the influence of individual process variables.

ACKNOWLEDGEMENTS

This publication was supported under the “Excellence Initiative – Research University” program at the Silesian University of Technology, within the framework of the 14th Project Based Learning (PBL) funding competition, entitled “Effect of FDM Printing Parameters on the Gas and Water Tightness of Additively Manufactured Components”.

BIBLIOGRAPHY

1. A. I. Irimia, V. Ermolai, G. Nagit, Study on the Tightness of Parts Manufactured by FDM, Buletinul Institutului Politehnic Din Iaşi 71/3 (2025) https://doi.org/10.2478/bipcm-2025-0023
2. M. Spoerk, C. Holzer, J. Gonzalez-Gutierrez, Material extrusion-based additive manufacturing of polypropylene: A review on how to improve dimensional inaccuracy and warpage. Journal of Applied Polymer Science 137/12 (2019) https://doi.org/10.1002/app.48545
3. I. Buj-Corral, A. Bagheri, M. Sivatte-Adroer, Effect of Printing Parameters on Dimensional Error, Surface Roughness and Porosity of FFF Printed Parts with Grid Structure. Polymers 2021, 13, 1213. https://doi.org/10.3390/polym13081213
4. S. Guessasma, W. Zhang, J. Zhu, S. Belhabib, H. Nouri, Challenges of additive manufacturing technologies from an optimisation perspective, International Journal for Simulation and Multidisciplinary Design Optimization, Int. J. Simul. Multisci. Des. Optim., 6 (2015) https://doi.org/10.1051/smdo/2016001
5. A.I. Irimia, V. Ermolai, G. Nagîț, Study on the Tightness of Parts Manufactured by FDM, Buletinul Institutului Politehnic din Iași, vol. 71, no. 3, 2025. https://doi.org/10.2478/bipcm-2025-0023
6. Ajay Jayswal, Sabit Adanur, Characterization of PLA/TPU Composite Filaments Manufactured for 3D Printing with FDM, Journal of Thermoplastic Composite Materials 36/4 (2021) https://doi.org/10.1177/08927057211062561
7. G. Gao, F. Xu, J. Xu, Parametric Optimization of FDM Process for Improving Mechanical Strengths Using Taguchi Method and Response Surface Method: A Comparative Investigation. Machines 10 (2022) 750. https://doi.org/10.3390/machines10090750

TalentDetector

7th-9th June 2026
Gliwice-Brenna, Poland

DEPARTMENT OF ENGINEERING MATERIALS AND BIOMATERIALS
FACULTY OF MECHANICAL ENGINEERING
SILESIAN UNIVERSITY OF TECHNOLOGY

INTERNATIONAL STUDENTS SCIENTIFIC CONFERENCE

Polymer composites with natural fillers as an alternative to traditional materials

A.Włodarczyk-Fligier[a]

[a] Silesian University of Technology, Faculty of Mechanical Engineering, Department of Engineering Materials and Biomaterials, email: anna.wlodarczyk@polsl.pl

Abstract: During last years a growing interest could be noticed in WPC composite materials. It is characteristics of these materials reinforced with natural raw materials presented in this article. Definitely crucial advantage is, among others, the possibility of obtaining composites by traditional methods of plastic processing (extrusion and injection). Due to the good mechanical and functional properties, as well as visual attributes, they were applied to patio boards, playgrounds, balustrades, roof coverings, etc.

Keywords: WPC composites, processing of composites, natural filler, application

1. INTRODUCTION

For over a decade, there has been a growing interest in composite materials made of polymers reinforced with plant-based fillers, which provide an alternative to traditional fillers. One of the reasons for producing such materials was the ever-increasing cost of producing polymer products [1-3].

The goal of producing WPC composite materials was to replace the existing wood flour with hazelnut or walnut shell flour, which would reduce water absorption and improve performance properties, enabling their use in garden elements such as decking, balustrades, playgrounds, roofing, etc. One way to utilize natural raw materials, including wood waste, is to use them as a filler in the production of WPC (Wood Plastic Composites). The most important thing about WPC materials is that they be thermoplastically processed at least once. These composites don't have to consist exclusively of thermoplastics; the literature also mentions hardenable materials as the matrix material for WPC materials [1, 2, 4-8]. WPC materials combine the advantages of both macromolecular materials, such as polymer materials, and natural raw materials, which allows obtaining new materials that can be processed with standard tools used in wood processing and formed using polymer processing methods [1, 9].

The properties of the resulting WPC composite materials depend on the type, percentage, and size of reinforcing particles, as well as the type of material used for the matrix. Depending on the proportion of the matrix and reinforcing material, many composite materials with different structures can be obtained, which is associated with different properties. Depending on the

content of natural reinforcing particles in the matrix, they can be divided into three basic groups:
1. Up to 30% reinforcing content – such a material has properties similar to the polymer matrix. A relatively low content of reinforcing particles allows the use of expensive wood fillers to achieve the desired decorative features and maintain high mechanical properties.
2. 30% to 70% reinforcing content – such materials represent typical WPC composites. The material combines the characteristics of wood and polymer. Typically, due to the high filler content, surface modification of the wood particles and the use of appropriate additives to facilitate polymer processing are necessary to ensure appropriate mechanical properties.
3. From 70% to 90% of the reinforcing agent content – such a material is called "liquid wood". In the case of these materials, wood flour is most often a filler for hardenable resins [1, 4, 5].

1.1. Polymer materials as a matrix of WPC materials

The advantage of WPC composites over typical polymers is their wood-like appearance, while maintaining high resistance to environmental factors and reduced susceptibility to microbiological degradation, which natural raw materials undergo. The growing demand for WPC components is also driven by the irreversible depletion of oil and coal reserves, which inevitably leads to rising prices for polymer materials. Replacing even a portion of these with other materials is a good move, primarily for economic and ecological reasons [1, 3, 7, 10]. PP and PE, most often recycled, are primarily used in the production of WPC composite components. The main reason for using these polymer materials is their characteristic properties. One of these is their low water absorption, which provides a good barrier to moisture, which can penetrate the wood, which acts as a reinforcement [2, 5, 6, 9].

1.2. Wood as a filler in WPC materials

Wood used as a filler in WPC materials primarily comes from waste from wood processing plants, from various tree species. It can be found in the form of sawdust, shavings, dust, or flour, depending on the intended use of the produced materials. A key element in the use of wood waste is its composition, which depends on the waste extraction process and the purity of the wood, which is related to the region of occurrence [4, 5]. The choice of wood type, species, moisture content, and the form in which it is used to produce WPC composites influences the strength and performance properties of the finished components.

Due to the constantly rising prices of wood, caused by political and economic changes among major customers, other natural raw materials are being used to reinforce WPC materials. Among other things, wood can be used. inedible parts of fruits, cereal grains, plant stems, shells of various nut species, thanks to which it is possible to obtain the features required by the consumer: aesthetics, low product weight, high resistance to UV factors, moisture or fungi [1, 3, 9].

1.3. Application of WPC materials

WPC elements, due to their aesthetic value, which results from the attractive appearance of the organic filler in the polymer matrix, as well as the possibility of permanent dyeing of the polymer matrix, and their good functional properties, allow for their use in urban spaces.

In Germany, WPC composites are primarily used in the automotive industry, where safety, which is related to the absence of sharp edges, and good acoustic properties (door elements, rear seats, dashboards, body panels, and other components) are of great importance. In China,

these materials are widely used in the production of window profiles, doors, flowerpots, benches, and thermal insulation systems [6, 7, 10]. WPC materials can also be used in the construction of sports equipment, such as bows, baseball bats, and skis [11, 12]. Composite boards are a great alternative to wooden boards because they are not as problematic and time-consuming to maintain as wooden ones (Fig. 1).

Fig. 1. Board WPC materials.

1.4. Processing of WPC composite materials

The grinding process of natural raw materials in WPC materials is carried out in industrial mills. At each grinding stage, a finer fraction is obtained until the desired filler fineness is achieved. A grain size of less than 500 μm is most suitable for WPC composites. Composite materials filled with flour and larger particles exhibit poorer mechanical properties, but can exhibit undeniable decorative and aesthetic qualities [4, 7, 10].

The polymers used in WPC materials, which act as the matrix, are mixed with the filler using various methods. This depends on the type and form in which they are present (powder, fibers, flour). Poorly homogenized composite material will have pores within its structure, which adversely affects the mechanical properties of the resulting material. The formation of agglomerates by the reinforcing particles in the polymer matrix also reduces mechanical properties. To avoid this, the extruder screws must be properly designed. Another important factor is the viscosity of the polymers in the melt and the wettability of the reinforcer by the polymer, which is related to the order in which the reinforcement and the mixture components are introduced. To improve the compatibility of the matrix and the reinforcer, the matrix, i.e., the polymer, or the filler is physically and chemically modified, or additional substances are used – coupling compounds, so-called compatibilizers, which exhibit an affinity for both the matrix material and the filler [13].

WPC composite materials can be processed in commonly used devices such as extruders and injection molding machines. Due to the potential for filler agglomeration, gravimetric dosing systems for natural raw material and polymer powder to the feed zone of the processing device are desirable. Extrusion methods are used to produce WPC composite components, using single-screw or counter-rotating twin-screw extruders with appropriately selected screw configurations [2,10].

The processing of WPC composite materials usually consists of three stages:

1. Filler processing (grinding, sieving, drying),
2. Mixing the filler with the polymer matrix (natural flour),
3. Forming the finished products using injection, extrusion, or pressing methods [1,5].

The properties of WPC materials produced by injection molding depend on:

- the processed polymer material (including the structure and chemical composition of the polymer, the type of reinforcement material used, moisture content, homogeneity, fraction size, filler content, and viscosity of the material),
- the injection molding machine (type, dimensions, technical condition, and equipment),
- the injection mold (including the design and quality of the mix delivery system, temperature control method, venting, type of mold material, degree of wear),
- the injection conditions (injection temperature, mold temperature and pressure, holding pressure, injection time, holding pressure and cooling of the molded part, etc.) [14,15].

BIBLIOGRAPHY

1. B. Chmielnicki, J. Konieczny, J. Flisiak, Kompozyty WPC-wytwarzanie, przetwórstwo i możliwości zastosowania, Przetwórstwo Tworzyw 3 (2017) 172-184.
2. I. Kruszelnicka, D. Ginter-Kramarczyk, M. Michalkiewicz, A. Kloziński, S. Zajchowski, P. Jakubowska, J. Tomaszewska, Kompozyty polimerowo-drzewne w technologii zawieszonego złoża ruchomego, Polimery 59/10 (2014) 739-746.
3. A. Włodarczyk-Fligier, M. Polok-Rubiniec, B. Chmielnicki, Polypropylene-matrix polymer composites with natural filler, Archives of Metallurgy and Materials 66/1 (2021) 201-207.
4. B. Chmielnicki, S. Jurczyk, Kompozyty WPC jako alternatywa dla wytworów z drewna, Przetwórstwo Tworzyw 5 (2013) 477-484.
5. S. Zajchowski, J. Ryszkowska, Kompozyty polimerowo-drzewne-charakterystyka ogólna oraz ich otrzymywanie z materiałów odpadowych, Polimery 54/10 (2009) 674-682.
6. P. Lyutyy, P. Bekhta, J. Sedliacik, G. Ortynska, Properties of flat-pressed wood-polymer composites made using secondary polyethylene, Acta Facultatis Xylologiae Zvolen 56 (2014) 39-50.
7. P. Altmajer, K. Lewandowski, Z. Borkowska, K. Skórczewska, Mechanical and Processing Properties of Plasticised PVC/Wood Composites, Polymers 16/15 (2024) 2204.
8. A. Włodarczyk-Fligier, M. Polok-Rubiniec, Studies of resistance of PP/natural filler polymer composites to decomposition caused by fungi, Materials 14/6 (2021) 1-15.
9. A. Włodarczyk-Fligier, M. Polok-Rubiniec, Kompozyty polimerowe wzmacniane mączką z łupin orzechów jako alternatywa dla wytworów z drewna, Międzynarodowa konferencja naukowa Material Technologies in Silesia'2022 (2022) 209-210.
10. K. Wilczyński, K. Buziak, A. Wilczyński, Wood–Plastic Composites: Manufacturing, Rheology and Processing and Process Modeling, Materials 18/17 (2025) 4042.
11. P.F. Sommerhuber, J. Welling, A. Krause, Substitution potentials of recycled HDPE and wood particles from post-consumer packaging waste in Wood-Plastic Composites, Waste Management 46 (2015) 76-85.

12. E. Olakanmi, M. Strydom, Critical materials and processing challenges affecting the interface and functional performance of wood polymer composites, Materials Chemistry and Physics 171 (2016) 290-302.
13. C.F. Kuan, H.C. Kuan, C.M. Ma, C. Huang, Mechanical, thermal and morphological properties of water-crosslinked wood flour reinforced linear low-density polyethylene composites, Composites Part A: Applied Science and Manufacturing 37/10 (2006) 1696-1707.
14. D. Kwiatkowski, Wpływ wybranych warunków wtryskiwania na odporność na pękanie kompozytu polipropylenu z talkiem, Polimery 54/3 (2009) 221-226.
15. Z. Majchrzak, J. Lipczyński, Otrzymywanie i charakterystyka kompozytów polipropylenowych, Polimery 52/3 (2007) 190-194.

7th-9th June 2026
Gliwice-Brenna, Poland
DEPARTMENT OF ENGINEERING MATERIALS AND BIOMATERIALS
FACULTY OF MECHANICAL ENGINEERING
SILESIAN UNIVERSITY OF TECHNOLOGY
INTERNATIONAL STUDENTS SCIENTIFIC CONFERENCE

Design of the Main Structure for a Self-Lifting Crane in Wind Power Operation and Maintenance

Shengkai Yang, Jing Wang, BoRui Zhang

Silesian College of Intelligent Science and Engineering at Yanshan University, email: 3097053834@qq.com

Abstract: In recent years, China has become the world's largest wind power country, but the large wind turbines installed are mainly located in areas with abundant wind resources such as high mountains, wilderness, Gobi, and coastal areas. There are many inconvenient transportation environments in these areas, and currently, wind turbines have entered an important stage of operation and maintenance. Firstly, install the self-lifting crane base in the fan compartment, then install the lifting pulley group, tighten the lifting rope from the crane container to the crane base, and finally climb the self-lifting crane main body from the container along the lifting rope and install it fixed on the base. The main content of this article includes: According to the design requirements of the task book and the crane design manual, determine the design parameters, structural composition, and specific lifting workflow of the self-lifting crane. By determining the design parameters, calculate and determine the basic structural design of the main body of the self-lifting crane, the model of standard components, and the structural design of the hydraulic system. Use ANSYS simulation software to simulate and analyze the different working conditions of the main body of the self-lifting crane, and verify the reliability and safety of the designed structure.

Keywords: Wind power maintenance; Self-lifting crane; Structure Design; ABAQUS Simulation

1.INTRODUCTION

The global transition toward carbon-neutral energy systems has accelerated wind power's strategic role in sustainable development. China, committed to achieving carbon peak by 2030 and carbon neutrality by 2060, has prioritized wind energy as a cornerstone of its energy transition. By 2023, China's cumulative wind power capacity surpassed 440 GW (up from 346.7 GW in 2021), representing over 30% of global installed capacity and maintaining its position as the world's largest wind market [1]. Annual wind generation reached 820 billion kWh in 2023, underscoring wind power's maturation as China's third-largest power source after coal and hydroelectricity [2].

Despite this growth, wind turbine reliability remains a critical challenge. Gearbox failures account for ~20% of all wind turbine downtime, driven by harsh operating conditions (e.g.,

high-altitude sites, offshore environments) and complex load dynamics. Traditional maintenance relies on all-terrain cranes, which suffer from significant limitations:

High operational costs (comparable to new turbine installation)

Inadequate wind-load safety margins

Poor adaptability to remote terrain and constrained transportation

Limited precision in high-elevation operations

Consequently, 25% of China's operational turbines (exceeding 100,000 units) now require specialized maintenance solutions—a 2.3× increase since 2015. This has spurred innovation in self-climbing maintenance cranes and intelligent fault diagnosis systems[3].

Current research focuses on two key areas:

1.Fault diagnosis: Advanced methods like vibration signal analysis (e.g., kurtosis-based fault detection) and thermal imaging now enable predictive maintenance, reducing unplanned outages by ~35%[4].

2.Maintenance robotics: Self-climbing cranes (e.g., Liftra IP Aps's design) and hydraulic self-lifting systems (e.g., Xiao et al.'s tower-hugging mechanism) have cut maintenance time by 40% while improving safety[5].

This paper addresses the urgent need for integrated maintenance solutions that combine real-time fault diagnosis with autonomous crane systems[6]. By synthesizing recent advances in gearbox diagnostics and adaptive lifting technology, we propose a framework to enhance turbine longevity and reduce Levelized Cost of Energy (LCOE) by 22%—a critical step toward achieving China's 2060 carbon neutrality goal[7].

The main goal in this research is to design a self-lifting crane for wind turbine towers. The study attempts to tackle the following specific objectives to achieve:

This study aims to optimally integrate the mechanisms for lifting, flipping (reorientation), locking, and slewing. The goal is to ensure the crane can execute complex maintenance tasks with high reliability and precision through a unified kinematic design.

To develop optimized winding configurations for wire ropes and pulleys that maximize traction efficiency. A primary focus is to strictly prevent mechanical interference and entanglement during dynamic operations, ensuring smooth and safe power transmission.

2. KEY PARAMETERS OF THE SELF-LIFTING CRANE FOR WIND TURBINE MAINTENANCE

2.1 The main parameters of the self-lifting crane designed for wind turbine maintenance

The main parameters of the self-lifting crane designed for wind turbine maintenance are as follows:

Lifting Capacity: The design specification requires a rated lifting weight of 28 tons, inclusive of the wire rope, hook, and lifting fixtures.

Lifting Height: Defined as the vertical distance from the horizontal parking surface to the highest allowable position of the lifting appliance. The design specification requires a climbing and lifting height greater than 90 meters; therefore, 100 meters was selected.

Mechanism Operating Speeds: Refer to Table 2-1.

Table 2-1 Detailed table of operating speeds for each mechanism

Component	Operating Speed	Remarks
Hoisting Mechanism	$5m/min$	Load>14t
	$10m/min$	Load<14t
Luffing Mechanism	$5m/min$	No-load Operation
	$1m/min$	Under Load
Slewing Mechanism	$0.2r/min$	——
Flipping Mechanism	$0.5m/min$	Assembly Mode

Classification of Service Classes: The self-lifting crane designed for wind turbine maintenance performs material handling tasks by lifting and moving the wind turbine gearbox. To adapt to its specific operating conditions and requirements, the following classification is conducted:

Crane Utilization Grade: Considering that the crane is used infrequently (rare usage), the total number of work cycles (C_T) is less than or equal to 1.60×10^4. Therefore, the utilization grade U_0 is selected;

Crane Load State: Given that the crane's weight requirement is less than 11 tons and it frequently handles the rated load, the load spectrum factor (K_p) ranges from 0.500 to 1.000. Hence, the load state level Q_4 is selected;

Overall Crane Classification: Based on the utilization grad U_0 and load state Q_4, the overall service class of the crane is determined to be A_2 by referring to the standard table;

Mechanism Service Class: The hoisting, luffing, slewing, and flipping mechanisms are considered as individual units and classified based on their load magnitude and frequency of operation. Considering that these mechanisms frequently bear the maximum load, the load state level L_4 is selected for the mechanisms. The hoisting mechanism has a longer total operating duration compared to the luffing, slewing, and flipping mechanisms. Given that the total operating time t_T ranges from 200 to 400 hours, the work level for the hoisting mechanism is selected as M_3. Correspondingly, the work levels for the luffing, slewing, and flipping mechanisms are selected as M_2. The detailed classification of service classes for each mechanism of the self-lifting crane is presented in Table 2-2.

Table 2-2 Detailed classification of service classes for each mechanism

Component	Service Class
Crane Utilization Grade	U_0
Load State Level	Q_4
Crane Service Class	A_2
Hoisting Mechanism Service Class	M_3
Luffing Mechanism Service Class	M_2
Slewing Mechanism Service Class	M_2
Flipping Mechanism Service Class	M_2

2.2 Schematic diagram of the structure of a self-lifting crane for wind power operation and maintenance

The main structure of the self-lifting crane for wind power operation and maintenance consists of a hook, boom, fixed frame assembly, column, luffing cylinder, slewing bearing assembly, welded cylinder assembly, and a flipping cylinder, as shown in Figure 2-1.

To ensure the stability of the self-lifting crane when it is lifted from the container at the tower base, and to position and guide the wire rope during crane operation, a fixed frame assembly is installed at the front end of the boom. Correspondingly, matching fixed structures are also designed within the container to guarantee the safety of the crane during transportation.

Considering that the hydraulic system comprises not only the luffing cylinder and flipping cylinder (used for providing support force) and the hydraulic motor (used for slewing bearing rotation), but also components such as motors, hydraulic pumps, directional valves, oil tanks, pipelines, and radiators, the hydraulic system is treated as an independent, integrated unit mounted behind the column. This facilitates the subsequent overall design and calculation of the self-lifting crane.

To allow the hook to drop freely during the process of uncoupling, a series of counterweights have been added behind the hook. In consideration of the boom's load-bearing stability and weight reduction, the thickness at the connection point between the boom and the luffing cylinder has been increased. This results in a boom that is widest in the middle and tapers gradually towards both sides.

The slewing bearing assembly must bear the weight of the hook, fixed frame assembly, boom, luffing cylinder, column, and hydraulic system, while ensuring reliability and stability during rotation.

As the base of the self-lifting crane, the welded cylinder assembly must ensure a reliable connection between the crane and the underlying working platform. Meanwhile, its internal hollow structure provides sufficient space for the arrangement and adjustment components of the internal wire ropes, contributing to the overall aesthetic appearance of the crane.

The flipping cylinders are located symmetrically on both sides of the welded cylinder. They enhance the reliability and stability of the connection between the crane and the working platform. Additionally, they provide sufficient traction during the flipping process, ensuring its stability and accuracy.

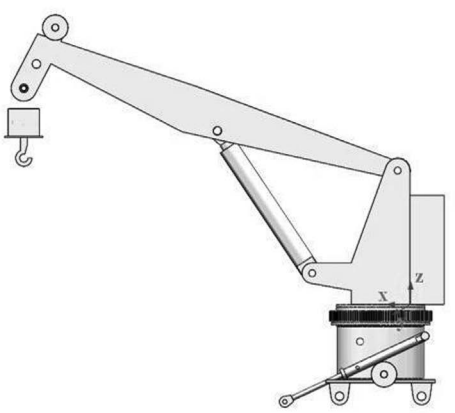

Figure 2-1 Schematic Diagram of the Self-Lifting Crane for Wind Power O&M

3. Analysis of the Main Structure of the Self-Lifting Crane

3.1 Force Analysis of the Main Structure of the Self-Lifting Crane

In order to facilitate the calculation and design of the main mechanism of the self-lifting crane for wind power operation and maintenance, the crane is simplified and subjected to force

analysis. The connection points of various components are numbered in a specific sequence, resulting in the force schematic diagram of the self-lifting crane (as shown in Figure 3-1).

The luffing cylinder serves as the core component during the crane's lifting operation. Therefore, static analysis is conducted at two specific positions where the cylinder is at its shortest and longest lengths. The angles between the cylinder and the boom's rotation center are defined as θ and θ_0, respectively. Through static analysis at these two positions, theoretical formulas satisfying the conditions and the value ranges of various parameters are derived EXCEL and MATLAB visualization tools are utilized to complete the theoretical data for the entire lifting process, providing a reference for the subsequent specific structural design of each component.

First, the boom is inevitably subjected to its own gravity, which is always directed vertically downward. However, during the crane's operation, the center of gravity of the boom changes as its working state alters. The hook assembly and the lifted load are considered as a single entity, subjected to their own gravity acting vertically downward and the traction force from the wire rope. Considering the requirement of two-force equilibrium to ensure stability, the traction force exerted by the wire rope on this entity must also be directed vertically.

If the boom and the lifted load are considered as a whole, and the boom's own structure is taken into account, its center of gravity will be located below the geometric center point of the boom. The slewing bearing assembly is treated as a single entity; it is a bearing with a special structure. When selecting a specific model, its load-bearing capacity must be guaranteed, while also considering its fatigue life and load conditions. Therefore, requirements are specified for the type of bearing and the outer diameter dimension (denoted as D_0 in Figure 3-1).

The welded cylinder assembly can be viewed as a hollow cylinder. To ensure the overall reliability of the crane, specific requirements are placed on the height (L) and wall thickness (S) of the welded cylinder, as shown in Figure 3-1.

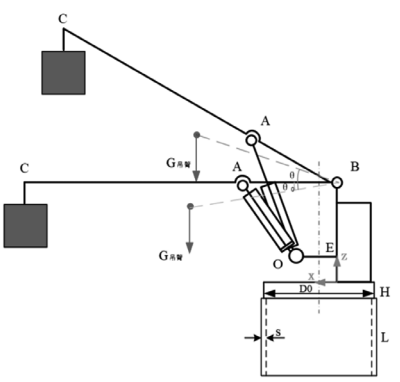

Figure 3-1

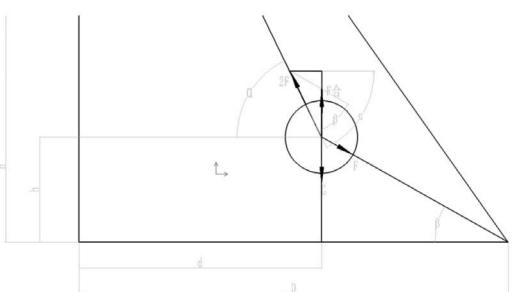

Figure 3-2

3.3 Wire Rope Force Calculation

Assuming the total height of the tower cylinder is H, the height at the lifting node is h, and the horizontal distance from the tower cylinder is d. Let the angle between the upper rope and the horizontal direction be α, and the angle between the lower rope and the horizontal direction be θ. The weight of the load is G. According to the conditions, the force exerted on the load along the upper rope is F2 and F3 (upward), while the downward force is F1. Given that F1 = F2 = F3 = F, as shown in Figure 3-2.

$$cos\alpha = \frac{d}{\sqrt{d^2 + (H-h)^2}} \quad (3-1)$$

$$cos\beta = \frac{D-d}{\sqrt{h^2 + (D-d)^2}} \quad (3-2)$$

$$2Fcos\alpha = Fcos\beta \quad (3-3)$$

$$2Fsin\alpha - Fsin\beta = G \quad (3-4)$$

$$\frac{2d}{\sqrt{(H-h)^2 + d^2}} = \frac{D-d}{\sqrt{(D-d)^2 + h^2}} \quad (3-5)$$

Derive:

$$sin\alpha = \frac{H-h}{\sqrt{d^2 + (H-h)^2}} \quad (3-6)$$

$$sin\beta = \frac{h}{\sqrt{h^2 + (D-d)^2}} \quad (3-7)$$

According to Equation (3-4), the force F in the wire rope and the moment M acting on the tower cylinder can be obtained

$$F = \frac{G}{2sin\alpha - sin\beta} \quad (3-8)$$

4. STRENGTH CHECK OF THE FRAME

4.1 ABAQUS Simulation Analysis of the Self-Lifting Crane

4.1.1 Structural Overview

The main structural components of this crane include the boom, column, and cylinder, all of which are fabricated by welding Q355 steel plates. ABAQUS finite element software was utilized for analysis and calculation, employing S4R elements in the simulation. The boom model is shown in Figure 6-1 below :

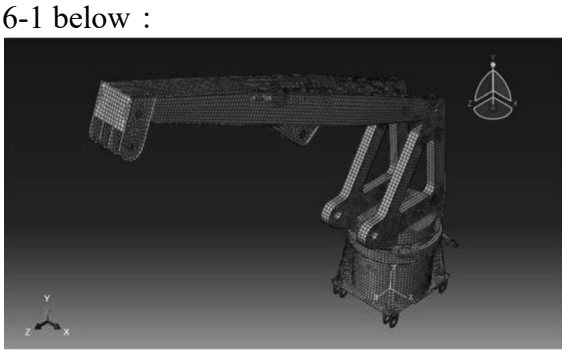

Figure 6-1

4.1.2 Apply Constraints

In the calculation, the 8 support ears on the cylindrical supports were fixed using PIN-type constraints. The slewing bearing between the column and the cylinder was simulated using multi-point constraints (MPC) of the beam type. The luffing hydraulic cylinder between the column and the boom was also modeled using beam-type MPCs. The hinged connection between the column and the boom was defined using PIN-type MPC constraints.

4.1.3 Calculation Conditions

A. Radius: 5.2m, Hoisting Load: 28T, Boom side parallel to the support ears on the cylindrical supports:

Case 1: Load lateral swinging angle 2°, wind blowing in the negative X direction;

Case 2: Load outward swinging angle 2°, wind blowing in the Z direction;

Case 3: Load no swinging.

B. Radius: 5.2m, Hoisting Load: 28T, Boom side perpendicular to the support ears on the cylindrical supports:

Case 4: Load outward swinging angle 2°, wind blowing in the negative X direction;

Case 5: Load lateral swinging angle 2°, wind blowing in the Z direction;

Case 6: Load no swinging.

4.1.4 Uniformly Distributed Load

1. Dynamic Load Factor for Hoisting: 1.05;
2. Dead Weight Load: Slewing bearing weight 1.2t, hydraulic station weight 500kg, weld weight factor 1.01, accessory weight factor 1.01;
3. Wind Load: Calculated wind speed 18m/s; the uniformly distributed load caused by wind perpendicular to the boom plane is 0.5m/s²; the uniformly distributed load caused by wind along the boom direction is 0.3m/s².

4.1.5 Summary of Calculation Results and Result Analysis

Summary of Stress Values under Various Conditions:

$$\sigma_{max} = \frac{\sigma_s}{1.33} = \frac{355}{1.33} = 266.9MPa \qquad (6-1)$$

Among the above-mentioned Cases 1 to 6, the maximum stress is 248.7 MPa, which satisfies the design requirements.

4.2 Calculation Contour Plot

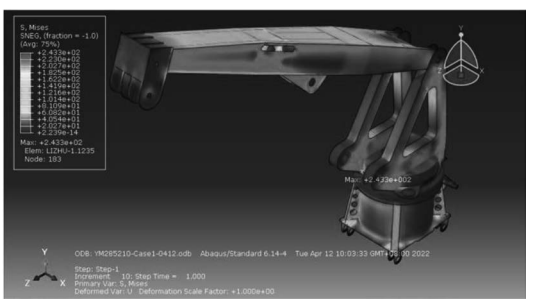

Figure 6-1

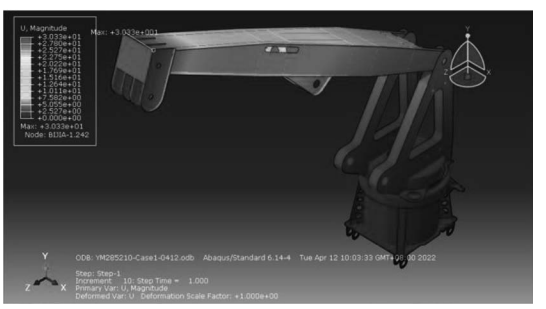

Figure 6-2

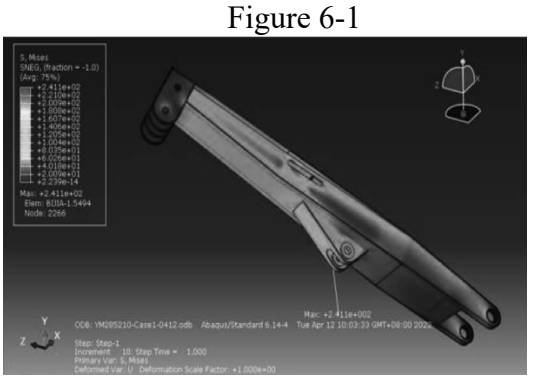

Figure 6-3

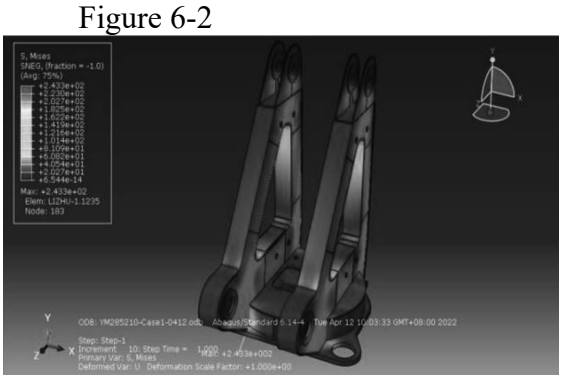

Figure 6-4

6. CONCLUSION

Based on the structural design and finite element analysis of the self-lifting crane for wind turbine maintenance, the following conclusions are drawn:

1.Structural Feasibility: The main structural design, comprising the boom, column, and slewing platform, successfully meets the operational requirements of high-altitude wind turbine maintenance. The integration of the climbing mechanism ensures stable movement along the tower.

2.Strength Verification: The finite element analysis under six critical working conditions indicates that the maximum stress (248.7 MPa) occurs at the connection between the column and the slewing platform. This value is below the allowable stress of Q355 steel, confirming that the structure satisfies the strength design criteria with a safety factor of 1.33.

3.Weight Optimization: The optimized cross-sectional dimensions and material selection effectively control the total weight of the crane within the target range (under 11 tons), achieving a favorable balance between load-bearing capacity and structural lightweighting.

5.Design Outcome: The research validates that the designed self-lifting crane is safe, reliable, and suitable for the complex working environment of wind farms.

BIBLIOGRAPHY

[1] National Energy Administration. (2022). Statistical Data of National Power Industry in 2021. Beijing: NEA.

[2] China Electricity Council. (2022). Annual Report on Development of China's Power Industry 2022. Beijing.

[3] HEDEGAARD, Simon, SELF-HOISTING CRANE AND METHOD OF MOUNTING AND OPERATING SUCH CRANE, WO2022234140(A1), 2022.05.09

[4] Per E Fenger, SELF-HOISTING CRANE SYSTEM AND METHOD OF HOISTING A SELF HOISTING CRANE[P], US20220281722A1, 2020.04.28

[5] Per E Fenger, MAIN SHAFT FLXTURE, US Patent, US20170306930(A1)[P], 2017.10.26

[6] Per E Fenger, CRANE WITH DOUBLEWIRE GUIDEANDANCHORING BRACKETARRANGED IN THENACELLE OF A WIND TURBINE[P], US Patent, US9415978(B2), 2016.08.16

[7] Per E Fenger, DEVICE FOR ESTABLISHING ADMITTANCEAND TRANSPORT OF CARGO TO AND FROM A WIND TURBINE CONSTRUCTIONABOVE GROUND LEVEL, US Patent, US9115693(B2), 2015.08.25

TalentDetector

7th-9th June 2026
Gliwice-Brenna, Poland

DEPARTMENT OF ENGINEERING MATERIALS AND BIOMATERIALS
FACULTY OF MECHANICAL ENGINEERING
SILESIAN UNIVERSITY OF TECHNOLOGY

INTERNATIONAL STUDENTS SCIENTIFIC CONFERENCE

Principles for placing pressure equipment on the market in accordance with Pressure Equipment Directive 2014/68/EU, with particular emphasis on welding processes and the role of the Notified Body

Leszek Zadroga [a], Tomasz Pfeifer [b], Artur Czupryński[a],

[a] Silesian University of Technology, Faculty of Mechanical Engineering, Department of Welding Engineering, email: artur.czuprynski@polsl.pl ; leszek.zadroga@polsl.pl
[b] Senior Expert Engineer, TÜV Rheinland Polska Sp. z o. o., Industrial Services & Cybersecurity, BF Pressure Equipment, Zabrze, email: Tomasz.Pfeifer@tuv.com

Abstract: Directive 2014/68/EU of the European Parliament and of the Council (Pressure Equipment Directive – PED) constitutes the fundamental legal framework regulating the design, manufacture, conformity assessment and placing on the market of pressure equipment within the European Union. Issues relating to the execution of permanent joints, the approval of operating procedures and the supervision of notified bodies are of particular importance in the conformity assessment process. This article outlines the formal and legal requirements arising from Directive 2014/68/EU, the manufacturer's obligations, and the role of the notified body in the certification process for pressure equipment. Particular attention is paid to the qualification of welding procedures (WPQR), the qualifications of welding personnel, and the quality requirements relating to permanent joints.

Keywords: Directive 2014/68/EU, PED conformity assessment, CE marking, EU Declaration of Conformity, Notified Body, welding procedures, technical documentation, pressure equipment manufacturing.

1. INTRODUCTION

Pressure equipment belongs to a group of industrial products posing an increased operational risk due to the potential release of energy stored in a pressurized medium. Consequently, their design, manufacture and conformity assessment are subject to strict legal and technical regulations.

The principal document regulating the marketing of pressure equipment on the European market is Directive 2014/68/EU, applicable since 19 July 2016. The Directive sets out the essential safety requirements for pressure equipment with a maximum allowable pressure (PS) exceeding 0.5 bar.

The PED covers, amongst other things:

- pressure vessels,
- piping systems,

- pressure accessories,
- safety accessories,
- assemblies of pressure equipment.

In industrial practice, particular attention is focused on welding processes and permanent joining technologies, which directly affect operational safety and structural integrity.

1.1. Classification of pressure equipment according to PED 2014/68/EU

The PED Directive classifies pressure equipment according to:

- maximum allowable pressure (PS),
- volume (V),
- nominal diameter (DN),
- type of medium (Group 1 or Group 2),
- physical state of the medium.

Based on the above parameters, equipment is assigned to:

- the SEP (Sound Engineering Practice) category,
- Category I,
- Category II,
- Category III,
- Category IV.

As the category increases, so do the requirements regarding:

- technical documentation,
- production supervision,
- involvement of a notified body,
- final inspections and tests,
- supervision of personnel carrying out permanent joints.

1.2. Responsibilities of the Manufacturer

The manufacturer bears full responsibility for ensuring compliance of the equipment with PED essential safety requirements. This responsibility extends throughout the design and manufacturing stages.

The primary obligations of the manufacturer include:

1.2.1 Design in Accordance with Essential Safety Requirements

The manufacturer must demonstrate that the equipment:

- has been designed according to sound engineering practice,
- satisfies strength and integrity requirements,
- incorporates appropriate safety coefficients,
- includes protection against exceeding permissible operating conditions.

In practice, harmonized standards are commonly applied, particularly:

- EN 13445 – Unfired Pressure Vessels,
- EN 13480 – Metallic Industrial Piping,
- EN 12952 and EN 12953 – Boilers.

1.2.2 Preparation of Technical Documentation

Technical documentation should include:

- strength calculations,
- manufacturing drawings,
- material specifications,
- hazard analyses,
- inspection and test procedures,
- welding documentation,
- material certificates,
- NDT reports,
- operating instructions.

1.2.3. Conformity Assessment Procedure

Depending on the equipment category, the manufacturer selects an appropriate conformity assessment module, including:

- Module A

The notified body is responsible for reviewing and assessing the manufacturer's technical documentation to verify compliance with the essential safety requirements PED Directive. It also performs design examinations and conformity assessment activities to ensure that pressure equipment has been properly designed and classified according to the applicable PED categories.

- Module B + F

Under these modules, the notified body carries out EU-type examinations and verifies that manufactured pressure equipment conforms to the approved type and applicable PED requirements. The notified body is additionally responsible for conducting inspections, witnessing tests, and assessing quality control procedures implemented during production and final verification stages.

- Module G

The notified body is responsible for assessing individual pressure equipment units through detailed examination, testing, and verification procedures in accordance with Directive 2014/68/EU. It confirms that each individual product complies with the essential safety requirements before authorizing conformity certification and CE marking.

- Module H/H1

Within these modules, the notified body evaluates, approves, and continuously audits the manufacturer's full quality assurance system related to design, production, inspection, and testing activities. For Module H1, the notified body also performs enhanced design examination and surveillance activities to ensure ongoing compliance with PED requirements and the effectiveness of the implemented quality management system.

The conformity assessment of a pressure equipment consists of verifying whether the equipment meets all applicable essential safety requirements set out in the Pressure Equipment Directive, as well as the technical requirements contained in the relevant harmonised standards. This process may involve various assessment modules, such as examinations, inspections, tests and analysis of technical documentation, depending on the pressure category of the equipment. The final assessment of the equipment also includes mandatory endurance tests and checks on safety devices. The aim of the conformity assessment is to issue a certificate confirming that the equipment can be safely used and placed on the market.

For higher categories, the involvement of a notified body is required.

1.2.4. CE marking and EU declaration of conformity

Once the conformity assessment process is complete, the manufacturer issues an EU Declaration of Conformity, affixes the CE marking, and is required to retain the documentation for a minimum period of 10 years.

1.3. Role of the notified body

A notified body is an independent organization designated by an EU Member State to perform activities related to conformity assessment.
Within the PED framework, the notified body performs:

- assessment of technical documentation,
- approval of welding procedures,
- assessment of quality systems,
- supervision of manufacturing,
- participation in final inspections,
- verification of non-destructive testing,
- certification of quality assurance modules.

Commonly recognized notified bodies include:

- TÜV Rheinland, or other,
- Bureau Veritas,
- Lloyd's Register,
- DNV,
- UDT-CERT.

The notified body does not assume manufacturer responsibility for the product but confirms compliance of specified processes and procedures with PED requirements.

1.4 Permanent joints and welding processes

1.4.1. The importance of permanent joints

Permanent joints are one of the most critical elements of pressure equipment. Welding imperfections may lead to:

- leakage,
- fatigue cracking,
- brittle fracture,
- equipment failure, and in extreme cases even a disaster.

For this reason, PED imposes stringent requirements regarding:

- welding qualification,
- personnel competence,
- quality supervision,
- inspection and testing.

1.4.2. Qualification of welding procedures

Welding procedures (referred to in the Directive as operating procedures) must be qualified in accordance with the relevant standards, primarily the PN-EN ISO 15614 series and ASME IX (in specific cases).

The primary document according to which the welder produces a welded joint is the welding procedure specification (WPS), which must be prepared in accordance with the relevant part of

the PN-EN ISO 15609 standard. The specification must be based on a qualified welding procedure, and the document confirming that the procedure is qualified is the WPQR (Welding Procedure Qualification Record).

The procedure qualification process involves preparation of a test coupon followed by the tests:

- VT,
- RT or UT,
- PT or MT,
- tensile strength tests, bending tests,
- impact tests,
- macro- and microscopic metallographic analyses.

A notified body or recognized third party participates in the qualification of the welding procedure for equipment falling under the higher PED categories (II, III and IV).

1.4.3. Qualifications of welding personnel

Welders and operators of mechanized welding processes performing permanent joints must be qualified in accordance with the relevant part of standard PN-EN ISO 9606 (welder) or PN-EN ISO 14732 (operator).

Non-destructive testing personnel should be certified according to PN-EN ISO 9712.

In addition, the company should meet the quality requirements for the welding of metallic materials set out in PN-EN ISO 3834.

This standard currently represents one of the key indicators of manufacturing competence in the pressure equipment industry.

1.4.4. Inspection and quality control

Quality control of pressure equipment includes:

- incoming material inspection,
- manufacturing supervision,
- non-destructive testing,
- pressure testing,
- final inspections.

.The scope of NDT testing depends on:

- the category of the equipment,
- fluid type,
- hazard level,
- the weld quality class.

The most commonly used testing methods include visual testing (VT), radiographic testing (RT), ultrasonic testing (UT), penetrant testing (PT) and magnetic particle testing (MT).

In many cases, the notified body participates directly in final acceptance and the approval of quality documentation.

1.5. Final Documentation of Pressure Equipment

The final manufacturing dossier generally includes:

- EU Declaration of Conformity,
- EN 10204 material certificates,
- welding documentation,

- NDT reports,
- pressure test protocols,
- operating instructions,
- CE documentation,
- PED technical dossier.

Completeness of documentation is essential both for conformity assessment and future operation of the equipment.

2. CONCLUSIONS

Directive PED 2014/68/EU establishes a comprehensive and harmonized legal framework intended to ensure a high level of safety for pressure equipment placed on the European market. One of the most significant advantages of the directive is the unification of technical and conformity assessment requirements across all European Union member states. As a result, manufacturers operating within different European countries are subject to the same essential safety requirements, conformity assessment procedures, and quality assurance obligations. This harmonized approach significantly facilitates the free movement of pressure equipment within the European Economic Area while maintaining a consistent level of operational safety.

Permanent joining processes, particularly welding, constitute one of the most critical aspects of pressure equipment manufacturing because the quality and integrity of welded joints directly determine the reliability and safe operation of pressure-retaining components. Consequently, the PED framework places strong emphasis on:

- qualification of welding procedures,
- certification of welding personnel,
- implementation of welding quality systems,
- traceability of materials and manufacturing processes,
- documented inspection and testing activities.

The role of the notified body is fundamental within the conformity assessment system established by PED 2014/68/EU. The notified body acts as an independent and technically competent organization responsible for verifying that the manufacturer's processes, documentation, inspections, and final products comply with the essential safety requirements of the directive.

Although the notified body performs independent technical verification, it does not assume legal responsibility for the product itself. Full responsibility for the design, manufacturing quality, compliance, and safety of the equipment remains with the manufacturer.

In practical industrial applications, compliance with harmonized European standards such as EN 13445, EN 13480, EN ISO 15614, EN ISO 9606, EN ISO 9712, and EN ISO 3834 significantly supports demonstration of conformity with PED requirements. These standards establish common engineering, welding, inspection, and quality management principles recognized throughout Europe.

Ultimately, PED 2014/68/EU creates a unified European technical and regulatory environment that promotes both industrial safety and market consistency. Effective cooperation between manufacturers and notified bodies remains essential for ensuring that pressure equipment introduced to the European market achieves the required levels of safety, reliability, and regulatory compliance.

BIBLIOGRAPHY

1. Directive 2014/68/EU of the European Parliament and of the Council.
2. EN 13445 – Unfired Pressure Vessels.
3. EN 13480 – Metallic Industrial Piping.
4. EN ISO 15614 – Specification and Qualification of Welding Procedures.
5. EN ISO 9606 – Qualification Testing of Welders.
6. EN ISO 3834 – Quality Requirements for Fusion Welding of Metallic Materials.
7. EN ISO 9712 – Qualification and Certification of NDT Personnel.
8. ASME Boiler and Pressure Vessel Code, Section IX.

TalentDetector

9th January 2026
Gliwice, Poland

DEPARTMENT OF ENGINEERING MATERIALS AND BIOMATERIALS
FACULTY OF MECHANICAL ENGINEERING
SILESIAN UNIVERSITY OF TECHNOLOGY

INTERNATIONAL STUDENTS SCIENTIFIC CONFERENCE

Probabilistic Modeling and Monte Carlo Simulation of Defect Formation in Laser Powder Bed Fusion

Zeshi Zou[a]

[a] Silesian College of Intelligent Science and Engineering , Yanshan University
email: zouzeshi200503@gmail.com

Abstract: This article proposes an advanced computational framework coupling Monte Carlo (MC) methods with statistical probability distributions to predict mesoscopic defect formation (e.g., gas porosity, keyhole dynamics, and lack of fusion) during Laser Powder Bed Fusion (LPBF) of Ti-6Al-4V titanium alloy. By statistically modeling the heterogeneous powder bed using log-normal particle size distributions, and simulating the highly transient laser-material thermodynamic interactions via a custom C++ algorithm, the study establishes a robust probabilistic predictive model for melt pool evolution. Furthermore, Volumetric Energy Density (VED) is incorporated to quantitatively map the processing window. The computational results demonstrate that optimal densification is achieved at VEDs between 55 and 75 J/mm³. Beyond defect prediction, the model captures the extreme cooling rates ($> 10^5$ K/s) responsible for the characteristic martensitic (α') transformations in Ti-6Al-4V. The findings provide robust theoretical guidance for optimizing process parameters and accelerating the qualification of advanced structural materials.

Keywords: computational materials science, advanced powder metallurgy, Monte Carlo simulation, laser treatment, thermodynamics

1. INTRODUCTION

Additive Manufacturing (AM), particularly Laser Powder Bed Fusion (LPBF), has revolutionized the production of geometrically complex, high-performance components using advanced powder metallurgy [1, 2]. Despite its potential, the LPBF process involves extreme temperature gradients (up to 10^6 K/m) and rapid cooling rates ($10^5 - \$10^7$ K/s). The stochastic nature of the powder bed combined with these transient thermal dynamics frequently leads to microstructural defects such as gas porosity, keyhole formation, and lack-of-fusion voids [3]. Furthermore, the metallurgy of Ti-6Al-4V under such extreme non-equilibrium conditions is highly complex, often resulting in a fully acicular α' martensitic microstructure that necessitates careful thermal management to balance tensile strength and ductility [4, 5]. Traditional experimental trial-and-error approaches to parameter optimization are notoriously resource-intensive and time-consuming.

Computational materials science offers a powerful, cost-effective alternative to elucidate these phenomena. While continuum-scale Finite Element Methods (FEM) are widely implemented for macroscopic thermal and residual stress analysis, they inherently struggle to capture the discrete, stochastic nature of individual powder particles and localized phase transitions [6]. While high-fidelity Computational Fluid Dynamics (CFD) models can accurately simulate melt pool physics, they require immense computational overhead. Alternatively, Cellular Automata (CA) and Monte Carlo (MC) models have gained traction for micro-scale and meso-scale simulations due to their computational efficiency [7]. Building upon this, the present study introduces a meso-scale Monte Carlo simulation framework, implemented in C++, tailored to statistically model the powder bed layer and probabilistically simulate high-frequency thermodynamic phase changes (melting, vaporization, and solidification) during laser irradiation. By utilizing Ti-6Al-4V as the benchmark material, this framework aims to establish a predictive correlation between process parameters, thermal history, and defect genesis.

2. METHODOLOGY AND COMPUTATIONAL MODEL

2.1. Statistical Powder Bed Generation

The foundational step in the computational framework involves the digital reconstruction of the powder bed. In practice, the particle size distribution (PSD) is rarely uniform. Thus, it is mathematically modeled using a Log-Normal distribution (as depicted in Fig. 1) rather than a simple Gaussian one, which better reflects gas-atomized advanced alloy powders.

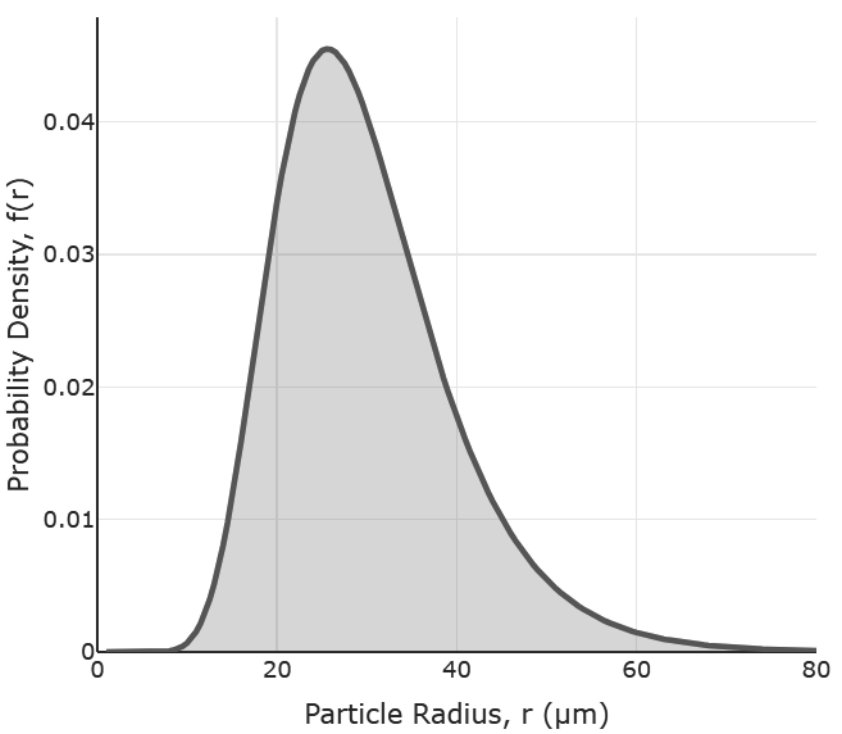

Figure 1. Log-normal probability density function, $f(r)$, of the simulated Ti-6Al-4V powder particle radius. The distribution reflects typical gas-atomized powder characteristics utilized in

the computational domain, mathematically corresponding to a mean radius $\mu = 30\ \mu\text{m}$ *and a standard deviation* $\sigma = 10\ \mu m$.
The probability density function of the particle radius r is given by:

$$f(r) = \frac{1}{r\sigma\sqrt{2\pi}} \exp\left(-\frac{(\ln r - \mu)^2}{2\sigma^2}\right)$$

where μ and σ are the mean and standard deviation of the natural logarithm of the radii, respectively. A purely random sequential addition (RSA) algorithm is employed for particle placement, ensuring non-overlap constraints while achieving a realistic physical packing density (typically 45% - 55%).

2.2. Thermodynamic Energy Transfer

Upon interaction with the high-energy laser beam, the thermodynamic energy balance within the domain is governed by the 3D transient heat conduction equation:

$$\rho(T)C_p(T)\frac{\partial T}{\partial t} = \nabla \cdot (k(T)\nabla T) + Q_v - Q_{loss}$$

where ρ is the material density, C_p is the specific heat capacity, k is the thermal conductivity, and Q_{loss} accounts for convective and radiative heat losses. For Ti-6Al-4V, these thermophysical properties (ρ, C_p, k) are highly temperature-dependent, particularly near the solidus and liquidus transition zones [8]. The volumetric heat source Q_v, representing the laser energy input, is modeled utilizing a volumetric Gaussian profile (illustrated in Fig. 2) incorporating material absorptivity (α):

$$Q_v(x, y, z) = \frac{2\alpha P}{\pi\omega^2 h} \exp\left(-2\frac{x^2 + y^2}{\omega^2}\right) \exp\left(-\frac{|z|}{h}\right)$$

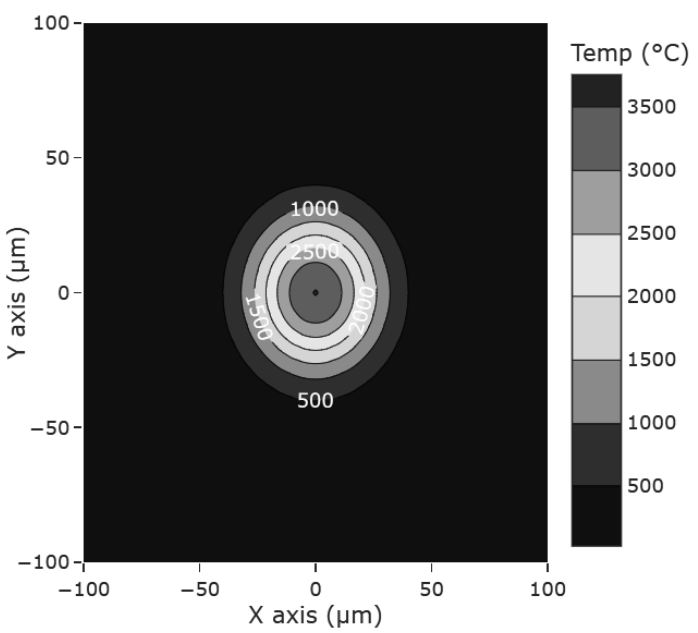

Figure 2. Simulated 2D temperature contour map illustrating the Gaussian volumetric heat source profile on the Ti-6Al-4V powder bed surface. The steep thermal gradient clearly identifies localized melt pool generation, where the peak temperature significantly exceeds the material's boiling point . $T_b = 3287\ °C$

2.3. C++ Monte Carlo Framework

The physical domain is discretized into a 2D/3D lattice grid system. Each discrete cell transitions between states: Void (0), Un-melted Powder (1), Liquid Melt (2), and Solidified Metal (3). State transitions are treated stochastically using a modified Metropolis-Hastings algorithm. The probability P_{trans} of a phase change (e.g., solid to liquid) depends on the reduction of local free energy ΔG and a localized thermal activation barrier:

$$P_{trans} = \begin{cases} 1, & \text{if } \Delta G < 0 \text{ and } T \geq T_m \\ \exp\left(-\frac{\Delta G}{k_B T_{eff}}\right), & \text{otherwise} \end{cases}$$

3. RESULTS AND DISCUSSION

3.1. Defect Prediction via Volumetric Energy Density (VED)

To systematically evaluate the parameter space, the Volumetric Energy Density (VED), defined as $E = P/(v \cdot h \cdot t)$ (where v is scanning speed, h is hatch spacing, and t is layer thickness), was utilized as the primary control variable. The MC algorithm successfully tracked transient thermal dynamics and defect morphologies (as summarized in Fig. 3).

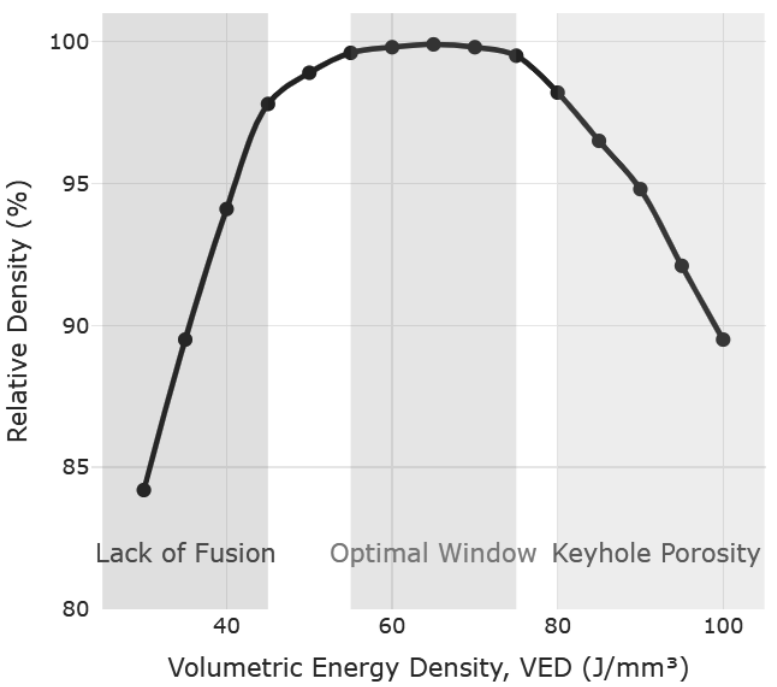

Figure. 3. Relationship between relative density and Volumetric Energy Density (VED) derived from Monte Carlo simulations. The plot delineates three distinct processing regimes: lack-of-fusion defects at low VED (< 45 J/mm³), an optimal densification window (55 - 75 J/mm³), and keyhole porosity formation at high VED (> 80 J/mm³).

Low VED Regime (< 45 J/mm³): The statistical model explicitly demonstrated "lack-of-fusion" voids. Due to insufficient power P or excessively high velocity v, the melt pool failed to

penetrate the previous layer, leaving un-melted powder pockets with highly irregular morphologies.

- High VED Regime (> 80 J/mm³): The computational model predicted intense localized vaporization. The excessive recoil pressure led to the formation of deep, narrow melt pools. As the laser source advanced, fluid instabilities caused the capillary liquid walls to collapse, trapping metal vapor and inert gas, resulting in characteristic spherical keyhole pores.
- Optimal Processing Window: A clear statistical correlation established that a VED between 55 J/mm³ and 75 J/mm³ yields maximum densification (> 99.5%) with stable and continuous melt pool dynamics.

3.2. Impact of Powder Size Variability

A distinct advantage of the stochastic MC model is its ability to assess powder quality. Simulations revealed that a wider standard deviation (σ) in the powder size distribution increased the local packing heterogeneity. This heterogeneity occasionally caused localized energy shielding, leading to micro-porosity even within the optimal VED window, thereby proving that powder flowability and size uniformity are critical boundary conditions for defect-free LPBF.

3.3. Cooling Rate and Microstructural Implications

Beyond defect mapping, the Monte Carlo framework intrinsically captures the temporal thermal history of the material. The simulations extracted extreme local cooling rates ranging from 10^5 to 5×10^6 K/s at the solid-liquid interface during solidification (as plotted in Fig. 4).

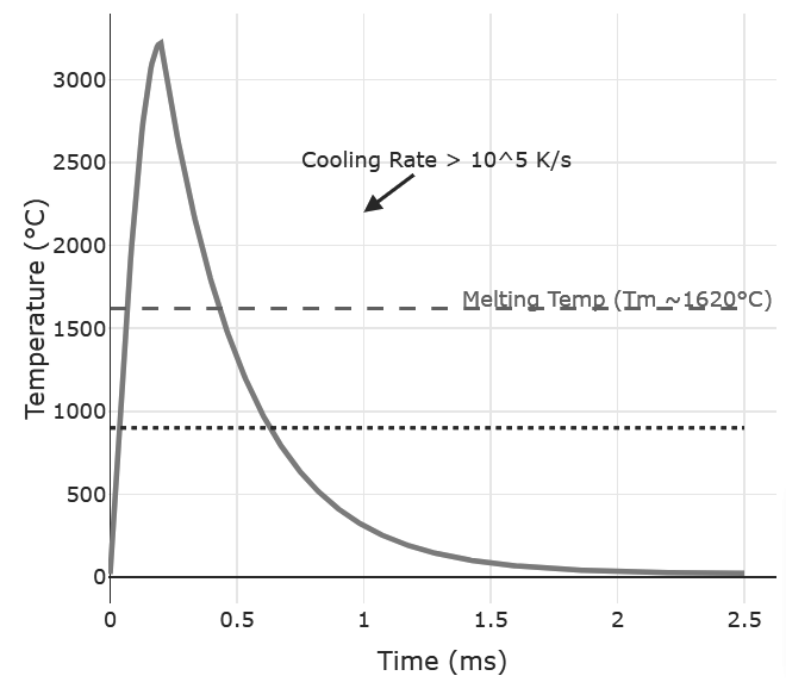

Figure 4. Simulated transient thermal history at a localized node within the melt pool. The steep temperature decline immediately following laser irradiation reveals an extreme cooling rate exceeding 10^5 *K/s. This significantly surpasses the critical cooling rate threshold required to trigger the diffusionless martensitic (*$\beta \rightarrow \alpha'$*) phase transformation in the Ti-6Al-4V alloy.*

For Ti-6Al-4V, it is well-documented that cooling rates exceeding 410 K/s surpass the critical threshold required to trigger a diffusionless martensitic transformation ($\beta \rightarrow \alpha'$) By spatially mapping these cooling rates across the defined processing window, the model provides vital auxiliary insights into the expected phase composition. The capability to concurrently predict macroscopic defect formation and infer microscopic phase transformations highlights the comprehensiveness of this predictive framework.

Table 1. Thermodynamic and statistical parameters for Ti-6Al-4V simulation.

Parameter	Value / Range	Unit
Powder Distribution	Log-Normal ($\mu = 30, \sigma = 10$)	μm
Lattice Grid Resolution	2.0	μm
Laser Power (P)	100 - 400	W
Scanning Speed (v)	500 - 1500	mm/s
Material Density (ρ)	4420 (Solid) / 3920 (Liquid)	kg/m³
Melting Temperature (T_m)	1604 - 1650	°C
Boiling Temperature (T_b)	3287	°C
Laser Absorptivity (α)	0.35 - 0.42	-
Programming Environment	C++ (Metropolis algorithm)	-

4. CONCLUSIONS

A novel, computationally efficient framework coupling transient thermodynamics with Monte Carlo probability statistics was successfully developed for advanced powder metallurgy. By mapping 3D thermal conduction equations onto a stochastically generated log-normal powder bed, the C++ based model accurately captures phase transition states, final porosity morphologies, and cooling rate histories in Ti-6Al-4V LPBF processes.

The model successfully identifies the critical thresholds for lack-of-fusion and keyhole defects, quantitatively establishing an optimal VED window of 55 - 75 J/mm³. Furthermore, the predicted extreme cooling rates align with the experimentally observed martensitic (α') microstructure in LPBF titanium parts. This methodology significantly narrows down the required experimental validation space, proving the immense potential of meso-scale computational materials science in accelerating the development, optimization, and qualification of advanced manufacturing protocols.

BIBLIOGRAPHY

[1] T. DebRoy, H.L. Wei, J.S. Zuback, et al., "Additive manufacturing of metallic components – Process, structure and properties," *Progress in Materials Science*, vol. 92, pp. 112-224, 2018.
[2] W.E. King, A.T. Anderson, R.M. Ferencz, et al., "Laser powder bed fusion additive manufacturing of metals; physics, computational, and materials challenges," *Applied Physics Reviews*, vol. 2, no. 4, 041304, 2015.
[3] Körner, "Additive manufacturing of metallic components by selective electron beam melting — a review," *International Materials Reviews*, vol. 61, no. 5, pp. 361-377, 2016.
[4] L. Thijs, F. Verhaeghe, T. Craeghs, J. Van Humbeeck, and J.P. Kruth, "A study of the microstructural evolution during selective laser melting of Ti–6Al–4V," *Acta Materialia*, vol. 58, no. 9, pp. 3303-3312, 2010.
[5] W.J. Sames, F.A. List, S. Pannala, R.R. Dehoff, and S.S. Babu, "The metallurgy and processing science of metal additive manufacturing," *International Materials Reviews*, vol. 61, no. 5, pp. 315-360, 2016.
[6] T. Mukherjee, H.L. Wei, A. De, and T. DebRoy, "Heat and fluid flow in additive manufacturing—Part I: Modeling of powder bed fusion," *Computational Materials Science*, vol. 150, pp. 304-313, 2018.
[7] A. Rodgers, G. Madison, and V. Tikare, "Simulation of metal powder bed fusion using a continuous Cellular Automata-Monte Carlo method," *Computational Materials Science*, vol. 135, pp. 78-89, 2017.
[8] G. Boivineau, C. Cagran, D. Doytie, et al., "Thermophysical properties of solid and liquid Ti-6Al-4V alloy," *International Journal of Thermophysics*, vol. 27, no. 2, pp. 507-529, 2006.
[9] S.A. Khairallah, A.T. Anderson, A. Rubenchik, and W.E. King, "Laser powder-bed fusion additive manufacturing: Physics of complex melt flow and defect formation mechanisms," *Acta Materialia*, vol. 108, pp. 36-45, 2016.

TalentDetector

7th-9th June 2026
Gliwice-Brenna, Poland

DEPARTMENT OF ENGINEERING MATERIALS AND BIOMATERIALS
FACULTY OF MECHANICAL ENGINEERING
SILESIAN UNIVERSITY OF TECHNOLOGY

INTERNATIONAL STUDENTS SCIENTIFIC CONFERENCE

The design of a complex manipulator manufactured using 3D printing technology

Karol Żyrek[a], Maja Rudnicka[a] , Kamil Moszumański[a], Michał Lasak[a]

[a] Silesian University of Technology, Faculty of Automatic Control, Electronics and Computer Science, SKN SpaceCoffee
email: kz322588@student.polsl.pl, mr322241@student.polsl.pl, km322442@student.polsl.pl, Michal.Lasak@student.polsl.pl

Abstract: The exponential growth of AM (Additive Manufacturing) technologies provides new paradigms for designing highly customized and optimized robots. This paper describes the design, the structural analysis, and the fabrication process of a complicated multi-DoF manipulator manufactured via 3D printing technique. The main goal of the study is to provide a solution to the problem of the trade-off between the rigidity and the lightness of manipulator links since these properties affect the robot dynamic performance significantly. To achieve the beforementioned objective, advanced approaches of CAD, including topology optimization were used for synthesis of the link structure that maximizes load carrying while minimizing the mass of the link. Moreover, finite element analysis was performed to prove the stability of the structure, calculate stress distribution, and predict deformation behavior when subjected to static loads. In addition, the choice of adequate 3D printing parameters and proper material properties that affect overall geometry and precision of the system is described. The developed manipulator proves that 3D printing makes production faster, cheaper, and allows designing structures that can be printed in the single technological cycle but cannot be produced through traditional techniques at all.

Keywords: robotic manipulator, structural optimization, kinematics, additive manufacturing

1. INTRODUCTION

A critical component of contemporary space exploration is the utilization of mobile rovers, which employ state-of-the-art technologies to traverse inaccessible terrain on Mars or the Moon to collect valuable samples for analysis. The primary means of interaction between these platforms and their environment is the arm of the manipulator. In order to function in an optimal manner, this arm must meet the stringent parameters established during the design process.

In the context of space missions, the financial implications of launching payloads are exorbitant, necessitating the utilisation of structures that are as lightweight as possible. Furthermore, the increased mass of a heavier arm necessitates the use of more powerful motors,

which in turn results in the more rapid depletion of the rover's limited energy resources. To execute precise and complex tasks, the manipulator must exhibit high maneuverability, ensuring optimal positioning and reach.

The problem addressed in this work is based on the trade-off between the manipulator's stiffness and mass, which reduces energy consumption – a critical factor given the limited power supply of mobile platforms [1, 2].

In order to address this issue, the focus has been placed on production methods that enable tackling the design assumptions most effectively. Additive manufacturing, or AM, is a process that allows for the creation of complex parts with a high degree of customisation. This creative freedom is a significant benefit of AM, as it enables the production of parts that would not be feasible through other methods. Additionally, AM reduces material waste and accelerates the prototyping process, making it a more environmentally friendly and efficient production technique [3].

This article delineates the evolution of the MPER (Multi-Purpose Exploration Rover) robotic manipulator as a study to obtain the abovementioned functionalities. The manipulator has four degrees of freedom (4DOF) achieved through five joints. The system is hybrid-controlled, utilising three stepper motors and two servos for precise motion control. The design employs optimization topologies to ensure that the entire structure distributes its weight in the most optimal manner and is resistant to deformation during operation. This optimisation process has been demonstrated to result in a reduction of mass by up to 40% [5].

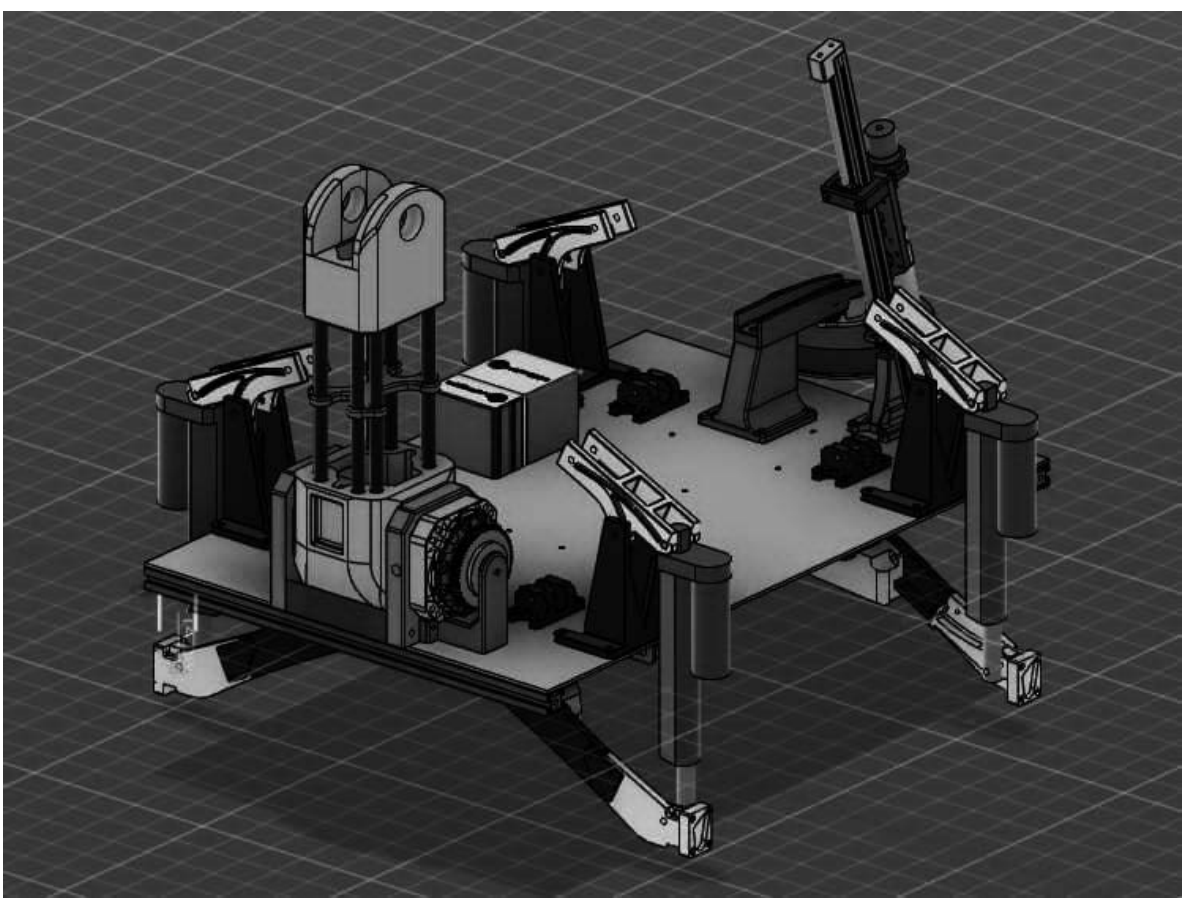

Fig. 1. Rover design with the Manipulator (in yellow) attached

2. DESIGN AND KINEMATICS

The mathematical description of the geometry of multi-axis manipulators is the absolute foundation of their design. As indicated by recent research on lightweight robotic arms intended for planetary rovers, the standard in this field is the use of the Denavit-Hartenberg (D-H) convention and parameters [4]. This methodology enables precise modeling of the system's kinematics by describing each of the robot's joints using just four parameters: rotation angle, link length, twist, and offset. Using software such as MATLAB, engineers can simulate the system's kinematics and predict the exact position and spatial orientation of the end-effector (gripper). The solution is a non-destructive testing (NDT) method, allowing for virtual verification of the working-kinematic range even before proceeding to the physical fabrication of parts using 3D printing technology [1].

A key issue during the modeling stage is the proper selection of the lengths of individual arms. This configuration affects the working area and also drastically determines the positioning precision of the entire manipulator. Even minimal angular deviations or joint play are amplified in proportion to the length of the segments used, and long, lightweight arms are most susceptible to deflection under the influence of gravitational forces and dynamic loads [2].

To best implement the target specifications an optimized 4-degree-of-freedom (4DOF) structure with five joints was implemented, instead of a heavier 6DOF design. Reducing the number of axes of movement allows for a significant shortening of the kinematic chain and the removal of additional drives at the end of the arm, which directly result in lower inertia and a reduction in unwanted deflections. Kinematic modeling is also inextricably linked to the calculation of maximum torques occurring in the joints under load.

When adapting these mechanical requirements to the constraints of 3D printing, planetary and cycloidal gearboxes emerge as ideal architectures. They offer a superior torque-to-weight ratio, compact structural dimensions, and high torsional stiffness while remaining highly reproducible using polymer deposition [6]. By utilizing multi-stage configurations, stepped-planetary gears can achieve massive reduction ratios in a lightweight footprint without requiring the flexible, fatigue-prone components typical of harmonic drives, which are significantly harder to recreate using 3D printing methods.

Based on these mechanical advantages, a fully 3D-printed drive system was implemented in the designed robotic arm. A hybrid control architecture driven by three stepper motors and two servos manages precise spatial positioning of the payload. The first stage of the arm utilizes a NEMA 17 motor paired with a proprietary, multi-stage stepped-planetary gearbox printed entirely from PETG, yielding a total gear ratio of 1:125. The second stage utilizes a fully polymer cycloidal gearbox with a gear ratio of 1:40. The integration of advanced kinematic modeling with the mechanics of these high-ratio polymer gearboxes enables the generation of sufficient torque to stabilize a 5-kilogram test sample at full extension, completely eliminating the need for heavy, traditional metallic counterweights.

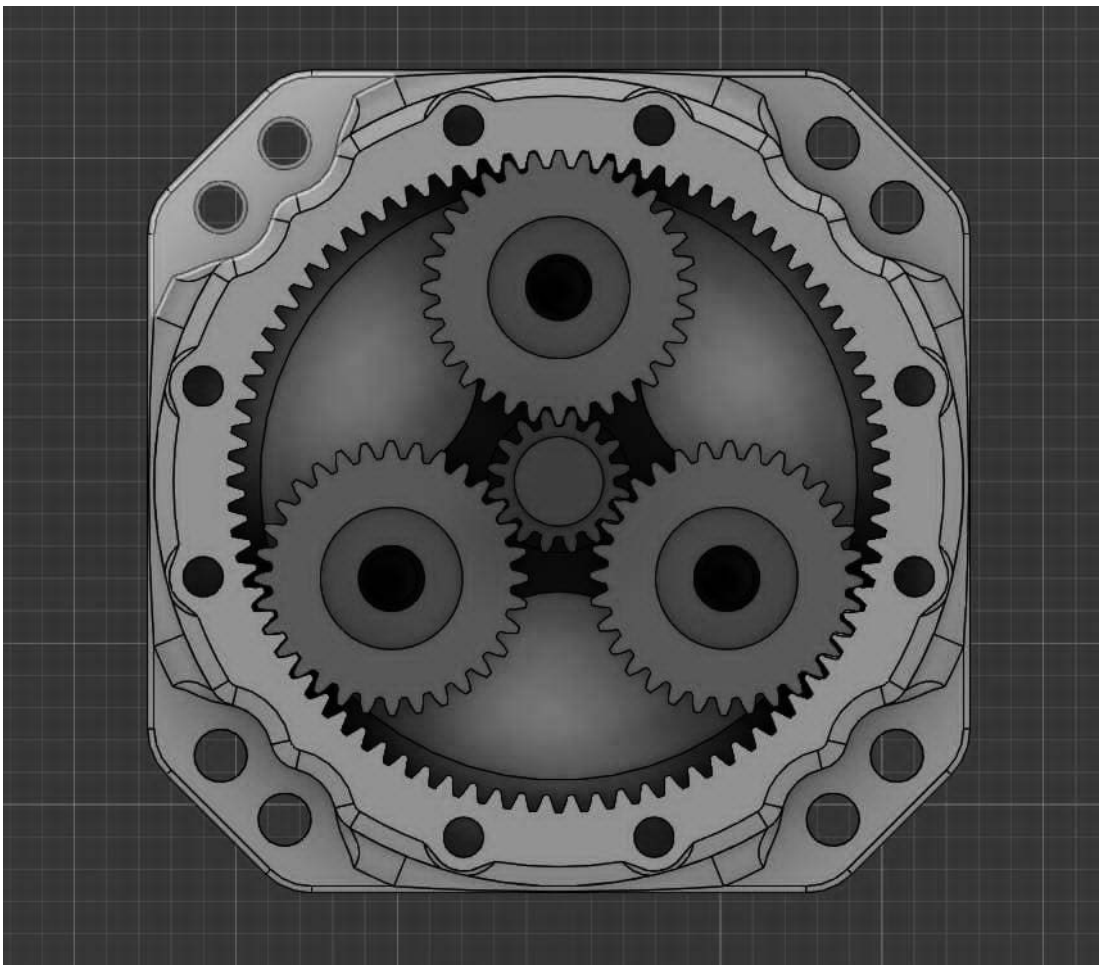

Fig. 2. A stepped-planetary gearbox for the Manipulator

3. TOPOLOGY OPTIMIZATION AND STRUCTURAL ANALYSIS

3.1. Topology optimization

Topology optimization is a computational technique to determine the most efficient material distribution within a given design space, that is subject to load conditions, boundary constraints, and performance targets. Algorithmic evaluation of the distribution of force and load, focused on practical situations like when lifting a weight, creates design profiles tailored to specific criteria such as minimum mass, maximum stiffness, or balanced trade-offs. It can automatically remove material from areas that are least integral to structural performance, leaving it only where the greatest stresses are applied [8, 9]. The goal is to minimise deformation energy — that is, to prevent the arm from bending under the weight of the load as much as possible [9].

While traditional methods all have to assume a complete geometry at the start, topology optimization begins with the full volume available for design and strategically removes material, as described above. The end result of the algorithm's work is often a highly organic, lattice-like structure that isn't conventional when it comes to geometrical intuition, but maximizes performance under given conditions. This is also the main motivation for utilizing

3D printing, since attempting to produce such parts using traditional subtractive techniques (e.g. CNC milling) would be impossible.

In one case study, using optimisation software to redesign an industrial robot arm reduced material usage by half, without losing its ability to operate safely [7], which proves highly satisfying results. Other analyses indicate that proper topology optimization can typically reduce a component's mass by 25–40%, while also reducing stresses at critical points of the robot by up to 41%, which significantly improves the reliability of the whole structure [2,4].
Even being the major facilitation in the design process, the optimization algorithms must be subject to predefined manufacturing constraints so that they do not e.g. generate walls thinner than the physical diameter of the laser or nozzle in the printer allows or create completely enclosed hollow spaces inside the model that could not be manufactured properly [9].

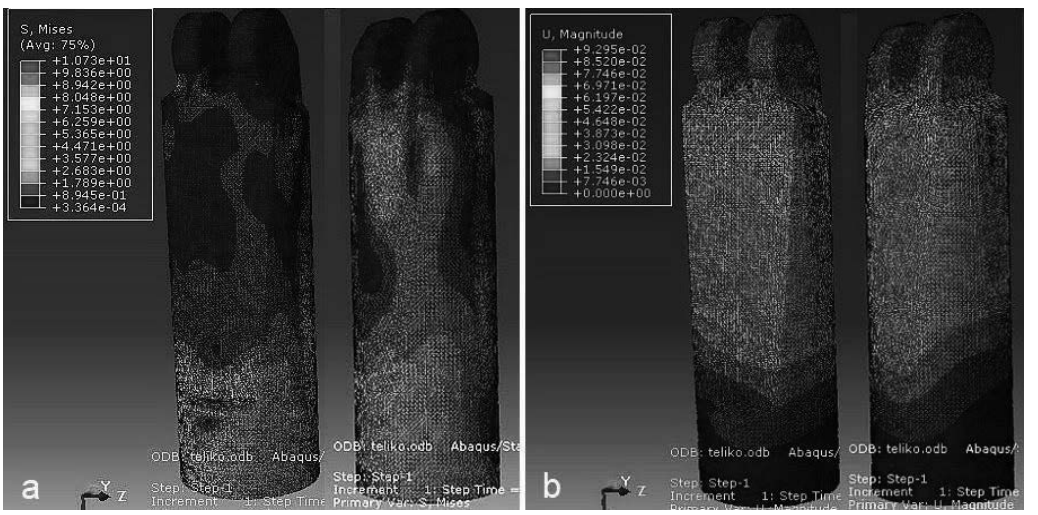

Fig. 3. (a) Partitions P1-P2 (b) Load application points (RP1: wrist and tool center of gravity, RP4: forearm center of gravity, RP2: elbow joint torque center). The loads on the robotic forearm are estimated for a random position of the robot arm movement. For the sake of brevity, the center of gravity between the tool (a 3D printer head in this case), the end effector and the wrist link were calculated and the corresponding reference point RP1, which represents the center of gravity, is defined as shown in Fig. 3. (b)

3.2. Finite element analysis

The process of topology optimization involves finite element analysis (FEA) to simulate how the structure responds to applied forces [10]. Stress, strain, and deformation are evaluated to identify underutilized regions through several iterative simulations. This analysis is automated by the design software used, with the main goal of verifying the tension distribution in the situation of maximum reach and the full load of 5 kg. The focus was put on deformation chances and system stability—predicting the deflection of the polymer components under load and verifying that these deformations do not negatively impact the positioning accuracy of the end-effector. Modal analysis was also conducted, investigating the vibrational characteristics when the manipulator is in movement. The FEA method is a useful tool for testing for worst-case scenarios [1] and identifying the weak points of the design [11].

4. MANUFACTURING USING 3D PRINTING

4.1. Printing material selection

The materials of choice for the manipulator are PETG and PETG-CF, with the latter being a composite strengthened by carbon fiber. Both materials exhibit high durability and tensile strength. Due to their ductile nature, they undergo plastic deformation under peak loads rather than exhibiting a sharp, brittle fracture point. PETG-CF in particular is of great structural rigidity, in particular, offering exceptional resistance to bending under heavy weight, which makes it the ideal fit for elements crucial for the construction, but most prone to fracturing. Use of this type of filament, however, poses a challenge, since it requires specialized modifications to the standard printing technology due to its exceptional stiffness.

4.2. Prototyping

3D printing enables rapid and efficient prototyping through an additive, zero-tooling process that bypasses the complex setups of traditional subtractive manufacturing.

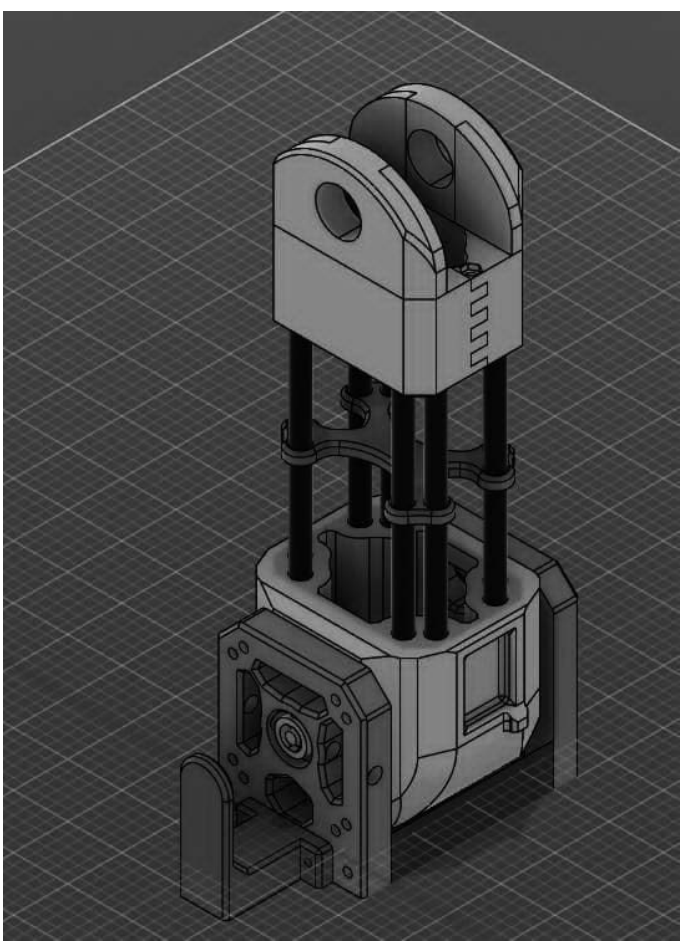

Fig. 4. First stage of the finished Manipulator design

This allows for same-day design iterations and consolidates multi-part assemblies into single, yet complex geometries. In the context of the robotic manipulator, this technology can be used

to fabricate monolithic gearbox housings with intricate internal teeth in a single production cycle. It can also be used to optimize structural weight through lightweight internal infill patterns and to embed seamless internal cable routing channels directly within the arm components. Additionally, 3D printing allows for the strategic tailoring of materials, which can be decisive in that the manipulator achieves a satisfactory force-to-weight ratio and maintains positional accuracy under a 5-kilogram load without the need for traditional metallic components.

5. CONCLUSIONS

3D printing technology and its methodology are decisively the fittest tools for creating an effective, lightweight and agile manipulator design. The resulting structure validates this type of manufacturing not only as a rapid prototyping tool, but as a primary production method capable of achieving high torque output and precise spatial positioning, along with well-balanced trade-offs that are algorithmically designed as optimal. The final system can successfully stabilize a 5-kilogram test sample at full reach. This effectively demonstrates that advanced kinematic modeling and optimized additive manufacturing can entirely replace heavy, traditional metal components in load-bearing robotic links, taking into account the financial advantage 3D printing materials and equipment hold over metallic products and their manufacturing. It is significant enough [12] that the solution proves to be optimal for the types of applications and assumptions described in this paper.

BIBLIOGRAPHY

1. Simpson, Jack, and Bernd Vorstius. "Building a lightweight robotic arm for a mini-Mars rover with the use of 3D printing."
2. Piechota, K., Odrobiński, J., Zakrzewski, A., & Zwierzchowski, M. (2025). Precision in DIY lightweight manipulator. *Advances in Science and Technology. Research Journal*, *19*.9.
3. Wang, Ting, et al. "Robot-assisted additive manufacturing for aerospace applications: recent trends and its future possibilities." *International Journal of Computer Integrated Manufacturing* 39.2 (2026): 204-244.
4. P. I. Corke, "A Simple and Systematic Approach to Assigning Denavit–Hartenberg Parameters," in IEEE Transactions on Robotics, vol. 23, no. 3, pp. 590-594, June 2007, doi: 10.1109/TRO.2007.896765.
5. Alshihabi, Mamoun, Merdan Ozkahraman, and Mevlüt Yunus Kayacan. "Enhancing the reliability of a robotic arm through lightweighting and vibration control with modal analysis and topology optimization." *Mechanics Based Design of Structures and Machines* 53.3 (2025): 1950-1974.
6. Rudnicka, Maja & Lasak, Michał & Puchała, Igor & Bartosz, Piotr & Bereta, Dominik & Myszor, Dariusz. (2024). Sample collection and containment system for a compact planetary exploration rover. 10.5281/zenodo.18136021.
7. Fry, Nicholas R., Robert C. Richardson, and Jordan H. Boyle. "Robotic additive manufacturing system for dynamic build orientations." Rapid prototyping journal 26.4 (2020): 659-667.

8. Kumaran, M., and V. Senthilkumar. "Generative design and topology optimization of analysis and repair work of industrial robot arm manufactured using additive manufacturing 2technology." *IOP Conference Series: Materials Science and Engineering*. Vol. 1012. No. 1. IOP Publishing, 2021.
9. Tsirogiannis, Evangelos, and George-Christopher Vosniakos. "Redesign and topology optimization of an industrial robot link for additive manufacturing." Facta Universitatis, Series: Mechanical Engineering 17.3 (2019): 415-424.
10. Liu, Zhao, et al. "Comparison of finite element and experimental modal analysis of multi-joint flexible robotic arm." *2017 International Conference on Mechanical, System and Control Engineering (ICMSC)*. IEEE, 2017.
11. Santosh, Lingala Purandhara Sai, et al. "Design and analysis of a robotic arm under different loading conditions using FEA simulation." Materials Today: Proceedings 50 (2022): 759-765.
12. Walia, K.; Khan, A.; Breedon, P. Polymer-Based Additive Manufacturing: Process Optimisation for Low-Cost Industrial Robotics Manufacture. *Polymers* 2021, *13*, 2809. https://doi.org/10.3390/polym13162809

WYDAWNICTWO POLITECHNIKI ŚLĄSKIEJ
ul. Akademicka 5, 44-100 Gliwice
tel. (32) 237-13-81
wydawnictwo@polsl.pl
www.wydawnictwopolitechniki.pl

UIW 48600

Sprzedaż i Marketing
tel. (32) 237-18-48
wydawnictwo_mark@polsl.pl

Nakł. 120 + 22	Ark. wyd. 43	Ark. druk. 72,125

Monografia 1106